

Advances in Delivery Science and Technology

Anette Müllertz
Yvonne Perrie
Thomas Rades *Editors*

Analytical Techniques in the Pharmaceutical Sciences



 Springer

Advances in Delivery Science and Technology

Series editor

Michael J. Rathbone

More information about this series at <http://www.springer.com/series/8875>

Anette Müllertz • Yvonne Perrie • Thomas Rades
Editors

Analytical Techniques in the Pharmaceutical Sciences

 Springer

Editors

Anette Müllertz
Bioneer: FARMA
Department of Pharmacy
University of Copenhagen
Copenhagen Ø, Denmark

Yvonne Perrie
Strathclyde Institute of Pharmacy
and Biomedical Sciences
Glasgow, Scotland

Thomas Rades
Department of Pharmacy
University of Copenhagen
Copenhagen Ø, Denmark

ISSN 2192-6204 ISSN 2192-6212 (electronic)
Advances in Delivery Science and Technology
ISBN 978-1-4939-4027-1 ISBN 978-1-4939-4029-5 (eBook)
DOI 10.1007/978-1-4939-4029-5

Library of Congress Control Number: 2016943084

© Controlled Release Society 2016

This work is subject to copyright. All rights are reserved by the Publisher, whether the whole or part of the material is concerned, specifically the rights of translation, reprinting, reuse of illustrations, recitation, broadcasting, reproduction on microfilms or in any other physical way, and transmission or information storage and retrieval, electronic adaptation, computer software, or by similar or dissimilar methodology now known or hereafter developed.

The use of general descriptive names, registered names, trademarks, service marks, etc. in this publication does not imply, even in the absence of a specific statement, that such names are exempt from the relevant protective laws and regulations and therefore free for general use.

The publisher, the authors and the editors are safe to assume that the advice and information in this book are believed to be true and accurate at the date of publication. Neither the publisher nor the authors or the editors give a warranty, express or implied, with respect to the material contained herein or for any errors or omissions that may have been made.

Printed on acid-free paper

This Springer imprint is published by Springer Nature
The registered company is Springer Science+Business Media LLC New York

Preface

Progress in all areas of the pharmaceutical sciences, from drug discovery and biopharmaceutics to drug delivery and pharmaceutical technology, has long been strongly connected to the development and application of analytical techniques. Without the development of HPLC and its application to plasma samples, there would be no plasma concentration time curves and no development of the concept of bioavailability. Without solid-state analytical techniques, like X-ray powder diffraction and thermal analysis, the importance of the solid-state form of a drug on its pharmaceutical performance could not have been studied, let alone understood, to name but two examples. This list could continue endlessly. But analytical techniques have also evolved as pharmaceutical questions have been more clearly stated. An example for this is the continuous development of dissolution testing, initially used for the quality control of dosage form, to now also having physiologically relevant dissolution testing aiming to understand the performance of a dosage form *in vivo*.

This book brings together a large range of analytical techniques of specific relevance to the pharmaceutical sciences. The techniques are introduced to understand their theoretical background, but also to highlight their pharmaceutical applications. The book therefore, we hope, is equally interesting and enlightening for skilled experts in the field of pharmaceutical sciences, as for young and beginning researchers, including undergraduate and postgraduate students.

In our attempt to try to bring order into the plethora of analytical techniques available today for the pharmaceutical scientist, we have divided the techniques in this book according to their principle of measurement. The reader will find chapters on spectroscopic techniques, diffractometric techniques, thermal techniques, separation techniques, and many more. Whilst many methods probing the molecular, particulate and bulk level are included, we are not claiming to have covered all techniques available. We have aimed to collect the major techniques of particular value to the pharmaceutical scientist today, techniques that formed the basis and introduced other techniques. We further elaborate by explaining how their use in drug and dosage form research should be facilitated.

The pharmaceutical sciences and the analytical sciences will continue to be intertwined in a fruitful and beneficial co-evolution ultimately to the benefit of patients and society. We hope that through you, the reader, this book can make a small contribution to this.

Copenhagen, Denmark
Glasgow, UK
Copenhagen, Denmark

Anette Müllertz
Yvonne Perrie
Thomas Rades

Contents

Part I Spectroscopic and Spectrometric Techniques

- 1 UV/Vis Spectrophotometry and UV Imaging** 3
Jesper Østergaard
- 2 Fluorescence Spectroscopy: Basic Foundations and Methods** 29
Luis A. Bagatolli
- 3 Mid and Near Infrared Spectroscopy** 61
Gabriele Reich
- 4 Raman Spectroscopy** 139
Keith C. Gordon and Sara J. Fraser-Miller
- 5 Pharmaceutical Terahertz Spectroscopy and Imaging** 171
J. Axel Zeitler
- 6 Circular Dichroism Spectroscopy for Structural
Characterization of Proteins** 223
Søren Vrønning Hoffmann, Mathias Fano, and Marco van de Weert
- 7 Applications of Mass Spectrometry in Drug
Development Science** 253
Ulrike Leurs, Ulrik H. Mistarz, and Kasper D. Rand

Part II Diffractometric Techniques

- 8 An Overview of Powder X-ray Diffraction
and Its Relevance to Pharmaceutical Crystal Structures** 293
Kenneth Shankland
- 9 Single-Crystal X-ray Diffraction** 315
Andrew D. Bond

10 Applications of Small Angle X-ray Scattering in Pharmaceutical Science	339
Ben J. Boyd and Thomas Rades	
Part III Thermal Techniques	
11 Thermal Analysis of Pharmaceuticals	363
Sheng Qi	
12 Isothermal Microcalorimetry	389
S. Gaisford	
Part IV Separation Techniques	
13 HPLC/UHPLC	413
Steen Honore Hansen	
14 Capillary-Based Techniques for Physical-Chemical Characterization of Drug Substances and Drug Delivery Systems	439
Jesper Østergaard, Susan W. Larsen, and Henrik Jensen	
15 Asymmetrical Flow Field Flow Fractionation: A Useful Tool for the Separation of Protein Pharmaceuticals and Particulate Systems	467
Julia Engert, Roman Mathaes, and Gerhard Winter	
Part V Imaging Techniques	
16 Light and Electron Microscopy	491
Heike Bunjes and Judith Kuntsche	
17 Vibrational Spectroscopic Imaging	523
Sara J. Fraser-Miller, Jukka Saarinen, and Clare J. Strachan	
18 Magnetic Resonance Imaging and Its Applications to Solid Pharmaceutical Dosage Forms	591
M.D. Mantle	
19 Mass Spectrometry Imaging of Pharmaceuticals: From Tablets to Tissues	629
Ivan M. Kempson and Clive A. Prestidge	
20 Applications of AFM in Pharmaceutical Sciences	649
Dimitrios A. Lamprou and James R. Smith	
Part VI Techniques to Characterize Particles	
21 Particle Size Analysis of Micro and Nanoparticles	677
Elisabeth Kastner and Yvonne Perrie	

22 Particle Size Measurements in Aerosols	701
Regina Scherließ	
Part VII Rheological Techniques	
23 Rheology in Pharmaceutical Sciences	719
Johanna Aho, Søren Hvidt, and Stefania Baldursdottir	
Part VIII Release and Uptake Testing Techniques	
24 Evaluating Oral Drug Delivery Systems: Dissolution Models	753
Ragna Berthelsen, Anette Müllertz, and Thomas Rades	
25 Evaluating Oral Drug Delivery Systems: Digestion Models	773
Ragna Berthelsen, Philip Sassene, Thomas Rades, and Anette Müllertz	
26 Application of Cell Culture and Tissue Models for Assessing Drug Transport	791
Carsten Uhd Nielsen and Birger Brodin	
Index	823

Contributors

Johanna Aho Department of Pharmacy, University of Copenhagen, Copenhagen, Denmark

Luis A. Bagatoli MEMPHYS—Center for Biomembrane Physics, University of Southern Denmark, Odense, Denmark

Stefania Baldursdottir Department of Pharmacy, University of Copenhagen, Copenhagen, Denmark

Ragna Berthelsen Department of Pharmacy, University of Copenhagen, Copenhagen, Denmark

Andrew D. Bond Department of Chemistry, University of Cambridge, Cambridge, UK

Ben J. Boyd Drug Delivery, Disposition and Dynamics and ARC Centre of Excellence in Convergent Bio-Nano Science and Technology, Monash Institute of Pharmaceutical Sciences, Monash University Parkville, Parkville, VIC, Australia

Birger Brodin Department of Pharmacy, University of Copenhagen, Copenhagen, Denmark

Heike Bunjes Technische Universität Braunschweig, Institute of Pharmaceutical Technology, Braunschweig, Germany

Julia Engert Department of Pharmacy, Pharmaceutical Technology and Biopharmaceutics, Ludwig-Maximilians-University Munich, Munich, Germany

Mathias Fano Bioneer:FARMA, Copenhagen, Denmark

Sara J. Fraser-Miller Department of Chemistry, Dodd-Walls Centre, University of Otago, Dunedin, New Zealand

Formulation and Industrial Pharmacy Unit, Division of Pharmaceutical Chemistry and Technology, Faculty of Pharmacy, University of Helsinki, Helsinki, Finland

Simon Gaisford UCL School of Pharmacy, Dodd-Walls Centre, University College London, London, UK

Keith C. Gordon Department of Chemistry, University of Otago, Dunedin, New Zealand

Steen Honoré Hansen Department of Pharmacy, Faculty of Health and Medical Sciences, University of Copenhagen, Copenhagen, Denmark

Søren Vrønning Hoffmann ISA, Department of Physics and Astronomy, Aarhus University, Aarhus, Denmark

Søren Hvidt The Department of Chemistry – Institute of Science and Environment, Roskilde University, Roskilde, Denmark

Henrik Jensen Department of Pharmacy, Faculty of Health and Medical Sciences, University of Copenhagen, Copenhagen, Denmark

Elisabeth Kastner Strathclyde Institute of Pharmacy and Biomedical Sciences, University of Strathclyde, Glasgow, Scotland

Ivan M. Kempson Future Industries Institute, University of South Australia, Mawson Lakes, SA, Australia

Judith Kuntsche Department of Physics, Chemistry and Pharmacy, University of Southern Denmark, Odense, Denmark

Dimitrios A. Lamprou Strathclyde Institute of Pharmacy and Biomedical Sciences (SIPBS), University of Strathclyde, Glasgow, UK

Susan W. Larsen Department of Pharmacy, University of Copenhagen, Copenhagen, Denmark

Ulrike Leurs Department of Pharmacy, Faculty of Health and Medical Sciences, University of Copenhagen, Copenhagen, Denmark

M.D. Mantle Department of Chemical Engineering and Biotechnology, University of Cambridge, Cambridge, UK

Roman Mathaes Department of Pharmacy, Pharmaceutical Technology and Biopharmaceutics, Ludwig-Maximilians-University Munich, Munich, Germany

Ulrik H. Mistarz Department of Pharmacy, Faculty of Health and Medical Sciences, University of Copenhagen, Copenhagen, Denmark

Anette Müllertz Bioneer:FARMA, Department of Pharmacy, University of Copenhagen, Copenhagen, Denmark

Carsten Uhd Nielsen Department of Physics, Chemistry and Pharmacy, University of Southern Denmark, Odense, Denmark

Jesper Østergaard Department of Pharmacy, Faculty of Health and Medical Sciences, University of Copenhagen, Copenhagen, Denmark

Yvonne Perrie Strathclyde Institute of Pharmacy and Biomedical Sciences, Glasgow, Scotland

Clive A. Prestidge School of Pharmacy and Medical Sciences, University of South Australia, Adelaide, Australia

Sheng Qi School of Pharmacy, University of East Anglia, Norwich, UK

Thomas Rades Department of Pharmacy, University of Copenhagen, Copenhagen, Denmark

Kasper D. Rand Department of Pharmacy, Faculty of Health and Medical Sciences, University of Copenhagen, Copenhagen, Denmark

Gabriele Reich Department of Pharmaceutical Technology and Biopharmaceutics, Institute of Pharmacy and Molecular Biotechnology, University of Heidelberg, Heidelberg, Germany

Jukka Saarinen Formulation and Industrial Pharmacy Unit, Division of Pharmaceutical Chemistry and Technology, Faculty of Pharmacy, University of Helsinki, Helsinki, Finland

Philip Sassene Department of Pharmacy, University of Copenhagen, Copenhagen, Denmark

Regina Scherließ Department of Pharmaceutics and Biopharmaceutics, Kiel University, Kiel, Germany

Kenneth Shankland School of Pharmacy, University of Reading, Reading, UK

James R. Smith School of Pharmacy and Biomedical Sciences, University of Portsmouth, Portsmouth, UK

Clare J. Strachan Formulation and Industrial Pharmacy Unit, Division of Pharmaceutical Chemistry and Technology, University of Helsinki, Helsinki, Finland

Marco van de Weert University of Copenhagen, Copenhagen, Denmark

Gerhard Winter Department of Pharmacy, Pharmaceutical Technology and Biopharmaceutics, Ludwig-Maximilians-University Munich, Munich, Germany

J. Axel Zeitler Department of Chemical Engineering and Biotechnology, University of Cambridge, Cambridge, UK

Editor's Biography

Anette Müllertz is professor at the Department of Pharmacy, University of Copenhagen, Denmark. She is head of Bioneer:FARMA, funded by the Danish Ministry of Science and Technology to establish research-based scientific services within the area of Drug Development. After receiving her Ph.D. degree in lipid nutrition at the Technical University of Denmark, she worked for Novo Nordisk A/S on the development of, e.g. structured lipids, digestive lipases, and digestion models. At the University of Copenhagen, she is head of the Rational Oral Drug Delivery Research Group, which focuses on developing predictive biopharmaceutical tools for oral drug development and lipid-based formulations. She has contributed to over 130 publications in international peer-reviewed journals and 10 book chapters. She is also a winner of the AAPS Lipid-Based Drug Delivery Award. She is a driving force in the EU sponsored Innovative Medicines Initiative Consortium Oral Biopharmaceutics Tools (OrBiTo) and is in the steering committee of two AAPS Focus Groups (FGs), The Lipid-based Drug Delivery FG and the QbD and Product Performance FG. She is in the advisory board for the *Journal of Pharmaceutical Sciences* and editor for the *Journal of Drug Delivery Science and Technology*.

Yvonne Perrie is Professor of Drug Delivery within the Strathclyde Institute of Pharmacy and Biomedical Sciences at the University of Strathclyde, Scotland. She graduated with First-Class Honours in Pharmacy from Strathclyde University and earned a Ph.D. from the University of London under the supervision of Prof. Gregoriadis. Prof. Perrie's research is multi-disciplinary and focuses on the development of drug carrier systems for the delivery of drugs and vaccines to enhance patient care globally. Prof. Perrie is a Director-at-large for the Controlled Release Society. She is Editor-in-Chief of both the *Journal of Liposome Research and Pharmaceutics*; she is also Associate Editor for the *Journal of Drug Targeting* and the *Journal of Pharmacy and Pharmacology*.

Thomas Rades is the Research Chair in Pharmaceutical Design and Drug Delivery at the Department of Pharmacy, University of Copenhagen, Denmark. Dr. Rades obtained his Ph.D. from the Technical University of Braunschweig, Germany, and has developed an international reputation for his research on solid drugs and dosage forms as well as in vaccine delivery. Research in both areas aim to improve drug therapy through appropriate formulation and the characterization of medicines; another objective is to increase an understanding of the physico-chemical properties of drugs and medicines. Dr. Rades has published more than 325 papers in international peer-reviewed journals. He is an editor of the *Journal of Pharmaceutical Sciences*, the *European Journal of Pharmaceutics*, and *Biopharmaceutics*. Dr. Rades holds an honorary doctorate from Åbo Akademi University (Finland); he is an Eminent Fellow of the Academy of Pharmaceutical Sciences (UK), a Fellow of the New Zealand Institute of Chemistry, and a member of the College of Fellows of the Controlled Release Society.

His studies combine the physical, chemical, and biological sciences and technology with analytics to optimally formulate drugs and vaccines.

Part I
Spectroscopic and Spectrometric
Techniques

Chapter 1

UV/Vis Spectrophotometry and UV Imaging

Jesper Østergaard

Abstract The present chapter describes typical instrumentation and principles of UV/Visible spectrophotometry and UV imaging measurements. The absorption of light as a function of wavelength depends on the structural properties of molecules as well as the solvent in which they are dissolved, including solvent polarity, pH, temperature and the presence of complexing agents. The absorbance measured for an analyte can be linearly related to concentration through Lambert-Beer's law. Instrument related and chemical parameters causing deviations from Lambert-Beer's law are discussed in relation to quantitative applications of spectrophotometry. Practical issues to be considered in quantitative analysis are briefly covered, as is the use of UV/Vis spectrophotometry for compound identification and physico-chemical profiling, including pK_a and kinetic studies. Recent UV imaging equipment facilitating spatially (2D) resolved absorbance measurements in real-time is described and selected applications in drug dissolution and release testing reviewed.

Keywords Absorbance • Dissolution/release testing • Drug quantification • Kinetics • Lambert-Beer's law • Physicochemical profiling • Spectrophotometer • UV imaging • UV/Visible spectrophotometry • UV/Visible spectroscopy

1 Introduction

Light is electromagnetic radiation characterized by a number of waves having different wavelengths or photons carrying varying amounts of energy. Pharmaceutical applications of ultraviolet-visible (UV-vis) spectrophotometry concern light in the wavelength range 190–800 nm. The relevant ultraviolet (UV) range is from 190 to 400 nm and the visible region, recognized by the human eye, is from 400 to 800 nm. Light is characterized by the wavelength λ defined as the distance between two crests of a wave and the energy of the light (E) is related to the wavelength by:

J. Østergaard (✉)

Faculty of Health and Medical Sciences, Department of Pharmacy, University of Copenhagen, Universitetsparken 2, Copenhagen 2100, Denmark

e-mail: jesper.ostergaard@sund.ku.dk

$$E = \frac{ch}{\lambda} \quad (1.1)$$

where h is the Planck's constant and c is the speed of light. Consequently, light with different wavelengths holds different amounts of energy; the lower the wavelength the higher the energy. This has implications for the interaction of light with matter. Molecules absorb light when the incident photon possesses energy equal to the energy difference between two allowed states of the valence electrons. Thus absorption of light occurs when energy from the photon promotes an electron to a higher energy state. The excited molecules give up the absorbed energy through the radiation of heat returning to their initial ground state. The ability of a molecule to absorb light as a function of wavelength is represented in a UV-visible absorption spectrum and will depend on the molecular structure. Functional groups and structural elements absorbing light are termed chromophores. The UV-visible spectrum may be helpful in compound identification and for determination of physical chemical properties. However, the main application of UV-vis spectrophotometry is related to the quantification of compounds.

2 Principles of Measurement

2.1 Lambert-Beer's Law

The absorption of UV and visible light is quantitatively described by the laws of Lambert and Beer. According to the law of Lambert, each layer of the medium through which the light is passing absorbs an equal fraction of light which is independent of the intensity of the incident light; thus, along the light path there is an exponential decay in the light intensity. Beer's law states that the amount of light absorbed is proportional to the number of chromophores present in the medium that the light is passing through. In other words, the amount of absorbed light is proportional to the concentration of the absorbing species (chromophores). These two laws are often combined into what is often referred to as Lambert-Beer's, Beer-Lambert's or simply Beer's law:

$$\log_{10} \left(\frac{I_o}{I} \right) = \log_{10} \left(\frac{1}{T} \right) = A = \epsilon bc \quad (1.2)$$

where I_o is the intensity of the incident light, I is the intensity of the transmitted light, T is the transmittance given by (I/I_o) , A is the absorbance, ϵ is the molar absorption coefficient (unit: $\text{L mol}^{-1} \text{cm}^{-1}$), b is the light path (the length of medium through which the light is passing; commonly given in cm), and c is the concentration of the absorbing molecule (mol L^{-1}). Lambert-Beer's law is valid only if the light is monochromatic, that is, the radiation is of only a single

wavelength. The laws of Lambert and Beer apply to mixtures containing several absorbing molecules (1, 2, 3...n) provided interactions between the molecules affecting their spectra are absent:

$$A = \epsilon_1bc_1 + \epsilon_2bc_2 + \epsilon_3bc_3 + \cdots + \epsilon_nbc_n \quad (1.3)$$

Frequently, different concentration units are applied. It may be convenient to use the specific absorbance ($A_{1\text{ cm}}^1\%$) for conversion between absorbance and concentration when the molecular weight (M_r) is unknown or the concentrations given in gram or milligram per volume:

$$A = A_{1\text{ cm}}^1\%bc = \frac{10\epsilon}{M_r}bc \quad (1.4)$$

As will be apparent from the following the absorbance of molecule is dependent on the solvent, pH, molecular interactions, and temperature in addition to structure and wavelength.

2.2 *Deviations from Lambert-Beer's Law and Sources of Error*

The proportionality between absorbance and concentration inferred by Eq. (1.2) is not always observed, causes for deviation from Lambert-Beer's law may be of chemical as well as instrumental origin (Fifield and Kealey 2000; Hage and Carr 2011; Sommer 1989). At high drug or analyte concentrations (typically >0.01 M) deviations from linearity may be observed due to refractive index changes and because the close proximity of the absorbing molecules will affect their charge distribution and lead to alterations in their absorptivity. Furthermore, the compounds should not take part in reactions, such as self-association reactions and chemical degradation which may lead to changes in absorbance. Particles present in the sample will also lead to deviations from Lambert-Beer's law due to light scattering.

Experimentally it is not possible obtain monochromatic radiation. In practice the sample is exposed to polychromatic radiation of a certain wavelength range ($\Delta\lambda$), the more narrow the band of wavelengths, the better since polychromatic radiation leads to deviations from Lambert-Beer's law. This deviation is most significant when there is a large variation in the molar absorption coefficient ϵ as indicated in Fig. 1.1. Consequently, for quantitative work, a relatively narrow wavelength range where there is only a small change in absorptivity should be selected; this is normally found at the absorption maximum. A compromise is sought since a narrow slit width (spectral bandwidth) leads to a low energy throughput and thereby reduced sensitivity due to signal-to-noise degradation. On the other hand, an overly

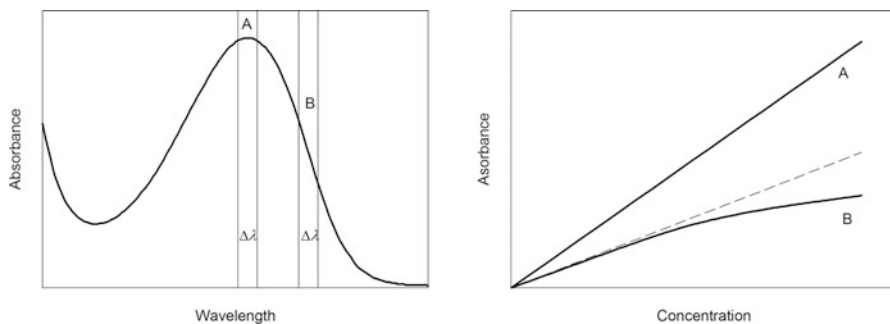


Fig. 1.1 Effect of wavelength selection and polychromatic light on calibration curves. *Left*, UV absorbance spectrum. *Right*, calibration curves

large slit width of the monochromator (or band pass of a band pass filter) will lead to deterioration of spectral details (Görög 1995; Sommer 1989).

Deviation from Lambert-Beer's law can also occur due to stray light. This is light that reaches the detector without having passed through the sample due to light scattering within the instrumentation or light entering from outside the instrument. As apparent from Eq. (1.5) stray light will give rise to negative deviations from Lambert-Beer's law:

$$A = \log_{10} \left(\frac{I_o + I_s}{I + I_s} \right) \quad (1.5)$$

where I_s is the stray light intensity. Errors due to stray light are most predominant at wavelengths where the intensity of the light source is low.

3 Instrumentation

The basic components for UV/Visible spectrophotometry include a light source, a wavelength selector, a sample compartment (often a cuvette or flow cell) and a detector. Two optical configurations are applied normal optical setup where wavelength selection occurs before the light passes the sample and the reverse optical configuration where dispersion of the light occurs after the sample. Two basic types of detectors are used, photomultiplier tubes or semiconductors, the latter including photodiodes and charge coupled devices. Below the basic features of common types of spectrophotometers (single beam spectrophotometer, double beam spectrophotometer and array detector spectrophotometer) and a relatively new UV imaging instrument are outlined.

3.1 Single Beam Spectrophotometers

The classical single-beam UV spectrophotometer commonly employs deuterium arc (160–375 nm) and tungsten-halogen (350–2500 nm) lamps as the light sources. A monochromator is placed between the light sources and the sample for selecting a narrow wavelength range to be passed through the sample. The intensity of the light escaping the sample is measured using a photo multiplication tube or a photodiode (Fig. 1.2). For absorbance measurements to be made according to Eq. (1.2) measurement of I_0 and I is needed. However, the light will to some extent be reflected and/or absorbed at the interfaces encountered in the spectrophotometer, e.g., the walls of the sample cuvettes, leading to a decrease in light intensity. Since we are interested in the absorbance of a drug substance dissolved in a suitable solvent or solution (reference), the decreases in light intensity not related to the analyte are taken into account by measurement of the light intensity passing through the sample relative to a measurement performed using an identical cuvette containing only the solvent. In the single-beam instrument these measurements must be made one at a time which requires that the absorbance of the blank is adjusted to zero followed by measurement of the sample. Thus with aid of the instrument the absorbance is determined according to:

$$A \cong \log_{10} \left(\frac{I_{ref}}{I_{sample}} \right) \quad (1.6)$$

rather than Eq. (1.2). I_{ref} and I_{sample} are the intensities of the light transmitted through the reference (sample holder + solvent) and sample (sample holder + solution), respectively. It is crucial for measurements in the single-beam instrument that all other parameters, than the drug substance (analyte) concentration, are kept constant. Thus, the solvent/solution as well as the sample container (often a cuvette) should be the same or similar to avoid errors. This also put demands to the constancy of the radiation output of the light source, the detector and the electronics since the measurement of the sample of interest and the reference are separated in time. To compensate for variation in light intensity provided by the lamp, some systems have an electronic compensation system, a so called split-beam arrangement, diverting part of the light before passing the sample allowing stabilization of source intensity (Rouessac and Rouessac 2007).

3.2 Double Beam Spectrophotometers

In the classical double-beam UV-vis spectrophotometer (Fig. 1.2), the time gap between reference and sample measurement is eliminated. Using a chopper the beam is split into two parallel beams, one passing through a reference cell and the other through the sample cell (Fig. 1.2). This setup, where the absorbance values of

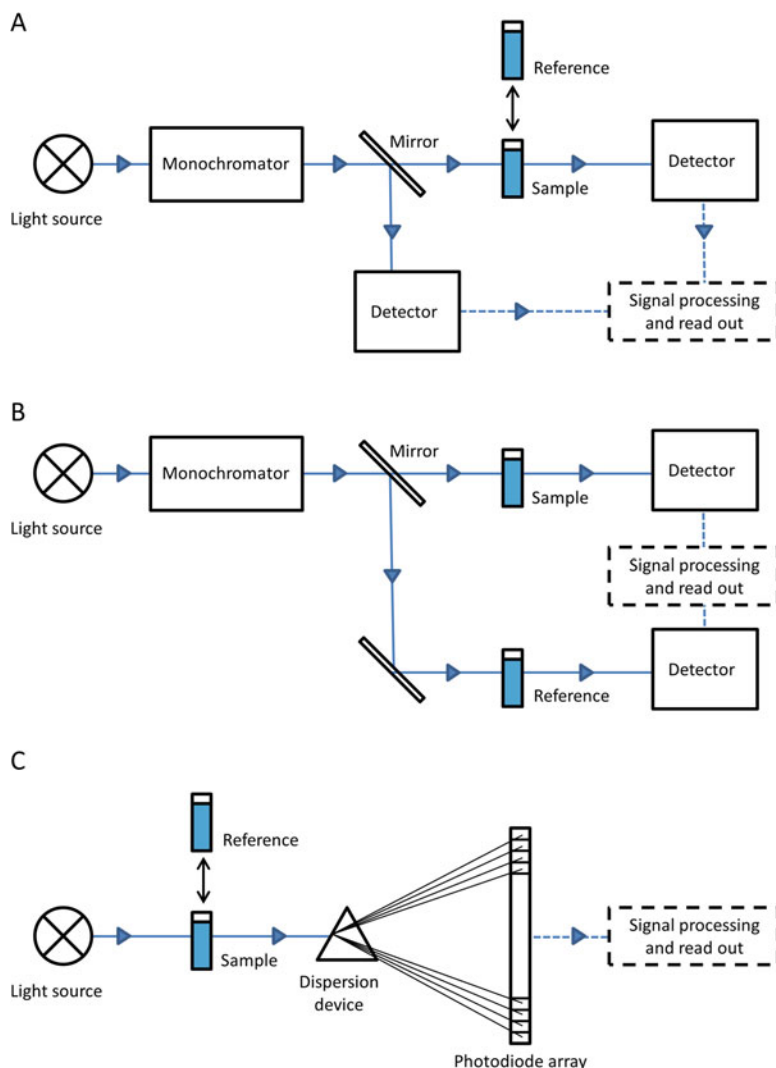


Fig. 1.2 Schematic representation of the general design of a (a) single beam spectrophotometer with split-beam design, (b) double beam spectrophotometer, and (c) photodiode array spectrophotometer

the reference and sample are measured simultaneously allows measurements to be done faster and with greater accuracy since error due to drift is eliminated. High performance instruments are usually equipped a deuterium arc and a tungsten-halogen lamp, a double monochromator for reducing stray light and allow for the selection of spectral bandwidth. The scanning of an absorbance spectrum may take several minutes since the wavelength scan is achieved by the monochromator

physically rotating. Overly fast recording speed may lead to distortion of the absorbance bands and displacement of maxima (Görög 1995).

3.3 Photodiode Array and Charge-Coupled Device Spectrophotometers

Many newer spectrophotometers do not have a monochromator and photo multiplication tube but rely on the reversed optical design utilizing a photodiode array (PDA) or a charge-coupled device (CCD) detector for wavelength selection and detection. A photodiode is a photosensitive element capable of measuring the intensity of light striking it. A schematic representation of a PDA UV-vis spectrophotometer is shown in Fig. 1.2. The sample is irradiated with polychromatic light which after transmission through the sample hit a reflection grating which disperses the light onto the array according to wavelength. Each photodiode measures the light intensity for a defined wavelength interval depending on its position in the array. The PDA can be read very fast as compared to spectrophotometers using a scanning monochromator for wavelength selection allowing UV-vis spectra to be recorded within ~100 ms as compared to ≥ 1 min. The wavelength resolution of PDA spectrophotometers is determined by the number and size of the photodiodes. CCDs utilize different photosensitive elements and are increasingly replacing PDAs as detectors in spectrophotometers. The performance of CCDs is better approaching that photomultiplier tubes (Skoog et al. 1998). In addition, CCDs are two-dimensional thus providing more detector elements, pixels. PDA and CCD spectrophotometers are often made in single-beam configuration utilizing either a deuterium arc and a tungsten-halogen lamp or a xenon arc lamp as the light source.

3.3.1 Micro-volume Spectrophotometers

In traditional UV-vis spectrophotometers, a quartz cuvette or flow cell is used for maintaining the well-defined light path needed for quantitative work. However, cuvette-free spectrophotometers are available with variable, short light paths minimizing the need for sample dilution of concentrated samples as well as allowing measurements to be performed with minute sample volumes (0.3–2 μL) (Implen GmbH 2014; Picodrop Ltd 2014; Thermo Fischer Scientific Inc 2014). This type of spectrophotometer is of interest when the sample volume is sparse and finds wide use in protein quantification and nucleic acid analysis. Figure 1.3 exemplifies one of the strategies taken in micro-volume spectrophotometry.

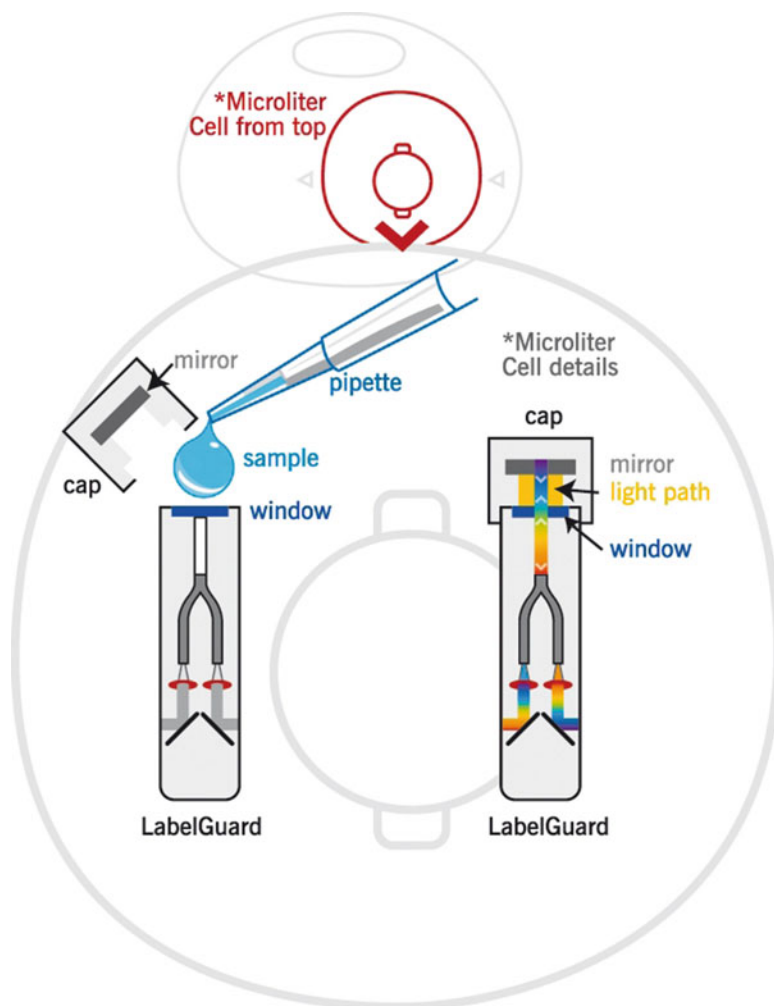


Fig. 1.3 Schematic representation of micro-volume spectrophotometer measurement cell design (Implen NanoPhotometer). A droplet ($0.3\text{--}3.5\ \mu\text{L}$) is pipetted on the window and positioning of the cap ensures a well-defined light path. White light passes through the sample twice due to reflection at the mirror in the cap. The spectrophotometer uses a monochromator placed between the sample compartment and the detector for wavelength selection. Reproduced with courtesy of Implen GmbH

3.3.2 UV Fiber Optic Probes

Optical fibers have led to the development of additional types of spectrophotometers. Among these UV-vis fiber optic probes, often comprising a pulsed Xenon lamp and an array detector, have attracted a lot of interest, particularly in relation to dissolution testing and pK_a determination. Figure 1.4 shows the schematic of

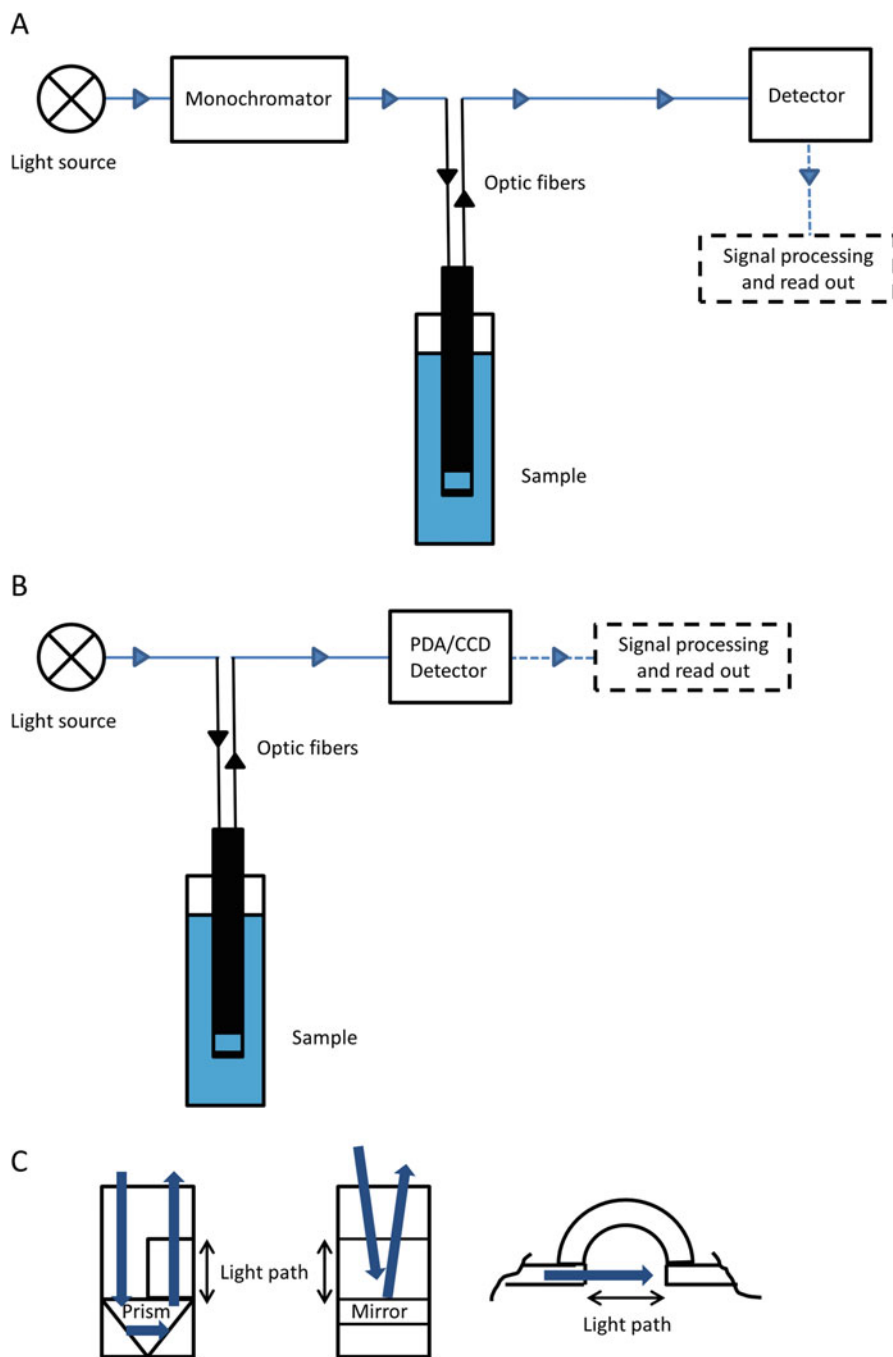


Fig. 1.4 Schematic representation of fiber optic probe spectrophotometers. Fiber optic probe systems utilizing (a) monochromator and (b) PDA/CCD detector. Schematic representations of (c) selected probe designs. Modified from Inman et al. (2001) and Rouessac and Rouessac (2007)

UV-vis fiber optic probe designs. Special light shield designs facilitate the use of optic probes for absorbance measurement even in the presence of normal/outside light. With the use of array detectors, real time monitoring with full range UV-scans can be achieved with the additional benefit of eliminating sample handling. Since sample filtration is not performed in in situ concentration monitoring using fiber optic probes as normally done in off-line UV/Vis spectrophotometric or HPLC analysis special attention has to be directed at matrix effects. In addition to light absorbed by the analyte, the apparent absorbance may change due to particulates originating from excipients as well as the analyte (drug) subject to investigation. Procedures have been developed capable of taking into account effects of particles scattering light (Wiberg and Hultin 2006). However, awareness is rising that nanoparticles (excipient or drug) capable of both absorbing and scattering UV light represent a complex scenario (Van Eerdenbrugh et al. 2011).

3.4 UV Imaging

The types of spectrophotometers discussed so far are designed for absorbance measurements in homogeneous solutions. UV imaging instrumentation has occurred which facilitates spatially resolved absorbance measurements (Østergaard et al. 2010, 2014a). The key components of the commercially available UV imaging instruments are a pulsed Xe lamp, a band pass filter for wavelength selection, fiber optic cable, a quartz flow cell or cuvette and a $7 \times 9 \text{ mm}^2$ complementary metal oxide semiconductor (CMOS) sensor chip as sketched in Fig. 1.5. The sensor array composed of $7 \times 7 \text{ }\mu\text{m}^2$ pixels (photosensitive elements) is used to provide the spatial resolution and consequently only a single wavelength can be applied. Most CMOS sensor chips are not sufficiently sensitive to light at wavelengths below $\sim 250 \text{ nm}$ and the system utilizes a special Actipix[®] technology for converting light from the UV range to the visible range upon emergence from the sample prior to striking the array. The working wavelength range explored for the system is 200–640 nm, thus, the instrument is not limited to the UV wavelength range. The configuration is in most aspects similar to a single-beam spectrophotometer in the sense that reference images have to be attained prior to inserting and imaging the sample subject to study.

4 Applications of UV/Visible Spectrophotometry

4.1 Qualitative Analysis

Which compounds absorb light in the UV and visible wavelength range and what determines the appearance of their absorbance spectrum? As discussed above the

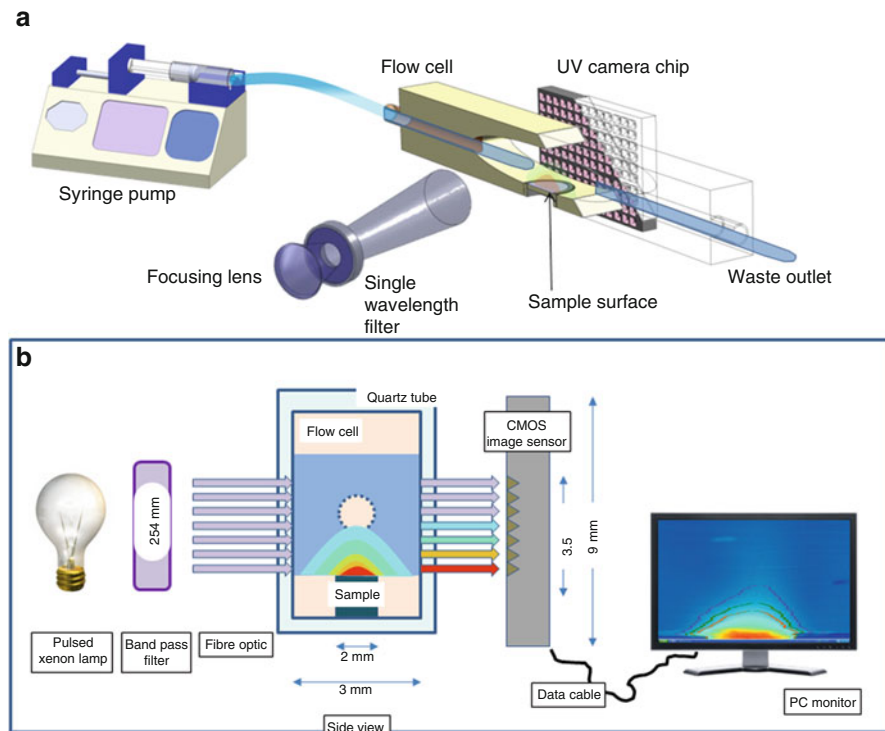


Fig. 1.5 Schematic representation of commercially available UV imaging instrumentation. (a) Key components of the instrument. (b) Side view of flow cell. With permission from Springer Science + Business. Copyright ©2010 (Østergaard et al. 2010)

absorption of UV and visible light is due to the excitation of electrons to higher energy levels. Excitation of electrons in C-H and C-C single bonds requires a lot of energy and is restricted to wavelengths below 185 nm (the vacuum UV region). Compounds that absorb light in the UV-vis range above ~185 nm contain electrons taking part in chemical bonding and are shared by several atoms, or, unshared electrons localized about an O, N, S or halogen atom. The saturated functional groups containing O, N, S or halogen atoms are termed auxochromes because they exhibit limited absorbance themselves but significantly affect the absorbance of a molecule (shifting λ_{\max} towards longer wavelengths and increasing ϵ) when the unshared electron pair can interact with aromatic rings or conjugated double bonds. Functional groups absorbing light are called chromophores. Double and triple bonds, e.g., C=C, N=N, C=N, C=O, C \equiv C, and C \equiv N are examples of chromophores. They have relatively weak absorbance above 200 nm when occurring isolated. If the chromophores are separated by at least two single bonds, interaction between the chromophores is absent and the spectrum approximates the sum of the spectra of the individual chromophores. However, the conjugation of chromophores, allowing delocalization of the π -electrons, leads to shift of the absorbance

maxima (λ_{\max}) towards longer wavelengths (bathochromic shifts) and increased absorptivities (hyperchromic shifts) (Fifield and Kealey 2000; Görög 1995; Rouessac and Rouessac 2007; Skoog et al. 1998). The following terminology is commonly applied when describing changes in UV spectra due to environmental or structural changes leading to changes in electron distribution of a molecule:

Bathochromic (red) shift: shift of λ_{\max} towards longer wavelength

Hypsochromic (blue) shift: shift of λ_{\max} towards shorter wavelength

Hyperchromic shift: increase in absorptivity

Hypochromic shift: decrease in absorptivity

Molar absorption coefficients vary in the range 0–10⁵ in UV-vis spectrophotometry. The magnitude of ϵ depends on the size of the chromophore and the probability that a collision with the photon leads to excitation/transition. It follows from above that compounds having many double and triple bonds, aromatic rings and O, N and halogens tend to absorb light strongly. Based on semi-empirical rules it is possible to estimate or calculate λ_{\max} from structural properties for a number of molecules (Görög 1995). This may, however, be of limited value in practical work. The environment to which the molecule is exposed will affect the shape of the spectrum. Important environmental parameters include temperature, pH, ionic strength, solvent properties (refractive index, polarity, permittivity, donor power or acid-base properties), chemical equilibria, and presence of surfactants or complexation agents. The absorbance spectrum of a compound may depend on instrument parameters slit width and scanning speed, broad band passes and high scanning speeds leading to the distortion of the spectrum (Sommer 1989).

Due to the dependence of the absorbance spectrum on the molecular structure alluded to above, UV-visible spectrophotometry may be helpful in compound identification. UV-vis spectrophotometry is included in the pharmacopoeia as a secondary method for compound identification. It may be applied together with one or two additional methods for compound identification as an alternative to infrared (IR) spectroscopy which is the primary method. Absorbance spectra have less features and details and UV spectrophotometry, thus, is less specific than IR spectroscopy. By comparison to a reference spectrum it is possible to render probable that the material is the intended substance or not and to assess whether it may be contaminated with impurities absorbing light in the UV or visible range (Hansen et al. 2012). Furthermore, absorbance spectra serves as an important starting point for development of quantitative analytical methods using spectrophotometry or separation techniques, e.g., HPLC or capillary electrophoresis (CE), applying UV-vis detection.

4.2 Quantitative Analysis

The basis for quantitative spectrophotometric analysis in the UV-visible range is Lambert-Beer's law (Eq. (1.2)). Frequently, a calibration curve is first constructed

by measurement of standard solutions of known concentrations at a selected wavelength (often λ_{\max}) providing suitable sensitivity. This is followed by measurement of the absorbance of the compound of interest, the analyte, under similar conditions. It is important that the matrix of the standards and samples is identical, e.g., with respect to solvent composition, pH and temperature, otherwise significant errors may be introduced. In cases where it is not possible to prepare standard solutions matching the composition of the sample matrix, the procedure of standard addition may be applied. In standard addition, known quantities of the pure analyte are added to the sample while the absorbance of the sample is measured before and after addition of the analyte. In this way calibration is done in the sample minimizing possible matrix effects and the analyte is quantified using Lambert-Beer's law (Hansen et al. 2012; Skoog et al. 1998). For complex samples, separation of the sample components prior to spectrophotometric analysis as in HPLC or CE is often the preferred approach although quantitative analysis in multicomponent systems as covered briefly below may constitute a feasible option.

For determination of the content or purity of pharmaceutical raw materials UV spectrophotometric assays are described in the pharmacopoeia. Detailed examples and guidance on how to perform such assays can be found elsewhere (Hansen et al. 2012; Watson 2005). The content range specified for a well-defined chemical compound is strict and depends to a large extent on the precision of the analytical method applied. For UV spectrophotometric assays the range is often 97.0–103.0 % (w/w) because three times the standard deviation is within 3 %. The upper limit is above 100 % because of the analytical uncertainty and lack of specificity and may be lower to accommodate the presence of impurities (Hansen et al. 2012). Assays for content can usually be performed with better precision using titration (range 99.0–101.0 %) or HPLC (range 98.0–102.0 %). Convenience, simplicity of operation and method development, and instrument availability may merit the use of UV-vis spectrophotometry. For verification of instrument performance the wavelength scale, absorbance scale, resolution and stray light limits should be checked (Council of Europe 2014).

UV-vis spectrophotometry may be applied to determine the quantitative composition of samples containing multiple analytes. It is a prerequisite that the individual spectra of the analytes are known and that the absorbance values for the individual analytes are additive, i.e., that Eq. (1.3) is valid. In the simplest case, a solution containing two components 1 and 2 at concentrations C_1 and C_2 , measurement at two wavelengths λ_a and λ_b is sufficient for quantification. From standard solutions of known concentrations of the individual analytes the wavelengths λ_a and λ_b are selected and the molar absorption coefficients ϵ_1^a , ϵ_2^a , ϵ_1^b and ϵ_2^b are determined. Solving the set of two simultaneous equations upon measurement of the absorbance of the sample at λ_a and λ_b (b is the light path of measurement cuvette, often 1 cm):

$$\lambda_a: A_a = \epsilon_1^a b C_1 + \epsilon_2^a b C_2 \quad (1.7)$$

$$\lambda_b: A_b = \varepsilon_1^b b C_1 + \varepsilon_2^b b C_2 \quad (1.8)$$

will provide the composition of the sample in form of C_1 and C_2 . A similar procedure is feasible for three-component systems but becomes impractical and inefficient when additional compounds are present. The approach works well when the UV-vis spectra of the analytes are very different; close similarity of the individual analyte spectra will lead to less precision since small measurement errors can lead to large variations in the result. Impurities not taken into account constitute an additional source of error. The simple approach illustrated above is hardly used today, quantitative analysis software is applied and a large number of data points from the spectra are utilized providing increased selectivity and accuracy in addition to convenience. In addition to multi-wavelength linear regression analysis, methods based on partial least squares, principal component regression or multiple least squares find use in multi component quantification (Görög 1995; Perkampus 1992; Rouessac and Rouessac 2007; Sommer 1989).

To conclude this section it is worth to note that a variety of more specialized spectrophotometric approaches for quantification has been established, e.g., difference spectrophotometry, derivative spectrophotometry, dual-wavelength spectrophotometry and spectrophotometric titration (Görög 1995; Perkampus 1992; Sommer 1989).

4.3 Physicochemical Properties

4.3.1 pK_a Values

As alluded to above, a change in solution pH often affects a change in absorbance spectrum of a drug substance. Figure 1.6 shows the pH dependent changes in the absorbance spectra of pyridoxine HCl (pK_a 4.90; 8.89 (Avdeef 2012)). The determination of ionization constants and pK_a values is possible from such absorbance changes. Two isobestic points are indicated in Fig. 1.6. At such intersection points in the spectra the molar absorptivities of the two forms are identical, consequently this wavelength cannot be used for pK_a determination. The apparent acidity constant (mixed constant) for a monoprotic acid HA is given as:

$$K'_a = \frac{a_{H^+} [A^-]}{[HA]} = \frac{a_{H^+} \alpha}{1 - \alpha} \quad (1.9)$$

where a_{H^+} is the hydronium ion activity, $[HA]$ and $[A^-]$ are the concentrations of HA and A^- , respectively, and α is the degree of dissociation ($\alpha = [A^-]/([HA] + [A^-])$). The absorbance of a solution containing the acid HA and the conjugate base A^- at the total concentration $C_t = [HA] + [A^-]$ is:

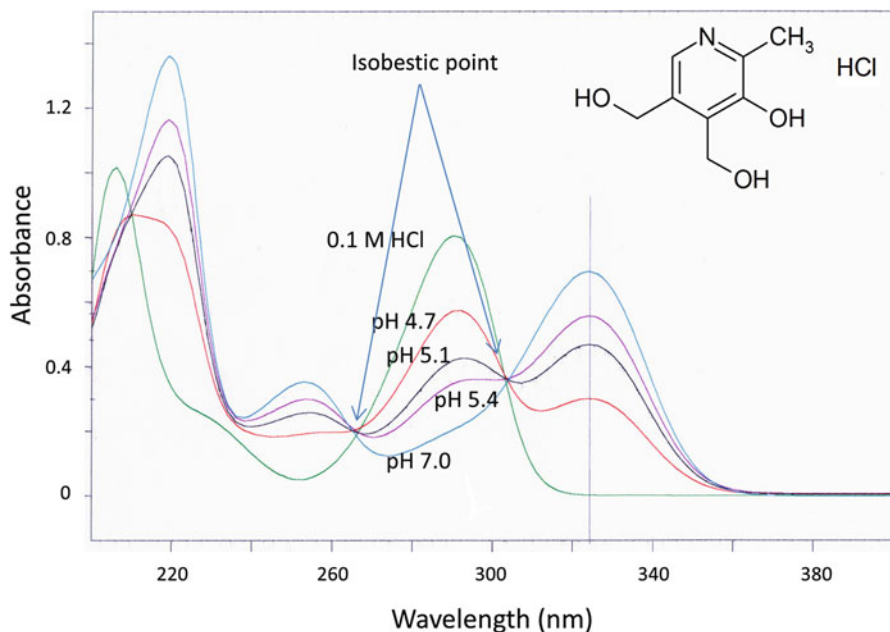


Fig. 1.6 UV spectra of pyridoxine at various pH

$$A = \epsilon_{HA}b[HA] + \epsilon_{A^-}b[A^-] \quad (1.10)$$

The absorbance, A_{HA} , of a solution containing HA entirely at the acidic form ($C_t = [HA]$) is given by:

$$A_{HA} = \epsilon_{HA}bC_t \quad (1.11)$$

and, similarly, for the absorbance, A_{A^-} , for a solution containing HA entirely on the deprotonated form ($C_t = [A^-]$):

$$A_{A^-} = \epsilon_{A^-}bC_t \quad (1.12)$$

The absorbance of a solution containing HA and A^- may be expressed in terms of the total acid concentration and the degree of dissociation, α :

$$A = \epsilon_{HA}b(1 - \alpha)C_t + \epsilon_{A^-}b\alpha C_t \quad (1.13)$$

which upon insertion of Eqs. (1.11) and (1.12) leads to:

$$A = (1 - \alpha)A_{HA} + \alpha A_{A^-} \quad (1.14)$$

Substitution of Eq. (1.14) into the acidity constant (Eq. (1.9)) and rearrangement leads to:

$$pK'_a = pH - \log \frac{A_{HA} - A}{A - A_{A^-}} \quad (1.15)$$

Equation (1.15) allows the determination of the mixed pK'_a from solutions of HA on its fully protonated and deprotonated forms and a solution of known pH when a wavelength for detection can be found where the acid and base forms have different absorptivity (Connors 1987; Perkampus 1992). Thermodynamic pK_a values can be determined by inclusion of the Debye-Hückel equation. For polyprotic compounds, such as pyridoxine HCl, the procedure outlined here requires the pK_a values to differ four units. Again, effective advanced data analysis procedures utilizing the entire absorbance spectra have been developed (Avdeef 2012; Tam and Takács-Novák 1999, 2001).

4.3.2 Equilibrium Constants and Complexation

UV and visible spectrophotometry can be applied broadly to the characterization of equilibria and complexation phenomena. The determination of acidity constants touched upon in the previous section can be considered a special case hereof. Frequently, molecular interactions lead to changes in electron distribution and consequently altered absorbance spectra. Spectrophotometry has for instance been used for determination of drug substance—cyclodextrin complexation (Connors 1987; Mura 2014). Connors has detailed approaches and equations for data analysis (Connors 1987).

4.3.3 Kinetics and Reaction Monitoring

Spectrophotometry is a powerful method for monitoring chemical reaction kinetics, provided that there is proportionality between absorbance and concentration for both reactants and products, i.e. adherence to Lambert-Beer's law, and that there is an experimentally satisfactory difference between the absorbance of the reactants and the products (Connors 1990; Jencks 1987; Perkampus 1992). The experimental conditions can often be selected in a manner that the reaction under investigation follows pseudo first order kinetics and under such conditions determination of the rate constant or half-life is particularly convenient. For the reaction:



the initial conditions ($t = 0$) are $[R] = [R]_0$ and $[P] = 0$ and mass balance considerations define

$$[R]_0 = [R] + [P] = [P]_\infty \quad (1.17)$$

where $[R]_0$ is the reactant concentration at $t=0$ and $[P]_\infty$ is the product concentration when the reaction has come to completion. Lambert-Beer's law provides the relations below:

$$A_0 = \varepsilon_R b [R]_0 \quad (1.18)$$

$$A_\infty = \varepsilon_P b [P]_\infty \quad (1.19)$$

$$A_t = \varepsilon_R b [R] + \varepsilon_P b [P] \quad (1.20)$$

where A_0 , A_t and A_∞ are the absorbance of the reaction mixture at $t=0$, $t=t$ and $t=\infty$. The absorbance values can be substituted into the integrated first order equation:

$$\ln \frac{[R]}{[R]_0} = -kt \quad (1.21)$$

leading to Eq. (1.22a) or (1.22b) depending on A_0 or A_∞ attaining the larger value:

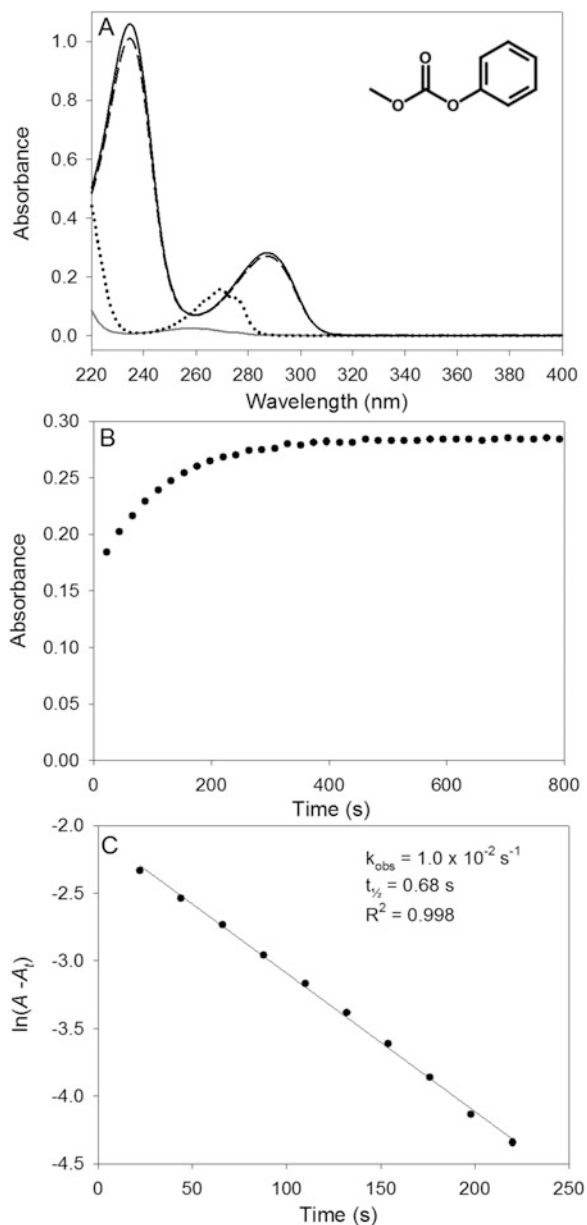
$$\ln \frac{A_t - A_\infty}{A_0 - A_\infty} = -kt \quad (1.22a)$$

$$\ln \frac{A_\infty - A_t}{A_\infty - A_0} = -kt \quad (1.22b)$$

The determination of the pseudo first order rate constant for the hydrolysis of ethyl phenyl carbonate in alkaline solution by UV spectrophotometry is shown in Fig. 1.7 (Østergaard and Larsen 2007). The UV spectra of ethyl phenyl carbonate, the reaction products and phenolate are shown in Fig. 1.7a. The change in absorbance as a function time at the selected wavelength 287 nm and data analysis in accordance with Eq. (1.22b) are depicted in Fig. 1.7b, c, respectively. The hydrolysis of ethyl phenyl carbonate and a series of related carbonate esters was investigated in a prodrug context with the aim of characterizing the susceptibility towards hydrolysis in a wide pH range and generation of pH-rate profiles. UV spectrophotometry is well-suited for these simple systems where reactants and products are well defined. Analysis at several wavelengths, for instance using a diode array spectrophotometer, increases confidence that secondary reactions are not occurring during incubation (the determined rate constant should be independent of the wavelength). However, for complex reactions the use of a separation method such as HPLC may be advantageous in elucidating the reaction processes, although also more labor intensive. Perkampus describes rate equations in which concentration has been substituted with absorbance for second order reactions as well as consecutive and parallel reactions (Perkampus 1992). Also, special equations have been derived for the systems where it is not feasible to follow the reaction to completion (Connors 1990; Jencks 1987; Perkampus 1992).

UV-vis spectrophotometry is feasible for kinetic studies lasting less than 1 min to hours and even days. In kinetic experiments, the mixing of the reactants leads to a

Fig. 1.7 Application of UV spectrophotometry to monitor the hydrolysis of ethyl phenyl carbonate in 0.01 M NaOH at 37 °C. **(a)** UV spectra of ethyl phenyl carbonate ($1.1 \cdot 10^{-4}$ M) in H₂O (gray trace) and upon incubation in 0.01 M NaOH (black solid trace) and of phenol ($1.0 \cdot 10^{-4}$ M) in H₂O (dotted trace) and in 0.01 M NaOH (dashed trace). **(b)** Absorbance at 287 nm as a function of time for reaction mixture initially containing $1.0 \cdot 10^{-4}$ M ethyl phenyl carbonate in 0.01 M NaOH at 37 °C. **(c)** Plot of $\ln(A_\infty - A_t)$ versus time (equivalent to Eq. (1.22b) for determination of the rate constant k_{obs}). Data from Østergaard and Larsen (2007). *Note: Only one of six experiments conducted in parallel is shown. Hence, the relatively few data points and lack of data points in the early phase of the reaction due to the time required for starting and mixing six solutions*



dead-time (perhaps 5–10 s in a cuvette-based spectrophotometer) in which reliable data cannot be obtained. Special stopped-flow spectrophotometers should be applied for monitoring very fast processes where effective mixing allows monitoring of reactions on the millisecond scale. For experiments lasting for longer periods of time special cuvettes or cells should be used to prevent vaporization and

instrument drift must be avoided. Good temperature control is often maintained by the use of a water bath and circulating water. Investigation of kinetics by spectrophotometry is attractive because spectrophotometers capable of operating several cells at the same time are available and handling and disturbance of the sample subject to study are avoided. The sample, however, has to be photochemically stable.

Enzyme kinetics is a related huge area of application of UV/Vis spectrophotometry. Accounts on the use of spectrophotometric assays for characterization of enzyme catalyzed reactions is given elsewhere (John 1992).

4.3.4 Dissolution Testing

In formulation development and as a part of quality control dissolution testing is widely employed and therefore deserves special mentioning. The USP dissolution testing apparatus 2 is the most commonly used device for oral solid dosage forms. Traditionally, samples are withdrawn manually over time and analyzed by HPLC or spectrophotometry. The approach is labor intensive, prone to operator errors and provides limited number of data points on the dissolution profile due to sample capacity limitations (Lu et al. 2003; Mirza et al. 2009; Wiberg and Hultin 2006; Zhang et al. 2013). Consequently, fiber optic probes (Sect. 3.3) have received a great deal of attention by providing continuous monitoring of the dissolution process and improved data precision by eliminating manual steps. Changes in the hydrodynamic conditions due to immersion of the fiber optic probe into the dissolution medium must be anticipated. Turbid media may also represent an issue to which attention must be directed. Various types of dedicated instrumentation and software provide a large degree of user friendliness and efficient use of the information captured in the recorded UV spectra from dissolution testing.

5 Applications of UV Imaging

Spectroscopic imaging methods providing spectrally, spatially, and temporally resolved information is increasingly used in pharmaceutical research including drug dissolution and release testing (Kazarian and Ewing 2013; Kempe et al. 2010; Mantle 2013; Windbergs et al. 2009). UV imaging offers a complementary approach for conducting dissolution and release testing, relative to Fourier transform infrared (FTIR), coherent anti-Stokes Raman scattering (CARS), terahertz and magnetic resonance imaging (MRI) by focusing on molecules in solution or in the dissolved state. Selected applications of this comparatively simple format for chemical imaging are presented in the following. A detailed review can be found elsewhere (Østergaard et al. 2014a).

5.1 Drug Dissolution

The dissolution of lidocaine from a single crystal into phosphate buffer, pH 7.4, exemplifies the opportunities associated with UV imaging in relation to dissolution testing (Østergaard et al. 2011). Figure 1.8 shows a lidocaine crystal (~ 3 mm in length) mounted in a flow-through dissolution cell. The flow-through cell was filled with buffer prior to stopping the flow while UV imaging was performed at 254 nm. The UV absorbance maps (images) obtained show the spatially resolved distribution of lidocaine next to the crystal. The absorbance values represent apparent lidocaine concentrations because of averaging across the light path ($b = 3$ mm). Figure 1.8 shows the appearance of natural convection in the cell due to density gradients forming during dissolution of lidocaine. Concentrated, dense lidocaine solution drops to the bottom of the flow-through cell leading to the asymmetric concentration distribution. The image in Fig. 1.8 is constructed from the read out of $\sim 50,000$ pixel units (4×4 pixel binning). The quantitative attributes of UV spectrophotometry are maintained in the imaging setup and the amount of lidocaine dissolved was calculated from the UV images (Østergaard et al. 2011). In Fig. 1.8, the lidocaine crystal is readily apparent, however, the ability to detect only at one wavelength at a time constitutes a limitation of the imaging approach. Having a single wavelength available only, may make it difficult, and sometimes not

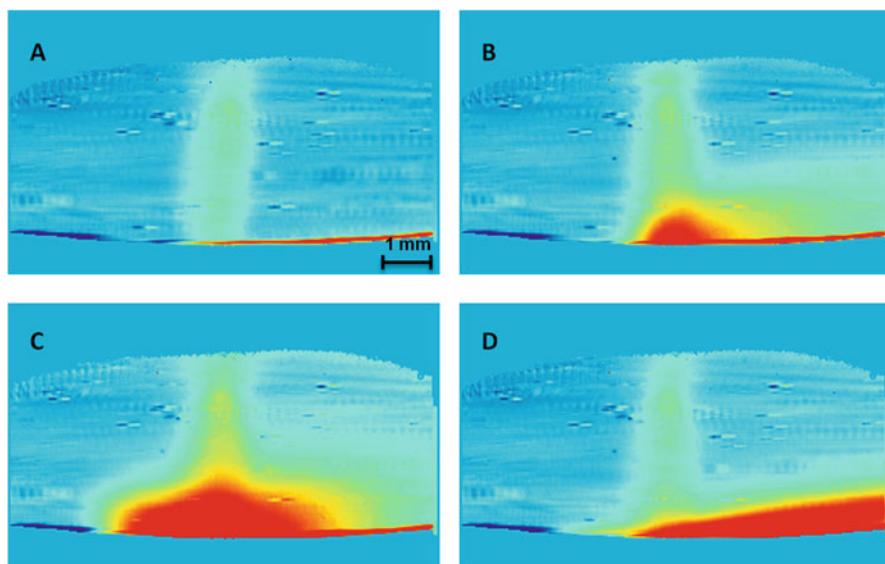


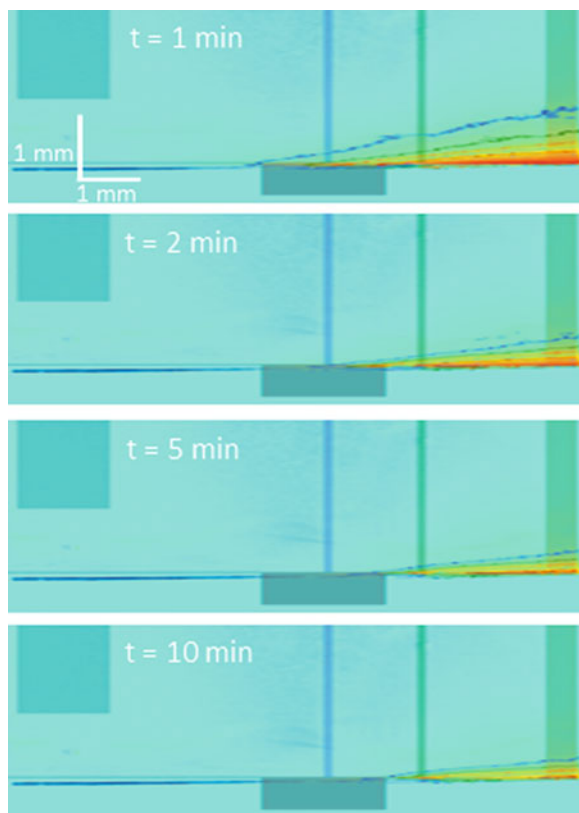
Fig. 1.8 UV imaging of lidocaine dissolution from single crystal positioned vertically in 0.067 M phosphate buffer, pH 7.4. UV images obtained at 254 nm in flow cell, (a) immediately upon filling of the cell ($t = 0$ min), (b) 2 min upon arresting flow, (c) 5 min upon arresting flow, and (d) during flushing the cell with phosphate buffer. With permission from John Wiley and Sons. Copyright © 2011 Wiley-Liss, Inc. (Østergaard et al. 2011)

possible, to differentiate between absorbance, light scattering and physical blocking of light. Thus interpretation of images from dissolution and release experiments involving complex matrixes may be challenging.

Currently the main application of the commercially available UV imaging systems is in dissolution imaging utilizing a flow-through setup (Østergaard et al. 2014a). The Sirius SDI UV imaging instrument is essentially a flow-through alternative to the miniaturized rotating disk intrinsic dissolution testing instrumentation with imaging functionality. It should not be compared to the USP apparatus 4 because the small size will not allow introduction of most intact formulations, such as tablets and capsules, into the system.

Figure 1.9 shows typical UV images obtained during dissolution imaging utilizing the setup illustrated in Fig. 1.5 (Østergaard et al. 2014b). A compact of the drug theophylline (~3 mg) is placed in the shaded region of the image with the surface of the compact flush with the bottom of the flow cell. Dissolution of theophylline from the compact is seen as an increased absorbance downstream from the compact position. Real-time imaging at the sample surface provides information on drug dissolution as well as additional possible dissolution related processes such as compact disintegration, swelling and precipitation events. Using the molar

Fig. 1.9 Selected UV absorbance maps for the dissolution of theophylline anhydrate in water as studied by UV imaging with *in situ* Raman spectroscopy at 1.0 mL/min and 297 nm. Intense red color indicates high absorbance and the contours represent the iso-absorbance lines. With permission from John Wiley and Sons. Copyright © 2014 Wiley Periodicals, Inc. and the American Pharmacists Association (Østergaard et al. 2014b)



absorptivity of the drug and knowledge of flow rate and profile dissolution rates can be calculated from the images leading to dissolution rate versus time profiles. Dissolution UV imaging is still in its infancy; however, the most important applications appear to be ranking of solid forms (polymorphs, hydrates, salts, cocrystals) according to their dissolution rate/behavior for guiding form selection (Boetker et al. 2011; Gordon et al. 2013; Hulse et al. 2012; Niederquell and Kuentz 2014; Østergaard et al. 2011, 2014b; Qiao et al. 2013). Also, troubleshooting or problem solving in cases of unexpected dissolution behavior seem to be an important application. To this end the combination of UV imaging with in situ Raman spectroscopy appears particularly promising since both information of the solution phase and the solid phase is obtained (Østergaard et al. 2014b).

5.2 Drug Diffusion and Release

Provided that the matrix is (sufficiently) transparent at the selected wavelength UV imaging may also constitute an approach for studying drug diffusion and release in gel matrixes. Hydrogels based on the non-ionic poly(ethylene oxide)-poly(propylene oxide)-poly(ethylene oxide) (PEO-PPO-PEO) triblock copolymer Pluronic F127 and on agarose have been applied to UV imaging examining low-molecular weight, peptide and protein diffusion and release behavior (Jensen et al. 2014; Ye et al. 2011). Drug diffusion and release can be studied in quartz cells by positioning the drug-loaded gel or formulation in contact with the acceptor medium which may be a blank hydrogel or an aqueous solution. Real-time absorbance measurement provides spatially (2D) and temporally resolved absorbance maps which with the use of a calibration curve can be converted into concentration maps or images. Image analysis together with Fick's second law form the basis for extracting release rates for various types of formulations and determination of analyte diffusion coefficients (Gaunø et al. 2013; Jensen et al. 2014; Østergaard et al. 2010; Pajander et al. 2012; Ye et al. 2011, 2012). Applications of this kind are very much in their infancy, however, with the advent of larger area imaging systems, UV imaging is likely to become an attractive approach in formulation development giving direct insights into concentration gradients and release processes in real-time.

6 Conclusions and Perspectives

UV and visible spectrophotometry is a widely used analytical method in pharmaceutical research and most likely will continue to be so. Different types of spectrophotometers are available, however, they have in common that are relatively easy to use and provide data, which are easy to evaluate and interpret with short measurement times. Lambert-Beer's law relates absorbance to concentration and provides

the basis for quantitative measurements. Quantification is the main application of UV-vis spectrophotometry, but it also finds use in physicochemical profiling of drug substances such as pK_a determination and kinetic studies. Furthermore, the appearance of absorbance spectra and molar absorption coefficients are helpful in compound identification. UV imaging providing spatially and temporally resolved absorbance measurements has recently been introduced and holds promise in the monitoring of drug transport processes, concentration gradients and related events in drug dissolution and release studies.

References

- Avdeef A (2012) Absorption and drug development. Solubility, permeability and charge state, 2nd edn. Hoboken, Wiley
- Boetker JP, Savolainen M, Koradia V, Tian F, Rades T, Müllertz A, Cornett C, Rantanen J, Østergaard J (2011) Insights into the early dissolution events of amlodipine using UV imaging and Raman spectroscopy. *Mol Pharm* 8:1372–1380
- Connors KA (1987) Binding constants. The measurement of molecular complex stability. Wiley, New York
- Connors KA (1990) Chemical kinetics. The study of reaction rates in solution. VCH Publishers, New York
- Council of Europe (2014) 2.2.25 Absorption spectrophotometry, ultraviolet and visible. In: European Pharmacopoeia, 8.2 edn. Strasbourg, pp 40–42
- Fifield FW, Kealey D (2000) Principles and practice of analytical chemistry, 5th edn. Blackwell, Oxford
- Gaunø MH, Vilhelmsen T, Larsen CC, Boetker JP, Wittendorf J, Rantanen J, Østergaard J (2013) Real-time in vitro dissolution of 5-aminosalicylic acid from single ethyl cellulose coated extrudates studied by UV imaging. *J Pharm Biomed Anal* 83:49–56
- Gordon S, Naelapää K, Rantanen J, Selen A, Müllertz A, Østergaard J (2013) Real-time dissolution behavior of furosemide in biorelevant media as determined by UV imaging. *Pharm Dev Technol* 18:1407–1416
- Görög S (1995) Ultraviolet-visible spectrophotometry in pharmaceutical analysis. CRC Press, Boca Raton
- Hage DS, Carr JD (2011) Analytical chemistry and quantitative analysis. Prentice Hall, Boston
- Hansen SH, Pedersen-Bjergaard S, Rasmussen KE (2012) Introduction to pharmaceutical chemical analysis. Wiley, Chichester
- Hulse WL, Gray J, Forbes RT (2012) A discriminatory intrinsic dissolution study using UV area imaging analysis to gain additional insights into the dissolution behaviour of active pharmaceutical ingredients. *Int J Pharm* 434:133–139
- Implen GmbH (2014) NanoPhotometer® P-Class. <http://www.implen.de/nanophotometer>
- Inman GW, Wethington E, Baughman K, Horton M (2001) System optimization for in situ fiber-optic dissolution testing. Hydrodynamic effects, system performance, and applications. *Pharm Technol* 25:92–100
- Jencks WP (1987) Catalysis in chemistry and enzymology, 2nd edn. Dover, Mineola
- Jensen SS, Jensen H, Cornett C, Møller EH, Østergaard J (2014) Insulin diffusion and self-association characterized by real-time UV imaging and Taylor dispersion analysis. *J Pharm Biomed Anal* 92:203–210
- John RA (1992) Photometric assays. In: Eienthal R, Danson MJ (eds) Enzyme assays. A practical approach. Oxford University Press, Oxford, pp 59–92

- Kazarian SG, Ewing AV (2013) Applications of Fourier transform infrared spectroscopic imaging to tablet dissolution and drug release. *Expert Opin Drug Deliv* 10:1207–1221
- Kempe S, Metz H, Mäder K (2010) Application of electron paramagnetic resonance (EPR) spectroscopy and imaging in drug delivery research—chances and challenges. *Eur J Pharm Biopharm* 74:55–66
- Lu X, Lozano R, Shah P (2003) In-situ dissolution testing using different UV fiber optic probes and instruments. *Dissolut Technol* 10:6–15
- Mantle MD (2013) NMR and MRI studies of drug delivery systems. *Curr Opin Colloid Interface Sci* 18:214–227
- Mirza T, Liu Q, Vivilecchia R, Joshi Y (2009) Comprehensive validation scheme for in situ fiber optics dissolution method for pharmaceutical drug product testing. *J Pharm Sci* 98:1086–1094
- Mura P (2014) Analytical techniques for characterization of cyclodextrin complexes in aqueous solution: a review. *J Pharm Biomed Anal* 101:238–250, <http://dx.doi.org/10.1016/j.jpba.2014.02.022>
- Niederquell A, Kuentz M (2014) Biorelevant dissolution of poorly soluble weak acids studied by UV imaging reveals ranges of fractal-like kinetics. *Int J Pharm* 463:38–49
- Østergaard J, Lenke J, Jensen SS, Sun Y, Ye F (2014a) UV imaging for in vitro dissolution and release studies: initial experiences. *Dissolut Technol* 21(4):27–38
- Østergaard J, Larsen C (2007) Bioreversible derivatives of phenol. 2. Reactivity of carbonate esters with fatty acid-like structures towards hydrolysis in aqueous solutions. *Molecules* 12:2396–2412
- Østergaard J, Meng-Lund E, Larsen SW, Larsen C, Petersson K, Lenke J, Jensen H (2010) Real-time UV imaging of nicotine release from transdermal patch. *Pharm Res* 27:2614–2623
- Østergaard J, Ye F, Rantanen J, Yaghmur A, Larsen SW, Larsen C, Jensen H (2011) Monitoring lidocaine single-crystal dissolution by ultraviolet imaging. *J Pharm Sci* 100:3405–3410
- Østergaard J, Wu JX, Naelapää K, Boetker JP, Jensen H, Rantanen J (2014) Simultaneous UV imaging and Raman spectroscopy for measurement of solvent-mediated phase transformations during dissolution testing. *J Pharm Sci* 103:1149–1156
- Pajander J, Baldursdóttir S, Rantanen J, Østergaard J (2012) Behaviour of HPMC compacts investigated using UV-imaging. *Int J Pharm* 427:345–353
- Perkampus H-H (1992) UV-VIS spectroscopy and its applications. Springer, Berlin
- Picodrop Ltd. (2014) Microlitre spectrometry in a pipette tip. <http://picodrop.com/index.asp>
- Qiao N, Wang K, Schlindwein W, Davies A, Li M (2013) In situ monitoring of carbamazepine-nicotinamide cocrystal intrinsic dissolution behaviour. *Eur J Pharm Biopharm* 83:415–426
- Rouessac F, Rouessac A (2007) Chemical analysis. Modern instrumentation methods and techniques, 2nd edn. Wiley, Chichester
- Skoog DA, Holler FJ, Nieman TA (1998) Principles of instrumental analysis, 5th edn. Saunders College Publishing, Philadelphia
- Sommer L (1989) Analytical absorption spectrophotometry in the visible and ultraviolet. The principles. Elsevier Science Publishers, Amsterdam
- Tam KY, Takács-Novák K (1999) Multiwavelength spectrophotometric determination of acid dissociation constants: Part II. First derivative vs target factor analysis. *Pharm Res* 16:374–381
- Tam KY, Takács-Novák K (2001) Multi-wavelength spectroscopic determination of acid dissociation constants: a validation study. *Anal Chim Acta* 434:157–167
- Thermo Fischer Scientific Inc. (2014) NanoDrop Products. <http://nanodrop.com/Products.aspx>
- Van Eerdenbrugh B, Alonzo DE, Taylor LS (2011) Influence of particle size on the ultraviolet spectrum of particulate-containing solutions: Implications for in-situ concentration monitoring using UV/Vis Fiber-optic probes. *Pharm Res* 28:1643–1652
- Watson DG (2005) Pharmaceutical analysis. A textbook for pharmacy students and pharmaceutical chemists, 2nd edn. Elsevier Churchill Livingstone, Edinburgh
- Wiberg KH, Hultin U-K (2006) Multivariate chemometric approach to fiber-optic dissolution testing. *Anal Chem* 78:5076–5085

- Windbergs M, Jurna M, Offerhaus HL, Herek JL, Kleinebudde P, Strachan CJ (2009) Chemical imaging of oral solid dosage forms and changes upon dissolution using coherent anti-Stokes raman scattering microscopy. *Anal Chem* 81:2085–2091
- Ye F, Yagmur A, Jensen H, Larsen SW, Larsen C, Østergaard J (2011) Real-time UV imaging of drug diffusion and release from Pluronic F127 hydrogels. *Eur J Pharm Sci* 43:236–243
- Ye F, Larsen SW, Yagmur A, Jensen H, Larsen C, Østergaard J (2012) Real-time UV imaging of piroxicam diffusion and distribution from oil solutions into gels mimicking the subcutaneous matrix. *Eur J Pharm Sci* 46:72–78
- Zhang Y, Bredael G, Armenante PM (2013) Dissolution of prednisolone tablets in presence of an arch-shaped fiber optic probe in a USP dissolution testing apparatus 2. *J Pharma Sci* 102:2718–2729

Chapter 2

Fluorescence Spectroscopy: Basic Foundations and Methods

Luis A. Bagatolli

Abstract Fluorescence spectroscopy is a powerful experimental tool used by scientists from many disciplines. During the last decades there have been important developments on distinct fluorescence methods, particularly those related to the study of biological phenomena. This chapter discusses the foundations of the fluorescence phenomenon, introduces some general methodologies and provides selected examples on applications focused to disentangle structural and dynamical aspects of biological processes.

Keywords Light absorption, fluorescence emission • Fluorescence lifetime • Fluorescence polarization • FRET • Fluorescence instrumentation • Fluorophores • Raster imaging correlation spectroscopy

1 A Brief Historical Overview

The oldest known recorded observations on bioluminescent phenomena in nature were made in China, dating roughly from 1500 to 1000 BC regarding glow-worms and fireflies; however, until the full flowering of alchemy in Europe (sixteenth and seventeenth centuries) no effort was directed at understanding and applying knowledge of such phenomena. Luminescence is the spontaneous emission of radiation from a substance. Particularly, the process involves emission of radiation from species in electronically (or vibrationally) excited states not in thermal equilibrium with its environment (Lakowicz 2006; Valeur and Berberan-Santos 2013). There are various types of luminescence and they are classified according to the mode of excitation. For example, fluorescence and phosphorescence are luminescence phenomena in which the excitation mode corresponds to absorption of light (one or more photons) (Lakowicz 2006; Valeur and Berberan-Santos 2013). Thus, to understand fluorescence (or phosphorescence) we need to concern ourselves with how molecules interact with electromagnetic waves (Jameson et al. 2003).

L.A. Bagatolli (✉)

MEMPHYS—Center for Biomembrane Physics, University of Southern Denmark,
Campusvej 55, Odense M 5230, Denmark
e-mail: bagatolli@bmb.sdu.dk

The phenomenon of fluorescence was first described by N. Monardes in 1565. He reported a blue color emerging from an infusion prepared with wood of a Mexican tree called “Coatl” (in Nahuatl language), “Palo Azul” (in Spanish, “blue stick”), or “*Lignum Nephriticum*” (“kidney wood”, scientific name *Eysenhardtia polystachya*). Infusions of this wood (known to Mesoamericans prior to the European invasion) are still used to treat renal and urinary conditions (Fig. 2.1a). This spontaneous emission of radiation was studied by R. Boyle (1664)

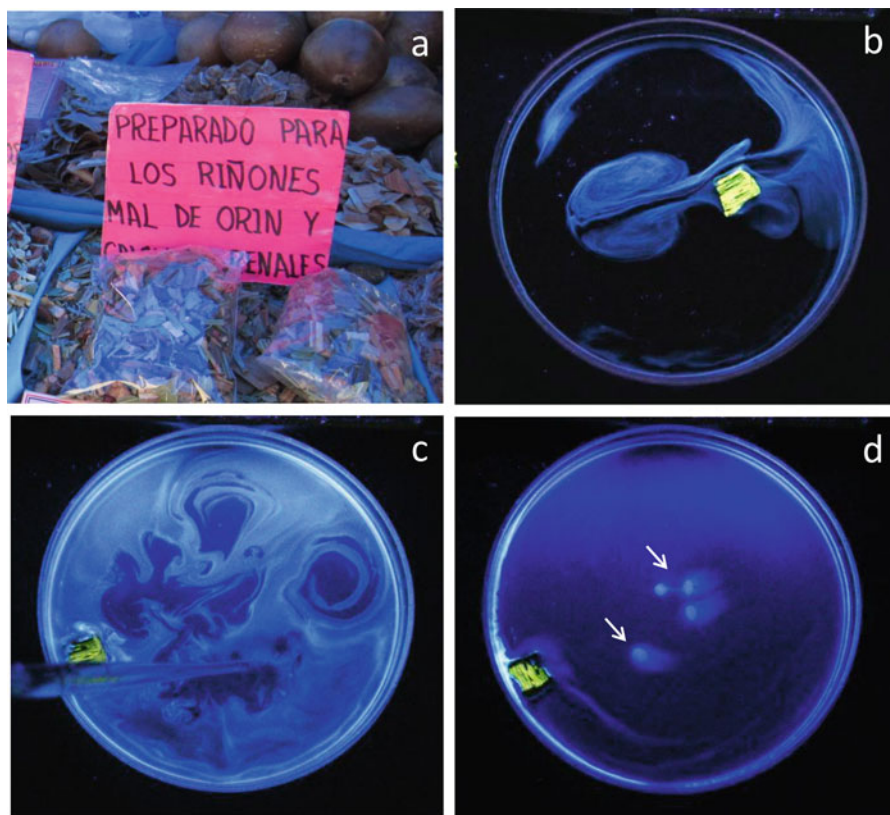


Fig. 2.1 (a) A picture from a market in Tepoztlán (Mexico) showing how the “Palo Azul” is commercialized. The sign (in Spanish) reads “. . .for kidneys (riñones), urinary pain and burning sensation (mal de orin) and kidney stones (calculos renales)”. (b) A piece of this wood is immersed in a basic solution (NaOH) and after a few minutes the fluorescent compound is extracted. Note that a fluorescent signal also emerges from the surface of the wood (which is dry). (c) Addition of HCl to the solution. The dark areas are the result of a quenching mechanism caused by the decrease of the pH where the acid was added. (d) Addition of NaOH pellets to the solution (white arrows). The fluorescence recovery near the pellets is caused by the increase in the local pH. The images in (b), (c) and (d) were taken using a UV lamp as excitation source. The picture included of the Mexican market was kindly provided by Rosario Colin

and I. Newton (1665), among others, in the mid-1600s but its physical basis was not understood (Valeur and Berberan-Santos 2013). Boyle described an interesting property of this infusion, which is the quenching of the fluorescence by addition of acid and its restoration by addition of alkali, constituting one of the first reports on pH indicators (Fig. 2.1b–d). The compound responsible for this phenomenon was identified centuries later and reported to be an end product of a spontaneous oxidation of a flavonoid present in the plant (Acuna et al. 2009). Similarly, phosphorescence was described in 1602 by V. Casciarolo, an Italian shoe-maker. After calcination of a heavy stone (Bologna stone) he noticed that the stone spontaneously glowed after exposure to daylight. The stone contains barium sulfate that after reduction by coal yields barium sulfide, a phosphorescent compound (Valeur and Berberan-Santos 2013). The phenomenon was discussed by Galileo Galilei, among others, who described it “. . . as a certain quantity of fire and light to which the stone was exposed being trapped in the stone and then slowly released from it”, comparing light absorption to that of water by a sponge. As will be discussed later, the best parameter to distinguish phosphorescence from fluorescence is precisely the time scale in which emission occurs after absorption of light.

It was not until the mid-1800s when J. Herschel and G.C. Stokes provided a more systematic description of the fluorescence phenomenon (Lakowicz 2006; Valeur and Berberan-Santos 2013). Using quinine sulfate,¹ Stokes demonstrated that the spontaneous emission of radiation occurs at wavelengths longer than that of the excitation light (a phenomenon presently known as the “Stokes shift”). It was Stokes who coined the term fluorescence to describe this light-induced luminescence. Solid theoretical foundations of fluorescence spectroscopy were not, however, established until the middle of the twentieth by pioneers including Enrique Gaviola, Jean and Francis Perrin, Peter Pringsheim, Sergei Vavilov, Theodore Förster, Alexander Jablonski, and more recently Gregorio Weber (Jameson 1998). A complete chronological list with names and their contributions can be found in Valeur and Berberan-Santos (2013, p. 4).

2 Foundations of the Fluorescence Phenomenon and Typical Fluorescent Parameters

The energy of a photon and therefore the frequency (ν) of the radiation (emitted or absorbed) is given by the Bohr frequency condition:

$$h\nu = \Delta E \quad (2.1)$$

¹ This compound gives the particular bitter flavor to “tonic water”. Due to the presence of quinine sulfate, this beverage emits blue light when it is illuminated with a UV excitation light source.

where ΔE is the energy difference between two electronic states and h is the Planck constant. This relation is often expressed in terms of the wavelength of the radiation as:

$$h\frac{c}{\lambda} = \Delta E \quad (2.2)$$

where c is the speed of light and λ is the wavelength. Notice that the energy is inversely proportional to the wavelength, e.g. ultraviolet (UV) radiation has a shorter wavelength than infrared light (IR), therefore higher energy.

As mentioned, fluorescence is a spontaneous emission of radiation -preceded by absorption of light- from electronically (or vibrationally) excited states species which retain spin multiplicity. This definition generally applies to aromatic organic molecules (conjugated systems) involving $\pi \rightarrow \pi^*$ and $n \rightarrow \pi^*$ transitions (for a more detailed explanation using molecular orbital theory see Valeur and Berberan-Santos (2013, Chap. 2)). Once a molecule is excited to higher energy electronic states ("excited states", S_1 , S_2) it can release this excess of energy by emitting light (fluorescence) therefore returning to the ground state (S_0). However, it is important to consider that there are many other possible pathways for this energy loss or de-excitation (such as intramolecular charge transfer, conformational changes, energy transfer and other radiationless decay pathways) that compete with fluorescence. Consequently, the efficiency with which a molecule emits fluorescent light depends on the rate of fluorescence emission relative to the rate of all other deactivation processes. Figure 2.2 shows a Perrin-Jablonski diagram for molecules (which is an extension of the Bohr-Grottrian diagram for atoms proposed in the 1920s), which illustrates the different processes that can occur between absorption and emission of light. The transitions between distinct states are depicted as colored vertical lines. When an electronic transition takes place it is accompanied by the excitation of vibrations of the molecule, that is, during absorption (~ 10 fs) the nuclei are static but the electrons have acquired extra energy, thus generating coulombic forces among the nuclei (*Franck-Condon principle*). The time scale of the absorption process is fast compared with fluorescence (femtosecond versus nanoseconds) and absorption usually promotes electrons to higher vibrational levels of the electronic excited states (S_1 , S_2). Upon absorption, the system experiences a non radiative process named internal conversion (10^{-12} s or less) which relaxes the system to the lowest vibrational level of S_1 (Fig. 2.2). The energy released during this particular process is generally transferred to the surrounding media (e.g. solvent). The system finally reaches the ground state (S_0) in few nanoseconds by emitting light (fluorescence), typically reaching higher vibrational levels in the ground state, and quickly relaxes (10^{-12} s) to lower vibrational levels reaching thermal equilibrium. Alternatively, the system may experience a type of transition called intersystem crossing, which involves a change in spin multiplicity (occurring in 10^{-10} s). This process leads to the phenomenon of phosphorescence (Fig. 2.2). The characteristic emission of phosphorescence occurs at a much longer time scales, in the order of micro to milliseconds. If the temperature of the system is

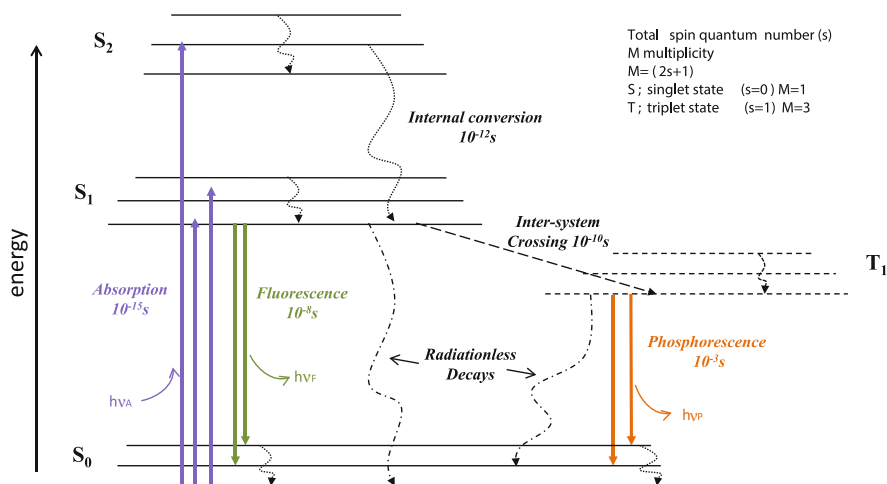


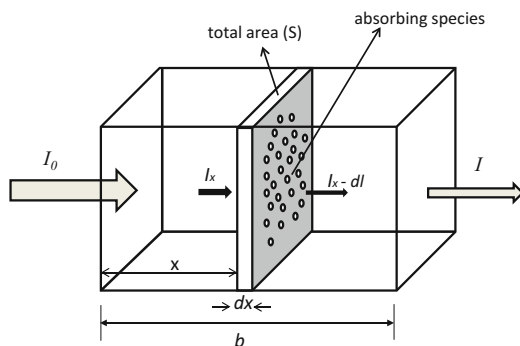
Fig. 2.2 Perrin-Jablonski diagram illustrating different processes occurring between absorption and emission of light. The time scale of the different processes is indicated in the figure. See text for details

very low, the time of the phosphorescence decay can reach minutes. Some important general rules can be elaborated from the Perrin-Jablonski diagram as will be discussed in the following sections.

Absorption of light can also occur by the simultaneous absorption of two or more photons of low energy (infrared light). This phenomenon is termed multiphoton excitation and was theoretically predicted by Marie Goeppert-Mayer early in the 1930s (Lakowicz 2006; Valeur and Berberan-Santos 2013; Diaspro et al. 2006; Ustione and Piston 2011; Bloksgaard et al. 2013). The probability of the occurrence of this phenomenon is particularly low (“forbidden” in quantum mechanical terms) compared to one photon absorption, but achievable using specialized lasers as excitation sources. This mode of excitation also leads to fluorescence, and it is exploited in fluorescence microscopy since it possesses an inherent sectioning effect (Diaspro et al. 2006; Ustione and Piston 2011; Bloksgaard et al. 2013). One of the characteristics of multiphoton absorption is that the radiation absorbed is of longer wavelengths than the fluorescent emission, exactly the opposite of what happens in one photon absorption.

To conclude, it is noteworthy to mention that practically all fluorescence data required for any research project will fall into one of the following categories: fluorescence lifetime, fluorescence quantum yield, fluorescence excitation and emission spectra, or fluorescence polarization. Some general aspects of these distinct (but related) categories will be discussed in the following subsections, including a brief introduction to absorption and derivation of the Beer-Lambert law.

Fig. 2.3 A diagram representing a hypothetical absorbing system used to derive the Beer-Lambert law (see text)



2.1 Absorption and the Beer-Lambert Law

Absorption of light is a central process in fluorescence spectroscopy. Some fundamental properties of this phenomenon are captured in the Beer-Lambert law, which connects the magnitude of light absorption with the concentration of absorbing species in solution. Let us consider a collimated beam of monochromatic light with intensity I_0 striking a solution containing a given absorbing molecule. After passing through the path length b of the sample, which contains n light absorbing molecules/cm³, the intensity of the light reduces to I (Fig. 2.3). Consider now a cross-section of the sample having an area S and an infinitesimal thickness dx placed at a distance x from the surface. The number of absorbing species in this selected portion of the sample is represented as the product of n , S and dx as $=nSdx$. Let σ be the effective cross section² for the absorbing molecules in cm². The area fraction where light gets absorbed *due to each absorbing species* (i.e. *the fractional area for each molecule*) would be $=\sigma/s$ and consequently, the *total fractional area where light gets absorbed for all molecules present in the selected portion of the sample* would be represented by the product $=nSdx \times \sigma/s = \sigma ndx$. If I_x is the light entering the selected infinitesimal portion of the sample, and the light absorbed is dI , the light exiting this infinitesimal portion would be $=I_x - dI$ (Fig. 2.3). The fraction of light absorbed then would be $=\frac{dI}{I_x}$. This quantity is directly proportional to the fractional area occupied by all the molecules in the slab, thus

$$\frac{dI}{I_x} = -\sigma ndx \quad (2.3)$$

where the negative sign is placed to indicate absorption of light. If we integrate Eq. (2.3) from $x = 0$ to $x = b$, where b is the path length (in cm), we get:

² Absorption cross section is a measure of the probability of light absorption occurring in a given compound.

$$\ln \frac{I_0}{I} = \sigma nb \quad (2.4)$$

Equation (2.4) is the Beer-Lambert law. Transforming the number of molecules per cm^3 to concentration (using Avogadro's number and converting cm^3 to liters) we obtain:

$$\ln \frac{I_0}{I} = 6.023 \times 10^{20} \sigma cb \quad \text{or} \quad \log \frac{I_0}{I} = \frac{6.023 \times 10^{20} \sigma}{2.303} cb \quad (2.5)$$

If the absorption cross section is related to the molar extinction coefficient (ϵ) (as $\epsilon = 2.614 \times 10^{20} \sigma$), Eq. (2.5) transforms to the well know Beer-Lambert equation as:

$$A = \epsilon cb \quad (2.6)$$

In Eq. (2.6), A is the absorbance (or optical density; $\log \frac{I_0}{I}$). This parameter has no dimensions, therefore the units of ϵ are $\text{M}^{-1} \text{cm}^{-1}$.

This law governs the amount of light that will be absorbed in terms of the number of absorbing species, the intensity of their absorption and the distance the light travels through the sample. Too high absorbance can be detrimental to correctly measure the concentration of given absorbing species, also compromising accurate measurement of fluorescence. For instance, fluorimeters are designed to detect fluorescent light (which is isotropically emitted) in an orthogonal configuration, i.e. the detectors are placed at 90° respect to the incident excitation beam (see section 4), with the emission optics typically focused in the center of the cuvette. This geometry allows a more complete elimination of the unabsorbed excitation light from the fluorescence signal. However if the sample has a high absorbance, the excitation light will be strongly absorbed near the wall of the cuvette (Fig. 2.4),

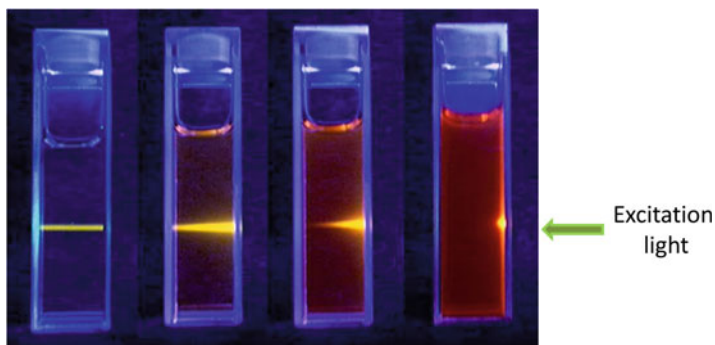


Fig. 2.4 Light absorption and the inner filter effect. The cuvettes contain solutions of Rhodamine B in ethanol and are excited with a green laser. The corresponding absorbance in these solutions (left to right) are 0.04, 1, 3 and >30 . Reprinted from Jameson et al. (2003), with permission from Elsevier

resulting in a weak emission intensity at the center of the cuvette even though the concentration of the fluorescent compound³ is high. Moreover, this phenomenon can cause a distortion of the shape of the emission spectrum due to self-absorption of fluorescent light, particularly at wavelengths where emission and absorption spectra overlap. This is known as the “inner filter effect” and must be taken into account to perform adequate fluorescence measurements (Lakowicz 2006; Valeur and Berberan-Santos 2013; Jameson et al. 2003). A practical way to avoid this effect is to keep the absorbance of the sample below ~ 0.1 . If this is not possible, fluorescence measurements in highly absorbing samples require other strategies, such as the use of special cuvettes with different geometries or shorter path lengths (for details see Lakowicz (2006), Valeur and Berberan-Santos (2013), and Jameson et al. (2003)).

2.2 Fluorescence Lifetimes and Fluorescence Quantum Yields

The fluorescence lifetime (τ) and fluorescence quantum yield (Φ_F) are characteristic parameters of the fluorescence decay. The former refers to the average time a fluorescent molecule resides in the electronic excited state and defines a window of observation of dynamic phenomena. In other words, processes occurring in time scales similar to that of the fluorescence lifetime can affect the fluorescence decay and consequently be detected. Representative examples are those fluorophores that respond to solvent relaxation and polarity, such as the case of 6-acyl-2-dimethylaminonaphthalene compounds (PRODAN, LAURDAN) (Weber and Farris 1979), or the case of 1-anilino-8-naphthalenesulfonate (1,8-ANS) that changes its characteristic lifetime from picoseconds in water to ~ 16 ns when bound to serum albumins (Bagatolli et al. 1996a) (see Sect. 5).

The lifetime of the excited state is defined as:

$$\tau = \frac{1}{\Gamma + k_{nr}} \quad (2.7)$$

where Γ and k_{nr} are the rates of radiative and non radiative decays, respectively. k_{nr} is the sum of all non radiative decays competing with fluorescence. The lifetime of a fluorophore in the absence of non-radiative processes is called the *intrinsic* or *natural lifetime* (τ_n) and it is defined as:

$$\tau_n = \frac{1}{\Gamma} \quad (2.8)$$

³ which will be referred to as “fluorophores” in the rest of this chapter (notice that this type of molecules can be also referred as “fluorescent probes”, or “fluorescent dyes”).

This parameter can be theoretically calculated from the absorption spectra, extinction coefficient and the emission spectra of the fluorophore (see below) using the Strickler-Berg equation (Strickler and Berg 1962):

$$\tau_n^{-1} = 2.88 * 10^{-9} n^2 \left\langle \bar{\nu}_f^{-3} \right\rangle \int_{\Delta\nu_a} \varepsilon(\bar{\nu}) d\ln(\bar{\nu}) \quad (2.9)$$

where

$$\left\langle \bar{\nu}_f^{-3} \right\rangle = \frac{\int_{\Delta\nu_e} F(\bar{\nu}) d\nu}{\int_{\Delta\nu_a} F(\bar{\nu}) \nu^{-3} d\nu} \quad (2.10)$$

n is the refractive index, ε is the molar absorption coefficient, $\Delta\nu_e$ and $\Delta\nu_a$ correspond to the experimental limits of the emission and absorption bands (S_0 and S_1 transitions), respectively, and $F(\nu)$ describes the spectral distribution of the emission of photons per wavelength interval. Equation (2.9) does not consider interactions of fluorophores with the medium (solvent) and other deactivation processes, so the agreement of the calculated values with those obtained experimentally is generally not better than 20% (Jameson et al. 2003).

The fluorescence quantum yield, in turn, refers to the fraction of excited molecules that return to the ground state emitting fluorescence photons. It is defined as the rate of the fluorescence emission divided by the sum of the rates of all deactivation processes:

$$\Phi_F = \frac{\Gamma}{\Gamma + k_{nr}} \quad (2.11)$$

Considering Eqs. (2.7) and (2.8), Eq. (2.11) can be expressed as:

$$\Phi_F = \frac{\tau}{\tau_n} \quad (2.12)$$

If the incidence of non-radiative deactivation processes is small, the value of the experimental lifetime will approach the natural lifetime and Φ_F will tend to 1, indicating that every photon absorbed by the molecule is transforming into a fluorescence photon. The use of fluorophores with a high Φ_F is experimentally convenient since fluorescence photons can be easily detected at low fluorophore concentrations (generally as low as 10^{-9} M using a fluorometer). A practical way to measure Φ_F of a given fluorophore is by comparing its fluorescence yield with a standard, see Lakowicz (2006), Valeur and Berberan-Santos (2013), and Jameson et al. (2003). Tables listing quantum yields of various fluorescent molecules (including standards) can be found in Valeur and Berberan-Santos (2013, pp. 272 and 522).

2.3 Fluorescence Emission Spectra

The wavelength dependence of the fluorescence emission can be analyzed by constructing a spectrum, which reports the intensity of the emitted light versus the wavelength (or alternatively frequency). This can be mathematically expressed as:

$$\int_0^{\infty} F_{\lambda}(\lambda) d\lambda_F = \Phi_F \quad (2.13)$$

where $F_{\lambda}(\lambda)$ represents the fluorescence spectrum, which is characteristic of a given compound in particular conditions. Generally the fluorescence spectrum is reported together with the corresponding absorption spectrum as shown in Fig. 2.5a. In

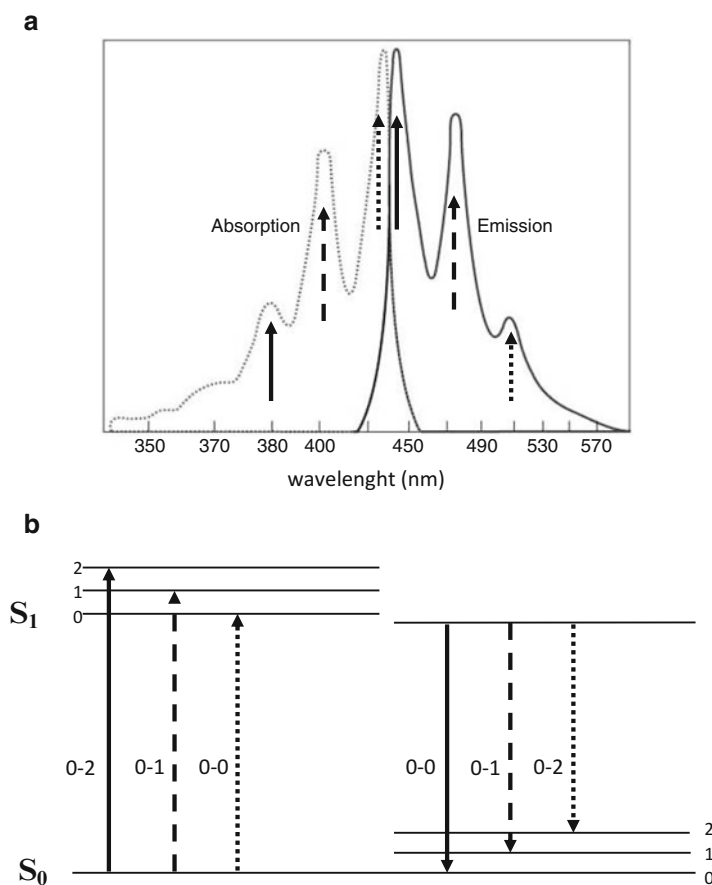


Fig. 2.5 (a) Normalized absorption and emission spectra of perylene in benzene. (b) Simplified Perrin-Jablonski diagram illustrating the mirror image rule

solvents, these spectra exhibit broad and somehow structure-less bands (and not a discrete line at a given wavelength as Fig. 2.2 may suggest), which means that each electronic state consists of an almost continuous manifold of vibrational levels. If the energy difference between the low vibrational levels of S_0 (and S_1) is low enough ($\nu \sim 500 \text{ cm}^{-1}$), excitation can then occur from a vibrationally excited level of the S_0 state (Valeur and Berberan-Santos 2013), which explains why the absorption spectrum can partially overlap the fluorescence emission spectrum (see Fig. 2.5a). In any case, the energy gap between the electronic states S_0 and S_1 is much larger than between vibrational levels, so the likelihood of finding a molecule in S_1 at room temperature is nearly zero.

As mentioned above, the most conspicuous difference between the absorption and the fluorescence spectrum of a given compound is their relative position on the wavelength axis, i.e. the Stokes shift (see Fig. 2.5a). This property is explained by the energy difference of the corresponding electronic transitions (see Fig. 2.2). As expected from Eq. (2.2), the absorption spectrum is located at shorter wavelengths because the magnitude of ΔE associated with the light absorption process is larger than the ΔE of fluorescent emission.

Another important feature of the fluorescence emission spectrum is that its position on the wavelength axis is generally independent of the wavelength used for excitation. This phenomenon has been called Kasha's rule and is a consequence of vibrational relaxation among the excited electronic states (internal conversion, Fig. 2.2). A consequence of the internal conversion is that fluorescence generally originates from the lowest vibrational levels of S_1 . However, some exceptions to the rule have been reported, as for example azulene which emits fluorescence mostly from S_2 (Murata et al. 1972). Finally, it is interesting to notice that the characteristic absorption and fluorescence spectra of some aromatic hydrocarbons (e.g. perylene, anthracene, naphthalene) show vibronic structures, which are specular (Fig. 2.5a). This is interpreted as evidence of similar energy spacing between vibrational levels (along with Franck Condon factors which determine the relative intensities of the vibronic bands) of S_0 and S_1 (Fig. 2.5b), causing the apparent symmetry of the absorption and emission spectra. This effect is known as the "mirror image rule". However, it is important to remark that changes in fluorophore geometry or charge distribution between the excited and ground states often degrade this phenomenon.

To summarize, the fluorescence emission spectrum gives information of all plausible processes occurring during the excited state. The emission spectrum is a fingerprint of a given fluorophore in particular environmental conditions (polarity, temperature, viscosity, pH, ionic strength, etc.) and constitutes a very interesting piece of information to examine potential changes occurring in the local environment of the fluorophore. As an example, the fluorescence response of 6-propionyl-2-dimethylaminonaphthalene (PRODAN) to the polarity of different solvents (Weber and Farris 1979) is shown in Fig. 2.6.

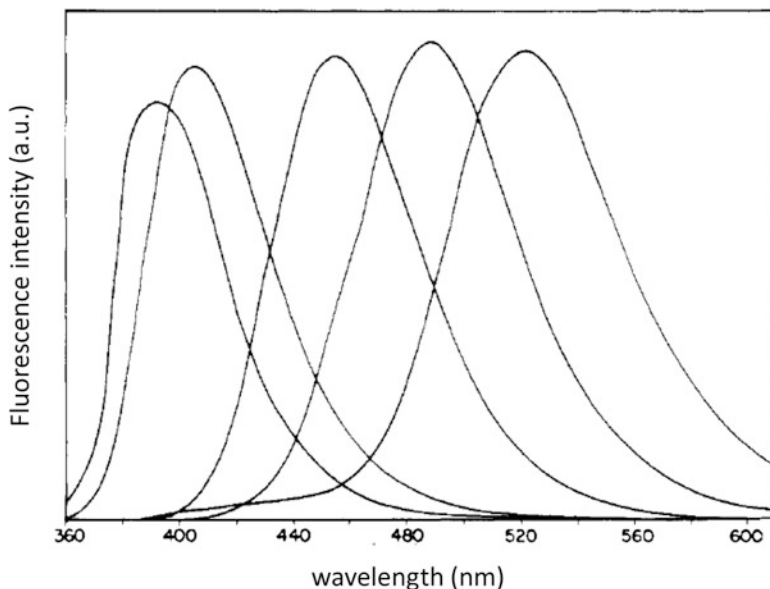


Fig. 2.6 Technical fluorescence spectra of PRODAN solutions excited at 350 nm. The successive maxima correspond (from *left to right*) to cyclohexane, chlorobenzene, dimethylformamide, ethanol, and water. The heights do not reflect relative fluorescence yields. Reprinted with permission from Weber and Farris (1979). Copyright (2013) American Chemical Society

2.4 Fluorescence Excitation Spectra

The excitation spectrum is defined as the fluorescent intensity measured as a function of excitation wavelength at a constant emission wavelength. Generally, this is strongly related to the fluorophore's absorption spectrum, i.e. identical in shape to the absorption spectrum, provided that there is a single species in the ground state. However, if several species are present, or a sole species exists in different forms in the ground state (tautomeric forms, complexes or aggregates) the excitation and absorption spectra are no longer superimposable. Some particular fluorescent molecules, such as the Ca^{2+} indicator fura-2 (Johnson 2010a), shows Ca^{2+} concentration dependent changes in the excitation spectrum. This phenomenon is used to determine changes in Ca^{2+} cellular levels using ratiometric approaches (Isasi et al. 1995), i.e. the fluorescence intensity ratio measured between two excitation wavelengths at a fixed emission wavelength.

2.5 Fluorescence Polarization

The polarization state of fluorescence emission is an important aspect studied since the mid-1800s. In the 1920s F. Weigert found that the fluorescence emission of fluorescent molecules dissolved in glycerol (a very viscous solvent) was partially polarized (Valeur and Berberan-Santos 2013; Jameson et al. 2003). The observed extent of depolarization was found to be dependent on the molecular size and the viscosity of the media, and therefore related to molecular rotations. An important contribution to the understanding this behavior is the work of F. Perrin, who in 1926 derived an equation (now known as the Perrin equation) relating polarization to molecular size, fluorescence lifetime, temperature and solvent viscosity (Perrin 1926). During the 1950s G. Weber made several important contributions (theoretical and experimental (Weber 1952)) to the understanding of fluorescence polarization, with interesting applications to the study of biological systems.

Fluorescence polarization measurements are based on the principle of photoselective excitation of fluorophores by polarized light. If the incident light is linearly polarized the probability of excitation is proportional to the cosine square of the angle between the fluorophore's absorption transition moment⁴ and the electric vector of the excitation light. Under these conditions, fluorophores with their absorption transition moments aligned parallel to the electric vector of the excitation light will be favorably excited. Thus, a solution of fluorophores illuminated by linearly polarized light will render an anisotropic distribution of excited fluorophores, with a concomitant anisotropic fluorescence emission (Fig. 2.7). Any changes in the direction of the transition moment happening during the fluorescence lifetime of the excited state will cause this anisotropic distribution to decrease, inducing a partial or total depolarization of the fluorescence emission light. Common sources of depolarization are non-parallel absorption and emission transition moments, molecular motion (particularly rotational diffusion, see Fig. 2.7), or transfer of the excitation energy to a chemically identical molecule with different orientation (homo-molecular resonance energy transfer). Fluorescence polarization measurements thus, provide an excellent tool to explore molecular mobility (e.g. rotation of macromolecules), molecular shape and size (proteins), macromolecular interactions (protein-protein or protein-ligand), fluidity of a given medium and order parameters in lipid bilayers (see (Lakowicz 2006; Valeur and Berberan-Santos 2013; Jameson et al. 2003; Weber 1952; Eftink 1994)). For example, a widely used technique for clinical analysis for drugs or metabolites is a fluorescence polarization -based immunoassay that uses a special instrument commercialized by Abbot, i.e. the Abbot TDx apparatus (Jameson et al. 2003).

⁴ A transition moment is the electric dipole moment associated with the transition between two electronic states. In general the transition dipole moment is a complex vector quantity. Its direction gives the polarization of the transition, which determines how the system will interact with an electromagnetic wave of a given polarization.

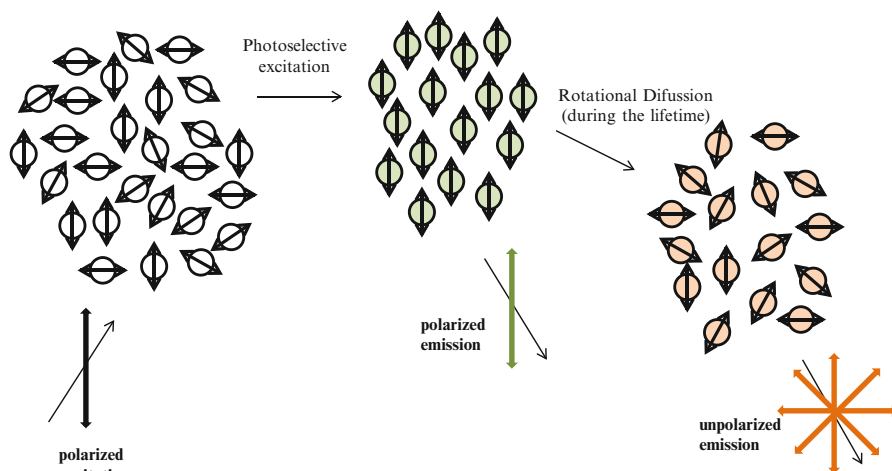


Fig. 2.7 Photoselection effect and the outcome of molecular rotation in the polarization of fluorescence emission light

Relevant mathematical expressions for polarization (P) and anisotropy (r) (both parameters describe the same phenomenon) are:

$$P = \frac{I_{\parallel} + I_{\perp}}{I_{\parallel} + I_{\perp}} \quad (2.14)$$

$$r = \frac{I_{\parallel} + I_{\perp}}{I_{\parallel} + 2I_{\perp}} \quad (2.15)$$

where I_{\parallel} and I_{\perp} are the fluorescence intensities of the vertically and horizontally polarized emission, when the sample is excited with vertically polarized excitation light. In order to measure these parameters a fluorometer equipped with polarizers is required (see Sect. 4 below). Further information on this topic can be found in more comprehensive sources, such as Lakowicz (2006), Valeur and Berberan-Santos (2013), Jameson et al. (2003), and Jameson and Ross (2010).

2.6 Other Useful Fluorescence Related Methods

2.6.1 Quenching of Fluorescence

The measurement of a decrease in the fluorescent intensity of a given fluorophore by addition of ions (Cu^{2+} , I^{-}) or other molecules (acrylamide, O_2) offers a wealth of information. Two processes are involved in this type of phenomenon: (i) a collisional process occurring during the excited state lifetime, named *collisional*

quenching, characterized by a concomitant decrease of the fluorophore's fluorescence lifetime (i.e. the excited state is depleted by collisions of the quencher with the fluorophore, decreasing the probability of fluorescence emission); and (ii) the formation of complexes in the ground state, named *static quenching*, that does not affect the lifetime of the fluorophore. For the former mechanism (collisional quenching) kinetic information of the process can be gleaned using the Stern-Volmer equation:

$$\frac{\tau_0}{\tau} = \frac{F_0}{F} = 1 + k_q\tau_0[Q] \quad (2.16)$$

where F and F_0 are the fluorescence intensity of the fluorophore in absence and presence of the quencher, k_q is the bimolecular quenching constant, τ_0 the fluorescence lifetime of the fluorophore in absence of the quencher and Q the concentration of the quencher. If the quenching process is static equation (2.16) is modified to:

$$\frac{F_0}{F} = 1 + K_s[Q] \quad (2.17)$$

where K_s is an association constant (Lakowicz 2006).

The accessibility of fluorophores to quenchers can be used to determine the location of fluorophores on membranes (Bagatolli et al. 1995) or proteins (Eftink and Ghiron 1981). Additionally, this approach can be used to study membrane or protein dynamics (Lakowicz 2006). For example, in 1973 Lakowicz and Weber reported an O_2 quenching study using a series of distinct proteins (Lakowicz and Weber 1973a, b), revealing that these macromolecules undergo rapid structural fluctuations on the nanosecond time scale. The general conclusion derived from this study was that the functional properties of proteins are not properly represented by rigid models that do not include rapid structural fluctuations, which was the accepted view in 1973.

2.6.2 Förster Resonance Energy Transfer (FRET)

This phenomenon is based on *non-radiative* transfer of energy between two molecules, called donor and acceptor. The transfer of energy is operated by a dipole-dipole interaction that depends on the distance between the molecules, the relative orientation of the dipoles and the extent of overlap between the emission spectrum of the donor and the absorption spectrum of the acceptor. The donor is always a fluorophore while the acceptor does not need to be fluorescent. A complete theory of resonance energy transfer via dipole-dipole interactions was developed by Theodor Förster in 1946 (Clegg 2009). This process may happen also between identical molecules and it is called homo-FRET (for a comprehensive review of homo-FRET see (Jameson et al. 2003)). The rate of energy transfer (k_T) is given by:

$$k_T = \frac{1}{\tau_d} \left(\frac{R_0}{R} \right)^6 \quad (2.18)$$

where τ_d is the fluorescence lifetime of the donor in the absence of acceptor and R the distance between the centers of the donor and acceptor molecules. R_0 is the Förster critical distance at which 50 % of the excitation energy is transferred to the acceptor and is defined as:

$$R_0 = 0.211 (n^{-4} \Phi_{Fd} k^2 J)^{1/6} \quad (2.19)$$

where n is the refractive index of the medium (usually between 1.2 and 1.4), Φ_{Fd} is the fluorescence quantum yield of the donor in absence of acceptor, k^2 is an orientation factor for the donor/acceptor dipole-dipole interaction and J is the normalized spectral overlap integral between the donor fluorescence emission spectrum and the acceptor absorption spectrum.

The efficiency of energy transfer (E) can be expressed as:

$$E = \frac{k_T}{k_T + \sum_{i \neq T} k_i} \quad (2.20)$$

where k_T is the rate of transfer and k_i are all other deactivation processes.

Experimentally, E can be calculated from the fluorescence lifetimes or emission intensities of the donor determined in absence (τ_d and F_d respectively) and presence (τ_{da} or F_{da} respectively) of the acceptor as:

$$E = 1 - \frac{\tau_{da}}{\tau_d} \quad \text{or} \quad E = 1 - \frac{F_{da}}{F_d} \quad (2.21)$$

The distance between the molecules that constitute a given FRET pair can then be calculated, knowing the corresponding Förster critical distance R_0 , as:

$$R = \left(\frac{1}{E} - 1 \right)^{1/6} R_0 \quad (2.22)$$

Distances can generally be measured between $\sim 0.5 R_0$ and $\sim 1.5 R_0$. The information obtained from this method is analogous to a hypothetical “spectroscopic ruler”, allowing the determination of distances between molecules from 10 to 100 Å! Typical applications use of FRET to monitor protein-protein interactions (e.g. one labeled with the donor and the other with the acceptor) or structural changes of macromolecules labeled with the donor-acceptor pair at different positions (Coutinho et al. 2007). Further reading (including examples) can be found in Lakowicz (2006), Valeur and Berberan-Santos (2013), and Clegg (2009).

2.6.3 Fluorescence Fluctuations-Based Approaches

The fluorescence properties and methods presented in the previous subsections can also be implemented in fluorescence microscopy, where the phenomena can yield spatially resolved information (Lakowicz 2006; Valeur and Berberan-Santos 2013). Spatial resolution provides information not available from classical fluorescence spectroscopy experiments in a cuvette, where only average bulk-sample information is obtained. Several fluorescence microscopy methods have been developed that rely on the analysis of fluorescence fluctuations. These approaches have become increasingly popular in the last few years (Lakowicz 2006; Valeur and Berberan-Santos 2013; Digman and Gratton 2012; Jameson et al. 2009), offering very interesting applications on structurally complex specimens such as cells and tissues (Digman and Gratton 2012; Jameson et al. 2009; Brewer et al. 2013). Here particular emphasis will be placed on one of these methods, called raster imaging correlation spectroscopy (RICS), and illustrate this method with an example in Sect. 5. RICS provides spatially resolved information on the diffusion coefficients of fluorophores using the temporal and spatial information inherent to the fluorescence scanning confocal image⁵ (Digman and Gratton 2012; Digman et al. 2005a, b). The principle of the technique is best explained by considering a diffusing fluorescent particle during scanning confocal image acquisition. Because of its inherent diffusion and the finite time of the scanning system, this fluorescent particle can be detected in multiple pixels, leading to a characteristic spatial distribution of the signal. Thus, information on the particle's travels in the sample can be obtained using a 2D spatial correlation analysis of the image, which provides information on diffusion coefficients of fluorophores from the regions of interest. Additionally, the technique also provides information on the number of fluorescently labeled particles in the sample. For this type of analysis the physical characteristics of the laser scanning confocal microscope (such as the pixel dwell time, line scanning time, and pixel size) must be known (Digman and Gratton 2012; Digman et al. 2005a, b). Moreover, the joint diffusion of molecules (which implies spatial colocalization of these molecular species) can be studied using cross-correlation RICS (cc-RICS). This approach can detect for example, whether two distinct fluorophores diffuse together or not (Brewer et al. 2013). The spatial resolution in this type of experiments is ~ 250 and ~ 600 nm in the radial and axial directions, respectively.

⁵The principle of confocal imaging was patented in 1957 by Marvin Minsky and aims to overcome some limitations of traditional wide-field fluorescence microscopes, which lack resolution in the axial direction. A confocal microscope uses scanned point illumination and a pinhole in an optically conjugate plane in front of the detector to eliminate out-of-focus signal. As only light produced by fluorescence very close to the focal plane a section with variable width (in the order of 0.6 μm or more) can be obtained.

3 Fluorescence Markers and Reporters

Many different types of fluorophores have been characterized to perform studies in biological systems. This includes a large selection organic molecules (which is the main focus in this chapter) as well as some inorganic compounds (e.g. quantum dots (Lakowicz 2006; Valeur and Berberan-Santos 2013)). Fluorophores are used, generally in very low amounts, to stain certain structures (tissues, cells, or other materials), as a substrate for enzymatic reactions, as sensors (whose fluorescence decay is affected by processes in the local environment of the fluorophore) or covalent tags of macromolecules serving as affinity markers or bioactive reagents (e.g. antibodies, peptides).

Depending on whether they are constituent parts of the systems under study, fluorescent molecules can be divided in two families. The first contains naturally occurring fluorescent compounds which can be analyzed directly in the systems of interest. Representative examples are the aromatic amino acids phenylalanine (ex/em 260 nm/282 nm), tyrosine (ex/em 280 nm/305 nm) and tryptophan (ex/em 280, 295 nm/305–350 nm); green fluorescent protein (GFP, see below); and cofactors such as NADH (Ex/Em 340/460 nm), FAD⁺ (ex/em 450 nm/540 nm) and porphyrins (ex/em 550 nm/620 nm). A typical experimental application with such fluorophores is the use of the fluorescence emission spectra of aromatic amino acids to monitor denaturation of proteins (or interactions involving these macromolecules). This experimental strategy is based on the polarity sensitive nature of the fluorescence emission spectrum, which drastically changes when the structure of the protein is unfolded (Eftink 1994).

The second family is composed of fluorophores that are added to the system under study. The number of molecules in this family is very large and continuously growing (Johnson 2010b) and comprises fluorescent markers -that can be non-covalently or covalently attached to macromolecules- and fluorescent reporters, i.e. molecules sensitive to pH or other ions (e.g. Ca²⁺, K⁺, Na⁺), oxidation states, polarity or membrane potential. Examples of these compounds are rhodamine, fluorescein, dialkylcarbocyanines (e.g. DiI, DiO), perylene, pyrene, Cy3, Cy5, DAPI, DPH, parinaric acid, 1,8-ANS, LAURDAN, PRODAN, or the Bodipy, Atto and Alexa derivatives (just to mention few, see Fig. 2.8 for some examples). One of the many examples of applications of *extrinsic* fluorescent molecules is the case of the amphiphilic fluorophore LAURDAN (Bagatolli 2013), which is used to study structural and dynamical aspects of artificial and biological membranes. The fluorescence decay of LAURDAN is responsive to water dipolar relaxation processes, which drastically depend on membrane lateral structure. For example, during a phase transition process in model bilayers, the lateral packing of the membrane changes from a crystalline-ordered to a liquid-disordered structure, disturbing the associated interfacial water dynamics. During this process LAURDAN fluorescent emission shows a shift in the emission maximum of ~50 nm (from blue to green), making it a very sensitive tool to study membrane lateral structure (Bagatolli 2006, 2013; Parasassi and Gratton 1995; Parasassi et al. 1998). LAURDAN is chemically related with PRODAN, whose

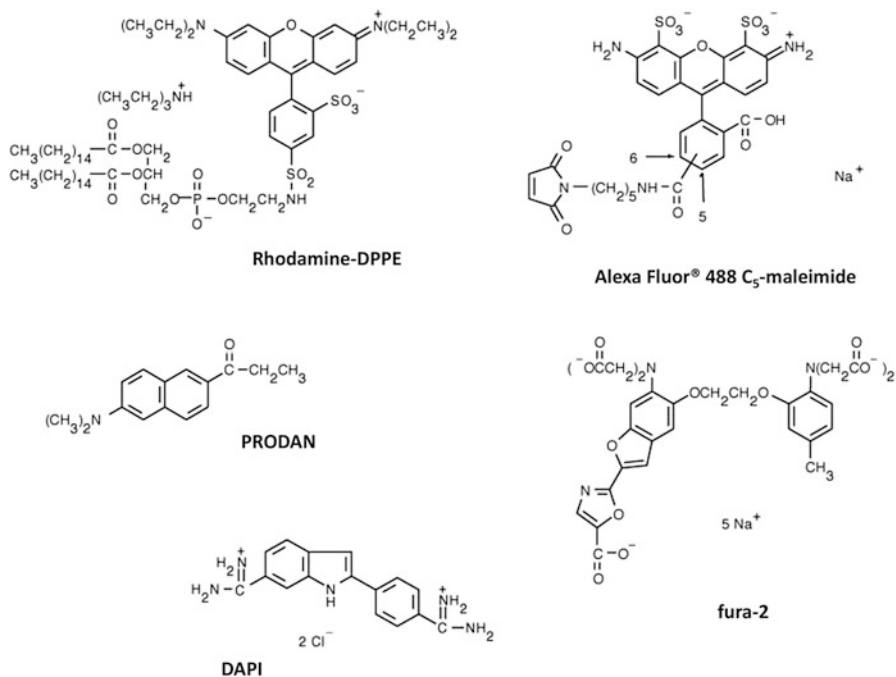


Fig. 2.8 Representative selection of extrinsic fluorescent molecules, including a membrane marker (Rhodamine-DPPE), a polarity sensitive fluorophore (PRODAN), a Ca²⁺ indicator (fura-2), a DNA marker (DAPI) and a thiol reactive probe (Alexa Fluor[®] 488 C₅-maleimide) which is used to label proteins containing cysteine residues

spectral response to solvents is shown in Fig. 2.6. PRODAN is also used to study the lateral structure of membranes (Parasassi et al. 1998) and also to monitor conformational changes in proteins (Lasagna et al. 1996).

To conclude with this section fluorescent proteins, which comprise a special subfamily of extrinsic fluorophores, will be briefly discussed. Recent progress in understanding protein interactions (and protein distributions) in cellular systems has been largely based on labeling methods making use of the green fluorescent protein (GFP) (Tsien et al. 1998). GFP is a protein composed of 238 amino acids (26.9 kDa), isolated from the jellyfish *Aequorea victoria*, which exhibits bright green fluorescence when exposed to blue light. GFP has a major absorption peak at 395 nm and a minor one at 475 nm. Its emission peak is at 509 nm, which is in the lower green portion of the visible spectrum. In cell and molecular biology, the GFP gene is frequently used as a marker by genetically fusing GFP to the protein of interest. The GFP gene can be introduced into organisms and maintained in their genome through breeding, injection with a viral vector, or cell transformation. This strategy constitutes an important advantage when compared with the use of regular fluorescent markers, where targeting a specific protein inside a cell is virtually impossible without disrupting the cell. To date, the GFP gene has been introduced and expressed in many bacteria, yeast and other fungi, fish (such as zebrafish),

plant, fly, and mammalian cells, including human, and used to produce biosensors in modified forms (Tsien et al. 1998). Martin Chalfie, Osamu Shimomura and Roger Y. Tsien were awarded the 2008 Nobel Prize in chemistry “for the discovery and development of the green fluorescent protein, GFP”. This strategy also encompasses the use of other fluorescent proteins from other organisms, or mutations on GFP, that give access to different fluorescent colors.

4 Some Instrumental Considerations

Fluorometers are general-purpose instruments designed to measure fluorescence spectra, polarization and/or lifetime. A typical fluorometer includes a light source, a specimen chamber with integrated optical components, and high sensitivity detectors (Fig. 2.9). Recalling that fluorescence light is isotropically distributed in space (it can be detected in all directions); the optical paths for excitation and emission light detection are placed along the orthogonal axis (“T” configuration, see

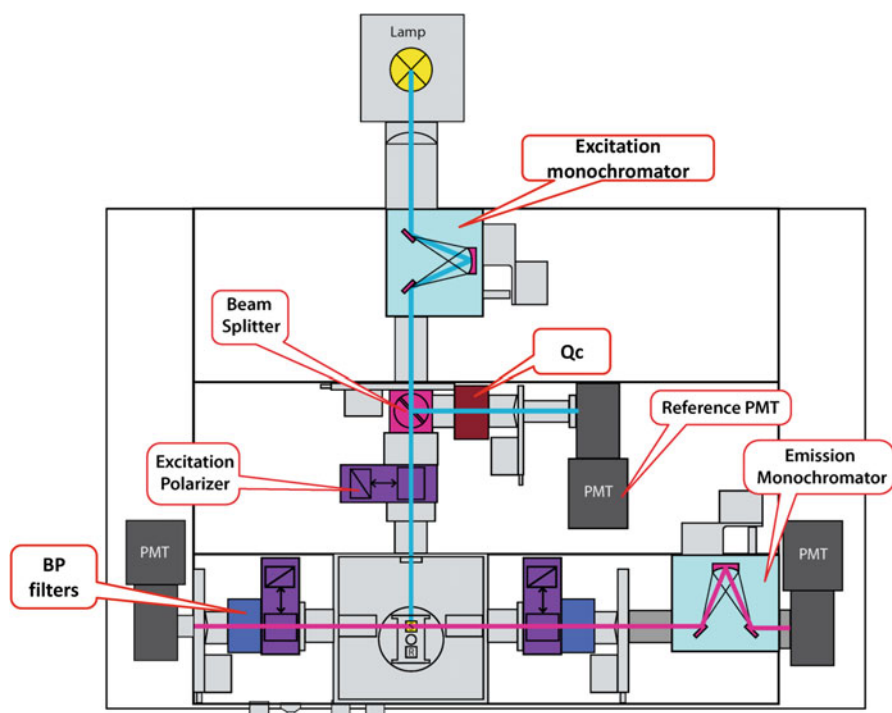


Fig. 2.9 Schematic diagram of a fluorometer (revised with permission from commercial literature from ISS, Champaign, IL). The principal components include the xenon arc lamp, excitation and emission monochromators, three slots to adapt band pass (BP) filters, a quartz beam splitter, a quantum counter solution (Qc), three photomultiplier tubes (PMT) and three calcite prism polarizers

Fig. 2.9). This orthogonal arrangement ensures minimal leakage of excitation light into the fluorescence emission detection side. Common excitation sources used in commercially available fluorimeters are Xenon Arc Lamps, which provide a relatively uniform intensity over a broad spectral range from the UV to the near IR. Alternatively, monochromatic light sources such as light emitting devices (LEDs, e.g. diodes, laser diodes and lasers) are used as well, particularly for dynamic measurements (e.g. fluorescence lifetimes). High sensitivity photodetectors are commonly used in fluorimeters, such as photomultipliers (allowing acquisition in analog or photon counting mode) or charged coupled device cameras (see Lakowicz 2006, Chap. 2)). For spectral measurements monochromators or band pass filters are placed in the excitation and emission light path to select specific spectral bands (see Fig. 2.8) (Jameson et al. 2003). Some commercial equipment such as the one described in Fig. 2.9 also includes polarizers, allowing fluorescence polarization or anisotropy measurements (Sect. 2.5).

4.1 Steady State Fluorescence Excitation and Emission Spectra

There are some practical aspects concerning measurements of fluorescence spectra that are important to recognize. One of them is illustrated in Fig. 2.10, which corresponds to an emission scan obtained in absence of fluorophores using simply water. In this particular case the excitation wavelength was placed at 300 nm. Different peaks are apparent in this “fluorophore-less” spectrum, corresponding to

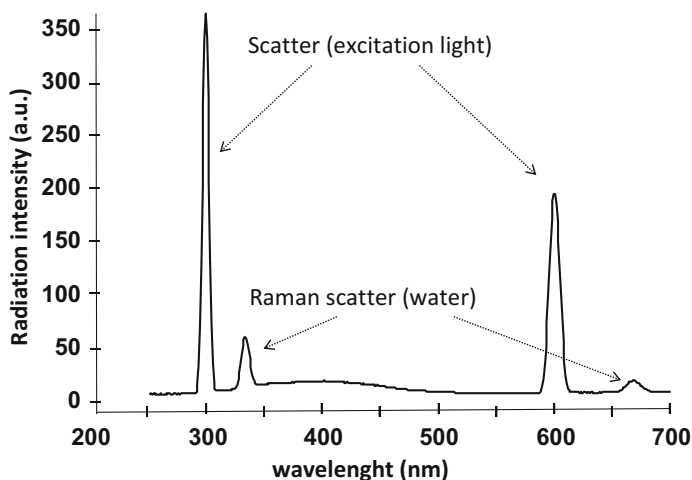


Fig. 2.10 Emission scan from 250 to 700 nm with excitation at 300 nm, peaks correspond (from left to right) to Rayleigh scatter (300 nm), Raman scatter (334 nm), second order Rayleigh (600 nm) and second order Raman (668 nm)

Rayleigh scatter of the excitation light and the Raman scatter of water. Under particular experimental conditions these effects can alter the shape of emission spectra. The Rayleigh scatter is prominent precisely at wavelength regions corresponding to the excitation wavelength, and it is generally avoided by choosing appropriate spectral bands for the acquisition of fluorescence spectra (e.g. excluding the excitation wavelength). Additional long pass band filters excluding the excitation wavelength can be placed in front of the detector to minimize this effect. The Rayleigh scatter is particularly important in turbid samples (e.g. membrane suspensions), and its effect can be circumvented by different strategies involving alternative cuvette geometries or cuvettes with shorter optical lengths (Lakowicz 2006; Jameson et al. 2003). The Raman effect corresponds to a quasi-elastic scatter of water (O-H stretching mode) and this peak may become relevant when very low concentrations of fluorophores (or fluorophores with a low Φ_F) are used. An important feature of the Raman peak is its dependence on the excitation wavelength, something that does not occur for fluorescence (recall Kasha's rule discussed in Sect. 2.3)). A simple equation to identify the position of the water Raman peak is given by the following equation:

$$\frac{1}{\lambda_R} = \frac{1}{\lambda_{Ex}} - 0.00034 \quad (2.23)$$

where λ_R and λ_{Ex} are the Raman and excitation wavelengths respectively (Jameson et al. 2003). Another important instrumental factor known as Wood's anomaly, refers to a surface plasmon polariton process occurring on the surface of the diffraction gratings placed in the monochromators (Jameson et al. 2003; Maystre 2012). This phenomenon that results in a wavelength dependent -horizontally polarized- additional signal may affect the shape of fluorescence emission spectra. It can be eliminated by placing the emission polarizer in a vertical position. Although different adjustments can be implemented by the user concerning the acquisition of fluorescence emission spectra (Jameson et al. 2003), the fluorometer manufacturers generally provide correction files that can correct the output data for slit size, position of polarizers, Wood's anomalies, etc.

The acquisition of excitation spectra also requires corrections since the energy response of the excitation source (lamps) is not constant along the UV-visible- near IR range. This correction is generally performed with a quantum counter, usually a concentrated solution of Rhodamine B in ethylene glycol, which has a linear fluorescence emission response in a broad excitation wavelength range (200–600 nm). The idea behind this procedure is to perform a simultaneous ratiometric measure between the fluorescence intensities of the sample and the quantum counter at the different excitation wavelengths. By applying this procedure, any energy fluctuation coming from the excitation source will be eliminated during the acquisition of the excitation spectra. The quantum counter is generally placed in a reference channel in the fluorometer, as indicated in Fig. 2.9. A complete list of quantum counters with proper references can be found in Lakowicz (2006, pp. 52). Last but not least, it is important to consider that cuvettes used to measure fluorescence have intrinsic absorption properties depending on the cuvette material.

For example, quartz cuvettes are required to measure absorption and fluorescence in the UV spectral range since glass or plastic absorb light at these wavelengths. The same considerations apply to solvents used in the experiments since many organic solvents show strong light absorption, particularly in the UV region.

4.2 Fluorescence Lifetimes

There are two different ways to measure fluorescence decays, termed “time domain” and “frequency domain” techniques (Lakowicz 2006; Valeur and Berberan-Santos 2013; Jameson et al. 2003). The former directly measures the time decay of fluorescent emission after a short pulse (shorter than the lifetime) of excitation light. The latter indirectly measures the lifetime by analyzing the extent of demodulation and phase shift of the fluorescence light with respect to a modulated excitation light. The frequency domain method will be briefly referred to below. For further reading on the theoretical, experimental and instrumental aspects of these methods (Lakowicz 2006; Valeur and Berberan-Santos 2013; Jameson et al. 2003; Gratton et al. 1984) are highly recommended.

In multifrequency domain measurements the fluorophore is excited by a light source oscillating at a high frequency (generally in the MHz range to overlap the nanosecond time range of fluorescence lifetimes) (Gratton et al. 1984). The resultant fluorescence signal is also modulated at the same frequency but, since there is a finite fluorescence lifetime, is phase-delayed and amplitude-demodulated. The phase delay and modulation ratio contain the lifetime information of the fluorophore (equations are included in Fig. 2.11) and can be measured using heterodyning or homodyning detection techniques (Gratton et al. 1984). A typical data representation is shown in Fig. 2.11 (inset). Measurements generally require the use of fluorescence lifetime standards. Further details regarding experimental considerations (polarization effects, proper selection of standards) and more comprehensive instrumental information can be found in Lakowicz (2006), Valeur and Berberan-Santos (2013), and Jameson et al. (2003).

Generally, the time dependent fluorescence intensity decay can be described as:

$$I_t = \alpha e^{-\frac{t}{\tau}} \quad (2.24)$$

where I_t is the intensity at time t , α is a normalization term (the pre-exponential factor) and τ is the lifetime. This expression assumes that the decay is monoexponential (63% of the molecules have decayed prior to $t = \tau$ and 37% decay at $t > \tau$), which is not always the case (sometimes two or more exponents are required to properly fit the data). Other models used to fit fluorescence decays make use of Gaussian and Lorentzian distributions (Alcala et al. 1987a, b, c). More recently, an approach named “phasor analysis” which offers a “model free analysis” has proven very useful to perform lifetime analysis (both in cuvette and microscopy experiments) (Digman et al. 2008; Stefl et al. 2011). To conclude with this section it

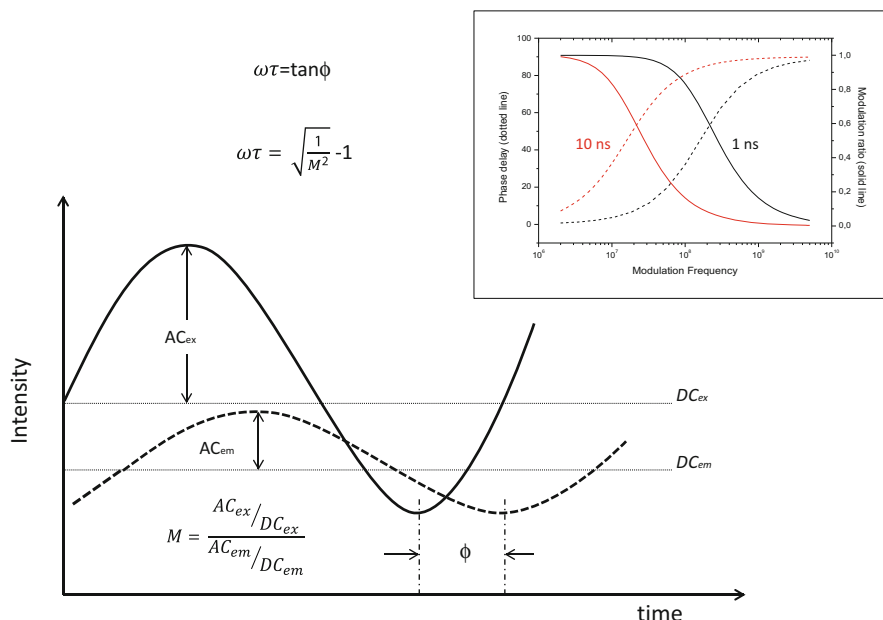


Fig. 2.11 Sketch showing the definitions of the phase angle and the demodulation of fluorescence emission. The mathematical expressions relating the phase angle (ϕ) and modulation ratio (M) with the lifetime are included at the *top* of the figure. The *inset* illustrates two simulations assuming single exponential decays of 1 and 10 ns respectively, where the evolution of M and ϕ vs. the modulation frequency of the excitation light is shown

should be mentioned that fluorescence lifetime measurements can also be performed in a fluorescence microscope. This technique is called fluorescence lifetime image (FLIM) (van Munster and Gadella 2005) and allows spatially resolved lifetime information. This information is particularly useful to study complex specimens such as cells or tissues, where the degree of labeling cannot be easily controlled. In contrast to fluorescence intensity, fluorescence lifetime is independent of the probe concentration (Bloksgaard et al. 2013), providing a direct indication of changes in the fluorophore's environment.

5 Pharmaceutical Applications

5.1 Human Serum Albumin: Drug Interactions Studied by Fluorescence Methods

1-Anilino-8-naphthalenesulfonate (1,8-ANS) is a fluorescent molecule that binds with high affinity to hydrophobic surfaces of proteins (Hawe et al. 2008) as well as membranes (Slavik 1982). The fluorescence properties of this molecule are

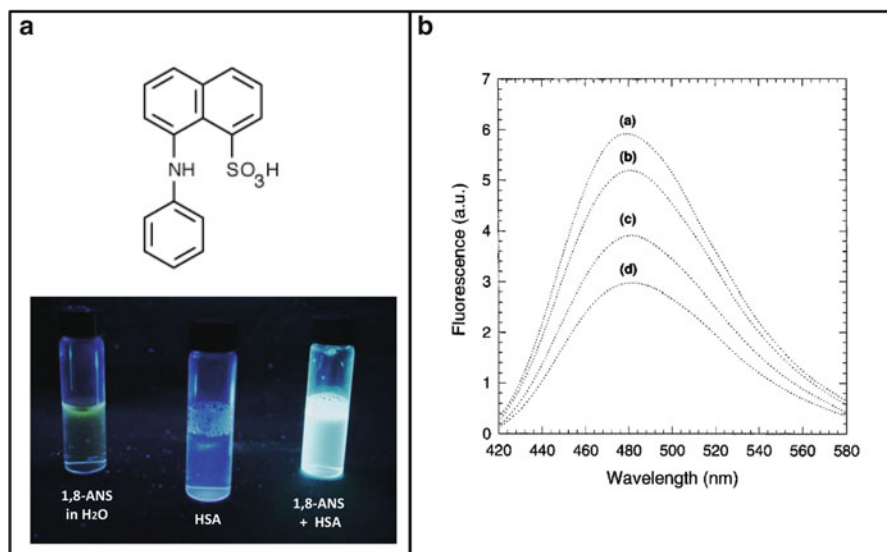


Fig. 2.12 (a) Molecular structure of 1,8-ANS and a picture comparing the fluorescent response of 1,8-ANS in water and in a solution of human serum albumin. From this picture the increase in the fluorescence quantum yield of the probe in presence of the protein is apparent. (b) Displacement of 1,8-ANS by diazepam. The graph shows the steady state fluorescence spectra of the fluorophore bound to HSA in the absence (a) or in the presence of 25 μM (b), 100 μM (c), or 150 μM (d) diazepam. 1,8-ANS and HSA concentrations were 12.5 μM and 1.25 μM, respectively. The calculated dissociation constant for diazepam was 1×10^{-5} M. Adapted from Bagatolli et al. (1996b)

extremely sensitive to polarity. For example, the Φ_F of 1,8-ANS is very low in water ($\Phi_F = 3.5 \times 10^{-3}$) compared with methanol ($\Phi_F = 0.21$) or bound to nonpolar surfaces of proteins ($\Phi_F = 0.67$ for bovine or human serum albumins) (Bagatolli et al. 1996a, b) (Fig. 2.12a). Thus, these properties make 1,8-ANS well suited for determining the affinity of hydrophobic ligands to their corresponding binding proteins (Hawe et al. 2008).

The interaction of 1,8-ANS with serum albumins was first reported in 1954 by G. Weber (Weber and Laurence 1954) and in many papers since (Weber and Young 1964; Weber and Daniel 1966; Daniel and Weber 1966). This section will concentrate on one study performed with human serum albumin (HSA) using frequency domain fluorometry (Bagatolli et al. 1996a). This work showed that HSA has two distinguishable fluorescent sites, depending of the ANS/serum albumin ratio. Above a 1:1 mol ratio of 1,8-ANS:HSA, the fluorescence emission spectra can be resolved into two components: (i) component 1 with a fluorescence lifetime of 16 ns ($\Phi_F = 0.67$) and a $\sim\lambda_{\max}$ of 478 nm (which is dominant below the 1:1 mol ratio); and (ii) component 2 with an average fluorescence lifetime of 3 ns ($\Phi_F = 0.11$) and a $\sim\lambda_{\max}$ of 483 nm. This information allowed fitting the binding of the fluorophore with a model of two independent binding sites, with dissociation constants of

1.15×10^{-6} M (capacity of 1 mol of 1,8-ANS per mol of HSA, site 1) and 1.27×10^{-5} M (capacity of 2.34 mol of 1,8-ANS per mol of HSA, site 2). The fluorescent site 1 was related to the IIIA subdomains of the protein (He and Carter 1992) and is implicated in the binding of many different drugs (such as diazepam or aspirin) (Bagatolli et al. 1996a). One of the results of this study was an easy steady-state method to perform competition experiments with different drugs interacting with HSA (see Fig. 2.12b) (Bagatolli et al. 1996b). This approach offered several advantages over classical methods such as equilibrium dialysis techniques: it is faster, cheaper, and requires a simple mathematical treatment to extract dissociation constants. It has also been successfully applied to study the interaction of herbicides with serum albumins (Rosso et al. 1998).

5.2 Do Liposomes Penetrate Skin?

Liposomes have been suggested as delivery systems for drugs through the skin (Cevc 1997, 2003, 2004; van Kuijk-Meuwissen et al. 1998). Although studies applying different techniques have been conducted to document the penetration of liposomes into skin such as transmission electron microscopy (Bouwstra and Honeywell-Nguyen 2002; Honeywell-Nguyen et al. 2004, 2006), tape stripping (Honeywell-Nguyen et al. 2004), laser scanning confocal and multiphoton excitation fluorescence microscopy (van Kuijk-Meuwissen et al. 1998; Alvarez-Roman et al. 2004; Cevc et al. 2002; Carrer et al. 2008; Simonsson et al. 2011), no conclusive evidence has been presented so far to answer how exactly it is that liposomes facilitate transdermal penetration of drugs. Recently, ccRICS has been applied to evaluate *the integrity* of liposomes during transdermal penetration experiments (Bloksgaard et al. 2013; Brewer et al. 2013). As mentioned above (Sect. 2.6) this technique can determine whether or not two different fluorescent species diffuse together. The strategy presented in this work is based on the production of liposomes labeled with two different fluorophores (Brewer et al. 2013), one placed in the liposome membrane and another in the liposome lumen (summarized in Fig. 2.13a); a high cross correlation is expected between the two fluorescent signals *if, and only if*, the liposomes are intact and the “cargo” travels with the vesicle. While a maximum extent of cross correlation is observed for liposomes in buffer, a sporadic cross correlation was obtained on the surface of the skin and, interestingly, no cross correlation at all was measured within the skin stratum corneum (SC; the outermost layer of skin where the barrier function of the tissue occurs) as indicated in Fig. 2.13b (Brewer et al. 2013). Remarkably, measures within the SC showed that the diffusion coefficients measured for both fluorescent labels were not different in presence or absence of liposomes. In addition, RICS measurements in the presence of liposomes showed that the *number of fluorescent molecules* obtained for the membrane marker differ between buffer and the skin SC. This observation rules out cargo leakage from the liposomes, suggesting that

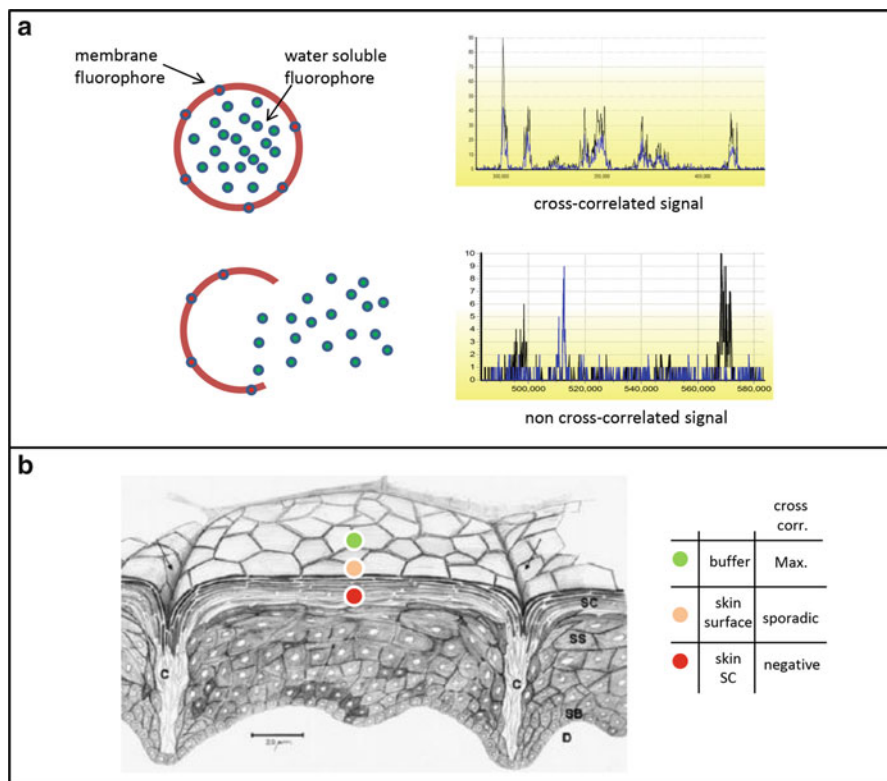


Fig. 2.13 (a) Sketch of doubly labeled liposomes and the corresponding fluorescence fluctuations for both fluorophores (*black and blue lines*) when liposomes are intact or destroyed by the addition of detergent. (b) A graphical representation summarizing the RICS results showing the cross-correlated signal in buffer (far from the skin surface), the sporadic cross-correlation at the skin surface and the lack of correlation deep into the skin stratum corneum

liposomes start to burst as soon as they reach the skin surface (Brewer et al. 2013). Finally, it was also shown that when liposomes are injected in the skin directly below the SC, the cross-correlation is maintained. All these results led to the conclusion that the integrity of liposomes is highly compromised by the skin barrier. With regard to the spatially resolved information provided by imaging, RICS allows to construct diffusion maps of fluorophores in the tissue at different depths (Fig. 2.14). This capability of the technique provides relevant information to explore tissue heterogeneity (Bloksgaard et al. 2013; Brewer et al. 2013).

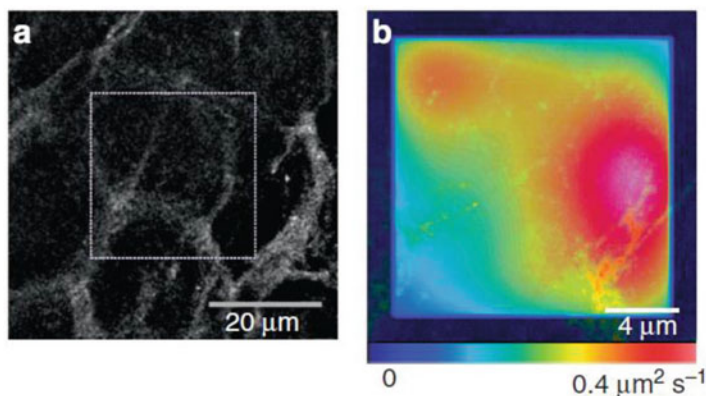


Fig. 2.14 Spatially resolved diffusion (diffusion maps) of ATTO 647N Streptavidin at 2 μm under the stratum corneum (SC) surface. ATTO 647N Streptavidin is a water soluble protein covalently labeled with the ATTO 647N fluorophore. **(a)** Intensity image of the SC. The white box indicates the area where diffusion was measured. **(b)** Diffusion coefficient map positioned on top of the corresponding intensity image showing the spatial distribution of the diffusion coefficients of ATTO 647N Streptavidin. Note that diffusion is not homogeneous across the sample. Adapted from Brewer et al. (2013)

6 Concluding Remarks

Fluorescence spectroscopy embraces a broad number of different methodologies allowing the study of different physical processes in biological systems. The contents presented in this chapter are intended to introduce basic concepts, including few useful experimental tips for beginners in the field, mostly related to cuvette experiments. Readers with an interest in these topics may wish to consult more comprehensive sources such as *Principles of Fluorescence Spectroscopy* (third edition) by J. Lakowicz or *Molecular Fluorescence: Principles and Applications* (second edition), an excellent text by B. Valeur and M. N. Berberan-Santos ((Lakowicz 2006; Valeur and Berberan-Santos 2013) respectively, quoted throughout this chapter). Additionally, many advanced fluorescence topics (including fluorescence microscopy-based approaches) are also covered in the series *Topics in Fluorescence Spectroscopy* (Volumes 1–6, edited by J. Lakowicz, Kluwer Academic Publishers), and several volumes of *Methods in Enzymology* (Volumes 246, 278 and 360) have dealt with issues in fluorescence spectroscopy.

Acknowledgments The author wants to thank the Danish National Research Foundation (which supports MEMPHYS-Center for Biomembrane Physics) and Drs. David Jameson and Roberto Stock for the critical reading of this manuscript.

References

- Acuna AU, Amat-Guerri F, Morcillo P, Liras M, Rodriguez B (2009) Structure and formation of the fluorescent compound of *Lignum nephriticum*. *Org Lett* 11(14):3020–3023
- Alcala JR, Gratton E, Prendergast FG (1987a) Interpretation of fluorescence decays in proteins using continuous lifetime distributions. *Biophys J* 51(6):925–936
- Alcala JR, Gratton E, Prendergast FG (1987b) Fluorescence lifetime distributions in proteins. *Biophys J* 51(4):597–604
- Alcala JR, Gratton E, Prendergast FG (1987c) Resolvability of fluorescence lifetime distributions using phase fluorometry. *Biophys J* 51(4):587–596
- Alvarez-Roman R, Naik A, Kalia YN, Fessi H, Guy RH (2004) Visualization of skin penetration using confocal laser scanning microscopy. *Eur J Pharm Biopharm* 58(2):301–316
- Bagatolli LA (2006) To see or not to see: lateral organization of biological membranes and fluorescence microscopy. *Biochim Biophys Acta* 1758(10):1541–1556
- Bagatolli LA (2013) LAURDAN fluorescence properties in membranes: a journey from the fluorometer to the microscope. In: Mely Y, Duportail G (eds) *Fluorescent methods to study biological membranes*, vol 13, Springer series on fluorescence. Springer, Berlin, pp 3–36
- Bagatolli LA, Montich GG, Ravera M, Perez JD, Fidelio GD (1995) Fatty acid indole fluorescent derivatives as probes to measure the polarity of interfaces containing gangliosides. *Chem Phys Lipids* 78(2):193–202
- Bagatolli LA, Kivatinitz SC, Aguilar F, Soto MA, Sotomayor CP, Fidelio GD (1996a) Two distinguishable fluorescent modes of 1-anilino 8-naphthalenesulfonate bound to Human Albumin. *J Fluoresc* 6:33–40
- Bagatolli LA, Kivatinitz SC, Fidelio GD (1996b) Interaction of small ligands with human serum albumin IIIA subdomain. How to determine the affinity constant using an easy steady state fluorescent method. *J Pharm Sci* 85(10):1131–1132
- Bloksgaard M, Brewer J, Bagatolli LA (2013) Structural and dynamical aspects of skin studied by multiphoton excitation fluorescence microscopy-based methods. *Eur J Pharm Sci* 50(5):586–594
- Bouwstra JA, Honeywell-Nguyen PL (2002) Skin structure and mode of action of vesicles. *Adv Drug Deliv Rev* 54:S41–S55
- Boyle R (1664) *Experiments and considerations touching colours*. Henry Herringman, London
- Brewer J, Bloksgaard M, Kubiak J, Sorensen JA, Bagatolli LA (2013) Spatially resolved two-color diffusion measurements in human skin applied to transdermal liposome penetration. *J Invest Dermatol* 133(5):1260–1268
- Carrer DC, Vermehren C, Bagatolli LA (2008) Pig skin structure and transdermal delivery of liposomes: a two photon microscopy study. *J Control Release* 132(1):12–20
- Cevc G (1997) Drug delivery across the skin. *Expert Opin Investig Drugs* 6(12):1887–1937
- Cevc G (2003) Transdermal drug delivery of insulin with ultradeformable carriers. *Clin Pharmacokinet* 42(5):461–474
- Cevc G (2004) Lipid vesicles and other colloids as drug carriers on the skin. *Adv Drug Deliv Rev* 56(5):675–711
- Cevc G, Schatzlein A, Richardsen H (2002) Ultradeformable lipid vesicles can penetrate the skin and other semi-permeable barriers unfragmented. Evidence from double label CLSM experiments and direct size measurements. *Biochim Biophys Acta* 1564(1):21–30
- Clegg R (2009) Förster resonance energy transfer—FRET: what is it, why do it, and how it's done. In: Gadella TWJ (ed) *FRET and FLIM techniques*, vol 33, pp 1–57
- Coutinho A, Garcia C, Gonzalez-Rodriguez J, Lillo MP (2007) Conformational changes in human integrin α IIb β 3 after platelet activation, monitored by FRET. *Biophys Chem* 130(1–2):76–87
- Daniel E, Weber G (1966) Cooperative effects in binding by bovine serum albumin. I. The binding of 1-anilino-8-naphthalenesulfonate. Fluorimetric titrations. *Biochemistry* 5(6):1893–1900

- Diaspro A, Bianchini P, Vicidomini G, Faretta M, Ramoino P, Usai C (2006) Multi-photon excitation microscopy. *Biomed Eng Online* 5:36
- Digman MA, Gratton E (2012) Scanning image correlation spectroscopy. *Bioessays* 34 (5):377–385
- Digman MA, Brown CM, Sengupta P, Wiseman PW, Horwitz AR, Gratton E (2005a) Measuring fast dynamics in solutions and cells with a laser scanning microscope. *Biophys J* 89 (2):1317–1327
- Digman MA, Sengupta P, Wiseman PW, Brown CM, Horwitz AR, Gratton E (2005b) Fluctuation correlation spectroscopy with a laser-scanning microscope: exploiting the hidden time structure. *Biophys J* 88(5):L33–L36
- Digman MA, Caiolfa VR, Zamai M, Gratton E (2008) The phasor approach to fluorescence lifetime imaging analysis. *Biophys J* 94(2):L14–L16
- Eftink MR (1994) The use of fluorescence methods to monitor unfolding transitions in proteins. *Biophys J* 66(2 Pt 1):482–501
- Eftink MR, Ghiron CA (1981) Fluorescence quenching studies with proteins. *Anal Biochem* 114 (2):199–227
- Gratton E, Jameson DM, Hall RD (1984) Multifrequency phase and modulation fluorometry. *Annu Rev Biophys Bioeng* 13:105–124
- Hawe A, Sutter M, Jiskoot W (2008) Extrinsic fluorescent dyes as tools for protein characterization. *Pharm Res* 25(7):1487–1499
- He XM, Carter DC (1992) Atomic structure and chemistry of human serum albumin. *Nature* 358 (6383):209–215
- Honeywell-Nguyen PL, Gooris GS, Bouwstra JA (2004) Quantitative assessment of the transport of elastic and rigid vesicle components and a model drug from these vesicle formulations into human skin in vivo. *J Investig Dermatol* 123(5):902–910
- Honeywell-Nguyen PL, Groenink HWW, Bouwstra JA (2006) Elastic vesicles as a tool for dermal and transdermal delivery. *J Liposome Res* 16(3):273–280
- Isasi SC, Bianco ID, Fidelio GD (1995) Gangliosides raise the intracellular Ca^{2+} level in different cell types. *Life Sci* 57(5):449–456
- Jameson D (1998) Gregorio Weber, 1916–1997: a fluorescent lifetime. *Biophys J* 75:419–421
- Jameson DM, Ross JA (2010) Fluorescence polarization/anisotropy in diagnostics and imaging. *Chem Rev* 110(5):2685–2708
- Jameson D, Crony JC, Moens P (2003) Fluorescence: basic concepts, practical aspects and some anecdotes. *Methods Enzymol* 360:1–43
- Jameson DM, Ross JA, Albanesi JP (2009) Fluorescence fluctuation spectroscopy: ushering in a new age of enlightenment for cellular dynamics. *Biophys Rev* 1(3):105–118
- Johnson ID (2010a) Indicators for Ca^{2+} , Mg^{2+} , Zn^{2+} and other metal ions. In: *The molecular probes handbook: a guide to fluorescent probes and labeling technologies*, 11th edn. Life Technologies Corporation, sect 19.12
- Johnson ID (2010a) *The molecular probes handbook: a guide to fluorescent probes and labeling technologies*, 11th edn. Life Technologies Corporation, Carlsbad
- Lakowicz JR (2006) *Principles of fluorescence spectroscopy*, 3rd edn. Springer, New York
- Lakowicz JR, Weber G (1973a) Quenching of fluorescence by oxygen. A probe for structural fluctuations in macromolecules. *Biochemistry* 12(21):4161–4170
- Lakowicz JR, Weber G (1973b) Quenching of protein fluorescence by oxygen. Detection of structural fluctuations in proteins on the nanosecond time scale. *Biochemistry* 12 (21):4171–4179
- Lasagna M, Vargas V, Jameson DM, Brunet JE (1996) Spectral properties of environmentally sensitive probes associated with horseradish peroxidase. *Biochemistry* 35(3):973–979
- Maystre D (2012) Theory of Wood's anomalies. In: Enoch S, Bonod N (eds) *Plasmonics*, vol 167, Springer series in optical sciences. Springer, Berlin, pp 39–83
- Murata S, Iwanaga C, Toda T, Kokubun H (1972) Fluorescence and radiationless transitions from the second excited states of azulene derivatives. *Ber Bunsenges Phys Chem* 76:1176–1183

- Newton I (1665–1666) *Of colours*. Cambridge University Library, Cambridge
- Parasassi T, Gratton E (1995) Membrane lipid domains and dynamics as detected by LAURDAN fluorescence. *J Fluoresc* 5(1):59–69
- Parasassi T, Krasnowska EK, Bagatolli LA, Gratton E (1998) LAURDAN and Prodan as polarity sensitive fluorescent membrane probes. *J Fluoresc* 8(4):365–373
- Perrin F (1926) Polarisation de la lumière de fluorescence. Vie moyenne des molécules dans l'état excité. *J Phys Radium* 7:390–401
- Rosso SB, Gonzalez M, Bagatolli LA, Duffard RO, Fidelio GD (1998) Evidence of a strong interaction of 2,4-dichlorophenoxyacetic acid herbicide with human serum albumin. *Life Sci* 63(26):2343–2351
- Simonsson C, Madsen JT, Graneli A, Andersen KE, Karlberg AT, Jonsson CA, Ericson MB (2011) A study of the enhanced sensitizing capacity of a contact allergen in lipid vesicle formulations. *Toxicol Appl Pharmacol* 252(3):221–227
- Slavik J (1982) Anilinonaphthalene sulfonate as a probe of membrane composition and function. *Biochim Biophys Acta* 694(1):1–25
- Steffl M, James NG, Ross JA, Jameson DM (2011) Applications of phasors to in vitro time-resolved fluorescence measurements. *Anal Biochem* 410:62–69
- Strickler SJ, Berg RA (1962) Relationship between absorption intensity and fluorescence lifetime of molecules. *J Chem Phys* 37:814–822
- Tsien CL, Fraser HS, Long WJ, Kennedy RL (1998) Using classification tree and logistic regression methods to diagnose myocardial infarction. *Stud Health Technol Inform* 52 (Pt 1):493–497
- Ustione A, Piston DW (2011) A simple introduction to multiphoton microscopy. *J Microsc* 243 (3):221–226
- Valeur B, Berberan-Santos MN (2013) *Molecular fluorescence. Principles and applications*, 2nd edn. Wiley-VCH Verlag y Co, Weinheim
- van Kuijk-Meuwissen MEMJ, Junginger HE, Bouwstra JA (1998) Interactions between liposomes and human skin in vitro, a confocal laser scanning microscopy study. *Biochim Biophys Acta Biomembr* 1371(1):31–39
- van Munster EB, Gadella TW (2005) Fluorescence lifetime imaging microscopy (FLIM). *Adv Biochem Eng Biotechnol* 95:143–175
- Weber G (1952) Polarization of the fluorescence of macromolecules. I. Theory and experimental method. *Biochem J* 51(2):145–155
- Weber G, Daniel E (1966) Cooperative effects in binding by bovine serum albumin. II. The binding of 1-anilino-8-naphthalenesulfonate. Polarization of the ligand fluorescence and quenching of the protein fluorescence. *Biochemistry* 5(6):1900–1907
- Weber G, Farris FJ (1979) Synthesis and spectral properties of a hydrophobic fluorescent probe: 6-propionyl-2-(dimethylamino)naphthalene. *Biochemistry* 18(14):3075–3078
- Weber G, Laurence DJ (1954) Fluorescent indicators of adsorption in aqueous solution and on the solid phase. *Biochem J* 56 (325th Meeting):xxxi
- Weber G, Young LB (1964) Fragmentation of bovine serum albumin by pepsin. I. The origin of the acid expansion of the albumin molecule. *J Biol Chem* 239:1415–1423

Chapter 3

Mid and Near Infrared Spectroscopy

Gabriele Reich

Abstract Vibrational spectroscopy in the mid (MIR) and near infrared (NIR) range provides structural information on virtually any organic compound and thus presents many interesting perspectives in both qualitative and quantitative analysis. These two techniques are powerful analytical tools for the identification and molecular characterization of pharmaceutical raw materials, intermediates and final dosage forms. NIR spectroscopy being fast, noninvasive, multiparametric, robust and easy to interface with a process, perfectly matches the measurement system requirements within the process analytical technology (PAT) framework. This chapter focuses on modern pharmaceutical MIR and NIR applications and covers (1) basic principles of both techniques including recent advances in instrumentation, sampling and data processing, (2) characterization of solid drug molecules and excipients, (3) nondestructive analysis of solid oral dosage forms, (4) secondary structural analysis of protein therapeutics, and (5) real-time process monitoring and control in drug substance and drug product manufacture. Strategies of MIR and NIR signal processing and multivariate NIR method implementation are highlighted and practical challenges of specific applications discussed. Finally, theoretical and practical aspects of NIR in vivo applications are briefly reviewed. Overall, the analytical versatility of infrared spectroscopy to be applied in various fields of pharmaceutical development, production and quality control is demonstrated and potential benefits and limitations of the distinct wavelength regions are scrutinized.

Keywords Noninvasive analysis • Spectral sampling • Signal processing • Multivariate calibration • Method validation • Solid-state analysis • Timely measurements • Process understanding • Process control

G. Reich (✉)

Department of Pharmaceutical Technology and Biopharmaceutics, Institute of Pharmacy and Molecular Biotechnology, University of Heidelberg, Im Neuenheimer Feld 329, Heidelberg 69120, Germany

e-mail: gabriele.reich@uni-hd.de

1 Theoretical Background, Instrumentation and Data Analysis

1.1 The Origin of Mid and Near Infrared Spectra

Infrared (IR) spectroscopy uses the spectral range between 12,500 and 20 cm^{-1} , which can be further subdivided in the far-IR (FIR: 400–20 cm^{-1}), the mid-IR (MIR: 4000–400 cm^{-1}) and the near-IR (NIR: 12,500–4000 cm^{-1}) (Fig. 3.1). Spectral signals in the MIR and NIR range are absorption bands as a consequence of molecular vibrations. Sample absorbance is recorded at each wavelength (nm) and, except for dispersive NIR instruments, plotted against the inverse of the wavelength, i.e. the wavenumber (cm^{-1}).

Absorbance in the MIR range originates from two types of fundamental vibrations, namely stretching and bending (Chalmers and Griffiths 2001; Griffiths and De Haseth 2007). The vibrational frequencies can simplistically be described by a mechanical ‘balls-on-spring’ model and correlated with molecular parameters based on a harmonic oscillator approximation by considering the strength of the bond and the mass of the atoms as main variables. As molecular systems according to quantum mechanics can only have some discrete energy levels with transitions solely between adjacent levels, the radiation energy for a fundamental vibration to occur should match exactly the difference between the ground level ($\nu = 0$) and the first excitation level ($\nu = 1$). However, energy match is not sufficient. For a vibration to be active in the MIR, a molecular interaction of the electrical oscillating field of the electromagnetic wave is required. As this is only possible, if the vibration induced displacement of the atoms also induces a modulation of the molecular dipole moment, the electric field vector of the radiation must oscillate with the same frequency as the molecular dipole moment. As a consequence, MIR spectroscopy is specifically sensitive to polar functionalities (Table 3.1).

Frequency and intensity of the absorbed radiation depend on the strength of the bond, the atoms the molecule is composed of, the extent of the dipole moment

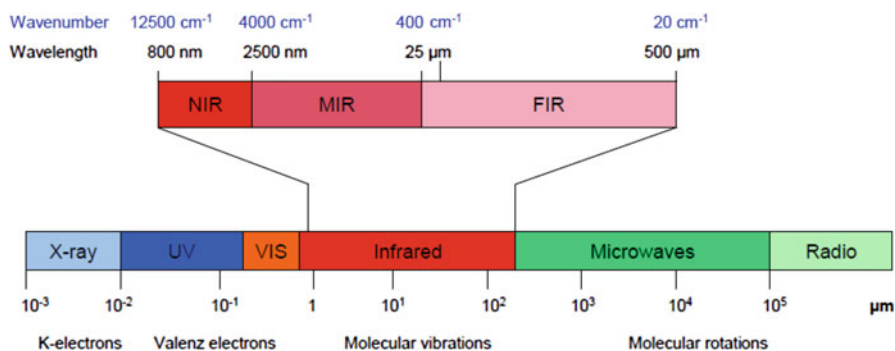


Fig. 3.1 Infrared spectral regions within the electromagnetic spectrum

Table 3.1 Characteristics of mid and near infrared spectroscopy

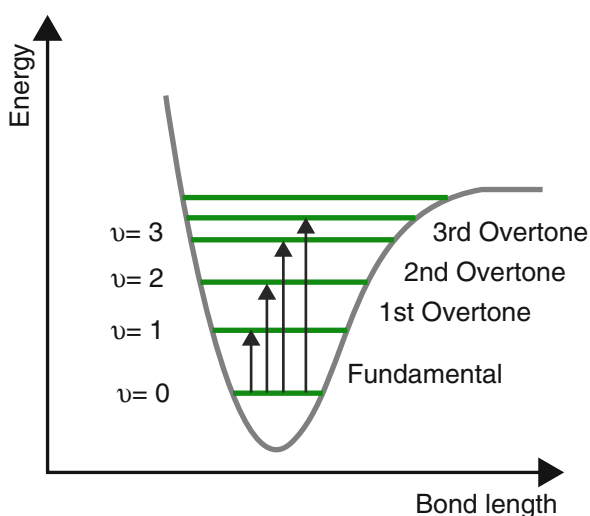
	<i>Mid</i> infrared spectroscopy	<i>Near</i> infrared spectroscopy
Vibrations	Fundamentals	Overtones Combinations
Wavenumber range	4000–400 cm ⁻¹	12,500–4000 cm ⁻¹
Radiation (Light source)	Polychromonatic radiation (Globar tungsten)	
Spectral principle	Absorption	
Absorption coefficient	High	Low
Absorbance peaks	Numerous and well resolved	Broad and overlapped
Selection rules	Change in dipole moment	Change in dipole moment Anharmonicity
Functionalities	Polar groups	X-H groups (i.e. CH/OH/ NH groups)
Structural selectivity	High	Low
Quantitative measurements	Beer's law	
Sample preparation	Dilution required (e.g. KBr) (except ATR-IR)	Not required
Sample size	Small volume (μl)	Large
	Low thickness (μm)	Thickness up to cm
Monochromator Detection principles	FT-IR	Grating
		FT-IR
		AOTF
		Diode-array
Light-fiber optics	Chalcogenide or AgCl (<10m)	Quartz (>100m)
	Limited	
Probes	ATR	Transmission
		Transflection
		Diffuse reflectance

change and the chemical environment. Hence, position, intensity and width of MIR absorption peaks provide information about the molecular structure of the sample including inter- and intramolecular interactions such as hydrogen bondings. As absorbance is strong in the MIR range, most samples have to be diluted or measured in the attenuated total reflectance (ATR) mode (see Sect. 1.2). In addition, measurements in the mid-IR are very sensitive to water, i.e. the strong water band around 3700–3000 cm⁻¹ can obscure absorption bands from other groups thus potentially providing problems to measurements of aqueous samples. The use of a purge gas such as nitrogen is therefore compelling. On the other hand, peaks are numerous providing an absorption pattern, i.e. a spectral fingerprint that is unique for each material. Thus, MIR spectroscopy is an analytical technique that has traditionally been applied in many fields of pharmaceutical drug product development and manufacture. Historically most important is its use for the chemical identification of raw materials including drug substances, excipients and packaging materials. Innovative MIR applications will be outlined in Sects. 3, 4 and 6.

Absorption bands occurring in the NIR region originate from overtones and combinations of fundamental vibrations of $-\text{CH}$, $-\text{NH}$, $-\text{OH}$ and $-\text{SH}$ groups. In addition to a change in the dipole moment, key features determining their frequency and intensity are anharmonicity and Fermi resonance. Additional electronic transitions may occur in the short-wave NIR region, the so-called Herschel region ($12,500\text{--}8500\text{ cm}^{-1}$; $800\text{--}1200\text{ nm}$), which due to its very high optical transparency is almost exclusively used for biomedical applications and thus also called the ‘window of body’ (see also Sect. 8). Most of the pharmaceutical NIR applications are performed in the region $1200\text{--}2500\text{ nm}$ which is dominated by absorption bands resulting from overtones and combinational vibrations. In the following, the physical basis of their origin will be briefly described.

The energy curve of an oscillating molecule is strongly affected by intramolecular interactions resulting in non-symmetric vibrations around the equilibrium position and non-identical spacings between the energy levels that a molecule can attain. This situation can be described by the quantum mechanical model of an *anharmonic oscillator* (Fig. 3.2). Selection rules for anharmonic systems do not exclude transitions with $\Delta\nu > 1$. Thus, transitions with $\Delta\nu = 2$ or 3 are possible, although with lower probability at higher quantum number (ν). NIR overtone bands originate from such multilevel energy transitions that occur at multiples of the fundamental vibrational frequency according to their degree of anharmonicity (Reich 2005; Siesler 2008). Combination bands, on the other hand, result from vibration interactions. Their frequencies are the sums of multiples of each interacting frequency. The degree of anharmonicity is determined by the mass difference between the atoms of a covalent bond and the local electronic environment, i.e. the molecular dipole moment resulting from the impact of neighbouring groups and hydrogen bondings. As a consequence, anharmonic vibrations induce a modification of the dipole moment that is not linearly dependent on the nuclear displacement.

Fig. 3.2 Anharmonic oscillator model



The NIR region is dominated by absorption bands arising from vibrations of X-H bonds with a high dipole moment and a large interatomic mass difference, and thus a large anharmonicity. The overtone and combination band pattern is further complicated by effects resulting from coupling or resonance between vibrations of the same functional group, which makes band assignment difficult. Fermi resonance, for instance, occurs between a fundamental vibration and an overtone at low frequency difference. It leads to a significant band splitting with a greater separation of the two peaks and an intensification of the overtone band. Moreover, resonance effects between combination bands and high order overtones of hydrocarbons have to be considered.

In conclusion, NIR absorption bands are typically broad, overlapping and 10–100 times weaker than their corresponding mid-IR bands. The low absorption coefficient is an advantage, since it permits a high penetration depth and thus nondestructive measurements of strongly absorbing and highly scattering samples such as solids. Band shifts associated with inter- and intramolecular hydrogen bondings are even more pronounced than in the mid-IR. On the other hand, sensitivity and selectivity are low and call for multivariate data processing to relate spectral information to specific sample properties. Absorption and scatter effects contained in diffuse reflectance and transmittance spectra can be used to simultaneously evaluate chemical and physical sample characteristics. However, scatter effects resulting from random physical sample variations may also pose analytical problems to be managed in method development. Key features of MIR and NIR spectroscopy are summarized in Table 3.1.

1.2 *MIR Instrumentation and Sampling*

FT technique: Modern MIR spectrometers are *Fourier transform infrared (FTIR)* instruments (Griffiths and De Haseth 2007). Due to their improved acquisition mode and overall performance, they have almost entirely replaced dispersive instruments. The main optical part of an FT-IR spectrometer is the interferometer. A common instrumental setup is the two-beam Michelson interferometer consisting of two mutually perpendicular plan mirrors and a beam splitter. The radiation beam coming from the light source is collimated by a mirror or lens and directed to the interferometer, where it is split into two parts by the beam splitter. One part propagates to the fixed mirror, is reflected there and thus travels back to the beam splitter. The other part is directed towards the movable mirror, where it is also reflected back. The two split beams are recombined at the beam splitter and directed out to be focused on the detector.

As the split beams are spatially coherent, they interfere upon recombination. The interference pattern, i.e. the radiation intensity of the recombined beam is a function of the optical path difference and thus the position of the movable mirror. A plot of light intensity (I) versus the optical path difference (d) produces the interferogram, which is recorded by the detector. As each wavelength (λ) produces its own

interference pattern, the interferogram contains the spectral information necessary to be transformed by Fourier analysis from a time domain into a frequency domain, i.e. into a spectrum. Advantages of the FT technique are rapid data collection and a high signal to noise (S/N) ratio, which is important for accurate measurements. In rapid scan FT instruments the movable mirror is moved at a maximum speed of 10 cm/s providing a time resolution of 10 ms at 12 cm^{-1} optical resolution.

In a special type of FTIR spectroscopy, named *photoacoustic spectroscopy* (FTIR-PAS), the interferogram is recorded by an acoustic detector. Intensity modulated IR radiation available in form of the interferogram generates heat waves in the sample, which is placed in a cavity cell filled with a transfer gas (e.g. helium). The heat waves induce sound signals in the surrounding transfer gas, which can be detected by a sensitive microphone (Wartewig and Neubert 2005). Advanced FTIR and FTIR-PAS spectrometers allow the interferogram to be recorded in a *step scan mode*, i.e. the movable mirror is stopped at different positions to obtain time-resolved intensity measurements. The time resolution is limited by the response time of the detector, but can be in the order of nanoseconds. With FTIR-PAS, frequency modulation at each mirror position enables controllable depth profiling of the sample.

Two-dimensional (2D) FT-IR spectroscopy is a new tool to study transient molecular structures and dynamics by monitoring excitation and subsequent relaxation processes caused by external perturbations (Noda 1990; Baiz et al. 2012a, b). A vibrational spectrum is spread over two frequency axes to provide information about vibrational couplings by means of cross peaks. Hence, the 2D approach allows enhancement of spectral resolution, which is very useful to study structural connectivity such as in proteins. Ultrafast lasers are used to perform measurements within picoseconds or faster.

Sampling techniques for measurements in the mid-IR strongly depend on the chemical, physical and spectral characteristics of the sample and the parameter to be determined. Three main setups are in common use: (1) transmission, (2) attenuated total reflectance (ATR), and (3) diffuse reflectance (DRIFT) (Griffiths and De Haseth 2007). Additional configurations for specific applications comprise PAS and chemical imaging (CI) or hyphenated techniques such as TG-IR. The development and use of fiber optics for real-time measurements continues to grow. In the following the basic principles of transmission, ATR and DRIFT measurements will be briefly explained and their practical pros and cons discussed.

Transmission measurements are feasible with liquid and solid samples. Due to the high absorbance coefficient in the mid-IR region, solid samples have to be diluted with a nonabsorbing substance such as KBr and pressed into a pellet. For pharmaceutical applications it is important to consider that the high pressure applied in pellet formation may lead to structural artefacts (see also Sect. 3). Liquid samples are presented in ZnSe, BaF₂ or CaF₂ cuvettes. A short pathlength of typically 5 μm is required when dealing with aqueous protein solutions, since water exhibits strong absorption bands in the mid-IR, which overlap the amide I band and some of the side chain bands of proteins (see also Sect. 6).

In the *ATR setup* the sample is placed in direct contact to an internally reflecting material with a high index of refraction (e.g. ZnSe). The light beam that is transmitted through the ATR element is reflected at the crystal/sample interface, thereby penetrating a few microns into the sample. The evanescent wave can interact with the sample resulting in absorption so that the light reaching the detector contains sample information. The intimate contact between the sample and the ATR element is, however, crucial. The ATR setup can be mounted onto a benchtop instrument or implemented in an immersion probe. With the benchtop setup small amounts of liquids, semi-solids and powders can be analyzed. Different designs of the ATR cell including configurations for diffusion studies are available. Due to the low penetration depth of the MIR light into the sample, the optical pathlength is small enough to allow aqueous solutions to be measured. The method is quick and no sample preparation is needed. With an ATR immersion probe real-time monitoring of chemical reactions and crystallization processes is feasible (see Sects. 4.1 and 4.2). As the sampling depth in an ATR setup is very small, it does not allow measurements throughout the bulk sample. This is, however, an advantage, when dealing with slurries in crystallization processes to ensure that crystallized material does not interfere with the liquid phase signal.

In a *DRIFT setup*, IR radiation reflected from rough sample surfaces is collected. In principle, the incident light is partly reflected by the sample surface (i.e. specular reflectance), partly scattered, and partly transmitted into the sample. The transmitted part may be absorbed or diffracted, resulting in diffusely scattered light. Contrary to the specularly reflected part, which is usually eliminated by the DRIFT accessory, the diffuse reflected light collected over various angles thus contains absorptivity information from the sample. Due to the measurement principle, DRIFT spectroscopy can be used for noninvasive evaluation of solid samples including characterization of polymorphic forms (see Sect. 3.2). Ideally, minimal sample preparation is required. However, results may be compromised by very large particles or a very wide particle size distribution affecting spectral quality or by strongly absorbing compounds that require dilution with KBr.

1.3 NIR Instrumentation and Sampling

A NIR spectrometer is basically composed of a light source, a monochromator, a sample holder or a sample presentation interface, and a detector (Reich 2005). Different instruments can be distinguished according to their optical configuration, the light source (e.g. a tungsten-halogen lamp or super-luminescent LEDs), the type of detector (e.g. PbS, InGaAs), the scan rate, the measuring mode, the sampling technique, the vibration tolerance and the protection against environmental conditions such as dust, humidity and solvents (Workman and Burns 2008). Various optical configurations are available to separate the polychromatic NIR radiation into monochromatic frequencies. Broadband, discrete filter photometers and light-emitting diode (LED)-based instruments only cover a selected narrow spectral

range of approx. 50–100 nm. Diffraction gratings, interferometers, diode arrays, acousto-optical tunable filters (AOTF) and micro-electro-mechanical systems (MEMS) optical tunable filters provide full range spectra. Selection of the appropriate configuration strongly depends on the application to be performed with the instrument. The most important criteria to be considered comprise the required S/N ratio, photometric and wavelength accuracy, spectral resolution, potential stray light effects and measurement speed. The decision for a specific instrumental setup, i.e. spectrometer and sampling configuration strongly depends on the sample type, the required analytical sensitivity and reliability, ease of use and potential implementation needs. The latter aspects require laboratory and process analyzers to be distinguished.

NIR laboratory analyzers intended for pharmaceutical off-line or at-line quality control measurements require a high analyte sensitivity, whereas measurement speed is of lower importance. For raw material identification purposes, hand-held miniaturized NIR spectrometers based on e.g. a thin-film linearly variable filter (LVF) as the dispersive element have gained popularity (Sorak et al. 2012; Alcalá et al. 2013). State-of-the-art lab instruments for reliable quantitative analysis are FT-NIR spectrometers. The appropriate spectral sampling technique is determined by the optical properties of the sample matrix, i.e. transparent samples are measured in transmittance mode, whereas the analysis of turbid liquids or semi-solids and solids may be performed in diffuse reflectance, diffuse transmittance or transflectance mode, depending on the absorption and/or scatter characteristics of the sample (Reich 2005). In case of solids, spectral quality is further affected by the sample presentation. This issue will be discussed in more detail in Sect. 2.1.

Process analyzers are intended for on-line or in-line measurements to provide real-time process information. Fast and rugged NIR instruments are thus required, preferably with no moving parts to enable numerous scans per second without being sensitive to vibrations. Established NIR analyzer formats for real-time PAT applications include the scanning grating monochromator, the grating polychromator photodiode array spectrometer, AOTF analyzers, and process FT-NIR instruments (Simpson 2010). AOTF analyzers are extremely fast (100 scans/s), whereas FT instruments provide the best spectroscopic performance and long-term spectral reproducibility. Emerging technologies further comprise compact MEMS-based grating and FT spectrometer devices (Simpson 2010). Selection of the appropriate process analyzer technology certainly depends on the process dynamics, the required accuracy, the intended flexibility and the environmental conditions. Interfacing is another demanding aspect to be considered when implementing a PAT application. Various NIR probe designs for on-line and in-line analysis of solids or clear to opaque liquids including contact and non-contact configurations with sampling options in reflectance, transmission or transflectance mode are commercially available. For pharmaceutical PAT applications, the ability of separating the spectrometer from the point of sampling at a long distance by means of quartz light-fiber optics or applying multiple remote control points is certainly an advantage of NIRS over MIRS (see Table 3.1). Practical challenges associated with the implementation of real-time PAT applications in both drug substance and drug product manufacture will be discussed in Sects. 4 and 7, respectively.

1.4 Spectral Data Analysis

MIR Signal Processing: Absorbance bands in the mid-IR are often directly interpretable due to peak specificity resulting from characteristic vibrations of certain atomic groups at typical, so-called ‘group’ frequencies, regardless of the structure of the rest of the molecule. Band assignment based on these group frequencies can therefore be used to diagnose certain functional groups and structural moieties. On the other hand, absorption bands in the range $<1500\text{ cm}^{-1}$ mainly result from strongly coupled vibrations that are specific for a single molecule. The spectral pattern of this ‘fingerprint’ region is therefore especially useful for chemical identification purposes.

Identification of a substance is usually performed by visual or computer-aided comparison of the IR absorption spectrum of the sample with a reference spectrum from a spectroscopic library or a reference sample. Prerequisite for a proper diagnosis is that both spectra were measured under the same conditions. Quantitative analysis is generally feasible, since absorption intensity in the mid-IR is proportional to the concentration of the absorbing component. Lambert-Beer’s law can be applied directly, if well resolved absorption bands have been identified.

Complex overlapping bands representing different structural features such as those found in FT-MIR spectra of proteins call for resolution enhancement prior to band assignment. Common approaches are Fourier self-deconvolution (FSD) (Byler and Susi 1986) or the use of second derivative spectra. Once the underlying features have been resolved, a curve fitting procedure can be applied to estimate quantitatively the area of each component representing a certain secondary structure. Challenges associated with the use of resolution enhancement and curve fitting for protein secondary structural analysis will be discussed in Sect. 6.1. Alternatively, the ‘spectral correlation coefficient’ based on absorption intensities may be calculated (Prestrelski et al. 1993) or a comparison of the ‘area of overlap’ between baseline-corrected and area-normalized second derivative spectra may be performed to quantify overall MIR spectral similarity (Kendrick et al. 1996). Peak fitting of non-deconvoluted spectra followed by multivariate regression is an additional approach that may be applied (Vonhoff et al. 2010). Overall, it can be concluded that in mid-IR spectroscopy band assignment is still more popular than multivariate data analysis.

Multivariate NIR Data Analysis: Since NIR spectra are typically composed of broad overlapping absorption bands which contain chemical and physical sample information, the analytical raw data are hardly selective. Qualitative or quantitative analysis therefore require multivariate classification or regression based calibration modeling to be performed. To selectively relate spectral variables to specific sample properties, it is usually necessary to eliminate, reduce or at least standardize the influence of interfering information contained in the spectra and enhance relevant information from the analyte by signal preprocessing prior to calibration modeling. In the following, the most frequently applied mathematical and multivariate statistical methods for NIR data processing will be shortly discussed. For a

more detailed treatise of the subject matter the reader is referred to the comprehensive textbooks of Martens and Naes (2001) and Naes et al. (2002) and the more recent reviews of Xiabo et al. (2010) and Rajalahti and Kvalheim (2011).

Data Pretreatments: Scatter effects and path length variations, resulting from variable physical sample properties or sample collection, and hardware or process noise are the most prominent spectral interferences compromising the prediction performance of an NIR method. Scatter-induced baseline offsets can be effectively reduced by e.g. multiplicative scatter correction (MSC) or standard normal variate (SNV). Normalization algorithms are applicable to compensate for baseline shifts and intensity differences resulting from path length variations. Derivatives remove constant offsets and provide a better resolution of overlapping peaks. However, to avoid amplification of spectral noise, derivation should be applied only in combination with Taylor or Savitzky Golay smoothing algorithms. A special pretreatment algorithm, which removes non-correlated, systematic variation in the spectral data set X that is orthogonal to the response data set Y and thus of no predictive value, is Orthogonal Signal Correction (OSC). OSC can effectively reduce the complexity of multivariate NIR calibration models by using correlated variation only. Overall, proper selection of the pretreatment strategy is crucial for the results obtained from NIR measurements, since signal preprocessing strongly affects the robustness of a NIR method whether qualitative or quantitative.

Multivariate classification methods: In qualitative NIR analysis, multivariate classification methods, also known as pattern recognition methods, are used to group samples with similar chemical and/or physical characteristics according to their spectral similarity. *Unsupervised* classification methods do not require any a priori knowledge about the samples within a class. They simply produce clusters and thus provide valuable information about subpopulations within a spectral data set. Classification can be performed by hierarchical methods leading to a dendrogram or visually by principal component analysis (PCA). PCA decomposes the spectral data matrix into orthogonal components whose linear combinations approximate the original data. The new variables are called principal components (PC), latent variables (LV), eigenvectors or simply factors, and account for the largest possible variance in the data set. The PCs are obtained in a sequential way with each PC being described by a score vector and a loading vector. The score value indicates how a certain spectrum is related to other sample spectra in that PC. Score plots thus reveal characteristic patterns (i.e. clusters, trends or outliers) in the spectral data. The loading vector provides information about spectral features captured by the corresponding PC. Loading plots can therefore be applied to interpret the patterns observed in the score plot. Since scores and loadings contain the covariance structure of a spectral data set, PCA enables different sources of variation to be easily recognized and spectral variability to be efficiently reduced to only a few PCs capturing the dominant variation pattern. Some other multivariate methods such as soft independent modeling of class analogies (SIMCA) and principal component regression (PCR) therefore rely on PCA to perform classification or regression.

For pharmaceutical identification and/or qualification purposes, *supervised* classification methods are applied to construct spectral libraries with a training set of samples of known category membership, thus providing pre-specified classification rules that are used to allocate unknown samples to the most probable subgroup. Supervised classification methods can operate either in the wavelength space or in a factor space. In any case, mathematical criteria have to be established for parametrizing spectral similarity. Similarity can be expressed by either a correlation coefficient (CV) or a distance measure such as the Euclidian or Mahalanobis distance. The correlation coefficient is a rather robust parameter for identity testing, while distance-based methods also enable product qualification to be performed. Algorithms comprise linear discriminant analysis (LDA), quadratic discriminant analysis (QDA), K nearest neighbours (KNN), SIMCA and partial least squares discriminant analysis (PLS-DA). What they have in common is the need to define a threshold for discriminating between classes or evaluating spectral similarity or dissimilarity. Challenges associated with the threshold definition will be discussed in Sect. 2.2.

Multivariate regression methods: For quantitative analysis, the multivariate information contained in NIR spectral data requires multivariate calibration modeling based on reference data. Method development comprises several critical steps which will be discussed in more detail in Sect. 2.1. Herein, the most prominent algorithms used to relate the spectral variations to the analytical target property will be briefly explained.

The most frequently applied regression methods are principal component regression (PCR) and partial least squares regression (PLSR). Both methods try to establish a linear relation between the spectral information and the analytical target property based on reference values. PCR uses the PC scores, i.e. the largest variation in the spectrum to perform regression on the sample property to be predicted, whereas PLSR decomposes both the spectral data matrix X and the response matrix Y into latent variables that reflect the maximum covariance between the two. The advantage of PLS regression modeling over PCR is obvious, namely to find the variables in X that best describe the related response values Y to be predicted. With both methods, the optimum number of latent variables is crucial for the model robustness and highly dependent on the sample characteristics and the analytical target parameter. If spectral data and target property are not linearly related, non-linear calibration methods such as locally weighted regression (LWR), artificial neural networks (ANN) or support vector regression (SVR) have to be applied. For further details concerning LWR and ANN, the interested reader is referred to the textbook of Naes et al. (2002).

Multivariate curve resolution (MCR) is an alternative approach to PCA and PLS for multivariate spectral data analysis, when calibration samples are not readily available or difficult to prepare such as in pharmaceutical production settings. In MCR, also known as soft modeling or mathematical resolution, it is assumed that each spectrum can be described as the sum of N pure underlying spectra. The purpose of the MCR modeling procedure is to estimate the pure underlying spectra for each spectrum. Hence, the advantage of MCR as compared to PLS is that a calibration data set is not strictly required. Moreover, model interpretation is often easier.

2 Practical Challenges of Multivariate NIR Method Implementation

Implementation of a multivariate NIR method comprises the following distinct steps:

1. Definition of the analytical target parameter(s)
2. Selection of the appropriate instrumental setup and sampling strategy
3. Multivariate calibration model development
4. Method validation
5. Method transfer to routine use
6. Model maintenance

Challenges inherent to the development of reliable and robust multivariate NIR methods depend on the analytical target and the complexity of the system to be analyzed. Defining the scope and purpose of the analysis and considering a priori knowledge prior to calibration development is thus important in both qualitative and quantitative NIR methods to properly select a representative calibration sample set, determine the adequate spectral acquisition and sampling mode and choose the appropriate spectral data processing algorithms to compensate for potential interfering spectral effects and provide sample classification or quantification. Subsequent validation of the calibration model is another demanding step for method implementation and routine use. This section is intended to discuss the most critical issues to be considered in qualitative and quantitative NIR method development, validation, transfer and maintenance.

2.1 Qualitative Analysis

Within the pharmaceutical supply chain, nondestructive qualitative NIR analysis based on supervised classification algorithms (see Sect. 1.4) plays a major role for the identification and qualification of both raw materials and dosage forms. Specifically critical in qualitative NIR method development is (1) the variable selection step, (2) the choice of the classification algorithm and (3) the threshold definition to ensure adequate selectivity (Blanco and Romero 2001; Alvarenga et al. 2008).

Interpretation of scores and loadings obtained from a PCA usually helps with *variable selection* and identification of analyte-specific spectral regions for subsequent classification modeling. For the specific identification of an active pharmaceutical ingredient (API) in a solid dosage form, *distance-based supervised methods* operating with the first few PCs as input variables usually provide good prediction performance and long-term accuracy, i.e. high robustness. In case of raw material identification and qualification, *size-independent and robust correlation methods* are well suited to construct the general identification library. To further distinguish between similar compounds in subcascading qualification libraries, distance-based methods are again more suitable.

Irrespective of the modeling method, the most crucial step in terms of selectivity is the definition of the *threshold value* being the boundary assigned to a specific group of the library. Setting the appropriate threshold is an iterative procedure to be performed in conjunction with the external validation, i.e. the threshold value is successively changed until an acceptable identification performance of the independent validation samples is achieved. If the threshold thus defined does not allow the desired selectivity to discriminate between similar compounds, a smaller sublibrary should be used to define the appropriate threshold.

Finally, for a qualitative NIR method to comply with the validation criteria given in the ICH Q2 documents (ICH Q2 (R1) 2005), specificity and robustness must be proven. Distance-based classification methods operating in the dimension-reduced factor space are usually more specific and robust as compared to correlation methods operating in the wavelength space. The latter provide, however, the advantage to easily update the library by incorporating new variabilities, e.g. new products or additional spectra of an existing product.

2.2 Quantitative Analysis

Selectivity, accuracy and robustness are key elements of a quantitative NIR method. Due to the multivariate nature of NIR spectra including chemical and physical sample information, method development requires a thorough understanding of all variables affecting method performance.

A high signal-to-noise ratio is, for instance, needed for assaying a low dose API in a complex powder or tablet formulation, whereas *spectral resolution* is not a major issue when determining physical characteristics such as tablet hardness primarily associated with baseline shifts (Reich 2005). Selection of the appropriate spectral *sampling strategy* depends on the optical properties of the sample matrix, the analytical target parameter and the specific application (i.e. static or dynamic). When dealing with powders, granules or pellets measured in reflectance mode, prediction accuracy strongly depends on the spectral reproducibility, i.e. sample homogeneity and compactness (Reich 2005). The reflectance mode is well suited for the analysis of tablet coatings (see Sect. 7.7) and capsule shells (Reich 2005). It reveals, however, some limitations when measuring highly inhomogeneous tablets, multilayer tablets or tablets with a thick coating, since the spectral information depth is limited (Saeed et al. 2011). The same is valid for nondestructive capsule content analysis. Transmittance measurements usually scan a larger volume of the dosage form and thus provide a better overall quantitative description of a tablet or capsule fill matrix. In fact, improved accuracy and robustness of tablet and capsule assays performed in transmittance mode have been reported, despite a reduced wavelength range being available for the analysis (Xiang et al. 2009a, b; Warnecke et al. 2013).

The greatest difficulty in developing a robust quantitative NIR method is the selection of a *representative calibration sample set*. In fact, the sample set should

span a sufficiently wide concentration range of the analytical target parameter and encompass all expected chemical and physical variabilities to enable the selective prediction of real life, e.g. production samples with normal and abnormal target characteristics. In case of drug content determination, ICH guidelines (ICH Q2 (R1) 2005) recommend to use a range of $\pm 20\%$ around the nominal value for calibration modeling. In addition, collinearity between concentration values of API and excipients should be kept as low as possible to avoid pseudo-correlations (Xiang et al. 2009c). In case of low dose products, this can be accomplished by statistically designed placebos with excipient concentrations in the range of $\pm 5\%$ of their nominal value (Blanco and Peguero 2010).

Since intra-batch and batch-to-batch variability in pharmaceutical production are usually low, normal production samples are not sufficient to span the concentration range of the analyte required for calibration modeling. Sample manufacture with variable API and/or the excipient concentrations well above and below the target value is usually not applicable in the production setting. On the other hand, only production samples contain the spectral signature of the production process that is necessary to reflect physical matrix variability (Cogdill et al. 2005a). In view of this technically and economically challenging situation, various approaches have been proposed to efficiently design and manufacture calibration samples for the development of robust quantitative NIR calibration models to be applied in routine production. Those include the combination of lab and production samples (Blanco and Peguero 2010), the use of laboratory samples only with process-related physical matrix variability being included via calculation of a process spectrum (Blanco et al. 2011) or modeling strategies based on reduced sample sets with artificial data augmentation and/or orthogonal projections (Pieters et al. 2013). In any case, statistically designed experiments are highly recommendable to define the composition and number of calibration samples.

The *reference method* has to be carefully selected, since the accuracy of the reference method determines the accuracy of the NIR method. For content uniformity analysis, the sample size of the reference analysis should be comparable with the spectral sample size (see also Sect. 7.1). Moreover, the time between the NIR measurements and the reference analysis can be crucial. Moisture content determination, for instance, requires reference analysis to be performed directly after NIR analysis, i.e. without any lag time (see also Sect. 4.3).

Multivariate calibration modeling is the next step in method development. The goal is to selectively relate the spectral information to the sample properties of interest, i.e. the reference values. Since variable positioning, packing density and/or process-related variations in physical sample characteristics result in wavelength dependent baseline shifts, normalization and/or derivative transformations are usually required for reliable and robust calibrations to be developed, especially when measuring content uniformity of solids. On the other hand, baseline correction should be made with care when determining physical sample characteristics such as particle size, tablet porosity or hardness. In either case, spectral pretreatments prior to regression modeling are crucial and should be performed based on scientific rationales.

As outlined in Sect. 1.4, the *algorithms* most frequently used for quantitative NIR calibration modeling are principal components regression (PCR) and partial least squares regression (PLSR). Both methods allow several parameters of interest to be modeled and thus to be determined simultaneously. In addition, they can handle noise-related variability and collinearity of spectral data. The choice of the calibration method is mainly determined by the sample characteristics and the number of components to be simultaneously analyzed. PLS usually leads to more parsimonious calibration models of higher precision, since the first few PLS factors are most correlated to the parameter of interest and less prone to errors. For large data sets, PLS is often faster to implement and optimize than PCR. When dealing with very complex systems, enhanced variations of the PLS algorithm, namely interval variable selection (IVS)-PLS or orthogonal signal correction (OSC)-PLS can improve prediction performance by further reducing the complexity of the model (Abrahamson et al. 2003; Blanco et al. 2001). Other options to select the optimal number of latent variables are net analyte signal (NAS) correction (Sarracuga and Lopez 2009; Pieters et al. 2013) or pure-component projection (PCP) (Cogdill and Anderson 2005). NAS splits the information of the spectral matrix X in contributions related to the analyte and those related to other sources of variability. PCP utilizes the spectral information of pure sample constituents. Quadratic versions of the PCR or PLS algorithms can be useful to model non-linear phenomena. When a large variation of chemical and physical variables has to be managed such as in QbD-based product development, deconvolution by parallel factor analysis (PARAFAC) prior to regression is also an option (Alcalà et al. 2009). Alternatively, LWR or ANN (Chalus et al. 2007; Chen et al. 2001) can be favourably applied for non-linear calibration modeling.

Regardless of the regression algorithm applied, the goal is to find the most accurate and precise calibration model possible. Statistical indicators for a preliminary estimate of the goodness of fit are R-squared (R^2_{cal}), the root mean squared error of calibration (RMSEC) and the bias. Once outliers have been identified, the optimal number of factors in the model have to be determined by an internal test-set or leave-one-out cross validation procedure. The next step is the “real” NIR *method validation* based on independent samples, which is intended to assess how well the selected calibration model will perform on future samples in routine use. In robust calibration models containing all sources of expected variation, the root mean squared error of prediction (RMSEP) is equal or nearly equal to the root mean squared error of cross validation (RMSECV) and both validation approaches recommend more or less the same number of factors to determine the best model. In fact, the optimal number of factors depends on the model complexity and the data set used to determine the model.

Statistical indicators such as R^2_{cal} , R^2_{pred} , RMSEC, RMSECV, RMSEP, slope, intercept and bias certainly do not provide all quantitative information needed to comply with the general pharmaceutical regulatory requirements on method validation comprising specificity, accuracy, precision, valid range of application, robustness (ICH Q2 (R1) guideline 2005) and suitability of the method for its intended use (Ph. Eur. 2.2.40). In fact, in chemometric statistics no information is

given about the suitability of the method for its intended use or the range over which the method can provide results of acceptable accuracy (De Bleye et al. 2012). Hence, additional approaches are needed to address these issues. One such ICH compliant approach summarized in so-called accuracy profiles (Mantanus et al. 2009) is based on β -expectation tolerance intervals defining the “interval where an expected proportion of NIR results will fall with a defined probability β ” (Chavez et al. 2013). If the β -expectation tolerance limits are within the acceptance limits, a method can be considered as valid over the whole concentration range. A few practical applications of this approach have already been described in the literature (Mantanus et al. 2010a, b). The method is especially valuable for PAT applications to ensure “quality, reliability and accuracy of the individual results for the intended purpose of the NIR method” (De Bleye et al. 2012).

A problem with many calibrations is that the conditions used for calibration modeling are somewhat different to the measurement conditions in routine analysis. Eventually *calibration maintenance*, also referred to as *calibration transfer*, is needed. Calibration transfer operations can be classified as either data transformation or model update techniques (Blanco et al. 1998; Cogdill et al. 2005a; Bouveresse and Campbell 2008). Data transformation techniques include signal processing and empirical methods such as direct orthogonalization (DO) algorithms and regression-based transformations (e.g., direct standardization (DS) or piecewise direct standardization (PDS)). DO algorithms reduce undesirable spectral variation not associated with the analyte, whereas DS and PDS estimate a transfer function to predict the spectral information of a master instrument from a slave instrument. Empirical data transformation is useful for planned events such as calibration transfer to a new instrument or instrument maintenance (Cogdill et al. 2005a; Sulub et al. 2008; Boiret et al. 2011). Major challenges are the design of the calibration transfer data set and the selection of the appropriate algorithm. Model updating is required, if model performance in routine analysis is or starts getting poor, since a subset of variations such as a change in the API or excipient source, effect of routine wear of processing equipment or changes in environmental conditions during the NIR measurements has not been included in the model. To correct for the new spectral variances, additional sample spectra have to augment the primary calibration. Efficient model updating, however, requires proper weighting of the new samples with techniques such as the Tikhonov regularization (TK) to minimize the number of samples needed to update the new conditions. The TK approach has been successfully applied by Farrell et al. (2012) to improve the performance of a NIR lab calibration model for API content determination of tablets in full production.

Overall, it is obvious that industrial implementation of a pharmaceutical NIR application is an iterative and multistep procedure. Current perspectives of the regulatory authorities regarding NIR method development, validation and maintenance have been outlined in the EMA guideline on the ‘use of NIRS by the pharmaceutical industry and the data requirements for new submissions and variations’ (EMA 2014) and the most recent U.S.F.D.A. draft guidance on the ‘development and submission of near infrared analytical procedures’ (U.S.F.D.A. 2015).

3 Application in Solid-State Characterization of Drug Molecules and Excipients

The majority of pharmaceutical drug products are solid dosage forms. Hence, most raw materials and intermediates in pharmaceutical development and production are solid compounds. Typically, APIs are manufactured in a stable crystalline form. The amorphous state has attracted considerable interest as a means to improve the dissolution rate and thus enhance bioavailability of poorly water-soluble, e.g. BCS class II APIs. Moreover, excipient grades with tailored solid-state characteristics such as amorphous/crystalline ratio, particle size and/or water content have gained importance. Since processability, stability and bioavailability of pharmaceutical solids are closely related to their solid-state properties, adequate methods for their analysis should be available.

A variety of molecular and particulate level analytical techniques have been described for the identification, characterization and quantification of diverse solid-state forms including polymorphs and solvates and/or to determine the degree of crystallinity in an amorphous compound. Typically, a combination of techniques is required, as no single method can provide all information about the solid-state form. The same is true for the analysis of bulk level properties. Vibrational spectroscopy plays a major role in solid-state analysis on a molecular level. Contrary to MIRS, NIR spectra can provide additional information on particulate and bulk level properties, e.g. particle size and moisture content.

Within the last two decades, numerous research papers and reviews have been published noting the potential and limitations of MIRS and NIRS as applied to pharmaceutical solid-state characterization. Off-line, at-line and in-line applications have been described and their analytical performance as compared to other techniques has been demonstrated. In the following, a representation of some of these applications will be provided and the rationale behind the different approaches will be outlined. In this section, the focus will be on lab analysis only, whereas real-time PAT applications for monitoring moisture content, solid-state transformations and particle size during pharmaceutical unit operations in API and drug product manufacture will be discussed in Sects. 4 and 7, respectively.

3.1 Determination of Water Content and Hydration State

Evaluation of batch-to-batch variability and/or storage-induced changes in water content and/or the state of hydration is part of pharmaceutical raw material qualification. Nondestructive NIR transmittance and reflectance measurements are a reliable and efficient noninvasive alternative to traditional methods for the determination of both water content and state of water.

Due to the large anharmonicity of the OH-bonds of water, the NIR absorption bands of water are strong with five maxima at 760, 970, 1170, 1450 and 1940 nm for

bulk water. The most intense band at 1940 nm results from the combination of OH stretching and bending vibrations; the band at 1450 nm can be assigned to the first overtone of the OH stretching vibrations. The specific band to be used for water detection and quantification depends on the required level of sensitivity and selectivity. Since the exact positioning of the O–H bands depends on the hydrogen bonding intensity, band shifts are indicative of molecular interactions. This feature allows water-solid interactions to be investigated with NIRS, i.e. bulk water to be distinguished from bound water and bound water including hydrates to be determined. In addition to a slight shift towards higher wavelengths, hydrate water bands are sharper than bulk water bands, since the energetic state of water molecules within a crystal lattice is rather uniform. NIRS is thus a powerful technique to distinguish between different hydrates or the anhydrate and the hydrate form of the same compound (Zhou et al. 2003; Higgins et al. 2003; Cao et al. 2006).

Considering the overall high sensitivity to water, it is not surprising that NIR moisture content determination of pharmaceutical solids, including APIs, excipients and drug products, has been described extensively in the literature. MLR and PLSR calibration modeling as well as peak area analysis (Brülls et al. 2007) have been used for NIR moisture assays. Earlier work has been comprehensively reviewed by Blanco et al. (1998) and Luypaert et al. (2007) and hence, will not be outlined in detail herein. Instead, the lessons learned from these applications and some of the results obtained in more recent studies will be briefly discussed.

The NIR detection limit for moisture assay was demonstrated to be as low as 0.04 % (Grohganz et al. 2010a). Method accuracy is comparable with KFT reference analysis, i.e. usually not an issue. NIR measurements are certainly more adequate than KFT when dealing with highly hygroscopic compounds (Zhou et al. 1998; Stokvold et al. 2002), since noninvasive measurements can be performed through glass bottles and vials, i.e. the sample can be kept inside the tightly closed packaging material without being exposed to ambient air at any time. This clearly reduces measurement errors resulting from handling and transfer of samples as required in lab analysis and allows stability testing to be performed in a reliable and efficient manner (Stokvold et al. 2002). The high NIR sensitivity to moisture and the noninvasive nature of the method enable a very low moisture content of spray- and freeze-dried materials to be determined with a prediction accuracy in the range between 0.08 % (Stokvold et al. 2002) and 0.5 % (Yip et al. 2012). The large difference in method accuracy between different applications reflect the impact of potential spectral interferences resulting from a ‘natural’ process-induced variation in cake density, morphology and solid-state characteristics not represented in the calibration sample set and/or in ‘artificially moisturized’ calibration samples. In case of mannitol, for instance, the formation of different polymorphic forms including a metastable hemihydrate strongly depends on the conditions used to adjust the moisture content. In fact, Grohganz et al. (2009, 2010a, b) could demonstrate that NIR spectral features attributed to the moisture content of freeze-dried mannitol or mannitol containing products are typically found in the loadings of the higher PCs (PC4 or PC5), whereas differences in density, morphology, polymorphic and/or pseudopolymorphic forms account for

most of the variation and are thus observed in the first PCs. This clearly emphasizes that large ‘natural’ sample sets and an algorithm such as PLS, which can find covariability between NIR spectral data and reference data, are needed for robust moisture calibration modeling. Successful method development and validation for NIR moisture assay of freeze-dried mannitol containing products with an RMSECV of 0.149 % in the moisture range of 0.15–4.27 % has been reported by Grohganz et al. (2010b).

Yip et al. (2012) proposed an alternative multivariate approach called Main and Interactions of Individual Principal Components Regression (MIPCR) to improve the NIR model performance with only a limited set of calibration samples by including interaction terms accounting for spectral interferences affecting the water related absorption bands. The MIPCR approach was found to be applicable for total moisture assay even in the presence of artificially modified mannitol samples. Interestingly, the state of hydration and its impact on the observed structural interferences has not been elucidated, although qualitative and quantitative analysis of the different states of water in freeze-dried mannitol has already been described earlier by Cao et al. (2006).

Nondestructive identification and quantification of the hydrate form of two drug compounds, forming single and multiple hydration states depending on the storage conditions, has been described by Higgins et al. (2003). Detailed analysis of the OH band shifts in combination with multivariate classification of the NIR spectra enabled the mechanism of hydration to be elucidated, the different hydrogen bonding pattern of the different hydrate forms to be distinguished and thus the conditions for stability of the drug substance to be identified. The spectral differences between anhydrate and hydrate form(s) in the water band region have been widely used for noninvasive stability screening of drug molecules such as azithromycin (Blanco et al. 2005), caffeine (Krzyzaniak et al. 2007) and imidafenacin (Uchida and Otsuka 2011). A fully validated NIR method for the nondestructive quantification of storage-induced transformations of azithromycin with a limit of quantification comparable to XRPD has been reported by Blanco et al. (2005).

NIR spectral changes beyond the water band resulting from structural differences between the hydrate and anhydrate form have also been used for identification and quantification purposes (Higgins et al. 2003; Vora et al. 2004). This approach has also been applied to elucidate the structural reorganisation of theophylline upon dehydration and rehydration in a study with the hyphenated DVS-NIR technique, which combines gravimetric data obtained from dynamic vapor sorption (DVS) with spectral data from NIRS (Vora et al. 2004).

Spectral differences between the anhydrate and the hydrate form(s) of a compound in the mid-IR are usually observed as shifts in the fingerprint region. Hydrates reveal an additional water absorbance band at approx. $3200\text{--}3400\text{ cm}^{-1}$ depending on the hydrogen bonding intensity. Due to the wealth of information contained in the MIR spectra, the method has been used extensively to detect solid-solid transformations of channel-type hydrates. Most of the studies have been performed with a diffuse reflectance setup, although particle size effects on spectral

quality have to be considered. The work published has been summarized in the reviews of Joergensen et al. (2009), Heinz et al. (2009) and Chieng et al. (2011). An example demonstrating the potential of DRIFTS is given by Kojima et al. (2008). The authors used XRPD, TG/DTA and DRIFTS to characterize the hydrate forms of ampicilline and nitrofurantoin. DRIFTS, being sensitive to changes in hydrogen bonding between water and API, could detect hydrate formation before XRPD.

Overall, it is obvious that NIRS is a powerful tool for the assessment of hydrate forms, since NIR spectra are even more sensitive to different hydrogen bondings than MIR spectra. On the other hand, MIR spectroscopy is well suited to detect subtle structural differences between the hydrate and anhydrate form of the same compound and/or to determine slight conformational changes during multiple solid-state transformations. Hence, it is still a valuable tool in early development especially when combined with DSC such as in the one-step simultaneous DSC-FTIR microspectroscopy described by Lin (2015).

3.2 Identification and Quantification of Polymorphic Forms

X-ray powder diffraction (XRPD) is certainly the most straightforward analytical technique for polymorph identification on the particulate level, since it provides direct information on the crystalline lattice. MIR spectroscopy, on the other hand, can provide distinct information about the molecular structure and conformation including intra- and intermolecular interactions, i.e. the hydrogen bonding pattern of a solid organic compound. Hence, it is a valuable and sensitive tool to characterize different polymorphic forms on the molecular level. It has been widely used as an alternative or a complementary technique to Raman spectroscopy to discriminate between different polymorphs on both, the qualitative and quantitative level. Numerous MIR applications usually in combination with XRPD and DSC can be found in the scientific literature. An extensive list of early papers is given in the review of Bugay (2001), whereas later work has been summarized and carefully reviewed by Heinz et al. (2009) and Chieng et al. (2011). The following discussion will focus on a few examples to demonstrate the potential and challenges of MIR applications in polymorphic analysis.

The MIR spectrum of a solid crystalline material is complex with only a certain percentage of the spectral information being readily interpretable. Hence, direct band assignment to certain molecular features is usually not feasible. Multivariate analysis of MIR spectral data, however, provides versatile options for polymorph screening and qualitative characterization of different polymorphic forms. Multivariate calibration modeling has also facilitated the quantitative characterization of the polymorphic composition of crystalline pharmaceutical bulk material. Braga and Poppi (2004), for instance, used PLSR in combination with NAS to determine the polymorphic purity of carbamazepine. Calibration modeling based on XRPD reference data was performed with binary mixtures in the range of 80–100 % (w/w) of form III in I measured in diffuse reflectance mode. The maximum absolute error

of the validated method was 2 %. Various multivariate methods, namely multivariate statistical process control (MSPC), SIMCA and OSC have been applied prior to PLS regression to estimate the complex polymorphic composition of sulfathiazole bulk material with a prediction error comparable to the XRPD reference method (Pöllänen et al. 2005).

The diffuse reflectance setup used in the aforementioned studies has been the most important sampling technique in quantitative polymorph analysis, since the measurements are noninvasive and the polymorphic forms remain intact due to limited sample preparation. However, reproducible sample homogeneity and consistent particle size of all constituents are issues to be considered, when developing a quantitative assay. The ATR mode requires less material and very little sample preparation. Disadvantages of the method are the low penetration depth of the MIR radiation and potential artefacts resulting from pressure-induced transformations. The combination of a variable temperature stage with MIRS, such as in hot-stage FTIR or DSC-FTIR microspectroscopy, is certainly the prime setup for polymorphic transformation studies in early development (Hsu et al. 2010; Wang et al. 2010a; Lin 2014).

The opportunity to measure noninvasively through glass bottles and use remote fiber optics for in-line applications has directed the interest towards NIR spectroscopy for both, polymorph screening and quantification. The number of publications noting NIRS in these fields has grown significantly over the last 15 years. An extensive list of papers can be found in the review of Chieng et al. (2011). Early studies revealed the reliability of NIR/PCA for fast polymorph screening (Aaltonen et al. 2003) and demonstrated, for instance, that polymorphs of sulfathiazole in binary mixtures can be determined down to 0.3 % w/w (Patel et al. 2001). Within the last decade, several studies have been conducted to compare the performance of NIRS with XRPD (Ziémons et al. 2011) and/or other spectroscopic techniques such as Raman (Heinz et al. 2007; Kogermann et al. 2007; Croker et al. 2012), ATR-FTIR (McArdle et al. 2005) or a combination of the two (Hu et al. 2010; Schönlichler et al. 2013). In addition, hyphenated NIR/Raman spectroscopy has been evaluated (Aaltonen et al. 2007a). Lessons learned from these studies will be briefly summarized hereafter.

NIRS is well suited for quantification of polymorphs in binary and ternary mixtures and often outperforms other spectroscopic techniques. McArdle et al. (2005) could demonstrate that NIRS offers significant advantages in quantitative accuracy and is also more convenient to use than both ATR-IR and XRPD. Schönlichler et al. (2013) observed pressure-induced polymorphic transitions with ATR-IR spectroscopy thus providing evidence that ATR-IR is often not the appropriate method. Some authors even revealed a slight advantage of the NIR method over Raman in both accuracy and limit of detection (Heinz et al. 2007; Hu et al. 2010; Croker et al. 2012; Schönlichler et al. 2013). The complementary information obtained from hyphenated Raman/NIR techniques in conjunction with PCA (Aaltonen et al. 2007a) or PLS-DA (Kogermann et al. 2007) is valuable when complex phase transformations occur including multiple anhydrate/hydrate forms. In those cases, the sensitivity of NIRS to water and hydrogen bondings can provide

the information necessary to distinguish between the hydrate and anhydrate form (s), whereas Raman spectroscopy reveals information about intramolecular differences of the molecular backbone.

To date, most of the quantitative NIR studies have been performed with well-characterized model compounds such as carbamazepine, indomethacin or sulfathiazole. Nevertheless, the results clearly indicate that NIRS is a reliable alternative to XRPD. In a comparative study using accuracy profiles, a statistical approach based on β -expectation tolerance intervals, the interchangeability of the two methods has been demonstrated for binary polymorphic mixtures of fluconazole (Ziémons et al. 2011). The huge potential of in-line NIR applications for monitoring process-induced polymorphic and/or pseudopolymorphic transformations during API and drug product manufacture will be outlined in Sects. 4 and 7.

3.3 *Cocrystal Characterization*

Within the last decade, pharmaceutical cocrystals composed of an API and at least one additional component have gained increasing interest to address technological, biopharmaceutical and stability issues (Qiao et al. 2011). As for any crystalline material, XRPD is the standard analytical method to identify new cocrystal forms. Spectroscopic analysis can provide complementary information to better understand the molecular interactions and determine the functional groups being involved in the cocrystal formation. Since cocrystal formation is usually based on structural units of homo- (e.g., acid-acid) or heterosynthons (e.g., acid-amide) that are stabilized by hydrogen bonds, mid-IR spectroscopy is a powerful tool to characterize cocrystals and distinguish cocrystals from salts. Depending on the intermolecular interactions, spectral changes relative to the parent solids range from only slight band shifts to clearly different spectral features. Molecular characterization of cocrystals by means of MIR has been reported for e.g. benzamide-benzoic acid (Brittain 2009), carbamazepine-saccharin (Jayasankar et al. 2006), piracetam-dihydrobenzoic acid isomers (Liao et al. 2010), indomethacin-saccharin (Basavoju et al. 2008; Zhang et al. 2012a, b) and theophylline-citric acid (Lin et al. 2013). ATR-IR in combination with XRPD and DSC allowed the mechanisms underlying carbamazepine-saccharin cocrystal formation upon cogrinding and storage to be investigated (Jayasankar et al. 2006). Spectral analysis provided valuable information regarding the different rates of cocrystallization between the hydrated and the anhydrous form of carbamazepine as well as the impact of water and process-induced amorphous phases on storage-induced transformations. Childs et al. (2007) used MIR analysis in combination with single crystal data to distinguish between cocrystal, salt and complex formation of theophylline with various cofomers. Different polymorphic forms of carbamazepine-saccharin and carbamazepine-nicotinamide cocrystals have been determined by a combination of MIRS and XRPD. In a recent paper, XRPD, DSC, ATR-IR and Raman

spectroscopy were compared in terms of quantification of ibuprofen-nicotinamide cocrystals and its co-formers (Soares and Carneiro 2014). In this study, Raman spectroscopy revealed the most precise PLS results, since the differences between the physical mixture and the cocrystal were more distinct in the Raman spectra than in the MIR spectra.

Cocrystal screening and quantification with NIRS has also been reported, although to a lower extent. One reason for this is the lower selectivity of the method as compared to MIR or Raman spectroscopy, which makes direct assessment of cocrystal formation more difficult, especially when dealing with different solid-state forms of the API. In a study performed by AllesØ et al. (2008), for instance, positive verification of indomethacin-saccharin cocrystal formation by NIRS/PCA was feasible only when including a set of reference samples representing different solid-state combinations, e.g. the two different polymorphs and the amorphous form of the API in physical mixtures with the guest molecule. In contrast, Raman spectroscopy allowed straightforward interpretation of the sample spectra and thus direct assessment of cocrystal formation including solid-state-transitions.

The successful application of NIRS for real-time monitoring of co-crystal formation has been reported by Kelly et al. (2012) and Sarraguca et al. (2014). Kelly et al. (2012) used a high temperature probe to monitor the formation of ibuprofen-nicotinamide cocrystals during solvent free continuous crystallization in a twin screw extruder. Second derivative spectra revealed band shifts related to the hydrogen bonds formed between ibuprofen (O-H/C=O) and nicotinamide (NH and NH/C=O) upon cocrystal formation. PLS calibration modeling was performed based on XRPD reference data and reliable predictions were obtained by excluding temperature effects on the spectra. NIR on-line monitoring of furosemide-adenine cocrystallization by solvent evaporation has been described recently (Sarraguca et al. 2014). The main events during the cocrystallization process, namely nucleation and solvent evaporation were clearly distinguished in a score plot thus contributing to a better understanding and control of the process. PCA could distinguish between furosemide, adenine and the cocrystal, the formation of which was verified by XRPD and ATR-IR. Both, ATR-IR and NIRS identified the carboxyl acid group of furosemide and the amine group of adenine as the functional groups involved in hydrogen bondings upon cocrystal formation. Overall, it is obvious that MIRS and NIRS are valuable tools to evaluate cocrystal formation on a molecular level.

3.4 Assessment of Crystallinity and Amorphous State

Process- and/or storage-induced recrystallization is one of the major issues to be considered when dealing with amorphous solids. Crystalline materials, on the other hand, may be accidentally rendered partly amorphous by mechanical and/or thermal stress. In either case, significant changes in material performance have to be

expected. Hence, analytical methods capable to detect and/or quantify subtle changes in the amorphous/crystalline ratio, preferably in a fast and nondestructive manner, are required in both early development and later production (Shah et al. 2006; Einfal et al. 2013).

Typically, the amorphous form of a given drug molecule or excipient gives rise to MIR and NIR spectra that differ significantly from their crystalline counterparts. The spectral differences are mainly related to conformational and intermolecular differences. The amorphous state is characterized by a wider range of conformations as compared to the crystalline state which typically leads to a band broadening in both, MIR and NIR spectra. Moreover, the differences in local intermolecular interactions, i.e. the overall hydrogen bonding pattern between amorphous and crystalline solids are reflected by characteristic band shifts and intensity differences. In fact, MIRS and NIRS in conjunction with MVDA are valuable tools to probe the amorphous state on a molecular level and/or provide quantitative information on the degree of crystallinity of a solid compound.

Numerous studies have been performed to compare MIRS and/or NIRS with Raman spectroscopy in terms of sensitivity to identify and characterize subtle structural differences in amorphous and crystalline phases, method accuracy and limit of detection (Heinz et al. 2007, 2008; Savolainen et al. 2007a, b). Moreover, hyphenated techniques such as gravimetric dynamic vapor sorption (DVS) in combination with NIRS have been reported as a fast and reliable means to evaluate stress-induced changes in the amorphous/crystalline ratio (Moran and Buckton 2009). Readers interested in a comprehensive coverage of the different topics are referred to some excellent review articles (Shah et al. 2006; Heinz et al. 2009; Chieng et al. 2011; Einfal et al. 2013). Hereafter, some examples will be discussed in more detail.

MIR spectroscopy is a powerful analytical tool in early development to learn more about the distinct differences in the hydrogen bonding pattern and strength between the crystalline and amorphous state of the same compound or structurally related compounds (Tang et al. 2002; Kaushal et al. 2008). MIRS can also provide molecular information to improve the understanding how downstream processing and storage conditions will impact the chemical and physical stability of amorphous drug molecules. Studies based on DRIFT measurements in combination with XRPD comprise the evaluation of milling (Chieng et al. 2006, 2008; Zhang et al. 2009) and comilling effects (Chieng et al. 2009). In situ measurements in a controlled humidity transmission cell have been performed to investigate the effect of relative humidity on the recrystallization kinetics of amorphous nifedipine (Chan et al. 2004) and nitrendipine (Chan et al. 2007). Peak heights were used to monitor the devitrification process and the conversion of a transient crystalline form to the stable crystalline form in a semiquantitative manner (Chan et al. 2004). Quantification of the amount of undesired amorphous cyclosporine in crystalline samples based on FT-MIR transmittance measurements in conjunction with multivariate PLS calibration modeling has been reported by Bertacche et al. (2006). Recently, ATR-IR has been applied to co-amorphous naproxen and indomethacin systems to

characterize their molecular interactions (Löbmann et al. 2011). In a second study, vibrational modes from theoretical calculations could be matched with the experimentally observed MIR spectra (Löbmann et al. 2013).

NIRS has been successfully applied to quantify the amorphous/crystalline ratio of various model compounds including sucrose, lactose, indomethacin and miokamycin. PLS calibration modeling based on binary mixtures revealed that low amounts of amorphous and crystalline material can be determined to within 1 % and 0.5 % (w/w), respectively (Fix and Steffens 2004). Good overall agreement between NIRS data and XRPD data has been demonstrated by several authors. The high sensitivity of NIRS to low levels of crystallinity is specially valuable when measuring lyophilized compounds through glass vials (Bai et al. 2004). Reliable NIR quantification of the amorphous form and two different polymorphs of indomethacin in ternary mixtures has been demonstrated by Heinz et al. (2007). Moreover, the sensitivity of NIRS to conformational changes and variation in intermolecular bondings enabled amorphous indomethacin samples prepared by milling, quench-cooling and spray-drying to be distinguished (Savolainen et al. 2007a). Recent papers describe the use of NIRS to quantitatively monitor the conversion of sulfathiazole and sulfamerazine polymorphs into the amorphous form during cryomilling (Hu et al. 2013; Macfhionnghaile et al. 2014). NIRS has also been applied for in situ stability testing of amorphous indomethacin, i.e. to monitor the transformation to different polymorphs when stored in 96-well plates at low or high relative humidity (Otsuka and Tanabe 2012). Another interesting application in early drug development is the real-time NIR monitoring of the recrystallization kinetics of small amorphous drug particles during acoustic levitation (Rehder et al. 2013). High speed NIR measurements enabled the fast solid-solid transformations to be detected and quantified with adequate accuracy by means of MCR.

Due to the sensitivity of NIR spectra to water, challenges associated with the general hygroscopicity of an amorphous material and the different water-solid interactions of the crystalline and amorphous state have to be considered, when developing a quantitative calibration model for monitoring solid-solid transformations. On the other hand, a combination of gravimetric and spectroscopic measurements on the same sample can provide the information necessary to understand the mechanism and kinetics of water uptake and/or release during a phase transformation and its impact on the transformation kinetics and dynamics. A modulated DVS/NIR technique, for instance, was applied to elucidate the variable crystallization behavior of spray-dried amorphous trehalose samples prepared from solutions of different solute concentration (Moran and Buckton 2009). NIR spectra revealed differences in the extent of hydrogen bonding upon modulated exposure to high relative humidity. These differences were closely related to a different short-range order in the amorphous samples. The outcome of this study significantly improved the understanding how structural manipulation upon spray-drying can impact the ability of amorphous trehalose to crystallize when exposed to high relative humidity.

4 Use as Real-Time PAT Tools in Drug Substance Manufacture

In 2004, the United States Food and Drug Administration published the process analytical technology (PAT) guidance for industry (USFDA 2004a) and the final report on pharmaceutical cGMPs for the twenty-first century (USFDA 2004b) to promote significant changes in the development and manufacture of pharmaceuticals. Since then, much progress towards multivariate process monitoring for real-time detection of failures and improved operational control has been made in both, primary and secondary manufacture. Hereafter, a brief description how MIR and/or NIR sensors can be successfully implemented in API manufacturing is provided and a few applications in process development and routine production are discussed. PAT tools in secondary manufacture are outlined in Sect. 7.

4.1 Reaction Monitoring

The chemical synthesis of an API usually comprises multiple steps and the reaction mixtures of each step may contain transient species in multiple phases, which makes physical sampling and off-line analytics challenging. In situ analysis, instead, can provide the real-time information facilitating screening and optimization of reaction conditions, identification of steady state in flow chemistry reaction monitoring, evaluation of catalyst deactivation kinetics and reaction end point control.

Spectroscopic methods have been widely applied to API reaction monitoring usually in combination with e.g. FBRM and mass spectrometry to gain information from the liquid, solid and gas phase, respectively. MIRS is certainly the primary spectroscopic PAT tool in API reaction monitoring due to its high specificity, but in recent years, the number of NIR applications has also been growing significantly. Within the last two decades, numerous papers have been published describing the use of ATR-FTIR or NIR probes for real time API reaction monitoring and control. Reaction types investigated include alkylation (Wiss et al. 2005; Wiss and Ermini 2006; Cervera-Padrell et al. 2012), epoxidation (Ge et al. 1995), esterification (Blanco et al. 2006a, 2007) and hydrogenation (Marziano et al. 2000; Andanson et al. 2010; Kiefer et al. 2012). Most of the published work reports on laboratory scale applications during development aiming to improve yield, control product quality and/or ensure operational safety. A few papers also describe end point determination and process verification in the production scale (Wiss et al. 2005; Wiss and Ermini 2006; Cervera-Padrell et al. 2012; Clegg et al. 2012).

The availability of highly flexible and miniaturized ATR-IR immersion probes based on robust fiber optics with high chemical and pressure resistance has extended the versatility of the applications with respect to the experimental setup and the reaction volume ranging from 1 mL to litres (Heise et al. 2003; Blum and

John 2012). Applications in a nitrogen or argon purged glove box (Minnich et al. 2007) as well as in miniaturized flow reactors are feasible (Chanda et al. 2013). Moreover, the use of ATR-FTIR probes for exothermic reaction monitoring under cryogenic conditions such as in the synthesis of organolithium intermediates has been reported (Li 2010; Lumpi et al. 2012). Temperature induced spectral artefacts leading to differing thermal expansion coefficients of the probe materials can be corrected by fast Fourier transformation (FFT).

The availability of rugged NIR spectrometer and low cost, robust NIR probes with a high sample penetration depth in combination with the opportunity to use longer fiber-optics as compared to MIRS has promoted industrial NIR applications in API reaction monitoring (Wiss et al. 2005). In conjunction with MVDA, the method can be highly selective as demonstrated in several papers (Blanco et al. 2006a, 2007). Moreover, transfer to the production area is facilitated (Wiss and Ermini 2006). A recent example is the successful development and industrial implementation of a robust in-line NIR method for monitoring and control of the continuous synthesis of an API intermediate by a Grignard alkylation reaction (Cervera-Padrell et al. 2012). API synthesis can now be performed with significantly higher yields and lower impurity levels. Overall, it can be concluded that both, ATR-IR and NIR probes are adequate tools for real-time monitoring of many chemical reactions relevant to API synthesis. The individual choice certainly depends on the specific process constraints and the required specificity and/or selectivity.

4.2 Crystallization

Crystallization is one of the most critical steps during API manufacture, since it determines the purity and physical characteristics of the drug molecule. Design of a robust crystallization process thus requires a thorough understanding of how the operation conditions affect the outcome with respect to the desired polymorph, crystal shape and particle size. In situ analysis is favourable, since analytical artefacts associated with sample isolation can be minimized. Numerous papers have been published describing the use of MIR or NIR spectroscopy usually in combination with focus beam reflectance measurements (FBRM) for real-time monitoring of crystallization processes. The advances made within the past 20 years have been comprehensively reviewed and discussed by Yu et al. (2007) and Nagy and Braatz (2012). Most of the published work has been performed in laboratory scale for screening and optimization of operational conditions. Only a few more recent papers describe setups for production scale operations (Nagy and Braatz 2012; Nagy et al. 2013; Sanzida and Nagy 2013; Helmdach et al. 2013; Simone et al. 2015).

ATR-FTIR probes in conjunction with MVDA are the prime tool for in-situ solubility measurements in cooling and anti-solvent crystallization thus enabling the level of supersaturation to be determined. The rationale behind this approach is

the fact that only the liquid solution being in close contact with the probe is measured without interference from crystal formation. Within the last decade, there has been an evolution from simple to more complex applications of the ATR-FTIR method most often in combination with FBRM or PVM to identify the onset of nucleation (Zhou et al. 2006; Nagy et al. 2008; Kee et al. 2009, 2011; Barrett et al. 2010; Duffy et al. 2012). Raman spectroscopy may provide complementary information to further characterize the polymorphic form and/or determine polymorphic transitions in the process slurry (Schöll et al. 2006).

Closed-loop supersaturation control of crystallization processes based on ATR-FTIR in-situ measurements has been reported by Alatalo et al. (2010), Barrett et al. (2010) and Duffy et al. (2013). Calibration transfer between process scales has recently been described by Helmdach et al. (2013). The authors established a univariate model based on peak integration which could be transferred from the lab to the pilot plant. Application of indirect hard modeling (IHM) could successfully compensate for variable operation parameters such as water vapor inside the spectrometer, variable bending radius of the moving fiber optics and minor encrustations of the sensor. Method implementation in the pilot plant was thus feasible without time-consuming and cost-intensive modifications of the existing setup, i.e. the ATR-IR probe was simply connected to a transmission flow cell within a loop to the reactor.

As an alternative to ATR-IR measurements, the use of NIR transreflectance probes for the determination of solute concentrations during crystallization is gaining increasing interest, especially for production scale operations. This trend can be explained by the fact that NIR fiber optic probes are cheap and more robust and versatile than ATR-IR setups. However, unlike ATR-IR, spectral information is strongly affected by solid matter, an issue that has to be considered in calibration development (Zhou et al. 2006; Li et al. 2008; Kadam et al. 2010). In principle, the NIR spectral information gained in one single measurement from both, the solution and the solid phase can be used to simultaneously predict the solute concentration, the solvent and/or anti-solvent composition, the onset of crystallization and the polymorphic form. The use of in situ NIRS in combination with a new genetic algorithm and support vector machine approach for the simultaneous characterization of multiple properties of the solid and the liquid phase during seeded and unseeded cooling crystallization of L-glutamic acid has been demonstrated by Ma and Wang (2011). Schaefer et al. (2013) used an on-line NIR configuration with a transmission probe to control an industrial seeded API crystallization process by monitoring both the API concentration and the residual solvent content. The PLS models developed at lab scale were tested in the industrial pilot plant and validated according to the ICH Q2 (R1) guideline, using the accuracy profile approach (Schaefer et al. 2014). It is worth mentioning that this method has been approved by the European Medicines Agency (EMA).

Despite a lower specificity for structural differences of polymorphs as compared to Raman probes, NIR setups were found to be capable to detect polymorphic transformations in addition to nucleation and crystal growth, even in the presence of water (Simone et al. 2015). Overall, it is evident that complementary PAT tools are

favourable for the robust detection of CQAs in API crystallization processes. To select the optimal sensor configurations, a composite sensor array (CSA) capable to integrate and analyze the signals from different sensors has recently been developed (Simone et al. 2015). In fact, the CSA concept proposed by the authors is a step forward towards implementation of automated decision support and control systems in API crystallization processes.

4.3 Drying

Critical quality attributes (CQAs) to be controlled upon API drying are the residual content of moisture and/or organic solvents and the solid-state form. In spray drying, particle size and morphology and, in case of poorly water-soluble drug substances, the amorphous state may be additional characteristics to be controlled.

NIR spectroscopy is a reliable in-line technique for real-time end point control of drying processes (Hicks et al. 2003; Märk et al. 2010; Schneider and Reich 2011a, b). It enables product moisture content or residual organic solvents to be quantified and solid-state transformations to be monitored in a noninvasive manner (Zhou et al. 2003; Kogermann et al. 2008; Touil et al. 2012). Hence, disadvantages and risks associated with manual sampling followed by lab analysis with Karl Fischer titration (KFT), gas chromatography (GC) or loss on drying (LOD), especially when dealing with hygroscopic or cytotoxic compounds, can be avoided.

Schneider and Reich (2011a) describe the successful application of in-line NIRS for monitoring and control of both water and organic solvent content of two model substances in a rotating suspension dryer, which combines centrifugation, washing and thermal drying in one filter basket. Though NIR method implementation was challenging due to equipment and process constraints, the information gained from the process trajectories were valuable to control the process and ensure product quality. The advantage of using a noninvasive in situ NIRS sampling approach for monitoring the moisture content upon filter drying of a cytotoxic compound has been demonstrated by Hicks et al. (2003). Despite significant variability in wet cake density during optimization of the workup, i.e. filtration procedure, the PLS calibration model based on KFT reference data covering the range of 0–15 % moisture content revealed a SEP of 0.99 % w/w, indicating adequate method accuracy. Märk et al. (2010) used an on-line NIRS setup to monitor the fluid bed drying (FBD) process of an antibiotic substance. Assay, water content and residual solvent were recorded simultaneously with high accuracy based on PLS models developed with HPLC, KFT and GC as reference methods. The system proved to work stable and could be automated to a certain extent for process end point determination.

Regarding method accuracy, spectral effects induced by the process dynamics and reference sampling issues were found to be most critical. The impact of air dynamics in a fluid bed dryer (FBD) on NIR spectral quality has been described by

Green et al. (2005). Schneider and Reich (2011b) showed that the influence of spectral uncertainty on the prediction error of NIR measurements resulting from high-frequency fluctuations can be dominant at a low S/N ratio. The authors provide an efficient optimization approach to reduce spectral uncertainty to a minimum. The approach was successfully applied to a challenging NIR in-line method in a rotating suspension dryer for monitoring water and ethanol content of a model substance (Schneider and Reich 2011a). Sampling issues in FBD were investigated in detail by Green et al. (2005) and more recently by Heigl et al. (2013). Both studies reveal that the way in which reference sampling is performed has a significant impact on the accuracy of the NIR in-line method accuracy. Most crucial are the downtime between thief-probing a sample and its actual analysis and the sample amount available for reference analysis (Heigl et al. 2013). This is especially important when measuring residual volatile organic solvents (Schneider and Reich 2011a, b).

In conclusion, it is evident that multiple NIR in-line measurements are more representative of the drying process than temporally sparse off-line tests and more straightforward with respect to end point control. The low penetration depth compared to other methods such as microwave resonance technology can be compensated by the measurement frequency. An additional advantage of using in-line NIRS for end point control of an API drying process is the opportunity to simultaneously monitor the conversion to the preferred solid-state form.

Zhou et al. (2003) were the first who described in-line NIR monitoring of a drying process with concomitant distinction between surface and bound water of a drug substance forming different hydrates. The study revealed that NIRS can serve as a reliable PAT tool to ensure that the desired hydrate form is achieved. Since then, NIR monitoring of API dehydration upon FBD has been reported extensively, although mainly for granules rather than pure APIs (see Sect. 7.2). However, the lessons learned from these studies clearly indicate that in-line NIRS in combination with MVDA is a straightforward and reliable PAT approach to monitor and control drying induced pseudopolymorphic transformations.

An in-line NIR method to simultaneously monitor moisture content, dehydration and polymorphic transformation of theophylline upon stirred bed vacuum drying has recently been described by Touil et al. (2012). In this study, reliable quantification of the different solid state forms based on PLS calibration modeling was first demonstrated. The real-time NIR spectral information could then be used to investigate the impact of process parameters on both, the drying and the solid-state transformation kinetics. This enabled a detailed insight into the dehydration and transformation process. In addition, the input parameters of a process controller could be identified.

The utility of NIRS for at-line solid state analysis of spray-dried products including determination of moisture content, particle size and amorphous content has also been demonstrated (Savolainen et al. 2007a; Maltesen et al. 2012). Hence, noninvasive real-time monitoring of these CQAs during the process should be feasible by means of a NIR probe at the glass vessel of the spray-dryer.

5 Application on Solid Oral Dosage Forms

Manufacture of solid oral dosage forms such as tablets and capsules comprises multiple steps, each having an impact on the final drug product performance. Hence, to assess the status of the product and finally confirm batch release, fast at-line, in-line or on-line analysis of the critical quality attributes (CQAs) in different steps across the manufacturing process is helpful in both development and routine production. Moreover, efficient stability testing heavily relies on rapid analytical procedures.

The dual dependence of the NIR signal on chemical and physical sample characteristics allows various analytical targets (i.e. CQAs) to be simultaneously determined in a nondestructive manner. Although sometimes quite challenging, determination of chemical, physical and even related biopharmaceutical CQAs from one single NIR measurement is feasible and reliable when properly performed (Reich 2005; Anderson et al. 2008). In fact, NIR identification and quantification of the API in intermediates and finished dosage forms may comprise solid-state characterization, i.e. analysis of polymorphic or pseudopolymorphic form composition (Blanco and Villar 2003; Blanco et al. 2005). NIRS is also gaining some importance for the molecular characterization of drug/polymer interactions in solid dispersions of poorly soluble drugs (Rahman et al. 2010a, b; Zidan et al. 2012), which has traditionally been performed by FT-MIR spectroscopy (Taylor and Zografis 1997; Liu and Desai 2005; Huang et al. 2011; Karolewicz et al. 2012). The moisture content of powders, granules, pellets, tablets and capsules can be reliably determined with NIRS, as reviewed by Luypaert et al. (2007) and reported by Mantanus et al. (2009) and Corredor et al. (2011). The potential of NIRS for nondestructive quality control and stability testing of hard and soft capsules including shell/fill interactions and shell crosslinking has been verified by Reich (2005). Off-line and at-line measurements to simultaneously determine blend uniformity (BU) and particle size of pharmaceutical powder blends or granules and content uniformity (CU), hardness, coating thickness and/or dissolution of tablets have also been widely demonstrated (Blanco et al. 2006b, c; Chen et al. 2001; Cogdill et al. 2005a, b, c; Reich and Frickel 1999, 2000; Frickel and Reich 2000; Reich 2000a, b, 2001; Moes et al. 2008; Tabasi et al. 2008a, b, c; Weißner 2006; Weißner et al. 2006a, b; Wu et al. 2013).

In the following, the potential of MIRS and NIRS for characterizing solid dispersions and the rationale behind the NIR approach to measure particle size, tablet hardness and drug dissolution including challenges to be managed when the measurements are performed in the lab settings will be discussed in more detail. Lessons that can be learned from lab measurements, including method constraints and limitations, are also valuable for real-time PAT applications, which are discussed in Sect. 7.

5.1 Molecular Characterization of Solid Dispersions

Solid dispersions based on hydrophilic or amphiphilic polymers have gained increasing interest as a formulation platform for poorly water-soluble drug

molecules. In product development, FT-MIR spectroscopy is a well-established analytical tool to characterize solid dispersions, i.e. to probe the nature and extent of molecular interactions between polymer and API. The rationale behind this approach is a shift and broadening of the absorption bands of functional groups forming hydrogen bonds upon interaction. Changes in wavelength, band width and/or intensity can also provide information on the solid-state form of both drug substance and polymer. Hence, FTIR spectra can be used to identify molecular interactions directly after production and evaluate stability, i.e. the tendency of the amorphous API to recrystallize upon storage. Numerous papers report on the successful application of FT-MIR spectroscopy in combination with other analytical techniques such as XRPD, DSC and DVS to investigate drug/polymer combinations including indomethacin/PVP (Taylor and Zografi 1997), nifedipine/PEG (Huang et al. 2011), carbamazepine/Soluplus[®] and carbamazepine/ hydromelllose acetate succinate (Alshahrani et al. 2015). MIRS has also been applied as complementary analytical technique to characterize drug/cyclodextrin inclusion complexes. Studies comprise, for instance, omeprazole/methyl-beta-cyclodextrin (Figueiras et al. 2007), loratadine/hydroxypropyl-beta-cyclodextrin (Lin et al. 2010) and gemfibrozil/dimethyl-beta-cyclodextrin (Aigner et al. 2012).

Recently, NIR spectroscopy in combination with MVDA has gained importance in stability studies e.g., to detect drug recrystallization including polymorphic transformations (Maniruzzaman et al. 2014) and to quantify drug crystallinity upon storage (Zidan et al. 2012). NIR in-line applications are expected to be extremely useful to monitor phase transformations during production, e.g. in hot melt extrusion as demonstrated by Maniruzzaman et al. (2014). This latter aspect is discussed in more detail in Sect. 7.4.

5.2 *Challenges of Particle Size Determination*

NIR measurements of particle size in diffuse reflectance rely on particle size dependent scatter effects resulting in nonlinear baseline shifts. However, reliable quantitative calibration modeling is usually not an easy task, since correlation of spectral information with particle size is often hampered by complex interrelated material and particle size dependent absorption and scatter effects (Burger et al. 1998; Shi and Anderson 2010). In fact, different chemometric approaches have to be applied depending on the application, i.e. the mean particle size, the particular particle size distribution, the refractive indices and the absorption properties of the particulate matter under investigation. Most crucial for NIR quantification of mean particle size are large particle size differences. This can be attributed to the fact that particle size effects on the absorption coefficient are more pronounced for small particles ($\leq 90 \mu\text{m}$) than for large particles. Moreover, sample presentation is of utmost importance, since spectral reproducibility is strongly affected by sample compactness. Considering these issues, it is obvious that NIRS is not the first choice when accurate particle size measurements are required.

NIR spectra can, however, provide a rough estimate of the particle size when the method is anyhow used for the determination of other CQAs. In addition, the multivariate spectral information can be used to predict the performance of granules or powders upon further processing (Otsuka et al. 2003; Otsuka and Yamane 2009).

5.3 *Nondestructive Tablet Hardness Testing*

Nondestructive NIR hardness testing of tablets has been described by several groups (Blanco et al. 2006b, c; Tabasi et al. 2008a; Weißner 2006; Weißner et al. 2006b; Wu et al. 2013). Early work has been thoroughly reviewed by Reich (2005). Reflectance as well as transmission measurements have been reported. Both methods are generally applicable; due to density variations in different regions of the tablet, hardness is, however, better predicted by transmission measurements (Reich 2000b, 2001).

Spectral effects that can be used for calibration development depend on the range of hardness levels to be included in the model and the tablet ingredients. Irrespective of the formulation, a “primary” spectral effect of wavelength-dependent baseline shifting with increasing hardness resulting from a decrease in tablet porosity is observed at low hardness levels (Fig. 3.3). At higher hardness levels, a pressure-induced “secondary” spectral effect, namely a peak shifting arising from changes in interparticulate and/or intermolecular bondings can be

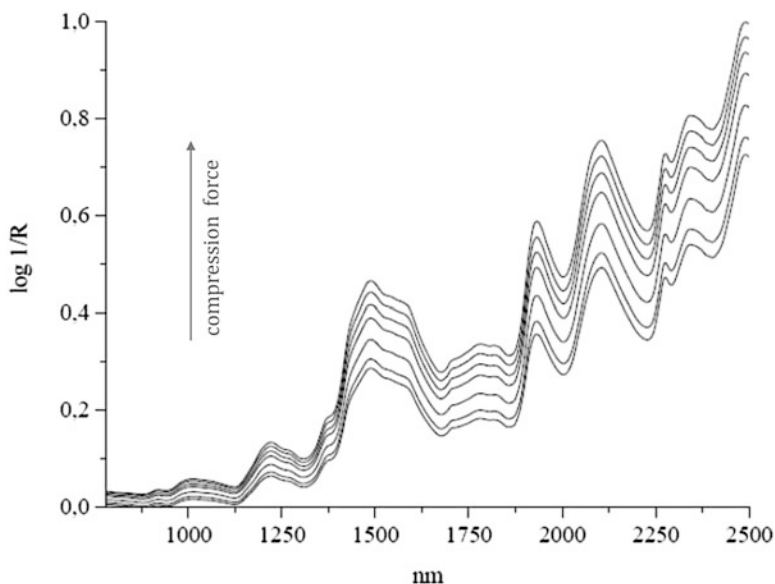


Fig. 3.3 NIR reflectance spectra of tablets with different hardness levels

observed. The secondary effect strongly depends on the material properties, being most pronounced with excipients such as microcrystalline cellulose grades that reveal a pressure-induced plastic deformation (Reich 2000a, b, 2001).

Primary effects can be favourably modeled by reducing the relevant spectral information to slope and intercept, i.e. a best-fit line through each spectrum. This approach based on reflectance spectra was found to be insensitive to slight formulation changes (Kirsch and Drennen 1999). Multivariate PCR or PLS methods (Shah et al. 2007; Tanabe et al. 2007; Tabasi et al. 2008a, b, c; Weißner 2006) and ANN (Chen et al. 2001; Wu et al. 2013) have been applied to both transmission or reflectance spectra to model additional secondary effects. These models are certainly more sensitive to formulation changes, since they also rely on material specific spectral effects. Indeed, differences in primary and secondary spectral effects can be used in tablet formulation and process development to better understand the consolidation characteristics of different formulations (Reich 2000a, b, 2001). To this end, a global calibration model including eight different excipients has been developed by Weißner et al. (2006b).

5.4 Nondestructive Prediction of Dissolution Performance

Prediction of drug dissolution from NIR spectra of immediate release (IR) tablets relies on formulation and/or pressure induced differences in tablet morphology (i.e. particle size, density, porosity) and interparticular bondings (Blanco and Alcalá 2006; Donoso and Ghaly 2005; Freitas et al. 2005; Otsuka et al. 2007; Weißner et al. 2006a; Weißner et al. 2007). Since IR tablets are usually manufactured with tight tolerances, quantitative modeling of drug dissolution of commercialized IR tablet products is usually challenging without additional lab samples. To reduce the calibration effort, augmentation of the calibration sample set with samples from stability, i.e. samples stored under ICH conditions has been reported in the literature. However, this approach should be performed with care, since temperature- and/or moisture-induced spectral effects are different from e.g. pressure-induced spectral effects and thus not always applicable to reflect the dissolution performance under normal storage conditions. Thus, a qualitative NIR “conformity” approach is often a better option to verify drug dissolution of IR tablets.

Contrary to IR tablets, the dissolution performance of IR capsule products is often related to microstructural features of the capsule shell (Reich 2004). Nondestructive NIR determination of storage-induced disintegration and/or dissolution changes of hard and soft capsules therefore usually relies on chemical changes resulting from capsule shell crosslinking (Gold et al. 1997, 1998; Reich 2005). Since rate and extent of crosslinking are affected by shell formulation, fill composition and storage conditions (i.e. temperature, relative humidity), development of reliable quantitative calibration models requires a thorough understanding of the impact of all variables on both capsule crosslinking and NIR spectra. Spectral interferences to be considered are variable moisture effects and temperature-induced structural changes not related to crosslinking (Reich 2005).

Quantitative NIR calibration modeling is usually easier to perform when dealing with modified release (MR) film coated tablets. Since drug dissolution rate of film coated MR tablets depends on film thickness and uniformity, samples taken from various time points during the manufacturing process can be used for calibration development. Applications based on both transmission and reflectance spectra have been described in the literature (Kirsch and Drennen 1995; Reich and Frickel 1999; Frickel and Reich 2000). The latter approach however, may not be applicable to tablets with a very thick coating containing a high amount of pigments.

In case of matrix tablets, drug release rate usually depends on the concentration and distribution of a sustained release polymer used as filler and/or binder. Moreover, pressure-induced physical effects may contribute to the dissolution profile. Interpretation of PCA scores and loadings can be helpful for variable selection to be used in quantitative NIR calibration modeling (Tabasi et al. 2009). Multilayer tablets containing an immediate release (IR) and a controlled release (CR) layer are most challenging, since NIR spectral information from both layers are required for dissolution modeling. A successful industrial NIR application has been reported by Weißner et al. (2006a). Robust calibration models for the prediction of the sustained release profile based on reflectance spectra from the CR layer could be developed with samples from production and stability testing. Moreover, batch-to-batch variability of the initial dissolution rate could be attributed to a variable distribution of the disintegrant in the IR layer (Weißner 2006).

5.5 Simultaneous Determination of Multiple CQAs

Considering the NIR applications outlined above, the potential of the method becomes obvious, namely to allow several CQAs such as identity, drug content, hardness and dissolution of solid oral dosage forms to be determined from one single nondestructive measurement. The multivariate NIR spectral information, however, may cause analytical problems, if not adequately handled. This is due to the fact that each CQA, if not the analytical target, has to be considered as an interfering parameter in the calibration development process. In fact, most challenging is how to achieve the required selectivity and accuracy for each analytical target parameter in a certain application. Examples of robust and reliable industrial NIRS calibrations for the simultaneous determination of drug content, tablet hardness and drug dissolution of three tablet products with different release profiles, namely IR tablets, enteric coated tablets and sustained release multilayer tablets, can be found in the PhD thesis of Weißner (2006). In case of the IR tablet product, the validated method gained FDA approval. Moreover, excipient-independent models have been developed for both NIR drug assay and tablet hardness determination with the potential to be applied in early product development followed by transfer to production.

6 Application in Protein Formulation Development

6.1 Evaluation of Protein Secondary Structural Changes and Beyond

One of the major challenges when formulating protein therapeutics is to preserve a 'native-like' structure of the protein during processing, shipping and upon long term storage. Biopharmaceutical product development therefore requires the application of complementary analytical techniques that enable local and global structural perturbations to be evaluated. MIR spectroscopy is a well-established analytical tool for estimating secondary structural changes of proteins in solid and solution state (Manning 2005). The technique has been applied in stability testing of aqueous protein solutions (Dong et al. 1990; Fabian et al. 1993; Jiang et al. 2011), in formulation and process optimization of freeze-dried (Carpenter et al. 1998; Chang et al. 2005; Abdul-Fattah et al. 2007; Al-Hussein and Giessler 2013), spray-dried (French et al. 2004; Maury et al. 2005; Schüle et al. 2007) and spray-freeze-dried (Constantino et al. 2002) products as well as in controlled release product development (Van de Weert et al. 2000; Jorgensen et al. 2003; McFearin et al. 2011).

The rationale behind this approach is the conformational sensitivity of the MIR absorption bands of the protein backbone, the so called normal modes (A, B, I-VII) of the amide group. Most widely used for protein secondary structural analysis is the amide I band between 1600 and 1700 cm^{-1} originating from the C=O stretching vibration of the amide group. The conformational sensitivity of the amide I band includes hydrogen bondings and coupling between transition dipoles. Hence, protein secondary structural features such as α -helix, β -sheet, turns and random coil display distinct amide I frequencies (Barth and Zscherp 2002; Barth 2007).

Due to the overlap of water bands and the amide I protein bands, accurate subtraction of the water spectra resulting from traces of water vapor in the air and/or the sample solution itself is inevitable for a reliable protein secondary structural analysis. Modern FT-MIR spectrometers with a high S/N ratio enable high quality difference spectra to be obtained even for proteins in highly diluted aqueous solutions. When measuring in transmission mode, a small cell path length (e.g. 5–10 μm) and a protein concentration of >10 mg/mL are recommended. Noninvasive measurements in both solid and solution state became feasible with the ATR sampling technique. In fact, the low amount of sample required for analysis (typically in the range of 10–100 μg), the short measuring time and a high time resolution (down to 1 μs with moderate effort) have certainly been recognized as important advantages of the FT-MIR technique. Noteworthy is, that for comparative measurements it is mandatory to apply the same physical sampling mode (Van de Weert et al. 2001).

MIR signal processing is, however, less straightforward when dealing with proteins rather than small drug molecules. This is due to the fact that proteins are

usually composed of various domains of different secondary structural elements. The amide I band is thus a complex composite of these structural features. Since the band width of the contributing components is usually greater than the separation between the maxima of adjacent peaks, individual component bands are overlapped and not resolved. Spectral analysis therefore requires mathematical methods to resolve the individual bands. Common approaches can be classified into: (1) methods based on band narrowing and decomposition of the broad amide I band into its components or (2) multivariate techniques, i.e. pattern recognition methods. Since most pharmaceutical applications still rely on procedures of the first category, their strengths and weaknesses will be briefly discussed.

To enhance the resolution of the amide I band of a protein, i.e. to decompose the overlapped peaks into their principal bands, two procedures have been widely used, namely *Fourier self deconvolution* (FSD) and calculation of the *second derivative* of the absorption spectrum. Since both procedures amplify the spectral noise, the degree of band narrowing is limited by the S/N ratio of the spectrum. This means that the full width of half height (FWHH) of the bands has to be greater than the resolution of the instrument. A high S/N ratio is therefore required for resolution enhancement with FSD or derivation. An issue potentially encountered with both FSD and derivation of amide I spectra is the disproportional amplification of water vapour induced bands. Careful purging of the spectrometer with dry air or nitrogen is thus inevitable when analyzing proteins.

The FSD method, first proposed by Kauppinen et al. (1981), provides the advantage to preserve the profile, area and position of the bands and therefore allows 'real' quantitative calculations. On the other hand, its application requires the setting of the FWHH of the line shape function and the truncation frequency of the apodization function, which is practically restricted, since the FSD algorithm deconvolves all bands with the same FWHH of the line shape function, irrespective of their bandwidths. Thus, derivation is often preferred, since it does not require any a priori information about the FWHH of the individual bands of each component.

A widely applied method to extract quantitative information from resolution-enhanced amide I spectra is *curve fitting*, initially proposed by Byler and Susi (1986). This procedure provides fractional areas of the bands assigned to different secondary structural features by iterative adjustments of height, width and position of the individual component bands with best fit being achieved by assuming that the components have Gaussian band shapes. Band narrowing by means of FSD followed by curve fitting analysis reveals some limitations for the assessment of the absolute content of secondary structural elements, since the choice of the input parameters is subjective. It is, however, a valuable procedure in pharmaceutical product development to assess relative secondary structural changes associated with the manufacture and storage of protein pharmaceuticals.

An alternative approach to evaluate protein stability issues is the evaluation of the overall *spectral similarity* or *dissimilarity* in the amide I region. A straightforward and reliable method of this category is the calculation of the 'area of overlap' of baseline-corrected area-normalized second derivative spectra (Kendrick et al. 1996). Method qualification to be included in regulatory filings has been

described by Jiang et al. (2011). In certain cases, it might be more reasonable to simply compare the relative height and width of a single ‘marker’ band, instead of evaluating the global spectral similarity. An additional opportunity to avoid arbitrary spectral deconvolution is the use of chemometric data processing, i.e. to perform *multivariate calibration modeling* of the non-deconvoluted FTIR spectra. Interestingly, PCA or PLS have not been widely applied in FT-MIR secondary structural analysis, although Vonhoff et al. (2010) clearly demonstrated the feasibility and reliability of such an approach.

Within the last three decades, numerous papers have clearly demonstrated the great potential of FT-MIR spectroscopy for biopharmaceutical product development. Challenges associated with the application on antibody formulations and polymeric protein delivery systems will be highlighted and discussed in Sects. 6.2 and 6.3.

NIR applications in secondary structural analysis of protein formulations are still limited, although the sensitivity of the method to structural changes of various types of proteins in solid and solution state has been demonstrated (Bai et al. 2005; Izutzu et al. 2006). Bai et al. (2005) reported that structural changes of two different model proteins upon freeze-drying with different concentrations of sucrose were clearly reflected in NIR bands assigned to amide A/I, A/II, B/II and CH stretching modes. Moreover, thermal-induced perturbations of freeze-dried proteins could be verified. Multivariate PLS calibration modeling revealed a good correlation between the NIR data and the FT-MIR spectral information of the amide I band. Izutzu et al. (2006) used seven different proteins in solid and solution state to confirm the reliability of NIRS for the distinction of secondary structural features. Besides hydrogen-bonding patterns being specific for each protein, normalized second-derivative solvent-compensated NIR spectra of the proteins in aqueous solution suggested characteristic bands in the combination and first overtone region indicative of α -helix or β -sheet structures. In addition, NIR analysis was capable to assess thermal unfolding and subsequent intermolecular β -sheet structure formation of heat-treated bovine serum albumin in both solution and the freeze-dried state. The use of NIRS as a PAT tool in freeze-drying to detect formulation and process induced structural perturbations of a model IgG in real-time has recently been described by Pieters et al. (2012). Details of this application are outlined in Sect. 7.8.

FT-MIR spectroscopy will certainly remain the primary tool for protein structural analysis in early development. However, NIR measurements clearly reveal some distinct advantages for formulation screening, in routine quality control and long-term stability testing. In fact, NIR reflectance measurements can be performed directly through the closed glass vial (Kamat et al. 1989; Muzzio et al. 2011) with no instrument purging and/or maintenance of a dry environment around the sample being required, thus reducing analysis time and minimizing potential artefacts that may arise from sample preparation and/or inaccurate data processing. Contrary to MIRS, the dual nature of NIR spectra provides physical and chemical sample information and thus enables product CQAs other than the protein secondary structure such as moisture content (see Sect. 3.1) and solid state characteristics

(see Sects. 3.2 and 3.4) to be determined simultaneously. Qualitative and quantitative analysis of complex formulations is certainly facilitated by means of multivariate processing of the NIR spectral data. This latter aspect has been evaluated in a few studies in terms of formulation and process optimization. In formulation screening of freeze-dried products, for instance, the use of NIRS for simultaneous investigation of several CQAs has been verified by Grohganz et al. (2010b). Versatile samples could be classified according to their excipient composition, moisture content and solid-state form of mannitol thus enabling adequate formulations to be selected. Lee et al. (2011b) applied NIRS to investigate the polymorphic variation of spray-dried mannitol as a function of particle size and in the presence low levels of lysozyme used as model protein. Simultaneous determination of moisture content and aerodynamic particle size of spray-dried insulin powders for pulmonary delivery by means of NIRS has been reported by Maltesen et al. (2012). The study was designed to gain process understanding and replace traditional analytical techniques. The use NIR chemical imaging for high-throughput screening of freeze-dried protein formulations in well plates has recently been described by Trnka et al. (2014). Overall, it is obvious that NIR spectroscopy is a versatile analytical tool for the noninvasive characterization of protein formulations, since multiple CQAs can be recorded simultaneously. Its potential in this field has certainly not been fully exploited yet.

6.2 Challenges of Antibody Formulations

Monoclonal antibodies (mAbs) represent the leading group of biopharmaceutical products. As multidomain proteins with structurally independent regions, their stability profile is rather complex. A major issue is their tendency to aggregate during downstream processing, shipping and/or upon long-term storage with distinct 'hot spots' following different pathways. To gain insight into the local and global conformational and colloidal effects contributing to the overall structural stability of a specific mAb, an array of complementary analytical tools has to be applied (Neergaard et al. 2014; Cerasoli et al. 2014). Since FT-MIR spectroscopy is specially sensitive to changes in the intra- and intermolecular β -sheet pattern, it can be used as a versatile tool to provide information about population averaged secondary structural changes of mAb formulations.

MIR spectra of antibody molecules with preserved native structure usually reveal two characteristic bands in the amide I region, namely a strong one at $1630\text{--}1640\text{ cm}^{-1}$ and a weak one at $1680\text{--}1690\text{ cm}^{-1}$ reflecting the presence of an intramolecular antiparallel β -sheet structure (Murphy et al. 2012). Additional bands at 1670 cm^{-1} can be ascribed to turns. Temperature-induced conformational changes of mAbs in aqueous solution are usually reflected by an intensity decrease of both β -sheet bands with a concomitant shift of the $1630\text{--}1640\text{ cm}^{-1}$ band to lower frequencies. A band at $1615\text{--}1625\text{ cm}^{-1}$ is indicative of an intermolecular β -sheet structure of aggregates that are formed upon heat treatment (Hawe

et al. 2009). Indeed, extensive secondary structural changes associated with temperature-induced unfolding and precipitation have been assessed for IgG antibodies (Hawe et al. 2009; Cerasoli et al. 2014; Telikepalli et al. 2014). A high-throughput thermal stability assay based on ATR-FTIR imaging has been described by Boulet-Audet et al. (2014). Furthermore, it could be demonstrated that extensive stirring also leads to aggregates with non-native structural features (Telikepalli et al. 2014), while freeze-thawing and shaking usually provides aggregates with a more or less preserved, i.e. native-like secondary structure (Hawe et al. 2009; Joubert et al. 2011; Telikepalli et al. 2014).

FT-MIR spectroscopy has also been applied to evaluate secondary structural changes of antibodies upon freeze- or spray-drying (Andya et al. 2003; Abdul-Fattah et al. 2007; Schüle et al. 2007; Tian et al. 2007; Wang et al. 2010b; Murphy et al. 2012), shipping-like stress (Telikepalli et al. 2015) and long-term storage in a freeze- or spray-dried form (Cleland et al. 2001; Chang et al. 2005; Maury et al. 2005; Park et al. 2013). Distinct drying-induced secondary structural perturbations towards enhanced β -sheet structure resulting from harsh process conditions or an inadequate formulation are clearly reflected in the amide I spectral region. Studies with model IgGs and therapeutic mAbs or fragments also revealed that a more or less “native-like” secondary structure can be preserved upon freeze- or spray-drying when antibodies are formulated with an adequate amount of stabilizer, e.g. sucrose, trehalose, surfactants (Chang et al. 2005; Abdul-Fattah et al. 2007). Moreover, a correlation between retention of a native-like secondary structure upon drying, as determined by FTIR, and storage stability in the solid state has been demonstrated (Maury et al. 2005, 2012; Abdul-Fattah et al. 2007).

Subtle secondary structural differences resulting from different formulations and/or perturbations upon long-term storage are best reflected by a detailed examination of different amide I bands, i.e. by comparing the frequency shift and bandwidth of more than one β -sheet marker band of the FTIR spectrum. The rationale behind this approach is the different sensitivity of the low ($\leq 1640\text{ cm}^{-1}$) and high ($\geq 1680\text{ cm}^{-1}$) frequency band of the antiparallel β -sheet motifs of antibody molecules to various types of distortions (Demirdöven et al. 2004). The low frequency band ($\leq 1640\text{ cm}^{-1}$) is sensitive to distortions along the hydrogen bond direction between different strands of the β -sheets (e.g. number of strands, degree of twisting of the β -sheets and hydrogen bond strength), whereas the high frequency band ($\geq 1680\text{ cm}^{-1}$) reflects distortions along the strand direction. Interestingly, only a few studies have yet focused on multiple marker bands within the amide I envelope when evaluating antibody formulations with respect to their long term stability (Cleland et al. 2001; Abdul-Fattah et al. 2007; Murphy et al. 2012).

Distinct differences in the relative intensity and bandwidth of the high and low frequency β -sheet bands of a monoclonal antibody (i.e. rhuMab HER2), when freeze-dried in the absence and presence of stabilizers, have been described by Cleland et al. (2001). Compared to the stabilizer-free product, formulations containing sucrose or mannitol revealed a higher intensity of the low frequency ($\leq 1640\text{ cm}^{-1}$) band, a slight red shift and a reduced bandwidth of the high

frequency band ($\geq 1680\text{ cm}^{-1}$). Although not discussed further within this paper, the spectral effects clearly indicate effects over the entire β -sheet structure with less distortion of the β -strands upon addition of sucrose or mannitol.

Upon spray-drying of IgG solutions, Maury et al. (2005) revealed an intensity increase of the β -sheet bands at the cost of the 1661 cm^{-1} band reflecting turns. Noteworthy is that obvious structural differences between formulations with and without sorbitol, reflected by quantitative differences in the relative peak area of the high and low frequency β -sheet bands, have not been discussed either, although drying-induced aggregation was remarkably different between the two formulations.

In a study with different formulations of a model IgG1 antibody, Abdul-Fattah et al. (2007) emphasized that the β -sheet ratio, i.e. the intensity ratio between the 1690 cm^{-1} band and the 1640 cm^{-1} band, was more sensitive to secondary structural changes caused by the drying method (i.e. spray-drying, freeze-drying, foam drying) than the correlation coefficient. However, frequency shifts and changes in bandwidths have not been evaluated.

A detailed examination of the amide I spectral region including changes in band position, peak height and bandwidth of both the high and low frequency β -sheet band was performed by Murphy et al. (2012) in a study designed to evaluate the effect of sucrose and sorbitol on the stability of a lyophilized IgG1 antibody. A red shift of the high frequency band upon addition of increasing amounts of sucrose, consistent with the observations made by Cleland et al. (2001), reflects reduced distortions along the strand direction in the presence of a lyoprotectant. The observed decrease in the bandwidth of both β -sheet bands with increasing amounts of sucrose clearly indicates a greater homogeneity across the entire β -sheet structure when the sugar content is increased, likely arising from a decreased molecular mobility. Since the trend in bandwidth narrowing was further amplified upon addition of sorbitol, a substance known to dampen β -relaxations, it can be assumed that the spectral changes reflect both reduced global and local fluctuations in the β -sheet structure when the IgG is embedded in a sucrose/sorbitol matrix. This interpretation is consistent with FTIR data on carboxy-myoglobin indicating that the protective effect of stabilizers can be explained by a strong coupling of the protein surface to the surrounding stabilizer matrix (Giuffrida et al. 2004). Evidence that local rather than global perturbations are often responsible for mAb aggregation has recently been provided by hydrogen/deuterium exchange mass spectrometry (HDX-MS) (Manikwar et al. 2013; Moorthy et al. 2014).

Overall, it can be concluded that the potential of MIR spectroscopy in protein formulation development including mAbs has not been fully exploited yet. The combined use of the hydration water bending modes and protein spectral features other than the amide I band can certainly provide additional information about protein dynamics in the solid state and thus improve our understanding of matrix effects (Cordone et al. 2005; Cottone et al. 2005; Mallamace et al. 2014). Moreover, local conformational changes in distinct Fc and Fab regions of mAbs, not detectable in classical FTIR spectra, may be reflected by 2D-FTIR spectroscopy optionally combined with site-specific H/D exchange (Demirdöven et al. 2004; Lefèvre

et al. 2004; Kammerzell and Middaugh 2007; Kammerzell et al. 2009; Baiz et al. 2012a, b). This can certainly improve our understanding of conformational effects on mAb aggregation pathways. In addition, it can be expected that NIR spectroscopy will gain further importance as PAT tool in mAb lyophilization (see Sect. 7.8).

6.3 *Noninvasive Analysis of Polymeric Protein Delivery Systems*

Being noninvasive, FTIR spectroscopy is also an interesting tool for evaluating protein secondary structure within biodegradable polymeric delivery systems such as PLGA films (Carrasquillo et al. 1999; van de Weert et al. 2002) and microspheres (Fu et al. 1999; Yang et al. 1999; van de Weert et al. 2000; Keles et al. 2014). Model proteins such as hen egg lysozyme (Fu et al. 1999; van de Weert et al. 2000, 2002) and bovine serum albumin (BSA) (Fu et al. 1999) and therapeutically relevant proteins such as recombinant human growth hormone (rhGH) (Carrasquillo et al. 1999; Yang et al. 1999; Keles et al. 2014) have been investigated with respect to their tendency to unfold and/or aggregate during the encapsulation process and/or upon release.

Fu et al. (1999) performed a quantitative study based on FSD and Gaussian curve fitting applied to FT-MIR transmission spectra obtained from lysozyme and BSA in solution, as freeze-dried powders and within PLGA microspheres. In this study, the authors provided evidence that KBr pellet formation and subtraction of the interfering PLGA matrix background did not create any spectral artefacts compromising protein secondary structural analysis. It is, however, important to note that the polymer background cannot be fully eliminated by subtraction of the spectrum of blank microspheres, since the spectral characteristics of blank microspheres and the polymer matrix of protein-loaded microspheres are not identical. Within the microspheres, both proteins revealed a significantly reduced α -helix content as compared to the lyophilized powder, thus indicating conformational changes upon encapsulation. The spectral data also evidenced that trehalose (at a 1:10 ratio of protein:sugar) was able to fully preserve the α -helix content of BSA within the PLGA microspheres, whereas the lysozyme secondary structure could not be stabilized at the equivalent protein:sugar ratio.

Van de Weert et al. (2000) used qualitative FTIR measurements to demonstrate the tendency of lysozyme to form aggregates when entrapped in biodegradable polymers thus compromising the release profile. In a first paper, the authors used different measurement modes, namely transmission to analyse the protein conformation and ATR, PAS and FTIR imaging to elucidate the protein distribution on the surface and within the PLGA microsphere matrix. Irrespective of the measuring mode, a characteristic band of non-covalent aggregates at 1625 cm^{-1} was observed in the second derivative spectra corresponding to protein adsorbed to the cavity

walls inside the microspheres. Formation of intermolecular β -sheet aggregates was also detected by FT-MIR when lysozyme was entrapped in PEG-based amphiphilic multiblock copolymer films (Van de Weert et al. 2002). Contrary to PLGA microspheres, quantitative protein release was observed indicating that aggregation was reversible.

A different FT-MIR approach to screen formulations with respect to their effect on conformational changes and aggregation of rhHG upon microencapsulation and under release conditions has been demonstrated by Yang et al. (1999). Second derivative amide I spectra obtained after successful PLGA microsphere background subtraction were used to compare the protein secondary structure of dried and rehydrated samples of different composition. A significant loss of the native α -helical structure was observed upon microencapsulation, even in the presence of mannitol, trehalose or zinc-precipitation. Upon rehydration complete rhGH refolding to the native structure was detected for the trehalose formulation and the zinc-precipitated rhGH. On the contrary, excipient-free and mannitol containing rhGH microspheres revealed intermolecular β -sheet formation, i.e. aggregation during rehydration.

A recent application describes the use of ATR-IR imaging for in situ monitoring of hGH release from single PLGA microparticles during dissolution in D₂O. With this setup, the hGH release mechanism and the impact of gamma-irradiation on the release kinetics could be elucidated (Keles et al. 2014). The use of NIRS in combination with MVDA for noninvasive in situ monitoring of matrix hydration, polymer degradation and protein release profiles from PLGA matrices has been demonstrated by Schönbrodt (2004) and Reich (2005). Real-time in situ monitoring of both polymer degradation and protein release of polyethylene glycol acrylate (PEGA) hydrogel nanoparticles by means of a fiber-optic ATR-FTIR probe has been reported by McFearin et al. (2011). The feasibility of nondestructive NIR protein quantification within lipid matrices has also been demonstrated (Schönbrodt et al. 2006). Overall, it is obvious that both mid and near infrared spectroscopy are versatile tools for characterizing controlled release protein delivery systems.

7 Use as Real-Time PAT Tool in Batch and Continuous Drug Product Manufacture

Currently, NIRS is the most versatile analytical technique for in-line and on-line monitoring of pharmaceutical manufacturing processes. It has been successfully applied in both batch and continuous manufacture to gain process understanding and enable process control. Applications comprise real-time monitoring of unit operations in solid drug product manufacture including powder blending, high shear wet granulation, fluid bed operations, hot melt extrusion, freeze-drying, roller compaction, pelletization, encapsulation, tableting, coating and packaging. Challenges in pharmaceutical NIR process monitoring and control encompass:

- the probe design
- the mechanical and optical probe interface
- adequate location(s) and number of sensors within the process equipment
- the process environment and dynamics
- the analytical target parameter(s)
- the sampling strategy, e.g. data collection, measurement speed, sample size
- multivariate data processing and interpretation
- adequate reference samples and accuracy of reference data
- data utilization and storage

In the following sections, specific challenges and options related to the implementation and application of a NIRS method for real-time monitoring of the most relevant unit operations in pharmaceutical secondary manufacture will be highlighted and the most recent and prominent literature data discussed. Detailed information on earlier work can be found in review articles of Reich (2005), Räsänen and Sandler (2007) and De Beer et al. (2011a).

7.1 *Blending*

Powder blending is one of the most critical unit operations in the manufacture of solid dosage forms. Traditional off-line analyses to assess blend homogeneity are time consuming, destructive and often hampered by sampling errors. Moreover, they usually do not provide all the real-time information needed to understand and effectively control the process such as whole matrix fingerprinting including information about excipient blending performance. Considering these disadvantages, the value of implementing noninvasive and multivariate in-line methods such as NIRS for blend monitoring is obvious: namely to provide process trajectories of single components, i.e. API and excipients or the whole powder mix and to determine the blending end point in real-time.

Within the last two decades, numerous NIR applications for real-time monitoring of batch blending processes including bin blender, V-blender, Y-blender and Nauta mixer have been described and extensively reviewed by Reich (2005), Räsänen and Sandler (2007) and De Beer et al. (2011a). Recent reports are also dealing with applications to continuous powder blending processes (Vanarase et al. 2010; Martínez et al. 2013; Vanarase et al. 2013; Colón et al. 2014). In the following the most critical issues to be considered when developing an in-line NIR method for a batch or a continuous blending process will be outlined and discussed in more detail.

For the accurate and precise estimation of blending end-points, multiple NIR *sampling points* at different locations of the blender are highly recommended, since it has been demonstrated that only information from multiple positions allow a temporally and spatially resolved process monitoring (El-Hagrasy et al. 2001; Shi et al. 2008; Scheibelhofer et al. 2013). This allows, for instance, zones with

different mixing kinetics to be identified (Scheibelhofer et al. 2013). Of particular importance for a reliable evaluation of blend homogeneity is the estimation of the *sample size* being analysed by the NIR sensor relative to the size of the final dosage form. The spectral sample size depends on the NIR sampling optics, the spectral acquisition mode and the powder properties. The beam size of the NIR probe determines the sample area being illuminated, whereas the blend composition affects the wavelength dependent penetration depth of the NIR radiation. Powder movement during dynamic spectral acquisition further enlarges the sample volume being analysed as compared to a static measurement, but also enhances potential sources of error and thus measurement uncertainties. Since measurement speed is not an issue for modern NIR instruments, the state-of-the-art NIR sampling strategy for the assessment of blend homogeneity is the dynamic spectral acquisition mode at a speed that allows spectral averaging to compensate for interfering spectral fluctuations. Considering these constraints, it is evident that the impact of spectral sampling effects and powder blend properties on the effective sample size should be considered prior to NIR method development.

Equally challenging to method development is the selection of an appropriate *data processing strategy* and the adequate statistics to reliably estimate process variations and blending end-points. In fact, numerous qualitative and quantitative NIR methods have been developed and evaluated for their potential use in blend end-point determination of batch processes. Depending on the algorithm applied, different answers related to the blend composition will be obtained.

Qualitative methods simply rely on time-dependent changes of spectral features reflecting compositional changes. One of the most common approaches is to calculate the Moving Block Standard Deviation (MBSD) between consecutive spectra (Sekulic et al. 1996; Storme-Paris et al. 2009; Momose et al. 2011). Spectral data are arranged in a time by wavelength matrix and the standard deviation (SD) of the intensity values is determined over a predefined time window or block, followed by the calculation of a mean value over all wavelengths. Finally, the mean SD is plotted as a function of time and the blending end-point is determined as the time interval at which the SD profile reaches a minimum value. Other approaches for the qualitative assessment of powder blend homogeneity comprise the use of e.g. principal component analysis (PCA), dissimilarity indices, SIMCA (Sekulic et al. 1998), Hotelling's T^2 statistics (Maesschalck et al. 1998), and principal component modified bootstrap error-adjusted single-sample technique (El-Hagrasy et al. 2006).

Puchert et al. (2011) presented a multivariate approach called Principal Component Scores Distance Analysis (PC-SDA). The method comprises a PCA of pretreated spectra followed by the calculation of Euclidian distances between PC scores as a function of blend time and the determination of MBSDs of successive PC scores distances in a multidimensional space. This approach enables the estimation of a time-window during blending in which spectral variability decreases to a preset minimum, i.e. below a threshold value. To develop a solid statistical rationale for blend end-point determination based on QbD principles, predefined spectra with low variability from normal production samples are used as calibration

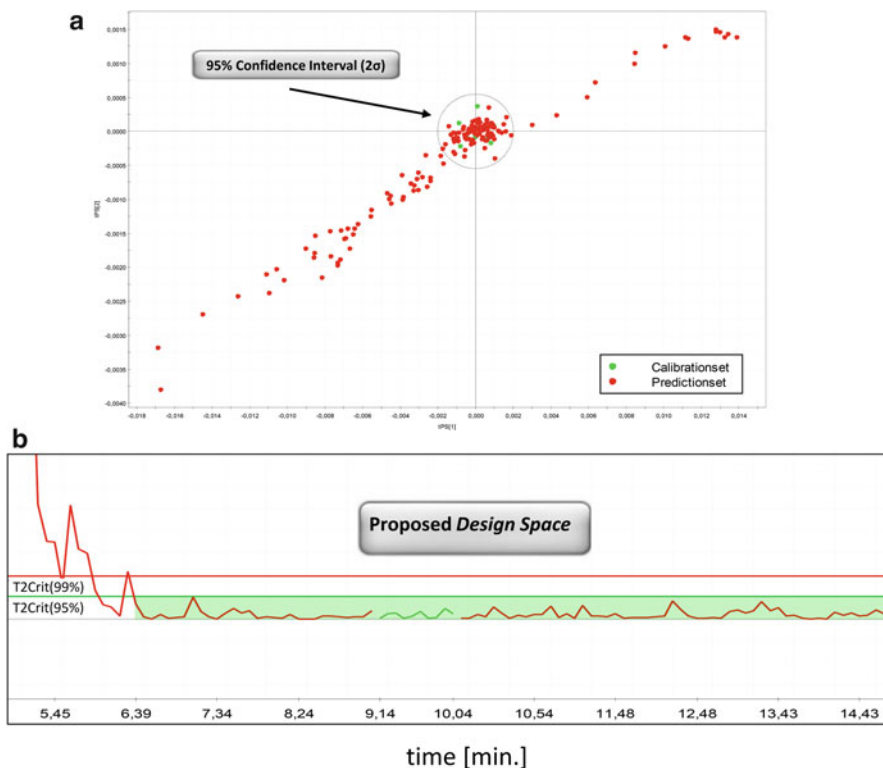


Fig. 3.4 PC-SDA method: (a) score plot of NIR calibration and prediction set with 95 % confidence interval and (b) corresponding Hotelling's T^2 chart with the proposed design space for blend homogeneity

set to compute a 95 % confidence interval which describes the boundary of a multivariate target end-point space, i.e. the overall design space for blend homogeneity (Fig. 3.4). Hotelling's T^2 statistics is then applied to monitor and report blend homogeneity in a straightforward univariate manner, which is useful for pharmaceutical dossiers and QbD filings. The method is easy to implement in an industrial setting, since it can be applied when only production samples are available for calibration modeling. As for other qualitative approaches, the method provides information on the homogeneity of the 'whole' formulation, while ensuring that a possible absence of the API or an excipient will be noticed.

Quantitative approaches based on a regression model ensure specificity to the parameter of interest, i.e. the API and/or an excipient, since each individual component in the formulation can be modeled independently. This provides the advantage to assess time-dependent deviations from target concentrations (Fig. 3.5). Hence, selective PLS regression models are valuable for a more detailed understanding of the mixing behavior of individual formulation components or whenever quantitative results are needed. Quantitative NIR model development is, however, time-consuming, cost-intensive and laborious, as it requires specially

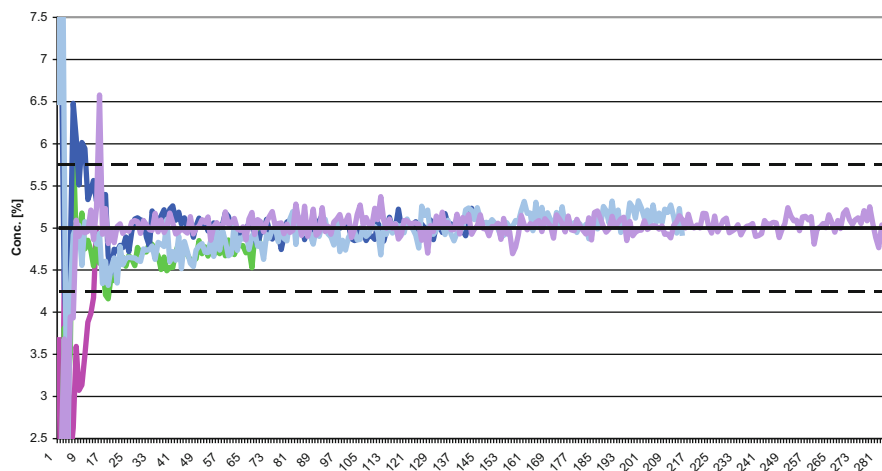


Fig. 3.5 Real-time NIR quantification of drug substance at 5 % w/w target concentration during a powder blending process in a bin blender

designed calibration sample sets covering concentration variations beyond the normal operating conditions. Careful validation has to be performed to calculate the appropriate number of PLS factors and ensure model parsimony. A lean PLS approach to be applied in early product development has been evaluated by Bakri et al. (2010). From a time and cost perspective, mixed strategies combining a qualitative method to evaluate global homogeneity and a regression model to predict the API concentration may be straightforward. For such an approach, MCR is a versatile option, since qualitative and quantitative modeling is feasible depending on the mathematical constraints selected (Igne et al. 2014). In fact, selection of a suitable NIR blend control strategy for a batch blending process is a case by case decision, which should be made by carefully considering the pros and cons of the different approaches. A comprehensive list of the most prominent modeling strategies including statistics to estimate blend homogeneity in batch blending processes is given by Puchert et al. (2011).

To date, only a few studies describe NIR applications for monitoring continuous blending processes with both single or multi-point NIR probes being mounted at the outlet of the blender. Contrary to batch processes, an NIR method to be used in continuous blending has to monitor blend variations after steady state has been achieved (Vanarase et al. 2010). Method precision is thus extremely important, which implies that the analytical error should be known and kept as small as possible (Martínez et al. 2013; Vanarase et al. 2013). To this end, parameters that might interfere with the accuracy and precision of the NIR results have to be identified and carefully evaluated (Colón et al. 2014; Martínez et al. 2013). Spectral sensitivity to changes in mass flow and rotation speed, for instance, have to be included in the calibration model. When blend uniformity is assessed by the RSD, the number of scans to be averaged has to be optimized according to the sample size

of interest. Variograms and fast Fourier transform (FFT) analysis are effective tools to investigate blend variability and optimize the NIR sampling rate (Colón et al. 2014).

7.2 *Wet Granulation*

Wet granulation is a dynamic particle size enlargement process consisting of three distinct subphases, e.g. mixing, granulation and drying. It is usually performed in a fluidized bed granulator or a high shear mixer. Regardless of the technology applied, the granulation phase is a complex combination of several overlapping processes, namely (1) wetting and particle nucleation, (2) consolidation and particle growth, and (3) attrition and breakage. Hence, process development and control inevitably requires real-time assessment of CQAs. The cross-sensitivity of NIR spectra to chemical and physical sample properties offers the possibility of simultaneously determining moisture content, particle size, content uniformity and solid-state characteristics, thus enabling real-time process adjustments and end point determination based on a single measurement. Hereafter, the potential of NIRS for monitoring wet granulation processes will be highlighted and critical issues discussed.

Fluid Bed Granulation: Fluid bed granulation (FBG), if under control, is a very efficient process, since it allows mixing, granulation and drying to be performed in a single unit operation (Burggrave et al. 2013). Development of an in-line NIR method is, however, a challenge due to the dynamic complexity of the process including the sample heterogeneity with dramatic morphological changes as a function of process time. Reliable collection of NIR spectra is extremely challenging during the initial phase, since probe fouling, i.e. contamination of the probe head is likely to occur. Solutions to this problem include the use of an air supply system or a special interface design. A comparison between three interface configurations, namely (1) a sensor head measuring through a side window, (2) a reflection fiber probe inserted in the process chamber, and (3) the same fiber probe with a pan collecting the product in front of its window, was recently performed in our own lab (Schneider and Reich 2012). Best results were achieved with the sensor head (1) followed by the inserted fiber probe (2).

With a suitable probe design and interfacing, reliable spectral information for moisture profiling throughout the different process stages can be obtained, provided that the spectral sampling rate is in accordance with the process dynamics and reference sampling and analysis for PLS calibration modelling are performed in an appropriate way (Green et al. 2005; Heigl et al. 2013). Identification of the distinct subphases (Rantanen et al. 2001) and process end point determination (Findlay et al. 2005; Peinado et al. 2011) are thus feasible. Moreover, spectral changes associated with the loss of water upon fluid bed drying (FBD) can be favourably used to provide information on API dehydration. Successful in-line applications in this field have been described by e.g. Räsänen et al. (2003) and Aaltonen

et al. (2007b). To reflect sample heterogeneity during the granulation process, multipoint NIR methods with several probes at different locations of the process chamber, as reported by Leskinen et al. (2010), are certainly recommendable. Moreover, formulation- and process-induced changes of the reflection and refractive properties of the granules should be considered during method development (Rantanen et al. 2000). The challenge of industrial NIR method validation according to ICH Q2 (R1) guidelines, when dealing with a dynamic fluidized bed process, has recently been discussed by Peinado et al. (2011).

Approaches to simultaneously determine changes in moisture content and particle size during FBG and/or FBD have been described by Findlay et al. (2005), Nieuwmeyer et al. (2007) and Alcala et al. (2010). In the first two applications, PLS model accuracy for particle size determination was strongly affected by the dynamically changing moisture content of the granules. In the work of Alcala et al. (2010), NIR spectral information during the spraying phase was found to be dominated by particle size changes. This allowed PLS models for the determination of three different classes of particles, namely large, medium and small size to be developed. However, accuracy was also an issue indicating that in complex dynamic wet granulation processes accurate particle size determination from real-time NIR spectra remains challenging and calls for complementary PAT tools such as focused beam reflectance measurements (FBRM). In fact, a combination of several analyzers such as NIR and Raman spectroscopy (Aaltonen et al. 2007b), NIRS and FBRM (Tok et al. 2008), or multipoint NIR probes, acoustic emission and a flash topography particle size analyser (Leskinen et al. 2010) can be valuable for enhanced process knowledge and control (Lourenco et al. 2012; Burggrave et al. 2013).

High shear wet granulation: NIRS is also a valuable PAT tool for fingerprinting high shear wet granulation (HSWG) processes. Rantanen et al. (2005) could demonstrate that in-line NIRS in combination with MVDA can be used to monitor the granulation progress and detect the end point of each process stage, namely mixing, spraying and wet massing. Score plots were used to distinguish between the individual subphases. For a better understanding of the chemical and physical changes occurring throughout the process, each stage was analyzed separately by distinct interpretation of the PC loadings. The RMS value of the scores of all contributing PCs was used to evaluate homogeneity of major and minor components in the mixing phase. In the spraying phase, spectral information is dominated by the water addition. Thus, a PLS regression model could accurately determine the amount of water in the wet mass. To gain information related to the particle growth in the wet massing phase, OSC was applied to remove the water contribution from the NIR signal. A rough estimate of the mean particle growth was thus feasible. However, robust PLS models for granule size determination with high accuracy could not be achieved. Due to the interacting variables changing the optical properties of the granules during wet massing, it is difficult to selectively extract the physical information related to the particle size distribution. Once again, this clearly indicates the limitations of in-line NIRS for particle size monitoring in wet

granulation processes. Nevertheless, in-line NIR data from a high shear granulation process have been used to predict granule and tablet properties, e.g., mean particle size, porosity and hardness (Luukkonen et al. 2008). Moreover, NIR determination of polymorph conversion of an API in wet granulation has been described by Li et al. (2005).

The benefits of a combination of chemical information from in-line NIR spectra and physical information from impeller torque and temperature measurements for enhanced process understanding have been described by Jorgensen et al. (2004a, b). Due to the sensitivity of NIR spectra to both bulk and hydrate water, spectral changes during wet granulation can provide additional information on potential anhydrate/hydrate transformations. Only recently, Otsuka et al. (2014) used real-time NIR spectra to simultaneously monitor the dynamic changes of the moisture content within the formulation and the corresponding anhydrate/monohydrate transformation pathway of theophylline during HSWG at different temperatures. Process parameters could be effectively adjusted and controlled based on the multivariate NIR measurements comprising quantification of water adsorbed to the formulation ingredients and theophylline monohydrate formation.

Twin screw granulation: Twin screw granulation (TSG) is a continuous alternative to HSWG. For a better understanding and control of the TSG process, implementation of complementary PAT tools for real-time monitoring of CQAs has recently been described (Fonteyne et al. 2012, 2013). NIR spectroscopy was found to be an appropriate technique for monitoring the moisture content of the granules (Chablani et al. 2011) and the solid-state properties of the API (Fonteyne et al. 2013). Only recently, the potential of NIR chemical imaging as a research tool for visualization and understanding of the granulation liquid mixing and distribution during continuous TSG has been demonstrated (Kumar et al. 2014; Vercruyssen et al. 2014). Actually, more real-time studies with different PAT tools are needed to fully understand the impact of raw material characteristics and process variables on the agglomerate formation in a twin screw granulator. NIRCI is certainly a valuable tool for process optimization, whereas NIR in-line measurements can provide at least some of the multivariate information needed to control the process. In any case, selection of the appropriate NIR instrument specification will be decisive for the success of the application.

7.3 *NIR in Roller Compaction*

Roller compaction with subsequent crushing of the obtained ribbons is a dry granulation process of growing importance, since it eliminates moisture and heat and can be applied in continuous production. During the last decade, NIRS in-process analysis has been evaluated by several groups.

Gupta et al. (2004), Gupta et al. 2005a, b) published a series of papers, in which they related key quality attributes such as relative density, tensile strength, Young's modulus and moisture content to real-time NIR spectral information obtained

during roller compaction. In the first paper (Gupta et al. 2004), the authors used the nonlinear upward shift in the spectral baseline to monitor the effect of different roll speeds and feed rates on the strength of the roll-compacts and to further predict the PSD after milling. The slope of the best-fit line through the real-time NIR spectra was used for the spectral correlations. In the following, PLS regression models for the simultaneous real-time prediction of chemical, physical and mechanical key quality attributes were developed (Gupta et al. 2005a, b). Good agreement between off-line reference data and real-time NIR predictions could be demonstrated, provided that the calibration samples represented the conditions of the real-time measurements with respect to the degree of elastic recovery and the environmental conditions.

Density monitoring with NIR spectral slope and roll gap as process critical control parameters was performed by Soh et al. (2007) for raw material evaluation. Roll speed dependent fluctuations observed in real-time NIR spectra were investigated with Fast Fourier Transform (FFT) analysis and identified as the eccentricity of the rolling motion of rollers (Feng et al. 2008). Based on this result, a new control kit was installed to reduce the motion-induced variability of the real-time NIR spectra. Acevedo et al. (2012) compared three different approaches of spectral data analysis, namely spectral slope, PCA and PLS, to evaluate changes in the ribbon density distribution resulting from variable operational conditions. As one could expect, PCA was more sensitive to slight density differences than the spectral slope, since not only physical, but also chemical, i.e. structural information was considered. The prediction accuracy of the PLS models depended on the reference method (e.g., caliper, pycnometer, in-line laser). Differences in principle and density range captured by the different reference methods and the difficulty to match the sample volume analysed by the NIR sensor were found to be responsible for the low prediction accuracy of all models. These results are consistent with experiences in our own lab, indicating that real-time NIR quantification of physical and mechanical properties often suffers from inadequate reference measurements.

Difficulties associated with the low penetration depth of NIR radiation (Austin et al. 2013) or the probe design and the dynamic changes of the distance between the NIR probe and the ribbon surface (Quyet et al. 2013) have been addressed recently. In this context, microwave resonance sensing has been recommended as a more accurate alternative to NIR measurements for both moisture and density determination (Austin et al. 2013). This is certainly an option, especially when transferability between formulations is desirable and/or the experimental setup for real-time NIR measurements including interfacing of the sensor provides difficulties. Due to undulations of the ribbon surface, selection of the appropriate NIR probe size and the optimal measuring distance are, for instance, critical when dealing with industrial ribbed roller compacts. Simulations and experimental findings both revealed that performance fluctuations are less pronounced with a large NIR probe size measuring at a short distance (Quyet et al. 2013). This latter aspect is especially important in a continuous production setting (McAuliffe et al. 2014).

7.4 *Hot-Melt Extrusion*

Hot-melt extrusion (HME) is a continuous manufacturing technology that can be applied to either provide a sustained drug release profile or enhance solubility and/or the dissolution rate of poorly soluble drug substances upon formation of solid solutions or solid dispersions. In any case, the distribution and solid-state characteristics of the API and its molecular interactions with the excipient matrix are CQAs affecting product stability and dissolution performance. Real-time assessment of these CQAs can be effectively performed by in-line NIR spectroscopy (Markl et al. 2013; Saerens et al. 2014). Compared to Raman spectroscopy, NIRS is easier to implement and less sensitive to external changes (Krier et al. 2013). Hence, NIRS has been successfully applied for real-time troubleshooting by monitoring material behavior and changes in the solid-state of an API as a function of variable HME process settings, e.g. temperature and screw speed (Almeida et al. 2012; Saerens et al. 2012), and to identify critical process parameters, namely screw design and number of feeders (Wahl et al. 2013). PLS models have been developed to determine the composition of multicomponent formulations (API, surfactant and polymer) at the exit of both single- (Tumuluri et al. 2004) and twin-screw extruders (Saerens et al. 2012). Moreover, the extent of drug/polymer interactions (Almeida et al. 2012; Saerens et al. 2012) and the formation of ibuprofen/nicotinamide co-crystals have been monitored (Kelly et al. 2012).

In HME applications, the NIR probe is most often mounted after the screws close to the extrusion die. Probe design and measurement mode depend on the formulation (Saerens et al. 2013). Spectral data processing requires temperature effects on the NIR spectra as well as intensity variations caused by path length variation to be considered. Overall, NIRS has already demonstrated to be a versatile tool for HME process development and multivariate process control (Markl et al. 2013; Saerens et al. 2014). The method has great potential to further investigate extrusion mixing dynamics and monitor rheological properties and related microstructural features of different HME formulations.

7.5 *Pelletization*

Interestingly, only a few papers are available on NIR applications for in-process analysis of pelletization. Those comprise in-line configurations for moisture content determination (Radtke et al. 1999; Mantanus et al. 2009) and API quantification (Mantanus et al. 2010a, b) during matrix pellet manufacture in a rotary fluidized bed. Mantanus et al. (2010a, b) applied accuracy profiles based on β -expectation tolerance intervals (for further details see Sect. 2.2) to evaluate the predictive performance of the PLS model in compliance with the ICH Q2(R1) regulatory documents. At-line NIRS in combination with Raman spectroscopy (Sandler et al. 2005) or XRPD (Römer et al. 2007) was applied to increase the understanding

of API solid-state transformations during pelletization. In the study of Sandler et al. (2005), NIR spectra provided valuable information about the state of water in the pellet formulations, but could not be used to detect hydrate formation of nitrofurantoin and theophylline because of saturation of the water signal. Hydrate formation was visible only in the Raman spectra. However, NIRS allowed process-induced transformations of erythromycin A dihydrate during extrusion-spheronization and drying to be detected (Römer et al. 2007). Those two examples clearly indicate once again that successful NIR process applications require a priori process knowledge and analytical expertise to take advantage of the information obtained and/or make use of complementary information from additional PAT tools.

7.6 *Tabletting and Capsule Filling*

High speed tabletting and capsule filling machines require non-segregating powder blends or granule mixtures with good flowability to ensure content uniformity and consistent dissolution performance of the final product. Process efficiency and product performance therefore rely on real-time assessment of blend uniformity from the very beginning to the very end of the process. To date, different NIR approaches regarding sensor location have been described in the literature.

To detect segregation problems of particulate matter during voiding, NIR sensors have been implemented in the feed hopper of a tablet press (Barajas et al. 2007). Benedetti et al. (2007) described a prototype sampling interface enabling in-line measurements of the flowing powder mixtures to be performed under stable optical conditions to reduce the impact of air diffusion, changes in packing density and flow velocity on measurement precision and accuracy. More recent work describes NIR sensors being mounted in a defined position on the feed frame of the tablet press to monitor the powder directly before filling the die (Liu and Blackwood 2012; Ward et al. 2013; Wahl et al. 2014). This approach provides the opportunity to assess the API concentration in the blend immediately before tablet compression and relate the NIR signal directly to the weight corrected tablet potency determined from stratified tablet samples (Ward et al. 2013). The method is applicable to batch and continuous tabletting processes and can be used as a development tool to understand powder mixing dynamics within the feed frame and/or identify and control powder segregation events (Wahl et al. 2014). However, difficulties have been reported regarding variations in sample presentation resulting from powder movements caused by the paddle wheel agitation. Optimization of probe distance, spectral preprocessing and averaging are effective means to reduce the spectral noise, i.e. to obtain a robust and accurate method.

Practical approaches to control of the final product during tabletting or capsule filling have also been reported. In capsule filling machines working according to the intermittent principle, real-time determination of drug content of individual capsules during the filling process is technically feasible with a NIR reflectance probe mounted at the dosing station. Spectral acquisition can be triggered directly after

capsule filling and weight check, i.e. before the capsule body is transferred to the closing station. To reduce spectral interference of variable capsule shell properties (e.g. moisture content) the spot size of the probe head should be smaller than the diameter of the capsule body. Karande et al. (2010) demonstrated that real-time NIR quantification of individual tablet components (e.g. API and excipients) during the manufacturing process with a rotary tablet press is feasible with a high degree of accuracy. In this study, a diffuse reflectance probe with a 3.18 mm spot size was mounted adjacent to the tablet ejection area. At a production rate of 6000 tablets/h, measurements were carried out with an integration time of 100 ms. Dynamic spectral sampling triggered while the tablets were passing underneath the probe head enabled a larger tablet surface area to be scanned compared to a stationary measurement. This enabled content uniformity problems towards the end of the process, not evident from stratified sampling results, to be detected.

In a recent paper, in-line NIR measurements were applied to determine the drug content of both powder mixtures and tablets during a continuous direct compression tableting process (Järvinen et al. 2013). Reliable measurements were carried out at a production speed of 25,000–125,000 tablets/h with NIR probes being installed in the discharge chute of the continuous mixer and the compression area of the tablet press. In fact, the ultimate approach towards better process understanding and real time release (RTR) is a combination of several NIR sensors at different locations of a capsule filling or tableting machine reflecting real-time uniformity problems during voiding and dosing, demonstrating content uniformity and eventually replacing hardness and dissolution testing. Ideally, machine settings are adjusted within a closed loop control system.

7.7 Coating

Film coating of pellets and tablets is a multivariate unit operation commonly used to improve patient compliance or address biopharmaceutical issues such as gastroresistance and sustained drug release. To improve process efficiency and ensure consistent product quality, in-line measurements of CQAs such as coating thickness and/or uniformity are required. Within the last decade, several studies have clearly demonstrated that NIRS is an appropriate in-line PAT tool for coating process monitoring (Knop and Kleinebudde 2013). NIRS has been applied in fluid bed (Andanson et al. 2010; Bogomolov et al. 2010; Lee et al. 2010, 2011a, b) and pan coating operations (Perez-Ramos et al. 2005; Römer et al. 2008; Gendre et al. 2011a, b; Möltgen et al. 2012, 2013) to determine the average weight gain and/or mean thickness of functional and non-functional coatings of both tablets and pellets. In addition, real-time NIR prediction of dissolution performance of sustained release coated tablets has been evaluated (Gendre et al. 2011b). Univariate as well as multivariate calibrations have been developed and applied for coating end point determination. Most critical to NIR method development and application are the probe positioning in the process equipment and the acquisition of reliable reference data to calibrate and validate the spectral information.

In fluid bed systems, the NIR probe is usually integrated in the cylinder wall (Lee et al. 2011a, b), whereas in pan coaters the probe is most often mounted above the moving tablet bed (Perez-Ramos et al. 2005; Gendre et al. 2011a, b). The exact position should ensure that no spray liquid will hit the measuring window. Probe positioning inside the rotating tablet bed of an industrial scale pan coater has been described by Möltgen et al. (2012). The immersion probe used in this setup was equipped with a gas rinsing nozzle to enable in-process cleaning of the optical sapphire window. Irrespective of the probe interface, spectral effects resulting from changing conditions during the process such as the variation in density of the tablet bed associated with a change in bed-probe distance and changes in the spray rate and/or the exhaust air temperature have to be considered. Analyzer sensitivity to changing operation parameters has been investigated in detail by Möltgen et al. (2012) in an industrial scale HPMC coating process. PC score plots enabled visualization of process dynamics with trajectories reflecting changes in process conditions. Each step of the process, namely preheating, spraying and drying could be distinguished (Fig. 3.6) and the dominating factors, i.e. temperature, moisture, coating growth, change in tablet bed density, core/coat interactions and their spectral effects could be identified. The distinct spectral separation of the HPMC coating growth and the tablet moisture content in different PCs enabled the simultaneous real-time monitoring of both product CQAs. A selective and accurate iPLS weight gain calibration model based on calibration samples dominated by the coating growth was successfully applied to monitor a challenging pan coating process, i.e. to quantify the growth of a very thin HPMC coating on heart-shaped tablets. PLS batch level modelling was further applied to statistically designed experiments to diagnose CPPs (Möltgen 2014).

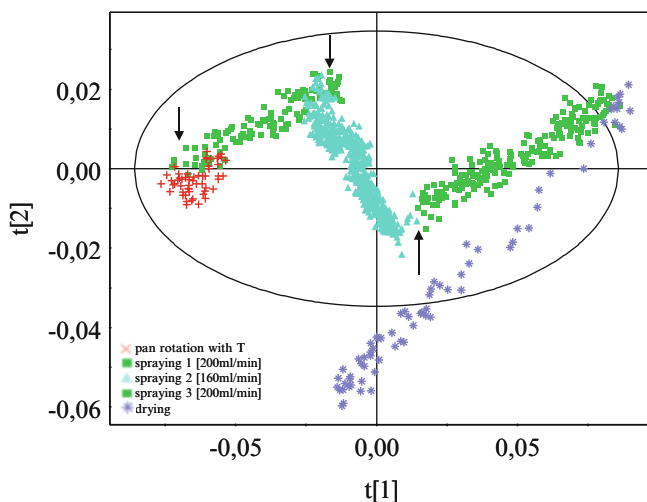


Fig. 3.6 PC score plot of in-line NIR spectra indicating the different steps during a pan coating process

To monitor the progress of a film coating process, various metrics and thus different reference methods including an analytical balance, a micrometer gauge, terahertz pulsed imaging (TPI) and various microscopic techniques (e.g. LM, CLSM, SEM) have been applied for quantitative calibration modelling. Each of these methods has its limitations (Möltgen et al. 2012, 2013). Hence, a multivariate approach for direct NIR coating thickness determination without the need of reference sampling would be advantageous. Such an approach has recently been described by Möltgen et al. (2013). The method, called ‘science-based’ (SBC) or ‘matched filter’ calibration, isolates the analytical signal from the spectral noise without varying reference values. Contrary to PLS calibration modelling, estimates of the NIR coating signal (response spectrum) and the spectral noise (covariance matrix) are made by the user directly and then matched to the actual measurement situation thus minimizing the mean-squared prediction error upon calculation of the regression vector. In the study of Möltgen et al. (2013), calibration was performed with a pure coating polymer response spectrum scaled to absorption units (AU) per μm . The covariance matrix contained various noise estimates, namely hardware noise floor, process noise, and for improved selectivity and robustness, extra noise associated with two interfering components, i.e. spectral information of water and core, respectively. The SBC method was successfully applied to an industrial scale HPMC coating process and enabled real-time NIR measurements of the average film coat thickness even in the range of 8–28 μm with a detection limit of $0.64 \pm 0.03 \mu\text{m}$ root-mean square (RMS).

Overall, it can be expected that the number of in-line NIR applications to industrial coating processes will significantly increase within the next decade. During process development, complementary techniques such NIRCI (Möltgen et al. 2012) or TPI (Ho et al. 2009) are highly recommended, since they can provide additional information on coating integrity and/or inter- and intra-tablet coating uniformity.

7.8 Freeze-Drying

Spectroscopic in situ monitoring of a freeze-drying process was first demonstrated with a custom-built single-reflection ATR-MIR accessory (Remmele et al. 1997). The first NIR application was published by Brülls et al. (2003). In this study, the measurements were also performed invasively by placing the NIR fiber-optic probe in the center of the vial 1 mm above the bottom, thus compromising the product which is not acceptable for a sterile and sensitive drug product. Despite this disadvantage, the setup was capable to detect the freezing point of a PVP model formulation, completion of ice formation, and transition from the frozen solution to an ice-free material. Moreover, desorption rate and drying end point could be determined.

Nowadays, it is technically feasible to spectroscopically monitor freeze-drying processes in a non-invasive manner. In a series of papers, De Beer et al. (2009a, b, 2011b) have investigated the pros and cons of NIRS for this purpose. The importance of using complementary process analysers for understanding and control of a freeze-drying process could be demonstrated by comparing Raman and NIR spectroscopy for in-line monitoring of various CQAs during lyophilization of a mannitol solution. NIRS is well suited to monitor the behavior of water and ice. It has also been applied to provide information about formulation changes of a multicomponent system even during the freezing step (Rosas et al. 2014). However, ice provides huge NIR signals thus potentially hiding spectral information associated with the product solid-state characteristics. Hence, to gain information on excipient crystallization and/or polymorphic transformations during freezing and primary drying of aqueous solutions, it is most often recommended to collect additional spectral information from a Raman probe (De Beer et al. 2011b).

During lyophilization of protein formulations, NIRS is also a valuable tool for real-time monitoring of protein unfolding and interactions with lyoprotectants when sublimation is completed (Pieters et al. 2012). The amide A/II band near 4850 cm^{-1} arising from N-H stretching vibrations and N-H bending coupled with C-N stretching, though less sensitive to protein secondary structural changes than the amide I band in the MIR region, was sufficiently selective to monitor the dehydration-induced unfolding of a IgG protein during the secondary drying phase. In the presence of sucrose as lyoprotectant, water substitution could be verified by a decrease of the amide A/II frequencies reflecting hydrogen bond interactions between the protein backbone and the lyoprotectant.

Despite the great advantage of simultaneously monitoring multiple CQAs in a non-invasive manner, the single-vial analysis has been considered restricted to formulation development, since it does not enable variations within the freeze dryer shelf to be detected. In fact, a multipoint NIR measurement setup for real-time moisture content quantification during freeze-drying including method validation has recently been described by Kauppinen et al. (2013, 2014). The benefits of a multipoint NIR setup for process development, namely to monitor samples at different locations within the shelf, are certainly evident. However, interfacing of the NIRS sensors in an industrial GMP environment remains challenging. Major technical issues to overcome are related to the physical dimensions of the NIR probes and the fragility of the optical fibers which make installation of the measurement setup and loading of the vials extremely difficult. Probe heads may interfere with the tight array of the vials thereby altering the heat transfer to the vials under analysis. Additional challenges to be considered are the location and minimum number of NIR probes, the small sample size being captured by each of the NIR probe relative to the cake volume, the cake shrinkage and/or the potential sample collapse.

8 In Vivo Applications

The low absorptivity of NIR radiation enabling a high penetration depth and thus a long optical pathlength is favorable for in vivo applications. Measurements through tissue, muscle, fat and body fluids are feasible and have been evaluated extensively. Biomedical applications comprise medical monitoring and tissue analysis.

8.1 Medical Monitoring

Medical monitoring is performed exclusively in the wavelength range of 600–1300 nm, the so-called ‘therapeutic window’. As bands in this region are very weak, it shows a very high optical transparency. Moreover, since electronic transitions occur in this region, it allows tissue physiology such as blood and tissue oxygenation, respiratory status or ischaemic damage to be monitored. Analytical key compounds for these in vivo applications are chromophores such as haemoglobin in blood, myoglobin in muscle tissue and cytochrome c oxidase in cellular mitochondrial membranes. Miniaturized pulse oximeter for blood oxygen monitoring are commercially available and in routine use. Cerebral blood flow analysis and brain monitoring are special areas of interest in paediatrics, neonatology and cardio-thorac-vascular surgery. A hot topic is functional cerebral imaging based on pulsatile spectra. For further information on transcranial dynamic NIR imaging the interested reader is referred to a paper of Hu et al. (2009).

NIR molecular probes based on organic fluorophores have gained practical importance for in vivo measurements, i.e. cellular and tissue imaging in the wavelength range between 700 and 900 nm (Zhang et al. 2012a, b). NIR dye-encapsulated nanoparticles with tumor specific ligands can be used for tumor targeting (Luo et al. 2011). They hold great promise for diagnostic and therapeutic applications in the treatment of cancer (Yuan et al. 2013, 2014).

8.2 Tissue Analysis

The use of NIRS for the noninvasive measurement of blood glucose and the NIR/MIR in situ analysis of human tissue including skin profiling and cancer diagnosis are additional topics of interest. In vivo applications in these fields have certainly profited from the in vitro experience gained in clinical chemistry (e.g., NIR analysis of plasma and whole blood samples), medical diagnosis (e.g., FTIR/NIR analysis of isolated tissues including chemical imaging) and biopharmaceutical analysis (e.g., FTIR-ATR and FTIR-PAS studies with artificial and biological membranes including drug penetration). Prospects and challenges associated with monitoring of blood glucose and skin profiling will be briefly outlined.

Noninvasive measurement of blood glucose: The use of NIR spectroscopy in combination with MVDA for noninvasive monitoring of glucose in human tissue has been studied extensively over the last two decades. The rationale for probing blood glucose by scanning through or measuring in the skin is the fact that there is a correlation between the glucose level in the tissue and in the venous/arterial blood. Early studies made use of the shorter wavelength region between 800 and 1300 nm with a high penetration depth for diffuse reflectance measurements e.g., at the finger tip. PLS prediction results revealed RMSEP values ranging between 18 and 34 mg/dL (Robinson et al. 1992; Müller et al. 1997). Successful measurements at the oral mucosa with an RMSEP of 36.4 mg/dL have been reported by Heise et al. (1998). A comprehensive overview of the early work in this field can be found in some book chapters (Heise 2002; Du et al. 2008) and a more recent review of Ozaki (2012).

All studies clearly reveal that the development of a reliable *in vivo* blood glucose assay is extremely challenging due to the variable physiological conditions of skin tissue (e.g. body temperature) and the very weak signals of glucose obtained from measurements through the skin. The interfering matrix information in the spectra and the background noise are extremely high, leading to a very low S/N ratio of the glucose peak. The quality of the NIR spectra is, however, critical for a reliable assay. Improvements were made by using NIR radiation in the region of 1300–1900 nm with a penetration depth of only a few mm, thus enabling spectral acquisition selectively from the dermis. An instrument was developed with a sensor containing several inlet fibers illuminating the skin and a detecting fiber at an adequate distance to collect the scattered light from a controlled penetration depth (Maruao et al. 2003). Due to the strong absorption of water and the interference with information from other components, method accuracy strongly depends on the appropriate wavelength interval(s) used for calibration modeling. Kasemsumran et al. (2006) evaluated two wavelength selection methods, namely moving window partial least squares regression (MWPLSR) and searching combination moving window partial least squares (SCMWPLS). PLS models based on the optimized spectral region selected by SCMWPLS revealed best statistical performance (RMSEV = 17–25 mg/dL) and best clinical accuracy.

Noninvasive skin profiling: The human skin is easily accessible for noninvasive spectroscopic analysis. Spectral information gained from different sublayers e.g., cellular substructures can thus be used for skin diagnosis and drug penetration studies. NIR diffuse reflectance measurements in combination with skin impedance spectroscopy have been successfully applied to distinguish between malignant and benign skin tumours (Bodén et al. 2013). Moreover, structural and compositional changes of human skin upon contact with chemicals have been investigated with NIR spectroscopy. For a better understanding of drug penetration in the skin, depth resolved investigations with e.g. FTIR-PAS have been described (Gotter et al. 2008). Due to the frequency modulation of the light beam, this technique is extremely useful for depth profiling in the time course of drug penetration processes.

All examples clearly demonstrate that controlled penetration depth of the measured light is a key element for reliable MIR/NIR *in vivo* applications. In

combination with imaging systems and appropriate multivariate methods for spectral data analysis, advanced MIR/NIR techniques are powerful tools with further prospects in diversified biopharmaceutical and biomedical areas.

9 Concluding Remarks

MIR and NIR spectroscopy have matured into prominent analytical techniques in both laboratory and manufacturing settings. Both techniques provide molecular level information and have increasingly been adopted as powerful PAT tools in primary and secondary pharmaceutical manufacture. Major benefits are that materials in different physical states can be analyzed in a fast and noninvasive manner. For identification and structural characterization, MIR spectral information is more straightforward, since it features strong and well resolved absorption bands of fundamental vibrations thus enabling direct band assignment to be performed in many cases. NIRS is very unique, as it is concerned with a mix of overtones and combination bands. Instruments are robust and flexible to implement in various process environments. The spectra contain a wealth of chemical and physical sample information in broad overlapping spectral bands and therefore require multivariate data analysis to achieve the desired selectivity. Adding up the specific pros and cons of the two techniques, it is obvious that MIRS is more specific, whereas NIRS is more versatile and can provide information not accessible by any other analytical technique. Those differences are important to consider when selecting the adequate analytical tool for a specific application. Overall, it can be expected that innovative hardware and software concepts coupled with advanced control systems will continue to support pharmaceutical product development, manufacture and quality control. NIRS will certainly play a key role in real-time PAT settings of continuous pharmaceutical manufacturing processes, whereas ultrafast multipulse 2D-MIR spectroscopy can pave the way for advanced biotechnological and biomedical applications and major contributions to the understanding of the local and global conformational stabilization of protein therapeutics.

References

- Aaltonen J, Rantanen J, Siiriä S et al (2003) Polymorph screening using near-infrared spectroscopy. *Anal Chem* 75:5267–5273
- Aaltonen J, Strachan CJ, Pöllänen K et al (2007a) Hyphenated spectroscopy as a polymorph screening tool. *J Pharm Biomed Anal* 44:477–483
- Aaltonen J, Kogermann K, Strachan JC et al (2007b) In-line monitoring of solid-state transitions during fluidisation. *Chem Eng Sci* 62:408–415
- Abdul-Fattah AM, Truong-Le V, Yee L et al (2007) Drying-induced variations in physico-chemical properties of amorphous pharmaceuticals and their impact on stability I: stability of a monoclonal antibody. *J Pharm Sci* 96:1983–2008

- Abrahamson C, Johannson J, Sparen A et al (2003) Comparison of different variable selection methods conducted on NIR transmission measurements on intact tablets. *Chemom Intell Lab Syst* 69:3–12
- Acevedo D, Muliadi A, Giridhar A et al (2012) Evaluation of three approaches for real-time monitoring of roller compaction with near-infrared spectroscopy. *AAPS PharmSciTech* 13:1005–1012
- Aigner Z, Berkesi O, Farkas G et al (2012) DSC, X-ray and FTIR studies of a gemfibrozil/dimethyl-beta-cyclodextrin inclusion complex produced by co-grinding. *J Pharm Biomed Anal* 57:62–67
- Alatalo HM, Hatakka H, Louhi-Kultanen M et al (2010) Closed-loop control of reactive crystallization. Part I: Supersaturation-controlled crystallization of L-glutamic acid. *Chem Eng Technol* 33:743–750
- Alcalà M, Roperó J, Vázquez R et al (2009) Deconvolution of chemical and physical information from intact tablets NIR spectra: two- and three-way multivariate calibration strategies for drug quantification. *J Pharm Sci* 98:2747–2758
- Alcala M, Blanco M, Bautista M et al (2010) On-line monitoring of a granulation process by NIR spectroscopy. *J Pharm Sci* 99:336–345
- Alcala M, Blanco M, Moyano D et al (2013) Qualitative and quantitative pharmaceutical analysis with a novel hand-held miniature near infrared spectrometer. *J Near Infrared Spectrosc* 21:445–457
- Al-Hussein A, Giessler H (2013) Investigation of histidine stabilizing effects on LDH during freeze-drying. *J Pharm Sci* 102:813–826
- Allesø M, Velaga S, Alhalaweh A, Cornett C et al (2008) Near-infrared spectroscopy for cocrystal screening. A comparative study with Raman spectroscopy. *Anal Chem* 80:7755–7764
- Almeida A, Saerens L, De Beer T et al (2012) Upscaling and in-line process monitoring via spectroscopic techniques of ethylene vinyl acetate hot-melt extruded formulations. *Int J Pharm* 439:223–229
- Alshahrani SM, Lu W, Park JB et al (2015) Stability-enhanced hot-melt extruded amorphous solid dispersions via combinations of Soluplus and HPMCAS-HF. *AAPS PharmSciTech*. doi:10.1208/s12249-014-0269-6
- Alvarenga L, Ferreira D, Altekruze D et al (2008) Tablet identification using near-infrared spectroscopy (NIRS) for pharmaceutical quality control. *J Pharm Biomed Anal* 48:62–69
- Andanson JM, Jutz F, Baiker A (2010) Simple in situ monitoring of a complex catalytic reaction network at high pressure by attenuated total reflection Fourier transform infrared spectroscopy. *Appl Spectrosc* 64:286–292
- Anderson CA, Drennen JK, Ciurczak EW (2008) Pharmaceutical applications of near-infrared spectroscopy. In: Burns DA, Ciurczak EW (eds) *Handbook of near infrared spectroscopy*, 3rd edn. CRC Press, Boca Raton
- Andya JD, Hsu CC, Shire SJ (2003) Mechanisms of aggregate formation and carbohydrate excipient stabilization of lyophilized humanized monoclonal antibody formulations. *AAPS PharmSci* 5:Article 10
- Austin J, Gupta A, McDonnell R et al (2013) The use of near-infrared and microwave resonance sensing to monitor a continuous roller compaction process. *J Pharm Sci* 102:1895–1904
- Bai SJ, Rani M, Suryanarayanan R et al (2004) Quantification of glycine crystallinity by near-infrared (NIR) spectroscopy. *J Pharm Sci* 93:2439–2447
- Bai S, Nayar R, Carpenter JF, Manning MC (2005) Noninvasive determination of protein conformation in the solid state using near infrared (NIR) spectroscopy. *J Pharm Sci* 94:2030–2038
- Baiz CR, Peng CS, Reppert ME et al (2012a) Coherent two-dimensional infrared spectroscopy: quantitative analysis of protein secondary structure in solution. *Analyst* 137:1793–1799
- Baiz C, Reppert M, Tokmakoff A (2012b) Amide I two-dimensional infrared spectroscopy: methods for visualizing the vibrational structure of large proteins. *J Phys Chem A* 117:5955–5961

- Bakri B, Weimer M, Hauck G, Reich G (2010) Implementation of NIR blend monitoring in early development: evaluation of calibration design and spectrometer configuration. Poster presented at AAPS annual meeting and exposition, New Orleans 2010
- Barajas MJ, Cassiani AR, Vargas W et al (2007) Near-infrared spectroscopic method for real-time monitoring of pharmaceutical powders during voiding. *Appl Spectrosc* 61:490–496
- Barrett M, McNamara M, Hao HX et al (2010) Supersaturation tracking for the development, optimization and control of crystallization processes. *Chem Eng Res Des* 88:1108–1119
- Barth A (2007) Infrared spectroscopy of proteins. *Biochim Biophys Acta* 1767:1073–1101
- Barth A, Zscherp C (2002) What vibrations tell us about proteins. *Q Rev Biophys* 35:369–430
- Basavoju S, Boström D, Velaga SP (2008) Indomethacin-saccharin cocrystal: design, synthesis and preliminary pharmaceutical characterization. *Pharm Res* 25:530–541
- Benedetti C, Abatzoglou N, Simard JS et al (2007) Cohesive, multicomponent, dense powder flow characterization by NIR. *Int J Pharm* 336:292–301
- Bertacche V, Pini E, Stradi R et al (2006) Quantitative determination of amorphous cyclosporine in crystalline cyclosporine samples by Fourier transform infrared spectroscopy. *J Pharm Sci* 95:159–166
- Blanco M, Alcalá M (2006) Content uniformity and tablet hardness testing of intact pharmaceutical tablets by near infrared spectroscopy: a contribution to process analytical technologies. *Anal Chim Acta* 557:353–359
- Blanco M, Peguero A (2010) Influence of physical factors on the accuracy of calibration models for NIR spectroscopy. *J Pharm Biomed Anal* 52:59–65
- Blanco M, Romero MA (2001) Near-infrared libraries in the pharmaceutical industry: a solution for identity confirmation. *Analyst* 26:2212–2217
- Blanco M, Villar A (2003) Development and validation of a method for the polymorphic analysis of pharmaceutical preparations using near infrared spectroscopy. *J Pharm Sci* 92:823–830
- Blanco M, Coello J, Iturriaga H et al (1998) Near-infrared spectroscopy in the pharmaceutical industry. *Analyst* 123:135R–150R
- Blanco M, Coello J, Montoliu I, Romero MA (2001) Orthogonal signal correction in near-infrared calibration. *Anal Chim Acta* 434:125–132
- Blanco M, Valdés D, Llorente I et al (2005) Application of NIR spectroscopy in polymorphic analysis study of pseudo-polymorphs stability. *J Pharm Sci* 94:1336–1342
- Blanco M, Castillo M, Peinado A et al (2006a) Application of multivariate curve resolution to chemical process control of an esterification reaction monitored by near-infrared spectroscopy. *Appl Spectrosc* 60:641–647
- Blanco M, Alcalá M, González JM et al (2006b) A process analytical technology approach based on near infrared spectroscopy: tablet hardness, content uniformity, and dissolution test measurements of intact tablets. *J Pharm Sci* 95:2137–2144
- Blanco M, Alcalá M, González JM et al (2006c) Determination of dissolution profiles in intact pharmaceutical tablets by NIR spectroscopy. *Process Anal Technol* 3:25–28
- Blanco M, Castillo M, Beneyto R (2007) Study of reaction processes by in-line near-infrared spectroscopy in combination with multivariate curve resolution: esterification of myristic acid with isopropanol. *Talanta* 72:519–525
- Blanco M, Cueva-Mestanza R, Peguero A (2011) NIR analysis of pharmaceutical samples without reference data: Improving the calibration. *Talanta* 85:2218–2225
- Blum MM, John H (2012) Historical perspective and modern applications of attenuated total reflectance Fourier transform infrared spectroscopy (ATR-FTIR). *Drug Test Anal* 4:298–302
- Bodén I, Nyström J, Lundskog B et al (2013) Non-invasive identification of melanoma with near-infrared and skin impedance spectroscopy. *Skin Res Technol* 19:e473–e478
- Bogomolov A, Engler M, Melicher M et al (2010) In-line analysis of a fluid bed pellet coating process using a combination of near infrared and Raman spectroscopy. *J Chemom* 24:544–557
- Boiret M, Meunier L, Ginot YM (2011) Tablet potency of tianeptine in coated tablets by near infrared spectroscopy: model optimization, calibration transfer and confidence intervals. *J Pharm Biomed Anal* 54:510–516

- Boulet-Audet M, Byrne B, Kazarian SG (2014) High-throughput thermal stability analysis of a monoclonal antibody by attenuated total reflection FT-IR spectroscopic imaging. *Anal Chem* 86:9786–9793
- Bouveresse E, Campbell B (2008) Transfer of multivariate calibration models based on near-infrared spectroscopy. In: Burns DA, Ciurczak EW (eds) *Handbook of near-infrared analysis*, 3rd edn. CRC Press, Boca Raton
- Braga JWB, Poppi RJ (2004) Figures of merit for the determination of the polymorphic purity of carbamazepine by infrared spectroscopy and multivariate calibration. *J Pharm Sci* 93:2124–2134
- Brittain HG (2009) Vibrational spectroscopic studies of cocrystals and salts. 1. The benzamide-benzoic acid system. *Cryst Growth Des* 9:2492–2499
- Brülls M, Folestad S, Sparèn A et al (2003) In-situ near-infrared spectroscopy monitoring in pharmaceutical industry. *Pharm Res* 20:494–499
- Brülls M, Folestad S, Sparèn A et al (2007) Applying spectral peak area analysis in near-infrared spectroscopy moisture assays. *J Pharm Biomed Anal* 44:127–136
- Bugay DE (2001) Characterization of the solid state: spectroscopic techniques. *Adv Drug Deliv Rev* 48:43–65
- Burger T, Fricke J, Kuhn J (1998) NIR radiative transfer investigations to characterize pharmaceutical powders and their mixtures. *J Near Infrared Spectrosc* 6:33–40
- Burggrave A, Monteyne T, Vervaeck C et al (2013) Process analytical tools for monitoring, understanding, and control of pharmaceutical fluidized bed granulation: a review. *Eur J Pharm Biopharm* 83:2–15
- Byler DM, Susi H (1986) Examination of the secondary structure of proteins by deconvolved FTIR spectra. *Biopolymers* 25:469–487
- Cao W, Mao C, Chen W et al (2006) Differentiation and quantitative determination of surface and hydrate water in lyophilized mannitol using NIR spectroscopy. *J Pharm Sci* 95:2077–2086
- Carpenter JF, Prestrelski SJ, Dong A (1998) Application of infrared spectroscopy to development of stable lyophilized protein formulations. *Eur J Pharm Biopharm* 45:231–238
- Carrasquillo KG, Constantino HR, Cordero RA et al (1999) On the structural preservation of recombinant human growth hormone in a dried film of a synthetic biodegradable polymer. *J Pharm Sci* 88: 166–173
- Cerasoli E, Ravi J, Garfagnini T et al (2014) Temperature denaturation and aggregation of a multi-domain protein (IgG1) investigated with an array of complementary biophysical methods. *Anal Bioanal Chem* 406:6577–6586
- Cervera-Padrell AE, Nielsen JP, Pedersen MJ et al (2012) Monitoring and control of a continuous Grignard reaction for the synthesis of an active pharmaceutical ingredient intermediate using inline NIR spectroscopy. *Org Process Res Dev* 16:901–914
- Chablani L, Taylor MK, Mehrotra A et al (2011) Inline real-time near-infrared granule moisture measurements of a continuous granulation-drying-milling process. *AAPS PharmSciTech* 12:1050–1055
- Chalmers JM, Griffiths PR (eds) (2001) *Handbook of vibrational spectroscopy*. Wiley, New York
- Chalus P, Walter S, Ulmschneider M (2007) Combined wavelet transform-artificial neural network use in tablet active content determination by near-infrared spectroscopy. *Anal Chim Acta* 591:219–224
- Chan KLA, Fleming OS, Kazarian SG et al (2004) Polymorphism and devitrification of nifedipine under controlled humidity: a combined FT-Raman, IR and Raman microscopic investigation. *J Raman Spectrosc* 35:353–359
- Chan KLA, Kazarian SG, Vassou D, Gionis V, Chryssikos GD (2007) In situ high-throughput study of drug polymorphism under controlled temperature and humidity using FT-IR spectroscopic imaging. *Vib Spectrosc* 43:221–226
- Chanda A, Daly AM, Foley DA et al (2013) Industry perspectives on process analytical technology: tools and applications in API development. *Org Process Res Dev* 19:63–83

- Chang L, Shephard D, Sun J et al (2005) Effect of sorbitol and residual moisture on the stability of lyophilized antibodies: implications for the mechanism of protein stabilization in the solid state. *J Pharm Sci* 94:1445–1455
- Chavez PF, De Bleye C, Sacré PY et al (2013) Validation methodologies of near infrared spectroscopy methods in pharmaceutical applications. *Eur Pharm Rev* 18:3–6
- Chen Y, Thosar SS, Forbess RA et al (2001) Prediction of drug content and hardness of intact tablets using artificial neural network and near-infrared spectroscopy. *Drug Dev Ind Pharm* 27:623–631
- Chieng N, Zujovic Z, Bowmaker G et al (2006) Effect of milling conditions on the solid-state conversion of ranitidine hydrochloride form I. *Int J Pharm* 327:36–44
- Chieng N, Rades T, Saville D (2008) Formation and physical stability of the amorphous phase of ranitidine hydrochloride polymorphs prepared by cryo-milling. *Eur J Pharm Biopharm* 68:771–780
- Chieng N, Aaltonen J, Saville D et al (2009) Physical characterization and stability of amorphous indomethacin and ranitidine hydrochloride binary systems prepared by mechanical activation. *Eur J Pharm Biopharm* 71:47–54
- Chieng N, Rades T, Aaltonen J (2011) An overview of recent studies on the analysis of pharmaceutical polymorphs. *J Pharm Biomed Anal* 55:618–644
- Childs SL, Stahly GP, Park A (2007) The salt-cocystal continuum: the influence of crystal structure on ionization state. *Mol Pharm* 4:323–338
- Clegg IM, Daly AM, Donnelly C et al (2012) Application of mid-infrared spectroscopy to the development and transfer of a manufacturing process for an active pharmaceutical ingredient. *Appl Spectrosc* 66:574–579
- Cleland JL, Lam X, Kendrick B et al (2001) A specific molar ratio of stabilizer to protein is required for storage stability of a lyophilized monoclonal antibody. *J Pharm Sci* 90:310–321
- Cogdill RP, Anderson CA (2005) Efficient spectroscopic calibration using net analyte signal and pure component projection methods. *J Near Infrared Spectrosc* 13:119–131
- Cogdill RP, Anderson CA, Drennen JK (2005a) Process analytical technology case study, Part III: Calibration monitoring and transfer. *AAPS PharmSciTech* 6:E284–E297
- Cogdill RP, Anderson C, Chrisholm R et al (2005b) Process analytical technology case study, Part I: Feasibility studies for quantitative near-infrared method development. *AAPS PharmSciTech* 6:E262–E272
- Cogdill RP, Anderson C, Chrisholm R et al (2005c) Process analytical technology case study, Part II: Development and validation of quantitative near-infrared calibrations in support of a process analytical technology application for real-time release. *AAPS PharmSciTech* 6:E273–E283
- Colón YM, Florian MA, Acevedo D et al (2014) Near infrared method development for a continuous manufacturing blending process. *J Pharm Innov* 9:291–301
- Constantino HR, Firouzabadian L, Wu C et al (2002) Protein spray freeze drying. 2. Effect of formulation variables on particle size and stability. *J Pharm Sci* 91:388–395
- Cordone L, Cottone G, Giuffrida S et al (2005) Internal dynamics and protein-matrix coupling in trehalose-coated proteins. *Biochim Biophys Acta* 1749:252–281
- Corredor CC, Bu D, Both D (2011) Comparison of near infrared and microwave resonance sensors for at-line moisture determination in powders and tablets. *Anal Chim Acta* 696:84–93
- Cottone G, Giuffrida S, Cicotti G et al (2005) Molecular dynamics simulation of sucrose- and trehalose-coated carboxy-myoglobin. *Proteins* 59:291–302
- Croker DM, Hennigan MC, Maher A et al (2012) A comparative study of the use of powder X-ray diffraction, Raman and near infrared spectroscopy for quantification of binary polymorphic mixtures of piracetam. *J Pharm Biomed Anal* 63:80–96
- De Beer TRM, Vercrusysse P et al (2009a) In-line and real-time process monitoring of a freeze drying process using Raman and NIR spectroscopy as complimentary process analytical technology (PAT) tools. *J Pharm Sci* 98:3430–3446

- De Beer TRM, Wiggenghorn M et al (2009b) Importance of using complementary process analyzers for the process monitoring, analysis, and understanding of freeze drying. *Anal Chem* 81:7639–7649
- De Beer T, Burggraeve A, Fonteyne M, Saerens L, Remon JP, Vervaet C (2011a) Near infrared and Raman spectroscopy for the in-process monitoring of pharmaceutical production processes. *Int J Pharm* 417:32–47
- De Beer TR, Wiggenghorn M, Hawe A et al (2011b) Optimization of a pharmaceutical freeze-dried product and its process using an experimental design approach and innovative process analyzers. *Talanta* 83:1623–1633
- De Bleye C, Chavez PF, Mantanus J et al (2012) Critical review of near-infrared spectroscopic methods validations in pharmaceutical applications. *J Pharm Biomed Anal* 69:125–132
- Demirdöven N, Cheatum CM, Chung HS et al (2004) Two-dimensional infrared spectroscopy of antiparallel β -sheet secondary structure. *J Am Chem Soc* 126:7981–7990
- Dong A, Huang P, Caughey WS (1990) Protein secondary structures in water from second-derivative amide I infrared spectra. *Biochemistry* 29:3303–3308
- Donoso M, Ghaly ES (2005) Prediction of tablets disintegration times using near-infrared diffuse reflectance spectroscopy as a nondestructive method. *Pharm Dev Technol* 10:211–217
- Du YP, Kasemsuran S, Jiang JH et al (2008) In vivo and in vitro near-infrared spectroscopic determination of blood glucose and other biomedical components with chemometrics. In: Burns DA, Ciurczak EW (eds) *Handbook of near-infrared analysis*, 3rd edn. CRC Press, Boca Raton
- Duffy D, Cremin N, Napier M et al (2012) In situ monitoring, control and optimization of a liquid-liquid phase separation crystallization. *Chem Eng Sci* 77:112–121
- Duffy D, Barrett M, Glennon B (2013) Novel, calibration-free strategies for supersaturation control in antisolvent crystallization processes. *Cryst Growth Des* 13:3321–3332
- Einfal T, Planinsek O, Hrovat K (2013) Methods of amorphization and investigation of the amorphous state. *Acta Pharm* 63:305–334
- El-Hagrasy AS, Morris HR, D'Amico F et al (2001) Near-infrared spectroscopy and imaging for the monitoring of powder blend homogeneity. *J Pharm Sci* 90:1298–1307
- El-Hagrasy AS, Delgado-Lopez M, Drennen JK (2006) A process analytical technology approach to near-infrared process control of pharmaceutical powder blending: Part II: qualitative near-infrared models for prediction of blend homogeneity. *J Pharm Sci* 95:407–421
- EMA Guideline on the use of near infrared spectroscopy by the pharmaceutical industry and the data requirements for new submissions and variations, January (2014)
- Fabian H, Schultz C, Naumann D et al (1993) Secondary structure and temperature-induced unfolding and refolding of ribonuclease T1 in aqueous solution. A Fourier transform infrared spectroscopic study. *J Mol Biol* 232:967–981
- Farrell JA, Higgins K, Kalivas JH (2012) Updating a near-infrared multivariate calibration model formed with lab-prepared pharmaceutical tablet types to new tablet types in fill production. *J Pharm Biomed Anal* 61:114–121
- Feng T, Wang F, Pinal R et al (2008) Investigation of the variability of NIR in-line monitoring of roller compaction process by using fast fourier transform (FFT) analysis. *AAPS PharmSciTech* 9:419–424
- Figueiras A, Carvalho RA, Ribeiro L et al (2007) Solid-state characterization and dissolution profiles of the inclusion complexes of omeprazole with native and chemically modified beta-cyclodextrin. *Eur J Pharm Biopharm* 67:531–539
- Findlay WP, Peck GR, Morris KR (2005) Determination of fluidized bed granulation end point using near-infrared spectroscopy and phenomenological analysis. *J Pharm Sci* 94:604–612
- Fix I, Steffens KJ (2004) Quantifying low amorphous or crystalline amounts of alpha-lactose-monohydrate using X-ray powder diffraction, near-infrared spectroscopy, and differential scanning calorimetry. *Drug Dev Ind Pharm* 30:513–523
- Fonteyne M, Soares S, Verduyck J et al (2012) Prediction of quality attributes of continuously produced granules using complimentary PAT tools. *Eur J Pharm Biopharm* 82:429–436

- Fonteyne M, Vercruyse J, Díaz DC et al (2013) Real-time assessment of critical quality attributes of a continuous granulation process. *Pharm Dev Technol* 18:85–97
- Freitas MP, Sabadin A, Silva LM et al (2005) Prediction of drug dissolution profiles from tablets using NIR diffuse reflectance spectroscopy: a rapid and nondestructive method. *J Pharm Biomed Anal* 39:17–21
- French DL, Arakawa T, Li T (2004) Fourier transform infrared spectroscopy investigation of protein conformation in spray-dried protein/trehalose powders. *Biopolymers* 73:524–531
- Frickel H, Reich G (2000) NIR spectroscopy of film-coated tablets—fast and nondestructive evaluation of film coat uniformity and drug release kinetics. *Proc Int Symp Contr Rel Bioact Mater* 27:740–741
- Fu K, Griebenov K, Hsieh L et al (1999) FTIR characterization of the secondary structure of proteins encapsulated within PLGA microspheres. *J Control Release* 58:357–366
- Ge Z, Thompson R, Cooper S et al (1995) Quantitative monitoring of an epoxidation process by Fourier transform infrared spectroscopy. *Process Control Qual* 7:3–12
- Gendre C, Boiret M, Genty M et al (2011a) Real-time predictions of drug release and end point detection of a coating operation by in-line near infrared measurements. *Int J Pharm* 421:237–243
- Gendre C, Genty M, Boiret M et al (2011b) Development of a process analytical technology (PAT) for in-line monitoring of film thickness and mass of coating materials during a pan coating operation. *Eur J Pharm Biopharm* 43:244–250
- Giuffrida S, Cottone G, Cordone L (2004) Structure-dynamics coupling between protein and external matrix in sucrose-coated and trehalose-coated MbCO: an FTIR study. *J Phys Chem* 108:15415–15421
- Gold TB, Buice RG Jr, Lodder RA et al (1997) Determination of extent of formaldehyde-induced crosslinking in hard gelatin capsules by near infrared spectroscopy. *Pharm Res* 14:1046–1050
- Gold TB, Buice RG Jr, Lodder RA et al (1998) Detection of formaldehyde-induced crosslinking in soft elastic gelatin capsules using near-infrared spectrophotometry. *Pharm Dev Technol* 3:209–214
- Gotter B, Faubel W, Neubert RH (2008) Optical methods for measurements of skin penetration. *Skin Pharmacol Physiol* 21:156–165
- Green RL, Thureau G, Pixley NC et al (2005) In-line monitoring of moisture content in fluid bed dryers using near-IR spectroscopy with consideration of sampling effects on method accuracy. *Anal Chem* 77:4515–4522
- Griffiths PR, De Haseth JA (2007) *Fourier transform infrared spectrometry*, 2nd edn. Wiley, New York
- Grohganz H, Fonteyne M, Skibsted E et al (2009) Role of excipients in the quantification of water in lyophilized mixtures using NIR spectroscopy. *J Pharm Biomed Anal* 49:901–907
- Grohganz H, Gildemyn D, Skibsted E et al (2010a) Towards a robust water content determination of freeze-dried samples by near-infrared spectroscopy. *Anal Chim Acta* 676:34–40
- Grohganz H, Fonteyne M, Skibsted E et al (2010b) Classification of lyophilized mixtures using multivariate analysis of NIR spectra. *Eur J Pharm Biopharm* 74:406–412
- Gupta A, Peck GE, Miller RW et al (2004) Nondestructive measurements of the compact strength and the particle-size distribution after milling of roller compacted powders by near-infrared spectroscopy. *J Pharm Sci* 93:1047–1053
- Gupta A, Peck GE, Miller RW et al (2005a) Real-time near-infrared monitoring of content uniformity, moisture content, compact density, tensile strength, and Young's modulus of roller compacted powder blends. *J Pharm Sci* 94:1589–1597
- Gupta A, Peck GE, Miller RW et al (2005b) Influence of ambient moisture on the compaction behavior of microcrystalline cellulose powder undergoing uni-axial compression and roller compaction: a comparative study using near-infrared spectroscopy. *J Pharm Sci* 94:2301–2313
- Hawe A, Kasper JC, Friess W et al (2009) Structural properties of monoclonal antibody aggregates induced by freeze-thawing and thermal stress. *Eur J Pharm Sci* 38:79–87

- Heigl N, Koller DM, Glasser BJ et al (2013) Quantitative on-line vs. off-line NIR analysis of fluidized bed drying with consideration of the spectral background. *Eur J Pharm Biopharm* 85:1064–1074
- Heinz A, Savolainen M, Rades T et al (2007) Quantifying ternary mixtures of different solid-state forms of indomethacin by Raman and near-infrared spectroscopy. *Eur J Pharm Sci* 32:182–192
- Heinz A, Strachan CJ, Atassi F et al (2008) Characterizing an amorphous system exhibiting trace crystallinity: a case study with saquinavir. *Cryst Growth Des* 8:119–127
- Heinz A, Strachan CJ, Gordon K et al (2009) Analysis of solid-state transformations of pharmaceutical compounds using vibrational spectroscopy. *J Pharm Pharmacol* 61:971–988
- Heise HM (2002) Applications of near-infrared spectroscopy in medical sciences. In: Siesler HW, Ozaki Y, Kawara S, Heise HM (eds) *Near-Infrared spectroscopy*. Wiley, Weinheim
- Heise HM, Marbach R, Bittner A (1998) Clinical chemistry and near infrared spectroscopy: technology for non-invasive glucose monitoring. *J Near Infrared Spectrosc* 6:349–359
- Heise HM, Küpper L, Butvina LN (2003) Novel infrared optical probes for process monitoring and analysis based on next-generation silver halide fibers. *Anal Bioanal Chem* 375:1116–1123
- Helmdach L, Feth MP, Minnich C et al (2013) Application of ATR-MIR spectroscopy in the pilot plant—scope and limitations using the example of paracetamol crystallizations. *Chem Eng Proc* 70:184–197
- Hicks MB, Zhou GX, Lieberman DR et al (2003) In situ moisture determination of a cytotoxic compound during process optimization. *J Pharm Sci* 92:529–535
- Higgins JP, Arrivo SM, Reed RA (2003) Approach to the determination of hydrate form conversions of drug compounds and solid dosage forms by near-infrared spectroscopy. *J Pharm Sci* 92:2303–2316
- Ho L, Cuppok Y, Muschert S et al (2009) Effects of film coating thickness and drug layer uniformity on in vitro drug release from sustained-release coated pellets: a case study using terahertz pulsed imaging. *Int J Pharm* 382:151–159
- Hsu CH, Ke WT, Lin SY (2010) Progressive steps of polymorphic transformation of gabapentin polymorphs studied by hot-stage FTIR microspectroscopy. *J Pharm Pharm Sci* 13:67–77
- Hu S, Maslov K, Tsytarov V et al (2009) Functional transcranial brain imaging by optical-resolution photoacoustic microscopy. *J Biomed Opt* 14:040503. doi:10.1117/1.3194136
- Hu Y, Erxleben A, Ryder AG et al (2010) Quantitative analysis of sulfathiazole polymorphs in ternary mixtures by attenuated total reflectance infrared, near-infrared and Raman spectroscopy. *J Pharm Biopharm* 53:412–420
- Hu Y, Macfhionnghaile P, Caron V et al (2013) Formation, physical stability, and quantification of process-induced disorder in cryomilled samples of a model polymorphic drug. *J Pharm Sci* 102:93–103
- Huang J, Li Y, Wigent RJ et al (2011) Interplay of formulation and process methodology on the extent of nifedipine molecular dispersion in polymers. *Int J Pharm* 420:59–67
- Igne B, de Juan A, Jaumot J et al (2014) Modeling strategies for pharmaceutical blend monitoring and end-point determination by near-infrared spectroscopy. *Int J Pharm* 473:219–231
- International Conference on Harmonization (ICH) of Technical Requirements for registration of Pharmaceuticals for human Use, Topic Q2 (R1): Validation of analytical Procedures: Text and Methodology. Geneva (2005) <http://bioforum.org.il/Uploads/Editor/karen/q2.r1.step4.pdf>. Accessed 23 June 2015
- Izutzu KI, Fujimaki Y, Kuwabara A et al (2006) Near-infrared analysis of protein secondary structure in aqueous solutions and freeze-dried solids. *J Pharm Sci* 95:781–789
- Järvinen K, Hoehe W, Järvinen M et al (2013) In-line monitoring of the drug content of powder mixtures and tablets by near-infrared spectroscopy during the continuous direct compression tableting process. *Eur J Pharm Sci* 48:680–688
- Jayasankar A, Somwangthanoj A, Shao ZJ et al (2006) Cocrystal formation during cogrinding and storage is mediated by amorphous phase. *Pharm Res* 23:2381–2392
- Jiang Y, Li C, Nguyen X, Muzammil S et al (2011) Qualification of FTIR spectroscopic method for protein secondary structural analysis. *J Pharm Sci* 100:4631–4641

- Joergensen AC, Strachan CJ, Pöllänen KH, Koradia V, Tian F, Rantanen J (2009) An insight into water of crystallization during processing using vibrational spectroscopy. *J Pharm Sci* 98:3903–3932
- Jorgensen L, Vermehren C, Bjerregaard S et al (2003) Secondary structure alterations in insulin and growth hormone water-in-oil emulsions. *Int J Pharm* 254:7–10
- Jorgensen AC, Rantanen J, Luukkonen P et al (2004a) Visualization of a pharmaceutical unit operation; wet granulation. *Anal Chem* 76:5331–5338
- Jorgensen AC, Luukkonen P, Rantanen J et al (2004b) Comparison of torque measurements and near-infrared spectroscopy in characterization of a wet granulation process. *J Pharm Sci* 93:2232–2243
- Joubert MK, Luo Q, Nashed-Samuel Y et al (2011) Classification and characterization of therapeutic antibody aggregates. *J Biol Chem* 286:25118–25133
- Kadam SS, van der Windt E, Daudey PJ et al (2010) A comparative study of ATR-FTIR and FT-NIR spectroscopy for in-situ concentration monitoring during batch cooling crystallization processes. *Cryst Growth Des* 10:2629–2640
- Kamat MS, Lodder RA, DeLuca PP (1989) Near-infrared spectroscopic determination of residual moisture in lyophilized sucrose through intact glass vials. *Pharm Res* 6:961–965
- Kammerzell TJ, Middaugh CR (2007) Two-dimensional correlation spectroscopy reveals coupled immunoglobulin regions of differential flexibility that influence stability. *Biochemistry* 46:9762–9773
- Kammerzell TJ, KJanai S, Liu JL et al (2009) Increasing IgG concentration modulates the conformational heterogeneity and bonding network that influence solution properties. *J Phys Chem B* 113:6109–6118
- Karande AD, Heng PW, Liew CV (2010) In-line quantification of micronized drug and excipients in tablets by near-infrared (NIR) spectroscopy: real time monitoring of tbleting process. *Int J Pharm* 396:63–74
- Karolewicz B, Górnaiak A, Owczarek A et al (2012) Solid dispersion in pharmaceutical technology. Part II. The methods of analysis of solid dispersions and examples of their application. *Polim Med* 42:97–107
- Kasemsumran S, Du YP, Maruo K et al (2006) Improvement of partial least squares models for in vitro and in vivo glucose quantifications by using near-infrared spectroscopy and searching combination moving window partial least squares. *Chemom Intell Lab Syst* 82:97–103
- Kauppinen JK, Moffatt DJ, Matsch HH et al (1981) Fourier transforms in the computation of self-deconvoluted and first-order derivative spectra of overlapped band contours. *Anal Chem* 53:1454–1457
- Kauppinen A, Toiviainen M et al (2013) In-line multipoint near-infrared spectroscopy for moisture content quantification during freeze-drying. *Anal Chem* 85:2377–2384
- Kauppinen A, Toiviainen M et al (2014) Validation of a multipoint near-infrared spectroscopy method for in-line moisture content analysis during freeze-drying. *J Pharm Biomed Anal* 95:229–237
- Kaushal AM, Chakraborti AK, Basal AK (2008) FTIR studies on differential intermolecular association in crystalline and amorphous states of structurally related non-steroidal anti-inflammatory drugs. *Mol Pharm* 5:937–945
- Kee NCS, Tan RBH, Braatz RD (2009) Selective crystallization of the metastable α -form of L-glutamic acid using concentration feedback control. *Cryst Growth Des* 9:3044–3061
- Kee NCS, Tan RBH, Braatz RD (2011) Semiautomated identification of the phase diagram for enantiotropic crystallizations using ATR-FTIR spectroscopy and laser backscattering. *Ind Eng Chem Res* 50:1488–1495
- Keles H, Naylor A, Clegg F et al (2014) Studying the release of hGH from gamma-irradiated PLGA microparticles using ATR-FTIR imaging. *Vib Spectrosc* 71:76–84
- Kelly AL, Gough T, Dhupal RS, Halsey SA et al (2012) Monitoring ibuprofen-nicotinamide cocrystal formation during solvent free continuous cocrystallization (SFCC) using near infrared spectroscopy as a PAT tool. *Int J Pharm* 426:15–20

- Kendrick BS, Dong A, Allison D et al (1996) Quantification of the area of overlap between second-derivative amide I infrared spectra to determine the structural similarity of a protein in different states. *J Pharm Sci* 85:155–158
- Kiefer J, Cöngel MA, Roth D et al (2012) Attenuated total reflection infrared difference spectroscopy (ATR-IRDS) for quantitative reaction monitoring. *Appl Spectrosc* 66:685–688
- Kirsch JD, Drennen JK (1995) Determination of film-coated tablet parameters by near-infrared spectroscopy. *J Pharm Biomed Anal* 13:1271–1281
- Kirsch JD, Drennen JK (1999) Nondestructive tablet hardness testing by near-infrared spectroscopy: a new and robust spectral best-fit algorithm. *J Pharm Biomed Anal* 19:351–369
- Knop K, Kleinebudde P (2013) PAT-tools for process control in pharmaceutical film coating applications. *Int J Pharm* 457:527–536
- Kogermann K, Aaltonen J, Strachan CJ et al (2007) Qualitative in situ analysis of multiple solid-state forms using spectroscopy and partial least squares discriminant modeling. *J Pharm Sci* 96:1802–1820
- Kogermann K, Aaltonen J, Strachan CJ et al (2008) Establishing quantitative in-line analysis of multiple solid-state transformations during dehydration. *J Pharm Sci* 97:4983–4999
- Kojima T, Yamauchi Y, Onoue S et al (2008) Evaluation of hydrate formation of a pharmaceutical solid by using diffuse reflectance infrared Fourier-transform spectroscopy. *J Pharm Biomed Anal* 46:788–791
- Krier F, Mantanus J, Sacré PY et al (2013) PAT tools for the control of co-extrusion implants manufacturing process. *Int J Pharm* 458:15–24
- Krzyzaniak JF, Williams GR, Ni N (2007) Identification of phase boundaries in anhydrate/hydrate systems. *J Pharm Sci* 96:1270–1281
- Kumar A, Vercautse J, Toiviainen M et al (2014) Mixing and transport during pharmaceutical twin-screw wet granulation: experimental analysis via chemical imaging. *Eur J Pharm Biopharm* 87:279–289
- Lee MJ, Park CR, Kim AY et al (2010) Dynamic calibration for the in-line NIR monitoring of film thickness of pharmaceutical tablets processed in a fluid-bed coater. *J Pharm Sci* 99:325–335
- Lee MJ, Seo DY, Lee HE et al (2011a) In line NIR quantification of film thickness on pharmaceutical pellets during a fluid bed coating process. *Int J Pharm* 403:66–72
- Lee YY, Wu JX, Yang M et al (2011b) Particle size dependence of polymorphism in spray-dried mannitol. *Eur J Pharm Sci* 44:41–48
- Lefèvre T, Arseneault K, Pézolet M (2004) Study of protein aggregation using two-dimensional correlation infrared spectroscopy and spectral simulations. *Biopolymers* 73:705–715
- Leskinen JTT, Okkonen MAH, Toiviainen S et al (2010) Labscale fluidized bed granulator instrumented with non-invasive process monitoring devices. *Chem Eng J* 164:268–274
- Li S (2010) Application of online reaction monitoring by Raman and infrared spectroscopy in early drug development: halogen-lithium exchange chemistry. *Am Pharm Rev* 13:62–67
- Li W, Worosila GD, Wang W et al (2005) Determination of polymorph conversion of an active pharmaceutical ingredient in wet granulation using NIR calibration models generated from the premix blends. *J Pharm Sci* 94:2800–2806
- Li RF, Wang XZ, Ababe SB (2008) Monitoring batch cooling crystallization using NIR: development of calibration models using genetic algorithm and PLS. *Part Part Syst Charact* 25:314–327
- Liao X, Gautam M, Grill A et al (2010) Effect of position isomerism on the formation and physicochemical properties of pharmaceutical co-crystals. *J Pharm Sci* 99:246–254
- Lin SY (2014) Molecular perspectives on solid-state phase transformation and chemical reactivity of drugs: metoclopramide as an example. *Drug Discov Today* 52:1224–1232. doi:[10.1016/j.drudis.2014.10.001](https://doi.org/10.1016/j.drudis.2014.10.001)
- Lin SY (2015) Molecular perspectives on solid-state phase transformation and chemical reactivity of drugs: metoclopramide as an example. *Drug Discov Today* 20:209–222
- Lin SY, Hsu CH, Sheu MT (2010) Curve-fitting FT-IR studies of loratadine/hydroxypropyl-beta-cyclodextrin inclusion complex induced by co-grinding. *J Pharm Biomed Anal* 53:799–803

- Lin HL, Hsu PC, Lin SY (2013) Theophylline-citric acid co-crystals easily induced by DSC-FTIR microspectroscopy or different storage conditions. *Asian J Pharm Sci* 8:19–27
- Liu Y, Blackwood D (2012) Sample presentation in rotary tablet press feed frame monitoring by near infrared spectroscopy. *Am Pharm Rev* May: 1–7
- Liu C, Desai KG (2005) Characteristics of rofecoxib-polyethylene glycol 4000 solid dispersions and tablets based on solid dispersions. *Pharm Dev Technol* 10:467–477
- Löbmann K, Laitinen R, Grohganz H et al (2011) Coamorphous drug systems: enhanced physical stability and dissolution rate of indomethacin and naproxen. *Mol Pharm* 8:1919–1928
- Löbmann K, Laitinen R, Grohganz H et al (2013) A theoretical and spectroscopic study of co-amorphous naproxen and indomethacin. *Int J Pharm* 453:80–87
- Lourenco V, Lochmann D, Reich G et al (2012) A quality by design study applied to an industrial pharmaceutical fluid bed granulation. *Eur J Pharm Biopharm* 81:438–447
- Lumpi D, Wagner C, Schoepf H et al (2012) Fibre-optic ATR-IR spectroscopy at cryogenic temperatures: in-line reaction monitoring on organolithium compounds. *Chem Commun* 48:2451–2453
- Luo S, Zhang E, Su Y et al (2011) A review of NIR dyes in cancer targeting and imaging. *Biomaterials* 32:7127–7138
- Luukkonen P, Fransson M, Bjorn IN et al (2008) Real-time assessment of granule and tablet properties using in-line data from a high shear granulation process. *J Pharm Sci* 97:950–959
- Luyptaert J, Massart DL, Vander Heyden Y (2007) Near-infrared spectroscopy applications in pharmaceutical analysis. *Talanta* 72:865–883
- Ma CY, Wang XZ (2011) Simultaneous characterization of multiple properties of solid and liquid phases in crystallization processes using NIR. *Particuology* 9:589–597
- Macfionnghaile P, Hu Y, Gniado K et al (2014) Effects of ball-milling and cryomilling on sulfamerazine polymorphs a comparative study. *J Pharm Sci* 103:1766–1778
- Maesschalck RD, Sanchez FC, Massart DL et al (1998) On-line monitoring of powder blending with near-infrared spectroscopy. *Appl Spectrosc* 52:725–731
- Mallamace F, Baglioni P, Corsaro C et al (2014) The influence of water on protein properties. *J Chem Phys* 141:165104
- Maltesen MJ, van der Weert M, Grohganz H (2012) Design of experiments-based monitoring of critical quality attributes for the spray-drying process of insulin by NIR spectroscopy. *AAPS PharmSciTech* 13:747–755
- Manikwar P, Majumdar R, Hickey JM et al (2013) Correlating excipient effects on conformational and storage stability of IgG1 monoclonal antibody with local dynamics as measured by hydrogen/deuterium-exchange mass spectrometry. *J Pharm Sci* 102:2136–2151
- Maniruzzaman M, Islam MT, Moradiya HG et al (2014) Prediction of polymorphic transformations of paracetamol in solid dispersions. *J Pharm Sci* 103:1819–1828
- Manning MC (2005) Use of infrared spectroscopy to monitor protein structure and stability. *Expert Rev Proteomics* 2:731–743
- Mantanus J, Ziémons E, Lebrun P et al (2009) Moisture content determination of pharmaceutical pellets by near infrared spectroscopy: method development and validation. *Anal Chim Acta* 642:186–192
- Mantanus J, Ziémons E, Lebrun P et al (2010a) Active content determination of non-coated pharmaceutical pellets by near-infrared spectroscopy: method development, validation and reliability evaluation. *Talanta* 80:1750–1757
- Mantanus J, Ziemons E, Rozet E et al (2010b) Building the quality into pellet manufacturing environment—feasibility study and validation of an in-line quantitative near infrared (NIR) method. *Talanta* 83:305–311
- Märk J, Karner M, Andre M et al (2010) Online process control of a pharmaceutical intermediate in a fluidized-bed drier environment using near-infrared spectroscopy. *Anal Chem* 82:4209–4215
- Markl D, Wahl PR, Menezes JC et al (2013) Supervisory control system for monitoring a pharmaceutical hot melt extrusion process. *AAPS PharmSciTech* 14:1034–1044

- Martens H, Naes T (2001) *Multivariate calibration*, Copyright 1989 by Wiley, reprinted with corrections
- Martínez L, Peinado A, Liesum L et al (2013) Use of near-infrared spectroscopy to quantify drug content on a continuous blending process: influence of mass flow and rotation speed variations. *Eur J Pharm Biopharm* 84:606–615
- Maruao K, Tsurugi M, Chin J et al (2003) Noninvasive blood glucose assay using a newly developed near-infrared system. *IEEE J Sel Top Quantum Electron* 9:322–330
- Marziano I, Sharp DCA, Dunn PJ et al (2000) On-line mid-IR spectroscopy as a real-time approach in monitoring hydrogenation reactions. *Org Process Res Dev* 45:357–361
- Maury M, Murphy K, Kumar S et al (2005) Spray-drying of proteins: effects of sorbitol and trehalose on aggregation and FT-IR amide I spectrum of an immunoglobulin G. *Eur J Pharm Biopharm* 59:251–261
- McArdle P, Gilligan K, Cunningham D et al (2005) Determination of the polymorphic forms of bicifadine hydrochloride by differential scanning calorimetry-thermogravimetric analysis, X-ray powder diffraction, attenuated total reflectance-infrared spectroscopy, and attenuated total reflectance-near-infrared spectroscopy. *Appl Spectrosc* 59:1365–1371
- McAucliffe MAP, O'Mahony GE et al (2015) The use of PAT and off-line methods for monitoring of roller compacted ribbon and granule properties with a view to continuous processing. *Org Process Res Dev* 19(1):158–166. doi:[10.1021/op5000013](https://doi.org/10.1021/op5000013)
- McFearin CL, Sankaranarayanan J, Almutin A (2011) Application of fiber optic ATR-FTIR methods for in situ characterization of protein delivery systems in real time. *Anal Chem* 83:3943–3949
- Minnich CB, Buskens P, Steffens HC, Bäuerlein PS, Butvina LN, Küpper L, Leitner W, Liauw MA, Greiner L (2007) Highly flexible fibre-optic ATR-IR probe for inline reaction monitoring. *Org Process Res Dev* 11:94–97
- Möltgen CV (2014) QbD/PAT method development for enhanced process understanding and control of a pharmaceutical pan coating process. Dissertation, University of Heidelberg
- Möltgen CV, Puchert T, Menezes JC et al (2012) A novel in-line NIR spectroscopy application for the monitoring of tablet film coating in an industrial scale process. *Talanta* 92:26–37
- Möltgen CV, Herdling T, Reich G (2013) A novel multivariate approach using science-based calibration for direct coating thickness determination in real-time NIR process monitoring. *Eur J Pharm Biopharm* 85:1056–1063
- Moes JJ, Ruijken MM, Gout E et al (2008) Application of process analytical technology in tablet process development using NIR spectroscopy: Blend uniformity, content uniformity and coating thickness measurements. *Int J Pharm* 357: 108–118
- Momose W, Imai K, Yokota S et al (2011) Process analytical technology applied for end-point detection of pharmaceutical blending by combining two calibration-free methods: simultaneously monitoring specific near-infrared peak intensity and moving block standard deviation. *Powder Technol* 210:122–131
- Moorthy BS, Schultz SG, Kim SG et al (2014) Predicting protein aggregation during storage in lyophilized solids using solid state amide hydrogen/deuterium-exchange with mass spectrometric analysis (ssHDX-MS). *Mol Pharm* 11:1869–1879
- Moran A, Buckton G (2009) Studies of the crystallization of amorphous trehalose using simultaneous gravimetric vapor sorption/near IR (GVS/NIR) and “modulated” GVS/NIR. *AAPS PharmSciTech* 10:297–302
- Müller UA, Mertes B, Fischbacher C et al (1997) Noninvasive blood glucose monitoring by means of near infrared spectroscopy: methods for improving the reliability of the calibration models. *Int J Artif Org* 20:285–290
- Murphy BM, Zhang N, Payne RW et al (2012) Structure, stability, and mobility of a lyophilized IgG1 monoclonal antibody as determined using second-derivative infrared spectroscopy. *J Pharm Sci* 101:81–91
- Muzzio CR, Dini NG, Simionato LD (2011) Determination of moisture content in lyophilized mannitol through glass vials using NIR micro-spectrometers. *Braz J Pharm Sci* 2:289–297

- Naes T, Isaksson T, Fearn T, Davies T (2002) *Multivariate calibration and classification*. NIR Publications, Chichester
- Nagy ZK, Braatz RD (2012) Advances and new directions in crystallization control. *Annu Rev Chem Biomol Eng* 3:55–75
- Nagy ZK, Fujiwara M, Braatz RD (2008) Modelling and control of combined cooling and antisolvent crystallization control. *J Process Control* 18:856–864
- Nagy ZK, Fevotte G, Kramer H et al (2013) Recent advances in the monitoring, modeling and control of crystallization systems. *Chem Eng Res Des* 91:1903–1922
- Neergaard MS, Nielsen AD, Parshad H et al (2014) Stability of monoclonal antibodies at high-concentration: head-to-head comparison of the IgG1 and IgG4 subclass. *J Pharm Sci* 103:115–127
- Nieuwmeyer FJS, Damen M, Gerich A et al (2007) Granule characterization during fluid bed drying by development of a near infrared method to determine water content and median particle size. *Pharm Res* 24:1854–1861
- Noda I (1990) Two-dimensional infrared (2D IR) spectroscopy: theory and applications. *Appl Spectrosc* 44:550–561
- Otsuka M, Tanabe H (2012) Stability test for amorphous materials in humidity controlled 96 well plates by near-infrared spectroscopy. *Drug Dev Ind Pharm* 38:380–385
- Otsuka M, Yamane I (2009) Prediction of tablet properties based on near infrared spectra of raw mixed powders by chemometrics: Scale-up factor of blending and tableting processes. *J Pharm Sci* 98:4296–4305
- Otsuka M, Mouri Y, Matsuda Y (2003) Chemometric evaluation of pharmaceutical properties of antipyrine granules by near-infrared spectroscopy. *AAPS PharmSciTech* 4:Article 47
- Otsuka M, Tanabe H, Osaki K et al (2007) Chemoinformetrical evaluation of dissolution property of indomethacin tablets by near-infrared spectroscopy. *J Pharm Sci* 96:788–801
- Otsuka M, Kanai Y, Hattori Y (2014) Real-time monitoring of changes of adsorbed and crystalline water contents in tablet formulation powder containing theophylline anhydrate at various temperatures during agitated granulation by near-infrared spectroscopy. *J Pharm Sci* 103:2924–2936
- Ozaki Y (2012) Near infrared spectroscopy—its versatility in analytical chemistry. *Anal Sci* 28:545–563
- Park J, Nagapudi K, Vergara C, Ramachander R, Laurence JS, Krishnan S (2013) Effect of pH and excipients on structure, dynamics, and long-term stability of a model IgG1 antibody upon freeze-drying. *Pharm Res* 30:968–984
- Patel AD, Luner PE, Kemper MS (2001) Low-level determination of polymorph composition in physical mixtures by near-infrared reflectance spectroscopy. *J Pharm Sci* 90:360–370
- Peinado A, Hammond J, Scott A (2011) Development, validation and transfer of a near infrared method to determine in-line the end point of a fluidized drying process for commercial production batches of an approved oral solid dose pharmaceutical product. *J Pharm Biomed Anal* 54:13–20
- Perez-Ramos JD, Findlay WP, Peck G et al (2005) Quantitative analysis of film coating in a pan coater based on in-line sensor measurements. *AAPS PharmSciTech* 6:E127–E136
- Pieters S, De Beer T, Kasper JC et al (2012) Near-infrared spectroscopy for in-line monitoring of protein unfolding and its interactions with lyoprotectants during freeze-drying. *Anal Chem* 84:947–955
- Pieters S, Saeyns W, Van den Kerkhof T et al (2013) Robust calibrations on reduced sample sets for API content prediction in tablets: definition of a cost-effective NIR model development strategy. *Anal Chim Acta* 761:62–70
- Pöllänen K, Häkkinen A, Huhtanen M et al (2005) DRIFT-IR for quantitative characterization of polymorphic composition of sulfathiazole. *Anal Chim Acta* 544:108–117
- Prestrelski SJ, Tedeschi N, Tsutomu A et al (1993) Dehydration-induced conformational transitions in proteins and their inhibition by stabilizers. *Biophys J* 65:661–671

- Puchert T, Holzhauser CV, Menezes JC et al (2011) A new PAT/QbD approach for the determination of blend homogeneity: combination of on-line NIRS analysis with PC Scores Distance Analysis (PC-SDA). *Eur J Pharm Biopharm* 78:173–182
- Qiao N, Li M, Schlindwein W et al (2011) Pharmaceutical cocrystals: an overview. *Int J Pharm* 419:1–11
- Quyett PV, Samanta AK, Liew CV et al (2013) A prediction model for monitoring ribbed roller compacted ribbons. *J Pharm Sci* 102:2667–2678
- Radtke G, Knop K, Lippold C (1999) In-process control of direct pelletisation in the rotary fluidized bed using NIR spectroscopy. *NIR News* 10:4–12
- Rahman Z, Zidan AS, Khan MA (2010a) Formulation and evaluation of a protein-loaded solid dispersion by non-destructive methods. *AAPS J* 12:158–170
- Rahman Z, Zidan AS, Khan MA (2010b) Risperidone solid dispersion of orally disintegrating tablet: its formulation design and non-destructive methods of evaluation. *Int J Pharm* 400:49–58
- Rajalahti T, Kvalheim OM (2011) Multivariate data analysis in pharmaceuticals: a tutorial review. *Int J Pharm* 417:280–290
- Rantanen J, Räsänen E, Tenhunen J et al (2000) In-line moisture measurement during granulation with a four-wavelength near infrared sensor: an evaluation of particle size and binder effects. *Eur J Pharm Biopharm* 50:271–276
- Rantanen J, Laine SJ, Antikainen OK, Mannermaa JP, Simula OE, Yliruusi J (2001) Visualization of fluid-bed granulation with self-organising maps. *J Pharm Biomed Anal* 24:343–352
- Rantanen J, Wikström H, Turner R et al (2005) Use of in-line near-infrared spectroscopy in combination with chemometrics for improved understanding of pharmaceutical processes. *Anal Chem* 77:556–563
- Räsänen E, Sandler N (2007) Near infrared spectroscopy in the development of solid dosage forms. *J Pharm Pharmacol* 59:147–159
- Räsänen E, Rantanen J, Mannermaa JP et al (2003) Dehydration studies using a novel multichamber microscale fluid bed dryer with in-line near-infrared measurement. *J Pharm Sci* 92:2074–2081
- Rehder S, Wu JX, Laackmann J et al (2013) A case study of real-time monitoring of solid-state phase transformations in acoustically levitated particles using near infrared and Raman spectroscopy. *Eur J Pharm Biopharm* 48:97–103
- Reich G (2000a) Fast and non-destructive quality control of gelatin capsule shells. In: Proceedings of third world meeting APV/APGI, Berlin, 3–6 April, pp 493–494
- Reich G (2000b) Use of NIR transmission spectroscopy for nondestructive determination of tablet hardness. In: Proceedings of third world meeting APV/APGI, Berlin, 3–6 April, pp 105–106
- Reich G (2001) Nondestructive determination of tablet hardness and consolidation characteristics using NIR transmission spectroscopy. Poster presented at AAPS Annual Meeting and Exposition, Denver, M 2283
- Reich G (2004) Formulation and physical properties of soft capsules. In: Podczeczek F, Jones BE (eds) *Pharmaceutical capsules*, 2nd edn. Pharmaceutical Press, London
- Reich G (2005) Near-infrared spectroscopy and imaging: basic principles and pharmaceutical applications. *Adv Drug Deliv Rev* 57:1109–1143
- Reich G, Frickel H (1999) Use of transmission spectroscopy to determine physical and functional film coat properties on tablets. *Proc Int Symp Control Rel Bioact Mater* 26:905–906
- Reich G, Frickel H (2000) NIR spectroscopy—a rapid method to evaluate gastroresistance and drug release kinetics of film-coated tablets. In: Proceedings of third world meeting APV/APGI, Berlin, 3/6 April, pp 627–628
- Remmele RL, Stushnoff C, Carpenter JF (1997) Real-time in situ monitoring of lysozyme during lyophilization using infrared spectroscopy: dehydration stress in the presence of sucrose. *Pharm Res* 14:1548–1555
- Robinson MR, Eaton RP, Haaland DM et al (1992) Noninvasive glucose monitoring in diabetic patients: a preliminary evaluation. *Clin Chem* 38:1618–1622

- Römer M, Heinamaki J, Miroshnyk I et al (2007) Phase transformations of erythromycin A dehydrate during pelletisation and drying. *Eur J Pharm Biopharm* 67:246–252
- Römer M, Heinämäki JI, Strachan CJ et al (2008) Prediction of tablet film-coating thickness using a rotating plate coating system and NIR spectroscopy. *AAPS PharmSciTech* 9:1047–1053
- Rosas JG, de Waard H, De Beer T et al (2014) NIR spectroscopy for the in-line monitoring of a multicomponent formulation during the entire freeze-drying process. *J Pharm Biomed Anal* 97:39–46
- Saeed M, Probst L, Betz G (2011) Assessment of diffuse transmission and reflection modes in near-infrared quantification—Part 2: Diffuse reflection information depth. *J Pharm Sci* 100:1130–1141
- Saerens L (2013) Spectroscopic process monitoring for quality assessment, visualization and understanding of pharmaceutical hot-melt extrusion. PhD Thesis, Ghent University
- Saerens L, Dierickx L, Quinten T et al (2012) In-line NIR spectroscopy for the understanding of polymer-drug interaction during pharmaceutical hot-melt extrusion. *Eur J Pharm Biopharm* 81:230–237
- Saerens L, Vervaeet C, Remon JP et al (2014) Process monitoring and visualization solutions for hot-melt extrusion: a review. *J Pharm Pharmacol* 66:180–203
- Sandler N, Rantanen J, Heinamaki J et al (2005) Pellet manufacturing extrusion-spheronization using process analytical technology. *AAPS PharmSciTech* 6:Article 26
- Sanzida N, Nagy ZK (2013) Iterative learning control for the systematic design of supersaturation controlled batch crystallization processes. *Comput Chem Eng* 59:11–121
- Sarracuga MC, Lopez JA (2009) The use of net analyte signal (NAS) in near infrared spectroscopy pharmaceutical applications: interpretability and figures of merit. *Anal Chim Acta* 642:179–185
- Sarracuga MC, Ribeiro PR, Santos AQ et al (2014) A PAT approach for on-line monitoring of pharmaceutical co-crystals formation with near infrared spectroscopy. *Int J Pharm* 471:478–484
- Savolainen M, Heinz A, Strachan C et al (2007a) Screening for differences in the amorphous state of indomethacin using multivariate visualization. *Eur J Pharm Sci* 30:113–123
- Savolainen M, Jouppila K, Pajamo O et al (2007b) Determination of amorphous content in the pharmaceutical process environment. *J Pharm Pharmacol* 59:161–170
- Schaefer C, Lecomte C, Clicq D et al (2013) On-line near infrared spectroscopy as a process analytical (PAT) tool to control an industrial seeded API crystallization. *J Pharm Biomed Anal* 83:194–201
- Schaefer C, Clicq D, Lecomte C et al (2014) A Process Analytical Technology (PAT) approach to control a new API manufacturing process: development, validation and implementation. *Talanta* 120:114–125
- Scheibelhofer O, Balak N, Koller DM et al (2013) Spatially resolved monitoring of powder mixing processes via multiple NIR probes. *Powder Technol* 243:161–170
- Schneider H, Reich G (2011a) PAT instrumentation of a suspension dryer for dynamic inline monitoring of solid-liquid separation, washing and thermal drying. *Pharm Ind* 73:927–936
- Schneider H, Reich G (2011b) Optimization of near-infrared spectroscopic process monitoring at low signal-to-noise ratio. *Anal Chem* 83:2172–2178
- Schneider H, Reich G (2012) Comparison of different probe arrangements for inline NIR measurements during fluid bed granulation. Paper presented at 26th international forum of process analytical technology (IFPAC), Baltimore, 22–25 January 2012
- Schöll J, Bonalumi D, Vicum L et al (2006) In situ monitoring and modeling of the solvent-mediated polymorphic transformation of L-glutamic acid. *Cryst Growth Des* 6:881–891
- Schönbichler SA, Bittner LKH, Weiss AKH et al (2013) Comparison of NIR chemical imaging with conventional NIR, Raman, and ATR-IR spectroscopy for quantification of furosemide crystal polymorphs in ternary powder mixtures. *Eur J Pharm Biopharm* 84:616–625
- Schönbrodt T (2004) Near-infrared spectroscopic characterization of monolithic matrix systems for parenteral drug delivery. Dissertation, University of Heidelberg

- Schönbrodt T, Mohl S, Winter G et al (2006) NIR spectroscopy—a non-destructive analytical tool for protein quantification within lipid implants. *J Control Release* 114:261–267
- Schüle S, Frieß W, Bechthold-Peters K et al (2007) Conformational analysis of protein secondary structure during spray-drying of antibody/mannitol formulations. *Eur J Pharm Biopharm* 65:1–9
- Sekulic SS, Ward HW, Brannegan DR et al (1996) On-line monitoring of powder blend homogeneity by near-infrared spectroscopy. *Anal Chem* 68:509–513
- Sekulic SS, Wakeman J, Doherty P, Hailey PA (1998) Automated system for the on-line monitoring of powder blending processes using near-infrared spectroscopy. Part II: Qualitative approaches to blend evaluation. *J Pharm Biomed Anal* 17:1285–1309
- Shah B, Kakumanu VK, Bansal AK (2006) Analytical techniques for quantification of amorphous/crystalline phases in pharmaceutical solids. *J Pharm Sci* 95:1641–1665
- Shah RB, Tawakkul MA, Khan MA (2007) Process analytical technology: chemometric analysis of Raman and near-infrared spectroscopic data for predicting physical properties of extended release matrix tablets. *J Pharm Sci* 96:1356–1365
- Shi Z, Anderson CA (2010) Pharmaceutical applications of separation of absorption and scattering in near-infrared spectroscopy (NIRS). *J Pharm Sci* 99:4766–4783
- Shi Z, Cogdill RP, Short SM et al (2008) Process characterization of powder blending by near-infrared spectroscopy: blend end-points and beyond. *J Pharm Biomed Anal* 47:738–745
- Siesler HW (2008) Basic principles of near-infrared spectroscopy. In: Burns DA, Ciuczak EW (eds) *Handbook of near-infrared analysis*, 3rd edn. CRC Press, Boca Raton
- Simone E, Saleemi N, Nagy ZK (2015) In situ monitoring of polymorphic transformations using a composite sensor array of Raman, NIR, and ATR-UV/vis spectroscopy, FBRM, and PVM for an intelligent decision support system. *Org Process Res Dev* 19:167–177
- Simpson MB (2010) Near-infrared spectroscopy for process analytical technology: theory, technology, and implementation. In: Bakeev KA (ed) *Process analytical technology*, 2nd edn. Wiley, Chichester
- Soares FL, Carneiro RL (2014) Evaluation of analytical tools and multivariate methods for quantification of co-former crystals in ibuprofen-nicotinamide co-crystals. *J Pharm Biomed Anal* 89:166–175
- Soh JP, Boersen N, Carvajal MT et al (2007) Importance of raw material attributes for modeling ribbon and granule properties in roller compaction: multivariate analysis on roll gap and NIR spectral slope as process critical control parameters. *J Pharm Innov* 2:106–124
- Sorak D, Herberholz L, Iwascek S et al (2012) New developments and application of handheld Raman, mid-infrared and near-infrared spectrometers. *Appl Spectrosc Rev* 47:83–115
- Stokvold A, Dyrstad K, Libnau FO (2002) Sensitive NIRS measurement of increased moisture in stored hygroscopic freeze dried product. *J Pharm Biomed Anal* 28:867–873
- Storme-Paris I, Clarot I, Esposito S et al (2009) Near infrared spectroscopy homogeneity evaluation of complex powder blends in a small-scale pharmaceutical preformulation process, a real life application. *Eur J Pharm Biopharm* 72:189–198
- Sulub Y, LoBrutto R, Vivilecchia R et al (2008) Content uniformity determination of pharmaceutical tablets using five near-infrared reflectance spectrometers: a process analytical technology (PAT) approach using robust multivariate calibration transfer algorithms. *Anal Chim Acta* 611:143–150
- Tabasi SH, Fahmy R, Bensley D et al (2008a) Quality by design, Part I: application of NIR spectroscopy to monitor tablet manufacturing process. *J Pharm Sci* 97:4040–4051
- Tabasi SH, Fahmy R, Bensley D et al (2008b) Quality by design. Part II: Application of NIR spectroscopy to monitor coating process for pharmaceutical coated product. *J Pharm Sci* 97:4052–4066
- Tabasi SH, Fahmy R, Bensley D et al (2008c) Quality by design. Part III: Study of curing process of sustained release polymer products using NIR spectroscopy. *J Pharm Sci* 97:4067–4086
- Tabasi SH, Moolchandani V, Fahmy R et al (2009) Sustained release dosage forms dissolution behavior prediction: a study of matrix tablets using NIR spectroscopy. *Int J Pharm* 382:1–6

- Tanabe H, Otsuka K, Otsuka M (2007) Theoretical analysis of tablet hardness prediction using chemoinformatic near-infrared spectroscopy. *Anal Sci* 23:857–862
- Tang XC, Pikal MJ, Taylor LS (2002) A spectroscopic investigation of hydrogen bond patterns in crystalline and amorphous phases in dihydropyridine calcium channel blockers. *Pharm Res* 19: 477–483
- Taylor LS, Zografi G (1997) Spectroscopic characterization of interactions between PVP and indomethacin in amorphous molecular dispersions. *Pharm Res* 12:1691–1698
- Telikepalli SN, Kumru OS, Kalonia C et al (2014) Structural characterization of IgG1 mAb aggregates and particles generated under various stress conditions. *J Pharm Sci* 103:796–809
- Telikepalli S, Kumru OS, Kim JH et al (2015) Characterization of the physical stability of a lyophilized IgG1 mAb after accelerated shipping-like stress. *J Pharm Sci* 104:495–507
- Tian F, Middaugh R, Offerdahl T et al (2007) Spectroscopic evaluation of the stabilization of humanized monoclonal antibodies in amino acid formulations. *Int J Pharm* 335:20–31
- Tok A, Goh XP, Ng W et al (2008) Monitoring granulation rate processes using three PAT tools in a pilot-scale fluidized bed. *AAPS PharmSciTech* 9:1083–1091
- Touil A, Peczalski R, Zagrouba F (2012) Monitoring of theophylline dehydration in a vacuum contact dryer by near-infrared spectroscopy. *Chem Eng Res Des*. doi:10.1016/j.cherd.2012.11.014
- Trnka H, Palou A, Panouillot PE et al (2014) Near-infrared imaging for high-throughput screening of moisture induced changes in freeze-dried formulations. *J Pharm Sci* 103:2839–2846
- Tumuluri SV, Prodduturi S, Crowley MM et al (2004) The use of near-infrared spectroscopy for the quantification of a drug in hot-melt extruded films. *Drug Dev Ind Pharm* 30:505–5011
- Uchida H, Otsuka M (2011) Quantitative analysis of pseudopolymorphic transformation of imidafenacin by application of a novel combination of near-infrared spectroscopy and a humidity-controlled 96-well plate. *J Pharm Pharmacol* 63:911–917
- USFDA (2004a) PAT—a framework for innovative pharmaceutical development, manufacturing, and quality assurance. <http://www.fda.gov/cder/guidance>
- USFDA (2004b) Final report on pharmaceutical cGMPs for the 21st century—a risk-based approach. <http://www.fda.gov/cder/gmp/gmp2004/GMPfinalreport2004.htm>
- USFDA Draft Guidance—Development and submission of near infrared analytical procedures, Guidance for Industry, March (2015)
- Van de Weert M, van't Hof R, van der Weerd J et al (2000) Lysozyme distribution and conformation in a biodegradable polymer matrix as determined by FTIR techniques. *J Control Release* 68:31–40
- Van de Weert M, Haris PI, Hennink WE et al (2001) Fourier transform infrared spectroscopic analysis of protein conformation: effect of sampling method and stress factors. *Anal Biochem* 297:160–169
- Van de Weert M, van Dijkhuizen-Radersma R, Bezemer JM et al (2002) Reversible aggregation of lysozyme in a biodegradable amphiphilic multiblock copolymer. *Eur J Pharm Biopharm* 54:89–93
- Vanarase AU, Alcalà M, Jerez Rozo JI et al (2010) Real-time monitoring of drug concentration in a continuous powder mixing process using NIR spectroscopy. *Chem Eng Sci* 65:5728–5733
- Vanarase AU, Järvinen M, Paaso J et al (2013) Development of a methodology to estimate error in the on-line measurements of blend uniformity in a continuous powder mixing process. *Powder Technol* 241:263–271
- Vercruyssen J, Toiviainen M, Fonteyne M et al (2014) Visualization and understanding of the granulation liquid mixing and distribution during continuous twin screw granulation using NIR chemical imaging. *Eur J Pharm Biopharm* 86:383–392
- Vonhoff S, Condliffe J, Schiffter H (2010) Implementation of an FTIR calibration curve for fast and objective determination of changes in protein secondary structure during formulation development. *J Pharm Biomed Anal* 51:39–45
- Vora KL, Buckton G, Clapham D (2004) The use of dynamic vapour sorption and near infra-red spectroscopy (DVS-NIR) to study the crystal transitions of theophylline and the report of a new solid-state transition. *Eur J Pharm Sci* 22:97–105

- Wahl PR, Treffer D, Mohr S et al (2013) Inline monitoring and a PAT strategy for pharmaceutical hot melt extrusion. *Int J Pharm* 455:159–168
- Wahl PR, Fruhmann G, Sacher S et al (2014) PAT for tableting: inline monitoring of API and excipients via NIR spectroscopy. *Eur J Pharm Biopharm* 87:271–278
- Wang SL, Wong YC, Cheng WT et al (2010a) A continuous process for solid-state dehydration, amorphization and recrystallization of metoclopramide HCl monohydrate studied by simultaneous DSC-FTIR microspectroscopy. *J Therm Anal Calorim* 104:261–264
- Wang B, Cicerone MT, Aso Y et al (2010b) The impact of thermal treatment on the stability of freeze-dried amorphous pharmaceuticals: II. Aggregation in an IgG1 fusion protein. *J Pharm Sci* 99:683–700
- Ward HW, Blackwood DO, Polizzi M et al (2013) Monitoring blend potency in a tablet press feed frame using near infrared spectroscopy. *J Pharm Biomed Anal* 80:18–23
- Warnecke S, Rinnan A, Alleso M et al (2013) Measurement of active content in escitaopram tablets by near-infrared transmission spectroscopy model that encompasses batch variability. *J Pharm Sci* 102:1268–1280
- Wartewig S, Neubert RHH (2005) Pharmaceutical applications of mid-IR and Raman spectroscopy. *Adv Drug Deliv Rev* 57:1144–1170
- Weißner BV (2006) Quantitative NIR Kalibrationsmodelle zur nichtinvasiven Tablettenanalytik in der pharmazeutischen Entwicklung und Produktion. Dissertation, Universität Heidelberg
- Weißner BV, Henck JO, Reich G (2006a) Development of reliable NIR calibration models for nondestructive dissolution testing. Poster presented at the AAPS Annual Meeting and Exposition, San Antonio, R 6010
- Weißner BV, Henck JO, Reich G (2006b) The potential of near infrared spectroscopy for tablet analysis in industrial formulation development and production. In: Proceedings of 5th World Meeting on Pharmaceutics, Biopharmaceutics and Pharmaceutical Technology, Geneva/Switzerland, 27–30 March 2006
- Weißner BV, Henck JO, Reich G (2007) Applied NIR spectroscopy: a reliable alternative to conventional drug dissolution tests. In: Proceedings of 2nd European Congress on Life Science Process Technology, Nuremberg/Germany, March 2007
- Wiss J, Ermini G (2006) Safety improvements of a Grignard reaction by controlling the reactant feed rate by on-line concentration monitoring using NIR. *Org Process Res Dev* 10:1282–1286
- Wiss J, Länzlinger M, Wermuth M (2005) Safety improvement of a Grignard reaction using on-line NIR monitoring. *Org Process Res Dev* 9:365–371
- Workman JJ, Burns DA (2008) Commercial NIR instrumentation. In: Burns DA, Ciuczak EW (eds) Handbook of near-infrared analysis, 3rd edn. CRC Press, Boca Raton
- Wu J, Luo W, Wang X et al (2013) A new application of WT-ANN method to control the preparation process of metformin hydrochloride tablets by near infrared spectroscopy compared to PLS. *J Pharm Biomed Anal* 80:186–191
- Xiabo Z, Jiewen Z, Povey MJW et al (2010) Variables selection methods in near-infrared spectroscopy. *Anal Chim Acta* 667:14–32
- Xiang D, LoBrutto R, Cheney J et al (2009a) Evaluation of transmission and reflection modalities for measuring content uniformity of pharmaceutical tablets with near-infrared spectroscopy. *Appl Spectrosc* 63:33–47
- Xiang D, Königsberger M, Wabuye B et al (2009b) Development of robust quantitative methods by near-infrared spectroscopy for rapid pharmaceutical determination of content uniformity in complex tablet matrix. *Analyst* 134:1405–1415
- Xiang D, Berry J, Buntz S et al (2009c) Robust calibration design in the pharmaceutical quantitative measurements with near-infrared (NIR) spectroscopy: avoiding the chemometric pitfalls. *J Pharm Sci* 98:1155–1166
- Yang TH, Dong A, Meyer J et al (1999) Use of infrared spectroscopy to assess secondary structure of human growth hormone within biodegradable microspheres. *J Pharm Sci* 88:161–16
- Yip WL, Gausemei I, Sande SA et al (2012) Strategies for multivariate modeling of moisture content in freeze-dried mannitol-containing products by near-infrared spectroscopy. *J Pharm Biomed Anal* 70:202–211

- Yu ZQ, Chew JW, Chow PS et al (2007) Recent advances in crystallization control: an industrial perspective. *IChemE* 85:893–905
- Yu J, Zhang X, Hao X et al (2014) Near-infrared fluorescence imaging using organic dye nanoparticles. *Biomaterials* 35:3356–3364
- Yuan A, Wu J, Tang X et al (2013) Application of near-infrared dyes for tumor imaging, photothermal, and photodynamic therapies. *J Pharm Sci* 102:6–28
- Zhang F, Aaltonen J, Tian F et al (2009) Influence of particle size and preparation methods on the physical and chemical stability of amorphous simvastatin. *Eur J Pharm Biopharm* 71:64–70
- Zhang GC, Lin HL, Lin SY (2012a) Thermal analysis and FTIR spectral curve-fitting investigation of formation mechanism and stability of indomethacin-saccharin cocrystals via solid-state grinding process. *J Pharm Biomed Anal* 66:162–169
- Zhang X, Bloch S, Akers W et al (2012b) Near-infrared molecular probes for in vivo imaging. *Curr Protoc Cytom Chapter 12:Unit12.27* doi:[10.1002/04](https://doi.org/10.1002/04)
- Zhou X, Hines P, Borer MW (1998) Moisture determination in hygroscopic drug substances by near infrared spectroscopy. *J Pharm Biomed Anal* 17:219–225
- Zhou GX, Ge Z, Dorwart J et al (2003) Determination and differentiation of surface and bound water in drug substances by near infrared spectroscopy. *J Pharm Sci* 92:1058–1065
- Zhou GX, Crocker L, Xu J et al (2006) In-line measurement of a drug substance via near infrared spectroscopy to ensure a robust crystallization process. *J Pharm Sci* 95:2337–2347
- Zidan AS, Rahman Z, Sayeed V et al (2012) Crystallinity evaluation of tacrolimus solid dispersions by chemometric analysis. *Int J Pharm* 423:341–350
- Ziémons E, Bourichi H, Mantanus J et al (2011) Determination of binary polymorphic mixtures of fluconazole using near infrared spectroscopy and X-ray powder diffraction: a comparative study based on pre-validation results. *J Pharm Biomed Anal* 55:1208–1212

Chapter 4

Raman Spectroscopy

Keith C. Gordon and Sara J. Fraser-Miller

Abstract This chapter describes how Raman spectroscopy may be used in the analysis of pharmaceutical problems. The basic ideas around the technique are discussed along with some of the key issues in measuring Raman spectra that may be relevant to pharmaceutical samples. The limitations and strengths of different instruments (dispersive and Fourier-transform) are described. The use of Raman spectroscopy is highlighted in a number of case studies that utilize multivariate techniques; polymorphism, drug delivery and counterfeit drug studies are described. Finally, new technologies that are set to further enhance Raman spectroscopy as a method for analysis, such as low frequency Raman, spatially offset Raman scattering, transmission Raman and spatial heterodyne Raman spectroscopy are discussed.

Keywords Raman • Chemometrics • Polymorphism • Drug delivery • Counterfeit medicines • Low frequency Raman

1 Introduction

Raman spectroscopy is a technique in which scattered light informs on the nature of the irradiated sample. This technique has been radically affected by technological developments over the last few decades (Zhu et al. 2014). This has seen the technique move from highly specialised laboratories with large and cumbersome equipment to the deployment of the experiment in handheld robust field devices. In this chapter we provide a basic introduction to the theory and experimental methodology of the technique, describe the historical development and the key technologies that have made the experiments much more readily available, highlight the use of Raman spectroscopy in a number of applications and describe the new frontiers of this science and its future directions and possibilities. We have focused on *spontaneous* Raman spectroscopy rather than the surfeit of interesting techniques that use non-linear response, such as femtosecond stimulated Raman spectroscopy

K.C. Gordon (✉) • S.J. Fraser-Miller (✉)
Department of Chemistry, Dodd-Walls Centre, University of Otago, Dunedin, New Zealand
e-mail: keith.gordon@otago.ac.nz; sara.miller@otago.ac.nz

(Kukura et al. 2007) and coherent anti-Stokes Raman spectroscopy (El-Diasty 2011), as these are not extensively used in commercial instruments.

2 Theory of Raman Scattering

A Raman spectrum shows the intensity of Raman transitions (along the y-axis) and the energies of those transitions (along the x-axis), as shown in Fig. 4.1. The y-axis generally does not have specific units but is couched as “relative intensity”—in certain specialized cases the Raman cross section (β , see Table 4.1, probability of the transition) is given. The x-axis is labeled in wavenumbers or Raman shift (both in cm^{-1}) and is sometimes given the symbol $\tilde{\nu}$. It is related to frequency (ν) and wavelength (λ) by: $c \times \tilde{\nu} = \nu = \frac{c}{\lambda}$, where c is the speed of light.

Electromagnetic radiation, or light as we call it, at the energies visible to the human eye, is a form of energy with both wave and particle type properties. Young and Fresnel’s diffraction experiments demonstrated wave like properties of light. Later James C. Maxwell developed a series of equations which describe light as the propagation of electromagnetic waves. A quanta of electromagnetic light is named a photon, and can be described as a massless particle with a specific energy.

Light can interact with molecules in a number of ways, it can be absorbed, emitted, and scattered. Here we focus on the inelastic scattering phenomena of Raman scattering. Raman scattering occurs when a photon (electromagnetic radiation) interacts with a molecule by inelastic scattering. The majority of photons hitting a given sample undergo elastic (Rayleigh) scattering where no energy is transferred between the photon and the sample. The probability of this occurring is quite low (about 10^{-5} for 1 m travel in air) nonetheless it is Rayleigh scattering that makes the sky blue as the process is a function of wavelength, namely λ^{-4} . Of these scattered photons a very small amount (a further one in 10^6) of photons will transfer energy between the molecule and the photon, this is considered inelastic (Raman) scattering (McCreery 2000).

The Raman effect can be nicely explained if we use the wave-model of light, as depicted in Fig. 4.2. If one considers light as an oscillating electromagnetic wave then (at ν Hz) the amplitude of the electric field, $E(t)$, varies as a sine or cosine function as given by Eq. (4.1).

$$E = E_0 \sin(2\pi\nu t) \quad (4.1)$$

This will cause the electrons in a molecule to follow the field—i.e. become polarized and create an induced dipole moment (μ), and that causes light scattering at the frequency of the oscillation, in this case ν , giving rise to the Rayleigh effect. If we think of the molecule as having a cloud of electrons about its nuclei, the ease with which those electrons follow the light field will determine the intensity (or likelihood of the scattering). We can think of the elasticity of the electron

Fig. 4.1 Low frequency Raman spectrum of crystalline griseofulvin measured using 785 nm excitation and showing Stokes and anti-Stokes scattering

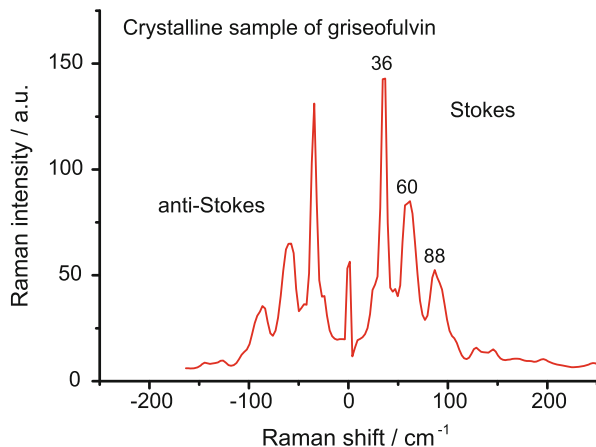


Table 4.1 Raman scattering cross sections for a series of molecules in liquid or solution with differing λ_{exc}

Compound	Raman shift (cm ⁻¹)	λ_{exc} (nm)	$\beta \times 10^{30}$ (cm ² sr ⁻¹ molecule ⁻¹)	Reference
Benzene	992	647	11	Petty et al. (1991)
		514.5	30	Shrötter et al. (1979)
		488.0	37	Shrötter et al. (1979)
		441.6	45	Shrötter et al. (1979)
		407	64	Trulson and Mathies (1986)
CHCl ₃	758	785.0	0.6	McCreery (2000)
		514.5	3.2	McCreery (2000)
Naphthalene in benzene	1382	514.5	82	McCreery (2000)
Anthracene in benzene	1402		540	McCreery (2000)
β -carotene in benzene	1520		1.1×10^7	McCreery (2000)

Note that β -carotene is in pre-resonance at 514.5 nm hence the large β -value

cloud as the polarizability, α and assume the sample is irradiated with light of ν_{laser} (Hz), then the dipole is described by Eq. (4.2).

$$\mu = \alpha \times E = \alpha \times E_0 \sin(2\pi\nu_{laser}t) \quad (4.2)$$

This model can provide more insight if we imagine how Raman scattering occurs. In Raman scattering the molecule vibrates at a frequency ν_{vib} so the stretchiness or elasticity of the electron cloud (α) is altered. The change in α with the vibration is called $\frac{\partial\alpha}{\partial q}$. This means the polarizability of the electrons, and thus the induced dipole (μ), in the vibrating molecule is a function of the driving field of the

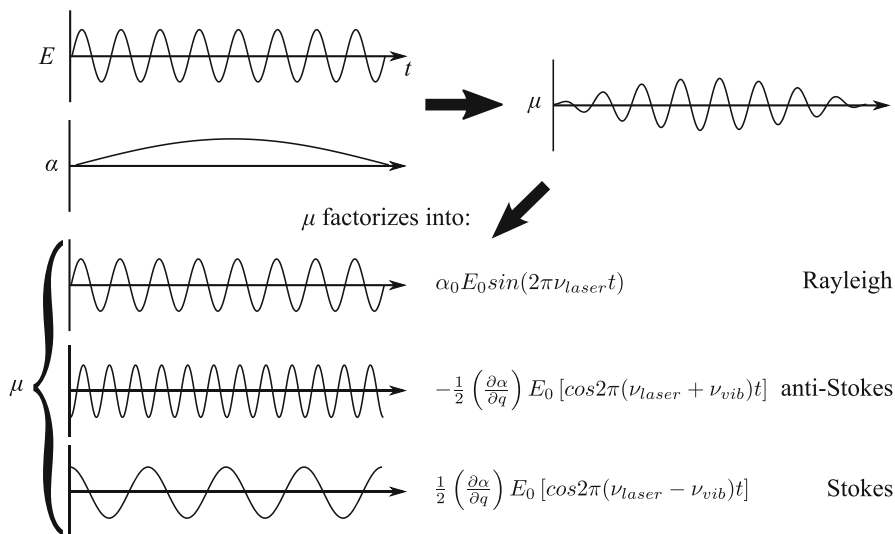


Fig. 4.2 Depiction of the interaction of an oscillating E -field and varying polarisability (α) resulting in an induced dipole (μ). The factorization of the μ signal is shown in its Rayleigh, anti-Stokes and Stokes scattering components

photon E_0 and the vibration. The polarizability is modulated by the vibration and becomes Eq. (4.3) and the dipole is now described by Eq. (4.4).

$$\alpha = \alpha_0 + \left(\frac{\partial \alpha}{\partial q} \right) \sin(2\pi \nu_{vib} t) \quad (4.3)$$

$$\mu = \alpha \times E = \left[\alpha_0 + \left(\frac{\partial \alpha}{\partial q} \right) \sin(2\pi \nu_{vib} t) \right] \times E_0 \sin(2\pi \nu_{laser} t) \quad (4.4)$$

Equation (4.4) may be factorised using the trigonometric relationship, Eq. (4.5), to give Eq. (4.6).

$$\sin A \sin B = \frac{1}{2} (\cos(A - B) - \cos(A + B)) \quad (4.5)$$

$$\begin{aligned} \mu &= \alpha_0 E_0 \sin(2\pi \nu_{laser} t) \\ &+ \frac{1}{2} \left(\frac{\partial \alpha}{\partial q} \right) E_0 [\cos 2\pi (\nu_{laser} - \nu_{vib}) t - \cos 2\pi (\nu_{laser} + \nu_{vib}) t] \end{aligned} \quad (4.6)$$

Equation (4.6) tells us that Raman scattering will occur at frequencies above and below the laser line (ν_{laser}) and this is observed. The photons scattered with *greater* energy than the laser line are called anti-Stokes lines and those with *lower* energy are called Stokes lines (Fig. 4.2). The Stokes lines correspond to transitions of the molecule from a $\nu = 0 \rightarrow \nu = 1$ vibrational state; the anti-Stokes corresponds to

$\nu = 1 \rightarrow \nu = 0$. The reason that the anti-Stokes lines are much weaker is that the population of molecules that are in the $\nu = 1$ state is lower than these transitions occur less frequently. The population of the respective states is related to the energy between them (ΔE) by the Boltzmann distribution, Eq. (4.7).

$$\frac{N_{\nu=1}}{N_{\nu=0}} = \exp\left[\frac{-\Delta E}{kT}\right] \quad (4.7)$$

At room temperature, for transitions at about 100 cm^{-1} $\frac{N_{\nu=1}}{N_{\nu=0}} = 0.62$, thus the anti-Stokes and Stokes lines have comparable intensity; but for 1000 cm^{-1} this ratio drops to 0.008. Thus anti-Stokes lines really only have appreciable intensity for low frequency vibrations as shown in Fig. 4.1.

Equation (4.6) also tells us that the intensity of the Raman effect is related to the change in *polarizability* with vibration $\left(\frac{\partial\alpha}{\partial q}\right)$. Molecules with electrons that are easy to polarize will give stronger Raman scattering than those held tightly. This has an important ramification for the study of pharmaceuticals in formulations and as most excipients are σ -bonded molecules like cellulose, starch etc. and most APIs contain π -electrons. This means that APIs give stronger Raman signals than the excipients (Fig. 4.3); one can consider this technique to have bias towards APIs as shown in Fig. 4.4. This is exemplified by the data shown in Table 4.1 which shows the Raman cross sections for different molecules and as a function of excitation wavelength. These data show that the Raman cross sections vary dramatically with the molecule, for example with benzene the Raman transition at 992 cm^{-1} is ten times more intense than the 758 cm^{-1} band of CHCl_3 . Furthermore the Raman cross section varies with λ_{exc} . Notably it becomes intense when the laser wavelength is coincident or approaching an electronic absorption energy of the analyte; this is the resonance Raman effect—it can enhance signals by 10^6 as seen for β -carotene. This can be problematic if coloring agents are added to the formulation as by their nature such agents are highly absorbing in the visible region, although new techniques (described in Sect. 5) can ameliorate this problem.

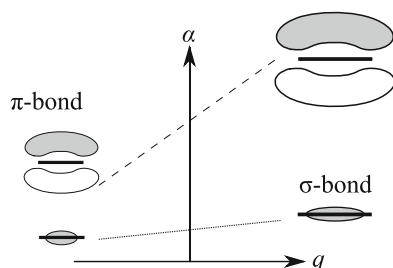
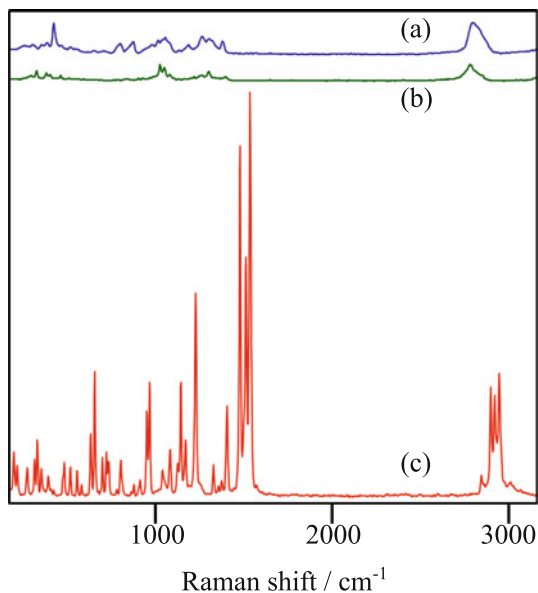


Fig. 4.3 Depiction of the changes in polarizability associated with the stretching of a σ -bond versus π -bond. The greater extent of the π orbitals means that α is greater for this bond type and change in α is also greater—thus these species give stronger Raman bands

Fig. 4.4 Raman spectra taken under identical conditions, $\lambda_{exc} = 1064$ nm, 85 mW; acquisition time 3 min; solid state samples: (a) corn starch; (b) cellulose and (c) carbamazepine



The Raman spectrum measures scattered photons and thus the background signal is a combination of ambient light (experiments are carried out in a darkened environment) plus detector readout noise; these can both be low. However there are two matters that have made measuring Raman spectra difficult and these both arise from the weakness of the signal. If we consider Fig. 4.1, the Raman band at 36 cm^{-1} is about 4–5 cm high. The Rayleigh scattering at 0 cm^{-1} (which has been filtered) would be over 10^5 times higher; hence unfiltered, the peak would be over 5 km tall! In addition to the Rayleigh scattering the second major drawback in measuring Raman spectra is fluorescence (or more generally emission). It is not atypical for the fluorescence quantum yield of compounds to exceed 0.01 (that is 1 in every 100 absorbed photons yields a fluorescence photon). The efficiency of this process is many orders of magnitude greater than either Rayleigh or Raman scattering (a typical β value is 10^{-17} , 10^6 – 10^{13} greater than those values for Raman scattering, Table 4.1) so that even a small amount of a fluorescent impurity can swamp the signal.

2.1 Dealing with Fluorescence

Molecular fluorescence generally occurs in the visible region of the spectrum; Fig. 4.5 shows a typical emission spectrum and a number of Raman laser excitation wavelengths. There are two methods using laser wavelength to avoid the problem of fluorescence: firstly tune to the *blue* of the fluorescence signal—this is an appealing solution because the Raman scattering is fundamentally stronger the

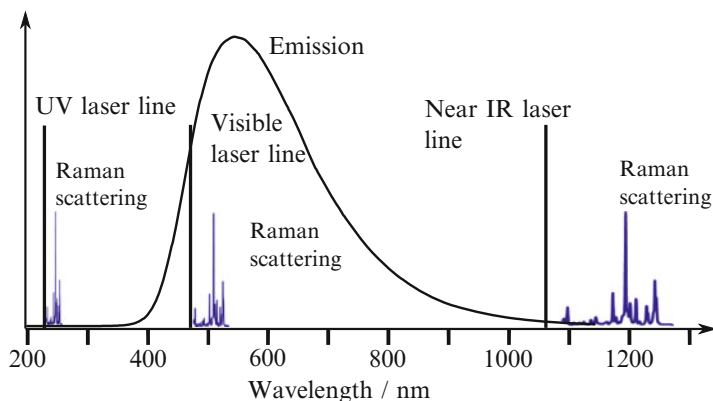


Fig. 4.5 Schematic showing a typical emission spectrum and the spectral ranges for Raman scattering (magnified $> \times 10^5$) with UV, visible and near-IR laser irradiation

shorter the wavelength. However the main drawbacks are the availability of laser sources in the UV and decomposition of the samples by far UV irradiation. Lasers available in the far UV are either pulsed in nature, such as excimer or solid-state lasers (which can readily damage samples) or are sourced from second harmonic generation of a continuous wave laser. In this case very powerful CW lasers are required to deliver useful laser power. Secondly, the laser can be tuned to the red—in Fig. 4.5 a 1064 nm excitation is shown. This avoids the emission but the Raman scattering is much weaker. If one considers a Raman band at 1000 cm^{-1} this scatters at 218 nm with 213 nm excitation and 1191 nm with 1064 nm excitation. The λ^{-4} difference corresponds to a scattering difference of 900:1.

There are a number of additional ways of removing or extracting Raman spectral data from highly emissive samples. One way is to use pulsed lasers with gated detection. This relies on the fact that Raman scattering is virtually an instantaneous process, taking femtoseconds (10^{-15} s) to occur, whereas emission is of the order of picoseconds (10^{-12} s). Thus if a detector is switched fast enough most of the emission can be gated out and not observed. Such methodologies have been used very effectively in Kerr-gating in which the Raman scattering is only measured for the 3 ps in which the laser irradiates the sample (Littleford et al. 2004). This type of temporal filtering can be very effective but is not commonly used because of the expense of ultrafast lasers and intensified CCDs (Ehn et al. 2013).

An alternate method was first developed by Mathies (Shreve et al. 1992); this uses the fact that emission spectra do not alter with small changes in excitation wavelengths whereas the Raman scattering photons are at $\nu_{\text{laser}} - \nu_{\text{vib}}$ Hz. Thus even a change of only 10 cm^{-1} in laser excitation wavenumber will shift the requisite Raman scattered photons by the same amount. Subtracting the two spectra from each other will lead to a difference spectrum revealing the Raman scattering

underlying the emission. This is called shifted excitation Raman difference spectroscopy and has been developed and is now used in some instruments (Cooper et al. 2013; Zhao et al. 2002).

Finally there is an additional method that relies on shifting of the spectrometer developed by Bell et al. (1998) that has been successful.

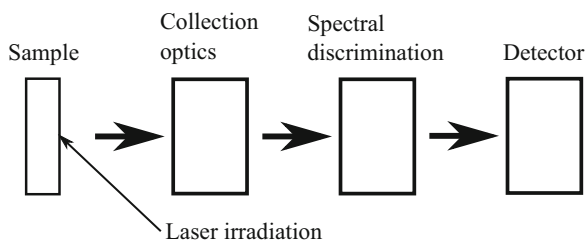
Although the gating methodologies and shifted excitation Raman difference spectroscopy are at present not routinely used the ease of re-tuning diode lasers or even LEDs (Adami and Kiefer 2013) to accommodate such experiments means that they will find greater use in conventional and commercial systems.

3 Experimental Methods

A schematic of a Raman experiment is shown in Fig. 4.6. In essence it involves irradiating the sample with light, collecting the scattered radiation, dispersing it into wavelength space and detection. The light source is now almost always a laser source, although prior to the advent of lasers atomic emission lines from arc lights (such as the 435 nm line from a mercury arc) were used as was filtered sunlight. The need for a laser source flows from the intrinsic paucity of the Raman signal coupled with the need for narrow spectral linewidth excitation. The peaks in the spectrum shown in Fig. 4.1 have a bandwidth of about 10 cm^{-1} . This is intrinsic to the vibrational transition from which the Raman scattering originates. If, however, a spectrally broad excitation source is used then the transition is broadened out as Raman scattering occurs from the range of ν_{laser} present. This effect is observed in Raman spectra measured with pulsed laser sources. When using picosecond pulsed laser excitation the short duration of the pulse causes increased spectral bandwidth (a pulse of 1 ps has a bandwidth of 30 cm^{-1} at $\lambda = 600\text{ nm}$) (Baker et al. 2007).

The collection optics may consist of lenses, mirrors or fibre-optic components. The energy discrimination of the scattering photons is accomplished with a spectrometer. Broadly speaking spectrometers fall into two categories; either dispersive or interferometer based.

Fig. 4.6 Block diagram of a Raman experiment comprising of an irradiated sample, collection optics, spectral discrimination (often achieved by a spectrograph) and detector



3.1 Dispersive Systems

Prior to the introduction of multi-channel detectors, particularly CCDs, Raman scattering was detected using photomultiplier tubes. To get a Raman spectrum a spectrograph was scanned through a range of wavelengths corresponding to the Raman shift values of interest. The disproportionate intensity of the Rayleigh line meant that spectrographs would be highly dispersive (separating different wavelengths very effectively) and this was often accomplished using a double monochromator—which is similar to the filter stage shown in Fig. 4.7. A double monochromator has two gratings and often five reflective optics (mirrors). One of the consequences of this is that the throughput of the instrument is lower than a single-stage spectrograph.

If one assumes that each mirror is 90% reflecting and the gratings are 70% efficient, then the maximum throughput for a double monochromator is 32%, for a single it is 55%. The other limitation of this method is that photomultipliers were used for detection. These are single element detectors thus the spectrum had to be scanned and data sequentially collected one wavenumber at a time to create a spectrum. As the scanning process is mechanical it can be difficult to add repeated acquisitions. With the advent of CCDs triple-spectrometers were used (Fig. 4.7). These have two parts: firstly a double monochromator set in what is called subtractive dispersion in which the first grating disperses the scattered radiation—the dispersed light is then filtered to block the Rayleigh line and the second grating refocuses the dispersed light to a point source; the second portion of the instrument is a single stage spectrograph, which has one grating to disperse the filtered light on to a CCD. The throughput of this instrument is only 13%.

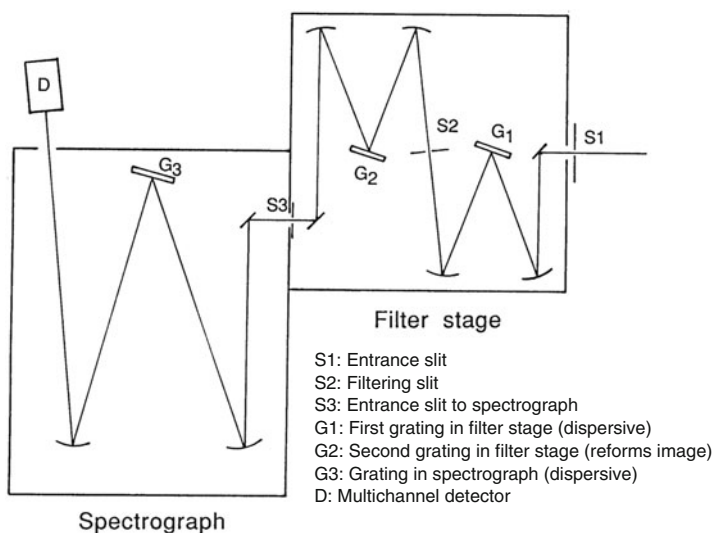


Fig. 4.7 Schematic of a triple spectrometer with filter stage and spectrograph

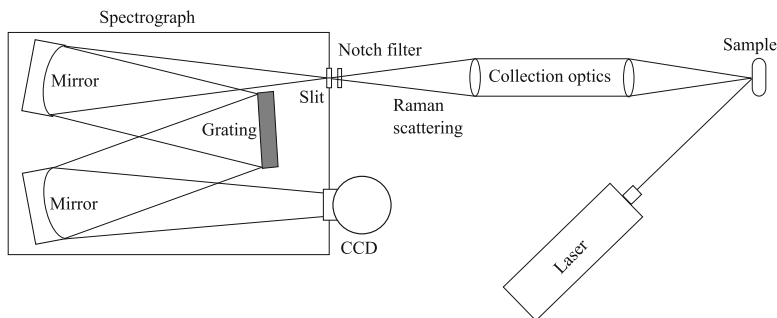


Fig. 4.8 Schematic of a Raman experiment using backscattering geometry and a Czerny-Turner spectrograph with a charge-coupled device (CCD) detector

The introduction of notch filters effectively revolutionized Raman spectrometer design. The use of single stage spectrographs with CCDs meant that instruments had high throughput and because of their relative simplicity, in terms of internal optics, they could be miniaturized for specific types of lasers. The importance of notch filters and new developments with regard to them is discussed in Sect. 5 (Fig. 4.8).

3.2 *Fourier Transform (FT) Systems*

The FT instrument works using a Michelson interferometer (Fig. 4.9) in which the Raman scattering, which has been filtered with notch filters to remove the Rayleigh line, is split (via a beamsplitter) and follows two paths to reflective optics. These are in turn reflected back to the beamsplitter and interfere either constructively or otherwise depending on the relative pathlengths that have been followed and the wavelength of the light. The criterion for constructive interference is given by $n\lambda = 2(M - F) = \delta$ where n is an integer value, λ is the wavelength, M and F are the distances from beamsplitter to moving and fixed mirrors respectively and δ is the retardation length. An interferogram is a plot of signal intensity versus δ . The spectrum, a plot of Raman shift versus Raman intensity, may be derived by the Fourier transform of the interferogram. The $\tilde{\nu}$ interferogram of sulfur and the resulting Raman spectrum is shown in Fig. 4.10. The interferogram is quite structured because there are only a few bands and thus only about ten sine waves are added together to form this. It is also noteworthy that the anti-Stokes bands show a dramatic fall off with higher values of $\tilde{\nu}$ in accord with the Boltzmann population.

In an FT or any interferometer-based experiment there are a number of factors that favour the technique. Firstly the Jacquinot advantage allows for a large beam diameter, that is there is no need to focus the image of the irradiated volume to a point source. This is a requirement of dispersive instruments. Secondly there is the Connes advantage—this is the addition of subsequent acquisitions which is possible because the retardation length of the interferogram is known with high precision.

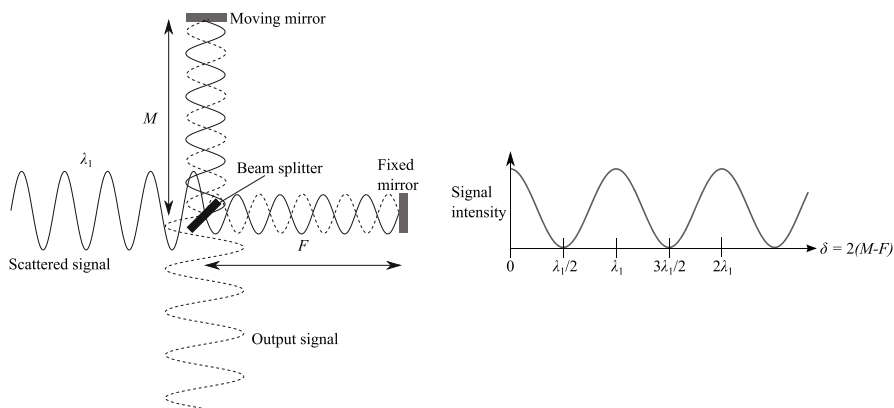


Fig. 4.9 Schematic of a Michelson interferometer and the associated interferogram (δ versus signal intensity) for a single wavelength (λ_1)

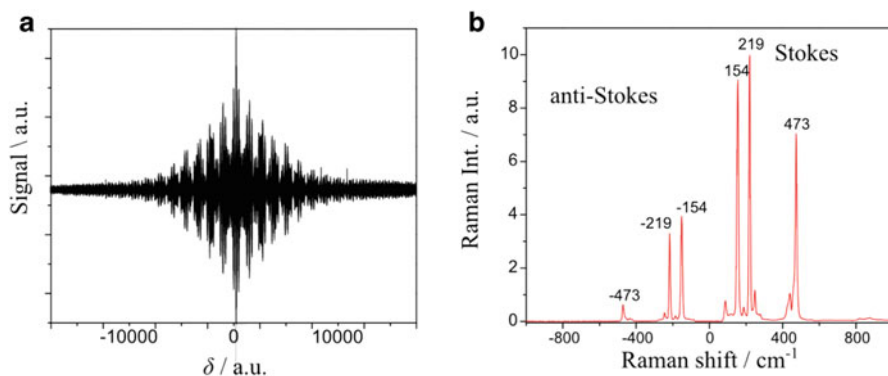


Fig. 4.10 Schematic of (a) an interferogram for a Raman spectrum and (b) the corresponding Fourier transformed frequency domain spectrum

Finally there is the Fellgett advantage. At each δ value, a number of wavelengths or Raman shift values are measured simultaneously. These are significant advantages over the point-by-point scanning instruments.

3.3 Spectral Correction

One issue that is prevalent in Raman spectra is that the Raman shifts for a particular molecule are intrinsic to that compound but the actual photon energies that are being measured vary depending on the excitation wavelength used. As has already been described a Raman shift of 1000 cm^{-1} corresponds to a scattered photon of 218 nm if one uses 213 nm excitation and 1290 nm with 1064 nm excitation.

Importantly the Raman spectrum can cover a wavelength range such that the detector being used may vary in sensitivity quite significantly. For example in a 1064 nm Raman spectrum measured from 400 to 4000 cm^{-1} the spectrum ranges from 1100 to 1560 nm and in that range a Ge detector (a commonly used detection element in FT systems) varies in sensitivity by one order of magnitude—peaking performance at 1400 nm (Chalmers and Dent 1997). In the case of a spectrum measured at 488 nm with CCD detection the Raman shift range corresponds to 498–590 nm and CCD sensitivities can easily vary by a factor of two (Janesick 2001). Thus the Raman spectrum will appear to have different band intensities depending on the excitation wavelength and the spectrometer type used (all of the optical elements have spectral variance in terms of throughput). Intensity corrections may be made but in almost all of the present literature the data presented are uncorrected and thus some care is required in interpreting data between different experiments, even if the same excitation wavelength is used as gratings can show very different spectral efficiencies.

4 Applications

Raman spectroscopy has many applications in the pharmaceutical sciences field. Raman spectroscopy can be used in many stages, from drug and formulation development to process control and post sale analysis.

Multivariate data analysis techniques, or chemometrics, have been a valuable tool for opening spectra up to interpretation, allowing quantification of compounds, and simplifying large spectral data sets. In the pharmaceutical industry multivariate techniques, such as partial least squares (PLS), have allowed quantification of compounds or properties of compounds to be quantified. An example of this may be quantification of pharmaceutical APIs and excipients.

The following sections consist of some background information on a selection of chemometric techniques commonly used for interpretation of Raman spectroscopy, followed by some specific examples where Raman spectroscopy is used in combination with chemometrics to quantify specific polymorphs of APIs, monitor drug delivery and detect counterfeit formulations.

4.1 *Chemometrics*

Raman spectroscopy of pharmaceutical systems can yield complex spectra with information contained across hundreds to thousands of points. Univariate methods for identification, quantification and classification are not ideal here as they cannot give the whole picture. Multivariate techniques are used to find differences, similarities and regions of co-variance across the spectra.

Pattern recognition can be a valuable tool in finding similarities and differences in large data sets. These data sets can be analysed by both unsupervised and supervised techniques. Unsupervised methods such as principal component analysis (PCA) and hierarchical cluster analysis (HCA) allow natural grouping and separation of the data without any prior knowledge; the groupings are based on the inherent nature of the data set without external groupings acting on the separation (Beebe et al. 1998). Supervised pattern recognition methods such as soft independent modeling of class analogy (SIMCA) and k-nearest neighbours (KNN) use class membership information in the models, and hence push the models to provide information for a specific application (Beebe et al. 1998). Supervised methods can be used to find what separating features lead to specific groupings.

Multivariate methods such as multiple linear regression (MLR), principal component regression (PCR) and partial least squares (PLS) can also be used to classify and quantify the samples using inverse multivariate calibration methods (Beebe et al. 1998).

Multivariate techniques for unsupervised (PCA) and supervised pattern recognition (SIMCA), and classification (SIMCA, PCR, PLS-DA) and quantification (PLSR) techniques are described in this section.

4.1.1 Principal Component Analysis (PCA)

PCA is a useful tool to reduce dimensionality in large datasets, allowing for human interpretation of datasets with hundreds of dimensions or variables, such as spectra, which may be simplified down to two or three dimensions called principal components (PCs) (Beebe et al. 1998).

PCA effectively decomposes the initial dataset such that

$$X = T \cdot P^T + E \quad (4.8)$$

where X is the initial dataset (matrix of i samples by k parameters), T is the scores, P^T is the loadings and E is the residuals, as illustrated in Fig. 4.11. The scores are the reduced dimensionality values for each given sample, i.e. the values assigned to each sample for a given PC. The loadings is effectively what variance each score or PC is describing and can be used to interpret the variances described across a given PC. The x-residuals are the remaining components not described by the PCs, often mainly noise, but can sometimes contain useful information.

A visual example of how PCA simplifies a three variable dataset is shown in Fig. 4.12, where it can be seen that none of the three variables give a good indication of the main variance in the data set. The description of variance across the dataset are best described using new axes or dimensions, namely PCs. The first principal component (PC1) describes the most variance in the sample, with the second principal component (PC2) describing further variance not described in PC1; each consecutive PC is describing variations in the data that are orthogonal to previous PCs. Calculation of the PCs occurs via least squares calculations where the

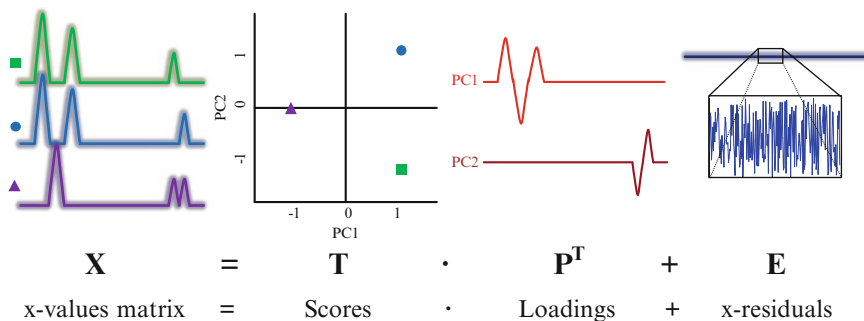
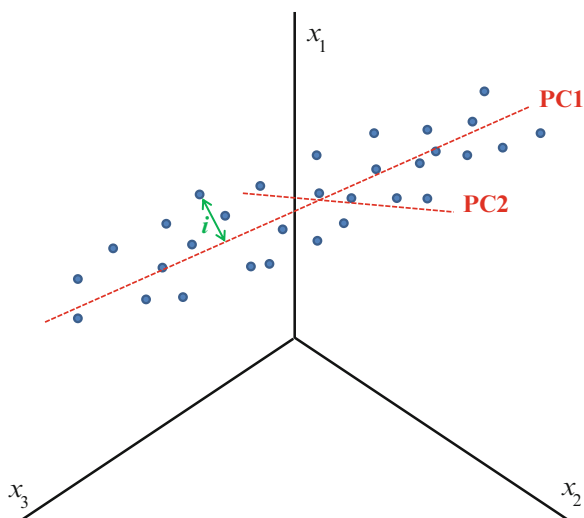


Fig. 4.11 Graphical representation of how PCA separates the initial series of spectra into scores, loadings and residual components

Fig. 4.12 Illustration of how PCA calculates the PCs in a three variable dataset by finding the line of most variance through minimising the sum of i^2



sum of the squared perpendicular distance of each point (i , Fig. 4.12) to a given PC is minimised.

4.1.2 Principal Component Regression (PCR)

PCR is a regression model which is based on multiple linear regression (MLR) in combination with PCA. MLR requires the X-variables to be linearly independent. In PCR, a PCA is run on the spectral data to remove collinearity in the dataset and then a MLR is run on the PCs. This removes the problem of co-linearity which makes MLR unstable in spectroscopic applications (Esbensen 2001) PCR decomposes the X matrix using PCA as seen in Eq. (4.8), then calculates the b -coefficients using MLR with the model

$$y = T \cdot b + f \quad (4.9)$$

where y is the vector containing concentration values to be modelled, T is the scores, b is a coefficient computed via MLR and f is the y -residuals from the MLR model (Software AS 2013). Unknown samples can then undergo a regression classification based on the PCR model.

4.1.3 Partial Least Squares (PLS)

PLS can be used for both quantification and classification by using the partial least squares regression (PLSR) and partial least squares discriminant analysis (PLS-DA) variations, respectively. PLS is an inverse method used for relating measurements and concentrations, inverse methods follow the same general equation relating a specific property such as concentrations (y) to the measurement matrix (X) and model coefficients (b) (Beebe et al. 1998).

$$y = Xb \quad (4.10)$$

PLSR is a regression model which is set up using two data matrices. A model is created to find the coefficients in the first matrix X , for example Raman spectra, that best predict the second matrix Y , for example concentration of a specific component. These model coefficients can then be applied to an unknown X dataset to predict a Y value (Esbensen 2001). PLS simultaneously solves Eq. (4.8) and the following

$$Y = T \cdot B + F \quad (4.11)$$

where Y is the vector or matrix containing concentration values to be modeled, T is the scores calculated via PLS, B is a coefficient and F is the y -residuals computed from the PLS model (Software AS 2013).

The PLS technique differs from PCR in that the first factors will directly relate to the prediction, unlike PCR where if the variance describing a particular parameter is small, it is not described until later factors. With PCR the model relies on the spectral variance alone, rather than co-variance with the Y -matrix which is maximised for each factor with PLS. More knowledge of a sample set and what part of the spectrum that differentiates between the classifications is required for PCR compared with PLS.

Selection of the appropriate number of factors is important for both PLS and PCR models. The number of factors needs to cover the variance within the model, but not over-fit the data. Generally, the appropriate number of factors can be selected using two guidelines:

1. At the point where the calibration and validation stop tracking closely. This means the calibration no longer models the data accurately, the model is over

fitting the data. If they track closely for all factors, then the second selection guideline needs to dominate the decision making.

- At the point when new factors do not contribute significantly to modelling the data.

A further analysis to test the validity of the model is to examine the loadings plots; these should contain signatures that correspond to real spectral features.

The resulting PLS model gives a reference versus predicted plot (also given with PCR), an example is shown in Fig. 4.13. This contains information as to how well the model has worked. Ideally the slope of a perfect model would be 1 as $predicted = reference$ and the offset would be 0.

The quality of a model can also be assessed using the root mean squared error of calculation (RMSEC) and the root mean squared error of prediction (RMSEP) which gives a measure of the error in the calculation and prediction of the model. The RMSEC is defined as

$$RMSEC = \sqrt{\frac{\sum_{i=1}^n (\hat{y}_{i,cal} - y_{i,cal})^2}{n}} \quad (4.12)$$

and the RMSEP is defined as

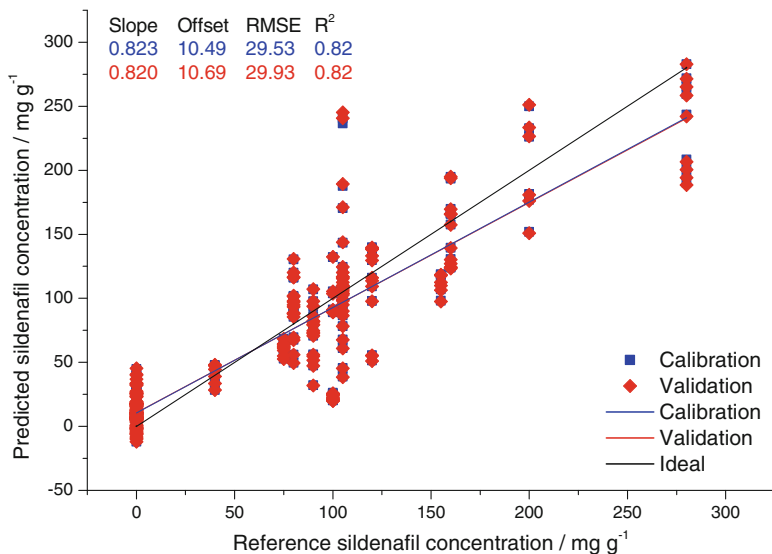


Fig. 4.13 Example of a PLS-R reference versus predicted plot. This is an example of sildenafil concentration in genuine and counterfeit medicines

$$RMSEP = \sqrt{\frac{\sum_{i=1}^n (\hat{y}_{i,val} - y_{i,val})^2}{n}} \quad (4.13)$$

where $y_{i,cal}$ is the given value (i.e. concentration) for the i^{th} calibration sample, $\hat{y}_{i,cal}$ is the fitted value (i.e. concentration) for the same sample, and n is the number of samples fitted in the model. $\hat{y}_{i,cal} - y_{i,cal}$ is considered the modeling error for each sample, and is the difference between the actual and fitted value for a given sample. RMSEP uses the validating test set values $y_{i,val}$ instead of the calibration samples $y_{i,cal}$ (Esbensen 2001; Beebe et al. 1998). Ideally a low value for RMSEC/P is desired as in a perfect model where *reference* = *predicted* the RMSEC/P is equal to 0.

To validate a model properly, a set of measurements independent of the model setup should be used to test the model. Often the 2/3rds to 1/3rd data ratio is used where 2/3rds of the data is used to create a model and 1/3rd used to test the model with the test set generating the RMSEP values.

The PLS-DA variation can be used to discriminate between classes. Instead of a range of values for the Y vector/matrix, each sample is given a value based on belonging (1) or not belonging (0) to the class of interest. Any new samples will be assigned a value by the model based on how close to 0 or 1 they are.

4.1.4 Soft Independent Modeling of Class Analogy (SIMCA)

SIMCA is a supervised pattern recognition method used to classify samples into given classes. A PCA model is created for each classification group and unknown samples are compared to this model using two parameters: the sample to model distance (S_i) and sample leverage (H_i). S_i is effectively the distance of a given sample to the center of the model and the H_i can be described as how much influence the sample would have on the model if it was included in the model, as demonstrated in Fig. 4.14a, b (Esbensen 2001).

If a sample is sufficiently close to the model i.e. if S_i is within distance bounds, and has a low leverage, it will be deemed to belong to the same class of the model (yellow region in Fig. 4.14c), otherwise it will not be regarded as a member of this class. The tightness of the model boundary can be adjusted using different significance or p-levels for S_i . The p-level can be adjusted between 0.1 and 25 % with a lower p-level (tighter boundary) more desirable as the evidence of difference is not as strong with a higher p-value.

This classification method is useful for classifying samples with a narrow classification bound, or when after PCA is applied there is visible separation of the group one wants to classify from samples that one does not want to classify.

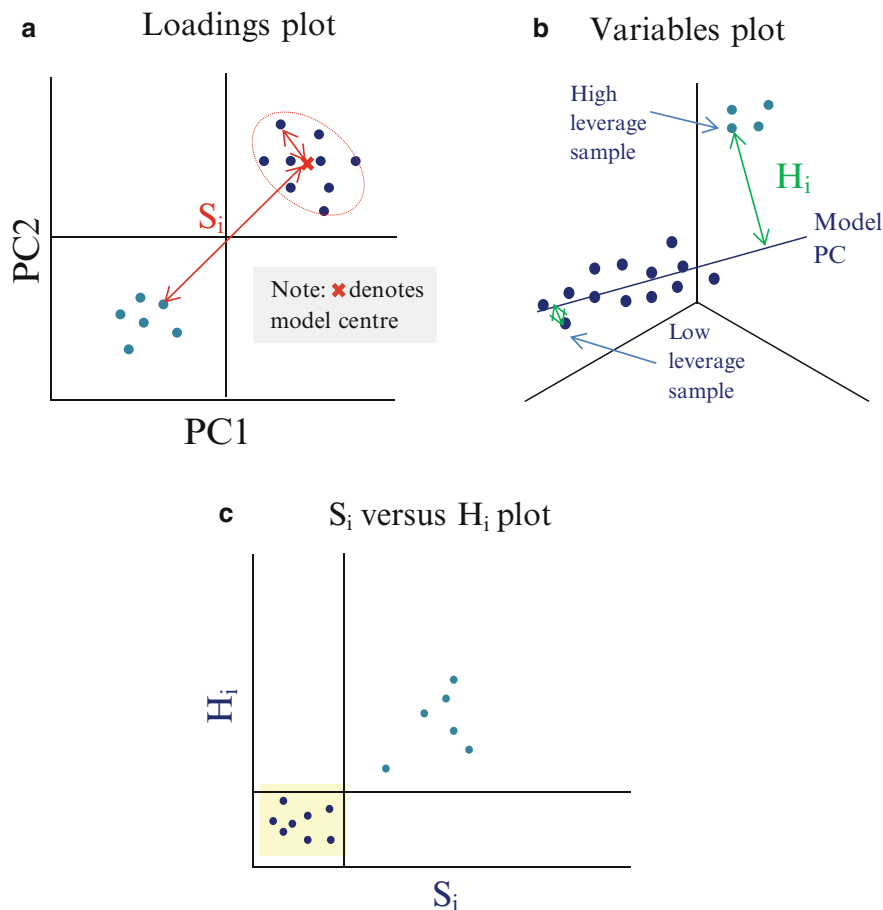


Fig. 4.14 Example of the parameters used in SIMCA classification; (a) sample to model distance (S_i), and (b) sample leverage (H_i). Image (c) shows how these parameters contribute to classify samples with the yellow region indicating the classification zone

4.1.5 Multiple Curve Resolution (MCR)

Multiple curve resolution (MCR) is a method used to find linear combinations of different components in a system. MCR effectively decomposes the initial data into the original components and their associated concentrations. The general equation that MCR follows is

$$X = YS^T + E \quad (4.14)$$

where X is the initial data matrix such as a series of spectra, Y is the concentration of the sources, S^T is the shape of the sources (i.e. pure component spectra) and E is the error matrix (Tauler and de Juan 2006; CAMO 2012).

Solving Eq. (4.14) can lead to multiple pairs for Y and S^T as a result of rotational and intensity ambiguities. Rotational ambiguity can be described as the differing shape of the sources and intensity ambiguity described as the differing magnitude of the sources. The transformation of Eq. (4.14) gives insight into the two sources of ambiguities.

$$X = YS^T - Y(TT^{-1})S^T = (YT)(T^{-1}S^T) = Y'S'^T \quad (4.15)$$

where $Y' = YT$ and $S'^T = T^{-1}S^T$ describe the X matrix as the Y and S^T matrices do, however the Y' and S'^T are not the sought solutions (Tauler and de Juan 2006; CAMO 2012).

To remove ambiguity in the resulting Y and S^T pairs, constraints may be placed on the problem. Common constraints which can be selected include non-negativity, unimodality and closure. Non-negativity constraint forces the values in the source concentrations (Y) and/or the source profiles (S^T) to be greater than or equal to 0. Unimodality constraint only allows one maximum per sample, this is used for monotonic profiles where only one component is increasing or decaying. Closure constraint is used for closed reaction systems where the overall balance of the components remains constant for all samples, it forces the sum of the components to equal a constant value for all samples. Constraints should be selected based on the nature of the sample set being studied (Tauler and de Juan 2006; CAMO 2012).

4.2 Polymorphism of Ranitidine Hydrochloride

Drug polymorphism is the phenomenon where a therapeutic drug can crystallise into different forms, with different physical and bioactive properties. Polymorphism can be a problem in drug development, with different solubilities, bioactivity and toxicity occurring in the different crystalline forms. In particular insoluble active pharmaceutical ingredients (API), such as those in biopharmaceuticals classification system class 2, the amorphous or metastable crystalline form is used to increase water solubility. The problem with using the amorphous or metastable forms is spontaneous crystallisation into the most thermodynamically stable form.

Raman spectroscopy can be used to identify the different polymorphs of a given API, the different polymorphs of the APIs can then be quantified using partial least squares regression (PLS).

A study by McGoverin et al. (2012) compared the ability of FT-Raman in a 180° backscattering arrangement and transmission Raman spectroscopy to quantify two different polymorphs of ranitidine hydrochloride. PLS was used to create models using both the backscattering and transmission arrangements, with various sampling times. The longer acquisition times lead to more stable models (10 s versus 1 or 5 s) for both transmission and 180° backscattering arrangements. The transmission

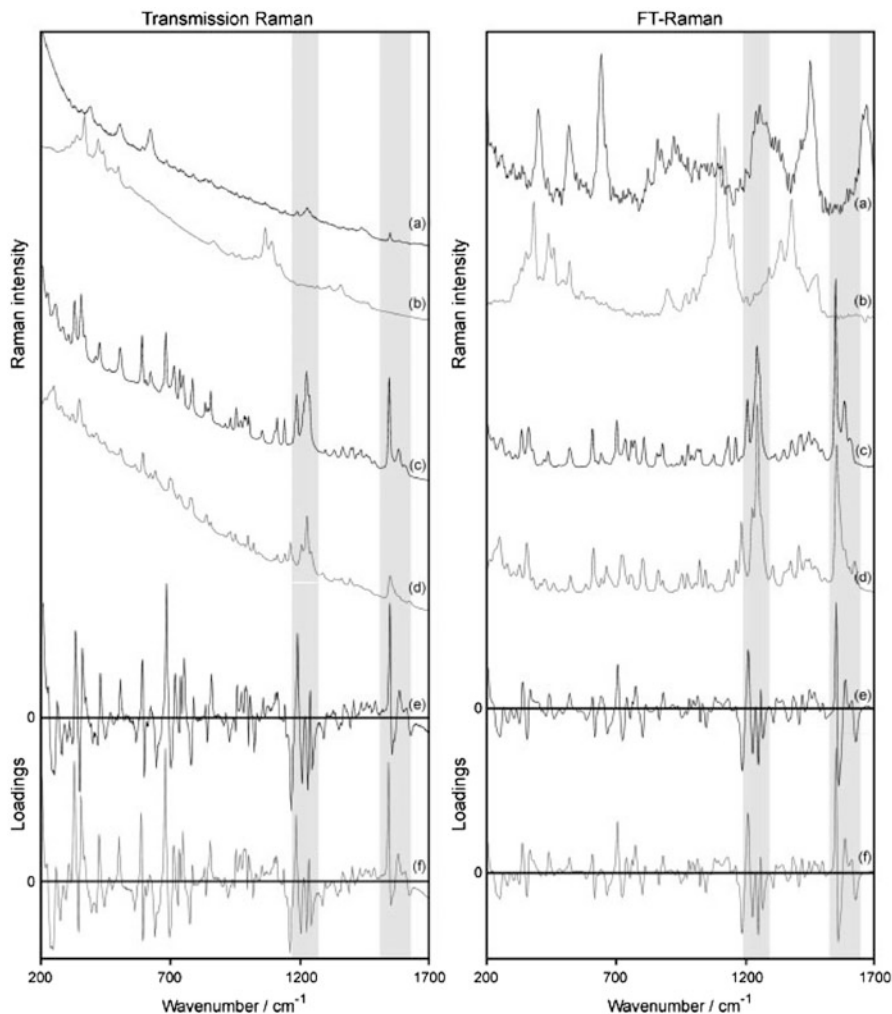


Fig. 4.15 Transmission (*left*) and FT-Raman (*right*) spectra of (a) gelatin capsule, (b) microcrystalline cellulose, (c) ranitidine hydrochloride form I and (d) ranitidine hydrochloride form II. The first PLS loadings for the 0–100% form I ranitidine hydrochloride calibrations is shown for the (e) capsules and (f) tablet models, where separation is clearly based on the differences between form I (positive weighting) and form II (negative weighting). Figure reprinted with permission from McGovern et al. (2012)

measurements tended to give more accurate quantification of polymorph I, this is believed to be due to the large sample volume being measured in transmission Raman, thus preventing subsampling of any one component in a mixture.

The Raman spectra taken from a gelatin capsule, microcrystalline cellulose and ranitidine hydrochloride in forms I and II, from transmission and FT setups are given in Fig. 4.15. The first loadings for the PLS models calculating the

concentration of form I in the 0–100 % range is shown for both tablets and capsules in Fig. 4.15, with positive loadings features associated with form I spectral features and negative loadings features associated with form II spectral features.

With the 0–100 % model for form I ranitidine hydrochloride, the content was predicted with an accuracy suitable for process control. This highlights the potential for Raman spectroscopy in transmission mode for in-line measurement during manufacturing processes.

4.3 *In Vivo Drug Delivery*

Melot et al. used confocal Raman spectroscopy to monitor the effectiveness of penetration enhancers for delivery of retinol through the stratum corneum (outer epidermal layer of skin) in vivo by non-invasive depth profiling (Mélot et al. 2009).

Four formulations of 0.3 % *trans*-retinol were applied to the skin on the forearm of male volunteers. The first formulation consisted of 99.7 and 0.3 % *trans*-retinol. The second contained 98.7 % *trans*-retinol and 1 % triton X 100, the triton X 100 is a lipid extractor type penetration enhancer. The third formulation contained 98.7 % MYRITOL[®] 318, 0.3 % *trans*-retinol. The second contained 98.7 % MYRITOL[®] 318, 0.3 % *trans*-retinol and 1 % oleic acid, the oleic acid is a lipid fluidiser type penetration enhancer. The final formulation is a model delivery system identified from ex vivo experiments, 70 % ethanol, 30 % propylene glycol and 0.3 % *trans*-retinol, propylene glycol is a well known penetration enhancer.

Raman spectra were collected prior to and up to 6 h after application of the *trans*-retinol formulas. The spectra were modeled using a multiple linear regression type algorithm, with each pure spectrum fitted instead of a single band, this is similar to multiple curve resolution. This gave a measure for the relative amounts of each of the major components spectra, with the major components being: the typical spectra of the stratum corneum, spectra of *trans*-retinol and myritol. These spectra are shown in Fig. 4.16.

An example of the absolute and normalised amounts of *trans*-retinol found in the skin at different depths and time periods is given in Fig. 4.17, where it was shown that the *trans*-retinol in ethanol and propylene glycol has the highest amount of *trans*-retinol penetrating into the skin, with the other formulations with penetration enhancers not performing as efficiently as the model delivery system.

Raman spectroscopy was able to determine in vivo the depth profile of *trans*-retinol over a 6 h time period. The *trans*-retinol in MTRITOL[®] 318 formulation was found to not penetrate in significant levels to depths greater than 5 μm , the formulations with penetration enhancers (oleic acid and triton X 100) enhanced delivery of *trans*-retinol into the skin, but did not act as effectively as the model delivery system of *trans*-retinol in ethanol and propylene glycol.

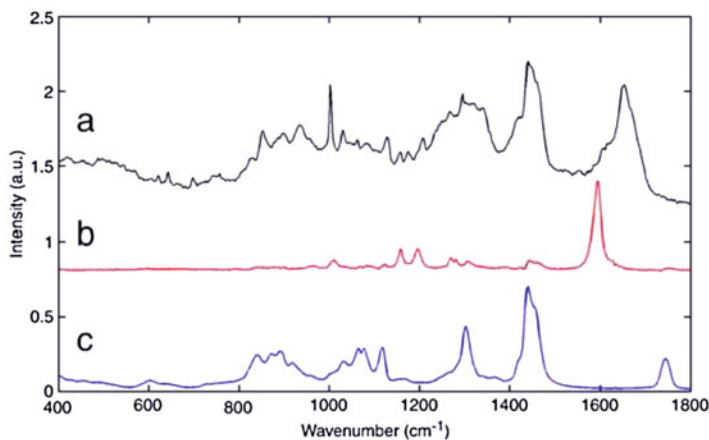


Fig. 4.16 Example spectra for the major components of interest. (a) Typical spectra of stratum corneum, (b) *trans*-retinol and (c) myrtilol. Figure reprinted with permission from Mélot et al. (2009)

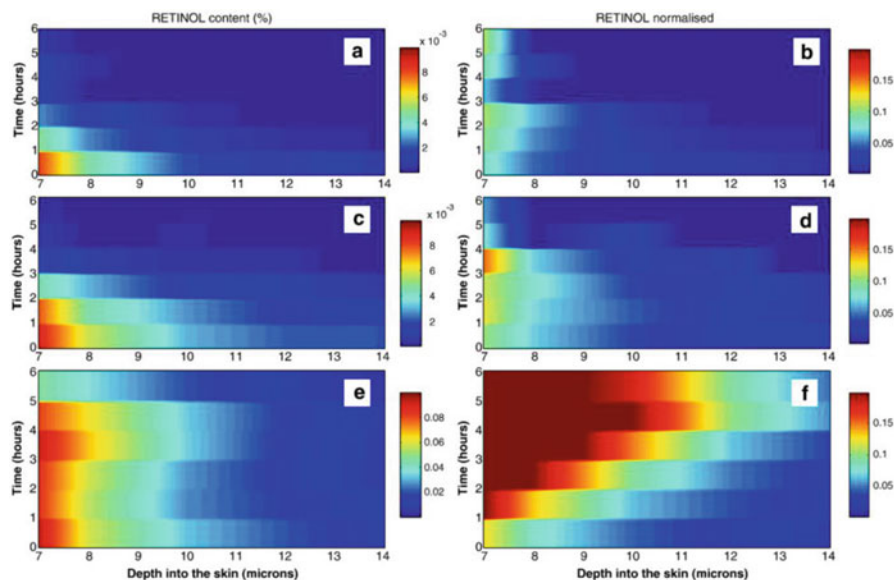


Fig. 4.17 The absolute (*left*) and normalised (*right*) profiles for *trans*-retinol after treatment with: (a, b) 0.3% *trans*-retinol in 98.7% MYRITOL[®] 318 and 1% triton X 100, (c, d) 0.3% *trans*-retinol in 98.7% MYRITOL[®] 318 and 1% oleic acid and (e, f) 0.3% *trans*-retinol in 70% ethanol and 30% propylene glycol. Figure reprinted with permission from Mélot et al. (2009)

4.4 Counterfeit Detection

Raman spectroscopy in combination with chemometrics can be used for the detection of counterfeit pharmaceuticals. Raman spectroscopy has been used by many research groups to detect, classify and even quantify the API in suspect products. Anti-malarial tablets have been measured and classified with Raman spectroscopy (de Veij et al. 2007), and spatially offset Raman spectroscopy (SORS) through blister packs, whereby characterising the samples without removal from the packaging (Ricci et al. 2007). Medicines used in the treatment of erectile dysfunction are commonly counterfeited and have been investigated using Raman spectroscopy (Trefi et al. 2008; de Veij et al. 2008; Degardin et al. 2011; Fraser et al. 2013) and Raman microscopy (Sacre et al. 2011).

Counterfeit and unregistered Cialis (tadalafil) were investigated using FT-Raman spectroscopy to classify genuine from counterfeit products, identify and attempt to quantify the API present in the samples. PCA of the products showed separation based on the API present along PC1, as seen in Fig. 4.18a, with spectral features leading to this separation associated with tadalafil (negative PC1 bands) and sildenafil (positive PC1 bands) spectra signals, shown in the loadings plots in Fig. 4.18b. PCA also gave groupings of some counterfeit products which are thought to come from the same manufacturer as seen in Fig. 4.18a.

SIMCA was able to correctly classify genuine from counterfeit and unregistered generic products. PLS-DA was able to identify the API present in the samples as sildenafil or tadalafil and the PLSR was able to loosely quantify the concentration of API in the tablets, whereby giving a rough indication of the risk associated with each counterfeit sample, whether it is sub-therapeutic or toxic levels (Fraser et al. 2013).

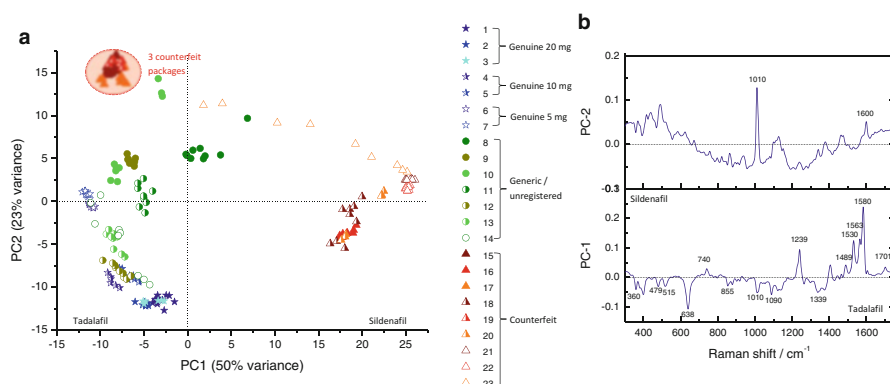


Fig. 4.18 Scores and loadings plot demonstrating the separation of counterfeit, generic and genuine Cialis samples. (a) Scores plot of PC1 versus PC2 and (b) the loadings for PC1 and PC2

5 New Technologies and Experimental Protocols

A number of new technologies have arisen in the past 5 years that have begun to have an impact on how Raman spectroscopy is being used in analytical applications.

5.1 Low Frequency Raman Spectroscopy

The spectrum in Fig. 4.1 shows Raman scattering bands down to 36 cm^{-1} ; this spectrum is measured using volume Bragg gratings to remove the intense Rayleigh scattering. The utility of low frequency Raman measurements has been exemplified in a study by Hédoux on indomethacin (Hédoux et al. 2009).

It is the nature of the low frequency modes that provide the utility of this spectral region. In general the frequencies or wavenumbers of transitions in this region are due to bond stretching or bending and in a harmonic approximation are related to the force constant k for the vibration and the reduced mass μ . For diatomics this is given by: $\tilde{\nu} = \frac{1}{2\pi} \sqrt{\frac{k}{\mu}}$. In general therefore stronger bonds vibrate at higher frequencies (thus for a C-C bond $\tilde{\nu} \sim 1100\text{ cm}^{-1}$ and for C = C $\tilde{\nu} \sim 1600\text{ cm}^{-1}$) and the presence of a light atom (H) results in vibrations at $\sim 3000\text{ cm}^{-1}$ because of the reduction in μ . The low frequency modes are due to very large μ , i.e. involving many atoms or molecules moving in concert, or due to low k . In a sense these two parameters are related; as the “vibration” involves many atoms or molecules the forces that hold these are intrinsically weaker than the forces that hold two atoms together. The low frequency modes may involve torsional motion of a single molecule or motion between two molecules (intermolecular vibrations). An example of this is shown in Fig. 4.19. This figure shows the normal modes of vibrations for a low frequency torsional mode (ν_{14}) and three key higher frequency modes (ν_{163} , ν_{207} and ν_{208}).

The Raman spectrum of griseofulvin with standard notch filters and volume Bragg grating (VBG) filters are shown in Fig. 4.20. It is notable that the spectrum taken using an FT instrument will only give data down to about 100 cm^{-1} ; however the spectrum using VBG filtering is able to measure right across the laser line, and accurately measure features down to 24 cm^{-1} for this sample. It is also notable how different the relative intensities of bands are. For example for the 1064 nm data the bands at 1617 and 1703 cm^{-1} are more intense whereas in the 785 nm data the bands around 653 cm^{-1} are stronger. This is due to the respective intensity biases in each experiment. Such bias is not problematic if data is measured on the same instrument but if data sets between experiments are compared this can become challenging. Many modern instruments now incorporate intensity correction as an automated feature. The low frequency modes in the vibrational spectrum may be associated with crystalline phonon modes; thus low frequency transitions can be

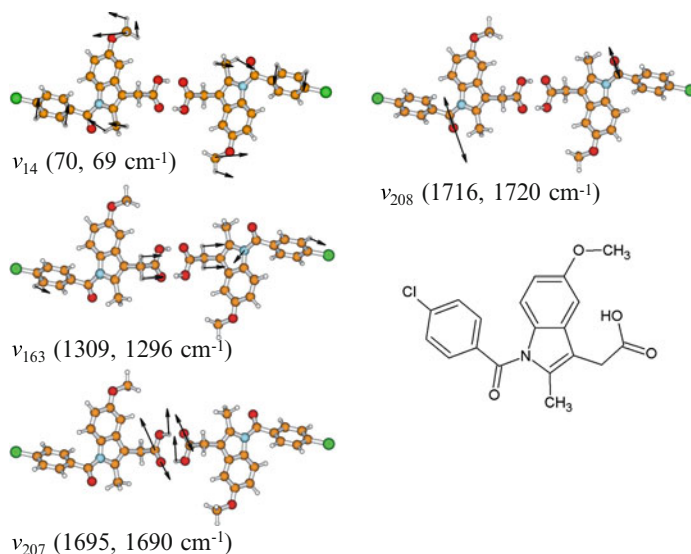


Fig. 4.19 Depiction of selected normal modes for indomethacin derived from density functional theory calculations of the dimer structure. The experimental and calculated wavenumbers are given in parentheses. Experimental data for ν_{14} from Hédoux et al. (2009) and for the other modes from Strachan et al. (2007a). The structure of the indomethacin monomer is shown

exquisitely sensitive to crystallinity, in crystalline samples these can be $50\times$ more intense than intramolecular vibrations. These low frequency modes can be much more sensitive to crystalline formation because of this. For amorphous material there is a broad Raman feature attributed to a boson peak; this may also be modeled as a quantifier for crystalline versus amorphous nature (Hédoux et al. 2009).

In absorption spectroscopy these energies lie in the far-infrared or THz region. THz spectroscopy has been used extensively to quantify crystallization and the presence of differing drug polymorphs (Strachan et al. 2005; Zeitler et al. 2005, 2007; Strachan et al. 2004a, b, 2007a, b). With the introduction of relatively inexpensive high quality notch filters that will allow conventional Raman spectrometers to measure down at low frequencies ($\sim 10\text{ cm}^{-1}$) the same type of experiments used effectively in THz spectroscopy will now be available to existing Raman laboratories.

5.2 Spatially Offset Raman Scattering (SORS)

The idea behind SORS is simple yet not immediately intuitive. In a conventional sampling arrangement the excitation laser is focused on to the sample and the collection optics are designed to image that irradiated volume. The maximum amount of scattered light is present there and thus the largest signals should be

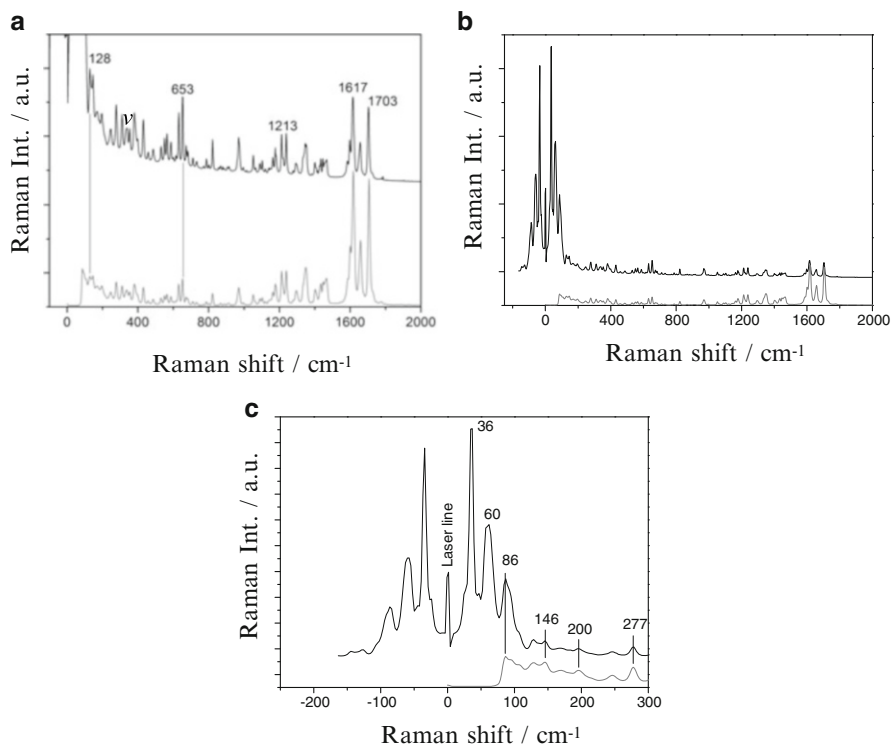


Fig. 4.20 Raman spectra of griseofulvin in the solid state measured with 1064 nm excitation using a Bruker IFS-55 interferometer bench equipped with FRA/106 Raman accessory (*lower spectra, gray*) and with 785 nm excitation and a backscattering geometry with a Princeton Instruments LS-785 spectrometer and Pixis CCD camera and VBG filtering (*upper spectra, black*). (a) Conventional spectral region; (b) full region showing intense phonon Stokes and ant-Stokes modes; (c) low frequency region

observed. In the SORS experiment a laser is focused on to the substrate as a tablet, but the imaging optics that collect the Raman scattering are moved away from the illuminated area (Fig. 4.21).

SORS was first described by Matousek et al. (2005) in which they showed that the technique could be used to reject the Raman scattering from the top layer of a sample in an experiment in which *trans*-stilbene (a strong Raman scattering molecule) was placed beneath a 1 mm layer of PMMA. As the offset was increased the signal fell off as would be expected, but importantly the offset sampled deeper inside the sandwiched sample and thus the spectrum of *trans*-stilbene was observed over that of PMMA; these offsets were not insignificant, being up to 2–4 mm. Effectively by offsetting the sampling optics, a different volume of the sample was analysed. This technique is very well suited to examining samples in which the surface is not representative of the bulk, such as coated tablets (Eliasson and Matousek 2007). It may also be used to quality control bulk pharmaceutical

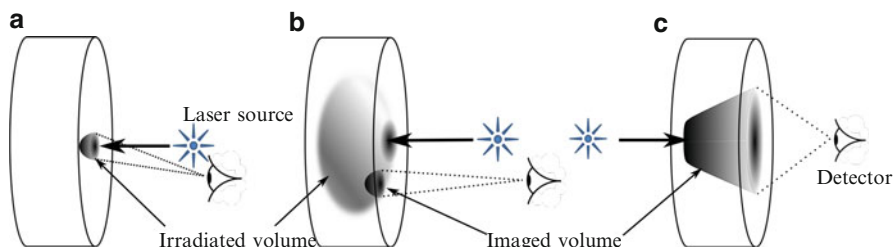


Fig. 4.21 Sampling arrangements for Raman scattering showing the irradiated volume from the laser and the collected sample volume for: (a) a conventional backscattering geometry; (b) a spatially offset geometry; (c) a transmission Raman geometry

ingredients without the recourse of removing them from their packaging, even when the packaging is completely opaque in the visible region, such as polypropylene (Bloomfield et al. 2013).

SORS is a technique that could only work with modern instrumentation, including the highly sensitive CCD detection and single stage, high throughput spectrographs (which in turn rely on notch filters to be effective). As described in Sect. 1, the probability of Raman scattering is low and thus a large number of photons strike the sample to yield a small number of Raman scattered photons (Table 4.1). It is this low probability that allows SORS to work as photons are able to scatter through the sample but this has another distinct effect; it takes time. This is exemplified in a study using picosecond time-resolved spectroscopy by Petterson et al. (2010). They showed the net photon migration was about 10^7 m s⁻¹; they also showed that with a 5 mm offset Raman signal was still detected 1 ns (1000 ps) after the laser pulse had irradiated the sample.

5.3 Transmission Raman

Transmission Raman spectroscopy developed after SORS and involves measuring the Raman scattering that is transmitted through a sample (Fig. 4.21c). In comparison with SORS it shows superior rejection of surface scattering for pharmaceutical samples (Matousek and Parker 2007) and with SORS is a key technology in the development of airport security devices to measure liquids in containers (as described at <http://www.cobaltlight.com>). A comparative study on ranitidine hydrochloride tablets showed the transmission spectroscopy gave better quantitation of API than FT-Raman and with a significantly shorter acquisition time (McGovern et al. 2012). A comparative study of propranolol tablets with concentrations of the API between 16 and 24 % w/w were examined and it was found that using the same excitation wavelength ($\lambda_{exc} = 785$ nm) and spectrometer a transmission geometry was about 25 % more accurate than backscattering. This was attributed to the greater sampled volume in the transmission mode (Johansson et al. 2007).

5.4 Spatial Heterodyne Raman Spectroscopy

One innovation that has recently been reported is the use of a spatial heterodyne spectrometer to obtain Raman spectra (Gomer et al. 2011). This experiment works by using interferometry with pulsed laser excitation. In a sense it is similar to FT techniques described earlier. However rather than use mirrors and obtain an interferogram point-by-point, this technique uses angled gratings to create an interference pattern which is imaged on to a CCD. There is a confluence of spectroscopic advantages in this method: firstly, there is no need for a point source thus the spectral image may have a large diameter—so there is a Jacquinot advantage; secondly, the interference pattern is measured by CCD thus all of the data is collected simultaneously, so there is a Fellgett advantage; thirdly, once set up the system has *no moving parts* this means that it is robust and is a technology that could be miniaturized. The interferogram is built up of a series of fringe patterns depending on the Raman shift scattered from the sample. The deconvolution of the interferogram gives a spectrum in fringe/cm (f) space that can be converted to Raman shift via the equation, $f = 4(\theta - \theta_L)\tan \theta_L$, where θ is the wavenumber from the sample, θ_L is the Littrow wavenumber (the wavenumber that corresponds to no interference) and $\tan \theta_L$ is the tan function of the Littrow angles that the gratings are set at. A schematic of the experiment and the interference pattern and spectrum (in fringe/cm) is shown in Fig. 4.22. The potential advantages of this type of spectrometer are significant. It is possible to image samples from many meters away and this utility has been recognized in the potential use of the instrument for exploration on Mars (Angel et al. 2012). The advantages offered by such an instrument could be used in bulk analysis of pharmaceuticals and drug delivery.

6 Conclusions

This chapter describes some aspects of spontaneous Raman scattering. The relative intensities of Raman scattering with regard to molecular polarizability and the issues associated with fluorescence are discussed. Experimental methods are described including dispersive and Fourier transform. Applications are described including the use of chemometrics in analysis. The use of Raman is highlighted in a number of case studies where ranitidine polymorphs are examined using conventional and transmission Raman spectroscopy, non-invasive depth profiling is described along with counterfeit detection.

A number of new technologies are described. These include: the use of notch filters to achieve low frequency Raman spectra which have great potential for the examination of polymorphs; the use of spatially offset Raman scattering to avoid fluorescence and detect through opaque containers; the use of transmission spectroscopy to investigate bulk and avoid surface effects; the use of spatial heterodyne

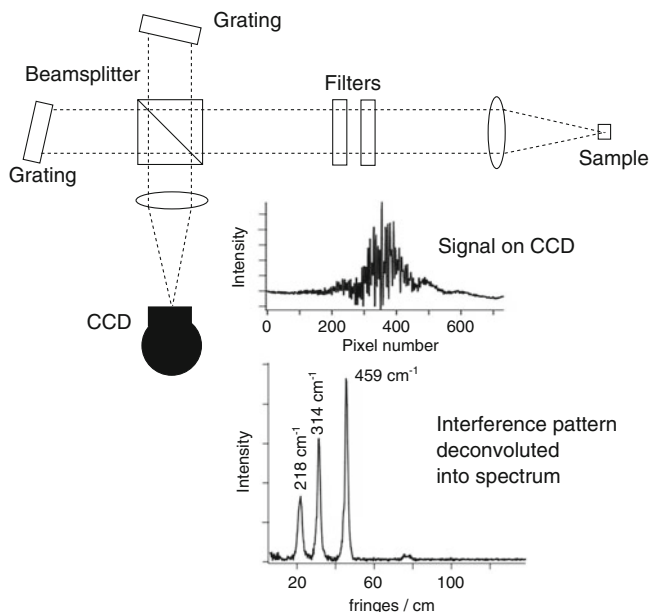


Fig. 4.22 Schematic of spatial heterodyne experiment showing grating angled at θ_L along with CCD output and deconvoluted fringe/cm spectrum and corresponding bands in Raman shift for CCl_4

spectroscopy as a new method of collecting Raman spectra without needing any moving parts in the instrument.

Raman spectroscopy has been transformed as an analytical technique in the pharmaceutical area over the last decade, however there remain a significant number of innovations that are yet to be deployed in commercial instruments. For example the use of notch filters will see low frequency Raman become standard on most instruments, the use of shifted excitation Raman difference spectroscopy will make fluorescence removal routine. Finally the possibility of spatial heterodyne Raman spectroscopy offers instruments with high throughput that could be robust and miniaturized.

References

- Adami R, Kiefer J (2013) Light-emitting diode based shifted-excitation Raman difference spectroscopy (LED-SERDS). *Analyst* 138:6258
- Angel SM, Gomer NR, Sharma SK, McKay C (2012) Remote Raman spectroscopy for planetary exploration: a review. *Appl Spectrosc* 66:137–150
- Baker R, Matousek P, Ronayne KL, Parker AW, Stone N, Rogers K (2007) Depth profiling of calcifications in breast tissue using picosecond Kerr-gated Raman spectroscopy. *Analyst* 132:48–53

- Beebe KR, Pell RJ, Seasholtz MB (1998) *Chemometrics a practical guide*, Wiley-Interscience series on laboratory automation. Wiley, New York
- Bell SEJ, Bourguignon ESO, Dennis A (1998) Analysis of luminescent samples using subtracted shifted Raman spectroscopy. *Analyst* 123:1729–1734
- Bloomfield M, Andrews D, Loeffen P, Tombling C, York T, Matousek P (2013) Non-invasive identification of incoming raw pharmaceutical materials using spatially offset Raman spectroscopy. *J Pharm Biomed Anal* 76:65–69
- CAMO (2012) The Unscrambler X supporting information. Software contents file. CAMO Software AS, Nedre Vollgate, Oslo, Norway
- Chalmers JM, Dent G (1997) *Industrial analysis with vibrational spectroscopy*. Royal Society of Chemistry, Cambridge
- Cooper JB, Abdelkader M, Wise KL (2013) Sequentially shifted excitation Raman spectroscopy: novel algorithm and instrumentation for fluorescence-free Raman spectroscopy in spectral space. *Appl Spectrosc* 67:973
- de Veij M, Vandenabeele P, Hall KA, Fernandez FM, Green MD, White NJ, Dondorp AM, Newton PN, Moens L (2007) Fast detection and identification of counterfeit antimalarial tablets by Raman spectroscopy. *J Raman Spectrosc* 38:181–187
- de Veij M, Deneckere A, Vandenabeele P, de Kaste D, Moens L (2008) Detection of counterfeit Viagra[®] with Raman spectroscopy. *J Pharm Biomed Anal* 46:303–309
- Degardin K, Roggo Y, Been F, Margot P (2011) Detection and chemical profiling of medicine counterfeits by Raman spectroscopy and chemometrics. *Anal Chim Acta* 705(1–2):334–341
- Ehn A, Levenius M, Jonsson M, Aldén M, Bood J (2013) Temporal filtering with fast ICCD cameras in Raman studies. *J Raman Spectrosc* 44(4):622–629
- El-Diasty F (2011) Coherent anti-stokes Raman scattering: spectroscopy and microscopy. *Vib Spectrosc* 55:1–37
- Eliasson C, Matousek P (2007) Noninvasive authentication of pharmaceutical products through packaging using spatially offset Raman spectroscopy. *Anal Chem* 79:1696–1701
- Esbensen KH (2001) *Multivariate data analysis—in practice*, 5th edn. CAMO Software AS, Nedre Vollgate, Oslo, Norway
- Fraser SJ, Oughton J, Batten WA, Clark ASS, Schmierer DM, Gordon KC, Strachan CJ (2013) Simultaneous qualitative and quantitative analysis of counterfeit and unregistered medicines using Raman spectroscopy. *J Raman Spectrosc* 44:1172–1180
- Gomer NR, Gordon CM, Sharma PLSK, Carter JC, Angel SM (2011) Raman spectroscopy using a spatial heterodyne spectrometer: proof of concept. *Appl Spectrosc* 65:849–857
- Hédoux A, Paccou L, Guinet Y, Willart JF, Descamps M (2009) Using the low-frequency Raman spectroscopy to analyze the crystallization of amorphous indomethacin. *Eur J Pharm Sci* 38(2):156–164
- Janesick JR (2001) *Scientific charge-coupled devices*. SPIE, Washington
- Johansson J, Sparén A, Svensson O, Folestad S, Claybourn M (2007) Quantitative transmission Raman spectroscopy of pharmaceutical tablets and capsules. *Appl Spectrosc* 61:1211–1218
- Kukura P, McCamant DW, Mathies RA (2007) Femtosecond stimulated Raman spectroscopy. *Annu Rev Phys Chem* 58:461–488
- Matousek P, Parker AW (2007) Non-invasive probing of pharmaceutical capsules using transmission Raman spectroscopy. *J Raman Spectrosc* 38:563–567
- Matousek P, Clark I, Draper E, Morris M, Goodship A, Everall N, Towrie M, Finney W, Parker A (2005) Subsurface probing in diffusely scattering media using spatially offset Raman spectroscopy. *Appl Spectrosc* 59(4):393–400
- McCreery RL (2000) *Raman spectroscopy for chemical analysis*. Wiley-Interscience, New York
- McGovernin CM, Hargreaves MD, Matousek P, Gordon KC (2012) Pharmaceutical polymorphs quantified with transmission Raman spectroscopy. *J Raman Spectrosc* 43:280–285
- Mélot M, Oudney PDA, Williamson AM, Caspers PJ, van der Pol A, Puppels GJ (2009) Studying the effectiveness of penetration enhancers to deliver retinol through the stratum corneum by in vivo confocal Raman spectroscopy. *J Control Release* 138:32–39

- Petterson IEI, Dvořák P, Buijs JB, Gooijer C, Ariese F (2010) Time-resolved spatially offset Raman spectroscopy for depth analysis of diffusely scattering layers. *Analyst* 135:3255–3259
- Petty CJ, Hendra PJ, Jawhari T (1991) A standardised intensity scale for Fourier transform Raman spectra of liquids. *Spectrochim Acta A* 47A:1189–1199
- Littleford RE, Matousek P, Towrie M, Parker AW, Dent G, Lacey RJ, Smith WE (2004) Raman spectroscopy of street samples of cocaine obtained using Kerr gated fluorescence rejection. *Analyst* 129:505–506
- Ricci C, Eliasson C, Macleod NA, Newton PN, Matousek P, Kazarian SG (2007) Characterization of genuine and fake artesunate anti-malarial tablets using Fourier transform infrared imaging and spatially offset Raman spectroscopy through blister packs. *Anal Bioanal Chem* 389:1525–1532
- Sacre PY, Deconinck E, Saerens L, De Beer T, Courselle P, Vancauwenberghe R, Chiap P, Crommen J, De Beer JO (2011) Detection of counterfeit Viagra by Raman microspectroscopy imaging and multivariate analysis. *J Pharm Biomed Anal* 56:454–461
- Shreve AP, Cherepy NJ, Mathies RA (1992) Effective rejection of fluorescence interference in Raman spectroscopy using a shifted excitation difference technique. *Appl Spectrosc* 46:707–711
- Shrötter HW, Klöckner HW, Weber A (1979) Raman spectroscopy of gases and liquids, topics in current physics. Springer, New York
- Software ASC (2013) The unscrambler[®] appendices: method references. PDF from CAMO website. [http://www.camo.com/downloads/U9.6 pdf manual/The Unscrambler Method References.pdf](http://www.camo.com/downloads/U9.6%20pdf%20manual/The%20Unscrambler%20Method%20References.pdf)
- Strachan CJ, Rades T, Newnham DA, Gordon KC, Pepper M, Taday PF (2004a) Using terahertz pulsed spectroscopy to study crystallinity of pharmaceutical materials. *Chem Phys Lett* 390:20–24
- Strachan CJ, Pratiwi D, Gordon KC, Rades T (2004b) Quantitative analysis of polymorphic mixtures of carbamazepine by Raman spectroscopy and principal components analysis. *J Raman Spectrosc* 35:347–352
- Strachan CJ, Taday PF, Newnham DA, Gordon KC, Zeitler JA, Pepper M, Rades T (2005) Using terahertz pulsed spectroscopy to quantify pharmaceutical polymorphism and crystallinity. *J Pharm Sci* 94:837–846
- Strachan CJ, Rades T, Gordon KC (2007a) A theoretical and spectroscopic study of gamma-crystalline and amorphous indometacin. *J Pharm Pharmacol* 59:261–269
- Strachan CJ, Rades T, Gordon KC, Rantanen J (2007b) Raman spectroscopy for quantitative analysis of pharmaceutical solids. *J Pharm Pharmacol* 59:179–192
- Tauler R, de Juan A (2006) Multivariate curve resolution. In: Gemperline P (ed) Practical guide to chemometrics, 2nd edn. CRC Press, Taylor and Francis Group, FL, pp 417–473
- Trefi S, Routaboul C, Hamieh S, Gilard V, Malet-Martino M, Martino R (2008) Analysis of illegally manufactured formulations of tadalafil (Cialis[®]) by H-1 NMR, 2D DOSY H-1 NMR and Raman spectroscopy. *J Pharm Biomed Anal* 47:103–113
- Trulson MO, Mathies RS (1986) Raman cross section measurements in the visible and ultraviolet using an integrating cavity: application to benzene, cyclohexane, and cacodylate. *J Chem Phys* 84:2068–2074
- Zeitler JA, Newnham DA, Taday PF, Pepper M, Gordon KC, Rades T (2005) Temperature dependent terahertz pulsed spectroscopy of carbamazepine tablets. *J Pharm Pharmacol* 57: S10–S10
- Zeitler JA, Taday PF, Gordon KC, Pepper M, Rades T (2007) Solid-state transition mechanism in carbamazepine polymorphs by time-resolved terahertz spectroscopy. *ChemPhysChem* 8:1924–1927
- Zhao J, Carrabba MM, Allen FS (2002) Automated fluorescence rejection using shifted excitation Raman difference spectroscopy. *Appl Spectrosc* 56:834–845
- Zhu X, Xu T, Lin Q, Duan Y (2014) Technical development of Raman spectroscopy: From instrumental to advanced combined technologies. *Appl Spectrosc Rev* 49:64–82

Chapter 5

Pharmaceutical Terahertz Spectroscopy and Imaging

J. Axel Zeitler

Abstract Terahertz spectroscopy and imaging have developed rapidly over the past decade as versatile analytical tools for the characterisation of drug delivery systems. In this chapter the technology that has enabled the recent surge of interest in using terahertz techniques is explained in terms of its basic principles and the specific implementations of pharmaceutical relevance. Using a number of examples and case studies an overview of the current state-of-the-art applications of terahertz radiation in pharmaceuticals is presented. In the field of spectroscopy this ranges from polymorph detection and quantification, detailed analysis of phase transitions to amorphous stability. Important imaging applications include non-destructive coating thickness measurements, characterisation of the microstructure of tablet matrices as well as liquid transport into tablets during disintegration.

Keywords Terahertz spectroscopy • Terahertz imaging • Polymorph detection • Solid-state properties • Phase transition • Amorphous • Crystallinity • Amorphous stability • Crystallisation • Film coating • Tablet porosity • Tablet hardness • Disintegration testing

1 Terahertz Radiation: Opportunities for Pharmaceutical Analysis

The term terahertz radiation refers to electromagnetic radiation in a part of the spectrum that was until very recently rather difficult to assess due to technical limitations. Such difficulties might seem somewhat unexpected given that the terahertz range is sandwiched between the well utilised regions of infrared and microwave radiation, but it is only since the late 1990s that scientists routinely access this region for spectroscopy without the need to revert to helium cooled bolometers for detection. The difficulty in performing spectroscopy and imaging at terahertz frequencies originates from the fact that electronic sources and detectors

J.A. Zeitler (✉)

Department of Chemical Engineering and Biotechnology, University of Cambridge, Pembroke Street, Cambridge CB2 3RA, UK
e-mail: jaz22@cam.ac.uk

of radiation rapidly drop in intensity or sensitivity at frequencies above the gigahertz range as it becomes increasingly more difficult to oscillate charge carriers in conducting materials at such high frequencies, thus limiting microwave sources and detectors to frequencies of typically less than 1 THz. In contrast, optical sources such as lasers and blackbody radiation sources that are commonly utilised in the infrared spectral range also drop significantly in power or become impractical in operation (e.g. bulky gas lasers) and hence limit the experimentally accessible spectral range. In addition, thermal background radiation emitted from objects at room temperature contributes significantly to the spectral intensity at terahertz frequencies which makes the detection of incoherent terahertz radiation emitted from typical sources such as globars or mercury arc lamps even harder, thus requiring cryogenically cooled bolometers.

Given this technical difficulty it is not surprising that for a long time spectroscopy and imaging applications at terahertz frequencies remained confined to a relatively small group of laboratories with specialised equipment (Chantry 1971; Möller and Rothschild 1971; Gebbie 1984). However, the work that has been carried out in these groups has revealed some very exciting properties of terahertz radiation that give rise to a range of opportunities in pharmaceutical analysis, three of which are highlighted in this chapter (Fig. 5.1): (1) The ability to probe the intermolecular interactions between hydrogen bonding molecules; (2) the low absorption of terahertz radiation by a range of materials, such as polymers, that are commonly used as excipients in pharmaceutical formulations; as well as (3) relatively low scattering losses in pharmaceutical dosage forms due to the long wavelength of the radiation (a frequency of 1 THz corresponds to a wavelength of 0.3 mm). For a detailed background of the current state of the art in terahertz spectroscopy the reader is referred to more specialist literature (Dexheimer 2007b; Peiponen et al. 2013; Parrott and Zeitler 2015).

The first applications of terahertz spectroscopy and imaging in a pharmaceutical sciences context emerged during the past decade and it is only thanks to the enormous technological advances that have been made in the 1990s that this development was possible. Modern terahertz spectroscopy and imaging is almost exclusively preformed using coherent terahertz radiation. In the majority of systems picosecond pulses of coherent terahertz radiation are generated either by photoconductive antennas or by non-linear optical effects from femtosecond near-infrared pulses that can be routinely generated from lasers.¹ The average power of such terahertz beams is very low (typically in the order of several micro Watts) yet it is possible to detect these pulses with very high sensitivity by exploiting their coherence property by means of time-gated detection schemes that work essentially in reverse to the emission process. The technology developed from early work by

¹ There is a growing number of other technologies available, such as photo mixing, that allows the generation of cw terahertz radiation by exploiting similar physical effects to those needed for the pulsed generation but the majority of applications reported in the pharmaceutical sciences thus far uses pulsed terahertz radiation and hence the description in this chapter is restricted to this technology.

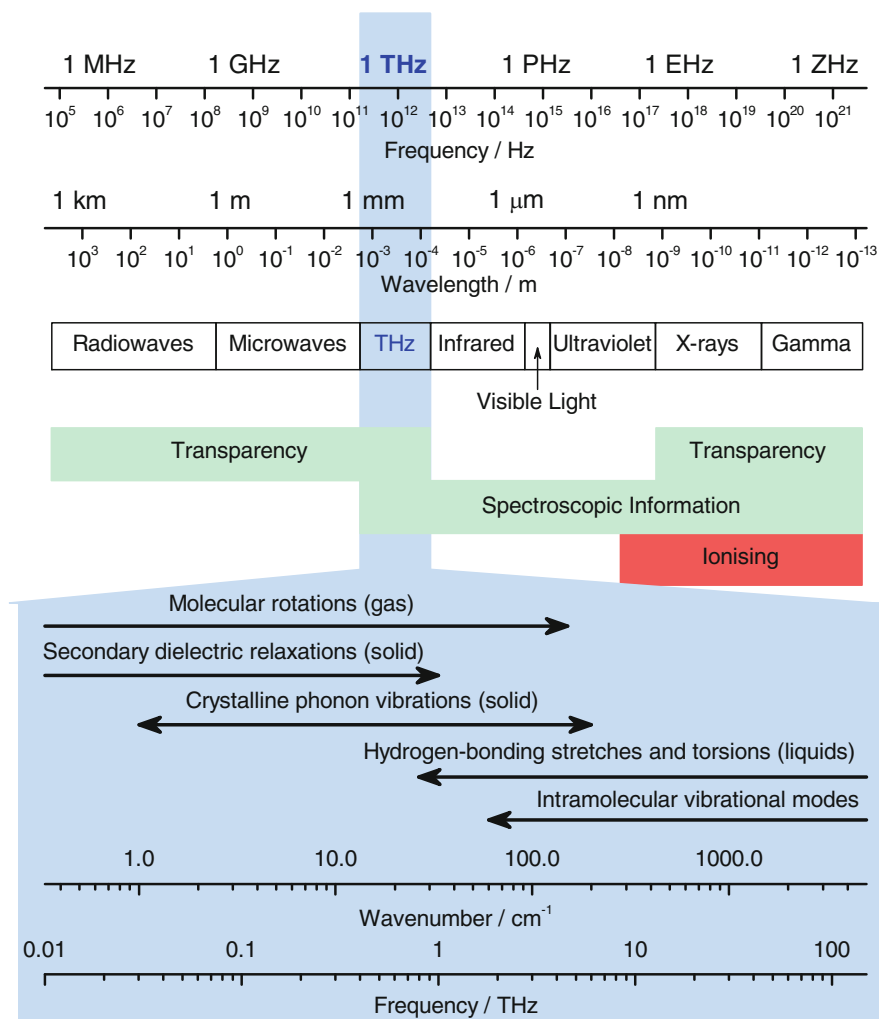


Fig. 5.1 The terahertz region of the electromagnetic spectrum

Auston in the 1970s that demonstrated how pulses of terahertz radiation can be generated and detected within a semiconductor substrate (Auston 1975). In the late 1980s Grischkowsky's group was able to demonstrate how such pulses of terahertz radiation could be coupled into free space (Fattinger and Grischkowsky 1989) and utilised for spectroscopy (Vanexter et al. 1989; Grischkowsky et al. 1990). It is this technology, which has been commercially available for the past 10 years, that has brought terahertz spectroscopy and imaging to a much larger group of scientists and which forms the basis for the applications introduced in this chapter. A number of recent review articles and books cover the details of terahertz time-domain spectroscopy (THz-TDS) and its development (Jepsen et al. 2010; Peiponen et al. 2013; Lee 2009; Bründermann et al. 2012; Dexheimer 2007b; Parrott and Zeitler 2015).

The chapter is structured into two main sections: terahertz spectroscopy and terahertz imaging. Each section is quite self contained, the former mainly referring to spectroscopic studies of solid state small organic molecular properties such as drug molecules that might be of interest during the development stage of a dosage form and the latter section containing a range of examples of imaging applications using pulsed terahertz radiation to investigate film coating properties and study the microstructure of dosage forms, which is equally interesting for product development as well as process control and quality assurance.

2 Terahertz Spectroscopy

2.1 *Phenomena That Can Be Studied By Terahertz Spectroscopy*

The photon energy of terahertz radiation ($0.1\text{--}6\text{ THz} \equiv 0.04\text{--}2.39\text{ kJ mol}^{-1}$) overlaps with hydrogen bond energies (typically $<20\text{ kJ mol}^{-1}$) and it is hence possible to investigate a wide range of molecular interactions in organic solids and liquids. In addition, in small organic molecular crystals the phonon vibrations as well as low energy intra-molecular motions such as bend and torsion modes are also observed at terahertz frequencies. This ability to probe molecular interaction in molecular crystals was demonstrated in a number of studies (Upadhyya et al. 2003; Walther et al. 2003; Shen et al. 2004). In a pharmaceutical context the fact that terahertz radiation is sensitive to intermolecular forces such as hydrogen bonds and lattice modes in crystals makes THz-TDS a valuable tool for material characterisation as outlined in Sect. 2.3 of this chapter.

In amorphous materials no distinct spectral features can be observed at terahertz frequencies. In glasses the loss of electromagnetic radiation at the higher frequency end of the spectral bandwidth is due to absorption into the vibrational density of states (VDOS), which follows a universal frequency dependence in this spectral range (Taraskin et al. 2006). Very valuable information can be extracted from these featureless spectra nonetheless: using the universal frequency dependence Parrott et al. quantitatively studied the charge distribution and its relationship to short-range and long-range order in a range of inorganic sodosilicate glasses (Parrott et al. 2010) and Zalkovskij et al. showed at the example of chalcogenide glasses that the VDOS dominates the absorption over a broad frequency range up to 12 THz (Zalkovskij et al. 2012). Coupled to the vibrational losses are the high frequency tails of the dielectric relaxation processes that still contribute to the absorption at terahertz frequencies (Sibik et al. 2014a). Pharmaceutical applications in the characterisation of amorphous drug molecules and formulations are still limited but Sect. 2.4 aims to provide an overview of what is currently known and what potential information could be extracted from terahertz spectra in the future.

In addition to solid samples interesting information on the intermolecular interactions in liquids can also be extracted from terahertz spectra (Ronne et al. 1999). Structurally liquids are quite similar to glasses though the relaxation processes take place at completely different time-scales and it is mainly through dipole relaxation processes that occur on femtosecond (fast, collision driven orientational relaxation) to picosecond (slow orientational relaxation) time-scales that radiation is absorbed at terahertz frequencies. In addition to the dielectric relaxation processes intermolecular stretching and libration processes contribute to the absorption of terahertz radiation by hydrogen bonding liquids (Yada et al. 2009). These relaxation processes can be quantified using Debye models, such as a simple two component model to resolve fast (femtosecond) and a slow (picosecond) relaxation process:

$$\hat{\epsilon}(\omega) = \epsilon_{\infty} + \frac{\Delta\epsilon_1}{1 + i\omega\tau_1} + \frac{\Delta\epsilon_2}{1 + i\omega\tau_2}. \quad (5.1)$$

For example in water at room temperature the two relaxation processes are $\tau_1 \approx 8$ ps and $\tau_2 \approx 170$ fs (here $\hat{\epsilon}$ is the complex dielectric loss, ω is the angular frequency and $\Delta\epsilon_i$ is a measure of the strength of the respective relaxation process). Additional terms have been added to this equation to account for the intermolecular stretching vibrations. As soon as other molecules, such as carbohydrates or proteins, are dissolved in water it is possible to distinguish between different populations of water molecules based on the change in the relaxational dynamics as the water molecules that are part of the solvation shell exhibit a significantly different dynamics compared to the bulk water molecules (Heugen et al. 2006; Ebbinghaus et al. 2010). In addition very interesting effects regarding the hydration of biomolecules were detected using terahertz spectroscopy (Knab et al. 2006; Markelz et al. 2007; He et al. 2008). In this chapter only solid samples are discussed and the interested reader is referred to the literature for further detail on terahertz spectroscopy of liquids (George and Markelz 2012; Falconer and Markelz 2012).

2.2 Optical Properties

The propagation of a plane wave of electromagnetic radiation through a material can be described by means of the complex refractive index \hat{n} , which is a frequency dependent characteristic of the material that the radiation traverses. As the plane wave enters the material its velocity changes and part of the wave is absorbed by the material:

$$\hat{n}(\omega) = n + i\kappa. \quad (5.2)$$

The real part of this expression, n , describes the change in velocity of the electromagnetic wave compared to its propagation in vacuo while the imaginary part of the refractive index, κ , which is also known as the extinction coefficient or

better the index of absorption, is related to the absorption, or decay, of the oscillation amplitude of the incident electric field

$$\alpha(\omega) = \frac{2\omega\kappa(\omega)}{c}, \quad (5.3)$$

where c is the speed of light in vacuum. The intensity of the transmitted field is proportional to the square of its amplitude and hence we can use Beer-Lambert law as in conventional infrared spectroscopy to describe the change in intensity upon absorption by

$$I = I_0 \exp(-\alpha(\omega)l), \quad (5.4)$$

where l is the thickness of the sample.

Using THz-TDS the electric field of the transmitted pulse is measured directly rather than its intensity and hence both the absorption coefficient, α , and refractive index, n , of materials can be extracted without any mathematical processing by means of the Kramers-Kronig relationship. For the most simple case of a freestanding pellet of sample material this is achieved by measuring a pulse of terahertz radiation that propagates through the empty spectrometer, or a blank reference sample pellet that only contains diluent such as polyethylene, E_{ref} , as well as the sample pulse E_{sam} . Both pulses are transformed into the frequency domain by means of the Fourier transformation and then the amplitude, $A(\omega)$, and the phase, $\phi(\omega)$, of the ratio of the two spectra $E_{\text{sam}}/E_{\text{ref}} \equiv A(\omega)\exp^{i\phi(\omega)}$ are calculated. The optical properties can subsequently be directly extracted as follows:

$$n(\omega) = 1 + \frac{c}{\omega l} \phi(\omega), \quad (5.5)$$

and

$$\alpha(\omega) = -\frac{2}{l} \ln \left(A(\omega) \frac{[n(\omega) + 1]^2}{4n(\omega)} \right). \quad (5.6)$$

Rather than in terms of α and n the complex refractive index can alternatively be expressed in terms of the dielectric losses ($\hat{\epsilon}$):

$$\hat{\epsilon}(\omega) = \epsilon'(\omega) - i\epsilon''(\omega) = \hat{n}(\omega)^2, \quad (5.7)$$

where ϵ' is the real and ϵ'' the imaginary part of the dielectric losses. It is hence possible to convert between the refractive index and the dielectric losses by

$$\begin{aligned} \epsilon'(\omega) &= n(\omega)^2 - \kappa(\omega)^2, \\ \epsilon''(\omega) &= 2n(\omega)\kappa(\omega) = \frac{n(\omega)\alpha(\omega)c}{\omega}. \end{aligned} \quad (5.8)$$

This ability to directly measure n , α , ϵ' and ϵ'' makes THz-TDS a very versatile technique as it can be used to study high frequency dielectric losses over a decade of frequency that is typically not accessible using dielectric spectroscopy techniques and at the same time THz-TDS is a very useful low frequency extension of far-infrared spectroscopy where FT-IR spectrometers are limited both in spectral brightness and detection sensitivity.

Like in FT-IR the vibrational modes that can be excited by THz-TDS are only the infrared active ones and hence low-frequency Raman spectroscopy techniques are ideally suited to complement the terahertz spectra in exactly the same way as these two techniques traditionally complement one another at higher frequencies.

2.3 *Crystal Structure of Drug Molecules*

2.3.1 **Polymorphism: Identification**

Early studies of pharmaceutically relevant molecules such as nucleosides, sugars and small organic molecules including drugs focused entirely on detecting vibrational modes in crystalline materials for identification of the respective substance (Walther et al. 2000, 2002; Fischer et al. 2002; Taday et al. 2003a; Upadhyya et al. 2003; Walther et al. 2003; Shen et al. 2003, 2004; Upadhyya et al. 2004; Ning et al. 2005; Lu et al. 2006). While these studies were very important to demonstrate the capabilities of THz-TDS to measure molecular interactions in hydrogen bonded crystalline solids, their applications in the pharmaceutical sector were limited at the time as although it was clear that such spectra were unique to a certain material the complex collective nature of the vibrational modes meant that the spectra could not be interpreted easily. However, the fact that organic molecular crystals exhibit distinct vibrational modes that can be used for the identification of a material was very interesting in the context of security screening applications as terahertz radiation is able to penetrate a number of optically opaque materials such as polymers and ceramics (Dobroiu et al. 2007).

The next breakthrough in the direct context of pharmaceutical analysis was the work reported by Taday et al. (2003b) where the authors showed at the example of ranitidine hydrochloride forms I and II that THz-TDS is an excellent technique to resolve different polymorphs of drug molecules. The results were particularly significant given that the complex polymorphism of drug molecules had become a widely debated topic in pharmaceutical analysis (Bernstein 2007) and the terahertz spectra clearly showed the high sensitivity of the method to resolve subtle differences in the crystal structure using vibrational spectroscopy. Even though it was still not yet possible to assign these vibrational modes to specific motions the advantage of the technique was that each crystal polymorph clearly had very different spectral features. Compared to infrared and Raman spectroscopy, where often subtle spectral shifts dominate the differences between different polymorphs, the terahertz spectra of the two forms of ranitidine studied by Taday et al. were completely different.

This proof-of-principle study was followed by a number of more detailed investigations. Strachan et al. highlighted the general applicability of this method to investigate pharmaceutical polymorphism (Strachan et al. 2004). In this context the study also emphasised that materials in their amorphous state do not exhibit any specific vibrational feature in the terahertz frequency range, which was previously pointed out already in a more general context by Walther et al. (2003). Yamaguchi et al. showed that pure enantiomers have different vibrational features at terahertz frequencies compared to the racemic compounds but no difference was found between the respective D- and L- enantiomers (Yamaguchi et al. 2005). In the absence of sufficiently powerful computational methods to calculate the intermolecular and low energy intramolecular vibrational motions in crystalline materials a series of three papers from the NTT Basic Research Laboratories in Japan presented some elegant experiments to separate the intra- and intermolecular vibrational modes by studying the intensity of the modes depending on the propagation of the terahertz field through different crystal axis in large single crystals (Rungsawang et al. 2006a, b) as well as by loading molecules into mesoporous silica to suppress intermolecular motions (Ueno et al. 2006b; Ueno and Ajito 2007). At the example of sulfathiazole the sensitivity of THz-TDS was demonstrated to resolve the subtle differences between a large number of different polymorphic forms, here five polymorphs, of the same compound (Fig. 5.2) (Zeitler et al. 2006).

In addition to resolving different polymorphic forms THz-TDS was found to resolve a range of hydrate forms (Fig. 5.3) (Zeitler et al. 2007a; Kogermann et al. 2007; Liu and Zhang 2006) and cocrystals (Nguyen et al. 2007; Parrott et al. 2009) further confirming the sensitivity of the technique to subtle changes in intermolecular interactions. The results of these studies demonstrated that THz-TDS is a useful technique to complement information on the crystal structure from diffraction techniques commonly used in crystallography: while the average position of the atoms in an organic molecular crystal can be resolved to a high precision even based on powder diffraction data there are samples where the powder diffraction pattern of two materials can look almost identical yet the terahertz spectral fingerprint looks vastly different allowing for easy identification of the respective solid state forms (Parrott et al. 2009). The ability to resolve such subtle differences between, in this case, two cocrystals originates from the fact that rather than probing the structure of the material THz-TDS measures the dynamics resulting from the low energy bonding interactions in such materials.

2.3.2 Quantification

Not long after the first applications of THz-TDS to identify polymorphs of drug molecules were reported it was demonstrated how the technique can be applied to quantify the amount of one polymorph in the presence of another (Strachan et al. 2005). At the example of different polymorphs of four different drug molecules Strachan et al. showed that it is possible to discern polymorph impurities of as little as 0.5 % and reliably quantify the amount of the minor component down to

Fig. 5.2 The terahertz transmission spectra of five different polymorphic forms of sulfathiazole. All forms can clearly be distinguished from one another (baseline removed for clarity, modified from Zeitler et al. 2006)

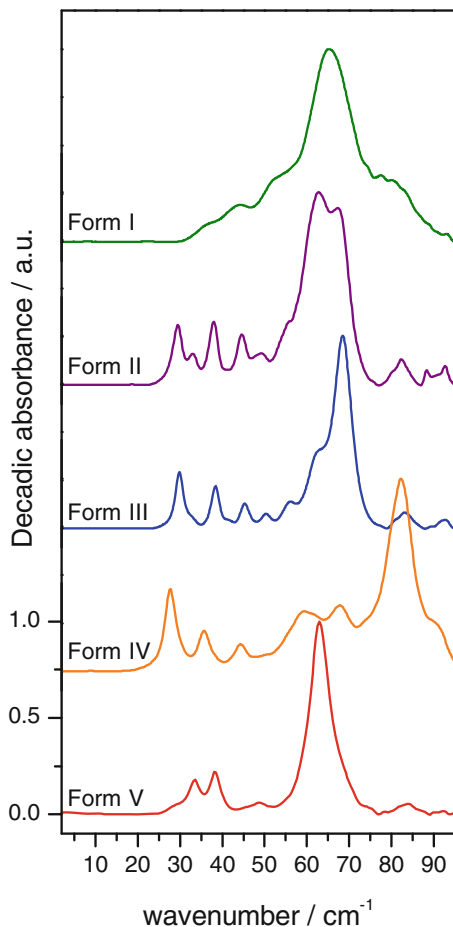
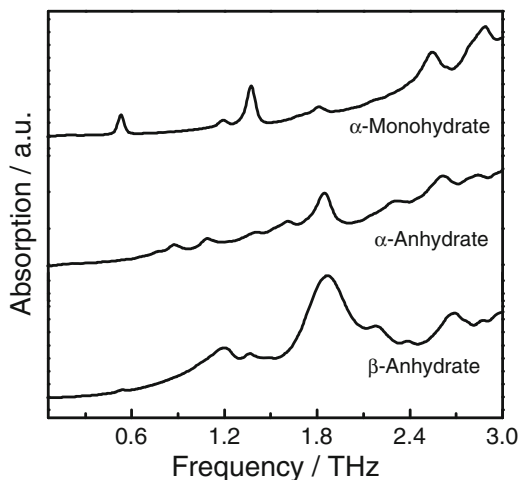


Fig. 5.3 Terahertz spectra of different hydrous and anhydrous forms of lactose. From the spectra it is immediately obvious that the intermolecular interactions rather than the chemical structure of the molecules dominate the vibrational spectra at terahertz frequencies



concentrations of 2%. In this study the authors mainly used multivariate data analysis techniques (partial least squares regression) for the quantitative analysis. The performance of THz-TDS was comparable to other vibrational spectroscopy techniques as well as X-ray powder diffraction and similar to other techniques the absolute detection and quantification thresholds were found to vary depending on the relative strength of the spectral features in the respective polymorph. The study further demonstrated that THz-TDS is a good technique to quantify trace crystallinity in an amorphous matrix.

Almost exactly at the same time as the paper by Strachan et al. was published Yamaguchi et al. showed how THz-TDS can be used to quantify the amount of pure enantiomer in a mixture with the racemic compound based on the absorption intensity of a single spectral feature (Yamaguchi et al. 2005).

Ueno et al. also used univariate analysis (absorbance at fixed frequencies corresponding to the spectral features) to quantify a range of amino acids and their mixtures from the terahertz transmission spectra (Ueno et al. 2006a). Good linearity of the spectral response to varying sample concentration was confirmed and the authors were able to resolve even mixtures of three amino acids simultaneously.

While both the work of Strachan et al. as well as that of Ueno et al. were based on transmission spectra Cogdill et al. showed that drug/excipient mixtures can also be quantified in reflection (Cogdill et al. 2006). Flat faced tablets were prepared made from up to three different materials (one drug, a crystalline excipient and an amorphous excipient) and the spatial distribution of the constituent materials was resolved by mapping over the samples.

Following these initial studies the ability to quantify drug molecules in the solid state at terahertz frequencies has attracted considerable interest and studies were published on a range of samples: mefenamic acid (Otsuka et al. 2010) theophylline (Hisazumi et al. 2011), diclofenac (King et al. 2011b), illicit drugs (Chen et al. 2011), sodium salicylate in mannitol/lactose tablet (Hisazumi et al. 2012b) as well as ternary mixtures of lactose, fructose and citric acid (El Haddad et al. 2014).

The ability to measure relatively small amounts of crystalline material in an amorphous matrix due to the pronounced difference between a crystalline (sharp peaks) and amorphous material (homogeneously increasing background) was investigated in quite some detail over a range of pharmaceutically relevant systems: crystallinity of threhalose dihydrate (Takeuchi et al. 2012), trace crystallinity in freeze-dried amino acid/gelatine mixtures (Darkwah et al. 2013), crystallinity of sucrose (Ermolina et al. 2014), crystallinity of cellulose (Vieira and Pasquini 2014). All these studies show that THz-TDS is a useful technique to study the presence of small amount of crystalline phase in a largely amorphous matrix (Fig. 5.4). This will be discussed in more detail in Sect. 2.4.1 in the context of crystallisation studies. It is important to note in this context that THz-TDS is not as sensitive or robust to detect trace amounts of amorphous phase in a largely crystalline matrix.

This point becomes clear in two studies where crystalline lactose was partially converted into the amorphous state using a ball mill and the amount of residual crystallinity was monitored over the milling process time (Smith et al. 2015a, b). When attempting to quantify the change in crystallinity it is important to keep in

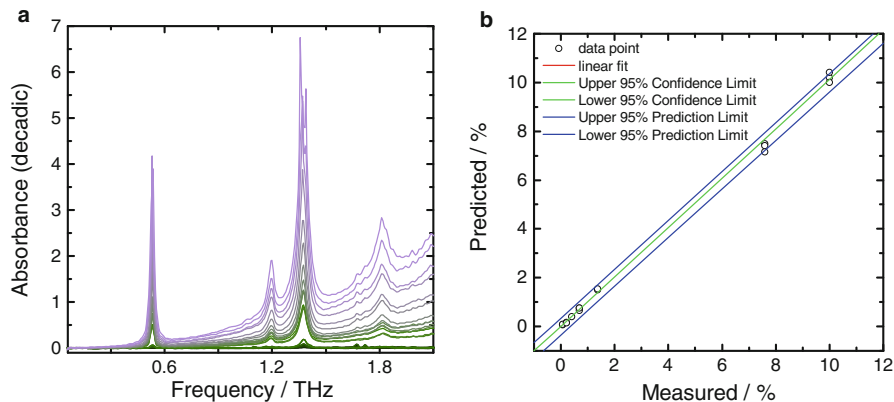


Fig. 5.4 (a) Terahertz spectra of crystalline lactose α -monohydrate at low concentrations in an amorphous polyethylene matrix; (b) corresponding linear fit of the absorption feature at 0.56 THz

mind that a growing amount of amorphous phase will increase the background absorption of the terahertz spectra due to the collapse of the crystalline lattice modes into the VDOS (see Sect. 2.4 for details). At the same time the reduction in particle size will affect the amount of scattering which is also lead to systematic changes in the baseline absorption (smaller particles scatter less, hence the spectral baseline will reduce). It would therefore be potentially limiting the sensitivity of the THz-TDS to remove the baseline by means of baseline subtraction or any other pre-processing techniques that are commonly used in chemometrics in order to quantify the crystallinity by peak height or area of the remaining crystalline modes.

Using multivariate spectral analysis a THz-TDS method was developed to quantify API content within a tablet matrix (Wu et al. 2008). Rather than measuring pure drug these measurements demonstrated that it is possible to develop quantitative models even in the presence of a range of excipients.

2.3.3 Interpretation of Terahertz Spectra

When the first spectroscopy studies of organic molecular crystals were published about 15 years ago one of the most significant limitations of THz-TDS compared to mid-infrared spectroscopy was that the spectra could only serve as a fingerprint. As outlined in the previous section this did not limit some of the applications of THz-TDS such as polymorph identification and quantification of crystalline fractions. However, the assignment of spectral features to particular vibrational motions was not possible hence preventing a bigger impact of the technique to study more fundamental properties in crystalline samples and phase transition mechanisms.

In the mid-infrared, spectra can be analysed based on the fact that certain modes, such as the $-\text{CH}$ or the $>\text{C}=\text{O}$ stretch, are always observed around well defined frequencies that are characteristic to the functional groups. In addition, an

absorption band often exhibits a typical strength that further aids the band assignment. At lower frequencies in the mid-infrared, in the so-called fingerprint region, increasing complexity of the vibrational modes occurs yet nowadays it is almost trivial to calculate, for any molecule based on its chemical structure alone, both the frequency and intensity of all these intramolecular modes from first principles using density functional theory (DFT). Given that interactions between neighbouring atoms dominate and longer interaction distances rarely extend beyond the individual molecule the calculations of such localised normal modes can be performed for a single molecule. Using as little computational power as that of a portable computer it is possible to solve such calculations within a matter of hours on computational packages such as Gaussian 09.

However, these techniques cannot be readily applied to calculate accurate terahertz vibrational modes (Tomerini and Day 2012). Given the lower energy of the vibrations the associated motions can no longer be sufficiently modelled based on an individual molecule surrounded by vacuum, as is the case for the mid-infrared DFT calculations. At terahertz frequencies it is typically not a simple stretch or bend of an individual bond that leads to a spectral feature but the collective motions of the atoms within a molecule. Initial attempts to resolve terahertz vibrational modes based on simple DFT methods based on a single molecule or a small cluster of a few isolated molecules (Fischer et al. 2002; Takahashi et al. 2009) were soon superseded by more sophisticated computational approaches that explicitly take the periodic nature of the crystalline lattice into account (Allis et al. 2006; Day et al. 2006). DFT calculations under periodic boundary conditions are computationally much more demanding and the resources required to successfully get such a calculation to converge to the tight energy criteria is immense compared to a single molecule DFT mid-infrared calculation: at present the calculations readily take weeks of computation time on high performance computing clusters running on hundreds of processor cores in parallel.

Thus far broadly three different types of methods have been successfully demonstrated for the calculation of terahertz spectral modes: atom-atom potential methods (Day et al. 2006; Li et al. 2010), periodic DFT methods (Allis et al. 2006; Jepsen and Clark 2007; Takahashi et al. 2009; King et al. 2011a; Kambara et al. 2010; Singh et al. 2012; Juliano et al. 2013; Delaney et al. 2013a) and molecular dynamics simulations (Katz et al. 2014). Each of these approaches comes with their own merits and limitations. For a detailed review of the background to these techniques the reader is referred to the excellent summary by Tomerini and Day (2012) as well as a recent review article on this topic by Takahashi (2014). Even though enormous progress has been achieved in the assignment of molecular motions to vibrational features observed at terahertz frequencies Tomerini and Day point out a number of limitations that currently restrict all three computational approaches: the effect of surface effects on the modes at terahertz frequencies, the interaction of sample with binder in a transmission experiment (Burnett et al. 2013) as well as the effect of disorder (Li et al. 2010) and impurities in the crystals.

However, with the refinement of the periodic DFT methods to better account for the dispersion in the intermolecular interaction it is becoming increasingly straightforward to assign vibrational modes at terahertz frequencies, making THz-TDS a very powerful technique for spectroscopic solid-state analysis. Over the past three years a number of studies have demonstrated the potential of this approach to study the solid-state properties of drug molecules and their complex phase behaviour on the molecular level (King et al. 2011b; Delaney et al. 2012, 2013a, b; Singh et al. 2012; Juliano et al. 2013; Pellizzeri et al. 2014).

2.3.4 Polymorphism: Fundamental Properties

As Threlfall recently reminded the pharmaceutical community so felicitously: “The commonest misperception, easily acquired merely by reading the literature, is that polymorphism is a simple, well-understood phenomenon and that polymorphs are well behaved” (Threlfall 2014). Through the advances made in recent years in making terahertz spectroscopy available commercially to pharmaceutical analysis together with the advent of the computational methods described in the previous section it is now possible to use the spectral observations at terahertz frequencies to better study some of the fundamental properties of the weak intermolecular interactions that govern polymorphism in organic molecular crystals.

Terahertz spectroscopy has proven to be a very sensitive probe to investigate disorder in crystalline materials. As mentioned briefly before, terahertz spectra reveal the differences in the molecular dynamics that is caused by local disorder in a crystal compared to techniques that provide information based on atomic position, such as X-ray (for heavy atoms such as C, N, O) or neutron diffraction. For example it was found that the spectra of the cocrystals of theophylline with the chiral or racemic form of malic acid have very different terahertz spectra even though their structures are very similar. This was explained by the symmetry breaking which occurs for the lattice modes in the chiral cocrystal due to the conformational stress caused by the need of one of the enantiomer having to fit into the same lattice position as its stereoisomer in the crystal structure of the racemic cocrystal (Parrott et al. 2009).

In crystalline benzoic acid a temperature dependent disorder is observed for the position of the hydrogen atom in the carboxylic acid group. By means of computational simulations Li et al. were able to demonstrate the profound effect of this subtle disorder on the vibrational modes at terahertz frequencies (Li et al. 2010). Aided by computational methods King, Hakey and Korter were able elucidate the interplay between intramolecular torsions and lattice modes that governs the spectral differences between the enantiopure and racemic form of serine (King et al. 2010a) and ibuprofen (King et al. 2010b). The group was furthermore able to refine the accuracy of their computational techniques to investigate the effect of solvates, specifically hydrates, on the terahertz spectrum compared to its anhydrous

counterpart (King and Korter 2010; King et al. 2010a, 2011c). It was found that vibrational modes originating from the small and relatively loosely bonded water molecules dominated the terahertz spectra.

Further examples that both demonstrate the high sensitivity of THz-TDS for supermolecular structure and explain this sensitivity at the molecular level by means of computational techniques are the studies recently published by Tim Korter's group on the conformational disorder in irbesartan (Delaney et al. 2012), the discussion of the interplay between conformational strain and cohesion binding that was found to play a key role in the stability of gabapentin polymorphs (Delaney et al. 2013a, b) as well as aripiprazole, (Delaney et al. 2013a) and how THz-TDS can play an important role as a complementary technique to X-ray diffraction in the characterisation of new polymorphs (Pellizzeri et al. 2014).

In the context of this discussion it is interesting to note that with increasing degree of crystalline disorder the vibrational peaks that are observed at terahertz frequencies typically broaden and loose intensity. This effect is particularly pronounced when intramolecular rotations remain possible even once the molecule is locked into its crystal structure: the increased intramolecular flexibility that is associated with the crystalline disorder directly affects the complex motions that govern the terahertz vibrational modes.

2.3.5 Crystalline Phase Transitions

Given its fast spectral acquisition rate and the insensitivity to sample temperature due to its coherent detection scheme, THz-TDS is ideally suited to investigate the complex phase transition behaviour that can be observed in drug molecules. A number of studies have shown how polymorphic phase transitions can be resolved as a sample of drug material is heated and a new polymorph emerges by means of solid state transformation (Zeitler et al. 2005, 2006; Upadhyya et al. 2006). By analysing the kinetics of such processes it is possible to explain the molecular mechanism of the transformation processes (Zeitler et al. 2007a).

It is equally possible of course to use this method to analyse the dehydration behaviour of hydrate forms as the water molecules leave the crystal structure with increasing temperature (Liu and Zhang 2006; Zeitler et al. 2007a). Given the sensitivity of THz-TDS to crystallinity it is very easy to spot the collapse of crystal structure that is associated with the dehydration of some drug molecules that result in the formation of an amorphous phase from which subsequent crystallisation of an anhydrous form can typically be observed.

One aspect that makes THz-TDS unique compared to other vibrational spectroscopy techniques when it comes to the investigation of the dehydration behaviour of hydrates is that the rotational transitions of water molecules in the vapour phase exhibit characteristic absorption lines at terahertz frequencies. These lines are distinct in that they are much narrower and quite intense and hence can be easily identified. During in situ analysis of the dehydration process it is often possible to identify the underlying solid state transition as well as the evaporation step of the

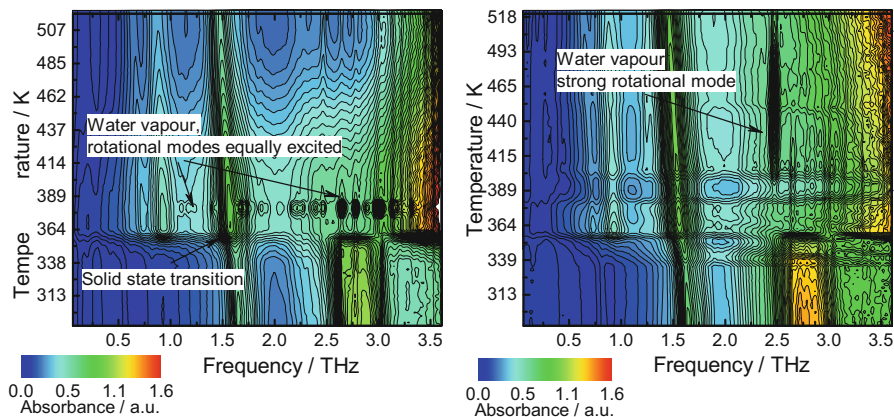


Fig. 5.5 Dehydration of theophylline monohydrate observed by in situ THz-TDS

water molecules from the sample surface. These steps can occur simultaneously or they can be separated into distinct steps (Fig. 5.5) (Zeitler et al. 2007a). Naturally the sample preparation can influence the loss of water given that a small amount of drug material is typically embedded in a porous matrix of polymer for a THz-TDS experiment (Kogermann et al. 2007).

Besides temperature induced phase transformations THz-TDS has been used to study solid state synthesis of co-crystals through grinding (Nguyen et al. 2007; Hongwei and Zhiyong 2011; Liu et al. 2011; Du et al. 2013).

Due to the sensitivity for crystalline disorder discussed in the previous section THz-TDS is a useful probe to resolve phase transitions in such materials. At the example of simvastatin Tan and Zeitler showed how THz-TDS can detect the polymorphic transitions between three different forms of simvastatin (Tan and Zeitler 2015). In this sample the spectra showed no distinct peaks appearing or disappearing (much in line with XRPD analysis that resolves no major changes in the crystal packing across the polymorphs) yet a detailed analysis of the absorption intensity and peak width can clearly reveal the respective phase transitions.

2.4 Amorphous Materials

When investigating amorphous materials terahertz spectroscopy can provide very interesting insights into the interplay between high frequency dielectric relaxation processes, that are well known to play a fundamental role in the stability of the disordered state, and the vibrational modes that break down into a vibrational density of states (VDOS) in the amorphous phase. The majority of the absorption of terahertz radiation by disordered solids is via coupling to the vibrational density of states (VDOS) (Taraskin et al. 2006), which is sometimes also referred to as the

microscopical peak.² A general introduction into the physics of THz-TDS of amorphous materials can be found in Sibik and Zeitler (2015).

2.4.1 Onset of Crystallisation

Compared to the spectral baseline in crystalline samples the VDOS leads to relatively strong monotonous absorption and it can be used as a very sensitive probe for crystallisation. It is this sensitivity that a number of studies have exploited to try and detect, and ultimately better understand the molecular changes associated with, the onset of crystallisation from the amorphous phase.

By heating a sample of amorphous quench cooled carbamazepine through its glass transition temperature, T_g , it was demonstrated that this change in molecular dynamics is reflected in the absorption of terahertz radiation and that the lower frequencies increase in absorption while at higher frequencies (above 1 THz) a decrease in absorption is observed as the material changes from a glass into a supercooled liquid (Zeitler et al. 2007d). Crystallisation is associated with a dramatic change in the spectra: the VDOS splits into the well defined phonon-like vibrational modes that are characteristic for organic molecular crystals and sharp peaks emerge while the baseline absorption drops significantly.

In a similar fashion the onset of crystallisation was investigated in a sample of paracetamol (Fig. 5.6) (Sibik et al. 2014b). In this study supercooled paracetamol

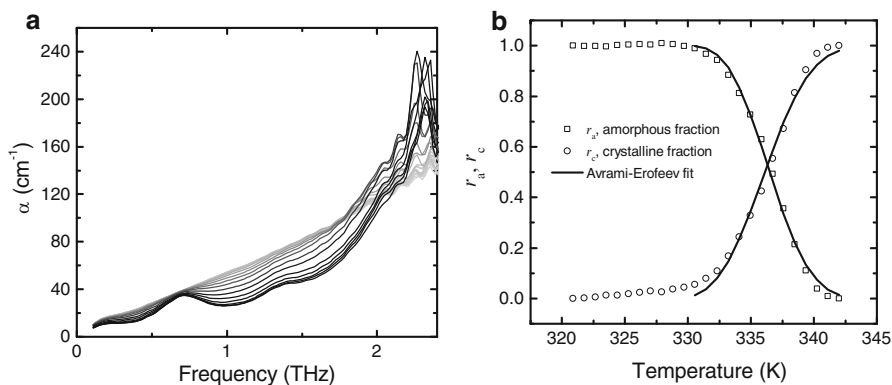


Fig. 5.6 (a) Terahertz spectra of paracetamol crystallising from the amorphous phase. As the crystallisation progresses distinct vibrational modes emerge from the VDOS. (b) Kinetics of the crystallisation process and corresponding fit using the Avrami-Erofeev model (modified from Sibik et al. 2014b)

² Any excess density of states beyond the Debye level is generally referred to as the ‘Boson peak’. Some authors refer to the whole VDOS peak as the ‘Boson peak’, which is technically not correct and further confusion can arise from the discussion of Raman and neutron scattering experiments where this peak is typically much stronger than in dielectric/THz spectra.

was also heated above its T_g and crystallisation of one of its polymorphs occurred. Upon further heating the phase transitions into two further polymorphs was observed. As the sample in this study was sandwiched between two windows rather than a free standing pellet, as in the carbamazepine study, it was also possible to observe the melt of the material at higher temperatures. Using the terahertz spectra together with a fit to a power law, that was previously developed (Sibik et al. 2013), it was possible to determine the crystallisation kinetics very precisely. The temperature of the onset of crystallisation as extracted from the THz-TDS spectra was found to match very well with the deviation of the heat capacity from its baseline during the DSC measurement.

Using a related type of power law fit McIntosh et al. also studied the crystallisation kinetics of an amorphous material (McIntosh et al. 2013). But rather than heating their specimen of amorphous lactose the authors exposed it to elevated levels of humidity and observed the subsequent crystallisation.

2.5 Stability of Amorphous Drugs Below T_g

In addition to the work into characterising crystallisation processes above T_g it is very interesting from a stability point of view to understand the mechanisms that govern the crystallisation of glasses below T_g . Several dielectric spectroscopy studies have highlighted the importance of the secondary relaxation processes in this context, in particular that of the Johari-Goldstein (JG) β -relaxation (Bhattacharya and Suryanarayanan 2009; Grzybowska et al. 2010). In an amorphous material typically both primary and secondary relaxation processes take place and these processes can be observed using dielectric spectroscopy. The primary relaxation can be considered as a molecular diffusion process and it can no longer be observed at temperatures below the glass transition temperature, T_g , as the viscosity of the material becomes too large (Angell et al. 2000). In fact, the T_g is often defined as the temperature when the α relaxation exceeds 1000 s ($T_{g,\alpha}$). In addition, there are a number of secondary relaxations that can be observed at higher frequencies and which are explained in terms of intra-molecular flexibility (Grzybowska et al. 2010) or inter-molecular mobility. For THz-TDS of particular importance is the so-called JG relaxation processes in this context, in particular that of the Johari-Goldstein (JG) β -relaxation process (Johari 1970) as well as the fast β relaxation process. Due to its inter-molecular nature, they are thought to play a major role during the crystallisation from the disordered state (Grzybowska et al. 2010). Given that the secondary relaxation processes are typically observed at frequencies around 10^6 Hz it is surprising that THz-TDS measurements are sensitive to these relaxation processes. Capaccioli et al. show that it is the caged molecule dynamics that are probed at terahertz frequencies (Capaccioli et al. 2015). This caged dynamics manifests itself as the 'nearly constant losses' (NCL) in the susceptibility spectra (see Ngai 1998, 2003 for details on the coupling model) and refers to molecules that are confined by the anharmonic intermolecular potential.

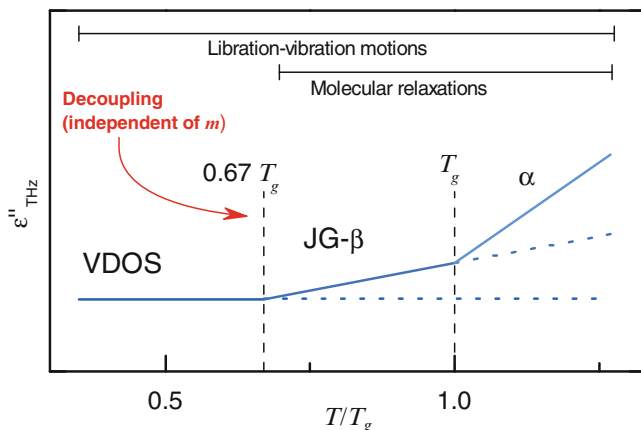


Fig. 5.7 Schematic of the thermal decoupling process of the molecular relaxation processes from the VDOS, or microscopic peak, in supercooled hydrogen-bonded liquids (modified from Sibik et al. 2014a)

The NCL process is fundamentally linked to the JG β -relaxation, and by means of the coupling model also to the α relaxation and hence both processes can be detected using THz-TDS.

At the example of a set of polyalcohols as well as sorbitol/water mixtures Sibik et al. investigated how the dielectric relaxation processes and the VDOS interact when the temperature of the samples is varied (Sibik et al. 2013, 2014a). As the samples are cooled from a supercooled liquid into a glass and further to temperatures well below T_g three features were observed in the dielectric losses of all samples (Fig. 5.7): the VDOS peak can be seen at temperatures well below the glass transition. Its shape and frequency is almost independent of temperature and it persists into the liquid phase at higher temperatures. As outlined above the origin of this peak is due to librational/torsional modes that exist in disordered solids but not in crystals. At higher temperatures, but still below the glass transition $0.65T_g < T < T_g$, an additional β -relaxation process was observed that showed strong temperature dependence and which was mainly attributed to JG β -relaxation. Interestingly, compelling evidence was found in all samples for a secondary glass transition at $T_{g,\beta} \approx 0.65T_g$. Given that the sample materials span a wide range of fragilities this phenomenon is clearly not related to the glass fragility and it appears to be a universal feature of hydrogen bonded glasses. At temperatures above T_g , the α -relaxation processes dominated the spectra. The authors highlighted that the thermal changes in the losses at terahertz frequencies originate from a universal change in the hydrogen bonding structure of the samples that was previously not reported (Sibik et al. 2014a).

Recent results with partially crystalline naproxen confirm these results (Sibik et al. 2015). Amorphous naproxen is highly unstable with a strong tendency to crystallise even if quench cooled and stored at low temperatures. In the study, a sample of naproxen melt was quenched into liquid nitrogen. As the spectra in

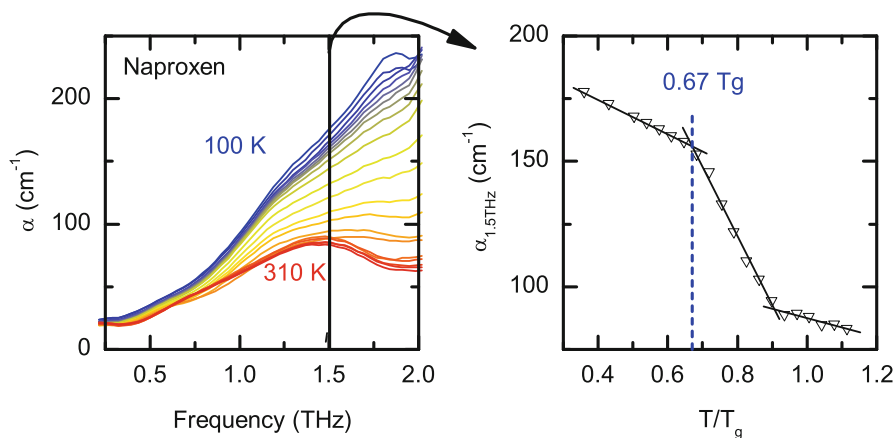


Fig. 5.8 Terahertz spectra of a sample of amorphous naproxen that contains seed crystals from 100 to 310 K with 10 K step increments (*left*). Terahertz absorption of naproxen at 1.5 THz as a function of rescaled temperature T/T_g (*right*). Modified from Sibik et al. (2015)

Fig. 5.8 suggest given the monotonous increase in absorption with frequency and the absence of strong vibrational modes, the resulting sample was mostly amorphous. However, the sample is not fully amorphous as the spectra exhibit a weak shoulder at around 1.2 THz in the absorption spectra at 100 K, indicating the presence of trace crystallites in the quench-cooled sample. In contrast to the temperature dependent absorption observed for pure amorphous phases, where an overall increase in absorption is observed due to the shift of the dielectric relaxation processes to higher frequencies with increasing temperature, the sample of amorphous naproxen that contains seed crystals steadily crystallises even at temperatures well below T_g . Nucleation has already occurred and crystal growth is observed with increasing temperature which is characterised by a decrease in the overall absorption losses while simultaneously a peak emerges from the shoulder and red-shifts with increasing temperature. What is extremely interesting in this context is that the results show that the crystallisation of amorphous naproxen commences at temperatures well below T_g in the presence of seed crystals.

Further analysis of the data shows that there is a significant change in the crystallisation kinetics at $T_{g,\beta} \approx 0.67T_g$. At temperatures above this point the crystallisation rate increases by about 3.5 times. This coincides exactly with the temperature where the secondary relaxation enters the terahertz frequency range which, as already stated, plays a crucial role in the crystallisation of glasses below T_g . Thus, one must be very careful when evaluating the stability of a glass at temperatures above the secondary glass transition associated with the β process, here $\approx 0.67T_g$ as this state is inherently unstable (albeit the crystallisation rate of naproxen is quite an extreme case of course).

Sibik et al. were also able to demonstrate that the three temperature regimes that were identified in samples of polyalcohols (characterised by $T_{g,\beta}$ and $T_{g,\alpha}$) are also present in samples of drug molecules (Sibik et al. 2015). After scaling the

Fig. 5.9 Scaled absorption at 1 THz of amorphous paracetamol, flufenamic acid, indomethacin, and simvastatin. The *solid lines* show the linear fits across the relevant thermal regions to extract the strength of the JG β -relaxation process from THz-TDS data (Sibik et al. 2015)

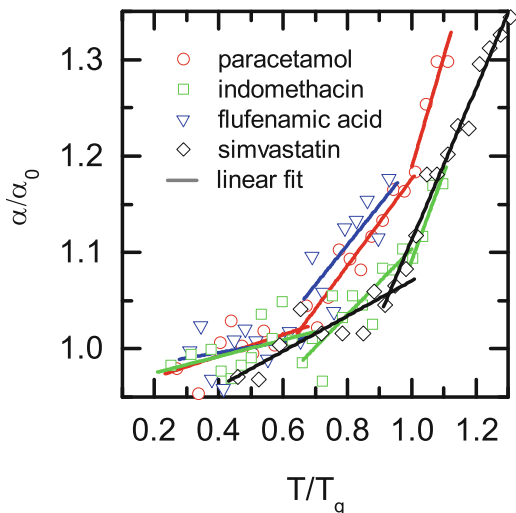


Table 5.1 Stability t_{stable} of amorphous drugs expressed as time before any crystallisation was detected at 277 and 298 K, glass-transition temperature T_g ($=T_{g,\alpha}$) determined by DSC, together with the linear-fit analysis of absorption losses, $\alpha/\alpha_0(T/T_g) = A + BT/T_g$, as shown in Fig. 5.9

Sample	t_{stable} at 277 K	t_{stable} at 298 K	T_g (K)	$T_{g,\beta}$ (K)	$T_{g,\beta}/T_g$	B_2
Flufenamic acid	4 days	1 day	285	160	0.55	0.42 ± 0.15
Paracetamol	45 days	1 day	297	194	0.65	0.45 ± 0.05
Indomethacin	136 days	7 days	318	243	0.76	0.34 ± 0.09
Simvastatin	>84 days	>220 days	303	–	–	0.18 ± 0.03

B_2 is the linear coefficient obtained from fits in the temperature region between T_β and T_g

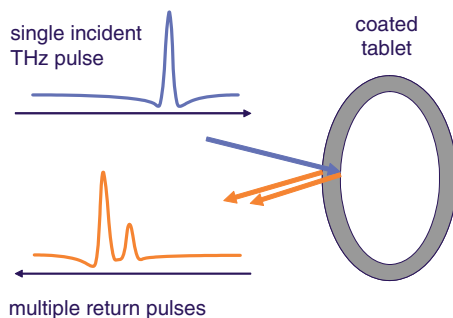
absorption to be able to compare the change in behaviour between different samples it was possible to measure the strength of the JG β -relaxation from the slope of a linear fit between $0.67T_g$ and T_g (Fig. 5.9). An excellent correlation was found between this property and the stability of the drug molecules against crystallisation as measured during XRPD stability studies (Table 5.1). It was shown that fast (GHz-THz) molecular processes are governing the stability and crystallisation at temperatures below T_g and that the molecular mobility is facilitating, rather than actively driving, the structural changes while it was acknowledged that other factors, such as thermodynamics, also play a key role in the crystallisation process.

3 Terahertz Imaging

3.1 Measurement Principle

In contrast to the previous section, where we were concerned with the spectral response of the interaction between terahertz radiation and a given sample material,

Fig. 5.10 Measurement principle of terahertz pulsed imaging (TPI) of coating structures on tablets



the measurement principle in terahertz pulsed imaging (TPI) exploits the time-domain profile of the terahertz pulse rather than its frequency components. Conceptually the measurement is similar to that of a radar or ultrasound experiment: a pulse of radiation is focused onto an object and the reflections that occur at structures below its surface are delayed in time relative to the reflection from the surface. By measuring the delay between the reflections (the so-called time-of-flight) it is possible to precisely determine the depth where this reflection originated from within the sample.

In the pharmaceutical sciences the most successful application for this measurement technique is in the characterisation of coating structures that are applied to tablets (Fig. 5.10). Both sugar coatings and film coatings have been characterised (Fitzgerald et al. 2005; Zeitler et al. 2007b) but the majority of the work that has been reported to date is on polymer film coatings. TPI works very well in this application because polymers and other tablet excipients are relatively transparent at terahertz frequencies and hence it is possible for the terahertz pulse to penetrate deep into the tablet.

As the terahertz pulse is propagating into the tablet a reflection will occur whenever a change in refractive index occurs. This change in refractive index can either be due to the propagation of the pulse from one type of material into another or it can be due to a distinct difference in density of the sample matrix which in turn is reflected in a change in optical density. The amplitude of the reflection is governed by the relative difference in refractive indices of the two adjacent layers that the pulse is propagating through. The reflection coefficient r is defined as

$$r_{01} = \frac{n_1 - n_0}{n_0 + n_1}, \quad (5.9)$$

where n_0 and n_1 are the refractive indices of the two media that the terahertz pulse is propagating through and the subscript in r_{01} denotes that the reflection occurs at the interface between medium 0 and medium 1 (Fig. 5.11). Note that the direction of the reflected pulse (i.e. the sign of its amplitude) can be either positive or negative, depending on the relative change in refractive indices that the terahertz pulse is traversing.

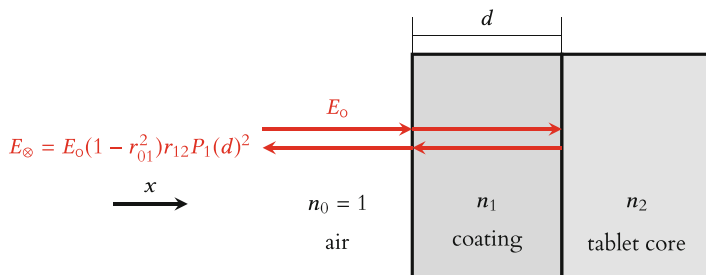


Fig. 5.11 Schematic of a basic 1-D model of the propagation of electromagnetic radiation into a single coating layer of thickness d with refractive index \tilde{n}_1 from free space (refractive index \tilde{n}_0). The tablet core is characterised by a refractive index of \tilde{n}_2 . The terahertz pulse propagates from the source (not shown, to the left of the sample) to the detector (not shown, also to the left of the sample) along x . E_0 denotes the electric field generated at the emitter while E_{\otimes} is the electric field measured by the detector that originates from the coating/core interface

Typically the terahertz pulse is propagating through air ($n_0 = 1$) before it reflects off the tablet surface and hence Eq. (5.11) simplifies to

$$r_{01} = \frac{n_1 - 1}{1 + n_1}. \quad (5.10)$$

Subsequent reflections from further layer structures deeper in the tablet (interface between the coating and the tablet core, additional coating layers, interfaces in bi-layered tablets) can be treated in the same manner:

$$r_{12} = \frac{n_2 - n_1}{n_1 + n_2}. \quad (5.11)$$

It is important to remember from Eq. (5.2) that the refractive index is frequency dependent and a complex number that also accounts for the absorption of the material (we should really refer to it as $\hat{n}(\omega)$). However, most polymers that are used for pharmaceutical coating are almost completely transparent at terahertz frequencies ($\kappa \approx 0.006$), typically no vibrational modes are observed in the spectral range and the real part of the refractive index is almost constant over the spectral bandwidth used in typical instruments and hence $\hat{n}(\omega)$ can be approximated by its average real part n as the propagation term P can be neglected:

$$P_1(d) = \exp\left(\frac{-i\omega\tilde{n}_1d}{c}\right) \quad (5.12)$$

Here c is the speed of light in vacuum and d is the thickness of the coating layer.

It is possible to calculate the amplitude of any subsequent reflections below the surface analytically, however the expressions start becoming increasingly more

complex. For example the amplitude from the coating/core interface in a single layer coated tablet is

$$E_{\otimes} = -\frac{4n_1(n_1 - n_2)}{(1 + n_1)^2(n_1 + n_2)}, \quad (5.13)$$

and further layers can be included in a similar fashion. To facilitate the calculation it is far easier to describe this by matrix algebra and suitable 1-D propagation methods have been described in the literature (Shen and Taday 2008; Su et al. 2014).

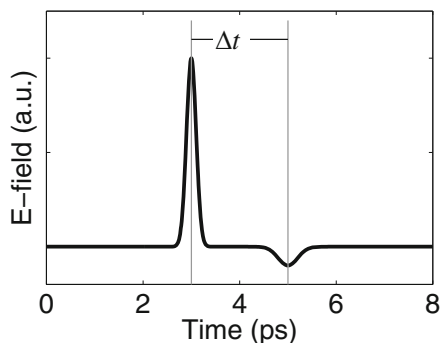
Using the real part of the refractive index n of the material the thickness of the coating layer can then be extracted from the measurement of the time-of-flight, Δt (Fig. 5.12):

$$d_{\text{TPI}} = \frac{\Delta t c}{2n}. \quad (5.14)$$

Apart from the assumption that absorption from the polymer coating is negligible the other simplification that is typically made in the analysis of the terahertz waveform is to assume that the reflection occurs at normal angle to the sample surface from a beam that can be described by a plane wave. In all of the commercially available TPI systems this is not true and most commonly the reflection angle is about 30° to the normal and a short focal length is used to achieve tight focusing and minimal interaction with the atmosphere. However, given the small coating thickness (typically $\ll 200 \mu\text{m}$ and at most a few hundreds of micrometer thick) these approximations do not result in significant errors.

The only variable that needs to be calibrated in order to obtain an absolute thickness of the coating structure is the refractive index of each polymer layer. Russe et al. showed that the refractive index is independent of the coating thickness and varies between values of 1.5 and 2.1 for typical coating formulations, depending on pigment content. The exact value can be determined either using THz-TDS or by calibration with an independent technique such as X-ray microtomography (Russe et al. 2012). It was also demonstrated that small

Fig. 5.12 The thickness of the structure that the pulse propagated through can be extracted using the time-of-flight between reflections together using Eq. (5.14)



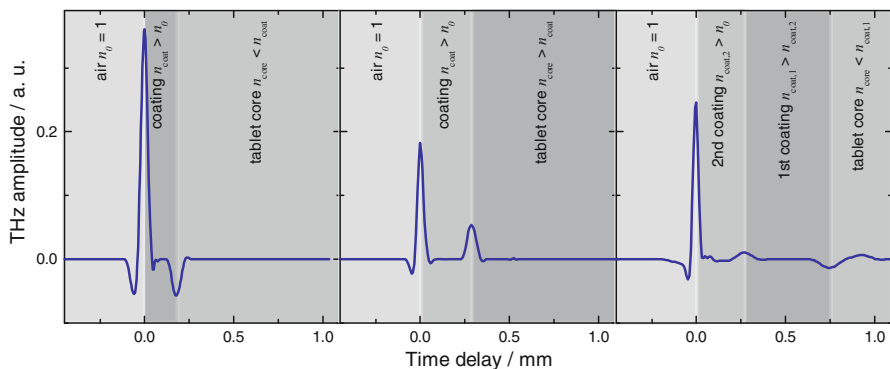


Fig. 5.13 Terahertz time-domain waveforms after signal processing of three samples of coated pharmaceutical tablets. The first two samples are coated with a single polymer layer. The first reflection is due to the interface between free space (air $n_0 = 1$) and the polymer coating. The second reflection originates from the interface between the polymer coating and the tablet core. In the sample on the left the refractive index on the coating material, n_{coat} , is higher than the refractive index of the tablet core, n_{core} , and hence a negative peak is observed. The opposite is the case for the sample in the centre. Here, $n_{\text{coat}} < n_{\text{core}}$, resulting in a second positive peak. In the third sample (*right*) there are two coating layers on top of one another. The first layer which is coated directly onto the core has a higher refractive index compared to the outermost second layer (modified from Zeitler and Shen 2012)

variations in water content in the coating material have negligible influence on the absolute value of its refractive index (Niwa et al. 2014).

In Fig. 5.13 three examples of TPI reflected waveforms are shown to illustrate the reflections that can be observed for a range of coating systems and to highlight the fact that both positive and negative reflection peaks can occur as well as the fact that the technique is able to resolve multiple layer structures in the same measurement.

Other properties that can be derived from the TPI measurement are the surface reflection peak intensity (also referred to as terahertz electric field peak strength, TEFPS) which is defined as the magnitude of the reflection coefficient from the tablet surface relative to the reference reflection from a mirror:

$$\text{TEFPS} = \frac{r_{01}}{E_0} \times 100\%. \quad (5.15)$$

The interface index (TII) is defined as the magnitude of the reflection coefficient from the interface between the coating and the inner tablet normalised to the reflection coefficient from the interface between the coating and the surface:

$$\text{TII} = \frac{E_{\otimes}}{r_{01}} \times 100\%, \quad (5.16)$$

where TEFPS is the peak intensity, E_0 is the amplitude of the reference incident terahertz pulse, TII is the terahertz interface index. Both parameters are strongly

affected by the refractive index of the tablet coating layer and can be used to provide information on relative coating density over the surface of the tablet (Ho et al. 2010; May et al. 2013). The interface index may also denote the changes in the physicochemical properties at the interface between the coating and the inner tablet.

3.2 *Instrumentation*

There are currently two imaging systems on the market that are specifically designed to image pharmaceutical dosage forms. Figure 5.23 shows the schematic diagram of a typical TPI system (in this case the TPI imaga 2000, TeraView Ltd., Cambridge, UK).

In TPI measurements, the transient electric field of the terahertz pulses is recorded as a function of the time delay between the terahertz pulse and the optical probe pulse. By sweeping the optical delay using a rapid variable delay stage, the entire terahertz waveform can be measured in less than 10 ms. Recent advances in laser technology have made it possible to further reduce the measurement acquisition time by employing a second laser the phase of which can be controlled electronically to time-gate the detector hence removing the need of a mechanical delay line. In such systems data acquisition rates of less than 1 ms are routinely possible (Figs. 5.14 and 5.15).

To acquire a TPI map of a tablet the terahertz waveforms are measured at 200 μm steps over the entire surface of a sample. There are currently no array detectors for TPI measurements and hence the maps have to be acquired by point mapping over the surface of the object of interest. Most pharmaceutical tablets have curved surfaces and, hence, a precise model of the surface shape and curvature of the tablet under investigation is the prerequisite for a reliable and quantitative TPI measurement. Such a topological surface model can be obtained in a fully automated measurement before the terahertz map is acquired by using a laser gauge that operates with a visible laser beam (Zeitler et al. 2007b). This model is subsequently used to present the tablet sample to the terahertz optics and keeping the tablet precisely at the focal position with sample surface always perpendicular to the terahertz sensor (Shen and Taday 2008). Consequently, no sample preparation is required and most pharmaceutical solid dosage forms with common shapes and surface curvatures can be directly imaged using this type of instrument (Zeitler et al. 2007b).

3.3 *Film Coating*

Out of all the work that has focused on applications of TPI in the pharmaceutical literature investigations into the integrity and uniformity of film coating structures

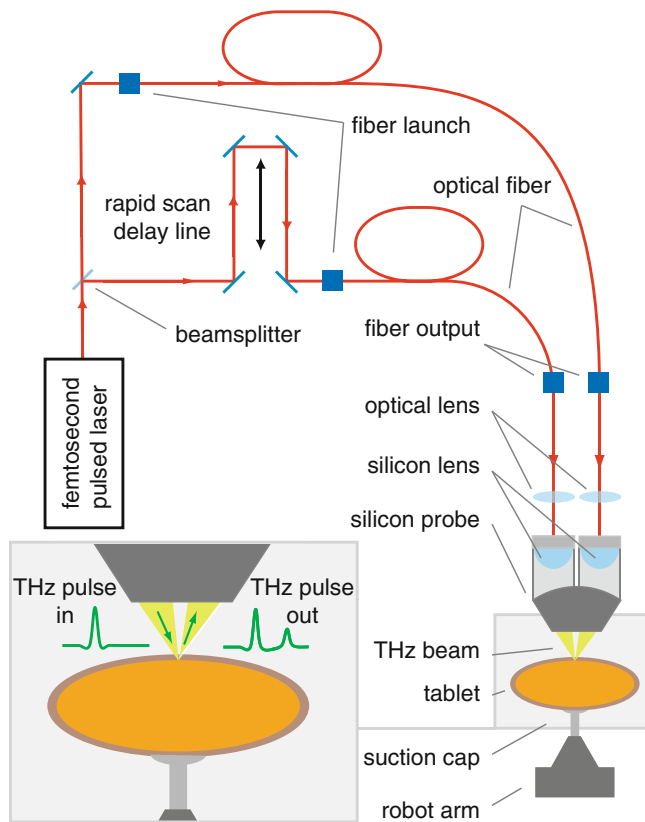


Fig. 5.14 Schematic diagram of a typical terahertz imaging setup used to image pharmaceutical tablets. The tablet samples are manipulated using a six-axis robotic arm. The system is capable of automatically point mapping over the entire surface of an arbitrarily shaped tablet. This configuration is utilised in the TPI imaga 2000 instrument by TeraView Ltd. (modified from Zeitler et al. 2007b)

clearly dominate. For such coating characterisation the TPI technique has significant advantages compared to competing technologies:

- TPI is non-destructive: optical microscopy requires samples to be microtomed; techniques such as laser induced breakdown spectroscopy locally destroy the sample (Brock et al. 2012).
- TPI provides excellent contrast between the different coating structures even when the coating layers are transparent and even if the differences in refractive indices between the layers are quite subtle. The lack of contrast is one of the disadvantages of X-ray microtomography ($X\mu$ CT) (Russe et al. 2012).
- Given TPI operates at such long wavelength (mm to hundreds of micrometers) scattering from particles (e.g. pigment) or air bubbles in the coating structure as well as from the tablet core is negligible and therefore the contrast between layers is not blurred and it is possible to measure structures deep below the

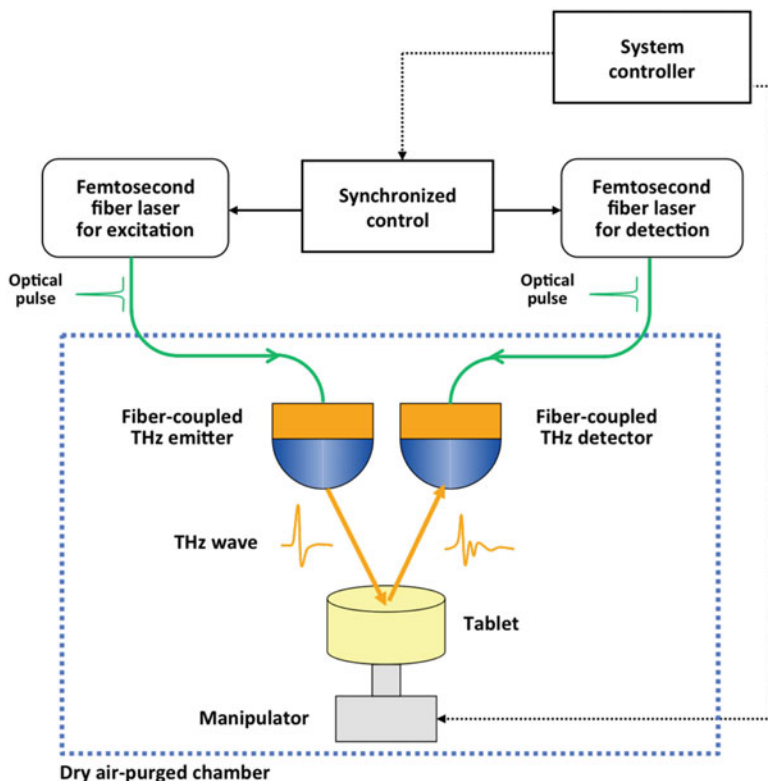


Fig. 5.15 Alternative design for TPI instrumentation that deploys a second ultrafast laser instead of a mechanical delay line for the time-gated detection of the terahertz pulse. This configuration is employed by the TAS7500IM instrument by Advantest Inc.

surface of a tablet. Scattering is the major limitation of optical coherence tomography (OCT) when applied to pharmaceutical coatings in particular when pigments are present in the coating layer.

- The image acquisition is relatively fast for an entire tablet (tens of minutes); signal processing is instantaneous and not computationally demanding. This is in contrast to X μ CT where acquisition and data processing takes hours.
- The TPI measurement is a direct measurement of the coating structure and not an indirect technique such as other spectroscopic imaging methods (NIR, Raman), where a change in spectral intensity needs to be calibrated into a coating thickness by means of chemometric models.
- Due to the implementation of the point mapping measurement where the tablet is always at focus and normal to the optics there are no aberrations and intensity fluctuations over the tablet surface as often the case in global imaging methods such as NIR imaging (Maurer and Leuenberger 2009).

- Using TPI it is possible to measure very thick coating structures ($\gg 100 \mu\text{m}$) as terahertz radiation can penetrate the coating material easily. This is a major limitation for OCT as well as NIR and Raman spectroscopy/imaging techniques, where penetration is limited to much thinner structures.

However, like with all methods there are of course also significant limitations of the TPI technique. Some of the disadvantages are:

- It is not possible to measure the coating structures at any tablet features that exhibit strong local curvature such as sharp edges at the crown of the tablet or in embossings (Brock et al. 2013a). Such structures can be much better resolved with X μ CT.
- The internal volume of the sample cannot be fully resolved and the spatial resolution is decreasing the deeper within the sample the measurement originates from. This is largely due to the optics used for TPI measurements, which is optimised to resolve relatively thin structures near the surface of the sample. Again X μ CT is a very good method to analyse such structures, as is magnetic resonance imaging (Zeitler and Gladden 2009).
- Coating structures with a thickness of less than $35 \mu\text{m}$ cannot be easily resolved as the measurement requires the two reflection peaks to be well resolved in the time-domain. It is possible to use advanced data extraction techniques for this purpose but this requires further calibration of the measurement (Ho et al. 2009a; Su et al. 2014). OCT techniques are much better suited for such thin structures (Zhong et al. 2011).
- Due to the long wavelength of terahertz radiation the TPI technique is difficult to perform for coated pellets. Only pellets of sufficiently large dimensions ($>500 \mu\text{m}$) can be measured reliably. OCT typically operates at NIR frequencies and can readily image much smaller pellets (Li et al. 2014)

3.3.1 Coating Uniformity

Figure 5.16 shows an example of how the TPI measurement can be used to investigate the coating uniformity during a film coating process. At regular intervals during the coating operation samples were removed from the coating pan and analysed using TPI. The resulting coating maps show the spatial distribution of the coating layer thickness over the surface of the tablets. The thickness distribution can be summarised by histogram plots and the results show that in this process good uniformity was achieved for each tablet. This method is an ideal tool for formulation and process development (Ho et al. 2009b).

In a further study TPI was compared to NIR imaging to resolve the layer thickness growth during a film coating process (Maurer and Leuenberger 2009). The NIR and TPI results were in good agreement and the authors pointed out that due to the low power of the TPI sensor the terahertz measurement did not cause any temperature increase in the sample, which is advantageous as heating the coating

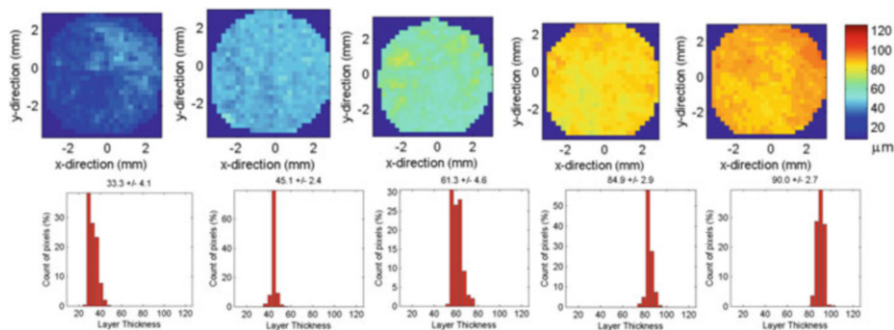


Fig. 5.16 TPI maps of the thickness distribution over the surface of biconvex tablets with process time. The tablets were sampled during the process and measured off-line. Coating process times are from left to right: 1, 2, 3, 4 and 5 h

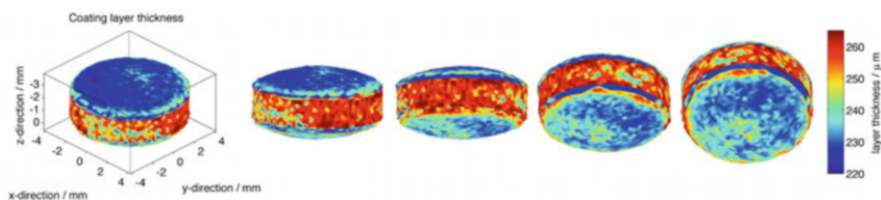


Fig. 5.17 Coating thickness distribution over all surfaces of a biconvex tablet (modified from Zeitler and Shen 2012)

during the measurement might lead to changes in its structure through curing, which could occur during the NIR measurements.

In spite of this excellent uniformity on the convex surfaces of the tablet it is very important to also consider the influence of the tablet geometry on the relative coating thickness distribution. Figure 5.17 highlights a commonly encountered situation where the centre band area of a biconvex tablet exhibits a significantly different amount of coating compared to the top and bottom surfaces. This behaviour can easily be explained by the relative exposure times and frequencies of these surfaces in the spray zone of the coating pan but it elegantly highlights the shortcoming of applying simplistic quality metrics such as weight gain to monitor and control the film coating process. While the thickness of the centre band is very often thinner compared to the top and bottom surface, this is not always the case as illustrated in Fig. 5.17, as the mechanical forces during the coating operation vary significantly depending on process scale and it hence can be possible for low density thick coating structures to form around the crown of the tablet during small scale coating or at low pan load (Ho et al. 2008).

As demonstrated by Ho et al. it is possible to detect a range of coating defects using TPI, both defects that are visible on the surface of the tablet and ones that extend far deeper into the coating and/or tablet core (Ho et al. 2007). This was confirmed in a later study by resolving cracks in the coating structure between

neighbouring parts of embossings (Maurer and Leuenberger 2009). Niwa and Hiraishi further highlighted how TPI can be used to resolve surface defects following film coating of tablets (Niwa and Hiraishi 2014). Using the TPI technique it was possible to spatially resolve areas with high surface roughness on the tablet faces and quantify their extend. Given the relatively long wavelength of the terahertz technique this application is however somewhat limited to defects of sufficient size and other techniques, including imaging methods at visible frequencies, may well be equally suited to resolve such kind of surface defects.

The TPI technique is also very attractive when analysing thick coating structures that would be difficult to penetrate using other sensing modalities. This effect was highlighted in a recent study by Vynckier et al. where TPI was used to analyse the thickness of a drug-loaded polymer layer that was co-extruded with a tablet shaped modified release core to form a monolithic drug delivery system using the process of calendering (Vynckier et al. 2015). Not only was it possible to measure the coating thickness ($>400\ \mu\text{m}$) but it was also possible to measure the presence of an air gap between the structures where delamination occurred as well as quantify its thickness.

3.3.2 Functional Coatings

For simple cosmetic coatings it does not matter too much whether the relative thickness varies over the surface of a tablet as long as all surfaces have a coating that exceeds a minimum thickness which provides the desired colour and gloss characteristics. This can even be true for some functional coatings: as long as no holes in the coating are present and a minimum thickness has formed that is sufficient to act as a barrier the absolute thickness of an enteric coating layer is not critical for its function (Spencer et al. 2008); the same is true also for moisture barrier coatings (Zhang et al. 2013) and probably also for light protective layers. The situation is however radically different when the coating acts as a diffusion barrier for sustained release applications or if it contains an active pharmaceutical ingredient (API) and hence has to comply with strict content uniformity requirements.

One type of formulations where active diffusion membranes are applied to the dosage form is the push-pull osmotic system (PPOS) where a semi-permeable coating is used to allow selective mass transport of water into the tablet core due to typically high salt concentration in the tablet core. The solubilised drug dispersion is then released through a small hole that is applied into the diffusion membrane after the coating process. Small variations in the mean coating thickness of the diffusion membrane were shown to directly correlate with the drug release characteristics of such dosage forms (Malaterre et al. 2009).

In active coating content uniformity is typically analysed by destructive and time consuming high performance liquid chromatography (HPLC) assays combined with dissolution testing. This traditional quality control method is accurate and precise but can only be applied to a limited number of samples per coating batch

due to its destructive nature and the cost and time associated with it. Brock et al. showed that TPI can be developed into a suitable non-destructive quality control technique to reliably quantify the API content of active coating (Brock et al. 2012). An additional advantage is that for each sample the TPI measurement takes less than one hour, which is typically less than the HPLC method given the significant sample preparation time and prior drug dissolution.

TPI is an excellent tool to help with the development of a coating process and finding the best process parameters to operate the coater with. In combination with a design of experiment (DoE) the TPI measurements can provide much more insight into the effect of the process variables on the quality and characteristics of the coated product than other surrogate parameters such as the coating weight gain. As demonstrated by Brock et al. this information can be applied to find the best process conditions to ensure good intra-tablet coating uniformity (Brock et al. 2013b) while also keeping the inter-tablet uniformity as well controlled as possible (Brock et al. 2014) (Fig. 5.18).

The coating thickness measurements were found to correlate directly to the API content of the coating material as determined by HPLC analysis for the tablets that had been coated with an active coating (Fig. 5.19). By replacing slow and expensive routine HPLC assays with TPI measurements a clear opportunity has emerged to save time and cost in the coating development process. The TPI method is not capable of providing the same information as the HPLC method can in terms of providing an impurity profile and resolving other chemical constituents but if the aim in routine end product quality testing to release a batch of tablets is to determine content uniformity the dissolution test and associated HPLC method could be replaced by TPI testing, in which case it would be even possible to test a much larger number of tablets per batch to build up even better confidence in the coating quality.

The general applicability of the TPI method was further confirmed in a study by Niwa, Hiraishi and Terada on the impact of the process conditions on the coating

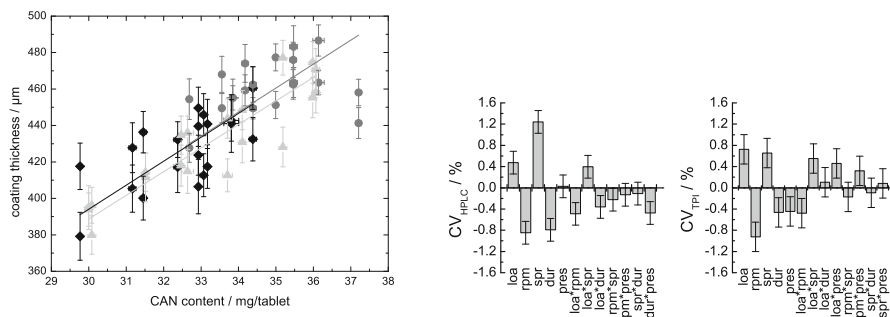


Fig. 5.18 Correlation of the drug content in the active coating layer with the layer thickness as measured by TPI (*left*); and coefficient plots for the analysis of a 2^{5-1} design of experiments for the active coating process at pilot scale. The y-axis represents the coefficient of variation of the respective property (modified from Brock et al. 2014)

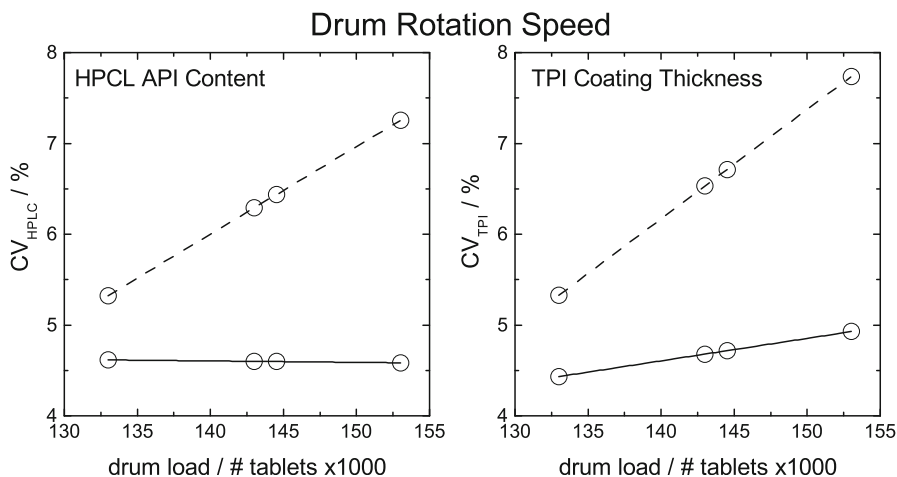


Fig. 5.19 Interaction of drum load with drum rotation speed in the HPLC (*left*) and TPI model (*right*). *Dashed line*: low factor level, *solid line*: high factor level (modified from Brock et al. 2014)

properties of enteric coatings, where the terahertz coating maps were directly compared to virtual cross-sections through the coatings as measured by X μ CT (Niwa et al. 2014).

Beyond using TPI in combination with DoE coating runs to explore the effect of coating process variable on the coating quality it is also possible to utilise computer simulations to develop a better process understanding and validate the theoretical results of such simulations using TPI experiments. Freireich et al. recently presented a new method based on discrete element modelling (DEM) together with two additional methods to perform the coating step onto the tablets following the DEM simulation (Freireich et al. 2015). These two methods account for the influence of the shadowing by neighbouring tablets to the simulated spray and the simulation is able to resolve the intra-tablet coating uniformity for a range of different tablet shapes. For all samples the tablet top and bottom surfaces were found to have thicker coatings than the centre bands. The experimental coating data displayed similar features as those found in the simulations (Fig. 5.20). The observed coating thickness distribution is consistent with the concept that the more readily a tablet can roll on the tablet bed in the coater and expose its surfaces to the spray, the more uniformly coated it will be. It is important to note that although randomly selected tablets from the DEM simulations displayed similar coating distributions with respect to the centre band vs. the other tablet surfaces, the coating distribution on an individual tablet can vary significantly from the coating thickness distribution averaged over all of the tablets (top row in Fig. 5.20). Hence, a large number of tablets needs to be sampled and averaged to estimate a meaningful statistics of the population.

Another type of coating structure that can be analysed by TPI is the diffusion barrier membrane in sustained release coatings. Here the thickness and porosity of

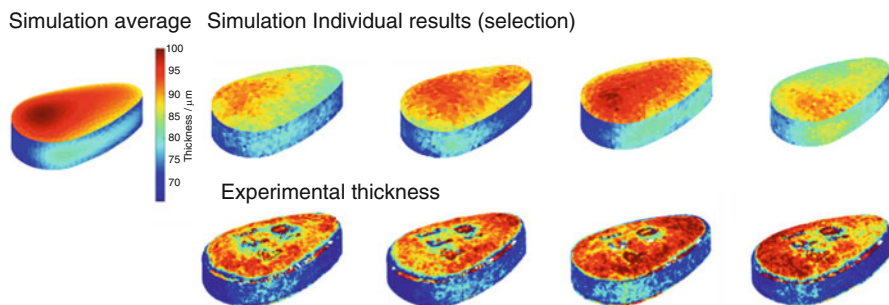


Fig. 5.20 Intra-tablet coating thickness distribution modelled by computer simulation (*top*). The average coating thickness distribution based on 770 tablets is plotted on the top left, while the coating distributions for four tablets chosen randomly in the DEM simulation after 1800 s process time are plotted on the right. The experimental TPI measurements of four samples also removed at 1800 s process time are shown for comparison (*bottom*) (modified from Freireich et al. 2015)

the coating is of critical importance for the release rate of the API which is contained in the tablet core. Ho et al. demonstrated that TPI has similar predictive power to dissolution testing for such structures which is very attractive given the long release periods that need to be tested by dissolution experiments for such sustained release formulations (drug release is designed to take place over days) (Ho et al. 2008, 2009a). Using multivariate calibration that is able to resolve the reflection peak from the coating/core interface even for very thin layers where the reflection is merged into the surface reflection it was possible to develop a quantitative model that could be used to predict the mean dissolution time (MDT) of a coated sustained release formulation (Fig. 5.21).

In addition to the potential to speed up quality testing of the finished coated product the TPI method also has merit to better understand the changes in coating microstructure during scale-up operations. At the example of the sustained release coatings discussed above Ho et al. showed that both TEFPS and coating layer thickness measured by TPI showed better correlation with the MDT for batches coated under different process conditions compared to the weight gain (Fig. 5.22). In this experiment two batches were coated with the same nominal polymer weight gain, one at lab scale and the other at pilot scale. The TPI measurements revealed that the pilot scale samples released slower but exhibited a thinner, more dense coating layer as the mechanical force on the coating was significantly larger at pilot scale compared to the lab scale process. The thicker, more porous coating that was formed at lab scale conditions allowed for faster diffusion and hence faster mass transport and faster drug release.

A similar effect was found when comparing different types of coating equipment at the same process scale. Haaser et al. showed that the coating structure of tablets coated in a pan coater was different to that of the same tablet cores being coated in a fluid bed, even though the tablet cores and the coating formulation was identical (Haaser et al. 2013). This difference in coating structure as characterised by the layer thickness and the interface index (TII, Eq. (5.16)) resulted in significant

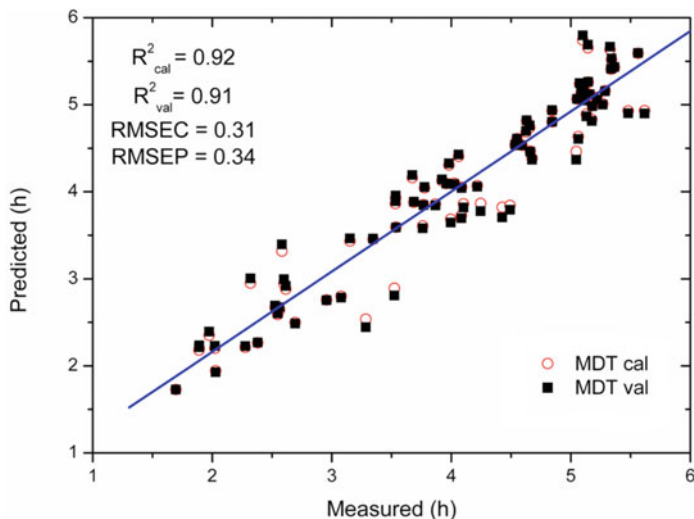


Fig. 5.21 Measured versus predicted MDT based on the multivariate calibration model of the terahertz time-domain waveforms. Both calibration and validation data points are presented here (modified from Ho et al. 2009a)

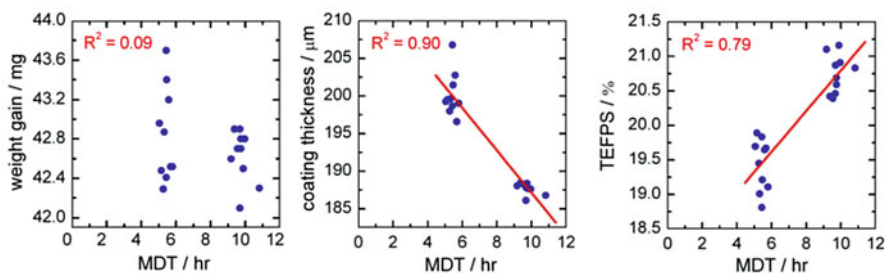


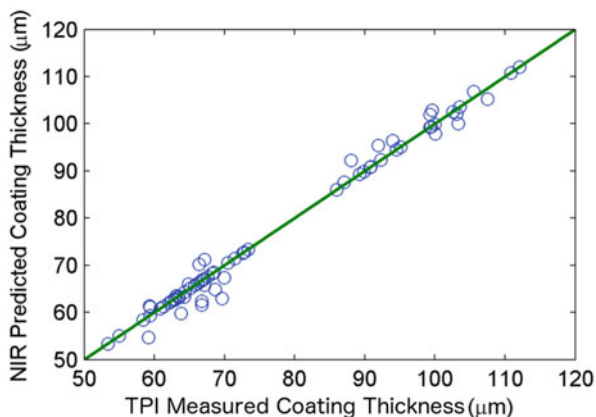
Fig. 5.22 Corellation of the mean dissolution time (MDT) with the weight gain of polymer that was coated, the coating layer thickness and TEFPS as measured by TPI. The red trendline is plotted as a guide for the eye (modified from Ho et al. 2008)

differences in drug release from the API in the tablet core. Again, the coating layer was designed to act as a diffusion barrier and the changes in drug release kinetics were attributed to the effects that the differences in mass and heat transfer as well as mechanical stress that are specific to the type of coating process had on the resulting coating microstructure.

3.3.3 Calibration of Process Sensors

The advantage of being able to measure absolute coating thickness following minimal calibration requirements of measuring the refractive index of the coating

Fig. 5.23 TPI can be used to accurately measure the coating thickness on tablets over a range of thicknesses to build an NIR calibration dataset for quantitative multivariate analysis (modified from Zhong et al. 2010)



material, makes TPI an attractive reference method for the calibration of spectroscopic in-line sensors such as NIR or Raman fibre coupled probes that are more robust and less expensive compared to TPI.

Although frequently used for process control of film coating operations NIR and Raman sensors cannot directly measure the coating thickness of a tablet. In such measurements the thickness of the coating layer is inferred by the change in spectral signatures that are either unique to the coating or to the core: e.g. as the intensity of vibrational modes that are unique to the API in the tablet core decreases the polymer film that covers that tablet surface increases. This information is used to build an indirect chemometric model which would typically be used to calibrate the spectral signature against polymer weight gain based on a training data set that is measured using a set of coated tablets with varying weight gain. Using TPI the calibration can be made directly against coating thickness rather than the surrogate parameter weight gain. This concept has been demonstrated for both NIR (Zhong et al. 2010; Gendre et al. 2011) and Raman (Müller et al. 2012) sensors and it has been shown to significantly reduce the number of samples required as well as the model development time.

Using the coating thickness measured by TPI is a far more accurate variable to calibrate the chemometric models against compared to the variation in tablet core weight as it is very difficult to provide meaningful weight gain parameters for thin coating layers where the polymer weight gain is similar to the variation in tablet core mass. For thin samples, where the TPI is limited by its minimum thickness resolution, OCT is an excellent technique and the combination of OCT and TPI is very promising to cover the entire range of coating thickness for calibration (Zhong et al. 2011).

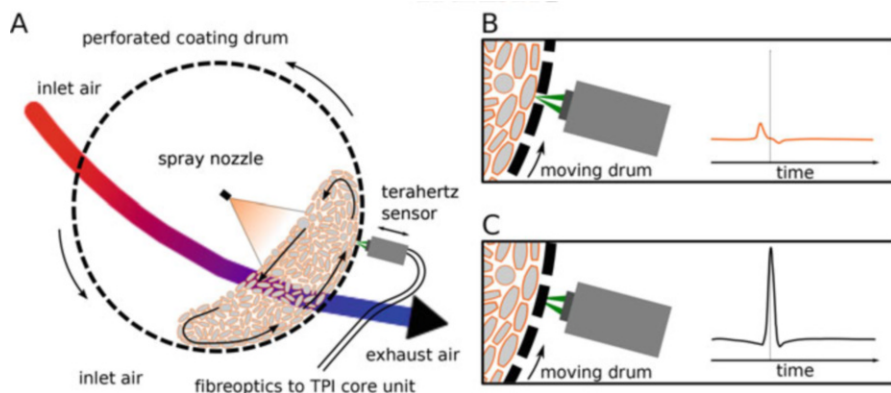


Fig. 5.24 (a) Schematic diagram of the pan coater fitted with the terahertz coating sensor, (b) successful terahertz measurement of the coating thickness of a tablet in the coating pan through a single hole of the drum mesh and (c) measurement of a reference reflection from the mesh. The terahertz pulse is shifted in phase and is much larger in amplitude allowing an easy discrimination between the reference waveforms from the drum mesh and the coating measurements from the tablets in the coater (modified from May et al. 2011)

3.3.4 In-Line Sensing

As discussed previously in this section, while a high resolution surface map of an entire tablet takes tens of minutes to acquire, one single TPI time-domain reflection waveform can be measured in less than 10 ms. This fast acquisition rate can be exploited to measure the coating thickness of individual randomly moving tablets in a perforated pan coater by placing a TPI sensor on the outside of the drum and measuring through its perforation (Fig. 5.24) (May et al. 2011).

The sensor measures a continuous stream of reflected waveforms, each one acquired in less than 10 ms. From this data stream the waveforms that correspond to reflections from tablets that are in focus and oriented normal to the TPI sensor ('tablet hits') are identified using a selection algorithm. The process is facilitated by the unique reflection characteristics that can be defined for each 'hit' in terms of peak position, width and intensity amongst other parameters (Fig. 5.25). Even though the majority of the tablets will align themselves with their face to the drum wall the hit rate for this algorithm is low, yet sufficient to measure the inter-tablet coating thickness distribution in the pan. During 10 min measurement time about 72,000 THz waveforms are collected of which there are 200-300 hits, corresponding to a hit rate of less than 5 %, as identified using very conservative criteria for the waveform selection algorithm. Using the tablet thickness measurements of hundreds of tablets makes it possible to derive meaningful statistics of the coating thickness distribution within the coater in real time while the process is in progress.

The TPI in-line measurements that were acquired during the coating process of a batch of 150 kg of tablets revealed that the inter-tablet coating thickness

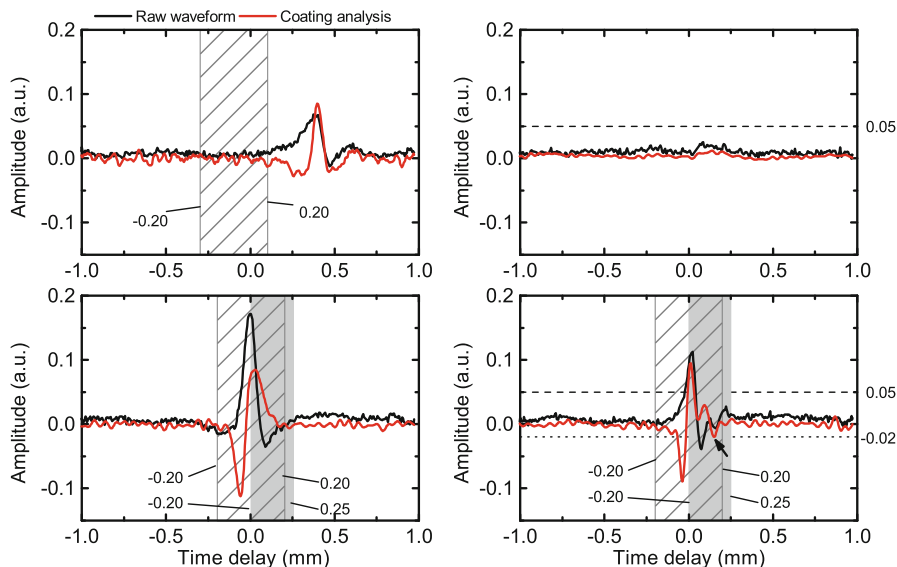


Fig. 5.25 Real-time signal processing for in-line TPI sensing. Examples of three rejected waveforms (a–c) and one accepted waveform (d). Reflection outside the primary pulse position range (a), the primary pulse amplitude range (b) and the secondary pulse amplitude range (c), and an accepted waveform that satisfies all these criteria (d) with an arrow highlighting the coating/core interface (modified from Lin et al. 2015)

distribution within the coating pan is much wider than would be expected based on the off-line analysis of the sample that was removed from the pan during the same period. Based on the off-line measurement of more than 20 tablets the operator would assume a relatively tight distribution of coating thickness for the tablet population in the coater ($\approx \pm 20\%$) while the in-line sensor clearly demonstrates that the actual distribution shows a variation of $> \pm 100\%$ (Fig. 5.26).

The TPI in-line sensor measurements are acquired using a prototype sensor and currently this technology is not yet available commercially. However, the results highlight the potential for this technology to improve the understanding of film coating, a very complex process that is presently dominated by empirical control strategies.

3.4 Chemical Imaging

Given the unique combination of spectral signatures that can be investigated using THz-TDS (see Sect. 2) and the ability to penetrate pharmaceutical excipients and resolve structures at depth, it is only natural to try and combine both approaches for depth resolved hyperspectral imaging. The principle of a basic two-dimensional chemical mapping analysis was demonstrated by Shen et al. (2005b) and more

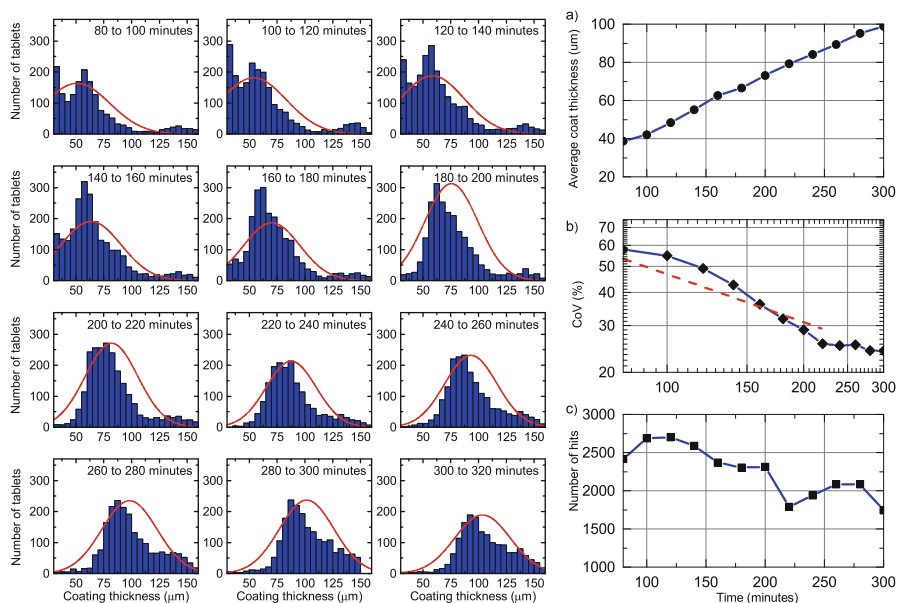


Fig. 5.26 *Left*: histogram of tablet coating thicknesses inside a production scale coating during operation. The large thickness values ($>150 \mu\text{m}$) acquired do not represent reliable measurements and are artefacts due to relaxed acceptance criteria. Baffles were removed from the coater after 200 min process time. *Right*: corresponding mean (a), inter-tablet variability (b), and number of tablet hits (c). Lines are plotted to guide the eye (modified from Lin et al. 2015)

advanced depth resolved three-dimensional datasets were introduced shortly afterwards by the same group (Shen et al. 2005a). The concept was further refined using model pharmaceutical compacts of simple geometry to show the ability to spatially resolve different chemical entities (Cogdill et al. 2006). Using a transmission setup the method was also demonstrated to be able to locate a fraction of cocrystal in a polyethylene matrix (Charron et al. 2013). Apart from tablets TPI was used in the pharmaceutical context to investigate the homogeneity of API in transdermal patches (Sakamoto et al. 2009).

By combining the ability of THz-TDS to quantify different solid-state modifications as discussed in Sect. 2.3.2 with mapping tablets in transmission Ajito et al. used terahertz imaging to show the distribution of different formulation ingredients and their homogeneity (Fig. 5.27) (Ajito et al. 2014).

The same concept can also be used to follow phase transitions in tablets. In a proof-of-principle study Hisazumi et al. used theophylline prepared into tablets by mixing with microcrystalline cellulose and magnesium stearate to demonstrate how the moisture induced transformation from the anhydrous form to the hydrate and back can be monitored using terahertz imaging (Fig. 5.28) (Hisazumi et al. 2012a).

It was also demonstrated that spectral information can be extracted in reflection imaging from buried layers or structures within tablets even if they are coated (Takeuchi et al. 2014).

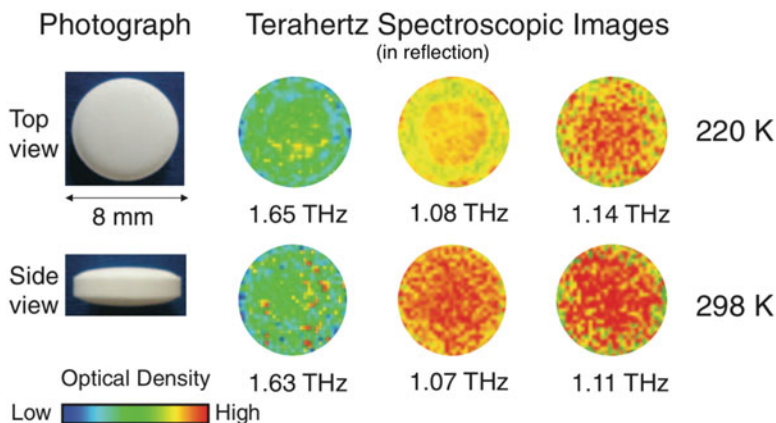


Fig. 5.27 Temperature-dependent THz-TDS transmission images of a commercial tablet containing 10 mg of famotidine. The peaks at 1.65, 1.08, and 1.14 THz, measured at 220 K correspond to famotidine polymorphic form A, form B, and D-mannitol, respectively (modified from Ajito et al. 2014)

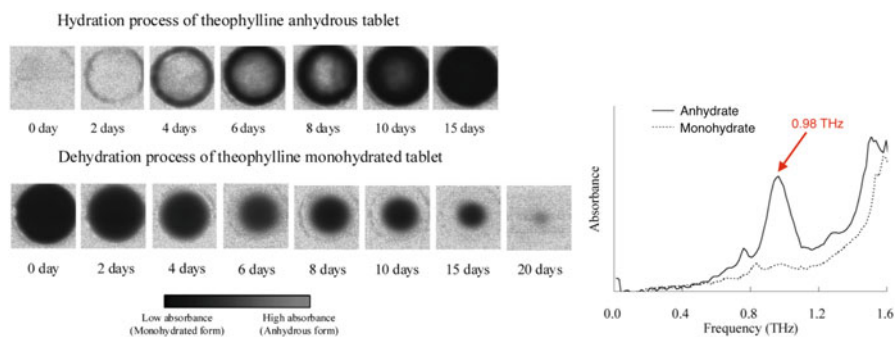


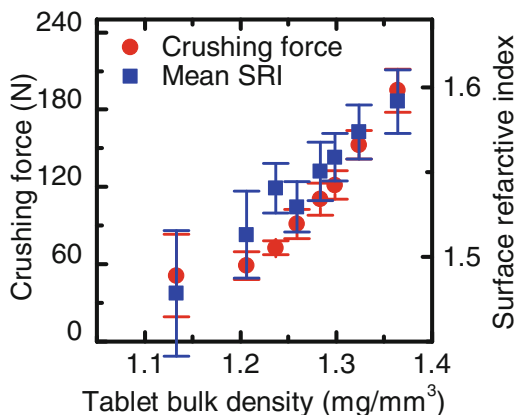
Fig. 5.28 Chemical mapping in transmission at 0.98 THz for theophylline in the tablets during storage (*left*). The strong spectral feature at 0.98 THz corresponds to the anhydrate form (*right*) and it is possible to resolve the solid state transformation process over time as the sample gets hydrate and dehydrated (modified from Hisazumi et al. 2012a)

3.5 Tablet Microstructure

3.5.1 Tablet Density/Hardness

Apart from measuring the thickness of coating structure and chemical imaging a number of other TPI applications have been reported in recent years. As outlined in the introduction to this section in Eq. (5.10) the amplitude of the first reflection (from the surface of the tablet) is related to the refractive index of the surface.

Fig. 5.29 Average crushing force and surface refractive index (SRI) as functions of bulk density for biconvex lactose tablets prepared by direct compression (modified from May et al. 2013)



This information can be used to estimate the density of flat faced tablets by calibrating the change in amplitude either using univariate or multivariate calibrations models, that can also specifically take into account the spectral components of the refractive index (Palermo et al. 2008).

Using a set of tablets compressed into either flat-faced or biconvex geometries May et al. investigated the applicability of TPI to resolve the subtle changes in refractive index associated with the variation in tablet density resulting from different compaction pressures (May et al. 2013). The results showed a clear correlation between the surface refractive index and the tablet bulk density (Fig. 5.29). It was also shown that the crushing force, i.e. the tablet hardness, can be correlated with the surface refractive index as measured by TPI.

3.5.2 Cracks and Delamination

In addition to investigating structures in the immediate vicinity of the tablet surface such as coatings, surface defects and density it is also possible to investigate structures far below the surface of the dosage form. At the example of a tri-layered tablet it was demonstrated that structures up to 2 mm below the surface of the tablet can be resolved in a standard TPI measurements (Zeitler et al. 2007a, b, c, d). Despite this proven ability to penetrate the tablet matrix this type of analysis is not yet used as commonly compared to film coating analysis. The optics of commercial TPI systems are optimised to resolve thin structures near the surface of the object of interest with the best possible lateral spatial resolution and hence typically the focal length of the optics are short and the terahertz beam is strongly converging.

In recent years the application of advanced imaging modalities that are commonly used at other frequencies such as e.g. three-dimensional synthetic aperture techniques which have been extensively used for radar imaging were demonstrated successfully at terahertz frequencies (Henry et al. 2012). With further development

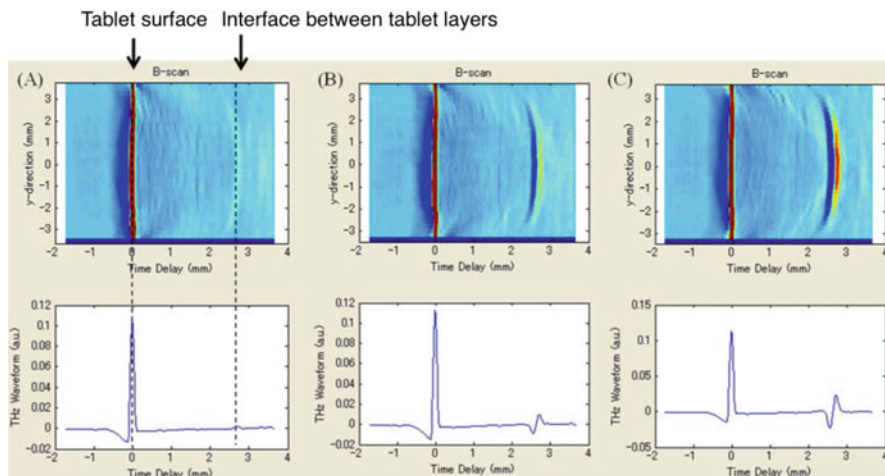


Fig. 5.30 TPI virtual cross sections showing the internal structure of three bi-layer tablets that were compressed under different conditions. Note that the x -axis is in units of time-delay equivalent to a refractive index of $n_{\text{air}} = 1$ (modified from Niwa et al. 2013)

of optimised and automated image reconstruction algorithms for TPI, which might also take scattering into account explicitly, such techniques are set to significantly extend the applications for TPI to resolve the microstructure deep within pharmaceutical dosage forms (Sakamoto et al. 2012), where currently applications are somewhat limited by diffraction and scattering effects.

Even given the present limitations in terms of the missing adaptability of commercially available TPI optics as well as the need for further development of advanced image processing techniques, there are a range of applications beyond coating analysis that can already be realised with the existing technology. Niwa et al. showed how TPI can be used to detect delamination between and the risk of rack formation in bilayered tablets (Niwa et al. 2013). Due to the large difference in refractive index between air ($n_{\text{air}} = 1$) and the tablet matrix ($n_{\text{tablet}} \approx 1.5$) a strong reflection is observed when layers delaminate, i.e. air pockets form at the interface that delaminates or forms a crack (Fig. 5.30). Compared to other reference techniques such as X μ CT the TPI method is much faster and the authors state that the reflection amplitude at the interface can be used to estimate the risk for delamination even in tablets that do not yet exhibit a crack.

3.5.3 Porosity

Besides direct imaging applications where physical or chemical properties of the tablets are resolved in lateral directions there are a number of largely unexplored applications when imaging in axial direction. There have been a number of papers from Peiponen et al. (Juuti et al. 2009; Tuononen et al. 2010a, b; Ervasti et al. 2011;

Bawuah et al. 2014a, b) that have shown the interplay between tablet excipients, their porous matrix and the optical properties in THz-TDS and how such effects can be quantified e.g. using effective medium approximations. Such applications are exciting because of the wealth of physical information that can be extracted from a tablet using a non-destructive transmission measurement. In a single measurement it is possible to quantify the porosity, weight and potential drug content of a tablet and given a large volume of the tablet is sampled the results are representative of the bulk behaviour of the sample. This opens a range of potential applications for process analytical technology (PAT) applications given the high penetrative power of terahertz radiation and the short measurements duration (milliseconds) required for transmission measurements that could complement the presently used destructive weight/thickness/hardness measurements following tablet compaction.

In a recent paper Peiponen et al. developed this concept further and highlighted the possibility of directly extracting mechanical properties from a tablet transmission measurement (Peiponen et al. 2015). By determining the tablet porosity it is then possible to use well established power law relationships to determine the corresponding Young's modulus of the tablet sample under investigation.

3.5.4 Disintegration Testing

It is possible to combine the ability of terahertz radiation to penetrate deep into pharmaceutical tablets with the high temporal resolution of the measurement as well as the high contrast that can be achieved with TPI (Yassin et al. 2015a, b). At the example of rapidly disintegrating oral formulations and a specially designed flow-loop it was demonstrated that TPI can be used to investigate the mass transport of dissolution medium within the tablet matrix by one-dimensional imaging experiments (Yassin et al. 2015a). The terahertz pulse exhibits reflections from the tablet surface as well as from the penetrating liquid front (Fig. 5.31). The TPI data can then be analysed to extract the position of the penetration front within the tablet as well as its swelling characteristics upon contact with dissolution medium.

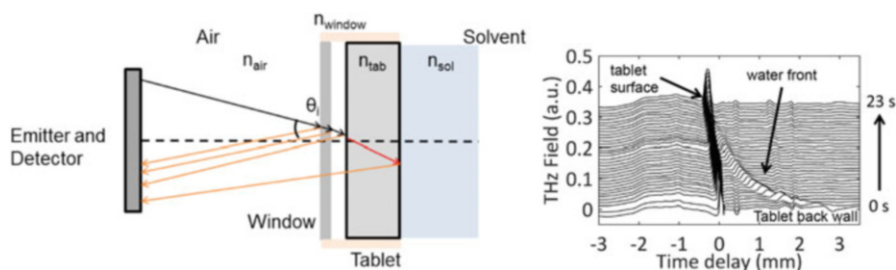


Fig. 5.31 Measurement principle (*left*) and example of penetration of water into a 1.5 mm thick matrix of microcrystalline cellulose (MCC) at 10% porosity (*left*). There is a clear peak at the interface between the wetted and unwanted MCC and the mass transport characteristics in the matrix can be extracted using the position of the peak over time (unpublished results)

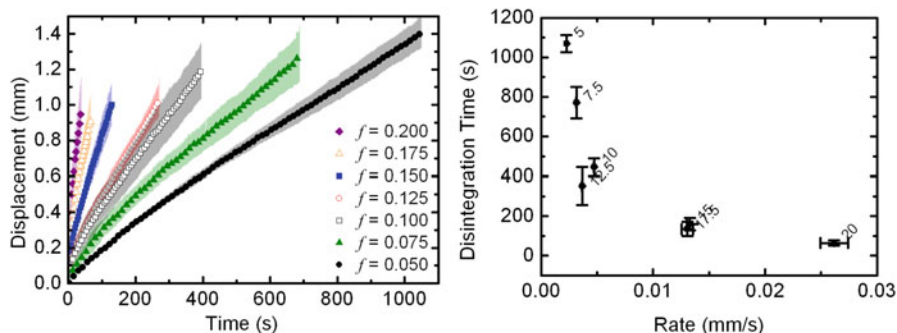


Fig. 5.32 Water penetration into MCC tablets of varying porosity (*left*) and corresponding disintegration times as a function of the liquid ingress rate (*right*). The data points are labelled by their corresponding porosity (unpublished results)

By systematically varying the formulation (filler, disintegrants, lubricants) as well as the microstructure (porosity, compaction characteristics, particle size) it is possible to use the TPI technique to develop a fundamental understanding of the tablet disintegration process (Fig. 5.32). The TPI method makes it possible to complement the previously developed swelling analysis and models (Lowenthal 1972; Dees 1980; Julian Quodbach and Kleinebudde 2015) and develop mathematical models of the process which in turn will allow for rational design of disintegration behaviour.

4 Conclusions

Terahertz technology has been applied to a wide range of applications in the pharmaceutical sciences over the past decade. Even though still in its infancy the technology has demonstrated a clear potential to help with the understanding of fundamental processes that are of critical importance for the stability and performance of modern medicines.

The unique ability of terahertz radiation to study the weak molecular interactions in hydrogen bonding systems make terahertz spectroscopy an ideal probe to resolve the structures and dynamics of drug molecules as well as the interplay between drug molecules and excipients. As a spectroscopic technique THz-TDS is much faster compared to crystallography measurements and is hence particularly suited for in situ measurements, though of course it cannot provide the full crystallographic information such as the unit cell structure albeit its high sensitivity to crystallographic properties.

For imaging applications TPI stands out as a technology that combined sufficiently high spatial resolutions (in particle in depth) with high penetrative power that gives unparalleled insights into the microstructure of a dosage form well

beyond its coating. Future developments will undoubtedly lead to more affordable and more robust instrumentation together with better understanding how to interpret the complex vibrational spectra at terahertz frequencies as well as further enhancements in image reconstruction at depth and better ways to resolve chemical information from structures embedded in the dosage forms.

References

- Ajito K, Kim JY, Ueno Y, Song HJ, Ueda K, Limwikrant W, Yamamoto K, Moribe K (2014) *Nondestructive multicomponent terahertz chemical imaging of medicine in tablets*. *J Electrochem Soc* 161(9):B171–B175. doi:[10.1149/2.0201409jes](https://doi.org/10.1149/2.0201409jes)
- Allis DG, Prokhorova D, Korter T (2006) Solid-state modeling of the terahertz spectrum of the high explosive HMX. *J Phys Chem A* 110(5):1951–1959
- Angell CA, Ngai KL, McKenna GB, McMillan PF, Martin SW (2000) Relaxation in glassforming liquids and amorphous solids. *J Appl Phys* 88(6):3113–3157. doi:[10.1063/1.1286035](https://doi.org/10.1063/1.1286035)
- Auston D (1975) Picosecond optoelectronic switching and gating in silicon. *Appl Phys Lett* 26(3):101–103
- Bawuah P, Pierotic Mendia A, Silfsten P, Pääkkönen P, Ervasti T, Ketolainen J, Zeitler JA, Peiponen KE (2014a) Detection of porosity of pharmaceutical compacts by terahertz radiation transmission and light reflection measurement techniques. *Int J Pharm* 465(1–2):70–76. doi:[10.1016/j.ijpharm.2014.02.011](https://doi.org/10.1016/j.ijpharm.2014.02.011)
- Bawuah P, Silfsten P, Ervasti T, Ketolainen J, Zeitler JA, Peiponen KE (2014b) Non-contact weight measurement of flat-faced pharmaceutical tablets using terahertz transmission pulse delay measurements. *Int J Pharm* 476(1–2):16–22. doi:[10.1016/j.ijpharm.2014.09.027](https://doi.org/10.1016/j.ijpharm.2014.09.027)
- Bernstein J (2007) *Polymorphism in molecular crystals*. Oxford University Press, Oxford
- Bhattacharya S, Suryanarayanan R (2009) Local mobility in amorphous pharmaceuticals—characterization and implications on stability. *J Pharm Sci* 98(9):2935–2953. doi:[10.1002/jps.21728](https://doi.org/10.1002/jps.21728)
- Brock D, Zeitler JA, Funke A, Knop K, Kleinebudde P (2012) A comparison of quality control methods for active coating processes. *Int J Pharm* 439:289–295. doi:[10.1016/j.ijpharm.2012.09.021](https://doi.org/10.1016/j.ijpharm.2012.09.021)
- Brock D, Zeitler JA, Funke A, Knop K, Kleinebudde P (2013a) Critical factors in the measurement of tablet film coatings using terahertz pulsed imaging 102(6):1813–1824. doi: [10.1002/jps.23521](https://doi.org/10.1002/jps.23521)
- Brock D, Zeitler JA, Funke A, Knop K, Kleinebudde P (2013b) Evaluation of critical process parameters for intra-tablet coating uniformity using terahertz pulsed imaging. *Eur J Pharm Biopharm* 85(3 Pt B):1122–1129. doi:[10.1016/j.ejpb.2013.07.004](https://doi.org/10.1016/j.ejpb.2013.07.004)
- Brock D, Zeitler JA, Funke A, Knop K, Kleinebudde P (2014) Evaluation of critical process parameters for inter-tablet coating uniformity of active-coated GITS using Terahertz Pulsed Imaging. *Eur J Pharm Biopharm* 88:434–442. doi:[10.1016/j.ejpb.2014.06.016](https://doi.org/10.1016/j.ejpb.2014.06.016)
- Bründermann E, Hübers HW, Kimmitt MF (2012) *Terahertz techniques*. Springer, Heidelberg
- Burnett AD, Kendrick J, Russell C, Christensen J, Cunningham JE, Pearson AR, Linfield EH, Davies AG (2013) Effect of molecular size and particle shape on the terahertz absorption of a homologous series of tetraalkylammonium salts. *Anal Chem* 85(16):7926–7934. doi:[10.1021/ac401657r](https://doi.org/10.1021/ac401657r)
- Capaccioli S, Ngai KL, Thayyil MS, Prevosto D (2015) Coupling of caged molecule dynamics to JG β -relaxation: I. *J Phys Chem B* 119(28):8800–8808. doi:[10.1021/acs.jpcc.5b04408](https://doi.org/10.1021/acs.jpcc.5b04408)
- Chantry GW (1971) *Submillimetre spectroscopy: guide to the theoretical and experimental physics of the infrared*, 1st edn. Academic, New York

- Charron DM, Ajito K, Kim JY, Ueno Y (2013) Chemical mapping of pharmaceutical cocrystals using terahertz spectroscopic imaging. *Anal Chem* 85(4):1980–1984. doi:[10.1021/ac302852n](https://doi.org/10.1021/ac302852n)
- Chen Y, Ma Y, Lu Z, Peng B, Chen Q (2011) Quantitative analysis of terahertz spectra for illicit drugs using adaptive-range micro-genetic algorithm. *J Appl Phys* 110(4):044902. doi:[10.1063/1.3624737](https://doi.org/10.1063/1.3624737)
- Cogdill R, Short S, Forcht R, Shi Z, Shen Y, Taday PF, Anderson CA, Drennen J (2006) An efficient method-development strategy for quantitative chemical imaging using terahertz pulsed spectroscopy. *J Pharm Innov* 1(1):63–75
- Darkwah J, Smith G, Ermolina I, Mueller-Holtz M (2013) A THz spectroscopy method for quantifying the degree of crystallinity in freeze-dried gelatin/amino acid mixtures: an application for the development of rapidly disintegrating tablets. *Int J Pharm* 455(1–2):357–364. doi:[10.1016/j.ijpharm.2013.06.073](https://doi.org/10.1016/j.ijpharm.2013.06.073)
- Day GM, Zeitler JA, Jones W, Rades T, Taday PF (2006) Understanding the influence of polymorphism on phonon spectra: lattice dynamics calculations and terahertz spectroscopy of carbamazepine. *J Phys Chem B* 110(1):447–456. doi:[10.1021/jp055439y](https://doi.org/10.1021/jp055439y)
- Dees PJ (1980) The mechanism of tablet disintegration. PhD thesis, Leiden
- Delaney SP, Pan D, Galella M, Yin SX, Korter TM (2012) Understanding the origins of conformational disorder in the crystalline polymorphs of Irbesartan. *Cryst Growth Des* 12(10):5017–5024. doi:[10.1021/cg300977e](https://doi.org/10.1021/cg300977e)
- Delaney SP, Pan D, Yin SX, Smith TM, Korter TM (2013a) Evaluating the roles of conformational strain and cohesive binding in crystalline polymorphs of aripiprazole. *Cryst Growth Des* 13(7):2943–2952. doi:[10.1021/cg400358e](https://doi.org/10.1021/cg400358e)
- Delaney SP, Smith TM, Korter TM (2013b) Conformation versus cohesion in the relative stabilities of gabapentin polymorphs. *RSC Adv* 4(2):855. doi:[10.1039/c3ra43887b](https://doi.org/10.1039/c3ra43887b)
- Dexheimer SL (2007b) Terahertz spectroscopy. Principles and applications. CRC Press, Boca Raton
- Dobroui A, Sasaki Y, Shibuya T, Otani C, Kawase K (2007) THz-wave spectroscopy applied to the detection of illicit drugs in mail. *Proc IEEE* 95(8):1566–1575
- Du Y, Xia Y, Zhang H, Hong Z (2013) Using terahertz time-domain spectroscopic technique to monitor cocrystal formation between piracetam and 2,5-dihydroxybenzoic acid. *Spectrochim Acta A Mol Biomol Spectrosc* 111(C):192–195. doi:[10.1016/j.saa.2013.03.081](https://doi.org/10.1016/j.saa.2013.03.081)
- Ebbinghaus S, Meister K, Born B (2010) Antifreeze glycoprotein activity correlates with long-range protein-water dynamics. *J Am Chem Soc* 132(35):12210–12211
- El Haddad J, de Miollis F, Sleiman JB, Canioni L, Mounaix P, Bousquet B (2014) Chemometrics applied to quantitative analysis of ternary mixtures by terahertz spectroscopy. *Anal Chem* 86(10):4927–4933. doi:[10.1021/ac500253b](https://doi.org/10.1021/ac500253b)
- Ervasti T, Silfsten P, Ketola J, Peiponen KE (2011) A study on the resolution of a terahertz spectrometer for the assessment of the porosity of pharmaceutical tablets. *Appl Spectrosc* 66(3):319–323. doi:[10.1366/11-06315](https://doi.org/10.1366/11-06315)
- Ermolina I, Darkwah J, Smith G (2014) Characterisation of crystalline-amorphous blends of sucrose with terahertz-pulsed spectroscopy: the development of a prediction technique for estimating the degree of crystallinity with partial least squares regression. *AAPS PharmSciTech* 15(2):253–260
- Falconer RJ, Markelz AG (2012) Terahertz spectroscopic analysis of peptides and proteins. *J Infrared Millim Terahertz Waves* 33(10):973–988. doi:[10.1007/s10762-012-9915-9](https://doi.org/10.1007/s10762-012-9915-9)
- Fattinger C, Grischkowsky DR (1989) Terahertz beams. *Appl Phys Lett* 54(6):490–492
- Fischer B, Walther M, Jepsen PU (2002) Far-infrared vibrational modes of DNA components studied by terahertz time-domain spectroscopy. *Phys Med Biol* 47(21):3807–3814. doi:[10.1088/0031-9155/47/21/319](https://doi.org/10.1088/0031-9155/47/21/319)
- Fitzgerald A, Cole B, Taday PF (2005) Nondestructive analysis of tablet coating thicknesses using terahertz pulsed imaging. *J Pharm Sci* 94(1):177–183. doi:[10.1002/jps.20225](https://doi.org/10.1002/jps.20225)
- Freireich B, Kumar R, Ketterhagen W, Su K, Wassgren C, Zeitler JA (2015) Comparisons of intratablet coating variability using DEM simulations, asymptotic limit models, and experiments. *Chem Eng Sci* 131:197–212. doi:[10.1016/j.ces.2015.03.013](https://doi.org/10.1016/j.ces.2015.03.013)

- Gebbie HA (1984) Fourier transform spectroscopy—recollections of the period 1955–1960. *Infrared Phys* 24(2–3):105–109. doi:[10.1016/0020-0891\(84\)90056-3](https://doi.org/10.1016/0020-0891(84)90056-3)
- Gendre C, Genty M, Boiret M, Julien M, Meunier L, Lecoq O, Baron M, Chaminade P, Péan JM (2011) Development of a Process Analytical Technology (PAT) for in-line monitoring of film thickness and mass of coating materials during a pan coating operation. *Eur J Pharm Sci* 43(4):244–250. doi:[10.1016/j.ejps.2011.04.017](https://doi.org/10.1016/j.ejps.2011.04.017)
- George DK, Markelz AG (2012) Terahertz spectroscopy of liquids and biomolecules. In: *Terahertz spectroscopy and imaging*. Springer, Berlin, pp 229–250. doi:[10.1007/978-3-642-29564-5_9](https://doi.org/10.1007/978-3-642-29564-5_9)
- Grischkowsky DR, Keiding S, Vanexter M, Fattinger C (1990) Far-infrared time-domain spectroscopy with terahertz beams of dielectrics and semiconductors. *J Opt Soc Am B* 7(10):2006–2015
- Grzybowska K, Paluch M, Grzybowski A, Wojnarowska Z, Hawelek L, Kolodziejczyk K, Ngai KL (2010) Molecular dynamics and physical stability of amorphous anti-inflammatory drug: celecoxib. *J Phys Chem B* 114(40):12792–12801. doi:[10.1021/jp1040212](https://doi.org/10.1021/jp1040212)
- Haaser M, Naelapaa K, Gordon KC, Pepper M, Rantanen J, Strachan CJ, Taday PF, Zeitler JA, Rades T (2013) Evaluating the effect of coating equipment on tablet film quality using terahertz pulsed imaging. *Eur J Pharm Biopharm* 85(3):1095–1102. doi:[10.1016/j.ejpb.2013.03.019](https://doi.org/10.1016/j.ejpb.2013.03.019)
- He Y, Ku P, Knab J, Chen J, Markelz A (2008) Protein dynamical transition does not require protein structure. *Phys Rev Lett* 101(17):178103–178104. doi:[10.1103/PhysRevLett.101.178103](https://doi.org/10.1103/PhysRevLett.101.178103)
- Henry SC, Zurk LM, Schecklman S, Duncan DD (2012) Three-dimensional broadband terahertz synthetic aperture imaging. *Opt Eng* 51(9):091603-1–091603-9. doi:[10.1117/1.OE.51.9.091603](https://doi.org/10.1117/1.OE.51.9.091603)
- Heugen U, Schwaab G, Brundermann E, Heyden M, Yu X, Leitner D, Havenith M (2006) Solute-induced retardation of water dynamics probed directly by terahertz spectroscopy. *Proc Natl Acad Sci U S A* 103(33):12301–12306. doi:[10.1073/pnas.0604897103](https://doi.org/10.1073/pnas.0604897103)
- Hisazumi J, Suzuki T, Nakagami H, Terada K (2011) Quantification of pharmaceutical polymorphs and prediction of dissolution rate using theophylline tablet by terahertz spectroscopy. *Chem Pharm Bull* 59(4):442–446. doi:[10.1248/cpb.59.442](https://doi.org/10.1248/cpb.59.442)
- Hisazumi J, Suzuki T, Wakiyama N (2012a) Chemical mapping of hydration and dehydration process of theophylline in tablets using terahertz pulsed imaging. *Chem Pharm Bull (Tokyo)* 60(7):831–836. doi:[10.1248/cpb.c11-00007](https://doi.org/10.1248/cpb.c11-00007)
- Hisazumi J, Watanabe T, Suzuki T (2012b) Using terahertz reflectance spectroscopy to quantify drug substance in tablets. *Chem Pharm Bull (Tokyo)* 60(12):1487–1493. doi:[10.1248/cpb.c12-00524](https://doi.org/10.1248/cpb.c12-00524)
- Ho L, Mueller R, Romer M, Gordon KC, Heinamaki J, Kleinebudde P, Pepper M, Rades T, Shen YC, Strachan CJ, Taday PF, Zeitler JA (2007) Analysis of sustained-release tablet film coats using terahertz pulsed imaging. *J Control Release* 119(3):253–261. doi:[10.1016/j.jconrel.2007.03.011](https://doi.org/10.1016/j.jconrel.2007.03.011)
- Ho L, Mueller R, Gordon KC, Kleinebudde P, Pepper M, Rades T, Shen Y, Taday PF, Zeitler JA (2008) Applications of terahertz pulsed imaging to sustained-release tablet film coating quality assessment and dissolution performance. *J Control Release* 127(1):79–87. doi:[10.1016/j.jconrel.2008.01.002](https://doi.org/10.1016/j.jconrel.2008.01.002)
- Ho L, Mueller R, Gordon KC, Kleinebudde P, Pepper M, Rades T, Shen Y, Taday PF, Zeitler JA (2009a) Monitoring the Film Coating Unit Operation and Predicting Drug Dissolution Using Terahertz Pulsed Imaging. *J Pharm Sci* 98(12):4866–4876. doi:[10.1002/jps.21766](https://doi.org/10.1002/jps.21766)
- Ho L, Mueller R, Gordon KC, Kleinebudde P, Pepper M, Rades T, Shen Y, Taday PF, Zeitler JA (2009b) Terahertz pulsed imaging as an analytical tool for sustained-release tablet film coating. *Eur J Pharm Biopharm* 71(1):117–123. doi:[10.1016/j.ejpb.2008.06.023](https://doi.org/10.1016/j.ejpb.2008.06.023)
- Ho L, Mueller R, Krueger C, Gordon KC, Kleinebudde P, Pepper M, Rades T, Shen Y, Taday PF, Zeitler JA (2010) Investigating dissolution performance critical areas on coated tablets: a case study using terahertz pulsed imaging. *J Pharm Sci* 99(1):392–402. doi:[10.1002/jps.21845](https://doi.org/10.1002/jps.21845)

- Hongwei L, Zhiyong W (2011) Investigation of solid-state reaction by terahertz time-domain spectroscopy. *Nucl Sci Tech* 22:139–143
- Jepsen PU, Clark S (2007) Precise ab-initio prediction of terahertz vibrational modes in crystalline systems. *Chem Phys Lett* 442(4-6):275–280
- Jepsen PU, Cooke DG, Koch M (2010) Terahertz spectroscopy and imaging—modern techniques and applications. *Laser Photonics Rev* 5(1):124–166. doi:10.1002/lpor.201000011
- Johari GP (1970) Viscous liquids and the glass transition. II. Secondary relaxations in glasses of rigid molecules. *J Chem Phys* 53(6):2372–2388. doi:10.1063/1.1674335
- Julian Quodbach PK, Kleinebudde P (2015) A critical review on tablet disintegration. *Pharm Dev Technol* 00(00):1–12. doi:10.3109/10837450.2015.1045618
- Juliano TR, King MD, Korter TM (2013) Evaluating London dispersion force corrections in crystalline nitroguanidine by terahertz spectroscopy. *IEEE Trans Terahertz Sci Technol* 3(3):281–287. doi:10.1109/TTHZ.2013.2254483
- Juuti M, Tuononen H, Prykäri T, Kontturi V, Kuosmanen M, Alarousu E, Ketolainen J, Myllylä R, Peiponen KE (2009) Optical and terahertz measurement techniques for flat-faced pharmaceutical tablets: a case study of gloss, surface roughness and bulk properties of starch acetate tablets. *Meas Sci Technol* 20(1):015,301. doi:10.1088/0957-0233/20/1/015301
- Kambara O, Tominaga K, Ji N, Sasaki T, Wang HW, Hayashi M (2010) Mode assignment of vibrational bands of 2-furoic acid in the terahertz frequency region. *Chem Phys Lett* 498(1–3):86–89. doi:10.1016/j.cplett.2010.08.047
- Katz G, Zybin S, Goddard WA III, Zeiri Y, Kosloff R (2014) Direct MD simulations of terahertz absorption and 2D spectroscopy applied to explosive crystals. *J Phys Chem Lett* 5(5):772–776. doi:10.1021/jz402801m
- King M, Korter T (2010) Effect of waters of crystallization on terahertz spectra: anhydrous oxalic acid and its dihydrate. *J Phys Chem A* 114(26):7127–7138. doi:10.1021/jp101935n
- King M, Buchanan W, Korter T (2010a) Investigating the anharmonicity of lattice vibrations in water-containing molecular crystals through the terahertz spectroscopy of L-serine monohydrate. *J Phys Chem A* 114(35):9570–9578. doi:10.1021/jp105384x
- King MD, Buchanan WD, Korter TM (2010b) Understanding the terahertz spectra of crystalline pharmaceuticals: terahertz spectroscopy and solid-state density functional theory study of (S)-(+)-ibuprofen and (RS)-ibuprofen. *J Pharm Sci* 100(3):1116–1129. doi:10.1002/jps.22339
- King MD, Buchanan WD, Korter TM (2011a) Application of London-type dispersion corrections to the solid-state density functional theory simulation of the terahertz spectra of crystalline pharmaceuticals. *Phys Chem Chem Phys* 13(10):4250–4259. doi:10.1039/c0cp01595d
- King MD, Buchanan WD, Korter TM (2011b) Identification and quantification of polymorphism in the pharmaceutical compound diclofenac acid by terahertz spectroscopy and solid-state density functional theory. *Anal Chem* 83(10):3786–3792. doi:10.1021/ac2001934
- King MD, Davis EA, Smith TM, Korter TM (2011c) Importance of accurate spectral simulations for the analysis of terahertz spectra: citric acid anhydrate and monohydrate. *J Phys Chem A* 115(40):11039–11044
- Knab J, Chen J, Markelz A (2006) Hydration dependence of conformational dielectric relaxation of lysozyme. *Biophys J* 90(7):2576–2581. doi:10.1529/biophysj.105.069088
- Kogermann K, Zeitler JA, Rantanen J, Rades T, Taday PF, Pepper M, Heinämäki J, Strachan CJ (2007) Investigating dehydration from compacts using terahertz pulsed, Raman, and near-infrared spectroscopy. *Appl Spectrosc* 61(12):1265–1274. doi:10.1366/000370207783292136
- Lee YS (2009) Principles of THz science and technology. Springer, Boston
- Li R, Zeitler JA, Tomerini D, Parrott EPJ, Gladden LF, Day G (2010) A study into the effect of subtle structural details and disorder on the terahertz spectrum of crystalline benzoic acid. *Phys Chem Chem Phys* 12(20):5329–5340. doi:10.1039/b926536h
- Li C, Zeitler JA, Dong Y, Shen YC (2014) Non-destructive evaluation of polymer coating structures on pharmaceutical pellets using full-field optical coherence tomography. *J Pharm Sci* 103(1):161–166. doi:10.1002/jps.23764

- Lin H, May RK, Evans MJ, Zhong S, Gladden LF, Shen Y, Zeitler JA (2015) Impact of processing conditions on inter-tablet coating thickness variations measured by terahertz in-line sensing. *J Pharm Sci* 104(8):2513–2522. doi:[10.1002/jps.24503](https://doi.org/10.1002/jps.24503)
- Liu H, Zhang X (2006) Dehydration kinetics of D-glucose monohydrate studied using THz time-domain spectroscopy. *Chem Phys Lett* 429(1–3):229–233
- Liu X, Liu G, Zhao H, Zhang Z, Wei Y, Liu M, Wen W, Zhou X (2011) The quantitative monitoring of mechanochemical reaction between solid l-tartaric acid and sodium carbonate monohydrate by terahertz spectroscopy. *J Phys Chem Solids* 72(11):1245–1250. doi:[10.1016/j.jpcs.2011.07.011](https://doi.org/10.1016/j.jpcs.2011.07.011)
- Lowenthal W (1972) Disintegration of tablets. *J Pharm Sci* 61(11):1695–1711. doi:[10.1002/jps.2600611102](https://doi.org/10.1002/jps.2600611102)
- Lu M, Shen J, Li N, Zhang Y, Zhang C, Liang L, Xu X (2006) Detection and identification of illicit drugs using terahertz imaging. *J Appl Phys* 100(10):103104. doi:[10.1063/1.2388041](https://doi.org/10.1063/1.2388041)
- Malaterre V, Pedersen M, Ogorka J, Gurny R, Loggia N, Taday PF (2009) Terahertz pulsed imaging, a novel process analytical tool to investigate the coating characteristics of push-pull osmotic systems. *Eur J Pharm Biopharm* 74(1):21–25
- Markelz A, Knab J, Chen J, He Y (2007) Protein dynamical transition in terahertz dielectric response. *Chem Phys Lett* 442(4–6):413–417
- Maurer L, Leuenberger H (2009) Terahertz pulsed imaging and near infrared imaging to monitor the coating process of pharmaceutical tablets. *Int J Pharm* 370(1–2):8–16. doi:[10.1016/j.ijpharm.2008.11.011](https://doi.org/10.1016/j.ijpharm.2008.11.011)
- May R, Evans MJ, Zhong S, Warr I, Gladden LF, Shen Y, Zeitler JA (2011) Terahertz in-line sensor for direct coating thickness measurement of individual tablets during film coating in real-time. *J Pharm Sci* 100(4):1535–1544. doi:[10.1002/jps.22359](https://doi.org/10.1002/jps.22359)
- May R, Su K, Han L, Zhong S, Elliott JA, Gladden LF, Evans M, Shen Y, Zeitler JA (2013) Hardness and density distributions of pharmaceutical tablets measured by terahertz pulsed imaging. *J Pharm Sci* 102:2179–2186. doi:[10.1002/jps.23560](https://doi.org/10.1002/jps.23560)
- McIntosh AI, Yang B, Goldup SM, Watkinson M, Donnan RS (2013) Crystallization of amorphous lactose at high humidity studied by terahertz time domain spectroscopy. *Chem Phys Lett* 558:104–108. doi:[10.1016/j.cplett.2012.12.044](https://doi.org/10.1016/j.cplett.2012.12.044)
- Möller KD, Rothschild WG (1971) Far-infrared spectroscopy. Wiley-VCH Verlag, Weinheim
- Müller J, Brock D, Knop K, Zeitler JA, Kleinebudde P (2012) Prediction of dissolution time and coating thickness of sustained release formulations using Raman spectroscopy and terahertz pulsed imaging. *Eur J Pharm Biopharm* 80(3):690–697. doi:[10.1016/j.ejpb.2011.12.003](https://doi.org/10.1016/j.ejpb.2011.12.003)
- Ngai KL (1998) Relation between some secondary relaxations and the α relaxations in glass-forming materials according to the coupling model. *J Chem Phys* 109(16):6982. doi:[10.1063/1.477334](https://doi.org/10.1063/1.477334)
- Ngai KL (2003) An extended coupling model description of the evolution of dynamics with time in supercooled liquids and ionic conductors. *J Phys Condens Matter* 15(11):S1107–S1125
- Nguyen K, Friscic T, Day G, Gladden LF, Jones W (2007) Terahertz time-domain spectroscopy and the quantitative monitoring of mechanochemical cocrystal formation. *Nat Mater* 6(3):206–209. doi:[10.1038/nmat1848](https://doi.org/10.1038/nmat1848)
- Ning L, Jingling S, Jinhai S, Laishun L, Xiaoyu X, Meihong L, Yan J (2005) Study on the THz spectrum of methamphetamine. *Opt Express* 13(18):6750–6755
- Niwa M, Hiraishi Y (2014) Quantitative analysis of visible surface defect risk in tablets during film coating using terahertz pulsed imaging. *Int J Pharm* 461(1–2):342–350. doi:[10.1016/j.ijpharm.2013.11.051](https://doi.org/10.1016/j.ijpharm.2013.11.051)
- Niwa M, Hiraishi Y, Iwasaki N, Terada K (2013) Quantitative analysis of the layer separation risk in bilayer tablets using terahertz pulsed imaging. *Int J Pharm* 452(1–2):249–256. doi:[10.1016/j.ijpharm.2013.05.010](https://doi.org/10.1016/j.ijpharm.2013.05.010)
- Niwa M, Hiraishi Y, Terada K (2014) Evaluation of coating properties of enteric-coated tablets using terahertz pulsed imaging. *Pharm Res* 31(8):2140–2151. doi:[10.1007/s11095-014-1314-6](https://doi.org/10.1007/s11095-014-1314-6)

- Otsuka M, Nishizawa J, Shibata J, Ito M (2010) Quantitative evaluation of mefenamic acid polymorphs by terahertz-chemometrics. *J Pharm Sci* 99(9):4048–4053
- Palermo R, Cogdill R, Short S, Drennen Iii J, Taday PF (2008) Density mapping and chemical component calibration development of four-component compacts via terahertz pulsed imaging. *J Pharm Biomed Anal* 46(1):36–44. doi:[10.1016/j.jpba.2007.10.023](https://doi.org/10.1016/j.jpba.2007.10.023)
- Parrott EPJ, Zeitler JA, Friscic T, Pepper M, Jones W, Day G, Gladden LF (2009) Testing the sensitivity of terahertz spectroscopy to changes in molecular and supramolecular structure: a study of structurally similar cocrystals. *Cryst Growth Des* 9(3):1452–1460. doi:[10.1021/cg8008893](https://doi.org/10.1021/cg8008893)
- Parrott EPJ, Zeitler JA, Simon G, Hehlen B, Gladden LF, Taraskin SN, Elliott SR (2010) Atomic charge distribution in sodosilicate glasses from terahertz time-domain spectroscopy. *Phys Rev B Condens Matter* 82(14):140203(R). doi:[10.1103/PhysRevB.82.140203](https://doi.org/10.1103/PhysRevB.82.140203)
- Parrott EPJ, Zeitler JA (2015) Terahertz time-domain and low-frequency Raman spectroscopy of organic materials. *Appl Spectrosc* 69(1):1–25
- Peiponen KE, Zeitler JA, Kuwata-Gonokami M (eds) (2013) Terahertz spectroscopy and imaging, Springer series in optical sciences, vol 171. Springer, Berlin. doi:[10.1007/978-3-642-29564-5](https://doi.org/10.1007/978-3-642-29564-5)
- Peiponen KE, Bawuah P, Chakraborty M, Juuti M, Zeitler JA, Ketolainen J (2015) Estimation of Young's modulus of pharmaceutical tablet obtained by terahertz time-delay measurement. *Int J Pharm* 489(1–2):100–105. doi:[10.1016/j.ijpharm.2015.04.068](https://doi.org/10.1016/j.ijpharm.2015.04.068)
- Pellizzeri S, Delaney SP, Korter TM, Zubieta J (2014) Using terahertz spectroscopy and solid-state density functional theory to characterize a new polymorph of 5-(4-pyridyl)tetrazole. *J Phys Chem A* 118(2):417–426. doi:[10.1021/jp412142w](https://doi.org/10.1021/jp412142w)
- Ronne C, Jensby K, Madsen GKH, Nielsen OF, Keiding SR (1999) THz time domain spectroscopy of liquids. In: Chamberlain JM (ed) *Industrial lasers and inspection (EUROPTO series)*, SPIE, pp 266–275. doi:[10.1117/12.361045](https://doi.org/10.1117/12.361045)
- Rungsawang R, Ueno Y, Tomita I, Ajito K (2006a) Angle-dependent terahertz time-domain spectroscopy of amino acid single crystals. *J Phys Chem B* 110(42):21259–21263
- Rungsawang R, Ueno Y, Tomita I, Ajito K (2006b) Terahertz notch filter using intermolecular hydrogen bonds in a sucrose crystal. *Opt Express* 14(12):5765–5772
- Russe IS, Brock D, Knop K, Kleinebudde P, Zeitler JA (2012) Validation of terahertz coating thickness measurements using X-ray microtomography. *Mol Pharm* 9(12):3551–3559. doi:[10.1021/mp300383y](https://doi.org/10.1021/mp300383y)
- Sakamoto T, Portieri A, Taday PF (2009) Detection of tulobuterol crystal in transdermal patches using terahertz pulsed spectroscopy and imaging. *Pharmazie* 64(6):361–365. doi:[10.1691/ph.2009.9022](https://doi.org/10.1691/ph.2009.9022)
- Sakamoto T, Portieri A, Arnone DD, Taday PF, Kawanishi T, Hiyama Y (2012) Coating and density distribution analysis of commercial ciprofloxacin hydrochloride monohydrate tablets by terahertz pulsed spectroscopy and imaging. *J Pharm Innov* 7(2):87–93. doi:[10.1007/s12247-012-9130-1](https://doi.org/10.1007/s12247-012-9130-1)
- Shen Y, Taday PF (2008) Development and application of terahertz pulsed imaging for nondestructive inspection of pharmaceutical tablet. *IEEE J Sel Top Quantum Electron* 14(2):407–415. doi:[10.1109/2007.JSTQE.911309](https://doi.org/10.1109/2007.JSTQE.911309)
- Shen Y, Upadhya P, Linfield E, Davies A (2003) Temperature-dependent low-frequency vibrational spectra of purine and adenine. *Appl Phys Lett* 82(14):2350–2352
- Shen Y, Upadhya P, Linfield E, Davies A (2004) Vibrational spectra of nucleosides studied using terahertz time-domain spectroscopy. *Vib Spectrosc* 35(1–2):111–114
- Shen Y, Taday PF, Newnham D, Kemp M, Pepper M, Hwu R, Linden K (2005a) 3D chemical mapping using terahertz pulsed imaging. In: *Terahertz and gigahertz electronics and photonics IV*, pp 24–31. doi:[10.1117/12.591472](https://doi.org/10.1117/12.591472)
- Shen Y, Taday PF, Newnham D, Pepper M (2005a) Chemical mapping using reflection terahertz pulsed imaging. *Semicond Sci Technol* 20(7):S254–S257
- Sibik J, Zeitler JA (2015) *Study of disordered materials by terahertz spectroscopy*. Wiley, New York, p 26

- Sibik J, Shalaev EY, Zeitler JA (2013) Glassy dynamics of sorbitol solutions at terahertz frequencies. *Phys Chem Chem Phys* 15(28):11931–11942. doi:[10.1039/c3cp51936h](https://doi.org/10.1039/c3cp51936h)
- Sibik J, Elliott SR, Zeitler JA (2014a) Thermal decoupling of molecular-relaxation processes from the vibrational density of states at terahertz frequencies in supercooled hydrogen-bonded liquids. *J Phys Chem Lett* 5(11):1968–1972. doi:[10.1021/jz5007302](https://doi.org/10.1021/jz5007302)
- Sibik J, Sargent MJ, Franklin M, Zeitler JA (2014b) Crystallization and phase changes in paracetamol from the amorphous solid to the liquid phase. *Mol Pharm* 11(4):1326–1334. doi:[10.1021/mp400768m](https://doi.org/10.1021/mp400768m)
- Sibik J, Löbmann K, Rades T, Zeitler JA (2015) Predicting crystallization of amorphous drugs with terahertz spectroscopy. *Mol Pharm* 12(8):3062–3068. doi:[10.1021/acs.molpharmaceut.5b00330](https://doi.org/10.1021/acs.molpharmaceut.5b00330)
- Singh R, George DK, Benedict JB, Korter TM, Markelz AG (2012) Improved mode assignment for molecular crystals through anisotropic terahertz spectroscopy. *J Phys Chem* 116(42):10359–10364. doi:[10.1021/jp307288r](https://doi.org/10.1021/jp307288r)
- Smith G, Hussain A, Bukhari NI, Ermolina I (2015a) Quantification of residual crystallinity in ball milled commercially sourced lactose monohydrate by thermo-analytical techniques and terahertz spectroscopy. *Eur J Pharm Biopharm* 92:180–191. doi:[10.1016/j.ejpb.2015.02.026](https://doi.org/10.1016/j.ejpb.2015.02.026)
- Smith G, Hussain A, Bukhari NI, Ermolina I (2015b) Quantification of residual crystallinity of ball-milled, commercially available, anhydrous β -lactose by differential scanning calorimetry and terahertz spectroscopy. *J Therm Anal Calorim* 121(1):327–333. doi:[10.1007/s10973-015-4469-4](https://doi.org/10.1007/s10973-015-4469-4)
- Spencer J, Gao Z, Moore T, Buhse L, Taday PF, Newnham D, Shen Y, Portieri A, Husain A (2008) Delayed release tablet dissolution related to coating thickness by terahertz pulsed image mapping. *J Pharm Sci* 97(4):1543–1550. doi:[10.1002/jps.21051](https://doi.org/10.1002/jps.21051)
- Strachan CJ, Rades T, Newnham D, Gordon KC, Pepper M, Taday PF (2004) Using terahertz pulsed spectroscopy to study crystallinity of pharmaceutical materials. *Chem Phys Lett* 390(1–3):20–24. doi:[10.1016/j.cplett.2004.03.117](https://doi.org/10.1016/j.cplett.2004.03.117)
- Strachan CJ, Taday PF, Newnham DA, Gordon KC, Zeitler JA, Pepper M, Rades T (2005) Using terahertz pulsed spectroscopy to quantify pharmaceutical polymorphism and crystallinity. *J Pharm Sci* 94(4):837–846. doi:[10.1002/jps.20281](https://doi.org/10.1002/jps.20281)
- Su K, Shen YC, Zeitler JA (2014) Terahertz sensor for non-contact thickness and quality measurement of automobile paints of varying complexity. *IEEE Trans Terahertz Sci Technol* 4(4):432–439. doi:[10.1109/TTHZ.2014.2325393](https://doi.org/10.1109/TTHZ.2014.2325393)
- Taday PF, Bradley IV, Amone DD (2003a) Terahertz pulse spectroscopy of biological materials: L-glutamic acid. *J Biol Phys* 29(2-3):109–115. doi:[10.1023/A:1024424205309](https://doi.org/10.1023/A:1024424205309)
- Taday PF, Bradley IV, Amone DD, Pepper M (2003b) Using terahertz pulse spectroscopy to study the crystalline structure of a drug: a case study of the polymorphs of ranitidine hydrochloride. *J Pharm Sci* 92(4):831–838. doi:[10.1002/jps.10358](https://doi.org/10.1002/jps.10358)
- Takahashi M (2014) Terahertz vibrations and hydrogen-bonded networks in crystals. *Crystals* 4(2):74–103. doi:[10.3390/cryst4020074](https://doi.org/10.3390/cryst4020074)
- Takahashi M, Kawazoe Y, Ishikawa Y, Ito H (2009) Interpretation of temperature-dependent low frequency vibrational spectrum of solid-state benzoic acid dimer. *Chem Phys Lett* 479(4–6):211–217. doi:[10.1016/j.cplett.2009.08.017](https://doi.org/10.1016/j.cplett.2009.08.017)
- Takeuchi I, Tomoda K, Nakajima T, Terada H, Kuroda H, Makino K (2012) Estimation of crystallinity of trehalose dihydrate microspheres by usage of terahertz time-domain spectroscopy. *J Pharm Sci* 101(9):3465–3472. doi:[10.1002/jps.23147](https://doi.org/10.1002/jps.23147)
- Takeuchi I, Shimakura K, Ohtake H, Takayanagi J, Tomoda K, Nakajima T, Terada H, Makino K (2014) Nondestructive analysis of structure and components of tablet coated with film by the usage of terahertz time-domain reflection spectroscopy. *J Pharm Sci* 103(1):256–261. doi:[10.1002/jps.23797](https://doi.org/10.1002/jps.23797)
- Tan NY, Zeitler JA (2015) Probing phase transitions in simvastatin with terahertz time-domain spectroscopy. *Mol Pharm* 12(3):810–815. doi:[10.1021/mp500649q](https://doi.org/10.1021/mp500649q)

- Taraskin SN, Simdyankin S, Elliott SR, Neilson J, Lo T (2006) Universal features of terahertz absorption in disordered materials. *Phys Rev Lett* 97:055504
- Threlfall T (2014) Polymorphism—polymorph myths and misperceptions. *Eur Pharm Rev* 19 (3):24–29
- Tomerini D, Day GM (2012) Computational methods for the assignment of vibrational modes in crystalline materials. In: *Terahertz spectroscopy and imaging*. Springer, Berlin, pp 151–190. doi:[10.1007/978-3-642-29564-5_7](https://doi.org/10.1007/978-3-642-29564-5_7)
- Tuononen H, Fukunaga K, Kuosmanen M, Ketolainen J, Peiponen KE (2010a) Wiener bounds for complex permittivity in terahertz spectroscopy: case study of two-phase pharmaceutical tablets. *Appl Spectrosc* 64(1):127–131
- Tuononen H, Gornov E, Zeitler JA, Aaltonen J, Peiponen KE (2010b) Using modified Kramers-Kronig relations to test transmission spectra of porous media in THz-TDS. *Opt Lett* 35 (5):631–633
- Ueno Y, Ajito K (2007) Terahertz time-domain spectra of aromatic carboxylic acids incorporated in nano-sized pores of mesoporous silicate. *Anal Sci* 23(7):803–807
- Ueno Y, Rungsawang R, Tomita I, Ajito K (2006a) Quantitative measurements of amino acids by terahertz time-domain transmission spectroscopy. *Anal Chem* 78(15):5424–5428
- Ueno Y, Rungsawang R, Tomita I, Ajito K (2006b) Terahertz time-domain spectra of inter- and intramolecular hydrogen bonds of fumaric and maleic acids. *Chem Lett* 35(10):1128–1129
- Upadhyaya P, Shen Y, Davies A, Linfield E (2003) Terahertz time-domain spectroscopy of glucose and uric acid. *J Biol Phys* 29(2–3):117–121. doi:[10.1023/A:1024476322147](https://doi.org/10.1023/A:1024476322147)
- Upadhyaya P, Shen Y, Davies A, Linfield E (2004) Far-infrared vibrational modes of polycrystalline saccharides. *Vib Spectrosc* 35(1–2):139–143
- Upadhyaya P, Nguyen K, Shen Y, Obradovic J, Fukushige K, Griffiths R, Gladden LF, Davies A, Linfield E (2006) Characterization of crystalline phase-transformations in theophylline by time-domain terahertz spectroscopy. *Spectrosc Lett* 39(3):215–224
- Vanexter M, Fattering C, Grischkowsky DR (1989) Terahertz time-domain spectroscopy of water-vapor. *Opt Lett* 14(20):1128–1130
- Vieira FS, Pasquini C (2014) Determination of cellulose crystallinity by terahertz-time domain spectroscopy. *Anal Chem* 86(8):3780–3786. doi:[10.1021/ac4035746](https://doi.org/10.1021/ac4035746)
- Vynckier AK, Lin H, Zeitler JA, Willart JF, Bongaers E, Voorspoels J, Remon JP, Vervaeet C (2015) Calendering as a direct shaping tool for the continuous production of fixed-dose combination products via co-extrusion. *Eur J Pharm Biopharm* 96:125–131. doi:[10.1016/j.ejpb.2015.07.023](https://doi.org/10.1016/j.ejpb.2015.07.023)
- Walther M, Fischer B, Schall M, Helm H, Jepsen PU (2000) Far-infrared vibrational spectra of all-trans, 9-cis and 13-cis retinal measured by THz time-domain spectroscopy. *Chem Phys Lett* 332(3–4):389–395
- Walther M, Plochocka P, Fischer B, Helm H, Jepsen PU (2002) Collective vibrational modes in biological molecules investigated by terahertz time-domain spectroscopy. *Biopolymers* 67 (4–5):310–313
- Walther M, Fischer B, Jepsen PU (2003) Noncovalent intermolecular forces in polycrystalline and amorphous saccharides in the far infrared. *Chem Phys* 288(2–3):261–268
- Wu H, Heilweil EJ, Hussain A, Khan M (2008) Process analytical technology (PAT): quantification approaches in Terahertz spectroscopy for pharmaceutical application. *J Pharm Sci* 97 (2):970–984
- Yada H, Nagai M, Tanaka K (2009) The intermolecular stretching vibration mode in water isotopes investigated with broadband terahertz time-domain spectroscopy. *Chem Phys Lett* 473(4–6):279–283. doi:[10.1016/j.cplett.2009.03.075](https://doi.org/10.1016/j.cplett.2009.03.075)
- Yamaguchi M, Miyamaru F, Yamamoto K, Tani M, Hangyo M (2005) Terahertz absorption spectra of L-, D-, and DL-alanine and their application to determination of enantiometric composition. *Appl Phys Lett* 86(5):053903-1–053903-3

- Yassin S, Goodwin DJ, Anderson A, Sibik J, Wilson DI, Gladden LF, Zeitler JA (2015a) The disintegration process in microcrystalline cellulose based tablets, Part 1: influence of temperature, porosity and superdisintegrants. *J Pharm Sci* 104(10):3440–3450. doi:[10.1002/jps.24544](https://doi.org/10.1002/jps.24544)
- Yassin S, Su K, Lin H, Gladden LF, Zeitler JA (2015b) Diffusion and swelling measurements in pharmaceutical powder compacts using terahertz pulsed imaging. *J Pharm Sci* 104(5):1658–1667. doi:[10.1002/jps.24376](https://doi.org/10.1002/jps.24376)
- Zalkovskij M, Zoffmann Bisgaard C, Novitsky A, Malureanu R, Savastru D, Popescu A, Jepsen PU, Lavrinenko AV (2012) Ultrabroadband terahertz spectroscopy of chalcogenide glasses. *Appl Phys Lett* 100(3):031901. doi:[10.1063/1.3676443](https://doi.org/10.1063/1.3676443)
- Zeitler JA, Gladden LF (2009) In-vitro tomography and non-destructive imaging at depth of pharmaceutical solid dosage forms. *Eur J Pharm Biopharm* 71(1):2–22. doi:[10.1016/j.ejpb.2008.08.012](https://doi.org/10.1016/j.ejpb.2008.08.012)
- Zeitler JA, Shen YC (2012) Industrial applications of terahertz imaging. In: *Terahertz spectroscopy and imaging*. Springer, Berlin, pp 451–489. doi:[10.1007/978-3-642-29564-5_18](https://doi.org/10.1007/978-3-642-29564-5_18)
- Zeitler JA, Newnham DA, Taday PF, Strachan CJ, Pepper M, Gordon KC, Rades T (2005) Temperature dependent terahertz pulsed spectroscopy of carbamazepine. *Thermochim Acta* 436(1–2):71–77. doi:[10.1016/j.tca.2005.07.006](https://doi.org/10.1016/j.tca.2005.07.006)
- Zeitler JA, Newnham DA, Taday PF, Threlfall TL, Lancaster RW, Berg RW, Strachan CJ, Pepper M, Gordon KC, Rades T (2006) Characterization of temperature-induced phase transitions in five polymorphic forms of sulfathiazole by terahertz pulsed spectroscopy and differential scanning calorimetry. *J Pharm Sci* 95(11):2486–2498. doi:[10.1002/jps.20719](https://doi.org/10.1002/jps.20719)
- Zeitler JA, Taday PF, Gordon KC, Pepper M, Rades T (2007a) Solid-state transition mechanism in carbamazepine polymorphs by time-resolved terahertz spectroscopy. *ChemPhysChem* 8(13):1924–1927. doi:[10.1002/cphc.200700261](https://doi.org/10.1002/cphc.200700261)
- Zeitler JA, Taday PF, Pepper M, Rades T (2007b) Relaxation and crystallization of amorphous carbamazepine studied by terahertz pulsed spectroscopy. *J Pharm Sci* 96(10):2703–2709. doi:[10.1002/jps.20908](https://doi.org/10.1002/jps.20908)
- Zeitler JA, Kogermann K, Rantanen J, Rades T, Taday PF, Pepper M, Aaltonen J, Strachan CJ (2007c) Drug hydrate systems and dehydration processes studied by terahertz pulsed spectroscopy. *Int J Pharm* 334(1–2):78–84. doi:[10.1016/j.ijpharm.2006.10.027](https://doi.org/10.1016/j.ijpharm.2006.10.027)
- Zeitler JA, Shen Y, Baker C, Taday PF, Pepper M, Rades T (2007d) Analysis of coating structures and interfaces in solid oral dosage forms by three dimensional terahertz pulsed imaging. *J Pharm Sci* 96(2):330–340. doi:[10.1002/jps.20789](https://doi.org/10.1002/jps.20789)
- Zhang Q, Gladden LF, Avalle P, Zeitler JA, Mantle M (2013) Terahertz pulsed imaging and magnetic resonance imaging as tools to probe formulation stability. *Pharmaceutics* 5(4):591–608. doi:[10.3390/pharmaceutics5040591](https://doi.org/10.3390/pharmaceutics5040591)
- Zhong S, Shen Y, Shen H, Evans M, May R, Zeitler JA, Warr I (2010) Near-infrared spectroscopy for non-destructive coating analysis calibrated by terahertz pulsed imaging. In: *35th international conference on infrared millimeter and terahertz waves (IRMMW-THz)*, pp 1–2. doi:[10.1109/ICIMW.2010.5612668](https://doi.org/10.1109/ICIMW.2010.5612668)
- Zhong S, Shen YC, Ho L, May R, Zeitler JA, Evans M, Taday PF, Pepper M, Rades T, Gordon KC, Mueller R, Kleibubde P (2011) Non-destructive quantification of pharmaceutical tablet coatings using terahertz pulsed imaging and optical coherence tomography. *Opt Lasers Eng* 49(3):361–365. doi:[10.1016/j.optlaseng.2010.11.003](https://doi.org/10.1016/j.optlaseng.2010.11.003)

Chapter 6

Circular Dichroism Spectroscopy for Structural Characterization of Proteins

Søren Vrønning Hoffmann, Mathias Fano, and Marco van de Weert

Abstract The large size, physicochemical complexity and rather labile nature of proteins present significant challenges in delivery of pharmaceutical proteins. First, the native structure of a given protein drug molecule must be characterized in order to define the active compound. Next, for the successful development of a formulation or drug delivery system for said molecule, compatibility of the system with the protein should be demonstrated. This is a challenging task as formulations and delivery systems often contain chromophores or particulates that absorb or scatter light, preventing the direct use of several of the most commonly used techniques for structural characterization.

The single most important spectroscopic method for the rapid elucidation of protein structure in solution is circular dichroism (CD) spectroscopy. In this chapter, an overview of the method is given, with a discussion of the instrumentation, several specific examples of applications and general experimental recommendations for CD experiments, including a special perspective on challenging samples as may be encountered in pharmaceutical sciences.

Keywords Circular dichroism (CD) • Synchrotron radiation CD • Secondary, tertiary and quaternary structure • Protein folding

S.V. Hoffmann

ISA, Department of Physics and Astronomy, Aarhus University, Ny Munkegade 120, Aarhus C 8000, Denmark

M. Fano (✉)

Bioneer:FARMA, Universitetsparken 2, Copenhagen Ø 2100, Denmark

e-mail: mathias.fano@sund.ku.dk

M. van de Weert

University of Copenhagen, Universitetsparken 2, Copenhagen Ø 2100, Denmark

1 Fundamentals of Circular Dichroism Spectroscopy

1.1 Physical Basis for Circular Dichroism

Chirality is at the heart of circular dichroism (CD) spectroscopy. A molecule is chiral if it has a mirror image which cannot be superimposed on itself after a proper rotation (Anslyn and Dougherty 2005; Barron 2009), in the same way as a right hand cannot be transformed into a left hand by a simple rotation. Proteins are chiral since their monomer units, amino acids, are chiral and exist as both a left and a right handed enantiomer. As an example, the two enantiomers of alanine are shown in Fig. 6.1. Amino acids commonly found in proteins are of the left handed form.

Light may also act as a true chiral object (Barron 2004). When produced in a circular polarization state, the electric field vector of the electromagnetic radiation traces out a helical motion in space as shown in Fig. 6.1. Circularly polarized light (CPL) may either rotate in a left (l-CPL) or right (r-CPL) handed motion, and the two polarizations states are, just as chiral molecules, a mirror image of each other, and thus cannot be superimposed by a proper rotation.

In normal absorption spectroscopy, which is routinely carried out in molecular biology and chemistry laboratories, the light source is unpolarized, and does not distinguish between enantiomers of chiral molecules. Likewise, absorption of circularly polarized light by a *non*-chiral molecule will, due to the lack of symmetry, not depend on the handedness of the light. However, circularly polarized light will be absorbed by a chiral molecule to different extents depending on if the light is left or right handed polarized. Circular dichroism spectroscopy takes advantage of this. The circular dichroism is defined as the difference in absorption between left (A_L) and right (A_R) handed polarized light:

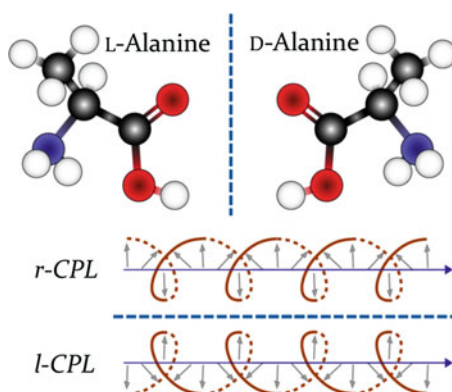


Fig. 6.1 The two enantiomers of the amino acid alanine (*top*) are mirror images of each other via a reflection through the plane indicated as a *dotted line*. The polarization vector (the electric field vector of the electromagnetic radiation) traces out a helix in circularly polarized light (*bottom*). The right and left-handed form of circularly polarized light are mirror images of each other

$$\Delta A = A_L - A_R \quad (6.1)$$

Notice that although absorption is always positive, the differential absorption may give rise to both positive and negative CD signals. For a sample of known concentration (c) measured in a sample container (cuvette) of pathlength (l) the differential extinction coefficient $\Delta\epsilon$ is related to the differential absorption ΔA via the Beer-Lambert law:

$$\Delta A = \Delta\epsilon \cdot c \cdot l \quad (6.2)$$

Circular dichroism spectroscopy measures this difference as a function of wavelength, so it is understood that ΔA and $\Delta\epsilon$ are wavelength dependent. In the case of proteins, CD is generally determined in the region 170–320 nm, encompassing the absorbance of the peptide bonds and several side-chains (see Sect. 2.2).

In quantum chemistry, absorption is described in terms of the electric dipole operator $\boldsymbol{\mu}$. When a molecule absorbs a photon the excitation of the molecule must result in a net change of the molecules dipole moment or, in other words, a linear displacement of the charge in the molecule, see Fig. 6.2. This is of course also required for a molecule to have a CD signal: no absorption implies that there can be no differential absorption either. However, a linear displacement of charge in the molecules does not have the symmetry to give rise to a differential absorption of circularly polarized light. For this, a rotational motion of the charge is also required.

Circular dichroism is described in quantum mechanical terms via the rotational strength operator R (Cantor and Shimmel 1980; Rosenfeld 1929):

$$R = \text{Im}(\boldsymbol{\mu} \cdot \boldsymbol{m}) \quad (6.3)$$

Where Im denotes the imaginary component and \boldsymbol{m} is the magnetic dipole operator. The difference between the electric and the magnetic dipole is illustrated in Fig. 6.2.

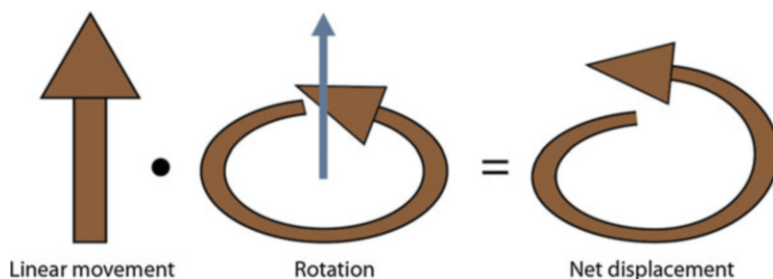


Fig. 6.2 Both an electric dipole moment (*left*) and a magnetic dipole moment (*middle*) are required for a differential absorption between left and right hand polarized light. Note that the direction (*blue arrow*) of the magnetic dipole moment is perpendicular to the circular motion. The result is a net helical displacement (*right*)

Since the rotational strength R is the product of both the electric and magnetic dipole, the net movement of charge in the molecule upon excitation (photon absorption) has to be displaced in a linear and circular motion, or in other words make a helical twist. It is tempting to think that a helical structure like the α -helix secondary structure in proteins should then be the perfect arrangement for a strong CD signal (which it coincidentally is), but the difference between the wavelength of the light (typically 200 nm) and the pitch of the α -helix (0.54 nm) does not warrant such a conclusion (Nordén et al. 2010). The net electron displacement under light absorption may either give rise to a positive ($\boldsymbol{\mu}$ and \boldsymbol{m} parallel) or negative ($\boldsymbol{\mu}$ and \boldsymbol{m} antiparallel) rotational strength and hence CD signal.

1.2 Instrumentation

The typical CD spectrometer is a bench-top instrument. Although the optical layout and instrument form differs between manufacturers, the overall principles are mostly the same. A schematic of a CD instrument is shown in Fig. 6.3.

The typical instrument consists of the following: a UV light source, typically a Xe-arc lamp, and a monochromator unit which selects and scans the wavelength. The light from the monochromator is linearly polarized (often with a MgF_2 Rochon type polarizer) after which a photo elastic modulator (PEM) converts the light into alternating left and right hand circularly polarized light at a high frequency, usually 50 kHz. The light passes through a sample (often in aqueous solution) after which the transmitted intensity is detected, mostly with a UV sensitive photo multiplier tube (PMT).

In normal (unpolarized) spectroscopy the desired signal typically lies between 0.1 and up to 1.5 absorbance units, but the difference between the absorbance of left and right hand circularly polarized light may be less than one ten thousandth of an absorbance unit. The subtraction of a direct measurement of the left and right circularly polarized light absorbances is therefore an unattractive, and mostly

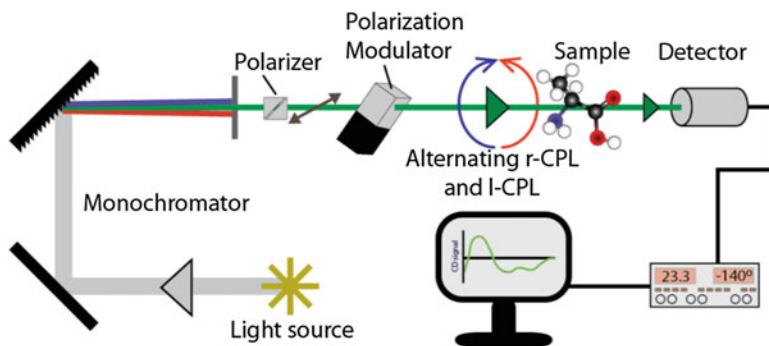


Fig. 6.3 Schematic representation of the optical layout of a typical CD spectrometer

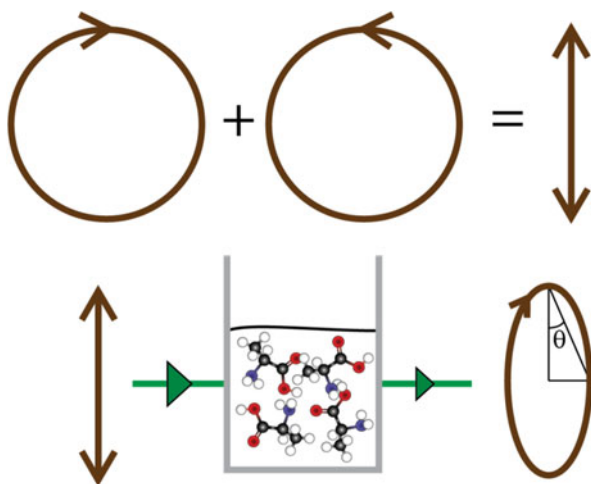
impossible, way of obtaining the CD signal. The fast oscillation between the two polarizations produced by the PEM offers an elegant and precise way of acquiring the CD signal. By filtering the signal from the detector to only contain the component which oscillates with the same frequency and phase as the PEM (by means of a lock-in amplifier), the small CD signal is extracted.

The natural unit for CD signals, following from the definition $\Delta A = A_L - A_R$, is Delta Absorbance. For direct comparison between samples measured at various concentrations and sample pathlengths the differential extinction coefficient $\Delta\epsilon$ is used. For protein samples, the far UV CD signal originates mostly from the secondary structure, i.e. from the relative orientation between pairs of amino acids. The relevant concentration to use when converting ΔA to $\Delta\epsilon$ is therefore the molar concentration of the peptide bond. Traditionally the pathlength of the typical cuvette for holding the sample is measured in cm, and the $\Delta\epsilon$ units therefore becomes $M^{-1} \text{ cm}^{-1}$. When using these units, the CD signal is called Delta Epsilon or Molar Circular Dichroism. The Delta Epsilon is important as it allows direct comparison between CD of proteins of different lengths, masses and amino acid compositions.

However, many other units are in use, and it can often be confusing to distinguish between them, even for the trained CD spectroscopist. The reader is referred to e.g. (Janes and Wallace 2009; Cantor and Shimmel 1980) if conversion between units is needed. However, one unit for ΔA is often used on bench-top instruments for historical reasons: θ measured in millidegrees, and therefore warrants a short description. Plane polarized light may be represented by the sum of two opposite handedness circularly polarized waves of equal intensity, see Fig. 6.4. If plane polarized light is passed through a chiral sample with non-zero CD, the light exits the sample slightly elliptical described by the ellipticity angle θ .

The effect is usually very small, so the angle is measured in millidegrees. There is a direct correlation between the ellipticity and ΔA :

Fig. 6.4 Linear polarized light can be considered as a superposition of two circularly polarized waves of opposite handedness (*top*). If linearly polarized light (*bottom*) is passed through a sample with non-zero CD signal the light exits as elliptical polarized light described by the ellipticity angle θ



$$\theta(\text{millidegrees}) = \Delta A \cdot \{1000 \cdot \ln(10) \cdot 180/4\pi\} = \Delta A \cdot 32982$$

So that the Delta Epsilon may be calculated as

$$\Delta \epsilon = \theta(\text{millidegrees}) / (c(\text{M}) \cdot l(\text{cm}) \cdot 32982)$$

where l is the pathlength and c is the concentration.

1.3 General Requirements for CD Measurements

Circular Dichroism is essentially an absorbance technique. Much of the same considerations that go into measuring the absorbance of a sample are therefore also valid and important for CD measurements. The sample needs to have an appropriate absorbance: if too low the measurement is not meaningful (nothing to measure), and if too high essentially no light will reach the detector. For the most accurate measurements the absorbance peak of the analyte should be in the range of 0.8–1, whereas absorbance (usually in the low wavelength end of the spectrum) of the entire sample (i.e. including solvent, buffers and salts) should be kept below 1.5. Two obvious means of adjusting the measured absorbance are change of pathlength and concentration, the latter in form of dilutions or up-concentrating. For the former, different types of cuvettes and cells for holding liquid samples are commercially available, and a few useful types are shown in Fig. 6.5. Typical pathlengths used for CD spectroscopy in the far UV are in a range of 0.1–1 mm. Longer cuvettes (of 1 cm or sometimes more) are used in the near UV spectral



Fig. 6.5 Different types of cuvettes for holding liquid samples. *Left:* Rectangular type cuvettes, here shown with a pathlength of 1 mm and 1 cm, but shorter types are also available. *Middle:* A 0.1 mm pathlength round cell with Teflon stoppers shown with a homemade Cu-holder. *Right:* Demountable round cell (0.1 mm pathlength) consisting of a flat and a hollow quartz plate, shown together with a Teflon and a Viton O-ring (bottom). These may be mounted in the cell holder shown above

region. These cuvettes and cells are mostly made of high quality Suprasil quartz. Highly specialized cells with shorter pathlengths down to a few micrometers also exist of both Suprasil and CaF₂ (Wien and Wallace 2005). For the shortest pathlengths the cells are demountable so that the optical surfaces may be easily cleaned from sample residues. A word of caution regarding the sample holders to use for CD spectroscopy: cuvettes and cells which otherwise work fine for normal absorbance spectroscopy, may introduce spurious effects in the CD signal due to strain or stress induced birefringence in the quartz. It is important to use sample holders which are designed and tested for CD spectroscopy use.

Samples measured with CD spectroscopy are more than often complex mixtures, especially for samples of pharmaceutical interest, of ingredients like water, buffers, salts, carbohydrates, lipids, preservatives (all constituting the solvent) and of course the chiral analyte (often protein or peptide). All these constituents potentially absorb in the UV spectral range (see Sect. 4.2), and therefore pose a limit to the lowest wavelength measurable, which may limit the structural information available in the CD spectrum. The influence of the solvent absorption may be minimized by changing the composition: e.g. lowering the chloride ion concentration (typically from salt and hydrochloric acid), using less absorbing buffers like sodium phosphate and using smaller (and therefore less scattering) lipid vesicles. When this is not desirable, or when the constitution of the solvent only can be changed to a certain level, the pathlength of the cell may be shortened. However, it is naturally important to avoid that the concentration of the protein becomes too low for meaningful CD signals to be measured. A rule of thumb is that a cell/cuvette pathlength of 0.1 mm requires a protein concentration of about 1 mg/ml (also see Sect. 4.2). Although this is a very rough estimate, which depends on the type and structure of the protein, it may be considered as a starting guideline for the choice of concentration.

An important prerequisite for obtaining a high quality CD spectrum of e.g. a protein does not only require acquisition of the sample spectrum, but also a carefully obtained reference or baseline spectrum. Although this is generally good practice for all absorption measurements, it is of a higher importance for CD spectroscopy, due to the small signal. As it is the spectrum of the protein which is of interest, the CD signal of the solvent has to be recorded and subtracted. This reference CD spectrum should be recorded on the same solvent used for making up the sample, and if the sample has been dialysed, keep and use the dialysate for reference. The baseline spectrum will show CD signals primarily from two sources: other or residual chiral substances in the solvent and CD signals originating from strain induced birefringence in the optics of the system, including the cuvette/cell. It is therefore good laboratory practice not only to record the baseline spectrum of the same solvent, but also in the same cell mounted under the same conditions (holder, rotation, position and sometimes even the same operator). Keep in mind that subtracting a badly obtained (or even noisy) baseline from an otherwise good sample spectrum degrades the final CD spectrum, and although tedious, it is recommended to plan carefully obtained reference spectra into the CD spectroscopy characterization protocol.

2 Characterizing Protein Structure Using CD

2.1 Protein Structure

A protein is a polymer of amino acids and often assumes a specific three-dimensional structure under physiologically relevant conditions, a conformation typically referred to as the native state. The native state is often also the active conformation although some proteins are largely unordered in their native states, typically requiring some degree of folding for activity (Dobson 2003; Uversky and Dunker 2010) while others possess a higher degree of organization than the active conformation, e.g. insulin that can form relatively stable dimeric and hexameric assemblies. In addition to their fundamental amino acid building blocks, proteins are often further modified by different chemical functionalities, either by covalent modification or through the binding of cofactors. However, most of their basic chemical, physical and conformational properties are generally given by the sequence of amino acids and we therefore limit the following discussion to the peptide part of proteins.

Proteins are assembled from 20 different L- α amino acids linked through peptide bonds. The lone pair of the backbone α -amino group is delocalized, resulting in double bond character and conformations restricted to trans and cis, the latter effectively only observed prior to proline residues. Therefore, the conformation of the peptide chain is effectively determined by the dihedral backbone angles, φ and ψ (Fig. 6.6). The numerical values of φ and ψ found in proteins are restricted or biased in two ways: (i) by sterical constraints due to the side chains, making certain conformations physically impossible, and (ii) by specific stabilization of certain interrelated values of φ and ψ through hydrogen bonds between peptide carbonyl groups and hydrogen atoms of the α -amino groups. The latter specific pattern of hydrogen bonds and backbone angles are characteristic of different elements of *secondary structure*, as shown in Table 6.1. Segments of secondary structure sometimes form so-called supersecondary structural elements or structural motifs, which are specific combinations of secondary structural elements that are observed in multiple proteins. Proteins which share structural motifs do not necessarily have a related function.

The topology of the entire peptide chain is referred to as the tertiary structure. Generally, a protein is only referred to as possessing a tertiary structure if said structure is stabilized through side chain interactions, in addition to backbone

Fig. 6.6 The three backbone angles φ , ψ and ω in proteins as illustrated for dialanine

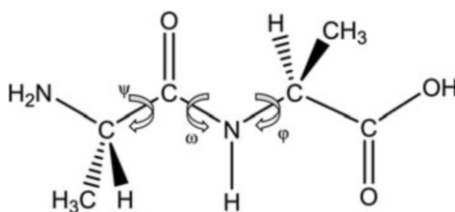
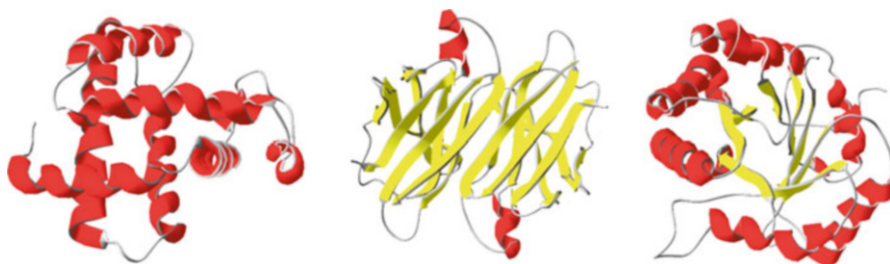


Table 6.1 Overview of important secondary structure elements in proteins and typical values for φ and ψ

Element	Φ	Ψ	Comment	References
Right handed α -helix	-62	-41	The most abundant secondary structure element, constituting 30–35 % of known structures	Barlow and Thornton (1988)
β -sheet, parallel	-119	113	Sheet structures are common and may form between units that are distant in primary sequence or between chains	IUPAC (1970)
β -sheet, antiparallel	-139	135		
Polyproline II helix (PPII)	-75	145	Unfolded proteins contain significant amounts of PP2 structure, also found in “unordered” regions of folded proteins	Adzhubei et al. (2013)
3_{10} -helix	-71	-18	Angles depend strongly on the position in the helical structure	Barlow and Thornton (1988)
π -helix	-57	-70	Present in about 15 % of known protein structures	Fodje and Al-Karadaghi (2002)
β -turn, type 1	-64, -90	-27, -7	One example out of many turn structures. Values refer to angles between the first and the second and between the second and third amino acid in the turn	Hutchinson and Thornton (1994)

**Fig. 6.7** Three-dimensional structures of an all- α protein (myoglobin, 1MBN.pdb), an all- β protein (prealbumin, 2PAB.pdb) and an α/β protein (triose phosphate isomerase, 7TIM.pdb). All figures were created using Swiss PDBViewer

interactions. For globular proteins this typically involves the formation of a hydrophobic core in which hydrophobic amino acids are shielded from the solvent water. As a rule of thumb, a length of about 50 amino acids is required for the formation of a globular structure with a hydrophobic core. A single, globular unit, or domain, is often classified according to topology and secondary structure content as either all- α , all- β , $\alpha + \beta$ or α/β (Levitt and Chothia 1976; Schaeffer and Daggett 2011). Examples of three of these folds are shown in Fig. 6.7.

Proteins that self-associate in order to form oligomeric structures are said to possess a quaternary structure. Oligomeric states may be the active, native state of

the protein, exemplified by haemoglobin, or a stable, but inactive conformer, which is the case for insulin. Self-association can also lead to undesired and uncontrollable oligomerization, generally referred to as aggregation.

All proteins exist in various conformational states depending particularly on the solvent properties and the temperature. The unfolded state is usually reserved for describing a somewhat hypothetical conformational state where no persistent self-interaction and thereby no persistent structure exists. Such a polypeptide chain should exhibit molecular dimensions similar to those expected from a random-coil polymer and additionally no residual local structure should exist (Fitzkee and Rose 2004). Since the unfolded state can be better described as a large number of fluctuating conformational states of similar free energy, the term *denatured state ensemble* is also commonly used. In a secondary structural context, these conformations are typically referred to as unordered/disordered, random or, preferably, irregular structure. Often, slight conformational changes lead to structures that possess significant native state character. These states may be described as non-native or denatured, the latter implying a lack of activity.

2.2 *Far UV and Near UV CD of Proteins*

Proteins contain a number of UV chromophores, most importantly the peptide bond and the aromatic side chains of tryptophan, tyrosine and phenylalanine. The peptide bond is a relatively weak chromophore but the sheer abundance of this group in proteins results in significant absorption in the far UV range, below 250 nm. The strongest CD signal in the far UV range is that of the α -helix, up to three times more intense than spectra of β strand structures. Furthermore, α helical structure is often quite easy to identify due to the intense positive peak at 192 nm and the minima at 208 and 222 nm. In addition to lower intensity, β strand structures vary much more conformationally than helices do and hence, the far UV CD spectra of proteins rich in sheets may appear very different from each other. In Fig. 6.8, examples of far UV CD spectra of three proteins of different folds are shown, along with a spectrum of ferredoxin, with an almost 50 % content of irregular structure.

The aromatic groups absorb both in the far UV range and in the near UV range, 250–320 nm. Furthermore, the disulfide bond formed between two cysteine residues absorbs in the near UV region. The absorption in the near UV range is routinely used for the determination of protein concentration since the absorption coefficient can be predicted with reasonable accuracy. Neither the disulfide nor the aromatic side chains are chiral by nature; however, when located in a chiral environment, circular dichroism may be observed due to induced chirality. The interior of a globular protein generally constitutes such an environment, meaning that the near UV CD spectrum of a protein is sensitive to changes in the tertiary structure. In some cases, near UV CD spectroscopy may also be applied to monitor changes in quaternary structure if self-association of individual monomers is accompanied by changes in the microenvironment of these side chains. Near UV

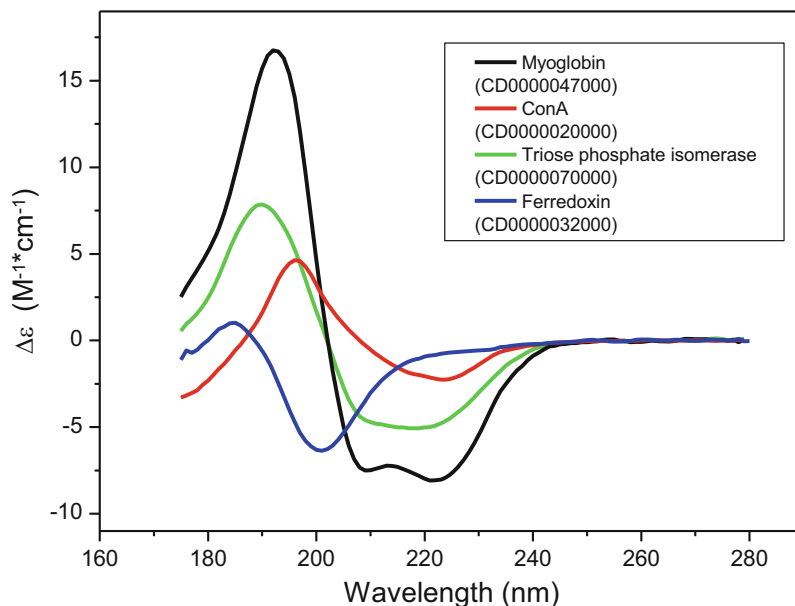


Fig. 6.8 Examples of far UV CD spectra of proteins with high content of α helix (myoglobin, *black*), β strand (concanavalin A, *red*), an α/β protein (triose phosphate isomerase, *green*) and a protein with a high content of irregular structure (ferredoxin, *blue*). Note that especially for proteins of high β strand content, the appearance of far UV CD spectra vary considerably. CD data were obtained from the online database of far UV CD spectra, PCDDDB, with the accession IDs shown in the *inset* (Whitmore et al. 2011)

CD bands are typically wide and overlapping and it is rarely possible to assign spectral features to certain amino acid side chains or to a given type of structure. For this reason, and probably also due to the fact that a near UV CD spectrum requires about 50 times more protein, near UV CD is not as commonly used as far UV CD. For examples of near UV CD spectra and their practical use, see Chap. 3.

Far UV and near UV CD spectroscopy thus gives information on the physical structure of proteins in solution, information that sometimes can be immediately interpreted as representing certain structural elements. Even disregarding this latter fact, CD is an invaluable tool for rapidly monitoring conformational changes, for instance when judging structural similarity of protein variants or for assessing conformational changes as a function of different conditions such as pH, ionic strength and temperature.

2.3 Estimation of Secondary Content by Far-UV CD

Different secondary structure elements give rise to characteristic CD spectra and a quantitative estimate of the secondary structure content of a given sample can therefore be obtained on basis of its far UV CD spectrum. Since the Beer-Lambert

law applies for CD spectroscopy, the measured spectrum is then taken as the sum of the individual contributions plus a noise term, a common feature of all methods for estimating secondary structural content (Greenfield 2006). The experimental data set is compared to a set of proteins with known CD spectra and known atomic structure from which the secondary structure content can be extracted using computer programs such as DSSP (Kabsch and Sander 1983) or STRIDE (Frishman and Argos 1995). Widely used mathematical strategies include least squares fitting (e.g. Saxena and Wetlaufer 1971), ridge regression (Provencher and Glöckner 1981), singular value decomposition (Hennessey and Johnson 1981) and neural networks (Andrade et al. 1993).

Most of the programs referred to above are freely available for non-commercial use, either as download or upon request. In addition, several have been implemented in downloadable programs such as CDPro (<http://lamar.colostate.edu/~sreeram/CDPro/CDPro.htm>; Sreerama and Woody 2000) or at webpages where analysis can be performed online (e.g. Dichroweb, <http://dichroweb.cryst.bbk.ac.uk>; Whitmore and Wallace 2008). It should be noted that both the choice of protein reference sets and of program can significantly influence the output. Therefore, it is always a good idea to compare the results obtained using different fitting routines and reference datasets.

For some types of samples, precise protein concentration is difficult to define or determine, for instance when working with proteins that are encapsulated in particulate carriers or aggregated, film-forming samples. Therefore, methods have also been developed for estimation of secondary content without knowledge of the protein concentration. One approach plots the measured ellipticity divided by the recorded absorbance, the so-called Kuhn g -factor (McPhie 2001), while another uses quadratic equations of ellipticities at given wavelengths relative to ellipticities at 207 nm (Raussens et al. 2003).

3 CD Spectroscopy in Pharmaceutical Sciences

The activity and stability of a peptide or protein is strongly correlated to their three-dimensional structure. Characterization of this three-dimensional structure is thus an important element for understanding the physicochemical and physiological behavior of these compounds. This characterization can be a daunting task due to the inherent complexity of these large molecules. Moreover, most methods only provide information on some aspects of the three dimensional structure, and thus a combination of methods is generally required to obtain a comprehensive overview. Each method has its own set of strengths and weaknesses, and the reader should be aware that the results of different methods can at times lead to what appears to be opposite conclusions. Thus, while we discuss only CD in this chapter, it is generally not advised to use this as the only method to characterize peptide or protein structure.

3.1 *CD in Early Stage Development*

In the early stages of pharmaceutical development, there usually is only a limited amount of material available. Yet, it may be important to obtain information on the folding of the peptide or protein, for example to compare to expectations from published data or predictive models. Since CD requires little material, in particular for far UV CD, it is an excellent first choice to perform such measurements.

A good example in this respect is the development of a biosimilar, i.e. a generic version of an already marketed protein drug. Due to the high complexity of proteins in terms of structure and production, regulatory agencies use the concept of “similarity” to allow for unavoidable small differences between the biosimilar and the comparator (innovator) product. For small molecule generic products it is sufficient to show chemical equivalence and bioequivalence, but biosimilars require a more comprehensive comparison. This includes using a range of structural characterization methods that should show the biosimilar is essentially the same (“similar” enough). A company wishing to develop such a biosimilar can benefit greatly from assuring early in the production process that the protein that is produced has the right (comparable) folding as that of the comparator product. If major deviations are observed the process can be optimized before large scale production is started. Also at the further development stages CD can be used to compare the biosimilar and comparator protein.

Beyond the low material consumption of CD, an added advantage is that spectra can be obtained and analyzed within an hour, which also allows a rapid screening of the effect of e.g. pH on the structure of the peptide or protein. The latter can help identify solution conditions that may compromise the structural integrity of the compound, but which may occur during production. For example, a common method for virus inactivation during protein purification involves lowering the pH and maintaining this pH for a prolonged period of time (minutes to hours). If major structural rearrangements are observed at this pH, this raises significant concerns about the stability of the protein.

An example of the use of CD to characterize the protein fold as a function of pH is given in Fig. 6.9. Here the near UV CD spectra of two monoclonal antibodies with very high sequence identity (>95 %) are shown in the range of pH 4–9. The observed differences are rather subtle, but the spectrum at pH 4 stands out most for the IgG4. At this pH a clear difference with the spectra at the other pH values is observed around 270–290 nm; the dichroic signal in this region is likely due to tyrosine and tryptophan residues and thus suggests there is a change in structure around one or more of these residues. No such differences are observed for the IgG1. At pH 4 both antibodies convert into a gel within 2 weeks storage at 40 °C, whereas the samples at higher pH do not form a gel even after 8 weeks of storage. Thus, the relatively small difference in the spectra may be indicative of a structural change that is highly detrimental to the stability of the IgG4 antibody. However, the IgG1 is equally susceptible to gel formation at pH 4, but does not show the same spectral deviation. This shows both the usefulness and limitations in using CD to predict potential stability issues upon varying the pH.

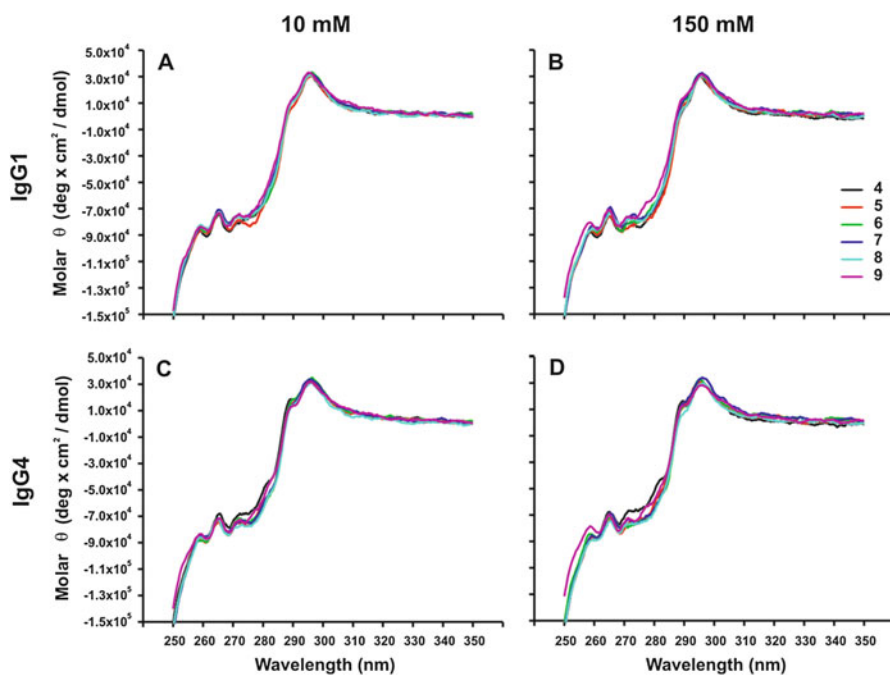


Fig. 6.9 Near UV CD spectra of an IgG1 and IgG4 monoclonal antibody at different pH values and two different ionic strengths. The spectra at pH 4 show a clear deviation from the other pH values around 270–290 nm for the IgG4, which is where a dichroic signal of tyrosine and tryptophan is expected. Reprinted with permission from Neergaard et al. (2014) © 2013 Wiley Periodicals, Inc. and the American Pharmacists Association

CD is also commonly used to determine unfolding thermodynamics, either by determining the structural changes as a function of temperature or as a function of denaturant concentration (e.g., urea or guanidine). Unfolding as a function of temperature helps identification of temperatures to avoid during production and during accelerated storage stability studies, as unfolding greatly accelerates various degradation reactions. Unfolding using denaturants allows the determination of the change in free energy upon unfolding at any temperature. This information can be used to construct a protein stability curve (Becktel and Schellman 1987).

3.2 Applications of CD in Formulation Research

Pharmaceutical protein formulations often contain a number of excipients to assure efficacy and long-term storage stability of the product. These excipients may include buffers, tonicity agents, preservatives and stabilizing agents. As in the case with pH discussed in the previous section, CD can be used to determine any structural changes induced by the added excipients. In addition, the effect of the excipient on thermal- or denaturant-induced unfolding can be investigated.

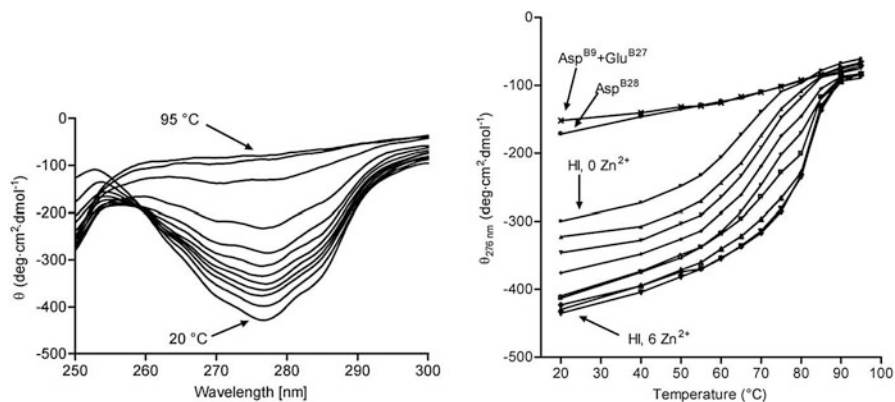


Fig. 6.10 *Left:* Near UV CD spectra of 0.6 mM insulin with 0.5 mM Zn^{2+} at varying temperatures. From the bottom (largest negative signal) to the top, temperatures range from 20 to 95 °C. The strong negative ellipticity is due to the insulin hexamer formation placing the tyrosines in a conformationally restricted environment. *Right:* Thermal scanning of ellipticity in the near UV range. The ellipticity at 276 nm is shown as a function of temperature. Thermal scans were performed with 0.6 mM human insulin in 7 mM phosphate buffer at pH 7.4 with varying amounts of Zn^{2+} . From the top to the bottom curve, the Zn^{2+} concentration is 0, 0.05, 0.1, 0.15, 0.2, 0.3, 0.4, 0.5, and 0.6 mM. Thermal scans with zinc-free insulin Asp^{B28} and Asp^{B9}Glu^{B27} in 7 mM phosphate buffer at pH 7.4, both known to be monomeric, are also indicated in the graph. Reprinted with permission from Huus et al. 2005. © 2005, American Chemical Society

An example of such studies is shown in Fig. 6.10 for insulin (Huus et al. 2005). Insulin is known to form multimers (dimers, tetramers, hexamers) upon increasing concentration and addition of certain metal ions, in this case Zn(II). The formation of dimers and hexamers places the tyrosine residues in a more ordered environment, which in turn causes a significant dichroic signal for these residues. Thus, the multimerization can be followed by CD (Fig. 6.10, left panel). The right panel shows the thermal melting curves as followed by CD for insulin in different multimeric forms (dimer or hexamer) as a result of the relative amount of Zn (II) added. The apparent transitions in the CD signal as a function of temperature fit well with those obtained by differential scanning calorimetry.

The insulin hexamer can undergo further structural changes upon addition of certain ligands like phenol or m-cresol. The latter are commonly used as preservatives in formulations and their presence is usually a concern due to their hydrophobic nature and potential negative effects on protein stability. However, the insulin hexamer has been found to contain six specific binding sites for these preservatives. Upon binding of these ligands, part of the B-chain of insulin folds into an α helix in a highly cooperative manner. In principle, human insulin can exist in three different allosteric states: T6, T3R3, and R6 states, with the latter being the final state formed upon addition of sufficient phenolic ligands. Also, various other ligands may cause such transitions, or induce further stabilization of the R6 state.

The change in structure upon preservative binding can be followed by CD as the increased content of α -helix corresponds to a more negative dichroic signal around 208 and 222 nm. Dichroic changes in the near UV region are also expected, but those can be more difficult to observe due to the strong absorbance of phenolic compounds in this region (see also Fig. 6.12). A ligand that is transparent in the near-UV region is the thiocyanate anion, which can cause a structural rearrangement from T6 to T3R3, but not to R6. The resulting changes in the near UV CD spectra are shown in Fig. 6.11a, with Fig. 6.11b showing the changes at 256 and 276 nm as a function of thiocyanate concentration (Huus et al. 2006). Note that both wavelengths can be used to follow the thermal unfolding (Fig. 6.11c).

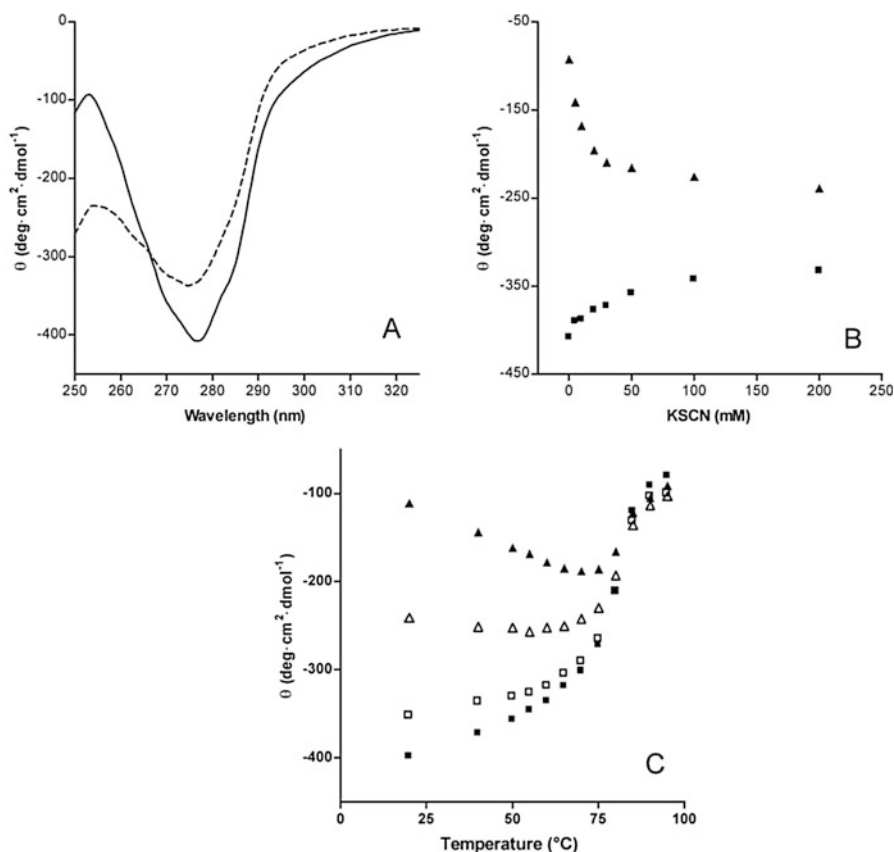


Fig. 6.11 Effect of the thiocyanate anion and heating on the near UV- CD spectrum of human insulin. Samples contained 0.6 mM human insulin with 5 Zn²⁺/hexamer in 7 mM phosphate at pH 7.4. (a) Spectra collected in the absence (full line) and presence of 200 mM KSCN (dashed line). (b) The effect of increasing KSCN concentrations on the near UV CD signal at 256 nm (filled triangle) and 276 nm (filled square). (c) Effect of heating on the near UV CD signal at 256 nm (triangles) and 276 nm (squares) in the absence (filled symbols) and presence of 100 mM thiocyanate (open symbols). Reproduced from Huus et al. 2006 with kind permission from Springer Science and Business Media

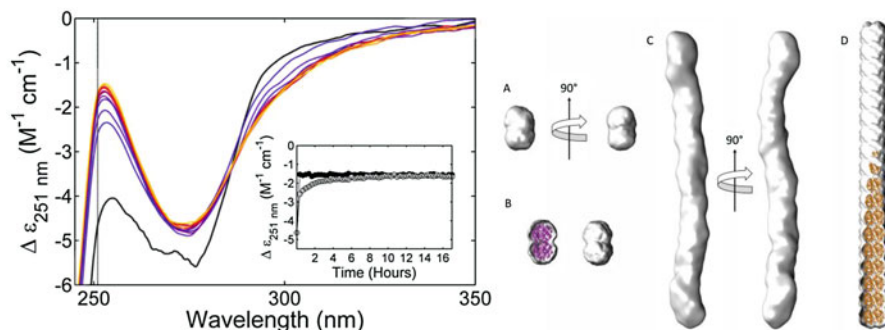


Fig. 6.12 *Left*: the self-association of Lys^{B29} (N^ε-ω-carboxyheptadecanoyl) des(B30) human insulin containing 6 Zn(II) ions per hexamer was followed by near UV CD. The allosteric change from R3T3 (or rather, dodecamers in the form of T3R3R3T3) to T6 (T6T6) can be followed at 251 nm (marked with a *broken line*). The measurements prior to self-assembly in the presence of high concentrations of phenol is shown in *black* (1070 μM insulin). This spectrum is comparatively noisy due to high absorption of phenol in particular around 270–280 nm. After buffer exchange over a NAP5 column, the conformational change can be followed in the sample (800 μM insulin) (from *purple* to *yellow*). Here the samples from 0 to 8 and 16 h are shown. The *inset* shows the development of $\Delta\epsilon_{251\text{nm}}$ during the 17 h in a buffer containing 0 (*black circles*) and 0.6 mM phenol (*grey circles*). In the latter case the transition is significantly slower. Adapted with permission from Jensen et al. (2013). © 2013, American Chemical Society. *Right*: Ab initio models of the SEC-purified dihexamer (a) and the fully self-associated sample after 48 h (c). The models are averaged and filtered of ten individual models calculated by the program Dammin. Two models of a R3T3T3R3-dihexamer (b) created from crystal structures 1MS0 and 1TRZ, respectively, and a T6-multihexamer (18 hexamers) (d) are shown for comparison. Reprinted with permission from Jensen et al. (2013) © 2013, American Chemical Society

The various allosteric changes of insulin are also of importance to understand the assembly process of large associates of certain lipidated insulins, such as insulin degludec (marketed as Levemir® by Novo Nordisk) and its close relative Lys^{B29} (N^ε-ω-carboxyheptadecanoyl) des(B30) human insulin (Steensgaard et al. 2013; Jensen et al. 2013). In the presence of phenolic ligands, these lipidated insulins primarily form dodecamers with the water-exposed sides consisting of insulin in the R-state, whereas the interacting interfaces between two hexamers consist of insulin molecules in the T-state. That is, these dodecamers are in a R3T3T3R3 configuration. Upon removal of the ligand a transition from R to T state is observed, causing a spatial rearrangement of the lipid chains that allows them to interact with other dodecamers and form large linear complexes (Fig. 6.12).

3.3 Application of CD for Advanced Drug Delivery Systems

Almost all protein drugs are administered parenterally due to the often very poor bioavailability through other routes and high costs of the protein drug. A variety of advanced drug delivery systems are currently under investigation to alleviate the

poor patient compliance common for parenteral delivery, but also to target the system to the desired site of action. For example, a number of products on the market contain PEGylated or lipidated variants of the parent protein. These modifications can significantly increase circulation time, thus reducing administration frequency. Also here CD is a commonly used technique to assess structural integrity and structural changes upon modification, as already shown above for insulin degludec and Lys^{B29} (N^ε-ω-carboxyheptadecanoyl) des(B30) human insulin (Fig. 6.12a).

A yet largely unsuccessful but heavily investigated approach is to encapsulate the protein drug or associate it to a carrier system. In the case of association of proteins to e.g. liposomal delivery systems, the aim is generally to (passively) target the system to its site of action. This reduces systemic exposure and thereby potential undesirable side-effects. However, the increasing complexity of such systems makes the proper characterization of the structural integrity of the protein even more difficult. The potential high scattering by liposomes means that it may be difficult to determine the whole far UV CD spectrum. In such cases it may still be possible to assess structural integrity by overlaying the CD spectra over a spectral region where scattering is limited enough to allow such a comparison. Such an approach is illustrated in van Slooten et al. (2000).

The scattering by particulate systems need not always be a major problem. For example, Sarmiento et al. (2007), were able to measure the far UV CD spectra of insulin entrapped in alginate/chitosan nanoparticles (Fig. 6.13), even though these particles were in the size-range of about 1 μm. Apparently, these particles have a refractive index that is quite similar to that of water, thus significantly reducing scattering. Moreover, by careful adaptation of concentration and cell path length,

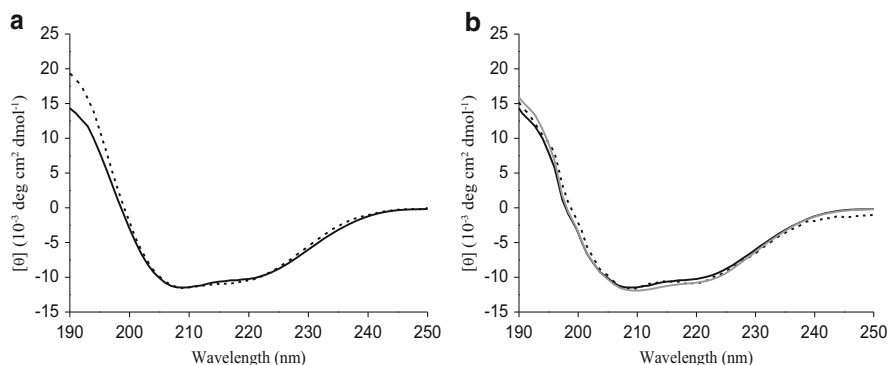


Fig. 6.13 *Left:* Far UV CD spectrum of human insulin in 0.01 M HCl solution (*solid line*) and entrapped in alginate/chitosan nanoparticles prepared with alginate:chitosan mass ratio of 4.3:1 at pH 4.7 (*dashed line*). *Right:* Far UV CD spectrum of human insulin in solution (*black solid line*), insulin released into pH 1.2 buffer from alginate/chitosan nanoparticles (*dashed line*) and insulin released into pH 6.8 buffer from alginate/chitosan nanoparticles (*grey solid line*) prepared with alginate:chitosan mass ratio of 4.3:1 prepared at pH 4.7. Adapted with permission from Sarmiento et al. (2007), © 2007, Elsevier

the negative impact of scattering can be reduced even further. CD can then also be used to investigate the structural integrity of the released protein, as also demonstrated in Fig. 6.13 for the insulin-loaded alginate/chitosan particles. Further details on measuring scattering sample may be found in the next Sect. 3.4.

3.4 RIME/Synchrotron Radiation CD

If challenges remain with scattering of the delivery system, further steps may include the use of synchrotron radiation circular dichroism or by refractive index matching; i.e. the adjustment of the refractive index of the solution to that of the scattering system. These methods are reviewed below based on recent literature dealing with index matching and synchrotron radiation CD on oil/water scattering systems, but the methods outlined are also valid for liposomal delivery systems and nanoparticles.

The study of protein conformational structure changes upon their incorporation into oil-water interfaces is particularly challenging. As emulsions are used in both the food and pharmaceutical industries, their stability is of outmost importance. Proteins, as macromolecular surfactants, are often used as emulsifiers (Dickinson 1999; Wilde 2000; Damodaran 2005; Murray 2011) due to their amphiphilic nature, and understanding their structure at oil/water (o/w) interfaces is therefore highly relevant.

From a spectroscopic point of view, emulsions may at a first glance be deemed unfit for analysis due to their highly scattering nature. The small oil droplets produce a very turbid and seemingly non-transparent solution for light wavelengths similar to, and smaller than, the size of the droplets. The scattering originates from refraction at the interface due to the higher refractive index (RI) of oil compared to water ($n = 1.333$): hexadecane has a refractive index of $n = 1.434$ and triglycerides around $n = 1.46$ (Zhai et al. 2010). The Refractive Index Matched Emulsion (RIME) method was developed to circumvent this problem (Husband et al. 2001). Glycerol is added to the water phase to effectively increase the refractive index of the water/glycerol solution to match the index of the oil under study. This eliminates refraction at the o/w interface making the solution transparent. The refractive index of glycerol is close to $n = 1.47$ (Physical Properties of Glycerine and Its Solutions 1963) and a 58% (v/v) addition to the aqueous phase removes the turbidity of a water/hexadecane emulsion rendering it accessible to spectroscopic studies. There are however several issues which should be considered before using the RIME method for protein folding studies. Firstly, the method is not useful for triglyceride oils often used in emulsions: the refractive index of triglycerides is so high that nearly 100% glycerol is needed to match the refractive index, rendering the method useless for these high RI oils. Secondly, all cosolvents, including glycerol, may change a protein's structure and functionality: glycerol acts as a stabilizer of the native state of some proteins as well as increasing the thermal stability (McClements 2002). Such refractive index matching may therefore have a

significant impact on the system under investigation, and this approach should be treated with appropriate caution. Thirdly, although glycerol is transparent in the visible and near UV spectral range, the added absorbance of both glycerol and the oil under study limits the lowest accessible wavelength in that far UV to a point where secondary structure prediction may become uncertain and erroneous even on high light flux CD instruments (*vide infra*).

The use of high brightness Synchrotron Radiation (SR) as a source for circular dichroism (SRCD) offers significant advantages over lamp based conventional circular dichroism (cCD) spectrometers (Janes and Wallace 2009; Wallace et al. 2011; Miles and Wallace 2006; Wallace 2009). The continuously high flux of light from SR sources into the VUV spectral region extends the accessible wavelength range over which a protein CD spectrum may be acquired. This effectively increases the informational content of the spectra (Toumadje et al. 1992; Wallace and Janes 2001) which, in combination with a better signal-to-noise ratio compared to cCD instruments, leads to better and more accurate secondary structure determination. In conjunction with newly developed protein reference basis spectra sets (Lees et al. 2006) which utilizes the extended wavelength range, even on membrane proteins (Abdul-Gader et al. 2011), SRCD has become a powerful tool for study of protein structures under difficult conditions like e.g. high absorption buffers and excipients, scattering, small sample amounts etc. With several SRCD beam lines throughout Europe and Asia (Miles et al. 2007; Wallace et al. 2011) and a new line planned in South America (Brazil), SRCD is both an established and available technique.

Several studies (Zhai et al. 2010, 2011, 2012; Wong et al. 2012; Day et al. 2014) of emulsions all carried out at the Aarhus University CD1 beam line (Miles et al. 2007, 2008) have shown that SRCD is a viable and powerful technique for investigations of protein structure change upon oil/water interface adsorption. It was shown (Zhai et al. 2010) that the combination of a SRCD instrument, the use of short pathlength sample cells (0.1 mm) and by carefully recording a reference baseline of the emulsion enables differentiation of the adsorbed protein signal from that of the light scattering droplets. Compared to the non-RI matched study by Husband et al. (2001), where only a very noisy spectrum of an emulsion with β -lactoglobulin down to only about 220 nm was obtained (i.e. essentially no spectral features), the new method allowed measurements of β -Ig in both tricaprylin (a triglyceride) and hexadecane emulsions down to 180 nm (Zhai et al. 2011), revealing a significant secondary structural change (increase of the α -helical content from 16 % up to 50 %) upon interface adsorption in the emulsion. Likewise α -lactalbumin shows a doubling of the helical content from about 30 % to nearly 60 % from the solution to the emulsion phase (Zhai et al. 2012), and also both beta-casein and deamidated gliadins show increased helical structure upon adsorption while the β -sheet content is reduced (Wong et al. 2012). Although these findings may indicate a propensity toward increased helical content, globular proteins like lysozyme, bovine serum album and myoglobin in contrast show a decreased helical content at oil/water interfaces compared to their structure in solution (Day et al. 2014).

4 Practical Considerations and Recommendations

4.1 Calibration and Maintenance of CD Instruments

A well-kept and properly calibrated CD instrument is essential for reliable high quality CD spectra to be obtained. Although this must always be considered at normal good laboratory practice, it is of even greater importance for studies of pharmaceutical relevance where e.g. day-to-day and batch-to-batch structure and function is investigated.

The most basic parameter of a spectrometer is the light intensity, which deteriorates during the lifetime of the spectrometer, often as a result of a drop in lamp performance over time. For all CD spectrometers, the detector high voltage (often denoted HT) is recorded alongside the CD signal. The HT is varied such that when a high intensity of light hits the detector, the HT is low, and when the detector records low levels of light, the HT is set higher. This means that when a spectrum is recorded for wavelengths across an absorption peak in a sample, the HT signal will also peak. The measured CD signal is only valid as long as the HT signal is below a certain voltage (as defined by each individual manufacturer for each model), and it is important to truncate CD spectra for wavelengths shorter than the wavelength where the HT hits this cut-off level. As the HT signal depends on the light level hitting the detector, reference HT spectra taken at regular intervals on the instrument, with no sample in the compartment, are valuable records of the instrument performance and will aid in determining when an instrument is due for service, simply by comparing with the HT spectrum taken with the instrument when it was new (or when last serviced).

A well-functioning CD spectrometer must also be wavelength calibrated. Many manufacturers of UV/Vis spectrometer and accessories offer filters with distinct absorption peaks at various wavelengths, but a 40 g/L solution of holmium oxide in 10% (v/v) perchloric acid is easily made, and will, sealed in a 10 mm cuvette, provide several absorption peaks at wavelengths above 240 nm for reliable calibration (Travis et al. 2005).

The spectrometer's ability to measure accurately the CD signal unperturbed in the entire wavelength range of the sample spectrum is obviously of the highest importance. Nevertheless, large variations have been observed between instruments of different makes and age (Miles et al. 2003), rendering direct comparison between spectra acquired in different laboratories difficult, showing that accurate CD signal calibration on a regular basis is mandatory for well-maintained instruments. The golden standard is the measurement of the CD spectrum of (1S)-(+)-10-camphorsulfonic acid (CSA) in a wavelength range from 330 nm down to at least 190 nm. To obtain reliable measurements at the low wavelength end, the CSA sample needs to be measured in a short pathlength sample cell of 1 mm or preferably 0.1 mm. The differential extinction coefficient at the positive 290 nm peak is $\Delta\epsilon = 2.36 \text{ M}^{-1} \text{ cm}^{-1}$, and to eliminate the uncertainty in the literature about the absolute amplitude of the peak near 191 nm, it has been suggested that the ratio

of the two peaks is set to 2.0 at a temperature of 25 °C so that $\Delta e = -4.72 \text{ M}^{-1} \text{ cm}^{-1}$ (Miles et al. 2003). It is important to measure the CSA spectrum at the correct temperature, as the ratio is temperature dependent. The hygroscopic nature of CSA makes the concentration determination impossible by simply weighing. Instead, the absorbance of CSA at 285 nm can be used with an extinction coefficient of $\epsilon_{285\text{nm}} = 34.6 \text{ M}^{-1} \text{ cm}^{-1}$ (Miles et al. 2004). A practical concentration of CSA of about 7 mg/mL is useful for CD measurements in a 0.1 mm pathlength sample cell, corresponding to a measured absorbance measured at 285 nm in a 1 cm cuvette of 1.008.

A reliable calibration of sample cuvette and cell pathlengths is a necessary condition for accurate comparison between measurements. Long pathlength cells (1 cm) may have deviations from the nominal length of up to about 1 %, which in general is acceptable. However, for short pathlength cells very large discrepancies from the manufacturer's specifications have been observed: up to 18 μm pathlength for a nominally 10 μm cell. Depending on pathlength, two methods for measuring the path length can be used: From 0.1 mm up to 1 cm cells the absorbance at 373 nm of potassium chromate (K_2CrO_4) in an alkaline solution of 50 mM KOH may be used, and for cells with pathlength of 0.1 mm and below an interference technique is required.

The generally accepted value for the extinction coefficient of potassium chromate at 373 nm is $\epsilon_{373} = 4830 \text{ M}^{-1} \text{ cm}^{-1}$ (Haupt 1952). However, variations in the apparent molar extinction coefficient with concentration have been reported (Burke and Mavrodineanu 1977; Burke et al. 1972) varying from $4830 \text{ M}^{-1} \text{ cm}^{-1}$ at a concentration of $c = 0.7 \times 10^{-4} \text{ M}$ to $4814 \text{ M}^{-1} \text{ cm}^{-1}$ for $c = 2.1 \times 10^{-4} \text{ M}$. The latter higher concentration corresponds to a very reasonable absorbance of $A = 1.01$ for pathlength determination in a 1 cm cuvette, i.e. using the often quoted extinction coefficient of $4830 \text{ M}^{-1} \text{ cm}^{-1}$ will introduce a mere 0.4 % error at this concentration.

When measuring the absorbance spectrum of a dry cell interference fringes from multiple reflections off the two cell windows may be observed, and is useful for a very accurate (down to 0.1 μm) determination of the pathlength. The effect is small for cells with a nominal pathlength of 0.1 mm and stronger for shorter pathlengths. An example of such a measurement is shown in Fig. 6.14, and represents a particularly difficult interference fringe measurement of a nominally 0.1 mm pathlength cell. The measurement for such a (comparably) long pathlength cell has to be made with a slow scanning rate (down to 5 nm/min), but for shorter pathlength cells good data may be collected at a considerable faster speed. By counting the number of fringes n between two wavelengths λ_1 and λ_2 the pathlength (PL) may be calculated as (Miles and Wallace 2006)

$$PL[\mu\text{m}] = 0.001 \cdot n \cdot \frac{1}{2} \cdot (\lambda_2 \cdot \lambda_1) / (\lambda_2 - \lambda_1)$$

where the wavelengths are measured in units of nm. Using this formula, the pathlength of the nominally 100 μm (0.1 mm) cell is found to be 104.5 μm , i.e. a 4.5 % deviation, which must be considered to be significant. Another method for

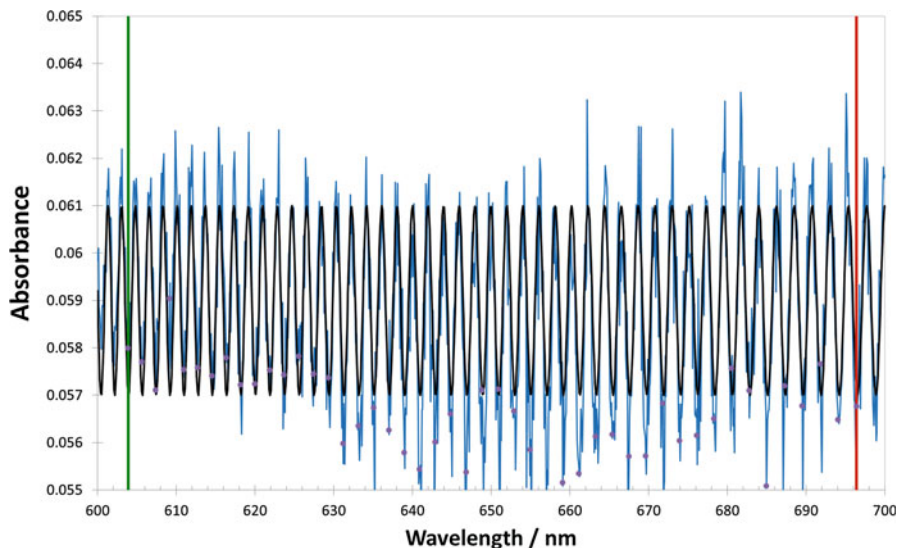


Fig. 6.14 The absorbance spectrum (*light blue*) of an empty cell with a nominally 0.1 mm pathlength measured at a scanning speed of 5 nm per min on an EVO300 spectrometer (Thermo). This represents a particular difficult cell to measure, illustrating the validity of the method. By counting the number of fringes (marked with *dots*) over a range of wavelengths marked with the *green* and *red line*, the pathlength may be accurately calculated. Another method is by fitting (black) the fringes. The actual pathlength is determined to be 0.1045 mm, a non-neglectable deviation from the nominal value

finding the pathlength, also illustrated in Fig. 6.14, is to fit the absorbance to the following function;

$$Absorbance = Amplitude \cdot \cos^2(2 \cdot \pi \cdot PL \cdot 1000/\lambda) + offset$$

which represents the absorbance variation of the interference fringes. The *Amplitude* represents the variation of the absorbance and the offset is the mean value. Both these methods are very precise, and we find that the two methods yield pathlengths within less than 0.1 μm (i.e. 0.1 %) of each other, giving confidence in that the correct value has been determined.

4.2 Sample Preparation and Data Acquisition

In addition to instrument performance, the successful execution and interpretation of a CD experiment depends on the attention given to experimental design and the care and precaution taken when analyzing the results.

Sample preparation: The first critical parameters relates to the purity, concentration and solvent of the protein under investigation. Since the Beer-Lambert law applies in CD spectroscopy, the measured CD signal from a protein sample is the sum of the contributions of all proteins present in the sample. Assessment of purity is therefore critical and should be performed using chromatographic and/or electrophoretic methods, including analysis carried out under native conditions. Suitable techniques include reduced/non-reduced SDS-PAGE, capillary electrophoresis and HPLC methods, primarily size exclusion chromatography. Roughly, three main approaches are taken in order to determine the concentration of a protein: (1) methods based on quantitative determination of the total content of a given protein constituent, e.g. amino acid and Kjeldahl analysis. These are considered the most accurate methods but are not generally available or employed in protein chemistry laboratories. (2) Spectroscopic methods based on absorption of light in the near-UV range. The absorption of light in the near-UV range by a protein completely unfolded in 6 M GdnHCl is exactly the same as the equivalent concentration of the aromatic chromophores dissolved in this solvent (Edelhoch 1967). Since sequence information is usually available today, the extinction coefficient for the protein in 6 M can be calculated. More often used though less accurate, is the estimation of an extinction coefficient of the native protein based on typical extinction coefficients for the aromatic chromophores in native proteins. One should be aware that using this procedure might introduce an error of up to 20 % in the estimation of the extinction coefficient, translating into the same error in protein concentration (Pace et al. 1995). (3) The use of extrinsic dyes that bind to proteins. These approaches can be very sensitive and therefore useful if quantitation of very small amounts of protein is needed. However, the staining response due to binding is very protein-specific and for this reason alone, the use of extrinsic dyes is not recommended in this context. For further details and examples of experimental protocol, the reader is referred to the literature (Noble and Bailey 2009).

The solvent for CD spectroscopic investigations should be as transparent as possible in the examined wavelength range. This means that care needs to be taken when selecting the appropriate buffer and salt for adjusting the ionic strength, if needed. In cases where the experimental conditions can be chosen freely, low concentrations of an inorganic buffer salt such as phosphate is typically selected in order to extend the lower wavelength limit. Buffers containing amino groups such as Tris are less desirable and buffers containing carboxylates or aromatic groups should be avoided. It is recommended both to consult the literature for further information (Kelly et al. 2005; Greenfield 2006) and to examine the absorbance of potential buffers using an ordinary UV spectrophotometer.

The protein concentration may also be optimized. At a given pathlength, a high concentration of protein results in a high signal but also higher noise, eventually leading to a lower signal to noise ratio. Conversely, at low concentrations, the signal diminishes while the noise is not strongly affected. The optimal concentration depends on several factors, e.g. the wavelength range of interest and the structural content, which determines the magnitude of the molar CD signal. A good starting point for far UV CD measurements are 0.1–0.2 mg/mL in a 1 mm cell. In the near

UV range suitable concentrations can be estimated by determining the absorbance around 280 nm (see above) and adjusting the concentration to give an absorbance of ca. 1 absorbance unit. In order to improve performance in the very far UV range, samples can be degassed and centrifuged in order to remove particulates. Filtration through a non-adsorbing filter-type of small pore size may also be performed but it should be evaluated if this adversely affects the sample under investigation.

Data acquisition. In addition to careful calibration and maintenance described in the previous section, a few control spectra are useful to perform. First, an air measurement can be performed in order to check instrument performance and possible CD signals in the absence of any objects in the light path. Second, a scan with the empty CD cell could be performed in order to check the quality of the cell. Finally, the reference spectrum ideally containing the same solvent components as the protein sample is measured. When subsequently measuring a number of protein samples, attention must be paid to potential baseline drift. This is especially important for near UV CD where the measured signal is often small and even a small drift can therefore be notable.

Typically, 3–5 scans are measured and averaged. It is strongly recommended not to let the instrument auto-average scans but to save or at least inspect all scans. For most commercial instruments, it is also possible to adjust the bandwidth of the light passing through the monochromators, which affects the spectral resolution. A narrow bandwidth increases resolution, but the concomitant decrease in light intensity may cancel out this advantage when the reduction in signal to noise ratio becomes a limiting factor. Due to differences in both hardware and software between different commercial CD instruments, the reader is encouraged to study the recommendations of the manufacturer concerning instrumental settings for optimal CD measurements.

4.3 Common Pitfalls and Errors

In the previous sections, critical technical and practical aspects regarding the successful acquisition of CD spectra have been presented. Failing to acknowledge these aspects may result in spurious data that may lead the researcher to erroneous conclusions. A number of these issues evidently compromises published results while others cannot be identified unequivocally. Therefore, we here present a brief list of pitfalls and common errors that can often be easily avoided.

Measurement at excessive HT (detector gain). Probably the most commonly occurring error is the presentation of data recorded at excessive absorbances. Recorded data need to be truncated at the wavelength at which the specified maximal detector gain (given by the high tension, HT, value) is exceeded. If measurements at lower wavelengths are sought after, one may consider optimizing the buffer composition, decreasing the protein concentration, or using a shorter pathlength or an instrument providing higher photon flux, i.e. synchrotron CD.

No subtraction of background spectrum. In addition to CD from the protein under investigation, raw CD data are the result of contributions from the instrumental hardware, sample cell and the buffer. A presented protein CD spectrum should always be the result of subtraction of an appropriate reference spectrum from the sample spectrum. In most cases, the nature of the appropriate reference is obvious: the same buffer used for dissolving the protein (or preferably, a dialysate) measured in the same sample cell using the same instrumental settings. In other cases, the reference spectrum is more difficult to define, for instance when examining poorly soluble proteins or aggregates hereof which may result in scattering artefacts not directly related to conformational content.

Overinterpretation of secondary structure fits. The typical root mean square deviation of estimates of the relative content of different secondary structure elements are in the range 5–15 % depending on the type of secondary structure element, the protein under investigation and the fitting strategy employed (Sreerama and Woody 2004). These numbers refer to the estimation of the conformational content of the model proteins constituting the protein reference sets. Model proteins are well characterized and typically available at high purities, which minimizes some of the uncertainties that lead to errors in concentration. The listed accuracies of secondary structure estimation should therefore be considered best-case and not necessarily common scenarios.

References

- Abdul-Gader A, Miles AJ, Wallace BA (2011) A reference dataset for the analyses of membrane protein secondary structures and transmembrane residues using circular dichroism spectroscopy. *Bioinformatics* 27:1630–1636
- Adzhubei AA, Sternberg MJE, Makarov AA (2013) Polyproline-II helix in proteins: structure and function. *J Mol Biol* 425:2100–2132
- Andrade MA, Chacón P, Merelo JJ, Morán F (1993) Evaluation of secondary structure of proteins from UV circular dichroism spectra using an unsupervised learning neural network. *Protein Eng* 6:383–390
- Anslyn EV, Dougherty DA (2005) Stereochemistry (Chapter 6). In: *Modern physical organic chemistry*. University Science Books, USA
- Barlow DJ, Thornton JM (1988) Helix geometry in proteins. *J Mol Biol* 201:601–619
- Barron LD (2004) *Molecular light scattering and optical activity*. Cambridge University Press, Cambridge
- Barron LD (2009) An introduction to chirality at the nanoscale. In: Amabilino DB (ed) *Chirality at the nanoscale: nanoparticles, surfaces, materials and more*. Wiley, Weinheim
- Becktel W, Schellman J (1987) Protein stability curves. *Biopolymers* 11:1859–1877
- Burke RW, Deardorff ER, Menis O (1972) Liquid absorbance standards. *J Res Natl Bur Stand A* 76A:51–64
- Burke RW, Mavrodineanu R (1977) Certification and use of acidic potassium dichromate solutions as an ultraviolet absorbance standard—SRM 935. National bureau of standards special publications. U.S. Government Printing office, Washington
- Cantor CR, Shimmel PR (1980) *Biophysical chemistry part II*. Freeman, New York
- Damodaran S (2005) Protein stabilization of emulsions and foams. *J Food Sci* 70:R54–R66

- Day L, Zhai J, Xu M, Jones NC, Hoffmann SV, Wooster TJ (2014) Conformational changes of globular proteins adsorbed at oil-in-water emulsion interfaces examined by synchrotron radiation circular dichroism. *Food Hydrocolloids* 34:78–87
- Dickinson E (1999) Adsorbed protein layers at fluid interfaces: interactions, structure and surface rheology. *Colloids Surf B* 15:161–176
- Dobson CM (2003) Protein folding and misfolding. *Nature* 426:884–890
- Edelhoch H (1967) Spectroscopic determination of tryptophan and tyrosine in proteins. *Biochemistry* 6:1948–1954
- Fitzkee NC, Rose GD (2004) Reassessing random-coil statistics in unfolded proteins. *Proc Natl Acad Sci U S A* 101:12497–12502
- Fodje MN, Al-Karadaghi S (2002) Occurrence, conformational features and amino acid propensities for the π -helix. *Protein Eng* 15:353–358
- Frishman D, Argos P (1995) Knowledge-based protein secondary structure assignment. *Proteins* 23:566–579
- Greenfield N (2006) Using circular dichroism spectra to estimate protein secondary structure. *Nat Protoc* 1:2876–2890
- Haupt GW (1952) An alkaline solution of potassium chromate is a transmittancy standard in the ultra violet. *J Res Natl Bur Stand* 48:414–416
- Hennessey JP Jr, Johnson WC Jr (1981) Information content in the circular dichroism of proteins. *Biochemistry* 20:1085–1094
- Husband FA, Garrod MJ, Mackie AR, Burnett GR, Wilde PJ (2001) Adsorbed protein secondary and tertiary structures by circular dichroism and infrared spectroscopy with refractive index matched emulsions. *J Agric Food Chem* 49:859–866
- Hutchinson EG, Thornton JM (1994) A revised set of potentials for β -turn formation in proteins. *Protein Sci* 3:2207–2216
- Huus K, Havelund S, Olsen HB, van de Weert M, Frokjaer S (2005) Thermal dissociation and unfolding of insulin. *Biochemistry* 44:11171–11177
- Huus K, Havelund S, Olsen HB, van de Weert M, Frokjaer S (2006) Chemical and thermal stability of insulin: effects of zinc and ligand binding to the insulin zinc-hexamer. *Pharm Res* 23:2611–2620
- IUPAC-IUB Commission on Biochemical Nomenclature (1970) Abbreviations and symbols for the description of the conformation of polypeptide chains. *J Biol Chem* 245:6489–6497
- Janes RW, Wallace BA (2009) An introduction to circular dichroism and synchrotron radiation circular dichroism spectroscopy. In: Wallace BA, Janes RW (eds) *Modern techniques for circular dichroism and synchrotron radiation circular dichroism spectroscopy*. Advances in biomedical spectroscopy, vol 1. IOS Press, Amsterdam, p 1–18.
- Jensen MH, Wahlund PO, Toft KN, Jacobsen JK, Steensgaard DB, van de Weert M, Havelund S, Vestergaard B (2013) Small angle X-ray scattering-based elucidation of the self-association mechanism of human insulin analogue lys(B29)(N ϵ)- ω -carboxyheptadecanoyl des(B30). *Biochemistry* 52:282–294
- Kabsch W, Sander C (1983) Dictionary of protein secondary structure: pattern recognition of hydrogen-bonded and geometrical features. *Biopolymers* 22:2257–2637
- Kelly SM, Jess TJ, Price NC (2005) How to study proteins by circular dichroism. *Biochim Biophys Acta* 1751:119–139
- Lees JG, Miles AJ, Wien F, Wallace BA (2006) A reference database for circular dichroism spectroscopy covering fold and secondary structure space. *Bioinformatics* 22:1955–1962
- Levitt M, Chothia C (1976) Structural patterns in proteins. *Nature* 261:552–558
- McClements DJ (2002) Modulation of globular protein functionality by weakly interacting cosolvents. *Crit Rev Food Sci Nutr* 42:417–471
- McPhie P (2001) Circular dichroism studies of proteins in films and in solution: estimation of secondary structure by g-factor analysis. *Anal Biochem* 293:109–119

- Miles A, Wien F, Lees J, Rodger A, Janes R, Wallace B (2003) Calibration and standardisation of synchrotron radiation circular dichroism and conventional circular dichroism spectrophotometers. *Spectroscopy* 17:653–661
- Miles AJ, Wien F, Wallace BA (2004) Redetermination of the extinction coefficient of camphor-10-sulfonic acid, a calibration standard for circular dichroism spectroscopy. *Anal Biochem* 335:338–339
- Miles AJ, Wallace BA (2006) Synchrotron radiation circular dichroism spectroscopy of proteins and applications in structural and functional genomics. *Chem Soc Rev* 35:39–51
- Miles AJ, Hoffmann SV, Tao Y, Janes RW, Wallace BA (2007) Synchrotron radiation circular dichroism (SRCD) spectroscopy: new beamlines and new applications in biology. *Spectroscopy* 21:245–255
- Miles AJ, Janes RW, Brown A, Clarke DT, Sutherland JC, Tao Y, Wallace BA, Hoffmann SV (2008) Light flux density threshold at which protein denaturation is induced by synchrotron radiation circular dichroism beamlines. *J Synchrotron Radiat* 15:420–422
- Murray BS (2011) Rheological properties of protein films. *Curr Opin Colloid Interface Sci* 16:27–35
- Neergaard MS, Nielsen AD, Parshad H, Van De Weert M (2014) Stability of monoclonal antibodies at high-concentration: head-to-head comparison of the IgG1 and IgG4 subclass. *J Pharm Sci* 103:115–127
- Noble JE, Bailey MJA (2009) Quantitation of protein. *Methods Enzymol* 463:73–95
- Nordén B, Rodger A, Daffron T (2010) Linear dichroism and circular dichroism. A text-book on polarized-light spectroscopy. RCS Publishing, Cambridge
- Pace CN, Vajdos F, Fee L, Grimsley G, Gray T (1995) How to measure and predict the molar absorption coefficient of a protein. *Protein Sci* 4:2411–2423
- Physical Properties of Glycerine and Its Solutions (1963) Physical properties of glycerine and its solutions. Glycerine Producers' Association, New York
- Provencher SW, Glöckner J (1981) Estimation of globular protein secondary structure from circular dichroism. *Biochemistry* 20:33–37
- Raussens V, Ruyschaert J-M, Goormaghtigh E (2003) Protein concentration is not an absolute prerequisite for the determination of secondary structure from circular dichroism spectra: a new scaling method. *Anal Biochem* 319:114–121
- Rosenfeld L (1929) Quantenmechanische theorie der natürlichen optischen aktivität von flüssigkeiten und gasen. *Z Phys* 52(161–174):921
- Sarmento B, Ferreira DC, Jorgensen L, van de Weert M (2007) Probing insulin's secondary structure after entrapment into alginate/chitosan nanoparticles. *Eur J Pharm Biopharm* 65:10–17
- Saxena VP, Wetlaufer DB (1971) A new basis for interpreting the circular dichroic spectra of proteins. *Proc Natl Acad Sci U S A* 68:969–972
- Schaeffer RD, Daggett V (2011) Protein folds and protein folding. *Protein Eng Des Sel* 24:11–19
- Sreerama N, Woody RW (2000) Estimation of protein secondary structure from circular dichroism spectra: comparison of CONTIN, SELCON, and CDSSTR methods with an expanded reference set. *Anal Biochem* 287:252–260
- Sreerama N, Woody RW (2004) Computation and analysis of protein circular dichroism spectra. *Methods Enzymol* 383:318–351
- Stensgaard DB, Schluckebier G, Strauss HM, Norrman M, Thomsen JK, Friderichsen AV, Havelund S, Jonassen I (2013) Ligand-controlled assembly of hexamers, dihexamers, and linear multihexamer structures by the engineered acylated insulin degludec. *Biochemistry* 52:295–309
- Toumadje A, Alcorn SW, Johnson WC Jr (1992) Extending CD spectra of proteins to 168 nm improves the analysis for secondary structure. *Anal Biochem* 200:321–331
- Travis JC, Acosta JC, Andor G et al (2005) Intrinsic wavelength standard absorption bands in holmium oxide solution for UV/visible molecular absorption spectrophotometry. *J Phys Chem Ref Data* 34:41–56

- Uversky VN, Dunker AK (2010) Understanding protein non-folding. *Biochim Biophys Acta* 1804:1231–1264
- van Slooten ML, Visser AJ, van Hoek A, Storm G, Crommelin DJ, Jiskoot W (2000) Conformational stability of human interferon- γ on association with and dissociation from liposomes. *J Pharm Sci* 89:1605–1619
- Wallace BA, Janes RW (2001) Synchrotron radiation circular dichroism spectroscopy of proteins: secondary structure, fold recognition and structural genomics. *Curr Opin Chem Biol* 5:567–571
- Wallace BA (2009) Protein characterization by synchrotron radiation circular dichroism spectroscopy. *Q Rev Biophys* 42:317–370
- Wallace BA, Gekko K, Hoffmann SV, Lin Y-H, Sutherland JC, Tao Y, Wien F, Janes RW (2011) Synchrotron radiation circular dichroism (SRCD) spectroscopy: an emerging method in structural biology for examining protein conformations and protein interactions. *Nucl Instr Meth Phys Res A* 649:177–178
- Whitmore L, Wallace BA (2008) Protein secondary structure analyses from circular dichroism spectroscopy: methods and reference databases. *Biopolymers* 89:392–400
- Whitmore L, Woollett B, Miles AJ, Klose DP, Janes RW, Wallace BA (2011) PCDDDB: the protein circular dichroism data bank, a repository for circular dichroism spectral and metadata. *Nucleic Acids Res* 39:D480–D486
- Wien F, Wallace BA (2005) Calcium fluoride micro cells for synchrotron radiation circular dichroism spectroscopy. *Appl Spectrosc* 59:1109–1113
- Wilde PJ (2000) Interfaces: their role in foam and emulsion behaviour. *Curr Opin Colloid Interface Sci* 5:176–181
- Wong BT, Zhai J, Hoffmann SV, Augustin M, Wooster TJ, Day L (2012) Conformational changes to deamidated wheat gliadins and β -casein upon adsorption to oil-water emulsion interfaces. *Food Hydrocolloids* 27:91–101
- Zhai J, Miles AJ, Pattenden LK, Lee T-H, Augustin MA, Wallace BA, Aguilar M-I, Wooster TJ (2010) Changes in beta-lactoglobulin conformation at the oil/water interface of emulsions studied by synchrotron radiation circular dichroism spectroscopy. *Biomacromolecules* 11:2136–2142
- Zhai J, Wooster TJ, Hoffmann SV, Lee T-H, Augustin MA, Aguilar M-I (2011) Structural rearrangement of β -lactoglobulin at different oil-water interfaces and its effect on emulsion stability. *Langmuir* 27:9227–9236
- Zhai J, Hoffmann SV, Day L, Lee T-H, Augustin MA, Aguilar M-I, Wooster TJ (2012) Conformational changes of α -lactalbumin adsorbed at oil-water interfaces: interplay between protein structure and emulsion stability. *Langmuir* 28:2357–2367

Chapter 7

Applications of Mass Spectrometry in Drug Development Science

Ulrike Leurs, Ulrik H. Mistarz, and Kasper D. Rand

Abstract Mass spectrometry (MS) offers the capability to identify, characterize and quantify a target molecule in a complex sample matrix and has developed into a premier analytical tool in drug development science. Through specific MS-based workflows including customized sample preparation, coupling to liquid chromatography and different ionization principles, both qualitative and quantitative analysis of small and large drug compounds can be achieved at an unprecedented sensitivity.

Here, we review the basic principles of MS and tandem MS, including ionization, mass analysis and detection, as well as fragmentation techniques and coupling of MS to chromatographic separation. As the structural integrity of protein drugs during purification, formulation and delivery is of critical importance to ensure drug efficacy and safety, an overview over current approaches for primary and higher-order structure analysis of proteins by mass spectrometry will be given as well as related workflows for quantitative MS analysis. Established “top-down” and “bottom-up” protein analyses with MS will be recapitulated, and the use of emerging technologies such as hydrogen/deuterium exchange mass spectrometry (HDX-MS) for higher-order protein structure analysis will be discussed.

Keywords Qualitative and quantitative mass spectrometry • Small molecules and protein biopharmaceuticals • Higher-order structure (HOS) elucidation • Hydrogen/deuterium exchange mass spectrometry (HDX-MS) • Pharmacokinetics and mass spectrometry

1 Mass Spectrometry in Drug Development

Over the last 30 years mass spectrometry (MS) has undergone a remarkable development in terms of increased sensitivity, throughput and faster sample preparation. MS applications are now characterized by their high sensitivity and low

U. Leurs • U.H. Mistarz • K.D. Rand (✉)

Department of Pharmacy, Faculty of Health and Medical Sciences, University of Copenhagen, Copenhagen, Denmark

e-mail: kasper.rand@sund.ku.dk

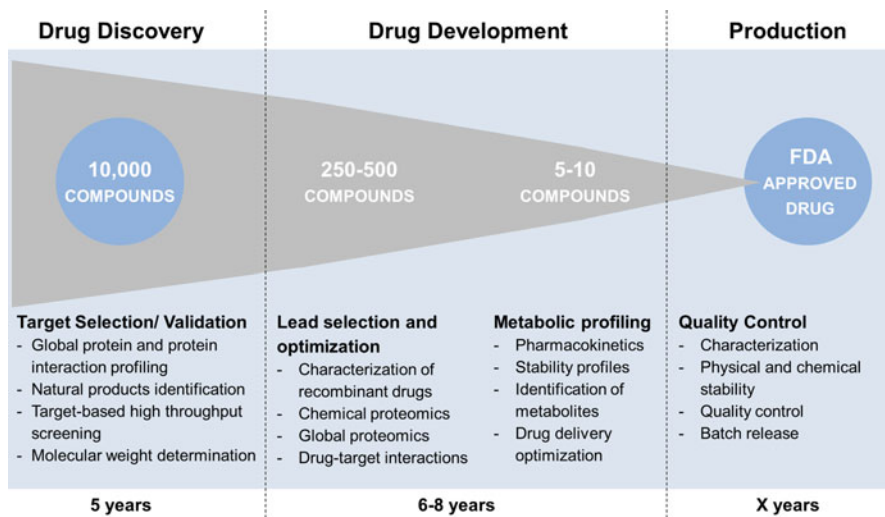


Fig. 7.1 Applications of mass spectrometry throughout the drug discovery, development and production process

sample consumption, while providing high mass accuracy with isotopic resolution for mass analysis even of large biomolecules. For these reasons MS has, within the last two decades, become an indispensable tool for researchers working in drug development science. Its low limit of detection (down to zepto moles), as well as the speed and vast diversity of applications make MS the method of choice in many areas of drug research. Figure 7.1 gives an overview of the many instances of MS-based analyses throughout the drug development process.

Early in the drug discovery progress, MS can be used to unravel the biological effect of a potential drug on an enzyme, a cell or in an organism (Glish and Vachet 2003). A subdivision of these applications is often referred to as *proteomics*, *metabolomics* and other “*omics*”; they involve the identification and quantification of proteins that are expressed in specific organisms or tissues across distinct functional or disease-relevant states. Of direct utility in drug discovery is *chemical proteomics* which involves enrichment and identification of unknown endogenous protein receptors targeted by a synthetic ligand or drug from biological material (Jeffery and Bogyo 2003; Rix and Superti-Furga 2009; Corradini et al. 2015). Later on in the drug discovery process, MS is used routinely by medicinal chemists to monitor chemical reactions during drug synthesis and product validation. In the case of protein pharmaceuticals, MS is used extensively for initial characterization and optimization of the recombinant expression products (Leurs et al. 2015). In later steps of the drug development process, formulation scientists use MS for stability testing and formulation development. For instance, MS has evolved to be a gold standard for quality control during manufacturing of both small molecule and large protein pharmaceuticals (Glish and Vachet 2003; Leurs et al. 2015). LC-MS

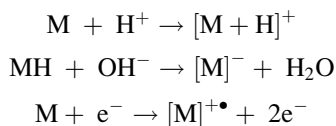
analysis is also routinely used to analyze and quantify metabolites from pharmacokinetic studies.

1.1 The Mass Spectrometer

During mass analysis, the molecular weight of an analyte compound is measured in relation to its charge, expressed as the m/z (ratio of mass to charge) value. Hence, MS requires the analyte to be ionized prior to mass analysis; i.e. be able to *take up* or *abstract a proton*. Hence, mass spectrometers can acquire data in both positive and negative mode, depending on the nature of the analyte. A mass spectrometer consists of three main parts: the ion source, the mass analyzer and the detector.

1.1.1 Ion Sources

The first step of any mass spectrometric analysis is the ionization of the analyte. The process of ionization refers to the transition of the analyte into the gas-phase as an ion by either taking up or detaching a proton, forming either cations or anions. Ionization can be achieved through direct and indirect charge transfer reactions, or by irradiating a volatile analyte with electrons:



The part of the mass spectrometer where the ionization takes place is called the ion source. Generally speaking, there are two different approaches to ionization—*hard* or *soft ionization*. The two differ according to the amount of internal energy that is deposited in the analyte as a result of ionization. *Hard ionization* is considered to be a harsh ionization method because high amounts of energy are imparted onto the analyte during the ionization process. This can lead to dissociation of covalent bonds in the analyte molecule (a process called fragmentation). In contrast to that, *soft ionization* maintains a low internal energy in the analyte during ionization, resulting in less or no fragmentation. Hard ionization has a long history in the analysis of small molecules, whereas soft ionization is a more recent development. Soft ionization methods are nowadays often used preferably in the analysis of both small molecules, as well as of larger peptides and protein molecules.

Examples for hard ionization methods are e.g. *electron ionization* (or electron impact, EI) and *chemical ionization* (CI). In EI, the analyte is vaporized and ionized by irradiation with high energy electrons. CI utilizes a reagent gas that is irradiated with electrons to produce an ionization plasma which in turn can react with the volatile analyte to yield ions. Both ionization methods induce fragmentation of the

analyte due to covalent bond dissociation, resulting in fragment ions with m/z values lower than the molecular weight of the analyte. Since both EI and CI require the ion source to be under high vacuum (1×10^{-8} bar), they are not readily coupled to liquid chromatography (LC). However, coupling of EI and CI sources to gas chromatography (GC) systems is routine as the chromatographic system used during GC is operated at vacuum. A further consequence of the required high vacuum inside the source is that only volatile organic compounds can be analyzed by EI and CI. Though EI and CI can provide a high degree of structural information about the analyte, they are increasingly supplanted by softer ionization techniques. An alternative to the hard ionization methods EI and CI is atmospheric pressure chemical ionization (APCI) which can circumvent some of their disadvantages. APCI is analogous to CI; however it operates at atmospheric pressure and can therefore be coupled to LC systems. The analyte eluting from the LC system is introduced as a thin fog into the APCI source via a nebulizer using nitrogen gas. The solvent is then evaporated in a heated desolvation/vaporization chamber. The hot gas carrying the analyte is then ionized along a corona discharge electrode. Ions produced enter the mass analyzer through a small inlet which allows the high-vacuum inside to be maintained.

The two most common soft ionization methods are matrix-assisted laser desorption/ionization (MALDI) and electrospray ionization (ESI), their principle mechanisms are illustrated in Fig. 7.2. MALDI ionization is a two-step process. The first step is the co-crystallization of the analyte with a matrix on a stainless steel target. The matrix normally consists of small organic molecules that have strong absorption at the incoming wavelength of the laser, typically 337 or 350 nm. The co-crystallized sample is then subjected to a laser beam under high vacuum, leading to desorption of the matrix material. The matrix material absorbs the energy from the laser beam, causing its ablation (Karas and Bahr 1990). In the resulting hot plume of ions and neutral molecules, proton transfer reactions lead to ionization of the analyte. The exact mechanism of ionization in MALDI is still discussed and remains to be elucidated. Because the matrix molecules absorb most of the energy from the laser, the damage to the sample is minimal, meaning that the ionization can occur without fragmentation of the analyte. MALDI can therefore be used for the analysis of large, non-volatile and thermally labile compounds such as proteins, oligonucleotides and synthetic polymers. Furthermore, the indirect ionization through matrix absorption sets no limits in terms of molecular weight of the ionized analyte—indeed; proteins with molecular masses up to 300,000 Da have been analyzed by MALDI (Siuzdak 1994). Common MALDI matrices include sinapinic acid, α -cyano-4-hydroxycinnamic acid and 2,5-dihydroxybenzoic acid; all of those compounds share certain features:

- chromophoric — to allow strong absorption in the wavelength range of the laser
- low molecular weight — to allow easy ablation
- acidic — to serve as a proton source for the analyte during ionization.

As MALDI is a pulsed ionization technique, it is well suited for coupling to time-of-flight (TOF) analyzers. TOF analyzers allow analysis of ions over a wide mass

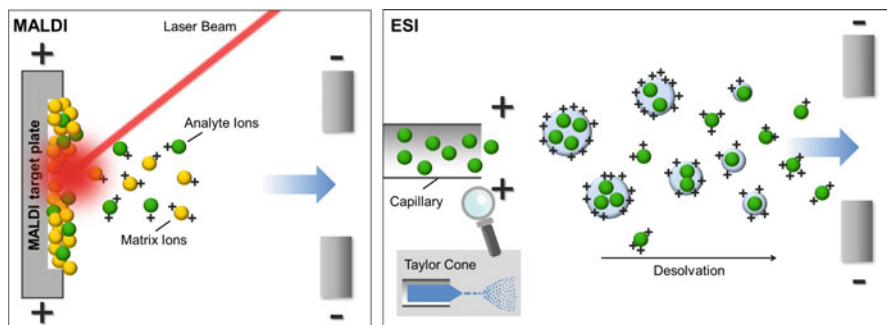


Fig. 7.2 Principles of MALDI and ESI ionization (Leurs et al. 2015)

range, and thereby complement MALDI ionization, which produces ions of low charge and thus large m/z values. Most MALDI MS instruments are therefore MALDI-TOF combinations. MALDI has a relatively high tolerance towards salts, buffer components and detergents, which can be very detrimental to other popular ionization techniques. In 2002, Koichi Tanaka was awarded the Nobel Prize in Chemistry for his work on soft laser desorption of biological macromolecules. A comprehensive overview of MALDI, the ablation/desorption process and different types of matrices has been given elsewhere (Karas and Bahr 1990; Hillenkamp and Peter-Katalini 2007).

Electrospray ionization (ESI) is another widely used soft ionization technique in MS. ESI produces ions by dispersing a solution containing the analyte by electrospray into a fine aerosol. To this end, a liquid passing through a capillary is subjected to a strong electric field at atmospheric pressure. The electric field is produced by applying a potential difference of 2–4 kV between the capillary and a cone shaped counter-electrode (skimmer) with a small orifice, which is placed in 0.3–2 cm distance from the capillary exit. The electrical field leads to an accumulation of charges at the liquid surface at the capillary exit. When the Coulombic repulsion of accumulating charges exceeds the surface tension of the liquid surface (Rayleigh limit), the shape of the liquid surface at the capillary exit assumes a so-called “Taylor cone”. From the Taylor cone, a jet of highly charged droplets is emitted into the ionization chamber (see Fig. 7.2). The solvent is then quickly evaporated from the droplets (a process also called *desolvation*) by a counter-current heated gas. The droplets then once again become unstable when they reach their Rayleigh limit, undergo Coulombic fission and thereby produce many smaller and more stable droplets. These droplets undergo repetitive rounds of desolvation and Coulombic fission, forming ever smaller droplets, until ultimately desolvated analyte ions emerge that are then extracted through the orifice of the skimmer into the mass spectrometer for mass analysis. To facilitate desolvation and increase ionization efficacy, solvents for ESI often consist of mixtures of water, acetonitrile and an acid as a proton source. Furthermore, the ion source can be heated to enhance desolvation. In high-flow ESI sources, an inert gas (e.g. N_2 or CO_2) is applied to assist nebulization, for example when coupled to an HPLC

system. ESI is the ion source of choice for LC-MS applications because it can be coupled “online” to an LC system.

ESI often produces multiply charged ions, resulting in a characteristic charge state envelope for larger molecules e.g. a protein, thereby effectively extending the mass range of the analyzer. Furthermore, some solution-phase information can be retained in ESI; enabling e.g. the analysis of higher-order structure and non-covalent interactions between a drug and its protein target by ESI. In 2002, John B. Fenn was awarded the Nobel Prize in Chemistry for his contributions in the development of ESI in the analysis of (bio)macromolecules. A comprehensive overview of ESI-MS and an explanation of the fundamentals of electrospray is given in “Electrospray and MALDI Mass Spectrometry: Fundamentals, Instrumentation, Practicalities, and Biological Applications” (Cole 2010).

The choice of the appropriate ionization technique depends on (i) the physical/chemical properties of the analyte, i.e. mass and polarity; (ii) the sample matrix and (iii) the requirements of a coupled chromatographic separation step prior to mass analysis. The diagram in Fig. 7.3 gives an overview of the application range of the different ionization methods with regards to molecular weight and sensitivity. As apparent from the illustration, ESI and MALDI have a very wide and high mass range, while EI and APCI are most suited for the analysis of small molecules.

1.1.2 Mass Analyzers

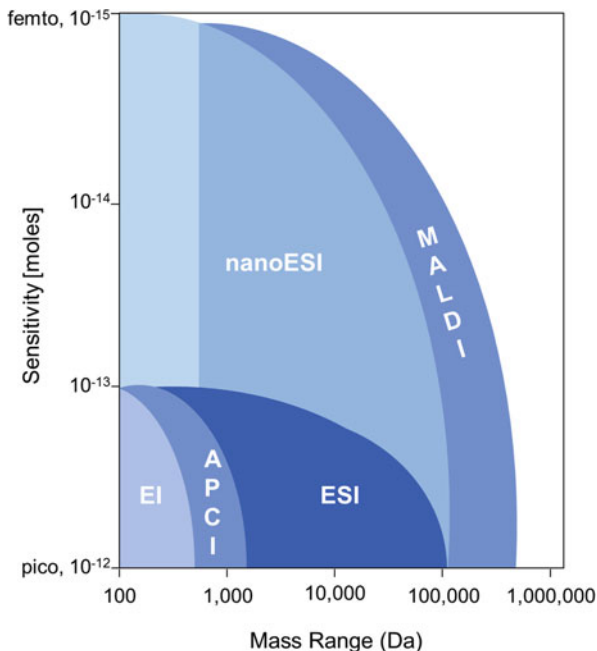
From the ion source, the produced ions are transported via electric fields to the mass analyzer where the ions are separated according to their m/z (ratio of mass to charge). Common mass analyzers include *time-of-flight (TOF)*, *quadrupoles*, *ion traps*. They can be grouped into *scanning* and *continuous* mass analyzers, depending on whether ions are allowed to pass through the analyzer over a certain time range (*scanning*), or detected at the same time (*continuous*). *TOF* mass analyzers use an electric field to accelerate the ions into a flight tube maintained at very low pressure (1×10^{-10} bar). After acceleration, the ions are allowed to drift in the field-free region inside the flight tube. The m/z of an ion is determined by measuring the time it requires to travel through the flight tube to the detector. The velocity (v) and time (t) an ion requires to travel to the detector can be described as

$$v = (2qU/m)^{1/2} \quad \text{and} \quad t = L/v$$

where q is the charge of the ion, L the length of the flight tube, m the nominal mass of the ion and U the potential applied to accelerate the ion. Thus, if the mass is high and the charge small, v is small and the ion reaches the detector later. If both mass and charge are small, v becomes bigger and the detector is reached quicker. In principal, TOF analyzers have no upper mass limit.

In a *quadrupole* mass analyzer, a radio frequency quadrupolar field is created between four parallel rods. These oscillating electrical fields are used to selectively

Fig. 7.3 Application range of different ionization techniques with regards to molecular weight of the analyte and sensitivity (Lim and Elenitoba-Johnson 2004)



stabilize or destabilize the trajectory of ions passing through the quadrupole. In contrast to a TOF analyzer, a quadrupole is a *scanning* mass analyzer, meaning that the quadrupole scans through different m/z ranges over time. Therefore, only ions in a certain m/z range can pass through the system at one time. Quadrupoles are considered low-resolution instruments and commonly have a mass range of 20–3,000 Da.

3D or Paul Ion trap mass analyzers store, or “trap” ions in a radio frequency (RF) and a direct current (DC) quadrupolar field created between a ring electrode and two end cap electrodes. To measure the mass of a stored ion, the ions are sequentially ejected from the trap to the detector by ramping the RF potential, thereby destabilizing the trajectories of ions with distinct m/z values. Because the ions repel each other inside the trap, their trajectories expand as a function of time. To prevent ion losses due to this expansion, the trap is maintained at a low pressure of helium gas, which neutralizes excess energy from the ions by collisional dampening.

In an *Orbitrap* mass analyzer, an electrostatic field with a quadro-logarithmic potential distribution is formed between an outer barrel-like electrode and a central inner spindle-like electrode. The ions entering this field start to orbit and oscillate along and around the inner electrode. The frequency of the oscillation of ions along the spindle-like electrode is proportional to the m/z value of the ions:

$$\omega = (z/m * k)^{1/2}$$

To detect the individual frequencies of ions, the image current from the oscillating ions is measured and converted into the frequency-domain using Fourier transformation. In contrast to the ion trap, no collisional cooling occurs inside the Orbitrap because it operates under very high vacuum (10^{-8} bar). The Orbitrap was invented by Alexander Makarov in the end of the 1990s (Makarov 2000).

Important characteristics of mass analyzers include (Marshall et al. 2002):

- **mass resolution:** the ability to distinguish between two peaks with close m/z values
- **mass accuracy:** the difference between the measured and the theoretical m/z value
- **mass range:** the m/z range of an analyzer
- **scan speed:** the number of scans per second of an analyzer over a given m/z range

The mass analyzers discussed earlier differ regarding these parameters. In terms of mass resolution, ion traps and quadrupoles can achieve a resolution of up to 4,000, and are considered low to medium resolution analyzers. TOF analyzers equipped with a reflectron often achieve a resolution of up to 50,000. One of the most powerful mass analyzers in terms of resolution is the Orbitrap with a resolution of 100,000 during routine operation. For target analytes with a mass below 2,000 Da, the mass accuracy of quadrupoles and ion traps often lies between 100 and 200 ppm, while TOF and Orbitrap analyzers routinely achieve a mass accuracy of <10 ppm (Hoffmann and Stroobant 2007). The high resolution and mass accuracy of both TOF and Orbitrap mass analyzers make them particularly suitable for the analysis of complex mixtures and large biomolecules.

As shown in Fig. 7.4a, the resolving power of a mass analyzer is defined as $R = m/\Delta m$, (where m is the mass of one compound and Δm is the mass difference to a peak with close m/z). However, Δm and thereby the resolution of a mass analyzer, can also be experimentally determined from a single peak as illustrated in Fig. 7.4b; being the same as twice the full width at half maximum height (FWHM) of a given peak. For further reading about mass analyzers and their physical properties, please refer to “Mass Spectrometry—Principles and Applications” (Hoffmann and Stroobant 2007).

1.1.3 Detectors

Once the ions have passed through the mass analyzer, they are detected and transformed into a useable signal by a detector. In general, two types of detectors can be distinguished: the so-called *point-ion-collectors* which detect arriving ions sequentially at one point. *Array collectors* on the other hand can detect arriving ions simultaneously along a plane. The detector measures the abundance of each

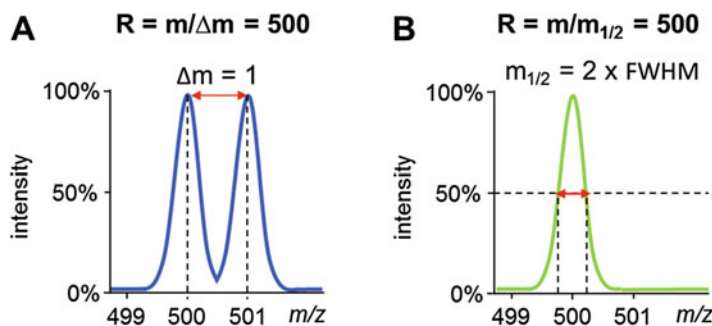


Fig. 7.4 (a) Definition of resolving power by measuring Δm between two peaks of close m/z . (b) Resolution defined as the full peak width at half maximum height (FWHM)

individual ion by recording either the induced charge or a current produced when the ion passes by or hits a surface. In most mass spectrometers, electron multipliers are used for this; however, also Faraday cups and ion-to-photon detectors can be used. Because only a small number of ions leave the mass analyzer at a time, signal amplification is often needed prior to detection. Many modern commercial instruments therefore use microchannel plate detectors. A review about detectors used in current mass spectrometry was published elsewhere (Koppelaar et al. 2005).

1.2 Tandem Mass Spectrometry

Tandem mass spectrometry, also called MS/MS or MS^2 , describes sequential mass analyses performed on the same population of ions, often following a gas-phase fragmentation event. The fragmentation of gas-phase ions occurring between the individual steps of mass analysis results in a change of the mass or charge of an ion. It can provide additional information about the structure and composition of the analyte. The ions that are selected for MS/MS analysis are often referred to as *precursor or parent ions*, while the ions formed after collision and detection are called *product ions*. The multiple steps of mass analysis required for MS/MS analysis can either be achieved by separating individual mass analyzers *in space*, or by operating one mass spectrometer differently *in time*.

For MS/MS *in space*, the individual mass spectrometer elements are physically separated. They are connected by e.g. a quadrupole, where the analyte ions are fragmented. The most common instrumental set up for MS/MS in space is the triple quadrupole (QqQ) shown in Fig. 7.5; a variation of the transmission quadrupole containing three consecutive quadrupole stages. The first quadrupole functions as a mass filter allowing only a certain m/z range into the second quadrupole that is used as a collision cell. Here, the precursor ion is fragmented into product ions, which are subsequently analyzed by the third quadrupole.

In contrast to this, the separation of ions in MS/MS *in time* is accomplished by trapping the ions and separating and/or colliding them in the same physical space;

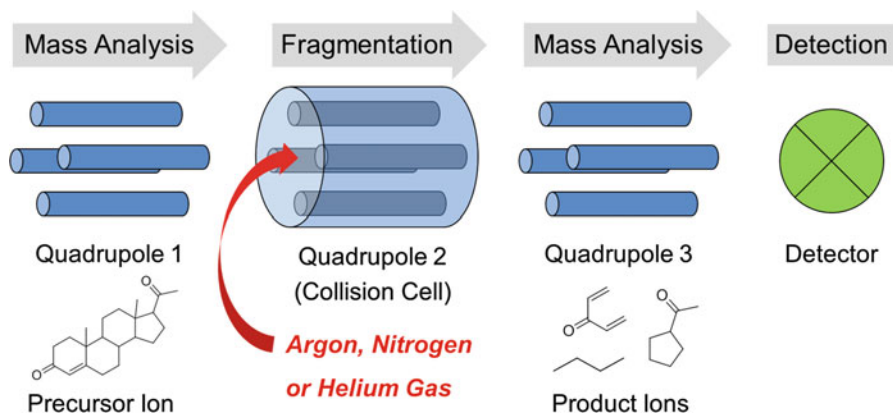


Fig. 7.5 Schematic set-up of a triple quadrupole QqQ mass spectrometer that enables tandem mass spectrometry (adapted from online sources). After selection of a precursor ion with a certain m/z value in the first quadrupole, the selected ions are fragmented in the collision cell (second quadrupole). The resulting fragment ions are then analyzed in the third quadrupole before reaching the detector

the different steps take place over time. For MS/MS in time, ion trap mass spectrometers can be used. Typically, the sequence of events is as follows: (i) selection of the precursor ion with one specific m/z value, all other ions are expelled from the trap. (ii) Fragmentation of the precursor ion in the trap, followed by (iii) analysis of the product ions. Multiple rounds of selection, fragmentation and analysis can be performed on the product ions. This process is referred to as MS^n , where n indicates the level of the MS/MS analysis.

1.2.1 Ion Activation in Tandem Mass Spectrometry

There are different ways of fragmenting ions for MS/MS analysis; the most common ones being *collision-induced dissociation* (CID, also known as collisionally activated dissociation CAD), *electron transfer dissociation* (ETD) and *electron capture dissociation* (ECD); all these processes can be summarized as *post-source* fragmentation techniques. For CID, gas-phase ions are collided with neutral gas atoms (He, N_2 or Ar). When an inert gas molecule collides with the analyte, some of its kinetic energy is converted into internal energy of the analyte; once this energy reaches a certain threshold, internal bonds within the analyte break (Jennings 1968). The degree of fragmentation can be controlled by altering (i) the collision energy (i.e. the kinetic energy of the analyte ions as they are accelerated into the cell), and (ii) the frequency of collisions experienced by the analyte in the collision cell (i.e. the collision gas pressure). In the case of ETD, an electron is transferred from a reagent radical anion (e.g. anthracene) to the analyte ion, thereby liberating Coulomb energy (Hunt et al. 2005). ECD describes in principal the same process as ETD, however there is no helper molecule, instead a free low-energy electron is

captured directly by the analyte (Zubarev et al. 2000). Fragmentation can also be provoked in the ion source. In an ESI mass spectrometer, such *in-source fragmentation* can be achieved by elevating the potential on the first skimmer cone in the ion source, thus providing more kinetic energy to the analyte ions. This causes more energetic collisions with the background gas present in the relatively high pressure of the ion source. In-source fragmentation can be used to selectively dissociate labile bonds (e.g. glycosidic bonds). A variant of in-source fragmentation referred to as *in-source decay* (ISD) can also be performed in MALDI by operating the laser significantly above the threshold for intact ion production (Brown and Lennon 1995, Hardouin 2007).

1.2.2 Scan Modes in Tandem Mass Spectrometry

A diverse range of different experimental sequences can be performed using MS/MS. Figure 7.6 shows an overview of different acquisition modes of a standard QqQ mass spectrometer (see Fig. 7.5 for a schematic setup). In *full scan mode*, the first quadrupole scans over a user-defined mass range, while the collision cell and the second quadrupole allow all ions to pass through to the detector. In *product ion scanning*, the first quadrupole (MS1) filters for a precursor ion at a set m/z value which is then being fragmented in the collision cell (second quadrupole). Subsequently, the third quadrupole (MS2) scans all product ions from the selected precursor ion over a user-defined mass range. In *precursor ion scanning*, MS1 scans over a user-defined mass range. All passing-through ions are fragmented in the collision cell and the product ions are filtered for a set m/z value in MS2. *Neutral loss scanning* scans the full mass range in MS1. After fragmentation, the second quadrupole scans for products with a defined mass off-set originating from a defined neutral loss of the precursor ions detected in MS1. In *selected reaction monitoring* (SRM), MS1 is set to filter for one m/z value, this precursor ion is then fragmented, and its products are filtered for a specific m/z value again in MS2. This means that both MS1 and MS2 are filtering and only need to scan a short mass range which will increase the sensitivity of the analysis of the specified precursor ion. In *multiple reaction monitoring* (MRM), several m/z values are set for both MS1 and MS2; MRM can be regarded as an extended version of SRM.

Application of MS/MS includes structure elucidation, high-sensitivity and high-selectivity analyses, as well as elementary analysis. Small molecule drugs fragment in distinct ways, yielding unique diagnostic fragments depending on their functional groups. Furthermore, the amino acid sequence of peptides can be analyzed by MS/MS, as will be explained later in this chapter. The use of MS/MS in protein analysis by peptide mapping will also be described in detail later in this chapter. Many pharmacological assays, e.g. for the monitoring of metabolites are MS/MS experiments such as SRM or MRM. Particularly for these applications, the classic QqQ instrumentation is more and more replaced by mass spectrometers where instead of the last quadrupole, an Orbitrap or TOF mass analyzer is employed. By replacing the last quadrupole, the resolution of the mass spectrometric analysis is increased: while quadrupoles typically only achieve resolutions up to 2000, TOF

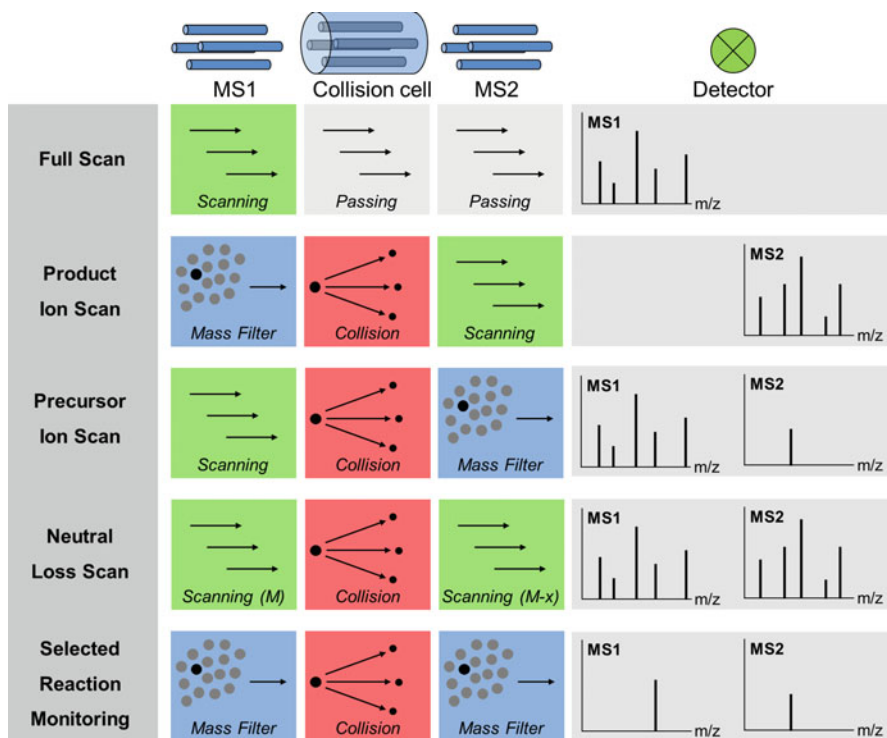


Fig. 7.6 Different scan modes in a standard QqQ mass spectrometer

and Orbitrap mass analyzers have resolutions from 40,000 to 100,000. This improved resolution facilitates the analysis of complex biological samples.

1.3 Coupling Mass Spectrometry to Chromatographic Separation

The coupling of mass spectrometry to a chromatographic system has a long history in pharmaceutical research and has been widely applied since the 1990s. It can be offline, if the analyte is collected and then analyzed. The mass spectrometer can however also be coupled online to the chromatographic system. The three main techniques employed in online coupling of MS are *gas chromatography* (GC), *capillary electrophoresis* (CE) and *liquid chromatography* (LC). Figure 7.7 gives an overview of commonly used chromatography-compatible ionization methods as a function of analyte polarity and molecular weight.

Gas chromatography coupled to mass spectrometry (GC-MS) is exclusively used for the analysis of volatile analytes. It is often coupled to CI and EI ion sources and therefore does not yield intact analyte ions, but fragments of the analyte. Hence, GC-MS delivers a high degree of structural information. GC-MS

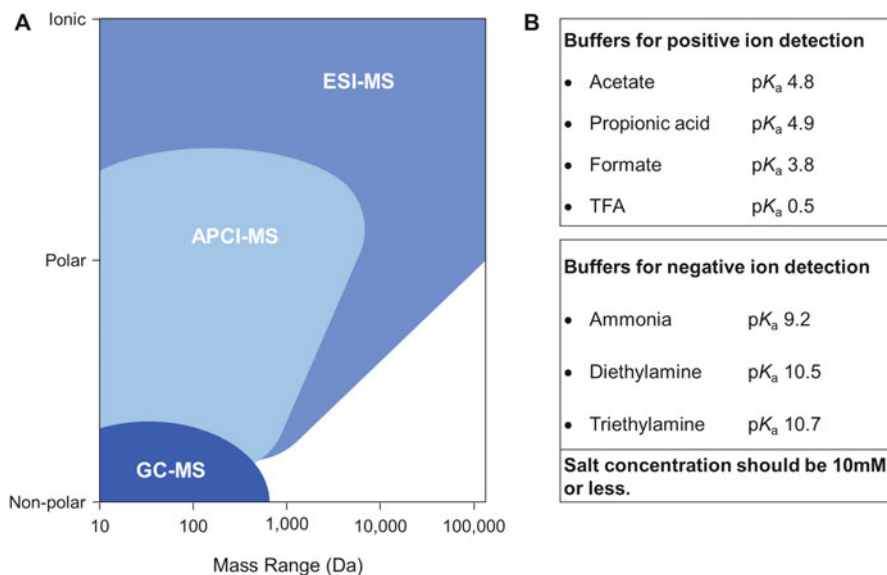


Fig. 7.7 (a) Application ranges of different ionization methods with regards to molecular weight and polarity of the analyte. (b) Solvents and buffers commonly used for LC-MS analyses and their pK_a values

is characterized by its very high sensitivity, minimal sample carry-over between runs, and short run-time (Ryhage 1964). As can be seen from Fig. 7.7, GC-MS is most suitable for the analysis of small, hydrophobic compounds. *liquid chromatography* (LC-MS) routinely used for the analysis of non-volatile compounds, both large and small. *Capillary electrophoresis* (CE-MS) has significant potential in terms of improved separation and absolute sensitivity but is still not a routine technique. LC-MS can be readily performed at a wide range of flow rates from nL/min up to ml/min. In order to achieve good resolution with LC-MS, many parameters may be altered, such as: type of solvent (basic vs. acidic), type of elution (isocratic vs. gradient), as well as the type of the column (normal vs. reversed phase). The goal of setting up a good LC-MS method is to minimize the run time while maintaining good chromatographic resolution (Ardrey 2003). While not as extensively used due to challenges in interfacing CE with MS, CE-MS methods provide very high sensitivity thus using only small sample quantities (Smith et al. 1989). Both CE and LC are mostly coupled to ESI or APCI ion sources, as they can accept high flow rates of solvent under atmospheric pressure. Figure 7.7 illustrates the optimal ranges for APCI- and ESI-MS with regards to molecular weight of the analyte and its polarity.

The most common solvents used for LC-MS analyses are acetonitrile and water; both are used at a low pH to enhance ionization of polar compounds by proton transfer. However, also volatile buffers such as ammonium acetate can be used if a higher pH is required for the analysis of e.g. basic compounds in negative ionization mode or larger biomolecules under native conditions. The table in Fig. 7.7 gives an

overview of buffers that are compatible and commonly used for mass spectrometric analysis.

A crucial step in obtaining good LC-MS data is the sample preparation. Firstly, the analyte has to be soluble in one of the LC solvents to prevent its precipitation in the LC system. Furthermore, the analyte concentration should not be too high as this may result in detector saturation, making the signal disproportional to the analyte concentration. Secondly, salts and detergents should be removed from the sample prior to the mass spectrometric analysis, as they may interfere with the ionization and evaporation process. Common ways of desalting/detergent removal include precipitation, solid-phase extraction (SPE), liquid-liquid extraction (LLE), or column switching (LC/LC). SPE and LLE will be described in more detail later in this chapter. For LC/LC, two or more (different) columns are used sequentially for sample clean-up. For example, a very dilute sample may be concentrated on a pre-column, while the flow-through containing contaminants is discarded. The flow-path can then be diverted to connect the first column to a second column with a different selectivity. Column switching increases the versatility of the chromatographic system and can protect the mass spectrometer from contaminants (Campins-Falco et al. 1993).

1.4 Representation of Mass Spectrometric Data

The data obtained from a simple mass spectrometric analysis can be represented solely by the mass spectrum. However, the coupling of MS to liquid chromatography and different MS/MS acquisition modes require additional forms of data representation, e.g. mass chromatograms. Such can be *total ion current chromatogram* (TIC), *base peak chromatogram* (BPC/BPI), *selected reaction monitoring chromatogram* (SRM) and *extracted ion chromatogram* (EIC/XIC). The TIC represents the summed intensities across the entire mass range at a given time (total number of ions that reaches the detector). But, especially in complex mixtures, the TIC provides very little information as several different species might co-elute and thereby obscure individual signals. The BPC is similar to the TIC, however it only represents the intensity of the most abundant peak in each spectrum at a given time. Therefore, the BPC can be considered as a “tidier” version of the TIC. The SRM is a chromatogram representing the intensity of a preselected m/z value over time. In contrast to the SRM, the EIC is a reconstructed chromatogram of a specific m/z value; thereby an analyte of interest can be extracted from a complex TIC. Another option of data representation are 3D contour maps, where the m/z values on the x-axis are plotted against the intensity on the y-axis and an additional experimental parameter such as time, or ion mobility, on the z-axis (Lanucara et al. 2014). Depending on the type of data acquisition, also UV and LC traces may have to be analyzed.

Figure 7.8 shows an example of an LC-MS/MS analysis of a mixture of peptides. From top to bottom, the TIC, the UV trace at 280 nm (diode array detector, DAD) and the EIC of $m/z = 613$ are shown. This example emphasizes how different types

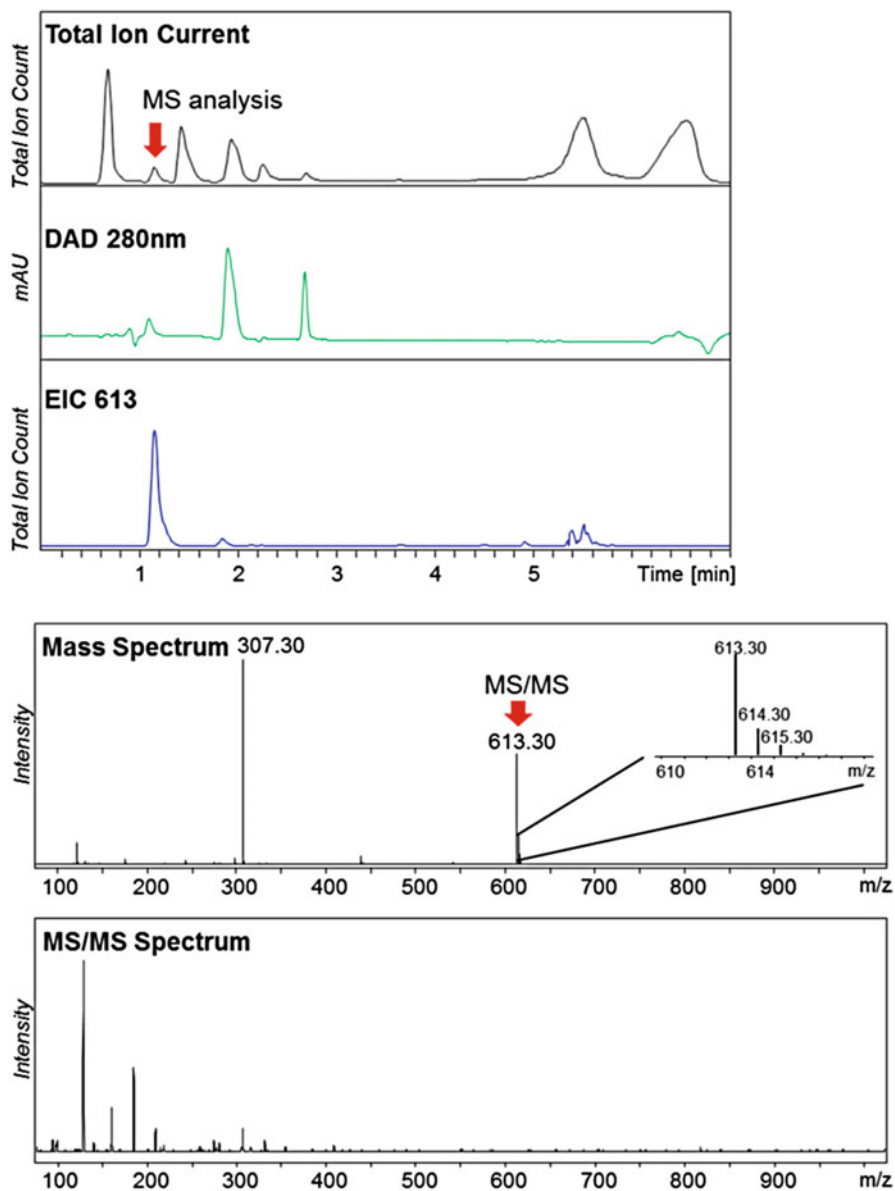


Fig. 7.8 LC-MS/MS analysis of a peptide mixture. Shown are the TIC (total ion current), the UV chromatogram (DAD) at $\lambda = 280$ nm, an EIC of $m/z = 613.30$, the mass spectrum at $R_t = 1.2$ min, as well as the corresponding MS/MS spectrum of $m/z = 613.30$

of data analysis can change how the data appears. In the TIC, there are a few very well separated peaks, from the UV trace it can be deduced that some but not all of them are UV active at 280 nm. The EIC shows only one peak which might be

misleading with regards to sample purity if TIC and UV trace are not taken into consideration. The second part of the figure shows the mass spectrum at R_t 1.2 min from m/z 100–1000. The zoom-in shows the isotopic distribution of the peptide. The respective m/z values are separated by 1, meaning that the peptide is a singly charged species. The second peak at m/z 307.30 is the corresponding doubly charged species. The second mass spectrum shows the MS/MS spectrum of fragment (product) ions of the precursor ion $m/z = 613$ after CID fragmentation.

1.5 Applications of Mass Spectrometry in Drug Development

Figure 7.1 earlier in the chapter emphasizes how essential MS has become throughout the whole drug discovery and development process. In particular, the coupling of MS to HPLC is widely used in drug development, combining the resolving power of the HPLC and the structural information obtained from MS. The advantage of MS over other analytical techniques is that molecular mass, structure and the purity of the sample can be probed in a single analysis. Hence, the analysis time per compound is decreased compared to other analytical techniques. This is of particular importance since more compounds enter the drug discovery process today than 20 years ago. This trend is due to the advent of high-throughput screenings and advances in synthetic organic chemistry. Applications of analytical MS in drug development can be divided into two areas: *qualitative MS*, e.g. identification and characterization of the structure of unknown compounds, and *quantitative MS*, e.g. for the quantification of an analyte in a (biological) sample.

2 Qualitative Analysis by Mass Spectrometry: Small Molecule Drugs

2.1 Mass Spectrum Interpretation

Apart from the m/z value, other useful information can be extracted from a mass spectrum. For example, the isotopic composition of an unknown compound can help to identify its elementary composition. Most elements in nature are isotopic mixtures; hence compounds do not only exhibit a single peak in the mass spectrum, but an isotopic cluster (see Fig. 7.9 for an overview of isotopic abundances of the most common elements). Especially chlorine, bromine, selenium and sulfur atoms have very distinct isotopic compositions that can be used for analytical purposes. An example is shown in Fig. 7.9a; depending on the substitution of ethene with chloro- and bromo-atoms, its isotopic cluster changes. In case of an unknown compound, the isotopic pattern can be used to deduce the elementary composition of a molecule. Hence, the isotopic distribution of a given m/z peak should be

inspected in order to correctly determine its charge state. Normally, the first peak in an isotopic cluster corresponds to the analyte ion containing only the lowest mass, and typically the most abundant, isotopes, e.g. ^{12}C , ^{14}N , ^1H . The second peak in the cluster corresponds to the analyte ion containing one ^{13}C (or to a much lesser extent a ^{15}N or a ^2H atom) increasing the mass of the ion by 1. If the ion has a charge state of 2, this mass increase will be divided by 2—resulting in a $\Delta m/z$ of 0.5. In this manner, the charge state of an ion signal in a mass spectrum can be determined from its isotopic distribution. For bigger molecules such as polymers and proteins, the isotopic distribution changes mainly as a function of the additional carbon atoms. With an increasing number of carbon atoms, the peaks corresponding to the relatively low abundance ^{13}C isotope accumulate and shift the isotopic distribution towards higher masses (see Fig. 7.9b and Sect. 3.1.1) (Wanner and Höfner 2007). Furthermore, similar m/z values might occur for different analytes depending on their charge states, especially when analyzing complex mixtures, thus necessitating the use of a high-resolution mass analyzer or MS/MS analysis.

Some important things to keep in mind when analyzing MS data include:

- Does the mass spectrometer operate in positive or negative ion mode i.e. is the analyte positively or negatively charged?
- Is the analyte singly, doubly or multiply charged?
- Is the analyte fragmented?
- Has the analyte formed adducts (e.g. with the matrix used for MALDI analysis, salts or reactive organic species such as epoxides)?
- What is the isotopic composition of the analyte (Br/Cl atoms)?

2.2 Monitoring Chemical Syntheses by MS

MS has become an indispensable tool for synthetic and medicinal chemists. It offers several advantages over traditional analytical techniques like thin-layer chromatography and NMR. These include short analysis time, easy data analysis and high sensitivity while requiring only minute amounts of analyte. LC-coupled mass spectrometry (LC-MS) can be used to (i) characterize newly synthesized compounds and synthetic intermediates; (ii) monitor chemical reactions and optimize those; as well as (iii) evaluate the final product by accurate mass analysis. Furthermore, MS is well suited to analyze fractions from chromatographic purifications, and spots from thin layer chromatography. Common side reactions of chemical synthesis include: oxidation (+16 Da), hydrolysis (−18 Da), decarboxylation (−44 Da), deamidation (+1 Da), as well as the formation of adducts. Apart from standard molecular weight determinations, tandem MS can be employed for structure elucidation of synthetic compounds, as described in Sect. 1.2. The different fragments that are obtained from MS/MS analysis can—together with the information from the precursor ion—help to elucidate the molecular structure of an unknown analyte. A technique termed “precursor ion fingerprinting” searches

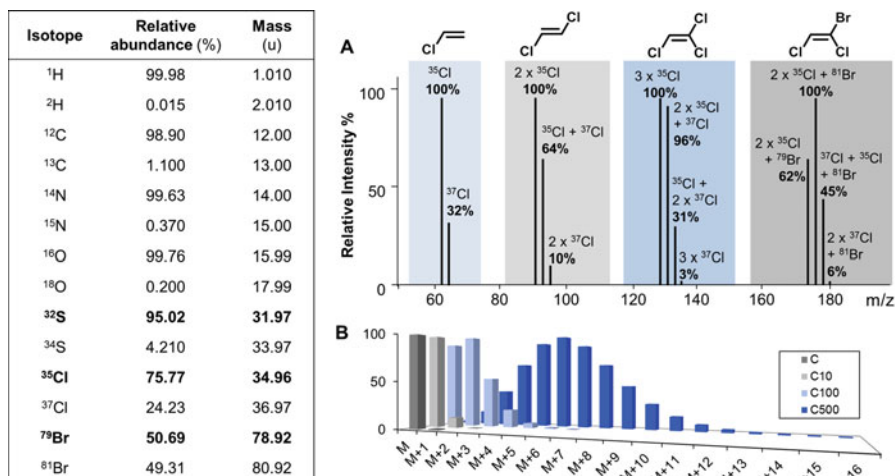


Fig. 7.9 Table of the isotopic abundances of the most common elements. (a) Mass spectrum showing the isotopic clusters of chloroethene, 1,2-dichloroethene, 1,1,2-trichloroethene and 1-bromo-1,2-dichloroethene. (b) Isotopic distribution as a function of number of carbon atoms. With increasing number of carbon atoms, the maximum of the isotopic distribution shifts towards higher masses. (Figure modified from Wanner and Höfner 2007)

fragments obtained from an MS/MS analysis of a given analyte against a library of product-ion spectra from known precursors.

Often, a sample clean-up step might be required prior to the MS analysis in order to warrant good results. Numerous reagents used in synthetic chemistry are not compatible with mass spectrometric analysis, as they might (i) contaminate the LC system, (ii) cause ion suppression, or (iii) contaminate the mass spectrometer. The difficulties associated with high salt concentrations and detergent content have been described earlier in this chapter. Apart from those, halogenated solvents can be problematic as they suppress ionization. Care should be taken when working with either very basic or acidic mixtures, as they can harm both the LC system, as well as the LC-MS interface.

A limitation of MS compared to NMR is its inability to distinguish between enantiomers and the ortho-, meta- and para-positions in aromatic rings. However, these disadvantages can in part be overcome by coupling the mass spectrometric analysis to chiral chromatography (Joyce et al. 1998).

2.3 Drug Delivery and Stability

An important step in drug development is the assessment of the stability of the active pharmaceutical ingredient (API) in a given formulation. Historically, the importance of excipients was underestimated; they were in general considered

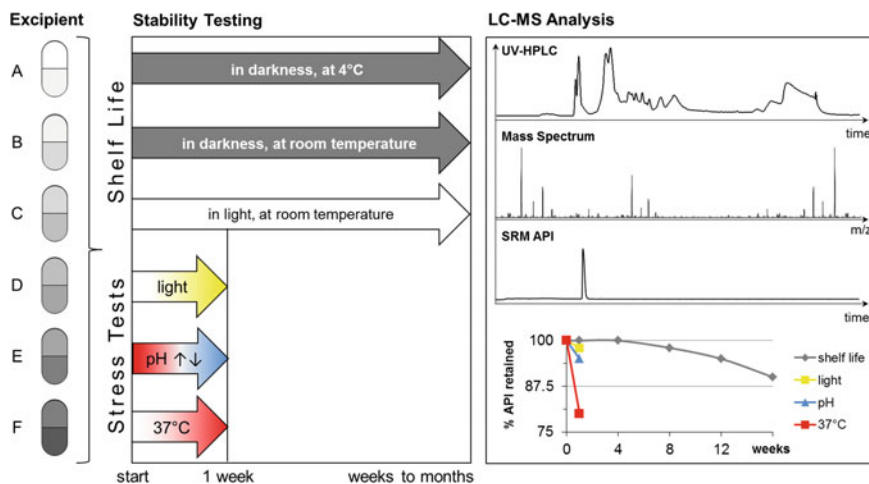


Fig. 7.10 Stability testing of a drug in the presence of different excipients (A–F). The different formulations are exposed to several stimuli, including long-term storage in darkness or light at different temperatures, and short-term stress-tests. The formulations are then analyzed by LC-MS regarding degradants identification and quantification of the active pharmaceutical ingredient (API)

cheap and standard fillers. However, with the advent of more sophisticated drugs and drug delivery systems, excipients can play an important role in e.g. stabilizing the drug and releasing it specifically at the desired site of action. When choosing a formulation, the shelf-life of a drug in the presence of different excipients has to be determined, and possibly toxic degradants need to be identified. MS is the method of choice to assess these parameters because of its high sensitivity and specificity.

The formulation for a new drug can be chosen from a wide panel of available excipients, a recent review stated that more than 1300 different excipients for oral drugs are available today (Zheng 2009). Points of consideration for choosing the right formulation are the hygroscopicity, oxidative potential, as well as the pH and temperature stability of the drug. Commonly, many different combinations of excipients, over different periods of time, and at different temperatures are evaluated for the formulation of a drug. A general workflow for such a study is shown in Fig. 7.10. Table 7.1 shows the most common degradations occurring in formulations, and their corresponding changes in m/z . In addition to long-term storage studies at room temperature, new drugs are also subjected to stress tests where they are exposed to e.g. oxidative, photolytic, hydrolytic and thermolytic stress. LC-MS has proven to be a viable tool for the detection of drug degradants from both long-term, and stress studies. Also for the assessment of drug safety, the information obtained from such formulation studies is of crucial importance. LC-MS analysis can accurately identify and quantify toxic degradants from a formulation, and thereby help to evaluate the drugs' safety profile.

Table 7.1 Common degradation pathways of drugs in formulations, the involved functional groups and the resulting shift in m/z

Common degradation pathways	Functional groups involved	ΔDa	Caused by
Hydrolysis	Nucleophilic centers, lactam groups	+18	Water in the formulation
Deamidation	-NH ₂	+0.98	
Deamination	-NHR	-	
Decarboxylation	-COOH	+45	
Oxidation	Double bonds, hydroxyl groups (single electron transfer)	+16 (air oxidation), different adducts	Can e.g. be caused by peroxides that originate from excipients such as polysorbate-80 or polyethylene glycol-400
Reduction	Primary/secondary amines	-	Can e.g. be caused by lactose in the formulation, which is a reducing sugar (Maillard reaction)
Photolysis	-OH, halogens	-	Can result in numerous reactions, including oxidation, eliminations and dehydrogenation
Dimerization	-SH	-	Can e.g. be caused by free thiol groups or in unsaturated aromatic systems
Dehydration	Sugars	-18	Formation of a double bond that is stabilized by resonance with neighboring functional groups

3 Qualitative Analysis by Mass Spectrometry: Large Molecule Drugs

Protein and peptide pharmaceuticals are large molecule drugs which can contain several hundreds of amino acids and have molecular masses from tens to hundreds of kDa. These drugs thus represent a different class of drug compounds to analyze and characterize at the molecular level compared to small molecule drugs. However, any modification of either the primary, secondary, tertiary or quaternary structure of a protein pharmaceutical can in principle impact its efficacy, bioavailability and immunogenicity (Tao et al. 2011). It is therefore important to be able to detect and characterize these modifications. MS has developed into a useful technique to characterize both primary and higher order structures of protein pharmaceuticals. As described earlier, soft ionization methods such as electrospray ionization (ESI) and matrix-assisted laser desorption/ionization (MALDI) can ionize large, polar protein molecules without breaking internal covalent bonds. The developments in soft ionization during recent years have allowed the implementation of a multitude of MS based workflows for the detailed analysis of protein pharmaceuticals. Nowadays, the chemical and physical stability of protein drugs, as well as their pharmacokinetics are routinely determined by MS (Chen et al. 2011).

3.1 Characterization of Peptide and Protein Pharmaceuticals: Primary Structure

The characterization of protein pharmaceuticals includes the determination of protein purity, molecular weight, amino acid sequence and post-translational modifications in relation to protein expression, formulation and storage. Figure 7.11 provides an overview of general workflows for primary structure analysis of protein pharmaceuticals by MS. The choice of a suitable MS workflow can vary depending on the nature of the protein, its formulation, modifications of interest and the available mass spectrometric setup. Most workflows can be grouped into “*top-down*” and “*bottom-up*” approaches that involve the analysis of intact or enzymatically digested proteins, respectively. The latter is commonly referred to as *peptide mass finger printing (PMF)* or simply *peptide mapping*. Top-down and bottom-up analyses are carried out using either MALDI-MS, or LC-coupled ESI-MS setups. MALDI-MS is often the first choice for primary structure analysis because of its ease-of-use, sensitivity, robustness, high tolerance for salts, buffers and detergents as well as a straightforward interpretation of the obtained spectra. In contrast to that, ESI-MS can be easily coupled to an LC system for higher-throughput analyses allowing separation of more complex samples and process automation (Holcapek et al. 2012).

3.1.1 Interpretation of Mass Spectra of Peptides and Proteins

Interpretation of mass spectra of larger peptides and proteins can be a complex and tedious task, compared to the analysis of small molecules. This is due to their large size, and the numerous functional groups that can carry a charge. As a result of that, the m/z of a protein observed in an ESI mass spectrum is normally not a single peak, but a so-called charge state envelope that consists of several peaks corresponding to the different charge states of the protein. In contrast to ESI, MALDI has a preference of yielding singly charged species, which simplifies the interpretation of MALDI mass spectra compared to ESI mass spectra. However, several software programs are available to assist the interpretation of protein mass spectra and automatically deconvolute these. *Deconvolution* describes the process of determining the molecular weight of a protein from a charge state envelope. Figure 7.12a shows an ESI mass spectrum of the protein cytochrome *c*, with the charge state envelope easily recognizable along the m/z axis. The inset (top right corner) shows the result of a software deconvolution of the spectrum yielding a single peak corresponding to the molecular weight of cytochrome *c*.

It is possible to determine the charge state and corresponding molecular mass of a protein based on the charge state distribution. To this end, two successive peaks are chosen from the charge state envelope, e.g. 773.438 and 824.932 from Fig. 7.12. The charge state of the protein can then be deduced from the m/z values of these two peaks using the following equation:

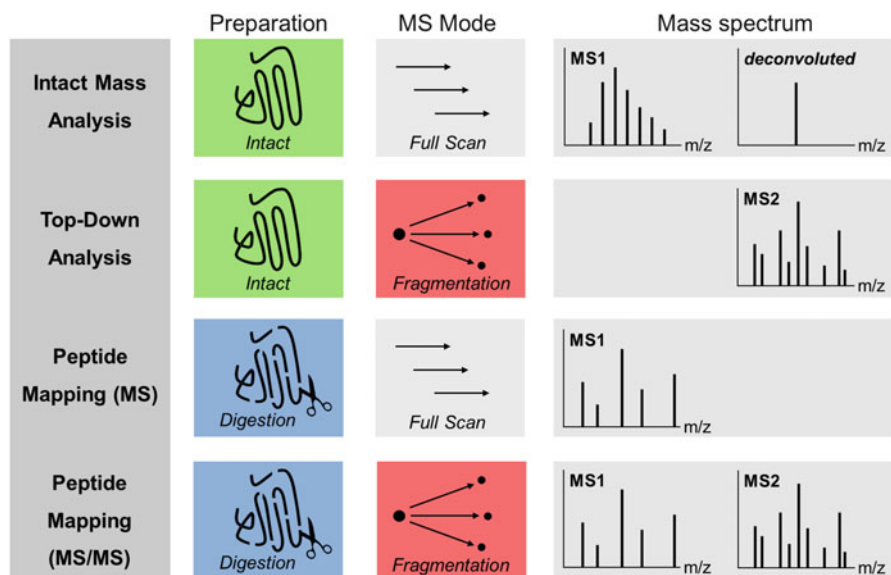


Fig. 7.11 Schematic overview of the different approaches for structural characterization of peptide and protein pharmaceuticals by MS. Intact mass analysis is performed without prior enzymatic digestion using either a full scan MS acquisition mode or a top-down MS/MS acquisition mode with ion fragmentation. Peptide mapping analysis includes an initial enzymatic digestion and either full scan MS acquisition mode or ion fragmentation MS/MS acquisition mode

$$n = \frac{\left(\frac{m}{z}\right)_{n+1} - 1}{\left(\frac{m}{z}\right)_n - \left(\frac{m}{z}\right)_{n+1}} = \frac{773.438 - 1}{824.932 - 773.438} = 15$$

Where the result is the charge state of $(m/z)_n$. The molecular mass of cytochrome *c* can be calculated accordingly:

$$m = \left(\frac{m}{z}\right)_n \cdot n - n = 15 \cdot 824.932 - 15 = 12359.30$$

As discussed earlier, peptides and proteins have distinct isotopic distributions, corresponding to the presence of different amounts of ^{13}C isotopes. Their mass can therefore be given as the monoisotopic mass or the average mass. The monoisotopic mass is the first peak of an isotopic distribution, while the average mass is the intensity-weighted average of all peaks of the isotopic distribution. Every peak in a charge state envelope of a protein has its own isotopic distribution (Fig. 7.12b); Fig. 7.13 shows such an isotopic distribution of a single charge state (2+) of a peptide. The monoisotopic mass of this peptide is the first peak of this distribution, containing only the most abundant isotopes, such as ^{12}C , ^{16}O and ^{14}N . The average mass is calculated as the weighted average of the different isotopic species present.

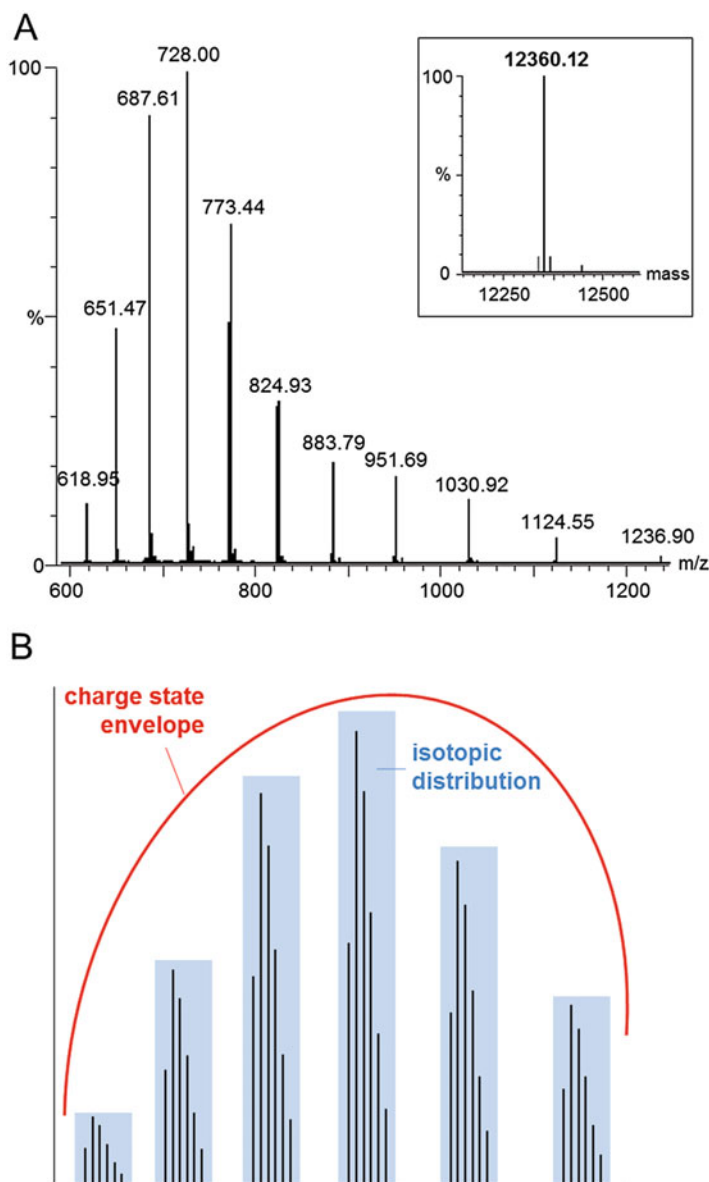


Fig. 7.12 (a) ESI-MS spectrum of the protein cytochrome *c* with a broad charge state envelope corresponding to the multiple protonation states of the protein. For example, peak 883.79 corresponds to cytochrome *c* with 14 charging protons $[M + 14H]^{14+}$ whereas peak 951.69 corresponds to $[M + 13H]^{13+}$. The inset shows the charge state deconvoluted spectrum (with altered x-axis i.e. mass) which yields a single peak corresponding to the mass of cytochrome *c*, obtained from deconvoluting the spectrum using the maximum entropy method of the MassLynx software (Waters Corp.). (b) Schematic mass spectrum of a protein with several charge states that are resolved to the isotopic distribution of each charge state by use of a high-resolution mass spectrometer (blue). The isotopic distribution is shown in blue bars of each charge state and the charge state envelope is indicated by a red bracket

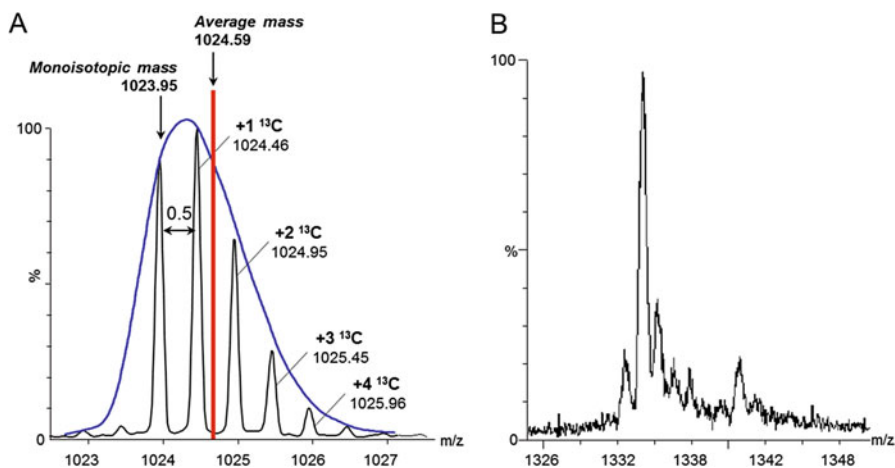


Fig. 7.13 (a) Doubly protonated state of a peptide ion (MW = 2045.9 g/mol), the red bar indicates the average mass. By measuring the distance between the isotopic peaks (0.5 Da) it is possible to determine the charge state of this isotopic distribution to be +2. Each isotopic peak represents the addition of a ^{13}C isotope, corresponding to a mass increase of +1 Da (0.5 Da for a doubly charged species). (b) A single mass spectrometric peak (13+) of Myoglobin (17 kDa). The single isotopic peaks cannot be distinguished due to insufficient resolution

Another option for determining the charge state and thus mass of a protein is through its isotopic distribution, if it can be resolved. This became feasible with the advent of high resolution MS, as now the isotopic peaks even for large biomolecules can be distinguished. By measuring the distance between the isotopic peaks and employing the equation shown below, the charge state of the protein can be calculated. In Fig. 7.13a, the distance between the isotopic peaks measures 0.5 m/z , revealing the charge state of this isotopic distribution to be 2.

$$n = \frac{1}{\Delta \frac{m}{z} = \frac{1}{0.5}} = 2$$

However, especially for large proteins containing posttranslational modifications, the resolution of the mass spectrometer might not be sufficient to resolve the isotopic distribution of a larger protein (Fig. 7.13b), or the isotopic resolution might be obscured due to overlapping isotopic patterns of differently modified species present in the sample.

3.1.2 Interpretation of Tandem Mass Spectra of Peptides and Proteins

Tandem MS is a valuable tool in determining the primary structure of peptides and proteins. Figure 7.14 shows the different fragment ions that can be formed through cleavage of the backbone of a peptide—using the *Roepstorff-Fohlman*

nomenclature (Roepstorff and Fohlman 1984). The fragments are occurring in pairs, cleavage between the carbonyl carbon and amide nitrogen yield both *b*- and *y*-ions, while cleavage between the amide nitrogen and the α -carbon leads to the formation of *c*- and *z*-ions. The numbering of *a*-, *b*- and *c*-ions originate from the amino-terminus, while the *x*-, *y*- and *z*-ions are numbered from the carboxyl-terminus as illustrated in Fig. 7.14a. Collision-induced dissociation (CID) yields primarily *b*- and *y*-ions with some *a*- and *x*-ions, while other types of fragmentation, like in-source decay (ISD) (Hardouin 2007), ETD (Syka et al. 2004) and ECD (Zubarev et al. 1999) primarily yield *c*- and *z*-ions.

De novo sequencing can be performed by fragmentation techniques like CID, ISD, ECD and ETD. Figure 7.14 shows an example of a CID spectrum of a peptide with a mass of 1003.45 Da, illustrating the sequencing of the amino acids constituting the peptide. Theoretically, the complete sets of both *b*- and *y*-ions obtained after fragmentation of a peptide confirm its entire sequence. In practice however, it is rarely possible to observe all *b*- and *y*-ions in one mass spectrum. Furthermore, the amino acid composition and the amount of collisional energy have an impact on which fragments are observed. In addition, the charge state of the peptide and the distribution of multiple charges along the peptide backbone have an impact on which fragments can be observed, as the charges might remain on solely the *b*- or *y*-ion after fragmentation, and thereby make the corresponding *b*- or *y*-ion uncharged and thereby not detectable by MS. Often, one can accurately identify a peptide sequence based solely on the recorded accurate mass of the precursor ion and a few consecutive fragment ions (*b*- or *y*- in the case of CID).

One of the limitations of peptide/protein sequencing by tandem MS is that the amino acids leucine and isoleucine are undistinguishable as they both have the exact same mass of 113.0841 g/mol (Table 7.2). This is also the case in the example shown in Fig. 7.14b. The mass of a particular fragment is related to the composition of amino acids, modifications and fragment type by the equation shown below:

$$m/z_{\text{fragment}} = \frac{m_{\text{amino acid}} + m_{\text{fragment ion type}} + m_{\text{modifications}}}{z}$$

Where m_{fragment} is the m/z value of the fragment ion, $m_{\text{amino acid}}$ is the monoisotopic mass of the amino acid, $m_{\text{fragment ion type}}$ is the mass difference for the fragment ion type (see Fig. 7.14a), $m_{\text{modifications}}$ is the mass of possible modifications to the side chains of the amino acid residues and z is the charge of the fragment ion. To calculate the m/z value of the y_4 -ion Asn-Thr-Asp-Glu from the peptide shown in Fig. 7.14b, the masses of the four amino acids are inserted into the equation (see Table 7.2), adding up to a mass of 478.16 Da which matches the peak of the y_4 ion shown in Fig. 7.14b:

$$\begin{aligned} m/z_{\text{fragment(NTDQ),y}} &= \frac{(114.04 + 101.05 + 115.03 + 129.04) + (19) + (0)}{1} \\ &= 478.16 \end{aligned}$$

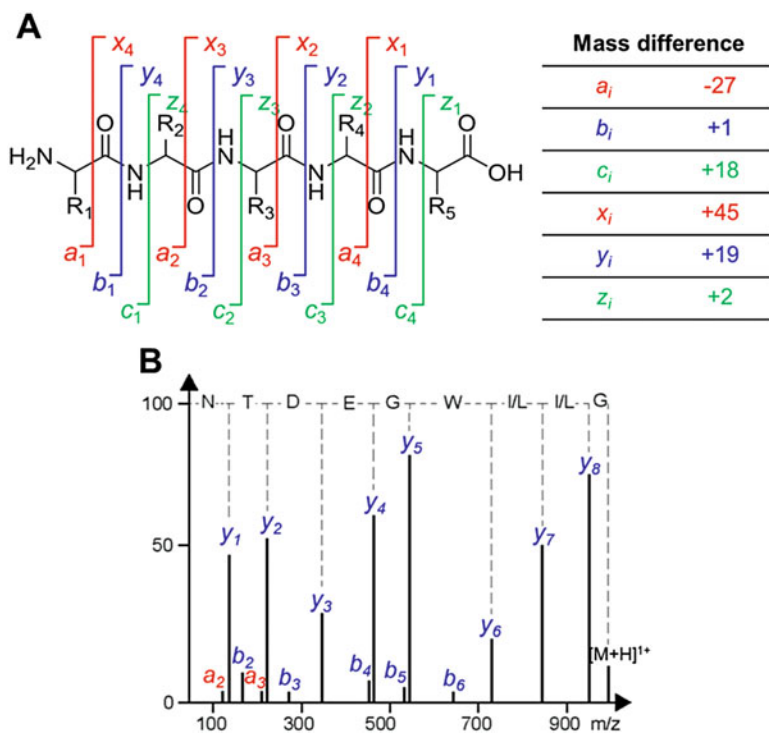


Fig. 7.14 (a) Peptide and protein fragmentation by tandem MS as defined by Roepstorff-Fohlman, and the corresponding mass differences of the fragments relative to the mass of the amino acid residues present in the fragment. (b) The peptide sequence G-I/L-I/L-W-G-E-D-T-N as sequenced by CID-MS/MS. The sequence is identified from the C-terminus through y-ions, and should be read from right to left in the spectrum

3.2 Analysis of Higher Order Structure of Protein Pharmaceuticals by Hydrogen/Deuterium Exchange Mass Spectrometry

A clear correlation exists between the higher order structure of pharmaceuticals and their function, efficacy, bioavailability and safety. It is therefore critical to control and analyze the higher order structure of protein pharmaceuticals during drug development. *Hydrogen/deuterium exchange mass spectrometry (HDX-MS)* has become a popular MS based tool to examine the conformation, dynamics and molecular interactions of proteins in solution. HDX-MS measures the rate and extent of hydrogen/deuterium exchange of backbone amide hydrogens of a protein placed in deuterated solvent. HDX is primarily dependent on the presence and relative strength of the hydrogen bonding of amide hydrogens in the target protein (i.e. the stability/dynamics of higher-order structure). The exchange of hydrogen by deuterium results in a mass change of +1 Da per exchange event, which can thus be

Table 7.2 Natural occurring amino acids with their corresponding 1- and 3-letter codes, as well as monoisotopic mass and average mass

Amino acid			Monoisotopic mass [g/mol]	Average mass [g/mol]
Glycine	Gly	G	57.0215	57.052
Alanine	Ala	A	71.0371	71.079
Serine	Ser	S	87.0320	87.078
Proline	Pro	P	97.0528	97.117
Valine	Val	V	99.0684	99.133
Threonine	Thr	T	101.0477	101.105
Cysteine	Cys	C	103.0092	103.145
Isoleucine	Ile	I	113.0841	113.160
Leucine	Leu	L	113.0841	113.160
Asparagine	Asn	N	114.0429	114.104
Aspartic Acid	Asp	D	115.0269	115.089
Glutamine	Gln	Q	128.0586	129.116
Lysine	Lys	K	128.0950	128.174
Glutamic Acid	Glu	E	129.0426	128.131
Methionine	Met	M	131.0405	131.199
Histidine	His	H	137.0589	137.141
Phenylalanine	Phe	F	147.0684	147.177
Arginine	Arg	R	156.1011	156.188
Tyrosine	Tyr	Y	163.0633	163.176
Tryptophan	Trp	W	186.0793	186.213

deduced from mass spectrometric analysis. HDX-MS is a sensitive and reliable technique that is capable of detecting and characterizing differences in the higher-order structure between protein states. Furthermore, HDX-MS can pinpoint any differences in conformation to a specific segment of the protein.

A protein contains three kinds of hydrogens:

- Hydrogens attached to carbons (non-exchangeable)
- Hydrogens attached to N, O or S on side chains or N/C-termini (exchangeable)
- Hydrogens attached to backbone amides (exchangeable)

During HDX, both the side chain hydrogens and backbone amide hydrogens are exchanged by deuterium over time. However, HDX-MS exclusively detects the labeling of the backbone amides, because the deuterium atoms on the side chains back-exchange to hydrogens rapidly during the LC step of the HDX-MS workflow. As mentioned above, the number of exchanged deuteriums along the protein backbone is highly dependent on the presence and stability of intra-molecular hydrogen bonding (i.e. conformational dynamics). Fast exchange occurs e.g. in loops, turns and unstructured regions, whereas slow exchange occurs in stable hydrogen-bonded structures such as α -helices and β -sheets (illustrated in Fig. 7.15). Hydrogen bonding can account for a 10^8 change in the amide exchange rate and the HDX half-life of amides in a protein often span a range from

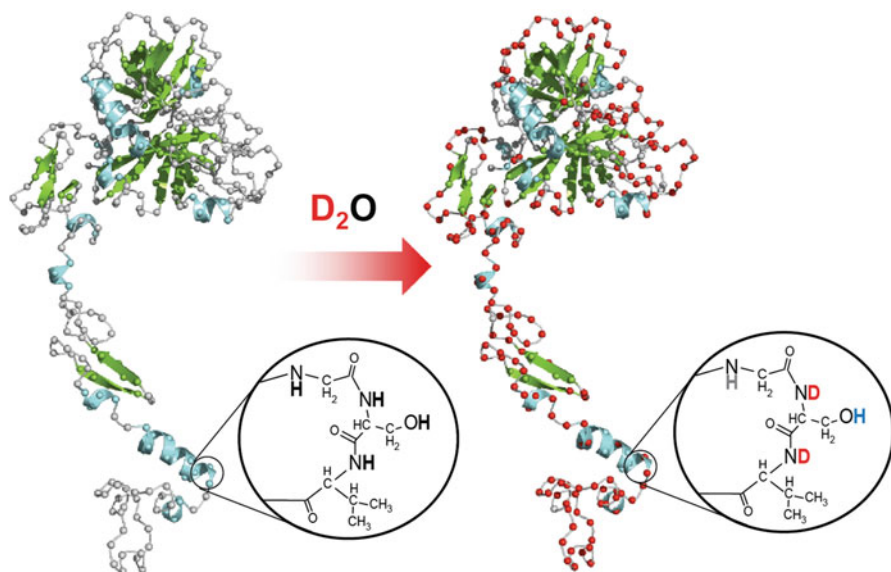


Fig. 7.15 Measuring the hydrogen/deuterium exchange of proteins by MS. When subjected to D_2O (red color), unstructured sections such as loops and turns exchange quicker with deuterium than structured hydrogen-bonded regions such as α -helices, β -sheets and parts hidden in the hydrophobic core of the protein. The red spheres indicate amide hydrogens that have exchanged with deuteriums, the grey spheres illustrate non-exchanged amide hydrogens. In the insert, the blue hydrogen indicate rapid exchanging hydrogens that back-exchange before MS detection, whereas the red hydrogens indicate backbone amide hydrogens measureable by LC-MS. The black hydrogens represent the non-exchanging hydrogens attached to carbon atoms

milliseconds to days (Bai et al. 1993). Thus, the measurement of HDX rates provides a highly sensitive analytical probe for characterizing local conformational environments in a protein (and the dynamics of such). Even small changes in conformation or dynamics between protein states can be revealed by local alterations in deuterium uptake. HDX-MS has therefore also emerged as a powerful tool for analyzing protein-drug and protein-protein interactions and the conformational perturbations that might be induced upon ligand binding. A popular application of HDX-MS is the mapping of perturbations sites of antibody biopharmaceuticals on target antigens (Pandit et al. 2012; Houde and Engen 2013; Jensen et al. 2015).

Analyzing the higher-order structure of protein pharmaceuticals by HDX-MS involves several steps. As shown in Fig. 7.16, these include labeling with deuterium, quenching (stopping) the labeling process, digestion of the protein(s) into peptides and LC separation of the peptides followed by mass analysis. Mass analysis of the intact protein as a function of labeling time provides a global view of the higher order structure. For local information, a bottom-up workflow employing a proteolytic digestion step, analogous to conventional peptide mapping, is performed allowing the measurement of deuterium uptake of individual peptides corresponding to small segments of the protein. A further increase in spatial

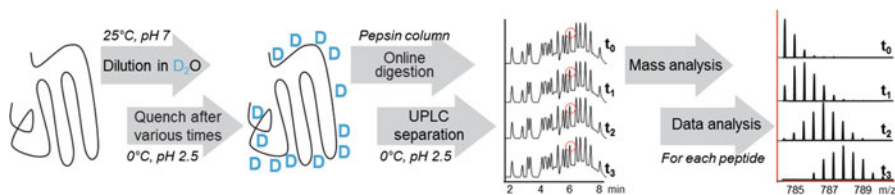


Fig. 7.16 Schematic workflow of a continuous labeling HDX-MS experiment. The protein is labeled by 20-fold dilution into the deuterated buffer at room temperature. The labeling is quenched after different periods of time by rapidly lowering the pH to 2.5 and the temperature to 0 °C. The different aliquots are injected in a cooled LC-MS setup which includes a pepsin column for online proteolysis, a subsequent reversed-phase trapcolumn for capturing peptides and desalting and a reversed-phase analytical column for UPLC separation of the digested peptides and lastly the mass spectrometer

resolution can be achieved by use of subsequent MS/MS to pinpoint the deuterium uptake to individual amino acid residues. The HDX-MS technique has seen significant technical improvements since its inception in 1993 (Zhang and Smith 1993), and nowadays labeling, digestion, separation and mass analysis can be automated and performed in one online workflow. Speed, reproducibility and robustness of HDX-MS have thus markedly improved making it suitable for more routine use across the drug development process: from drug discovery, over development to quality control and validation.

An overview of emerging HDX-MS applications in drug development science is shown in Fig. 7.17 and includes quality control, formulation development, comparison of biosimilars and the investigation of drug-target interactions. For further reading on the analysis and characterization of protein higher-order structure, we refer the reader to “Biophysical Characterization of Proteins in Developing Biopharmaceuticals” (Houde and Berkowitz 2015).

4 Quantitative Analysis by Mass Spectrometry

Quantitative analysis of a drug substance in samples of biological origin (bioanalysis) is an integral part of the drug development process. The goal of quantitative analysis by MS is to link the signal intensity of an analyte in a mass spectrum to a quantity of the analyte in a (biological) sample. The use of MS for quantitative purposes is widespread during the drug development process and normally executed by coupling a mass spectrometer to a chromatographic system and the use of one or more internal reference compounds/standards. Reference compounds are important, as the ionization response in ESI-MS is analyte-dependent. By using an internal standard, precise standard curves can be generated, allowing accurate quantification of the target analyte in complex samples. The choice of the chromatographic system depends on the nature of the analyte and the separation problem.

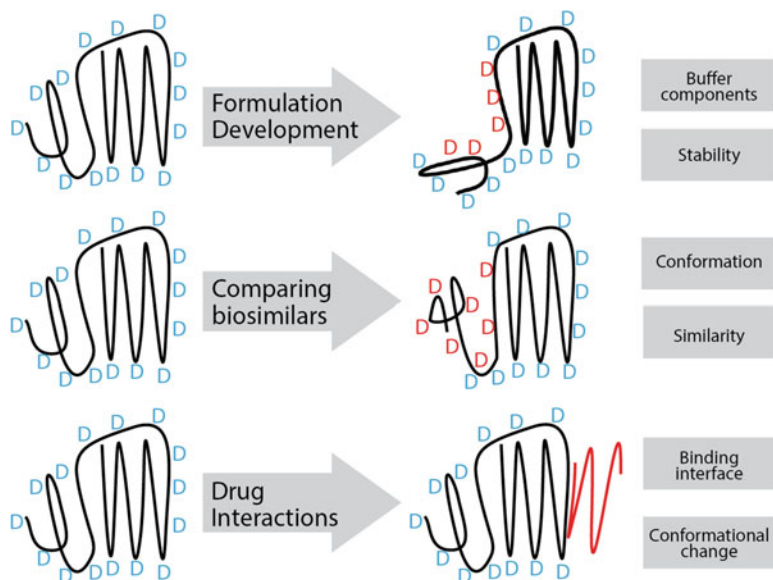


Fig. 7.17 Applications of HDX-MS in drug development: The effect on higher-order structure of formulation excipients, buffer components and long-term storage can be investigated. The conformation and similarity of related drug variants and biosimilars can be compared by HDX-MS. Protein-drug interaction sites and related conformational changes can be mapped by HDX-MS

4.1 Pharmacokinetics and Drug Metabolism

4.1.1 Pharmacokinetic Analysis by Quantitative LC-MS

Pharmacokinetics is a branch of pharmacology aiming at determining the fate of a drug in an organism after its administration. Important pharmacokinetic parameters of a new drug candidate include bioavailability, metabolism and clearance from circulation. LC-MS has become the preeminent tool for assessing these parameters because of its high sensitivity, specificity, repeatability, as well as ease of automation allowing high sample throughput. The fact that new drug candidates fail less often due to pharmacokinetic issues in later clinical phases today than 20 years ago, can at least in part be ascribed to improved LC-MS analyses (Frank and Hargreaves 2003). Samples from a pharmacokinetic study are often complex (e.g. blood and urine samples) and contain only trace amounts of the analyte. The most commonly employed MS experiments for *drug metabolism and pharmacokinetics (DMPK)* studies are consequently SRM and MRM. These provide the high sensitivity and specificity to analyze complex and dilute samples of biological origin. Traditionally, the MS systems used for DMPK studies are QqQ mass spectrometers which allow operation in SRM/MRM mode. However, classic QqQ combinations are increasingly being replaced by QTOF and Q-Orbitrap combinations as those offer

superior selectivity. A way of improving sensitivity and removing biological contaminants is to implement a sample clean-up step prior to the mass spectrometric analysis.

There are many drug delivery features that have to be assessed for new pharmaceutical compounds, e.g. their release, absorption, distribution, metabolism and excretion. The release is studied in order to determine how fast a drug is liberated from its formulation, i.e. after oral administration. Numerous model systems are available to study the dissolution of drugs *in vitro*. MS can be employed to quantify the released drug after different time points from such experiments. After the complete dissolution of the drug, it has to be absorbed into the systemic circulation in the small intestine. The most common *in vitro* assay measuring the permeability potential of a compound is the Caco-2 cell assay. MS is commonly used to analyze samples from this assay, as described in Li et al. (2003). Once the drug has entered the systemic circulation, it is distributed to different sites in the body. To analyze this process, samples can be taken from different body fluids and tissues. These can then be analyzed regarding their drug content by LC-MS(/MS). Once taken up into the systemic circulation, the drugs are also subject to metabolism, e.g. in the liver. Drug metabolism can be studied by MS both based on *in vivo* samples and *in vitro* e.g. from hepatocytes or microsomes (Korfmacher et al. 1999). The last feature remaining to be analyzed is the drugs' excretion from the body. It is important to determine which quantities of the drug the body disposes of over time, or if the drug accumulates irreversibly inside the body. Therefore, urine and feces samples need to be analyzed with regards to their drug content, which can be done routinely by MS.

Thus, many *in vitro* and *in vivo* pharmacokinetic experiments utilize MS as an analytical tool. Common sample preparation techniques to extract the drug from a biological sample will be described later in this chapter. For accurate quantitation, an *internal standard* and/or a *standard curve* should be used because the signal intensity in MS is compound dependent. The ideal standard curve is prepared by diluting the pure analyte in a matrix identical to that of the sample (e.g. blood or urine), and it should be linear over the relevant analytical concentration range. A more accurate way of quantifying an analyte is through an internal standard which is spiked into all samples including those used to make the standard curve. To this end, radio- or isotopically labeled analogues are often used because they exhibit similar properties in the sample clean-up process and the subsequent LC-MS analysis as the analyte, but can be distinguished due to their different mass (isotope labeled analogues) or by measuring their radioactivity prior to mass spectrometric analysis. These standards can thereby account for e.g. inadvertent losses during the sample preparation. Furthermore, radio- or isotopically labeled compounds can adjust for matrix effects which might hamper signal intensity of the analytes by e.g. co-elution of matrix components.

Important parameters for pharmacokinetic analysis by (LC-)MS include the *limit of detection* (LOD), as well as the *limit of quantitation* (LOQ). The LOQ is defined as at least 10× the standard deviation of the blank and where the quantitative response can be measured with high degree of confidence, the LOD is defined as at least 2–3× the standard deviation of the blank (Armbruster et al. 1994; Armbruster

and Pry 2008; Little 2015). Depending on the analyte, an SRM experiment performed on a QqQ mass spectrometer coupled to an appropriate LC system can detect pg/ml amounts of analyte, and quantify reliably down to ng/ml for proteins or down to fg/ml for small molecules. Both LOD and LOQ have to be determined for each compound and each experimental set up. A workflow for a typical pharmacokinetic analysis by LC-MS/MS using MRM and a radiolabeled internal standard is shown in Fig. 7.18.

4.1.2 Metabolite Identification by Quantitative LC-MS

One of the main concerns in the development of a new drug is its metabolism inside the organism. Today, metabolic stability can be assessed early on in the drug discovery process by *in vitro* assays, meaning that many compounds have to be analyzed. Commonly, radio- or isotope-labeled analogues of new drugs are used in metabolic studies to facilitate the identification of metabolites. After administration of the (radio)-labeled drug, an LC-MS or LC-/MS/MS analysis with online radioactivity detection is performed in order to identify and quantify metabolites. If the drug metabolites can be predicted, or are already known, an SRM or MRM experiment can be conducted in order to shorten analysis time and increase specificity and sensitivity. The mass spectrometer is then programmed to filter for one or more m/z value(s) of the intact drug in the first quadrupole, followed by fragmentation of these precursor ions in the second quadrupole. The third quadrupole can then either be set to scan for all product ions (*product ion scan*, compare Chap. 1.2.2 and Fig. 7.6), or to filter for one or more defined m/z values that represent specific fragmentation products of this drug metabolite (SRM/MRM, see Chap. 1.2.2 for more details and Fig. 7.18 for a typical workflow). To quantify drug metabolites, an isotope-labeled version of the metabolite can be added to the sample prior to analysis.

4.2 Sample Preparation for Mass Spectrometric Analyses

Samples of biological origin such as blood, bile, urine and tissue are typically not directly compatible with LC-MS analysis because of the presence of a range of highly abundant biomolecules such as fatty acids, lipids and protein components. Often also a concentration step is required prior to LC-MS analysis because of the low concentration of the analyte in the sample. A number of sample preparation techniques have been developed to achieve sample clean-up, increase the sensitivity of the analysis, and also the life time of the LC-MS system.

4.2.1 Protein Precipitation

Protein precipitation is commonly used to remove proteins from a biological sample by adding organic solvents and/or change the pH or salt concentration.

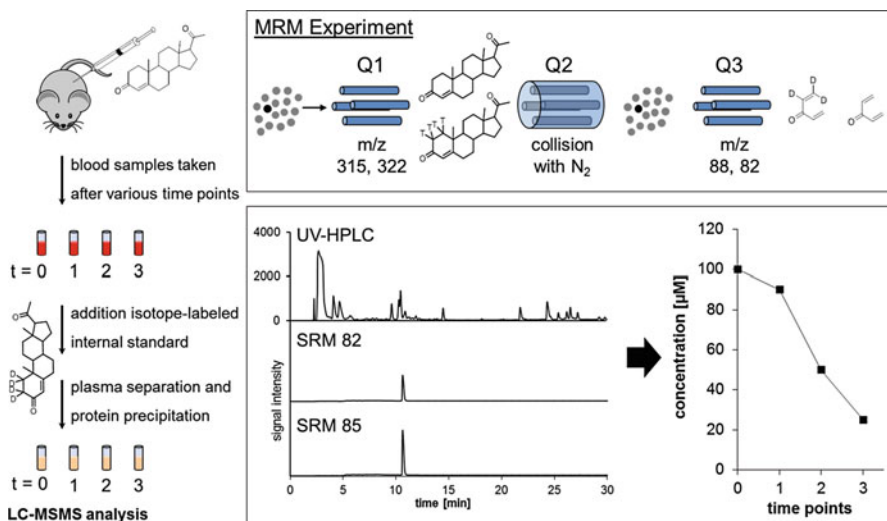


Fig. 7.18 Workflow for determination of pharmacokinetics of progesterone after i.v. administration in mice. After drug administration, blood samples are taken after different time points. The plasma is then separated from the sample, and the proteins are precipitated and removed. After addition of the isotope-labeled internal standard, the sample can be analyzed by LC-MS/MS and the signal of the analyte relative to the internal standard can be used to calculate the concentration of the analyte in the sample via a standard curve

The samples are then filtered or centrifuged in order to obtain the protein-free supernatant. Common reagents for protein precipitation include ammonium sulfate, methanol or acetone. When working with organic solvents, it is important to work under non-denaturing conditions, e.g. at 0 °C and neutral pH, as denaturation would increase the solubility of proteins and be detrimental to precipitation. When working with protein precipitation, additional steps for analyte concentration have to be performed because the sample is diluted by the addition of the precipitant. Even though protein precipitation is relatively easy, fast and cheap, it has several disadvantages which hamper its applicability towards LC-MS analysis. Firstly, many impurities are retained in the sample such as salts and endogenous small molecules, which can have a negative effect on sensitivity. Furthermore, protein precipitation is an offline sample clean-up technique which cannot be coupled online to the LC system.

4.2.2 Solid-Phase Extraction

One of the most common ways to purify and/or concentrate an analyte from a biological sample is solid-phase extraction (SPE). SPE relies on the affinity of either the analyte or the impurities in a solution towards a stationary phase. Depending on the affinity, either the analyte or the impurities are retained by the

stationary phase, while all other compounds pass by the stationary phase and can be either discarded or collected. If the analyte is retained on the stationary phase, it can be washed and the analyte then eluted. The purified and concentrated analyte can then be analyzed by LC-MS. There are many different types of stationary phases and their choice depends on the application. Common stationary phases for pharmaceutical research include reversed-phase SPE for the enrichment of peptides and proteins, as well as ion-exchange SPE for the enrichment of polar drugs. SPE can be easily automated using SPE cartridges that are organized in a block similar to a 96-well plate, allowing high sample throughput.

4.2.3 Turbulent Flow Chromatography

Another way for online sample clean-up of biological samples prior to LC-MS analysis is turbulent flow chromatography. Turbulent flow chromatography (TFC) separates compounds in two dimensions; first according to polarity by standard reversed phase HPLC, then by mass separation as a consequence of turbulent flow (Herman et al. 2012). TFC is based on the finding that the flow of a fluid through a tube becomes turbulent when the force of the fluid exceeds its resistance to flow by a factor of 2000–3000 (Reynolds 1961). In a chromatographic column which is a tube packed with particles of typically bead-like character, the flow becomes turbulent when the flow rate is increased sufficiently to make all flow paths in the column become turbulent. TFC can be used to separate small molecules from larger biomolecules. The reason for this is that small molecules can diffuse into the pores of the stationary phase, while larger molecules will be washed away. Many biological samples contain large amounts of proteins, making TFC an excellent tool for online sample clean-up of such samples. Though TFC efficiently removes compounds above 8000 Da, many other impurities from biological samples such as fatty acids are however not removed. Therefore, TFC often requires a second sample clean-up step.

4.2.4 Liquid-Liquid Extraction

Another offline sample preparation technique is liquid/liquid extraction (LLE). LLE is—while highly effective in removing impurities—very labor intensive and requires specialized glass ware and large volumes of organic solvents. Normally, a pH gradient is used to separate the analyte from impurities and the sample matrix. There have been efforts to semi-automate LLE; however these have proven to be insufficient for high-throughput workflows. However, an approach utilizing halogenated solvents that can be centrifuged to the bottom of an aqueous mixture in a 96-well plate has been successfully implemented for high-throughput workflows. Here, an autosampler adds the halogenated solvent to the biological sample, mixes by pipetting and then centrifuges the plate. The supernatant can then be injected to the LC-MS system. The advantages of this technique are that the method

development is relatively easy, and the samples are very clean. However, halogenated solvent waste is generated. Other more specialized but highly efficient types of sample preparation exist, for instance, various membrane based extraction methods (Gjelstad and Pedersen-Bjergaard 2013; Payan et al. 2013).

For further information on the quantification of large molecule drugs in biological samples by mass spectrometry we refer to (van den Broek et al. 2013).

References

- Ardrey RE (2003) Liquid chromatography-mass spectrometry: an introduction. Wiley, New York
- Armbruster DA, Pry T (2008) Limit of blank, limit of detection and limit of quantitation. *Clin Biochem Rev* 29(Suppl 1):S49–S52
- Armbruster DA, Tillman MD, Hubbs LM (1994) Limit of detection (Lod) limit of quantitation (Loq)—comparison of the empirical and the statistical, methods exemplified with GC-MS assays of abused drugs. *Clin Chem* 40(7):1233–1238
- Bai Y, Milne JS, Mayne L, Englander SW (1993) Primary structure effects on peptide group hydrogen exchange. *Proteins* 17(1):75–86
- Brown RS, Lennon JJ (1995) Sequence-specific fragmentation of matrix-assisted laser-desorbed protein peptide ions. *Anal Chem* 67(21):3990–3999
- Campins-Falco P, Herraiz-Hernandez R, Sevillano-Cabeza A (1993) Column-switching techniques for high-performance liquid chromatography of drugs in biological samples. *J Chromatogr* 619(2):177–190
- Chen G, Warrack BM, Goodenough AK, Wei H, Wang-Iverson DB, Tymiak AA (2011) Characterization of protein therapeutics by mass spectrometry: recent developments and future directions. *Drug Discov Today* 16(1–2):58–64
- Cole RB (2010) Electrospray and MALDI mass spectrometry: fundamentals, instrumentation, practicalities, and biological applications. Wiley, Oxford
- Corradini E, Klaasse G, Leurs U, Heck AJ, Martin NI, Scholten A (2015) Charting the interactome of PDE3A in human cells using an IBMX based chemical proteomics approach. *Mol Biosyst* 11(10):2783–2797
- Frank R, Hargreaves R (2003) Clinical biomarkers in drug discovery and development. *Nat Rev Drug Discov* 2(7):566–580
- Gjelstad A, Pedersen-Bjergaard S (2013) Challenges and new directions in analytical sample preparation. *Anal Bioanal Chem* 406:375–376
- Glish GL, Vachet RW (2003) The basics of mass spectrometry in the twenty-first century. *Nat Rev Drug Discov* 2(2):140–150
- Hardouin J (2007a) Protein sequence information by matrix-assisted laser desorption/ionization in-source decay mass spectrometry. *Mass Spectrom Rev* 26(5):672–682
- Herman JL, Edge T, Majors RE (2012) Theoretical concepts and applications of turbulent flow chromatography. *LCGC North America* 30(3):200–214
- Hillenkamp F, Peter-Katalini J (2007) MALDI MS: a practical guide to instrumentation, methods and applications. Weinheim, Wiley-VCH; [Chichester : John Wiley [distributor]]
- Hoffmann ED, Stroobant V (2007) Mass spectrometry: principles and applications. Wiley, Hoboken, NJ; Chichester: John Wiley [distributor]
- Holcapek M, Jirasko R, Lisa M (2012) Recent developments in liquid chromatography-mass spectrometry and related techniques. *J Chromatogr A* 1259:3–15
- Houde D, Engen JR (2013) Conformational analysis of recombinant monoclonal antibodies with hydrogen/deuterium exchange mass spectrometry. *Methods Mol Biol* 988:269–289

- Houde DJ, Berkowitz SA (2015) Biophysical characterization of proteins in developing biopharmaceuticals. D. J. H. A. Berkowitz. Elsevier, Amsterdam
- Hunt DF, Coon JJ, Syka JEP, Marto JA (2005). Electron transfer dissociation for biopolymer sequence analysis. *US* 11079147
- Jeffery DA, Bogyo M (2003) Chemical proteomics and its application to drug discovery. *Curr Opin Biotechnol* 14(1):87–95
- Jennings KR (1968) Collision-induced decompositions of aromatic molecular ions. *Int J Mass Spectrom Ion Phys* 1(3):227–235
- Jensen PF, Larraillet V, Schlothauer T, Kettenberger H, Hilger M, Rand KD (2015) Investigating the interaction between the neonatal Fc receptor and monoclonal antibody variants by hydrogen/deuterium exchange mass spectrometry. *Mol Cell Proteomics* 14(1):148–161
- Joyce KB, Jones AE, Scott RJ, Biddlecombe RA, Pleasance S (1998) Determination of the enantiomers of salbutamol and its 4-O-sulphate metabolites in biological matrices by chiral liquid chromatography tandem mass spectrometry. *Rapid Commun Mass Spectrom* 12 (23):1899–1910
- Karas M, Bahr U (1990) Laser desorption ionization mass spectrometry of large biomolecules. *Trends Anal Chem* 9(10):321–325
- Koppenaal DW, Barinaga CJ, Denton MB, Sperline RP, Hieftje GM, Schilling GD, Andrade FJ, Barnes JH (2005) MS detectors. *Anal Chem* 77(21):418A–427A
- Korfmacher WA, Palmer CA, Nardo C, Dunn-Meynell K, Grotz D, Cox K, Lin CC, Elicone C, Liu C, Duchoslav E (1999) Development of an automated mass spectrometry system for the quantitative analysis of liver microsomal incubation samples: a tool for rapid screening of new compounds for metabolic stability. *Rapid Commun Mass Spectrom* 13(10):901–907
- Lanucara F, Holman SW, Gray CJ, Eyers CE (2014) The power of ion mobility-mass spectrometry for structural characterization and the study of conformational dynamics. *Nat Chem* 6 (4):281–294
- Leurs U, Mistarz UH, Rand KD (2015) Getting to the core of protein pharmaceuticals—comprehensive structure analysis by mass spectrometry. *Eur J Pharm Biopharm* 93:95–109
- Li Y, Shin YG, Yu C, Kosmeder JW, Hirschelman WH, Pezzuto JM, van Breemen RB (2003) Increasing the throughput and productivity of Caco-2 cell permeability assays using liquid chromatography-mass spectrometry: application to resveratrol absorption and metabolism. *Comb Chem High Throughput Screen* 6(8):757–767
- Lim MS, Elenitoba-Johnson KS (2004) Proteomics in pathology research. *Lab Invest* 84 (10):1227–1244
- Little TA (2015) Method validation essentials, limit of blank, limit of detection, and limit of quantitation. *Biopharm Int* 28(4):48–51
- Makarov A (2000) Electrostatic axially harmonic orbital trapping: a high-performance technique of mass analysis. *Anal Chem* 72(6):1156–1162
- Marshall AG, Hendrickson CL, Shi SD (2002) Scaling MS plateaus with high-resolution FT-ICRMS. *Anal Chem* 74(9):252A–259A
- Pandit D, Tuske SJ, Coales SJ, E SY, Liu A, Lee JE, Morrow JA, Nemeth JF, Hamuro Y (2012) Mapping of discontinuous conformational epitopes by amide hydrogen/deuterium exchange mass spectrometry and computational docking. *J Mol Recognit* 25(3):114–124
- Payan MD, Li B, Petersen NJ, Jensen H, Hansen SH, Pedersen-Bjergaard S (2013) Nano-electromembrane extraction. *Anal Chim Acta* 785:60–66
- Reynolds A (1961) Dynamics of turbulent vortical flow. *Z Angew Math Phys* 12(2):149–158
- Rix U, Superti-Furga G (2009) Target profiling of small molecules by chemical proteomics. *Nat Chem Biol* 5(9):616–624
- Roepstorff P, Fohlman J (1984) Proposal for a nomenclature for sequence ions in mass spectra of peptides. *Biomed Mass Spectrom* 11:601
- Ryhage R (1964) Use of mass spectrometer as detector+analyzer for effluents emerging from high temperature gas liquid chromatography columns. *Anal Chem* 36(4):759–764

- Siuzdak G (1994) The emergence of mass spectrometry in biochemical research. *Proc Natl Acad Sci U S A* 91(24):11290–11297
- Smith RD, Udseth HR, Loo JA, Wright BW, Ross GA (1989) Sample introduction and separation in capillary electrophoresis, and combination with mass spectrometric detection. *Talanta* 36 (1–2):161–169
- Syka JE, Coon JJ, Schroeder MJ, Shabanowitz J, Hunt DF (2004) Peptide and protein sequence analysis by electron transfer dissociation mass spectrometry. *Proc Natl Acad Sci U S A* 101 (26):9528–9533
- Tao L, Ackerman M, Wu W, Liu P, Russell R (2011) Characterization of impurities and degradants using mass spectrometry. Wiley, Hoboken
- van den Broek I, Niessen WMA, van Dongen WD (2013) Bioanalytical LC–MS/MS of protein-based biopharmaceuticals. *J Chromatogr B* 929:161–179
- Wanner KT, Höfner G (2007) Mass spectrometry in medicinal chemistry. Weinheim, Wiley-VCH; Chichester : John Wiley [distributor]
- Zhang Z, Smith DL (1993) Determination of amide hydrogen exchange by mass spectrometry: a new tool for protein structure elucidation. *Protein Sci* 2(4):522–531
- Zheng J (2009) Formulation and analytical development for low-dose oral drug products. Wiley, New York
- Zubarev RA, Horn DM, Fridriksson EK, Kelleher NL, Kruger NA, Lewis MA, Carpenter BK, McLafferty FW (2000) Electron capture dissociation for structural characterization of multiply charged protein cations. *Anal Chem* 72(3):563–573
- Zubarev RA, Kruger NA, Fridriksson EK, Lewis MA, Horn DM, Carpenter BK, McLafferty FW (1999) Electron capture dissociation of gaseous multiply-charged proteins is favored at disulfide bonds and other sites of high hydrogen atom affinity. *J Am Chem Soc* 121:2857–2862

Part II
Diffraction Techniques

Chapter 8

An Overview of Powder X-ray Diffraction and Its Relevance to Pharmaceutical Crystal Structures

Kenneth Shankland

Abstract Single-crystal X-ray diffraction is one of the most powerful methods for the analysis of crystalline materials, but as active pharmaceutical ingredients are typically processed in the form of polycrystalline powders, powder X-ray diffraction assumes a particularly important role in their analysis. This chapter, which is targeted at pharmaceutical scientists, presents a brief introduction to the technique, before discussing the various ways in which it can be used to probe crystal structures, with a particular emphasis on the practicalities of data collection in the laboratory and on data analysis, leading ultimately to high-quality, refined crystal structures.

Keywords Powder diffraction • Pharmaceuticals • Crystal structure determination • Laboratory X-ray powder diffraction instrumentation • Physical form identification • Crystal structure verification • Rietveld refinement

1 Introduction

X-ray diffraction is one of the most powerful methods for the analysis of crystalline materials. In particular, single-crystal X-ray diffraction (SXD; see Chap. 9) is the definitive method for determining three-dimensional crystal structures, yielding accurate atomic coordinates and thermal parameters from which quantities such as molecular geometry and intermolecular distances can be derived. Availability of a representative single crystal is, of course, a pre-requisite, but there are many cases where crystallisation experiments yield only polycrystalline products e.g. with the mechanical grinding processes often used to produce co-crystals. In such cases, powder X-ray diffraction (PXRD) is the obvious alternative to SXD. As shall be seen, PXRD is intrinsically less ‘information rich’ than SXD, but can still yield crystal structures for materials ranging from small molecules through to proteins.

K. Shankland (✉)

School of Pharmacy, University of Reading, Reading RG6 6AD, UK

e-mail: k.shankland@reading.ac.uk

It finds particular utility in crystallographic phase identification and quantification, allowing one to answer important questions such as, “What is the crystal structure of polymorph A, how does its structure differ from that of polymorph B, and how much of polymorph A is present in a polycrystalline mixture of A plus B?”

This chapter differs from many other comprehensive articles and reviews of pharmaceutical powder diffraction (Randall et al. 2010; Brittain 2001; Shankland et al. 2013; Ivanisevic et al. 2010) in that it adopts a largely practical approach, with the intention of guiding the interested pharmaceutical analyst through a maze of PXRD opportunities. Although diffraction from crystals can be observed using X-rays, neutrons and electrons, the focus here is on the use of X-rays, which are by far the most widely used in practice. It is assumed that the reader is at least familiar with the fundamental concepts of crystal structures, such as lattice parameters, space groups, reflections and fractional coordinates; those who are not are referred to one of the many excellent introductory volumes available (Pecharsky and Zavalij 2005; Ooi 2009).

2 Background to the Technique

A typical PXRD pattern for a molecular organic material is shown in Fig. 8.1. The diffraction pattern consists of thousands of individual measurements of X-ray intensity, made at regular intervals along an arc that describes the angle of diffraction, 2θ , relative to the path of the incident X-ray beam. Peaks in the pattern are the result of the diffraction of X-rays by atoms in the crystal structure and are most conveniently thought of as X-ray reflections from individual lattice planes in the unit cell. Such reflections are only observed when Bragg’s law is satisfied i.e. $\lambda = 2d \sin \theta$, with λ = incident X-ray wavelength and d = the d -spacing of the reflection. Peak positions are thus a function of the size and shape of the unit cell. Reflection intensity, I , is proportional to the square of the structure factor modulus, $|F|$, where the structure factor for any given reflection hkl is given by

$$F_{hkl} = \sum_{j=1}^N f_j e^{2\pi i(hx_j + ky_j + lz_j)}$$

where N is the number of atoms in the unit cell, x , y and z are the fractional coordinates of the j th atom and f_j is the scattering factor of the j th atom. As such, it is clear that reflection intensities are a function of the atom types and their positions in the unit cell. Peak shapes and background scattering are the result of other factors, such as instrumental geometry, sample microstructure (i.e. crystallite size and strain), air scatter and sample amorphous content.

The PXRD pattern thus contains the key information that allows one, in principle, to determine the underlying three-dimensional crystal structure that gave rise to it. Specifically, peak positions can be used to determine the size and shape of the

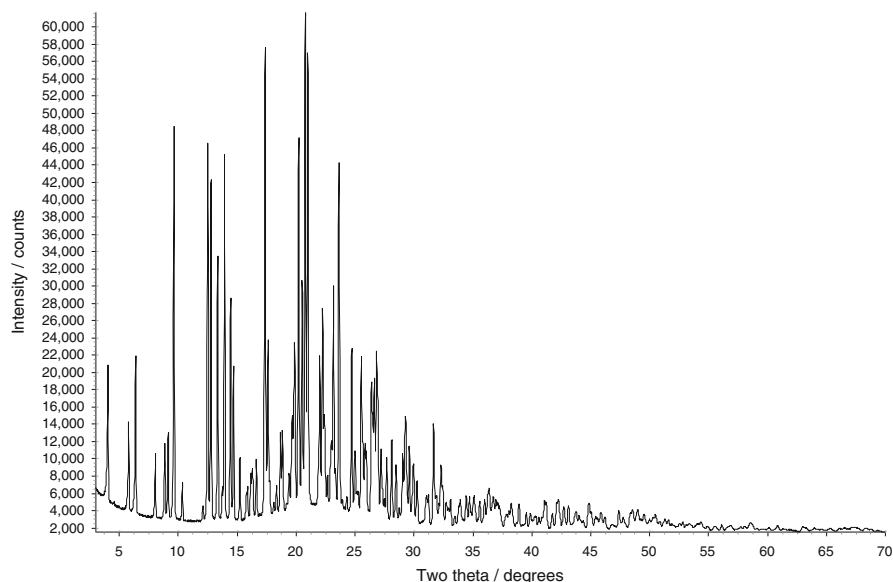


Fig. 8.1 A laboratory powder X-ray diffraction pattern of cyheptamide form II ($C_{16}H_{15}N_1O_1$, space group $P-1$, $Z' = 4$, $V = 2412.3 \text{ \AA}^3$; $\lambda = 1.54056 \text{ \AA}$). The pattern spans a d -spacing range of 29.36–1.34 \AA and contains contributions from around 2100 Bragg reflections

unit cell, whilst peak intensities can be used to determine the types of atoms present in the cell and their positions. Why then, is it so much more difficult to solve a crystal structure from PXRD data than from SXD data? The principal reason is that the PXRD pattern is a one-dimensional projection of diffraction that occurs in three dimensions¹ and a relatively small number of structure factors are measured in a typical PXRD experiment when compared with the number measured in a typical single-crystal experiment. For example, the data in Fig. 8.1 only extend to a resolution of 1.34 \AA , significantly less than the resolution of 0.84 \AA achieved in a typical SXD experiment; as each reflection intensity is a piece of information directly related to the crystal structure, much less information is therefore available to help solve and refine the structure. PXRD is further compromised by this collapse of diffraction from three dimensions to one, as reflections with similar d -spacings end up overlapping with one another in the pattern. This overlap problem becomes more severe at higher values of 2θ , where the number of reflections with similar d -spacings increases dramatically.² As a result, an individual discernible peak in the diffraction pattern may contain contributions from more than one reflection,

¹ A single crystal diffracts X-rays in three dimensions. A powder sample is ideally a random distribution of tiny single crystals, resulting in an orientationally averaged diffraction pattern in which reflections with identical d -spacings appear at identical 2θ values in the PXRD pattern.

² This can be seen in Fig. 8.7, where the tick marks lying on the x-axis indicate the positions of reflections in the diffraction pattern.

making it difficult to estimate the intensities of each contributing reflection. By way of example, the data set shown in Fig. 8.1 contains contributions from *ca.* 2100 reflections, but displays far fewer discernible peaks. It is also evident that at higher values of 2θ , the intensity of the observed diffraction ‘drops off’ (largely a consequence of the fact that the magnitude of the scattering factor, f_j , falls off with increasing diffraction angle) and reflections become increasingly difficult to distinguish from the background scattering as a result.

These factors conspire to make it difficult to extract a sufficient number of accurate reflection intensities from a PXRd pattern to make conventional methods of structure determination (i.e. the so-called ‘direct methods’ developed for SXD) work effectively. As will be seen in Sect. 3.8, however, this difficulty can often be overcome.

3 PXRd in the Laboratory Environment

This section focuses mainly on the instrumentation commonly found in laboratories where molecular materials are studied. For a concise general summary of laboratory-based PXRd, the reader is referred to the chapter of Louer (2002).

3.1 Radiation Source

The most commonly used X-ray tubes in the laboratory environment have copper anodes generating X-rays of wavelength 1.5418 Å (Cu $K\alpha$ radiation) and 1.3922 Å (Cu $K\beta$ radiation); the latter is normally filtered out (or monochromated, see below) to leave Cu $K\alpha$ radiation available for diffraction. Cu $K\alpha$ radiation consists of a mixture of two wavelengths, Cu $K\alpha_1$ ($\lambda = 1.54056$ Å) and Cu $K\alpha_2$ ($\lambda = 1.54439$ Å) and a primary monochromator³ can be used to select only the stronger Cu $K\alpha_1$ wavelength for diffraction. The main advantage of monochromatic incident radiation is that each reflection appears as only a single peak in the diffraction pattern, thus simplifying pattern analysis, though this gain comes at the cost of decreased incident beam intensity. A rotating anode source provides a much more intense source of X-rays that helps compensate for this loss, but at the cost of significantly greater initial expense, power consumption and maintenance. Of the other X-ray sources available (Cr, Fe, Co, Mo, Ag) the last two are finding increasing use in the collection of PXRd data for Pair Distribution Function analysis of seemingly X-ray amorphous materials (Dykhne et al. 2011), by virtue of their shorter wavelengths.

³ A primary monochromator selects a particular X-ray wavelength prior to it being incident upon the sample.

The remainder of this chapter will assume the use of monochromatic Cu $K\alpha_1$ radiation.

3.2 *Detector*

The most common detector type used on general purpose laboratory-based PXRD instrumentation is the position-sensitive detector (PSD) that can detect diffracted X-ray photons simultaneously over a range covering a few degrees 2θ . It combines good resolution with dramatically reduced count times relative to those of a conventional scintillation-based point detector. Two dimensional detectors that record entire diffraction rings are commonly used on diffractometers that are designed for high-throughput PXRD. The ability to collect entire diffraction rings and integrate around them to estimate diffracted intensity helps mitigate the effects of preferred orientation (see Sect. 3.3.1) and/or poor crystallite averaging from the small sample volumes that tend to be used in such situations.

3.3 *Instrumental Geometry*

3.3.1 *Reflection Geometry*

Reflection geometry is the most widely used instrumental setup as it combines simplicity of sample preparation with speed of data collection and ease of automation. The basic geometry is shown in Fig. 8.2, yielding good intensity and high instrumental resolution.⁴ The standard flat plate sample holder is extremely convenient for dealing with situations where relatively large amounts of sample (ca. 300 mg) are available and where recovery of the sample is desirable. When only very small amounts (a few mg) of material are available, it is common practice to use 'zero-background' silicon sample holders; the sample is lightly dusted onto the surface of the silicon crystal, which is normally smeared with an extremely thin layer of grease to aid adhesion of the powder. The sample is then, in general, not recoverable. Diffractometers can also be equipped with a robotic sample changer that allows large numbers of flat-plate samples to be pre-prepared, loaded into the diffractometer and then scanned in any given sequence.

The main limitation of this instrumental setup is that diffracted intensities can be significantly affected by preferred orientation; that is, when crystallites in the powder sample are not arranged randomly, leading to systematic distortion of reflection intensities. This is illustrated schematically in Fig. 8.3 and the effect

⁴ Instrumental resolution is frequently quoted in terms of the 'full width at half maximum' (FWHM) of a reflection obtained from a very sharply diffracting standard sample, when the instrumental contribution to the observed peak width exceeds that of the sample itself.

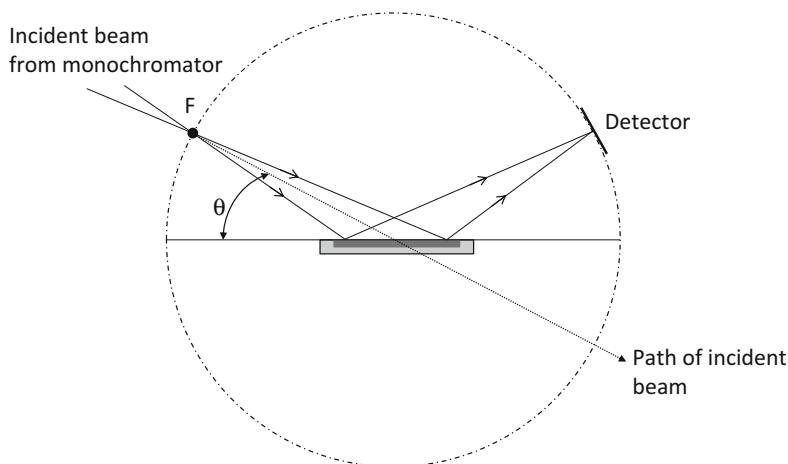


Fig. 8.2 A schematic diagram of the commonly-used Bragg-Brentano focusing instrument geometry. A convergent beam from the monochromated X-ray source focuses at point F on the diffraction circle (*dot-dashed* line), and diverges before hitting the sample. Upon diffraction from the sample, the beam focuses back on the diffraction circle giving high instrumental resolution. The detector scans over the circle in order to detect all the diffracted beams. The angle of incidence of the beam is θ and the diffracted angle from the incident beam path to the detector position is 2θ . The sample holder (*light grey*) holds a small amount of sample (*dark grey*) and lies at the centre of the circle

can be so severe as to render even the elementary identification of a sample by its PXRD pattern extremely difficult. Furthermore, observed peak positions can be also affected if the surface of the sample is not level or if the sample holder is under or over filled.

3.3.2 Transmission Geometry

The basic geometry is shown in Fig. 8.4, again yielding good intensity and high instrumental resolution. The sample is held in a thin walled glass capillary of diameter *ca.* 0.7 mm and is rotated around its axis in the X-ray beam. This setup is well suited to dealing with small amounts of sample (a few mg of material is sufficient for a 0.7 mm capillary) and when recovery of the sample is required. Smaller diameter capillaries (e.g. 0.3, 0.5 mm) can be used to reduce the amount of sample required still further, but as the irradiated volume of powder is much smaller, longer count times are needed to achieve counting statistics similar to those obtained from the 0.7 mm capillary.

The main advantage of this type of setup is that the effects of preferred orientation are minimised, giving rise to patterns with intensities that are much more likely to be representative of the underlying crystal structure. The main disadvantages are that: (a) it is not well suited to samples containing heavy atoms (e.g. Au, W) that absorb X-rays to a significant extent, though this is not generally a

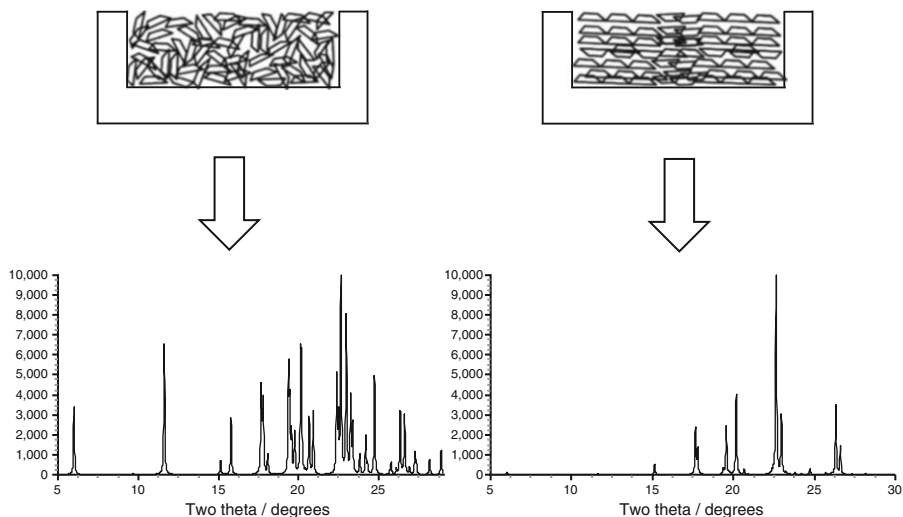


Fig. 8.3 The effect of preferred orientation upon observed diffraction in Bragg-Brentano geometry. The sample holder on the left hand side contains effectively a random distribution of sample crystallites, giving rise to a PXRD pattern that is representative of the underlying crystal structure. In the sample holder on the right, the sample crystallites are arranged in a non-random manner, giving rise to a PXRD pattern that is markedly different in terms of diffracted intensities from that generated by the random distribution

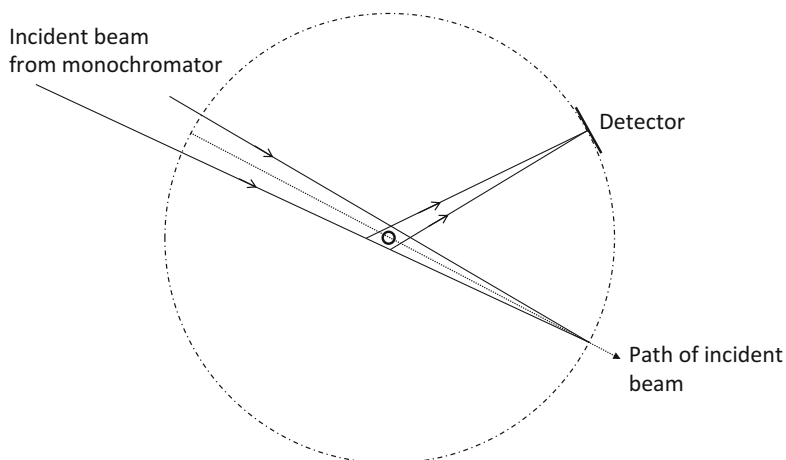


Fig. 8.4 A schematic diagram of a focusing transmission capillary instrument geometry. A convergent beam from the monochromated X-ray source focuses on the far side of the diffraction circle (*dot-dashed line*) after passing through the sample, giving high instrumental resolution. The sample is contained in a thin-walled glass capillary (*small dark circle*) at the centre of the diffraction circle, perpendicular to the plane of the paper. Upon diffraction from the sample, the beam focuses on the diffraction circle, over which the detector scans in order to collect all diffracted beams

problem for molecular organic materials; (b) it is not well suited to the automated running of large numbers of samples—only diffractometers at large central facilities (see Sect. 3.11) are routinely equipped with capillary sample changers, and capillary filling is a manual process that can be both tedious and difficult with powders that do not flow particularly well.

3.3.3 Reflection, Transmission or Both?

The choice of reflection or transmission modes depends very much upon the intended use. For situations where large numbers of samples need to be quickly screened and ‘fingerprinted’ (see Sect. 3.4), reflection geometry combined with an automated sample changer is an excellent choice. For structure solution and refinement, or for quantitative phase analysis, transmission geometry, with the sample mounted in a rotating capillary, is highly recommended. Very high throughput, 96-well plate configurations are also available in transmission (thin film) and reflection modes. It should be apparent from Figs. 8.2 and 8.4 that a single instrument can be converted between reflection and transmission relatively easily and the latest generation of diffractometers that feature ‘plug-and-play’ type optics make it easier than ever to have the best of both configurations.

Regardless of the mode of operation, a correctly aligned instrument is essential if reliable results are to be obtained. It is strongly recommended that alignment is checked on a regular basis using standard materials. Instruments are supplied with well-defined procedures for alignment, and calibration samples such as corundum and silicon. A Pawley refinement (see Sect. 3.7) of a standard sample is a particularly good way of checking the zero-point offset of a diffractometer; a value of *ca.* $\pm 0.007^\circ$ or smaller is indicative of excellent alignment.

3.4 *Fingerprint Identification of Physical Forms*

A PXRD pattern can be regarded as a ‘fingerprint’ of the crystal structure of the material under study and its importance as a means with which to identify specific crystallographic phases is evidenced by its central role in high-throughput physical form screening and its use in patents designed to protect physical forms. These aspects have been reviewed comprehensively elsewhere (Morissette et al. 2004; Florence 2009; Lemmerer et al. 2011). Given a small collection of PXRD patterns (e.g. *ca.* 10), visual assessment of pattern similarity in order to identify physical forms is feasible, but for much larger sets of data (such as one obtained from a 96-well plate polymorph screening experiment) it is prudent to use software to aid grouping and interpretation of patterns. The *PolySNAP* program (Barr et al. 2009) is one such software package that is optimised to handle large numbers (up to 1500) of patterns and group them not only in terms of their similarity to one another but also to any ‘reference patterns’ supplied. Any such program must take account of the

fact that the data collected from high-throughput PXRD experiments are generally subject to the influence of factors such as zero-point offset, preferred orientation and sample transparency. Whilst undoubtedly an invaluable aid to the initial assessment of PXRD data (and other data, including infra-red and Raman) from large numbers of samples, care must be exercised in drawing definitive conclusions from rapid screening data that have been quickly collected and are subject to some of the aforementioned confounding factors. For example, it has been remarked previously that the PXRD patterns of forms I and II of terephthalic acid are similar and that this might preclude their definitive identification by PXRD (Davey et al. 1994). This may well be the case with poor quality PXRD data, but an overlay of simulated patterns for these two crystal structures (Fig. 8.5) shows them to be only superficially similar; there are clear differences that are easily distinguished on a well-aligned laboratory diffractometer when due care is taken with sample preparation and presentation.

Ultimately, comparisons between PXRD patterns are much more straightforward if the underlying details of the crystal structure are known. The starting point for working out these details is determination of the size and shape of the unit cell.

3.5 Powder Indexing

Indexing a PXRD pattern is the process of determining the size and shape of a unit cell directly from the positions of the first 20 or so reflections in the pattern. The indexing process has been explained in considerable detail elsewhere (Werner 2002) and the focus here is on some of the practicalities involved.

A prerequisite for successful indexing is a PXRD data set collected on a well-aligned diffractometer.⁵ Although modern indexing programs such as *DICVOL*, *XCELL* and *TOPAS* can take zero-point offsets into account, they return more reliable solutions if supplied with reflection positions derived from good quality data. On a transmission capillary diffractometer equipped with a linear PSD, collection of data suitable for indexing over the range 2.5° – 40° 2θ takes only *ca.* 2 h. Reflection positions are best estimated using the peak fitting routines available in the indexing programs or the diffractometer's software suite. Broad peaks that may be composed of contributions from more than one reflection are preferably avoided and particular care should be taken when deciding whether or not to include the positions of weak peaks. In general, it is prudent to exclude *very weak* features from initial indexing attempts, as indexing programs are more tolerant of 'missing' input positions than they are of erroneous input positions. Supplied with around 20 input reflection positions, indexing programs will then suggest the most likely unit cells, ranked by some figure-of-merit, whose predicted reflection

⁵ The output of the indexing program *DICVOL91* includes the following line in its text output: "WARNING: ARE YOUR DATA IRREPROACHABLE?".

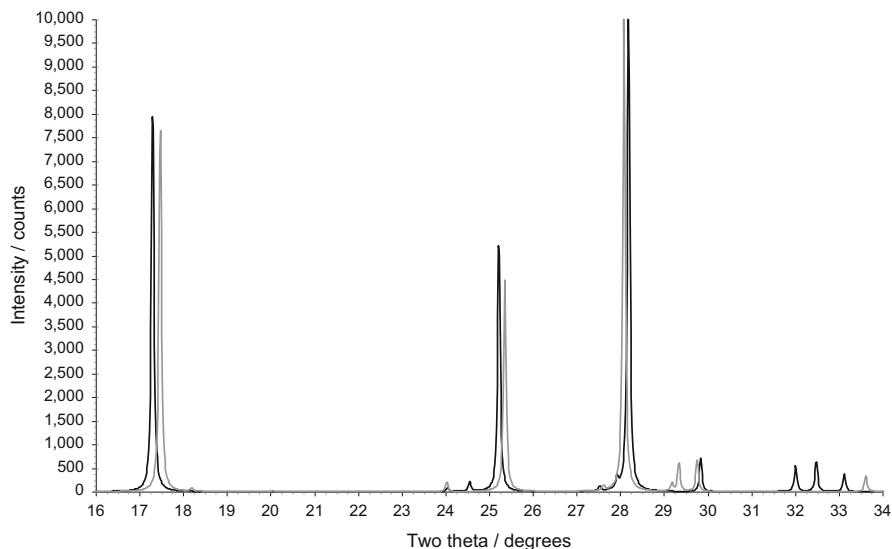


Fig. 8.5 Simulated PXRD patterns in the range 16° – 34° 2θ calculated using *Mercury* (Macrae et al. 2008), for terephthalic acid form 1 (black line, CSD refcode TEPHTH) and terephthalic acid form 2 (grey line, CSD refcode TEPHTH01, H-atoms added in calculated positions using *Mercury*). Whilst the patterns are superficially similar, the positions of the strong peaks are in fact well separated (e.g. the peaks at around 17.4° 2θ are separated by ca. 0.18°) and therefore easily distinguishable. The cluster of form 1 peaks at ca. 32° 2θ is also clearly diagnostic

positions best match those input. Candidate cells can be evaluated visually by plotting calculated peak positions for each cell against the observed PXRD data. For every peak in the diffraction pattern, there should be a corresponding calculated reflection position. If not, the cell is either incorrect or there are additional crystallographic phases (e.g. impurities) in the sample giving rise to PXRD features that cannot be explained by the candidate cell. If there is no peak to match a predicted reflection position, this is not necessarily indicative of an error in the cell; rather, the predicted reflection may well be a systematic absence (see Sect. 3.6).

For any promising unit cell, its volume (V_{cell}) should be crystallographically reasonable i.e. a multiple of the estimated molecular volume (V_{mol}) of the material under study. For example, if $V_{\text{mol}} \approx 250 \text{ \AA}^3$ and a candidate monoclinic cell has $V_{\text{cell}} = 995 \text{ \AA}^3$, then four molecules (a number consistent with a monoclinic solution) can fit in the cell. V_{mol} can be quickly and reliably estimated using the method of Hofmann (2002).

Whilst modern indexing programs can often tolerate the presence of some impurity lines in a PXRD pattern, intuition remains an important component in the indexing process. Figure 8.6 shows an example of a PXRD pattern collected from a sample of a 1:1 carbamazepine-indomethacin co-crystal that was produced by simple grinding of form III carbamazepine and γ -indomethacin powders. After initial indexing attempts failed, the pattern was checked for the presence of

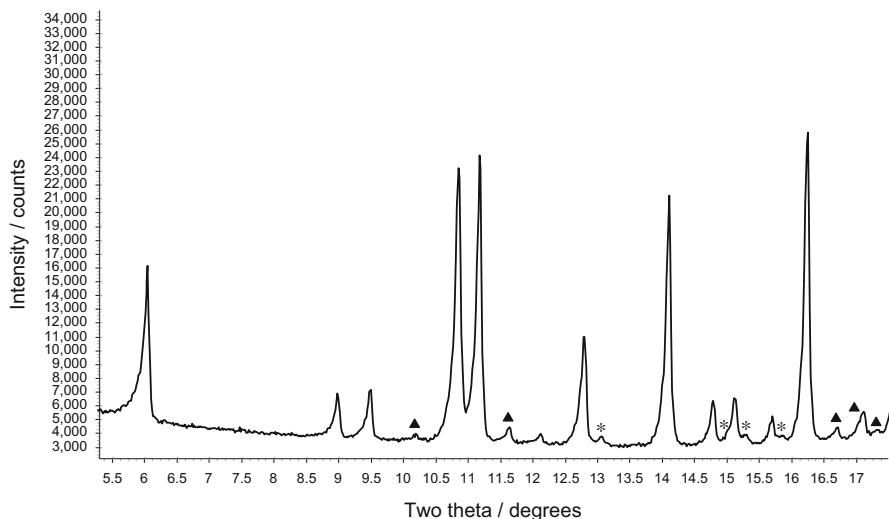


Fig. 8.6 A PXRD pattern collected from a sample of a 1:1 carbamazepine-indomethacin co-crystal produced by simple grinding. Weak peaks attributable to residual form III carbamazepine (*asterisk*) and γ -indomethacin (*filled triangle*) in the sample are indicated

contributions from residual form III carbamazepine and γ -indomethacin. Once two small subsets of weak reflections attributable to these phases were identified and eliminated from the indexing input, the co-crystal phase was easily indexed.

3.6 Space Group Determination

Indexing returns both the Bravais lattice type (e.g. triclinic, monoclinic, orthorhombic etc.) and the dimensions of the unit cell, but says nothing about the space group symmetry of the material being studied. For this, systematic absences⁶ in the PXRD pattern must be examined in order to determine the extinction symbol⁷ for the system under study. This concept is most easily explained by example. Consider a monoclinic unit cell returned by an indexing program. When the reflection positions calculated from this cell are plotted against the PXRD data, it might be noted that there are no observed peaks where the (0 1 0), (0 3 0), and (0 5 0) reflections are predicted to occur. The experienced crystallographer will immediately recognise

⁶ These are reflections that are predicted to appear for a unit cell with no space group symmetry, but which fail to appear in the diffraction pattern due to the effect of the underlying space group symmetry. Thus systematic absences can be used to help determine the space group symmetry.

⁷ The extinction symbol summarises the symmetry elements that are consistent with the observed systematic absences. Note that an extinction symbol can be consistent with more than one space group.

that these missing ('absent') reflections follow a trend: $0\ k\ 0$, $k = \text{odd}$ are all missing. This trend is associated with the presence of a 2_1 screw symmetry element along the b axis of the unit cell and assuming that these are the only absences noted, they will conclude that the extinction symbol is $P\ 1\ 2_1\ 1$. This leaves one further task—assignment of the correct space group, as extinction symbol $P\ 1\ 2_1\ 1$ is consistent with space groups $P\ 1\ 2_1\ 1$ and $P\ 1\ 2_1/m\ 1$; both space groups have identical systematic absences (Looijenga-Vos and Buerger 2005). The final decision as to which is correct is often made on the basis of the presence or absence of a centre of symmetry in the space group. For example, if the compound is a single enantiomer, then the centrosymmetric space group $P\ 1\ 2_1/m\ 1$ can be ruled out.

In practice, identifying systematic absences in a PXRD pattern is rarely as simple as outlined above, as several different classes of reflection may be absent and reflection overlap usually makes decisions about the presence or absence of a given reflection subjective at best. Fortunately, some PXRD data analysis programs are now equipped with routines that place the determination of the extinction symbol on a probabilistic basis, making selection a near-automatic task (Markvardsen et al. 2012).

3.7 Pawley Fitting for Phase Identification

Once a diffraction pattern has been collected, it can be compared visually or computationally with measured or calculated powder patterns of known crystalline forms (see Sect. 3.4). A much more powerful approach, however, is to use the underlying crystal structure directly in a Pawley refinement.⁸ This is a least-squares fit of a calculated powder diffraction pattern to an observed one, in which the least-squares variables are (typically) the unit cell parameters, a polynomial background, a set of peak shape parameters, a zero point offset and the intensity of each reflection present in the fitted data range. After the least-squares refinement has converged, the quality of the fit is assessed visually (see Fig. 8.7) and with the aid of a figure of merit such as R_{wp} (Young 1995) that quantify the goodness of fit. For a sample consisting of a single crystalline phase, all observed reflections should be accounted for by the input unit cell/space group and any residual misfit seen in the difference plot should be attributable only to small inaccuracies in the modelling of the peak shape. Significant misfit can be indicative of an incorrect unit cell/space group, or the presence of additional phases or impurities in the sample. As such, a good Pawley fit is valuable evidence of phase identity and purity. It is worth noting that multi-phase Pawley refinement can also be performed on a data set that contains contributions from more than one crystalline phase.

⁸For simplicity, we will consider only Pawley refinements here, whilst noting that the closely related Le Bail method of PXRD profile fitting can be used to the same end.

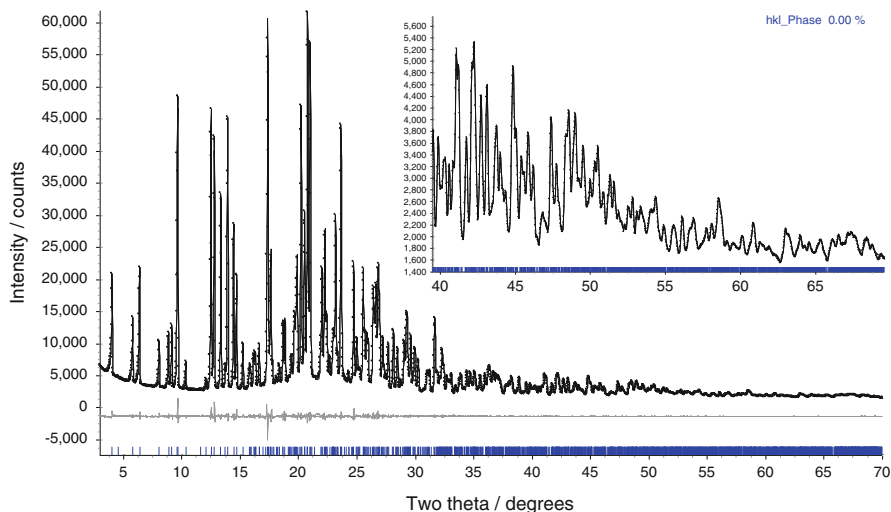


Fig. 8.7 A Pawley fit to the data shown in Fig. 8.1. The observed data points are shown as individual points, whilst the calculated pattern is shown as a *solid black line*. The difference between the *obs* and *calc* data is plotted as a *light grey line*. The high angle region of the pattern is shown in an expanded view as an *inset*. The *tick marks* along the x-axis show the calculated reflection positions. The R_{wp} for this fit is 1.631

Additionally, as the reflection intensities are least-squares variables in a Pawley refinement, the refinement can be used specifically to extract intensities from a PXRD pattern. These can then be used in a crystal structure determination attempt.

3.8 Crystal Structure Determination

Methods for crystal structure determination from powder diffraction data have developed in recent years to the extent that when assessed in terms of the number of atoms in the asymmetric unit of the crystal structure, reported powder structures span a similar range to those solved by all methods, albeit in a much smaller overall number (Shankland et al. 2013). Readers interested in methods for crystal structure determination from powder diffraction data (SDPD) are referred to a comprehensive review by Shankland in the forthcoming “International Tables for Crystallography Volume H: Powder diffraction” and an article on the principles underlying the use of powder diffraction data in solving pharmaceutical crystal structures (Shankland et al. 2013). Here, the discussion is limited to some of the key factors that should be considered by anyone setting out to solve a structure from PXRD data, having already exhausted the possibilities of growing a crystal suitable for SXD.

3.8.1 Is the Structure Solvable?

It is not possible to simply look at a 2D chemical sketch of a molecule and state definitively whether or not its crystal structure can be solved; there are too many unknowns, such as how well the powder sample will diffract, how sharp the diffraction features will be and what the value of Z' ⁹ for the crystal structure is. However, assuming $Z' = 1$ and sharp diffraction to moderate resolution (2 Å or better, equating to diffraction beyond *ca.* 45° 2 θ when using Cu $K\alpha_1$ radiation) then a study of published crystal structures suggests that the chances of solving a structure containing up to 50 non-H atoms and up to 15 degrees-of-freedom (DoF)¹⁰ using laboratory PXRD alone are very good (Shankland et al. 2013). Some additional general observations can be made in respect of factors that can increase the chances of obtaining a successful structure solution: (a) structures containing relatively heavy, strongly scattering atoms such as S, Cl and Br are more likely to be ‘solvable’ than molecules that contain only light (C, H, N, O) atoms; (b) the fewer the number of atoms in the structure, or the fewer the number of degrees of freedom, the more likely it is that a solution can be obtained.

3.8.2 Data Collection

As mentioned in Sect. 3.5, a data set suitable for indexing purposes can be collected in *ca.* 2 h and if a good Pawley fit to this data confirms the unit cell and space group, then a high-quality data set for structure solution *and* refinement should be collected. It is generally convenient to collect a single data set that can be used for both these purposes. As a general guide, data collected to 70° 2 θ using Cu $K\alpha_1$ radiation contains reflections to a minimum d -spacing (d_{\min}) of 1.35 Å and assuming good quality diffraction to this limit, a high-quality Rietveld refinement should be achievable (see Sect. 3.8.5). If the sample diffracts well to an even lower d_{\min} , then data should be collected to that limit if possible, as the higher resolution data will permit a more accurate Rietveld refinement.

The fall-off in diffracted intensity seen with increasing 2 θ (Sect. 2) can be compensated for during the data collection process by using a variable count time (VCT) scheme (Shankland et al. 1997). A general-purpose VCT scheme, suitable for structure solution and refinement, is given in Table 8.1. It may also be advantageous to collect data at low temperature (e.g. 150 K; see Sect. 3.10) in order to

⁹The number of crystallographically independent molecules in the asymmetric unit of the unit cell.

¹⁰The structural DoF for a molecular organic molecule are divided into external DoF (i.e. three positional and three orientational) and internal (i.e. the number of torsion angles that are free to rotate). Covalent bond lengths and bond angles are generally treated as fixed, well-defined quantities and so it is values for the various DoF that must be determined in order to solve the crystal structure.

Table 8.1 A sample VCT scheme for crystal structure solution and refinement

Scan number	Scan range/ $^{\circ}2\theta$	Time per step/s	Duration/h
1	2–22	2	0.65
2	22–40	4	1.18
3	40–55	15	3.68
4	55–70	24	5.88

The scheme is based on the use of Cu $K\alpha_1$ radiation, a linear PSD and a step size of $0.017^{\circ} 2\theta$. The total data collection time is *ca.* 12 h

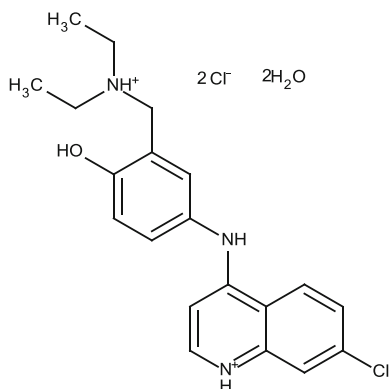
boost measured reflection intensities, particularly at high 2θ , assuming that the temperature change does not cause a phase transition.

3.8.3 Choice of SDPD Methodology

Whilst a great many methods for SDPD are available, in practice, only two are currently widely used: modified direct methods and global optimisation methods. Examples of pharmaceutical crystal structures solved by both methods are shown in Fig. 8.8. In the case of modified direct methods, the highly successful SXD direct methods of structure solution have been adapted to address the specific challenges presented by powder diffraction data. Modified direct methods of this type are to be found in the *EXPO* software package (Altomare et al. 2009) and are applicable to a broad range of problems that include inorganic, organic and organometallic structures, using diffraction data collected on standard laboratory instrumentation as well as on high-resolution synchrotron instruments. Importantly, modified direct methods do not require any *a priori* connectivity information, since the molecular connectivity is derived from electron density maps that are calculated as part of the SDPD process.

In the global optimisation approach to SDPD, the position, orientation and conformation of a molecular model of the compound under study is adjusted within the previously determined unit cell until such time as good agreement is obtained between observed and calculated PXRD data. The problem equates to one of locating the global minimum on an agreement factor (e.g. R_{wp}) hypersurface, whose dimensionality equals the number of DoF in the problem. Many computer programs that implement the global optimisation approach are available (Pagola and Stephens 2010; Engel et al. 1999; David et al. 2006; Favre-Nicolin and Černý 2004) and whilst implementation details and optimisation methods vary widely, they provide broadly similar functionality. The power of the global optimisation approach derives from its ability to incorporate prior information in the form of a 3D structural input model of the molecule being studied. This requirement for an initial structural model also constitutes its most obvious disadvantage—if the connectivity is not known then the SDPD attempt cannot proceed and if the connectivity is significantly in error,¹¹ then the SDPD attempt is destined to fail.

¹¹ Typical errors in construction of the input molecular model include the incorrect specification of chirality, cis-trans isomerism, N-atom pyramidalisation and flexible ring conformations.



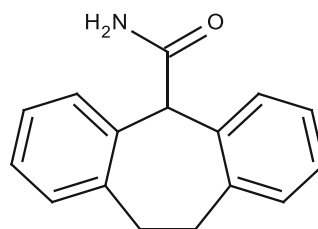
Amodiaquin dichloride dihydrate

$C_{20}H_{28}Cl_3 N_3 O_3$

$P2_1/c$, $V=2283.7\text{\AA}^3$, $Z'=1$

$N_{\text{atom}} = 57$, $N_{\text{nonH}} = 29$, $\text{DoF} = 30$

$d_{\text{min}} = 1.79\text{\AA}$



Cyheptamide form II

$C_{16}H_{15}N_1O_1$

$P-1$, $V=2411.7\text{\AA}^3$, $Z'=4$

$N_{\text{atom}} = 132$, $N_{\text{nonH}} = 72$, $\text{DoF}=28$

$d_{\text{min}} = 2.91\text{\AA}$ (soln.) $d_{\text{min}} = 1.34\text{\AA}$ (Riet)

Fig. 8.8 Two representative pharmaceutical crystal structures solved by (a) modified direct methods: amodiaquin dichloride dihydrate (Altomare et al. 2012) and (b) global optimisation: cyheptamide form II (Florence et al. 2008)

Provided that the connectivity is known, a 2D sketch or SMILES representation of a molecule can easily be converted to a set of 3D coordinates using molecular modelling software such as *Marvin* (ChemAxon 2013). The geometry of the resulting molecule is then preferably optimised using a density functional theory based program such as *CASTEP* (Clark et al. 2005). Alternatively, existing 3D crystal structures can be retrieved from the Cambridge Structural Database (Allen 2002) and modified if required. It is good practice to check the molecular geometry of the starting model using software such as *Mogul* (Bruno et al. 2004) which compares the geometry of the input model to that of similar structures found in the Cambridge Structural Database. Any problems identified in the model, such as bond lengths or angles that deviate significantly from commonly observed values, should be rectified before the model is used.

It is important to realise that any global optimisation SDPD attempt actually consists of multiple global optimisation runs, as no single run alone is guaranteed to find the global minimum. Depending on the complexity of the problem under study, it may take anywhere between a few seconds and a few days to complete an attempt on a conventional desktop PC; normally, as the number of DoF increases, so does the time taken to locate the global minimum. For a 'typical' molecular organic structure with ca. 15 DoF, the global minimum will normally be located in a matter of minutes.

3.8.4 Assessing the Structure Solution

Before proceeding to the structure refinement stage, the candidate structure solution must be assessed to see if it is viable, as it is quite possible for the best solution obtained by either direct methods or global optimisation to be completely incorrect. In the case of a direct methods solution, an electron density map of the best solution will be automatically generated and the user must assess it for chemical sense. This is not always straightforward, particularly when dealing with low-resolution PXRD data sets that yield low-resolution density maps where individual atoms may not be clearly visible, though recent software developments have helped significantly in this regard (Altomare et al. 2012). If the solution has been obtained using global optimisation methods, then the best solution will be the one with the best agreement factor (e.g. R_{wp} , see Sect. 3.8.3) and connectivity will already be present as a consequence of using a 3D input model. Initial solution assessment then becomes a two-stage process: (a) for a solution that fits the diffraction data satisfactorily, the ratio $R_{wp}^{soln}/R_{wp}^{Pawley}$ will be small, with a value of ca. 2–3 normally indicative of a correct structure that can be refined in a straightforward manner; (b) the packing of the molecules in the crystal structure solution should be chemically sensible with no atypical features, such as very short intermolecular contacts, to suggest that the structure is incorrect. It is important to note that some packing features that one might expect to see, such as particular hydrogen bonding motifs, may not show up in the initial structure solution.¹² Close examination of the crystal packing usually reveals that a simple operation on a functional group, such as a 180° rotation, is all that is needed to introduce a likely motif into the crystal structure and provide an improved model for subsequent refinement.

Ultimately, the refined crystal structure must make chemical and crystallographic sense *and* explain the observed PXRD data. If it does both, one may be confident that the correct crystal structure has been determined.

3.8.5 Rietveld Refinement

A Rietveld refinement (Young 1995) of a crystal structure against observed PXRD data is one in which the coordinates of the atoms in the crystal structure solution are adjusted in a least-squares fashion in order to minimise the difference between the observed and calculated PXRD data. As such, it is similar to a Pawley refinement except that the intensity of each reflection in the fitted range is now a function of the atom types and their positions in the crystal structure rather than a freely refined variable. A scale factor that relates the calculated intensities to the observed ones is also refined as part of the process. Many Rietveld refinement programs are available, all providing broadly similar capabilities e.g. *TOPAS* (Coelho 2003), *GSAS*

¹²Hydrogen atoms are sometimes poorly positioned in initial structure solutions, as a consequence of their weak contribution to the observed diffraction.

(Larson and Von Dreele 2000), *Fullprof* (Rodriguez-Carvajal 1993) and *X'Pert HighScore Plus* (PANalytical 2014).

Molecular organic crystal structures present some specific challenges in Rietveld refinement. PXRD data rarely extend to sufficient resolution to permit free refinement¹³ of all non-H atomic positions and reflection overlap results in a low observation-to-parameter ratio in the least squares. As such, free refinement of a moderately complex molecular organic structure against typical PXRD data (e.g. $d_{\min} \approx 1.4 \text{ \AA}$) will result in a structure in which the values of bond lengths, angles and torsions are likely to deviate significantly from expectation values — in other words, the improved fit to the data obtained by the least-squares comes at the expense of chemical sense. This issue can be addressed in one of two ways which are discussed below.

Chemical Restraints

Expectation values for bond lengths, bond angles, bond torsions and ring planarity in the molecule can be maintained during the least-squares refinement by the use of restraints. Whilst implementation varies from program to program, such restraints take the general form

```
<atomlist>, <value>, <esd>
```

For example, an instruction “C1 C2, 1.54, 0.001” may tell the least-squares that in refining the *xyz* coordinates of atoms C1 and C2, the distance between them should not deviate significantly from a value of 1.54 Å. Similarly, the instruction “C1 C2 C3, 109.5, 0.001” could be used to maintain a tetrahedral bond angle. The user must decide the relative weighting to be applied to the PXRD data and the restraint values employed in the refinement. A low weighting for the restraints will effectively result in a free refinement, whilst a high weighting will favour maintenance of initial geometry over improving the fit to the PXRD data. Performed with care, restrained Rietveld refinement can be particularly useful in allowing specific elements of a structure (e.g. the conformation of a ring) to ‘flex’ during refinement, in order to improve the fit.

Rigid Bodies

In a rigid-body Rietveld refinement, the least-squares variables are initially the same degrees of freedom employed during a global optimisation structure solution

¹³ A free refinement is defined here as one in which the *xyz* coordinates of each non-H atom in the asymmetric unit of the crystal structure are free to refine as least-squares variables. Thus a 35 non-H atom structure would have 105 least-squares variables to describe the atomic positions alone.

(see Sect. 3.8.1). This approach to refinement has the significant advantage that it maintains the chemical sense inherent in the global optimisation starting model, whilst allowing the position, orientation and conformation of the molecule to refine against the full PXRD data range. Additional flexibility (e.g. bond angles) can be introduced into the rigid body if required.

3.8.6 Final Structure Checking

The final step in reporting a refined crystal structure is to generate a Crystallographic Information File (CIF) that includes all the necessary crystallographic details such as the refined unit cell dimensions and the atomic coordinates, plus relevant metadata about the sample, the diffraction experiment and the PXRD data. A final check on the refined crystal structure should be carried out using the official IUCr structure-validation suite, *checkCIF/PLATON* (Spek 2009), accessible at <http://journals.iucr.org/services/cif/checking/checkfull.html>. Other useful tools available to help with CIF preparation include *MOGUL* (Bruno et al. 2004) for checking the refined molecular geometry and *EnCIFer* (Allen et al. 2004) for checking CIF format compliance.

3.9 Phase Quantification Using Rietveld Refinement

Rietveld refinement also offers the opportunity for the accurate quantification of crystalline phases in a polycrystalline sample. In a sample containing only a single crystalline phase, one may assume that all the observed Bragg scattering in a PXRD pattern collected from the sample is attributable to this single phase. If the sample contains two crystalline phases, then provided the crystal structures of both phases are known, a multi-phase Rietveld refinement can be performed. The values of the refined scale factors for each phase allow the Rietveld refinement to output the relative weight-percent of each phase present in the sample. The approach is a general one and can cope with the presence of several phases in the sample. A representative example, that of analysis of a mixture of form I and III carbamazepine, has been recently published (Antonio et al. 2011).

3.10 Sample Environment and Phase Transitions

One advantage of using PXRD in the study of materials is that it is relatively easy to subject a polycrystalline sample to variable temperature, pressure and humidity and measure the resultant changes in the PXRD data. Phase transitions that might result in the shattering of a single crystal are easily studied using a powder. In the laboratory environment, sample stages such as the Anton Paar TTK450 allow

Table 8.2 Notable features of synchrotron-based instrumentation and the advantages they confer in PXRD experiments

Feature	Advantages
High incident flux	Permits extremely high level of monochromation
	Enables use of complex sample environment
	Enables detection of very weak diffraction features
	Enables rapid data collection
Excellent alignment	Accurate peak positions aids indexing process
Large, efficient detectors	Enables rapid data collection
Tuneable wavelength	Enables exploitation of resonant scattering
High instrumental resolution	Increased resolution of overlapping reflections
Low background	Improved signal to noise ratio, especially at high 2θ
Robotic sample changer	Ability to queue capillary samples

materials to be studied in reflection over the temperature range 80–723 K and under conditions of controlled relative humidity. Measurements are subject to the aforementioned limitations of this geometry and heating/cooling also affects the height of the powder sample, which in turn affects the resultant peak positions. In capillary transmission geometry, a liquid nitrogen open-flow cooling device can be used to control the temperature of the sample in the range 80–500 K whilst maintaining the benefits of the transmission setup. The temperature of the sample will not match exactly that recorded by the cooling device but the small temperature offset can be easily determined by running a sample that exhibits a phase change at a known, well-defined temperature.

3.11 Alternatives to Laboratory-Based PXRD

The X-ray photon flux available at third generation synchrotron sources (such as the ESRF in France, the APS in the U.S.A., SPring-8 in Japan, the SLSA in Australia and Diamond in the U.K.) is many orders of magnitude greater than that produced by a conventional 2 kW sealed X-ray tube. This flux, when coupled with the extremely high-precision PXRD instrumentation present at synchrotron beamlines, confers a great many advantages relative to laboratory-based X-ray instrumentation (Table 8.2). As such, if a crystal structure cannot be solved from laboratory PXRD data, synchrotron radiation PXRD beamlines offer a powerful alternative. Access to PXRD beamlines is available on a peer-reviewed basis for new science proposals, or on a paid basis for commercial experiments. Many synchrotron beamlines offer postal services, with ‘data collection only’ and full structure determination options.

Acknowledgements The author gratefully acknowledges the many long-standing collaborations that have contributed to his work in the area of PXRD, but in particular those with Bill David, Tony Csoka, Anders Markvardsen, Alastair Florence, Norman Shankland and the staff of the Cambridge Crystallographic Data Centre.

References

- Allen FH (2002) The Cambridge Structural Database: a quarter of a million crystal structures and rising. *Acta Crystallogr B* 58:380–388. doi:[10.1107/s0108768102003890](https://doi.org/10.1107/s0108768102003890)
- Allen FH, Johnson O, Shields GP, Smith BR, Towler M (2004) CIF applications. XV. enCIFer: a program for viewing, editing and visualizing CIFs. *J Appl Crystallogr* 37:335–338. doi:[10.1107/s0021889804003528](https://doi.org/10.1107/s0021889804003528)
- Altomare A, Camalli M, Cuocci C, Giacovazzo C, Moliterni A, Rizzi R (2009) EXPO2009: structure solution by powder data in direct and reciprocal space. *J Appl Crystallogr* 42(6):1197–1202. doi:[10.1107/S0021889809042915](https://doi.org/10.1107/S0021889809042915)
- Altomare A, Cuocci C, Giacovazzo C, Moliterni A, Rizzi R (2012) COVMAP: a new algorithm for structure model optimization in the EXPO package. *J Appl Crystallogr* 45(4):789–797. doi:[10.1107/S002188981201953X](https://doi.org/10.1107/S002188981201953X)
- Antonio SG, Benini FR, Ferreira FF, Pires Rosa PC, Paiva-Santos CDO (2011) Quantitative phase analyses through the Rietveld method with X-ray powder diffraction data of heat-treated carbamazepine form III. *J Pharm Sci* 100(7):2658–2664. doi:[10.1002/jps.22482](https://doi.org/10.1002/jps.22482)
- Barr G, Dong W, Gilmore CJ (2009) PolySNAP3: a computer program for analysing and visualizing high-throughput data from diffraction and spectroscopic sources. *J Appl Crystallogr* 42:965–974. doi:[10.1107/s0021889809025746](https://doi.org/10.1107/s0021889809025746)
- Brittain HG (2001) X-ray diffraction III: pharmaceutical applications of x-ray powder diffraction. *Spectroscopy* 16(7):14–18
- Bruno IJ, Cole JC, Kessler M, Luo J, Motherwell WDS, Purkis LH, Smith BR, Taylor R, Cooper RI, Harris SE, Orpen AG (2004) Retrieval of crystallographically-derived molecular geometry information. *J Chem Inf Comput Sci* 44(6):2133–2144. doi:[10.1021/ci049780b](https://doi.org/10.1021/ci049780b)
- ChemAxon (2013) Marvin, 5.4.1.1 edn. ChemAxon
- Clark SJ, Segall MD, Pickard CJ, Hasnip PJ, Probert MJ, Refson K, Payne MC (2005) First principles methods using CASTEP. *Z Kristallogr* 220(5–6):567–570. doi:[10.1524/zkri.220.5.567.65075](https://doi.org/10.1524/zkri.220.5.567.65075)
- Coelho A (2003) TOPAS user manual, v3.1 edn. Bruker AXS GmbH, Karlsruhe
- Davey RJ, Maginn SJ, Andrews SJ, Black SN, Buckley AM, Cottier D, Dempsey P, Plowman R, Rout JE, Stanley DR, Taylor A (1994) Morphology and polymorphism in molecular-crystals—terephthalic acid. *J Chem Soc-Faraday Trans* 90(7):1003–1009. doi:[10.1039/ft9949001003](https://doi.org/10.1039/ft9949001003)
- David WIF, Shankland K, van de Streek J, Pidcock E, Motherwell WDS, Cole JC (2006) DASH: a program for crystal structure determination from powder diffraction data. *J Appl Crystallogr* 39:910–915. doi:[10.1107/s0021889806042117](https://doi.org/10.1107/s0021889806042117)
- Dykhne T, Taylor R, Florence A, Billinge SJL (2011) Data requirements for the reliable use of atomic pair distribution functions in amorphous pharmaceutical fingerprinting. *Pharm Res* 28(5):1041–1048. doi:[10.1007/s11095-010-0350-0](https://doi.org/10.1007/s11095-010-0350-0)
- Engel GE, Wilke S, König O, Harris KDM, Leusen FJJ (1999) PowderSolve—a complete package for crystal structure solution from powder diffraction patterns. *J Appl Crystallogr* 32(6):1169–1179. doi:[10.1107/S0021889899009930](https://doi.org/10.1107/S0021889899009930)
- Favre-Nicolin V, Černý R (2004) A better FOX: using flexible modelling and maximum likelihood to improve direct-space ab initio structure determination from powder diffraction. *Z Kristallogr Cryst Mater* 219(12):847–856. doi:[10.1524/zkri.219.12.847.55869](https://doi.org/10.1524/zkri.219.12.847.55869)
- Florence AJ (2009) Approaches to high-throughput physical form screening and discovery. In: Brittain HG (ed) *Polymorphism in pharmaceutical solids*, 2nd edn. Informa Healthcare, New York
- Florence AJ, Shankland K, Gelbrich T, Hursthouse MB, Shankland N, Johnston A, Fernandes P, Leech CK (2008) A catemer-to-dimer structural transformation in cyheptamide. *CrystEngComm* 10(1):26–28. doi:[10.1039/b712547j](https://doi.org/10.1039/b712547j)
- Hofmann DWM (2002) Fast estimation of crystal densities. *Acta Crystallogr B* 58:489–493. doi:[10.1107/s0108768101021814](https://doi.org/10.1107/s0108768101021814)

- Ivanisevic I, McClurg RB, Schields PJ (2010) Uses of X-ray powder diffraction in the pharmaceutical industry. In: Gad SC (ed) *Pharmaceutical Sciences Encyclopedia*. Wiley, New York. doi:[10.1002/9780470571224.pse414](https://doi.org/10.1002/9780470571224.pse414)
- Larson AC, Von Dreele RB (2000) *General Structure Analysis System (GSAS)*. Los Alamos National Laboratory Report
- Lemmerer A, Bernstein J, Griesser UJ, Kahlenberg V, Toebbens DM, Lapidus SH, Stephens P, Esterhuysen C (2011) A tale of two polymorphic pharmaceuticals: pyriithyldione and propyphenazone and their 1937 co-crystal patent. *Chemistry* 17(48):13445–13460. doi:[10.1002/chem.201100667](https://doi.org/10.1002/chem.201100667)
- Looijenga-Vos A, Buerger MJ (2005) Determination of space groups. In: Hahn T (ed) *International tables for crystallography, volume A: space-group symmetry*, 5th edn. Springer, Dordrecht
- Louer D (2002) Laboratory X-ray powder diffraction. In: David WIF, Shankland K, McCusker LB, Baerlocher C (eds) *Structure determination from powder diffraction data*. Oxford University Press, Oxford
- Macrae CF, Bruno IJ, Chisholm JA, Edgington PR, McCabe P, Pidcock E, Rodriguez-Monge L, Taylor R, van de Streek J, Wood PA (2008) Mercury CSD 2.0—new features for the visualization and investigation of crystal structures. *J Appl Crystallogr* 41:466–470. doi:[10.1107/s0021889807067908](https://doi.org/10.1107/s0021889807067908)
- Markvardsen AJ, David WIF, Johnston JC, Shankland K (2012) A probabilistic approach to space-group determination from powder diffraction data (vol A57, pg 47, 2001). *Acta Crystallogr A* 68:780. doi:[10.1107/s0108767312038305](https://doi.org/10.1107/s0108767312038305)
- Morissette SL, Almarsson O, Peterson ML, Remenar JF, Read MJ, Lemmo AV, Ellis S, Cima MJ, Gardner CR (2004) High-throughput crystallization: polymorphs, salts, co-crystals and solvates of pharmaceutical solids. *Adv Drug Deliv Rev* 56(3):275–300. doi:[10.1016/j.addr.2003.10.020](https://doi.org/10.1016/j.addr.2003.10.020)
- Ooi L (2009) *Principles of X-ray crystallography*. Oxford University Press, Oxford
- Pagola S, Stephens PW (2010) PSSP, a computer program for the crystal structure solution of molecular materials from X-ray powder diffraction data. *J Appl Crystallogr* 43(2):370–376. doi:[10.1107/S0021889810005509](https://doi.org/10.1107/S0021889810005509)
- PANalytical (2014) X'Pert HighScore Plus PANalytical B.V.
- Pecharsky VK, Zavalij PY (2005) *Fundamentals of powder diffraction and structural characterization of materials*. Springer, New York
- Randall C, Rocco W, Ricou P (2010) XRD in pharmaceutical analysis: a versatile tool for problem-solving. *Am Pharm Rev* 13:52–59
- Rodriguez-Carvajal J (1993) Recent advances in magnetic-structure determination by neutron powder diffraction. *Physica B* 192(1–2):55–69. doi:[10.1016/0921-4526\(93\)90108-i](https://doi.org/10.1016/0921-4526(93)90108-i)
- Shankland K, David WIF, Sivia DS (1997) Routine ab initio structure determination of chlorothiazide by X-ray powder diffraction using optimised data collection and analysis strategies. *J Mater Chem* 7(3):569–572. doi:[10.1039/a606998c](https://doi.org/10.1039/a606998c)
- Shankland K, Spillman MJ, Kabova EA, Edgeley DS, Shankland N (2013) The principles underlying the use of powder diffraction data in solving pharmaceutical crystal structures. *Acta Crystallogr C* 69:1251–1259. doi:[10.1107/s0108270113028643](https://doi.org/10.1107/s0108270113028643)
- Spek AL (2009) Structure validation in chemical crystallography. *Acta Crystallogr D* 65:148–155. doi:[10.1107/s090744490804362x](https://doi.org/10.1107/s090744490804362x)
- Werner P-E (2002) Autoindexing. In: David WIF, Shankland K, McCusker LB, Baerlocher C (eds) *Structure determination from powder diffraction data*. Oxford University Press, Oxford
- Young RA (ed) (1995) *The Rietveld method*. Oxford University Press, Oxford

Chapter 9

Single-Crystal X-ray Diffraction

Andrew D. Bond

Abstract Single-crystal X-ray diffraction is an extremely powerful technique to characterize small drug molecules in solid form. It is a mature technique that is becoming ever more automated, and it is increasingly viewed as “routine” in both industry and academia. On this basis, it is arguable how much the average formulation scientist needs to know about the technique: is it necessary to understand the inner workings of the “black box”, or is it sufficient just to trust the results produced by an automated analysis system? This chapter provides a brief outline of the principles, then considers some aspects that, in the author’s opinion, should still be understood to measure crystallographic data effectively and to interpret crystallographic results. The focus is on selected topics that are likely to be most relevant to pharmaceutical solid-form characterization.

Keywords Diffraction • X-ray • Single-crystal • SXRD • Absolute structure

1 Introduction

Single-crystal X-ray diffraction remains the “gold standard” technique to characterize small drug molecules in solid form. For a suitable crystalline sample, the analysis provides a complete three-dimensional picture of a molecule and the geometrical features of its interactions with other molecules in the solid state. In many cases, it can distinguish pharmaceutical salts from co-crystals by localising the positions of H atoms or provide an *ab initio* assessment of absolute configuration for chiral compounds. The technique is mature, and is viewed increasingly as “routine” in both industry and academia. This is largely due to some spectacular progress in laboratory instrumentation and associated software. Modern desktop single-crystal X-ray diffraction instruments can accept a mounted single crystal through an innocuous entry port, then within an hour or two return a fully refined crystal structure without requiring even the proverbial

A.D. Bond (✉)

Department of Chemistry, University of Cambridge, Lensfield Road, Cambridge CB2 1EW, UK

e-mail: adb29@cam.ac.uk

touch of a button. Quite often, the structures produced in this way are flawless. Furthermore, it is easy to check that they are flawless because the results can be submitted to sophisticated on-line validation systems that provide detailed reports within seconds. On this basis, it is arguable how much the average formulation scientist needs to know about the technique: is it necessary to understand the inner workings of the “black box”, or is it sufficient just to trust the results produced by an automated analysis system?

Certainly, the level of theoretical knowledge required to operate a modern single-crystal X-ray diffractometer is lower than it used to be. This chapter therefore provides only a brief outline of the principles, then goes on to consider some aspects that, in the author’s opinion, should still be understood to measure crystallographic data effectively and to interpret crystallographic results. The focus is on selected topics that are likely to be relevant to scientists involved with pharmaceutical solid-form characterization.

2 Theoretical Background of the Technique

X-ray diffraction can be viewed to encompass two physical processes: (i) scattering of X-rays by matter; (ii) interference of the scattered X-rays to produce a diffraction pattern. X-rays are scattered by any chemical sample (solid, liquid or gas), and therefore any chemical sample will produce a diffraction pattern. A simple maxim applies: *ordered objects yield ordered diffraction patterns*, or conversely *disordered objects yield disordered diffraction patterns*. The value of single-crystal X-ray diffraction comes from the fact that a crystal is highly ordered in three dimensions, and therefore it produces a diffraction pattern that is highly ordered in three dimensions. This makes it possible to interpret the diffraction pattern in a meaningful and robust way.

2.1 Anatomy of a Single-Crystal X-ray Diffraction Pattern

An X-ray diffraction pattern from a single crystal can be conceptually partitioned into the geometry of the pattern and the intensities of the diffracted beams (Fig. 9.1). Although the two aspects are obviously related by the crystal that produces them, they can usefully be viewed as distinct. The geometry of the pattern reflects the translational periodicity of the crystal lattice. The relationship between the lattice and the diffraction pattern is a reciprocal one: crystals with more compact lattices give diffraction patterns that are more spread out, while larger lattice parameters give diffraction patterns that are more compact. This also depends on the X-ray wavelength, with shorter wavelengths giving more compact diffraction patterns. The conceptual link between the crystal lattice and the geometry of diffraction is provided by Bragg’s law:

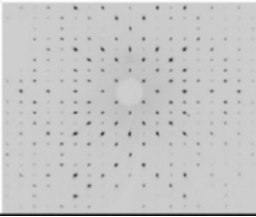
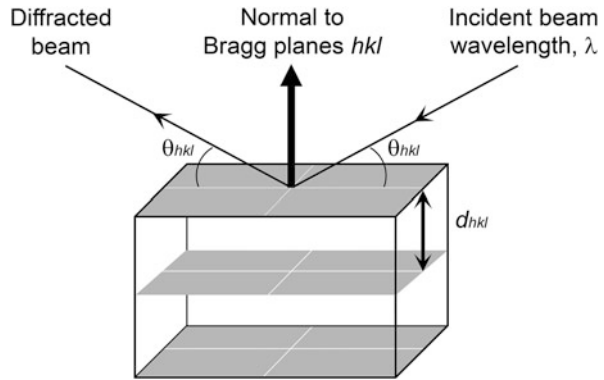
Geometry	Symmetry	Intensities
Lattice parameters Crystal orientation		Atom types and positions Displacement parameters Site occupancy factors

Fig. 9.1 Conceptual partitioning of the geometry and intensities in a single-crystal X-ray diffraction pattern. Symmetry impinges on both aspects

Fig. 9.2 Representation of the geometry of diffraction according to Bragg’s law. The incident beam, diffracted beam and normal to the Bragg planes are in a common plane



$$\lambda = 2d_{hkl} \sin \theta_{hkl} \tag{9.1}$$

where λ is the X-ray wavelength, θ_{hkl} is half the angle formed between the incident and diffracted beams, and d_{hkl} is the perpendicular distance between neighbouring lattice planes with Miller indices hkl . For single-crystal X-ray diffraction, a necessary condition is that the incident beam, diffracted beam and normal vector to the lattice planes are co-planar (Fig. 9.2). The hkl values assigned to each diffracted beam depend specifically on the unit cell that is chosen to describe the crystal lattice. A given crystal in a given orientation will always produce the same diffraction pattern, but the hkl values could be assigned in numerous ways depending on the unit cell that is used.

The intensities of the diffracted beams are determined by the distribution of atoms within the crystal. The relationship is defined by the structure factor equation, which is a mathematical description of the interference phenomenon:

$$F_{hkl} = \sum_{n=1}^N f_n \exp 2\pi i(hx_n + ky_n + lz_n) \tag{9.2}$$

The summation is taken over all N atoms in the unit cell and f_n is the atomic scattering factor of the n th atom, which has fractional coordinates x_n, y_n, z_n in the specified unit cell. The equation produces a value for one specific reflection with indices hkl , and a whole set of structure factor equations is required to describe the entire diffraction pattern. The diffracted intensity, I_{hkl} , is given by the structure factor multiplied by its complex conjugate, F_{hkl}^* , which is identical to the square of the structure factor modulus:

$$I_{hkl} = F_{hkl} \cdot F_{hkl}^* = |F_{hkl}|^2 \quad (9.3)$$

The summation in Eq. (9.2) shows that every atom in the unit cell makes a contribution to every diffracted beam, and therefore a complete set of diffracted intensities must be measured in order to determine a crystal structure from a diffraction pattern. It does not make any sense to measure some specific region of a diffraction pattern in the same way that a specific wavenumber region might be measured in an IR or Raman spectrum. The atomic scattering factors, f , depend on the number of electrons in the atom, and on the diffraction angle (Fig. 9.3). For real structures, Eq. (9.2) is extended to account for thermal or static displacement of the atoms, by introducing *displacement parameters*, which might be treated as isotropic (spherical) or anisotropic (ellipsoidal). In some cases, site occupancy factors might also be defined, which account for possible variation at the atomic site in different unit cells (see Sect. 4.2). The mathematical details are not mentioned here; it is sufficient to appreciate that displacement parameters and site occupancy factors serve to modulate the effective scattering from each atomic site. An example is shown in Fig. 9.3.

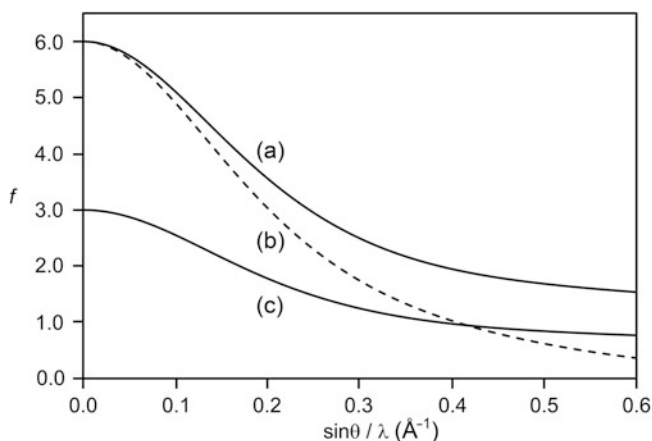


Fig. 9.3 Variation of the atomic scattering factor (f) for a C atom as a function of scattering angle (expressed as $\sin\theta/\lambda$). Line (a) shows a stationary spherical atom. Line (b) (dashed) shows the modulating effect of a typical isotropic displacement parameter. Line (c) shows the effect of a site occupancy factor equal to 0.5

Symmetry impinges on both the geometry and intensities of diffraction (Fig. 9.1). The geometrical features of the crystal lattice, and the resulting geometrical features of the diffraction pattern, are referred to as the *metric symmetry*. For the diffracted intensities, symmetry refers to equivalence of the intensity values. For example, reflections hkl and $-h-k-l$ are said to be symmetrically equivalent if $I_{hkl} = I_{-h-k-l}$. Since the diffracted intensities reflect the types and positions of the atoms within the unit cell, symmetry in the diffracted intensities must result from symmetry in the arrangement of the atoms. The symmetry of the atoms within the crystal is described by the crystal's *space group*, which refers to the collection of symmetry operators distributed through space. Therefore, symmetry in the diffracted intensities provides the information to determine the space group.

The geometry and intensity aspects of symmetry can sometimes be confused by the fact that the space group of a crystal can impose constraints on the geometry of the crystal lattice. For example, if there is a fourfold rotation axis relating the atomic positions within the crystal, the unit cell must have all of its angles equal to 90° and it must have identical axis lengths in the plane perpendicular to the fourfold axis if that symmetry is to be consistently repeated through the crystal structure. Thus, the space group symmetry (revealed by the diffracted intensities) can impose constraints on the metric symmetry (revealed by the geometry of the diffraction pattern). The converse is not true: symmetry in the diffraction geometry does not necessarily imply symmetry in the diffracted intensities.¹

2.2 Obtaining a Crystal Structure from a Diffraction Pattern

An overview of the process for obtaining an X-ray crystal structure is illustrated in Fig. 9.4. The translational periodicity of the crystal is obtained solely by measuring the geometry of the pattern. The angles observed for the diffracted beams are back-converted to yield dimensions (and orientation) of a periodic lattice that can produce that pattern. In the process, a unit cell is chosen to describe the lattice² and the pattern is indexed so that each diffracted beam is assigned hkl indices referring to the specified unit cell. The intensities of all diffracted beams are then established and used to deduce the types and positions of the atoms within the unit

¹“Negative correlations” can be specified. For example, the space group cannot be cubic if the metric symmetry is not cubic. But observing that the metric symmetry is cubic does not prove that the space group is cubic.

²Numerous unit cells could be chosen to describe a particular lattice. In practice, rules are defined to enable standard choices. The “reduced cell” is based on the three shortest independent distances between lattice points, with all angles either $<90^\circ$ or $\geq 90^\circ$. This defines a *primitive* cell, which contains only one independent lattice point. Non-primitive cells (containing more than one independent lattice point) might be defined if they better describe the symmetry of the structure. In that case, translational symmetry *within the unit cell* is defined in the list of space group operators.

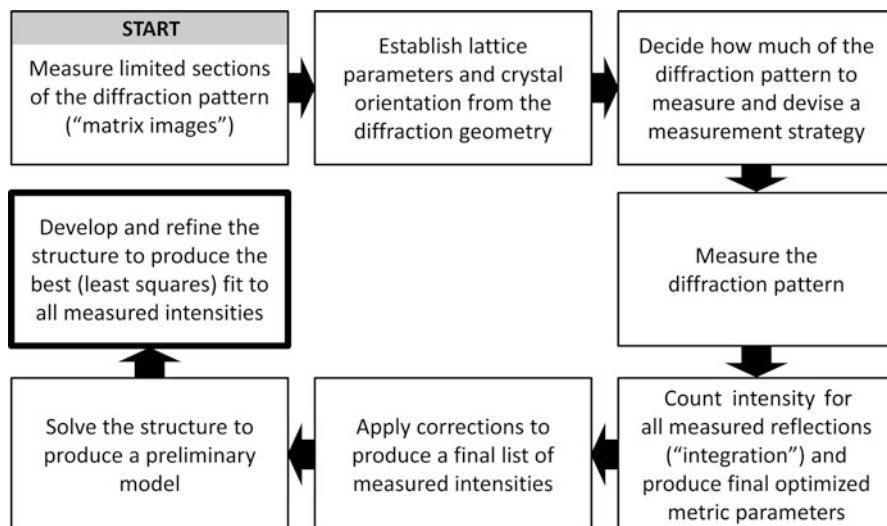


Fig. 9.4 Overview of the process for obtaining an X-ray crystal structure

cell by means of an inverse Fourier transform—essentially applying the structure factor equation, Eq. (9.2), in reverse. There is a problem at this stage, in that the structure factors F_{hkl} are complex numbers having modulus and phase, but the measured values of I_{hkl} reveal only the modulus $|F_{hkl}|$. This *phase problem* is generally overcome for small-molecule crystals by applying *direct methods*, or some variant thereof. This step is robustly automated, and the average user can safely view it as a “black box” (however, being aware of the implications of data quality for success—see Sect. 5.3.1). This step usually produces a first image of the structure that is more or less complete, and which can be developed (by Fourier syntheses) and refined (by least-squares methods) to produce the best fit to the diffraction pattern. This chapter does not consider methods for structure solution or describe structure refinement in any great detail—the interested reader is referred to more complete descriptions of these stages (Blake et al. 2009; Clegg 1998; Müller et al. 2006).

The metric features of the crystal lattice are optimized and finalized during the “data integration” stage, where the raw diffraction images are processed to establish the diffracted intensities. The fact that the metric features cannot subsequently be optimized any further is another manifestation of the practical independence of the geometry and intensities. The parameters that can be optimized during the structure refinement stage are those in Eq. (9.2), namely the atom types (expressed by the atomic scattering factors, f), atom coordinates (x, y, z) and displacement parameters (implemented as an extension to Eq. (9.2)), and perhaps site occupancy factors, with the aim to obtain the best fit to the complete set of diffracted intensities. It is necessary to make a choice for the crystal’s space group by examining systematic patterns in the intensity data and sometimes by considering the relationships

between the coordinates in the structure after it has been solved.³ The most probable group can usually be identified by the data processing and/or structure solution software, but it can be necessary to attempt structure refinement with several possible groups to establish which provides the best result. The choice of the space group decides which atoms in the unit cell are described by independent parameters and which are linked by a single set of parameters with a defined relationship between them. The consequence of choosing a space group with too much symmetry is therefore that the structure model is incorrectly constrained—*i.e.* it does not have enough free parameters to describe the data properly. Choosing a space group with too little symmetry (so-called “missed symmetry”) defines too many independent parameters that should actually be tied together, which leads to “over-description” of the data. It is also necessary to make a choice for the structure’s origin, *i.e.* the point considered to have coordinates 0,0,0. This is handled by the structure solution/refinement programs, but the user should be aware that different choices can be made, and that the same structure might be presented with different (but ultimately equivalent) sets of fractional coordinates.

3 Instrumentation and Software

Equipment for single-crystal X-ray diffraction (Fig. 9.5) has four basic components:

1. **A source, with associated optics, to provide the incident X-ray beam.** The conventional laboratory source has for many years been the “sealed tube”, in which a stream of electrons emitted from a tungsten filament is accelerated towards a metal target (anode) to generate X-rays. The most common anode materials are Cu and Mo, which emit characteristic X-rays with wavelengths close to 1.54 and 0.71 Å, respectively. The practical merits of these radiation types are discussed in Sect. 5.1. The sealed tube arrangement has a few practical disadvantages: (1) the power requirements are substantial, typically 1.5–2.0 kW; (2) the anode must be continuously cooled with a flowing water supply; (3) the X-ray intensity decreases quite rapidly, and the tubes must be replaced typically within a 1–2 year period. Many of these difficulties are overcome by newer *microfocus* sources, which produce greater X-ray flux over a smaller area, while operating at only 50 W. This is possible because the electrons accelerated towards the anode are focussed onto a very small area (diameter $\leq 100 \mu\text{m}$), which allows for more efficient design and cooling of the anode, and generation of a higher power density. Since the generator operates at a much lower power,

³ For example, a structure might be solved and initially refined in a non-centrosymmetric space group, but then it becomes clear from the atomic positions that a centre of inversion is actually present. Software for structure solution might also solve the structure in a lower symmetry space group, then provide a set of possible structures in various space groups for further examination.

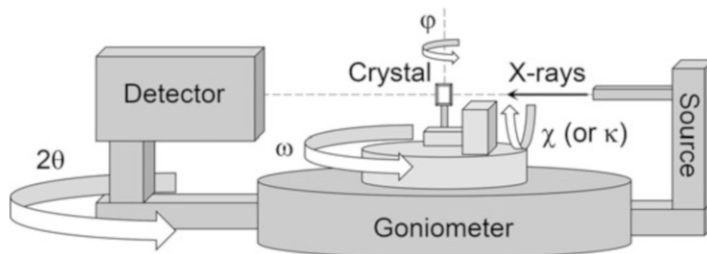


Fig. 9.5 Schematic illustration of a typical single-crystal X-ray diffractometer

the whole system can be cooled with air rather than flowing water. A microfocus source, combined with “multilayer optics” that can partially focus the X-ray beam produces a more intense beam for small-area measurements, while also being practically more convenient.

- 2. A motorized goniometer to orient and move the crystal.** The goniometer orients the crystal and detector with respect to the incident X-ray beam (Fig. 9.5). The detector moves around the 2θ axis, within the instrument’s horizontal plane. The goniometer typically has three further axes of movement to orient the crystal. Movement around the ω axis takes place in the horizontal plane of the instrument, the χ axis refers to elevation in the vertical plane, and movement around ϕ rotates the crystal around its local mount axis. Many instruments adopt “kappa geometry”, where a formal χ axis is replaced by a κ -axis, which swings the crystal within an inclined plane that moves with the ω circle. The formal details of the goniometer angles are of lesser importance here; the bottom line is that the goniometer must orient the crystal with respect to the incident beam to enable a suitable orientation for diffraction in such a way that the diffracted beam will fall onto the detector face. Recalling that the incident beam, diffracted beam and normal vector to the relevant Bragg planes lie in a common plane (Fig. 9.2), the crystal must be oriented so that the relevant normal vector (the “scattering vector”) lies close to the horizontal plane of the instrument if the diffracted beam is to be measured on the detector face.
- 3. A detector to measure the diffraction pattern.** Detectors for single-crystal X-ray diffraction are now almost exclusively 2D area detectors. Numerous technologies exist, but the dominant one in laboratory instruments over the past 25 or so years has been the charge-coupled device (CCD). CCD chips in X-ray detectors are identical to those in digital cameras, which means that they respond to visible light. A CCD X-ray detector comprises a 2D window with some material that converts X-rays to light, coupled to the CCD chip in a spatially-mapped manner. In some detectors, glass fibres are constructed as a taper to de-magnify a larger external active area onto a smaller CCD chip. Other detectors have 1:1 spatial correspondence between the active area and the chip, which can provide advantages in spatial resolution and sensitivity. At the time of writing, other technologies becoming prominent use active pixel sensors (“CMOS chips”) or hybrid pixel detectors that detect X-rays directly. Whatever

the technical nature of the detector, it can be viewed conceptually as a 2D array of pixels that map and count incoming X-rays.

4. **Control and data processing software.** The control software coordinates all aspects of data collection, including movement of the crystal and detector, synchronised opening and closing of the X-ray shutter and read-out of the diffraction images.⁴ Modern software systems are generally highly automated and can proceed through the entire measurement process with minimal user intervention. Some of the aspects that warrant caution in this respect are discussed in Sect. 5.

4 Applications of the Technique on Drug Compounds

For small-molecule drug compounds, single-crystal X-ray diffraction might be applied for many reasons, *e.g.* to establish chemical composition, polymorphic form or absolute structure. This section briefly considers a limited set of topics likely to be relevant for formulation scientists.

4.1 Dealing with H Atoms

According to Eq. (9.2), each atom in the unit cell contributes to the intensity of each diffracted beam to an extent that depends on the atomic scattering factor, f , which is related to the number of electrons in the atom. H atoms contain only one electron, so their individual contribution to the diffracted intensity is small. At room temperature, significant thermal motion will also serve to diminish their scattering contribution (Fig. 9.3). Nothing can be done about the number of electrons, but the thermal motion can be minimised by collecting data at low temperature. Since H atoms form the shortest covalent bonds (*ca* 1 Å), there is a requirement for high-resolution data (Sect. 5.3.1) if the positions of H atoms are to be resolved.⁵

For multi-component molecular crystals, where the distinction between a salt (containing ionized molecular species) or a co-crystal (containing neutral species) might depend on the location of one H atom within a hydrogen bond, room-temperature X-ray diffraction data may or may not deliver conclusive evidence. With a good crystal that produces significant diffracted intensity to high resolution (at least 0.85 Å), H atoms that are ostensibly static and ordered *should* be

⁴Newer instruments dispense with opening and closing of the X-ray shutter during data collection, and instead control the measurement and read-out time *via* electronics on the detector. This gives more precise time-keeping and the cumulative time saving over a long sequence of images can be significant.

⁵This section does not refer to the fundamental distinction between nuclear positions and the positions determined for H atoms by X-ray diffraction. See: Allen (1986).

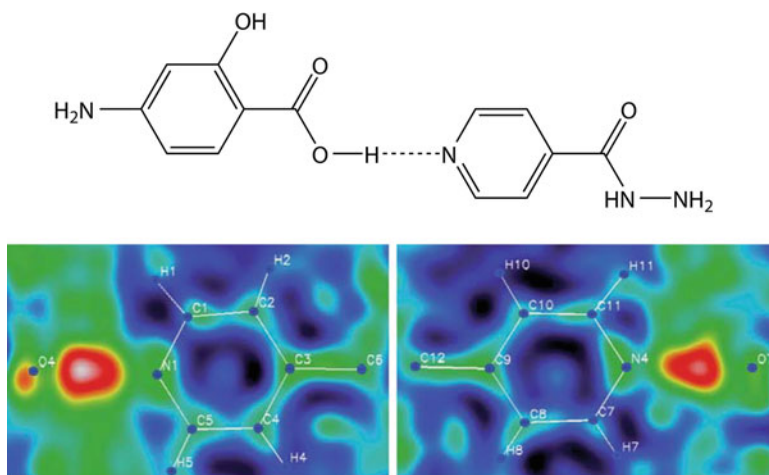


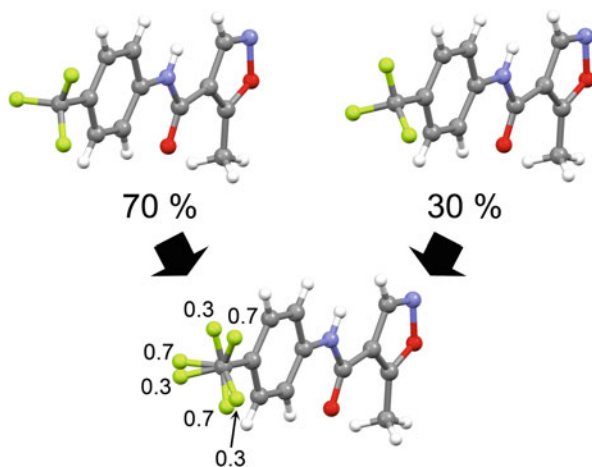
Fig. 9.6 Images of the electron density for two hydrogen bonds within an isoniazid/4-aminosalicylic acid co-crystal. On the *right*, the H atom lies close to the midpoint between the N and O atoms, while on the *left*, the H atom is displaced towards the O atom. The peaks are low in height and spread over a relatively large area, which means that positions established for the H atoms are relatively uncertain. Reproduced from (Grobelyny et al. 2011) with permission of The Royal Society of Chemistry.

distinguishable. Low-temperature data collection improves matters, but there is a risk that the H atom location or dynamics could change as a function of temperature. For example, Fig. 9.6 shows images of the electron density (from X-ray diffraction data at 220 K) for two distinct hydrogen bonds within an isoniazid/4-aminosalicylic acid crystal (Grobelyny et al. 2011). The electron density shows clear peaks corresponding to the H atoms, and the positions indicate that one hydrogen bond appears to be more symmetrical than the other. Variable-temperature measurements suggest that the symmetrical hydrogen bond becomes less symmetrical at room temperature (becoming more “co-crystal like” than “salt like”), but uncertainties associated with the H atom positions make it difficult to draw confident conclusions. In general, it is probably advisable to maintain a degree of scepticism concerning H atom positions determined from X-ray diffraction data, or at least to take careful note of the experimental conditions and data quality. Supplementary information from other techniques such as spectroscopy or computational methods is always valuable.

4.2 Dealing with Non-stoichiometry and Disorder

A fundamental assumption of single-crystal X-ray diffraction is that a crystal structure can be averaged into a single unit cell that is faithfully replicated through the entire crystal. If there should be some variability through the crystal, this will lead to a superposition of structures within the unit cell, so there will appear to be

Fig. 9.7 Example of a disordered CF_3 group in the crystal structure of leflunomide (Vega et al. 2006). The alternative molecular conformations are superimposed in the final set of atomic positions, requiring that the F atoms are assigned site occupancy factors less than 1.0



some atoms that are in mutually exclusive positions and only “partially present”. A typical example is a $\text{C}-\text{CF}_3$ group, which might display a variety of rotational orientations around the $\text{C}-\text{C}$ bond, which become averaged in the unit cell into several F atom positions distributed around a ring. If there are two distinct orientations of the CF_3 group, there will be six apparent F atom positions in the unit cell (Fig. 9.7). In a given molecule, all six of these atoms cannot actually be present, so each F atom must be represented with a *site occupancy factor* less than 1.0 (as mentioned in Sect. 2.1). In this case, there must be two distinct sets of three F atoms, each of which must describe a chemically acceptable CF_3 group, and the site occupancy factors for the two groups must sum to 1.0 (Fig. 9.7).

Since disorder generally results in a superposition of structures, it can be difficult to unravel the atomic sites in any rational way. One thing to bear in mind is the physical situation that is being modelled: disordered regions represent a superposition of structures, only one of which is present at any given location in the crystal, and each of which must be physically and chemically reasonable. In a good disorder model, it should be possible to identify sets of atoms in such a way as to say “either this set is present or this set is present”. Within each set, the chemical structure should be reasonable, and the sets should collectively describe the whole crystal. In many situations, disordered regions can become sufficiently complex to require *restraints*, which control interatomic distances or angles during refinement to ensure that the chemical structure remains reasonable.

In some situations, especially where a crystal might contain volatile solvents, there can be atoms or molecules that appear to be genuinely partially occupied, *i.e.* if an atom/molecule is not present at a particular site, nothing is present. For example, non-coordinated water molecules are often described with fractional site

occupancy in order to yield atoms with sensible displacement parameters.⁶ This might reflect a genuine physical situation, or it might just reflect the fact that a highly disordered region of electron density cannot adequately be described with individual atomic sites. In particularly severe cases, the electron density distribution in some region of the structure might be essentially uniform, so that it requires a great many closely-spaced partially occupied atomic sites in an effort to describe it. Caution should obviously be applied before assigning physical significance to the resulting atomic model. An alternative approach in such cases is to abandon any attempt to define atomic sites, and to treat highly disordered regions using a “continuous solvent area model” (the so-called *SQUEEZE* procedure; Van der Sluis and Spek 1990). Such methods are implemented by *modifying the intensity data*, so that the structure refinement can proceed in the usual manner, but with the disordered region left empty. Obviously, it is crucial in such cases to document that the data have been manipulated, and to understand that the empty regions in the final structure model are not really empty.⁷

Finally, it should be noted that disorder in crystals can be static (as has principally been described here), or dynamic. For example, a given CF_3 group might actually be rotating within the crystal, and the diffraction pattern, measured usually over a period of hours, provides a temporally-averaged picture. Dynamic disorder can sometimes be distinguished from static disorder by analysis of the structure as a function of temperature, but the two phenomena cannot be directly distinguished in a solitary crystal structure.

4.3 Dealing with Absolute Structure

Absolute structure applies to non-centrosymmetric crystal structures, which cannot be superimposed on their inversion-related counterpart. Non-centrosymmetric structures include chiral structures (non-superimposable on their mirror image), and also polar structures, which have a distinguishable orientation and which may or may not be chiral (Fig. 9.8). Frequently, chirality of a crystal's constituent molecules is of interest, and so it is important to appreciate the link between non-centrosymmetric crystal structures and chiral molecules. *Any* type of crystal structure can be non-centrosymmetric, regardless of whether the constituent molecules are chiral. However, an enantiomerically pure sample of a chiral molecule *must* crystallise in a non-centrosymmetric space group, and the absolute

⁶ The scattering contribution from a particular atom site is reduced either by defining a smaller site occupancy or a larger displacement parameter. Thus, occupancies and displacement parameters are correlated, and it can be necessary to fix one in order to refine the other. The two effects are not entirely indistinguishable, however, since they differ as a function of diffraction angle (Fig. 9.3).

⁷ This is particularly important when it comes to simulating powder X-ray diffraction patterns. The peak intensities in a pattern simulated from the model with empty regions will be different from the real situation where there is electron density in those regions.



Fig. 9.8 Schematic illustration of centrosymmetric, polar and chiral crystal structures

configuration of the molecules can be established by determining the crystal's absolute structure. In this way, single-crystal X-ray diffraction can provide an *ab initio* assessment of chirality for an enantiopure compound (Thompson and Watkin 2009).

4.3.1 Theoretical Background

The information to determine absolute structure lies in differences between the intensities of *Friedel pairs*, which are diffracted beams with indices hkl and $-h-k-l$. For a centrosymmetric crystal, Friedel pairs have equal intensity, but they become non-equivalent for non-centrosymmetric structures because of the “anomalous contribution” to the X-ray scattering. Anomalous scattering refers to X-rays scattered by a different physical mechanism (essentially absorption then re-emission), which imparts an additional phase change of 90° to the scattered X-rays. Mathematically, an extra component is added to the structure factor, which changes the resulting amplitude and phase according to Fig. 9.9. The result is that inversion-related models of a non-centrosymmetric structure give different sets of diffracted intensities, which allows them to be distinguished. Unfortunately, the magnitude of anomalous scattering is small. Cu radiation produces a more substantial effect than Mo, but the intensity difference between Friedel pairs remains minimal, especially for structures containing only light atoms (C, H, N, O). This means that great care must be taken when interpreting the results of an absolute-structure determination.

4.3.2 The Flack Parameter

The physical scenario of inversion-related non-centrosymmetric crystal structures is linked to a measured set of X-ray intensities by the Flack parameter, x :

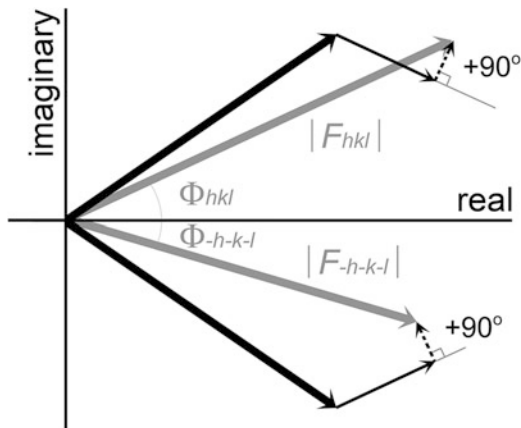


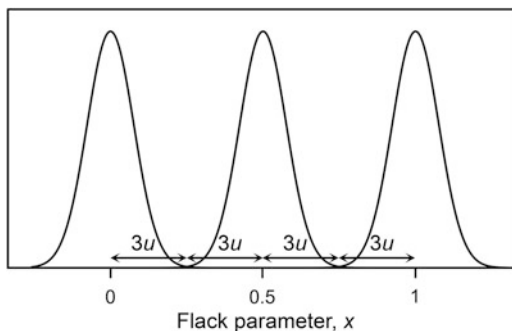
Fig. 9.9 Argand diagram showing differences between structure factors of Friedel pairs in a non-centrosymmetric crystal due to anomalous scattering. The *thick black vectors* represent the total contribution from atoms with no significant anomalous scattering: these have equal modulus and opposite phase (being the angle formed to the real axis). The *thin black vectors* show the effect of one atom with significant anomalous scattering: the atom has a regular scattering contribution (*solid line*) that has equal modulus and opposite phase, plus an anomalous scattering contribution (*dashed line*), which is turned by $+90^\circ$ with respect to the regular scattering. The resultant structure factors F_{hkl} and F_{-h-k-l} (*thick grey lines*) have different modulus and different phase. Since the diffracted intensity is $|F|^2$, a significant anomalous contribution means that $I_{hkl} \neq I_{-h-k-l}$

$$I_{hkl}(\text{obs}) = (1-x)I_{hkl}(\text{calc}) + xI_{-h-k-l}(\text{calc}) \tag{9.4}$$

Equation (9.4) states that the observed intensity of a diffracted beam, $I_{hkl}(\text{obs})$, comprises a linear combination of the intensities calculated from the structure model for the reflection hkl and its Friedel pair $h-k-l$. If the structure is non-centrosymmetric, $I_{hkl}(\text{calc}) \neq I_{-h-k-l}(\text{calc})$ (Fig. 9.9). In the ideal case (*i.e.* a perfect crystal, having either one handedness or the other), $I_{hkl}(\text{obs})$ must equal either $I_{hkl}(\text{calc})$ or $I_{-h-k-l}(\text{calc})$. If the model is correct, $I_{hkl}(\text{obs}) = I_{hkl}(\text{calc})$, which means that $x = 0$. If the model is inverted, $I_{hkl}(\text{obs}) = I_{-h-k-l}(\text{calc})$, which means that $x = 1$. Determining the absolute structure of a non-centrosymmetric crystal is therefore achieved by determining the value of x . If x should take a value between 0 and 1, this suggests that the crystal must be “part-way” between the inversion-related alternatives. This possibility is referred to as *inversion twinning*, which means physically that the crystal contains domains having one handedness and domains with the inverted structure. For a centrosymmetric crystal, $I_{hkl}(\text{calc}) = I_{-h-k-l}(\text{calc})$, so x is undefined.

When x is determined from experimental data, there are errors associated with the intensity measurements, which propagate through to an uncertainty on the value determined for x . A crucial question is how precisely must x be determined to make a valid conclusion about the absolute structure? If the value determined for x conforms to the expectations of a normal distribution, the width of the distribution will be $\pm 3u$, where u is the standard uncertainty. For the values $x = 0$ and 1 to be

Fig. 9.10 Non-overlapping normal distributions centred on $x = 0, 0.5$ and 1 . The physically meaningful range $0-1$ spans $12u$, which shows that $u \leq 1/12$ (≈ 0.08) if the values are to be statistically distinguished



clearly distinguishable from $x = 0.5$, normal distributions centred on $x = 0$ and 1 must not overlap with a distribution centred on $x = 0.5$ (Fig. 9.10). This defines a region of $12u$ over the range $x = 0 - 1$, which means that the largest permitted value of u is $1/12 \approx 0.08$. Thus, a general guideline for satisfactory determination of the absolute structure is that the refined value of x should be 0 (within $\pm 3u$) and have a standard uncertainty less than *ca* 0.1 . If the refined value of x is 1 with a standard uncertainty less than 0.1 , the handedness of the structure should definitely be inverted. If the refined value of x is somewhere between 0 and 1 , but with an acceptably low standard uncertainty, inversion twinning is confidently indicated. A standard uncertainty greater than 0.1 indicates that confident conclusions cannot be made (Flack and Bernardinelli 2000).

4.3.3 Improvements Using Differences and Quotients

In the last few years, methods have been developed (Parsons et al. 2013) that provide more precise indications of the Flack parameter, based on combinations of Friedel pairs, specifically differences (D) or quotients (Q):

$$D_{hkl} = I_{hkl} - I_{-h-k-l}$$

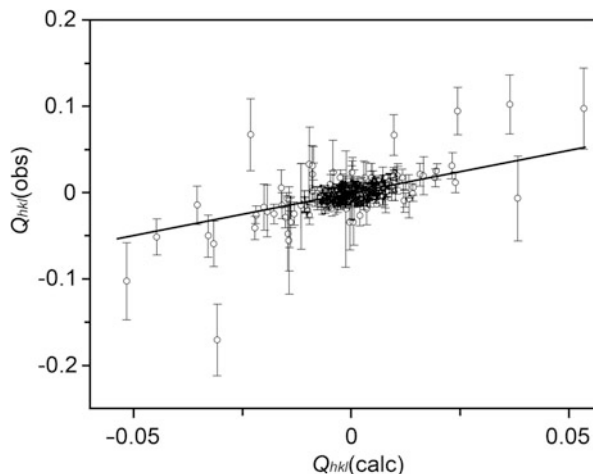
$$Q_{hkl} = [I_{hkl} - I_{-h-k-l}] / [I_{hkl} + I_{-h-k-l}]$$

Using the definition for the Flack parameter in Eq. (9.4), the following relationship is obtained:

$$\begin{aligned}
 D_{hkl}(\text{obs}) &= I_{hkl}(\text{model}) - I_{-h-k-l}(\text{model}) \\
 &= [(1-x)I_{hkl}(\text{calc}) + xI_{-h-k-l}(\text{calc})] - [(1-x)I_{-h-k-l}(\text{calc}) + xI_{hkl}(\text{calc})] \\
 &= (1-2x)[I_{hkl}(\text{calc}) - I_{-h-k-l}(\text{calc})] \\
 &= (1-2x)D_{hkl}(\text{calc})
 \end{aligned}
 \tag{9.5}$$

Here, “calc” refers to the refined crystal structure with its specific absolute structure, while “model” refers to the intensities calculated using the Flack parameter,

Fig. 9.11 $Q_{hkl}(\text{obs})$ vs. $Q_{hkl}(\text{calc})$ for a typical non-centrosymmetric crystal structure. The plot has a gradient of $1 + 2x$, and a least-squares fit provides a precise indication of the Flack parameter, x . Reproduced from (Parsons et al. 2013).



according to Eq. (9.4). Equation (9.5) shows that a plot of $D_{hkl}(\text{obs})$ vs. $D_{hkl}(\text{calc})$ should be linear with a slope of $(1-2x)$. An identical equation can be formulated for quotients (exchange D for Q), and the method is usually implemented by plotting $Q_{hkl}(\text{obs})$ vs. $Q_{hkl}(\text{calc})$. The quotients serve to “up-weight” the Friedel pairs with lower intensity. The value of x obtained by a least-squares fit to the “ Q plot” generally has a smaller associated uncertainty compared to conventional assessment of the Flack parameter (Fig. 9.11). This has a significant impact, especially in the pharmaceutical sciences, because it makes confident absolute structure determination viable for light-atom structures (containing only C, H, N, O) using a standard Cu X-ray source. The method is implemented post-refinement, which means that it can always be used, without imposing any additional requirements during the structure refinement stage. Since it relies on making a linear fit to the Q plot, the data set should be *complete* and should be checked for any outliers that might significantly skew the least-squares result.

5 Suggested Best Practices

There can be different aims for a single-crystal X-ray diffraction analysis, which might influence the overall strategy and best practices. In general, this section assumes that the analysis is being carried out as part of a pharmaceutical pre-formulation exercise, and that the aim is to provide the best possible characterisation of a crystalline drug for scientific and possibly legal/regulatory purposes.

5.1 Choice of Radiation

Available laboratory instruments are generally limited to Mo or Cu radiation. For most pharmaceutical applications, Cu is likely to provide the better option because of its stronger interaction with the sample and the benefits for absolute-structure determination of light-atom crystals (Sect. 4.3.3). Potential problems with absorption in the presence of heavier atoms are less likely for typical small-molecule drug compounds. Since diffraction patterns measured with Cu radiation are geometrically spread out compared to those measured with Mo, it will usually take longer to measure a data set using Cu radiation compared to Mo. However, this sacrifice in speed is far less significant with area-detector instruments, so it is unlikely to have any great impact outside of the most demanding high-throughput scenarios. Instruments with interchangeable Cu and Mo sources are available, but anecdotal accounts of owners in the pharmaceutical area suggest that the Mo source on such instruments is rarely used.

5.2 Temperature

Room temperature might be perceived to be the only temperature that is practically relevant for drug compounds. A common requirement is to match crystal structures to ambient powder X-ray diffraction patterns, which obviously requires room-temperature single-crystal data. However, the quality of single-crystal data generally increases at lower temperature, because the intensities are enhanced when the thermal motion of the atoms is minimized. This can be tremendously helpful to obtain the best possible data set for absolute-structure determination, for example. It can also help to localize H atoms or unravel disorder, although in this case there might be some concern about extrapolating low-temperature information back to ambient conditions. To define best practice, it would probably be ideal always to collect data at room temperature *and* at low temperature (usually 100 K, being the practical minimum for N₂ cryostats). This produces a “best” data set for more demanding refinement purposes and the most practically relevant ambient data set. It also has an advantage of checking for potential phase transformations or changes in proton position/mobility below room temperature. Duplicate data collections are much more practical on modern area-detector instruments, and a multi-temperature analysis can generally be programmed to proceed automatically.

5.3 Data Collection Strategy

The data collection strategy refers principally to how much of the diffraction pattern is measured, and how it is measured (*e.g.* counting time per reflection, measuring a given reflection more than once, *etc.*). The suggested best practice here is obvious: *assume nothing and measure everything—as well as possible!* There are several aspects to highlight.

5.3.1 Resolution

The resolution refers to the highest diffraction angle (lowest d_{hkl} value) that is measured. The d_{hkl} value is generally quoted because it is independent of the X-ray wavelength. Diffraction data measured to “low resolution” (which actually refers to a higher value of d_{hkl}) produces a less well defined image of the crystal structure. A guideline for molecular crystal structures is that data should be measured to $d_{hkl} \leq 0.85 \text{ \AA}$. For Cu radiation, this corresponds to $\theta_{\max} = 65^\circ$, and for Mo radiation, $\theta_{\max} = 25^\circ$. For direct methods of structure solution to be successful, data should generally be measured and observed to $d_{hkl} \leq 1 \text{ \AA}$. Some more modern developments may extend that estimate to $d_{hkl} \approx 1.2 \text{ \AA}$. When the structure is refined, lower-resolution data will lead to less precise atomic positions, probable problems defining (anisotropic) displacement parameters, and little-to-no chance to identify H atoms. The suggested best practice is to aim for 0.85 \AA where possible, and there is usually no need to go much beyond that.

5.3.2 What Fraction of the Diffraction Pattern Should Be Measured?

The data that must actually be measured (up to the specified angular resolution) depends on the symmetry of the diffraction pattern. If the pattern of intensities is genuinely symmetric, it is only necessary to measure the unique fraction. The main problem that can arise here is that most data-collection control software will attempt to identify symmetry in the diffraction pattern at an early stage, then use that to optimize the data-collection strategy. A common sequence (Fig. 9.4) is to collect a small portion (or portions) of the pattern in order to establish the lattice parameters, then the metric symmetry of the lattice is used to indicate the symmetry of the diffraction pattern as a whole. As stated in Sect. 2, the metric symmetry of the diffraction pattern does not necessarily reveal anything about symmetry in the diffracted intensities. If the metric symmetry appears to be higher than the actual symmetry of the diffraction pattern, a strategy based on the metric symmetry will miss some of the required data. Actually, chances are quite high that the metric symmetry *will* reflect the true symmetry of the diffraction pattern—but what if your most important sample was one of the exceptions? Of course, the worst-case scenario is only that the data might have to be re-collected after problems are uncovered,⁸ but this provides one example where the default actions on a modern diffractometer system might hide some assumptions that the user should understand.

⁸ Hopefully, the crystals are still available!

5.3.3 Centrosymmetric or Not?

A centrosymmetric crystal will produce a genuinely centrosymmetric diffraction pattern, and it is only necessary to measure one of each Friedel pair (*i.e.* to collect a “hemisphere” of data rather than a “full sphere”). For a non-centrosymmetric crystal structure, both reflections in each Friedel pair must be measured. Since non-centrosymmetric crystal structures can arise at any time, whether the constituent molecules are chiral or not, caution must be applied. In practice, samples that are known to be enantiopure *must* be flagged as non-centrosymmetric before the data collection strategy is calculated, which might mean making a change to default options. For other samples, the probable scenario is to assume centrosymmetry for speed, but be prepared to re-collect data (and be aware that it is necessary!) for structures that later are found to be non-centrosymmetric.

5.3.4 Completeness

Completeness refers to the fraction/percentage of *unique* data collected to the specified resolution. The obvious best practice is to aim for 100%. One of the advantages of the single-crystal technique over many others is the large number of observations that are made per parameter to be determined. For centrosymmetric structures, a guideline minimum is ten unique reflections to be measured per refined parameter. For non-centrosymmetric structures, this will usually be a little less than ten. If the completeness of the measured data falls below 100%, the ratio of observations to parameters decreases, and the resulting quality of the crystal structure decreases. There are (arguably) different degrees of seriousness concerning incomplete data sets. For example, missing data distributed at random throughout the entire data set is likely to cause fewer problems than systematic omission in a certain region of the diffraction pattern. For absolute-structure determination, failure to measure a sufficient number of Friedel pairs will lead to larger uncertainties and therefore less confident conclusions. For the quotient methods, it was previously noted that complete data sets are required in order to draw valid conclusions from the Q plot. With the speed of modern area-detector diffractometers, and for a standard crystalline sample (being stable over the duration of the data collection and having no other problems) there is no real excuse for collecting incomplete data sets. Therefore, 100% completeness (to the specified resolution) is suggested as the best practice.

5.3.5 Redundancy

Redundancy refers to measurement of the same data more than once. This could be measurement of reflections that are equivalent by symmetry, or it could be measurement of the same reflection in various crystal orientations. Repeated

measurement of the same observation reduces statistical error, so it is advisable always to measure data with as high a redundancy as possible. One advantage of area detectors is that they measure many reflections simultaneously, so it becomes practical (actually unavoidable) to measure data with a redundancy greater than 1. As always, there is a potential conflict between the desire for high redundancy and low data collection time. In general, an average redundancy of 5 is a good target, 10 is even better. Generally, the redundancy will be higher for low-angle reflections than high-angle reflections, so it might be advisable to focus on a certain redundancy target for the higher-angle reflections rather than the data set overall. For absolute-structure determination using quotient methods, the results become increasingly reliable with increasing redundancy, so a particularly valuable absolute structure determination warrants the time required to obtain a very high average redundancy of 10 or above.

5.3.6 Collection Time

The data collection time per image should be targeted to achieve observable data to the required angular resolution. Often, the software algorithms for integration are very effective for weak intensities, so reflections that are visible in the raw data images should certainly be statistically observable ($I > 2\sigma(I)$) in the final data set. Thus, the target collection time per image should be sufficient to see reflections out to the specified angular resolution in the raw images. The diffracted intensity will always decrease at higher angle, especially with room-temperature data (Fig. 9.3). This is minimized by lowering the temperature. For some crystals, it might be impossible to observe data to the desired resolution, or it could be that the higher-angle data require collection times so long that the lower-angle data overload the measurable intensity range of the detector. In that case, it could be practical to use different data collection times for low- and high-angle data—most modern diffractometer control packages can handle this approach. The principal best practice note for the user is to ensure that the target resolution limit is 0.85 \AA , and where possible that data are actually observed to this resolution.

5.4 Data Processing

Data processing refers to generation of a list of measured intensities from the raw diffraction images. This is exclusively a software task. The first step is *integration*, which involves counting up the measured intensities on a pixel-by-pixel basis. To achieve this in an efficient manner, the software has to know where it can expect to find intensity, which means that the geometry of diffraction must be established and the data set must be indexed. The software will assess the intensities measured at all pixels within a defined peak area (usually spanning several consecutive data

images) to produce the final summed intensity. The integration software incorporates methods for modelling and fitting peak profiles, which allows better assessment of weak reflections on the basis of information learned from well-defined strong reflections. The result of the integration is a list of raw measured intensities, with assigned *hkl* values referring to the specified unit cell.

The next step is to apply a sequence of corrections and optimisations to the intensities. Some fundamental corrections (Lorentz-Polarisation) must always be applied, and usually there are several distinct runs of data that must be merged and scaled relative to each other. When the merged data set has been created, the typical next step for an area-detector instrument is to apply a *multi-scan* correction, which works on the simple basis that “equivalent reflections should be equivalent”. Thus, the procedure looks for reflections that have been measured more than once, and/or should be equivalent under the specified symmetry of the diffraction pattern, and applies corrections to make them equivalent as far as possible. One of the factors corrected for is absorption, and multi-scan corrections are therefore commonly referred to as “absorption corrections.” This term is something of a left-over from point-detector instruments, where it was genuinely necessary to assess and correct for the effects of anisotropic absorption. Today it is misleading, because all kinds of systematic error are handled, *e.g.* poor centring of the crystal, beam inhomogeneity, *etc.* The multi-scan correction is an integral part of an area-detector based system, and it is a significant contributor to the quality of data that is obtained. It should not be viewed like a traditional absorption correction, and it should be applied in all cases.

Clearly, the effectiveness of the multi-scan correction relies on correct specification of the symmetry of the diffraction pattern. After the integration is completed, the information to make this assessment (namely a full list of diffracted intensities) is available, although any substantial systematic errors may potentially confuse the issue. A particularly important case is a non-centrosymmetric crystal, where the multi-scan process must not assume equivalence of Friedel pairs (for obvious reasons!). The multi-scan always benefits from higher redundancy, so for a fixed window of available time, it is usually better to collect more images and increase redundancy than to increase the individual image time.

5.5 Structure Checking Procedures

It has become standard practice for small-molecule crystal structures to be validated using automated checking procedures, principally the online *checkCIF* service provided by the International Union of Crystallography (IUCr 2014; Spek 2013). Such systems aim to identify problems or inconsistencies in single-crystal structures, and to advise when action might be taken. The *checkCIF* service has improved the general standard of single-crystal X-ray structures over the last decade or so, and it is absolutely recommended to pass any small-molecule

crystallographic results through this system.⁹ In line with the opening comments in this chapter, it is worth considering for a moment exactly what the checking system can and cannot do. The basis of the single-crystal X-ray diffraction technique is to make an experimental measurement of a crystal's diffraction pattern, then to derive a crystal structure from that diffraction pattern. The validity of the resulting crystal structure is judged by the question "how well does this structure match the measured diffraction pattern?" Any checking procedure that is going to address that question must be provided with the measured diffraction pattern. In the early days of *checkCIF*, only the refined crystal structure was provided, so the checking procedures were based solely on expectations compared to other refined crystal structures. There was in principle no guarantee that the structure was actually a fair representation of the data from which it was obtained! More recently (since *ca* 2011), the *checkCIF* service has also implemented checks on the structure factors that accompany the structure. So do the validation procedures now properly consider the experimental diffraction pattern? Actually not: the observed reflection data in such structure factor files is still a *secondary interpretation* of the measured diffraction pattern. The observed reflection intensities are derived from the measured diffraction images during the integration process, and that process can still be subject to inappropriate decisions by the operator or some automated procedure. For example, if a lattice is assumed to be centred, the integration process usually will not look for diffracted intensity in the positions that might indicate that the lattice is not centred. Thus, it will produce a list of observed reflection intensities that are entirely consistent with the assumed lattice centring, and a checking system cannot know that this could have been a poor choice.

The checking systems are very good at identifying technical mistakes that might have been made during structure refinement, *e.g.* missed symmetry, forgotten H atoms, incorrect chemical formula, *etc.*, and there is almost always a benefit in correcting such inconsistencies. They can also highlight features of a structure that appear to be unusual compared to expectations and therefore warrant checking, *e.g.* an unusual bond length, or an H atom that does not form any expected hydrogen bond. These expectations are usually defined in a sensible way, but it should be kept in mind that some structures may not actually conform to established expectations. Finally, they attempt to highlight experimental deficiencies, *e.g.* unsatisfactory resolution, completeness, data-to-parameter ratio, *etc.* Here, the well-informed user should always have the upper hand because they have actually done the experiment. A checking system may tell you that the data resolution is "too low", but it was not looking at your crystals or your data images, and it cannot tell you whether intensity was actually there to be measured. This category of warnings certainly can serve as a reminder that you may be dealing with sub-optimal data and that the derived results should not be "over interpreted", but they will never come as a surprise to a well-informed user that has carried out the entire analysis carefully and thoughtfully.

⁹ An interesting question in the pharmaceutical arena is whether submission of a crystal structure to a remote system such as *checkCIF* amounts to disclosure in the context of intellectual property.

6 Conclusion

The development of modern instrumentation for single-crystal X-ray diffraction has “raised the bar” for the quality of diffraction data and derived crystal structures. A good single crystal of a typical small-molecule drug compound will yield highly precise and reliable results on any modern instrument, and the automated validation procedures are consistent and reliable for these structures. For absolute-structure determination, which is one example of a key pharmaceutical application, the combination of highly precise intensity measurements and new methods for data analysis greatly enhance the possibilities to make confident *ab initio* conclusions from laboratory single-crystal X-ray measurements. Against this backdrop, it is possibly tempting to drift towards complacency and to pass the burden of understanding onto the instrument manufacturers and software writers. To some extent this is acceptable, but the user must retain a sufficient level of understanding to monitor the analysis, intervene where necessary, and properly evaluate the results. This chapter provides only a rather basic and pragmatic “primer”. Readers with an interest and opportunity to carry out single-crystal X-ray measurements are encouraged to spend time with their diffraction instruments, and to delve deeper into the underlying principles.

References

- Allen FH (1986) A systematic pairwise comparison of geometric parameters obtained by X-ray and neutron diffraction. *Acta Cryst B* 42:515–522
- Blake AJ, Cole JM, Evans JSO, Main P, Parsons S, Watkin DJ, Clegg W (2009) *Crystal structure analysis: principles and practice*. Oxford University Press, New York
- Clegg W (1998) *Crystal structure determination*. Oxford University Press, New York
- Flack HD, Bernardinelli G (2000) Reporting and evaluating absolute-structure and absolute-configuration determinations. *J Appl Cryst* 33:1143–1148
- Grobelyny P, Mukherjee A, Desiraju GR (2011) Drug-drug co-crystals: temperature-dependent proton mobility in the molecular complex of isoniazid with 4-aminosalicylic acid. *CrystEngComm* 13:4358–4364
- IUCr (2014) checkCIF. <http://checkcif.iucr.org>. Accessed 4 June 2016
- Müller P, Herbst-Irmer R, Spek AL, Scheider TR, Sawaya MR (2006) *Crystal structure refinement: a crystallographer’s guide to SHELXL*. Oxford University Press, New York
- Parsons S, Flack HD, Wagner T (2013) Use of intensity quotients and differences in absolute structure refinement. *Acta Cryst B* 69:249–259
- Spek AL (2013) Structure validation in chemical crystallography. *Acta Cryst D* 65:148–155
- Thompson AL, Watkin DJ (2009) X-ray crystallography and chirality: understanding the limitations. *Tetrahedron: Asymmetry* 20:712–717
- Van der Sluis P, Spek AL (1990) BYPASS: an effective method for the refinement of crystal structures containing disordered solvent regions. *Acta Cryst A* 46:194–201
- Vega D, Petragalli A, Fernández D, Ellena JA (2006) Polymorphism on leflunomide: stability and crystal structures. *J Pharm Sci* 95:1075–1083

Chapter 10

Applications of Small Angle X-ray Scattering in Pharmaceutical Science

Ben J. Boyd and Thomas Rades

Abstract Small angle X-ray scattering offers opportunities to better understand pharmaceutical systems across a range of length scales related to drug delivery. This contribution aims to highlight a range of areas in which SAXS can be deployed to better understand structure in pharmaceutically relevant materials from molecular to colloidal dimensions, with a focus on developing synchrotron techniques that provide new opportunities in time resolved kinetic studies.

Keywords X-ray scattering • Diffraction • Synchrotron • Self-assembly • Polymorphism • Grazing incidence • Time resolved

1 The Use of X-ray Scattering in Pharmaceutical Systems

Modern pharmaceutical science and materials-based drug delivery require a rich understanding of the structure of materials to progress from empirical-based testing to informed scientific design. This is especially the case in consideration of Quality by Design requirements of regulatory authorities in the development of new medicines. Many techniques are becoming available to the drug delivery scientist to characterize their materials, most of which are captured in this book. While general references on the topic of SAXS, and how to treat data obtained during well-conducted SAXS experiments can be found in several provided references (Bauwens 2012; Glatter and Kratky 1982; Guinier 1959; Lindner 1991), the purpose of this chapter is to provide the reader with some recent developments and opportunities in using small and wide angle X-ray scattering to understand

B.J. Boyd (✉)

Drug Delivery, Disposition and Dynamics and ARC Centre of Excellence in Convergent Bio-Nano Science and Technology, Monash Institute of Pharmaceutical Sciences, Monash University (Parkville Campus), 381 Royal Parade, Parkville, VIC 3052, Australia
e-mail: ben.boyd@monash.edu

T. Rades

Department of Pharmacy, University of Copenhagen, Universitetsparken 2,
Copenhagen 2100, Denmark

systems of pharmaceutical relevance, principally in solid state systems and soft matter self-assembled materials.

1.1 Diffraction for Different Length Scales

There are a multitude of subtleties in X-ray scattering, but whichever way you look at it diffraction techniques tell us about distance. The type of diffraction technique to select then is largely dependent on the length scale of the interaction that we wish to probe or measure. Diffraction may be used to probe distances between atoms in a specific molecule, distances between diffracting planes in a structured material, distances between particles in a dispersion of particles, distances across a particle in one or more dimensions. When the distances become too great and X-rays are no longer appropriate, light scattering typically becomes the technique of choice. Thus, X-ray scattering is a highly versatile technique for investigating the spatial arrangement in materials.

Other chapters in this book have done an excellent job in explaining the general concept of X-ray scattering and Bragg's Law in relation to extracting molecular level structural detail from the scattering data. The inverse proportionality between the dimension of the diffracting structures and angle, as dictated by Bragg's Law, means that *small angle* X-ray scattering in general refers to probing information at *larger length scales* (see Fig. 10.1), so rather than molecular level information, it is ensembles of molecules, self-assembled structures and particles. For those accustomed to the classical XRD terminology for solid state analysis, it should be noted that there is no cut off as such between 'SAXS' and 'WAXS' or 'XRD', and on

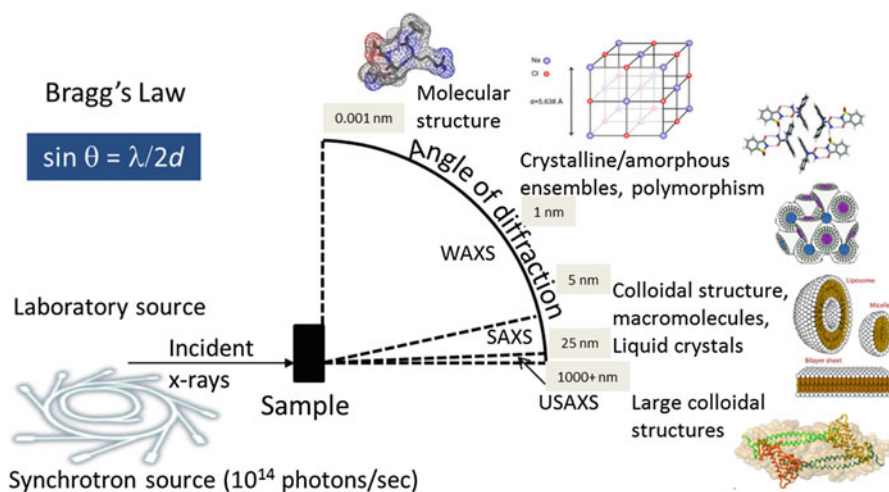


Fig. 10.1 Overview of the relationship between structural dimensions, scattering angle and terminology of techniques. Modified with permission from Dong and Boyd (2011)

modern X-ray systems it is typical to be able to position the detection system at the most useful distance from the sample. This is done in order to optimise the range of angle covered by the detector, from what would typically be considered to be small or ultra-small angle, out to wider angles sampled by classical XRD systems. It is also typical now to have two detectors to cover both regimes, and it then becomes a case of a potential compromise between coverage of a wide range of scattering angles, possibly with no gap between the range covered by the two detectors, and resolution at the detector.

X-rays used routinely in experimental structural studies may be from a laboratory benchtop-style instrument or from a synchrotron source. Laboratory X-ray scattering instruments have relatively low flux (typically $\sim 10^8$ photons/s) and hence are generally used for resolving structural information in 'static' equilibrium samples, as acquisition times of minutes to hours are required. This is however becoming less of an issue with new technologies, such as liquid metal jet microfocus sources providing up to 100-fold higher flux compared to common rotating anode sources, approaching 10^{12} photon/s, but are at this stage prohibitively expensive for most laboratories.

While materials at equilibrium (or close to it) are of interest in e.g. stability studies, materials in drug delivery could rarely be considered to be at equilibrium during either manufacture, or during administration and in vivo processing. In order to understand the behaviour of materials under kinetic situations, much more rapid acquisition is typically required than that achievable from a laboratory source. Further, the scattering contrast from organic materials is low, and together with the study of often dilute dispersed particulate materials for drug delivery, this means that the extra flux obtained from synchrotron sources is essential to obtaining quality kinetic and structural information in many systems. Synchrotron radiation is typically generated by accelerating electrons to close to the speed of light in a circular storage ring. The electrons are forced to bend around the ring using powerful electromagnetic fields, resulting in a loss of momentum; the consequent broad spectrum energy is emitted at a tangent to the ring path, and optics used to select the specific wavelengths desired depending on the type of experiment. Synchrotron X-ray radiation has significantly higher flux (typically $\sim 10^{13}$ photons/s) (Mandelkow and Holmes 1989) than the laboratory instruments, enabling diffraction patterns with sufficiently useful information to be obtained in milliseconds (Amenitsch et al. 1997). Further, the high flux means that unlike laboratory instruments, samples can be studied without a continuous vacuum. This opens a myriad of options for sample environments, relative to laboratory sources where the sample environment is completely under vacuum to minimise scattering from air. As such, synchrotron-based X-ray sources can be used for high throughput and time-resolved experiments as well as static samples.

The detection systems in both benchtop and synchrotron X-ray scattering facilities are largely similar. Image plates were commonplace until the relatively recent advent of position sensitive gas ionization detectors and more recently CCD and diode array detectors, which, coupled with fast computing capabilities, allow rapid acquisition times, and fast kinetic studies to be undertaken at synchrotron facilities.

2 Probing Larger Length Scales: Ultra Small Angle X-ray Scattering (USAXS)

To reiterate the relationship between distance and angle, Fig. 10.2 illustrates schematically the typical setup in terms of sample to detector distance to obtain maximum resolution on the detector. Some extra angular range at a fixed distance may also be obtained by offsetting the detector (with the drawback of reduced intensity from radial integration due to part of the scattering cone missing the detector at wider angles), or by manipulating the energy of the incoming X-rays. The ability to run true ultra-small angle X-ray scattering studies is therefore limited by the distance at which the detector may be positioned from the sample, by the physical distance as well as additional optics requirements. Despite potential applications in particle-based systems, USAXS has not found any direct application to date in mainstream pharmaceutical science. Some areas where there are likely to be future developments are described below.

A recent review of the use of USAXS to study larger scale polymer materials highlights a wide range of applications from a scattering perspective that could be readily applied to understand the assembly of polymer-drug conjugates for example (Zhang and Ilavsky 2010).

USAXS can also enable access to size structures typically probed using visible light. For example, dynamic light scattering is often used to probe larger scale structures in particle-based pharmaceutical systems such as liposomes, microparticles etc. The use of light as the probe is limited in the case of strongly absorbing materials and/or high volume fractions, and most systems need to be diluted prior to analysis which brings into question the representativeness of the measurement. However, the use of an X-ray equivalent to DLS, X-ray photon correlation spectroscopy, could enable study of significantly more concentrated systems. The technique, which requires a USAXS format to access the larger correlated size domains, has been used to investigate the size distribution in highly concentrated latex microparticle dispersions, which could be used for concentrated drug suspensions as one example (Zhang et al. 2011).

USAXS is also inherent in X-ray imaging, and although not directly related to structural elucidation in pharmaceutical materials or drug delivery systems, its ability to enable imaging of microstructure in tissues such as lung (Dong et al. 2014) should open opportunities for better understanding the interaction of delivery systems with tissues on administration, and indicate issues such as aggregation of particulate dosage forms in physiological fluids.

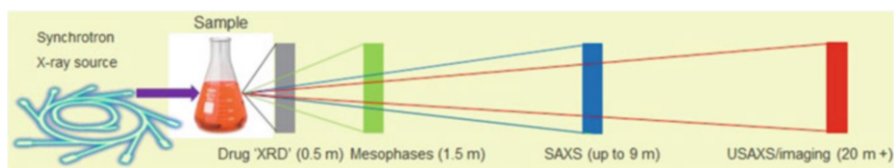


Fig. 10.2 Illustrating the sample to detector distances typically used in the different modes of 'small' angle X-ray scattering

3 Colloidal Scale Structures in Pharmaceutical Systems Probed Using SAXS

3.1 Drug Delivery Particles

Micellar systems are a common drug delivery vector for poorly water soluble drugs, enabling the required dose to be solubilized in a practical volume of aqueous medium (Kataoka et al. 2001; Torchilin 2001). They are also an important intermediate structure in the absorption of drugs and poorly soluble nutrients from the GI tract (Carey and Small 1970). Hence the structure of micelles, and the impact of drug solubilization on the structure is an important aspect of pharmaceutical science. SAXS can provide information such as size and shape of micelles as well as micelle aggregation number, radius of gyration and characteristic inter-headgroup spacing across the micelle core (Lipfert et al. 2007). Synchrotron SAXS has been used to observe the formation and transformation of micelles in real time (Hirai et al. 1995a, 1996; Liu et al. 1999; Lund et al. 2009; Schmolzer et al. 2002; Weiss et al. 2005).

In the pharmaceutical field, SAXS has been used to determine the effects of drug (Mackeben and Müller-Goymann 2000) and enzyme loading (Papadimitriou et al. 1994) on the structure of micelles. The effects of molecular structure of monomeric amphiphiles on micelle formation and structure has also been investigated (Dupuy et al. 1997; He et al. 2002; Salentinig et al. 2014; Zhang et al. 1999), aiding in selection of amphiphiles for formulation optimisation. Such studies may also provide insight into micelle interactions with other endogenous amphiphiles such as bile salts, and help to predict the fate of micelles after oral ingestion. SAXS studies on the effects of counterions (Joshi et al. 2007) and non-aqueous solvents (Aizawa 2010) on micelle structures also provide useful information for optimisation of micelle-based drug formulations.

Self nanoemulsifying and microemulsion drug delivery systems have also been studied using SAXS (Dora et al. 2012; Formariz et al. 2008; Nielsen et al. 2007; Schmiele et al. 2014) with droplet structure and likely location of components being better understood in these systems. Synchrotron SAXS has been used to study the interaction of microemulsions with proteins (Hirai et al. 2002, 1995b) and polymers (Hilfiker 1991).

SAXS can be also used to study the size, lamellarity and bilayer thickness in liposome drug delivery systems (Bouwstra et al. 1993; Glatter and Kratky 1982), and influence of drug loading on structure (Ristori et al. 2005; Salvati et al. 2007; Schütze and Müller-Goymann 1998; Wörle et al., 2006). Synchrotron SAXS has also been used to study the dynamics of the self-assembly of liposomes from micelles (Weiss et al. 2005, 2008). It is possible to use SAXS to distinguish between proteins encapsulated inside the liposome from those at the surface (Bouwstra et al. 1993; Skalko et al. 1998).

3.2 *Proteins in Solution vs. Protein Crystallography*

Structure-based drug design (SBDD) is a commonly used method in rational drug design (Anderson 2003; Williams et al. 2005). SBDD involves identifying the protein and/or enzyme involved in a specific metabolic or cell signal pathway, related to a particular disease state. Knowledge of the three-dimensional geometrical shape or structure of the target protein, allows drug compounds to be designed rationally to selectively interact with the target to bring about the desired effect. Nuclear magnetic resonance (NMR) and X-ray scattering are routinely used to derive the three dimensional structure of proteins and to study drug-protein target interaction for SBDD optimisation (Deschamps 2005; Scapin 2006; Takeuchi and Wagner 2006). Crystallography provides precision high-resolution protein structures, in the crystalline state, however the relationship between the crystalline structure and conformational state under physiological conditions is not readily determined. Protein crystallization required for protein crystallography often requires high concentrations of organic polymers, salts, and additives. Such conditions are very different from physiological systems and, as such, can alter protein-drug interactions.

Perhaps the most recent developments in this field are in the development of X-ray femtosecond lasers. These facilities provide a high intensity X-ray pulse with very short duration, sufficient to obtain scattering for resolving crystals at similar resolution to traditional crystallography. However, they require only very small crystallites, and are of particular use in the mesophase-mediated crystallization of membrane proteins such as G-protein coupled receptors, the most common drug target in biology today (Liu et al. 2014).

Although SAXS has lower resolution (>1 nm) and hence cannot provide information on protein structure at the atomic level, it can provide information on gross structural features such as shape, tertiary and quaternary structures under physiological conditions, and insights into protein function. SAXS has been used to characterize size and shape of biological macromolecules such as RNA (Rambo and Tainer 2010), proteins (Chacón et al. 2000; Hura et al. 2009), and protein complexes (Sardet et al. 1976) in biologically relevant solutions, and for the study of the effects of solution conditions on conformation (Ianeselli et al. 2010; Zhang et al. 2006). Furthermore, synchrotron SAXS can also provide time-resolved structural information, for example during protein folding or nucleotide hydrolysis (Davies et al. 2005; Kataoka et al. 1997; Zhu et al. 2004). The use and progress of SAXS for biological macromolecules, such as RNA and proteins in solution, has been comprehensively reviewed (Lipfert and Doniach 2007; Svergun and Koch 2003).

4 Mesoscale Structures

Materials of interest in the pharmaceutical field, particularly lipids for delivery, are often in the liquid crystalline state, with order in one or more dimensions, and liquid-like properties in other dimensions (Müller-Goymann 2002). There are two principal types of liquid crystals: thermotropic (TLCs) and lyotropic liquid crystals (LLCs). TLCs are formed by heating a crystalline solid or by cooling an isotropic melt, whereas LLCs are often formed by amphiphilic molecules on contact with water.

Liquid crystalline structure may be important in terms of both the state of the drug, or the use of liquid crystalline materials as a drug delivery matrix. Thermotropic liquid crystal forms of drug substances can enhance the solubility and dissolution rate of drugs (Bunjes and Rades 2005; Patterson et al. 2002; Rades and Müller-Goymann 1994), while lyotropic liquid crystals may be useful in a sustained release setting. Lyotropic liquid crystals may actually be formed by some drugs themselves on contact with water (Gutiérrez-Pichel et al. 2003; Mukerjee 1974). For example, antivirals (Rodríguez-Spong et al. 2008), phenothiazines (Attwood et al. 1974), non-steroidal anti-inflammatory drugs (Fini et al. 1995), among others (Schreier et al. 2000) are all surface active and have been shown to self-assemble in aqueous environments. The self-assembly of amphiphilic drugs may also affect their properties such as chemical stability (Kurz 1962; Wallace et al. 2010).

Importantly in the context of scattering, liquid crystals have a longer range of periodicity compared to solid crystals, making SAXS and/or WAXS appropriate for investigation of their internal nanostructures. Studies have demonstrated that the nanostructure of the lyotropic liquid crystal systems can have a significant bearing on the controlled release characteristics of the matrix (Fong et al. 2009; Lee et al. 2008) which in practical terms can be controlled by temperature, additives, or for some systems, pH (Borne et al. 2001; Caboi et al. 2001; Chang and Bodmeier 1997; Clogston et al. 2000; Dong et al. 2006; Engstroem and Engstrom 1992; Nakano et al. 2002). Hence, it is of great interest to understand their response to certain stimuli as this can provide a handle on ‘triggered’ drug release behaviour (Fong et al. 2009, 2010; Yagmur et al. 2008).

4.1 High Throughput Characterization

The virtues of high throughput techniques lie in rapid screening of material properties to enable fast selection of target structures for further development. In the case of traditional laboratory SAXS instruments, where 30 min or greater may be required to acquire a useful diffractogram, high throughput techniques are not achievable on a useful timescale. However the advent of synchrotron scattering approaches, where the acquisition time may be less than 1 s, have opened new

opportunities for high throughput screening of materials for pharmaceutical delivery, or indeed of solid state forms of drug substances under a vast array of conditions using microplate formats.

At the Australian Synchrotron (Kirby et al. 2013) there exists the capability to run samples loaded in multiwall microplates, such as the 96-well plate format illustrated in Panel **a** in Fig. 10.3, where the capillary is mounted on an XY translation stage, to allow automated rastering of the sample wells through the beam, with automated acquisition, typically 1 s per well, meaning that only a few minutes are required to obtain 96 diffractograms (Mulet et al. 2013). Mulet et al. have used this approach to rapidly screen the interactions of drugs with lipid mesophase structures (Mulet et al. 2010), as well as to identify the phase behaviour of new mesophase forming materials in high throughput fashion (Feast et al. 2014). We have used also this approach for rapid phase diagram determination, one example being to determine the phase diagram of mixtures of phytantriol and oleic acid in excess water at increasing pH to rapidly determine the optimal range for pH triggered formation of mucoadhesive particles (Du et al. 2014). There is also the option of running up to 90 samples in capillaries in a multicapillary temperature controlled holder (Panel **b** in Fig. 10.3) for rapid temperature-dependent phase diagrams when smaller sample sizes are required, or where the background scattering from the plastic plate is unacceptable.

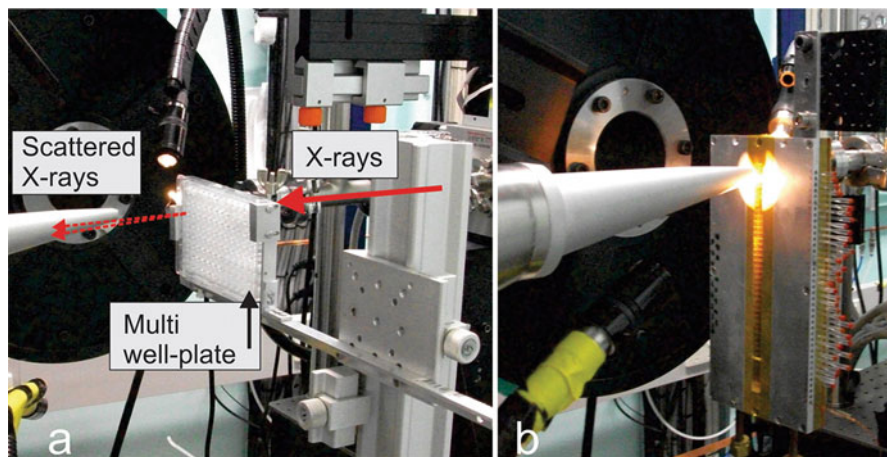


Fig. 10.3 Experimental sample environments at the Australian Synchrotron for high throughput screening of self-assembled structures; Panel **a** illustrates a 96 well plate configuration, while Panel **b** illustrates a multi (up to 90) capillary temperature controlled holder. In both cases the sample holder is mounted on an XY translation stage for automated movement through the X-ray beam and coordinated scattering acquisition (Reproduced with permission from Mulet et al. 2013)

4.2 Time Resolved Experiments

Synchrotron techniques provide huge opportunities to access time resolved structural details. The high X-ray flux and rapid acquisition capabilities of modern detectors has enabled micro- to milli-second data acquisition during transformations in materials under the influence of a wide range of physical and chemical stimuli at far greater temporal resolution than can be achieved on lab instruments. A number of such examples for self-assembled mesophase systems of pharmaceutical relevance where a range of different time domains have been studied are summarised in Table 10.1 below (see Sect. 5 for additional time-resolved examples on solid drug polymorphism).

One issue that new users to synchrotron facilities need to be mindful of in time resolved studies is the potential for beam damage, particularly for stationary samples exposed to multiple exposures at the same location. The high flux on sample is useful for getting a sufficient number of scattered photons onto the detector in a short period of time to allow resolution of fast processes, however, appropriate control experiments over the time domain but in the absence of the stimulus or change need to be conducted to ensure that the apparent time resolved changes in structure are not the result of, or substantially influenced by beam damage. Beam damage is usually non-reversible—so reversibility of a transition is usually a good indication that changes are not caused by beam damage. Strategies, such as moving the sample slightly between frames if possible, or using the minimal exposure time to obtain useful data may otherwise be necessary. Delays between frames are also useful. When the sample is in a flow through mode, such as

Table 10.1 Examples of pharmaceutically-relevant time-resolved SAXS studies across a range of time domains

System	Stimuli	Transition	Time domain	Reference
Zwitterionic and anionic surfactants	Mixing dissimilar solutions	Micelles to vesicles	5 ms	Weiss et al. (2005)
Phytantriol bulk cubic phase containing gold nanorods	Near infrared light	Cubic to hexagonal and inverse micellar phase	50 ms	Fong et al. (2010)
DOPG + monoolein	Addition of calcium	Vesicles to hexagonal phase	100 ms	Yaghmur et al. (2008)
Phytantriol bulk cubic phase containing spiropyran laurate	UV	Cubic to hexagonal phase	1 s	Fong et al. (2012)
Phytantriol + tributyrin dispersion	Enzyme	Lipid emulsion to cubosomes	1 s	Fong et al. (2014)
Medium chain triglycerides	Enzyme	Lipid emulsion to lamellar phase	5 s	Phan et al. (2013)

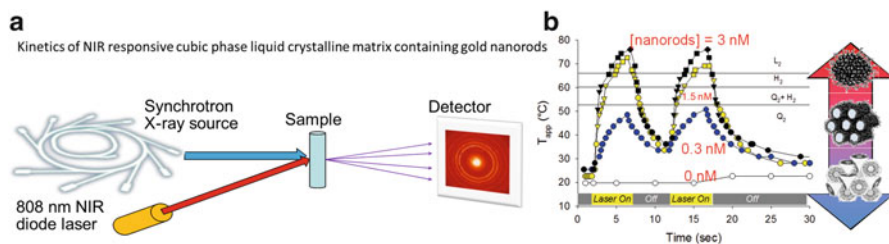


Fig. 10.4 Panel a: Light responsive liquid crystalline system with 50 ms data acquisition, converted to apparent temperature vs. time profiles shown in Panel b. Modified with permission from Fong et al. (2010)

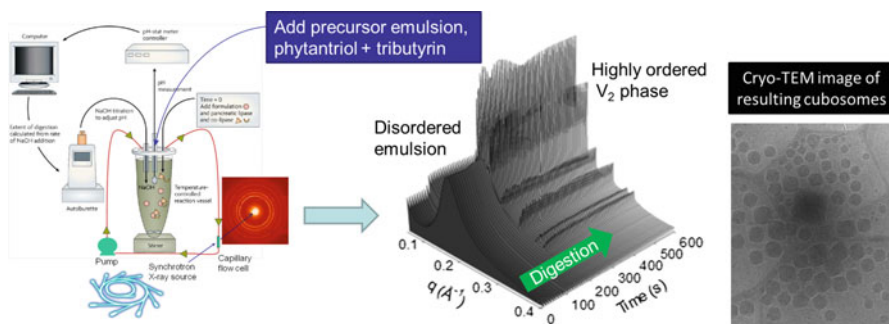


Fig. 10.5 Production of cubosomes from emulsion particles by digestion process monitored using *in situ* SAXS. Modified with permission from (Fong et al. 2014)

the enzymatic transition illustrated above, beam damage is likely to be much less of an issue as only a very small fraction of the sample is exposed in any one frame.

Two specific studies illustrating different capabilities in time-resolved studies of pharmaceutically relevant systems mentioned in Table 10.1 are elaborated on here. One involves the irradiation of gold nanorods embedded into a bulk cubic phase sample—the plasmonic particles act as ‘nanoheaters’ to induce temperature-driven phase transformations (Fong et al. 2010). In this case, a bulk phase sample was used, with a NIR laser used to irradiate the sample while in the beam (Panel a in Fig. 10.4), and care was taken to ensure that transitions were not the result of beam damage as mentioned above, indicated by the reversibility of the transitions. The data shows that the transitions are dependent on the gold nanorod concentration, and that the effect specifically requires the presence of the particles. With only a few seconds of irradiation, the apparent temperature of the matrix (as ‘felt’ by the lipid structures) was increased from 25 to 70 °C, and relaxed over a similar time frame as shown in Panel b in Fig. 10.4. The transitions in this systems have been directly linked to drug release *in vitro* and *in vivo* (Fong et al. 2009).

The second example involves the generation of highly structured cubic phase (V_2) particles, ‘cubosomes’ using an enzymatic process for application to *in situ* formation in the gut (Fong et al. 2014). Briefly, the disordered emulsion is added to a digestion vessel, illustrated schematically in Fig. 10.5, to which lipase is added in

the form of pancreatin to stimulate lipolysis. The digestion model has been used for many years, but only recently adapted with a pump and flow-through capillary to enable kinetic scattering information to be obtained in real time (Warren et al. 2011). The scattering, with 1 s frames, demonstrates the progression from a disordered emulsion precursor system, which, upon digestion of the tributyrin and partition of butyric acid away from the emulsion droplets, undergoes a transformation to cubosome particles. The cubosomes thus formed are all faceted particles, and there is a complete absence of liposomes which often contaminate cubosome preparations when produced using other approaches. The entire process occurred in less than 3 min, which would be missed using a laboratory source for this experiment.

4.3 Spatially Resolved Experiments

In contrast to time resolved studies in mesoscale drug delivery systems, there has been little study of spatially resolved structural detail in drug delivery systems. The high flux of synchrotron sources and purpose built beamlines with optics capable of controlling beam dimensions to less than 1 μm opens opportunities to conduct spatially resolved scattering on systems of pharmaceutical relevance where structural change over distance of microns is of interest or concern. The formation of mesoscale structures at the interface between oppositely charged surfactant and polymer systems has been recognised for some time, however the spatial resolution through these interfaces does not appear to have been studied. In the context of drug delivery these interfaces are important for example in DNA/cationic lipid complexes, or in mesostructured capsule formation. In the case of the latter, it has been recently shown that lamellar phase structures can form at the interface between bile salts and chitosan with application as novel controlled release materials (Tangso et al. 2014). In Fig. 10.6, a bile salt solution and chitosan solution were brought into

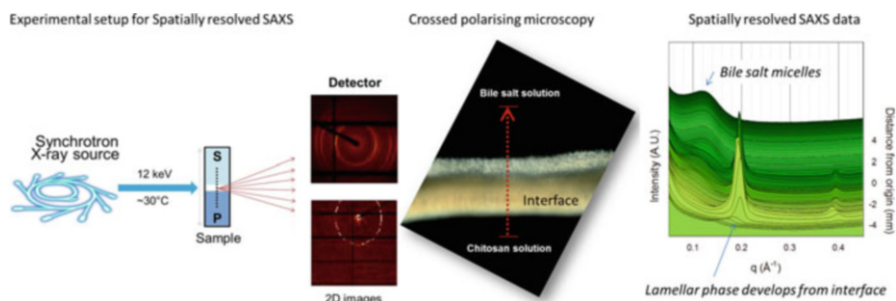


Fig. 10.6 Set up and example data for spatial structural scans across the interface formed between bile salt and chitosan solutions. The surfactant and polymer solutions are loaded from opposing ends of a flat capillary, and the structures formed at the interface are resolved by moving the capillary through the beam in a ‘line scan’ across the interface, acquiring the scattering profile at 100 μm intervals (Tangso et al. 2014)

contact, and a lamellar phase was found to form at the interface; this was somewhat surprising given that there is no lamellar phase in the binary surfactant-water phase diagram for the bile salt component. The lamellar phase was subsequently found to be temperature dependent, and forming capsules with lamellar structure in the shell, by dispersing droplets of one solution in the other, provided a novel temperature responsive controlled release system.

5 Probing Pharmaceutical Solid State Characteristics Using Scattering at Wider Angles

While the use of scattering analysis from powder diffraction studies has been well described in other chapters, the use of scattering from solid materials for understanding real time transformations in materials is a new development. Of particular current interest in the pharmaceutical field is the transformation between different solid state forms, e.g. amorphous to crystalline or polymorphic transition, on contact with aqueous media (Aaltonen et al. 2009). Drug polymorphism can have a significant impact on pharmaceutical properties such as apparent solubility, dissolution rate, density, etc. (Bernstein 2007; Hilfiker et al. 2006). These properties can directly impact on the quality and performance of drug products, by impacting stability, dissolution, and in some cases bioavailability. The classical means of analysing the solid state form of drug substances utilises laboratory scale XRD instrumentation. While the sample is not under vacuum, the acquisition time is typically 10 min or greater, precluding time resolution at the minutes to tens of minutes timescales *in situ*. In fact, in a review on solid state transformations in 2012, Greco and Bogner stated that “No *in situ* monitoring of solution-mediated phase transformation using XRPD has been reported” (Greco and Bogner 2012). The classical XRD format is also not readily amenable to samples dispersed in an aqueous environment.

Consequently, indirect methods such as Raman spectroscopy have been used to probe solid state transformations at the surface of a compact. The technique provides access to fast kinetic processes, however data analysis requires prior correlation of Raman spectra to known polymorphs, meaning that interpretation of the transformation may be confounded by metastable or unknown forms. The configuration of the experiment is such that the Raman probe acquires information from the surface of a compact pressed into a well holder, resulting in a low surface area compared to the *in vivo* case of a disintegrating tablet, meaning that the kinetics of the transformation may not be representative of the *in vivo* situation.

In order to address these shortcomings, a flow through approach coupled to synchrotron diffraction, using the *in situ* formation of a slurry was conceived that is then pumped through a capillary flow cell (Panel **a** in Fig. 10.7 (Boetker et al. 2012)). The approach provides a much greater surface area for transformation, with the high flux of the synchrotron source and the fast acquisition capabilities of

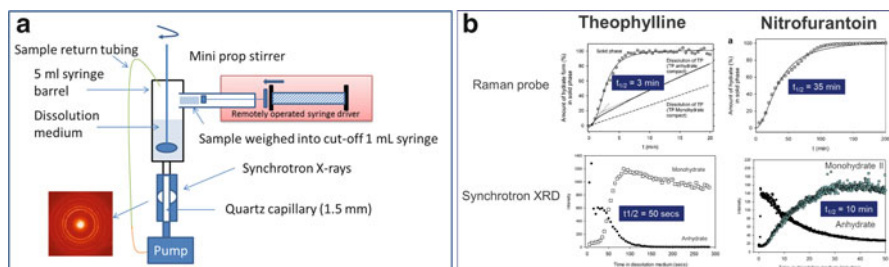


Fig. 10.7 Experimental setup for in situ XRD measurements (Panel a), and kinetics of transformation of anhydrate drug to hydrate form measured in situ using either the indirect Raman spectroscopic approach, or the direct synchrotron XRD method (Panel b). Modified with permission from Boetker et al. (2012)

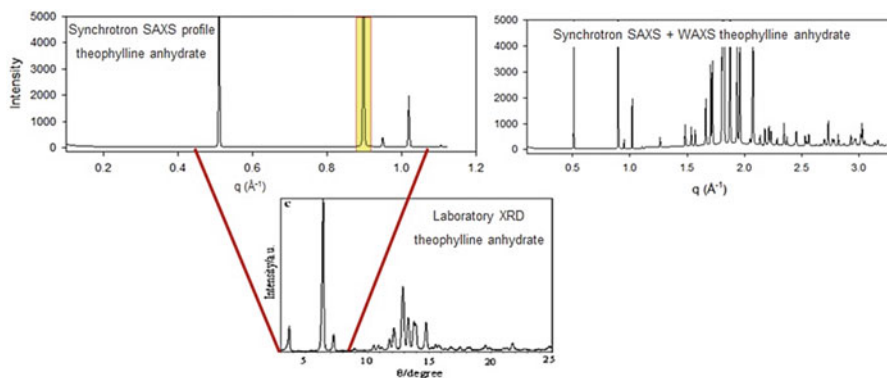


Fig. 10.8 Comparison of synchrotron integrated diffractograms on SAXS (top left) or SAXS + WAXS cameras (top right) compared to the laboratory literature XRD profile. Modified with permission from Boetker et al. (2012)

detector enabling the first real time in situ direct measurement of solid state forms using time resolved XRD. The consequent difference in kinetics was around three- to fourfold faster than the equivalent system across a range of drugs and types of transformations, as illustrated in Panel b in Fig. 10.7, where the transformation of theophylline or nitrofurantoin anhydrate to hydrate forms was more rapid when measured by *in situ* XRD than by Raman approaches.

Importantly, as a result of this study, it was also found that most crystalline forms of drug substances display diffraction at quite low angles, enabling optimization of resolution of the peaks and ready integration. For example, the radially integrated diffraction pattern obtained for theophylline anhydrate measured by synchrotron SAXS-WAXS with 1 s acquisition is illustrated below in Fig. 10.8, compared to the literature XRD pattern that took approximately 10 min to acquire. The sharpness of the low angle peaks is evident in the top left SAXS pattern, while for the combined SAXS-WAXS profile (manually compiled from separate SAXS

and WAXS camera acquisitions taken simultaneously) demonstrated the resolution of peaks in the wider angle region. It may also be possible to find examples where peaks occur at angles too low to observe on a laboratory XRD instrument, particularly those that form liquid crystalline structures as their morphological state.

While these results themselves are interesting and may have wider implications in concerns over the true kinetics of such transformation in the gastrointestinal tract, the study serves as a great example of the possibilities of coupling reasonably complex experimental setups, possible only because of the lack of need for vacuum, with the fast acquisition capabilities of the synchrotron to do experiments that are not possible on the laboratory equipment and are really only limited by imagination.

6 Alternative Small Angle X-ray Techniques

6.1 Anomalous SAXS (A-SAXS) in Pharmaceutical Systems

Typically, SAXS, particularly in soft matter, is often considered as a ‘non-specific’ technique, meaning that it is not discriminating on the basis of the material that it is probing, and provides only information on the structural element and not on molecular localization. However, it must be recalled that unlike neutrons, which are diffracted from nuclei within the material, X-rays are diffracted based on electron density. The strength of the diffraction effect then is related to what is termed the ‘scattering cross-section’. Hence, and in contrast to neutrons, the higher the atomic number of the element, generally the greater is the number of electrons, and a consequent increase in the scattering cross-section. This is illustrated schematically below in Fig. 10.9. In the case of neutrons, this relationship is not at all valid, the classical example of this is the difference in SLD between deuterium and hydrogen—chemically identical samples which have been fully deuterated will ‘look’ identical to X-rays, but will ‘look’ completely different to neutrons—this effect can be taken advantage of using the so called ‘contrast matching technique’ where components of a material can be made selectively transparent to neutrons to highlight localization of specific components of the material (Gradzielski 2012).

In the context of this book chapter, the above statements on scattering length density appear to exclude molecular definition in SAXS, however there is one tool available which has not received significant interest to date in pharmaceutical research which holds much promise. Certain elements exhibit a ‘K-edge’ phenomenon, whereby X-rays are absorbed by elements to a differing extent above and below a specific energy or wavelength. Lab instruments typically operate at a single wavelength, so one cannot take advantage of this effect on lab instruments, however modern synchrotron SAXS beamlines often have very fine control over the wavelength of X-rays incident on the sample, and hence the energy can be scanned with high precision. For example, at the SAXS/WAXS beamline at the Australian

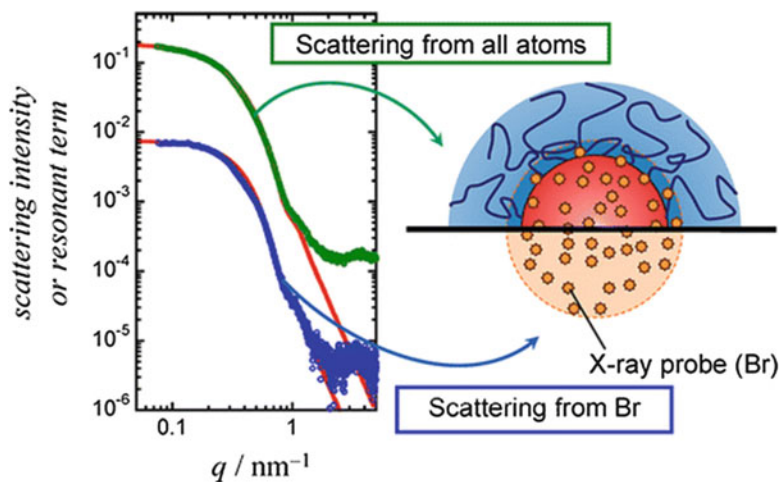


Fig. 10.11 Reproduced Graphical Abstract with permission from reference by Sanada et al. (2013) illustrating the use of K-edge contrast for a brominated drug loaded into a micellar system

with the corona as well as the core of the micelles. Although this is only one limited example, it is expected that given the relatively common occurrence of bromine in drug molecular structures, and the growing access to synchrotron sources with tunable wavelength of X-rays that many more examples of such studies will be published in the future.

6.2 Application of Grazing Incidence SAXS in Pharmaceutical Applications

Grazing incidence small angle X-ray scattering (GI-SAXS) is a surface specific form of SAXS, where the incident X-ray beam is impinged on the surface of the sample at a critical angle to allow surface propagation of the beam, enhancing the area over which scattering can be collected, and controlling the depth of penetration into the sample. Koradia et al. have demonstrated the use of GI-SAXS to study the surface of tablets of a range of drug substances (Koradia et al. 2012). They found that amorphous domains exist on the surface of tablets, which increase with compression load, and depth-dependent solid state transformations.

GI-SAXS has also been used to probe the swelling behaviour of polymers in controlled release formulations of clarithromycin. Time dependent swelling behaviour and drug localization at the surface were able to be discriminated (Gomez-Burgaz et al. 2009).

7 Concluding Remarks

The field of small angle X-ray scattering is evolving at a great pace, largely due to the availability of synchrotron sources. There are a wide range of studies to be explored in both the solid state and soft matter fields of pharmaceutical science, and hopefully this chapter has raised some awareness of some of the opportunities that are emerging. To think that opportunities in the scattering field are now completely known is folly—to quote Brian Kobilka (Winner 2012 Nobel Prize in Chemistry for his work on G-coupled protein receptors), “If I had obtained the GPCR crystals in 1995 or even in 2000, it would not have helped because it took time for the synchrotron microfocus technology to catch up to solve their structure” (private communication). It is inevitable that new opportunities will arise as facilities are developed, and new sample environments invented that enable unique application to understanding pharmaceutical materials and drug delivery systems that no-one has yet dreamt of. Specific challenges that not yet reality would include in vivo scattering on drug delivery materials, deconvolution of scattering in complex media, and increased development of molecule specific scattering approaches such as ASAXS.

References

- Aaltonen J, Alleso M, Mirza S, Koradia V, Gordon KC, Rantanen J (2009) Solid form screening—a review. *Eur J Pharm Biopharm* 71:23–37
- Aizawa H (2010) Morphology of polysorbate 80 (Tween 80) micelles in aqueous dimethyl sulfoxide solutions. *J Appl Cryst* 43:630–631
- Amenitsch H, Bernstorff S, Kriechbaum M, Lombardo D, Mio H, Rappolt M, Laggner P (1997) Performance and first results of the ELETTRA high-flux beamline for small-angle x-ray scattering. *J Appl Cryst* 30:872–876
- Anderson AC (2003) The process of structure-based drug design. *Chem Biol* 10:787–797
- Attwood D, Florence AT, Gillan JMN (1974) Micellar properties of drugs: properties of micellar aggregates of phenothiazines and their aqueous solutions. *J Pharm Sci* 63:988–993
- Bauwens CM (2012) X-ray scattering. Nova, New York
- Bernstein J (2007) Polymorphism in molecular crystals. Oxford University Press, Oxford
- Boetker J, Rades T, Rantanen J, Hawley A, Boyd BJ (2012) Structural elucidation of rapid solution-mediated phase transitions in pharmaceutical solids using in situ synchrotron SAXS/WAXS. *Mol Pharm* 9:2787–2791
- Borne J, Nylander T, Khan A (2001) Phase behavior and aggregate formation for the aqueous monoolein system mixed with sodium oleate and oleic acid. *Langmuir* 17:7742–7751
- Bouwstra JA, Gooris GS, Bras W, Talsma H (1993) Small angle X-ray scattering: possibilities and limitations in characterization of vesicles. *Chem Phys Lipids* 64:83–98
- Bunjes H, Rades T (2005) Thermotropic liquid crystalline drugs. *J Pharm Pharmacol* 57:807–816
- Caboi F, Amico GS, Pitzalis P, Monduzzi M, Nylander T, Larsson K (2001) Addition of hydrophilic and lipophilic compounds of biological relevance to the monoolein/water system. I. Phase behavior. *Chem Phys Lipids* 109:47–62
- Carey MC, Small DM (1970) The characteristics of mixed micellar solutions with particular reference to bile. *Am J Med* 49:590–608

- Chacón P, Diaz JF, Morán F, Andreu JM (2000) Reconstruction of protein form with X-ray solution scattering and a genetic algorithm. *J Mol Biol* 299:1289–1302
- Chang CM, Bodmeier R (1997) Effect of dissolution media and additives on the drug release from cubic phase delivery systems. *J Control Release* 46:215–222
- Clogston J, Rathman J, Tomasko D, Walker H, Caffrey M (2000) Phase behavior of a monoacyl-glycerol (Myverol 18-99K)/water system. *Chem Phys Lipids* 107:191–220
- Davies JM, Tsuruta H, May AP, Weis WI (2005) Conformational changes of p97 during nucleotide hydrolysis determined by small-angle X-ray scattering. *Structure* 13:183–195
- Deschamps J (2005) The role of crystallography in drug design. *AAPS J* 7:E813–E819
- Dong LA, Li J, Jian WS, Zhang L, Wu MS, Shi HL, Luo SQ (2014) Emphysema early diagnosis using X-ray diffraction enhanced imaging at synchrotron light source. *Biomed Eng Online* 13.
- Dong Y-D, Boyd BJ (2011) Applications of X-ray scattering in pharmaceutical science. *Int J Pharm* 417:101–111
- Dong YD, Larson I, Hanley T, Boyd BJ (2006) Bulk and dispersed aqueous phase behavior of phytantriol: effect of vitamin E acetate and F127 polymer on liquid crystal nanostructure. *Langmuir* 22:9512–9518
- Dora CL, Silva LFC, Putaux JL, Nishiyama Y, Pignot-Paintrand I, Borsali R, Lemos-Senna E (2012) Poly(ethylene glycol) hydroxystearate-based nanosized emulsions: effect of surfactant concentration on their formation and ability to solubilize quercetin. *J Biomed Nanotechnol* 8:202–210
- Du JD, Liu Q, Salentinig S, Nguyen T-H, Boyd BJ (2014) A novel approach to enhance the mucoadhesion of lipid drug nanocarriers for improved drug delivery to the buccal mucosa. *Int J Pharm* 471:358–365
- Dupuy C, Auvray X, Petipas C, Rico-Lattes I, Lattes A (1997) Anomeric effects on the structure of micelles of alkyl maltosides in water. *Langmuir* 13:3965–3967
- Engstroem S, Engstrom L (1992) Phase behaviour of the lidocaine-monoolein-water system. *Int J Pharm* 79:113–122
- Feast GC, Hutt OE, Mulet X, Conn CE, Drummond CJ, Savage GP (2014) The high-throughput synthesis and phase characterisation of amphiphiles: a sweet case study. *Chem Eur J* 20:2783–2792
- Finì A, Fazio G, Feroci G (1995) Solubility and solubilization properties of non-steroidal anti-inflammatory drugs. *Int J Pharm* 126:95–102
- Fong W-K, Hanley T, Boyd BJ (2009) Stimuli responsive liquid crystals provide ‘on-demand’ drug delivery in vitro and in vivo. *J Control Release* 135:218–226
- Fong W-K, Hanley TL, Thierry B, Kirby N, Boyd BJ (2010) Plasmonic nanorods provide reversible control over nanostructure of self-assembled drug delivery materials. *Langmuir* 26:6136–6139
- Fong W-K, Malic N, Evans RA, Hawley A, Boyd BJ, Hanley TL (2012) Alkylation of spiropyran moiety provides reversible photo-control over nanostructured soft materials. *Biointerphases* 7 (1–4):3
- Fong W-K, Salentinig S, Prestidge CA, Mezzenga R, Hawley A, Boyd BJ (2014) Generation of geometrically ordered lipid-based liquid crystalline nanoparticles using biologically relevant enzymatic processing. *Langmuir* 30(19):5373–5377
- Formariz TP, Chiavacci LA, Sarmiento VHV, Franzini CM, Silva AA Jr, Scarpa MV, Santilli CV, Egito EST, Oliveira AG (2008) Structural changes of biocompatible neutral microemulsions stabilized by mixed surfactant containing soya phosphatidylcholine and their relationship with doxorubicin release. *Colloids Surf B Biointerfaces* 63:287–295
- Glatter O, Kratky O (1982) Small angle X-ray scattering. Academic, London
- Gomez-Burgaz M, Torrado G, Torrado S (2009) Characterization and superficial transformations on mini-matrices made of interpolymer complexes of chitosan and carboxymethylcellulose during in vitro clarithromycin release. *Eur J Pharm Biopharm* 73:130–139
- Gradzielski M (2012) Dynamics of self-assembled systems studied by neutron scattering: current state and perspectives. *Eur Phys J Spec Top* 213:267–290

- Greco K, Bogner R (2012) Solution-mediated phase transformation: significance during dissolution and implications for bioavailability. *J Pharm Sci* 101:2996–3018
- Guinier A (1959) Heterogeneities in solid solutions. In: Frederick S, David T (eds) *Solid state physics*. Academic, New York, pp 293–398
- Gutiérrez-Pichel M, Barbosa S, Taboada P, Mosquera V (2003) Surface properties of some amphiphilic antidepressant drugs in different aqueous media. *Colloids Polym Sci* 281:575–579
- He, Garamus VM, Funari SS, Malfois M, Willumeit R, Niemeyer B (2002) Comparison of small-angle scattering methods for the structural analysis of octyl- β -maltopyranoside micelles. *J Phys Chem B* 106:7596–7604
- Hilfiker R (1991) SAXS studies on structure formation in microemulsion-triblock copolymer systems. *Ber Bunsen Ges Phys Chem* 95:1227–1232
- Hilfiker R, Blatter F, Raumer MV (2006) Relevance of solid-state properties for pharmaceutical products, polymorphism: in the pharmaceutical industry. Wiley-VCH Verlag GmbH & Co. KGaA, New York, pp 1–19
- Hirai M, Kawai-Hirai R, Iwase H, Hayakawa T, Kawabata Y, Takeda T (2002) Effect of proteins on dynamics of water-in-oil AOT microemulsions. *Appl Phys A Mater Sci Process* 74:s1254–s1256
- Hirai M, Kawai-Hirai R, Takizawa T, Yabuki S, Nakamura K, Hirai T, Kobayashi K, Amemiya Y, Oya M (1995a) Aerosol-OT reversed micellar formation at low water-surfactant ratio studied by synchrotron radiation small-angle X-ray scattering. *J Phys Chem* 99:6652–6660
- Hirai M, Takizawa T, Yabuki S, Hirai T, Hayashi K (1996) Thermotropic structural change of disialoganglioside micelles studied by using synchrotron radiation small-angle X-ray scattering. *J Phys Chem* 100:11675–11680
- Hirai M, Takizawa T, Yabuki S, Kawai-Hirai R, Oya M, Nakamura K, Kobashi K, Amemiya Y (1995b) Structure and reactivity of aerosol-OT reversed micelles containing [small alpha]-chymotrypsin. *J Chem Soc Faraday Trans* 91:1081–1089
- Hura GL, Menon AL, Hammel M, Rambo RP, Poole Ii FL, Tsutakawa SE, Jenney FE Jr, Classen S, Frankel KA, Hopkins RC, Yang S-j, Scott JW, Dillard BD, Adams MWW, Tainer JA (2009) Robust, high-throughput solution structural analyses by small angle X-ray scattering (SAXS). *Nat Methods* 6:606–612
- Ianeselli L, Zhang F, Skoda MWA, Jacobs RMJ, Martin RA, Callow S, Prévost S, Schreiber F (2010) Protein-protein interactions in ovalbumin solutions studied by small-angle scattering: effect of ionic strength and the chemical nature of cations. *J Phys Chem B* 114:3776–3783
- Joshi JV, Aswal VK, Goyal PS (2007) Combined SANS and SAXS studies on alkali metal dodecyl sulphate micelles. *J Phys Condens Matter* 19:196219
- Kataoka K, Harada A, Nagasaki Y (2001) Block copolymer micelles for drug delivery: design, characterization and biological significance. *Adv Drug Deliv Rev* 47:113–131
- Kataoka M, Kuwajima K, Tokunaga F, Goto Y (1997) Structural characterization of the molten globule of α -lactalbumin by solution X-ray scattering. *Protein Sci* 6:422–430
- Kirby NM, Mudie ST, Hawley AM, Cookson DJ, Mertens HDT, Cowieson N, Samardzic-Boban V (2013) A low-background-intensity focusing small-angle X-ray scattering undulator beamline. *J Appl Cryst* 46:1670–1680
- Koradia V, Tenho M, de Diego HL, Ringkjøbing-Elema M, Møller-Sønnergaard J, Salonen J, Lehto VP, Rantanen J (2012) Investigation of solid phase composition on tablet surfaces by grazing incidence X-ray diffraction. *Pharm Res* 29:134–144
- Kurz JL (1962) Effects of micellisation on the kinetics of the hydrolysis of monoalkyl sulfates. *J Phys Chem* 66:2239–2246
- Lee KWY, Nguyen T-H, Hanley T, Boyd BJ (2008) Nanostructure of liquid crystalline matrix determines in vitro sustained release and in vivo oral absorption kinetics for hydrophilic model drugs. *Int J Pharm* 365:190–199
- Lindner P (1991) Neutron, x-ray and light scattering: introduction to an investigative tool for colloidal and polymeric systems. In: *Proceedings of the European workshop on neutron, X-ray*

- and light scattering as an investigative tool for colloidal and polymeric systems, Bombannes, France, 27 May–2 June, 1990. North-Holland, Amsterdam
- Lipfert J, Columbus L, Chu VB, Lesley SA, Doniach S (2007) Size and shape of detergent micelles determined by small-angle X-ray scattering. *J Phys Chem B* 111:12427–12438
- Lipfert J, Doniach S (2007) Small-angle X-ray scattering from RNA, proteins, and protein complexes. *Annu Rev Biophys Biomol Struct* 36:307–327
- Liu L-Z, Cheng Z, Inomata K, Zhou S, Chu B (1999) Synchrotron SAXS and laser light scattering studies of aggregation behavior of poly(1,1-dihydroperfluorooctyl acrylate-*b*-vinyl acetate) diblock copolymer in supercritical carbon dioxide. *Macromolecules* 32:5836–5845
- Liu W, Wacker D, Wang C, Abola E, Cherezov V (2014) Femtosecond crystallography of membrane proteins in the lipidic cubic phase. *Philos Trans R Soc Lond B Biol Sci* 369:20130314.
- Lund R, Willner L, Monkenbusch M, Panine P, Narayanan T, Colmenero J, Richter D (2009) Structural observation and kinetic pathway in the formation of polymeric micelles. *Phys Rev Lett* 102:188301
- Mackeben S, Müller-Goymann CC (2000) Solubilization of timolol maleate in reversed micellar systems: measurement of particle size using SAXS and PCS. *Int J Pharm* 196:207–210
- Mandelkow E, Holmes K (1989) Synchrotron radiation as a source for X-ray diffraction the beginning, vol III, Synchrotron radiation in chemistry and biology. Springer, Berlin, pp 1–7
- Mukerjee P (1974) Micellar properties of drugs: micellar and nonmicellar patterns of self-association of hydrophobic solutes of different molecular structures—monomer fraction, availability, and misuses of micellar hypothesis. *J Pharm Sci* 63:972–981
- Mulet X, Conn CE, Fong C, Kennedy DF, Moghaddam MJ, Drummond CJ (2013) High-throughput development of amphiphile self-assembly materials: fast-tracking synthesis, characterization, formulation, application, and understanding. *Acc Chem Res* 46:1497–1505
- Mulet X, Kennedy DF, Conn CE, Hawley A, Drummond CJ (2010) High throughput preparation and characterisation of amphiphilic nanostructured nanoparticulate drug delivery vehicles. *Int J Pharm* 395:290–297
- Müller-Goymann CC (2002) Drug delivery—liquid crystals. In: Swarbrick J, Boylan JC (eds) *Encyclopedia of pharmaceutical technology*. Marcel Dekker, Inc., New York
- Nakano M, Teshigawara T, Sugita A, Leesajakul W, Taniguchi A, Kamo T, Matsuoka H, Handa T (2002) Dispersions of liquid crystalline phases of the monoolein/oleic acid/Pluronic F127 system. *Langmuir* 18:9283–9288
- Nielsen FS, Gibault E, Ljusberg-Wahren H, Arleth L, Pedersen AS, Mullertz A (2007) Characterization of prototype self-nanoemulsifying formulations of lipophilic compounds. *J Pharm Sci* 96:876–892
- Papadimitriou V, Xenakis A, Petit C, Pileni M (1994) Structural modifications of reverse micelles due to enzyme incorporation studied by SAXS. In: Ottewill R, Rennie A (eds) *Trends in colloid and interface science VIII*. Springer, Berlin, pp 226–228
- Patterson J, Bary A, Rades T (2002) Physical stability and solubility of the thermotropic mesophase of fenoprofen calcium as pure drug and in a tablet formulation. *Int J Pharm* 247:147–157
- Phan S, Hawley A, Mulet X, Waddington L, Prestidge CA, Boyd BJ (2013) Structural aspects of digestion of medium chain triglycerides studied in real time using sSAXS and cryo-TEM. *Pharm Res* 30:3088–3100
- Rades T, Müller-Goymann CC (1994) Melting behaviour and thermotropic mesomorphism of fenoprofen salts. *Eur J Pharm Biopharm* 40:277–282
- Rambo RP, Tainer JA (2010) Improving small-angle X-ray scattering data for structural analyses of the RNA world. *RNA* 16:638–646
- Ristori S, Oberdisse J, Grillo I, Donati A, Spalla O (2005) Structural characterization of cationic liposomes loaded with sugar-based carboranes. *Biophys J* 88:535–547

- Rodriguez-Spong B, Acciaccia A, Fleisher D, Rodriguez-Hornedo N (2008) pH-induced nanosegregation of ritonavir to lyotropic liquid crystal of higher solubility than crystalline polymorphs. *Mol Pharm* 5:956–967
- Salentinig S, Phan S, Darwish TA, Kirby N, Boyd BJ, Gilbert EP (2014) pH-responsive micelles based on caprylic acid. *Langmuir* 30:7296–7303
- Salvati A, Ristori S, Oberdisse J, Spalla O, Ricciardi G, Pietrangeli D, Giustini M, Martini G (2007) Small angle scattering and zeta potential of liposomes loaded with octa(carboranyl) porphyrazine. *J Phys Chem B* 111:10357–10364
- Sanada Y, Akiba I, Sakurai K, Shiraishi K, Yokoyama M, Mylonas E, Ohta N, Yagi N, Shinohara Y, Amemiya Y (2013) Hydrophobic molecules infiltrating into the poly(ethylene glycol) domain of the core/shell interface of a polymeric micelle: evidence obtained with anomalous small-angle X-ray scattering. *J Am Chem Soc* 135:2574–2582
- Sardet C, Tardieu A, Luzzati V (1976) Shape and size of bovine rhodopsin: a small-angle X-ray scattering study of a rhodopsin-detergent complex. *J Mol Biol* 105:383–398
- Scapin G (2006) Structural biology and drug discovery. *Curr Pharm Des* 12:2087–2097
- Schmiele M, Schindler T, Westermann M, Steiniger F, Radulescu A, Kriele A, Gilles R, Unruh T (2014) Mesoscopic structures of triglyceride nanosuspensions studied by small-angle X-ray and neutron scattering and computer simulations. *J Phys Chem B* 118:8808–8818
- Schmolzer S, Grabner D, Gradzielski M, Narayanan T (2002) Millisecond-range time-resolved small-angle X-ray scattering studies of micellar transformations. *Phys Rev Lett* 88:258301
- Schreier S, Malheiros SVP, de Paula E (2000) Surface active drugs: self-association and interaction with membranes and surfactants. Physicochemical and biological aspects. *Biochim Biophys Acta Biomembr* 1508:210–234
- Schütze W, Müller-Goymann CC (1998) Phase transformation of a liposomal dispersion into a micellar solution induced by drug-loading. *Pharm Res* 15:538–543
- Skalko N, Bouwstra J, Spies F, Stuart M, Frederik PM, Gregoriadis G (1998) Morphological observations on liposomes bearing covalently bound protein: studies with freeze-fracture and cryo electron microscopy and small angle X-ray scattering techniques. *Biochim Biophys Acta* 1370:151–160
- Svergun DI, Koch MHJ (2003) Small-angle scattering studies of biological macromolecules in solution. *Rep Prog Phys* 66:1735
- Takeuchi K, Wagner G (2006) NMR studies of protein interactions. *Curr Opin Struct Biol* 16:109–117
- Tangso KJ, Lindberg S, Hartley PG, Knott R, Spicer PT, Boyd BJ (2014) Formation of liquid crystalline structures in the bile salt—chitosan system and triggered release from lamellar phase bile salt—chitosan capsules. *ACS Appl Mater Interfaces* 6(15):12363–12371
- Torchilin VP (2001) Structure and design of polymeric surfactant-based drug delivery systems. *J Control Release* 73:137–172
- Wallace SJ, Li J, Nation RL, Prankerd RJ, Velkov T, Boyd BJ (2010) Self-assembly behavior of colistin and its prodrug colistin methanesulfonate: implications for solution stability and solubilization. *J Phys Chem B* 114:4836–4840
- Warren DB, Anby MU, Hawley A, Boyd BJ (2011) Real time evolution of liquid crystalline nanostructure during the digestion of formulation lipids using synchrotron small-angle X-ray scattering. *Langmuir* 27:9528–9534
- Weiss TM, Narayanan T, Gradzielski M (2008) Dynamics of spontaneous vesicle formation in fluorocarbon and hydrocarbon surfactant mixtures. *Langmuir* 24:3759–3766
- Weiss TM, Narayanan T, Wolf C, Gradzielski M, Panine P, Finet S, Helsby WI (2005) Dynamics of the self-assembly of unilamellar vesicles. *Phys Rev Lett* 94:038303
- Williams SP, Kuyper LF, Pearce KH (2005) Recent applications of protein crystallography and structure-guided drug design. *Curr Opin Chem Biol* 9:371–380
- Wörle G, Siekmann B, Bunjes H (2006) Effect of drug loading on the transformation of vesicular into cubic nanoparticles during heat treatment of aqueous monoolein/poloxamer dispersions. *Eur J Pharm Biopharm* 63:128–133

- Yaghmur A, Laggner P, Sartori B, Rappolt M (2008) Calcium triggered $L\alpha$ - H_2 phase transition monitored by combined rapid mixing and time-resolved synchrotron SAXS. *PLoS One* 3: e2072
- Zhang F, Allen AJ, Levine LE, Ilavsky J, Long GG, Sandy AR (2011) Development of ultra-small-angle X-ray scattering-X-ray photon correlation spectroscopy. *J Appl Cryst* 44:200–212
- Zhang F, Ilavsky J (2010) Ultra-small-angle X-ray scattering of polymers. *Polym Rev* 50:59–90
- Zhang F, Skoda MWA, Jacobs RMJ, Martin RA, Martin CM, Schreiber F (2006) Protein interactions studied by SAXS: effect of ionic strength and protein concentration for BSA in aqueous solutions. *J Phys Chem B* 111:251–259
- Zhang R, Marone PA, Thiyagarajan P, Tiede DM (1999) Structure and molecular fluctuations of n-alkyl- β -d-glucopyranoside micelles determined by X-ray and neutron scattering. *Langmuir* 15:7510–7519
- Zhu L, Qin Z-J, Zhou J-M, Kihara H (2004) Unfolding kinetics of dimeric creatine kinase measured by stopped-flow small angle X-ray scattering. *Biochimie* 86:127–132

Part III
Thermal Techniques

Chapter 11

Thermal Analysis of Pharmaceuticals

Sheng Qi

Abstract Thermal methods have been widely used and are well-established routine methods for pharmaceutical raw material and dosage form characterization. The conventional thermal methods all involve measuring a response from a material (usually in the form of energy/temperature or mass changes) as a result of applying heat to the sample. In this chapter the most widely used thermal analytical methods along with some more recently developed local thermal analysis and thermally based imaging methods are reviewed with regards to their working principle and applications in pharmaceutical product development. In the recent years, with the addition of the newly developed thermal imaging techniques, the capability of thermal analysis has broadened from conventional bulk sample analysis to also allowing more localized micron to sub-micron scale distribution and compositional analysis. The limitations of thermal methods for different applications are also discussed in relation to other characterization methods.

Keywords Differential scanning calorimetry • Hyper DSC • Thermogravimetric analysis • Localized thermal analysis • Amorphous • Crystallisation • Polymorphism • Physical stability

1 Introduction

The thermal properties of pharmaceutical raw materials and products are extremely important for understanding their processability and stability. Indeed, in many cases thermal measurements can be used to predict the physical and chemical stabilities of the materials. Thermal analytical methods include both classic thermal techniques, such as differential scanning calorimetry, for which the measurement of energy/temperature changes on heating are used to characterize a material's behaviour and more recently developed techniques where thermal methods are combined with other analytical techniques such as scanning atomic force microscopy. These have extended the capability of thermal analysis to allow imaging and

S. Qi (✉)

School of Pharmacy, University of East Anglia, Norwich, UK

e-mail: sheng.qi@uea.ac.uk

compositional identification. In this chapter, both conventional thermal analytical techniques as well as new developments in local thermal analysis and thermally based imaging technique are reviewed and the applications of these methods in the pharmaceutical field are discussed.

2 Theoretical Background of Thermal Analysis

2.1 Differential Scanning Calorimetry (DSC)

2.1.1 Conventional DSC

DSC is a thermal analysis technique, which was first commercially introduced in 1963 (Theeuwes et al. 1974). It provides qualitative and quantitative information as a function of time and temperature regarding thermal transitions in materials that involve endothermic or exothermic processes, or changes in heat capacity (Verdonck et al. 1999). In terms of instrumentation, there are two main types of DSC instruments, power compensation and heat flux. Power compensation DSC involves two separate furnaces for the reference and for the sample (Fig. 11.1). The common principle of power compensation DSC is to heat both the reference and the sample simultaneously in such a way that the temperature of the two is kept identical, and the difference in power required to maintain the temperature is measured (Reading and Craig 2006). Unlike power compensation DSC, which uses two furnaces, heat flux DSC uses two crucibles for the sample and for the reference within one furnace. They are both heated from the same source and the temperature difference between the sample and the reference over the heating profile is measured (Reading and Craig 2006).

For heat flux DSC, the output signal is then converted into the power difference as shown in the following equation:

$$dQ / dt = \Delta T/R \quad (11.1)$$

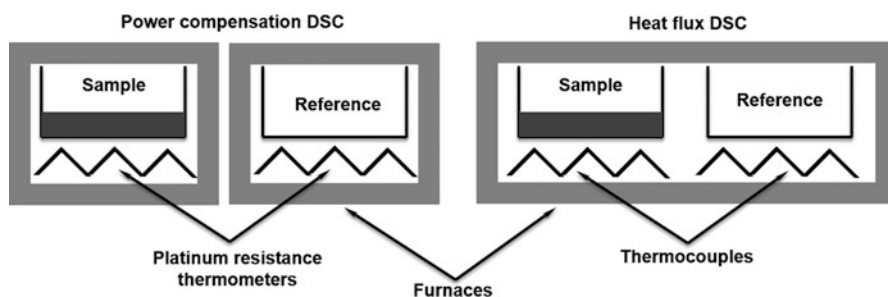


Fig. 11.1 Schematic illustrations of power compensation and heat flux DSC

where Q is the heat, t is the time, ΔT is the temperature difference between the sample and the reference and R is the thermal resistance of the heat paths between the furnace and the crucible. As described by Eq. (11.1), if the furnace and heat paths are truly symmetrical, the temperature difference between samples and reference is a measure of the difference in heat flow of the sample and reference. The total heat content of a material has a linear relationship to its heat capacity (C_p J/g °C), which is defined as the quantity of heat required to change the temperature of the material by 1 K:

$$C_p = dQ/dT \quad (11.2)$$

Rearranging this equation with time:

$$dQ / dt = C_p(dT/dt) \quad (11.3)$$

where dQ / dt is the heat flow and dT / dt is the heating rate. With this equation, the differential heat flow provides a measure of the sample heat capacity. DSC data is normally expressed as the heat flow as a function of temperature. Typical transitions can be measured using DSC including a range of first and second order phase transitions, such as melting, crystallisation, glass transition (T_g) and relaxation. As an example, Fig. 11.2 shows the thermal behaviour of amorphous paracetamol

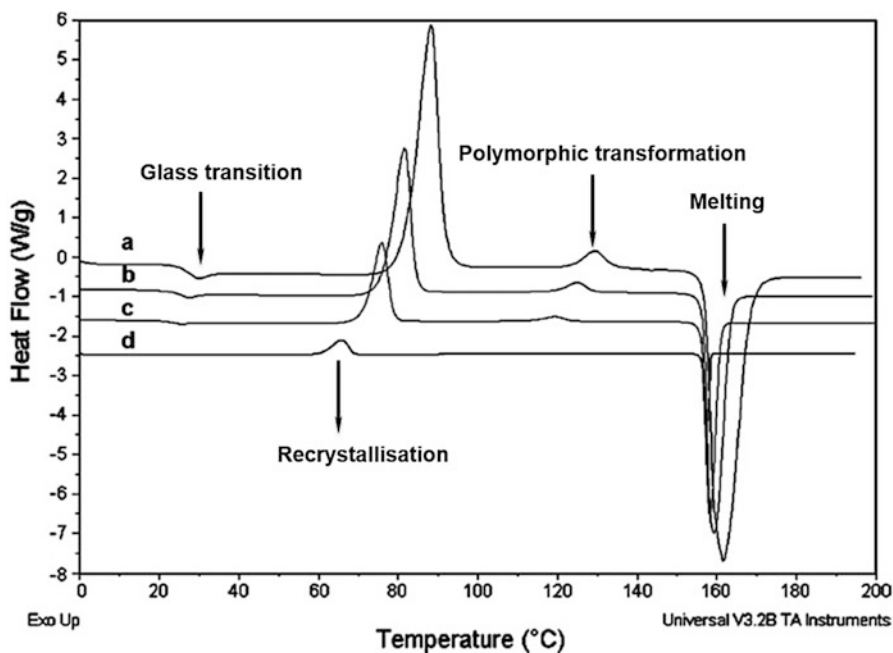


Fig. 11.2 DSC responses of amorphous paracetamol examined at (a) 20 °C/min; (b) 10 °C/min; (c) 5 °C/min; (d) 1 °C/min (Reproduced from Qi et al. 2008a, b)

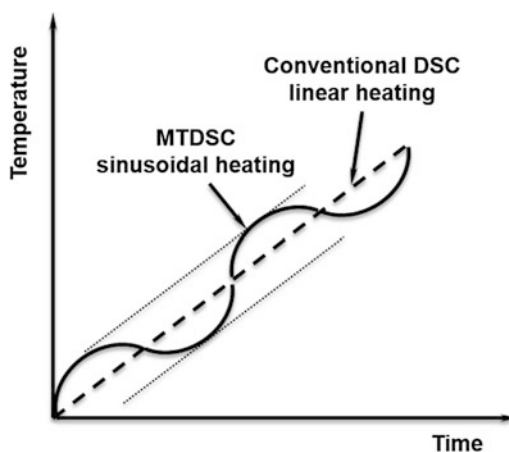
examined by DSC at different heat rates (Qi et al. 2008a, b). Due to the low T_g and physical instability of amorphous paracetamol on heating, glass transition, recrystallization, polymorphic form transformation and crystalline melting occurred as a sequence of responses of the sample heated in DSC (Qi et al. 2008a, b). It can be clearly seen that the crystallisation process is significantly affected by the heating rate of the DSC experiment, which highlighted the strong kinetic nature of the crystallisation behaviour.

2.1.2 Modulated Temperature Differential Scanning Calorimetry (MTDSC)

Conventional DSC mentioned above is a powerful tool to measure a wide range of thermal events such as melting accurately. However it often struggles to distinguish overlapping thermal events such as overlapped glass transitions and endothermic relaxation events, which can occur within the similar temperature range for many amorphous drugs and polymers (Reading and Craig 2006). MTDSC was designed to separate overlapping thermal events. Compared with conventional DSC, where a linear heating rate is applied, in MTDSC the sample follows a heating rate commonly with a sinusoidal modulated wave as seen in Fig. 11.3, and the uses of square and saw tooth modulated waves have also been reported. Sinusoidal modulation is overlaid on the linear ramp, namely, a perturbed heating or cooling process. As a result, there are three important parameters related to the MTDSC methodology, the average heating rate (the underlying heating rate), the amplitude of the modulation and the frequency of the modulation. Taking into account the contributions of these parameters, the heat flow signal of a MTDSC run can be described as follows:

$$dQ/dt = C_p \cdot dT/dt + f(t, T) \quad (11.4)$$

Fig. 11.3 Different scanning mode of conventional (linear) DSC and MTDSC (sine wave)



where dQ/dt is the total heat flow, dT/dt is the heating rate, C_p is the heat capacity, and $f(t,T)$ is a function of time and temperature that governs the response associated with the phase transition (Lacey et al. 2006). This equation shows that total heat flow is comprised of two contributions: one is a function of the heating rate (heating rate dependent and also called reversing component) and the other one is a function of time and temperature (temperature and time dependent and also called non-reversing component). The responses of heating rate dependent phase transitions tend to be larger when evaluated using faster heating rates and are often reversible transitions if multiple heating-cooling cycles applied. Temperature and time dependent transitions cannot be reversed once initiated and these transitions are termed as non-reversing transitions, such as relaxation and decomposition. Consequently, by separating heat signals into reversing and non-reversing components, overlapping reversing and non-reversing thermal events can be distinguished.

In addition to separating reversing and non-reversing thermal events, MTDSC is also able to measure the heat capacity more accurately in comparison to the conventional DSC. In MTDSC, the heat capacity data (C_p) is calculated by Lacey et al. (2006):

$$C_p = K_{cp}A_{MHF} / A_{MHR} \quad (11.5)$$

where K_{cp} is the heat capacity calibration constant, A_{MHF} is the amplitude of the modulated heat flow and A_{MHR} is the modulated heating rate. Therefore, the application of large amplitude in MTDSC can increase the heat capacity precision by reducing noise (Hill et al. 1999). In practice, adjusting the combination of amplitude, heating rate and period to suit the sample is extremely important for the effective use of MTDSC. As a rule of thumb, slow heating rate (<5 °C/min) should be used and the combination of all three parameters should allow at least six modulations over the course of the transition of interest.

2.1.3 Hyper DSC

High speed or high performance conventional DSC, also known as hyper DSC, operates at extremely fast heating rates from 200 °C/min up to 750 °C/min. Conventional DSC using slow (linear) heating rates (typically heating rate below 100 °C/min) can result in good resolution but poor sensitivity particularly for phase transitions that strongly affected by kinetic factors, whilst fast heating rates can result in poor resolution but good sensitivity (Gaisford 2008). Fast heating rates have the same total heat flow signal as in a DSC or MTDSC experiment. However as transitions occur over a shorter time period, the signal response to the thermal event appears larger (Lappalainen et al. 2006). One issue that can occur with conventional DSC with slow heating is that the heating process may alter the sample, before the thermal transition of interest is reached. Using fast heating rates these effects can be eliminated or reduced, allowing for the characterisation

of samples in their “as received” state (Gabbott et al. 2003). This technique is also of particular advantage for materials possessing properties that may change upon prolonged exposure to increased temperatures like amorphous products or formulations of biological molecules (Gaisford 2008). For example, Saunders and co-workers reported the sensitivity for detecting the amorphous content of spray dried lactose increased from 10 % (w/w) for conventional DSC to 1.5 % (w/w) for hyper DSC with 500 °C/min (Saunders et al. 2004).

2.2 Thermogravimetric Analysis (TGA)

TGA is one of the oldest thermal analytical procedures and has been used extensively in the study of material science. The technique involves monitoring the weight change of the sample in a chosen atmosphere (usually nitrogen or air) as a function of temperature. The measurement is operated by applying a temperature programme to a closed sample furnace containing an electronic microbalance (for holding the sample), which allows the sample to be simultaneously weighed and heated in a controlled manner, and the mass, time and temperature to be captured. In the pharmaceutical industry, TGA is routinely used for thermal stability and volatile components analysis of pharmaceutical materials (Pyramides et al. 1995). In research and development phase of a pharmaceutical formulation, TGA can also be used to facilitate the evaluation of processing temperatures of thermally based manufacturing processes such as hot melt extrusion. It can determine the thermal stability of the drugs and polymers upon heating to assist with selecting the operation temperature in hot melt extrusion to avoid thermal degradation occurred in process. As an empirical method, TGA is often used to measure the moisture or residue solvent contents in processed materials. However, the drawback is that it has no capability to identify the chemical composition of lost solvent. Therefore in some studies TGA has been coupled with spectroscopic detection methods such as gas chromatography (GC and GC-MS) to allow the chemical identification of the volatile material liberated from the sample.

2.3 Scanning Probe Based Thermal Analysis

The coupling of thermal analysis with atomic force microscopy (AFM) gives the new generation of thermal analysis with the capability to allow thermal measurement to be performed at the selected point of interest. Such technique is often known as localised thermal analysis (LTA). LTA is an extension of conventional AFM, replacing conventional probes with thermal probes. The tips of these probes are composed of material with high resistance to electrical current. When an electrical current is applied, it causes the tip of the probe to become heated (Harding et al. 2007). The probes have a unique advantage in that not only can they be used as

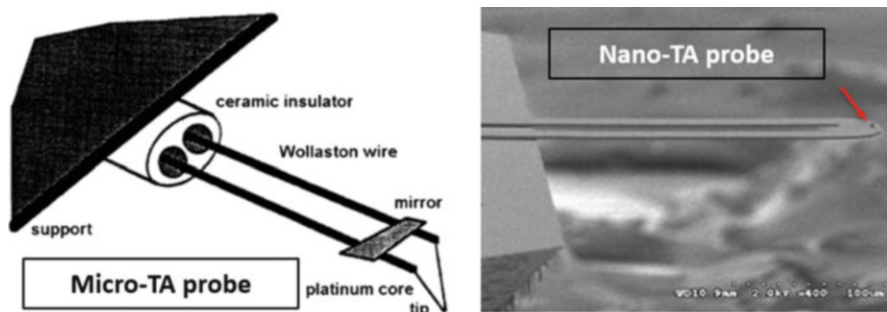


Fig. 11.4 Comparison of micro- and nano-thermal analysis probes: schematic design of micron size Wollaston wire thermal probe on the left and nano-TA probe on the right (Reproduced from Price et al. 1999 and Kjoller et al. 2010)

normal probes to generate topographical images but they can also be used as a localised heating source. The first LTA probe (called a Wollaston probe) was developed in 1994 and first used in 1996 by Hammiche et al. (1996). The probe consists of a 75 μm diameter silver wire with a 5 μm platinum filament core. The wire is manipulated to form a sharp point at which the silver is electrochemically removed to expose the filament (Fig. 11.4). This V-shaped wire is then used as the sensor to perform the functions mentioned above. As a result of the micron spatial resolution of the technique, the technique is known as micro-thermal analysis (μTA). There are several modes in which heated probes can be used but one of the most common is to carry out the thermal analysis on specific locations on a sample surface (Reading et al. 2001). Following the generation of a topographic image, the probe is placed in contact with a point of interest. The system monitors the position of the probe above the surface as the voltage is applied. Once the temperature at the end of the tip reach the softening temperature of the tested sample, such as a glass transition or melting transition, penetration of the tip into the sample will occur, which is reflected as a decreased deflection of the probe. Other applications of heated probe have also been reported. For example, the LTA probe can be used at a constant (heated) temperature as it is scanning across the sample, which is often known as heated-tip AFM. This temperature is normally selected as being above the softening temperature of one the components of interest in a multi-component sample. The image generated often can reveal the distribution of the components within the sample (Harding et al. 2007).

Recently, thermal probes with the similar dimensions to conventional tapping mode AFM probes have been invented, which allows the application of LTA studies at a increased spatial resolution (sub-micron) in comparison to the Wollaston probe (Reading et al. 2001). The new generation of thermal probe has a length of circa 200 μm and the height of the tip is below 1 μm (Harding et al. 2007). This provides the probe with a topographic spatial resolution of 5 nm (Kjoller et al. 2010). The probe is made of highly doped silica with boron or phosphorus which has a high electrical resistance (Harding et al. 2007). This allows the tip to be

heated when an electrical current is applied. With a sub-micron resolution, the technique is named nano-thermal analysis (nanoTA). A typical nanoTA tip is shown in Fig. 11.4.

A recent major development of LTA is the transition temperature mapping (TTM) technique (Kjoller et al. 2010). Instead of manually selecting the tested locations at the sample surface in conventional LTA, a defined region of interest at the surface of the sample can be selected. Within the selected region, each LTA tested point is a pixel of the final thermal image of the entire region produced. The LTA test at each point (pixel in the image) will stop once a thermal transition is detected and the probe will move on to the next adjacent point to continue the same process. The distance between the two consecutive pixels can be as close as 1 μm (Kjoller et al. 2010). As with other imaging techniques, the detected transition temperatures within that area are assigned a colour based on a particular palette and hence the coloured image is assembled based on different transition temperatures. As an imaging method, TTM can distinguish and reveal distribution of different materials or phases within a small area (i.e. 50 $\mu\text{m} \times 50 \mu\text{m}$). It can also “draw” the borderline between different phases in the same sample. Therefore, it can be useful to investigate the distribution of different materials within the sample at a sub-micron level (Qi et al. 2013). Figure 11.5 shows the possible identification crystallised region at the surface of an amorphous felodipine sample.

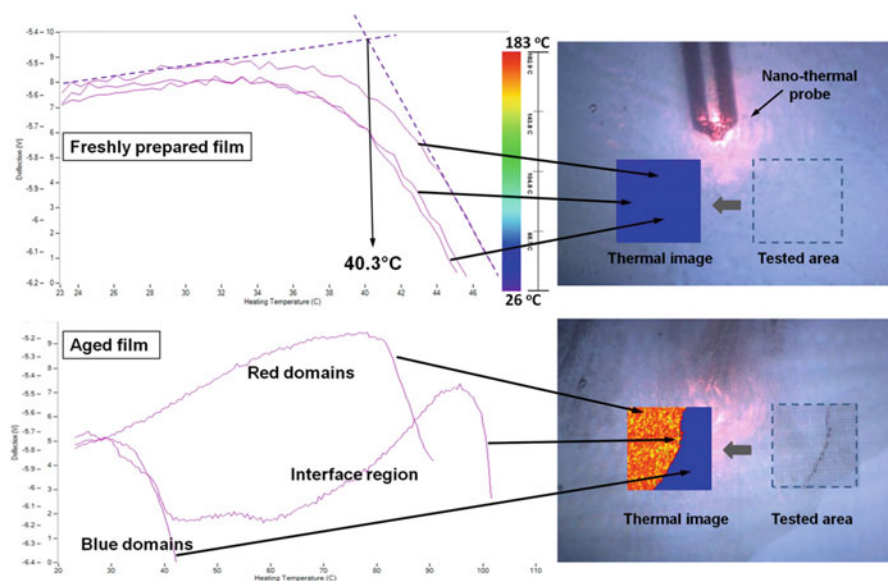


Fig. 11.5 Nano-TA profiles of the thin films of amorphous felodipine before and after aging (*left hand side panel*) and the optical images showing the tested areas on the film and the corresponding TTM images (*right hand side panel*) (Reproduced from Qi et al. 2013)

3 Physical and Chemical Phenomena Commonly Investigated Using Thermal Approaches

3.1 *Crystallisation*

Crystallisation is one of the most common processes that occur (both intentionally and unintentionally) for both active pharmaceutical ingredients and many excipient materials. It can take place in materials with low molecular weights, such as many drug molecules, lipids and salts, as well macromolecules including therapeutic proteins and polymers. The kinetic behaviour of crystallisation is often of significant importance in pharmaceutical formulation development and processing design in order to produce physically and chemically stable and effective medicines. Thermal analysis has been used to study the crystallisation behaviour of pharmaceutical materials in solution and in solid state (Málek 1999). The most commonly used approaches for studying crystallisation kinetics using thermal methods is applying Johnson-Mechl-Avrami (JMA) nucleation-growth model (Málek 1999). However, it should be emphasized that the JMA model is only valid if the crystallisation occurred under isothermal conditions at randomly dispersed second phase particles (Málek 1999). Although scanning thermal methods, such as DSC, often cannot accurately follow the isothermal crystallisation process the quantitative analysis of the formation of crystals over time by DSC (through measuring the melting enthalpy) can be used to construct the kinetic profile of the amount of crystallisation over time (Qi et al. 2008a, b, 2010a, b). These results can then be used in conjunction with the JMA model to explore the kinetic mechanism of the crystallisation process.

3.2 *Polymorphic Transformation*

Many pharmaceutical solids have more than one crystalline state with different lattice arrangements. The co-existence of different crystalline forms of the same chemical entity is known as polymorphism. Factors such as choice of solvent, temperature, additives, and preparation method can lead to the crystallisation of a substance into different polymorphic forms. Thermodynamically, there should be a single polymorph, which is the most stable form under a fixed condition. The importance of polymorphs in the pharmaceutical industry is that the physical properties of different polymorphs may be distinctively different. The physical properties of the crystalline material can have a direct impact on the dissolution rate and processability of the material. Furthermore, if the form obtained is not the most stable one, polymorphic transition may occur spontaneously. Thermal methods are the most frequently used characterization approach for determining the stability relationship between the polymorphs either being enantiotropic or monotropic (Burger and Ramberger 1979, Giron 2001). As seen in Fig. 11.6, for

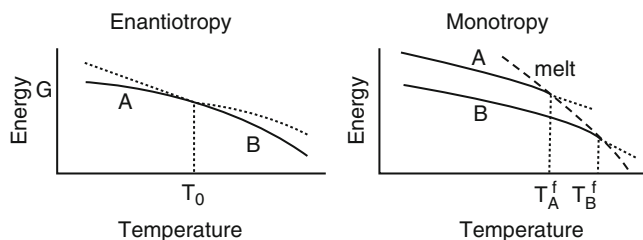


Fig. 11.6 Gibbs free energy diagrams of enantiotropic and monotropic polymorphs (Reproduced from Giron 2001)

enantiotropically related polymorphs, their free energies become equal at the transition temperature T_0 . Because the enthalpy of form A is lower than that of form B at T_0 , the transition is often detected as an endothermic transition by DSC. However, sometimes the transition temperature may be higher than the free energy crossing point which may lead to the melting of form A without polymorphic transformation. In this case, the enthalpy of fusion of form A is usually larger than that of form B. For monotropically related polymorphs, the stability relationship of the two polymorphs does not depend on the temperature below their melting points (no free energy crossing point). Therefore polymorphic transformation from metastable form B to form A may or may not occur on heating. If it occurs, this transition is an exothermic process. If it does not occur, metastable form B usually melts with a smaller enthalpy of fusion than that of the stable form A.

However, the kinetic influence from the conventional thermal scanning method often makes the polymorphic transformation data difficult to interpret. Recently, Qi and co-worker reported the development of modulated, quasi-isothermal and ultra-slow thermal method as a means of characterizing the α to γ indomethacin polymorphic transition (Qi and Craig 2012). By using both scanning and quasi-isothermal MTDSC to measure subtle heat capacity changes through the transformation, they were able to use Lissajous analysis to study the modulated heating signal in order to identify the poorly resolved polymorphic transformation (as seen in Fig. 11.7). Ultraslow heating rates (down to 0.04 °C/min) were also used to minimize the kinetic interference from the method. By combining these thermal methods, both kinetic and thermodynamic analyses of the polymorphic transformation via melt and recrystallization process between polymorphs of indomethacin was achieved.

3.3 Glass Transition

The glass transition temperature (T_g) is a kinetic parameter associated with molecular motion in an amorphous state, which can be measured using DSC and MTDSC. Below T_g the amorphous materials are “kinetically frozen” into the glassy state, and any further reduction in temperature only causes a small decrease in molecular

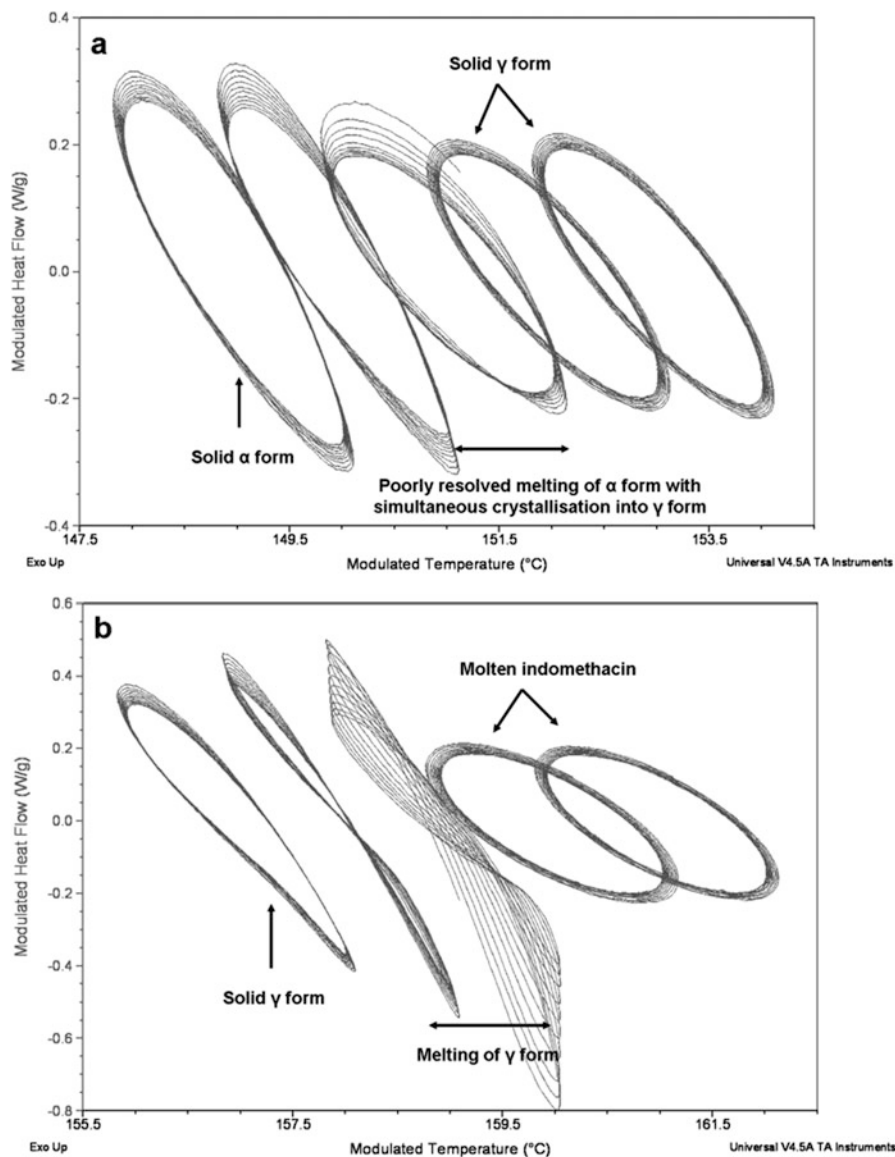


Fig. 11.7 Lissajous figures for the quasi-isothermal MTDSC studies of α indomethacin at the temperature range of (a) 148–153 $^{\circ}$ C; (b) 157–161 $^{\circ}$ C (Reproduced from Qi and Craig 2012)

motions of amorphous solids. Whereas above the T_g , amorphous solids will enter a rubbery state with significantly increased molecular motion (Hancock et al. 1995). Molecular motion has been related to the occurrence of the recrystallisation of amorphous solids and phase separation in amorphous solid dispersions (Hancock et al. 1995; Zhou et al. 2008).

For multicomponent amorphous systems, such as amorphous solid dispersions, glass transition temperatures can also be used as indicators to describe their physical state (Tobyn et al. 2009; van den Mooter et al. 2001). If a binary drug-polymer system is miscible, only a single T_g can be observed using DSC. The presences of two glass transitions indicate the presence of phase separation, which often is due to the poor miscibility between components (Craig et al. 2000). For miscible drug-polymer systems, if the T_g of the drug is lower than the T_g of the polymer, drugs can act as a plasticizer and reduces the T_g of the system. However this also manifests as an anti-plasticization effect provided by the polymer, which increases the T_g to a higher value in comparison to that of the pure amorphous drug, and stabilise the amorphous drug (Serajuddin 1999).

The Gordon-Taylor (G-T) equation is a useful tool in predicting the glass transition temperatures of drug-polymer solid dispersions (Tobyn et al. 2009; van den Mooter et al. 2001; Gordon and Taylor 1952). For completely miscible binary drug-polymer solid dispersions, the glass transition temperature of the system can be calculated by:

$$T_{gmix} = [(w_1 T_{g1}) + (K w_2 T_{g2})] / [w_1 + (K w_2)] \quad (11.6)$$

where T_{g1} , T_{g2} and T_{gmix} are the glass transition temperatures (in Kelvin) of component 1, 2 and the mixture, and w_1 and w_2 are the weight fractions of each component and K is a constant which can be calculated by:

$$K \approx (\rho_1 T_{g1}) / (\rho_2 T_{g2}) \quad (11.7)$$

where ρ_1 and ρ_2 are the true densities of each component. The application of the equation in predicting the miscibility of solid dispersions lies in the comparison between the theoretical and experimental T_{gmix} values of the system. The Gordon-Taylor equation relies on the assumption that the different components form an ideal mixture (Tobyn et al. 2009). Therefore, if the calculated and experimental T_{gmix} values are consistent, it may indicate that the system is miscible (Hancock and Zografi 1994). However, exceptions to this have been reported (Tobyn et al. 2009; van den Mooter et al. 2001; Khougazand and Clas 2000). The discrepancies of T_g s between the calculations from Gordon-Taylor equation and experimental data may be caused by two main reasons. Firstly, interactions between drugs and polymers in amorphous solid dispersions can affect the values obtained (van den Mooter et al. 2001). Positive deviation whereby the experimental value is higher than the G-T predicted value could occur if the interaction between drugs and polymers are stronger than what occurs between two drug molecules (Khougazand and Clas 2000), whereas negative deviation may be observed if the drug-polymer interaction is weaker than that between two drug molecules (Shamblin et al. 1998). Secondly, water sorption in amorphous solid dispersions can decrease the T_g value of the system via the strong plasticization effect of water sorption (Hancock and Zografi 1994; Roos 1997).

3.4 Molecular Mobility

The molecular mobility of drugs is commonly considered to be a key factor associated with the stability of amorphous solids and solid dispersions, since a high molecular mobility can lead to high tendency of recrystallisation and phase separation on aging (Hancock et al. 1995). On aging non-equilibrium amorphous materials tend to approach the equilibrium state by releasing the extra enthalpy and configurational entropy. This reducing extra energy process is termed as structural relaxation and the length of time over which the structural relaxation occurs is known as the relaxation time. Molecular mobility has a reciprocal relationship with the relaxation time constant (τ). In the Adam-Gibbs model (Hodge 1987), it is calculated as:

$$\tau = \tau_0 \exp(C / (TS_c)) \quad (11.8)$$

where τ is the molecular relaxation time constant, τ_0 is a constant, T is the absolute temperature, S_c is the configurational entropy, and C is a material dependent constant. This equation was further modified to the Adam-Gibbs-Vogel equation:

$$\tau = \tau_0 \exp(DT_0 / (T(1-T_0/T_f))) \quad (11.9)$$

where D is the strength parameter, T_0 is the temperature of zero molecular mobility, and T_f is the fictive temperature (Aso et al. 2004). The fictive temperature is defined as the temperature of intersection between the equilibrium liquid line and the non-equilibrium glass line. In most cases, T_f values are very close to T_g values, and therefore in calculations the T_f value can be replaced by the T_g value (Claudy et al. 1997; Badrinarayanan et al. 2007). By measuring the T_g and configurational entropy using thermal methods, the molecular mobility of amorphous solids can be estimated (Konno and Taylor 2008; Ahlneck and Zografı 1990).

3.5 Structural Relaxation

Two types of relaxations of amorphous materials have been defined at temperatures below and above the glass transition temperatures (Hancock and Zografı 1997). For molecules with low M_w , at temperatures below T_g , the dominant relaxation procedure is β -structural relaxation (also known as local molecular mobility), which can take place by means of the atomic movements within the molecular structure. For amorphous polymers, at temperatures below the T_g , β -structural relaxation refers to the vibrating of the side chains of the polymer (Böhmer et al. 1993). At temperatures higher than the T_g , the dominant relaxation is α -structural relaxation (also known as global molecular mobility), which could occur for both amorphous drug and polymer whereby an entire molecule will be mobilised (Böhmer et al. 1993).

These two types of relaxation can be detected by techniques such as DSC, dynamic mechanical analysis (DMA) and dielectric spectroscopy (Hancock and Zografi 1997; Bhugra et al. 2006; Hasegawa et al. 2009). For instance, when stored under ambient conditions for a certain time period, the relaxation enthalpy of amorphous indomethacin at the glass transition region can be detected on heating in DSC, and the relaxation enthalpy was a contribution of both α and β relaxations on aging (Hancock and Zografi 1997). For multicomponent system, such as solid dispersions, both relaxations of drugs and polymers are responsible for physical stability of the sample on aging (Hancock and Zografi 1997). As discussed earlier, the molecular mobility of an amorphous solid is associated with temperature, and will decrease with decreasing storage temperature leading to an increased physical stability. It has been used as an empirical practice that storing amorphous materials at temperatures 50 K below the T_g can sufficiently lower the molecular motions and leads to good physical stability of the amorphous material on aging (Hancock and Zografi 1997; Qian et al. 2010).

3.6 Dehydration and Decomposition

Dehydration and thermal decomposition behaviour of pharmaceutical active ingredients and excipients are commonly studied using TGA, or in some cases, TGA combined with FTIR, MS or GC/MS for identification of evaporated fume (Lever et al. 2000). In terms of dehydration studies, weight loss over the heating period is quantitatively related to the moisture loss within the sample (assuming no further thermally related decomposition occurs). Thermal decomposition temperatures can be identified by sharp and continuous significant weight loss of the samples during heating.

4 Applications of Thermal Analysis for the Characterisation of Pharmaceutical Raw Materials

4.1 Amorphous Drugs

Thermal analysis methods have been one of key streams of analytical techniques for the characterization of pharmaceutical amorphous solids including APIs and excipients. The physical parameters associated with their amorphous nature discussed earlier can all be fully investigated using thermal methods. For example, the α - and β -relaxation processes of amorphous indomethacin were studied using DSC (Vyazovkin and Dranca 2005). The β -relaxation was detected as a small endothermic relaxation peak that occurred in the similar temperature region of

the T_g . The activation of this relaxation process increased with increasing the annealing temperature of amorphous indomethacin. When the annealing temperature is well below the T_g , the β -relaxation fades significantly and leads to good physical instability of amorphous indomethacin (Vyazovkin and Dranca 2005). The crystallization kinetics of an amorphous API is another topic that has been widely studied using thermal methods such as DSC. Qi et al. reported the rapid but incomplete recrystallization behaviour of cyro-milled amorphous Etravirine at temperatures below the T_g of the amorphous drug measured using DSC and hyper DSC (Qi et al. 2010a, b). Furthermore, the effect of thermal history on the stability of amorphous material is also frequently studied using DSC. Amorphous paracetamol, as an example, shows a marked difference in recrystallization and polymorphic form conversion behaviour depending on the cooling rate that was used during sample preparation (Qi et al. 2008a, b).

4.2 *Pharmaceutical Polymers and Lipidic Excipients*

Thermal analysis methods are routine tests used in research and industry for the characterization of pharmaceutical polymers and lipids, including their T_g , melting and crystalline content and relaxation behaviour. Hydroxypropylmethylcellulose (HPMC) is a classical example of such practice. Ford reviewed the use of the thermal analysis for the characterization of HPMC as a raw excipient as well as in gels and formulated tablets. Various factors including pan types used for the analysis and thermal history of the sample were highlighted in the review in terms of their potential effect on the DSC data quality and interpretation of the results (Ford 1999). Semi-crystalline polymers such as PEGs are another example of a pharmaceutical excipient where thermal analysis is considered to be key for revealing the behaviour of the material. For example DSC has been used to investigate the miscibility of PEG and crystalline drug as a fast screening method for pre-formulation development (Thakral and Thakral 2013). Lipidic excipients such as TPGS, Gelucire and Poloxamer, all have distinct melting transitions which can be measured by DSC. Changes in the melting behaviour of these materials after drug incorporation or processing provide an indication of the occurrence drug-excipient interactions and the effect of processing on the excipients (Mosquera-Giraldo et al. 2014, Qi et al. 2008a, b).

4.3 *Polymer Blends*

Pharmaceutical polymer blends have been recently valued as a class of useful drug carrier materials with the advantage of having easily adjusted drug release profiles and enhanced formulation physical stability. The phase behaviour of a polymer blend can directly impact on the physical performance of the blends as a matrix.

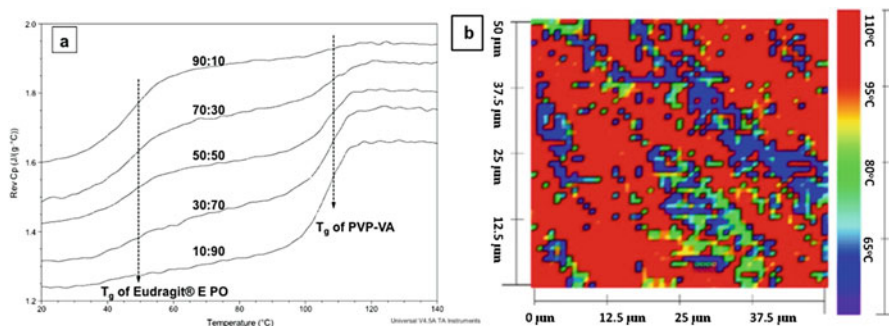


Fig. 11.8 (a) DSC profiles of the immiscible polymer blends with clearly separated two T_g s of the EUDRAGIT[®] EPO and Kollidon[®] VA 64 and (b) TTM result of the surface of hot melt extruded 50:50 (w/w) polymer blend (Reproduced from Yang et al. 2013)

Thermal analysis methods such as DSC, MTDSC, LTA and TTM have been all used to characterize pharmaceutical polymer blends. In Yang's study, MTDSC was used to estimate the miscibility between Eurgadit E PO and PVPVA by analyzing the T_g of the blend (Yang et al. 2013). Visualization of the phase separation of the processed polymer blend using TTM confirmed the immiscibility of the two polymers (as seen in Fig. 11.8). This immiscibility was found to be advantageous, enhancing the physical stability and *in vitro* dissolution rate of the formulation (Yang et al. 2013). MTDSC was used to investigate the influence of the PEG chain length on the miscibility of PEG/HPMC 2910 E5 polymer blends and the influence of polymer on the miscibility with itraconazole (Janssens et al. 2008). It was found that the polymer miscibility increased with decreasing chain length due to a decrease in the Gibbs free energy of mixing. Lower miscibility leads to more phase separated system indicated by a more rapid decrease of the T_g of the ternary solid dispersion and a high level of itraconazole recrystallization from the ternary solid dispersions. Marks and co-workers used DSC to assess the miscibility of the blends and to screen a wide range of polymer blends as potential carriers for oral drug delivery (Marks et al. 2014). As mentioned earlier, they also used T_g of the blend as a particular indicator to evaluate the miscibility between different combinations of hydrophilic and hydrophobic polymers.

5 Applications of Thermal Analysis for the Characterisation of Pharmaceutical Dosage Forms

5.1 Solid Dosage Forms

5.1.1 Physical Stability Evaluation

Thermal analysis has been widely used for monitoring the physical stability of solid dosage forms, such as detecting amorphous contents, polymorphic conversions of either API or crystalline excipients and excipient stabilities (lactose and crystalline

lipids as typical examples). Here solid dispersion formulations are used as an example to demonstrate how thermal methods can be used for not only monitoring but also predicting the physical stability of such formulations. An amorphous drug-polymer solid dispersion is a thermodynamically unstable system since the molecularly dispersed drugs (high energy level) in the system will tend to convert back to the more stable crystalline form (low energy level), leading to a physical instability on aging. Freshly prepared amorphous solid dispersions may have the drug molecularly dispersed in the polymeric carriers. On aging the physical instability of amorphous solid dispersions can be observed in the form of phase separation and recrystallization due to the relaxation of high energy-level drug molecules and molecular mobility of drugs under accelerated storage conditions. Recrystallization could then occur within the drug-rich phase whereby high concentration amorphous drug crystallizes to form the more stable crystalline state. Factors which can potentially affect the physical stability of amorphous solid dispersions have been investigated widely, and glass transition temperatures, molecular mobility, physical stability of amorphous drugs alone, miscibility between drugs and polymers and solid solubility of drugs in polymers have been considered to be key factors influencing the physical stability of solid dispersions (Hancock et al. 1995; Konno and Taylor 2008; Ng et al. 2013; Marsac et al. 2006). Amongst these, many can be studied using thermal analysis methods.

Crystallisation Tendency

Drug crystallization may take place if nuclei are present either in form of residual crystalline drug or foreign particles from the surrounding environment (Bruce et al. 2010). For an amorphous solid dispersion, drug crystallisation of a poorly water-soluble drug from the dispersion can significantly compromise the dissolution advantage an amorphous solid dispersion formulation can provide. Thermal analysis can be used as a tool for the evaluation of the tendency of crystallisation of amorphous drug either alone or present in a formulation, such as solid dispersions. For example, Yang used DSC and MTDSC to study the effect of milling on the physical stability of hot melt extruded solid dispersions (Yang et al. 2014). As seen in Fig. 11.9, DSC can clearly indicate the instability of milled amorphous solid dispersions formulations by the appearance of a recrystallization transition of the phase separated amorphous drug on heating and the separation of single T_g to a double T_g (Yang et al. 2014).

Quantitative Analysis of Crystallinity

The use of thermal methods including DSC and MTDSC for quantitative analysis of crystallinity of pharmaceutical materials including API, processed formulations and polymers has been widely reported (Grisedale et al. 2011; Kong and Hay 2002; Qi et al. 2010a, b). However, the absolute accuracy of the quantitative

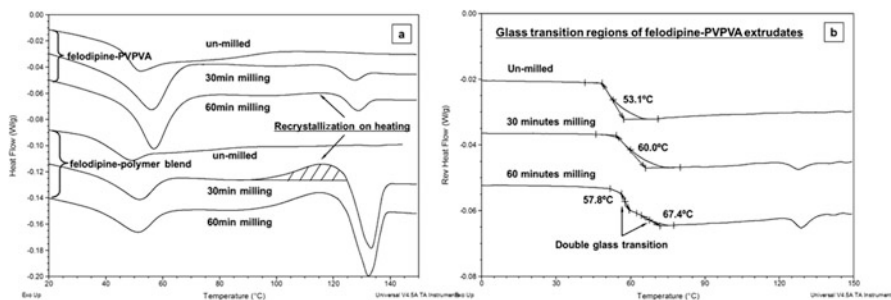


Fig. 11.9 (a) Total heat flow signals of the MTDSC results of 70% (w/w) felodipine loaded melt extrudates before and after milling; (b) reversing heat flow signals of 70% (w/w) felodipine–PVPVA melt extrudates before and after milling (Reproduced from Yang et al. 2014)

measurement of the crystalline content is still debatable. The common practice of using DSC for crystallinity measurement relies on the measurement of the enthalpy of the melting peak of the crystalline component and compares this to the melting enthalpy of the crystalline material with known purity. However, this often can only be used as an empirical approach for rough estimation of the crystallinity as the melting enthalpy of the crystalline material is affected by the presence of other excipients such as polymers and lipids. In addition, in many cases, recrystallization of the amorphous proportion of the material on heating during DSC testing can significantly affect the estimation of the crystalline content (Grisedale et al. 2011). Instead of using the melting enthalpy, heat capacity and recrystallization enthalpy can also be used to measure the amorphous content and as a means to indirectly calculate the crystalline content in a formulation with drug and excipients (Grisedale et al. 2011; Qi et al. 2010a, b).

Moisture-Induced Instability

Moisture can induce physical and chemical instability (such as degradation via hydrolysis reaction) in an API and in formulated pharmaceutical products (Ng et al. 2013; Ohtake and Shalaev 2013; Andronis et al. 1997; Rumondor et al. 2009). In terms of the physical instability of amorphous systems in particular, the sorption of moisture can promote the recrystallization of amorphous drug and phase separation of amorphous solid dispersions that initially containing molecularly dispersed drug in polymer matrices. The change in T_g and the presence of crystalline material in the samples after exposure to moisture, which can be measured using DSC and MTDSC, can often be used as indicators of physical instability.

5.1.2 Drug-Excipient Miscibility Estimation

As discussed earlier, for a solid dispersion, drug-polymer miscibility can significantly impact on the physical stability of system (Qian et al. 2010; Marsac et al. 2006; Li and Chiappetta 2008; Kawakami 2012). Miscibility is a concept originally applied the liquid solution theory to describe the mixing of two liquids whereby if two liquids are miscible a homogeneous solution by mixing of the two should be formed with any proportions of the two components. It has been applied in the polymer and pharmaceutical industries to describe whether the mixing of two polymers or drugs and polymers are thermodynamically favourable (Marsac et al. 2006, 2009; Higgins et al. 2005). Miscibility can be estimated by thermal methods based on the measurement of the melting point depression of the physical mixes of a crystalline drug and a polymer (Qian et al. 2010; Marsac et al. 2006, 2009; Hancock et al. 1997). Melting point depression method measures the reduced melting point of the crystalline drug when melted in the presence of a certain polymer. The melting point of a pure drug occurs when the chemical potential of the crystalline drug equals to the chemical potential of the molten drug. If the drug is miscible with a polymer, the chemical potential of the drug in the mixture with the polymer should be less than the chemical potential of the pure crystalline drug, and thus the reduced chemical potential will result in a depressed melting point of the drug in the presence of the miscible polymer (Nishi and Wang, 1975). In contrast, if the drug and polymer are immiscible, no melting point depression is expected due to the unchanged chemical potential brought by the presence of polymers.

Briefly, the melting point depression approach is a simple method to test the miscibility between drugs and polymers by running a physical mixture of the drug and the polymer in DSC on heating. The presence of a depressed melting point may indicate the drug and the polymer are miscible. Previously the melting point depression approach has been proved to be effective in predicting the miscibility between felodipine and nifedipine with PVP (Marsac et al. 2006). However, the depression of the melting point is heating rate dependent, which can affect the accuracy of the prediction.

Drug-polymer solid solubility is also a concept derived from solution theory, which considers the mixing of two liquids, solubility is defined as dissolving a solid-state material into a solvent until the equilibrium maximum concentration at a defined temperature and pressure (Qian et al. 2010; Marsac et al. 2006; Hancock et al. 1997). Several theoretical methods have been reported for the prediction of solid solubility of drugs in polymers (Marsac et al. 2006; Qi et al. 2010a, b; Hancock et al. 1997). Melting point depression combined with Flory-Huggins lattice based theory has been reported to predict solid solubility of felodipine and nifedipine in PVP (Marsac et al. 2006). The interaction parameter χ from Flory-Huggins theory can be calculated using the detected depressed melting points from drug-polymer physical mixtures with different ratios, and by further using the obtained interaction parathion the solid solubility of drugs in polymers can be predicted. However, the calculation used by this method is lengthy and in practice the depression of the drug melting is highly heating rate dependent. Therefore,

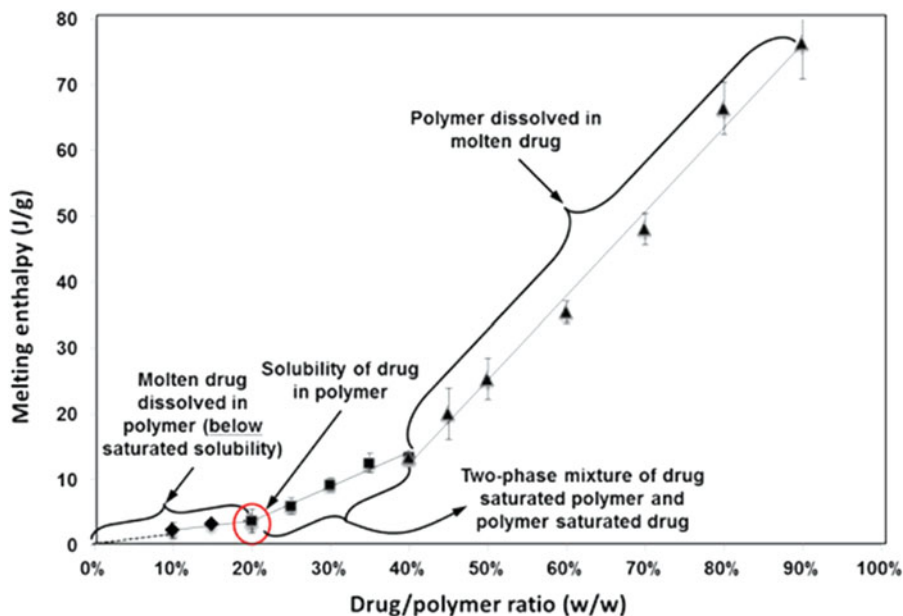


Fig. 11.10 Qi and Belton model prediction result of the miscibility between felodipine and EUDRAGIT E PO (Reproduced from Yang et al. 2014)

finding the appropriate experimental conditions for measuring melting point depression is also not straightforward.

Another thermal method for estimating drug-polymer solubility based on the measurement of melting enthalpy of crystalline drugs in physical mixtures with polymers by DSC was recently developed by Qi et al. (2010a, b). This model was a modification of a previous melting enthalpy based method (Felix et al. 1974). It assumed the dissolution of drugs in polymers on heating is endothermic and two possibilities, which involve drugs completely dissolved in polymers and *vice versa* were included in the model. The method was effectively used to predict the solubility of felodipine in Eudragit E PO, as seen in Fig. 11.10 (Yang et al. 2014). There are discrepancies between the solubility measured using this DSC based method and other prediction methods including melting point depression and solubility parameter methods. This is likely to be because of the nature of the characterization method, which is using the behaviour of the drug at temperatures close to the melting transition to predict the mixing behaviour with the polymer at ambient temperature.

5.1.3 Micro-scale Drug Distribution Uniformity Assessment

Although conventional thermal analysis methods are mostly used for characterize materials in bulk, the scanning and local thermal analysis have high precision for characterisation of materials at a micron to sub-micron scale. This offers the

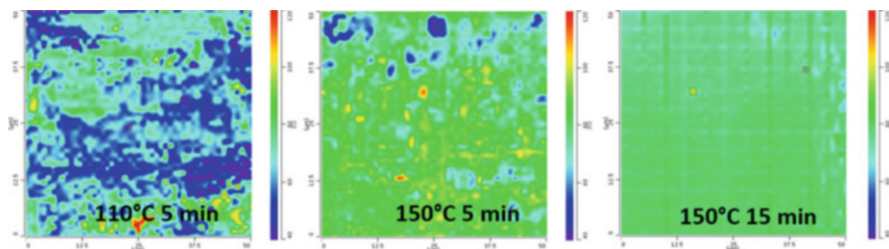


Fig. 11.11 TTM images of the surfaces of HME extrudates that processed at 110 and 150 °C with 5 min residence time and 150 °C with 15 min residence time (Reproduced from Moffat et al. 2014)

possibility of using these methods to study the distribution of drug or certain excipients within a formulation. This has been achieved by other imaging methods such as IR and confocal Raman imaging. However, each imaging method has advantages and limitations. The essential requirement for successful application of vibrational spectroscopic based imaging methods is to have sufficient separation of the vibrational bands used to identify the drug and excipients. If this is not available, local thermal analysis and thermal imaging method are good alternatives for studying the drug distribution within a dosage form by using the thermal transition temperature difference between the drug and other excipients. As seen in Fig. 11.11, Moffat used TTM to map out the micro-phase separation of a series of cyclosporine A containing solid dispersions processed using hot melt extrusion under different operational parameters (Moffat et al. 2014). The presence of colour-coded domains is an indication of the separation and distribution of phases (polymer-rich and drug-rich domains) in the formulation. The results clearly demonstrated that with increasing the processing temperature and residence time, a significant improvement in the homogeneity with a narrow distribution of transition temperatures could be obtained.

5.2 *Semi-solid and Liquid Dosage Forms*

DSC and high sensitivity DSC are also often used to characterize semi-solid and liquid formulations, such as semi-solid dispersions, gels and liquid suspensions. For semi-solid formulations, DSC can provide phase transition information relating to the formulation, which can be used to understand drug-excipient interactions. Gelucire 44/14 is one example of a semi-solid excipient and it has been widely used as semi-solid dispersion matrix for enhancing the *in vitro* dissolution and *in vivo* bioavailability of many poorly soluble drugs (da Fonseca Antunes et al. 2013). The broadening and depression of the melting transition of Gelucire and the disappearance of the melting peak of crystalline drug has been used an indication of the solubilisation of drug in the lipid and the formation of semi-solid dispersions (Hussein et al. 2012). DSC has a unique application in studying the

interactive behaviour of water molecules in the formulations with the polymer/surfactant in gels and solutions (Schulz et al. 2000). DSC can allow the identification of non-frozen water (highly interactive water bound with polymer/surfactants at a molecular level), freezable bound water, and free water by detecting the different melting transitions of different type of water (Schulz et al. 2000). DSC can also be used to study liquid suspensions. Qi used high sensitivity DSC to study the interactions of saturated fatty acids in alkaline buffer solution (Qi et al. 2008a, b). The in solution results confirmed the prediction of the occurrence of interactions observed in the DSC data of the dried fatty acids microspheres.

6 Conclusion

Thermal and mechanical analysis are extremely useful characterization methods for studying a highly diverse range of physical chemistry issues associated with drug and formulation development in the pharmaceutical industry. With the continuous development of new thermal analytical methods and thermal methods combined with spectroscopic and imaging methods, a wider range of sample forms and sizes can be studied and the application of thermal analysis in pharmaceutical product development and production is likely to be significantly extended.

References

- Ahneck C, Zografi G (1990) The molecular basis of moisture effects on the physical and chemical stability of drugs in the solid state. *Int J Pharm* 62:87–95
- Andronis V, Yoshioka M, Zografi G (1997) Effects of sorbed water on the crystallization of indomethacin from the amorphous state. *J Pharm Sci* 86:346–351
- Aso Y, Yoshioka S, Kojima S (2004) Molecular mobility-based estimation of the crystallization rates of amorphous nifedipine and phenobarbital in poly(vinylpyrrolidone) solid dispersions. *J Pharm Sci* 93:384–391
- Badrinarayanan P, Zheng W, Li Q et al (2007) The glass transition temperature versus the fictive temperature. *J Non-Cryst Solids* 353:2603–2612
- Bhugra C, Shmeis R, Krill S et al (2006) Predictions of onset of crystallization from experimental relaxation times I—Correlation of molecular mobility from temperatures above the glass transition to temperatures below the glass transition. *Pharm Res* 23:2277–2290
- Böhmer KLNR, Angell CA, Plazek DJ (1993) Nonexponential relaxations in strong and fragile glass formers. *J Chem Phys* 99:9
- Bruce CD, Fegely KA, Rajabi-Siahboomi AR et al (2010) The influence of heterogeneous nucleation on the surface crystallization of guaifenesin from melt extrudates containing Eudragit® L10055 or Acryl-EZE®. *Eur J Pharm Biopharm* 75:71–78
- Burger A, Ramberger R (1979) On the polymorphism of pharmaceuticals and other molecular crystals. II. *Microchim Acta* 72:273–316

- Claudy P, Jabrane S, Létouffé JM (1997) Annealing of a glycerol glass: enthalpy, fictive temperature and glass transition temperature change with annealing parameters. *Thermochim Acta* 293:1–11
- Craig DQM, Barsnes M, Royall P et al (2000) An evaluation of the use of modulated temperature DSC as a means of assessing the relaxation behaviour of amorphous lactose. *Pharm Res* 17:696–700
- da Fonseca Antunes AB, De Geest BG, Vervaeet C et al (2013) Gelucire 44/14 based immediate release formulations for poorly water-soluble drugs. *Drug Dev Ind Pharm* 39:791–798
- Felix T, Anwar H, Takeru H (1974) Quantitative analytical method for determination of drugs dispersed in polymers using differential scanning calorimetry. *J Pharm Sci* 63:427–429
- Ford JL (1999) Thermal analysis of hydroxypropylmethylcellulose and methylcellulose: powders, gels and matrix tablets. *Int J Pharm* 179:209–228
- Gabbott P, Clarke P, Mann T et al (2003) A high-sensitivity, high-speed DSC technique: measurement of amorphous lactose. *Am Lab* 35:17
- Gaisford S (2008) Fast-scan differential scanning calorimetry. *Eur Pharm Rev* 13:83–89
- Giron D (2001) Investigations of polymorphism and pseudo-polymorphism in pharmaceuticals by combined thermoanalytical techniques. *J Therm Anal Calorim* 64:37–60
- Gordon M, Taylor J (1952) Ideal copolymers and the second-order transitions of synthetic rubbers. I. Non-crystalline polymers. *J Appl Chem* 2:493–500
- Grisedale L, Jamieson MJ, Belton PS et al (2011) Characterization and quantification of amorphous material in milled and spray-dried salbutamol sulfate: a comparison of thermal, spectroscopic, and water vapor sorption approaches. *J Pharm Sci* 100:3114–3129
- Hammiche A, Pollock HM, Song M et al (1996) Localized thermal analysis using a miniaturized resistive probe. *Rev Sci Instrum* 67:4268–4274
- Hancock B, Zografi G (1994) The relationship between the glass transition temperature and the water content of amorphous pharmaceutical solids. *Pharm Res* 11:471–477
- Hancock BC, Zografi G (1997) Characteristics and significance of the amorphous state in pharmaceutical systems. *J Pharm Sci* 86:1–12
- Hancock B, Shamblin S, Zografi G (1995) Molecular mobility of amorphous pharmaceutical solids below their glass transition temperatures. *Pharm Res* 12:799–806
- Hancock BC, York P, Rowe RC (1997) The use of solubility parameters in pharmaceutical dosage form design. *Int J Pharm* 148:1–21
- Harding L, King W, Dai X et al (2007) Nanoscale characterisation and imaging of partially amorphous materials using local thermomechanical analysis and heated tip AFM. *Pharm Res* 24:2048–2054
- Hasegawa S, Ke P, Buckton G (2009) Determination of the structural relaxation at the surface of amorphous solid dispersion using inverse gas chromatography. *J Pharm Sci* 98:2133–2139
- Higgins JS, Tambasco M, Lipson JEG (2005) Polymer blends; stretching what we can learn through the combination of experiment and theory. *Prog Polym Sci* 30:832–843
- Hill VL, Craig DQM, Feely LC (1999) The effects of experimental parameters and calibration on MTDSC data. *Int J Pharm* 192:21–32
- Hodge IM (1987) Effects of annealing and prior history on enthalpy relaxation in glassy polymers. 6. Adam-Gibbs formulation of nonlinearity. *Macromolecules* 20:2897–2908
- Hussein A, El-Menshaweh S, Afouna M (2012) Enhancement of the in-vitro dissolution and in-vivo oral bioavailability of silymarin from liquid-filled hard gelatin capsules of semisolid dispersion using Gelucire 44/14 as a carrier. *Pharmazie* 67:209–214
- Janssens S, Denivelle S, Rombaut P et al (2008) Influence of polyethylene glycol chain length on compatibility and release characteristics of ternary solid dispersions of itraconazole in polyethylene glycol/hydroxypropylmethylcellulose 2910 E5 blends. *Eur J Pharm Sci* 35:203–210
- Kawakami K (2012) Miscibility analysis of particulate solid dispersions prepared by electrospray deposition. *Int J Pharm* 433:71–78
- Khoughazand KS, Clas D (2000) Crystallization inhibition in solid dispersions of MK-0591 and poly(vinylpyrrolidone) polymers. *J Pharm Sci* 89:1325–1334

- Kjoller K, Rose J, Sahagian K (2010) Transition temperature microscopy: nanoscale thermal analysis for micron- and submicron-scale devices. *Am Lab* 913:598
- Kong Y, Hay JN (2002) The measurement of the crystallinity of polymers by DSC. *Polymer* 43:3873–3878
- Konno H, Taylor L (2008) Ability of different polymers to inhibit the crystallization of amorphous felodipine in the presence of moisture. *Pharm Res* 25:969–978
- Lacey A, Price D, Reading M (2006) Theory and practice of modulated temperature differential scanning calorimetry. In: Reading M, Hourston D (eds) *Modulated temperature differential scanning calorimetry*. Springer, New York, pp 1–81
- Lappalainen M, Pitkänen I, Harjunen P (2006) Quantification of low levels of amorphous content in sucrose by hyperDSC. *Int J Pharm* 307:150–155
- Lever TJ, Price DM, Warrington SB (2000) Evolved gas collection from a thermogravimetric analyzer and identification by gas chromatography–mass spectrometry. In: *Proceedings of the twenty-eighth conference of the North American Thermal Analysis Society, Savannah, Georgia, October 2000*
- Li J, Chiappetta D (2008) An investigation of the thermodynamic miscibility between VeTPGS and polymers. *Int J Pharm* 350:212–219
- Málek J (1999) Crystallization kinetics by thermal analysis. *J Therm Anal Calorim* 56:763–769
- Marks JA, Wegiel LA, Taylor LS et al (2014) Pairwise polymer blends for oral drug delivery. *J Pharm Sci* 103:2871–2883
- Marsac P, Shamblin S, Taylor L (2006) Theoretical and practical approaches for prediction of drug–polymer miscibility and solubility. *Pharm Res* 23:2417–2426
- Marsac P, Li T, Taylor L (2009) Estimation of drug–polymer miscibility and solubility in amorphous solid dispersions using experimentally determined interaction parameters. *Pharm Res* 26:139–151
- Moffat JG, Qi S, Craig D (2014) Spatial characterization of hot melt extruded dispersion systems using thermal atomic force microscopy methods: the effects of processing parameters on phase separation. *Pharm Res* 31:1744–1752
- Mosquera-Giraldo L, Trasi NS, Taylor LS (2014) Impact of surfactants on the crystal growth of amorphous celecoxib. *Int J Pharm* 461:251–257
- Ng YC, Yang Z, McAuley WJ et al (2013) Stabilisation of amorphous drugs under high humidity using pharmaceutical thin films. *Eur J Pharm Biopharm* 84:555–565
- Nishi T, Wang TT (1975) Melting point depression and kinetic effects of cooling on crystallization in poly(vinylidene fluoride)-poly(methyl methacrylate) mixtures. *Macromolecules* 8:909–915
- Ohtake S, Shalaev E (2013) Effect of water on the chemical stability of amorphous pharmaceuticals: I. Small molecules. *J Pharm Sci* 102:1139–1154
- Price DM, Reading M, Hammiche A et al (1999) Micro-thermal analysis: scanning thermal microscopy and localised thermal analysis. *Int J Pharm* 192:85–96
- Pyramides G, Robinson JW, William Zito S (1995) The combined use of DSC and TGA for the thermal analysis of atenolol tablets. *J Pharm Biomed Anal* 13:103–110
- Qi S, Craig DQM (2012) The development of modulated, quasi-isothermal and ultraslow thermal methods as a means of characterizing the α to γ indomethacin polymorphic transformation. *Mol Pharm* 9:1087–1099
- Qi S, Avalle P, Saklatvala R, Craig DQM (2008a) An investigation into the effects of thermal history on the crystallisation behaviour of amorphous paracetamol. *Eur J Pharm Biopharm* 69:364–371
- Qi S, Deutsch D, Craig DQ (2008b) An investigation into the mechanisms of drug release from taste-masking fatty acid microspheres. *J Pharm Sci* 97:3842–3854
- Qi S, Weuts I, De Cort S et al (2010a) An investigation into the crystallisation behaviour of an amorphous cryomilled pharmaceutical material above and below the glass transition temperature. *J Pharm Sci* 99:196–208

- Qi S, Belton P, Nollenberger K et al (2010b) Characterisation and prediction of phase separation in hot-melt extruded solid dispersions: a thermal, microscopic and NMR relaxometry study. *Pharm Res* 27:1869–1883
- Qi S, Moffat JG, Yang Z (2013) Early stage phase separation in pharmaceutical solid dispersion thin films under high humidity: improved spatial understanding using probe-based thermal and spectroscopic nanocharacterization methods. *Mol Pharm* 10:918–930
- Qian F, Huang J, Hussain MA (2010) Drug-polymer solubility and miscibility: stability consideration and practical challenges in amorphous solid dispersion development. *J Pharm Sci* 99:2941–2947
- Reading M, Craig DQM (2006) Principles of differential scanning calorimetry. In: Craig DQM, Reading M (eds) *Thermal analysis of pharmaceuticals*. CRC Press, Boca Raton, pp 2–20
- Reading M, Price DM, Grandy DB et al (2001) Micro-thermal analysis of polymers: current capabilities and future prospects. *Macromol Symp* 167:45–62
- Roos YH (1997) Frozen state transitions in relation to freeze drying. *J Therm Anal* 48:535–544
- Rumondor AC, Marsac PJ, Stanford LA et al (2009) Phase behavior of poly(vinylpyrrolidone) containing amorphous solid dispersions in the presence of moisture. *Mol Pharm* 6:1492–1505
- Saunders M, Podlun K, Shergill S et al (2004) The potential of high-speed DSC (Hyper-DSC) for the detection and quantification of small amounts of amorphous content in predominantly crystalline samples. *Int J Pharm* 274:35–40
- Schulz P, Soltero JFA, Puig JE (2000) DSC analysis of surfactant-based microstructures. In: Garti N (ed) *Thermal behaviour of dispersed systems*. CRC Press, Boca Raton, pp 159–172
- Serajuddin ATM (1999) Solid dispersion of poorly water-soluble drugs: early promises, subsequent problems, and recent breakthroughs. *J Pharm Sci* 88:1058–1066
- Shamblin SL, Taylor LS, Zografis G (1998) Mixing behavior of colyophilized binary systems. *J Pharm Sci* 87:694–701
- Thakral S, Thakral NK (2013) Prediction of drug-polymer miscibility through the use of solubility parameter based Flory-Huggins interaction parameter and the experimental validation: PEG as model polymer. *J Pharm Sci* 102:2254–2263
- Theeuwes F, Hussain A, Higuchi T (1974) Quantitative analytical method for determination of drugs dispersed in polymers using differential scanning calorimetry. *J Pharm Sci* 63:427–429
- Tobyn M, Brown J, Dennis AB et al (2009) Amorphous drug-PVP dispersions: application of theoretical, thermal and spectroscopic analytical techniques to the study of a molecule with intermolecular bonds in both the crystalline and pure amorphous state. *J Pharm Sci* 98:3456–3468
- Van den Mooter G, Wuyts M, Blaton N et al (2001) Physical stabilisation of amorphous ketoconazole in solid dispersions with polyvinylpyrrolidone K25. *Eur J Pharm Sci* 12:261–269
- Verdonck E, Schaap K, Thomas LC (1999) A discussion of the principles and applications of modulated temperature DSC (MTDSC). *Int J Pharm* 192:3–20
- Vyazovkin S, Dranca I (2005) Physical stability and relaxation of amorphous indomethacin. *J Phys Chem B* 109:18637–18644
- Yang ZY, Nollenberger K, Albers J et al (2013) Microstructure of an immiscible polymer blend and its stabilization effect on amorphous solid dispersions. *Mol Pharm* 10:2767–2780
- Yang ZY, Nollenberger K, Albers J et al (2014) Molecular implications of drug-polymer solubility in understanding the destabilization of solid dispersions by milling. *Mol Pharm* 11:2453–2465
- Zhou D, Zhang GGZ, Law D et al (2008) Thermodynamics, molecular mobility and crystallization kinetics of amorphous griseofulvin. *Mol Pharm* 5:927–936

Chapter 12

Isothermal Microcalorimetry

S. Gaisford

Abstract Isothermal microcalorimeters (IMC) measure the heat change in a sample as it is held at a constant temperature—since nearly all processes, chemical and physical, occur with a change in heat, IMC analysis can be applied to the investigation of almost any material. The inherent sensitivity of the measurement means that small samples, or slow processes, may be investigated. This makes IMC a very powerful tool, especially in pharmaceutical analyses, since complex, heterogeneous samples can be studied directly. In this chapter, the basic principles of IMC are introduced, the most common experimental arrangements are defined and applications to pharmaceutical analyses are discussed. Applications discussed progress from preformulation characterization, through stability testing and amorphous content quantification to analyses of formulated products.

Keywords Isothermal microcalorimetry • Solution calorimetry • Isothermal titration calorimetry • Preformulation • Amorphous content

1 Introduction

All analytical techniques require the sample being analysed to possess some quality in order to effect analysis. There may be a requirement for, for instance, a chromophore or specific functional group. The net outcome is that while many analytical techniques are extremely sensitive, they can only be used to study samples with that particular functionality. Calorimeters are unique in the sense that the property they measure, heat (or enthalpy), is a universal accompaniment to chemical and physical change. This means calorimetry can be used, at least in principle, to study any sample, because regardless of the change occurring it is almost certain to result in a change in heat.¹ The only requirement is that the sample, or a representative

¹ It is noted that *a few* processes may occur with no change in heat, but these are unusual. An example is the Joule-Thompson expansion of a gas.

S. Gaisford (✉)

UCL School of Pharmacy, University College London, 29-39 Brunswick Square, London WC1N 1AX, UK

e-mail: s.gaisford@ucl.ac.uk

fraction of it, can be accommodated within the instrument. A further benefit is that there is no requirement for optical clarity of the sample; it is possible to study solid and heterogeneous samples directly. This is particularly advantageous for investigation of pharmaceutical samples, because it means calorimetry can be applied at all stages of product development, from identification of the drug substance through to characterization of the drug product.

Calorimeters can be divided into those that heat the sample during measurement (differential scanning calorimetry, DSC) and those that operate isothermally. DSC is a standard technique widely applied to identification and characterisation of physical forms, but is in the main used to study thermally-driven phase transitions. Isothermal microcalorimeters (IMC), conversely, are used to study time-dependent phase transitions or processes and can be constructed in numerous ways to allow investigation of a multitude of properties and processes. The two techniques are therefore complementary and together form a powerful suite that permits investigation and characterisation of many pharmaceutical materials. This chapter will explain the basic operating principles of IMC instruments and will discuss their broad application to pharmaceutical development.

2 Theoretical Background

Calorimetry (literal meaning; measurement of heat) is an extremely versatile technique, because when change occurs in a sample there is usually a concomitant change in heat content. In other words, *heat is a universal indicator of chemical and physical change*. The upshot is that calorimetry can detect, and potentially quantify, changes in a wide range of materials. The only properties required of the sample are that the process being followed results in a detectable quantity of heat and that the sample (or at least a representative part of it) fits within the calorimetric vessel. IMC is particularly suited to the measurement of pharmaceutical samples because it is sensitive enough to allow the analysis of samples non-destructively (that is, it does not cause any extra degradation other than that which would have occurred upon storage), directly under storage conditions. This means there is no need for elevated temperature stability studies (and hence no requirement for extrapolation of data, although clearly most processes occur faster at higher temperatures and it is possible to perform IMC measurements well above ambient conditions) and samples can be recovered and used in other studies (particularly important in the early stages of the drug discovery process when samples may only exist only in milligram quantities. It is important to note here that DSC analysis is usually destructive). IMC also imposes no requirements on the physical form of a sample, meaning that complex heterogeneous systems are open to investigation, as well as liquids and solids. Further, because both physical and chemical processes occur with a change in heat content, the technique is not limited in its detection ability to chemical degradation, in the way HPLC is for instance.

Calorimetry is one of the oldest analytical techniques, tracing its roots back to the ice calorimeters of Black and Lavoisier and Laplace (ca. 1780). In these early designs a sample is surrounded by ice. As the sample reacts, and so long as the process is exothermic, heat is exchanged with the ice, resulting in melting and formation of water. The volume of water produced is measured and the heat released is quantitatively determined by knowledge of the latent enthalpy of fusion of water. If, in addition, the rate of production of water droplets is observed, then information on the kinetics of the process can be inferred. IMC data therefore contain information on both the thermodynamics (heat, q , given the SI unit of Joules, J) and the kinetics (power, dq/dt , given the SI unit of Watts, W) of the system under investigation.

Modern instruments have not actually changed significantly since these early designs, save for the fact that modern electronics allow for the construction of apparatus that can measure both exothermic and endothermic events. In addition, most instruments operate with an inert reference material, which is used to correct for background noise and environmental fluctuations (and so are *differential*). An example of a typical commercial system is shown in Fig. 12.1.

Experimentally, there are only three methods by which changes in heat can be determined and all have been exploited in the design of IMC instruments. Indeed, it is a good idea to know the principles of operation on which any particular instrument is predicated, since it often impacts the type of sample that can be investigated or the way in which the experiment should be constructed.

In *power-compensation* calorimetry, an electrical element is used either to add or remove power from the calorimeter in order to maintain a particular temperature. The calorimeter is usually constructed to hold both a sample and an inert reference and the difference in power (ΔP) supplied by the element to the two sides is measured. The power output from the sample is the inverse of ΔP supplied by the element. In order to be able both to heat and cool, the element is usually of the Peltier type. Power-compensation designs are often used for DSC instruments, as they permit rapid changes in temperature, but they also feature in some isothermal instruments (in particular, those designed for isothermal titration calorimetry).

In *adiabatic* calorimetry there is no exchange of heat between the sample and its surroundings. Thus, heat release causes a rise in temperature and heat absorption causes a temperature fall. A thermometer is used to measure temperature and multiplication of the temperature change by an experimentally determined cell constant (effectively the heat capacity of the sample) produces the change in heat. In practice, constructing a true adiabatic shield around the sample is almost impossible, and so most instruments are designed to allow some heat exchange with the surroundings. The heat exchange is factored into the data conversion, usually by models based on Newton's law of cooling, and the instrument is said to operate under isoperibolic conditions. Many solution calorimeters are of an isoperibol design, and this has implications for the way experiments are performed (discussed below).

In *heat conduction* calorimetry the sample is surrounded by a heat-sink, which is maintained at a constant temperature. Between the sample and heat-sink is a

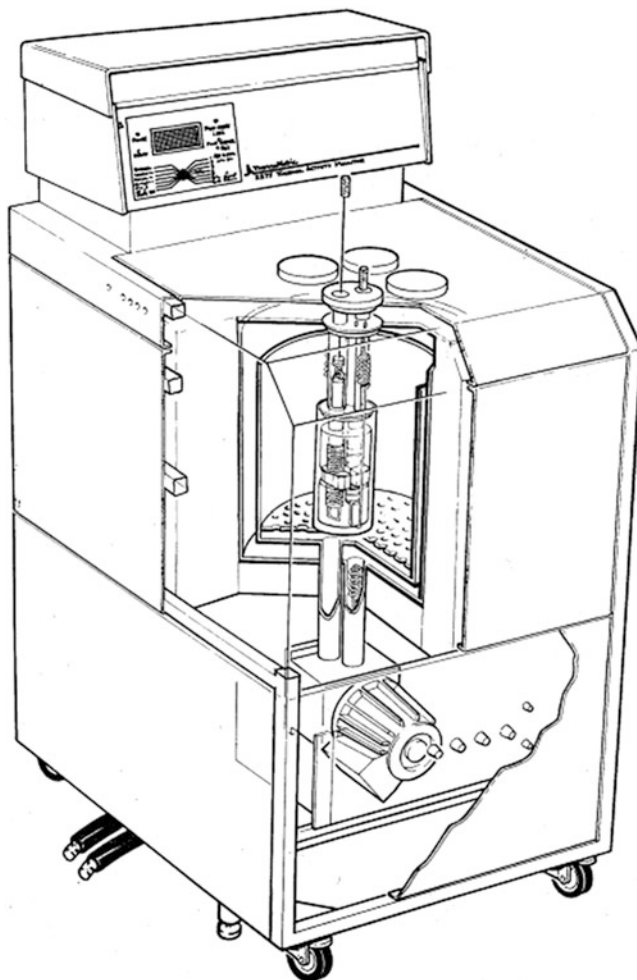


Fig. 12.1 Schematic view of an isothermal microcalorimeter (image courtesy of TA Instruments LLC)

thermopile (a collection of thermocouples wired in series); the thermopile, which generates a voltage in proportion to the temperature gradient across it, is the only direct connection between the sample and the heat-sink. If heat is produced by the sample, the temperature of the sample will rise and heat will flow to the heat-sink across the thermocouple. Conversely, if heat is absorbed by the sample, the temperature of the sample will fall and heat will flow from the heat-sink across the thermocouple. The amount of heat exchanged will quantitatively define the amount of voltage produced. The voltage signal is converted to power by multiplication with a cell constant. The cell constant is usually determined by calibration with an electrical resistance heater.

The arrangement of the sample in the calorimeter is also extremely important because it defines the type of measurement that can be performed or sample that can be studied. Common arrangements include;

Ampoule calorimetry: The sample is contained within a sealed ampoule that is held in the measuring position of the calorimeter. The ampoule is typically constructed from metal (stainless steel or an inert alloy, such as Hastelloy) or glass and will have a hermetic cap. Ampoules can contain solids, liquids or heterogeneous materials and may be reusable. If they can be autoclaved then they are particularly suited to study of microbiological samples. It is also possible to control the humidity of the atmosphere within the ampoule with the use of a mini-hygrostat containing a saturated salt solution. Ampoule calorimetry has the most general application, because virtually all types of sample can be accommodated.

Batch calorimetry: The sample chamber in the calorimeter is divided with a low partition, which allows liquid and/or solid samples to be loaded separately. Once measurement has begun, the chamber can be rotated, allowing the materials to mix. This arrangement is particularly suited to measuring heats of interaction and/or mixing.

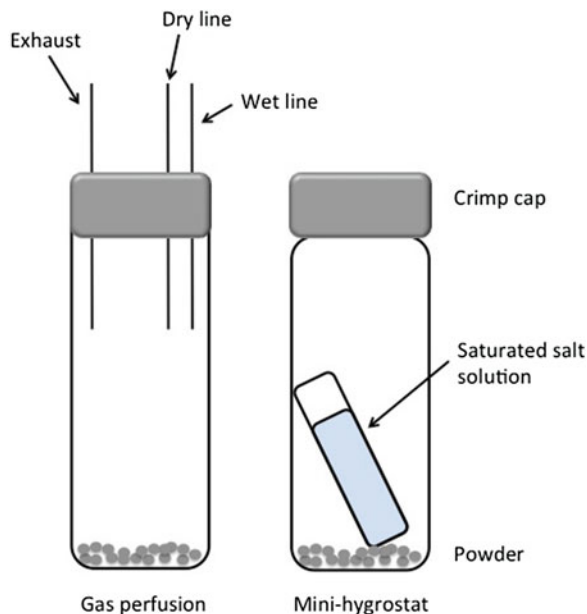
Solution, or ampoule-breaking, calorimetry: Solution calorimetry is not, as the name suggests, the study of solutions. Rather, it is similar in principle to batch calorimetry, where two materials are held in separate chambers prior to measurement. In this case one sample (usually a solid) is encapsulated in a small, sacrificial ampoule. The other sample (usually a liquid) is held in the main sample chamber. To commence measurement the ampoule containing the solid is broken, allowing the two materials to mix. Ampoules can be glass (often referred to as crushing ampoules) or metal (in which case the ampoule is constructed of several pieces which fall apart). Solution calorimeters are particularly suited to measurement of heats of dilution, dissolution or solution.

Flow calorimetry: In this case, a liquid sample is pumped through the sample chamber with a peristaltic pump. The system can be arranged so that the sample is recirculated through an external reservoir or pumped to waste. It is also possible to pump two liquids and arrange for them to mix in the sample chamber, in which case the system is referred to as a *flow-mix* calorimeter. Pharmaceutical applications of flow calorimetry are limited, but it has been used to study dissolution kinetics and it is highly suited to microbiological samples.

Isothermal titration calorimetry (ITC): ITC is probably the most widely used arrangement after ampoule calorimetry. The arrangement permits injection of a solution of ligand molecules into a solution of substrate molecules, and so it is a standard method for determining binding affinity of drug candidates to biological targets. From the heats of titration, it is possible to determine the enthalpy of binding and to construct a binding isotherm, from which the binding stoichiometry and affinity constant can be calculated.

Gas perfusion calorimetry: Here, the relative humidity (RH) or relative vapour pressure (RVP) of the atmosphere inside the sample chamber can be controlled during the course of an experiment. This is achieved either by placing a small reservoir of liquid (a mini-hygrostat) in the ampoule or by flowing a purge gas

Fig. 12.2 Schematic representations of the gas perfusion and mini-hydrostat methods for maintaining a specific RH above the sample



through the chamber using mass flow controllers, Fig. 12.2. In a typical arrangement of the latter, two gas lines are routed into the calorimeter. One is dry and the other passes through a series of reservoirs containing the vapour (usually water or ethanol). Proportional mixing of the flow rates of the two gas lines permits accurate control of the RH or RVP in the sample chamber. Gas perfusion calorimetry is particularly useful for investigating the stability of materials with respect to humidity (accelerated stability trial conditions are easily replicated for instance) or for determining amorphous contents.

It is extremely important to note here that it is imperative to select the correct form of calorimetry to maximise the information gleaned from the sample (an alternative view is to exercise caution that data are not misinterpreted because the experimental arrangement is not appropriate). The principles for instrument selection should become clearer through the applications discussed below.

3 Application of the Technique on Drug Molecules and Formulation Components

The potential applications for IMC in characterising actives and excipients are varied, and only brief summaries of the main areas are possible here. Beezer et al (1999), Gaisford and Buckton (2001) and O'Neill and Gaisford (2011) give more comprehensive reviews for the interested reader.

3.1 *Preformulation Characterisation*

The simplest IMC experiment involves only the placement of a small (typically up to 100 mg) amount of pharmaceutical powder into an ampoule. The power output is recorded with time. If the sample undergoes a process, such as chemical degradation or change in physical form (say, from amorphous to crystalline or from one polymorph to another) then a power is seen. Unlike in the case of DSC experiments where endothermic events are often recorded, the power seen by IMC is almost always exothermic, because the reaction occurs spontaneously (if endothermic powers are seen this is usually a result of water or solvent evaporation). Thus, one immediate use of IMC is simply to screen a new drug substance or excipient and see if any power is being produced. Absence of a measurable power gives confidence that the sample is stable. The presence of a power indicates some change is occurring and further investigation will be needed to determine the cause (Beezer et al 1998).

3.2 *Excipient Compatibility Screening*

This simple screening lends itself in particular to drug-excipient compatibility screening during preformulation design of a dosage form (Chadha and Bhandari 2014). The basic methodology is very simple. Samples of the API and excipient (s) in question are run individually to assess their response under the conditions of interest (temperature, RH etc.) against an inert reference. The materials are then run in binary mixtures (or tertiary or quaternary as necessary), usually in equi-mass ratios and under 100 % RH as this will ensure the maximum possible interaction and increase the probability of observing any interaction in the calorimeter. If no interaction is observed under these conditions then it is usually the case that the materials will not interact under less stressed conditions (Phipps et al 1998).

The calorimetric outputs observed for the individual samples are summed to give a theoretical response, representative of the calorimetric output should the two materials not interact. The theoretical response is compared with the actual calorimetric output for the real mixture. If the materials interact (i.e., there is some incompatibility) then the observed calorimetric response will differ from the theoretical response. The data may reveal an incompatibility whereby a degradation reaction is accelerated and hence the overall shape of the calorimetric curve will be the same (i.e., the mechanism is unchanged) but the rate will be greater. Alternatively the data may suggest that a new mechanistic pathway is possible in the presence of the excipient and the calorimetric curve will be notably different.

Thus, any difference from the theoretical output is an indication of interaction and possible incompatibility. At this stage the excipient can be rejected out of hand (if the goal is a preliminary screen) or investigated further if the excipient is essential for the formulation. Schmitt et al (2001) evaluated calorimetry as a

rapid and practical screen for predicting compatibility between binary mixtures of drug and excipients, using slurries to accelerate reaction. They showed it possible to predict relative stability within a functional class (binders, diluents etc.). Their study, although unable to provide quantitative information, predicted the worst-case incompatibility for a formulation with known stability problems.

3.3 Purity Determination

While DSC is more widely used for purity determination, an IMC method can be used so long as the sample undergoes a chemical reaction and that there are no other contributions to the calorimetric data. The calculation to establish the quantity of impurity present requires the reaction enthalpy to be known. The sample (accurately weighed) is allowed to react to completion and the area under the power-time curve (Q) is determined. In principle, Q must be equal to the product of the number of moles of reactant and the enthalpy for reaction. Therefore if the measured value for Q , obtained from the sample material, is divided by the value for Q obtained from a pure reference sample of the same material, then that ratio will indicate the percentage purity of the suspect material. This method has been used to estimate the purity of triacetin (a compound used for validation of isothermal calorimeters) by O'Neill (2002). The presence of an impurity was first suspected through a poor correlation with the accepted reaction enthalpy for the hydrolysis reaction and was confirmed from the results of a thin layer chromatography experiment.

3.4 Polymorph Stability

As for purity determination, DSC is widely used for identification of polymorphic form, but IMC can be useful for quantifying rates of conversion between forms providing the rate of conversion is reasonably fast (the extent of conversion, α , is >0.15 over the lifetime of the experiment (hours)).

For instance, Urakami and Beezer (2003) used IMC to quantify the stability of seratrodist polymorphs under controlled atmospheres of defined RH. Elevated temperatures (50–65 °C) were used to ensure that a sufficient fraction of the material had converted in order to perform the analysis. Not only was the enthalpy of transition measurable ($-5.70 \pm 1.13 \times 10^{-1} \text{ kJ mol}^{-1}$), quantification of conversion kinetics was possible using the Hancock-Sharp equation, Eq. (12.1). The Hancock-Sharp method involves plotting $\ln[\ln(1-\alpha)]$ versus $\ln t$ to obtain a series of straight lines, the slopes of which yield a parameter m . The value of this parameter indicates the mechanism of transformation.

$$\ln[\ln(1 - \alpha)] = \ln B + m \ln t \quad (0.15 \leq \alpha \leq 0.5) \quad (12.1)$$

Where B is a constant, m is a parameter that indicates mechanism and t is time.

Urakami and Beezer (2003) concluded that the mechanism of transformation of seratrodist is best described by the two dimensional growth of nuclei model. Since their study was conducted as a function of temperature it was also possible to calculate an activation enthalpy, thus permitting prediction of a shelf-life (based upon 90 % of Form II remaining, t_{90}) for a variety of conditions and storage temperatures. For example they predicted that the t_{90} for the transition of Form II to Form III was approximately 3900 days at 63 % RH and 298 K and 17.5 days at 63 % RH and 313 K.

It is also possible to use IMC to determine the relaxation rate of amorphous solids (an indicator of their likely propensity to crystallise). This is usually achieved by model fitting the power-time data to a modified stretch exponential function. Relaxation of amorphous pharmaceuticals has been demonstrated on a number of systems, including a series of disaccharides (Kawakami and Pikal 2005; Liu et al. 2002) and an amorphous maltose formulation (Kawakami and Ida 2003). Alem et al. (2010) compare the use of IMC with DSC for quantifying rates of relaxation.

3.5 *Enthalpy of Solution*

Measurement of the enthalpy of solution is useful because (i) it can be used to identify the compound or differentiate between physical forms, (ii) it should be equal but opposite to the enthalpy of fusion (determined with DSC) if mixing with the solvent is ideal, (iii) it can be used as the basis for determination of amorphous content (see below) and (iv) it can be used to determine interactions between drug and excipients.

Enthalpies of solution are measured with a solution (or ampoule-breaking) calorimeter. The (dry) sample is held within a chamber and is added to an excess of solvent. There are numerous examples where solution calorimetry has been used to measure the heat of solution of pure pharmaceuticals; Royall and Gaisford (2005) give a good overview.

In terms of polymorph characterisation, forms I and II of cyclopentiazide have been shown to have comparable enthalpies of solution ($\sim 6 \text{ kJ mol}^{-1}$) while form III has a higher enthalpy of solution of 15 kJ mol^{-1} (Gerber et al 1991). Similarly, solution calorimetry has been used to characterise the three polymorphic forms of a pre-clinical drug, Abbott-79175 (Li et al 1996) and the polymorphs of an angiotensin II antagonist agent (MK996) (Jahansouz et al. 1999).

Jain et al (2000) used solution calorimetry to probe the possible interactions between ampicillin and amoxicillin, a combination known to act synergistically. Traditional spectroscopic analysis was not possible because of the proximity of

their λ_{\max} values. Using solution calorimetry they were able to determine the enthalpies of solution at a variety of pH's as well as the excess molar enthalpies of solution of the binary mixture. From the low values of the excess molar enthalpies they concluded that the two antibiotics do not interact with each other to any great extent.

Alves et al (2005) report the measurement of the enthalpy of solution of diclofenac sodium and paracetamol individually and the excess molar enthalpy of binary mixtures in order to determine whether there was any interaction when in solution. It was reported that the enthalpies of solution of diclofenac sodium and paracetamol, at pH 7.0, were $50.24 \pm 0.04 \text{ kJ mol}^{-1}$ and $24.76 \pm 0.04 \text{ kJ mol}^{-1}$ respectively. Again the values of the excess molar enthalpy are small and indicated that little or no interaction existed.

3.6 Drug Stability

Drug stability is easily quantified by IMC. Further, it is possible to construct the experiment so that stability is determined in either the solid state (with control of relative humidity, RH) or in solution. If degradation follows first-order kinetics, analysis simply involves plotting $\ln(\text{power})$ versus time. The slope of the resulting straight line gives the rate constant. The enthalpy of reaction is determined by calculating the area under the power-time curve (heat, Q , in J) and dividing it by the number of moles of compound that has reacted. Analysis is more complicated if other higher or mixed-order kinetics are involved. A comprehensive overview is given in Gaisford et al. (2006).

Numerous examples of the use of IMC for determining drug stability in solution are in the literature. For example, Simoncic et al (2008) compared IMC with HPLC for determining the stability of perindopril erbumine in aqueous solution while Koenigbauer et al (1992) determined the activation energies for the degradation of several drugs, including phenytoin, triamterene, digoxin, tetracycline, theophylline and diltiazem. Roskar et al (2008) use IMC to determine the oxidative stability of various amino acids. Gaisford (2005) shows various examples of the use of IMC to study biopharmaceuticals.

Since water is difficult to remove entirely from a formulation, hydrolysis is a common cause of chemical instability. There are numerous examples in the literature where hydrolysis reactions have been studied calorimetrically. For instance, the degradation rate of meclufenoxate hydrochloride (MF), which hydrolyses in aqueous solution, has been determined using IC (Otsuka et al 1994). By plotting $\ln(\text{power})$ versus time, the degradation rate constants for MF at pH 6.4 and 2.9 were determined to equal $1.14 \times 10^{-4} \text{ s}^{-1}$ and $9.7 \times 10^{-7} \text{ s}^{-1}$ respectively. Comparison of these data with rate constant values determined using HPLC ($1.29 \times 10^{-4} \text{ s}^{-1}$ and $9.0 \times 10^{-7} \text{ s}^{-1}$) revealed the utility of the calorimetric technique. A similar approach has been used to determine the rate constants for ampicillin degradation in

aqueous buffers (Oliyai and Lindenbaum 1991) from pH 2 to 8 and a number of cephalosporins (Pikal and Dellerman 1989).

A typical formulated pharmaceutical may well have several independently degrading components and, although the degradation kinetics of the individual components of a medicine may be known, their behaviour in combination may be significantly different. Skaria et al (2005) studied aqueous solutions of binary mixtures of selected parabens. They found that the rate constants for degradation in binary systems were lower than those recorded for the pure compounds and suggested the most likely explanation was that the two reactants degraded to a common product, p-hydroxybenzoic acid. The data showed the sensitivity of IMC to subtle changes in reaction mechanism.

It is also possible to analyse quantitatively more complex reactions. For instance, Gaisford et al (1999) studied the acid catalysed hydrolysis of potassium hydroxylamine trisulfonate, because it follows a well characterised, three-step reaction mechanism. It was possible to model all stages of the reaction and determine rate constants and enthalpies for each step.

Analysis of reactions progressing in the solid state is more challenging, because kinetic schemes cannot be written on the basis of molecularity and so are written on the basis of the fraction of reaction completed (α). Sousa et al (2010, 2012) have discussed in some detail various approaches that can be used to interpret solid-state reactions studied with IMC. Where data are very complex, chemometric analysis may be of use. O'Neill et al (2007) discuss the role of chemometric analysis in the interpretation of stability data and Kong et al (2009) use chemometric analysis to aid interpretation of the effect of emodin on growth of *Candida albicans*.

3.7 Amorphous Content Quantification

Many pharmaceutical processing steps have the potential to render a crystalline material fully or partially amorphous. The potential consequences of amorphous content for drug product performance are significant (for instance in affecting powder flow, compression, stability or force of adhesion/cohesion), and so the need for assays capable of quantifying amorphous content is high. IMC is an excellent choice because, as ever, it is capable of studying powders and formulations directly, as a function of temperature and/or RH.

There are two ways of measuring amorphous content with IMC; solution calorimetry and gas perfusion calorimetry. The choice of technique is often driven by experimental factors. For instance, to use solution calorimetry a solvent must be available that is compatible with the instrument and in which the drug has an appreciable solubility. Gas perfusion calorimetry requires that a suitable plasticising vapour is available. Gaisford (2012) recently published a review of the use of IMC for quantifying amorphous contents.

The use of solution calorimetry for amorphous content quantification is predicated on the fact that the heat of solution ($\Delta_{\text{sol}}H$) comprises two components; an

endothermic energy needed to break the crystal lattice ($\Delta_{cl}H$) and an enthalpy of mixing with the solvent ($\Delta_{mix}H$) (Eq. (12.2)).

$$\Delta_{sol}H = \Delta_{cl}H + \Delta_{mix}H \quad (12.2)$$

If mixing with the solvent is ideal, the heat of mixing is zero (in practice, ideal mixing is unusual and so this value is often exothermic) and the heat of solution for a crystalline material is endothermic. However, amorphous materials have no crystal lattice barriers to overcome and so this component is zero. Hence, the heat of solution for an amorphous material will be zero if mixing is ideal and (usually) exothermic if not. The use of solution calorimetry as an assay then simply requires construction of a calibration plot of amorphous content (usually standards are prepared by blending crystalline and amorphous samples in appropriate mass ratios) versus heat of solution.

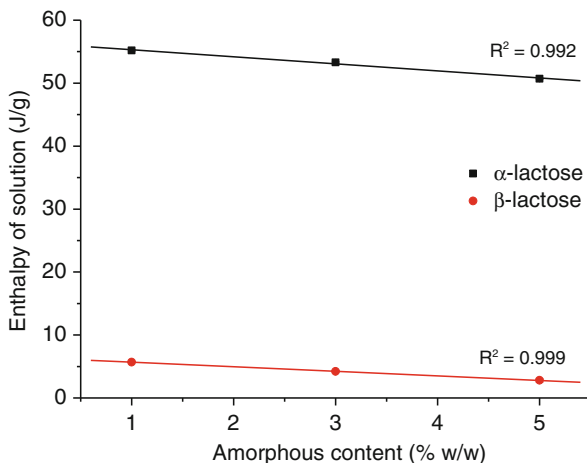
The first use of solution calorimetry for the quantitative measurement of the degree of crystallinity of pharmaceuticals was by Pikal et al (1978), who measured the heat of solution of various β -lactam antibiotics. Subsequent studies include the analysis of sulphamethoxazole from different sources (Guillory and Erb 1985), sucrose (Gao and Rytting 1997) and clathrate warfarin sodium (Gao and Rytting 1997). The issue of detection limits becomes important if the amorphous material is the minor component in what is a predominately crystalline sample. Hogan and Buckton (2000) assessed the applicability of solution calorimetry to study small amorphous contents in milled powders by preparing a calibration curve for lactose between 0 and 10 % w/w amorphous content. They found that the technique could quantify amorphous content to ± 0.5 % w/w but noted that care needed to be taken when preparing the ampoules, because ingress of even small amounts of humidity caused partial recrystallisation of the sample before measurement.

Usually, in experiments designed to measure degrees of crystallinity of amorphous content a solvent is selected in which the solute is freely soluble. This ensures complete dissolution of the sample within the time frame of the experiment. Harjunen et al (2004) studied the dissolution of lactose into saturated aqueous lactose solutions, a system where clearly the solute would not completely dissolve. Interestingly, they observed a linear relationship between the amorphous content of the lactose solute and the measured heat of solution in the saturated lactose solution ($\Delta_{sat}H$). Similarly, a linear relationship was found between the amorphous content of lactose and $\Delta_{sat}H$ in methanolic saturated solutions of lactose (Katainen et al 2003).

One potential limitation to this approach is where the sample exhibits polymorphism, in which case there may be more than one crystalline form present; if this is the case then for the calibration plot to be linear, it must be ensured that the crystalline material used to prepare the standards and the unknown sample contain the same proportions of the polymorphs. Similarly, Ramos et al (2005) showed that the anomeric composition of sugars also affected the calibration curve (Fig. 12.3).

For gas perfusion calorimetry, the humidity (or relative vapour pressure, RVP, if a solvent is used) of the atmosphere surrounding the sample is controlled. Two

Fig. 12.3 Calibration curves for α and β lactose prepared from enthalpy of solution data. The lines shown are linear regression fits; error bars are plotted but fall within the symbols (from Ramos et al 2005)



methods are available. In the simpler method, used where only a single RH is required, a small volume of a saturated salt solution is placed in a small glass tube (or mini-hygrostat) and housed in the calorimetric ampoule. Saturated salt solutions maintain fixed RH's in closed atmospheres, the specific RH being dependent on the salt used. RVP can be achieved by placing solvents or solvent mixtures in the mini-hygrostat. The principal advantages of this method are convenience and cost but it does have some limitations. The biggest is that the sample will start to wet as soon as the ampoule is sealed (which will be external to the instrument); there will then be a time delay while the ampoule is loaded into the calorimeter and thermal equilibrium is achieved. If the sample crystallises during this time then it will be almost impossible to recover quantitative data. Other disadvantages include the fact that the rate of water evaporation from (or condensation to) the reservoir will be dependent upon the cross-sectional area of the mini-hygrostat and the fact that the instrument will measure heats of evaporation and condensation since they occur directly in the ampoule. Khalef et al (2010) discuss the limitations of using saturated salt solutions for amorphous content quantification.

An alternative arrangement is to flow an inert carrier gas through the sample ampoule. Mass flow controllers mix two gas streams, one dry and one saturated with plasticising vapour, to vary the RH or RVP. The RH or RVP in the sample ampoule can thus be altered in either discrete steps or as a linear ramp. The immediate, and primary, advantage of this approach is that the flowing gas can be dry during the loading and equilibration phases; this ensures both that the water content of the sample at the start of each experiment is the same and that no data are lost prior to commencement of data capture. Another advantage is that the instrument does not record heats of evaporation and condensation from a salt reservoir. The obvious drawback is cost and complexity.

Cook et al (1996) reported the use of isothermal microcalorimetry to quantify amorphous contents of micronized drug particles and showed that amorphous contents correlated to energy input during milling. Giron et al (1997) used the

mini-hygrostat method to quantify amorphous contents in three pharmaceuticals, an experimental drug, an isoquinoline derivative and a peptide, and could detect amorphous contents less than 1 % w/w in each. The best analytical conditions were found to be different for each sample, the peptide in particular needing rather extreme conditions of 80 °C and 100 % RH.

Ahmed et al (1998) followed crystallisation of griseofulvin as a function of RH (65, 75 and 85 %) using salt solutions. The rate of crystallisation was determined via model fitting and was found to increase in proportion with RH. Vivoda et al (2011) use a mini-hygrostat to quantify amorphicity in lactose and nifedipine. Lehto and Laine (1998) used both the mini-hygrostat and IGPC methods to follow crystallisation of cefadroxil, noting that determination of the enthalpy of crystallisation was complicated by the effect of water expulsion immediately following crystallisation itself. Fiebich and Mutz (1999) used both the mini-hygrostat and IGPC methods to quantify amorphous contents in desferal. They show that both approaches allowed detection to 1 % w/w but that the IGPC method was particularly sensitive to small changes in the position of the baseline. Alam et al (2014) recently proposed a more accurate method using gas perfusion calorimetry based on heat of adsorption.

4 Application of the Technique on Dosage Forms

Perhaps more than any other analytical technique, IMC has the capacity to study processed and formulated samples directly and so the array of applications to which it has been put is vast. The range of applications broadly mirrors those described above, except the sample has more constituents and so the potential for reaction is often greater (and similarly, the data are harder to interpret).

Starting with processing, Qian et al (2012) used IMC to determine water uptake in naphthalene when milled with mesoporous silicon dioxide and correlated the data with the likelihood of recrystallizing the sample. Hulse et al (2009) use IMC to characterize the polymorphic composition of spray-dried mannitol samples. Gaisford et al (2010) and Höckerfelt et al (2009) both used IMC to determine the amorphous content of milled powders, noting that amorphous content increases while particle size remains constant.

Ziffels et al (2010) used IMC to quantify recrystallisation of partially amorphous lactose during and after compression while Al-Hallak et al (2008) used IMC to characterize the effect of compression forces on the stability of dibasic calcium phosphate dehydrate tablets. Simoncic et al (2007) were able to determine the stability of enalapril maleate in tablets with IMC and correlated their data with HPLC measurements. Calahan et al (2013) used IMC to follow the crystallisation of AMG 517 from HPMC-AS solid dispersions while Gaisford et al (2009a) were able to quantify the rate of crystallisation of indomethacin from HPMC films. Gaisford et al (2006) used IMC to determine the stability of busulfan in intravenous infusion bags.

Solution calorimetry has been used to study the actions of formulations directly. For instance, Gaisford et al (2004) used solution calorimetry to follow the acid neutralisation of magnesium trisilicate mixture BP. They showed that of the three active components in the mixture (magnesium carbonate, magnesium trisilicate and sodium bicarbonate), magnesium carbonate contributed most to the action of the product, followed by sodium bicarbonate. Conti et al. (2008) used solution calorimetry to investigate the mechanism of controlling release of diltiazem HCl from polymeric matrices. They noted that the drug showed no interaction with HPMC but an unfavourable interaction was seen with NaCMC. When the two polymers were used in combination a favourable interaction was seen, which correlated with zero-order release of the drug. The results indicated that solution calorimetry might be useful for screening and selecting polymer blends for use in controlled-release tablets. As well as highlighting potential chemical interactions between drugs and excipients, Conti et al (2006) also showed that solution calorimetry could be used to derive the swelling profiles of polymers in buffers, again helping in the development of modified-release formulations. Conti et al. (2007) has been changed to Conti et al. (2008) as per the reference list. Please check if okay. Yes, 2008 is correct

Ooi et al (2014) used gas perfusion calorimetry to flow pressurised metered dose inhaler model propellants through the sample chamber. They showed that the model propellant caused spray-dried beclometasone dipropionate to crystallise while spray dried salbutamol sulphate remained in its amorphous form.

While stability/compatibility studies are often strongly focused on the compounds within the formulation, the packaging material is also an integral part of the formulation and so should be considered during stability trials. The primary function of the packaging material is to protect the formulation from its environment. Further, the packaging itself is a chemical entity and hence may potentially interact with the formulation. Because of its invariance to physical form and its capacity to study relatively large samples isothermal calorimetry is ideally suited to investigate potential interactions between a formulation and its packaging.

The methodology for this aspect of formulation testing is largely the same as that described above for incompatibility testing. Here the formulation is now studied (rather than the individual components) in the presence of various packaging materials. Gaisford and O'Neill (2007) show the calorimetric output for a variety of packaging materials for a tablet susceptible to oxidation, Fig. 12.4. The tablet is shown individually (control experiment) and then sealed within a number of different packaging materials. It is clear that the tablet alone is relatively unstable. For this particular formulation Triplex packaging offers essentially no protection at all (i.e., the calorimetric response is identical in both cases). PVC provides little or no protection. The aluminium packaging material appears to offer a significantly better protection than all other materials in that the rate of change in the calorimetric output is reduced and hence it can be inferred that the degradative process is inhibited.

It is also possible to construct a calorimeter such that the sample is irradiated with light during measurement. Dhuna et al (2008) report the development of a

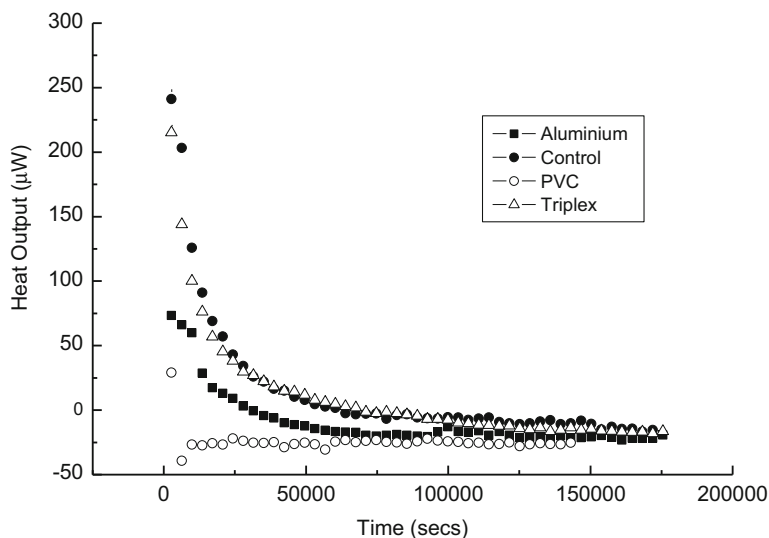


Fig. 12.4 A comparison of the effect of packaging materials on the power produced by a tablet formulation (from Gaisford and O'Neill 2007)

photocalorimeter and show its use in determining the photostability of nifedipine in the solid state.

5 Application of the Technique In Vivo

While it is feasible to construct a calorimeter large enough to accommodate humans (McLean and Tobin 1987), pharmaceutically in vivo applications really focus on microbiology and biotechnology (Krell 2008). Partly, this is due to the fact that growing organisms are easily monitored with IMC, even in complex or heterogeneous media. In addition, it is possible to study mixed bacterial populations or biofilms. Since the shape of bacterial growth curves is also unique to each organism, IMC can also be used to identify bacterial species (Boling and Blanchard 1973). It is thus possible to study the effect of antibiotics on bacteria or to investigate the growth and proliferation of bacteria on medical devices. For instance, Gaisford et al (2009b) and Said et al (2014a) used IMC to quantify the effect of silver-containing wound dressings against *S. aureus* and *P. aeruginosa* while Said et al (2014b) tested the efficacy of an anti-biofilm dressing. Similarly, human cell growth and interactions can be investigated directly (Santoro et al 2011). Calorimetry is also used in the clinic to identify sepsis or urinary tract infections (Braissant et al 2010).

Isothermal titration calorimetry (ITC) is widely used to investigate the binding thermodynamics of substrates to biological ligands (and so to optimise lead

compound design) but is also used to study systems designed to form spontaneously following oral delivery. Examples include its use to help design anionic liposaccharides for oral delivery (Abdelrahim et al 2012), to quantify the interaction of DNA with betaxolol (Sun et al 2010) and characterise the solubilisation of simvastatin with a range of surfactants (Patel et al 2007).

6 A “How to” Section (Example Protocols)

The ubiquity of heat² is the technique’s primary advantage and biggest drawback. It should be clear from the preceding text that IMC can be used to study almost any sample one might imagine but it is often the case that the data are complex in shape because they may comprise contributions from several simultaneous processes. It is also true that calorimetric data are extremely susceptible to systematic errors because of the accidental measurement of one or more of a range of processes (such as solvent evaporation and/or condensation, erosion, side reactions and so on) that may occur concurrently with the study process(es). These errors become proportionately more significant as the heat output from the study sample decreases. The majority of the effort in performing a calorimetric measurement should be devoted to setting up the experiment to ensure that erroneous or unexpected powers have not been accidentally introduced as a corollary of poor experimental design or execution.

It is clearly possible to design a wide range of calorimetric arrangements and it is important to understand the types of sample each is most suited to studying. The design of many instruments is a compromise between factors desirable for good calorimetric measurement and factors necessary to ensure a certain measurement function, meaning that careful experimental design and suitable calibration (preferentially using chemical test reactions) are essential precursors to accurate sample measurement. Selection of the most appropriate calorimeter design is critical when planning an experiment. Hopefully, the examples given in the previous section will direct the reader in making the best choice, but in general terms;

- Adiabatic solution calorimeters are really suited to reactions that progress to completion within 1–2 h, because of the inherent difficulties in making the necessary heat-loss corrections over longer time periods. They are not therefore suitable for stability assays, but are appropriate for dissolution processes
- Power compensation instruments have a lower detection limit but a better capacity to cope with high powers and are therefore usually used to study energetic reactions with large heat rates
- Heat conduction calorimeters, because they can measure micro and even nano-Watts are most suited, and most commonly used, for the study of long-term, low

²The author’s personal favourite definition; Heat does not come in different colours, Cooper et al. 2001.

energy reactions, typified by the degradation mechanisms often followed by pharmaceuticals.

7 A “Don’ts” Section (Common Mistakes People Make and How to Avoid Them)

It follows from above that a common mistake might be to select the wrong type of calorimeter design. A good principle would be to review the literature where similar samples have been studied, and note the type of calorimeter typically used. It is also critical that the sample is loaded properly, that no contaminants are on or in the system and that (if solvents or humidity are involved) that the sample chamber is hermetically sealed. A leaky seal will permit constant evaporation of the solvent, which will manifest as a constant, endothermic deflection from baseline. A further consideration is necessary if the solvent used is not ethanol. Methanol and most other organic solvents usually have the capacity to swell or degrade the o-rings forming the hermetic seal. If such an interaction is suspected, then an o-ring should be exposed to the solvent prior to measurement for confirmation and any o-rings in the instrument switched to a version made from a resistant polymer (for instance, Kalrez[®]).

A final consideration is to match the dynamic range of the instrument to the magnitude of the power being produced by the sample, if such a facility is available. Some high-sensitivity instruments have maximum dynamic ranges (for instance, the TAM 2277 system cannot measure powers larger than 3 mW).

References

- Abdelrahim AS, Simerska P, Toth I (2012) Development and characterization of anionic liposaccharides for enhanced oral drug delivery. *Int J Pharm* 430:120–128
- Ahmed H, Buckton G, Rawlins DA (1998) Crystallisation of partially amorphous griseofulvin in water vapour: determination of kinetic parameters using isothermal heat conduction microcalorimetry. *Int J Pharm* 167:139–145
- Alam S, Omar M, Gaisford S (2014) Use of heat of adsorption to quantify amorphous content in milled pharmaceutical powders. *Int J Pharm* 459:19–22
- Alem N, Beezer AE, Gaisford S (2010) Quantifying the rates of relaxation of binary mixtures of amorphous pharmaceuticals with isothermal calorimetry. *Int J Pharm* 399:12–18
- Al-Hallak MHDK, Xu ZH, Ghaffari F, Lobenberg R (2008) The effect of compression forces on the stability of dibasic calcium phosphate dehydrate tablets in the presence of glutamic acid hydrochloride monitored by isothermal calorimetry. *Thermochim Acta* 467:86–90
- Alves N, Bai G, Bastos M (2005) Enthalpies of solution of paracetamol and sodium diclofenac in phosphate buffer and in DMSO at 298.15 K. *Thermochim Acta* 441:16–19
- Beezer AE, Willson RJ, Mitchell JC, Hills AK, Gaisford S, Wood E, Connor JA (1998) Thermodynamic and kinetic parameters from isothermal heat conduction microcalorimetry. *Pure App Chem* 70:633–638

- Beezer AE, Gaisford S, Hills AK, Willson RJ, Mitchell JC (1999) Pharmaceutical microcalorimetry: applications to long-term stability studies. *Int J Pharm* 179:159–165
- Boling EA, Blanchard GC (1973) Bacterial identification by microcalorimetry. *Nature* 241:472–473
- Braissant O, Wirz D, Gopfert B, Daniels AU (2010) Biomedical use of isothermal microcalorimeters. *Sensors* 10:9369–9383
- Calahan JL, Zanon RL, Alvarez-Nunez F, Munson EJ (2013) Isothermal microcalorimetry to investigate the phase separation for amorphous solid dispersions of AMG 517 with HPMC-AS. *Mol Pharm* 10:1949–1957
- Chadha R, Bhandari S (2014) Drug-excipient compatibility screening—role of thermoanalytical and spectroscopic techniques. *J Pharm Biomed Anal* 87:82–97
- Conti S, Gaisford S, Buckton G, Conte U (2006) Solution calorimetry to monitor swelling and dissolution of polymers and polymer blends. *Thermochim Acta* 450:56–60
- Conti S, Gaisford S, Buckton G, Maggi L, Conte U (2008) The role of solution calorimetry in investigating controlled release processes from polymeric drug delivery systems. *Eur J Pharm Biopharm* 68:795–801
- Cook PA, Dellman CI, Horspool KR, Lukas TM, Marshall PV, Nichols G, Smith D, Ticehurst MD (1996) The characterisation and quantification of amorphous content of micronized drug particles. *Eur J Pharm Sci* 4:S181
- Cooper A, Johnson CM, Lakey JH, Nöllmann M (2001) Heat does not come in different colours: entropy-enthalpy compensation, free energy windows, quantum confinement, pressure perturbation calorimetry, solvation and the multiple causes of heat capacity effects in biomolecular interactions. *Biophys Chem* 93:215–230
- Dhuna M, Beezer AE, Connor JA, Clapham D, Courtice C, Frost J, Gaisford S (2008) LED-array photocalorimetry: instrument design and application to photostability of nifedipine. *J Pharm Biomed Anal* 48:1316–1320
- Fiebich K, Mutz M (1999) Evaluation of calorimetric and gravimetric methods to quantify the amorphous content of desferal. *J Therm Anal Cal* 57:75–85
- Gaisford S (2005) Stability assessment of pharmaceuticals and biopharmaceuticals by isothermal microcalorimetry. *Curr Pharm Biotech* 6:181–191
- Gaisford S (2012) Isothermal microcalorimetry for quantifying amorphous content in pharmaceuticals: a review of methods and data interpretation. *Ad Drug Del Rev* 64:431–439
- Gaisford S, Buckton G (2001) Potential applications of microcalorimetry for the study of physical processes in pharmaceuticals. *Thermochim Acta* 380:185–198
- Gaisford S, O'Neill MAA (2007) Pharmaceutical isothermal calorimetry. Informa Healthcare
- Gaisford S, Hills AK, Beezer AE, Mitchell JC (1999) Modelling and fitting of isothermal microcalorimetric data; applications to consecutive reaction schemes. *Thermochim Acta* 328:39–45
- Gaisford S, Royall PG, Greig DGT (2004) Solution calorimetry as a tool to study the neutralizing capacity of magnesium trisilicate mixture BP and its components. *Thermochim Acta* 417:217–221
- Gaisford S, O'Neill MAA, Thompson L, Chan K-L (2006) Shelf-life prediction of intravenous busulfan by isothermal calorimetry. *Hosp Pharm* 13:295–298
- Gaisford S, Verma A, Saunders M, Royall PG (2009a) Monitoring crystallisation of drugs from fast-dissolving oral films with isothermal calorimetry. *Int J Pharm* 380:105–111
- Gaisford S, Beezer AE, Bishop AH, Walker M, Parsons D (2009b) An in-vitro method for the quantitative determination of the antimicrobial efficacy of silver-containing wound dressings. *Int J Pharm* 366:111–116
- Gaisford S, Dennison M, Tawfik M, Jones M, Saunders M (2010) Following mechanical activation of salbutamol sulfate during ball-milling with isothermal calorimetry. *Int J Pharm* 393:74–78
- Gao D, Rytting JH (1997) Use of solution calorimetry to determine the extent of crystallinity of drugs and excipients. *Int J Pharm* 151:183–192
- Gerber JJ, van der Watt JG, Lötter AP (1991) Physical characterization of solid forms of cyclopenthiiazide. *Int J Pharm* 73:137–145

- Giron D, Remy P, Thomas S, Vilette E (1997) Quantitation of amorphicity by microcalorimetry. *J Therm Anal Cal* 48:465–472
- Guillory JK, Erb DM (1985) Using solution calorimetry to quantitate binary mixtures of three crystalline forms of sulfamethoxazole. *Pharm Manuf* 2(9):28–33
- Harjunen P, Lehto V-P, Koivisto M, Levonen E, Paronen P, Järvinen K (2004) Determination of amorphous content of lactose samples by solution calorimetry. *Drug Dev Ind Pharm* 30:809–815
- Höckerfelt H, Nyström C, Alderborn G (2009) Dry mixing transformed micro-particles of a drug from a highly crystalline to a highly amorphous state. *Pharm Dev Tech* 14:233–239
- Hogan SE, Buckton G (2000) The quantification of small degrees of disorder in lactose using solution calorimetry. *Int J Pharm* 207:57–64
- Hulse WL, Forbes RT, Bonner MC, Getrost M (2009) The characterization and comparison of spray-dried mannitol particles. *Drug Dev Ind Pharm* 35:712–718
- Jahansouz H, Thompson KC, Brenner GS, Kaufman MJ (1999) Investigation of the polymorphism of the angiotensin II antagonist agent MK-996. *Pharm Dev Tech* 4:181–187
- Jain DVS, Kashid N, Kapoor S, Chadha R (2000) Enthalpies of solution of ampicillin, amoxicillin and their binary mixtures at 310.15 K. *Int J Pharm* 201:1–6
- Kawakami K, Ida Y (2003) Direct observation of the enthalpy relaxation and the recovery process of maltose-based amorphous formulation by isothermal microcalorimetry. *Pharm Res* 20:1430–1436
- Kawakami K and Pikal MJ (2005) Calorimetric investigation of the structural relaxation of amorphous materials: evaluating the validity of methodologies. *J. Pharm. Sci.* 94:948–965
- Katainen E, Niemelä P, Päällysaho M, Harjunen P, Suhonen J, Järvinen K (2003) Evaluation of the amorphous content of lactose by solution calorimetry and raman spectroscopy. *Eur J Pharm Sci Abstracts* 19:S36
- Khalef N, Pinal R, Bakri A (2010) Limitations of amorphous content quantification by isothermal calorimetry using saturated salt solutions to control relative humidity: alternative methods. *J Pharm Sci* 99:2080–2089
- Koenigbauer MJ, Brooks SH, Rullo G, Couch RA (1992) Solid-state stability testing of drugs by isothermal calorimetry. *Pharm Res* 9:939–944
- Kong WJ, Wang JB, Jin C, Zhao YL, Dai CM, Xiao XH, Li ZL (2009) Effect of emodin on *Candida albicans* growth investigated by microcalorimetry combined with chemometric analysis. *Appl Microbiol Biotech* 83:1183–1190
- Krell T (2008) Microcalorimetry: a response to challenges in modern biotechnology. *Microbiol Biotech* 1:126–136
- Lehto V-P, Laine E (1998) Assessment of physical stability of different forms of cefadroxil at high humidities. *Int J Pharm* 163:49–62
- Li RCY, Mayer PT, Trivedi JS, Fort JJ (1996) Polymorphism and crystallisation behaviour of Abbott-79175, a second-generation 5-lipoxygenase inhibitor. *J Pharm Sci* 85:773–780
- Liu J, Rigsbee DR, Stotz C, Pikal MJ (2002) Dynamics of pharmaceutical amorphous solids: the study of enthalpy relaxation by isothermal microcalorimetry. *J Pharm Sci* 91:1853–1862
- McLean JA, Tobin G (1987) *Animal and human calorimetry*. Cambridge University Press, Cambridge
- O'Neill MAA (2002) PhD dissertation, University of Greenwich
- O'Neill MAA, Gaisford S (2011) Application and use of isothermal calorimetry in pharmaceutical development. *Int J Pharm* 417:83–93
- O'Neill MAA, Beezer AE, Tetteh J, Gaisford S, Dhuna M (2007) Application of chemometric analysis to complexity in isothermal calorimetric data. *J Phys Chem B* 111:8145–8149
- Oliyai R, Lindenbaum S (1991) Stability testing of pharmaceuticals by isothermal heat conduction calorimetry: ampicillin in aqueous solution. *Int J Pharm* 73:33–36
- Ooi J, Gaisford S, Boyd B, Traini D, Young PM (2014) Isothermal calorimetry: a predictive tool to model drug-propellant interactions in pressurized metered dose systems. *Int J Pharm* 461:301–309
- Otsuka T, Yoshioka S, Aso Y, Terao T (1994) Application of microcalorimetry to stability testing of meclizolam hydrochloride and *dl*- α -tocopherol. *Chem Pharm Bull* 42:130–132

- Patel R, Buckton G, Gaisford S (2007) The use of isothermal titration calorimetry to assess the solubility enhancement of simvastatin by a range of surfactants. *Thermochim Acta* 456:106–113
- Phipps M, Winnike RA, Viscomi F, Long ST (1998) Excipient compatibility assessment by isothermal microcalorimetry. *J Pharm Pharmacol* 50:6–9
- Pikal MJ, Dellerman KM (1989) Stability testing of pharmaceuticals by high-sensitivity isothermal calorimetry at 25 °C: cephalosporins in the solid and aqueous states. *Int J Pharm* 50:233–252
- Pikal MJ, Lukes AL, Lang JE, Gaines K (1978) Quantitative crystallinity determinations for β -lactam antibiotics by solution calorimetry: correlations with stability. *J Pharm Sci* 67:767–772
- Qian KK, Wurster DE, Bogner RH (2012) Spontaneous crystalline-to-amorphous phase transformation of organic or medicinal compounds in the presence of porous media, Part 3. Effect Moisture *Pharm Res* 29:2698–2709
- Ramos R, Gaisford S, Buckton G (2005) Calorimetric determination of amorphous content in lactose: a note on the preparation of calibration curves. *Int J Pharm* 300:13–21
- Roskar R, Vivoda M, Kmetec K (2008) Use of isothermal microcalorimetry for prediction of oxidative stability several amino acids. *J Therm Anal Cal* 92:791–794
- Royall PG, Gaisford S (2005) Application of solution calorimetry in pharmaceutical and biopharmaceutical research. *Curr Pharm Biotech* 6:215–222
- Said J, Dodoo CC, Walker M, Parsons D, Stapleton P, Beezer AE, Gaisford S (2014a) An *in-vitro* test of the efficacy of silver-containing wound dressings in simulated wound fluids. *Int J Pharm* 462:123–128
- Said J, Walker M, Parsons D, Stapleton P, Beezer AE, Gaisford S (2014b) An *in vitro* test of the efficacy of an anti-biofilm wound dressing. *Int J Pharm* 474:177–181
- Santoro R, Braissant O, Muller B, Wirz D, Daniels AU, Martin I, Wendt D (2011) Real time measurements of human chondrocyte heat production during *in vitro* proliferation. *Biotech Bioeng* 108:3019–3024
- Schmitt EA, Peck K, Sun Y, Deoffroy JM (2001) Rapid, practical and predictive excipient compatibility screening using isothermal microcalorimetry. *Thermochim Acta* 380:175–183
- Simoncic Z, Zupancic P, Roskar R, Gartner A, Kogej K, Kmetec V (2007) Use of microcalorimetry in determination of stability of enalapril maleate tablet formulations. *Int J Pharm* 342:145–151
- Simoncic Z, Roskar R, Gartner A, Kogej K, Kmetec V (2008) The use of microcalorimetry and HPLC for the determination of degradation kinetics and thermodynamic parameters of perindopril erbumine in aqueous solutions. *Int J Pharm* 356:200–205
- Skaria CV, Gaisford S, O'Neill MAA, Buckton G, Beezer AE (2005) Stability assessment of pharmaceuticals by isothermal calorimetry: two component systems. *Int J Pharm* 292:127–135
- Sousa L, Alem N, Beezer AE, O'Neill MAA, Gaisford S (2010) Quantitative analysis of solid-state processes studied with isothermal microcalorimetry. *J Phys Chem B* 114:13173–13178
- Sousa L, Beezer AE, Hansen LD, Clapham D, Connor JA, Gaisford S (2012) Calorimetric determination of rate constants and enthalpy changes for zero-order reactions. *J Phys Chem* 116:6356–6360
- Sun DZ, Xu XY, Liu M, Sun XJ, Zhang JY, Li LW, Di YY (2010) Microcalorimetric and spectrographic studies on the interaction of DNA with betaxolol. *Int J Pharm* 386:165–171
- Urakami K, Beezer AE (2003) A kinetic and thermodynamic study of seratrodist polymorphic transition by isothermal microcalorimetry. *Int J Pharm* 257:265–271
- Vivoda M, Roskar R, Kmetec V (2011) The development of a quick method for amorphicity determination by isothermal microcalorimetry. *J Therm Anal Cal* 105:1023–1030
- Ziffels S, Schwarz E, Steckel H (2010) Recrystallization behaviour of partially amorphous lactose during and after compression. *Pharmaz Industrie* 72:508–518

Part IV
Separation Techniques

Chapter 13

HPLC/UHPLC

Steen Honore Hansen

Abstract Separation techniques have become unavoidable in the drug development process. All samples must be considered to consist of several components. It is important to verify that a compound developed in the initial research phase primarily contain the expected compound and not a number of major impurities that may be responsible for effect or side effects, but even a “pure” API do always contain minor impurities which have to be controlled. The formulated drug products contain a lot of excipients and have to be tested for stability where new impurities may be formed. In the clinical trials samples of plasma, urine, tissue etc. also have to be analysed for the drug substance and its metabolites often in very low concentrations. Therefore all these samples must be considered as complex samples and separation is needed in order to determine each component in a selective and reliable way.

Liquid chromatography is most useful for such qualitative and quantitative analysis and is performed using high performance liquid chromatography (HPLC) or ultra high performance liquid chromatography equipment (UHPLC). Using these techniques high efficiency separations are achieved, and in this chapter these techniques are described in detail.

Keywords High performance liquid chromatography (HPLC) • Ultrahigh performance liquid chromatography (UHPLC) • Separation theory • Separation selectivity • Separation efficiency • Detection • API purity • Drug stability • Sample preparation • Validation

1 Introduction

High performance liquid chromatography (HPLC) was developed in 1960s (Huber 1969) and has since become the most commonly used chromatographic technique in areas like drug development, food analysis and environmental monitoring. In the

S.H. Hansen (✉)

Department of Pharmacy, Faculty of Health and Medical Sciences,
University of Copenhagen, Copenhagen, Denmark
e-mail: steen.honorehansen@sund.ku.dk

beginning of this millennium the technique was further developed into what is called ultrahigh performance liquid chromatography (UHPLC). At an early stage in the development HPLC was named high pressure liquid chromatography because of the relative high pressures used during analysis and with UHPLC the used pressures are even higher but the basic principles are the same.

Today these techniques are often just mentioned as liquid chromatography (LC).

1.1 Chromatographic Separation

A chromatographic technique involves two phases of which at least one is mobile and the other most often is stationary. The two phases move relative to each other and in most cases the mobile phase move through a bed of a stationary phase. The stationary phase may be a piece of paper (paper chromatography), particles of a suitable material placed as a thin layer on an inert support (thin-layer chromatography) or packed into a tube (a column) (column chromatography). Column chromatography can be executed using a liquid (liquid chromatography; LC) or a gas (gas chromatography; GC) as the mobile phase. Before HPLC came into play column chromatography was performed using gravity flow of the mobile phase.

The basic physico-chemical principle of chromatography is the partitioning of analytes between two immiscible phases. When a mixture of analytes is introduced into an LC system a number of separation mechanisms will influence the partition of analytes between the two phases. The two phases move relative to each other and in most cases one phase moves (the mobile phase) while the other is stationary (the stationary phase). Sample molecules introduced into the chromatographic system will be exposed to a number of interactions (diffusion, collisions, dipole-dipole interactions, hydrogen bonding, electrostatic interactions etc. as illustrated in Table 13.1) in the two phases simultaneous with the transport of the analytes through the system. The interactions taking place are dependent on the physical and chemical nature of the analytes as well as of the mobile and stationary phases and may result in different partition of analytes between the two phases and thus in

Table 13.1 Energy in bonds or of intermolecular forces

Type of bond/Intermolecular force	Example of interacting molecules	Energy in	
		Kj/mol	(Kcal/mol)
Covalent	$\text{RH}_2\text{C}-\text{CH}_2\text{R}$	400–1200	(100–300)
Ionic	$\text{R}_4\text{N}^+\text{OOC}-\text{R}$	200–800	(50–200)
Hydrogen bond	$\text{H}_3\text{COH}\cdots\text{HOH}$	20–50	(5–12)
Dipole-dipole	$\text{C}_6\text{H}_5\text{Cl}/\text{H}_3\text{CC}\equiv\text{N}$	12–40	(3–10)
Dipole-induced dipole	$\text{H}_3\text{CC}\equiv\text{N}/\text{C}_6\text{H}_6$	10–25	(2–6)
Dispersion/van der Waal	$\text{C}_6\text{H}_6/\text{C}_6\text{H}_{14}$	5–20	(1–5)

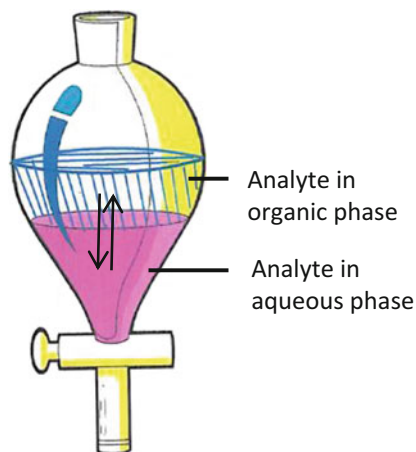
different migration rate through the system. A difference in migration rate of analytes in the system is synonymous with separation.

In this chapter an introduction to important separation principles in LC is given and how these principles can be used for separation, identification and quantification of analytes in the drug development process. The use of some chromatographic theory is needed in order to fulfill requirements from the health authorities controlling the quality of drug on the market. The quality of drugs and drug substances is regulated through the quality standards given in the international pharmacopoeias (e.g., Ph.Eur 2015; USP 2014). It is important to verify that a given chromatographic system is suitable for the intended purpose and this is done using a system suitability test. In such a test requirements to the number of theoretical plates, the retention factor and/or the resolution of given analytes are often stated and should be fulfilled before, during and after using the system. This will provide the highest reliability of the data produced.

1.2 Theory of Partition

Differential migration of individual compounds through the chromatographic system depends on the equilibrium distribution of each compound between the stationary phase and the mobile phase. Therefore, differential migration is determined by those experimental variables that affect this distribution such as the composition of the mobile phase, the composition of the stationary phase and the temperature (Snyder et al. 2010; Scott 1992). If we want to alter migration to improve separation, we must change one or more of these variables. The equilibrium distribution of an analyte in a two-phase system is given by the distribution constant, K_C (Fig. 13.1):

Fig. 13.1 An analyte have a certain distribution constant, K_C , for a given system of two immiscible phases at a given temperature and pressure



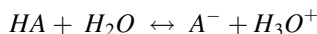
$$K_C = \frac{C_s}{C_m}$$

where C_s is the concentration of compound in the stationary phase and C_m is the concentration of compound in the mobile phase. The speed by which each compound migrates through the column is determined by the number of molecules of the compound which is statistically in the mobile phase at any instant, since sample molecules do not move through the column while they are in the stationary phase. The partitioning of molecules between the two phases is, however, a very rapid process. Retention of a compound is therefore determined by its distribution constant. Compounds with a large distribution constant have statistically a large portion of its molecules in the stationary phase and these compounds are strongly retained in the chromatographic system. Compounds with a small distribution constant have statistically a small portion of its molecules in the stationary phase and these compounds are less retained.

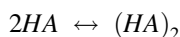
A compound appears to migrate smoothly through the column but at the molecular level the migration of a compound is highly discontinuous. Each time a molecule is transferred to the stationary phase, its migration is temporarily stopped while other molecules of the same kind pass further on. Some of these are immobilized a moment later and will be passed by the first molecule, and so on. Each molecule will thus follow a rapid, random alternation between the stationary and the mobile phase where the concentration of a compound, HA, in the stationary phase (s) and in the mobile phase (m) is determined by the distribution constant, K_C :

$$K_C = \frac{[HA]_s}{[HA]_m}$$

The distribution constant is a constant relating to specific molecular specie, but often the molecules can be present as different species e.g., by dissociating in a polar aqueous phase:



or form dimers in the organic phase:



These equilibria are very fast compared to the chromatographic process and it is therefore appropriate to look at the total distribution of all the species of a compound between the two phases:

$$D_C = \frac{[HA]_s + [A^-]_s + [(HA)_2]_s}{[HA]_m + [A^-]_m + [(HA)_2]_m} = \frac{[HA_{total}]_s}{[HA_{total}]_m}$$

The distribution between the two phases can also be expressed as the mass distribution ratio by multiplying the concentrations with the matching phase volumes:

$$D_m = \frac{[HA_{total}]_s \cdot V_s}{[HA_{total}]_m \cdot V_m} = \frac{((\text{amount of HA})_{total})_s}{((\text{amount of HA})_{total})_m}$$

1.3 Retention

The retention volume, V_R , of an analyte is the volume of mobile phase needed to elute the analyte to its maximum concentration from the chromatographic system (Fig. 13.2):

$$V_R = t_R \times F$$

where t_R is the corresponding retention time and F is the flow rate of the mobile phase in mL/min.

The hold-up volume (also named the dead volume), V_M , corresponds to the volume of mobile phase present in the system between the site of sample injection and the detection cell. This volume has to be moved out of the system before an

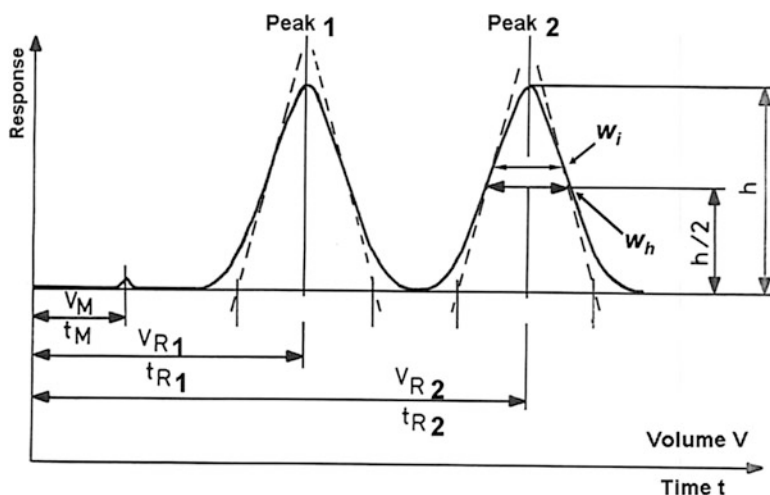


Fig. 13.2 A schematic chromatogram showing relevant chromatographic parameters

analyte injected and being only present in the mobile phase can reach the detector ($D_m \approx 0$).

When an analyte is eluted to its maximum concentration half of it has left the system in the mobile phase and the other half is still in the system distributed between the mobile and the stationary phase:

$$V_R \times [HA]_m = V_m \times [HA]_m + V_s \times [HA]_s$$

Thus

$$V_R = V_M + V_s \frac{[HA]_s}{[HA]_m} = V_M + V_s D_C,$$

and this leads us to:

$$V_R = V_M + V_M D_m = V_M (D_m + 1)$$

D_m is the mass distribution ratio of the analyte and is often referred to as the capacity factor, k or k' . Now k is the preferred designation and is more correctly called the retention factor.

For most purposes retention times are used instead of retention volumes resulting in the equations:

$$t_R = t_M (k + 1) \quad \text{and} \quad k = \frac{t_R - t_M}{t_M}$$

The correlation between retention and distribution ratio in a chromatographic system is obvious and the use of k -values makes it easy to compare chromatographic systems between different laboratories when using the same stationary and mobile phases but with different column dimensions and/or different connecting tubes.

1.4 Selectivity

The relative retention between two compounds, α , is equivalent to the ratio between their mass distribution values

$$\alpha = \frac{k_2}{k_1}$$

where k_2 is the retention factor of the later eluting compound and k_1 the retention factor of the first eluting compound. α is dependent of the nature of the

chromatographic phases and the temperature and its value should be kept within the range from 1.05 to 2 because larger values will result in unnecessary long analysis time.

Changing the selectivity in the separation is one of the most important ways to improve chromatographic separation and this is primarily done by changing the nature of the mobile and/or the stationary phase. Sometimes a change in column temperature may also affect the selectivity.

Please observe that the relative retention in Ph.Eur. is based on the ratio between retention times without correcting for the hold-up volume, t_M . This is done in order to avoid determination of t_M , but it may sometimes lead to a significant difference from the correct α -value for early eluting analytes.

1.5 Separation Efficiency

Molecules from a number of compounds in a mixture will after a chromatographic separation appear in separate bands if the compounds have different D_m -value (k-value). All molecules will migrate back and forth between the mobile and the stationary phase and the amount of each type of molecules present in the two phases is a statistical question dependent on the mass distribution ratio of each compound. The faster this exchange of molecules between the two phases is, the better will differences in partition ratios between analytes be expressed, and the more efficient the separation will be. In principle the molecules of an analyte should be brought into equilibrium between the two phases to express the distribution ratio. This will theoretically take place a number of times during the migration of the analytes through the column. Each equilibrium obtained can be considered equivalent to a theoretical plate also called the height equivalent to a theoretical plate, H. This theory is similar to the theory of theoretical plates in a distillation column (Martin and Synge 1941).

The number of theoretical plates, N, in a column is equivalent to the length, L, divided by H.

$$N = \frac{L}{H}$$

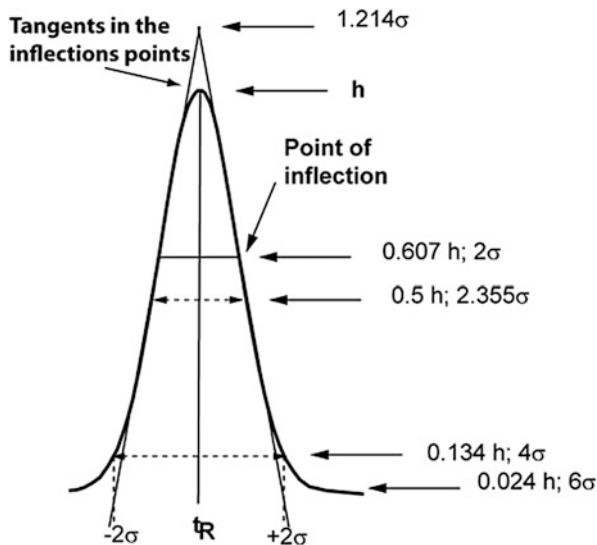
The plate height has the length σ^2/x , where σ is the standard deviation of the Gaussian peak (see Fig. 13.3) being equivalent to $1/4$ of the peak width, w, and x is the distance travelled.

For a peak just leaving the column the following equation is valid

$$N = \frac{Lx}{\sigma^2} = \frac{16(Lx)^2}{w_b^2}$$

and when using time units for column length and peak width we get

Fig. 13.3 A Gaussian peak with relevant parameters assigned



$$N = 16 \left(\frac{t_R}{w_b} \right)^2 = 5.54 \left(\frac{t_R}{w_h} \right)^2$$

where w_h is the peak width at half peak height and w_b is the peak width ($\sim 4\sigma$) at base line. It is therefore easy to calculate the number of theoretical plates for a certain compound using the chromatogram obtained. The number is dimensionless and the narrower the single peak, the more peaks can be separated and the higher the number N . The number of peaks possible to separate in a given chromatographic system assuming Gaussian peaks and a resolution of 1 is expressed as the peak capacity, PC:

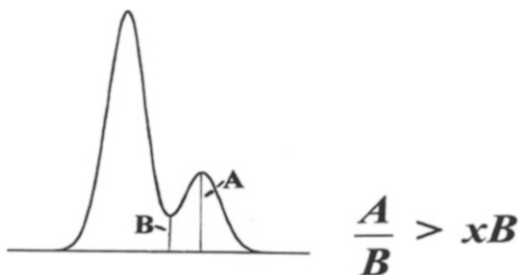
$$PC = 1 + \frac{\sqrt{N}}{4} \ln \left(\frac{t_R}{t_M} \right)$$

1.6 Resolution

The separation of two closely eluting, gaussian peaks can be expressed by the resolution, R_S ,

$$R_S = 2 \left(\frac{t_{R2} - t_{R1}}{w_{b1} + w_{b2}} \right) = 1.18 \left(\frac{t_{R2} - t_{R1}}{w_{h1} + w_{h2}} \right)$$

Fig. 13.4 Peak to valley-ratio



where t_{R2} and t_{R1} is the retention of the last and the first elution peak, respectively. The peak width may be measured at base line, w_b , or at half width, w_h .

When a resolution of 1.0 is achieved an overlap between the peaks is about 3 % and when $R_S = 1.5$ an overlap of only 0.2 % is present. Thus, with $R_S \geq 1.5$ the peaks are considered to be fully separated. However, this is only true when the peaks in question are of similar heights. If large differences in peak heights are present the minor peak may be compromised by a larger overlap from the major peak. In such cases another parameter for the resolution based on a peak to valley measurement can be used for characterization of the separation (Fig. 13.4).

An increase in resolution may preferably be achieved in two different ways: (1) by increasing the difference in retention (this is an increase in selectivity, α) or (2) by achieving more narrow peaks (this is an increase in efficiency, N). The change in α can be achieved by changing the constituents of the mobile phase (e.g., buffer (pH) and/or the organic solvent). The increase in efficiency is achieved by selecting a column containing a packing material with a smaller particle diameter (i.e., another column).

The resolution may also be expressed using the approximate formula

$$R_S = \frac{1}{4} \sqrt{N} \left(\frac{\alpha - 1}{\alpha} \right) \left(\frac{k}{k + 1} \right)$$

where efficiency, selectivity and retention are represented. From this it is directly deducible that it requires four times the number of theoretical plates to double the resolution, and as N is proportional to the length of the column an increase in analysis time of four will be the result. Therefore, a change in the selectivity is to be preferred. If it is possible to increase α from 1.05 to 1.10 the need for theoretical plates is decreased with a factor of 4 (Table 13.2). Thus an increase in relative retention will reduce the need for separation efficiency, and shorter columns may be used reducing the time of analysis accordingly. From Table 13.3 it can be learned that an increase in retention factor beyond 10 will only result in increase in analysis time without much improvement in separation.

Table 13.2 The required number of theoretical plates, N, as function of selectivity, α

α	$\left(\frac{\alpha}{\alpha-1}\right)^2$	Necessary number of N for $R_S = 1.5$ and $k = 2$
1.01	10,201	826,281
1.02	2601	210,681
1.03	1177	95,377
1.04	676	54,756
1.05	441	35,721
1.10	121	9801
1.15	58	4418
1.20	36	2916
1.25	25	2015
1.30	19	1514

Table 13.3 The required number of theoretical plates, N, as a function of retention

Retention factor k	Necessary number of N to obtain $R_S = 1.0$ for given α	
	$\alpha = 1.05$	$\alpha = 1.10$
0.1	853,780	234,260
0.2	254,020	69,700
0.5	63,500	17,420
1.0	28,220	7740
2.0	15,880	4360
5.0	10,160	2790
10	8540	2340
20	7780	2130

1.7 Summary on Theory

The basic of chromatography is partition of analytes between two immiscible phases. In LC the mobile phase is a liquid while the stationary phase is a solid or a liquid. A difference in distribution ratios is needed in order to obtain separation of analytes. From the theory outlined above a number of parameters can be highlighted: *Retention* can be expressed in time, t_R , or volume, V_R , units but could preferably be expressed as the retention factor, k , because this is identical to the mass distribution ratio, D_m . Values of k can be use when comparing similar LC system between laboratories independent of column dimensions. Separation efficiency of the chromatographic system is given by the number of theoretical plates, N , and the separation of an analyte from closely eluting peaks is expressed by the resolution, R_S .

These parameters are often used in the characterization of chromatographic system and are important parameters for evaluation of the suitability of a chromatographic system when used in system suitability tests in pharmacopoeias.

1.8 The Chromatographic Process

A minimum of knowledge about what is going on inside the analytical column during separation will ease the understanding of what is important when designing a new LC method.

When an analyte enters the chromatographic column the molecules will travel with the mobile phase in between particles and through pores in the column packing material. The molecules will therefore travel different distances which will result in distribution into a larger volume of mobile phase and thus a broader chromatographic peak when the analyte leave the column. This phenomenon is call EDDY diffusion (Fig. 13.5).

Furthermore, the molecules will be exposed to diffusion, which will have a significance in the longitudinal direction of the column and thus also lead to peak broadening. However, this contribution to the peak broadening will diminish with increasing flow-rate (Fig. 13.6).

Finally, the kinetics of the mass transfer of molecules between the two phases is important for the separation efficiency of the LC system. A fast exchange of the molecules between the two phases will promote the expression of the difference in mass distribution ratio between analytes and in this way increase separation efficiency. An increase in column temperature and a decrease in viscosity of the mobile and stationary phases will increase the exchange rate between phases and thus increase separation efficiency.

The individual contribution of the three parameters eddy diffusion, A, longitudinal diffusion, B, and mass transfer, C, to H as a function of the flow rate, u , of the mobile phase has been described in the classic van Deemter equation (Van Deemter et al. 1956)

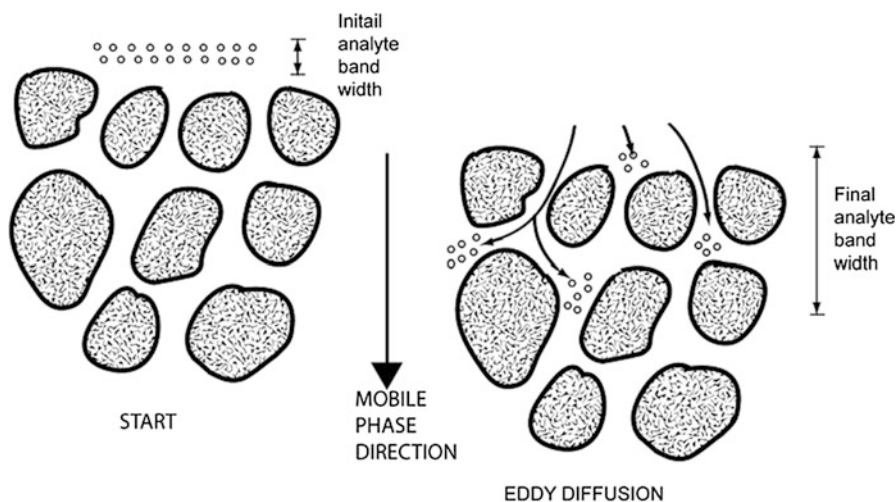


Fig. 13.5 Principle of EDDY diffusion

Fig. 13.6 Mass transfer of analyte between the chromatographic phases

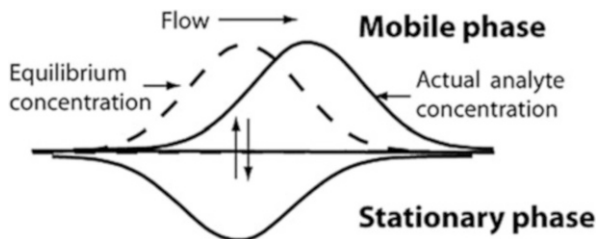
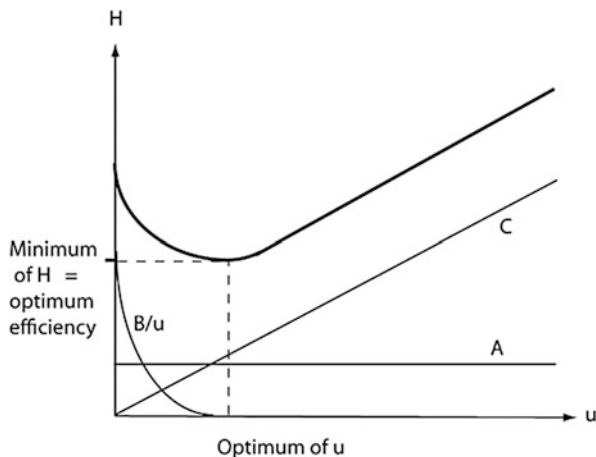


Fig. 13.7 The principle of a van Deemter plot



$$H = A + \frac{B}{u} + Cu$$

The van Deemter equation now exists in a number of refined versions (Huber and Hulsman 1967; Done and Knox 1972) but the basic principles are the same.

This can also be visualized in a diagram where the efficiency given as one theoretical plate, H , is plotted against the flow rate. The smaller the value of H , the more efficient is the system. From this Figure it is obvious that if loss in separation efficiency due to mass transfer can be minimized the flow rate may be increased leading to shorter analysis times. A deeper look into the van Deemter equation will also reveal that decreasing particle diameters of the column packing material will lead to increase in separation efficiency (Fig. 13.7).

1.9 Execution of HPLC/UHPLC

A basic HPLC equipment consists of a high pressure pump, a sample injection device, the separation column and a detector (Fig. 13.8).

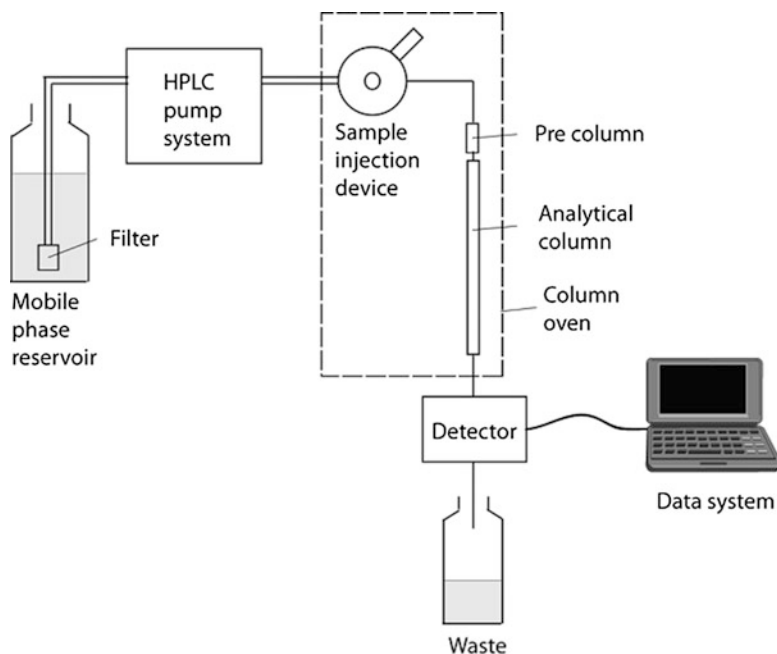


Fig. 13.8 Basic components of an HPLC system

The mobile phase is contained in a reservoir in which it also can be degassed. Water and polar organic solvents contain a certain amount of dissolved air. When the mobile phase is placed under pressure in the chromatographic system the solubility of the air increases, but when the pressure gradually decreases from the inlet to the outlet of the separation column the air may be released and form small bubbles that may disturb the detector signal. Therefore it is important to degas polar solvent prior to use in a pressurized LC system. Mixing of water and organic liquid will also result in release of air seen as bubbles. Therefore careful degassing of mobile phases is especially important when using gradient elution.

When samples contain a number of analytes with very different polarity (large span in distribution constants) gradient elution, where the eluting strength of the mobile phase is gradually increased during chromatography, is used. This has the advantage that late eluting peaks will be eluted earlier as sharper and higher peaks thus improving detection limits. The immediate reduction in analysis time observed is however somewhat lost due to the needed time for re-equilibration to the initial mobile phase condition. The correct re-equilibration is very important in order to keep constant retention times. If full re-equilibration is not achieved the retention of the analytes in the following chromatogram will be shorter—especially of the early eluting peaks. Gradient elution in the form of a washing step with strong eluting properties may also be useful in order to “clean” the column for strongly retained solutes.

The HPLC pump is designed to deliver a constant flow against a high pressure. In standard HPLC equipment the pressure limit is about 400 bar while it in UHPLC may be as high as 1500 bar. This puts a high demand on the technology in order to avoid leakages in the instrument. The constant flow is a must if reliable qualitative and quantitative data are to be obtained. Any particles in the mobile phase or in the sample will be deposited on top of the HPLC column and therefore a filter is placed on the solvent inlet line. If the separation column is gradually blocked due to injection of samples containing particles or material sticking onto the stationary phase the pump should compensate by increasing the pressure and keeping the flow rate constant.

Sample injection may be performed using a manual high pressure loop valve or by the use of an autosampler. The advantage of an autosampler is of course that the system will be able to work 24 h a day. Both injection devices should of course be able to withstand the high pressure in the system.

All partitioning between the mobile phase and the stationary phase are dependent on the temperature. The column system should be kept at a constant temperature. A larger difference in temperature between the sample (kept at room temperature) and the column (e.g., 50 or 60 °C) will result in peak broadening due to problems with mixing of liquids of different temperatures. This can be overcome by keeping the temperature of the capillary coming from the injection device to the column at the same temperature as the column.

The separation column (for HPLC and UHPLC) is the heart of the chromatographic system. It is in the column the analytes distribute between the two phases and in this way get separated. It is the composition of the mobile and the stationary phase that primarily control the separation. The separation principle is either straight phase (normal phase) chromatography, where the stationary phase is more polar than the mobile phase, or reversed phase chromatography, where the stationary phase is more nonpolar than the mobile phase.

For straight phase systems silica is often the preferred column packing material. Silica is an inorganic polymer formed by addition of acid to a silicate solution. However, silica from different manufacturers is often different in behavior due to different manufacturing processes. A typical mobile phase would be a mixture of heptane with 5 % of 2-propanol. However, if aqueous samples are injected into such a system the water will stick to the silica and gradually form an aqueous stationary phase and therefore such systems are difficult to keep in equilibrium. Straight phase systems are therefore not suitable for analysis of aqueous samples. In the beginning of the HPLC era silica contained a lot of metal ions (type A silica) which had an influence on the chromatographic performance, but now silica for chromatography is always highly purified (type B silica) (Gilroy et al. 2003) (Fig. 13.9).

It was a major break-through when stable stationary phases to be used in reversed phase chromatography became available in the beginning of the 1970s. Silica with chemically bonded stationary hydrophobic phases is used together with aqueous mobile phase made up of water and a miscible organic solvent like methanol or acetonitrile. The mobile phase can be further modified with a buffer to control pH and also with other additives. Reversed phase chromatography made

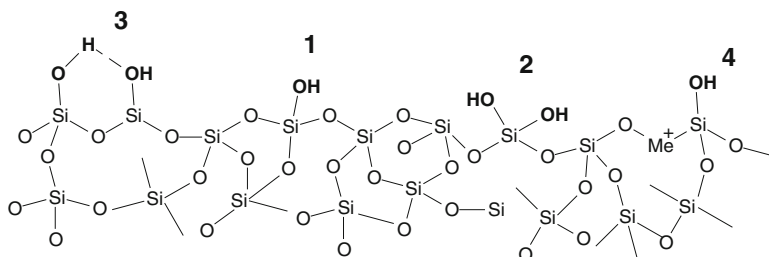


Fig. 13.9 Silica with (1) free (isolated) silanol groups, (2) geminal silanols, (3) associates silanols and (4) metal activated silanol group on the surface. The Si–O–Si bonds are the more hydrophobic siloxane bonds

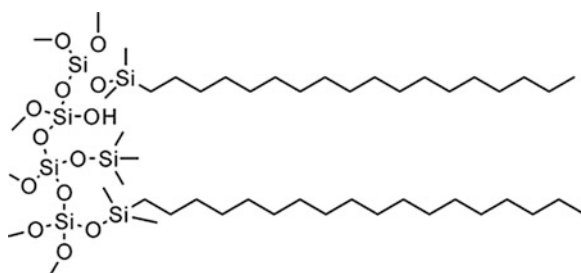


Fig. 13.10 Octadecylsilylsilica (ODS column packing material) for reversed-phase chromatography

it possible to directly analyse aqueous samples, and this principle has now become the far most used HPLC technique of all.

Basically the chemically bonded phase packing materials consist of silica material chemically modified with more or less hydrophobic organic molecules. The most used material is the octadecylsilylsilica (called ODS or C18 material, Fig. 13.10) which has C18 hydrocarbon chains on the surface. There seem to be no limit to the type of modification of the silica surface that can be performed. Presently (2014) there is close to one thousand different C18 materials on the market and they are all more or less different in their chromatographic characteristic because differences in manufacture of the silica and also in the bonding of the C18 groups. It is therefore recommended not to change the brand of a column packing material when first a method has been established.

A column packing material based on silica is not fully stable because very small amounts will dissolve over time. This is generally not a problem at low pH but at pH above ca. 8.5 silica dissolves and will disappear if no precautions are taken.

However, from the beginning of this millennium a number of column packing materials for reversed phase chromatography which can be operated at high pH, have become available.

Another direction of the technological development has been within particle size of the column packing materials. Starting out in about 1970 with solid core particles of about 40 μm in diameter having thin layer of porous silica on the surface smaller, fully porous particle sizes of 10 and 5 μm soon became available. In the 90s 3 μm became available and now column packing materials with particle sizes of 1.3–2 μm is state-of-the-art. It is remarkable that a number of the small particles now again are manufactured with a solid core and with a thin porous layer on the surface (DeStefano et al. 2008; Yoon et al. 2007). The decrease in particle diameter will of course lead to higher backpressures in the system. This can be overcome in two ways: a shorter column can be used because the smaller particles give more efficiency (higher number of theoretical plates) or by using higher pressures. Columns packed with 5 and 3 μm particles can be run in a standard HPLC system with a pressure limit of 400 bar (=40 Mega Pascals). But 1.5 μm particles require equipment that is able to run at a much higher backpressure and therefore UHPLC was developed. The chromatographic principles are the same as previously but new demand on the pumps, autosamplers and detectors had to be met. The pumps and autosamplers have to be able to withstand high pressures up to 1000–1500 bar (100–150 Mega Pascals) at the inlet side of the HPLC column. Using the column packing materials with 1.3–2 μm particles will provide very high number of theoretical plates and therefore the column dimensions can be reduced and analysis time and amount of mobile phase can be considerably reduced (see Tables 13.4 and 13.5). The high efficiency gives very narrow chromatographic peaks which means new demand on the detector cell volume to avoid that peaks separated on the column are mixed up in the detector cell. To fully explore the advantages (high efficiency and high speed of analysis) of UHPLC, UHPLC equipment is needed. On the other hand it is possible to use columns with 2–2.5 μm particles in standard chromatographic systems if the column length is not reduced too much (not below 50 mm). To do this it is important to optimize (reduce) the extra column volume which is in the connecting tubing from the injection device to the column and from the column to the detector incl. the detector cell volume.

Detection of analytes in the column effluent can be performed in many ways. The most widely used principle is spectrophotometry. A spectrophotometer equipped with a flow-through cell is all that is needed, but special requirements are needed.

Table 13.4 Effect of column length and particle size on column efficiency (N)

Column Length (mm)	Resolving Power N(5 μm)	Resolving Power N(3.5 μm)	Resolving Power N(1.8 μm)	Resolving Power N(1.3 μm)
150	12,500	21,000	-	-
100	8,500	14,000	-	-
75	6000	10,500	-	-
50	4,200	7,000	12,000	-
30	-	4,200	6,500	12,000
15	-	2,100	2,500	-

Table 13.5 Some typical HPLC columns and the corresponding eluent consumption

Column dimension (mm)	Particle size (μm)	Flow rate (mL/min)	Mobile phase consumption (Rel. %)	Injection volume (μL)	Volume of liquid in column (μL) Permeability = 0.6
250 \times 4.6	5	1.0	100*	20	2491
150 \times 4.6	3	1.0	60 (rel. to *) ^a	20	1495
150 \times 2.0	3	0.2	12 (rel. to *)	5	198
100 \times 2.0	2.5	0.2	8 (rel. to *)	5	132
50 \times 4.6	1.8	1.0	33 (rel. to \square)	20	498
100 \times 4.6	1.8	1.0	60 (rel. to *)	20	997

*relative to 250 \times 4.6 mm with 5 μm particles^arelative to 150 \times 4.6 mm with 3 μm particles**Table 13.6** Some selected, commercially available LC detectors and their typical performance

Detector	Lower limit of detection (ng)	Compatible with gradient elution
Ultra-violet (UV)	0.1–1	Yes
Fluorescence	0.001–0.01	Yes
Mass spectrometry (MS)	0.001–0.01	Yes
Electrochemical (ECD)	0.01–1	No
Refractive index (RI)	100–1000	No
Evaporative light scattering (ELSD)	0.1–1	Yes
Charged aerosol (CAD)	0.1–1	Yes

One of the first HPLC detectors developed had a mercury lamp as the light source. This provides discrete emission lines of which the line with the wavelength 2537 Å (254 nm) has the strongest light intensity giving the lowest limits of detection when used as detection wavelength. This is also the reason why many chromatographers still use 254 nm as the detection wavelength for their methods, although mercury lamps no longer are in use. Spectrophotometric detectors today are variable wavelength detectors able to detect at several wavelengths at the same time or diode array detectors where full UV spectra can be obtained in milliseconds and thus in each data point of the eluting peak. The spectrophotometric detector can be used in the wavelength range from 190 nm to about 800 nm but limitation may occur due to light absorbance of the mobile phase in the lower UV range.

Many other detection principles have been proposed and a number is commercially available and the most important of these are shown in Table 13.6. Of these detectors especially the mass spectrometer (MS) becomes more and more important because this detection principle provides not only quantitative information but also information on the molecular structure as well as much higher selectivity than the UV detector.

It is important to have a detection volume that is appropriate in relation to the peak width of the chromatographic peak. If the detection volume is too large two closely eluting but separated peaks will be mixed in the detector cell and will then

appear as one unresolved or only partly resolved peak. Accordingly, detector to be used for high efficiency separations should also have a fast electronic response. If the response factor of the detector is too long chromatographic separated peaks may appear as partly unresolved peaks in high efficiency systems.

1.10 LC in Drug Discovery, Development and Manufacturing

HPLC has since its commercialization in the late 1960s become the most important analytical chemical technique for analysis of drug substances and drugs. It is the work horse when identity and quantity of analytes are to be determined.

In the early discovery process a lot of molecules are to be tested in different assays. The quality (purity) of the test samples must be known to avoid wrong conclusions on the test result. Already at this stage LC coupled to MS are used to verify identity and purity of samples.

When lead substances have been selected they will be produced in a larger scale to be used in preliminary animal experiment. At the preclinical stage LC is used not only for quantitative analysis and purity testing but can also be used for determination of physico-chemical characteristics of the compound. Preclinical characterization parameters like pK_a , log P and log D values can be determined using LC (Chiang and Hu 2009). pK_a values can of course be determined using other techniques like UV-spectrophotometry or titration but especially determination of log P and log D values using reversed phase LC have shown to be useful.

In early drug discovery it is also important to obtain knowledge about the biotransformation of the drug substance in different animal species incl human (Zhang et al. 2007). Initially this is performed using isolated liver microsomes or intact hepatocytes from the different animal species. Preferably all drug metabolites found in humans should be qualified in the animal toxicity studies.

1.11 Drug Formulation and Stability

The analysis of dosage forms can easily be performed using LC. However, it should always be considered if a more simple approach can be applied for such analysis. If the dosage forms only contain one API having UV absorption and a number of non-UV absorbing excipients, quantitative UV measurements may be preferred. If the dosage forms contain UV absorbing excipients, contain more than one API or it is a question of a stability indicating method, LC is a logic choice. Such analysis are typically performed using reversed phase LC and with UV detection. The drug formulation is dissolved in the appropriate volume of mobile phase and after filtration or centrifugation the sample is injected onto the LC.

Although a “pure” API may be considered a multicomponent system because small amount of impurities always will be present the mixing of the API with excipients is a real multicomponent system. When creating such a formulation a number of items have to be considered in order to obtain a stable product. It is not only the compatibility between each individual ingredient but also possible presence of impurities in the excipients which may—being a impurity of a major component of the system compared to the amount of API—comprise a significant problem (Wu et al. 2011). Examples of this are the content of peroxides in polypyrrolidone resulting in oxidation of the API.

The API can also under certain conditions react with excipients and form new compounds—impurities. And if they amount to a certain level they have to be identified and qualified with respect to toxicity.

Examples: 5-aminosalicylic acid (5-ASA) a drug used to treat gut deceases was to be formulated as an enema. The API can easily be oxidized, a reaction which is catalyzed by trace metals e.g., iron and therefore citric acid was added partly as a buffer substance and partly for scavenging possible catalytic divalent cations. It lasted a while before it was discovered that the API and citric acid reacts with each other (Larsen et al. 2009). The product was assayed for content of 5-ASA by HPLC during the stability trial and because 5-ASA is an amino acid it elutes fairly early in a reversed phase system. However, the formed reaction products were amides and esters (Fig. 13.11) that had a considerably longer retention and therefore eluted as broad peaks in later chromatograms. Such broad peaks will first be detected when they have reached a significant amount. This is an example that shows that it can be a good idea to used gradient elution where late eluting impurities are more easily detected at an earlier stage in the drug development process.

In general citric acid and other multivalent carboxylic acid are likely to react with alcohol groups and with primary and secondary amines to form esters and amides, respectively. The reaction is of course much faster in solution compared to

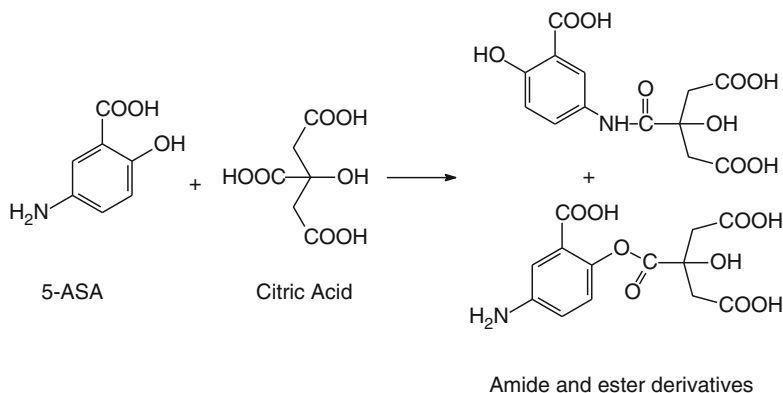


Fig. 13.11 Reaction between 5-aminosalicylic acid and citric acid forming the symmetrical citrates. The corresponding asymmetrical citrates are also formed

the solid state but even in solid state some micro environment with water may create an environment for such processes to take place.

Drug substances containing carboxylic acid groups can therefore also react with excipients having alcohol groups in their structure. An example of this is the drug substance cetirizine which has been shown to react with polyalcohols like sorbitol and glycerol as well as polyethylene glycols (Yu et al. 2010). Cetirizine is formulated as drops, syrups as well as tablets, and impurities being reaction products between the API and some excipients have been found in the liquid preparations.

2 Animal Experiments

Already at a very early stage in the drug development process biochemical *in vitro* systems comprising the use of cells or subcellular preparations are used. In order to be able to study the fate of the drug substance and possible transformations products in these systems more dedicated separation and detection techniques are required. HPLC is still a very important tool but now UHPLC seems to take over due to the very high separation efficiency. This combined with the latest developments in mass spectrometry is an extremely valuable tool for picking the needle in the haystack. This is becoming even more important in the analysis of biopharmaceutical often used at very low doses. It is not unusual to measure at a level of few picogram per mL of plasma.

Initial *in vitro* experiments with hepatocytes or subcellular fraction thereof take place in order to look at drug metabolism in different animal species as well as in humans. Also at this stage HPLC become unavoidable as metabolites have to be separated and even isolated and purified in a sufficient amount to be analysed by NMR (nuclear magnetic resonance) to give the final chemical structure. The NMR technology has developed into a level that makes it possible to elucidate the structure of sub milligram down to a few microgram of substance, and these amounts may be isolated using an analytical HPLC column. If larger amounts of metabolites are to be purified the possibility is to use larger columns and also for this purpose UHPLC technique is available.

A typical bioanalytical method consists of a sample preparation including a concentration step followed by LC-MS. The sample preparation is either performed using liquid-liquid extraction or using solid phase extraction followed by evaporation of the organic extract and reconstitution in the mobile phase. For extraction solid phase extraction columns in a 96 well-plate format can be used enabling high through put analysis.

3 Clinical Trials and Bioanalysis

After the preliminary animal toxicity studies have been performed and it has been verified that humans do not produce other metabolites than those observed in animal studies and when the formulation of the drug product is finalized the first clinical trials on healthy humans can take place.

The bioanalytical methods developed during animal studies can often be used to follow the plasma concentrations in clinical studies.

3.1 “How to” and “Don’t do”

Performing HPLC/UHPLC is in principle a very straight forward activity. Familiarize yourself with the hard-ware and soft-ware. Prepare the mobile phases and flush the instrument. Select and install your column (in more than 90 % of the cases reversed phase will be used typically with a C18 column packing material), and be sure to avoid dead volumes in the connections between tubing, column and detector. Bring your sample into solution and secure that the solution is free of particles (by centrifugation or filtration) and is compatible with the mobile phase (that the sample solvent has a similar or less strong elution effect on analytes compared to the mobile phase) and that no precipitation will occur (e.g., from proteins in biofluids). The detection principle should of course be compatible with the mobile phase (no strongly UV absorbing components if UV detection is used and only volatile constituents when MS is used).

Troubleshooting is an unavoidable part of performing HPLC/UHPLC. It is not possible to give a full presentation of this in the present text, but a help to solve problems can be found from manufacturers or in text books. Only the most common mistakes that can ruin the analysis are presented here.

One of the most encountered mistakes among unexperienced chromatographers is injection of samples dissolved in a solvent which is stronger eluting than the mobile phase. This may lead to peak broadening, peak distortion or even to disappearance of the peak. A typical example may arise when analysis of drug substances and drugs with low solubility in water are to be performed by reversed phase LC. Due to the solubility the samples may be dissolved in methanol, but if such a solution is injected into the reversed phase system where the mobile phase typically is a mixture of water and an organic solvent like methanol or acetonitrile, the sample solvent is stronger elution than the mobile phase. After injection the analyte molecules therefore prefer to stay in the sample solvent plug until it has been mixed with the mobile phase. If there is a large difference in elution strength of the sample solvent compared to the mobile phase (e.g., a mobile phase with a high water content) the analyte peak may be distorted or the analyte may even be eluted in the solvent front. Also a difference in pH may result in such problems which are shown in Fig. 13.12 where the ionisable compounds 4-aminobenzoic acid

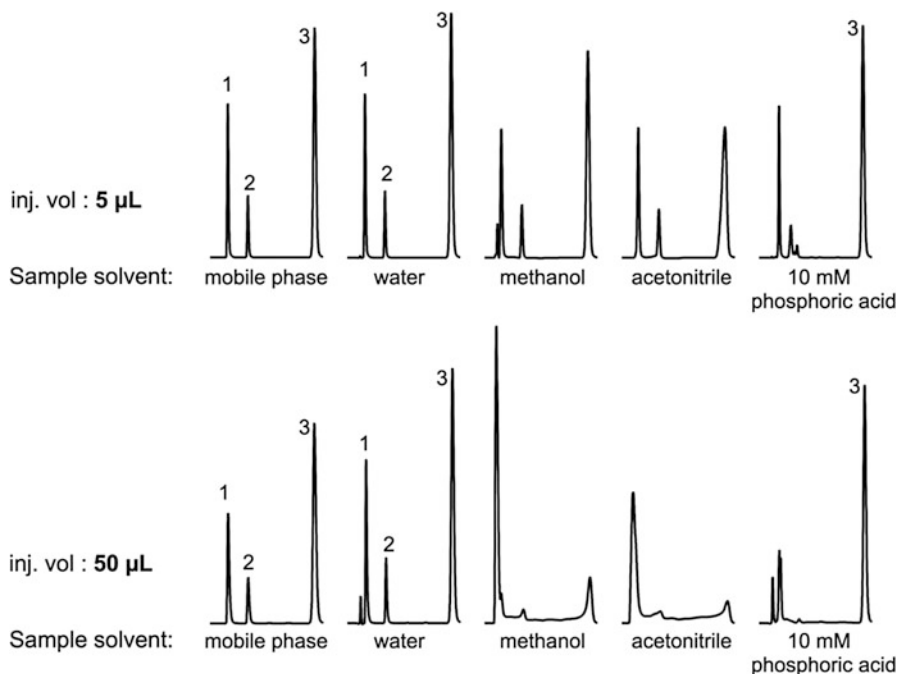


Fig. 13.12 Influence of sample solvent on the resulting chromatogram. Separation of 3 test solutes (1) 4-aminobenzoic acid, (2) aniline, (3) methylparaben in a reversed phase system with a C18 column and a mobile phase consisting of 15 % acetonitrile in 20 mM phosphate buffer pH 6.0. The solutes are dissolved in five different sample solvents and the samples are injected in a volume of 5 μL and 50 μL , respectively

and aniline is influenced by the difference in pH while the neutral compound methylparaben is unaffected of the discrepancy between the sample solvent and the pH of the mobile phase. The problems will of course increase with increasing sample volume as also shown.

If the solubility of the drug necessitate use of an organic solvent for dissolution it is important to validate if the sample can be used directly for LC analysis. Injection of increasing sample volumes into the LC will reveal if troubles can be expected. If it is necessary to dissolve the sample in neat methanol or acetonitrile a subsequently addition of small amounts of water (e.g., 5 or 10 %) to the sample will diminish the problems.

If possible the sample should be dissolved in the mobile phase or a solvent which is less strong eluting compared to the mobile phase, and all these considerations also applies for straight phase chromatography incl. HILIC where water is the stronger eluting solvent.

Samples ready for LC analysis should be completely free of particles and other items that may stick to the column (e.g., fat or constituents that may precipitate during injection). Therefore sample preparation is of the outmost importance.

Everything that is dissolved in the final sample should be able to pass through the analytical column. Otherwise items may build up on the column and gradually change its separation characteristic and efficiency or even block the column. A perfect sample preparation will avoid these problems.

When quantitative analysis is performed always measure the calibration standards in the same batch run as the samples. Use of calibration curves from a previous batch run can result in wrong results because the LC technique is not an absolute measurement but is based on comparison with calibration standards of known concentration. Because a number of parameters may change from batch run to batch run (temperature in the column, detector response, mobile phase composition etc.) calibration standards have to be measured in the same batch run.

Sometimes chromatographers are recommended to use a precolumn in order to protect the analytical column. In such a case it is important to realize that the precolumn is a part of the analytical column and any gradually change in retention time or column efficiency will be restored when changing the precolumn. These changes forth and back may have an influence on quantitative data and therefore validation is important.

3.2 Validation

Validation of an analysis method should be performed according to the ICH-guideline Q2(R1). Validation of a method is needed in order to prove that the method in question is suitable for the intended purpose. The validation should cover linearity, accuracy and precision. Limit of quantification and limit of detection is normally only needed for bioanalytical method. Furthermore, range and robustness may be validated (see guideline) especially if the method is to be transferred to another laboratory. The validation package can be more or less voluminous depending of where in the discovery, development or manufacturing process the method has to be used. However, some minimum validation must always be performed in order to prevent the production of unreliable analytical data. Please do remember that all analytical data are produced to be used for decisions for further action. Linearity, accuracy and precision should always be investigated.

4 Conclusions

Separation techniques have become most important to obtain qualitative and quantitative data throughout the process of drug development. HPLC with the further technological development into UHPLC (the borderline is difficult to set) allows qualitative and quantitative determination of several components in a

sample within a few minutes. With the coupling to different selective detectors—especially mass spectrometry—very sensitive and reliable analysis can be performed also on biofluids (plasma, urine etc.) with detection down into the femtomol range. Liquid chromatography has become extremely popular because aqueous samples can be handled in a simple way compared to what was necessary with gas chromatography where extraction to a volatile organic liquid was needed. In drug development HPLC/UHPLC is very useful from the early development phase, into the API characterization, the drug formulation process, the drug stability testing and the analysis of biofluids during clinical trials. But remember: Validation is a very important part of any method development to assure reliable data.

References

- Chiang PC, Hu Y (2009) Simultaneous determination of LogD, LogP, and pK(a) of drugs by using a reverse phase HPLC coupled with a 96-well plate auto injector. *Comb Chem High Throughput Screen* 12:250–257
- DeStefano JJ, Langlois TJ, Kirkland JJ (2008) Characteristics of superficially-porous silica particles for fast HPLC: some performance comparisons with sub-2- μm particles. *J Chromatogr Sci* 46:254–260
- Done JN, Knox JH (1972) Performance of packings in high speed liquid chromatography. II. Zipax. Effect of particle size. *J Chromatogr Sci* 10:606
- Gilroy JJ, Dolan JW, Snyder LR (2003) Column selectivity in reversed-phase liquid chromatography. IV. Type-B alkyl-silica columns. *J Chromatogr A* 1000:757–778
- Huber JFK (1969) High efficiency, high speed liquid chromatography in columns. *J Chromatogr Sci* 7:85–90
- Huber JFK, Hulsman JARJ (1967) A study of liquid chromatography in columns, the time of separation. *Anal Chim Acta* 38:305
- Larsen J, Staerk D, Cornett C, Hansen SH, Jaroszewski JW (2009) Identification of reaction products between drug substances and excipients by HPLC–SPE–NMR: ester and amide formation between citric acid and 5-aminosalicylic acid. *J Pharm Biomed Anal* 49:839–842
- Martin AJP, Synge RLM (1941) A new form of chromatogram employing two liquid phases. *Biochem J* 35(12):1358–1368
- The European Pharmacopoeia (2015) *Chromatographic separation techniques*, 8th edn. 2.2.46, pp 73–79
- The United States Pharmacopoeia 38 and National Formulary 33 (2014) 621 *Chromatography*, pp 424–434
- Scott RPW (1992) *Liquid chromatography column theory*. Wiley, New York
- Snyder LR, Kirkland JJ, Dolan JW (2010) *Introduction to modern liquid chromatography*, 3rd edn. Wiley, Hoboken
- Van Deemter JJ, Zuiderweg FJ, Klinkenberg A (1956) Longitudinal diffusion and resistance to mass transfer as causes of nonideality in chromatography. *Chem Eng Sci* 5:271–289
- Wu Y, Levons J, Narang AS, Raghavan K, Rao VM (2011) Reactive impurities in excipients: profiling, identification and mitigation of drug-excipient incompatibility. *AAPS Pharm Sci Tech* 12:1248–1263
- Yoon SB, Kim J-Y, Kim JH, Park YJ, Yoon KR, Park S-K, Yu J-S (2007) Synthesis of monodisperse spherical silica particles with solid core and mesoporous shell: mesopore channels perpendicular to the surface. *J Mater Chem* 17:1758–1761

- Yu H, Cornett C, Larsen J, Hansen SH (2010) Reaction between drug substances and pharmaceutical excipients: formation of esters between cetirizine and polyols. *J Pharm Biomed Anal* 53:745–750
- Zhang D, Zhu M, Humphreys WG (2007) *Drug metabolism in drug design and development*. Wiley, New York, pp 263–285

Chapter 14

Capillary-Based Techniques for Physical-Chemical Characterization of Drug Substances and Drug Delivery Systems

Jesper Østergaard, Susan W. Larsen, and Henrik Jensen

Abstract Physical chemical characterization of drug compounds and drug delivery systems is challenging when the amount of material for analysis is limited. Capillary-based methodologies based on capillary electrophoresis (CE) or Taylor Dispersion Analysis (TDA) present a number of advantages as they are characterized by being fast, require a very limited amount of sample material, are easy to automate and highly versatile. Different methods may be applied leading to a range of physical chemical properties being probed for the same sample using the same instrumentation. The term affinity CE covers a range of approaches for assessing important physical chemical parameters such as non-covalent affinity constants, pKa values as well as partition/distribution coefficients measured by quantifying partitioning into microemulsions and micelles. On the other hand, TDA provides data on diffusivities and hydrodynamic radius as well as viscosity. A variant of this technique termed Flow Induced Dispersion Analysis (FIDA) may be used to quantify non-covalent affinity interactions for charged as well as neutral species. The present chapter highlights novel features of capillary based methods in profiling physical chemical properties of drug compounds and drug delivery systems. A number of feasible applications are described, which may serve as an inspiration in delivery science and technology.

Keywords Capillary electrophoresis • Taylor dispersion analysis • Diffusion coefficient • Hydrodynamic radius • Affinity constant • pKa • Affinity shift capillary electrophoresis • Partition coefficient

J. Østergaard • S.W. Larsen • H. Jensen (✉)

Faculty of Health and Medical Sciences, Department of Pharmacy,
University of Copenhagen, Universitetsparken 2, Copenhagen, 2100, Denmark
e-mail: henrik.jensen@sund.ku.dk

1 Introduction

Characterization and analysis of drug substances is an integrated part of the drug development process. In the initial development phase, the amount of material available for characterization and analysis is often a limiting factor. While this problem has been apparent for many years, the trend towards an increasing focus on drugs based on biomacromolecules (peptides, proteins and DNA/RNA) has further highlighted these methodological challenges.

Faced with a few micrograms of a new chemical entity (NCE) some of the initial questions to be asked in a drug development program might be: Is the compound pure and stable? What is the solubility and perhaps acid base properties? What is the partition coefficient? Does the compound interact with plasma proteins? Using standard techniques, it may be possible to select only a few key properties to study simply due to lack of material. Later in the development, the selection and characterization and performance of the drug substances and drug delivery systems may be additionally limited by time consuming procedures.

The focus of the present chapter is capillary-based techniques, namely capillary electrophoresis (CE) and Taylor Dispersion Analysis (TDA) that are characterized by low sample volume requirements (microliters), automated and rapid methods. CE-based separation methods have therefore frequently been used as an approach for quantification of drug substances and impurities. However, the same general advantages also present capillary-based methods as an interesting choice for physical-chemical characterization such as for example assessment of partition behavior; acid dissociation constants (pK_a -values) and non-covalent interactions.

The current chapter will review the basis for CE, affinity CE and TDA. In addition to describing a number of useful physical-chemical characterization methods, the aim is to provide guidelines to select the most appropriate technique (s) in a given situation. The format of the present chapter prevents a detailed review of the entire body of literature covering the subject. The aim is to provide the reader with a practical tool that can be used in selecting methodology and be an aid in data treatment, analysis and interpretation. More specialized reviews are available in the literature (Henchoz et al. 2009; Heegaard and Kennedy 1999; Østergaard and Heegaard 2003, 2006; Jia 2005; Neubert and Rüttinger 2003). In addition, the table in Sect. 3 of the present chapter provides references to more specialized literature covering specific applications.

2 Capillary-Based Techniques for Application in Pharmaceutical Sciences

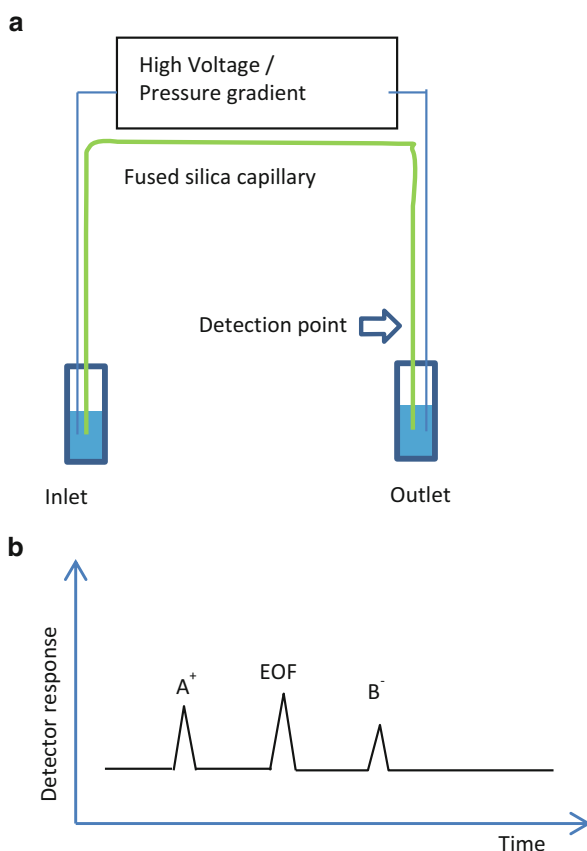
Capillary electrophoresis has been widely used as a separation method in bioanalysis (Kostal et al. 2008). Many applications involve quantification of an active pharmaceutical ingredient in plasma, drug formulations or crude products.

It should, however, be highlighted that in relation to drug development, capillary-based methods are highly relevant for screening and characterization of non-covalent interactions as well as determination of physical-chemical properties using only a minimum amount of material.

2.1 The Basics of Capillary-Based Analysis

The minimum requirement for conducting capillary electrophoresis (CE) based analysis is a high voltage power supply, a separation channel and a detector (Fig. 14.1). In TDA, a pressure gradient may be used to produce a hydrodynamic flow (Fig. 14.1). Usually, narrow bore fused silica capillaries (20–75 μm inner diameter) are used as the separation channel as they are relatively cheap and a wide variety of protocols exists for surface modification (see Sect. 3.2). In CE, charged

Fig. 14.1 Schematic representation of a capillary-based setup that may be used for physical-chemical characterization of drug substances and drug delivery systems (a). The electropherograms in CE are dependent on the capillary zeta potential, the applied potential and the charge of the investigated compound(s). In this example, the electrophoretic migration of positive species (A^+) is in the same direction as the EOF, whereas the electrophoretic migration of negatively charged species (B^-) is in the opposite direction of the EOF (b)



compounds are separated according to differences in their migration in an electrical field. The electrophoretic migration velocity, v_a , of an analyte is given by:

$$v_a = \mu_a \cdot E \quad (14.1)$$

where μ_a is the electrophoretic mobility and E is the field strength in the capillary. The field strength may be controlled experimentally as it is directly proportional to the applied potential difference between inlet and outlet of the capillary, V_{app} :

$$E = \frac{V_{app}}{l_c} \quad (14.2)$$

where l_c is the total capillary length.

In addition to the electrophoretic migration velocity, there is also an electroosmotic flow v_{eof} which is also dependent on the field strength according to:

$$v_{eof} = \mu_{eof} \cdot E \quad (14.3)$$

where μ_{eof} is the electroosmotic mobility defined as:

$$\mu_{eof} = \frac{\epsilon \cdot \zeta}{\eta} \quad (14.4)$$

Here ζ is the zeta potential of the inner capillary wall (related to the surface charge), ϵ is the relative permittivity of the run buffer solution and η is the run buffer viscosity. The “run buffer” is the solution present inside the capillary as well as at the inlet and outlet of the capillary during the separation. The run buffer filling the capillary will be transported through the capillary by the electroosmotic flow. Consequently, compounds are transported through the capillary by the combined action of the electroosmotic flow (EOF) and the electrophoretic migration. In some situations, the EOF is in the same direction as the electrophoretic mobility, whereas in other situations the electrophoretic mobility and EOF are in opposite directions. The polarity and inner surface charge of the capillary, the polarity of the applied potential difference and the charge of the compound being analyzed determines if the EOF and electrophoretic mobility will be operating in the same direction or in opposite directions (Fig. 14.1). In most cases, the EOF is in-itself not relevant for analysis, and is therefore solely measured in order to be able to correct for it in order to obtain the mobility of the species of interest (see later sections). The effective electrophoretic mobility corrected for the EOF is obtained as:

$$\mu_{eff} = \frac{l_c \cdot l_d}{V_{app}} \left[\frac{1}{t_a} - \frac{1}{t_{eof}} \right] \quad (14.5)$$

where l_d is the length from the capillary inlet to the detector and t_a and t_{eof} are the peak appearance times corresponding to the analyte and the EOF, respectively. The peak appearance time of the EOF is obtained by a charge neutral compound without electrophoretic mobility; such compounds, also termed EOF markers, are transported through the capillary exclusively by the EOF. According to Eq. (14.4), the direction and magnitude of the EOF depends on the surface zeta potential of the capillary. For example changing the surface charge from negative to positive will change the direction of the EOF. It should also be noted that if the EOF of the system and electrophoretic mobility of an analyte are in opposite directions, it is not always possible to observe both in the same run.

Due to the low samples volumes needed, an inherent limitation in capillary-based techniques is the relatively high detection limits. Most commercial systems for capillary electrophoresis have a built-in UV-Vis detector, but the short optical light path may prevent detection limits lower than the micromolar range. Further, for compounds lacking a suitable chromophore, as may be the case for many pharmaceutical excipients, UV-detection is not an option. Most commercially available CE systems can relatively easily be hyphenated with other detectors such as fluorescence (Annovazzi et al. 2004; Cao et al. 2013), capacitively coupled conductivity detection (CCCD)(Jensen et al. 2007), ElectroSpray Ionization Mass Spectrometry (ESI-MS)(Wan et al. 2005) and Inductively Coupled Plasma Mass Spectrometry (ICP-MS)(Nguyen et al. 2012, 2013a, b). Of these techniques, fluorescence is by far the most sensitive; however, many drug substances as well as excipients lack a suitable fluorophore. CCCD is a cost effective alternative compared to most other detection techniques and may in favorable cases have sensitivities in the micromolar range (Kuban and Hauser 2011). ESI-MS is a sensitive alternative in CE, but the limitations in the choice of buffer systems prevent the use of ESI-MS as a universal detection technique for pharmaceutically relevant systems. ICP-MS offers element specific detection and has advantages in detection of metal containing drug compounds (Nguyen et al. 2012, 2013a, b).

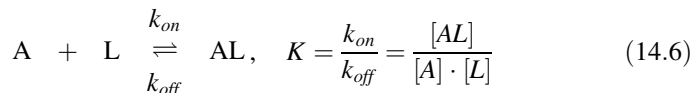
TDA rely on a hydrodynamic flow, which may be generated by a pressure gradient along the capillary as illustrated in Fig. 14.1. TDA is described in further detail in Sect. 2.3.

2.2 Techniques Based on Affinity Capillary Electrophoresis

Affinity capillary electrophoresis is an overall term for a variety of techniques used for assessing non-covalent interactions. In this section, we shall briefly discuss some of the most frequently applied approaches termed mobility shift affinity CE, affinity electrokinetic chromatography, pre-equilibrium capillary zone electrophoresis and frontal analysis capillary electrophoresis.

2.2.1 Mobility Shift Affinity CE

Mobility shift affinity CE is used to study solution equilibrium processes which may be represented as:



where K is the equilibrium constant corresponding to the equilibrium between A and L to form the complex AL (Zavaleta et al. 2006; Liu et al. 2009), k_{on} is the rate constant corresponding to complex formation (association) and k_{off} is the rate constant corresponding to complex dissociation. For the sake of clarity, we have represented the process as a simple 1:1 equilibrium, but the technique may also be used for other stoichiometries.

In mobility shift affinity CE, the entire capillary and the run buffer vials are filled with buffer containing the ligand L in various concentrations. The other binding partner, A, is injected as a small sample zone in the capillary and the electric field is applied. The most important requirement for this method is that at least one of the binding partners should be charged in order to have an effective electrophoretic mobility different from the complex AL. Another requirement is related to the binding kinetics, which should be fast compared to the analysis time. A mobility shift CE experiment is illustrated in Fig. 14.2.

Data analysis is simplified if L is present in large excess compared to A (the molecule detected). If L is present in large excess and/or K is high, the apparent effective mobility, μ_{eff} , measured experimentally will approach that of the complex AL. On the other hand if conditions are selected so that A and L do not bind (low concentration of A and/or L), the effective mobility measured corresponds to that of A. In general, the effective mobility will be related to the fraction of bound analyte A according to:

$$\mu_{eff} = \frac{[A]}{[A] + [AL]} \cdot \mu_A + \frac{[AL]}{[A] + [AL]} \cdot \mu_{AL} \quad (14.7)$$

where μ_A and μ_{AL} are the electrophoretic mobilities of A and AL, respectively. Combining Eq. (14.6) and Eq. (14.7) provides the binding isotherm:

$$\mu_{eff} = \frac{\mu_A + \mu_{AL} \cdot K \cdot [L]}{1 + K \cdot [L]} \quad (14.8)$$

Experimentally, μ_{eff} (obtained from Eq. (14.5)) is determined at various [L] to obtain the binding isotherm. A data fitting procedure will provide K and μ_{AL} . If L is in large excess compared to A, [L] can be approximated by the total ligand concentration.

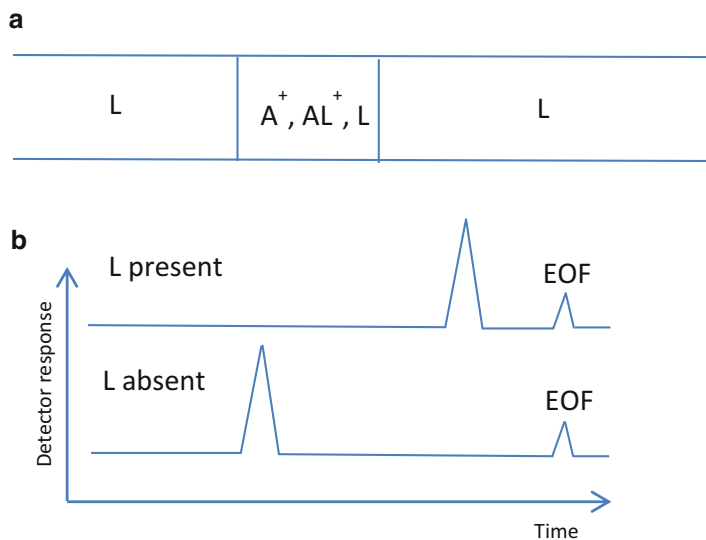


Fig. 14.2 Schematic distribution of A^+ , AL^+ and L in the capillary during a mobility shift CE experiment (a). Schematic illustration of electropherograms in the presence and absence of an interaction ligand where A is the compound detected (b). In this example, A^+ is positively charged and the interacting ligand L is neutral. In the presence of L , the apparent electrophoretic mobility of A is decreased due to complex formation

Mobility shift CE may be applied as a general methodology for assessing non-covalent interactions, which of the binding partners that should be selected as the analyte (the species detected) will depend on the properties of the molecules such as the absence or presence of suitable chromophores, solubility, as well as electrophoretic mobility.

2.2.2 Affinity Electrokinetic Chromatography (EKC)

In electrokinetic chromatography (EKC), a charged pseudo-stationary phase is added to the run buffer, which provides an electrodriven separation of neutral molecules based on the differential interaction or partitioning of the neutral analytes with the charged pseudo-stationary phase. The differential partitioning will confer different effective electrophoretic mobilities to the analytes. An affinity EKC experiment is illustrated in Fig. 14.3.

Due to these characteristics EKC is also an efficient technique for investigating partition behavior or drug lipophilicity (Terabe et al. 1984, 1985). The so-called pseudo-stationary phase is often a microemulsion or micellar solution. The effective mobility of an analyte is dependent on the fraction of analyte present in the aqueous phase x_{aq} and in the pseudo-stationary phase, x_{ps} according to:

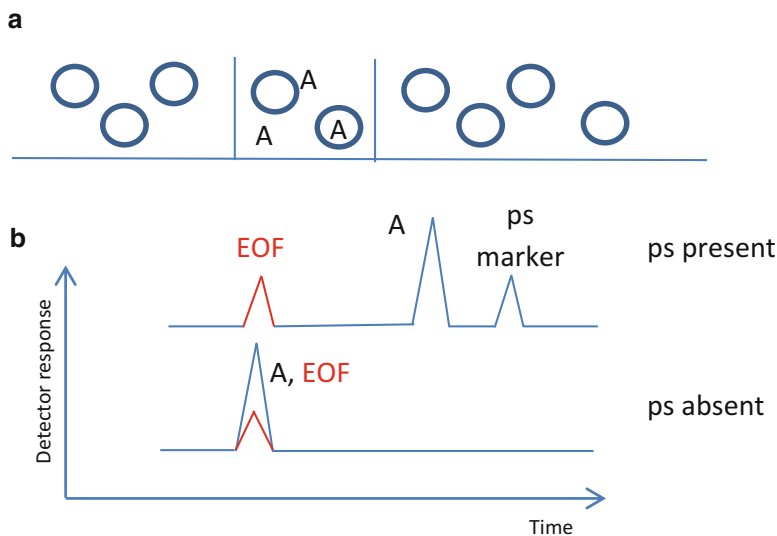


Fig. 14.3 Schematic distribution of the negatively charged pseudo-stationary phase (ps) (illustrated by *circles*) and the neutral compound A (the detected compound) during an EKC experiment (a). Electropherograms in the presence and absence of the ps (b). The ps marker is a molecule completely distributed into the ps. The EOF marker is a neutral molecule not interacting with the ps

$$\mu_{eff} = x_{aq}\mu_A + x_{ps}\mu_{ps} \quad (14.9)$$

where μ_A and μ_{ps} are the mobilities of the analyte and the pseudo-stationary phase, respectively.

The analyte is distributed into the pseudo-stationary phase according to the equilibrium partition coefficient:

$$P = \frac{[A]_{ps}}{[A]_{aq}} \quad (14.10)$$

Experimentally, the retention factor, k , is determined as:

$$k = \frac{n_{ps}}{n_{aq}} \quad (14.11)$$

where n_{ps} and n_{aq} are the amounts of A in the pseudo-stationary and aqueous phases, respectively. The retention factor is linked to the partition coefficient according to:

$$k = \frac{[A]_{ps}}{[A]_{aq}} \cdot \frac{V_{ps}}{V_{aq}} = P \cdot \frac{V_{ps}}{V_{aq}} \quad (14.12)$$

where V_{ps} and V_{aq} are the volumes of the pseudo-stationary and aqueous phases, respectively.

The retention factors for neutral and charged compounds, respectively, are obtained experimentally according to:

$$k = \frac{(t_A - t_{eof})}{\left[t_{eof} \left[1 - \frac{t_A}{t_{ps}} \right] \right]} \quad (14.13)$$

$$k = \frac{(t_A - t_0)}{\left[t_0 \left[1 - \frac{t_A}{t_{ps}} \right] \right]} \quad (14.14)$$

Here t_A , t_{eof} , t_{ps} and t_0 are the peak appearance times of the analyte in the presence of pseudo-stationary phase, the EOF peak appearance time, the pseudo-stationary phase migration time and the analyte peak appearance time in the absence of the pseudo-stationary phase, respectively. A highly lipophilic compound is usually employed to determine t_{ps} , by assuming 100% partitioning into the pseudo-stationary phase. Examples of electropherograms obtained in an EKC experiment are shown in Fig. 14.4 (Østergaard et al. 2003a). The dynamically coated capillary leads to a more optimal EOF (see Sect. 3.2).

2.2.3 Pre-equilibrium Capillary Zone and Frontal Analysis Capillary Electrophoresis

In pre-equilibrium zone and frontal analysis capillary electrophoresis, the sample contains the equilibrium binding mixture (A, L and AL), whereas the run buffer does not contain the interacting species. Upon sample injection, usually by pressure, the free (un-bound) analyte is separated from bound analyte, detected and subsequently quantified. In pre-equilibrium CZE, a narrow sample plug is injected and separation in the capillary leads to three peaks corresponding to A, L and AL (Østergaard and Heegaard 2006; Heegaard et al. 2008) whereas in capillary electrophoresis frontal analysis (CE-FA), a large sample zone (20–200 nL) is injected giving rise to a so called plateau peak (Fig. 14.5). If binding dissociation kinetics (k_{off}) is slow, CZE can be applied, however, it is important to carefully verify that the conditions are adequate (i.e., dissociation of the complex does not occur during initial separation) as it may otherwise result in erroneous binding parameters (Østergaard et al. 2005). The advantage of CE-FA is that systems exhibiting rapid on-and-off kinetics may be studied (Østergaard and Heegaard 2006; Vuignier et al. 2010a; Kraak et al. 1992). In contrast to CZE, plateau heights rather than peak areas are employed in CE-FA for data analysis. After separation of the

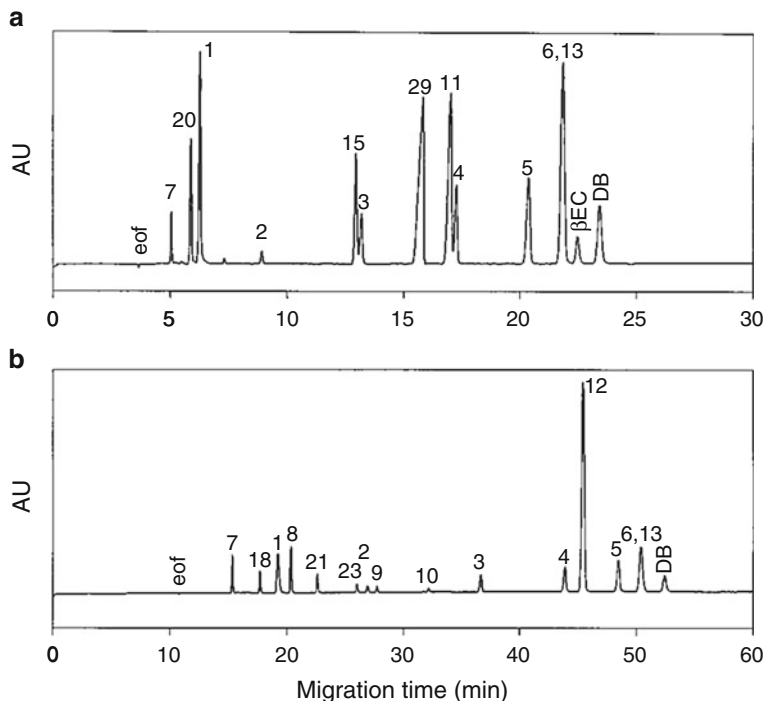


Fig. 14.4 Electrochromatograms of representative test solutes of small organic compounds. (a) Uncoated fused-silica capillary. The run buffer is a microemulsion consisting of 1.80 % w/w sodium dodecyl sulphate (SDS), 0.82 % w/w n-heptane, 6.49 % w/w 1-butanol in 0.1 M borate-0.05 M phosphate (pH 7.4). (b) Dynamically coated capillary (see also Sect. 3.2). Microemulsion: 2.16 % w/w SDS, 0.82 % w/w n-heptane, 6.49 % w/w 1-butanol in 0.05 M HCl (pH 1.4). In both examples UV detection at 214 nm were employed. From (Østergaard et al. 2003a) with permission

unbound and bound analyte, the plateau height corresponds to the amount of un-bound analyte. A schematic illustration of CZE and CE-FA experiments are provided in Fig. 14.5.

The concentration of free analyte is obtained from a standard curve obtained by injecting the analyte alone. In CE-FA, the achievement of a plateau is essential since this is an indication of the equilibrium being maintained during separation and that the height of the plateau is representative of the equilibrium concentration of the analyte in the original sample. An example is shown in Fig. 14.6.

The broader analyte plateau observed in the presence of a binding ligand is a result of the interaction affecting the migration of the complexed analyte. Fitting to an appropriate binding isotherm results in equilibrium binding parameters (Østergaard et al. 2002, 2003b). A prerequisite of both CZE and CE-FA is that free analyte and complex have different electrophoretic mobilities. CZE and CE-FA may in principle be performed on mixtures (for example plasma samples) as separation is an integrated part of these methods (Østergaard and Heegaard 2006).

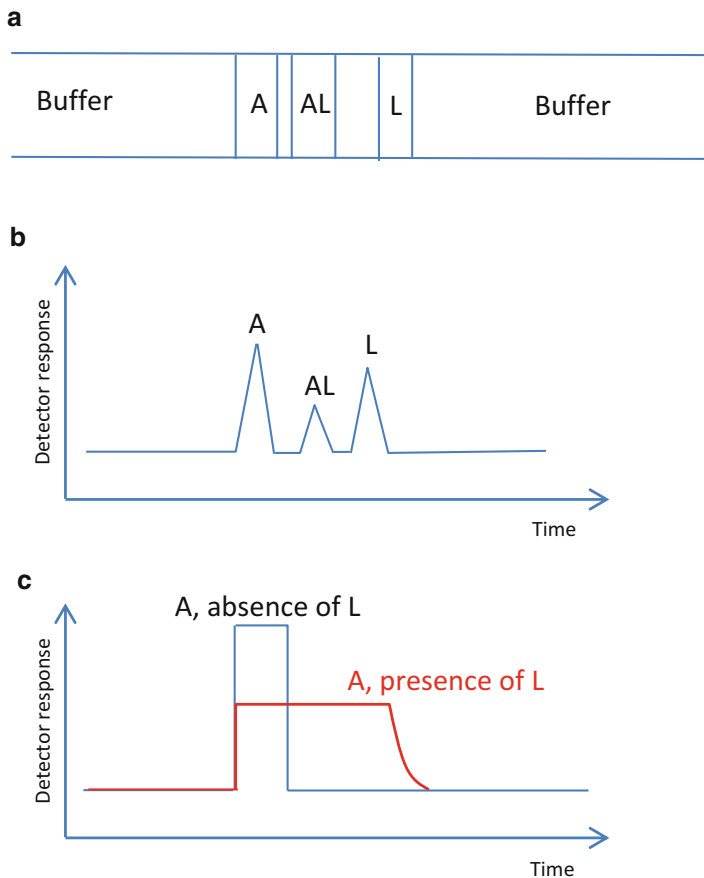


Fig. 14.5 Schematic illustration of the distribution of species in the separation capillary during CZE or CE-FA (a). Schematic illustration of the separation of A, AL and L in a CZE experiment with slow dissociation kinetics and a small sample volume (b). Detection of A in the presence and absence of L in a CE-FA experiment. A comparatively large sample volume is introduced into the capillary giving rise to plateau peaks the height of which is proportional to the concentration of A. In the presence of L, the plateau peak is lowered and becomes wider due to the binding equilibrium. In this illustration, the ligand being separated from A is not detected, but experimentally it is often seen in the electropherogram (c)

2.3 Techniques Based on Taylor Dispersion Analysis

Taylor dispersion analysis (TDA) is based on the dispersion of the injected compound(s) in a hydrodynamically driven flow (also called Hagen-Poiseuille flow) in a capillary (Taylor 1953, 1954). The dispersion is determined by the capillary dimensions, flow rate and the diffusivity of the measured substance. In principle TDA may be carried out using any equipment able to generate a hydrodynamic flow (Taylor 1953, 1954), whereas CE-based methods has the additional requirement of

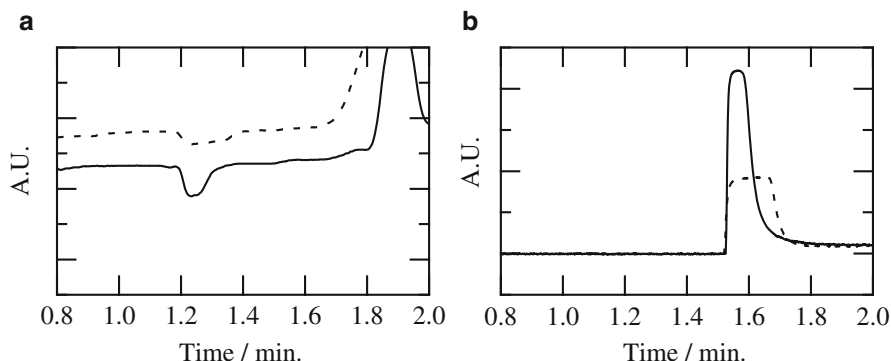


Fig. 14.6 Electropherograms of 0.5 mM 2-propylisoquinolinium bromide in 10 mM sodium phosphate buffer (pH 7.4) in the absence (*full line*) and presence of 5 mg/mL dextran sulfate (*broken line*), respectively. Contactless conductivity detection (**a**) and UV detection (**b**). The different peak appearance times are due to different detector positions on the capillary. The data in (**a**) and (**b**) refer to the same experiment. From (Jensen et al. 2007) with permission

a high voltage power supply (Fig. 14.1). A variation of TDA termed Flow Induced Dispersion Analysis (FIDA) may be used for determining non-covalent interactions (Jensen and Ostergaard 2010; Bielejewska et al. 2010). A schematic illustration of TDA and FIDA experiments are shown in Fig. 14.7.

Most CE systems have an internal pump which may be used to carry out a TDA experiment (Bello et al. 1994; Sharma et al. 2005; Østergaard and Jensen 2009), but more dedicated equipment has also been introduced (Ye et al. 2012) and in some cases, it has been advantageous to employ two detection windows (see Fig. 14.8) (Ye et al. 2012). Taylor dispersion analysis may be used to quantify diffusion coefficients (hydrodynamic size) (Bello et al. 1994; Sharma et al. 2005), as well as non-covalent interactions (Jensen and Ostergaard 2010).

2.3.1 Determination of Diffusion Coefficients by Taylor Dispersion Analysis

The golden standard in size determinations is based on dynamic light scattering. However, accurate measurement of diffusion coefficient (as measured by TDA) may give similar information. Recent studies have indicated good correlation between size measured by TDA and dynamic light scattering techniques (Hawe et al. 2011). TDA is better suited for measuring diffusivities of small molecules as compared to dynamic light scattering.

An example of a TDA experiment employing two detection windows is shown in Fig. 14.8. The second peak is lower and wider as compared to the first peak as a result of the dispersion occurring during the pressure driven flow.

The signal corresponding to the analyte adopts a Gaussian peak shape which experimentally may be analysed according to:

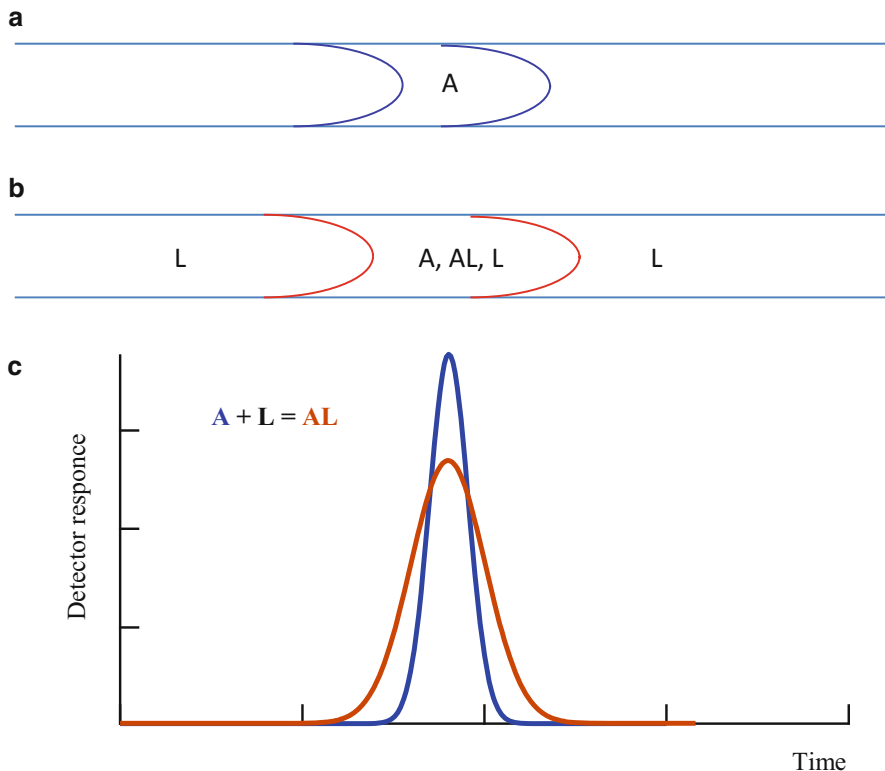


Fig. 14.7 Schematic illustration of the distribution of species in TDA (a) and FIDA (b). Taylorgrams in the absence of L (blue curve) and in the presence of L (red curve) where A is the detected molecule. The hydrodynamic flow employed in TDA and FIDA gives rise to relatively broad peaks compared to CE-based methods

$$\bar{C} = A + Be^{-\left(\frac{t-t_r}{2\sigma^2}\right)^2} \quad (14.15)$$

where \bar{C} is the analyte concentration across the capillary, A is a constant describing detector offset and B is a proportionality constant (depending on detector response, capillary radius, dispersion and the peak appearance time t_r), and σ^2 is the temporal variance. Provided certain conditions are fulfilled, the diffusion coefficient may be obtained from (Sharma et al. 2005):

$$D = \left(\frac{R_c^2}{24\sigma^2}\right)t_r \quad (14.16)$$

where R_c is the capillary radius. In the case where two detection windows are employed, the diffusion coefficient is obtained from a difference measurement (Ye et al. 2012):

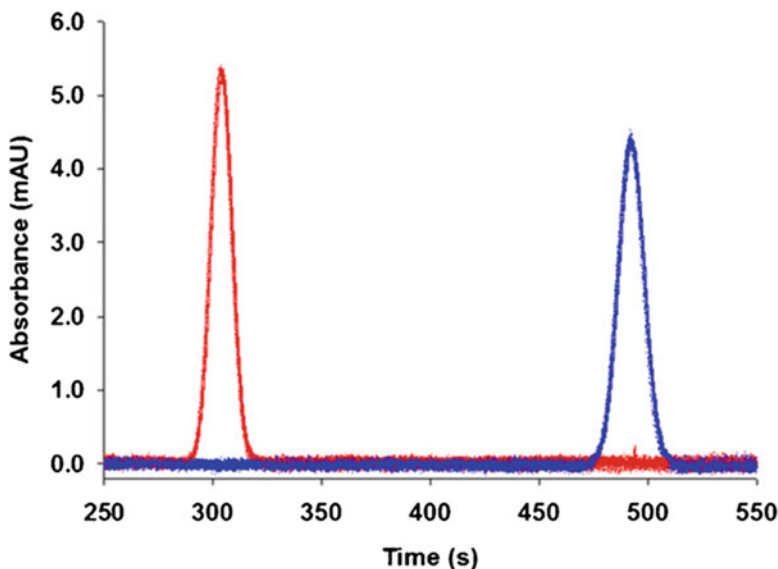


Fig. 14.8 Six superimposed dispersion profiles of 0.2 mg/mL phenol in water detected at 254 nm. The injected sample (33 nL (50 mbar for 7 s)) was forced through the capillary tube by a pressure drop of 50 mbar. Total length of the 75.6 μm i.d. capillary was 90.2 cm, with 30.7 and 50.9 cm to the first (*red trace*) and the second (*blue trace*) detection window, respectively. From (Ye et al. 2012), with permission

$$D = \frac{R_c^2}{24} \left[\frac{t_2 - t_1}{\sigma_2^2 - \sigma_1^2} \right] \quad (14.17)$$

where t_1 and t_2 are the peak appearance times corresponding to detector window 1 and 2, respectively, and σ_1^2 and σ_2^2 are the temporal variances corresponding to peak 1 and 2, respectively.

An advantage of using two detection points is that errors introduced by the finite width of the injected sample plug are minimized. Further details on TDA are available in the literature (Sharma et al. 2005; Østergaard and Jensen 2009; Cottet et al. 2007a, b, 2010; Ibrahim et al. 2013; Le Saux and Cottet 2008).

It may be of interest to convert measured diffusivities to apparent size by employing the Stokes-Einstein relation:

$$D = \frac{k_B T}{6\pi\eta R_h} \quad (14.18)$$

where k_B is the Boltzmann constant, T is the absolute temperature, η is the solvent viscosity and R_h is the hydrodynamic radius.

2.3.2 Assessment of Non-covalent Interactions from Dispersion Measurements

In FIDA, the apparent diffusion coefficient of an analyte A is measured in the presence of an interacting ligand L and under the assumption of rapid interaction kinetics; the non-covalent equilibrium binding constant, K , and the diffusivity of A and AL are obtained in the data analysis (Jensen and Ostergaard 2010) (see Fig. 14.7). In order for the method to be feasible, an additional requirement is that the complex, AL, is significantly larger than A (i.e., AL and A have different diffusivities).

The FIDA setup is very similar to the mobility shift ACE setup as the ligand is present in the run buffer in the capillary (Fig. 14.7). Important differences should, however, not be overlooked: the ligand should also be included in the sample and at the same concentration as in the run buffer. Since TDA is not a separation method, the presence of an inert marker or other impurities may affect the determination. The advantages of FIDA are mainly related to the simplicity in instrumentation (the only requirement is a hydrodynamic flow in a capillary tube and a detector), the low sample volume requirements and the fact that FIDA is not relying on the interacting species to be charged. In many cases, it can therefore be a supplement to ACE as it can address systems not applicable to CE. Further, the FIDA procedure also provides diffusivities of free analyte and complex which are not as easily obtained using other affinity methods.

3 Pharmaceutical Applications

The advantages of capillary-based techniques have been exploited in numerous studies of relevance to physical-chemical profiling of drug substances and drug delivery systems (Henchoz et al. 2009; Østergaard and Heegaard 2006; Jia 2005; Neubert and Rüttinger 2003; Jensen et al. 2013; El Deeb et al. 2013; Vuignier et al. 2010b). In this section some general features related to the determination of physicochemical properties using the capillary-based techniques are described in an overview format. Table 14.1 includes references to a number of selected applications of relevance to the techniques.

3.1 Affinity Capillary Electrophoresis and Taylor Dispersion Analysis

3.1.1 Acid Dissociation Constants (pK_a Values)

Determination of the effective electrophoretic mobility as a function of pH in a series of buffer solutions provides a convenient approach for determination of

Table 14.1 Selected applications of affinity capillary electrophoresis, electrokinetic chromatography and Taylor dispersion analysis for physicochemical characterization

Parameter	Method	Comments	Ref.
pK_a	Mobility shift ACE/CZE	Screening of pK_a values for drugs. Pressure assisted CE for increased throughput	Ishihama et al. (2002)
pK_a	Mobility shift ACE/CZE	Determination of pK_a for unstable drugs. Degradation products and impurities separated from main component. UV-Vis spectra applied to compound identification	Ørnkov et al. (2003)
Lipophilicity	EKC	Determination of octanol-water partition coefficients for 34 compounds including drugs and model prodrugs. Use of dynamically coated capillary for increasing EOF	Østergaard et al. (2003a)
Lipophilicity/ partitioning	CE-FA	Liposome-buffer distribution coefficients determined for charged drug substances. Validation by comparison to equilibrium dialysis	Franzen et al. (2009)
Plasma protein binding	CE-FA	Human serum albumin binding of 12 low-MW compounds using UV detection. Method development, estimation of binding parameters and displacement study	Østergaard et al. (2002)
Plasma protein binding	CE-FA	α_1 -acid glycoprotein and bovine serum albumin binding of selected drugs using CE-FA with MS detection	Vuignier et al. (2010b, 2012)
R_h , diffusion coefficient	TDA	Determination of diffusion coefficients and hydrodynamic radii of low-MW drugs substances in water, acetonitrile, methanol, isopropyl myristate, medium chain triglyceride, and propylene glycol. Simultaneous determination of solvent viscosity	Ye et al. (2012)
R_h	TDA	Sizing of selected peptides and proteins (MW 1–150 kDa). Effect thermal stressing and comparison with DLS	Hawe et al. (2011)
R_h , excipient interactions	TDA	Determination of drug-cyclodextrin (CD) complexation constants as well as drug and complex R_h	Jensen and Ostergaard (2010)

(continued)

Table 14.1 (continued)

Parameter	Method	Comments	Ref.
Excipient interactions	Mobility shift ACE	Alprostadiil-CD complexation studies with relevance for formulation performance	Schipper and Ramstad (2005)
Excipient interactions	Mobility shift ACE	Binding of NSAIDs to polyvinylpyrrolidone (PVP), vinylpyrrolidone-vinyl acetate copolymer	Jia et al. (2013)
Partitioning/ delivery system	EKC	Partitioning of cephalosporins into micelles, mixed micelles and microemulsions. Correlation of partition behavior with oral bioavailability in rabbit	Mrestani et al. (1998, 2010)
Delivery system	CE-FA, EKC and pre-equilibrium CZE	Characterization of PEGylated liposome formulation containing oxaliplatin or cisplatin. Membrane interactions, leakage, release and plasma protein interactions	Nguyen et al. (2013a), Franzen and Østergaard (2012), Franzen et al. (2011)
Delivery system	CE-FA	Binding of acylated-peptide ghrelin to liposomes. Effect of liposome net charge and peptide acyl chain on binding	Østergaard and Moeller (2010)

ionization constants (Jia 2005; Babic et al. 2007; Poole et al. 2004). Determination of pK_a values by CE can be considered a variant of mobility shift ACE and because CE is a separation method it is suited for characterization of impure as well as unstable compounds (Ôrnskov et al. 2003). The precise drug concentration does not need to be known since peak appearance times are applied for the quantification and due to the microscale format only small amounts of substance are required. As compared to potentiometric titration and UV spectrophotometric pK_a determination, CE may be more laborious because it is less well-supported in terms of software. From an experimental point of view, CE is attractive because of the autosampling capabilities of CE systems and is therefore well-suited for characterization of batches containing 5–10 compounds.

3.1.2 Partitioning and Lipophilicity

The partitioning of a drug substance between two immiscible solvents is not feasible for direct study by capillary-based methods; however, partitioning may be studied by EKC when a non-aqueous phase can be dispersed in an aqueous buffer. For instance, the partitioning of drug substances into micelles and microemulsion droplets by EKC is well established. As a micellar phase sodium dodecyl sulfate is most commonly applied but a wide range of anionic and cationic surfactants has been investigated. The solubilization capacity of surfactant

containing solutions may be estimated using EKC. Micellar EKC (MEKC) and microemulsion EKC (MEEKC) have shown to provide excellent surrogate methods for estimating octanol-water partition coefficients similar to liquid chromatography (Henchoz et al. 2009; Jia 2005; Wan and Holmen 2009). Microemulsions with compositions similar to that applied in Fig. 14.4 have shown to mimic octanol-water partitioning particularly well. The pseudo-stationary phase (partitioning phase) should be UV transparent, stable and carry charge for providing a large separation window. The analytes subject for characterization should ideally be neutral because determination of their mobility in the aqueous phase may be affected by drug-surfactant ionpairing for charged species. Micellar solutions and microemulsions are preferred pseudo-stationary phases due to their transparency, ease of preparation and stability; however, other phases involving vesicles and liposomes have been applied as well. Provided that the dispersed structures are sufficiently stable as is the case with liposomes, i.e., will not dissociate during dilution, frontal analysis CE may be an attractive alternative to the EKC format. CE-FA may be better suited for partitioning and lipophilicity determination of charged species than EKC (Franzen and Østergaard 2012). Attempts have been made to correlate EKC derived retention factors and partition coefficients with Caco-2 cell and skin permeability (Pascoe et al. 2006; Xian et al. 2008; Ørnskov et al. 2005; Wang et al. 2009) as well as with oral bioavailability (Wang et al. 2007).

3.1.3 Plasma Protein Binding

Lipophilicity and ionization state are of importance in describing the plasma protein binding properties of drug substances, which in turn affects drug distribution, clearance, metabolism and pharmacological efficacy (Trainor 2007). From the early start of ACE, characterization of plasma protein binding has been an area of significant interest as reviewed elsewhere (Østergaard and Heegaard 2003, 2006; Vuignier et al. 2010b; Oravcová et al. 1996) and here only a few illustrative studies are pointed out in Table 14.1. Often CE-FA will be the CE method of choice since, in general, the drug-plasma protein binding stoichiometry is unknown and mobility shift ACE is for most practical purposes limited to 1:1 interactions as higher order interactions are challenging to analyze (Sanger van de Griend et al. 1997), whereas for example human serum albumin most often binds several ligands and cannot be saturated. Affinity CE generally requires less material and is less labor intensive as compared to equilibrium dialysis and ultrafiltration and may therefore be an attractive characterization tool. However, for highly bound substances the relatively low sensitivity may constitute a limitation when applying CE with UV detection. Combination of frontal analysis CE with a mass spectrometer may be an approach to address this issue (Vuignier et al. 2012).

3.1.4 Diffusivity and Size

The diffusivity or the hydrodynamic radius are key parameters in drug transport in the pharmaceutical sciences. The hydrodynamic radius can also provide information on the self-association and aggregation state of molecules. Diffusion is a slow process but TDA performed in 50–100 μm inner diameter capillaries constitutes a relatively fast method for retrieving diffusion coefficients of molecules ranging from low-molecular weight drug substances, over polymers and proteins to nanoparticles in solution (Bello et al. 1994; Ye et al. 2012; Cottet et al. 2007b, c; Wan and Holmen 2009; Jensen et al. 2014; Belongia and Baygents 1997). In addition to the diffusion coefficient, a measure of solvent viscosity may be obtained from the TDA measurements (Ye et al. 2012). Sizing by TDA may offer an interesting alternative to size measurements by dynamic light scattering (DLS) where the measured scattering intensity for small particles is proportional to the particle diameter to the power of six whereas in TDA mass sensitive detectors are commonly used (Cottet et al. 2007a). DLS is more sensitive for detecting larger particles or aggregates. This may be to an extent where a few large particles may mask the light-scattering contribution of the small molecules in the sample (Filipe et al. 2013; Zölls et al. 2012). As detailed in Sect. 2.3, the diffusivity and hydrodynamic radius is determined from the dispersion of the peak in TDA, consequently a mixture of several compounds may constitute a challenge. However, it is possible at least for simple mixtures to deconvolute the signal and obtain size measures for the different molecules (Cottet et al. 2010). Another approach to analyze mixtures is to apply an electrophoretic separation step prior to TDA (Østergaard and Jensen 2009; Le Saux and Cottet 2008). The effective electrophoretic mobility determined by CE is related to the charge to size ratio of a molecule; hence, combination of CE with TDA may in certain cases be used for estimating the effective charge of analytes (Ibrahim et al. 2012, 2013; Li et al. 2011). In addition to the methods covered briefly here, molecular weight and pI determination of proteins are routinely determined by capillary gel electrophoresis analysis and capillary isoelectric focusing (cIEF), respectively (El Deeb et al. 2013).

3.1.5 Interactions with Excipients and Delivery Systems

The interaction and partitioning of drug substances with micelles, microemulsions or liposomes may provide information regarding drug lipophilicity. However, such studies may also provide data useful for guiding excipient selection or formulation development. For a range of excipients (or simple delivery vehicles) interaction or partition studies may be used to attain an estimate of solubilization capacities of various types of excipients. The most widely investigated excipients are likely to be cyclodextrins by mobility shift ACE and surfactants using MEKC. In case both the drug and cyclodextrin are uncharged, the Taylor dispersion analysis format detailed in Sect. 2.3 may be used for investigation of the complexation (Jensen and

Ostergaard 2010). CE has also been applied for the characterization of drug-polymer (polyelectrolyte) interactions. The relatively weak interactions between cationic drug molecules and polyelectrolytes such as dextran sulfate, chondroitin sulfate and hyaluronic acid have successfully been characterized by CE-FA (Jensen et al. 2007; Ye et al. 2013). Although more challenging due to the potential of capillary wall adsorption addressed briefly below, binding of proteins to cationic polymers have also been successfully investigated by frontal analysis CE (Zou et al. 2010). The types of excipients and drug delivery systems amendable for characterization using capillary-based systems is pretty much defined by the geometry of the capillary and the fact that the systems have to be dispersed in solution. Examples include interactions involving liposomes (Franzen and Østergaard 2012), dendrimers (Dribek et al. 2007) PLGA (Progent et al. 2002), polyvinylpyrrolidone (PVP), vinylpyrrolidone-vinyl acetate copolymer (Jia et al. 2013) as well as determination of critical micelle concentrations (CMCs)(Lin 2004). This is an area of research still in its infancy, however, due to the virtues of the capillary-based techniques, being in solution, automated and compound sparing, and the increased focus on nanoparticulate delivery systems it is likely to be a field with increasing activity. Liposomes illustrate the potential of applying capillary-based characterization methods to drug delivery systems. Surface charge, size, membrane interactions and permeability as well as drug encapsulation efficiency, leakage and release have been assessed by CE, EKC and TDA (Franzen and Østergaard 2012).

3.2 *Selecting the Appropriate Technique and Avoiding Pitfalls*

The techniques outlined above each have their strength and weaknesses, and method selection should therefore be based on a careful consideration. Below is listed a few paragraphs which is intended to be an aid in selecting the most appropriate technique(s).

3.2.1 **Effect of Solution Media on the Results**

If the system contains a highly UV-Vis absorbing background, detection schemes based on for example CCCD or MS may be used as UV-Vis absorption spectroscopy is not optimal. In some systems, a relatively large amount of substances, for instance cyclodextrins, are used which may have an impact on the viscosity of the sample solutions and separation buffers (Holm et al. 2011; Østergaard et al. 2012). This has to be taken into account in mobility shift ACE and EKC where measurements rely on mobilities. Corrected effective electrophoretic mobilities, μ^* , may be obtained by the “current correction method” or by separate viscosity measurements according to (Vespalec and Bocek 2000):

$$\mu' = \mu_{eff} \cdot \frac{I_0}{I} = \mu_{eff} \cdot \frac{\eta}{\eta_0} \quad (14.19)$$

where I_0 and I are the measured currents at zero and at a given ligand (cyclodextrin) concentration, respectively, and η_0 and η are the measured viscosities at zero and at a given ligand concentration, respectively. The “current correction method” is only feasible when the ligand is neutral. Viscosity measurements may readily be performed using a commercial CE instrument (Østergaard et al. 2003b). A special aspect to be considered in CE based methods is related to temperature control in the capillary. When a high voltage is applied, a current passes through the capillary resulting in Joule heating. As most physical-chemical parameters are temperature dependent it is a possible source of error that should be carefully evaluated (Holm et al. 2011; Østergaard et al. 2012). Joule heating can be minimized by choosing run buffers of low ionic strength and small electric fields. Several approaches have been described for quantifying and correcting for Joule heating (Kok 2000). In TDA, joule heating is not an issue.

Substantial difference in the ionic strength between sample and run buffer may result in sample stacking or de-stacking due to the non-homogeneous electric field. These artifacts are most pronounced for the large sample sizes employed in CE-FA.

3.2.2 What is the Kinetics of the System (Fast or Slow Binding/Partitioning)?

An important point to consider is the binding kinetics as it is relevant for the choice of methodology and since certain assumptions are made in the data analysis. Mobility shift ACE and TDA are suited for fast binding kinetics, in order for equilibrium to be maintained at all times during separation or hydrodynamic flow. Indications of (too) slow on-and-off kinetics in CE methods may become apparent as excessive peak broadening or peak splitting. In contrast, CZE should be used for binding systems characterized by slow on-and-off kinetics; it should be possible to separate the binding partners within a time frame that is short as compared to the dissociation kinetics. CE-FA is most optimal for fast binding kinetics. In many cases, the binding kinetics is not known beforehand. However, for a simple 1:1 interaction changing the concentration of analyte and/or ligand in a given assay should lead to similar equilibrium constants and is thus an option for controlling that the theoretical requirements are met.

3.2.3 Is Adsorption an Issue?

Capillary wall adsorption of the analytes is frequently an issue in capillary-based systems due to the high surface to volume ratio. The most common indications or clear warnings are tailing peaks due to adsorption to the inner surface of the

capillary and sub-optimal fitting of the data to the binding model. Fortunately a number of approaches can be taken to alleviate adsorption issues. A standard fused silica capillary is negatively charged at pH above 4 and therefore especially positively charged molecules may be prone to adsorption. Adsorption related problems will often be apparent as tailing peaks or even the complete disappearance of peaks and less reproducible migration times. The surface charge may be modified using an electrostatic dynamic coating procedure of a positively charged polymer (Bendahl et al. 2001), polymer physisorption (Gilges et al. 1994; Albarghouthi et al. 2003) or covalently modifying the capillary surface (chemisorption) (Cretich et al. 2005). Various types of capillary coatings may be employed to prevent or minimize adsorption and thereby optimize procedures. Additionally, it may be used for EOF optimization as illustrated in Fig. 14.4.

3.2.4 Is the Charge/Size Ratio on the Analyte and/or Ligand Optimal for the Assay?

The primary prerequisite for performing affinity studies by electrophoresis is the presence of a charge on one of the interacting species. Furthermore, the interaction has to lead to a significant change in mobility of the complex as compared to the free species. If this is not the case, or if the interacting species are uncharged, TDA based methods may be used. In TDA, there should be a change in size (diffusivity) upon binding (see paragraph 2.3).

4 Conclusions and Perspectives

The present chapter has highlighted the unique advantages of capillary-based techniques for physical-chemical characterization of drug substances and drug delivery systems: speed, low sample volume requirements, automation and versatility. From the examples referenced in Sect. 3, it should be apparent that capillary-based techniques present a highly versatile platform which may be used for assessment of many different parameters and systems. Yet, the full potential of capillary techniques for physical-chemical characterization remains to be realized outside the academic laboratories. This may in part be for historical reasons; capillary-based technologies have so far mainly been used in purely analytical chemical settings for quantification purposes. Hopefully, the future direction of the technology will be towards an increased adaptation in formulation development and characterization, as these areas can greatly benefit from the attractive features of capillary-based techniques. Although this holds for drug development in general, there can be no doubt that the trends towards an increasing focus on biopharmaceuticals will be a key driver in this process.

References

- Albarghouthi MN, Stein TM, Barron AE (2003) Poly-N-hydroxyethylacrylamide as a novel, adsorbed coating for protein separation by capillary electrophoresis. *Electrophoresis* 24:1166–1175
- Annovazzi L, Viglio S, Perani E, Luisetti M, Baraniuk J, Casado B, Cetta G, Iadarola P (2004) Capillary electrophoresis with laser-induced fluorescence detection as a novel sensitive approach for the analysis of desmosines in real samples. *Electrophoresis* 25:683–691
- Babic S, Horvat AJM, Pavlovic DP, Kastelan-Macan M (2007) Determination of pK_a values of active pharmaceutical ingredients. *Trends Anal Chem* 26:1043–1061
- Bello MS, Rezzonico R, Righetti PG (1994) Use of Taylor-Aris dispersion for measurement of a solute diffusion-coefficient in thin capillaries. *Science* 266:773–776
- Belongia BM, Baygents JC (1997) Measurements on the diffusion coefficient of colloidal particles by Taylor-Aris dispersion. *J Colloid Interface Sci* 195:19–31
- Bendahl L, Hansen SH, Gammelgaard B (2001) Capillaries modified by noncovalent anionic polymer adsorption for capillary zone electrophoresis, micellar electrokinetic capillary chromatography and capillary electrophoresis mass spectrometry. *Electrophoresis* 22:2565–2573
- Bielejewska A, Bylina A, Duszczek K, Fialkowski M, Holyst R (2010) Evaluation of ligand-selector interaction from effective diffusion coefficient. *Anal Chem* 82:5463–5469
- Cao LW, Tan XF, Li C, Wu C, Zhang ZD, Deng T, Meng JX (2013) Capillary electrophoresis-laser induced fluorescence detection of GABA and its analogs in human serum with solid-phase extraction and fluorescein-based probes. *Anal Methods* 5:6000–6008
- Cottet H, Biron JP, Martin M (2007a) Taylor dispersion analysis of mixtures. *Anal Chem* 79:9066–9073
- Cottet H, Martin M, Papillaud A, Souaid E, Collet H, Commeyras A (2007b) Determination of dendrigraft poly-L-lysine diffusion coefficients by Taylor dispersion analysis. *Biomacromolecules* 8:3235–3243
- Cottet H, Biron JP, Cipelletti L, Matmour R, Martin M (2010) Determination of individual diffusion coefficients in evolving binary mixtures by Taylor dispersion analysis: application to the monitoring of polymer reaction. *Anal Chem* 82:1793–1802
- Cretich M, Chiari M, Pirri G, Crippa A (2005) Electroosmotic flow suppression in capillary electrophoresis: chemisorption of trimethoxy silane-modified polydimethylacrylamide. *Electrophoresis* 26:1913–1919
- Dribek M, Le Potier I, Rodrigues A, Pallandre A, Fattal E, Taverna M (2007) Determination of binding constants of vasoactive intestinal peptide to poly(amidoamine) dendrimers designed for drug delivery using ACE. *Electrophoresis* 28:2191–2220
- El Deeb S, Wätzig H, Abd El-Hady D (2013) Capillary electrophoresis to investigate biopharmaceuticals and pharmaceutically-relevant binding properties. *Trends Anal Chem* 48:112–131
- Filipe V, Hawe A, Carpenter JF, Jiskoot W (2013) Analytical approaches to assess the degradation of therapeutic proteins. *Trends Anal Chem* 49:118–125
- Franzen U, Østergaard J (2012) Physico-chemical characterization of liposomes and drug substance-liposome interactions in pharmaceuticals using capillary electrophoresis and electrokinetic chromatography. *J Chromatogr A* 1267:32–44
- Franzen U, Jorgensen L, Larsen C, Heegaard NHH, Østergaard J (2009) Determination of liposome-buffer distribution coefficients of charged drugs by capillary electrophoresis frontal analysis. *Electrophoresis* 30:2711–2719
- Franzen U, Vermehren C, Jensen H, Ostergaard J (2011) Physicochemical characterization of a PEGylated liposomal drug formulation using capillary electrophoresis. *Electrophoresis* 32:738–748
- Gilges M, Kleemiss MH, Schomburg G (1994) Capillary zone electrophoresis separations of basic and acidic proteins using poly(vinyl alcohol) coatings in fused-silica capillaries. *Anal Chem* 66:2038–2046

- Hawe A, Hulse WL, Jiskoot W, Forbes RT (2011) Taylor dispersion analysis compared to dynamic light scattering for the size analysis of therapeutic peptides and proteins and their aggregates. *Pharm Res* 28:2302–2310
- Heegaard NHH, Kennedy RT (1999) Identification, quantitation, and characterization of biomolecules by capillary electrophoretic analysis of binding interactions. *Electrophoresis* 20:3122–3133
- Heegaard NHH, Schou C, Østergaard J (2008) Analysis of proteins in solution using affinity capillary electrophoresis. In: Zachariou M (ed) *Affinity chromatography: methods and protocols*, 2nd edn. Humana Press, Totowa, pp 303–338
- Henchoz Y, Bard B, Guillaume D, Carrupt P-A, Veuthey J-L, Martel S (2009) Analytical tools for the physicochemical profiling of drug candidates to predict absorption/distribution. *Anal Bioanal Chem* 394:707–729
- Holm R, Schönbeck C, Askjær S, Jensen H, Westh P, Østergaard J (2011) Complexation of tauro- and glyco-conjugated bile salts with α -cyclodextrin and hydroxypropyl- α -cyclodextrin studied by affinity capillary electrophoresis and molecular modelling. *J Sep Sci* 34:3221–3230
- Ibrahim A, Ohshima H, Allison SA, Cottet H (2012) Determination of effective charge of small ions, polyelectrolytes and nanoparticles by capillary electrophoresis. *J Chromatogr A* 1247:154–164
- Ibrahim A, Meyrueix R, Pouliquen G, Chan YP, Cottet H (2013) Size and charge characterization of polymeric drug delivery systems by Taylor dispersion analysis and capillary electrophoresis. *Anal Bioanal Chem* 405:5369–5379
- Ishihama Y, Nakamura M, Miwa T, Kajima T, Asakawa N (2002) A rapid method for pK_a determination of drugs using pressure-assisted capillary electrophoresis with photodiode array detection in drug discovery. *J Pharm Sci* 91:933–942
- Jensen H, Østergaard J (2010) Flow induced dispersion analysis quantifies noncovalent interactions in nanoliter samples. *J Am Chem Soc* 132:4070–4071
- Jensen H, Østergaard J, Thomsen AE, Hansen SH (2007) CE frontal analysis based on simultaneous UV and contactless conductivity detection: a general setup for studying noncovalent interactions. *Electrophoresis* 28:322–327
- Jensen H, Larsen SW, Larsen C, Østergaard J (2013) Physicochemical profiling of drug candidates using capillary-based techniques. *J Drug Del Tech* 23:333–345
- Jensen SS, Jensen H, Cornett C, Møller EH, Østergaard J (2014) Insulin diffusion and self-association characterized by real-time UV imaging and Taylor dispersion analysis. *J Pharm Biomed Anal* 92:203–210
- Jia Z (2005) Physicochemical profiling by capillary electrophoresis. *Curr Pharm Anal* 1:45–56
- Jia Z, Choi DK, Chokshi H (2013) Determination of drug-polymer binding constants by affinity capillary electrophoresis for aryl propionic acid derivatives and related compounds. *J Pharm Sci* 102:960–966
- Kok WT (2000) Capillary electrophoresis: instrumentation and operation. *Chromatographia* 51: S5–S89
- Kostal V, Katzenmeyer J, Arriaga EA (2008) Capillary electrophoresis in bioanalysis. *Anal Chem* 80:4533–4550
- Kraak JC, Busch S, Poppe H (1992) Study of protein-drug binding using capillary zone electrophoresis. *J Chromatogr* 608:257–264
- Kuban P, Hauser PC (2011) Capacitively coupled contactless conductivity detection for microseparation techniques—recent developments. *Electrophoresis* 32:30–42
- Le Saux T, Cottet H (2008) Size-based characterization by the coupling of capillary electrophoresis to Taylor dispersion analysis. *Anal Chem* 80:1829–1832
- Li SK, Liddell MR, Wen H (2011) Effective electrophoretic mobilities and charges of anti-VEGF proteins determined by capillary zone electrophoresis. *J Pharm Biomed Anal* 55:603–607
- Lin C-E (2004) Determination of critical micelle concentration of surfactants by capillary electrophoresis. *J Chromatogr A* 1037:467–478

- Liu X, Dahdouh F, Salgado M, Gomez FA (2009) Recent advances in affinity capillary electrophoresis (2007). *J Pharm Sci* 98:394–410
- Mrestani Y, El-Mokdad N, Ruttinger HH, Neubert R (1998) Characterization of partitioning behavior of cephalosporins using microemulsion and micellar electrokinetic chromatography. *Electrophoresis* 19:2895–2899
- Mrestani Y, Behbood L, Härtl A, Neubert RHH (2010) Microemulsion and mixed micelle for oral administration as new drug formulations for highly hydrophilic drugs. *Eur J Pharm Biopharm* 74:219–222
- Neubert RHH, Rüttinger H-H (2003) *Affinity capillary electrophoresis in pharmaceuticals and biopharmaceuticals*. Marcel Dekker, New York
- Nguyen TTTN, Østergaard J, Sturup S, Gammelgaard B (2012) Investigation of a liposomal oxaliplatin drug formulation by capillary electrophoresis hyphenated to inductively coupled plasma mass spectrometry (CE-ICP-MS). *Anal Bioanal Chem* 402:2131–2139
- Nguyen TTTN, Østergaard J, Sturup S, Gammelgaard B (2013a) Determination of platinum drug release and liposome stability in human plasma by CE-ICP-MS. *Int J Pharm* 449:95–102
- Nguyen TTTN, Østergaard J, Sturup S, Gammelgaard B (2013b) Metallomics in drug development: characterization of a liposomal cisplatin drug formulation in human plasma by CE-ICP-MS. *Anal Bioanal Chem* 405:1845–1854
- Oravcová J, Böhs B, Lindner W (1996) Drug-protein binding studies. New trends in analytical and experimental methodology. *J Chromatogr B* 677:1–28
- Ørnskov E, Linusson A, Folestad S (2003) Determination of dissociation constants of labile drug compounds by capillary electrophoresis. *J Pharm Biomed Anal* 33:379–391
- Ørnskov E, Gottfries J, Erickson M, Folestad S (2005) Experimental modelling of drug membrane permeability by capillary electrophoresis using liposomes, micelles and microemulsions. *J Pharm Pharmacol* 57:435–442
- Østergaard J, Moeller EH (2010) Ghrelin–liposome interactions. Characterization of liposomal formulations of an acylated 28-amino acid peptide using capillary electrophoresis. *Electrophoresis* 31:339–345
- Østergaard J, Heegaard NHH (2003) Capillary electrophoresis frontal analysis: principles and applications for the study of drug-plasma protein binding. *Electrophoresis* 24:2903–2913
- Østergaard J, Heegaard NHH (2006) Bioanalytical interaction studies executed by preincubation affinity capillary electrophoresis. *Electrophoresis* 27:2590–2608
- Østergaard J, Jensen H (2009) Simultaneous evaluation of ligand binding properties and protein size by electrophoresis and Taylor dispersion analysis in capillaries. *Anal Chem* 81:8694–8698
- Østergaard J, Schou C, Larsen C, Heegaard NHH (2002) Evaluation of capillary electrophoresis frontal analysis for the study of low molecular weight drug-human serum albumin interactions. *Electrophoresis* 23:2842–2853
- Østergaard J, Hansen SH, Larsen C, Schou C, Heegaard NHH (2003a) Determination of octanol-water partition coefficients for carbonate esters and other small organic molecules by microemulsion electrokinetic chromatography. *Electrophoresis* 24:1038–1046
- Østergaard J, Schou C, Larsen C, Heegaard NHH (2003b) Effect of dextran as a run buffer additive in drug-protein binding studies using capillary electrophoresis frontal analysis. *Anal Chem* 75:207–214
- Østergaard J, Hansen SH, Jensen H, Thomsen AE (2005) Pre-equilibrium capillary zone electrophoresis or frontal analysis: advantages of plateau peak conditions in affinity capillary electrophoresis. *Electrophoresis* 26:4050–4054
- Østergaard J, Jensen H, Holm R (2012) Affinity capillary electrophoresis method for investigation of bile salts complexation with sulbutyl ether- α -cyclodextrin. *J Sep Sci* 35:2764–2772
- Pascoe RJ, Masucci JA, Foley JP (2006) Investigation of vesicle electrokinetic chromatography as an in vitro assay for the estimation of intestinal permeability of pharmaceutical drug candidates. *Electrophoresis* 27:793–804
- Poole SK, Patel S, Dehring K, Workman H, Poole CF (2004) Determination of acid dissociation constants by capillary electrophoresis. *J Chromatogr A* 1037:445–454

- Progent F, Taverna M, Le Potier I, Gopée F, Ferrier D (2002) A study on the binding between polymers and peptides, using affinity capillary electrophoresis, applied to polymeric drug delivery systems. *Electrophoresis* 23:938–944
- Sanger van de Griend CE, Groningsson K, Arvidsson T (1997) Enantiomeric separation of a tetrapeptide with cyclodextrin—extension of the model for chiral capillary electrophoresis by complex formation of one enantiomer molecule with more than one chiral selector molecules. *J Chromatogr A* 782:271–279
- Schipper BR, Ramstad T (2005) Determination of the binding constant between alprostadil and alpha-cyclodextrin by capillary electrophoresis: implication for a freeze-dried formulation. *J Pharm Sci* 94:1528–1537
- Sharma U, Gleason NJ, Carbeck JD (2005) Diffusivity of solutes measured in glass capillaries using Taylor's analysis of dispersion and a commercial CE instrument. *Anal Chem* 77:806–813
- Taylor G (1953) Dispersion of soluble matter in solvent flowing slowly through a tube. *Proc R Soc London Ser A* 219:186–203
- Taylor G (1954) Conditions under which dispersion of a solute in a stream of solvent can be used to measure molecular diffusion. *Proc R Soc London Ser A* 225:473–477
- Terabe S, Otsuka K, Ichikawa K, Tsuchiya A, Ando T (1984) Electrokinetic separations with micellar solutions and open-tubular capillaries. *Anal Chem* 56:111–113
- Terabe S, Otsuka K, Ando T (1985) Electrokinetic chromatography with micellar solution and open-tubular capillary. *Anal Chem* 57:834–841
- Trainor GL (2007) The importance of plasma protein binding in drug discovery. *Expert Opin Drug Discov* 2:54–61
- Vespalec R, Bocek P (2000) Calculation of stability constants for the chiral selector-enantiomer interactions from electrophoretic mobilities. *J Chromatogr A* 875:431–445
- Vuignier K, Schappler J, Veuthey J-L, Carrupt P-A, Martel S (2010a) Improvement of a capillary electrophoresis/frontal analysis (CE/FA) method for determining binding constants: discussion on relevant parameters. *J Pharm Biomed Anal* 53:1288–1297
- Vuignier K, Schappler J, Veuthey J-L, Carrupt P-A, Martel S (2010b) Drug-protein binding: a critical review of analytical tools. *Anal Bioanal Chem* 398:53–66
- Vuignier K, Veuthey J-L, Carrupt P-A, Schappler J (2012) Characterization of drug-protein interactions by capillary electrophoresis hyphenated to mass spectrometry. *Electrophoresis* 33:3306–3315
- Wan H, Holmen AG (2009) High throughput screening of physicochemical properties and in vitro ADME profiling in drug discovery. *Comb Chem High Throughput Screen* 12:315–329
- Wan H, Östlund Å, Jönsson S, Lindberg W (2005) Single run measurements of drug-protein binding by high-performance frontal analysis capillary electrophoresis and mass spectrometry. *Rapid Commun Mass Spectrom* 19:1603–1610
- Wang Y, Sun J, Liu H, Wang Y, He Z (2007) Prediction of human drug absorption using liposome electrokinetic chromatography. *Chromatographia* 65:173–177
- Wang YJ, Sun J, Liu HZ, Liu JF, Zhang LQ, Liu K, He ZG (2009) Predicting skin permeability using liposome electrokinetic chromatography. *Analyst* 134:267–272
- Xian DL, Huang KL, Liu SQ, Xiao JY (2008) Quantitative retention-activity relationship studies by liposome electrokinetic chromatography to predict skin permeability. *Chin J Chem* 26:671–676
- Ye FB, Jensen H, Larsen SW, Yaghmur A, Larsen C, Østergaard J (2012) Measurement of drug diffusivities in pharmaceutical solvents using Taylor dispersion analysis. *J Pharm Biomed Anal* 61:176–183
- Ye F, Xie Y, Jensen H, Larsen SW, Yaghmur A, Larsen C, Østergaard J (2013) Interaction of amino acid and dipeptide α -naphthylamide derivatives with hyaluronic acid and human serum albumin studied by capillary electrophoresis frontal analysis. *Chromatographia* 76:49–57
- Zavaleta J, Chinchilla D, Brown A, Ramirez A, Calderon V, Sogomonyan T, Gomez FA (2006) Recent developments in affinity capillary electrophoresis: a review. *Curr Anal Chem* 2:35–42

- Zöls S, Tantipolphan R, Wiggenhorn M, Winter G, Jiskoot W, Friess W, Hawe A (2012) Particles in therapeutic protein formulations, part 1: overview of analytical methods. *J Pharm Sci* 101:914–935
- Zou T, Oukacine F, Le Saux T, Cottet H (2010) Neutral coatings for the study of polycation/multicharged anion interactions by capillary electrophoresis: application to dendrigraft poly-L-lysines with negatively multicharged molecules. *Anal Chem* 82:7362–7368

Chapter 15

Asymmetrical Flow Field Flow Fractionation: A Useful Tool for the Separation of Protein Pharmaceuticals and Particulate Systems

Julia Engert, Roman Mathaes, and Gerhard Winter

Abstract The focus of this chapter will be on asymmetrical flow field flow fractionation (AF4) for the separation and characterization of protein pharmaceuticals and particulate systems. The chapter will provide some background and historical information on field flow fractionation and the general working principle. In addition, a practical guide on how to use AF4 will be described and critical parameters for the development of a suitable separation method will be discussed. The use of AF4 for protein pharmaceuticals as well as particulate systems will be described and some examples given in the literature will be presented. Finally, a summary of the most recent trends in AF4 and an outlook will be given for potential application fields in the future.

Keywords Asymmetrical flow field flow fractionation • Protein pharmaceuticals • Separation

1 Introduction and General Principles of AF4

Asymmetrical flow field flow fractionation (AF4) is the most important representative of a group of separation technologies developed in the 1960s following one common principle, the field flow fractionation. Separations are carried out within a rectangular, flat channel where perpendicular to a laminar flow from inlet towards outlet a second field is applied. This field can be a temperature gradient, a thermal gradient, a magnetic field, a gravity field (created by centrifugation) or a flow field (Wahlund and Giddings 1987; Schimpf et al. 2000). The perpendicular field (called “cross-flow”) leads to a force that drives soluble or insoluble molecules and particles towards one of the channel walls (so-called accumulation wall). Under

J. Engert (✉) • R. Mathaes • G. Winter

Department of Pharmacy, Pharmaceutical Technology and Biopharmaceutics, Ludwig-Maximilians-University Munich, Butenandtstr. 5, Munich D-81377, Germany
e-mail: Julia.engert@cup.uni-muenchen.de

© Controlled Release Society 2016

A. Müllertz et al. (eds.), *Analytical Techniques in the Pharmaceutical Sciences*,
Advances in Delivery Science and Technology, DOI 10.1007/978-1-4939-4029-5_15

467

laminar flow conditions, the flow velocity across the channel thickness has a parabolic profile with the highest flow velocity at the center of the channel and slowest velocity at the walls. Smaller species diffuse back towards the middle of the laminar flow channel faster than larger species. At equilibrium, a steady state is established for each sample species at a certain distance from the channel wall. The mean thickness of this sample equilibrium layer is correlated to the retention time and physicochemical properties of the sample (Williams and Giddings 1994). By that, smaller species are eluted earlier, and when a detector is placed at the end of the separation channel, a fractogram similar to a chromatogram, can be established. Field-flow fraction (FFF) developed rather slowly in the first decade after its introduction in 1960 (Wahlund and Giddings 1987), and it lasted until about the year 2000 until the protein formulation community took real notice of the method (Klein and Huerzeler 1999; Fraunhofer and Winter 2004). This has several reasons, one of them being the fact that - at that time- a small number of suppliers had optimized AF4 systems so far, that they were commercially available for a reasonable price and could be used after a few hours of training by experienced HPLC users. This went along with the development of the asymmetrical version of flow field fractionation, that makes the systems much easier to build and to apply (Giddings 1993). Let us consider how a flow field is built up in a channel with laminar flow: The upper and lower wall of the channel have to be replaced by semipermeable membranes that allow liquid to be pumped into the channel and (on the other side) to be removed to create the cross flow (Fig. 15.1).

Such systems had been built e.g. by Giddings, and even though they worked very well (see application examples for liposomes, lipoplexes under 3.2), their setup was rather cumbersome. In a next step, the upper semipermeable wall was removed and

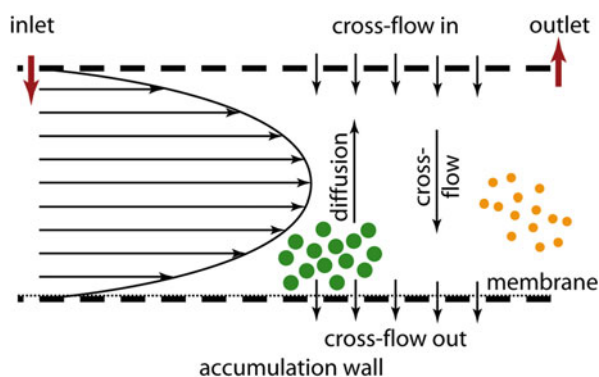


Fig. 15.1 Schematic illustration of the separation/fractionation principle of AF4. The parabolic flow profile of the channel flow transports the sample injected through the inlet through the AF4 channel. The cross-flow perpendicular to the channel flow forces the sample towards the accumulation wall. Separation/fractionation is then a result of two parameters taking place simultaneously. Smaller particles will diffuse back faster towards the channel center due to Brownian motion compared to larger particles. Secondly, particles located close to the accumulation wall will start to rotate and, as a consequence, will experience hydrodynamic lift forces back to the channel center

the cross-flow only achieved by pumping out water on the lower channel wall. Although the field would then be imperfect and “asymmetrical”, it serves the purpose perfectly as the movement of the analytes and their separation takes place close to the outlet wall and therefore the imperfection of the upper part of the channel plays no major role. This makes the systems finally cheaper and easier to handle which catalyzed its success (Wahlund and Giddings 1987).

Another driver for the increased interest in AF4 was the fact that in protein formulation sciences the relevance of aggregates and small, subvisible particles became more and more obvious, and particulate and nanoparticulate drug delivery systems needed more reliable analytics. As we will see in detail, AF4 can close certain gaps that other methods leave open, especially when size exclusion chromatography (SEC) as the standard for soluble macromolecules and optical methods measuring nanoparticles are considered. Before we discuss the method in more detail, a recent technical development shall be introduced. Hollow fiber FFF (sometimes called HF5) is the logical consequence when the AF4 principle is brought to its theoretical optimum. Why not transforming a channel with one semipermeable wall into a round tube where the entire wall surface can be used for removing liquid and creating a flow field? Existing technologies from hollow fiber dialysis modules were adapted to AF4 and the new “HF5” system was created (Reschiglian et al. 2014; Zattoni et al. 2008). With that, FFF reached a grade of convenience similar to column based chromatographic systems, where the user “plugs in” the separation device (now the “HF5 hollow fiber module”) and starts the run.

2 Practical Guide for AF4

Before carrying out a separation of a sample with AF4, we shall consider first the reasons to do so, namely the potential benefits over other methods and then how to run a sample and how to interpret the resulting fractogram. Of course, over the past decades excellent reviews have been written and handbooks edited, amongst which the books by Schimpf, Caldwell and Giddings are still considered as standard monographs (Schimpf et al. 2000; Caldwell 1988). The core of the AF4 method is the separation channel; all other peripheral compounds are comparable to standard chromatographic systems, be it the autosampler or the numerous detectors that can be used in line, like UV/VIS spectrophotometer, fluorimeter, refractive index (RI) detector, or multi-angle laser light scattering (MALLS) detector. Compared to a chromatographic column, an AF4 channel is first of all empty. No large surfaces, as they are typical for the column fill material, are provided and no inlet/outlet frits are needed. At least in theory, anything can be brought into the channel that is smaller than the channel height and everything leaves the channel eventually. Typical (inner) channel dimensions are a length of 10–40 cm, a width of 1–5 cm and a height of 100–500 μm (with more typically a height of 250–350 μm). With that, almost all types of protein aggregates and pharmaceutically relevant nanoparticles, even small microparticles can be loaded on an AF4 channel. Upper

size limits as for the standard SEC do not apply anymore. It is well known that due to sample filtration and the frit inlet of the SEC columns, one will always see only the soluble part of potential impurities and large species are systematically lost or underestimated. Thus, AF4 has a clear advantage over SEC in this respect. AF4 can also be used in a semi-preparative mode by applying larger channels. On the other hand, AF4 has a lower limit for molecules that can be analyzed. The cut-off of the semipermeable membrane that closes the channel is the limiting step. Cut-offs of about 10 kDa are standard. For smaller analytes one could use smaller cut-offs, like e.g., 5 kDa, but pressure in the system then rises and finally losses for molecules in size close to the cut-off make quantitative analytics impossible. Insulin may be named as the molecule marking the lower limit of AF4. As the channel is empty and unspecific to the type of analytes, they are only separated by their hydrodynamic radius, not by any other physical or chemical feature. However, certain molecules may bind unspecifically to dialysis membranes and therefore the general separation principle of AF4 may be somewhat compromised in these cases. Another feature of AF4 separation is that in practically all cases, the formulation in which the drug substance is dissolved can be used as a running buffer. This ensures that especially for aggregation phenomena, changes in pH, ionic strength, buffer type, surfactant concentration, and concentration of stabilizers that all could influence the analytical result can be avoided. As mentioned above, adsorption to the cross-flow wall can occur, and in such cases addition of surfactants or salts may be necessary. But molecules of this type often adsorb to other surfaces, too, and must be formulated with surfactant anyway to avoid losses during pharmaceutical fill and finish operations. Reschiglian et al. provided a concept that eliminates the membrane, but this could only be applied to very large particle/colloids in the sample and has therefore not found broader application (Reschiglian et al. 2000). Another argument that has been used in favor of AF4 versus SEC is the fact that the shear forces applied to a molecule or a colloidal particle are much lower in AF4 than in SEC. Higher overall pressure and the narrow spaces between the densely packed gel particles in an analytical column speak in favour of AF4 and data received from analytical ultracentrifugation (AUC), SEC and AF4 confirm this view in a way that aggregates are underestimated by SEC because they are “milled” down to smaller oligomers or dimers. On the other hand, AF4 is often criticized for its potential to artificially create aggregates. The main reason for that is the “focusing step” that is needed before an AF4 separation is started.

2.1 The Focusing Step

A sample injected into the running buffer of an AF4 channel would spread in a way that only weak, flat peaks will be achieved. To avoid this, after injecting a sample into the inlet area of the channel, forward flow and backflow are applied and the entire running buffer leaves the channel through the cross-flow membrane (Fig. 15.2). In that phase, a sharp band of the sample species is formed, preferably

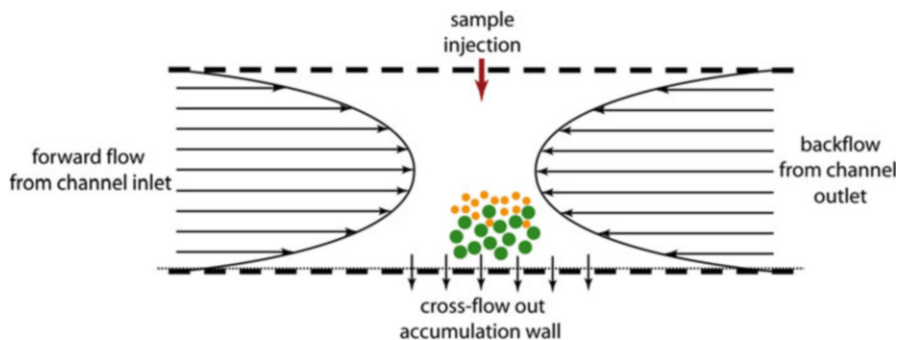


Fig. 15.2 Schematic illustration of the sample positioning during the focusing step applied in AF4. The flow from the channel inlet and the inversed flow from the channel outlet force the sample within a narrow band. Particles arrange at a distance to the accumulation wall according to their diffusion coefficient

close to the inlet side of the channel. Finally, the backflow is stopped and the regular separation starts with a forward flow plus a cross-flow. During the focusing step, the sample is concentrated in a band close to the membrane and under these conditions one could imagine that the higher concentration in the focus band and the microfluidics moving the molecules towards the membrane surface may induce aggregation. Control runs, if possible, are needed to exclude such artifacts (Litzén and Wahlund 1991).

2.2 Instrumentation

Before we consider performing (as a thought experiment) an AF4 run, we need to choose an instrument. The market is rather clearly laid out, as there are only two major competitors in Europe and North America. Both provide the user with excellent systems for more than 10 years; however, their technical philosophy is slightly different. Wyatt Technology (Wyatt Technology Europe GmbH, Dernbach, Germany), uses standard HPLC compounds for dosing the running buffer, for injecting the samples, and creating the linear and cross-flow; in fact, only a single pump is used. Whilst theoretically any system could be used, in practice the compounds are taken from Agilent. To exactly control the different flows, a “switchbox” with valves, pressure sensors, splitters etc. is used, called “Eclipse” system by Wyatt. Postnova (Postnova Analytics, Landsberg am Lech, Germany) uses a different approach. Several pumps provide the different flows and they are all custom-built as are the autosamplers, controllers etc. Both companies provide several detectors, with Wyatt having an emphasis on MALLS detectors. Due to the fact that Wyatt has built and optimized MALLS detectors and pertaining evaluation software systems for some decades, they rely on the SLS software package ASTRA but control the AF4/HF5 systems with a different software.

Postnova has one software package comprising fractionation run control and SLS evaluation, but has less SLS experience overall (Wyatt 1991; Roessner and Kulicke 1994).

MALLS detectors are common and relevant for AF4 applications, as they allow a direct and independent determination of the molecular size of an analyte. This is helpful and often used in SEC, too, but in AF4 two more aspects have to be considered. Firstly, retention times in AF4 are less easy to calibrate and to predict compared to the situation in SEC, therefore an independent method is needed. Secondly, the chance to have very large molecules or colloids running through the AF4 channel that cannot be separated by other methods so easily makes MALLS detection very attractive to estimate their size/molecular weight immediately in line (Wyatt 1991; Roessner and Kulicke 1994).

2.3 Separation

If we start an AF4 run, we first need to place the membrane into the separation channel (Fig. 15.3), equilibrate it with the running buffer, rinse the system and inject the sample. After focusing the sample band, the separation can start. For a given channel and membrane (only regenerated cellulose and polyethersulfone are on the market) the linear flow and the cross-flow are the only variables. The volume of the cross-flow enters the channel together at the inlet with the volume that finally leaves the channel at the outlet. Considering this, one becomes aware that the sample is diluted over the course of the separation run. Part of that is counteracted by the “up-concentration” during the focusing step. Another trick allows increasing the concentration of the analyte entering a detector after the channel. This feature is called “slot outlet” and uses the fact that the separation takes place slightly above the accumulation wall and the rest of the channel height is almost free of sample molecules. Consequently, only the part of the channel content next to the

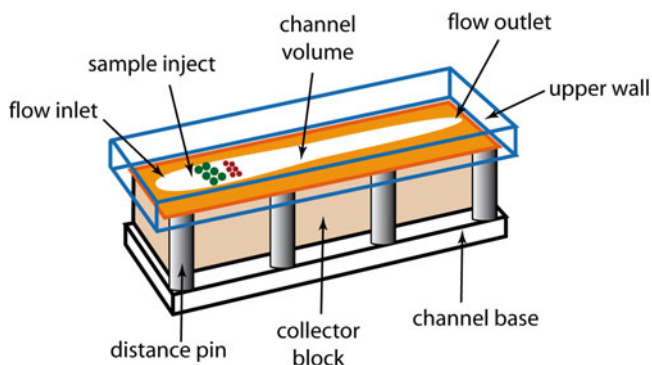


Fig. 15.3 Schematic drawing of a typical AF channel. Following sample injection and focusing samples are separated. Smaller particles (*red*) elute prior to larger particles (*green*)

accumulation wall is taken to the detector (“splitting” the flow), the rest is discarded. Before the optimal cross-flow is selected, a run without cross-flow is helpful to determine whether the sample is retained by the separation system as such, e.g., by adsorption to the membrane, and furthermore what molecule sizes are present in the sample before it has seen focusing and cross-flow. In case of strong membrane binding, albumin can be used to block such adsorption. Now the cross-flow is selected. Typically a cross-flow is not kept constant over the entire separation run but reduced over time (like a gradient) and finally set to 0 at the end. It is therefore a typical feature of an AF4 run, that all sample material that has been accumulated and not rolled towards the outlet according to the equilibrium distance from the wall, will then be released and detected as a wash off peak.

Larger species tend to elute not earlier than with this peak, and care has to be taken not to overestimate such species because of aggregates having formed at the accumulation surface and not being present in the sample as such. Theoretical calculations are possible to estimate the retention time of molecules or nanoparticles under given conditions (channel dimensions, fluxes, densities, viscosities, temperature) and allow indirectly to identify interactions that disturb the theoretical ideal diffusion behavior due to surface interaction and/or self-interaction of the analyte species (Giddings 1978).

In summary, the development of a suitable AF4 experimental set-up requires time and analysis of the various parameters having an influence on the quality of the resulting AF4 fractogram. Critical experimental parameters are the ionic strengths of the carrier liquid, the focus flow rate, the cross flow rate and the sample load. Some parameters may be more critical than others, but nonetheless, development of an appropriate AF4 method is time-consuming and non-trivial (Williams et al. 2001; Williams and Giddings 1994).

2.4 Steric Mode

Very large species within a sample show the so called “steric mode” elution behavior and elute in front of all the rest with the injection peak (Fig. 15.4). Although such steric mode pre-peaks are not regular shaped and not resulting from a quasi-equilibrium situation, they can deliver important qualitative information (Caldwell et al. 1979). The presence of very large species like oil droplets, agglomerates and particles can be confirmed in one run, a feature that SEC will not be able to deliver. Fraunhofer and Winter have shown that the presence of silicon oil droplets from prefilled syringes can be differentiated from protein drug aggregates (Fraunhofer and Winter 2004; Fraunhofer 2003). Gottschalk et al. went one step further and used the steric mode pre peak to quantify very large, particulate protein aggregates whereas the soluble, large aggregates run under normal separation mode (Gottschalk et al. 2006).

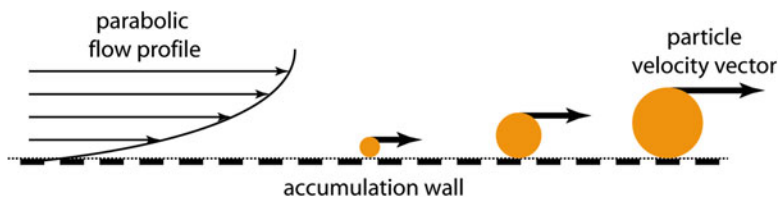


Fig. 15.4 Schematic illustration of the steric mode principle in AF4. Larger particles possess a higher particle velocity vector and are therefore eluted earlier compared to smaller particles from the AF4 channel

2.5 Benchmarking of AF4

2.5.1 Comparison to Electron Microscopy

Electron microscopy is widely used for the characterization of systems in the nano- and micrometer range. Scanning electron microscopy (SEM), transmission electron microscopy (TEM) and both cryo-SEM and cryo-TEM are currently utilized. Despite their advantages to fully elucidate the surface structure of a system, disadvantages are the tedious sample preparation and the time-consuming sample analysis. In addition, only a small fraction of the total sample can be analyzed. While in cryo-SEM and cryo-TEM samples are viewed in their frozen state, SEM and TEM usually require a drying and/or staining step, which may alter sample morphology and produce artifacts. In contrast to this, AF4 allows the analysis of a larger fraction of the total sample, gives detailed information about particle size, allows fractionation of different particle size fractions, and furthermore nanoparticles can be analyzed in liquid dispersion.

2.5.2 Comparison to Size Exclusion Chromatography

Size exclusion chromatography (SEC) is the standard method for the analysis and separation of proteins and other polymers of pharmaceutical relevance. Being the workhorse in every biopharmaceutical lab, SEC has matured to a very reliable and precise method. Qualification of the equipment and validation of the methods are common practice (Arakawa et al. 2010; Philo 2009). Still, SEC has its limitations and drawbacks. First, columns are very expensive, their standing times are often frustratingly short, especially when samples are rich in impurities, and the columns have to be selected for the samples under investigation, meaning that one needs different columns to cover a broad range of analytes. AF4 has certain advantages here. As already mentioned, one channel serves for the separation of all types of analytes from 5000 Da to particles of several hundreds of nanometers. Furthermore, it has been shown that SEC underestimates larger protein aggregates compared to AF4. For that reason, since the 1990s, AF4 received increasing interest as a new tool (“orthogonal method”) for protein, nucleotide and polymer research (Litzén

and Wahlund 1989; Litzén et al. 1993; Gabrielson et al. 2007; Carpenter et al. 2010). When it comes to the quantification of fragments, AF4 might have its weaknesses as small compounds can get lost due to the chosen membrane cut-off, but typical fragments formed from antibodies will be well retained, separated and detected. AF4 has therefore long been used as a trouble-shooting device and research instrument only, but now the first systems run under current good manufacturing practice (cGMP) conditions, and AF4 methods are used for the first products and projects for regulatory specifications.

2.5.3 Comparison to Analytical Ultracentrifugation

Although AF4 has shown its promises over SEC for larger particles and protein aggregates, AUC is often chosen when a method is sought where the interaction with the analytical separation systems can be reduced to practically zero and artifacts are very unlikely (Pauck and Coelfen 1998). Due to the mandatory presence of the channel membrane, AF4 can as a matter of principle not provide that. AUC is extremely expensive, needs experienced operators and specialists for interpretation, and by that, is not useful as a routine method accompanying product development, clinical supplies, scale up, and product release. In our eyes AUC should be used to control SEC and AF4 for their ability to detect relevant amounts of aggregates or colloids. Once qualified in that way, AF4, or in case of “easy” samples also SEC, could then be used for routine purposes.

3 Analysis of Particulate Systems

3.1 Nanoparticles

As described above, AF4 is a versatile tool for the analysis of various types of formulations. However, in particular for analytics of nanoparticulate formulations or particulates, it has been shown in various reports in the literature that AF4 offers additional attributes when it comes to sample analysis. Usually, nanoparticulate formulations are characterized by the classical analytical methods such as electron microscopy and dynamic light scattering (DLS). Electron microscopy allows investigating the surface of the nanoparticles, whereas analysis in terms of particle size and size distribution is cumbersome, since at least 10,000 particles must be counted in order to satisfy statistical requirements. DLS on the other hand does not provide any information on the surface characteristics of the sample, but can be utilized to calculate an average particle size and a size distribution according to the Stokes-Einstein equation. However, this technique is in principle only applicable to monodisperse formulations that contain perfectly spherical particles at an ideal concentration. AF4, on the other hand, allows obtaining information on particle size

while at the same time particles can be fractionated according to their size, should particles of different sizes be present in the formulation. In the following section an overview over different nanoparticulate formulations investigated by AF4 is given. A nice tutorial on how to select and develop a protocol for nanoparticle fractionation by AF4 can be found in Gigault et al. (2014a).

3.1.1 Human Serum Albumin Nanoparticles

John and Langer (2014) analyzed 150 nm human serum albumin (HSA) based nanoparticles in terms of particle size but also investigated the particle formation process using AF4. The authors report that the determination of an ideal cross flow for sample analysis is the main influencing parameter on the separation quality. Therefore, in a first step the cross flow should be varied. Cross-flow should be sufficiently high for particle separation, but at the same time as low as possible to achieve an optimal peak shape in the AF4 fractogram. In addition, the focusing step is highlighted as an important parameter. If the focusing step is too short or the focus flow too low, particles will not be fractionated completely. On the other hand, if the focus flow and the cross flow are increased to such an extent that the particles are located too close to the membrane, more time is needed for complete elution. In terms of particle concentration for AF4, a compromise needs to be found between a starting concentration that is sufficiently high (as the sample will be diluted during fractionation) but not too high since otherwise overloading effects of the channel will occur.

In addition to the analytical method for particle size characterization described above, the authors also utilized AF4 to observe HSA nanoparticle formation during the desolvation process, as well as characterized the size and degree of PEGylated HSA nanoparticles. Increasing amounts of ethanol were added for HSA desolvation which first resulted in the formation of protein aggregates and later in the formation of HSA nanoparticles. Covalent modification of HSA nanoparticles with PEG was observed by an increase in particle size and a time shift of the particle count rate. According to the author's reports, AF4 can be used to also quantify the degree of PEGylation when unbound PEG is previously removed from PEGylated nanoparticles.

3.1.2 Gelatin Nanoparticles

Fraunhofer et al. (2004) were able to show that AF4 is a powerful tool to characterize gelatin nanoparticles in addition to the characterization of gelatin bulk material and analysis of the nanoparticle drug-loading process. Using AF4, the authors were able to separate and quantify e.g., proteins and oligonucleotides, which were even more challenging, since the raw material of the nanoparticles was also of a proteinaceous nature. In addition, AF4 allowed confirming the heterogeneity of the gelatin molecular weight. In a further study, Zillies

et al. (2007) utilized AF4 to quantify the PEGylation efficiency of nanoparticles without further sample preparation.

3.1.3 Particles from Melt Extrusion

AF4 has also been reported as an analytical method to investigate and characterize the formation of structures or particles when solid dispersions prepared by melt-extrusion were dispersed in aqueous media (Kanzer et al. 2010). Kanzer et al. compared the size and size distribution obtained by either PCS or AF4 coupled with an online MALLS detector. In contrast to PCS, which only indicated submicron particles, AF4 allowed separating up to three different nanoparticulate fractions: colloidal polymer, nanoparticle aggregates and nanoparticulate aggregates of the incorporated drug (Kanzer et al. 2010), therefore providing a much deeper insight into the bulk phase of the dispersion compared to PCS.

3.2 *Liposomes, Liposomal Formulations and Lipoplexes*

Apart from solid nanoparticles, liposomes, liposomal formulations and lipoplexes have also been investigated. In the early days, classical flow field flow fractionation (FFF) has been employed to investigate the size and size distribution of liposomes. In 2006, Hupfeld et al. (2006) reported on the analysis of small liposomes. The authors used three different techniques to analyse liposomal size, namely PCS, SEC with subsequent PCS analysis, and FFF coupled with on-line static light scattering and RI detectors. While all three methods delivered useful results, the size distribution calculated was not identical. Bulk analysis of the liposomal preparation by PCS revealed a broad mono-modal or bimodal size distribution, whereas after fractionation by either SEC or AF4 smaller liposomes with a much narrower size distribution were obtained in addition to a broader peak representing larger particles. The authors concluded that bulk analysis of liposomal formulations by PCS often suffers from the limitation that PCS tends to underestimate smaller particles when at the same time larger particles are present. On the other hand, results obtained by FFF showed larger minimum liposome diameters, which the authors explained by the different detection limits of the PCS measurements and MALLS detection. Hence, fractionation of the sample prior to size analysis can result in more reproducible particle sizes (Hupfeld et al. 2006). In a consecutive study, Hupfeld et al. (2009) utilized AF4 to systematically investigate the effect of focus flow rate, cross flow rate, sample load and ionic strength of the carrier liquid on the retention behavior of liposomes separated by AF4. Varying the focus flow resulted in peak shifts and changes in peak shape, therefore for each formulation at first an optimal focus flow should be determined. Secondly, sample load had an effect on calculated geometric radii. Overloading effects of the channel may be observed when the sample load is too high, meaning that some larger particles do not reach

their expected position within the channel and remain in proximity to the parabolic flow profile. As a consequence, such particles will then elute earlier than expected. Another important aspect is the influence of the cross flow rate and the cross flow mode. Different constant cross flow rates were applied. While too small cross flow rates result in insufficient fractionation, high cross flow rates hinder complete elution of the sample. Therefore, in most cases a cross flow gradient is applied to obtain both satisfactory separation and complete elution. Lastly, the ionic strength of the carrier solution also impacted on the fractionation and size analysis of liposomes, since the retention of charged liposomes in a low or high ionic strength carrier medium may be different to highly purified or distilled water and also compared to the fractionation of uncharged liposomes. Not only does the zeta potential of the liposomes influence the location of the particles from the channel wall; the orientation of phosphatidyl choline groups within the liposome may also change upon an increase of the ionic strength, hence impacting on the zeta potential of the particles and consequently on the repulsive effects between individual liposomes as well as between liposomes and the accumulation wall (Hupfeld et al. 2010). Again, an optimal salt concentration needs to be found for sample analysis. If the salt concentration of the liposomal formulation is different to the carrier medium, shrinking and swelling effects of liposomes due to osmotic pressure can be observed (Hupfeld et al. 2010). Apart from liposome fractionation and size analysis, AF4 has recently been used to study drug transfer from liposomal formulations, using donor and acceptor liposomes and quantifying the amount of drug retained in the donor liposomes (Hinna et al. 2014).

FFF has further been used to analyze physical characteristics such as particle size and storage stability of self-assembled cationic lipid-DNA complexes (lipoplexes). These systems usually suffer from their heterogeneity, as free liposomes, DNA, and complexed DNA-liposomes are present in one single formulation. In 2001, Lee et al. studied the feasibility of an FFF system coupled with UV, RI and MALLS detectors. Exploring different ionic strengths of carrier liquids and types of membranes, the authors were able to establish a system which enabled them not only to study such complex systems of various lipid-DNA ratios, but also revealed that with MALLS detection the formation of aggregates upon storage became visible which was not observed with other techniques such as PCS (Lee et al. 2001). In addition, cationic lipid-DNA particle fractions can be fractionated using FFF which can be useful if structure-activity relationships of the different complexes need to be determined.

3.3 *Virus-Like Particles*

Virus-like particles (VLPs) as vaccine carriers have also been investigated using asymmetrical flow field-flow fractionation. Lang et al. (2009) report on the analysis of nicotine-conjugated VLP carriers, where AF4 was used as a complementary technique to DLS. The aim of this study was to investigate aggregated species of

VLPs, which is not possible by DLS or by SEC. The authors were able to separate VLP formulations into VLP fragments, monomers, dimers and oligomers/aggregates. AF4 was further used in the formulation development and testing of formulation stability over time. Chuan et al. (2008) reported an optimized AF4 method for the characterization of VLPs, and the authors focused on potential adsorption effects as well as on the separation of VLP fragments, monomer, dimer, and aggregates. AF4 was benchmarked against classical techniques such as TEM and DLS. Under optimized conditions, no sample aggregation effects were observed. VLP samples could be fractionated by AF4, and approximately 69 % of the VLPs showed a size between 15 and 35 nm, whereas the remaining fraction was composed of particles having a size range up to 100 nm. In addition to this, the authors reported that using AF4 even changes in the quaternary structure of the VLPs could be monitored. In a further study, Pease et al. (2009) analyzed four different types of VLPs: VLPs with and without packaged genomic DNA or protein, VLP with packaged foreign protein, VLP with packaged genomic DNA, and VLP assembled from VLP pentamers modified to express a foreign peptide sequence on the VLP surface.

3.4 *Polyplexes*

Noga et al. (2013) reported on the use of AF4 to investigate hydroxyethyl starch (HES)-coated polyplexes. In this study, the authors synthesized different HES-polyethylenimine (PEI) conjugates and used AF4 to investigate the rate of biodegradation upon incubation with alpha amylase (AA). The authors were able to show that degradation of HES in the presence of AA is rapid at the beginning and subsequently levels off after 4–6 h. Furthermore, lower molar substitution of HES showed higher degradation rates. The effect of molar mass on biodegradation was also investigated, showing that larger molecular weight HES (e.g., HES70) was degraded to a higher extent compared to lower molecular weight HES (e.g., HES 30). The authors explained this result by the better accessibility of α -1,4-glycosidic bonds of HES in the higher molecular weight HES molecules for AA.

3.5 *Non-spherical Nanoparticles*

In contrast to classical DLS measurements, field flow fractionation and in particular AF4 can also be used to analyze, quantify and separate particulate systems which are not perfect spheres, for example protein filaments or non-spherical particles. In 2004, Jores et al. (2004) reported on a study using symmetric flow field-flow fractionation to compare size and size distribution of solid lipid nanoparticles (SLNs) and nanostructured lipid carriers (NLCs) with DLS measurements. The colloidal structures were prepared from glyceryl behenate and medium chain

triglycerides in order to combine mixtures of solid and liquid lipids to increase drug loading and improve controlled release thereof. PCS indicated that SLN and NLC differed from a nanoemulsion with respect to Brownian motion due to asymmetric particle shapes, thereby also leading to higher polydispersity indices. The authors reported that using symmetric field-flow fractionation allows separation of isometric from asymmetric particles, as isometric particles will elute earlier. Here clearly the principle of field flow fractionation has great advantages compared to DLS in bulk, since isometric and asymmetric particles are separated before the measurement in field flow fractionation.

Further studies using classical FFF for non-spherical particles have been reported by Chun et al. (2008) for single wall carbon nanotubes (SWNTs). Here the authors characterized the rodlike structures according to their size by comparing the elution times of fractions of SWNTs to standard spherical particles.

Mathaes et al. (2013) utilized an AF4 system equipped with a MALLS detector for measuring the radius of gyration (geometric radius) and a DLS detector to determine the hydrodynamic radius of 40 nm spherical and stretched polystyrene particles. From the measurements, a shape factor (the quotient of the geometric radius to the hydrodynamic radius) can be calculated and enables to clearly distinguish spherical from elongated or rod-like particles. However, AF4 is limited in terms of particle size by the resolution of the DLS detector. In the presented study, the DLS only allowed to measure particles in the size range between 3 and 200 nm. Gigault et al. (2014b) also looked into the characterization of self-assembled nanofibers by AF4 to investigate the length of the nanofibers as well as their aggregation potential.

Care must be taken when non-spherical particles are analyzed by either FFF or AF4. Phelan Jr and Bauer (2009) highlight that up to a size of about 500 nm rodlike particles elute using FFF by a normal mechanism, whereas an inverse steric effect occurs when larger particles are separated. Alfi and Park further investigated this topic using FFF and concluded in their study that the separation behavior of rods and spheres also strongly depends on the conditions used for the fractionation procedure (Alfi and Park 2014).

4 Preparative Use of AF4

AF4 cannot only be used to fractionate and then analyze portions of sensitive samples such as proteins or antibodies, this technique can also be used to preparatively separate protein aggregates from monomer species (Freitag et al. 2011b). Separate fractions of aggregate species can then be analyzed in much more detail. Freitag et al. (2011b) utilized AF4 to separate and quantify fragments, monomer and soluble oligomers of a therapeutic antibody. The molecular weight of the detected species was calculated according to the fractogram obtained using the described AF4 method. It was possible to store the different fractions either at 2–8 °C for up to 3 weeks without any changes in the soluble oligomer fraction.

Alternatively, fractions were frozen in the deep freezer ($-80\text{ }^{\circ}\text{C}$) and subsequently gently defrosted in the refrigerator at $2\text{--}8\text{ }^{\circ}\text{C}$ without any changes in the peak position, retention time or loss of soluble oligomer due to adsorption phenomena. In addition to the excellent protein separation potential, AF4 can also be run using different ionic strength buffers; hence samples can be analyzed using any tonicity of the formulation which may later be used for *in vivo* studies. In a further study, Freitag et al. (2011a) were able to show that by using a rinsing/disinfection routine for the AF4 instrument, it was possible to obtain protein fractions with endotoxin levels far below the required 0.250 IU/mL for parenteral administration according to the monograph “water for injections” in the European Pharmacopoeia. This semi-preparative approach has not been published before, except for a circular AF4 variant (Maskos and Schupp 2003).

5 Recent Trends in AF4

In the following section, the most recent trends in using AF4 are summarized. The examples given here highlight that AF4 receives increasing attention from researchers not only in the pharmaceutical field, but also in various other disciplines and various different types of applications.

5.1 *Quantitative Characterization of IgG Aggregates*

Protein aggregates in pharmaceutical formulations receive growing attention due to the potential risk of aggregates to induce unwanted immunogenicity in patients. While a number of techniques is available for protein formulation characterization (SEC, DLS), it is recommended to utilize orthogonal methods for protein aggregate characterization such as AUC or AF4 (Carpenter et al. 2010). Ma et al. recently studied soluble aggregates formed in heat-stressed solutions of an IgG molecule to which polyacrylates were added for stabilization purposes (Ma et al. 2014). In contrast to other techniques it was possible with AF4 to obtain information on % IgG recovery in addition to quantify and size the fraction of IgG monomer or dimer in comparison to IgG aggregates.

5.2 *Separation of Different Types of Antibody Aggregates for Immunogenicity Testing In Vivo*

As described above, protein aggregates are linked to unwanted immunogenicity in patients. However, it is still a matter of debate if all aggregates in general are

responsible for immunogenicity, or if immunogenicity is only linked to certain types of aggregate species (soluble, insoluble, reversible, irreversible aggregates). Freitag et al. separated samples of a murine monoclonal antibody based on aggregate size by AF4, and the collected fractions were subsequently used to test immunogenicity in vivo (Freitag et al. 2014).

5.3 Separation and Quantification of Protein Aggregates by HF5

Fukuda et al. qualified the still not so extensively used HF5 method for the quantification of a monoclonal antibody and aggregates thereof in terms of precision, accuracy, linearity, and quantitation limit (Fukuda et al. 2014).

5.4 AF4 as an Additional Method to Gain Insight into Degradation Pathways of Antibody-Based Drug Candidates

Fincke et al. utilized AF4 in addition to spectroscopic techniques, DLS, differential scanning calorimetry (DSC), electrophoresis, visual inspection, and surface plasmon resonance (SPR) to investigate degradation pathways of three different antibody-based drug candidates upon exposure to elevated temperature (Fincke et al. 2014). This study highlighted the usefulness of AF4 as an orthogonal technique to classical bulk measurement techniques such as DLS.

5.5 Characterization of β -Cyclodextrin-Dextran Polymers for Poorly Water Soluble Drugs

di Cagno et al. (2014) evaluated the potential of different newly synthesized β -cyclodextrin-dextran polymers for parenteral administration of poorly water soluble drugs. The authors investigated the stability of the new substances in terms of aggregate formation by molecular weight, the ability to solubilize a poorly soluble drug as well as drug release properties.

5.6 *PLGA Nanoparticles Released from a Tablet*

Engel et al. (2014) reported on the use of AF4 as an analytical method to determine the release of PLGA nanoparticles embedded in a tablet. Two different sizes of PLGA nanoparticles (120 and 220 nm) were prepared and subsequently dried using either spray-drying or freeze-drying. This dry nanoparticle powder was then transformed into tablets by direct compaction using α -lactose-monohydrate, PEG 4000, polyvinylpyrrolidone, crosscarmellose sodium and silicon dioxide as further ingredients. Release of nanoparticles from the solid dosage forms was then analysed using AF4 without further treatment such as filtration. The authors report that nanoparticle release from the tablets was completed within 30 min, and the presence of nanoparticles in the release media could be clearly proven by AF4 as well as by DLS batch measurements. This is a very interesting approach as AF4 offers the possibility to quantify nanoparticle release and potentially released API in its soluble form by UV detection at the same time, given the concentration of the API is sufficiently high.

5.7 *Characterization of Cationic Polymers for Gene Delivery*

AF4 has also been investigated as a characterization technique for cationic polymers. Wagner et al. studied different cationic polymers for their applicability in gene delivery and used AF4 as an additional technique to AUC and NMR spectroscopy (Wagner et al. 2014). The authors describe that SEC and mass spectrometry (MS) often do not deliver meaningful results, in particular when cationic polymers are analyzed. For SEC, this is due to the fact that the cationic polymer strongly interacts with the stationary phase of the SEC column; therefore the authors investigated AF4 as an alternative technique since in AF4 no stationary phase is present. Nonetheless, care must be taken when choosing the channel membrane, as strong interactions with the membrane material may lead to peak deformation and broadening. Additionally, the ionic strengths of the eluent must be evaluated carefully when charged polymers are being fractionated as must be the amount of injected sample as overloading effects may occur due to electrostatic repulsion. In summary, AF4 was established as a reliable method to obtain conformational information and determine the molar mass and PDI of different polymers given that the molar mass of the polymer is larger than 15 kg mol^{-1} (Wagner et al. 2014).

5.8 *Characterization of Polymersomes Using AF4*

Till et al. investigated several polymersomes based on polyethylene block copolymers using AF4 and compared the results to classical characterization techniques such as electron and atomic force microscopy, as well as static light scattering (SLS) and DLS, and small-angle neutron scattering (Till et al. 2014).

5.9 *Quantification and Characterization of Nanoparticulate Additives in food*

In a recent study, Heroult et al. described the development of an AF4 method for the characterization and quantification of silica nanoparticles in a commercially available food product, coffee creamer (Heroult et al. 2014). The presence of nanoparticulate additives such as silver nanoparticles as antibacterial additives, titanium dioxide as whitener or silica as an anti-caking agent is widely performed in food industry. These excipients are also used in pharmaceuticals, therefore, the developed AF4 method may also be relevant for further studies.

6 Conclusion

In summary, AF4 has become a technique which is more and more relevant in the pharmaceutical setting and can be used as an orthogonal method to well-established classical characterization techniques. However, method development for AF4 remains to be non-trivial and may be a time-consuming procedure. Nonetheless, in some cases, AF4 may close an open gap that other techniques cannot capture. It will be interesting to see how AF4 will further evolve and in particular, if and how further developments of e.g., the HF5 system will proceed in the future.

Acknowledgements The authors wish to thank Dr.-Ing. Marcus Engert for preparing the schematic illustrations.

References

- Alfi M, Park J (2014) Theoretical analysis of the local orientation effect and the lift-hyperlayer mode of rodlike particles in field-flow fractionation. *J Sep Sci* 37(7):876–883. doi:[10.1002/jssc.201300902](https://doi.org/10.1002/jssc.201300902)
- Arakawa T, Ejima D, Li T, Philo JS (2010) The critical role of mobile phase composition in size exclusion chromatography of protein pharmaceuticals. *J Pharm Sci* 99(4):1674–1692. doi:[10.1002/jps.21974](https://doi.org/10.1002/jps.21974)

- Caldwell KD (1988) Field-flow fractionation. *Anal Chem* 60:959–971
- Caldwell KD, Nguyen TT, Myers MN, Giddings JC (1979) Observations on anomalous retention in steric field-flow fractionation. *Sep Sci Technol* 14:935–946
- Carpenter JF, Randolph TW, Jiskoot W, Crommelin DJA, Middaugh CR, Winter G (2010) Potential inaccurate quantitation and sizing of protein aggregates by size exclusion chromatography: essential need to use orthogonal methods to assure the quality of therapeutic protein products. *J Pharm Sci* 99(5):2200–2208. doi:[10.1002/jps.21989](https://doi.org/10.1002/jps.21989)
- Chuan YP, Fan YY, Lua L, Middelberg APJ (2008) Quantitative analysis of virus-like particle size and distribution by field-flow fractionation. *Biotechnol Bioeng* 99(6):1425–1433. doi:[10.1002/bit.21710](https://doi.org/10.1002/bit.21710)
- Chun J, Fagan JA, Hobbie EK, Bauer BJ (2008) Size separation of single-wall carbon nanotubes by flow-field flow fractionation. *Anal Chem* 80(7):2514–2523. doi:[10.1021/ac702362a](https://doi.org/10.1021/ac702362a)
- di Cagno M, Terndrup Nielsen T, Lambertsen Larsen K, Kuntsche J, Bauer-Brandl A (2014) β -Cyclodextrin-dextran polymers for the solubilization of poorly soluble drugs. *Int J Pharma* 468(1–2):258–263. doi:<http://dx.doi.org/10.1016/j.ijpharm.2014.04.029>
- Engel A, Plöger M, Mulac D, Langer K (2014) Asymmetric flow field-flow fractionation (AF4) for the quantification of nanoparticle release from tablets during dissolution testing. *Int J Pharma* 461(1–2):137–144. doi:<http://dx.doi.org/10.1016/j.ijpharm.2013.11.044>
- Fincke A, Winter J, Bunte T, Olbrich C (2014) Thermally induced degradation pathways of three different antibody-based drug development candidates. *Eur J Pharm Sci* 62:148–160. doi:<http://dx.doi.org/10.1016/j.ejps.2014.05.014>
- Fraunhofer W (2003) Asymmetrical flow field-flow-fractionation in pharmaceutical analytics—investigations in aggregation tendencies of pharmaceutical antibodies. Ph.D. thesis, Ludwig-Maximilians-University of Munich
- Fraunhofer W, Winter G (2004) The use of asymmetrical flow field-flow fractionation in pharmaceuticals and biopharmaceutics. *Eur J Pharma Biopharma* 58(2):369–383. doi:<http://dx.doi.org/10.1016/j.ejpb.2004.03.034>
- Fraunhofer W, Winter G, Coester C (2004) Asymmetrical flow field-flow fractionation and multiangle light scattering for analysis of gelatin nanoparticle drug carrier systems. *Anal Chem* 76(7):1909–1920. doi:[10.1021/ac0353031](https://doi.org/10.1021/ac0353031)
- Freitag AJ, Wittmann K, Immohr LI, Winter G, Myschik J (2011a) Asymmetrical flow field-flow fractionation—a preparative tool to obtain endotoxin-free protein Species. *GIT Lab J* 15:17–18
- Freitag AJ, Wittmann K, Winter G, Myschik J (2011b) The preparative use of flow field-flow fractionation (AF4). *LC GC Europe* 24(3):134–137
- Freitag A, Shomali M, Michalakakis S, Biel M, Siedler M, Kaymakcalan Z, Carpenter J, Randolph T, Winter G, Engert J (2014) Investigation of the immunogenicity of different types of aggregates of a murine monoclonal antibody in mice. *Pharm Res* 32(2):430–444. doi:[10.1007/s11095-014-1472-6](https://doi.org/10.1007/s11095-014-1472-6)
- Fukuda J, Iwura T, Yanagihara S, Kano K (2014) Separation and quantification of monoclonal-antibody aggregates by hollow-fiber-flow field-flow fractionation. *Anal Bioanal Chem* 406(25):6257–6264. doi:[10.1007/s00216-014-8065-4](https://doi.org/10.1007/s00216-014-8065-4)
- Gabrielson JP, Brader ML, Pekar AH, Mathis KB, Winter G, Carpenter JF, Randolph TW (2007) Quantitation of aggregate levels in a recombinant humanized monoclonal antibody formulation by size-exclusion chromatography, asymmetrical flow field flow fractionation, and sedimentation velocity. *J Pharm Sci* 96(2):268–279. doi:[10.1002/jps.20760](https://doi.org/10.1002/jps.20760)
- Giddings JC (1978) Displacement and dispersion of particles of finite size in flow channels with lateral forces: field-flow fractionation and hydrodynamic chromatography. *Sep Sci Technol* 13:241–245
- Giddings JC (1993) Field-flow fractionation: analysis of macromolecular, colloidal, and particulate materials. *Science* 260:1456–1465
- Gigault J, Pettibone JM, Schmitt C, Hackley VA (2014a) Rational strategy for characterization of nanoscale particles by asymmetric-flow field flow fractionation: a tutorial. *Anal Chim Acta* 809:9–24. doi:<http://dx.doi.org/10.1016/j.aca.2013.11.021>

- Gigault J, Zhang W, Lespes G, Charleux B, Grassl B (2014b) Asymmetrical flow field-flow fractionation analysis of water suspensions of polymer nanofibers synthesized via RAFT-mediated emulsion polymerization. *Anal Chim Acta* 819:116–121. doi:<http://dx.doi.org/10.1016/j.aca.2014.02.011>
- Gottschalk S, Lang R, Winter G (2006). Quantification of Insoluble Monoclonal Antibody Aggregates. Wyatt Application Note (<http://www.wyatt.com/files/literature/app-notes/fff-mals/insoluble-mab-aggregates.pdf>), retrieved 08/06/2016
- Heroult J, Nischwitz V, Bartzczak D, Goenaga-Infante H (2014) The potential of asymmetric flow field-flow fractionation hyphenated to multiple detectors for the quantification and size estimation of silica nanoparticles in a food matrix. *Anal Bioanal Chem* 406(16):3919–3927. doi:[10.1007/s00216-014-7831-7](https://doi.org/10.1007/s00216-014-7831-7)
- Hinna A, Steiniger F, Hupfeld S, Brandl M, Kuntsche J (2014) Asymmetrical flow field-flow fractionation with on-line detection for drug transfer studies: a feasibility study. *Anal Bioanal Chem* 406(30):7827–7813. doi:[10.1007/s00216-014-7643-9](https://doi.org/10.1007/s00216-014-7643-9)
- Hupfeld S, Holsaeter AM, Skar M, Frantzen CB, Brandl M (2006) Liposome size analysis by dynamic/static light scattering upon size exclusion-/field flow fractionation. *J Nanosci Nanotechnol* 6(8):1–7
- Hupfeld S, Ausbacher D, Brandl M (2009) Asymmetric flow field-flow fractionation of liposomes: optimization of fractionation variables. *J Sep Sci* 32(9):1465–1470. doi:[10.1002/jssc.200800626](https://doi.org/10.1002/jssc.200800626)
- Hupfeld S, Moen HH, Ausbacher D, Haas H, Brandl M (2010) Liposome fractionation and size analysis by asymmetrical flow field-flow fractionation/multi-angle light scattering: influence of ionic strength and osmotic pressure of the carrier liquid. *Chem Phys Lipids* 163(2):141–147. doi:<http://dx.doi.org/10.1016/j.chemphyslip.2009.10.009>
- John C, Langer K (2014) Asymmetrical flow field-flow fractionation for human serum albumin based nanoparticle characterisation and a deeper insight into particle formation processes. *J Chromatogr A* 1346:97–106. doi:<http://dx.doi.org/10.1016/j.chroma.2014.04.048>
- Jores K, Mehnert W, Drechsler M, Bunjes H, Johann C, Mäder K (2004) Investigations on the structure of solid lipid nanoparticles (SLN) and oil-loaded solid lipid nanoparticles by photon correlation spectroscopy, field-flow fractionation and transmission electron microscopy. *J Controlled Release* 95(2):217–227. doi:<http://dx.doi.org/10.1016/j.jconrel.2003.11.012>
- Kanzer J, Hupfeld S, Vasskog T, Tho I, Hölzig P, Mägerlein M, Fricker G, Brandl M (2010) In situ formation of nanoparticles upon dispersion of melt extrudate formulations in aqueous medium assessed by asymmetrical flow field-flow fractionation. *J Pharm Biomed Anal* 53(3):359–365. doi:<http://dx.doi.org/10.1016/j.jpba.2010.04.012>
- Klein T, Huerzeler C (1999) Characterization of biopolymers, proteins, particles and colloids by means of field-flow fractionation. *GIT Labor-Fachzeitschrift* 11:1224–1228
- Lang R, Winter G, Vogt L, Zürcher A, Dorigo B, Schimmele B (2009) Rational design of a stable, freeze-dried virus-like particle-based vaccine formulation. *Drug Dev Ind Pharm* 35(1):83–97. doi:[10.1080/03639040802192806](https://doi.org/10.1080/03639040802192806)
- Lee H, Williams SK, Allison SD, Anchordoquy TJ (2001) Analysis of self-assembled cationic lipid-DNA gene carrier complexes using flow field-flow fractionation and light scattering. *Anal Chem* 73:837–843
- Litzén A, Wahlund KG (1989) Application of an asymmetrical flow field-flow fractionation channel to the separation and characterization of proteins, plasmids, plasmid fragments, polysaccharides and unicellular algae. *J Chromatogr* 461:73–87
- Litzén A, Wahlund KG (1991) Zone broadening and dilution in rectangular and trapezoidal asymmetrical flow field-flow fractionation channels. *Anal Chem* 63:1001–1007
- Litzén A, Walter JK, Krischollek H, Wahlund KG (1993) Separation and quantitation of monoclonal antibody aggregates by asymmetrical flow field-flow fractionation and comparison to gel permeation chromatography. *Anal Biochem* 212:469–480

- Ma D, Martin N, Tribet C, Winnik F (2014) Quantitative characterization by asymmetrical flow field-flow fractionation of IgG thermal aggregation with and without polymer protective agents. *Anal Bioanal Chem* 406(29):7539–7547. doi:[10.1007/s00216-014-8200-2](https://doi.org/10.1007/s00216-014-8200-2)
- Maskos M, Schupp W (2003) Circular asymmetrical flow field-flow fractionation for the semipreparative separation of particles. *Anal Chem* 75(22):6105–6108. doi:[10.1021/ac034394z](https://doi.org/10.1021/ac034394z)
- Mathaes R, Winter G, Engert J, Besheer A (2013) Application of different analytical methods for the characterization of non-spherical micro- and nanoparticles. *Int J Pharma* 453(2):620–629. doi:[http://dx.doi.org/10.1016/j.ijpharm.2013.05.046](https://doi.org/http://dx.doi.org/10.1016/j.ijpharm.2013.05.046)
- Noga M, Edinger D, Kläger R, Wegner SV, Spatz JP, Wagner E, Winter G, Besheer A (2013) The effect of molar mass and degree of hydroxyethylation on the controlled shielding and deshielding of hydroxyethyl starch-coated polyplexes. *Biomaterials* 34(10):2530–2538. doi:<http://dx.doi.org/10.1016/j.biomaterials.2012.12.025>
- Pauck T, Coelfen H (1998) Hydrodynamic analysis of macromolecular conformation. A comparative study of flow field-flow fractionation and analytical ultracentrifugation. *Anal Chem* 70:3886–3891
- Pease LF, Lipin DI, Tsai D-H, Zachariah MR, Lua LHL, Tarlov MJ, Middelberg APJ (2009) Quantitative characterization of virus-like particles by asymmetrical flow field flow fractionation, electrospray differential mobility analysis, and transmission electron microscopy. *Biotechnol Bioeng* 102(3):845–855. doi:[10.1002/bit.22085](https://doi.org/10.1002/bit.22085)
- Phelan Jr FR, Bauer BJ (2009) Comparison of steric effects in the modeling of spheres and rodlike particles in field-flow fractionation. *Chem Eng Sci* 64(8):1747–1758. doi:<http://dx.doi.org/10.1016/j.ces.2008.10.006>
- Philo JS (2009) A critical review of methods for size characterization of non-particulate protein aggregates. *Curr Pharm Biotechnol* 10(4):359–372
- Reschiglian P, Melucci D, Zattoni A, Malló L, Hansen M, Kummerow A, Miller M (2000) Working without accumulation membrane in flow field-flow fractionation. *Anal Chem* 15(24):5945–5954
- Reschiglian P, Roda B, Zattoni A, Tanase M, Marassi V, Serani S (2014) Hollow-fiber flow field-flow fractionation with multi-angle laser scattering detection for aggregation studies of therapeutic proteins. *Anal Bioanal Chem* 406(6):1619–1627. doi:[10.1007/s00216-013-7462-4](https://doi.org/10.1007/s00216-013-7462-4)
- Roessner D, Kulicke WM (1994) On-line coupling of flow field-flow fractionation and multi-angle laser light scattering. *J Chromatogr A* 687:249–258
- Schimpf ME, Caldwell KD, Giddings JC (2000) *Field-flow fractionation handbook*. Wiley, New York
- Till U, Gaucher-Delmas M, Saint-Aguet P, Hamon G, Marty J-D, Chassenieux C, Payré B, Goudounèche D, Mingotaud A-F, Violleau F (2014) Asymmetrical flow field-flow fractionation with multi-angle light scattering and quasi-elastic light scattering for characterization of polymersomes: comparison with classical techniques. *Anal Bioanal Chem* 406(30):7841–7853. doi:[10.1007/s00216-014-7891-8](https://doi.org/10.1007/s00216-014-7891-8)
- Wagner M, Pietsch C, Tauhardt L, Schallon A, Schubert US (2014) Characterization of cationic polymers by asymmetric flow field-flow fractionation and multi-angle light scattering—a comparison with traditional techniques. *J Chromatogr A* 1325:195–203. doi:<http://dx.doi.org/10.1016/j.chroma.2013.11.049>
- Wahlund KG, Giddings JC (1987) Properties of an asymmetrical flow field-flow fractionation channel having one permeable wall. *Anal Chem* 59:1332–1339
- Williams PS, Giddings JC (1994) Theory of field-programmed field-flow fractionation with corrections for steric effects. *Anal Chem* 66:4215–4228
- Williams PS, Giddings MC, Giddings JC (2001) A data analysis algorithm for programmed field-flow fractionation. *Anal Chem* 73:4202–4211
- Wyatt PJ (1991) Absolute measurements with FFF and light scattering. *Polym Mater Sci Eng* 65:198–199

- Zattoni A, Rambaldi DC, Roda B, Parisi D, Roda A, Moon MH, Reschiglian P (2008) Hollow-fiber flow field-flow fractionation of whole blood serum. *J Chromatogr A* 1183(1–2):135–142. doi: <http://dx.doi.org/10.1016/j.chroma.2008.01.022>
- Zillies JC, Zwioerek K, Winter G, Coester C (2007) Method for quantifying the PEGylation of gelatin nanoparticle drug carrier systems using asymmetrical flow field-flow fractionation and refractive index detection. *Anal Chem* 79(12):4574–4580. doi: [10.1021/ac062135e](https://doi.org/10.1021/ac062135e)

Part V
Imaging Techniques

Chapter 16

Light and Electron Microscopy

Heike Bunjes and Judith Kuntsche

Abstract Microscopic techniques have a long history in pharmaceutical formulation research and development. They are especially useful for the study of systems containing particles of different length scales (like powders, granules, or colloidal suspensions) but can also be employed for the study of compact solid forms like tablets or of semisolids. As they yield a visual impression of the object of study they provide a rather natural way to the comprehension of sample behavior. As with all analytical techniques, however, there may be limitations and pitfalls that should be known in order to employ the methods correctly. This chapter explains the basic features of the microscopic techniques traditionally employed in pharmaceutical research—optical light microscopy as well as scanning and transmission electron microscopy with their respective variations. Apart from a short overview on instrumentation, the different sample preparation techniques are explained and a selection of pharmaceutical application examples is provided to illustrate the wealth of information that can be obtained and to stimulate a more detailed exploration of the possibilities of these fascinating methods.

Keywords Optical microscopy • Polarized light microscopy • Transmission electron microscopy • Cryoelectron microscopy • Freeze-fracture • Negative staining • Scanning electron microscopy • Energy dispersive X-ray spectrometry

H. Bunjes (✉)

Institut für Pharmazeutische Technologie, Technische Universität Braunschweig,
Mendelssohnstraße 1, Braunschweig 38106, Germany
e-mail: heike.bunjes@tu-braunschweig.de

J. Kuntsche

Department of Physics, Chemistry and Pharmacy, University of Southern Denmark,
Campusvej 55, Odense M 5230, Denmark
e-mail: kuntsche@sdu.dk

1 General Remarks on Microscopy in Pharmaceutical Formulation Research

Investigation by light or electron microscopy is a very helpful tool in formulation research as it yields visual images of the objects of interest. It is particularly suitable for the investigation of samples containing particles; Scanning Electron Microscopy (SEM) is also often used to visualize the surface structure of larger objects such as tablets. The high magnification that is employed upon microscopic investigation is a great advantage but also implies that only a small portion of the sample can usually be analyzed. Thus, investigators need to be very careful in selecting their samples and areas of investigation within the microscopic specimen appropriately in order to ensure that the data they obtain is representative for the whole sample. Several specimens usually need to be prepared and different areas of a specimen to be inspected in order to achieve this goal. Moreover, (electron) microscopic methods are prone to artifacts (e.g., resulting from unfavorable specimen-beam interactions in SEM or the preparation procedures usually required for Transmission Electron Microscopy (TEM) analysis). As a further complication, many microscopic techniques lead to two-dimensional projections of three-dimensional objects which needs to be taken into consideration upon interpretation of the images. Thus, although the principle of “seeing is believing” usually acts in favor of microscopic analysis, one should not simply trust everything that appears to be revealed in a microscopic image. A sound basic knowledge about the methods including their potential pitfalls helps to employ these powerful techniques adequately and to avoid misinterpretations. This chapter can only provide a glimpse into the fascinating field of microscopic investigation and reference to specialized textbooks is recommended to those who would like to apply the methods for their research (e.g., Carlton 2011; Flegler et al. 1995; Goldstein et al. 2003; Williams and Carter 2009). As with many other techniques, microscopy often is most useful when used in combination with other methods that can provide complementary information in particular on those facts that cannot adequately be unveiled by this technique.

2 Optical Microscopy

A lot of information can be obtained about pharmaceutical samples such as powders, suspensions or emulsions by just the simplest bright-field microscope, for example about particle morphology, size and homogeneity. Despite the comparative ease of use, low demands on instrumentation and sample preparation, optical microscopy is probably one of the most underestimated analytical techniques in modern pharmaceuticals.

This chapter will introduce the basic principles of optical microscopy (often also referred to as light microscopy) together with the different techniques used in

optical microscopy such as polarizing, phase contrast and differential interference contrast microscopy. Fluorescence microscopic techniques are not included as this would go beyond the scope of this chapter. Fluorescence imaging is, however, an emerging field in both biological and pharmaceutical science and the interested reader is referred to the large number of review articles focusing on fluorescence imaging (e.g., White and Errington 2005; Oheim et al. 2006; Vielreicher et al. 2013).

2.1 General Principles of Optical Microscopy

The main components of an optical microscope are the illumination source (often a halogen lamp), the condenser, the objective and the ocular (eyepiece). The general light path in an optical microscope is schematically shown in Fig. 16.1. Comprehensive information about the theory and principles of optical microscopy can be found, for example, on the websites of microscope manufacturers (e.g., www.opympusmicro.com, www.zeiss.com/microscopy).

Key parameters in microscopy are magnification and resolution. The total magnification of an optical microscope is provided by the magnification power of the objective (usually between $\times 4$ and $\times 100$) and the magnification provided by the ocular lens system (usually $\times 10$). When using an objective with a magnification power of $\times 40$ together with an ocular with $\times 10$ magnification, the total magnification will be $\times 400$. However, even the highest magnification is worthless, if the resolution is unsatisfactory. Resolution is the smallest distance between two objects where they can be clearly distinguished as two separate objects. The resolution R of the diffraction limited light microscope can be calculated by the equation introduced by Ernst Abbe (Eq. (16.1)) where R is a function of the wavelength (λ) of the light source used for sample illumination (shorter wavelengths increase the resolution), the refractive index (n) of the media between objective and sample and the half of the opening angle of the objective (θ):

$$R = \lambda / 2n \cdot \sin \theta = \lambda / 2 \cdot \text{NA} \quad (16.1)$$

The product ($n \cdot \sin \theta$) is known as the numerical aperture NA of an objective and provides convenient information about resolution of a given objective. The larger the opening angle of an objective (and thus the larger its aperture), the more of the diffracted light from the sample can be gathered and the higher the resolution of the sample image. Numerical apertures of objectives for optical microscopy range from 0.1 for very low magnification objectives (e.g., $\times 4$) up to about 0.9 for high magnification objectives (e.g., $\times 100$). By replacing air by a medium with higher refractive index (e.g., water or oil, Table 16.1) between the sample and the objective, higher numerical apertures can be achieved, e.g., up to 1.6 when using an immersion oil. The oil immersion technique requires specially designed

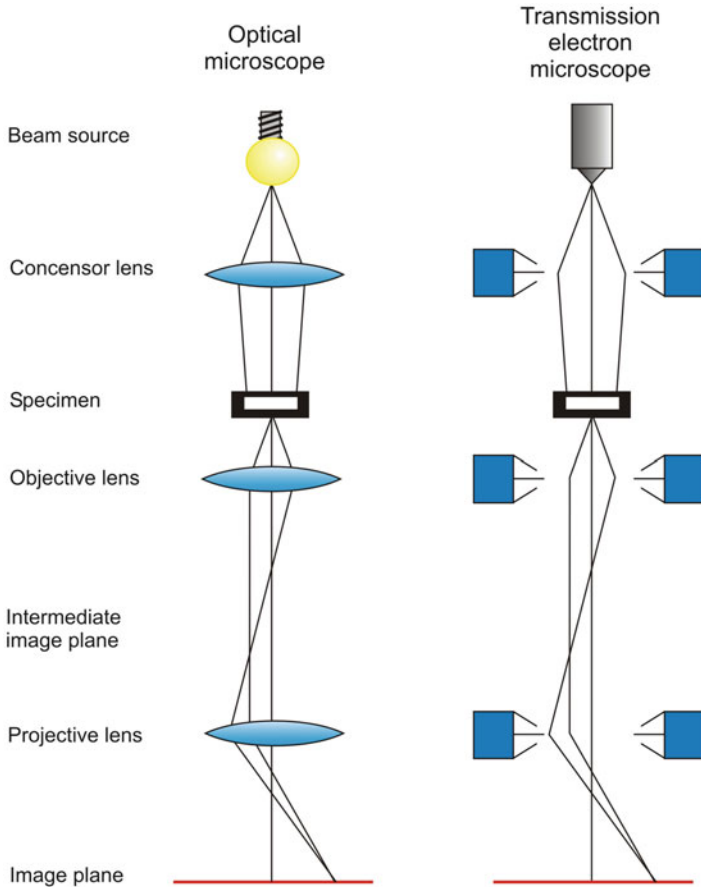


Fig. 16.1 Comparison of the setup of an (inverted) optical microscope with that of a transmission electron microscope

objectives (oil immersion objectives) and is generally used at high magnification (where a high resolution is required).

Another important characteristic of microscopic objectives is the correction for imaging errors (aberrations): Spherical aberrations (also known as aperture errors), chromatic aberrations (caused by dispersion effects) and aberrations caused by the field curvature (when using lenses with curved surface producing a curved image plane). Objectives with different degree of correction of aberrations (and consequently costs) are available (Abramowitz et al. 2002; Drent 2005; Piston 1998). Plane objectives generally provide correction for field curvature. Common types of objectives together with their degree of correction for optical aberrations, numerical aperture and magnification are summarized in Table 16.2.

Table 16.1 Common immersion media in optical microscopy (Abramowitz and Davidson 2014)

Material	Refractive index
Air	1.0003
Water	1.333
Glycerol	1.4695
Paraffin oil	1.480
Cedar wood oil	1.515
Synthetic oil	1.515

Table 16.2 Magnification, numerical aperture and working distance for common objectives (Spring et al. 2014)

Type of objective	Magnification	Numerical aperture	Working distance (mm)
Achromat correction for • SA with 1 color • CA with 2 colors	×4	0.10	30.00
	×10	0.25	6.10
	×20	0.40	2.10
	×40	0.65	0.65
	×100 (oil)	1.25	0.18
Plan achromat correction for • SA with 1 color • CA with 2 colors • FC	×4	0.10	30.00
	×10	0.25	10.50
	×20	0.40	1.30
	×40	0.65	0.57
	×100	0.90	0.26
	×100 (oil)	1.25	0.17
Plan fluorite correction for • SA with 2–4 colors • CA with 2–4 colors • FC	×4	0.13	17.10
	×10	0.30	16.00
	×20	0.50	2.10
	×40	0.75	0.72
	×100	0.90	0.30
	×100	1.30	0.20
	×100 (oil)	1.40	0.13
Plan apochromat correction for • SA with 3–4 colors • CA with 4–5 colors • FC	×4	0.20	15.70
	×10	0.45	4.00
	×20	0.75	1.00
	×40	0.95	0.14
	×100 (oil)	1.40	0.13

The price of the objectives increases with increasing degree of aberration correction (SA = spherical aberration, CA = chromatic/color aberration, FC = field curvature)

The condenser is primarily an optical lens system which focuses the light from the illumination source onto the sample. It usually is composed of a diaphragm with variable aperture and one or more lenses. In the up-right transmission light microscope, the condenser is located above the light source and below the sample. For special techniques used in optical microscopy (cf. Sect. 2.2) the condenser is equipped with special optical filters. The ocular lenses (eyepiece) focus the microscopic image onto the image plane (e.g., the eye) and usually also provide an

additional magnification (often $\times 10$). Modern microscopes are often equipped with a tri-ocular eyepiece facilitating connection to a camera. Finally, optimal illumination of the sample is a prerequisite for any convenient microscopic analysis and Köhler's illumination, introduced in 1893 by August Köhler, is still the predominant technique applied (Davidson and Fellers 2003; Goldberg 1980).

2.2 *Special Techniques in Optical Microscopy*

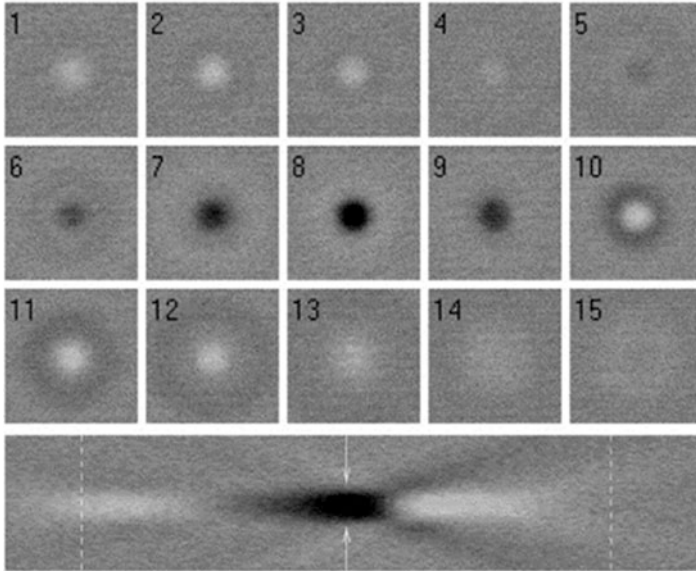
A limiting factor, especially with biological samples, is the poor contrast in normal bright field light microscopy. By introducing special filters in the light path, contrast of the image can be improved (phase contrast and differential interference contrast) or optical properties (birefringence) can be visualized by polarizing microscopy.

In the phase contrast technique (Elliot and Poon 2001; Pluta 1969), differences in refractive indices in sample structures are "converted" to bright-dark contrast thus providing contrast in a sample even if the differences in optical densities between the visualized structures are small. For this technique, a ring annulus is included in the condenser producing a hollow cone of light. A matching phase shift ring is located in the objective, resulting in an artificial phase difference of the light wave together with a reduction of light intensity. Due to these effects, an interference with the light that has been diffracted by the sample occurs and a phase contrast image is the result (Fig. 16.2 top). A disadvantage of the phase contrast technique is halo-formation and that it can only be used with thin samples.

A more sophisticated method to visualize samples with low contrast is the differential interference contrast setup (Elliot and Poon 2001) where differences in optical density in the sample are visualized as a difference in relief in the image (Fig. 16.2 bottom). However, the three-dimensionally appearing image is an optical effect and does not necessarily reflect the true structure of the sample. The optical setup is more complicated than that used in phase contrast microscopy and polarized light is required as light source. Special prisms (Wollaston prisms) are located in the condenser and in the objective. The prism in the condenser splits the polarized light into two beams, which have a slight difference in their traveling direction and the prism in the objective re-combines the beams. By passing the sample, both beams are affected when passing density boundaries and their optical path will be different when entering the second prism generating the differences in the relief and the three-dimensional appearance of the structure in the microscopic image.

Polarization microscopy (Oldenbourg 1996; Weaver 2003) is probably one of the most commonly used techniques of optical microscopy in the pharmaceutical field when investigating optically anisotropic (birefringent) samples such as crystalline or liquid crystalline materials. Two polarization filters are applied, one placed in the condenser (the polarizer providing polarized light for sample illumination) and another above the objective (the analyzer). The analyzer can be moved in and out of the light path and also allows adjustment of the angle respective to the

Phase contrast:



Differential interference contrast ($A = 1.4$, $A_C = 0.9$):

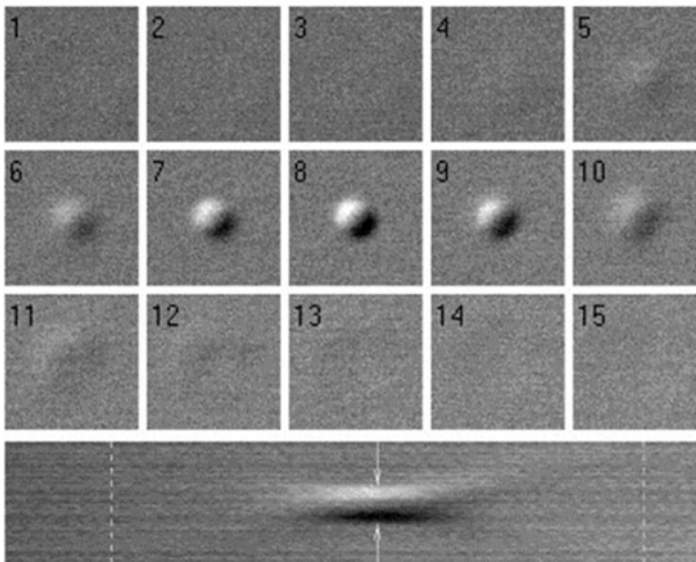


Fig. 16.2 Different contrast techniques used in light microscopy: microscopic images of a single PMMA sphere, radius $R_P = 550 \pm 7$ nm, refractive index $n_P = 1.49$, in decalin, $n_m = 1.47$. The top 15 images each (field of view $4.3 \mu\text{m} \times 4.3 \mu\text{m}$) form a series at varying degrees of defocus: $1.0 \mu\text{m}$ of forward axial (focusing) movement separate successive images, with no. 8 being in focus. The larger bottom images are a respective composite of 1-pixel-wide slices across the center of 165 images like the series above them, but with each separated by $0.11 \mu\text{m}$; this gives a quasi-side-on view; image no. 8 of the upper series is at the line indicated by the arrows; the dotted lines show the positions of images 1 and 15. Reprinted from Elliot and Poon 2001, Copyright (2001), with permission from Elsevier

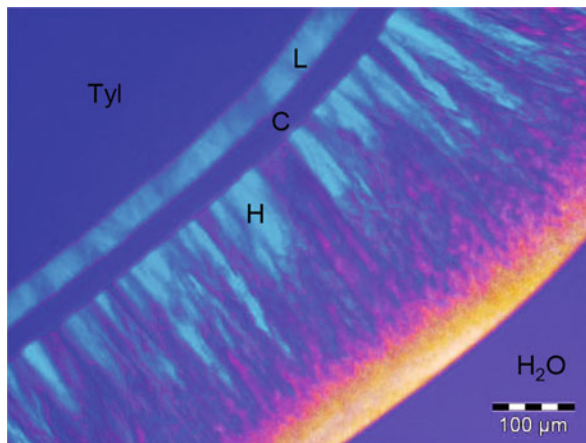
polarizer. If polarizer and analyzer are inserted into the optical path and the analyzer is oriented perpendicular to the analyzer (crossed polarizing filters), no light is passing when the sample is isotropic and the image appears dark. In contrast, viewing a birefringent sample, characteristic bright/dark patterns, which depend on the sample's birefringence, are observed. Often, a so-called λ -plate can be inserted in the light path just below the analyzer and the image of an isotropic sample with crossed polarizing filter will appear purple.

2.3 Applications of Optical Microscopy in Pharmaceutical Analysis

The pharmacopoeias, e.g., the European Pharmacopoeia (Ph.Eur.) suggest optical microscopy for the detection of sub-visible contaminations in infusions and injections (Ph.Eur. 2.9.19) and for the characterization of particles $>1 \mu\text{m}$ (Ph.Eur. 2.9.37). These monographs illustrate the two major applications of optical microscopy in pharmaceutical sciences: Quality control and material science.

Simple bright-field optical microscopy can already provide important information about a pharmaceutical sample, for example to detect drug precipitation in emulsions, particulate contaminations and the presence of undesired large particles in the μm -size range in colloidal dispersions. Differential interference contrast optical microscopy has been applied for stability evaluation of w/o/w multiple emulsions where coalescence of the internal aqueous phase could clearly be detected after storage of the samples (Hoppel et al. 2014). Optical microscopy provides an important analytical tool for quality control of colloidal formulations such as nanoparticle dispersions, nanoemulsions, liposomes and so on. Colloidal drug carrier systems have been intensively studied in the last decades especially with respect to drug targeting purposes but the number of approved nanomedicines (especially based on nanoparticles as drug carriers) is still unsatisfactory. Strict control of size and size distribution combined with physical stability present a main requirement for formulations intended for intravenous injection, but adequate physicochemical characterization and the lack of generally accepted standard methods for size determination together with problems of physical stability still present a serious challenge in the development of nanomedicines (Dawidczyk et al. 2014). Although optical microscopy allows rapid detection e.g., of drug precipitation in colloidal suspensions which may not be detectable by conventional particle sizing methods based on light scattering, optical microscopy is currently only rarely described for the characterization of colloidal dispersions in the scientific literature. Driscoll and co-workers used optical microscopy in addition to light scattering methods for stability evaluation of parenteral fat emulsions (Driscoll 2006). The limitations in detecting fractions of large particles by conventional light scattering methods (e.g., laser diffraction with sub-micron instrumentation) have also clearly been seen for drug nanosuspensions (Keck and Müller 2008; Keck

Fig. 16.3 Polarizing light micrograph of the liquid crystalline phases developing in the contact zone between the nonionic surfactant tyloxapol (Tyl) and water (H_2O): H: hexagonal; C: cubic; L: lamellar phase. Only the hexagonal and the lamellar phase exhibit birefringence



2010). These examples illustrate the usefulness of optical microscopy to get at least qualitative information about the presence of μm -particles in colloidal dispersions. For quality control and size determinations, optical microscopy should always be applied in addition to conventional light scattering methods.

The probably most frequently used application of (polarizing) optical microscopy in pharmaceutical analysis is material characterization, e.g., for the investigation of polymorphism (Bauer et al. 2001; Gilchrist et al. 2012; Nichols and Frampton 1998), crystallization behavior (Jurasin et al. 2011; Munk et al. 2012; Seefeldt et al. 2007; Tian et al. 2009; Wu et al. 2012), identification of liquid crystalline phases (Amar-Yuli and Garti 2005; Gong et al. 2011; Kuntsche et al. 2009b; Prehm et al. 2008) (Fig. 16.3) and phase behavior of mixtures (Benedini et al. 2011; Mercuri et al. 2012; Nonomura et al. 2009). In this context, microscopy is usually used in combination with other analytical techniques such as X-ray scattering/diffraction, differential scanning calorimetry and spectroscopic methods. If the microscope is equipped with a hot-stage sample holder (hot stage microscopy), phase transitions can be directly monitored and birefringence patterns observed at the different temperatures can facilitate phase identification. A comprehensive description about the use of polarizing microscopy and application of hot stage microscopy can be found in Carlton (2011).

Knowledge of solid state properties such as crystal modifications and crystal morphology are of uppermost importance as they determine, for example, solubility, dissolution rate as well as the efficiency of downstream processes such as milling (Chow et al. 2008). As an example, the influence of poly(N-isopropyl acrylamides) on the crystallization of nitrofurantoin as a model drug has recently been studied by Munk et al. (2012). Without the polymer, nitrofurantoin crystallizes from acetone-water mixtures forming needle-shaped crystals, whereas both a dendritic crystal morphology and uncontrolled crystallization of a metastable crystal modification (as identified by Raman spectroscopy) was observed in presence of the polymer (Fig. 16.4).

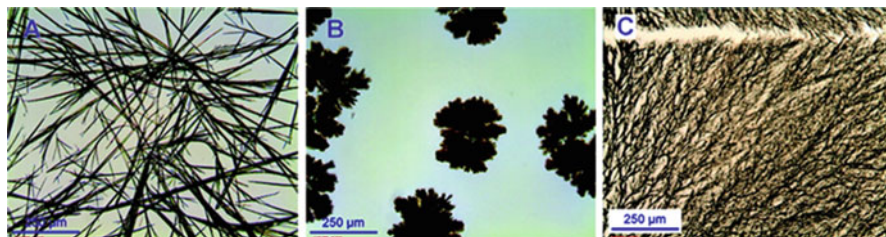


Fig. 16.4 Nitrofurantoin monohydrate (NFMH) crystallized from acetone:water mixtures in the presence of (A) no additive (needle growth of NFMH form II), (B) atactic poly(N-isopropyl acrylamide) (PNIPAM) (controlled dendritic growth of NFMH form II), (C) atactic PNIPAM (uncontrolled growth of NFMH form I). Reprinted with permission from Munk et al. 2012. Copyright (2012) American Chemical Society

3 Electron Microscopy

If higher resolution than achievable in light microscopy is required electron microscopic techniques can be employed to view the sample. The use of electron microscopic methods does, however, usually require more sophisticated sample preparation techniques and the sample is thus less close to its natural state upon observation. Two different types of instruments are typical for electron microscopy—transmission electron microscopes (TEMs) and scanning electron microscopes (SEMs). These two classes of instruments share some common basic features but also have fundamental differences as explained in the following.

3.1 General Setup of Electron Microscopes

Compared to a light microscope, most electron microscopes are rather large instruments. All of them consist of a microscopic column containing the electron source and the electron optical system, a sample stage or holder and detection systems that provide the data for the generation of electron microscopic images (Figs. 16.1 and 16.10). While electron beam generation and focusing are conceptually similar in TEM and SEM, the processes involved in image formation are fundamentally different. In the transmission setup, the image is detected much below the sample which is positioned in the upper part of the column. In conventional scanning electron microscopes, the sample forms essentially the lowest part of the setup and detection of the image generating data takes place in closer vicinity to and above the sample. Much shorter microscopic columns can thus be used in SEM as compared to TEM. In the following, after a short description of the common features of both types of instruments, the specificities of each technique will be outlined.

The electron beam is generated at the top of the column in an electron gun by thermionic or by field emission. For thermionic emission usually a tungsten hairpin

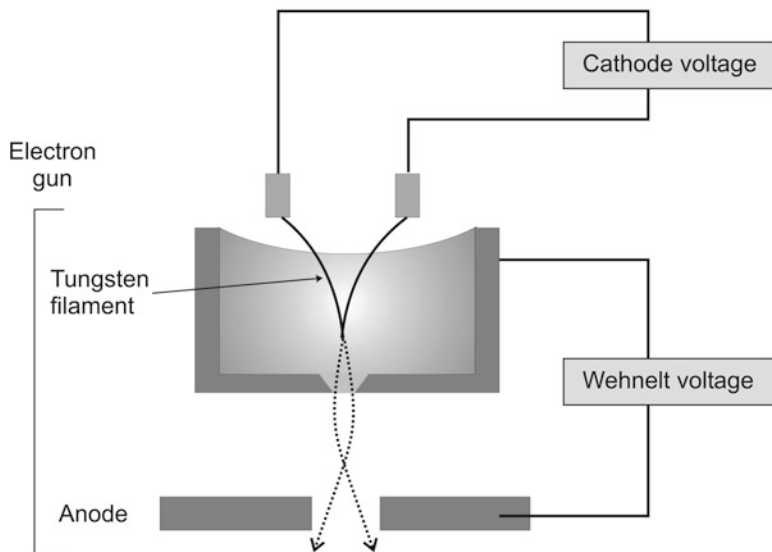


Fig. 16.5 Electron gun (filament setup) for beam generation in electron microscopes

wire (filament) or a lanthanum hexaboride (LaB_6) crystal with very fine tip is electrically heated resulting in the emission of electrons at the tip of the filament or crystal. The filament (or crystal) is operated at a very high negative potential and thus acts as a cathode (Fig. 16.5). The electrons emitted from the tip of the cathode are accelerated in an electric field towards a circle-shaped anode operated at zero potential. The electrons that pass the aperture in the center of the anode form the electron beam used for analysis. The cathode is surrounded by the Wehnelt cap set to an even higher negative potential than the cathode. Thus, the Wehnelt cap repels the electrons bringing them to a focus in front of the anode aperture. In field emission guns, electrons are “drawn” out of a very fine tungsten tip by a strong electric field applied between the emitting cathode and a first anode. The emitted electrons are accelerated toward a second anode; the potential between this anode and the cathode determines the accelerating voltage. Field emission can be accomplished in the cold or with the aid of heat to the tip (Schottky emission). Field emission guns combine high brightness of the electron beam with small beam size and narrow wavelength distribution of the emitted electrons; they are particularly useful for high resolution analysis in SEM. The costs for such instruments are, however, much higher than for those employing thermal emission.

The generated electron beam passes a set of electromagnetic lenses on its way down the column. Condenser lenses condense the beam and finally an objective lens focuses it onto the specimen. Apertures (small pieces of metal containing holes through which the beam must pass) can be used at different places of the column to e.g., shape the beam and to remove stray electrons. Usually, the whole electron microscopic setup is operated under high vacuum to avoid discharging effects due to ionization of gas molecules, scattering of the electrons as they interact with the gas molecules and, in particular, to protect the electron source from deleterious chemical reactions (e.g., oxidation) that could dramatically reduce their lifespan.

3.2 *Transmission Electron Microscopy (TEM)*

3.2.1 **The Transmission Electron Microscope**

The principal setup of a TEM (Williams and Carter 2009; Flegler et al. 1995) is similar to that of an inverted light microscope in which the sample is, however, illuminated by an electron beam focused by electromagnetic lenses (Fig. 16.1). Electrons that pass the specimen are projected onto a viewing screen or a photographic or electronic image recording device. Adequate sample preparation is a very important part of electron microscopic investigation by TEM. Since electrons cannot easily penetrate matter, only very thin samples can be studied. The contrast in TEM is obtained by the interaction of the electrons with the material (scattering). Heavy metals like lead, uranium and platinum strongly interact with the electrons and are, therefore, often used to improve the contrast (e.g., upon negative staining, see below). Since increasing acceleration voltage decreases the wavelength of the electrons the resolution of TEM becomes better at higher voltages. On the other hand, the contrast decreases with increasing acceleration voltage as the scattering of the electrons is inversely proportional to their velocity. In TEM investigations on colloidal drug carrier systems voltages between 80 and 200 kV are usually applied.

3.2.2 **Sample Preparation and TEM Investigation**

Negative staining is the most straightforward preparation method for the evaluation of colloidal particles by TEM (Friedrich et al. 2010; Harris 1997, 2007). A small drop of liquid sample is positioned on a TEM grid (small gold or copper grid with defined mesh size coated e.g., with a thin layer of carbon) which usually has been subjected to glow discharge in order to hydrophilize the carbon support film. During a short time of contact, particles present in the sample adsorb to the carbon support. After blotting excess sample and optional washing with water, a staining solution containing heavy metal salts which provide high contrast in the electron microscope (e.g., uranyl acetate, ammonium molybdate, or sodium phosphotungstate) is contacted with the grid. Excess solution is removed from the grid and the sample is air dried at room temperature. Dry samples can either be stored or directly be investigated in the electron microscope. Upon TEM observation, the colloidal particles appear bright against the darker background of the stain which interacts more strongly with the beam electrons than the usually organic matrix of the particles under investigation. Although the dried film of stain provides some sort of support for the colloidal particles, both staining and drying may result in structural alterations of the colloids which always need to be taken into consideration when interpreting negative staining TEM images. In particular “soft” particles like liposomes or emulsion droplets tend to collapse during sample preparation (Friedrich et al. 2010; Klang et al. 2013).

A closer approach to the native state of the particles is obtained when using freeze-fracturing (Severs 2007). This technique relies on the vitrification (i.e., transformation into the glassy state) of the liquid components of the sample (e.g., the aqueous dispersion medium) by extremely rapid cooling. The liquid sample is sandwiched between two copper or gold holders and subjected to freezing e.g., in liquid propane or melting nitrogen. This can be done manually or by using specialized equipment like a cryojet device. Under constant cooling in liquid nitrogen, the frozen sample is transferred to a freeze-fracturing unit where it is fractured under continued cooling and in high vacuum. The fracture planes develop predominantly along areas of the sample with weak molecular interactions (e.g., within lipid bilayers) (Meyer and Richter 2001). In order to obtain an observation plane with higher structuring the fractured sample can optionally be etched by water sublimation in vacuum leaving behind the non-volatile components of the sample. Afterwards, the sample surface is shadowed with a thin platinum/carbon layer (about 2 nm) usually at an angle of 45° with respect to the fracture surface. Subsequently, a thicker carbon layer (about 20–30 nm) is deposited onto the sample at an angle of 90° to improve stability of the film deposited on the sample surface. The sample is removed from the freeze-fracture device and the original sample cleaned away by rinsing with solvents to remove all organic residues. Thus, a “negative” replica of the fractured (and etched) sample plane is obtained that is placed on an electron microscopic grid to be viewed in the electron microscope. Due to the shadowing the images may adopt a somewhat “three-dimensional” appearance. The platinum/carbon replicas are stable over time and upon TEM observation; thus, they can be stored for later re-investigation. When obtained under optimal sample preparation conditions, freeze-fractured replicas reflect the original, native state of the sample and can provide valuable insights also into the interior of particles. Artifacts may, however, easily occur, e.g., due to an insufficient freezing rate that may induce crystallization or as a result of re-deposition of solvent molecules onto the sample plane after fracturing. Moreover, due to the many steps involved, sample preparation by freeze-fracturing is an intricate and rather time-consuming technique. With the more widespread availability of cryo-TEM instruments it has been replaced by this technique to some extent, although it remains an important source of ultra-structural information.

Investigation by cryo-TEM after plunge-freezing is the closest approach to the native state of the samples. After vitrification, colloids can directly be studied in their frozen-hydrated state. This way, information about the size, shape and internal structure of the particles may be obtained (Klang et al. 2012, 2013; Kuntsche et al. 2011). In contrast to the above mentioned techniques, which essentially rely on the preparation of suitable specimens, sample investigation by cryo-TEM additionally requires specialized electron microscopic equipment (see below). Detailed information on this technique can be taken from a large pool of dedicated literature (Friedrich et al. 2010; Grassucci et al. 2007, 2008; Harris 1997).

In most cases, specialized carbon-coated holey grids are used in cryo-TEM studies. Such grids consist of a squared copper mesh covered with a carbon-coated foil which is perforated by holes that can have different shapes. After fixation of the

TEM grid (previously submitted to glow discharge to hydrophilize the carbon) in the preparation chamber, a small droplet of sample is applied. Upon removal of excess sample by blotting with a filter paper a thin film of the sample forms in the holes of the grid (the sample must not be too viscous for this procedure). The sample is then immediately plunge-frozen, commonly in liquefied ethane cooled to liquid nitrogen temperature. As in freeze-fracturing, a very high cooling rate is required to vitrify the sample thereby avoiding the formation of crystalline ice. Automated vitrification systems with controlled humidity and/or temperature are available that help to ensure a reproducible sample preparation procedure (Egelhaaf et al. 2000). Under constant cooling, the grid with the vitrified sample is removed from the liquid ethane, excess ethane is blotted off and the sample is transferred into the cooled sample holder which is then quickly inserted into the electron microscope. Sample preparation for cryo-TEM thus requires strict control of sample environment over the whole process of preparation, transfer and electron microscopic investigation. Contact with atmospheric moisture needs to be avoided as it may lead to a contamination with ice on the vitrified specimen and/or on cooled parts of the equipment.

Apart from a specialized cryo-holder that ensures continuous cooling of the sample to about liquid nitrogen temperature upon microscopic observation the cryo-TEM should be equipped with a liquid nitrogen-cooled decontaminator close to the sample holder that collects water molecules being introduced into the vacuum system with the cooled holder or evaporating from the sample during observation. Often, cryo-holders allow tilting of the sample during observation thus providing access to information about the three-dimensional structure of the particles of interest which can be investigated from different angles (Barauskas et al. 2005; Kuntsche et al. 2010b). Sophisticated data evaluation even allows the reconstruction of the three-dimensional particle structure (Koning and Koster 2009). The colloidal structures embedded in the thin vitrified film are viewed under low dose conditions to avoid electron beam damage. In spite of this, the time period for viewing of the sample in cryo-TEM is often rather limited as most samples are sensitive to radiation.

Also in cryo-TEM artifacts may occur (Friedrich et al. 2010; Kuntsche et al. 2011; Burrows and Penn 2013). For example, cryogen residues can remain from the plunge-freezing process or there may be ice contamination due to a too high content of evaporated water in the microscopic column. Since the sample film usually becomes thinner in the middle of a hole of the grid, smaller particles are usually found in the middle part of the film. Very large particles may already be removed upon blotting when preparing the thin film to be vitrified.

3.2.3 Application of TEM in Pharmaceutical Formulation Research

TEM is particularly useful for the study of colloidal and nanostructured drug delivery systems. Often, the different preparation techniques are used in combination to obtain complementary information (Figs. 16.6 and 16.7). A lot of application

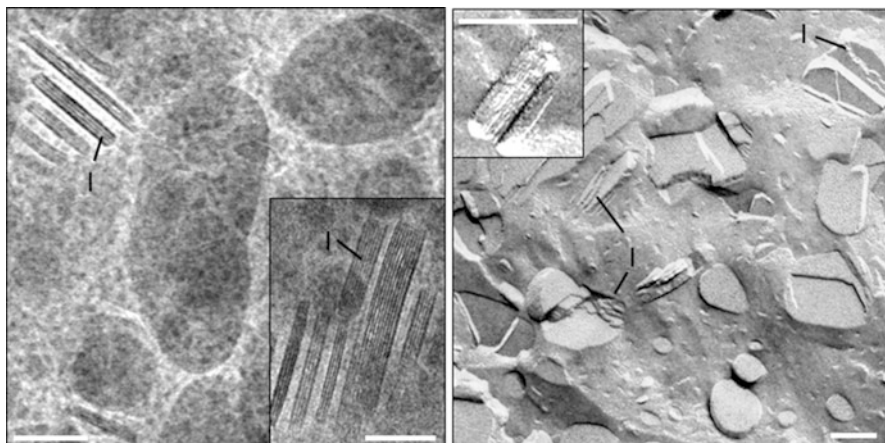


Fig. 16.6 Cryo (left) and freeze-fracture (right) transmission electron micrographs (bars represent 100 nm) of tristearin nanoparticles in the β -modification. The particles, which have a platelet-like shape, appear as elongated ellipsoidal structures in top-view and long rectangles in side-view. They display a layered internal structure (l) and tend to pack in stacks at this concentration (10% triglyceride). Reprinted with permission from Bunjes et al. 2007. Copyright (2007) American Chemical Society

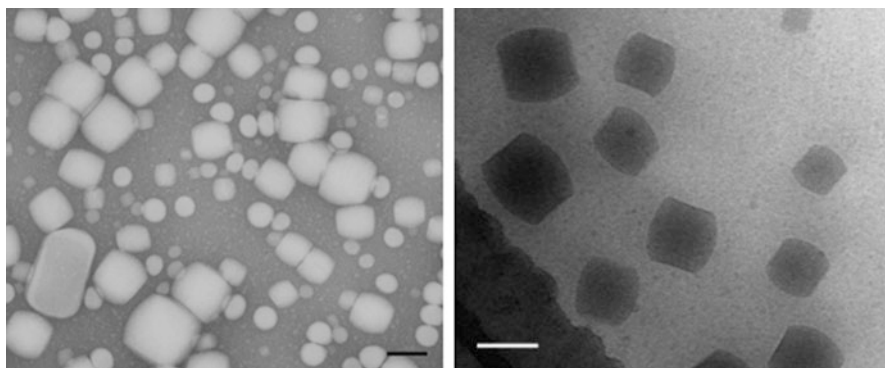
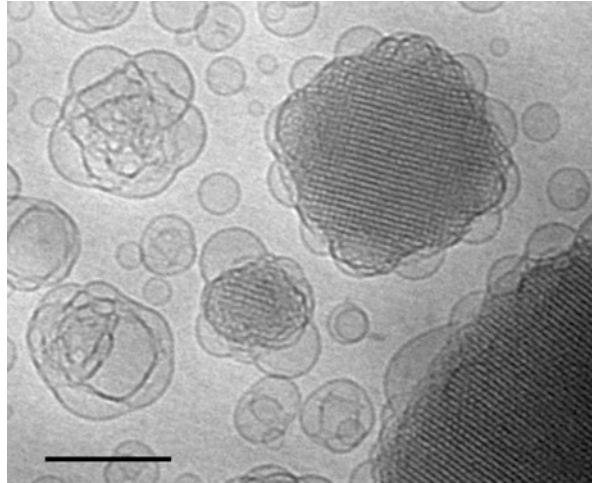


Fig. 16.7 TEM micrographs of supercooled cholesteryl myristate nanoparticles stabilized with polysorbate. The particles have a cylindrical shape that appears spherical in top-view and rectangular in side-view. Left: negative staining, scale bar: 140 nm; right: cryo-TEM, scale bar: 100 nm. Data from Kuntsche et al. 2010b

examples on pharmaceutically relevant systems can be found in extensive reviews on the use of transmission electron microscopy in pharmaceutical research (Klang et al. 2012, 2013; Kuntsche et al. 2011) and only a selection is presented in the following.

As a prominent example, the size, shape and lamellarity of liposomes have intensively been studied with TEM techniques (Almgren et al. 2000; Bibi et al. 2011; Hope et al. 1989). Structural alterations due to differences in bilayer

Fig. 16.8 Cryo-TEM micrograph showing the different colloidal structures in an aqueous dispersion of glycerol monooleate/poloxamer 407 after high pressure homogenization: Vesicles, cubic phase nanoparticles and particles of intermediate structure. Scale bar: 200 nm. Data from Kuntsche et al. 2008



composition and physical state can easily be visualized this way as can drug precipitation within liposomes as a result of gradient loading (Kuntsche et al. 2010a; Lauf et al. 2004; Li et al. 1998). Apart from liposomes, which originate from the liquid crystalline lamellar phase, nanoparticles based on other types of lyotropic mesophases, in particular the cubic and hexagonal phase, are being increasingly investigated in the field of drug delivery. Cryo-TEM is an invaluable characterization method for the corresponding dispersions, as it allows detailed visualization of the shape and the internal structure of the nanoparticles (Barauskas et al. 2005) (Fig. 16.8). This technique is even more important for characterizing internally structured nanoparticles without a periodic internal pattern (“sponge” nanoparticles), where the structure cannot be elucidated in detail by other methods (Barauskas et al. 2006). The cage-like ultrastructure of immunostimulating complexes (Iscoms) and related colloidal structures, that have an interesting potential as vaccine adjuvants, have intensively studied with TEM, in particular after negative staining (Demana et al. 2004; Madsen et al. 2010; Muhsin et al. 1989). The structure of complexes resulting from interaction of nucleic acids with cationic lipids, surfactants or polymers is well accessible to studies with cryo- and freeze-fracture TEM (Ainalem et al. 2009; Alfredsson 2005; Sternberg et al. 1994). Cryo-TEM in particular has also been employed to identify the various colloidal structures that may be formed by amphiphilic block copolymers (spherical and worm-like micelles, vesicles) being under investigation as alternative drug carrier systems (Rank et al. 2009; Velluto et al. 2008).

The different colloidal structures (e.g., emulsion droplets, vesicles formed by excess phospholipid) occurring in colloidal fat emulsions for parenteral nutrition or as drug carriers have also been studied by TEM techniques (Klang et al. 2012; Kuntsche et al. 2009a; Westesen and Wehler 1992). Moreover, TEM has led to valuable insights into the structure and morphology of solid lipid nanoparticles. Anisometric, platelet-shaped particles usually form upon crystallization of

spherical triglyceride nanodroplets after processing by melt-homogenization but other particle shapes (ranging from spherical over block-like to the often occurring platelets) may be observed in dependence on the composition and preparation process (Bunjes et al. 2007; Finke et al. 2013; Rosenblatt and Bunjes 2009). At higher concentration, platelet-like particles tend to self-organize in stacks (Bunjes et al. 2007; Unruh et al. 2002) (Fig. 16.6). Under favorable circumstances, even the lamellar organization of the triglyceride molecules within single crystalline particles can be observed (Bunjes et al. 2007; Rosenblatt and Bunjes 2009) (Fig. 16.6) Upon incorporation of liquid oils or drugs, liquid compartments sticking to the surface of the solid, platelet-like matrix of the nanoparticles may be formed as revealed by TEM images (Bunjes et al. 2001; Jores et al. 2004). Also the association of inorganic sunscreen pigments with solid lipid nanoparticles could be visualized (Villalobos-Hernández and Müller-Goymann 2005).

As a kind of intermediate between liquid emulsion droplets and solid lipid nanoparticles lipid nanoparticles in the supercooled smectic state have been prepared from cholesterol esters as drug delivery system for poorly water-soluble drugs. TEM studies revealed that—depending on the nature of the emulsifier used—these particles are of more or less clear cylindrical shape (Kuntsche et al. 2004, 2005, 2010b) (Fig. 16.7). Also for these dispersions, the presence of other colloids formed by the excess of emulsifier(s) could be observed in co-existence with the smectic lipid nanoparticles.

Examples for the use of TEM also include studies on nanoparticulate dispersions of pure drugs or drug conjugates. Examples are the visualization of the shape of amorphous and crystalline felodipine nanoparticles by cryo-TEM, cryo- and freeze-fracture TEM studies on supercooled ubidecarenone nanoparticles or the detection of shell-enclosed hexagonally structured nanoassemblies in aqueous dispersions of a gemcitabine squalene conjugate by cryo-TEM (Couvreur et al. 2008; Lindfors et al. 2007; Siekmann and Westesen 1995). Crystalline drug nanoparticles can be visualized in a rather straightforward manner by investigation of negatively stained specimens (Bitterlich et al. 2014) (Fig. 16.9).

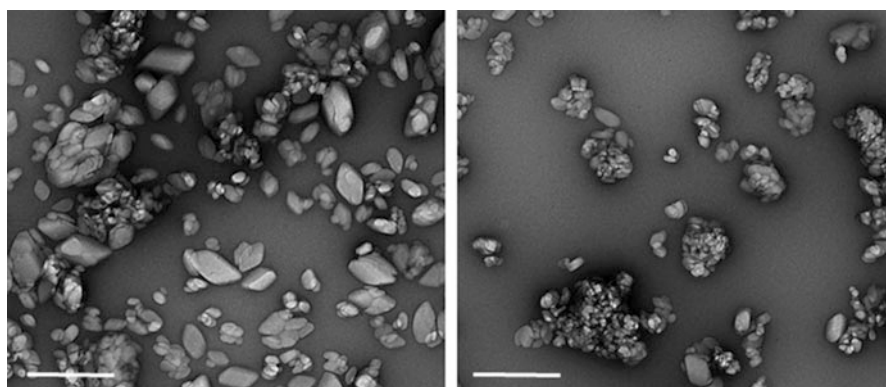


Fig. 16.9 TEM micrographs (negative staining) of a fenofibrate nanosuspension after 8 h (left) and 24 h (right) of grinding in a stirred media mill. Scale bars: 500 nm. Data from Bitterlich et al. 2014

In contrast to negative staining and cryo-TEM, TEM after freeze-fracturing can also be employed on semisolid and even solid systems. Thus, it has been used for the investigation of different kinds of liquid crystalline structures, vesicular phospholipid gels or semisolid emulsion systems as well as for solid lipid matrices (Attama et al. 2006; Brandl et al. 1997; Gašperlin et al. 1994; Müller-Goymann 1984; Paspaleeva-Kühn and Nürnberg 1992; Rades and Müller-Goymann 1997; Savic et al. 2005; Schütze and Müller-Goymann 1992).

3.3 Scanning Electron Microscopy (SEM)

Scanning electron microscopy (SEM) is a well established tool to investigate the morphology of particles and the topology of pharmaceutically relevant surfaces at high resolution. Although it may sometimes be operated at magnifications not much higher than those used in light microscopy the considerably higher depth of field provided by SEM allows unique insight into topological features of a sample. The SEM technique relies on the generation of a very fine electron beam that scans the sample surface in a point-wise, regular manner. The beam electrons penetrate the surface of the specimen and lead to a multitude of interactions with the sample atoms. These interactions give rise to the generation of different kinds of radiation (in particular electrons and X-rays) from the specimen surface that can be monitored by specialized detectors and used for imaging and element analysis. The most important SEM technique for pharmaceutical applications is surface imaging based on the detection of secondary electrons. This technique leads to the well-known “three-dimensional” grayscale images often included in monographs on pharmaceutical excipients (e.g., Rowe et al. 2009) and scientific publications on particulate pharmaceutical formulations. This section of the chapter will introduce the basics of the method and its applications with a particular focus on imaging by secondary electron detection. For more detailed insights, a lot of specialized literature is available, in particular with reference to biological and materials science but also with regard to pharmaceutical applications (e.g., Carlton 2011; Fleger et al. 1995; Goldstein et al. 2003; Klang et al. 2013).

3.3.1 The Scanning Electron Microscope

A sketch of a typical SEM-setup is provided in Fig. 16.10. SEMs are operated at lower accelerating voltages than TEMs. The accelerating voltage may be as high as 30 kV but SEMs that can operate at voltages below 1 kV are increasingly being used. Upon passage through the microscopic column the electron beam is condensed, and finally an objective lens focuses it as a small spot onto the specimen. Scan coils, which are usually situated within the objective lens, can deflect the beam and are used to move the beam spot in a raster pattern over the surface of the specimen. Magnification depends on the dimensions of the area scanned during

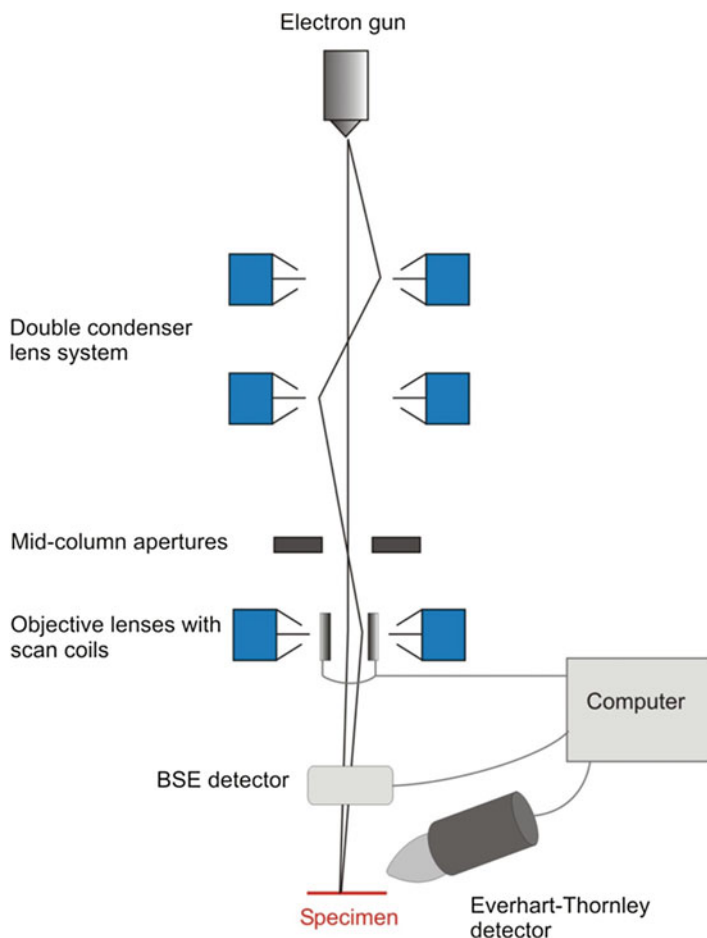


Fig. 16.10 Schematic illustration of the setup of a Scanning Electron Microscope

sample analysis (for higher magnification, the area is reduced). In order to achieve a high resolution, the spot size of the beam should be small (although spot size is not the only parameter determining resolution of a SEM). Interaction of the electron beam with the atoms of the specimen induces a multitude of effects (see Sect. 3.3.2). The resulting signals arising from the specimen's surface are recorded by corresponding detectors which are synchronized with the movement of the beam spot. Thus, the type or strength of a detector signal can be allocated to the corresponding position of the specimen's surface where the effect was produced. The release of so-called secondary electrons (SE) from the specimen is used for surface imaging. SE have a rather low energy and are monitored by a detector positioned at the side of the sample chamber. Usually, an Everhart-Thornley detector is used for this purpose (Fig. 16.11). The front structure (Faraday cage or collector screen) of this detector is positively charged (~ 300 V) and can thus collect

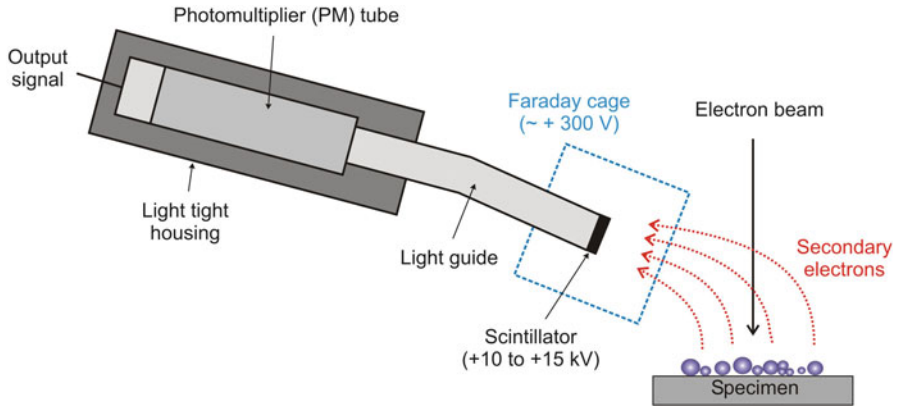


Fig. 16.11 Operating principle of an Everhart-Thornley detector

the low-energy SE emerging from anywhere on the specimen surface by electrostatic attraction. High energy electrons are not deflected by the relatively low potential of the Faraday cage and will only be detected if their path sends them directly into the opening of the detector. Electrons inside the Faraday cage are accelerated by a very high positive potential onto a small scintillator disc where they induce photon formation. By a light pipe, the photons are directed to a photomultiplier localized outside of the specimen chamber. Here, they cause the formation of an electron cascade thus amplifying the signal which is finally recorded and assigned to the respective spot on the specimen surface.

3.3.2 Electron Beam-Specimen Interactions

After entrance into the sample, the beam electrons undergo a multitude of interactions upon collision with the atoms of the sample. Thus, they get scattered, change direction and lose energy on their way. The interactions occur in a so-called interaction volume which has a pear- or droplet-like shape (Fig. 16.12). The size of the interaction volume increases with accelerating voltage and decreases with increasing atomic number. Within the interaction volume, the electrons undergo elastic or inelastic interactions with the sample atoms. Elastic interactions occur due to interaction with the nucleus of the specimen atoms. They do not cause much change in the energy of the electrons but lead to a deflection effect at a large angle. Elastic interaction may cause the electrons to be scattered back towards the direction of the primary beam (backscattered electrons, BSE). Due to their high energy, BSE can leave the specimen from a comparatively large depth of the interaction volume.

Inelastic interactions are due to interactions with the electron shell of the specimen atoms. They cause a large energy loss of the incident electron and its deflection at low angles. Inelastic interaction may lead to the release of weakly

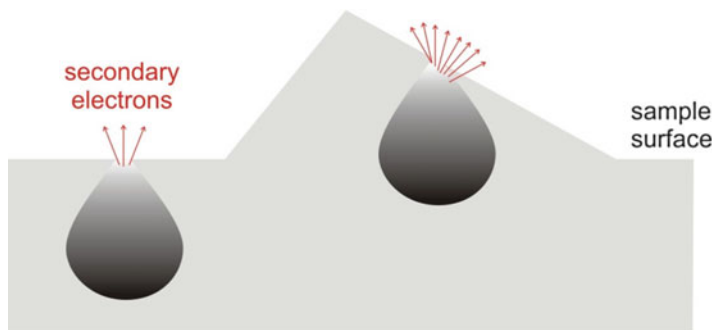


Fig. 16.12 Illustration of the pear-shaped interaction volume in which the different types of radiation that lead to image formation in SEM are created. Secondary electrons (SE) can leave the specimen only from areas close to the surface; thus, protruding parts of the specimen lead to a higher intensity in SE imaging

bound electrons from the orbital shell of the specimen atoms (secondary electrons, SE). Although SE may be generated throughout the interaction volume, only those in close vicinity (in the order of several nm) to the specimen surface can leave the specimen because of their low energy. In areas protruding from the sample surface, the fraction of SE that can leave the surface of the specimen is higher than in flat areas because more SE are generated at a distance close to the surface (Fig. 16.12). Therefore, the protruding areas appear brighter in the projection and an image of three-dimensional appearance is created. The topography of the sample is thus very well reflected in SE micrographs. The confinement of the origin of the SE created at the beam spot to a very narrow space leads to a high resolution of SE micrographs. The yield of SE increases with decreasing energy of the beam since the probability of interactions of the beam electrons with electrons from the outer shell of the specimen atoms increases when the beam electrons become slower. Thus, the resolution of surface images becomes better when the acceleration voltage is decreased. SE can also be generated by processes other than those outlined above. For example, BSE may liberate SE from other places in the specimen or even from components of the specimen chamber. Such effects decrease resolution but cannot be completely avoided.

BSE are not just a source of noise in SE micrographs but they can themselves be used for imaging. Images created from BSE detection do not reflect the surface topography in detail but can be used to analyze the composition of the sample surface. The yield of BSE generally increases with atomic number of the sample atoms albeit not in a linear manner. The intensity of electron backscattering thus reflects the sample composition. Organic materials composed solely of light atoms such as C, H, O, and N do not give rise to much backscattering. However, if components of higher atomic number are contained in the sample (for example, calcium phosphate as filling agent or API salts with inorganic counterions) contrast between areas of different composition, e.g., on a tablet surface, may be achieved

(Carlton 2011). BSE are detected close to the point where the electron beam enters the specimen chamber. As they can leave the specimen from a rather large part of the interaction volume and thus further away from the beam spot, the resolution of the corresponding images is lower than with SE detection.

3.3.3 Sample Preparation for SEM

The size of samples used for SEM is mainly limited by the size of the sample chamber; thus, samples can be rather large. In conventional SEM, sample thickness is not a problematic issue as only the sample surface is investigated. Sample preparation is often more straightforward in SEM compared with TEM. Dry powder or granule samples are usually mounted onto the sample holder of the SEM by using double-sided carbon adhesive tape (conductive). Powders can be sprinkled onto the tape or blown to it with the aid of an airstream. Also larger objects like tablets can be fixed by tape or they can be glued to the holder. To investigate the interior of tablets or larger particles, these objects may be broken or cut (preferably with a microtome). If particles agglomerate too strongly, they can be dispersed in a suitable volatile non-solvent and sprayed onto the holder or be deposited by filtration (e.g., using a Nuclepore filter). Filtration followed by drying is also well suitable for the preparation of particles from suspensions.

If the sample is non-conducting (as are most samples of pharmaceutical interest) it needs to be coated with a thin conductive layer unless investigated at very low accelerating voltage or in a low vacuum instrument. In most cases, sputter coating is used for that purpose. A sputter coating device (Fig. 16.13) consists of a vacuum-tight chamber containing an anode that holds the specimen to be coated and a cathode with the coating material (e.g., gold, palladium, carbon). After evacuation, the chamber is filled with argon gas and an electric field is generated between anode and cathode. At sufficiently high voltage an argon plasma is formed in which the argon atoms are ionized and accelerated towards the cathode. There, they liberate atoms from the coating material which distribute in the chamber and are deposited on the specimen. The process has to be controlled such that a thin (up to a few nm), continuous film is formed on the specimen; the film must not get too thick as it otherwise might cover details of the specimen's surface.

3.3.4 Environmental Scanning Electron Microscopy

Traditionally, the whole system of the SEM enclosing the electron beam (electron gun, column and sample chamber) operates under high vacuum. During the last decades, instruments that work with low vacuum in the sample chamber have become available. As these may help to overcome problems with charging of non-conducting samples and with vacuum sensitive samples they are used in some pharmaceutical applications. For example, so-called Environmental Scanning Electron Microscopes (ESEM) can operate under relatively high water vapor

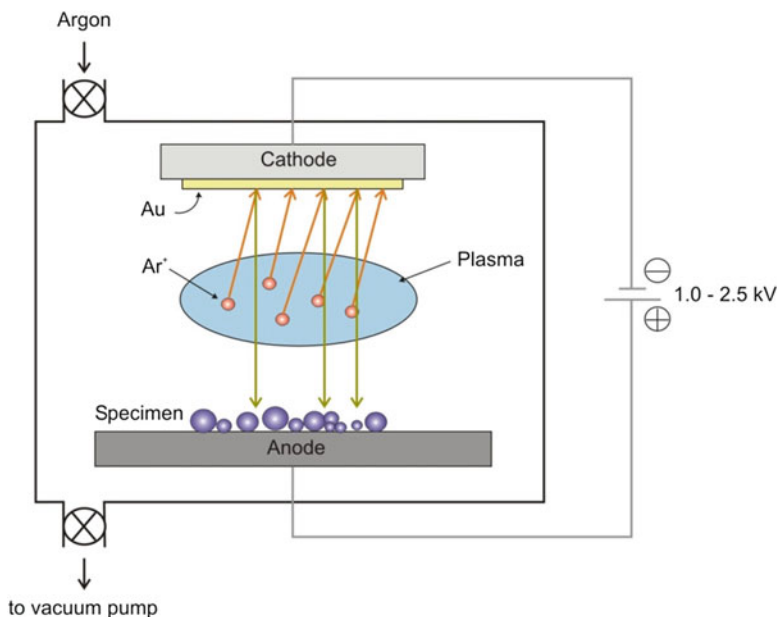


Fig. 16.13 Layout of a sputter coating device

pressures in the sample chamber but other low-vacuum devices have also been developed. Operation under low vacuum does not only allow investigating samples in a hydrated state close to ambient conditions but can also eliminate the need to coat samples with a conductive layer.

3.3.5 Energy Dispersive X-ray Spectrometry

Investigation of a sample by SEM cannot only lead to images but also to specific information on the chemical composition of the sample at specific sites. This type of investigation—energy dispersive X-ray spectrometry (EDX, often also referred to as EDS)—is based on the generation of X-rays upon interaction of the electron beam with the sample atoms. Apart from a continuous spectrum of X-rays (“Bremsstrahlung”) generated by the deceleration of the beam electrons due to interaction with the specimen atoms sharp X-ray signals are produced at wavelength positions that are specific for a given element. These signals are the basis for elemental mapping by EDX. They are generated when an inner shell electron of the specimen atom is hit by the electron beam and knocked out of its position. Its space is filled with an electron from a higher energy level electron shell and the energy difference is emitted as an X-ray photon with the corresponding energy. Replacement of the electron in the innermost shell (the K shell) can occur from the next higher level shell (the L shell) leading to K_{α} radiation or—less probably—from the even higher M shell yielding a smaller peak of the K_{β} radiation. There are also electron

transitions between the higher level shells (if present) altogether leading to a more or less complex spectrum of element-characteristic, sharp signals arising on top of the continuous spectrum. The X-ray detector records the X-ray spectra arising from the areas of interest in the specimen and the characteristic signals can be assigned to the corresponding elements.

3.3.6 Pharmaceutical Application of SEM and SEM/EDX

SEM imaging is extremely helpful to examine the size, shape and detailed morphology of particles and to understand morphology-related properties of substances, formulations or dosage forms (e.g., reviewed by Schmidt (2002)). The technique is thus abundantly used in the context of research and development especially on solid dosage forms and only a very limited number of examples can be referred to here. In the evaluation of pharmaceutical raw materials (drug substances and excipients) SEM images revealing the size, shape and morphology of the particles help to understand the processing properties and pharmaceutical performance of these materials (Kleinebudde 1997; Pitchayajittipong et al. 2010). The impact of different preparation procedures like precipitation or milling on important properties of the resulting drug or excipient particles can be investigated by SEM (Crisp et al. 2011; Ho et al. 2012; Kubavat et al. 2012; Otte and Carvajal 2011; Rasenack and Müller 2002). The structure of spray and freeze dried formulations is often examined with this method (Corveleyn and Remon 1997; Devi and Williams 2013; Littringer et al. 2013; Vehring 2008) (Fig. 16.14). The formation of interactive powder mixtures, where smaller particles (usually those of the active

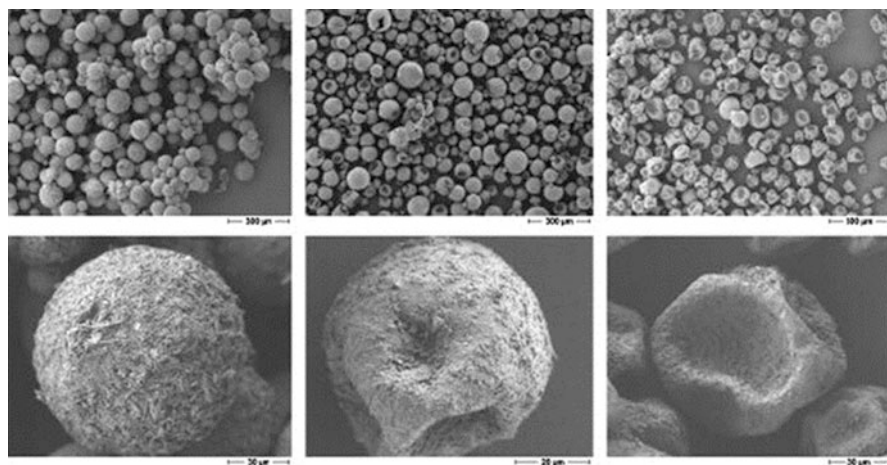


Fig. 16.14 SEM micrographs of mannitol samples spray dried at different outlet temperatures (left: 67 °C; middle: 84 °C; right: 102 °C. Scale bar 300 µm (top line), 30 µm (bottom left and right) 20 µm (bottom middle)). Reprinted from Littringer et al. 2013, Copyright (2013), with permission from Elsevier

substance) adhere to larger ones can easily be shown by SEM (Adi et al. 2007; Grasmeyer et al. 2013). Such interactive mixtures are highly relevant in formulations used in dry powder inhalers for which also other types of formulations are developed with the aid of SEM investigations (Healy et al. 2014; Hoppentocht et al. 2014). Images of tablet surfaces or cross-sections are very illustrative for the interpretation of deformation processes during tableting (Ghanam et al. 2010; Narayan and Hancock 2003) (Fig. 16.15). Similar images help to understand the

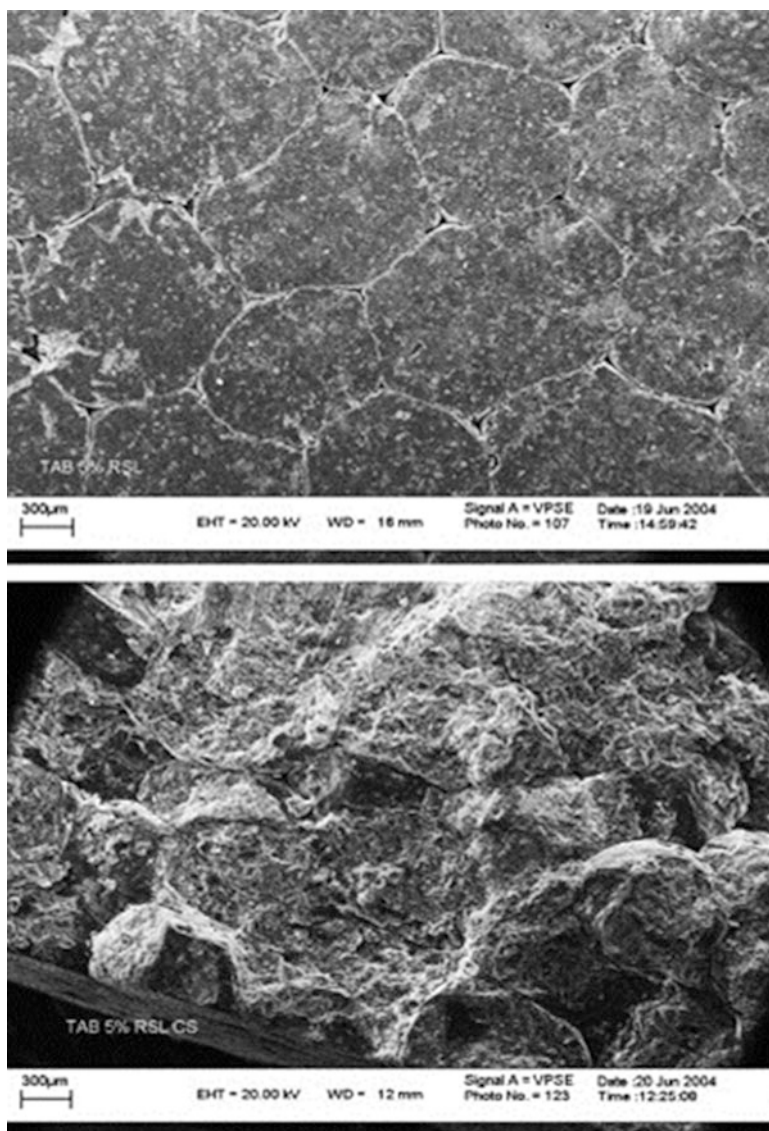


Fig. 16.15 SEM micrographs of a tablet prepared from ibuprofen-containing pellets coated with Eudragit; top: tablet surface, bottom: cross-section. Reprinted from Abbaspour et al. 2008, Copyright (2007), with permission from Elsevier

structure and formation of polymer layers upon coating of tablets, granules or other particles and their behavior upon processing (Abbaspour et al. 2008; Haaser et al. 2013; Jeong and Park 2008). In the field of parenteral dosage forms, the influence of production parameters on the morphology of polymer microparticles can be investigated and the structure and degradation of implants be analyzed (Cheng et al. 2009; Jeyanthi et al. 1996; Lee et al. 2012; Witt and Kissel 2001). SEM has also been applied to investigate particulate objects with sizes in the nanometer range, for example, to reveal the size and shape of the particles in drug nanosuspensions or of drug carrier nanoparticles (Bhakay et al. 2011; Finke et al. 2013; Gaumet et al. 2007; George and Ghosh 2013). In order to study “soft” structures in a close to their native situation a freeze-fracture technique (partly performed within the SEM instrument) is available and has been applied to lyotropic liquid crystalline cubic structures as well as other types of aqueous colloidal systems (Krauel et al. 2007; Rizwan et al. 2007).

For specific questions, the use of SEM in combination with energy dispersive X-ray spectrometry (SEM/EDX) can be a very interesting option. The possibility to identify particles or zones according to their elemental composition has, for example, been used to investigate the distribution of active ingredients or excipients in different kinds of solid dosage forms (Ghalanbor et al. 2010; Nagy et al. 2012; Pingali and Mendez 2014; Rajjada et al. 2013; van Eerdenbrugh et al. 2008). In these studies, the components of interest are identified by mapping the occurrence of a substance-specific element as indicator (e.g., sulfur for spironolactone, piroxicam or proteins, or Mg for magnesium stearate). There are also approaches to map a larger number of components, e.g., present at a tablet surface, by identifying phases of different composition using complex evaluation procedures (Scoutaris et al. 2014). Moreover, SEM/EDX analysis has proven to be an effective tool for the identification of foreign matter particles in tablets or drug nanosuspensions (Juhnke et al. 2012; Pajander et al. 2013).

4 Conclusion

Various microscopic techniques are available for the research on pharmaceutical formulations. They range from rather simple light microscopy to very advanced (and expensive) electron microscopic methods. Depending on the type of sample and question to be solved the right technique has to be chosen; however, different microscopic methods can often provide valuable complementary information. In particular for the more advanced techniques a certain degree of expertise is required in order to select the right preparation and measurement conditions for a given sample and to avoid misinterpretation of results. When used appropriately, microscopy can be extremely helpful to elucidate pharmaceutically relevant features of a sample as illustrated by numerous examples from the literature.

References

- Abbaspour M, Sadeghi F, Afrasiabi Garekani H (2008) Design and study of ibuprofen disintegrating sustained-release tablets comprising coated pellets. *Eur J Pharm Biopharm* 68:747–759
- Abramowitz M, Davidson MW (2014) Immersion media. <http://www.olympusmicro.com/primer/anatomy/immersion.html>. Accessed 30 Nov 2014
- Abramowitz M, Spring KR, Keller HE, Davidson MW (2002) Basic principles of microscope objectives. *BioTechniques* 33:772–781
- Adi H, Larson I, Stewart PJ (2007) Adhesion and redistribution of salmeterol xinafoate particles in sugar-based mixtures for inhalation. *Int J Pharm* 337:229–238
- Ainalem M, Carnerup AM, Janiak J, Alfredsson V, Nylander T, Schillén K (2009) Condensing DNA with poly(amido amine) dendrimers of different generations: means of controlling aggregate morphology. *Soft Matter* 5:2310–2320
- Alfredsson V (2005) Cryo-TEM studies of DNA and DNA–lipid structures. *Curr Opin Colloid Interf Sci* 10:269–273
- Almgren M, Edwards K, Karlsson G (2000) Cryo transmission electron microscopy of liposomes and related structures. *Coll Surf A* 174:3–21
- Amar-Yuli I, Garti N (2005) Transitions induced by solubilized fat into reverse hexagonal mesophases. *Colloids Surf B* 43:72–82
- Attama A, Schicke B, Müller-Goymann CC (2006) Further characterization of theobromae oil–beeswax admixtures as lipid matrices for improved drug delivery systems. *Eur J Pharm Biopharm* 64:294–306
- Barauskas J, Johnsson M, Tiberg F (2005) Self-assembled lipid superstructures: beyond vesicles and liposomes. *Nano Lett* 5:1615–1619
- Barauskas J, Misiunas A, Gunnarsson T, Tiberg F, Johnsson M (2006) “Sponge” nanoparticle dispersions in aqueous mixtures of diglycerol monooleate, glycerol dioleate, and polysorbate 80. *Langmuir* 22:6328–6334
- Bauer J, Spanton S, Henry R, Quick J, Dziki W, Porter W, Morris J (2001) Ritonavir: an extraordinary example of conformational polymorphism. *Pharm Res* 18:859–866
- Benedini L, Schulz EP, Messina PV, Palma SD, Allemandi DA, Schulz PC (2011) The ascorbyl palmitate–water system: phase diagram and state of water. *Colloids Surf A* 375:178–185
- Bhakay A, Merwade M, Bilgili E, Dave RN (2011) Novel aspects of wet milling for the production of microsuspensions and nanosuspensions of poorly water-soluble drugs. *Drug Dev Ind Pharm* 37:963–976
- Bibi S, Kaur R, Henriksen-Lacey M, McNeil SE, Wilkhu J, Lattmann E, Christensen D, Mohammed AR, Perrie Y (2011) Microscopy imaging of liposomes: from coverslips to environmental SEM. *Int J Pharm* 417:138–150
- Bitterlich A, Laabs C, Busmann E, Grandeury A, Juhnke M, Bunjes H, Kwade A (2014) Challenges in nanogrinding of active pharmaceutical ingredients. *Chem Eng Technol* 37:840–846
- Brandl M, Drechsler M, Bachmann D, Bauer K (1997) Morphology of semisolid aqueous phosphatidylcholine dispersions, a freeze fracture electron microscopy study. *Chem Phys Lipids* 87:65–72
- Bunjes H, Drechsler M, Koch MHJ, Westesen K (2001) Incorporation of the model drug ubidecarenone into solid lipid nanoparticles. *Pharm Res* 18:287–293
- Bunjes H, Steiniger F, Richter W (2007) Visualizing the structure of triglyceride nanoparticles in different crystal modifications. *Langmuir* 23:4005–4011
- Burrows ND, Penn RL (2013) Cryogenic transmission electron microscopy: aqueous suspensions of nanoscale objects. *Microsc Microanal* 19:1542–1553
- Carlton RA (2011) *Pharmaceutical microscopy*. Springer, New York
- Cheng L, Guo S, Wu W (2009) Characterization and in vitro release of praziquantel from poly (ϵ -caprolactone) implants. *Int J Pharm* 377:112–119

- Chow K, Tong HHY, Lum S, Chow AHI (2008) Engineering of pharmaceutical materials: an industrial perspective. *J Pharm Sci* 97:2855–2877
- Corveleyn S, Remon JP (1997) Formulation and production of rapidly disintegrating tablets by lyophilisation using hydrochlorothiazide as a model drug. *Int J Pharm* 152:215–225
- Couvreur P, Reddy LH, Mangenot S, Poupaert JH, Desmaële D, Lepître-Mouelhi S, Pili B, Bourgaux C, Amenitsch H, Ollivon M (2008) Discovery of new hexagonal supramolecular nanostructures formed by squalenylation of an anticancer nucleoside analogue. *Small* 4:247–253
- Crisp J, Dann S, Blatchford C (2011) Antisolvent crystallization of pharmaceutical excipients from aqueous solutions and the use of preferred orientation in phase identification by powder X-ray diffraction. *Eur J Pharm Sci* 42:568–577
- Davidson MW, Fellers TJ (2003) Understanding conjugate planes and Köhler illumination. <http://www.microscopyu.com/pdfs/KohlerIllumination.pdf>. Accessed 30 Nov 2014
- Dawidczyk CM, Russell LM, Searson PC (2014) Nanomedicines for cancer therapy: state-of-the-art and limitations to pre-clinical studies that hinder future developments. *Front Chem* 2:article 69
- Demana PH, Davies NM, Vosgerau U, Rades T (2004) Pseudo-ternary phase diagrams of aqueous mixtures of Quil A, cholesterol and phospholipid prepared by the lipid-film hydration method. *Int J Pharm* 270:229–239
- Devi S, Williams D (2013) Morphological and compressional mechanical properties of freeze-dried mannitol, sucrose, and trehalose cakes. *J Pharm Sci* 102:4246–4255
- Drent P (2005) Properties and selection of objective lenses for light microscopy applications. *Microsc Anal* 16:5–7
- Driscoll DF (2006) Lipid injectable emulsions: Pharmacopeial and safety issues. *Pharm Res* 23:1959–1969
- Egelhaaf SU, Schurtenberger P, Müller M (2000) New controlled environment vitrification system for cryo-transmission electron microscopy: design and application to surfactant solutions. *J Microsc* 200:128–139
- Elliot MS, Poon WCK (2001) Conventional optical microscopy of colloidal suspensions. *Adv Colloid Interf Sci* 92:133–194
- Finke JH, Schmolke H, Klages C, Müller-Goymann CC (2013) Controlling solid lipid nanoparticle adhesion by polyelectrolyte multilayer surface modifications. *Int J Pharm* 449:59–71
- Flegler SL, Heckman JW, Klomparens KL (1995) Scanning and transmission electron microscopy. An introduction. Oxford University Press, New York
- Friedrich H, Frederik PM, deWith G, Sommerdijk NAJM (2010) Imaging of self-assembled structures: interpretation of TEM and cryo-TEM images. *Angew Chem Int Ed* 49:7850–7858
- Gašperlin M, Kristl J, Šmid-Korbar J, Kerč J (1994) The structure elucidation of semisolid w/o emulsion systems containing silicone surfactant. *Int J Pharm* 107:51–56
- Gaumet M, Gurny R, Delie F (2007) Fluorescent biodegradable PLGA particles with narrow size distributions: preparation by means of selective centrifugation. *Int J Pharm* 342:222–230
- George M, Ghosh I (2013) Identifying the correlation between drug/stabilizer properties and critical quality attributes (CQAs) of nanosuspension formulation prepared by wet media milling technology. *Eur J Pharm Sci* 48:142–152
- Ghalanbor Z, Körber M, Bodmeier R (2010) Improved lysozyme stability and release properties of poly(lactide-co-glycolide) implants prepared by hot-melt extrusion. *Pharm Res* 27:371–379
- Ghanam D, Hassan I, Kleinebudde P (2010) Compression behaviour of κ-carrageenan pellets. *Int J Pharm* 390:117–127
- Gilchrist SE, Letchford K, Burt HM (2012) The solid-state characterization of fusidic acid. *Int J Pharm* 422:245–253
- Goldberg O (1980) Köhler illumination. *Microscope* 28:15–21
- Goldstein JI, Newbury DE, Echlin P, Joy DC, Lyman CE, Lifshin E, Sawyer L, Michael JR (2003) Scanning electron microscopy and X-ray microanalysis, 3rd edn. Springer, Boston

- Gong X, Moghaddam MJ, Sagnella SM, Conn CE, Danon SJ, Waddington LJ, Drummond CJ (2011) Lyotropic liquid crystalline self-assembly material behavior and nanoparticulate dispersions of a phytanyl pro-drug analogue of cepecitabine-A chemotherapy agent. *ACS Appl Mater Interfaces* 3:1552–1561
- Grasmeijer F, Hagedoorn P, Frijlink HW, de Boer HA, Haverkamp RG (2013) Mixing time effects on the dispersion performance of adhesive mixtures for inhalation. *PLoS ONE* 8, e69263
- Grassucci RA, Taylor DJ, Frank J (2007) Preparation of macromolecular complexes for cryo-electron microscopy. *Nat Protoc* 2:3239–3246
- Grassucci RA, Taylor D, Frank J (2008) Visualization of macromolecular complexes using cryo-electron microscopy with FEI Tecnai transmission electron microscopes. *Nat Protoc* 3:330–339
- Haaser M, Naelapää K, Gordon KC, Pepper M, Rantanen J, Strachan CJ, Taday PF, Zeitler JA, Rades T (2013) Evaluating the effect of coating equipment on tablet film quality using terahertz pulsed imaging. *Eur J Pharm Biopharm* 85:1095–1102
- Harris JR (1997) Negative staining and cryoelectron microscopy. The thin film techniques. *Microscopy handbooks*, vol 35. BIOS Scientific Publishers in association with the Royal Microscopical Society, Oxford, UK, Herndon, VA
- Harris JR (2007) Negative staining of thinly spread biological samples. In: Kuo J (ed) *Electron microscopy. Methods and protocols*, 2nd edn. Humana Press, Totowa, pp 107–142
- Healy AM, Amaro MI, Paluch KJ, Tajber L (2014) Dry powders for oral inhalation free of lactose carrier particles. *Adv Drug Deliv Rev* 75:32–52
- Ho R, Naderi M, Heng JYY, Williams DR, Thielmann F, Bouza P, Keith AR, Thiele G, Burnett DJ (2012) Effect of milling on particle shape and surface energy heterogeneity of needle-shaped crystals. *Pharm Res* 29:2806–2816
- Hope MJ, Wong KF, Cullis PR (1989) Freeze-fracture of lipids and model membrane systems. *J Microsc Tech* 13:277–287
- Hoppel M, Mahrhauser D, Stallinger C, Wagner F, Wirth M, Valenta C (2014) Natural polymer-stabilized multiple water-in-oil-in-water emulsions: a novel dermal drug delivery system for 5-fluorouracil. *J Pharm Pharmacol* 66:658–667
- Hoppentocht M, Hagedoorn P, Frijlink H, de Boer A (2014) Technological and practical challenges of dry powder inhalers and formulations. *Adv Drug Deliv Rev* 75:18–31
- Jeong S, Park K (2008) Development of sustained release fast-disintegrating tablets using various polymer-coated ion-exchange resin complexes. *Int J Pharm* 353:195–204
- Jeyanthi R, Thanoo B, Metha RC, DeLuca PP (1996) Effect of solvent removal technique on the matrix characteristics of polylactide/glycolide microspheres for peptide delivery. *J Control Release* 38:235–244
- Jores K, Mehnert W, Drechsler M, Bunjes H, Johann C, Mäder K (2004) Investigations on the structure of solid lipid nanoparticles (SLN) and oil-loaded solid lipid nanoparticles by photon correlation spectroscopy, field-flow fractionation and transmission electron microscopy. *J Control Release* 95:217–227
- Juhnke M, Martin D, John E (2012) Generation of wear during the production of drug nanosuspensions by wet media milling. *Eur J Pharm Biopharm* 81:214–222
- Jurasin D, Pustak A, Habus I, Smit I, Filipovic-Vincekovic N (2011) Polymorphism and mesomorphism of oligomeric surfactants: effect of the degree of oligomerization. *Langmuir* 27:14118–14130
- Keck C (2010) Particle size analysis of nanocrystals: improved analysis method. *Int J Pharm* 390:3–12
- Keck C, Müller RH (2008) Size analysis of submicron particles by laser diffractometry—90 % of the published measurements are false. *Int J Pharm* 355:150–163
- Klang V, Matsko NB, Valenta C, Hofer F (2012) Electron microscopy of nanoemulsions: an essential tool for characterisation and stability assessment. *Micron* 43:85–103
- Klang V, Valenta C, Matsko NB (2013) Electron microscopy of pharmaceutical systems. *Micron* 44:45–74

- Kleinebudde P (1997) The crystallite-gel-model for microcrystalline cellulose in wet granulation, extrusion, and sponification. *Pharm Res* 14:804–809
- Koning RI, Koster AJ (2009) Cryo-electron tomography in biology and medicine. *Ann Anat* 191:427–445
- Krauel K, Girvan L, Hook S, Rades T (2007) Characterisation of colloidal drug delivery systems from the naked eye to Cryo-FESEM. *Micron* 38:796–803
- Kubavat HA, Shur J, Ruecroft G, Hipkiss D, Price R (2012) Investigation into the influence of primary crystallization conditions on the mechanical properties and secondary processing behaviour of fluticasone propionate for carrier based dry powder inhaler formulations. *Pharm Res* 29:994–1006
- Kuntsche J, Westesen K, Drechsler M, Koch MHJ, Bunjes H (2004) Supercooled smectic nanoparticles: a potential novel carrier system for poorly water soluble drugs. *Pharm Res* 21:1834–1843
- Kuntsche J, Koch M, Drechsler M, Bunjes H (2005) Crystallization behavior of supercooled smectic cholesteryl myristate nanoparticles containing phospholipids as stabilizers. *Coll Surf B* 44:25–35
- Kuntsche J, Bunjes H, Fahr A, Pappinen S, Rönkkö S, Suhonen M, Urtti A (2008) Interaction of lipid nanoparticles with human epidermis and an organotypic cell culture model. *Int J Pharm* 354:180–195
- Kuntsche J, Klaus K, Steiniger F (2009a) Size determinations of colloidal fat emulsions: a comparative study. *J Biomed Nanotechnol* 5:384–395
- Kuntsche J, Koch MHJ, Fahr A, Bunjes H (2009b) Supercooled smectic nanoparticles: influence of the matrix composition and in vitro cytotoxicity. *Eur J Pharm Sci* 38:238–248
- Kuntsche J, Freisleben I, Steiniger F, Fahr A (2010a) Temoporfin-loaded liposomes: physico-chemical characterization. *Eur J Pharm Sci* 40:305–315
- Kuntsche J, Koch MH, Steiniger F, Bunjes H (2010b) Influence of stabilizer systems on the properties and phase behavior of supercooled smectic nanoparticles. *J Coll Interf Sci* 350:229–239
- Kuntsche J, Horst JC, Bunjes H (2011) Cryogenic transmission electron microscopy (cryo-TEM) for studying the morphology of colloidal drug delivery systems. *Int J Pharm* 417:120–137
- Lauf U, Fahr A, Westesen K, Ulrich AS (2004) Novel lipid nanotubes in dispersions of DMPC. *ChemPhysChem* 5:1246–1249
- Lee WL, Seh YC, Widjaja E, Chong HC, Tan NS, Joachim Loo SC (2012) Fabrication and drug release study of double-layered microparticles of various sizes. *J Pharm Sci* 101:2787–2797
- Li X, Hirsh DJ, Cabral-Lilly DZA, Gruner SM, Janoff AS, Perkins WR (1998) Doxorubicin physical state in solution and inside liposomes loaded via a pH gradient. *Biochim Biophys Acta* 1415:23–40
- Lindfors L, Skantze P, Skantze U, Westergren J, Olsson U (2007) Amorphous drug nanosuspensions. 3. Particle dissolution and crystal growth. *Langmuir* 23:9866–9874
- Littringer EM, Noisternig MF, Mescher A, Schroettner H, Walzel P, Griesser UJ, Urbanetz NA (2013) The morphology and various densities of spray dried mannitol. *Powder Technol* 246:193–200
- Madsen HB, Arboe-Andersen HM, Rozlosnik N, Madsen F, Ifversen P, Kasimova MR, Nielsen HM (2010) Investigation of the interaction between modified ISCOMs and stratum corneum lipid model systems. *Biochim Biophys Acta* 1798:1779–1789
- Mercuri A, Belton PS, Royall PG, Barker SA (2012) Identification and molecular interpretation of the effects of drug incorporation on the self-emulsification process using spectroscopic, micropolarimetric and microscopic measurements. *Mol Pharmaceutics* 9:2658–2668
- Meyer H, Richter W (2001) Freeze-fracture studies on lipids and membranes. *Micron* 32:615–644
- Muhsin Ö, Höglund S, Gelderblom HR, Morein B (1989) Quarternary structure of the immunostimulating complex (Iscom). *J Ultrastruc Mol Struc Res* 102:240–248
- Müller-Goymann CC (1984) Liquid crystals in emulsions, creams, and gels containing ethoxylated sterols as surfactant. *Pharm Res* 4:154–158

- Munk T, Baldursdottir S, Hietala S, Rades T, Kapp S, Nuopponen M, Kalliomäki K, Tenhu H, Rantanen J (2012) Crystal morphology modification by the addition of tailor-made stereocontrolled poly(N-isopropyl acrylamide). *Mol Pharmaceutics* 9:1932–1941
- Nagy ZK, Balogh A, Vajna B, Farkas A, Patyi G, Kramarics Á, Marosi G (2012) Comparison of electrospun and extruded Soluplus[®]-based solid dosage forms of improved dissolution. *J Pharm Sci* 101:322–332
- Narayan P, Hancock BC (2003) The relationship between the particle properties, mechanical behavior, and surface roughness of some pharmaceutical excipient compacts. *Mat Sci Eng A* 355:24–36
- Nichols G, Frampton CS (1998) Physicochemical characterization of the orthorhombic polymorph of paracetamol crystallized from solution. *J Pharm Sci* 87:684–693
- Nonomura Y, Nakayama K, Aoki Y, Fujimori A (2009) Phase behavior of bile acid/lipid/water systems containing model dietary lipids. *J Colloid Interf Sci* 339:222–229
- Oheim M, Micheal DJ, Geisbauer M, Madsen D, Chow RH (2006) Principles of two-photon excitation fluorescence microscopy and other nonlinear imaging approaches. *Adv Drug Del Rev* 58:788–808
- Oldenbourg R (1996) A new view on polarization microscopy. *Nature* 381:811–812
- Otte A, Carvajal MT (2011) Assessment of milling-induced disorder of two pharmaceutical compounds. *J Pharm Sci* 100:1793–1804
- Pajander J, Haugshøj KB, Bjørneboe K, Wahlberg P, Rantanen J (2013) Foreign matter identification from solid dosage forms. *J Pharm Biopharm Anal* 80:116–125
- Paspaleeva-Kühn V, Nürnberg E (1992) Participation of macrogolstearate 400 lamellar phases in hydrophilic creams and vesicles. *Pharm Res* 9:1336–1340
- Pingali KC, Mendez R (2014) Nanosmearing due to process shear—influence on powder and tablet properties. *Adv Powder Technol* 25:952–959
- Piston DW (1998) Choosing objective lenses: the importance of numerical aperture and magnification in digital optical microscopy. *Bio Bull* 195:1–4
- Pitchayajittipong C, Price R, Shur J, Kaerger JS, Edge S (2010) Characterisation and functionality of inhalation anhydrous lactose. *Int J Pharm* 390:134–141
- Pluta M (1969) A phase-contrast device with positive and negative image contrast. *J Microsc* 89:205–216
- Prehm M, Enders C, Anzahae MY, Glettner B, Baumeister U, Tschierke C (2008) Distinct columnar and lamellar liquid crystalline phases formed by new bolaamphiphiles with linear and branched lateral hydrocarbon chains. *Chem Eur J* 14:6352–6368
- Rades T, Müller-Goymann CC (1997) Electron and light microscopical investigation of defect structures in mesophases of pharmaceutical substances. *Colloid Polym Sci* 275:1169–1178
- Rajjada D, Genina N, Fors D, Wisaeus E, Peltonen J, Rantanen J, Sandler N (2013) A step toward development of printable dosage forms for poorly soluble drugs. *J Pharm Sci* 102:3694–3704
- Rank A, Hauschild S, Förster S, Schubert R (2009) Preparation of monodisperse block copolymer vesicles via a thermotropic cylinder – vesicle transition. *Langmuir* 25:1337–1344
- Rasenack N, Müller BW (2002) Dissolution rate enhancement by in situ micronization of poorly water-soluble drugs. *Pharm Res* 19:1894–1900
- Rizwan S, Dong Y, Boyd B, Rades T, Hook S (2007) Characterisation of bicontinuous cubic liquid crystalline systems of phytantriol and water using cryo field emission scanning electron microscopy (cryo FESEM). *Micron* 38:478–485
- Rosenblatt KM, Bunjes H (2009) Poly(vinyl alcohol) as emulsifier stabilizes solid triglyceride drug carrier nanoparticles in the α -modification. *Mol Pharmaceutics* 6:105–120
- Rowe RC, Sheskey PJ, Quinn ME (2009) *Handbook of pharmaceutical excipients*, 6th edn. Pharmaceutical Press, London
- Savic S, Vuleta G, Daniels R, Müller-Goymann CC (2005) Colloidal microstructure of binary systems and model creams stabilized with an alkylpolyglucoside non-ionic emulsifier. *Colloid Polym Sci* 283:439–451

- Schmidt PC (2002) Secondary electron microscopy in pharmaceutical technology. In: Swarbrick J, Boylan JC (eds) *Encyclopedia of pharmaceutical technology*, vol 3, 2nd edn. Marcel Dekker, New York, pp 2401–2435
- Schütze W, Müller-Goymann CC (1992) Mutual interactions between nonionic surfactants and gelatin—investigations in cubic liquid crystalline systems and micellar systems. *Colloid Polym Sci* 269:85–90
- Scoutaris N, Vithani K, Slipper I, Chowdhry B, Douroumis D (2014) SEM/EDX and confocal Raman microscopy as complementary tools for the characterization of pharmaceutical tablets. *Int J Pharm* 470:88–98
- Seefeldt K, Miller J, Alvarez-Nunez F, Nodriguez-Hornedo N (2007) Crystallization pathways and kinetics of carbamazepine-nicotinamide cocrystals form the amorphous state by *in situ* thermomicroscopy, spectroscopy and calorimetry studies. *J Pharm Sci* 96:1147–1158
- Sevens NJ (2007) Freeze-fracture electron microscopy. *Nat Protoc* 2:547–576
- Siekman B, Westesen K (1995) Preparation and physicochemical characterization of aqueous dispersions of coenzyme Q10 nanoparticles. *Pharm Res* 12:201–208
- Spring KR, Keller HE, Davidson MW (2014) Microscope objectives introduction. <http://www.olympusmicro.com/primer/anatomy/objectives.html>. Accessed 30 Nov 2014
- Sternberg B, Sorgi FL, Huang L (1994) New structures in complex formation between DNA and cationic liposomes visualized by freeze-fracture electron microscopy. *FEBS Lett* 356:361–366
- Tian F, Baldursdottir S, Rantanen J (2009) Effects of polymer additives on the crystallization of hydrates: a molecular-level modulation. *Mol Pharmaceutics* 6:202–2010
- Unruh T, Westesen K, Bösecke P, Lindner P, Koch MHJ (2002) Self-assembly of triglyceride nanocrystals in suspension. *Langmuir* 18:1796–1800
- van Eerdenbrugh B, Froyen L, van Humbeek J, Martens JA, Augustijns P, van den Mooter G (2008) Alternative matrix formers for nanosuspension solidification: dissolution performance and X-ray microanalysis as an evaluation tool for powder dispersion. *Eur J Pharm Sci* 35:344–353
- Vehring R (2008) Pharmaceutical particle engineering via spray drying. *Pharm Res* 25:999–1022
- Velluto D, Demurtas D, Hubbell JA (2008) PEG-b-PPS diblock copolymer aggregates for hydrophobic drug solubilization and release: cyclosporin A as an example. *Mol Pharmaceutics* 5:632–642
- Vielreicher M, Schürmann S, Detsch R, Schmidt MA, Buttereit A, Boccaccini A, Friedrich O (2013) Taking a deep look: modern microscopy technologies to optimize the design and functionality of biocompatible scaffolds for tissue engineering in regenerative medicine. *J R Soc Interface* 10:0263
- Villalobos-Hernández J, Müller-Goymann C (2005) Novel nanoparticulate carrier system based on carnauba wax and decyl oleate for the dispersion of inorganic sunscreens in aqueous media. *Eur J Pharm Biopharm* 60:113–122
- Weaver R (2003) Rediscovering polarized light microscopy. *American Lab* 35:55–61
- Westesen K, Wehler T (1992) Physicochemical characterization of a model intravenous oil-in-water emulsion. *J Pharm Sci* 81:777–786
- White NS, Errington RJ (2005) Fluorescence techniques for drug delivery research: theory and practice. *Adv Drug Del Rev* 57:17–42
- Williams DB, Carter CB (2009) *Transmission electron microscopy. A textbook for materials science*, 2nd edn. Springer, New York
- Witt C, Kissel T (2001) Morphological characterization of microspheres, films and implants prepared from poly(lactide-co-glycolide) and ABA triblock copolymers: is the erosion controlled by degradation, swelling or diffusion? *Eur J Pharm Biopharm* 51:171–181
- Wu JX, Xia D, van den Berg F, Amigo JM, Rades T, Yang M, Rantanen J (2012) A novel image analysis methodology for online monitoring of nucleation and crystal growth during solid state phase transformations. *Int J Pharm* 433:60–70

Chapter 17

Vibrational Spectroscopic Imaging

Sara J. Fraser-Miller, Jukka Saarinen, and Clare J. Strachan

Abstract Vibrational spectroscopy, which probes vibrations within and between molecules, may be divided into four classes: mid-infrared (MIR, also referred to as just infrared (IR)), near-infrared (NIR), terahertz/far-infrared (FIR), and Raman. These techniques, described in earlier chapters, have several features in common: they are rapid, non-destructive, and label-free and can yield information-rich data about both the chemical and physical (e.g. solid state form) properties of samples. NIR, IR and terahertz spectroscopies probe the absorption of infrared light of increasing wavelength (from NIR to terahertz regions). In contrast, Raman spectroscopy is based on a scattering phenomenon and may be used to probe vibrations that occur in both the MIR and terahertz regions. These techniques have become widespread for drug and dosage form characterisation during, for example, synthesis and pharmaceutical processing.

Often it is important to know the location of components within a sample. Thus, spectrometers can be coupled with devices (e.g. microscope, array detector) for spatially resolved analysis. With various setups, vibrational spectroscopic imaging may be performed on the macro-, micro-, and even nano-scales. The continuing fundamental advances in spectroscopic imaging technology are facilitating the increasingly widespread adoption of vibrational spectroscopic imaging for diverse analyses in the pharmaceutical setting.

In this chapter vibrational spectroscopic imaging methods based on IR, NIR, terahertz, and Raman signals will be described. The chapter begins with a description of the principles of the analytical methods and their variants, followed by an introductory description of spectroscopic data analysis methods. Finally, the pharmaceutical application of these methods will be described throughout the ‘lifecycle’ of the drug. This includes raw material (drug and excipient) and dosage form characterization, drug dissolution/release analysis, and imaging during drug delivery.

Keywords Mid-infrared (IR) • Near infrared (NIR) • Raman • Terahertz • Imaging • Microscopy • Mapping • Vibrational spectroscopy

S.J. Fraser-Miller • J. Saarinen • C.J. Strachan (✉)
Formulation and Industrial Pharmacy Unit, Division of Pharmaceutical
Chemistry and Technology, Faculty of Pharmacy, Viikinkaari 5E, P.O. Box 56,
University of Helsinki 00014, Finland
e-mail: sara.miller@otago.ac.nz; jukka.saarinen@helsinki.fi; clare.strachan@helsinki.fi

1 Vibrational Spectroscopic Imaging Methodology

1.1 Definitions of Imaging and Mapping

The terms imaging and mapping are often used interchangeably, with the term imaging used in this chapter to refer to image generation in general. However, more precisely, the appropriate term depends on the data acquisition method. Both methods result in a hypercube of data, spatial (x- and y-) and spectral (z-) information. Mapping involves collecting a whole spectrum (100–1000s of wavelengths) from a single point in space, and repeating this measurement from different grid positions. Imaging involves the collection of spatially resolved data representing a single wavelength, often carried out using a focal plane array (also known as a Staring array) or a charged couple device (CCD) as the spatially resolved detector. The sample can then be imaged using different wavelengths to build up the spectral hypercube (Fig. 17.1). Typically, mapping allows richer spectral data acquisition and sometimes a higher spatial resolution, but is usually slower for imaging a given area which can limit its feasibility (e.g. for dynamic samples).

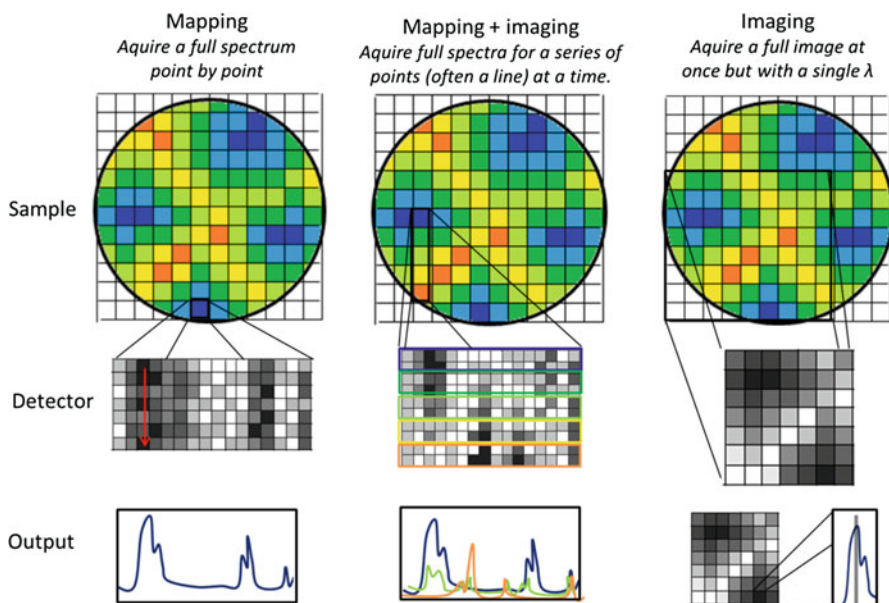


Fig. 17.1 Visualization of the differences between mapping and imaging setups. Mapping collects a full spectrum from one sampling position at a time, imaging collects spatial information at one wavelength at a time and mapping and imaging can be combined to collect full spectra for a series of positions at a time. All three methods result in a hypercube consisting of spatial information (x- and y-directions) and spectral information (z-direction)

To try and mitigate the disadvantages of each approach, some setups involve a merging of these two methods, such as gaining full spectral information for multiple spatial points, often in a line setup. An illustration of the differences between mapping and imaging methods and the merged version of the two is given in Fig. 17.1. The feasibility of these approaches is also affected by the spectroscopic technique employed. Instrumental and sampling variations for MIR, Raman, NIR and terahertz imaging are introduced below and also summarised in Table 17.1.

1.2 MIR

Mid-infrared (MIR) spectroscopy encompasses transitions in the energy range $4000\text{--}400\text{ cm}^{-1}$ (light with wavelengths of $2.5\text{--}25\text{ }\mu\text{m}$). These transitions are associated with fundamental vibrations where a molecule is excited from the ground ($v=0$) to the first vibrational excited state ($v=1$) and any associated rotational-vibrational transitions. The MIR transition is a single photon absorption event; this is illustrated in Fig. 17.2.

For a MIR transition to occur, a photon of the correct energy ($h\nu_1$) must interact with the sample with a vibrational transition associated with a change in dipole moment (μ). This means that vibrations where the dipole moment (δ^- through to δ^+) is altered are IR active. An example of a strongly IR active mode is an --O--H bond, with the O atom being δ^- and the H atom δ^+ . Stretching and compression along the O--H bond results in expansion and compression of the dipole moment (μ) meaning this vibrational mode is IR-active. This vibration and change in dipole moment is illustrated in Fig. 17.3a.

Experimentally, a MIR microscope includes an energy source (incandescent silicon carbide or synchrotron), a sample, a device to separate out the different wavelengths of light (spectrometer or gratings) and a detector (deuterated tri glycine sulphate (DTGS) or mercury cadmium telluride (MCT)). Often a Michelson interferometer is used as the spectrometer with the interferogram signal being converted to a spectrum using a Fourier transformation (FT). Imaging is possible by coupling an IR setup with microscope optics. While MIR spectroscopy may be used to probe diverse samples, it is very sensitive to water, making imaging samples in an aqueous medium difficult with this methodology.

In a confocal setup, the theoretical minimum sample spot diameter (d) is diffraction limited. This means that the theoretical minimum sample spot size is governed by the wavelength (λ) of light being used and the numerical aperture (NA) of the focusing objective by the equation

$$d \approx \frac{1.22\lambda}{NA} \quad (17.1)$$

Table 17.1 Comparison of vibrational spectroscopic imaging techniques

Aspect	Mid-infrared (MIR)	Near-infrared (NIR)	Raman	Coherent Raman	Terahertz
Spectral region	4000–200 cm^{-1}	12,300–4000 cm^{-1}	4000–20 cm^{-1}	4000–1200 cm^{-1}	2–133 cm^{-1}
Selection rule	Dipole moment change	Dipole moment change, anharmonicity	Polarisability change	Polarisability change	Refractive index difference (terahertz pulsed imaging based on reflection)/dipole moment change (terahertz spectroscopic mapping)
Typical vibrations	Fundamental intramolecular stretching and bending vibrations involving polar groups	Overtone and combinations (mainly OH, CH, NH)	Fundamental intramolecular stretching and bending vibrations involving non-polar and π -bonded groups, phonon vibrations (low frequency Raman)	Stretching vibrations involving non-polar and π -bonded groups (especially CH, CH ₂ and CH ₃ groups)	Phonon vibrations (crystals), intermolecular vibrations, molecular flexing
Signal intensity	Strong	Weak	Weak	Strong	Strong
Resolved bands in spectra	Common	Rare	Common	Common	Some (none for amorphous solids)
Common sampling setups	Transmission, ATR (micro/macro), near-field	Diffuse reflectance, transmission	Backscatter, transmission or spatially offset sampling arrangements, surface/tip-enhanced Raman	Forward scatter, (backward) scatter	Reflection, transmission
Quantitative/qualitative	Qualitative/quantitative	Qualitative/quantitative	Qualitative/quantitative	Qualitative (narrow-band CARS)/quantitative (SRS, multiplex CARS)	Qualitative/quantitative

Highest spatial resolution (depends on setup and sample)	Transmission: ~5–25 μm laterally (diffraction limited), signal from whole sample thickness for transmission. ATR: ~4 μm laterally, 100–300 nm up to 1–3 μm from surface axially). For near-field ~30 nm	Theoretically ~2 μm laterally (diffraction limited). In practice 10–100s of μm , due to need for thick sample and scattering effects in solid samples	~1 μm laterally, several microns axially. TERS: ~20–60 nm	~300 μm laterally, 1 μm axially. Tip-enhanced CARS: ~15–60 nm	150–200 μm laterally, 30–40 μm axially (reflection)/several mm (transmission)
Sensitivity to water	Strong	Strong	Weak	Weak	Strong
Problematic samples	Aqueous (ok with ATR), thick (samples must be ~10 μm or less except with ATR setup), rough	Aqueous, thin (less than 100 s of μm), strongly scattering	Fluorescing, thermally sensitive	Coloured (some)	Aqueous, very thin

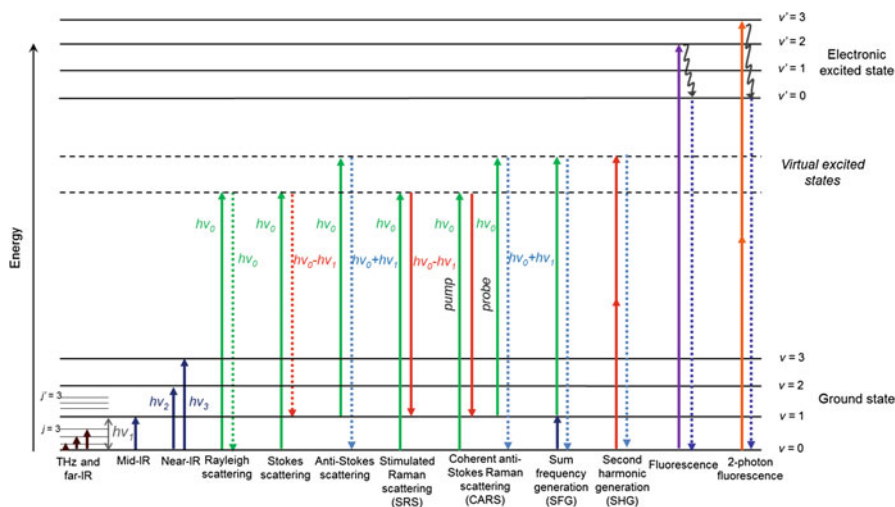


Fig. 17.2 The transitions involving absorption, emission and scattering of photons. The energy of an incident photon is $h\nu_0$, the energy difference between the ground ($\nu = 0$) and first vibrationally excited state ($\nu = 1$) is labelled $h\nu_1$. Infrared (IR) and near-infrared (NIR) are absorption processes which probe the fundamental and overtone vibrational transitions, respectively. Terahertz radiation probes the rotational and long range order (phonon) modes of the samples. Scattering processes can be elastic (Rayleigh) or inelastic (Raman). The inelastic processes can involve the incident photon contributing energy to the molecule via a vibrational transition ($h\nu_0 - h\nu_1$, Stokes scattering) or gaining energy from the molecule ($h\nu_0 + h\nu_1$, anti-Stokes scattering). Stimulated Raman scattering (SRS) involves the use of a second laser at energy $h\nu_0 - h\nu_1$ to stimulate the scattering process. Coherent anti-Stokes Raman scattering (CARS) is used to probe the anti-Stokes spectrum by using SRS to populate the vibrationally excited state which is then probed by another pass of the $h\nu_0$ laser. Sum frequency generation (SFG) uses two-photon excitation (with different energies) to induce anti-Stokes scattering, second harmonic generation (SHG) is a special case where the two photons are the same energy. The fluorescence pathway involves absorption of the photon into the excited state and emission from a lower level excited state back to the ground state. Two-photon fluorescence occurs when two photons induce an excitation to the electronic excited state with emission back down to the ground state. Although fluorescence is not classified as a vibrational event, it is shown here for comparison

From this it can be seen that with a change in the wavelength the minimum sample spot diameter will change. For example if a setup has an objective with a NA of 0.90, the spot size of the two extremes of the spectral window will vary by a factor of 10 with a resolution of $3.4 \mu\text{m}$ at 2500 nm and a resolution of $34 \mu\text{m}$ at $25,000 \text{ nm}$.

The approximate depth of field (L) is also dependent on the refractive index (n) of the sample by the equation

$$L \approx \frac{4n\lambda}{NA^2} \quad (17.2)$$

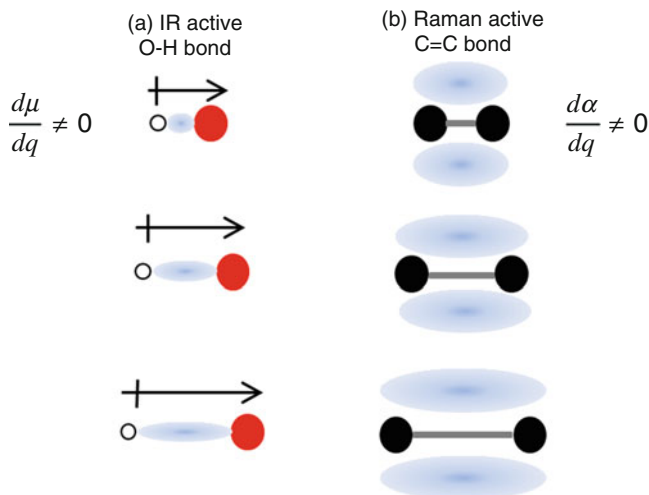


Fig. 17.3 Examples of (a) IR active (change in the dipole moment of the OH bond), and (b) Raman active (change in the polarisability of the C = C bond), modes

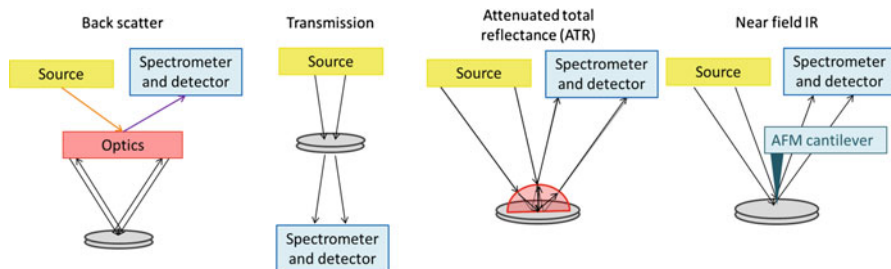


Fig. 17.4 Illustration of sampling methodology for backscatter, transmission, ATR and near-field methods

Hence materials with different refractive indices will give different sample volumes, this applies to all experiments which use diffraction based principals to minimise the sample spot size such as backscatter and attenuated total reflection (ATR) arrangements.

There are multiple sampling orientations employed in MIR imaging. These include backscattering, transmission and ATR setups (Griffiths and Mieso 2014; Grotheer et al. 2014). The different setups are employed to overcome various sampling issues. Near-field IR has also been employed to chemically image at a resolution smaller than the diffraction limited spot size. An illustration of these different sampling setups is given in Fig. 17.4.

1.2.1 Transmission

Transmission mode is where the source and detector are on opposite sides of the sample, and may be performed using mapping (sample stage is moved) or imaging (with focal plane array (FPA) detector). The sample needs to be thin ($\sim 10\ \mu\text{m}$ or less) for sufficient transmission of the infrared light and to not image a large sample volume. Embedding and microtoming is often necessary to obtain a suitable sample. This setup can produce spectral artefacts such as the Christiansen effect and Mie scattering in inhomogeneous samples (Griffiths and Misco 2014; Romeo et al. 2006; Pollard et al. 2007).

1.2.2 ATR-IR

A spherical ATR crystal with a high refractive index (e.g. germanium or silicon) can be used to improve the spatial resolution (in practice as good as approximately $4\ \mu\text{m}$ laterally) by refracting light into a tighter spot (Griffiths and Misco 2014). ATR-IR imaging is especially suited to imaging surface properties, since the evanescent wave responsible for image generation only penetrates approximately $1\text{--}3\ \mu\text{m}$ into the sample (depending on the crystal, angle of incidence of light and sample). The sample placed on the ATR crystal can be thick and thus sample preparation is often unnecessary, although the need for intimate contact between the sample surface and ATR crystal often requires sample compression onto the crystal. The setup is usually operated in imaging mode with a focal array detector, due to the challenges in reproducibly and non-destructively translating a micro-ATR crystal across the sample surface. Imaging may be performed in macro (without magnification) or micro (with microscope) modes depending on the desired spatial resolution (higher in micro) and field of view (smaller in micro). A challenge of the ATR-IR setup is to visually image the sample as the ATR crystal is often opaque to the visual spectrum. Instrumentation companies have devised clever solutions for this problem such as the LUMOS by Bruker Optics, where the sample is looked at optically before the ATR crystal is put in place for the spectral measurements.

1.2.3 Near-Field MIR

Atomic force microscopy (AFM) has been used in conjunction with MIR spectroscopy to image samples at a sub-diffraction limited resolution as low as $30\ \text{nm}$ (Higgins et al. 1996; Samson et al. 2006; Dazzi et al. 2012). By having the detector closer to the sample than the wavelength of light being used to illuminate the sample, the spatial resolution is much higher than with diffraction limited setups. A typical setup consists of the sample on an IR transparent prism with the IR light source coming from below. An AFM cantilever sits above the sample and detects

the thermal expansion and associated ring down (cantilever oscillations over time) of the sample associated with a transition of the same energy as the IR laser pulse. A spectrum is produced by plotting the ring down amplitude against excitation wavelength (Sonntag et al. 2014; Dazzi et al. 2012). Most studies using near-field IR look at biological systems (Cricenti et al. 2003; Gucciardi 2010; Keplinger et al. 2014) or polymer blends (Felts et al. 2013; Michaels et al. 2004; Vancso et al. 2005). The miscibility of pharmaceutical blends has also been studied with this technique (Sonntag et al. 2014; Dazzi et al. 2012; Van Eerdenbrugh et al. 2012).

1.3 NIR

Near infrared (NIR) spectroscopy covers the spectral region of $12,500\text{--}4000\text{ cm}^{-1}$ (0.8–2.5 μm wavelength). The transitions at these wavelengths tend to be overtone ($\nu = 0$ to $\nu = 2, 3, \dots$) and combination (two or more fundamental transitions excited simultaneously) vibrations. An example of an overtone transition is given in Fig. 17.2.

Like MIR, the active modes are associated with a change in the dipole moment. However in quantum mechanics the overtone transitions are forbidden. With anharmonicity (deviation from a simple harmonic oscillator) of the bond vibrations these transitions become allowed, so some transitions do occur. The molar absorptivity of these transitions are quite low, hence the signal is weaker than its MIR counterpart. The transitions seen in the NIR tend to be associated with X–H bonds, where X is often C, O, N or heavier atoms. NIR spectra often contain broad and complex spectral features whose precise origins can be difficult to identify. This kept NIR spectroscopy out of favour as a spectroscopic method until comparatively recently, when the use of multivariate data analysis to qualitatively and quantitatively analyse spectral differences has facilitated the use of NIR spectroscopy.

Like with MIR, there is a source (incandescent) which illuminates the sample, the resulting light is separated (spectrograph or gratings) and detected (Si-based CCDs and InGaAs). The orientations for sampling are transmission or diffuse reflectance modes. Focal plane array (FPA) detectors have allowed for faster spectroscopic imaging by collecting information from multiple points at once. This has allowed the use of NIR imaging to expand.

Like MIR, NIR is sensitive to aqueous environments. The diffraction limited spot size for NIR measurements is smaller (approximately 2–3 μm) than that for MIR. However, in practice, this spatial resolution is normally never achieved for two reasons: the inherently weak NIR signal requires samples hundreds of micrometres thick, and scattering of the NIR light with solid samples leads to spatial resolutions of tens to hundreds of micrometres depending on the sample.

1.4 Raman

1.4.1 Spontaneous

Raman spectroscopy is similar to MIR spectroscopy in that it probes the vibrational transitions in molecules, as seen in Fig. 17.2. Raman spectroscopy differs from MIR spectroscopy in the way in which these transitions are probed. MIR is a single photon absorption event whereas Raman is a two photon scattering event where the first photon hits the sample and a second photon is scattered back. The dominant scattering process is elastic scattering (Rayleigh scattering) which results in no energy change in the photons. One in every 10^6 – 10^8 photons will undergo spontaneous inelastic scattering, where the photon will lose or gain energy to or from the molecular vibrational energy levels; this is called Raman scattering.

The inelastic processes can involve the incident photon (energy of $h\nu_0$) contributing energy to the molecule resulting in a transition ($h\nu_0 - h\nu_1$), where energy given to the system from the scattered photon represents the energy gap between the ground and first vibrationally excited state (energy of $h\nu_1$). This is called Stokes scattering. The scattered photon may also gain energy from a transition between a vibrationally excited state falling back to the ground state ($h\nu_0 + h\nu_1$). This is called anti-Stokes scattering, and is weaker than the Stokes scattering due to the molecule needing to be in a vibrationally excited state when it interacts with the incident photon. This process is governed by a Boltzmann distribution which defines the relative population of energy states at a given temperature. Schematics of Rayleigh, Stokes and anti-Stokes transitions are given in Fig. 17.2.

The vibrational transitions that undergo IR absorption or Raman scattering are dependent on the nature of the vibrational modes. IR active modes require a change in the dipole moment in the vibration. An example of a strongly active IR transition is that of the O–H σ -bond stretch. The oxygen atom is more electronegative than the H, drawing electrons to itself and becoming slightly negative, denoted δ^- , whilst the hydrogen atom is slightly positive, denoted δ^+ . On extension and compression along the OH bond axis, the dipole is extended and compressed resulting in a change in the dipole moment, as seen in Fig. 17.3a. Conversely, Raman active transitions require a change in the polarisability (distortion of the electron cloud) of the vibrational mode. An example of a strongly Raman active system is C=C, where the π electron cloud is distorted with expansion and compression along the C=C axis as shown in Fig. 17.3b. This means that MIR and Raman are complementary techniques; molecules which are strongly IR active, such as water, tend to have a very weak Raman signal, and vice versa. Raman activity (or inactivity) can be used as an advantage when imaging pharmaceutical formulations. For example many APIs have high levels of conjugation, making them strongly Raman active, this means they have a strong signal compared with σ -bonded systems, which are common for many excipients.

Raman spectroscopy can be carried out using different experimental setups. The excitation photons are usually provided via a laser (historically arc emissions or

filtered sunlight were used). This light source is focused onto the sample and the scattered photons are collected, spectrally discriminated and detected. In modern times the two main methods of spectral discrimination and detection are Fourier transform (FT) and dispersive setups. FT systems are similar to those employed in FT-IR spectroscopy. Dispersive systems utilise a spectrograph to spatially separate the different wavelengths of light and image this signal onto a charged coupled device (CCD) detector. Raman imaging is experimentally carried out via coupling a Raman setup (CCD or FT based) to an optical microscope to enable measurements to be carried out on a small sample volume.

Like IR microscopy, the minimal sample volume measureable in a confocal setup is diffraction limited. The lateral resolution is described by Eq. (17.1) and the depth of field is described by Eq. (17.2). By changing the illuminating wavelength, the minimum sample spot diameter will change. For example if a setup has an objective with a NA of 0.90, the spot size at 785 nm will be 1.1 μm and at 532 nm will be 0.7 μm . The depth of field is also dependent on the refractive index of the sample. Therefore the approximate depth of field for Raman spectra of PMMA ($n = 1.5$) and silicon ($n = 3.4$) would be 3.9 and 8.9 μm , respectively, when measured at 532 nm with a NA of 0.9. It is important to remember that mixtures with components with varied refractive indexes will give a varied sample volumes, making any suggestions of a defined sample volume difficult (Everall 2010). Furthermore, in reality some low levels of signal will be detected from outside this sample volume. The relative amount of signal detected depends on the Raman scattering ability of the region being focused on and the nearby constituents. If the microscope is focused on a mixture component which is a poor Raman scatterer which is positioned above a component which is a good Raman scatterer, then the signal detected will likely contain signal associated with the neighbouring component. It is then hard to interpret if there are low levels of this component in the theoretical focal volume or if the component constitutes a nearby layer (McCreery 2000; Everall 2000a, b, 2009, 2010).

Further complicating the situation, when taking a series of measurements at varying depths, the position being measured within the sample may not be where one would expect it to be due to the change in refractive index of the air:sample interface. This means the spectra are collected from further into the sample than anticipated; this is called spherical aberration. To minimise the effects of spherical aberration, an oil immersion objective combined with an immersion fluid with the same refractive index as the sample is often used (Everall 2000b, 2009, 2010).

1.4.2 Coherent Raman

One of the challenges with Raman mapping and imaging is the inherently weak signal which can make analysis painfully slow. The Raman transition can be stimulated by the use of a second laser at the same frequency as the Stokes shifted light. Both anti-Stokes Raman spectroscopy (CARS) and stimulated Raman spectroscopy (SRS) utilise this phenomenon. CARS is a four photon

interaction, or four wave mixing process, where pump, Stokes scattering and probe photons interact with the sample to generate coherent anti-Stokes scattering (Cheng and Xie 2004). SRS is another form of coherent Raman imaging, but instead only pump and Stokes waves are utilised. When the difference in frequency between the two beams matches a vibrational mode a small fraction (about one millionth) of the incident energy is transferred between the two beams. To measure this small alteration, one of the input beams is intensity-modulated at high frequency. This modulation is transferred to the other beam and can be measured using sensitive photodetection. In contrast to CARS, SRS lacks a non-resonant background. The CARS and SRS processes are illustrated in Fig. 17.2.

Fully integrated commercial coherent Raman microscopes have only recently been commercialised with Leica being the first to market such a system (narrow-band CARS setup) around 2012. The major benefit of coherent Raman imaging (both CARS and SRS) compared to imaging based on spontaneous Raman scattering is the much more rapid imaging capability (several orders of magnitude). This allows video rate imaging which opens up the possibility for dynamic process analysis, as well as much shorter imaging times. In addition, coherent Raman imaging is inherently confocal (no requirement for a pinhole) with a slightly higher spatial resolution of approximately 200–400 nm laterally and 1 μm axially (inherent confocal nature) compared to conventional Raman mapping. Furthermore, autofluorescence (one-photon) interference, which can be a major problem when imaging pharmaceutical and cellular samples with conventional Raman microscopy, may be avoided in many cases. On the other hand spontaneous Raman mapping (less so imaging) gives richer spectral information which supports analysis of subtle spectral differences and analysis of complex mixtures.

Most coherent Raman microscope setups are also capable of detecting other non-linear optical phenomena during analysis (multimodal imaging). This includes sum frequency generation (SFG), including second harmonic generation (SHG) and two photon excited fluorescence (TPEF) (see Fig. 17.2 for schematics of these phenomena). SFG occurs when the energy of two photons is combined and the sample emits a photon with the higher energy. In SHG, the two incoming photons have the same energy. SFG occurs in situations which lack inversion symmetry. This includes non-centrosymmetric crystals (e.g. collagen and chiral pharmaceutical crystals) and boundaries.

The continual development of coherent Raman imaging systems capable of rapidly collecting CARS or SRS spectra (broadband or multiplex) are likely to provide richer spectral information in future and facilitate quantitative analysis. While spectra based on SRS and spontaneous Raman scattering are linear to concentration, CARS spectra are not (the resonant CARS signal scales quadratically with concentration). However, multiplex CARS spectroscopy allows quantitative analysis if the imaginary and linear to concentration component of the CARS signal is extracted, for example, by maximum entropy analysis (Rinia et al. 2007). For more information about quantitative CARS microscopy, readers are referred to an excellent review (Day et al. 2011a).

Several detailed reviews about coherent Raman imaging are available (Evans and Xie 2008; Zumbusch et al. 1999; Rodriguez et al. 2006). Reviews on coherent Raman imaging (and nonlinear optical imaging) tailored to a pharmaceutical audience have also been published (Strachan et al. 2011; Strachan 2012; Fussell et al. 2013b).

1.4.3 Near-Field Raman

The Raman signal can also be enhanced by near-field effects, this occurs when a sample is placed adjacent to a roughened metal surface, metal nanoparticles or between a sharpened tip and a metal surface. The techniques which utilise this are surface-enhanced Raman spectroscopy (SERS) and tip-enhanced Raman spectroscopy (TERS). The near-field or surface enhancement is believed to be due to a combination of three contributions: surface plasmon resonance, charge transfer between the molecule and metal conduction band and resonances within the adsorbed molecule (Lombardi and Birke 2009).

SERS imaging setups involve Raman microscopy with the sample of interest either applied to a roughened surface or metal nanoparticles applied to the sample surface. The spectra are collected using a wavelength of light which is associated with surface plasmon resonance of the roughened surface or metal nanoparticles. SERS signal only occurs in ‘hotspots’, which typically consist of sharp edges of nanoparticles or tight joins between two nanoparticles. Quantitative imaging with SERS using nanoparticles is very difficult as it is very much by chance as to whether the laser will be focused on a ‘hotspot’ to gain enhanced signal, making some components appear in higher concentrations by chance and not getting consistent spectra across the sample.

TERS overcomes this chance-based enhancement seen in SERS by using a nano-tip to generate enhancement in a given position. This can be done using scanning tunnelling microscope (STM) or atomic force microscopy (AFM) feedback setups for the tip (Schmid et al. 2013). Movement of this tip across a sample allows the generation of a spatially distributed spectral map with a spatial resolution approximately $100 \times$ smaller than that seen in diffraction limited systems (Sonntag et al. 2014; Pekdemir et al. 2012), some studies have obtained a resolution as low as 1.7 nm (Chen et al. 2014). TERS studies have focused on biological systems (Cialla et al. 2009; Elfick et al. 2010; Pekdemir et al. 2012), nanomaterials (Natelson et al. 2013; Saito et al. 2009) and method development (Dieringer et al. 2006; Poborchii et al. 2009). Recently, tip-enhanced CARS has also been reported (Furusawa et al. 2012). With the development of readily available TERS setups and manufactured tips it is likely that TERS will be more suitable for use in pharmaceutical applications.

1.5 Terahertz

Terahertz radiation lies between the MIR and microwave regions of the electromagnetic spectrum. It can be defined as having a frequency of between 0.05 and 4 THz, corresponding to $1.67\text{--}133\text{ cm}^{-1}$. It is somewhat synonymous with the far-infrared region, which has commonly been defined as having a spectral region of $400\text{--}10\text{ cm}^{-1}$ ($25\text{--}1000\text{ }\mu\text{m}$). In materials, terahertz radiation can induce rotational transitions (Fig. 17.2), low frequency bond vibrations, hydrogen-bonding stretches and torsion vibrations, and in solids, crystalline phonon vibrations (Chantry 1971; Möller and Rotschild 1971). Crystalline phonon vibrations can be thought of as collective vibrations constructed from the interaction of many intramolecular vibrations and require a periodic structure for propagation. Thus, crystalline materials are capable of sustaining crystalline phonon modes that appear as peaks in terahertz spectra, while amorphous materials lack the required long range order for phonon mode propagation and the energy associated with intermolecular vibrations is diffusely dissipated within the material, resulting in spectra that lack distinct peaks. Since the advent of commercially available terahertz spectrometers just over 10 years ago, the technique has been widely used for solid state analysis in pharmaceutical materials (e.g. (Strachan et al. 2004; Zeitler et al. 2007a); for more details see Terahertz Spectroscopy chapter in this book).

In terahertz pulsed imaging, structures within solid dosage forms can be resolved in three dimensions. Since most pharmaceutical excipients are (semi)transparent to terahertz radiation, some of the terahertz radiation will propagate into the sample. The core technology is the same as for terahertz pulsed spectroscopy (Shen 2011; Zeitler et al. 2007c). In short, terahertz pulses are generated using a femtosecond pulsed NIR laser that pumps a biased photoconductive antenna. The pulses are collimated and focused onto the sample, and the reflected or transmitted terahertz pulse is then collected and focused onto an unbiased photoconductive antenna for detection. Imaging may be performed using reflection (Fig. 17.5) or transmission setups.

In terahertz pulsed imaging involving reflection, structures within solid dosage forms can be resolved in three dimensions. Each time there is a boundary associated with a refractive index (RI) change, some of the terahertz pulse will be reflected. The terahertz pulse reflection is recorded as a time domain waveform. If the refractive indices of the different parts of a dosage form are known, the information about the dosage form may be directly converted into depth information (Fig. 17.6). The time domain waveform may be sequentially collected at multiple points across the sample surface to generate spatially-resolved information in three dimensions. With current commercially available terahertz imaging setups, different types of solid dosage forms (e.g. tablets, large pellets) are automatically rotated using a robotic arm allowing analysis to be performed from all directions with respect to the dosage form. Due to the longer wavelengths involved, lateral resolution at $150\text{--}250\text{ }\mu\text{m}$ in terahertz is poorer than for the other imaging techniques described in this chapter. However, information can be directly obtained deep (several

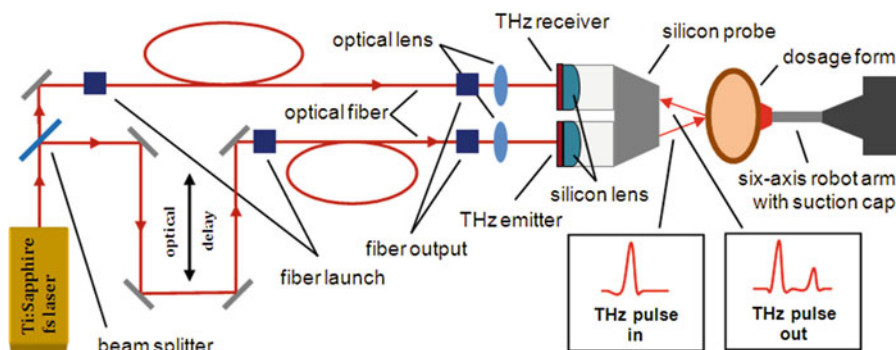


Fig. 17.5 Schematic of a terahertz pulsed imaging setup. The fs pulsed laser beam is split into probe and pump beams. Two optical fibres launch the beams and connect the spectroscopy unit to the terahertz emitter and detector within the imaging unit. The silicon lens setup (silicon probe) circumvents the need for nitrogen purging by minimizing the distance to the sample and therefore interference from water vapour absorption. A six-axis robotic arm is used to present the sample surface orthogonally to the terahertz radiation (based on a pre-generated topographic model) and thus the structure can be probed. From (Haaser et al. 2013a) with permission from Elsevier

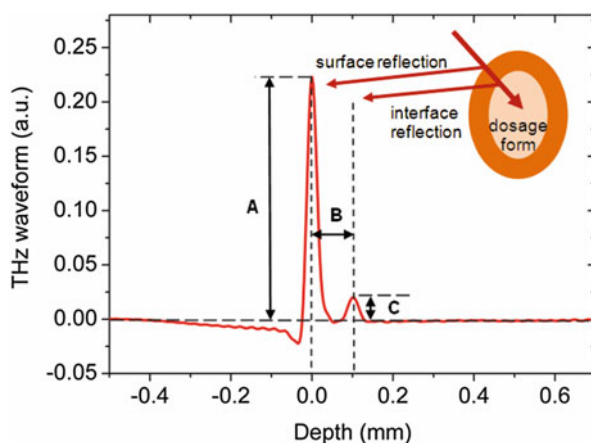


Fig. 17.6 A typical terahertz time-domain waveform calculated for a single-layer coated tablet. The first peak at 0 mm depth is due to the reflection at the surface of the coating layer. The peak at ~ 0.1 mm represents interface between the coating layer and the tablet core. From the terahertz waveform parameters such as (A) the peak intensity (directly related to changes of the RI and sensitive to signal scattering); (B) the time delay between the surface reflection and the coating/core interface reflection (used to calculate the coating thickness); and (C) the interface index (related to changes of the RI at the coating/core interface) are obtained. From (Haaser et al. 2013a) with permission from Elsevier

millimetres) into solid dosage forms with an axial resolution of 30–40 μm without any need for prior calibration standards. A single time domain waveform may be collected within milliseconds. Depending on the sample dimensions, a whole dosage form may be mapped within a few minutes.

In the transmission setup, the measurement is analogous to terahertz spectroscopy using transmission. However, the terahertz beam is focused onto the sample to obtain diffraction limited lateral spatial resolution. The terahertz signal is sequentially obtained for adjacent pixels as the focus is moved across the sample. The technique is sometimes referred to as terahertz spectroscopic imaging (but is most consistent with the mapping concept described at the start of this chapter). Using this transmission approach, the information is not sufficiently resolved in the z-direction for 3D imaging. Detailed spectral information can be obtained for 2D imaging. More detail about the technical aspects of terahertz imaging is provided in the Terahertz Spectroscopy chapter and briefly in Table 17.1.

2 Data Analysis

Converting spectroscopic data into an interpretable image can be done using univariate, bivariate and multivariate methods. Appropriate preprocessing before creating images based on the spectra is usually required. A brief outline of various preprocessing as well as uni-, bi- and multivariate analysis methods will be discussed here.

2.1 Spectral Preprocessing

Spectral preprocessing is often required to remove differences associated with spectral artefacts which are not associated with the chemical information of interest. For example, an enhanced baseline in a Raman spectrum can be associated with emission due to fluorescence or sample heating. This enhanced baseline hinders the direct use of a single band intensity to relate to a component's concentration, since the enhanced baseline gives the peak an enhanced intensity not associated with the single component concentration. Similar problems arise with variations in the spectral intensity scales due to focusing differences between samples and high noise signals masking spectral signals.

2.2 Noise Correction

Noise is the component of a spectrum which contains no useful information and consists of a random, often high frequency structure. The noise component of spectra comes from the detection of electrical and thermal sources by the detector, as well as statistics-based random events (Shaver 2001). The noise component of spectra is ideally minimised during spectral acquisition. This can be achieved by increasing the acquisition time and co-addition of multiple scans for most

spectroscopic techniques or also increasing the laser power or changing to a shorter laser wavelength for Raman spectroscopy (Shaver 2001; Adams 2004).

Post data acquisition, the high frequency noise component of spectra can be reduced artificially by smoothing methods which use a moving window to smooth the spectra. An example of this is moving average smoothing. Moving average smoothing artificially reduces the noise component of the spectra by taking portions of the spectra (windows), calculating the average value of that segment of the spectrum (window of $2n + 1$ x -values) and replacing the centre value in the segment with the average for the $2n + 1$ points. The process is then repeated by moving the window along by one point spectrum value. This continues for all x -values in the spectrum by moving the window along (CAMO 2012; Beebe et al. 1998). Similarly, a polynomial can be fitted to the window and used to find the centre value instead of an average, this is called Savitzky-Golay smoothing (Savitzky and Golay 1964; Steinier et al. 1972).

The segment size is an important parameter in smoothing methods. If the segment size is too narrow then little to no noise reduction will occur. Similarly, if the segment size is too large, the resolution between close-lying bands may be lost. The ideal segment size depends on the spectra in question.

2.3 Baseline Correction

Baseline correction is used to remove elevated baselines associated with sampling orientation, diffuse scattering or sample emission. The selection of an appropriate baseline correction method is important. If the baseline profile is curved then a polynomial baseline is appropriate or if the spectra are not noisy then a derivative of the spectra can be taken. If the baseline is linear and just offset then a linear baseline correction or baseline offset correction is appropriate.

Linear baseline correction acts to remove a linear slope from a given spectrum by creating a straight line between two endpoints. This method works well for smaller ranges of data, or spectra with an approximately linear slope in the baseline, such as those associated with different foci. However, when a spectrum has a curved baseline then this baseline correcting technique is not effective. The mathematical representation of linear baseline correction for a single spectrum is

$$\mathbf{x} = \bar{\mathbf{x}} + \alpha + \beta\mathbf{x} \quad (17.3)$$

where \mathbf{x} is the vector representing the spectrum as a whole, $\bar{\mathbf{x}}$ is the spectral vector representing the spectral features of interest (i.e. in this case the spectra), α and β are the estimated slope and offset which are based on at least two points which are thought to contain only baseline information (Beebe et al. 1998).

An n -order polynomial can be fitted to a spectrum with a specific number of approximate baseline points. The polynomial is subtracted from the spectrum to

remove large, curving baselines. This is particularly useful for fluorescence and thermal type baselines.

Differentiation acts to remove the effects of the baseline by replacing each point in the spectrum with the slope at each point in the spectrum calculated from a chosen window size. However, this also decreases the signal-to-noise ratio of the spectra and changes the band shape, making complex spectra harder to interpret. Differentiation can also be used to distinguish shoulders and small bands hidden within large bands (Adams 2004).

2.4 *Scaling and Scatter Correction*

Differences in scale can occur due to changes in the optical path length (focus) and variation in the sample surface. The scale and nature of the spectra will be different depending on sample focus, with differences in intensity and sample volume being measured from focusing slightly above, at, or below the sample surface. Correction of the scale differences can be performed by normalisation methods, such as mean and peak normalisation, or by scatter correcting methods, such as standard normal variate (SNV) and multiplicative scatter correction (MSC), which also correct for some differences in the baseline.

Mean normalisation calculates a new value for each point along a given sample x_j by dividing each point x_k for that sample by the mean of the sample \bar{x}_i as shown here

$$X_{i,k} = \frac{X_{i,k}}{|\bar{X}_i|} \quad (17.4)$$

where $X_{i,k}$ is a matrix (or vector if $i = 1$) with i samples and k variables per sample. Each x -value of the samples of the matrix $X_{i,k}$ is divided by the average for the sample in the data matrix (\bar{X}_i) (CAMO 2012).

Peak normalisation (or area normalisation) corrects for differences in the scale between spectra by taking the integral of a specific band, representative of a specific component which may be used as an internal standard. The area under the curve is normalised to equal one, with the rest of the spectra correspondingly scaled.

The SNV transformation removes scatter effects by centering and scaling each spectrum independently in the data set. Mathematically SNV transforms the dataset by the equation

$$x_{i,k}^{\text{SNV}} = \frac{x(i,k) - \bar{x}_i}{\sigma} \quad (17.5)$$

where x_i are the spectral values of a sample (i), \bar{x} is the mean of all the x_i in the sample and σ is the standard deviation of the sample (Barnes et al. 1989; CAMO 2009–2012).

MSC also acts to correct for both baseline slope and offset effects. MSC fits a regression line to each sample spectrum, with the regression line for each spectrum described by

$$x_{i,k} = a + b\bar{x}_k + \eta_i \quad (17.6)$$

where x_1, \dots, x_k are the spectral values of a sample, and $\bar{x}_1, \dots, \bar{x}_k$ are the average values from the calibration samples. The a and b coefficients, for intercept and slope, respectively, are calculated using least squares regression for each wavelength (CAMO 2012; Isaksson and Naes 1988).

The coefficients a and b , found in the above equation, are then applied to the following equation

$$x_i^{\text{MSC}} = \frac{x_i - a}{b} \quad (17.7)$$

where the MSC corrected x points (x_i^{MSC}) are equal to the initial point value (x_i), subtracted by the baseline of the spectrum (a) and then divided by the slope of the spectrum (b) (CAMO 2012; Isaksson and Naes 1988).

2.5 Univariate Analysis

Univariate images are based on a single variable from the spectra, such as peak intensity at a single wavelength or the integral of a band. This is a very simple method which is easy to implement and interpret. The limitations of this method include the potential to exclude valuable information and to get false intensities based on baseline and scale of the spectra (if not properly preprocessed). Furthermore, non-overlapping spectral bands are generally required.

2.5.1 Peak Intensity

Peak intensity false colour maps are commonly used for looking at the spatial distribution of a single component (Balss et al. 2008; Franzen and Windbergs 2014; Rizi et al. 2011; van Apeldoorn et al. 2004). A requirement for this imaging analysis to work is the presence of an intense band representing the chemical of interest which is not masked by signal from other components. The spectra also need to be appropriately preprocessed so that differences due to scale are not contributing to the image.

2.5.2 Peak Integral

Peak integral false colour maps are similar to peak intensity maps, where a single variable is used to create an image of the spatial distribution of a specific component (Almeida et al. 2012; Balss et al. 2008). The single variable used is the integral (area under the curve) of a band. The way in which the integral is calculated is important, such as the creation of a linear baseline between integral endpoints in a spectrum with an enhanced baseline. Like peak intensity, the chosen band needs to be located in a spectral region where it is not masked by other constituents. The selection of appropriate preprocessing is again very important, particularly a normalization method to remove differences based in sample focus. Small changes to the band intensity, band-width and peak position tend to be hidden in this measurement.

2.5.3 Bandwidth

The bandwidth or full width half maximum (FWHM) has been used to look at how a given component changes across a sample (Vervaeck et al. 2013). The bandwidth is useful for looking at the crystallinity of a drug distributed across a sample, with a broader band indicative of a more amorphous structure.

2.6 *Bivariate Analysis*

Bivariate imaging is a popular method of imaging analysis (Balss et al. 2008; Breitenbach et al. 1999; Karavas et al. 2007; Zhang et al. 2007). Bivariate images consist of a ratio between two parameters such as the peak intensities or integrals of two independent bands. The use of two bands can be considered an internally normalised method, where the relative amounts of two different sample components are directly compared across the imaged sample.

2.7 *Multivariate Analysis*

Multivariate methods utilise many variables, this means a whole spectrum with its associated components contribute to the image. Common multivariate methods used for imaging include principal component analysis (PCA), classical least squares (CLS), partial least squares regression (PLSR), multiple curve resolution (MCR; also known as multivariate curve resolution) and band target entropy minimization (BTEM). A brief introduction into what these techniques can do is given here. Appropriate preprocessing is important for multivariate analysis

methods, for example in PCA if there is variance associated with scale and baseline they will appear in the model and possibly hide the more interesting differences associated with the chemical or physicochemical composition.

2.8 Principal Component Analysis (PCA)

PCA is a tool used to significantly reduce the dimensionality in large datasets. For example spectra with hundreds to thousands of variables can be reduced to, for example, two or three dimensions called principal components (PCs) (Beebe et al. 1998). This simplification is based on the variance across the dataset, with each spectrum represented as a single point in 2D or 3D PC space. The variance across each reduced dimension (PC) can be interpreted back to the spectra via the loadings plot (what the variance in a given PC looks like). If a loadings plot shows spectral differences of interest, the values of each individual spectrum for the PC can be used to create a false colour map showing the distribution based on the separating features. In pharmaceutical applications the separating features might be associated with different formulation ingredients (active drug, different excipients) or the distribution of different solid state forms of a single component. It is important to note that this is a qualitative method; PCA cannot be used to quantify components.

2.9 Classical Least Squares (CLS)

CLS is a quantitative method which is used in well-defined systems where all the components are known and pure spectra have been acquired (Beebe et al. 1998). CLS requires that there is a linear relationship between measurement and concentration. The concentration of a given component from CLS is used to create the false colour images of the spatial distribution of a single component. This method is often used for quantitatively mapping the spatial distribution of an API (Balogh et al. 2014; Breitzkreitz et al. 2013; Nagy et al. 2012).

2.10 Partial Least Squares Regression (PLS)

PLS is another quantitative method which also requires a linear relationship between measurement and concentration. However, unlike CLS, it is more robust to less defined systems which may contain additional undefined ingredients (CAMO 2009–2012; Beebe et al. 1998). A model is created based on known mixtures and their concentrations; this is then used for unknowns to give the predicted concentration of a given formulation component. These concentrations can be used to create false colour maps of the given component distribution across a sample.

2.11 Multiple Curve Resolution (MCR)

MCR is a qualitative and/or quantitative method used to find linear combinations of pure components in a mixture or system. MCR decomposes the initial series of spectra into the pure component spectra and their relative concentrations (CAMO 2009–2012; R. and A. 2006). To quantify based on these curves, some known mixtures are required to calibrate the concentrations. Like CLS and PLS, the concentrations given from MCR can be used to spatially map the distribution of ingredient concentrations using false colour maps.

2.12 Band Target Entropy Minimization (BTEM)

BTEM is a self-modelling curve resolution technique which does not require reference spectra or prior information to find pure constituents (Chew et al. 2002; Widjaja et al. 2002, 2003a, b; Widjaja and Seah 2008). Like MCR, the output of this analysis gives the pure component spectra and the relative amounts of those components.

3 Pharmaceutical Applications

3.1 Drugs and Dosage Forms

Vibrational spectroscopic imaging of drugs and dosage forms during preformulation, formulation and processing has been investigated extensively with MIR, NIR, terahertz and Raman spectroscopic techniques over the last two decades. A selection of studies in which various drugs and dosage forms have been imaged using the aforementioned imaging techniques are presented in Table 17.2 and some of these are highlighted in more detail below. In this and the subsequent sections on imaging drug release/dissolution and drug delivery, the examples are intended to illustrate the types of analyses that are possible rather than form a comprehensive review of all pharmaceutical applications.

3.2 MIR Imaging

In pharmaceuticals, FTIR imaging has been most widely used to characterise component distribution in solid dosage forms (Table 17.2), for example tablets (Roggo et al. 2005a; Ricci et al. 2007) and microsphere matrices (van der Weert et al. 2000; Mei et al. 2003; Chan and Kazarian 2004b). One example of drug distribution

Table 17.2 Selected studies involving vibrational spectroscopic imaging of drugs and dosage forms

Technique	Purpose	Sample type	Conclusions	Reference
FTIR	Study FTIR imaging as a high-throughput analysis tool	Solutions with PEG and ibuprofen/nifedipine	It was possible to analyse ca. 100 samples simultaneously when FTIR was combined with a microdroplet device	Chan and Kazarian (2005)
FTIR	High-throughput visualization of crystallization	Thin drug films	It was possible to monitor drug crystallization	Chan et al. (2007)
FTIR	Image the distribution and secondary structure of enzyme	<i>Candida antarctica</i> lipase B in polymeric matrix	IR imaging revealed that enzyme was localised in an external shell of the polymer matrix	Mei et al. (2003)
FTIR	Analyse contaminated tablets and tablets with different dissolution profiles	Tablets	No contamination was observed and chemical composition of the surface of the tablets explained different dissolution profiles	Roggo et al. (2005a)
FTIR	Visualise lysozyme distribution and conformation in PLGA microspheres	PLGA/lysozyme microspheres	Protein was homogeneously distributed in the spheres	van der Weert et al. (2000)
Hot stage FTIR thermomicroscopy	Obtain information about the solid state of the drug	Pure drug, carbamazepine	Different polymorphic forms were detected	Rustichelli et al. (2000)
FTIR	Characterise genuine and counterfeit anti-malarial tablets	Tablets	FTIR together with other vibrational spectroscopy techniques could be used to visualise the compositions in tablets	Ricci et al. (2007)
FTIR	Study water sorption in a pharmaceutical formulation	Tablets, PEG/griseofulvin	FTIR revealed that water sorption occurs mostly in PEG areas, no changes in drug distribution were observed	Chan and Kazarian (2004b)
Raman	Study drug distribution in a transdermal drug delivery device	Oestradiol patch	Oestradiol crystals were observed in a drug patch	Armstrong et al. (1996)

(continued)

Table 17.2 (continued)

Technique	Purpose	Sample type	Conclusions	Reference
Raman	Visualise the drug distribution in vaginal rings	Silicone elastomer reservoir-type vaginal ring, HIV microbicide candidate	The drug was observed in the core and the sheath of the ring	Bell et al. (2007)
Raman and NIR	Visualise drug distribution within tablets	Tablets	Drug and excipients were possible to observe using Raman + NIR together	Clarke et al. (2001)
Raman	Study solid structure including distribution, physical state and presence of polymorphs	Hot melt solid dispersion, nimodipine/PEG	It was observed that part of the drug existed in the form of crystals and the drug was not uniformly distributed	Docoslis et al. (2007)
Raman	Identify particle composition, size and size distribution	Beclomethasone nasal sprays	The API could be discriminated from excipients and the general shape of the API could be identified	Doub et al. (2007)
Raman	Study distribution of API and ingredients on granule surfaces	Granules	Ingredient distribution could be specifically analysed	Fujimaki et al. (2009)
Raman	Study API distribution and solid state	Melted solid dispersion	API distribution and co-existence of crystal and amorphous forms could be visualised	Furuyama et al. (2008)
Raman	Observe if a poorly water-soluble drug is dispersed in polymeric matrix as amorphous nanodispersions or molecular dispersions	Solid dispersions, felodipine	Combined methods showed that felodipine forms amorphous nanodispersions in PVP over a certain concentration range	Karavas et al. (2007)
Raman	Characterization of drug polymorphs	Tablets, chloramphenicol palmitate	Raman together with multivariate data analysis revealed the presence of various polymorphs in the tablets	Lin et al. (2006)
Raman	Study solid state of API	Thermal inkjet dispensed prednisolone	Two different polymorphs were observed in the samples	Melendez et al. (2008)

Raman	Study physical status of API and understand drug release properties	Extruded and electrospun samples drug-polymer matrices, spirinolactone	The electrospun method showed efficient amorphisation	Nagy et al. (2012)
Raman	Study the evolution of drug content inhomogeneity as a function of granulation time	Ibuprofen granules	Raman mapping could be used to observe drug distribution in granules	Poutiainen et al. (2011)
Raman	Visualise tulobuterol in transdermal tapes	Transdermal film	Visualisation of drug distribution in tapes was achieved; it was also possible to detect differences in crystal growth	Sakamoto et al. (2009)
Raman	Image two drug molecules in a dry powder inhaler formulation	Metered-dose inhaler deposits	Both APIs could be observed	Sasic and Harding (2010)
Raman	Study how different manufacturing methods affect component distribution and API solid state	Tablets, imipramine	Tablets made by different manufacturing techniques could be distinguished	Vajna et al. (2010)
Raman	Probe content uniformity of a lipid based powder for inhalation	Inhalation powder	Homogenous distribution of API was successfully employed	Schoenherr et al. (2009)
Raman	Study drug distribution in combination pressurised meter-dose inhalers	Metered-dose inhaler deposits, salbutamol, beclomethasone dipropionate	APIs could be mapped successfully	Steele et al. (2004)
Raman	Study tablet compositions from tablets made by different manufacturing methods	Tablets, Isoptin SR-E, Isoptin SR	Raman techniques revealed that both tablets contained the same excipients and distribution of components was successfully mapped	Vajna et al. (2011b)
Raman	Characterization of drug-excipient interactions between drug and cyclodextrins	Lyophilised powder	Raman mapping was found to be suitable to detect traces of pure crystalline API	Vajna et al. (2011a)
Raman	Visualise amorphous domains in the surface of sorbitol disks	Sorbitol disk	Raman microscopy could be used to detect amorphous and crystalline sorbitol	Ward et al. (2005)

(continued)

Table 17.2 (continued)

Technique	Purpose	Sample type	Conclusions	Reference
Raman	Detection of minor components in tablets	Tablet	Raman microscopy together with suitable data treatment revealed excipients in as small concentrations as 0.2 wt%	Widjaja and Seah (2008)
Raman	Detection of trace crystallinity	Hot melt extruded polymer dispersions	Trace crystallinity could be detected	Widjaja et al. (2011)
Raman	Observing crystalline and amorphous drug on the surface of the tablet	Tablets	It was possible to image the distribution of crystalline and amorphous API on the surface of the tablet	Nakamoto et al. (2013)
Raman	Visualise component distribution in a pharmaceutical tablet	Bilayer tablet	Components could be mapped using Raman microscopy and multivariate data-analysis	Zhang et al. (2005)
CARS	Study spontaneous formation of lipid structures in emulsions	Dodecane emulsions	CARS could be used to image variation in composition of emulsions	Pautot et al. (2003)
CARS	Visualise the distribution of drug in an inhalation mixture	Mixture of lactose carrier particles and micronised drug	The drug distribution was able to be visualised	Fussell et al. (2014a)
CARS	Visualise the drug distribution and solid state in drug-loaded silica particles	MCM-41 silica particles loaded with itraconazole and griseofulvin	It was possible to see different distribution patterns between the two drugs and that the drug was amorphous	Fussell et al. (2014b)
SRS	Image API and excipients within tablets	Amlodipine besylate tablets	API and excipients could be detected from tablets	Slipchenko et al. (2010)
NIR	Detect API and excipients in tablets	Tablets	API and excipients could be mapped with multivariate data-analysis	Gendrin et al. (2007)
NIR	Create chemical images of each ingredient in a formulation which had problems in processing	Blends and tablets	Chemical images could be created together with multivariate data-analysis, such as PCA	Clarke (2004)

NIR	Identify counterfeit medicines	Tablets, bisoprolol	Near infrared chemical imaging with multivariate data-analysis was effective technique for detecting counterfeits	Puchert et al. (2010)
NIR	Study how process-related changes affect dissolution	Tablets	NIR could be used to detect qualitatively differences due to granulation, compaction force and coating parameters	Roggo et al. (2005b)
NIR	Visualise drug and excipients distribution in a tablet and compare different calibration approaches	Tablets	PLSI method proved to be the most accurate method to create chemical images	Ravn et al. (2008)
NIR	Study powder blend homogeneity	Powders, salicylic acid, lactose	NIR imaging could be used to visualise powder homogeneity and mixing level	El-Hagrasy et al. (2001)
NIR	Study powder blend homogeneity	Tablets	NIR spectral imaging could be used to ensure the tablet blend quality qualitatively and quantitatively	Lyon et al. (2002)
NIR	Study powder blend homogeneity and compare different multivariate data-analysis techniques	Binary mixtures, ibuprofen and starch	Often combinations of different multivariate data-analysis methods are preferred	Amigo et al. (2008)
NIR	Study how grinding time affect the distribution of chemical components in a tablet	Tablets	NIR with chemometrics revealed the components distribution as a function of time	Awa et al. (2008)
NIR	Quantify the distribution of major and minor components in a tablet	Tablets	The best results were obtained with NIR when an augmented version of multivariate curve resolution was used	Amigo and Ravn (2009)
NIR	Form density profiles in a tablet	Tablets, lactose, magnesium stearate	Results showed that NIR chemical imaging can be also used to monitor density of substances in tablets	Ellison et al. (2008)

(continued)

Table 17.2 (continued)

Technique	Purpose	Sample type	Conclusions	Reference
NIR	Image over-the-counter drug tablets	Tablets, particles	Using PCA, API and excipients could be imaged from the tablet	Koehler et al. (2002)
NIR	Study the distribution of API and excipients in a tablet and visualise the coating thickness and the coating distribution	Tablets	The distribution of components could be visualised as well as the coating thickness and distribution of the coating material	Palou et al. (2012)
NIR	Studying homogeneity of protein-sugar mixtures	Tablets	NIR imaging is a suitable technique for studying the homogeneity of dried protein formulations	Jovanovic et al. (2006)
NIR	Use NIR chemical imaging for studying content uniformity of tablets	Tablets	NIR chemical imaging could be used to study content uniformity of tablets	Lee et al. (2006)
3D TPI	The first example of non-destructive imaging and comparison of structures of different sugar coatings on tablets	Two brands of sugar-coated ibuprofen tablets	First application of TPI for pharmaceutical analysis. Multiple coating layers could be resolved as well as differences in coating thickness between brands. There was good agreement with photographs of cross-sections	Fitzgerald et al. (2004)
3D TPI	The first example of whole dosage form imaging of various coatings and interfaces in a range of solid dosage forms	Film-coated tablets, sugar-coated tablets, multilayered controlled release tablets, soft gelatin capsules	Non-destructive and rapid spatial and statistical analysis of multiple layers possible up to 3 mm within tablets. In soft gels, the thickness of the gelatin layer and seal characterization was possible	Zeitler et al. (2007b)

3D TPI	Non-destructive analysis of coating layer thickness, reproducibility, and uniformity sustained-release coated tablets	Ten sustained-release coated tablets from same lab-scale batch	Coating thickness was determined around entire tablets and was generally thinner for the central band than the tablet faces. Defects were characterised. Results were in good agreement with destructive optical microscopy	Ho et al. (2007)
3D TPI	Detection of differences in film coating thickness and drug layer uniformity of multilayered, sustained-release coated, standard size pellets	Pellets (1 mm diameter and high curvature) with a sugar starter core, metoprolol succinate layer and Kollicoat® SR:Kollicoat® IR polymer of different thicknesses	TPI could be used for film coating and drug layer thickness determination. The sampling setup used did not allow imaging over the entire surface of each pellet	Haaser et al. (2013b)
3D TPI	TPI was used to investigate the effect of the coating equipment on film coating structure and the results were correlated with subsequent dissolution behaviour	Six tablets each from fluid bed and drum coater coated with the same amount of the same delayed release coating formulation under recommended process conditions	A lower mean coating thickness and higher density for tablets coated in the drum coater compared to fluid bed coated tablets was imaged. This was correlated with a slower drug release	Haaser et al. (2013c)
TPI	Quantitative analysis of layer separation risk in bilayer tablets	Bilayer tablets (8 mm, biconvex) with lactose (130 mg, layer A) and mannitol (100 mg, layer B)	TPI could non-destructively detect cracks between component layers and predict the likelihood of separation	Charron et al. (2013) and Niwa et al. (2013)
3D TPI	Quantitative analysis of hardness and surface density distribution	Biconvex and flat-faced lactose monohydrate tablets prepared directly compressed with rotary tablet press	Surface refractive index (SRI) was mapped across tablet surfaces. SRI was strongly correlated with crushing strength, density and hardness	May et al. (2013)

(continued)

Table 17.2 (continued)

Technique	Purpose	Sample type	Conclusions	Reference
Terahertz spectroscopic imaging	Quantitative transmittance mapping of co-crystal and co-crystal former distribution in compacts	Compacts containing caffeine-oxalic acid cocrystal, or caffeine or oxalic acid in polyethylene matrix	Terahertz spectroscopic imaging could be used to resolve the domains of co-crystals and co-crystal formers. Co-crystal concentration determined matched the known total concentration	Charron et al. (2013)
Terahertz spectroscopic imaging	Terahertz spectroscopic imaging combined with component spatial pattern analysis for detection and identification of drugs concealed in envelopes	D-methamphetamine hydrochloride, DL-3,4-methylenedioxymethamphetamine hydrochloride (MDMA), and aspirin. Approx. 20 mg of each substance was placed in 10 mm ² polyethylene bags, which were then placed inside a paper envelope	Non-destructive detection and imaging of the drugs possible at a concentration of ~20 mg/cm ²	19

imaging involved the model protein (lysozyme) in poly(lactic-co-glycolic acid) (PLGA) microspheres, prepared by w-o-w solvent evaporation and imaged using transmission FTIR imaging (van der Weert et al. 2000). The microspheres (~ 150 μm volume-adjusted diameter) were embedded in Technovit 7100 (containing hydroxyethyl-methacrylate) and slices of approximately 5 μm thickness were prepared. It was possible to visualise the protein distribution (with diffraction limited spatial resolution) based on the absorbance intensity of characteristic IR bands: amide bands at 1550 cm^{-1} (amide II) and at 1650 cm^{-1} (amide I), and PLGA at 1756 cm^{-1} (spectral resolution 4 cm^{-1}). The embedding material surrounding the microspheres could be visualised using the characteristic band at 1720 cm^{-1} . From the false colour images lysozyme was found primarily inside the microspheres. The lack of lysozyme on the surface of the microspheres was confirmed from IR spectra obtained with an ATR setup (not spatially resolved) and FTIR-photoacoustic spectroscopy (FTIR-PAS). This analysis was then used to explain the lysozyme release behaviour. It was previously observed that there was a burst release of lysozyme from the microspheres and it was thought that it was due to the lysozyme localization on the surface. However FTIR imaging and IR spectroscopy showed that there was no lysozyme on the surface area of the microspheres. The reason for this burst release was apparently the diffusion of protein from cavities through water-filled pores in the PLGA matrix.

As mentioned above, water gives a strong signal in IR spectra. This water sensitivity can be used to monitor water sorption into pharmaceutical products. Water sorption during storage can cause solid state changes. FTIR imaging was used to study water sorption in thin films ($\sim 12\text{ }\mu\text{m}$) containing a mixture of polyethylene glycol (PEG) 80% (w/w) and griseofulvin 20% (w/w) (Chan and Kazarian 2004b). They placed samples on a BaF₂ disc that was located in a controlled temperature and humidity cell. The humidity conditions were modified by changing the ratio of dry and wet incoming air. The sorption of water could be imaged in transmission mode with a $15\times$ transmission objective and a 64×64 FPA detector producing a field of view of $266\times 266\text{ }\mu\text{m}$ with a spectral resolution of 16 cm^{-1} . Griseofulvin and PEG had characteristic IR bands at 1540 and 1240 cm^{-1} respectively, which could be used for imaging the distribution of these substances on the surface of the film (Chan and Kazarian 2004b). Water sorption was imaged using the broad water band at $3700\text{--}3100\text{ cm}^{-1}$. The temperature was kept constant at $25\text{ }^\circ\text{C}$ and the sample was exposed to relative humidity (RH) values of 0.5, 60, 70, 80 and 90%. The spectroscopic images revealed that griseofulvin was not homogeneously distributed in the PEG matrix, with separate areas of griseofulvin distinguishable in the matrix. Based on the IR spectra, the PEG was also found in the griseofulvin-rich areas, but not vice versa. Water sorption occurred mostly in the areas rich in PEG. By looking at the images obtained and based on semi-quantitative data achieved by integrating the absorbance of the broad water band, relatively little water sorption was observed at RHs from 0.5 to 60%. Above 60% RH, the amount of sorbed water increased substantially and doubled when the RH reached between 80 and 90%.

FTIR imaging has also been used to image polymeric solutions (Chan and Kazarian 2005) and solid state form distribution in pure drugs (Rustichelli et al. 2000; Chan et al. 2007) (see Table 17.2 for further examples). Whilst the resolution of FTIR imaging setups are diffraction limited to at best around 4 μm , the relatively new and exciting near-field techniques such as AFM-IR spectroscopy can reveal chemically specific information at nanoscale resolution. Van Eerdenbrugh et al. have used near-field IR imaging via the coupling of AFM to MIR spectroscopy to look at the micro- and nanostructure of a felodipine:poly(acrylic acid) blends (Van Eerdenbrugh et al. 2012). The instrument used was a nanoIR in contact mode with the spatial resolution of around 100 nm. The nano-IR imaging showed that the discrete sub-micrometre domains seen in the 50:50 mix consisted of felodipine rich amorphous regions and the continuous phase was dominantly poly(acrylic acid). Selected wavelengths were used to give false colour images of the blends based on the chemical constituents to give sub-micrometre scale chemical images.

3.3 Raman Imaging

3.3.1 Spontaneous Raman

Since APIs often contain strongly Raman scattering moieties, such as double bonded and especially aromatic groups, Raman microscopy can potentially be a more sensitive method than MIR imaging to detect API distribution in a wide range of pharmaceuticals. Other distinguishing features compared to MIR imaging include a generally higher spatial resolution (approximately 1 μm for a confocal setup), more flexible sampling arrangements, and minimal water sensitivity. Drug distribution has been imaged in, for example, powders (Vajna et al. 2011a), granules (Fujimaki et al. 2009), tablets (Widjaja and Seah 2008; Vajna et al. 2010, 2011b; Nakamoto et al. 2013), solid dispersions (Furuyama et al. 2008), inhalation formulations (Sasic and Harding 2010; Schoenherr et al. 2009; Steele et al. 2004) and transdermal tapes (Sakamoto et al. 2009).

While both imaging and mapping have been used, mapping appears to be the more common approach despite longer acquisition times (Gordon and McGovern 2011), perhaps due to the combined advantages of the possibility for confocality, a higher spatial resolution, and richer spectral information. Indeed, the spectra obtained with Raman mapping have been subjected to diverse univariate, bivariate and multivariate analysis methods to maximise spectral interpretation. The multivariate methods include *K*-means clustering (KM), PCA, CLS and MCR (Zhang et al. 2005). Zhang et al. directly compared the use of different multivariate data analysis methods and the resulting chemical maps (Zhang et al. 2005). Direct CLS was selected as a multivariate method that requires reference spectra of pure components. PCA, MCR and cluster analysis were chosen as methods that do not require reference information (unsupervised methods). The sample was a bilayer tablet that had two chemically and optically distinguishable layers (a stock placebo

blend from lactose, Avicel® and magnesium stearate was prepared and divided into two portions with 2 % red dye in one layer and 5 % sodium benzoate (API) in the second layer). The Raman spectra were collected using a 785 nm excitation laser through a $50\times$ objective. The sampling area was $400\times 400\ \mu\text{m}$ with a step size of $10\ \mu\text{m}$ in the x - and y -directions. All of the multivariate data-analysis methods had some strengths and weaknesses in this particular study. Since, direct CLS required reference spectra of samples it was considered to be the most accurate method and false-colour images obtained using other methods were directly compared to those obtained using direct CLS. The PCA images resembled direct CLS images to some degree (and were considered an effective method for exploratory data-analysis). KM cluster analysis was a useful tool to automatically separate the image into areas containing similar chemical composition. In this case, the MCR images were similar to the direct CLS images (with MCR it is important to ensure the calculated resolved component spectra resemble those of the pure components before any false colour images are interpreted). In general, the most suitable data analysis methods are both sample and even instrument specific, and not necessarily obvious. This study, therefore serves as an example to show that careful data analysis method selection and testing is just as important as spectroscopic imaging method selection.

Besides imaging drug (and excipient) distribution, Raman microscopy can be used to study polymorph and crystallinity distribution in pharmaceuticals since different solid state forms of an API usually have different Raman spectra. Nakamoto et al. showed how crystalline and amorphous forms of ethosuximide (ESM) can be distinguished in a model tablet containing ESM together with several excipients (lactose monohydrate, microcrystalline cellulose, hydroxyl-propyl-cellulose and magnesium stearate) (Nakamoto et al. 2013). One batch was a placebo, one contained 100 % of crystalline ESM and the other three batches contained amorphous ESM in varying proportions. One of the batches was almost completely amorphous (2.5 % crystallinity). Raman spectra of the excipients and ESM were recorded using a Horiba LabRAM ARAMIS system with a 532.09 nm diode laser and a $50\times$ objective. The excipients did not have any Raman peaks in the $2000\text{--}1500\ \text{cm}^{-1}$ region, leaving a clear window for the ESM signal. Crystalline ESM had two peaks at 1758.3 and $1705.2\ \text{cm}^{-1}$ and amorphous ESM had one peak at $1767.6\ \text{cm}^{-1}$. Differences in the spectra allowed visualization of crystalline and amorphous ESM on the surface of a tablet. A direct CLS model was used after baseline correction and normalization to create the images. Crystalline ESM was found on the surface of the tablets containing 100 % crystalline ESM and amorphous ESM was found on the surface of tablets containing ESM mostly in the amorphous state. It was also possible to detect areas of amorphous ESM among the crystalline ESM on the surface of tablets containing both forms of ESM.

Imaging approaches are potentially capable of very early detection of solid state changes, such as phase separation and crystallisation during storage (compared to non-microscopic spectroscopic analysis), since, if data at enough pixels are collected, some are likely to represent those of the newly formed solid state form or phase separated component. Furthermore, the different forms/components may be detected with Raman microscopy even if the API is at a low concentration in the

formulation. This heightened potential for sensitive detection by collecting data at multiple pixels needs to be balanced with the drawback of increased data collection time compared to macroscopic spectroscopic analysis.

3.3.2 Coherent Raman

CARS microscopy is the most widely investigated coherent Raman imaging method in pharmaceuticals. The earliest drug formulations imaged with CARS microscopy were emulsions (Pautot et al. 2003). Emulsions and other lipid based formulations are particularly suitable for coherent Raman microscopy, since lipid structures contain many C–H stretching modes that give strong CARS signals at wavelengths easily detected with current setups. Other lipid based formulations that have been imaged include solid lipid extrudates and lipid based matrix tablets (Jurna et al. 2009; Windbergs et al. 2009).

Recently, CARS microscopy has been used to image protein distribution in lipid microparticles (Christophersen et al. 2015). Lysozyme distributions inside solid lipid microparticles (SLMs) prepared from different lipid excipients and by different techniques were imaged and dissolution profiles of these different SLMs were compared to obtain information about how drug distribution and preparation method affect drug release and dissolution. The lipid excipients were glyceryl trimyristate, glyceryl distearate and glyceryl monostearate. SLMs were prepared by melting and mixing the lipid with either an aqueous protein solution (w/o/w method) or powdered protein (s/o/w method), followed by mixing with a polyvinyl alcohol solution. The CARS microscope was the first commercialised fully integrated CARS setup, and was capable of narrowband CARS imaging (Leica TCS SP8 CARS microscope). To identify suitable CARS wavenumbers (shifts) for imaging the different components, CARS spectra of the lipids and lysozyme were first recorded between 2700 and 3300 cm^{-1} (this involved manual tuning of the optical parametric oscillator (OPO) sequentially to each CARS shift). The lipids had a peak maximum at about 2860 cm^{-1} (CH_2 stretching), while lysozyme had a peak maximum at 2940 cm^{-1} (Fig. 17.7c). The spectrally overlapping signals were separated using a cluster analysis algorithm in the microscope software, with weighting factors for the two components (represented by 2860 and 2940 cm^{-1} for lipid and protein respectively), applied individually for each sample. Lysozyme could be visualised within virtual cross sections of all the SLMs using CARS, with the data for each image taking seconds to record (Fig. 17.7a). Lysozyme had localised in the core of SLMs prepared by the w/o/w method from glyceryl trimyristate and glyceryl distearate. The CARS images were compared with transmission electron microscopy (TEM) images, which confirmed that these particles had a well-defined shell structure (Fig. 17.7b). The situation was different in the case of SLMs prepared by w/o/w method from glyceryl monostearate. In some cases the lysozyme had distributed unevenly into many small cavities or close to the surface within a hollow space. TEM pictures revealed that this could be because of a loose shell structure of these particles. The

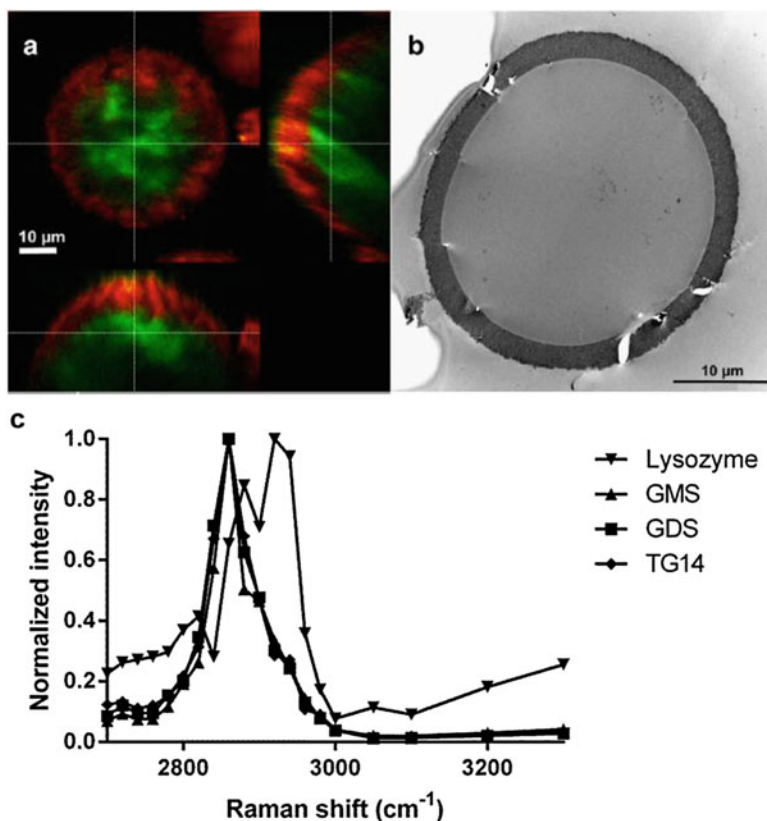


Fig. 17.7 (a) Overlay of CARS images at 2860 cm^{-1} (red, representing lipid) and 2940 cm^{-1} (green, representing lysozyme) of a lysozyme loaded trimyristin (TG14) solid lipid microparticle prepared by the w/o/w method. The cross-sectional projections show the lysozyme encapsulated in the hollow core. (b) Transmission electron microscopy image of solid lipid microparticle. (c) Normalised CARS spectra of lysozyme, glyceryl monostearate (GMS), glyceryl distearate (GDS), and TG14. Adapted from Christophersen et al. (2015) with permission from Elsevier

glyceryl monostearate and glyceryl distearate SLMs prepared by the s/o/w method, had a similar drug distribution compared to the w/o/w particles. However in SLMs made from glyceryl tristearate, the drug was localised in a smaller area. Also TEM images revealed that the hollow core-shell structure was missing. The particles prepared with different excipients and preparation methods exhibited substantially different lysozyme release profiles, which could be explained by the different lysozyme distributions. This is just one example that illustrates the potential of coherent Raman imaging to reveal important information about drug distribution and subsequently drug release behaviour.

Polymer dispersions are also suitable for CARS analysis. Kang et al. have used CARS microscopy for imaging paclitaxel drug distribution and release from a polymer film (Kang et al. 2007). Paclitaxel distribution was detected in many

types of polymer films with a lateral resolution of $0.3\ \mu\text{m}$ and a depth resolution of $0.9\ \mu\text{m}$, which is higher than what can be achieved with diffraction limited spontaneous Raman imaging/mapping setups.

In several cases, the advantages of the superior 3D spatial resolution and imaging speed of coherent Raman microscopy compared to conventional Raman microscopy have been demonstrated for the same type of dosage form. Spontaneous Raman microscopy has been used to image two active pharmaceutical ingredients (APIs) in inhalation blends (Sasic and Harding 2010). The chemical images formed based on these spectra revealed the presence of both APIs on the surface of lactose. However the chemical images were quite pixilated, with a lateral spatial resolution of $\sim 5\ \mu\text{m}$. CARS microscopy was used by Fussell et al for the same purpose, albeit with a better spatial resolution of about $0.4\ \mu\text{m}$ laterally and $1\ \mu\text{m}$ axially (Fussell et al. 2014a). Budesonide and salmeterol distribution was determined in an inhalation powder mixture with lactose carrier particles. The CARS microscope was a homebuilt system consisting of a picosecond pulsed laser operating at $1064\ \text{nm}$ combined with an OPO that were used to tune the Stokes beam to suitable CARS resonances for the different components ($2888\ \text{cm}^{-1}$ for lactose, $3046\ \text{cm}^{-1}$ for budesonide and $3050\ \text{cm}^{-1}$ for salmeterol). The laser beams were focused onto the inverted microscope using $60\times$ and $40\times$ objectives. Using the intensities at the selected frequencies for each component, it was possible to visualise salmeterol (Fig. 17.8) and budesonide distribution on the surface of lactose carrier particles. Often electron microscopy is used for imaging drug particles on the surface of a lactose carrier particle with very good spatial resolution. In this study images taken by CARS microscopy were compared to those taken with scanning electron microscopy (SEM). SEM is not a chemically specific method and therefore identification of drug particles is based on the morphological properties of a material, which might be difficult or impossible at times. In this study, after 0.5 min of mixing the inhalation blend, it was possible to detect salmeterol on the surface of lactose just by looking the SEM pictures based on a typical plate-like morphology. The chemically-specific CARS images confirmed this. Prolonged mixing causes plastic deformation and aggregation; hence the plate-like salmeterol particles were not detected after 600 min of mixing from SEM images. CARS microscopy revealed that the round-shaped particles on the surface of lactose were salmeterol in a different morphology.

This study clearly highlights some of the benefits of CARS microscopy compared to imaging based on spontaneous Raman scattering. Better spatial resolution can be achieved when CARS microscopy is used, allowing detection of submicron particles. With the use of image analysis software, it is possible to form particle size distribution profiles from CARS images. In the same study, Fussell et al. compared the size distribution of budesonide particles based on CARS image analysis method and laser diffraction analysis. The CARS image analysis method produced slightly larger particle sizes. Inherent confocality is also a benefit in CARS microscopy, allowing depth scanning. A nice example of this was included in this study where a lactose particle was scanned from bottom to top allowing visualization of drug penetration and surface curvature. As shown, CARS microscopy can be an

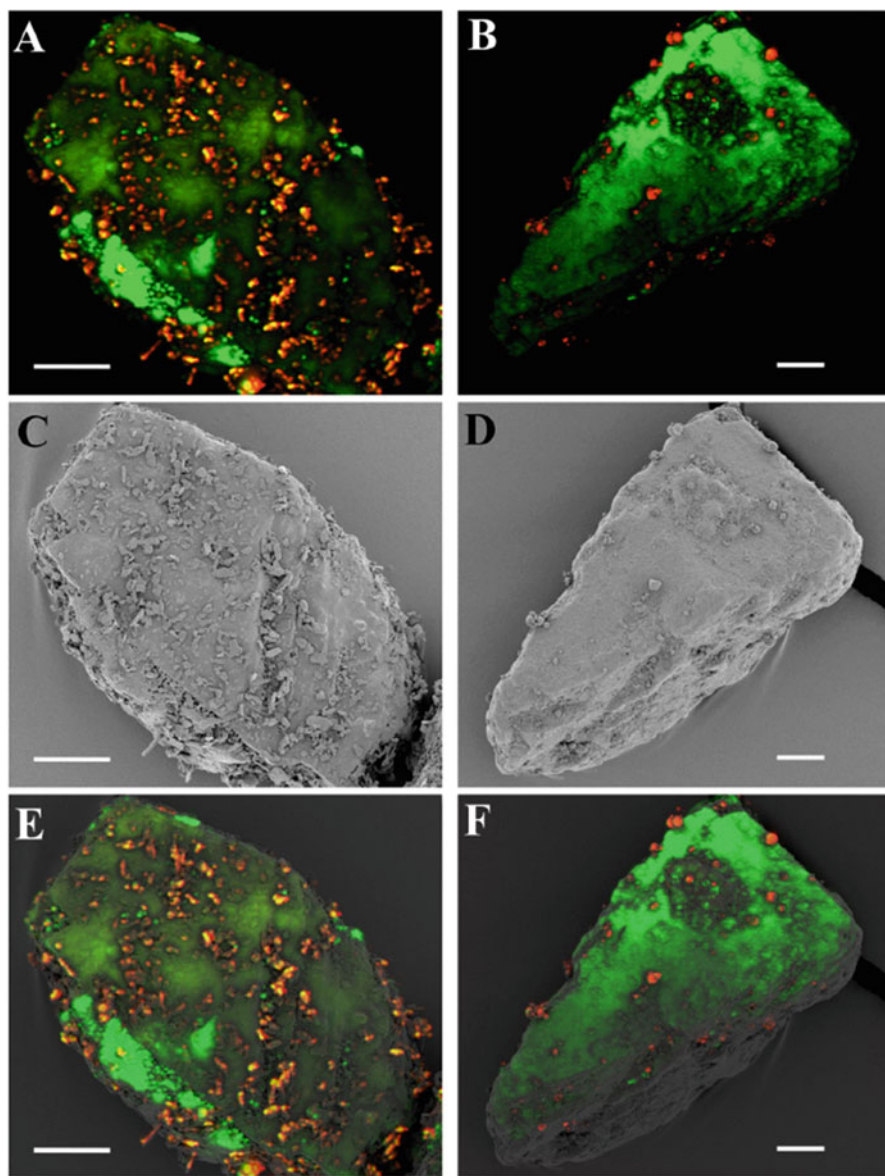


Fig. 17.8 CARS (A+B), SEM (C+D) and combined CARS and SEM images (E+F) of salmeterol (*red*) and lactose (*green*) mixtures after 0.5 (*left*) and 600 min of mixing (*right*). Scale bars represent 20 μm . Reproduced from (Fussell et al. 2014a) with permission from John Wiley and Sons

extremely rapid method for imaging the distribution of substances of interest (video-rate for narrowband CARS imaging, compared to minutes for (spontaneous) Raman imaging and minute to hours for Raman mapping). One of the limitations of conventional narrowband CARS setups is that imaging at a single wavelength for each component of interest limits specificity. Obtaining the CARS signal at multiple Raman shifts can take some time because the energy difference between the Stokes laser and pump lasers has to be changed manually as many times as there are wavenumbers to be detected. However, approaches to much more rapidly obtain CARS signals at multiple wavelengths (CARS spectra) for hyperspectral imaging using narrow-band CARS sources have been and are being developed. In the study by Fussell et al. described above, a hyperspectral imaging setup using an OPO-based approach to rapidly scan through multiple CARS shifts it took about 4 min to measure a spectrum from 3800 to 3100 cm^{-1} (Garbacik et al. 2012). Broadband CARS sources are another approach to rapidly (in minutes) obtain CARS spectra for imaging. As described earlier in this chapter, such data can also allow quantitative analysis with advanced spectral processing (Day et al. 2011b).

Stimulated Raman scattering (SRS) has also been used to image component distribution in dosage forms. Slipchenko et al. used SRS imaging to detect amlodipine besylate (API) and four excipients within pharmaceutical tablets (Slipchenko et al. 2010). The results were directly compared to the images obtained by confocal Raman mapping and CARS imaging. With SRS, the API and all the excipients were successfully visualised with a lateral spatial resolution of 0.62 μm , which was better than for the confocal Raman microscope with a lateral spatial resolution of a few μm . The imaging speed in SRS was also much faster; it took 1 s per pixel with confocal Raman mapping, compared with 100 μs per pixel for SRS. This study also demonstrated the benefit of SRS imaging over CARS microscopy by the absence of a non-resonant background signal. SRS spectra are also linear to concentration which facilitates quantitative analysis.

3.4 *Near-Infrared Imaging*

NIR spectroscopy is a rapid spectroscopic imaging method with a lower spatial resolution in practice than MIR imaging. However, it is fast, with a more flexible, non-contact sampling setup. The technique has become popular for imaging intermediate products during pharmaceutical processing (Table 17.2). NIR imaging has been used for example to control powder blend homogeneity (El-Hagrasy et al. 2001; Jovanovic et al. 2006) and tableting (Ellison et al. 2008). It has also been used to understand how process related changes affect tablet dissolution (Roggo et al. 2005b). For example, the chemical composition of the surface of tablet cores has been used to explain the differences in drug dissolution rate. It has also been used to visualise API and excipients in final pharmaceutical formulations to be able to confirm the quality of the product (Amigo and Ravn 2009; Ravn

et al. 2008). In a similar manner, Puchert et al. (2010) used NIR imaging to distinguish counterfeit medicines from genuine ones.

It is possible to get a very large amount of spectroscopic data in a comparatively short time using NIR spectroscopic imaging (Amigo et al. 2008). Although this can be useful, careful data treatment is especially important when NIR imaging is used since the overlapping signals originate from both chemical and physical sample properties. Univariate and many multivariate chemometric data processing methods have been applied to NIR spectroscopic imaging. Univariate data analysis can be used when a sample contains few substances in which the main spectral variation of interest is expected to result from physical phenomena (e.g. baseline shift). Such an analysis was performed by Ellison et al., in which the density variation of lactose monohydrate tablets with different amounts of magnesium stearate (0, 0.25 and 1 %) was imaged (Ellison et al. 2008). The absorbance at 2120 nm, representing baseline shift, was chosen to image density distribution. In order to get quantitative data from each pixel, a calibration curve was constructed based on the measured densities of tablets and corresponding average absorbance intensities at 2120 nm. False colour images revealed that the density was higher at the edges than the centre of the tablets. Density changes in the tablets correlating with upper and lower punch forces were also visible.

Many types of multivariate data-analysis methods are used for extracting the information from NIR data sets. These methods include partial least squares (PLS) (Palou et al. 2012; Gendrin et al. 2007), classical least squares (CLS), principal component analysis (PCA), multivariate curve resolution (MCR), cluster analysis (Amigo et al. 2008) and self-modelling curve resolution (SMCR) (Awa et al. 2008). In addition, new data treatment methods such as linear image signature (LIS) have been developed (Puchert et al. 2010). While the best methods depend on the sample, PLS analysis has been proven accurate in several examples (Gendrin et al. 2007; Jovanovic et al. 2006; Palou et al. 2012).

Palou et al. (2012) used NIR imaging with PLS analysis to study the distribution of API and five excipients (API and excipients #1 and #2 accounted for 95 % of the tablet content) in a tablet and also to quantify the thickness and surface distribution of the film coating. Spectra of pure samples were used to form a calibration model. The tablets were then imaged from six different directions: four outer sides and both internal surfaces after splitting the tablet into two. The PLS model was then used to predict the concentrations of each of the excipients on each imaging spot in the tablet. The concentrations achieved using the PLS model were very close to the nominal values for the API and the excipients. The distribution of the components could be seen from the false colour images calculated with PLS. High concentrations of API and excipient #2 were observed from the same areas while high concentrations of API and excipient #1 were complementary. This was attributed to API and excipient #2 being mixed first together before addition of the other excipients. The minor excipients were distributed homogeneously. In addition, PLS was also used to quantify the thickness and the distribution of the coating. The model was successfully used to quantify the mean coating thickness of the samples.

It was also observed that the coating material was not uniformly distributed on the tablet surface.

One of the pharmaceutical manufacturing processes that can be monitored using NIR spectroscopic imaging is powder blending. El-Hagrasy et al. used this technique noninvasively to monitor powder blend homogeneity of mixtures of salicylic acid and lactose and to determine the end-point for mixing (El-Hagrasy et al. 2001). A V-blender was used for mixing and there were optical ports installed on the blender that allowed the NIR spectra to be recorded with fibre optics. The blender was stopped at predetermined times to collect NIR spectra and samples for UV spectroscopy (reference method). UV spectroscopy revealed that the mixture was sufficiently homogeneously mixed after 16 min of mixing. Similar end-points were also achieved from NIR spectra treated with suitable algorithms and NIR images could be used to visualise this. Images were collected using an InSb imaging camera that had a discrete bandpass filter that allowed the salicylic acid absorbance band at 1656 nm to be recorded. It was possible to see that the mixture reached homogeneity after 14–16 min. It was concluded that NIR spectroscopy and imaging could be used to define the endpoint of mixing as well as UV spectroscopy. One advantage of using imaging is that the large sample mass could be used statistically to improve the reliability of the end-point determination.

These examples show how NIR spectroscopic imaging can be used as a rapid and non-invasive method to obtain information from all stages of drug manufacturing, starting from quality assurance of raw materials to analysis of finished drug products such as tablets and capsules. NIR imaging is especially well suited to real time processing analysis for controlling and optimising manufacturing of medicines (process analytical technology).

3.5 Terahertz Imaging

Terahertz imaging of drugs and dosage forms has been reviewed in some detail in a number of publications (e.g. (Haaser et al. 2013b; Shen 2011; Smith and Arnold 2011; Zeitler et al. 2007c)). A few examples that illustrate some of the breadth of published pharmaceutical applications are highlighted below and in Table 17.2. For a more complete treatment terahertz imaging applications in this book, the reader is referred to the Terahertz Spectroscopy chapter in this book.

Terahertz pulsed imaging (TPI) is particularly well suited to imaging layered structures of large dosage forms such as tablets, with tablet coating analysis being the most widely published pharmaceutical application of TPI to date. The first proof-of-principle analysis in this context was that of Fitzgerald et al. (Fitzgerald et al. 2004; Wallace et al. 2004), in which sugar coatings of two brands of over-the-counter ibuprofen tablets were imaged and compared. A 1 mm² area was raster scanned and the thickness of the sugar coatings of both brands was determined (results were verified using cut cross-sections of the tablets). In contrast to the innovator product, multiple coating layers were detected for the generic product.

The success of this proof-of-principle study provided justification for developing an imaging setup with a robotic six-axis arm capable manipulating the presentation of tablets to the terahertz beam such that entire tablet surfaces could be mapped (e.g. Imaga2000, Teraview Ltd, Cambridge). As a result, almost all subsequent publications of 3D TPI for pharmaceutical dosage form imaging have involved imaging of whole tablets. This was first demonstrated by Zeitler et al. who imaged entire film-coated tablets, sugar-coated tablets, multi-layered controlled release tablets, and even the gelatin coating of soft gelatin capsules (Zeitler et al. 2007b).

In contrast to other vibrational spectroscopic imaging methods, terahertz imaging can often easily detect interfaces at least 2 mm below the tablet surface of coated tablets (Zeitler et al. 2007b). A flurry of publications in the last few years have shown 3D TPI to be suitable for detailed analysis of coating thickness distribution variation, imaging coating structure defects, density analysis (see examples in Table 17.2). One of the most widely investigated pharmaceutical applications of TPI is for controlled release coating analysis, since the structure of such coatings is critical to drug release behaviour.

The resonance of the rotational modes of water with terahertz radiation effectively precludes terahertz sampling in an aqueous environment. Nevertheless, dosage form coating properties have been investigated and directly correlated to drug release behaviour, and therefore TPI may potentially be used to predict drug release from coated dosage forms, so long as the drug release is limited by diffusion through the coating rather than dissolution of the drug itself. Coating thickness, as determined by TPI, has in some cases been directly correlated to drug release of sustained release coatings. Furthermore, if the coating around the central band is thinner (as determined by TPI), drug can be released faster from this region than from the tablet sides. In other cases an inverse relationship between coating thickness and drug release rate has been observed, i.e. a higher coating thickness measured with TPI was associated with a faster drug release (e.g. Ho et al. 2008). Coating density, obtained from coating thickness combined with weight gain and/or the terahertz electric field peak strength signal, was found to be different in these samples. A higher coating density was correlated with a slower drug release (Ho et al. 2010). Changes in coating structure (density, extra interfaces, thickness) due to different processing conditions, including coating method, scale up, and process interruptions have been detected with TPI and correlated to changes in drug release behaviour. This topic has recently been discussed (Haaser et al. 2013a). In this context, TPI is an effective tool to understand and even predict drug release behaviour from controlled release systems.

More recently, TPI has also been shown to be of value with much smaller dosage forms (Haaser et al. 2013b). Standard size pellets (approximately 1 mm diameter) with a sugar starter core, metoprolol succinate drug layer, and finally a sustained-release polymeric coating were analysed with respect to drug layer and polymer coating thickness and as well as coating density. Both the drug (approx. 40 μm in all batches) and polymeric coatings thicknesses (approx. 40 μm (batch I), 60 μm (batch II) and 100 μm (batch III)) could be accurately determined (Fig. 17.9, SEM was used as a reference technique). Only a small area on each pellet was

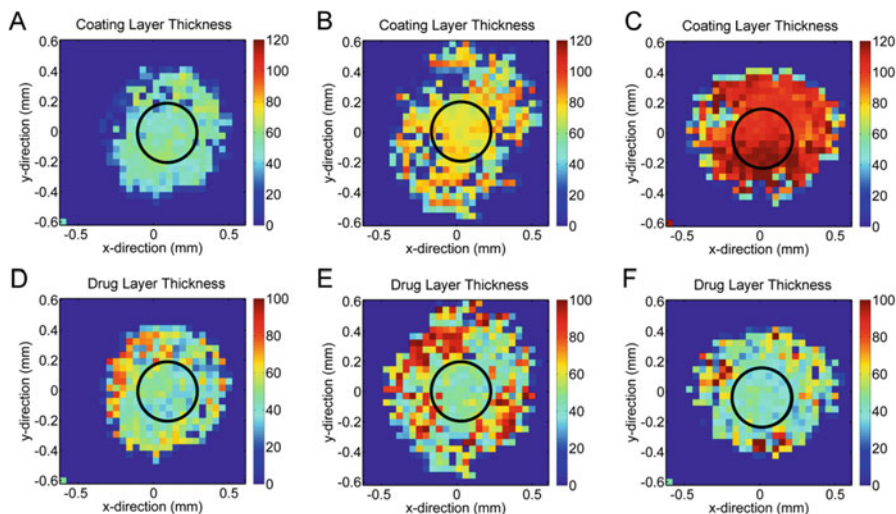


Fig. 17.9 Coating (*top*) and drug (*bottom*) layer thickness of a pellet imaged using terahertz pulsed imaging from batch I (**A, D**), Batch II (**B, E**) and batch III (**C, F**). The *black* circles indicate the areas used for coating and drug layer thickness calculation. *Dark blue* pixels in the pellet area correlate with measurement failure (and were excluded from calculations). The colour scale bars are in μm . Reproduced from (Haaser et al. 2013b) with permission from Elsevier

imaged due to the sampling setup restrictions and high curvature of the pellets. Nevertheless, subsequent dissolution testing on the same pellets showed that the calculated thicknesses were directly correlated with drug release.

Transmission 2D terahertz spectroscopic mapping, in which terahertz spectra are sequentially obtained across the sample, has been used for chemical and solid state mapping. The lateral spatial resolution is also approximately 200 μm for this setup (diffraction limited), while the axial resolution is over 2 mm (Charron et al. 2013). Charron et al. quantitatively mapped caffeine-oxalic acid co-crystal and co-crystal former distribution in compacts (Charron et al. 2013). Polyethylene was used as a transparent and highly compressible albeit not very pharmaceutical matrix former. The peak intensity for the cocrystal at 1.56 THz (at 120 K) was established to be linear to concentration, and was used to quantitatively map cocrystal concentration mapped across the compacts. With sampling at each pixel traversing the entire thickness of the compact, excellent agreement was found between total cocrystal content according to the mapping results and known concentration (Charron et al. 2013) Another example of terahertz spectroscopic mapping in drug and dosage form characterisation is the mapping of illicit drugs within polyethylene bags and paper envelopes (Kawase et al. 2003). Transmission terahertz spectroscopic mapping obviously suffers in terms of spatial resolution compared to other techniques in this chapter, including TPI imaging based on refractive index changes. Nevertheless, it may, for example, be of value in sensitive solid state mapping if other methods are not sufficiently solid state sensitive or non-destructive sampling at depth is required.

3.6 Drug Release and Dissolution

Drug dissolution and release processes are affected by a number of interacting chemical and physical phenomena, many of which may themselves change during interaction of the drug or dosage form with the biological medium (e.g. excipient swelling or dissolution, porosity changes, drug distribution changes, chemical reactions, etc). Imaging of the dosage forms during drug release and/or dissolution can help in obtaining a mechanistic understanding and subsequent optimization of drug release behaviour. Vibrational spectroscopic imaging has some advantages compared to other currently used imaging methods for analysis, including the high chemical specificity without the need for coloured components (c.f. visual photography) or magnetic moments (magnetic resonance imaging). As illustrated below, in some cases the imaging is sufficiently rapid to allow *in situ* imaging.

Imaging drug release and/or dissolution has been carried out via both MIR and Raman-based methodologies. Raman-based methods have the advantage of having generally weak water signals which facilitates visualization of the drug and dosage form in an aqueous environment. Since water strongly absorbs all forms of infrared light, NIR, MIR and terahertz imaging have generally not been considered techniques of choice for imaging drug release/dissolution. On the other hand, this problem has been effectively circumvented in MIR imaging by using adapted ATR sampling setups (in which water as well as drug and excipients may all be imaged simultaneously).

3.7 MIR Imaging

Macro-FTIR ATR imaging has been used to image *in situ* the dissolution of tablets (van der Weerd and Kazarian 2004; van der Weerd et al. 2004). In these studies Van der Weerd et al. invented a diamond ATR plate system in which a tablet could be directly compressed on the surface of the diamond. With water flowing at 1 mL min^{-1} through the system, the tablet changes could be analysed over time with a Bruker Optics IFS66S step scan spectrometer with a 64×64 MCT FPA detector with a spectral resolution of 16 cm^{-1} , field of view of $820 \times 1140 \text{ }\mu\text{m}$ and nominal spatial resolution of 13–18 μm .

In the first study, the model tablet consisted of hydroxypropyl methylcellulose (HPMC) and caffeine 20% (w/w) (van der Weerd et al. 2004). Spectral data sets were acquired at 8 min intervals. For image formation, the first image represented the dry sample and images were also presented after the water flow had been on for 0, 40, 80, 160 and 190 min. The individual components were imaged at each time point based on absorbances specific to each component: $960\text{--}1130 \text{ cm}^{-1}$ for HPMC, $1680\text{--}1720 \text{ cm}^{-1}$ for caffeine and $3200\text{--}3500 \text{ cm}^{-1}$ for water. Even though the spatial resolution was not especially high (approximately 15 μm), areas of caffeine particles in the HPMC matrix could be distinguished. Just after the addition

of water, the water associated closely with the HPMC. Over time, the caffeine and HPMC absorbance decreased as water penetrated into the tablet. Interestingly, the caffeine particles moved counter to the water flow during the experiment, probably due to the HPMC swelling. Spectra extracted from different areas of the sample after 40 min of water flow were also analysed visually. Four areas were chosen, representing, (a) the inner region of the tablet, (b) a caffeine particle, (c) the area outside the tablet core and d) the tablet surface at the beginning of the water flow. Caffeine peaks were also apparent in the spectrum recorded from the inner regions of the tablets, although the signal could not be seen in the images due to insufficient spatial resolution. HPMC peaks were also observed from the outer areas of the tablet indicating the relocation of tablet material by diffusion or gel formation.

The FTIR imaging of tablet dissolution was extended with a more quantitative analysis (van der Weerd and Kazarian 2004). PLS analysis was used to reduce the large amount of data in the original data sets. Originally a data cube with $64 \times 64 \times 700$ pixels was obtained, where 64×64 pixels formed the spatial dimensions and 700 wavenumbers represented the spectral dimension. After PLS reduction it was possible to express a complete infrared spectrum in one value. Three independent PLS regression models were used, and the resulting values were the concentrations of niacinamide, HPMC and water (the three components in the model tablet). Based on these PLS models, images at different time points were constructed, and it was possible to see how water penetrated into the tablet and reduced the concentrations of HPMC and niacinamide. A UV spectrometer was also added to the system and the results obtained by FTIR images were compared to the dissolution profiles obtained by UV spectroscopy; a strong correlation between the dissolution profiles obtained through FTIR imaging and UV spectroscopy was observed.

Other examples are listed in Table 17.3, and drug dissolution and release using ATR-IR analysis has also been reviewed in detail elsewhere (Kazarian and Ewing 2013). While the types of dosage forms that can be analysed is limited due to the need for contact optics, a clear advantage of this method includes the ability to (quantitatively) image drugs, excipients and water during the same *in situ* measurement.

3.8 Raman Imaging

3.8.1 Spontaneous Raman

A few studies have featured Raman microscopy for imaging drug dissolution and release processes (Table 17.3). Extrudates containing the drug theophylline anhydrate (50 % w/w) and the lipid tripalmitin, with or without the water-soluble polyethylene glycol (PEG) (25 % w/w) have been analysed (Haaser et al. 2011). Dissolution testing was performed using US Pharmacopeia apparatus 1. Extrudates

Table 17.3 Selected studies involving vibrational spectroscopic imaging of drug release and dissolution

Technique	Purpose	Sample type	Conclusions	Reference
FTIR	<i>In situ</i> imaging of tablet dissolution	Tablets	Drug dissolution could be followed and compared to dissolution tests	Rustichelli et al. (2000) and van der Weerd et al. (2004)
FTIR	Study drug release from polymer film	PEO polymer film with testosterone	False colour images revealed two distinct delivery mechanisms	Coutts-London et al. (2003)
FTIR	Image dissolution of solid dispersion	Solid dispersion, nifedipine/PEG	It was observed that nifedipine started to crystallise at a concentration of 10 wt%	Chan and Kazarian (2004a)
FTIR	Image dissolution of solid dispersion	Solid dispersion, ibuprofen/PEG	Crystallization of ibuprofen could be observed and it was concluded that this slows overall drug dissolution	Kazarian and Chan (2003)
FTIR	Study the diffusion of nicotine in ethanol/water into a polymer membrane	Ethylene-vinyl acetate (EVA) polymer and nicotine/ethanol/water solution	Distribution of each component in the polymer could be visualised	Rafferty and Koenig (2002)
Raman + FTIR	Study drug diffusion from a semisolid formulation	Dithranol in white soft paraffin	IR could be used for observing the lateral distribution of API and Raman could be used for observing 3D diffusion	Grotheer et al. (2014)
Raman	Image a matrix dosage form during dissolution	Solid lipid extrudates	Drug distribution and release were successfully mapped using Raman microscopy	Haaser et al. (2011)
Raman	Investigate the physical structure of solid lipid extrudates and relate the structure to dissolution behaviour	Solid lipid extrudates	Raman mapping could be used for detecting micrometre size differences on the surface of matrices and their effect on dissolution	Windbergs et al. (2010)
CARS	Visualise the solid state changes in theophylline and its effect on dissolution	Theophylline anhydrate and monohydrate	Theophylline solid state conversion correlated with dissolution rate changes	Fussell et al. (2013a)

(continued)

Table 17.3 (continued)

Technique	Purpose	Sample type	Conclusions	Reference
CARS	Study paclitaxel distribution in PEG/PLGA blends and its release	PEG/PLGA polymer films on a cover glass	CARS microscopy showed that drug release is closely related to its distribution	Kang et al. (2006, 2007)
CARS	Study drug release from oral drug formulations and monitoring solid state changes	Theophylline tablets and extrudates	It was possible to follow drug release and solid state changes with CARS microscopy	Jurna et al. (2009) and Windbergs et al. (2009)
CARS	Study lipid digestion	Glycerol trioleate, porcine pancreatic lipase	Multiplex CARS microscopy could be used to observe lipid digestion	Day et al. (2010)

were removed from the dissolution media periodically, and transverse sections of the extrudates were prepared with a razor blade and mounted onto microscope slides. A dispersive confocal Raman microscope was used for point-by-point mapping the extrudate cross-section with an excitation wavelength of 785 nm, spectral region 65–1520 cm^{-1} , and 20 \times (lateral resolution $\sim 14 \mu\text{m}$) and 50 \times (lateral resolution $\sim 4 \mu\text{m}$) objectives. Theophylline had a resolved Raman peak at 554 cm^{-1} , tripalmitin had two peaks at 1100 cm^{-1} and 1130 cm^{-1} and PEG had a double peak at 844 and 860 cm^{-1} , from which normalised peak areas were used to calculate drug distribution in the Raman mapping studies. After 120 min of dissolution of the binary extrudates (without PEG), 17 % (w/w) of theophylline anhydrate was released according to UV–Vis spectroscopy. Assuming a boundary that would recede uniformly based on Higuchi kinetics, the Raman signal from theophylline would be observed close to a 45 μm zone from the edge of the extrudate. It was possible to detect drug loss from this 45 μm zone, although the drug boundary was not uniformly receding. In the ternary system extrudates, the PEG dissolved rapidly from within the matrix and after 30 min it was completely dissolved (Fig. 17.10). The fast polymer dissolution increased the exposed surface area of the drug, resulting in faster drug release compared with the binary system. This study showed how Raman microscopy can be a useful tool for high resolution imaging of controlled release formulations and their changes during drug release. The acquisition time for each image was several hours, which precludes *in situ* analysis. However, this meant that an official pharmacopeia dissolution testing setup without modification could be used. Raman imaging could be used for faster image acquisition (using just a few wavenumbers) which might be possible *in situ* depending on the application.

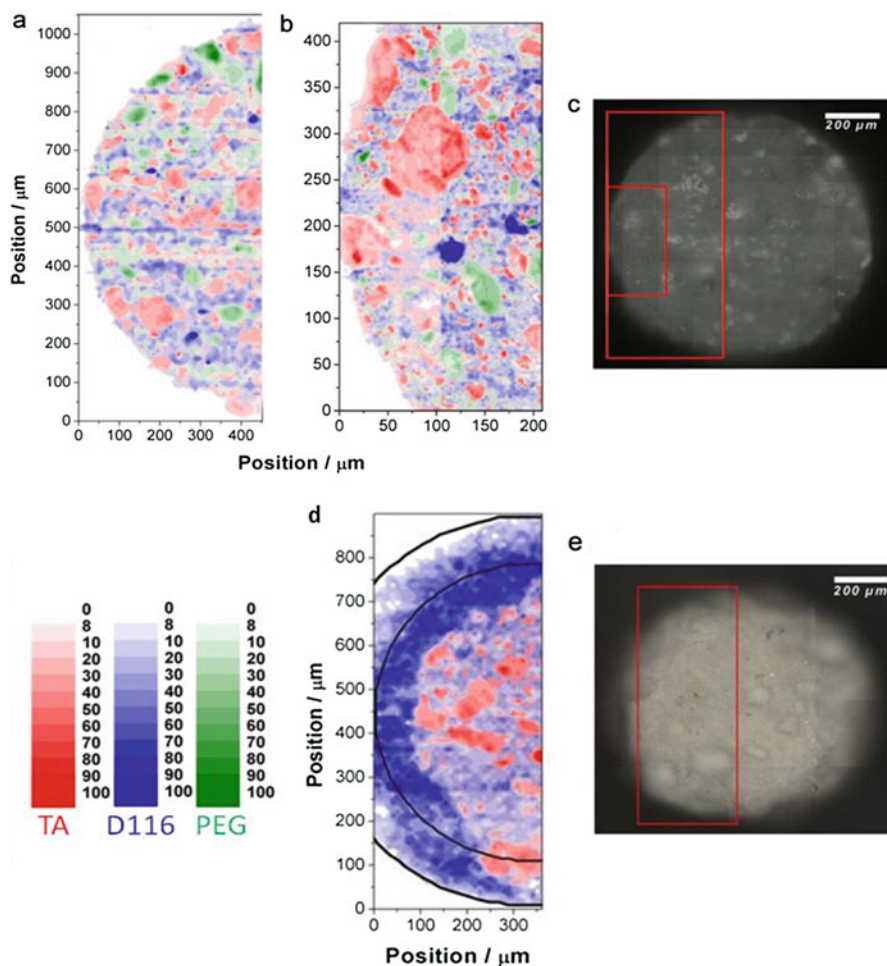


Fig. 17.10 Cross-section of an extrudate containing tripalmitin (*blue*, 1100 cm^{-1}), theophylline anhydrate (*red*, 554 cm^{-1}), and polyethylene glycol (*green*, 844 and 860 cm^{-1}). Raman map of all three components recorded before dissolution testing with (a) a $20\times$ objective, and (b) a $50\times$ objective. (c) Corresponding optical microscopy image with rectangles depicting areas mapped in (a) and (b). Raman map of all three components recorded after dissolution testing for 30 min with (d) a $20\times$ objective (note absence of PEG signal above 8% threshold, and that there was no evidence of theophylline monohydrate formation). (e) Corresponding optical microscopy image with rectangle depicting corresponding area mapped in (d). For further details see original publication. Reproduced from (Haaser et al. 2011) with permission from John Wiley and Sons

3.8.2 Coherent Raman

There are several studies over the last decade in which CARS microscopy has been used for imaging drug release. Kang et al. investigated paclitaxel in polymer films (Kang et al. 2006, 2007). They investigated the structure affecting the release of paclitaxel from poly(ethylene glycol)/poly(lactic-co-glycolic acid) (PEG/PLGA) blends. They observed that paclitaxel was partitioned into the PEG phase. On the surface of the films, the addition of PEG caused an accelerated burst release of paclitaxel. Inside the film, paclitaxel was distributed differently and its release retarded by the continuous PLGA matrix.

Theophylline drug release from lipid formulations have been studied using CARS microscopy (Jurna et al. 2009; Windbergs et al. 2009). In these studies lipid based solid oral drug formulations, similar to those described above for the spontaneous Raman mapping, were investigated. Theophylline anhydrate and monohydrate were combined with tripalmitin. Tablets made from the powdered substances were prepared, and extrudates of theophylline and tripalmitin were also used. Samples were imaged 30 and 180 min after addition of dissolution media (purified water) and compared to the images taken before dissolution. The CARS microscope used a 1064 nm laser combined with an OPO for narrowband CARS imaging with manual tuning to different resonances. The imaging was performed using $20\times$ objectives. Initially Raman spectra from pure compounds were measured to find the suitable resonances for CARS imaging. Tripalmitin, theophylline monohydrate and theophylline anhydrate had peaks at 2880, 3109 and 3123 cm^{-1} respectively. Because the theophylline peaks overlapped it was not possible to selectively image one solid state form at a time. However, the signal at 3109 cm^{-1} could be used to non-selectively detect both forms of theophylline. Since theophylline monohydrate had a needle-like morphology (compared to more prismatic morphology for the anhydrate form), this could be used to distinguish between these two solid forms. Tablets made from powdered theophylline monohydrate and tripalmitin, powdered theophylline anhydrate and tripalmitin and from extrudes of the theophylline anhydrate and tripalmitin, were imaged. It was observed that theophylline monohydrate dissolved completely in water over a 180 min time period and after 30 min there were only a few theophylline monohydrate needles visible. The theophylline monohydrate needles had left visible voids in the insoluble tripalmitin matrix, which indicated that the tripalmitin matrix stayed intact during the dissolution and hence the drug release was completely diffusion controlled. When tablets made from powdered theophylline anhydrate and tripalmitin were imaged, an interesting observation was made. After 30 min of dissolution, the signal from theophylline was still visible. However typical needle like morphology for theophylline monohydrate was observed, which strongly suggested that the transition from the anhydrate to monohydrate form had occurred. After 180 min all theophylline appeared to have dissolved (no drug signal present). This suggested that the dissolution process had multiple stages. First the anhydrate dissolved, leading to a supersaturated solution with

respect to the less soluble monohydrate. The monohydrate form crystallised out of solution and finally the two forms of theophylline dissolved. Theophylline anhydrate tablets made from extrudates were also imaged. Interestingly no needle like morphology was observed after 30 or 180 min of dissolution. This suggested that when the extrudates are used for tableting, theophylline monohydrate is not formed during the dissolution process.

The need for speed for *in situ* analysis of dosage forms during dissolution testing has also been one of the major motivations for the introduction of CARS imaging for the analysis of drug release over the last decade. In the studies described above with tripalmitin and theophylline, a flow-through cell was also used. This flow-through cell allowed *in situ* visualization of the tripalmitin-theophylline matrices during dissolution. Fussell et al. improved this *in situ* system and added a UV spectrometer to the setup (Fussell et al. 2013a). Directly compressed compacts made from theophylline anhydrate and theophylline monohydrate were imaged during dissolution *in situ* with dissolution monitored simultaneously via UV-vis absorbance of the solution. Theophylline monohydrate crystal growth on the surface of the theophylline anhydrate compacts was observed when the samples were imaged by CARS microscopy at 2952 cm^{-1} . Besides the visual observation of crystal growth, CARS spectra collected using hyperspectral CARS imaging were used to confirm the solid-state identity. A peak shift in the theophylline spectrum was observed from 3120 to 3105 cm^{-1} , due to the conversion from the anhydrate to monohydrate form. The dissolution curves obtained by UV absorbance spectroscopy also gave valuable information. When the anhydrate form was used, a peak in theophylline concentration occurred, after which the concentration dropped rapidly. This drop can be explained by the anhydrate form of theophylline reaching supersaturation, which caused precipitation and crystal growth of the less soluble monohydrate. When a methyl cellulose solution was used as the dissolution medium, the dissolution profiles were quite different. There was no significant difference in the dissolution profiles of compacts made from theophylline monohydrate, but the decrease in dissolution rate when anhydrate compacts were used disappeared. There was a two-fold increase in dissolution rate when compacts made from the anhydrate form were used and this could have been interpreted to mean that there was no conversion to monohydrate. However CARS microscopy images showed that there was growth of monohydrate crystals and this growth was slower compared to the situation when water was used as a dissolution medium. These images obtained by CARS microscopy show in principle how helpful it can be to have a visualization method to directly observe how the structures of drugs and dosage forms change during drug dissolution and release.

3.9 Drug Delivery

Many novel medicines are developed so that they target specific tissues or cells. During drug development it is helpful to visualise how well this targeting is

achieved. Electron microscopy approaches, especially variants of TEM, are used to track particles, such as nanocarriers, on the cellular level. However, the technique is restricted to particulate level analysis, is not chemically specific, and not suitable for *in situ* analysis. Fluorescence microscopy is one commonly used method that is chemically specific, can track drug in solution and is suitable for *in situ* analysis. Usually the cell nucleus and possibly other organelles are stained and the drug and/or carrier particles are tagged with a fluorescent dye to monitor drug penetration into and localization within the cells. However, there are also several disadvantages to this method. Firstly, fluorescent dyes can alter the chemical situation at the cellular level, due to the presence of externally added molecules that do not normally belong to the cellular environment. Secondly, fluorescence imaging tends to suffer from photobleaching which can make image interpretation more difficult. Thirdly, the fluorescent tags may dissociate from their target structure (especially if physically bound), potentially leading to erroneous interpretations. These problems can be avoided if chemically-specific, label-free methods are employed. Vibrational spectroscopic imaging methods have the potential to overcome these drawbacks, and are beginning to be used for the label free chemically specific imaging of delivery of pharmaceuticals on the cellular and tissue levels. Some challenges of these methods include the limitation of penetration depth in biological systems, distortion of the sample position and volume and sensitivity to water. CARS and other variants of coherent Raman imaging have a promising future in this respect as they are rapid, can be used to image within biological samples *in situ* including live cell cultures, and have a low water sensitivity and a high spatial resolution (Strachan et al. 2011).

3.10 MIR Imaging

There are only a few publications in which MIR spectroscopy imaging has been used to image drug delivery to cells and tissues (Table 17.4). One reason for this is the wavelength region of MIR from about 2.5 to 15.5 μm limiting spatial resolution. Even though it is possible to achieve a true diffraction-limited spatial resolution (Nasse et al. 2011), the smallest object size that can be seen by a standard microscope based on a MIR light is around 2.5 μm , and thus novel nano-based medicines cannot be visualised. Also, the presence of water in cellular environments can be a problem especially when living cells are imaged, since the strong water absorbance often masks peaks of interest. However, there have been developments in IR spectroscopic imaging that facilitate cell imaging and thus promote interest in the topic (Holman et al. 2009; Mariangela et al. 2013; Petibois et al. 2010). One of these developments is the use of a synchrotron radiation beam, which allows very bright illumination. In addition, attenuated total reflection (ATR) IR has been used to overcome the water signal interference. In this method, cells are cultured on ATR crystals (Mariangela et al. 2013). Microfluidics systems have also been built to minimise the water interference (Holman et al. 2009).

Table 17.4 Selected studies involving vibrational spectroscopic imaging of drug delivery

Technique	Purpose	Sample type	Conclusions	Reference
Synchrotron FTIR	Characterise β -Amyloid areas in brain tissues	Tissue sample	β -Amyloid was spectrally resolved from tissues with a resolution of about the size of a cell	Choo et al. (1996) ^a
Synchrotron and conventional FTIR	Demonstrate the capability of modern FTIR instruments	Tissue	Diffraction-limited resolution in all wavelengths was obtained (micrometre resolution)	Nasse et al. (2011) ^a
FTIR	Study changes in tumour gliomas	Tissue	FTIR could discriminate between normal, tumoral, peri-tumoral and necrotic tissues in brain structures	Beljebbar et al. (2008) ^a
FTIR	Study penetration of fatty acids through the pig skin	Tissue, pig ear	Fatty acids could be imaged in the skin	Cotte et al. (2004) ^a
FTIR	Image living microbial cells in open-channel microfluidic platform	Bacterial cells	Synchrotron FTIR imaging could be applied to image cellular responses in bacterial cells in an open-channel microfluidic platform	Holman et al. (2009)
FTIR	Invent suitable FTIR based imaging platform for real-time cell imaging	U87 human glioma cells, the human cerebral microvascular endothelial cells (hCMEC/D3)	It was possible to distinguish chemically specific areas (amide I band, CH stretching and CO stretching) relatively rapidly	Petibois et al. (2010) and Yao et al. (2012) ^a
FTIR	Develop ATR device suitable for <i>in-vivo</i> cell imaging	Cells	Chemically specific areas from cells could be distinguished (nucleus and cytosolic extensions)	Mariangela et al. (2013) ^a
Raman	Visualise drug distribution and metabolism in colon cancer cells	SW480 cells, erlotinib	It was possible to visualise drug in the vicinity of cells	Pautot et al. (2003)
Raman	Visualise drug distribution in cancer cells	MDA-435 cells, paclitaxel	Paclitaxel drug could be visualised inside the living cells with a help of data-analysis techniques	Ling et al. (2002)

(continued)

Table 17.4 (continued)

Technique	Purpose	Sample type	Conclusions	Reference
CARS	<i>In-vivo</i> video-rate imaging of tissue	Mouse ear tissue	CARS microscopy could be used for detecting glands and individual cells	Evans et al. (2005) ^a
CARS	Visualise the lipid distribution in meibomian glands	Tissue sample, eye	Differences in lipid compositions in different areas in meibomian gland could be visualised	Lin et al. (2011) ^a
CARS	Visualise drug distribution in different organs after administration	Tissue samples, deuterated quaternary ammonium glycol chitosan nanoparticles	Nanoparticles could be observed in different tissues after administration	Garrett et al. (2012)
SRS	Visualise drug permeation through the porcine skin	Porcine skin, ibuprofen/propylene glycol solution	It was possible to see how ibuprofen crystallised on the surface of the porcine skin	Belsey et al. (2014)
SRS (SRL)	Quantitative imaging of DMSO in aqueous solution and in fat tissue	Tissue, MCF7 cells, DMSO aqueous solution	It was possible to quantitatively map DMSO in aqueous solution and in fat tissue	Zhang et al. (2013) ^a
CARS	Monitor lipid droplet transport in cells	Y-1 cells	Lipid droplet trafficking was detected label-free	Nan et al. (2006) ^a
CARS	Study PLGA nanoparticle uptake in cells	Human mesothelial cells (CRL-9444)	CARS images showed that PLGA nanoparticles did not internalise as easily as predicted	Xu et al. (2009)
CARS	Quantitative imaging of individual cellular lipid droplets	Linolenic acid, palmitic acid, HeLa cells, 3 T3-L1 cells	It was possible to visualise the formation and growth of lipid droplets	Bonn et al. (2009) ^a

^aThese examples do not include drug molecules, but feature imaging of cells and tissues potentially useful in future drug delivery imaging research

IR spectroscopic imaging has been used for biomedical applications, mostly involving studies where tumour tissues have been imaged (Beljebbar et al. 2008; Choo et al. 1996; Lasch et al. 2004). One of the few publications in which FTIR microscopy has been used for drug delivery analysis on the cellular level is a study where bacterial cells have been imaged with FTIR microscopy and changes in bacterial biofilm due to exposure to antimicrobial agents have been followed (Holman et al. 2009). A special open-channel microfluidic system was developed

for this purpose and, for example, antibacterial agent mitomycin-C uptake in *E. coli* biofilm was successfully followed over an 8 h time period. It was possible to see the increased signal from mitomycin-C and decreased signal from proteins (amide III).

Another example of MIR microscopy in a drug delivery context involved the uptake of penetration enhancers into pig skin (Cotte et al. 2004). Pig ear skin was treated with perdeuterated molecules of palmitic acid and myristic acid in propylene glycol. The skin was treated with the solutions in Franz diffusion cells and after exposure to the fatty acid, sections of 4–5 μm were prepared and placed on zinc sulphide IR transparent windows. IR spectra for image formation were collected using a Nic-Plan IR microscope coupled to a Magna 560 FT-IR spectrometer using a synchrotron beam with a spectral resolution of 8 or 4 cm^{-1} . It was possible to distinguish protein (amide I and II, 1650 and 1550 cm^{-1}) and lipid (CH stretching, 2700–3000 cm^{-1}) peaks from the propylene glycol only treated skin. From samples treated with perdeuterated fatty acids, peaks due to carbon-deuterium (CD) stretching at around 2000 and 2300 cm^{-1} were visible. These CD peaks, that were absent in untreated skin, allowed perdeuterated fatty acid penetration into the pig skin to be imaged. The signal distribution from D-palmitic acid was limited to the inner layers of the stratum corneum. However, signal from D-myristic acid was found deeper in the skin, and indeed had penetrated almost the full depth of the epidermis.

3.11 Raman Imaging

Raman microscopy, in all its forms, is gaining much interest as a label-free imaging tool in drug delivery applications due to its comparatively high spatial resolution, high drug sensitivity, lack of water sensitivity, and flexible non-contact sampling possibilities.

3.11.1 Spontaneous Raman

Examples of spontaneous Raman imaging in drug delivery are presented in Table 17.4. Spontaneous Raman microscopy has been used to image the cancer drug erlotinib and its fate when applied to cells (El-Mashtoly et al. 2014). Erlotinib is a drug that targets an epidermal growth factor receptor (EGFR) where it acts as a tyrosine kinase receptor inhibitor. In this study human colorectal adenocarcinoma cells (SW 480) were cultured on CaF_2 windows and were incubated for 12 h with erlotinib at a concentration of about 100 μM . Erlotinib is a poorly water-soluble drug, so 6 % captisol (β -cyclodextrin derivative) was used to increase its dissolution in water. After incubation, the cells were fixed and imaged via Raman microscopy. The Raman microscope used was a confocal Raman microscope with a 532 nm Nd:YAG laser and a 60 \times objective. Based on integration of Raman intensity in the C–H stretching region (2800–3050 cm^{-1}) it was possible to distinguish some cell

organelles, including the nucleus from the surrounding cytoplasm. Erlotinib could be observed from the integrated Raman intensity of the $C\equiv C$ region ($2085\text{--}2140\text{ cm}^{-1}$), located in the spectrally silent region of the cells. Hierarchical cluster analysis (HCA) was also used to group areas with similar spectra. The HCA images were formed from 11 clusters. Clustering revealed the cell nucleus, and it was possible to identify different areas within the cytosol that exhibited similar spectral features. The erlotinib drug was also nicely distinguished in one cluster. After 12 h of incubation some of erlotinib started to associate with the cells. 3D Raman imaging revealed that the drug was located within the cells. The fate of the erlotinib was further investigated to see if any metabolites could be observed inside the cells. The spectrum from erlotinib collected from within the cells was measured and revealed that erlotinib was free from its carrier, based on the absence of the 1053 cm^{-1} band representing captisol. The spectra of erlotinib within the cells were different to that of the free erlotinib; this suggests that the erlotinib had been metabolised. It was further speculated that this metabolite could be identified based on knowledge about different metabolism routes and taking into account the fact that the metabolite had a Raman peak at 1006 cm^{-1} , associated with trigonal ring deformation of the phenyl group and using quantum chemical calculations. Raman spectra of a synthetic metabolite confirmed that the metabolite was desmethyl-erlotinib, which had almost identical spectra to the spectra of erlotinib inside the cells.

A major barrier to Raman imaging of biological samples is autofluorescence of cellular components, which can overwhelm and mask the Raman signal. Biological samples exhibit significant fluorescence especially when illuminated with visible light (e.g. at 532 nm). Established techniques to reject fluorescence include changing the laser wavelength (to the near infrared or UV range) or photobleaching. However, these approaches can be slow, increase the risk of sample damage, and may not sufficiently reject sample fluorescence. Time-resolved Raman microscopy, in which the sub-picosecond Raman signal is separated from the nanosecond-scale fluorescence signal is a potential approach, but to the best of the authors' knowledge, has not yet been used to characterise drug delivery in biological samples due to the current lack of availability of such Raman microscopes. Another challenge is sensitivity. Surface enhanced Raman techniques offer an excellent opportunity for dissolved drug on and nanoparticle analysis on the cellular level (with less than 100 nm resolution), especially if research efforts to improve signal intensity reproducibility are successful.

3.11.2 Coherent Raman

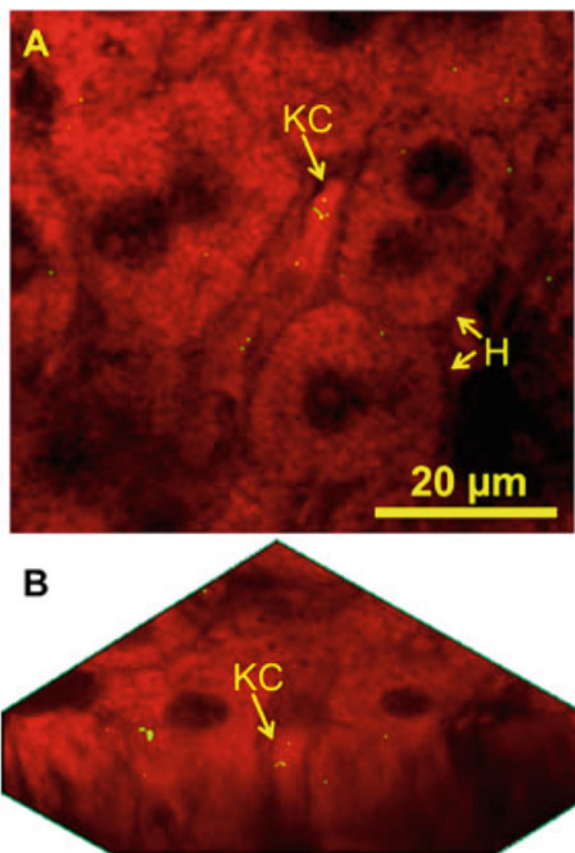
There are many features of coherent Raman imaging that make it especially suitable for imaging drugs in a biological environment. In addition to it being label-free, inherently confocal, rapid (video-rate), non-destructive, non-contact and suitable for imaging samples with high aqueous contents as already described, it is worth mentioning that the use of NIR wavelengths in coherent Raman imaging facilitates

analysis in biological samples. Such light penetrates deeper into tissues than visible light (used in one-photon fluorescence imaging). Tissue and cell damage is also minimised, since the anti-Stokes signal is stimulated allowing well tolerated laser powers and irradiation time to be minimised. These features make it perfectly feasible to image live cell and tissue cultures (Evans et al. 2005; Zumbusch et al. 1999; Rodriguez et al. 2006; Evans and Xie 2008; Strachan et al. 2011). Coherent Raman microscopes are generally also capable of measuring other non-linear optical phenomena, which can be combined with Raman analysis (multimodal imaging). Second harmonic generation (SHG) only occurs in materials with a non-centrosymmetric structure (Strachan et al. 2011). Collagen is a typical example of this kind of material in biological samples. Two-photon excited fluorescence (TPEF) can be used to detect auto-fluorescent endogenous materials like keratin or fluorescent exogenous materials (Li et al. 2009). For example, Mouras et al. imaged cancerous breast tissue using multimodal imaging; they could detect connective tissue using TPEF, proteins using CARS and fibrous connective tissues using SHG (Mouras et al. 2010). Coherent Raman imaging (with and without complimentary non-linear optical signals) has been used much more frequently in biomedical than pharmaceutical applications with many types of tissues and individual cells having been imaged (Evans et al. 2005; Lei et al. 2011; Lin et al. 2011; Evans and Xie 2008; Rodriguez et al. 2006). These studies form a basis for drug delivery applications where tissues and cells are imaged with drug formulations. In pharmaceutical drug delivery applications, coherent Raman imaging methods have been mostly used for imaging dermal and transdermal administration. Evans et al. used CARS microscopy for imaging an ear of an anaesthetised mouse *in vivo* (Evans et al. 2005). The system was capable of a spatial resolution of 0.3 μm laterally and 1.5 μm axially. The mouse ear was flattened with methylcellulose gel on a borosilicate coverslip. By using the signal at 2845 cm^{-1} (CH_2 stretching), different structures of skin involving lipids could be detected at different depths. On the surface of the skin it was possible to detect corneocytes of the stratum corneum. From depths of around 20–40 μm below the surface of the skin, sebaceous glands were visible. Large adipocyte cells were observed in the dermis from depths of about 60–80 μm and smaller adipocytes were found in the subcutaneous layer from depths of about 100 μm . Mineral oil was then applied to the skin and the penetration of the oil was monitored based on the increasing intensity of CARS signal taken at 2845 cm^{-1} below the skin surface. It was possible to image the penetration of the mineral oil in real time through the stratum corneum.

SRS imaging has also been used to follow chemical penetration through the skin. Belsey et al. imaged the penetration of ketoprofen in deuterated propylene glycol solution into porcine skin (Belsey et al. 2014). The drug permeation was imaged so that the lasers were sequentially tuned to match suitable Raman shifts, with 2855 cm^{-1} corresponding to the skin lipids, 2120 cm^{-1} corresponding to C–D stretching in propylene glycol and 1599 cm^{-1} corresponding to C–C stretching in ketoprofen. In this study it was possible to obtain semi-quantitative data for ketoprofen permeation into the skin. Ketoprofen crystallization on the surface of the skin, which affected the permeation process, was also imaged.

Other drug delivery routes have also been probed, including the parenteral and oral routes. Label-free imaging of non-fluorescing drugs at low concentrations (compared to those found in the skin) is challenging. However, nanoparticle imaging in which higher concentrations within the focal volume are achieved is currently more feasible. For example, Garrett et al. investigated deuterated quaternary ammonium glycol chitosan nanoparticle distribution in the different tissues after parenteral and peroral administration to mice (Garrett et al. 2012) (Fig. 17.11). The deuterated nanoparticles had a Raman peak at 2100 cm^{-1} , whereas lipid rich cellular structures could be detected using the signal at 2840 cm^{-1} . The nanoparticles were formulated in sodium chloride 0.9 % for intravenous injection and in water for oral administration. The size of the nanoparticles was about 350 nm, but they formed larger aggregates in sodium chloride ranging from 0.5 to 1.5 μm . After i.v. injection, harvested brains and livers were cut into 0.5 mm thick slices and mounted between coverslips for imaging. Transverse sections of jejunum were also imaged after oral administration of the nanoparticles. The nanoparticles were rarely detected in the brain parenchyma, and mostly found around the blood vessel endothelia. The polymer may have interacted with the

Fig. 17.11 Mouse liver containing Kupffer cells (KC) and hepatocytes (H) harvested 25 min after IV dosing with deuterated quaternary ammonium glycol chitosan nanoparticles. A two-dimensional x - y slice (A) and a three-dimensional reconstruction (B) of a CARS z-stack obtained from combining images of livers taken at the CH_2 resonance representing lipid (red, 2840 cm^{-1}) and the CD_2 resonance representing the nanoparticles (green). Reproduced from (Garrett et al. 2012) with permission from John Wiley and Sons



glycocalyx to enhance drug uptake into the brain. In the liver, the two most common cell types, hepatocytes and Kupffer cells, were detected. The nanoparticles were not internalised into the hepatocytes, and were instead found in the intercellular space between the cells. However, nanoparticles were found inside Kupffer cells which may mean that these nanoparticles undergo biodegradation in the Kupffer cells. CARS images taken from the jejunum after oral administration revealed that no particles were found to have been transported across the villi; the nanoparticles were visible in the mucus layer of the jejunum. This study showed the potential of coherent Raman imaging for label free detection of non-fluorescent nanoparticles for drug delivery in different organs after administration. Such analysis may lead to more efficient and optimised development of drug delivery systems involving nanoparticles. The technique is also well suited to imaging nanoparticle interactions in (live) cell cultures and although work is underway in this area, publications are still lacking.

Ongoing developments in optical sources and techniques (e.g. SRS, quantitative analysis) as well as further instrument commercialisation are likely to rapidly expand the pharmaceutical application of this technology. In particular, as the sensitivity of the technique improves, *in situ* (quantitative) label free imaging of drug on the subcellular level may become routinely possible in the future, which will help to open up the area of cellular-level pharmacokinetics.

4 Conclusions

The concept of vibrational spectroscopic imaging has been introduced along with a brief introduction of imaging and mapping using MIR, NIR, terahertz (far-IR) and Raman spectroscopic techniques. The analysis considerations and methods were briefly considered. Examples of imaging using these techniques were given for various applications within the areas of drugs and dosage forms, drug release and dissolution, and finally drug delivery. Different techniques shine for different applications, such as MIR for monitoring water sorption into drug formulations during storage, NIR for rapid imaging during pharmaceutical processing, TPI for analysis of solid state structures at depth, and variants of Raman for probing drug release and delivery. Coherent Raman imaging provides exciting possibilities for imaging at speed, especially *in situ* imaging in live cellular and tissue samples. Continuing technological developments of vibrational spectroscopic imaging (e.g. surface enhanced techniques) will further increase analytical potential, and it is expected that the application of vibrational spectroscopic imaging in the pharmaceutical setting will continue to accelerate.

References

- Adams MJ (2004) Chemometrics in analytical spectroscopy. In: RSC analytical spectroscopy monographs, 2nd edn. Royal Society of Chemistry, London
- Almeida A, Brabant L, Siepmann F, De Beer T, Bouquet W, Van Hoorebeke L, Siepmann J, Remon JP, Vervaeke C (2012) Sustained release from hot-melt extruded matrices based on ethylene vinyl acetate and polyethylene oxide. *Eur J Pharm Biopharm* 82(3):526–533. doi:[10.1016/j.ejpb.2012.08.008](https://doi.org/10.1016/j.ejpb.2012.08.008)
- Amigo JM, Ravn C (2009) Direct quantification and distribution assessment of major and minor components in pharmaceutical tablets by NIR-chemical imaging. *Eur J Pharm Sci* 37(2):76–82. doi:[10.1016/j.ejps.2009.01.001](https://doi.org/10.1016/j.ejps.2009.01.001)
- Amigo JM, Cruz J, Bautista M, Maspoch S, Coello J, Blanco M (2008) Study of pharmaceutical samples by NIR chemical-image and multivariate analysis. *TRAC-Trend Anal Chem* 27(8):696–713. doi:[10.1016/j.trac.2008.05.010](https://doi.org/10.1016/j.trac.2008.05.010)
- Armstrong GL, Edwards HGM, Farwell DW, Williams AC (1996) Fourier transform Raman microscopic study of drug distribution in a transdermal drug delivery device. *Vib Spectrosc* 11(2):105–113
- Awa K, Okumura T, Shinzawa H, Otsuka M, Ozaki Y (2008) Self-modeling curve resolution (SMCR) analysis of near-infrared (NIR) imaging data of pharmaceutical tablets. *Anal Chim Acta* 619(1):81–86. doi:[10.1016/j.aca.2008.02.033](https://doi.org/10.1016/j.aca.2008.02.033)
- Balogh A, Dravavöelgyi G, Farago K, Farkas A, Vigh T, Soti PL, Wagner I, Madarasz J, Pataki H, Marosi G, Nagy ZK (2014) Plasticized drug-loaded melt electrospun polymer mats: characterization, thermal degradation, and release kinetics. *J Pharm Sci* 103(4):1278–1287. doi:[10.1002/jps.23904](https://doi.org/10.1002/jps.23904)
- Balss KM, Lianos G, Papandreou G, Maryanoff CA (2008) Quantitative spatial distribution of sirolimus and polymers in drug-eluting stents using confocal Raman microscopy. *J Biomed Mater Res A* 85A(1):258–270. doi:[10.1002/jbm.a.31535](https://doi.org/10.1002/jbm.a.31535)
- Barnes RJ, Dhanoa MS, Lister SJ (1989) Standard normal variate transformation and de-trending of near-infrared diffuse reflectance spectra. *Appl Spectrosc* 43(5):772–777. doi:[10.1366/0003702894202201](https://doi.org/10.1366/0003702894202201)
- Beebe KR, Pell RJ, Seasholtz MB (1998) Chemometrics a practical guide. Wiley-interscience series on laboratory automation. Wiley, New York
- Beljebbar A, Amharref N, Leveques A, Dukic S, Venteo L, Schneider L, Pluot M, Manfait M (2008) Modeling and quantifying biochemical changes in C6 tumor gliomas by Fourier transform infrared imaging. *Anal Chem* 80(22):8406–8415. doi:[10.1021/ac800990y](https://doi.org/10.1021/ac800990y)
- Bell SEJ, Dennis AC, Fido LA, Malcolm RK, Sirimuthu NMS, Toner CF, Woolfson AD (2007) Characterization of silicone elastomer vaginal rings containing HIV microbicide TMC120 by Raman spectroscopy. *J Pharm Pharmacol* 59(2):203–207. doi:[10.1211/jpp.59.2.0007](https://doi.org/10.1211/jpp.59.2.0007)
- Belsey NA, Garrett NL, Contreras-Rojas LR, Pickup-Gerlaugh AJ, Price GJ, Moger J, Guy RH (2014) Evaluation of drug delivery to intact and porated skin by coherent Raman scattering and fluorescence microscopies. *J Control Release* 174:37–42. doi:[10.1016/j.jconrel.2013.11.002](https://doi.org/10.1016/j.jconrel.2013.11.002)
- Bonn M, Muller M, Rinia HA, Burger KNJ (2009) Imaging of chemical and physical state of individual cellular lipid droplets using multiplex CARS microscopy. *J Raman Spectrosc* 40(7):763–769. doi:[10.1002/jrs.2253](https://doi.org/10.1002/jrs.2253)
- Breitenbach J, Schrof W, Neumann J (1999) Confocal Raman-spectroscopy: analytical approach to solid dispersions and mapping of drugs. *Pharm Res* 16(7):1109–1113. doi:[10.1023/a:1018956304595](https://doi.org/10.1023/a:1018956304595)
- Breitkreitz MC, Sabin GP, Polla G, Poppi RJ (2013) Characterization of semi-solid self-emulsifying drug delivery systems (SEDDS) of atorvastatin calcium by Raman image spectroscopy and chemometrics. *J Pharm Biomed Anal* 73:3–12. doi:[10.1016/j.jpba.2012.03.054](https://doi.org/10.1016/j.jpba.2012.03.054)
- CAMO (2009–2012) The Unscrambler X supporting information. Software contents file
- CAMO (2012) The Unscrambler appendices: method references

- Chan KLA, Kazarian SG (2004a) FTIR spectroscopic imaging of dissolution of a solid dispersion of nifedipine in poly(ethylene glycol). *Mol Pharm* 1(4):331–335. doi:[10.1021/mp049973m](https://doi.org/10.1021/mp049973m)
- Chan KLA, Kazarian SG (2004b) Visualisation of the heterogeneous water sorption in a pharmaceutical formulation under controlled humidity via FT-IR imaging. *Vib Spectrosc* 35 (1–2):45–49. doi:[10.1016/j.vibspec.2003.11.005](https://doi.org/10.1016/j.vibspec.2003.11.005)
- Chan KLA, Kazarian SG (2005) Fourier transform infrared imaging for high-throughput analysis of pharmaceutical formulations. *J Comb Chem* 7(2):185–189. doi:[10.1021/cc049840q](https://doi.org/10.1021/cc049840q)
- Chan KLA, Kazarian SG, Vassou D, Gionis V, Chryssikos GD (2007) In situ high-throughput study of drug polymorphism under controlled temperature and humidity using FT-IR spectroscopic imaging. *Vib Spectrosc* 43(1):221–226. doi:[10.1016/j.vibspec.2006.07.015](https://doi.org/10.1016/j.vibspec.2006.07.015)
- Chantry GW (1971) *Submillimetre spectroscopy: a guide to the theoretical and experimental physics of the far infrared*. Academic, London
- Charron DM, Ajito K, Kim JY, Ueno Y (2013) Chemical mapping of pharmaceutical cocrystals using terahertz spectroscopic imaging. *Anal Chem* 85(4):1980–1984. doi:[10.1021/ac302852n](https://doi.org/10.1021/ac302852n)
- Chen C, Hayazawa N, Kawata S (2014) A 1.7 nm resolution chemical analysis of carbon nanotubes by tip-enhanced Raman imaging in the ambient. *Nat Commun* 5:3312. doi:[10.1038/ncomms4312](https://doi.org/10.1038/ncomms4312)
- Cheng JX, Xie XS (2004) Coherent anti-Stokes Raman scattering microscopy: instrumentation, theory, and applications. *J Phys Chem B* 108(3):827–840. doi:[10.1021/jp035693v](https://doi.org/10.1021/jp035693v)
- Chew W, Widjaja E, Garland M (2002) Band-target entropy minimization (BTEM): an advanced method for recovering unknown pure component spectra. Application to the FTIR spectra of unstable organometallic mixtures. *Organometallics* 21(9):1982–1990. doi:[10.1021/om0108752](https://doi.org/10.1021/om0108752)
- Choo LP, Wetzel DL, Halliday WC, Jackson M, LeVine SM, Mantsch HH (1996) In situ characterization of beta-amyloid in Alzheimer's diseased tissue by synchrotron Fourier transform infrared microspectroscopy. *Biophys J* 71(4):1672–1679
- Christophersen PC, Birch D, Saarinen J, Isomäki A, Nielsen HM, Yang M, Strachan CJ, Mu H (2015) Investigation of protein distribution in solid lipid particles and its impact on protein release using coherent anti-Stokes Raman scattering microscopy. *J Control Release* 197:111–120. doi:[10.1016/j.jconrel.2014.10.023](https://doi.org/10.1016/j.jconrel.2014.10.023)
- Cialla D, Deckert-Gaudig T, Budich C, Laue M, Moller R, Naumann D, Deckert V, Popp J (2009) Raman to the limit: tip-enhanced Raman spectroscopic investigations of a single tobacco mosaic virus. *J Raman Spectrosc* 40(3):240–243. doi:[10.1002/jrs.2123](https://doi.org/10.1002/jrs.2123)
- Clarke F (2004) Extracting process-related information from pharmaceutical dosage forms using near infrared microscopy. *Vib Spectrosc* 34(1):25–35. doi:[10.1016/j.vibspec.2003.08.005](https://doi.org/10.1016/j.vibspec.2003.08.005)
- Clarke FC, Jamieson MJ, Clark DA, Hammond SV, Jee RD, Moffat AC (2001) Chemical image fusion. The synergy of FT-NIR and Raman mapping microscopy to enable a more complete visualization of pharmaceutical formulations. *Anal Chem* 73(10):2213–2220. doi:[10.1021/ac001327i](https://doi.org/10.1021/ac001327i)
- Cotte M, Dumas P, Besnard M, Tchoreloff P, Walter P (2004) Synchrotron FT-IR microscopic study of chemical enhancers in transdermal drug delivery: example of fatty acids. *J Control Release* 97(2):269–281. doi:[10.1016/j.jconrel.2004.03.014](https://doi.org/10.1016/j.jconrel.2004.03.014)
- Coutts-Lendon CA, Wright NA, Mieso EV, Koenig JL (2003) The use of FT-IR imaging as an analytical tool for the characterization of drug delivery systems. *J Control Release* 93 (3):223–248. doi:[10.1016/j.jconrel.2003.06.003](https://doi.org/10.1016/j.jconrel.2003.06.003)
- Cricenti A, Generosi R, Luce M, Perfetti P, Margaritondo G, Talley D, Sanghera JS, Aggarwal ID, Tolk NH, Congiu-Castellano A, Rizzo MA, Piston DW (2003) Chemically resolved imaging of biological cells and thin films by infrared scanning near-field optical microscopy. *Biophys J* 85 (4):2705–2710. doi:[10.1016/s0006-3495\(03\)74693-1](https://doi.org/10.1016/s0006-3495(03)74693-1)
- Day JPR, Rago G, Domke KF, Velikov KP, Bonn M (2010) Label-free imaging of lipophilic bioactive molecules during lipid digestion by multiplex coherent anti-Stokes Raman scattering microspectroscopy. *J Am Chem Soc* 132(24):8433–8439. doi:[10.1021/ja102069d](https://doi.org/10.1021/ja102069d)

- Day JPR, Domke KF, Rago G, Kano H, H-O H, Vartiainen EM, Bonn M (2011a) Quantitative coherent anti-Stokes Raman scattering (CARS) microscopy. *J Phys Chem B* 115 (24):7713–7725. doi:[10.1021/jp200606e](https://doi.org/10.1021/jp200606e)
- Day JPR, Domke KF, Rago G, Kano H, H-O H, Vartiainen EM, Bonn M (2011b) Quantitative coherent anti-Stokes Raman scattering (CARS) microscopy. *J Phys Chem B* 115 (24):7713–7725. doi:[10.1021/jp200606e](https://doi.org/10.1021/jp200606e)
- Dazzi A, Prater CB, Hu Q, Chase DB, Rabolt JF, Marcott C (2012) AFM-IR: combining atomic force microscopy and infrared spectroscopy for nanoscale chemical characterization. *Appl Spectrosc* 66(12):1365–1384
- Dieringer JA, McFarland AD, Shah NC, Stuart DA, Whitney AV, Yonzon CR, Young MA, Zhang XY, Van Duyne RP (2006) Surface enhanced Raman spectroscopy: new materials, concepts, characterization tools, and applications. *Faraday Discuss* 132:9–26. doi:[10.1039/b513431p](https://doi.org/10.1039/b513431p)
- Docoslis A, Huszarik KL, Papageorgiou GZ, Bikiaris D, Stergiou D, Georgarakis E (2007) Characterization of the distribution, polymorphism, and stability of nimodipine in its solid dispersions in polyethylene glycol by micro-Raman spectroscopy and powder X-ray diffraction. *AAPS J* 9(3):E361–E370. doi:[10.1208/aapsj0903043](https://doi.org/10.1208/aapsj0903043)
- Doub WH, Adams WP, Spencer JA, Buhse LF, Nelson MP, Treado PJ (2007) Raman chemical imaging for ingredient-specific particle size characterization of aqueous suspension nasal spray formulations: a progress report. *Pharm Res* 24(5):934–945. doi:[10.1007/s11095-006-9211-2](https://doi.org/10.1007/s11095-006-9211-2)
- Elflick APD, Downes AR, Mouras R (2010) Development of tip-enhanced optical spectroscopy for biological applications: a review. *Anal Bioanal Chem* 396(1):45–52. doi:[10.1007/s00216-009-3223-9](https://doi.org/10.1007/s00216-009-3223-9)
- El-Hagrasy AS, Morris HR, D'Amico F, Lodder RA, Drennen JK (2001) Near-infrared spectroscopy and imaging for the monitoring of powder blend homogeneity. *J Pharm Sci* 90 (9):1298–1307. doi:[10.1002/jps.1082](https://doi.org/10.1002/jps.1082)
- Ellison CD, Ennis BJ, Hamad ML, Lyon RC (2008) Measuring the distribution of density and tableting force in pharmaceutical tablets by chemical imaging. *J Pharm Biomed Anal* 48 (1):1–7. doi:[10.1016/j.jpba.2008.04.020](https://doi.org/10.1016/j.jpba.2008.04.020)
- El-Mashtoly SF, Petersen D, Yosef HK, Mosig A, Reinacher-Schick A, Koetting C, Gerwert K (2014) Label-free imaging of drug distribution and metabolism in colon cancer cells by Raman microscopy. *Analyst* 139(5):1155–1161. doi:[10.1039/c3an01993d](https://doi.org/10.1039/c3an01993d)
- Evans CL, Xie XS (2008) Coherent anti-Stokes Raman scattering microscopy: chemical imaging for biology and medicine. In: *Annual review of analytical chemistry*, vol 1. pp 883–909. doi:[10.1146/annurev.anchem.1.031207.112754](https://doi.org/10.1146/annurev.anchem.1.031207.112754)
- Evans CL, Potma EO, Puoris'haag M, Cote D, Lin CP, Xie XS (2005) Chemical imaging of tissue in vivo with video-rate coherent anti-Stokes Raman scattering microscopy. *Proc Natl Acad Sci U S A* 102(46):16807–16812. doi:[10.1073/pnas.0508282102](https://doi.org/10.1073/pnas.0508282102)
- Everall NJ (2000a) Confocal Raman microscopy: why the depth resolution and spatial accuracy can be much worse than you think. *Appl Spectrosc* 54(10):1515–1520
- Everall NJ (2000b) Modeling and measuring the effect of refraction on the depth resolution of confocal Raman microscopy. *Appl Spectrosc* 54(6):773–782
- Everall NJ (2009) Confocal Raman microscopy: performance, pitfalls, and best practice. *Appl Spectrosc* 63(9):245A–262A
- Everall NJ (2010) Confocal Raman microscopy: common errors and artefacts. *Analyst* 135 (10):2512–2522. doi:[10.1039/c0an00371a](https://doi.org/10.1039/c0an00371a)
- Felts JR, Cho HN, Yu MF, Bergman LA, Vakakis AF, King WP (2013) Atomic force microscope infrared spectroscopy on 15 nm scale polymer nanostructures. *Rev Sci Instrum* 84(2):023709. doi:[10.1063/1.4793229](https://doi.org/10.1063/1.4793229)
- Fitzgerald AJ, Cole BE, Taday PF (2004) Non-destructive analysis of tablet coating thicknesses using terahertz pulsed imaging. *J Pharm Sci* 94(1):177–183
- Franzen L, Windbergs M (2014) Accessing Raman spectral variability in human stratum corneum for quantitative in vitro depth profiling. *J Raman Spectrosc* 45(1):82–88. doi:[10.1002/jrs.4428](https://doi.org/10.1002/jrs.4428)

- Fujimaki Y, Matsubara T, Sakamoto T, Sasakura D, Miura T, Takekawa M, Hiyama Y (2009) Distribution of ethenzamide and other ingredients on granule surfaces studied by Raman microspectroscopy and mapping. *Pharmazie* 64(5):316–322. doi:[10.1691/ph.2009.8291](https://doi.org/10.1691/ph.2009.8291)
- Furusawa K, Hayazawa N, Catalan FC, Okamoto T, Kawata S (2012) Tip-enhanced broadband CARS spectroscopy and imaging using a photonic crystal fiber based broadband light source. *J Raman Spectrosc* 43(5):656–661. doi:[10.1002/jrs.3151](https://doi.org/10.1002/jrs.3151)
- Furuyama N, Hasegawa S, Hamaura T, Yada S, Nakagami H, Yonemochi E, Terada K (2008) Evaluation of solid dispersions on a molecular level by the Raman mapping technique. *Int J Pharm* 361(1–2):12–18. doi:[10.1016/j.ijpharm.2008.05.009](https://doi.org/10.1016/j.ijpharm.2008.05.009)
- Fussell A, Garbacik E, Offerhaus H, Kleinebudde P, Strachan C (2013a) In situ dissolution analysis using coherent anti-Stokes Raman scattering (CARS) and hyperspectral CARS microscopy. *Eur J Pharm Biopharm* 85(3):1141–1147. doi:[10.1016/j.ejpb.2013.08.012](https://doi.org/10.1016/j.ejpb.2013.08.012)
- Fussell AL, Isomäki A, Strachan CJ (2013b) Nonlinear optical imaging—introduction and pharmaceutical applications. *Am Pharm Rev* 16(6):54–63
- Fussell AL, Grasmeyer F, Frijlink HW, de Boer AH, Offerhaus HL (2014a) CARS microscopy as a tool for studying the distribution of micronised drugs in adhesive mixtures for inhalation. *J Raman Spectrosc* 45(7):495–500. doi:[10.1002/jrs.4515](https://doi.org/10.1002/jrs.4515)
- Fussell AL, Mah PT, Offerhaus H, Niemi S-M, Salonen J, Santos HA, Strachan C (2014b) Coherent anti-Stokes Raman scattering microscopy driving the future of loaded mesoporous silica imaging. *Acta Biomater* 10(11):4870–4877. doi:[10.1016/j.actbio.2014.07.021](https://doi.org/10.1016/j.actbio.2014.07.021)
- Garbacik ET, Herek JL, Otto C, Offerhaus HL (2012) Rapid identification of heterogeneous mixture components with hyperspectral coherent anti-Stokes Raman scattering imaging. *J Raman Spectrosc* 43(5):651–655. doi:[10.1002/jrs.4064](https://doi.org/10.1002/jrs.4064)
- Garrett NL, Lalatsa A, Begley D, Mihoreanu L, Uchehgbu IF, Schoetzlein AG, Moger J (2012) Label-free imaging of polymeric nanomedicines using coherent anti-stokes Raman scattering microscopy. *J Raman Spectrosc* 43(5):681–688. doi:[10.1002/jrs.3170](https://doi.org/10.1002/jrs.3170)
- Gendrin C, Roggo Y, Collet C (2007) Content uniformity of pharmaceutical solid dosage forms by near infrared hyperspectral imaging: a feasibility study. *Talanta* 73(4):733–741. doi:[10.1016/j.talanta.2007.04.054](https://doi.org/10.1016/j.talanta.2007.04.054)
- Gordon KC, McGoverin CM (2011) Raman mapping of pharmaceuticals. *Int J Pharm* 417(1–2):151–162. doi:[10.1016/j.ijpharm.2010.12.030](https://doi.org/10.1016/j.ijpharm.2010.12.030)
- Griffiths PR, Misco EV (2014) Infrared and Raman instrumentation for mapping and imaging. In: *Infrared and Raman spectroscopic imaging*, 2nd edn. Wiley-VCH, Weinheim
- Grotheer E, Vogel C, Kolomiets O, Hoffmann U, Unger M, Siesler HW (2014) FT-IR and NIR spectroscopic imaging: principles, practical aspects, and applications in material and pharmaceutical science. *Infrared and Raman spectroscopic imaging*, 2nd edn. Wiley-VCH, Weinheim
- Gucciardi PG (2010) Applications of scanning near-field optical microscopy in life science. In: *Biosystems investigated by scanning probe microscopy*. Springer, Berlin. doi:[10.1007/978-3-540-85039-7_3](https://doi.org/10.1007/978-3-540-85039-7_3)
- Haaser M, Windbergs M, McGoverin CM, Kleinebudde P, Rades T, Gordon KC, Strachan CJ (2011) Analysis of matrix dosage forms during dissolution testing using Raman microscopy. *J Pharm Sci* 100(10):4452–4459. doi:[10.1002/jps.22609](https://doi.org/10.1002/jps.22609)
- Haaser M, Gordon KC, Strachan CJ, Rades T (2013a) Terahertz pulsed imaging as an advanced characterisation tool for film coatings—A review. *Int J Pharm* 457(2):510–520. doi:[10.1016/j.ijpharm.2013.03.053](https://doi.org/10.1016/j.ijpharm.2013.03.053)
- Haaser M, Karrout Y, Velghe C, Cuppok Y, Gordon KC, Pepper M, Siepmann J, Rades T, Taday PF, Strachan CJ (2013b) Application of terahertz pulsed imaging to analyse film coating characteristics of sustained-release coated pellets. *Int J Pharm* 457(2):521–526
- Haaser M, Naelapää K, Gordon KC, Pepper M, Rantanen J, Strachan CJ, Taday PF, Zeitler JA, Rades T (2013c) Evaluating the effect of coating equipment on tablet film quality using terahertz pulsed imaging. *Eur J Pharm Biopharm* 85:1095–1102. doi:[10.1016/j.ejpb.2013.03.019](https://doi.org/10.1016/j.ejpb.2013.03.019)

- Higgins DA, VandenBout DA, Kerimo J, Barbara PF (1996) Polarization-modulation near-field scanning optical microscopy of mesostructured materials. *J Phys Chem* 100(32):13794–13803. doi:[10.1021/jp9609951](https://doi.org/10.1021/jp9609951)
- Ho L, Muller F, Romer M, Gordon KC, Heinamaki J, Kleinebudde P, Pepper M, Rades T, Shen YC, Strachan CJ, Taday PF, Zeitler JA (2007) Analysis of tablet film coating quality using terahertz pulsed imaging. *J Pharm Pharmacol* 59:52
- Ho L, Müller R, Gordon KC, Kleinebudde P, Pepper M, Rades T, Shen Y, Taday PF, Zeitler JA (2008) Applications of terahertz pulsed imaging to sustained-release tablet film coating quality assessment and dissolution performance. *J Control Release* 127(1):79–87. doi:[10.1016/j.jconrel.2008.01.002](https://doi.org/10.1016/j.jconrel.2008.01.002)
- Ho L, Muller R, Kruger C, Gordon KC, Kleinebudde P, Pepper M, Rades T, Shen YC, Taday PF, Zeitler JA (2010) Investigating dissolution performance critical areas on coated tablets: a case study using terahertz pulsed imaging. *J Pharm Sci* 99(1):392–402
- Holman H-YN, Miles R, Hao Z, Wozei E, Anderson LM, Yang H (2009) Real-time chemical imaging of bacterial activity in biofilms using open-channel microfluidics and synchrotron FTIR spectromicroscopy. *Anal Chem* 81(20):8564–8570. doi:[10.1021/ac9015424](https://doi.org/10.1021/ac9015424)
- Isaksson T, Naes T (1988) The effect of multiplicative scatter correction (MSC) and linearity improvement in NIR spectroscopy. *Appl Spectrosc* 42(7):1273–1284. doi:[10.1366/0003702884429869](https://doi.org/10.1366/0003702884429869)
- Jovanovic N, Gerich A, Bouchard A, Jiskoot W (2006) Near-infrared imaging for studying homogeneity of protein–sugar mixtures. *Pharm Res* 23(9):2002–2013. doi:[10.1007/s11095-006-9037-y](https://doi.org/10.1007/s11095-006-9037-y)
- Jurna M, Windbergs M, Strachan CJ, Hartsuiker L, Otto C, Kleinebudde P, Herek JL, Offerhaus HL (2009) Coherent anti-Stokes Raman scattering microscopy to monitor drug dissolution in different oral pharmaceutical tablets. *J Innov Opt Health Sci* 2(1):37–43. doi:[10.1142/s1793545809000322](https://doi.org/10.1142/s1793545809000322)
- Kang E, Wang H, Kwon IK, Robinson J, Park K, Cheng J-X (2006) In situ visualization of paclitaxel distribution and release by coherent anti-stokes Raman scattering microscopy. *Anal Chem* 78(23):8036–8043. doi:[10.1021/ac061218s](https://doi.org/10.1021/ac061218s)
- Kang E, Robinson J, Park K, Cheng J-X (2007) Paclitaxel distribution in poly(ethylene glycol)/poly(lactide-co-glycolic acid) blends and its release visualized by coherent anti-Stokes Raman scattering microscopy. *J Control Release* 122(3):261–268. doi:[10.1016/j.jconrel.2007.05.007](https://doi.org/10.1016/j.jconrel.2007.05.007)
- Karavas E, Georgarakis M, Docoslis A, Bikiaris D (2007) Combining SEM, TEM, and micro-Raman techniques to differentiate between the amorphous molecular level dispersions and nanodispersions of a poorly water-soluble drug within a polymer matrix. *Int J Pharm* 340(1–2):76–83. doi:[10.1016/j.ijpharm.2007.03.037](https://doi.org/10.1016/j.ijpharm.2007.03.037)
- Kawase K, Ogawa Y, Watanabe Y, Inoue H (2003) Non-destructive terahertz imaging of illicit drugs using spectral fingerprints. *Opt Express* 11(20):2549–2554. doi:[10.1364/oe.11.002549](https://doi.org/10.1364/oe.11.002549)
- Kazarian SG, Chan KLA (2003) “Chemical photography” of drug release. *Macromolecules* 36(26):9866–9872. doi:[10.1021/ma035210l](https://doi.org/10.1021/ma035210l)
- Kazarian SG, Ewing AV (2013) Applications of Fourier transform infrared spectroscopic imaging to tablet dissolution and drug release. *Expert Opin Drug Deliv* 10(9):1207–1221. doi:[10.1517/17425247.2013.801452](https://doi.org/10.1517/17425247.2013.801452)
- Keplinger T, Konnerth J, Aguié-Beghin V, Rueggeberg M, Gierlinger N, Burgert I (2014) A zoom into the nanoscale texture of secondary cell walls. *Plant Methods* 10(1):1
- Koehler FW, Lee E, Kidder LH, Lewis EN (2002) Near infrared spectroscopy: the practical chemical imaging solution. *Spectrosc Eur* 14(3):12–19
- Lasch P, Haensch W, Naumann D, Diem M (2004) Imaging of colorectal adenocarcinoma using FT-IR microspectroscopy and cluster analysis. *Biochim Biophys Acta* 1688(2):176–186. doi:[10.1016/j.bbadis.2003.12.006](https://doi.org/10.1016/j.bbadis.2003.12.006)
- Lee E, Huang WX, Chen P, Lewis EN, Vivilecchia RV (2006) High-throughput analysis of pharmaceutical tablet content uniformity by near-infrared chemical imaging. *Spectroscopy* 21(11):24–32

- Lei TC, Ammar DA, Masihzadeh O, Gibson EA, Kahook MY (2011) Label-free imaging of trabecular meshwork cells using coherent anti-Stokes Raman scattering (CARS) microscopy. *Mol Vis* 17(283-84):2628–2633
- Li D, Zheng W, Qu JY (2009) Imaging of epithelial tissue in vivo based on excitation of multiple endogenous nonlinear optical signals. *Opt Lett* 34(18):2853–2855
- Lin W-Q, Jiang J-H, Yang H-F, Ozaki Y, Shen G-L, Yu R-Q (2006) Characterization of chloramphenicol palmitate drug polymorphs by Raman mapping with multivariate image segmentation using a spatial directed agglomeration clustering method. *Anal Chem* 78 (17):6003–6011. doi:[10.1021/ac0520902](https://doi.org/10.1021/ac0520902)
- Lin C-Y, Suhaimi JL, Nien CL, Miljkovic MD, Diem M, Jester JV, Potma EO (2011) Picosecond spectral coherent anti-Stokes Raman scattering imaging with principal component analysis of meibomian glands. *J Biomed Opt* 16(2):021104. doi:[10.1117/1.3533716](https://doi.org/10.1117/1.3533716)
- Ling J, Weitman SD, Miller MA, Moore RV, Bovik AC (2002) Direct Raman imaging techniques for study of the subcellular distribution of a drug. *Appl Optics* 41(28):6006–6017. doi:[10.1364/ao.41.006006](https://doi.org/10.1364/ao.41.006006)
- Lombardi JR, Birke RL (2009) A unified view of surface-enhanced Raman scattering. *Acc Chem Res* 42(6):734–742. doi:[10.1021/ar800249y](https://doi.org/10.1021/ar800249y)
- Lyon RC, Lester DS, Lewis EN, Lee E, Yu LX, Jefferson EH, Hussain AS (2002) Near-infrared spectral imaging for quality assurance of pharmaceutical products: analysis of tablets to assess powder blend homogeneity. *AAPS PharmSciTech* 3(3):E17. doi:[10.1208/pt030317](https://doi.org/10.1208/pt030317)
- Mariangela C-G, Seydou Y, Diego S, Sabine C, Augusto M, Petibois C (2013) Experimental ATR device for real-time FTIR imaging of living cells using brilliant synchrotron radiation sources. *Biotechnol Adv* 31(3):402–407. doi:[10.1016/j.biotechadv.2011.11.009](https://doi.org/10.1016/j.biotechadv.2011.11.009)
- May RK, Su K, Han L, Zhong S, Elliott JA, Gladden LF, Evans M, Shen Y, Zeitler JA (2013) Hardness and density distributions of pharmaceutical tablets measured by terahertz pulsed imaging. *J Pharm Sci* 102(7):2179–2186. doi:[10.1002/jps.23560](https://doi.org/10.1002/jps.23560)
- McCreery R (2000) Raman spectroscopy for chemical analysis. In: *Chemical analysis*, vol 157. Wiley-Interscience, New York
- Mei Y, Miller L, Gao W, Gross RA (2003) Imaging the distribution and secondary structure of immobilized enzymes using infrared microspectroscopy. *Biomacromolecules* 4(1):70–74. doi:[10.1021/bm025811t](https://doi.org/10.1021/bm025811t)
- Melendez PA, Kane KM, Ashvar CS, Albrecht M, Smith PA (2008) Thermal inkjet application in the preparation of oral dosage forms: dispensing of prednisolone solutions and polymorphic characterization by solid-state spectroscopic techniques. *J Pharm Sci* 97(7):2619–2636. doi:[10.1002/jps.21189](https://doi.org/10.1002/jps.21189)
- Michaels CA, Gu XH, Chase DB, Stranick SJ (2004) Near-field infrared imaging and spectroscopy of a thin film polystyrene/poly(ethyl acrylate) blend. *Appl Spectrosc* 58(3):257–263. doi:[10.1366/000370204322886582](https://doi.org/10.1366/000370204322886582)
- Möller KD, Rotschild WG (1971) *Far-infrared spectroscopy*. Wiley series in pure and applied optics. Wiley, New York
- Mouras R, Rischitor G, Downes A, Salter D, Elfick A (2010) Nonlinear optical microscopy for drug delivery monitoring and cancer tissue imaging. *J Raman Spectrosc* 41(8):848–852. doi:[10.1002/jrs.2622](https://doi.org/10.1002/jrs.2622)
- Nagy ZK, Balogh A, Vajna B, Farkas A, Patyi G, Kramarics A, Marosi G (2012) Comparison of electrospun and extruded soluplus (R)-based solid dosage forms of improved dissolution. *J Pharm Sci* 101(1):322–332. doi:[10.1002/jps.22731](https://doi.org/10.1002/jps.22731)
- Nakamoto K, Urasaki T, Hondo S, Murahashi N, Yonemochi E, Terada K (2013) Evaluation of the crystalline and amorphous states of drug products by nanothermal analysis and Raman imaging. *J Pharm Biomed Anal* 75:105–111. doi:[10.1016/j.jpba.2012.11.020](https://doi.org/10.1016/j.jpba.2012.11.020)
- Nan XL, Potma EO, Xie XS (2006) Nonperturbative chemical imaging of organelle transport in living cells with coherent anti-stokes Raman scattering microscopy. *Biophys J* 91(2):728–735. doi:[10.1529/biophysj.105.074534](https://doi.org/10.1529/biophysj.105.074534)

- Nasse MJ, Walsh MJ, Mattson EC, Reininger R, Kajdacsy-Balla A, Macias V, Bhargava R, Hirschmugl CJ (2011) High-resolution Fourier-transform infrared chemical imaging with multiple synchrotron beams. *Nat Methods* 8(5):413–416. doi:[10.1038/nmeth.1585](https://doi.org/10.1038/nmeth.1585)
- Natelson D, Li YJ, Herzog JB (2013) Nanogap structures: combining enhanced Raman spectroscopy and electronic transport. *Phys Chem Chem Phys* 15(15):5262–5275. doi:[10.1039/c3cp44142c](https://doi.org/10.1039/c3cp44142c)
- Niwa M, Hiraishi Y, Iwasaki N, Terada K (2013) Quantitative analysis of the layer separation risk in bilayer tablets using terahertz pulsed imaging. *Int J Pharm* 452(1–2):249–256. doi:[10.1016/j.ijpharm.2013.05.010](https://doi.org/10.1016/j.ijpharm.2013.05.010)
- Palou A, Cruz J, Blanco M, Tomas J, de los Rios J, Alcalá M (2012) Determination of drug, excipients and coating distribution in pharmaceutical tablets using NIR-CI. *J Pharm Anal* 2:90–97
- Pautot S, Frisken BJ, Cheng JX, Xie XS, Weitz DA (2003) Spontaneous formation of lipid structures at oil/water lipid interfaces. *Langmuir* 19(24):10281–10287. doi:[10.1021/la034532f](https://doi.org/10.1021/la034532f)
- Pekdemir ME, Ertürkan D, Külah H, Boyacı IH, Özgen C, Tamer U (2012) Ultrasensitive and selective homogeneous sandwich immunoassay detection by surface enhanced raman scattering (SERS). *Analyst* 137(20):4834–4840
- Petibois C, Cestelli-Guidi M, Piccinini M, Moenner M, Marcelli A (2010) Synchrotron radiation FTIR imaging in minutes: a first step towards real-time cell imaging. *Anal Bioanal Chem* 397(6):2123–2129. doi:[10.1007/s00216-010-3817-2](https://doi.org/10.1007/s00216-010-3817-2)
- Poborchii V, Tada T, Kanayama T, Geshev P (2009) Optimization of tip material and shape for near-UV TERS in Si structures. *J Raman Spectrosc* 40(10):1377–1385. doi:[10.1002/jrs.2417](https://doi.org/10.1002/jrs.2417)
- Pollard MJ, Griffiths PR, Nishikida K (2007) Investigation of the Christiansen effect in the mid-infrared region for airborne particles. *Appl Spectrosc* 61(8):860–866. doi:[10.1366/000370207781540123](https://doi.org/10.1366/000370207781540123)
- Poutiainen S, Pajander J, Savolainen A, Ketolainen J, Jarvinen K (2011) Evolution of granule structure and drug content during fluidized bed granulation by X-ray microtomography and confocal Raman spectroscopy. *J Pharm Sci* 100(12):5254–5269. doi:[10.1002/jps.22719](https://doi.org/10.1002/jps.22719)
- Puchert T, Lochmann D, Menezes JC, Reich G (2010) Near-infrared chemical imaging (NIR-CI) for counterfeit drug identification—a four-stage concept with a novel approach of data processing (Linear Image Signature). *J Pharm Biomed Anal* 51(1):138–145. doi:[10.1016/j.jpba.2009.08.022](https://doi.org/10.1016/j.jpba.2009.08.022)
- R. T. A. dJ (2006) Multivariate curve resolution. In: Gemperline P (ed) *Practical guide to chemometrics*, 2nd edn, Ch. 11. CRC Press, Taylor and Francis Group, Boca Raton, FL, pp 417–473
- Rafferty DW, Koenig JL (2002) FTIR imaging for the characterization of controlled-release drug delivery applications. *J Control Release* 83(1):29–39. doi:[10.1016/s0168-3659\(02\)00135-9](https://doi.org/10.1016/s0168-3659(02)00135-9)
- Ravn C, Skibsted E, Bro R (2008) Near-infrared chemical imaging (NIR-CI) on pharmaceutical solid dosage forms—comparing common calibration approaches. *J Pharm Biomed Anal* 48(3):554–561. doi:[10.1016/j.jpba.2008.07.019](https://doi.org/10.1016/j.jpba.2008.07.019)
- Ricci C, Eliasson C, Macleod NA, Newton PN, Matousek P, Kazarian SG (2007) Characterization of genuine and fake artesunate anti-malarial tablets using Fourier transform infrared imaging and spatially offset Raman spectroscopy through blister packs. *Anal Bioanal Chem* 389(5):1525–1532. doi:[10.1007/s00216-007-1543-1](https://doi.org/10.1007/s00216-007-1543-1)
- Rinia HA, Bonn M, Müller M, Vartiainen EM (2007) Quantitative CARS spectroscopy using the maximum entropy method: the main lipid phase transition. *ChemPhysChem* 8(2):279–287
- Rizi K, Green RJ, Khutoryanskaya O, Donaldson M, Williams AC (2011) Mechanisms of burst release from pH-responsive polymeric microparticles. *J Pharm Pharmacol* 63(9):1141–1155. doi:[10.1111/j.2042-7158.2011.01322.x](https://doi.org/10.1111/j.2042-7158.2011.01322.x)
- Rodriguez LG, Lockett SJ, Holtom GR (2006) Coherent anti-stokes Raman scattering microscopy: a biological review. *Cytometry A* 69A(8):779–791. doi:[10.1002/cyto.a.20299](https://doi.org/10.1002/cyto.a.20299)

- Roggo Y, Edmond A, Chalus P, Ulmschneider M (2005a) Infrared hyperspectral imaging for qualitative analysis of pharmaceutical solid forms. *Anal Chim Acta* 535(1–2):79–87. doi:[10.1016/j.aca.2004.12.037](https://doi.org/10.1016/j.aca.2004.12.037)
- Roggo Y, Jent N, Edmond A, Chalus P, Ulmschneider M (2005b) Characterizing process effects on pharmaceutical solid forms using near-infrared spectroscopy and infrared imaging. *Eur J Pharm Biopharm* 61(1–2):100–110. doi:[10.1016/j.ejpb.2005.04.005](https://doi.org/10.1016/j.ejpb.2005.04.005)
- Romeo M, Mohlenhoff B, Diem M (2006) Infrared micro-spectroscopy of human cells: causes for the spectral variance of oral mucosa (buccal) cells. *Vib Spectrosc* 42(1):9–14. doi:[10.1016/j.vibspec.2006.04.009](https://doi.org/10.1016/j.vibspec.2006.04.009)
- Rustichelli C, Gamberini G, Ferioli V, Gamberini MC, Ficarra R, Tommasini S (2000) Solid-state study of polymorphic drugs: carbamazepine. *J Pharm Biomed Anal* 23(1):41–54. doi:[10.1016/S0731-7085\(00\)00262-4](https://doi.org/10.1016/S0731-7085(00)00262-4)
- Saito Y, Verma P, Masui K, Inouye Y, Kawata S (2009) Nano-scale analysis of graphene layers by tip-enhanced near-field Raman spectroscopy. *J Raman Spectrosc* 40(10):1434–1440. doi:[10.1002/jrs.2366](https://doi.org/10.1002/jrs.2366)
- Sakamoto T, Matsubara T, Sasakura D, Takada Y, Fujimaki Y, Aida K, Miura T, Terahara T, Higo N, Kawanishi T, Hiyama Y (2009) Chemical mapping of tulobuterol in transdermal tapes using microscopic laser Raman spectroscopy. *Pharmazie* 64(3):166–171. doi:[10.1691/ph.2008.8217](https://doi.org/10.1691/ph.2008.8217)
- Samson JS, Wollny G, Brundermann E, Bergner A, Hecker A, Schwaab G, Wieck AD, Havenith M (2006) Setup of a scanning near field infrared microscope (SNIM): imaging of sub-surface nano-structures in gallium-doped silicon. *Phys Chem Chem Phys* 8(6):753–758. doi:[10.1039/b512780g](https://doi.org/10.1039/b512780g)
- Sasic S, Harding L (2010) Global illumination Raman chemical imaging of a combination of two drug molecules in a dry powder inhaler formulation. *Anal Methods* 2(10):1528–1535. doi:[10.1039/c0ay00371a](https://doi.org/10.1039/c0ay00371a)
- Savitzky A, Golay MJE (1964) Smoothing + differentiation of data by simplified least squares procedures. *Anal Chem* 36(8):1627–1639. doi:[10.1021/ac60214a047](https://doi.org/10.1021/ac60214a047)
- Schmid T, Opilik L, Blum C, Zenobi R (2013) Nanoscale chemical imaging using tip-enhanced Raman spectroscopy: a critical review. *Angew Chem Int Ed* 52(23):5940–5954. doi:[10.1002/anie.201203849](https://doi.org/10.1002/anie.201203849)
- Schoenherr C, Haefele T, Paulus K, Francese G (2009) Confocal Raman microscopy to probe content uniformity of a lipid based powder for inhalation: a quality by design approach. *Eur J Pharm Sci* 38(1):47–54. doi:[10.1016/j.ejps.2009.05.011](https://doi.org/10.1016/j.ejps.2009.05.011)
- Shaver JM (2001) Handbook of Raman spectroscopy from the research laboratory to the process line. Practical spectroscopy. Marcel Dekker, New York
- Shen YC (2011) Terahertz pulsed spectroscopy and imaging for pharmaceutical applications: a review. *Int J Pharm* 417(1–2):48–60
- Slipchenko MN, Chen H, Ely DR, Jung Y, Carvajal MT, Cheng J-X (2010) Vibrational imaging of tablets by epi-detected stimulated Raman scattering microscopy. *Analyst* 135(10):2613–2619. doi:[10.1039/c0an00252f](https://doi.org/10.1039/c0an00252f)
- Smith RM, Arnold MA (2011) Terahertz time-domain spectroscopy of solid samples: principles, applications, and challenges. *Appl Spectrosc Rev* 46(8):636–679
- Sonntag MD, Pozzi EA, Jiang N, Hersam MC, Van Duyne RP (2014) Recent advances in tip-enhanced Raman spectroscopy. *J Phys Chem Lett* 5(18):3125–3130. doi:[10.1021/jz5015746](https://doi.org/10.1021/jz5015746)
- Steele DF, Young PM, Price R, Smith T, Edge S, Lewis D (2004) The potential use of Raman mapping to investigate in vitro deposition of combination pressurized metered-dose inhalers. *AAPS J* 6(4):41–44
- Steinier J, Termonia Y, Deltour J (1972) Smoothing and differentiation of data by simplified least squares procedure. *Anal Chem* 44(11):1906–1909. doi:[10.1021/ac60319a045](https://doi.org/10.1021/ac60319a045)
- Strachan C (2012) Applications of Raman, CARS and SRS imaging in dosage form development. *Eur Pharm Rev* 17(2):41–48

- Strachan CJ, Rades T, Newnham DA, Gordon KC, Pepper M, Taday PF (2004) Using terahertz pulsed spectroscopy to study crystallinity of pharmaceutical materials. *Chem Phys Lett* 390 (1–3):20–24
- Strachan CJ, Windbergs M, Offerhaus HL (2011) Pharmaceutical applications of non-linear imaging. *Int J Pharm* 417(1–2):163–172. doi:[10.1016/j.ijpharm.2010.12.017](https://doi.org/10.1016/j.ijpharm.2010.12.017)
- Vajna B, Farkas I, Szabo A, Zsigmond Z, Marosi G (2010) Raman microscopic evaluation of technology dependent structural differences in tablets containing imipramine model drug. *J Pharm Biomed Anal* 51(1):30–38. doi:[10.1016/j.jpba.2009.07.030](https://doi.org/10.1016/j.jpba.2009.07.030)
- Vajna B, Farkas I, Farkas A, Pataki H, Nagy Z, Madarasz J, Marosi G (2011a) Characterization of drug-cyclodextrin formulations using Raman mapping and multivariate curve resolution. *J Pharm Biomed Anal* 56(1):38–44. doi:[10.1016/j.jpba.2011.05.005](https://doi.org/10.1016/j.jpba.2011.05.005)
- Vajna B, Pataki H, Nagy Z, Farkas I, Marosi G (2011b) Characterization of melt extruded and conventional Isoptin formulations using Raman chemical imaging and chemometrics. *Int J Pharm* 419(1–2):107–113. doi:[10.1016/j.ijpharm.2011.07.023](https://doi.org/10.1016/j.ijpharm.2011.07.023)
- van Apeldoorn AA, van Manen HJ, Bezemer JM, de Bruijn JD, van Blitterswijk CA, Otto C (2004) Raman imaging of PLGA microsphere degradation inside macrophages. *J Am Chem Soc* 126 (41):13226–13227. doi:[10.1021/ja0459936](https://doi.org/10.1021/ja0459936)
- van der Weerd J, Kazarian SG (2004) Combined approach of FTIR imaging and conventional dissolution tests applied to drug release. *J Control Release* 98(2):295–305. doi:[10.1016/j.jconrel.2004.05.007](https://doi.org/10.1016/j.jconrel.2004.05.007)
- van der Weerd J, Chan KLA, Kazarian SG (2004) An innovative design of compaction cell for in situ FT-IR imaging of tablet dissolution. *Vib Spectrosc* 35(1–2):9–13. doi:[10.1016/j.vibspec.2003.11.004](https://doi.org/10.1016/j.vibspec.2003.11.004)
- van der Weert M, van't Hof R, van der Weerd J, Heeren RMA, Posthuma G, Hennink WE, Crommelin DJA (2000) Lysozyme distribution and conformation in a biodegradable polymer matrix as determined by FTIR techniques. *J Control Release* 68(1):31–40. doi:[10.1016/s0168-3659\(00\)00227-3](https://doi.org/10.1016/s0168-3659(00)00227-3)
- Van Eerdenbrugh B, Lo M, Kjoller K, Marcott C, Taylor LS (2012) Nanoscale mid-infrared imaging of phase separation in a drug-polymer blend. *J Pharm Sci* 101(6):2066–2073. doi:[10.1002/jps.23099](https://doi.org/10.1002/jps.23099)
- Vancso GJ, Hillborg H, Schonherr H (2005) Chemical composition of polymer surfaces imaged by atomic force microscopy and complementary approaches. In: Anantawaraskul S (ed) *Polymer analysis, polymer theory. Advances in polymer science*, vol 182. Springer Verlag, Berlin Heidelberg, Germany, pp 55–129. doi:[10.1007/b135560](https://doi.org/10.1007/b135560)
- Vervaeck A, Saeuens L, De Geest BG, De Beer T, Carleer R, Adriaensens P, Remon JP, Vervaeck C (2013) Prilling of fatty acids as a continuous process for the development of controlled release multiparticulate dosage forms. *Eur J Pharm Biopharm* 85(3):587–596. doi:[10.1016/j.ejpb.2013.02.003](https://doi.org/10.1016/j.ejpb.2013.02.003)
- Wallace VP, Taday PF, Fitzgerald AJ, Woodward RM, Cluff J, Pye RJ, Arnone DD (2004) Terahertz pulsed imaging and spectroscopy for biomedical and pharmaceutical applications. *Faraday Discuss* 126:255–263
- Ward S, Perkins M, Zhang JX, Roberts CJ, Madden CE, Luk SY, Patel N, Ebbens SJ (2005) Identifying and mapping surface amorphous domains. *Pharm Res* 22(7):1195–1202. doi:[10.1007/s11095-005-6027-4](https://doi.org/10.1007/s11095-005-6027-4)
- Widjaja E, Seah RKH (2008) Application of Raman microscopy and band-target entropy minimization to identify minor components in model pharmaceutical tablets. *J Pharm Biomed Anal* 46(2):274–281. doi:[10.1016/j.jpba.2007.09.023](https://doi.org/10.1016/j.jpba.2007.09.023)
- Widjaja E, Li CZ, Garland M (2002) Semi-batch homogeneous catalytic in-situ spectroscopic data. FTIR spectral reconstructions using band-target entropy minimization (BTEM) without spectral preconditioning. *Organometallics* 21(9):1991–1997. doi:[10.1021/om010933j](https://doi.org/10.1021/om010933j)
- Widjaja E, Crane N, Chen TC, Morris MD, Ignelzi MA, McCreadie BR (2003a) Band-target entropy minimization (BTEM) applied to hyperspectral Raman image data. *Appl Spectrosc* 57 (11):1353–1362. doi:[10.1366/000370203322554509](https://doi.org/10.1366/000370203322554509)

- Widjaja E, Li CZ, Chew W, Garland M (2003b) Band-target entropy minimization. A robust algorithm for pure component spectral recovery. Application to complex randomized mixtures of six components. *Anal Chem* 75(17):4499–4507. doi:[10.1021/ac0263622](https://doi.org/10.1021/ac0263622)
- Widjaja E, Kanaujia P, Lau G, Ng WK, Garland M, Saal C, Hanefeld A, Fischbach M, Maio M, Tan RBH (2011) Detection of trace crystallinity in an amorphous system using Raman microscopy and chemometric analysis. *Eur J Pharm Sci* 42(1–2):45–54. doi:[10.1016/j.ejps.2010.10.004](https://doi.org/10.1016/j.ejps.2010.10.004)
- Windbergs M, Jurna M, Offerhaus HL, Herek JL, Kleinebudde P, Strachan CJ (2009) chemical imaging of oral solid dosage forms and changes upon dissolution using coherent anti-Stokes Raman scattering microscopy. *Anal Chem* 81(6):2085–2091. doi:[10.1021/ac8020856](https://doi.org/10.1021/ac8020856)
- Windbergs M, Haaser M, McGoverin CM, Gordon KC, Kleinebudde P, Strachan CJ (2010) Investigating the relationship between drug distribution in solid lipid matrices and dissolution behaviour using Raman spectroscopy and mapping. *J Pharm Sci* 99(3):1464–1475. doi:[10.1002/jps.21894](https://doi.org/10.1002/jps.21894)
- Xu P, Gullotti E, Tong L, Highley CB, Errabelli DR, Hasan T, Cheng J-X, Kohane DS, Yeo Y (2009) Intracellular drug delivery by poly(lactic-co-glycolic acid) nanoparticles, revisited. *Mol Pharm* 6(1):190–201. doi:[10.1021/mp800137z](https://doi.org/10.1021/mp800137z)
- Yao S, Moenner M, Engdahl A, Petibois C (2012) Use of synchrotron-radiation-based FTIR imaging for characterizing changes in cell contents. *Anal Bioanal Chem* 404(5):1311–1316. doi:[10.1007/s00216-012-6223-0](https://doi.org/10.1007/s00216-012-6223-0)
- Zeitler JA, Kogermann K, Rantanen J, Rades T, Taday PF, Pepper M, Aaltonen J, Strachan CJ (2007a) Drug hydrate systems and dehydration processes studied by terahertz pulsed spectroscopy. *Int J Pharm* 334(1–2):78–84
- Zeitler JA, Shen YC, Baker C, Taday PF, Pepper M, Rades T (2007b) Analysis of coating structures and interfaces in solid oral dosage forms by three dimensional terahertz pulsed imaging. *J Pharm Sci* 96(2):330–340
- Zeitler JA, Taday PF, Newnham DA, Pepper M, Gordon KC, Rades T (2007c) Terahertz pulsed spectroscopy and imaging in the pharmaceutical setting—a review. *J Pharm Pharmacol* 59(2):209–223
- Zhang L, Henson MJ, Sekulic SS (2005) Multivariate data analysis for Raman imaging of a model pharmaceutical tablet. *Anal Chim Acta* 545(2):262–278. doi:[10.1016/j.aca.2005.04.080](https://doi.org/10.1016/j.aca.2005.04.080)
- Zhang G, Flach CR, Mendelsohn R (2007) Tracking the dephosphorylation of resveratrol triphosphate in skin by confocal Raman microscopy. *J Control Release* 123(2):141–147. doi:[10.1016/j.jconrel.2007.08.001](https://doi.org/10.1016/j.jconrel.2007.08.001)
- Zhang D, Wang P, Slipchenko MN, Ben-Amotz D, Weiner AM, Cheng J-X (2013) Quantitative vibrational imaging by hyperspectral stimulated Raman scattering microscopy and multivariate curve resolution analysis. *Anal Chem* 85(1):98–106. doi:[10.1021/ac3019119](https://doi.org/10.1021/ac3019119)
- Zumbusch A, Holtom GR, Xie XS (1999) Three-dimensional vibrational imaging by coherent anti-Stokes Raman scattering. *Phys Rev Lett* 82(20):4142–4145. doi:[10.1103/PhysRevLett.82.4142](https://doi.org/10.1103/PhysRevLett.82.4142)

Chapter 18

Magnetic Resonance Imaging and Its Applications to Solid Pharmaceutical Dosage Forms

M.D. Mantle

Abstract Nuclear magnetic resonance (NMR) in the form of both spectroscopy and imaging are powerful tools in most areas of scientific research. NMR spectroscopy yields quantitative information such as chemical species concentration and their three-dimensional molecular structure. The addition of pulsed magnetic field gradients to a spectroscopic experiment then provides non-invasive localised information in three spatial dimensions, i.e., a magnetic resonance image. This powerful combination of magnetic resonance imaging with NMR spectroscopy makes it possible to probe local chemical, physical and mass transport phenomena (in the form of diffusion and flow) and is particularly suited to study the dissolution behaviour of solid pharmaceutical dosage forms. This Chapter will focus on the fundamentals of the theory behind quantitative magnetic resonance spectroscopy and imaging, and highlights the importance of understanding the origins of the various magnetic resonance contrast mechanisms that are inherent in the systems discussed. Examples will be drawn from both model and real pharmaceutical solid dosage forms undergoing dissolution testing in a USP-IV dissolution cell under pharmacopeial conditions to illustrate the ideas discussed in the main text.

Keywords Nuclear magnetic resonance • Magnetic resonance imaging • Dissolution • Solid dosage forms • Quantitative • Mass-transport • T_1 and T_2 relaxation

1 Introduction

It is fair to say that nuclear magnetic resonance (NMR), in the form of magnetic resonance imaging (MRI) and NMR spectroscopy are worldwide phenomena that collectively provide unrivalled information in many areas of medical, physical,

M.D. Mantle (✉)

Department of Chemical Engineering and Biotechnology, University of Cambridge, Pembroke Street, Cambridge CB2 3RA, UK

e-mail: mdm20@cam.ac.uk

chemical, biological and engineering sciences. In the last 70 years six Nobel prizes have been awarded for magnetic resonance related phenomena, which illustrates the global importance and impact of the technique. MRI and NMR spectroscopy whilst relying on the same fundamental physical phenomena are generally thought of as quite separate analytical tools. NMR spectroscopy of both solids and liquids provides chemical and structural information whilst MRI provides spatial information. Of course, experienced magnetic resonance practitioners and researchers know that, in principle, any NMR spectroscopic technique can also be spatially localised. For example, the use of *chemical shift imaging* techniques can yield a two dimensional spatial image from an object that also has chemical spectra from every single pixel element that constitutes that image. This chapter will mainly focus on the theory behind, and applications of MRI to solid dosage forms used in pharmaceutical research. Some of the earliest published work concerning MRI and pharmaceutical research dates back to the work of Rajabisiahboomi et al. (1994) who used traditional spin echo magnetic resonance imaging to investigate the swelling of hydrating hydroxypropylmethylcellulose (HPMC) tablets. Today, there is a large collection of published material concerning the use of magnetic resonance imaging and its application to pharmaceutical science. There are several comprehensive recent reviews (Melia et al. 1998; Richardson et al. 2005; Zeitler and Gladden 2009; Nott 2010; Mantle 2013) outlining the application of magnetic resonance to pharmaceutically relevant research and the interested reader is urged to consult these for a detailed discussion of the subject. The aims of this chapter are:

- To provide the reader with a sound knowledge of the underlying theory of NMR and MRI.
- To provide current examples of state-of-the art MRI research pertaining to solid dosage forms.
- To give some practical hints and tips commonly adopted by MRI practitioners to optimise the fidelity of the acquired data.

2 Overview of Magnetic Resonance Theory

The complete theory of NMR and MRI is long and complex and thus the interested reader is referred to several excellent texts on the subject for a thorough treatment (Callaghan 1993; Haacke et al. 1999; Levitt 2001; Liang and Lauterbur 2000). The next three sections outline the basic fundamental theory behind nuclear magnetic resonance spectroscopy and magnetic resonance imaging and describe how chemical and spatial information are obtained from nuclear spin systems.

2.1 The Origins of Nuclear Magnetic Resonance

When nuclei with non-zero nuclear spin angular momentum, denoted by quantum number, I , (e.g., for hydrogen nuclei (^1H) in water $I = \frac{1}{2}$) are placed in a strong homogenous magnetic field, B_0 , (typically between 1 and 10 T), the nuclear spin energy levels split into $(2I + 1)$ possible orientations. For hydrogen nuclei two such energy levels exist: the high energy state aligned against the direction of the external field B_0 denoted by the symbol $|\beta\rangle$ $\Rightarrow -\frac{1}{2}$ and a low energy state aligned with the direction of B_0 , denoted by symbol $|\alpha\rangle$ $\Rightarrow +\frac{1}{2}$ (see Fig. 18.1a). At equilibrium the individual magnetic moments, $\mu_{\alpha,\beta}$ of each hydrogen nucleus that are associated with the quantum mechanical spin states $|\alpha\rangle$ and $|\beta\rangle$ distribute

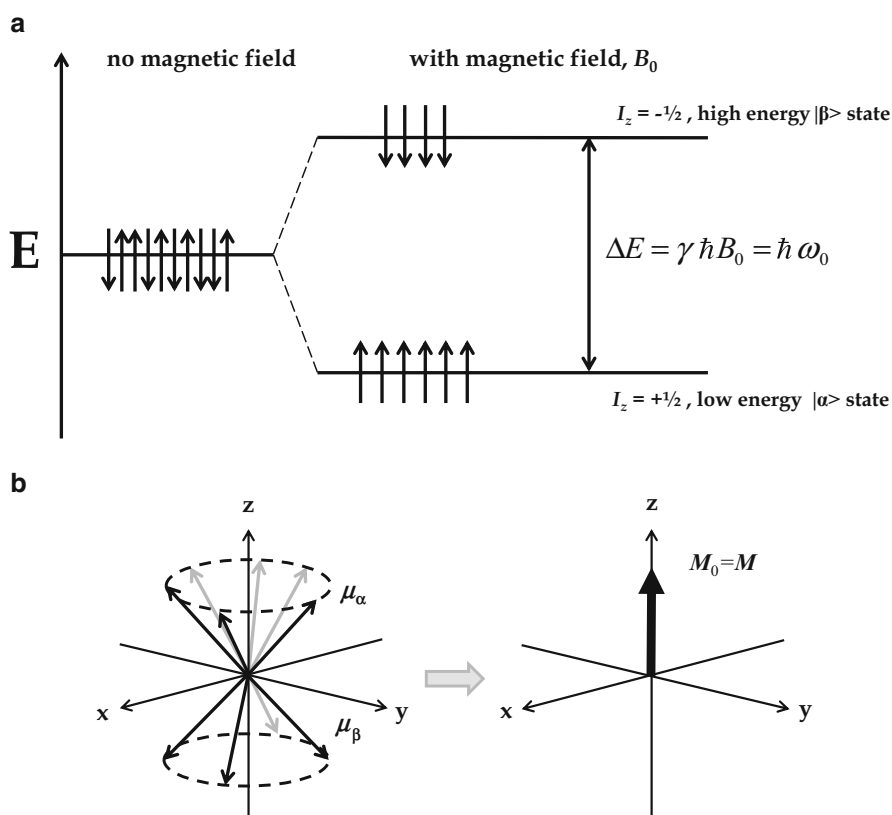


Fig. 18.1 (a) Splitting of the otherwise degenerate nuclear spin energy levels when nuclear ensemble with spin $I = \frac{1}{2}$ is placed into a strong magnetic field B_0 . (b) Precession of the individual magnetic moments, $\mu_{\alpha,\beta}$, about the main B_0 field which is directed along the z-axis. The summation over all $\mu_{\alpha,\beta}$ gives rise to a net magnetisation, $M_0 = M$

themselves between the two energy levels according to Boltzmann's distribution given by:

$$\frac{N_\beta}{N_\alpha} = \exp\left[-\frac{\Delta E}{kT}\right] \quad (18.1)$$

Where N_α is the population of magnetic moments in the lower energy state and N_β the population of magnetic moments in the higher energy state, ΔE the difference in energy between the two states $|\alpha\rangle$ and $|\beta\rangle$, k is Boltzmann's constant and T is the temperature. In terms of classical mechanics and the standard vector picture of NMR (Levitt 2002) (see Fig. 18.1b) the individual magnetic moments do not align perfectly with or against the main magnetic field B_0 and instead *precess* in a conical fashion about the external magnetic field B_0 at a well defined frequency known as the Larmor frequency, ω_0 , given by:

$$\omega_0 = \gamma B_0 = \Delta E \quad (18.2)$$

where γ is the gyromagnetic ratio of the nuclei under investigation. The (vector) summation of the individual nuclear magnetic moments $\sum_{i=1}^{N_A} \mu_{i(\alpha,\beta)}$, where N_A is

Avagadro's number, gives rise to a macroscopic net magnetisation vector, $\mathbf{M}_0 = \mathbf{M}$, aligned parallel to the direction of the magnetic field, B_0 . Note: that the vector sum of the x - and y -components of $\boldsymbol{\mu}$ is zero. This process is summarised in Fig. 18.1b.

In order to obtain a simple NMR spectrum of a sample, we must disturb the magnetisation vector, \mathbf{M}_0 , from its equilibrium position. Practically this is implemented by exposing the system/sample to electromagnetic energy of appropriate frequency, $\hbar\omega_0$ (radio-frequency (r.f.)), via a radio frequency coil that surrounds the sample itself. If a r.f. pulse is applied (Fig. 18.2a) to the spin system at equilibrium a resonant absorption occurs between these nuclear spin energy levels.

In terms of the classical magnetisation vector shown in Fig. 18.2b the action of the excitation pulse, in this case a pulse of r.f. applied at right angles (along x') to the direction of the superconducting field, is therefore to rotate \mathbf{M} about the x' -axis. In this example, the r.f. excitation is applied with a fixed power B_1 and for a sufficient time that \mathbf{M} is rotated to lie along the y' -axis in the x' - y' plane.¹ If this condition is met, the r.f. pulse is referred to as a $(\pi/2)_{x'}$ (or 90°) pulse where the " x' " subscript indicates the direction or phase of the applied r.f. pulse; here it has been applied

¹ In terms of the spin populations shown in Fig. 18.1a, a 90° r.f. pulse equalises the populations of both the $|\alpha\rangle$ and $|\beta\rangle$ energy states resulting in a non-equilibrium situation, i.e., the spin system has excess energy. Similarly a 180° r.f. inversion pulse would invert the initial equilibrium resulting in an excess population in the higher energy state.

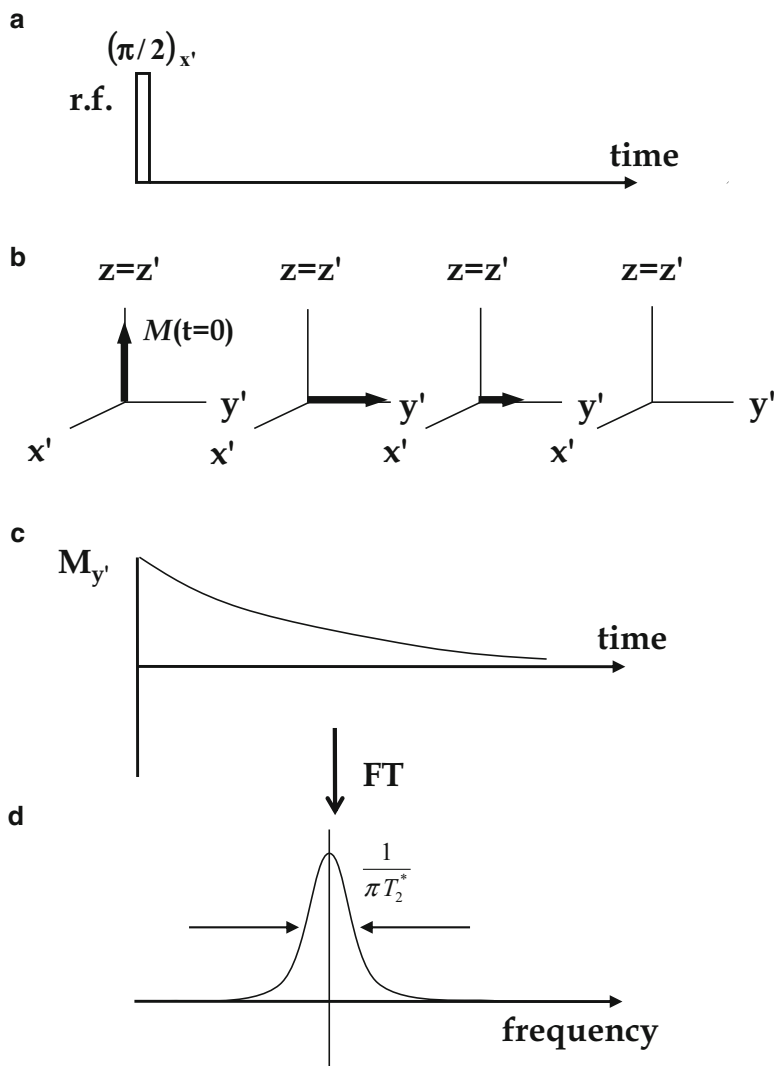


Fig. 18.2 (a) The behaviour of the magnetisation vector in the rotating frame of reference is shown in response to the application of a single $(\pi/2)$ r.f. pulse along x' . (b) The decay of the magnetisation vector in the x' - y' plane yields the received time-domain signal, called the Free Induction Decay (FID), shown in (c). The result of a Fourier transform of the FID is the spectrum shown in (d). If a liquid state sample is studied the full-width at half-maximum-height of the spectral signal is $1/\pi T_2^*$ (see Eq. (18.5))

along the x' direction in the rotating frame of reference and has rotated \mathbf{M} through $\pi/2$ rad. In general the rotation angle or “tip” angle, θ , of a r.f. pulse is given by:

$$\theta = \gamma B_1 t_p \quad (18.3)$$

where B_1 is the power and t_p the length of the r.f. pulse respectively. The processes shown in Fig. 18.2 are represented in the *rotating* frame of reference which is adopted to simplify the representation of the action of the r.f. pulses. In this rotating frame representation, the MR time domain signal, following r.f. excitation, is measured by acquiring the signal (i.e., the magnitude of the magnetisation vector) aligned along y' as a function of time; this signal will decay with time due to the recovery of the magnetisation along z' and, at shorter timescales, due to the loss of phase coherence of the spin isochromats comprising the net magnetisation vector along the y' axis (Fig. 18.2c). These decay processes are termed the spin-lattice (T_1) and spin-spin relaxation (T_2) processes and are key to obtaining quantitative information from the sample of interest; T_1 and particularly T_2 relaxation will be discussed further in the next Sect. 2.2. The decay of the magnetisation along the y' -axis is recorded as a decaying oscillatory voltage that is induced in the r.f. coil used for excitation. This induced analogue voltage is usually in the micro-volts range and is pre-amplified into milli-volts before subsequent digitisation. Fourier transform of this time-domain signal yields the frequency domain spectral response in which the area under the spectral peak (with appropriate calibration) gives a quantitative measure of both the number of molecules of a given molecular species and the number of ^1H nuclei within that molecule (Fig. 18.2d). Different chemical, i.e., electron environments present in chemical bonds will modify slightly (parts per million, ppm) the B_0 field experienced at the nucleus giving slightly different resonance frequencies for the individual active nuclei within a sample leading to the chemical specificity of the NMR experiment. For example, a simple “pulse acquire” experiment on a tube of ethanol will after Fourier transformation yield a ^1H NMR spectrum with three distinct peaks with intensities in the ratio of 1:2:3 corresponding to the $-\text{OH}$, $-\text{CH}_2-$ and $-\text{CH}_3$ chemical moieties. Thus NMR is an intrinsically chemically specific, quantitative measurement. This is the essential attribute which makes it such a powerful tool in many areas of scientific research.

2.2 Nuclear Spin Relaxation (T_1 and T_2)

This section outlines the principles behind T_1 and T_2 nuclear spin relaxation processes and how they can affect the interpretation of the acquired data. Immediately after a $(\pi/2)$ r.f. excitation pulse the two energy levels of our spin $\frac{1}{2}$ system have equal populations of $|\alpha\rangle$ and $|\beta\rangle$ spin states. In this situation the nuclear spin system has excess energy and must return to thermal equilibrium by a process known as *relaxation*. A number of different relaxation times characterise different mechanisms (Levitt 2002) for this re-distribution of energy. The most important are the spin-lattice relaxation (T_1) and spin-spin relaxation (T_2) time constants. These time constants characterise the physicochemical environment of the molecules being studied. T_1 relaxation characterises the energy exchange between the excited spin and the surrounding physical environment (i.e., the lattice), while T_2 is

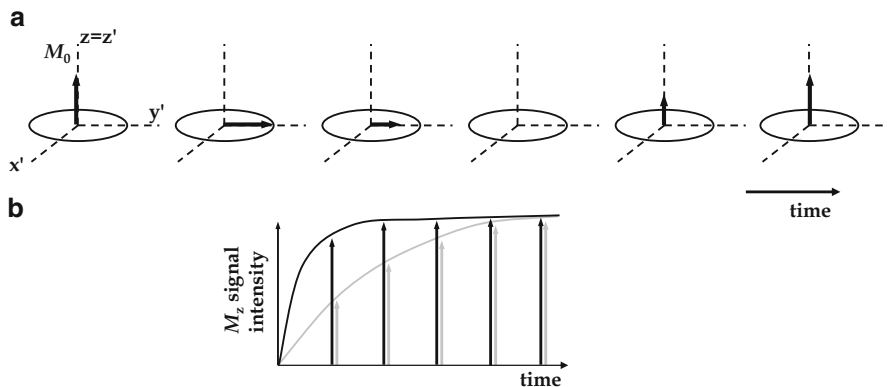


Fig. 18.3 (a) The action of the $\pi/2$ pulse (applied along the x' direction) is to rotate the magnetisation vector into the $x'-y'$ plane, along the y' direction. At timescales longer than T_2 , the magnetisation recovers back along the direction of the magnetic field B_0 , with a characteristic time constant T_1 . (b) Two different species within the same sample may have different characteristic T_1 values. In this example, the species associated with the *black arrows* has a shorter T_1 than the species associated with the *grey arrows*; the arrows indicate the magnitude of the acquired signal intensity following the initial r.f. excitation. If data are acquired at long times after r.f. excitation, equal signal intensity will be acquired from both species if they both have the same (spin) number density. However, if data are acquired very soon after the excitation pulse, the acquired signal will be predominantly associated with the species characterised by the shorter T_1 . This illustrates the principle of relaxation contrast

associated with entropy-exchange processes within the spin system. In general distinct chemical species will have their own T_1/T_2 characteristics which will vary depending on the physical state in which that species exists.

2.2.1 Spin-Lattice Relaxation, T_1

We have seen that at thermodynamic equilibrium and before the application of the r.f. excitation pulse the net macroscopic magnetisation vector, \mathbf{M} , is aligned along the direction of the static magnetic field B_0 (see Fig. 18.3a). It is the magnitude of this vector that provides the quantitative measurement of the number of nuclear spins excited within the sample.

After excitation by a $(\pi/2)_{x'}$ r.f. pulse the magnetisation vector lies along the y' -axis. The spin systems then act to return to equilibrium via a monotonic increase in the magnitude of the magnetisation vector back along z' as a function of time. After a few milli-seconds only a fraction of the magnetisation will have been re-established along z' . If we wait times $\sim 5-7$ times longer than T_1 , the full magnitude of M_0 will have recovered along z' . The magnitude of the magnetisation vector (Fig. 18.3b) along z' , $M_{z'}$, as a function of the 'waiting' time, τ , can be written down analytically for any specific r.f. pulse sequence. Equation (18.4)

describes the recovery of the magnetisation back along z' for a saturation recovery pulse sequence:

$$M_z(\tau) = M_0 \left[1 - \exp\left(-\frac{\tau}{T_1}\right) \right] \quad (18.4)$$

By recording M_z for several τ values and fitting these data to Eq. (18.4), both the T_1 and the value of M_0 (which quantifies the number of initially excited spins) are obtained.

2.2.2 Spin-Spin Relaxation, T_2

On time-scales of less than or equal to that of T_1 , spin-spin relaxation processes occur. An important spin-spin relaxation time constant is T_2^* which characterises a faster decay of the magnetisation along y' and includes the effects of both B_0 magnetic field heterogeneities and irreversible spin-spin interactions on the loss of phase coherence of the magnetisation following excitation. The simple pulse-acquire sequence (with no refocusing) shown in Fig. 18.4a gives a time-domain

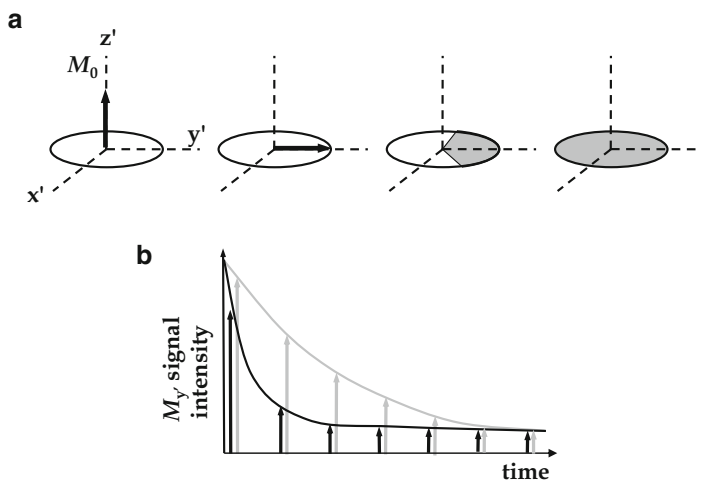


Fig. 18.4 (a) Similar to Fig. 18.3, the $\pi/2$ rotates the magnetisation vector into the $x'-y'$ plane. The individual spin isochromats then dephase in the $x'-y'$ plane, as shown by the increasing size of the shaded region with time. (b) A plot of the M_y values for two different characteristic T_2^* values yields two different decay curves shown as *grey* and *black* curves in (b). Again, choosing a suitable time to collect the data after the initial excitation pulse will lead to different amounts of each species being reflected in the acquired data

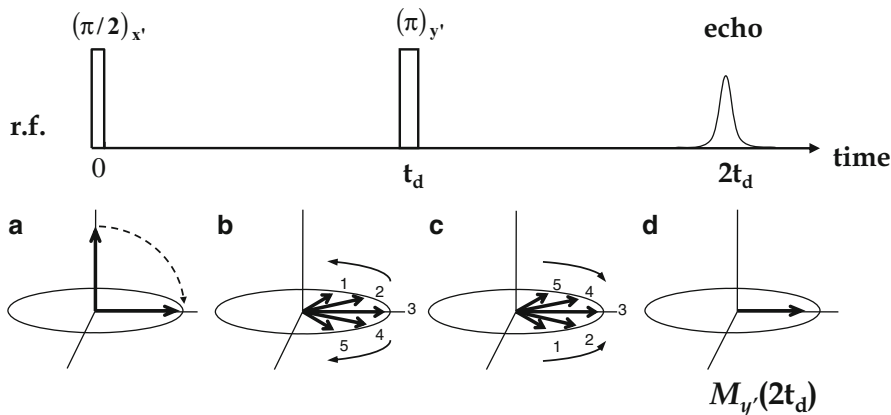


Fig. 18.5 A Hahn spin echo pulse sequence used to determine T_2 . (a) A $(\pi/2)_{x'}$ pulse rotates M_0 into the y' -direction, and (b) the spin isochromats dephase with time. At a time t_d later, a $(\pi)_{y'}$ pulse is applied along the y' -axis causing the spins to 'refocus' (c) along the y' -axis to form an 'echo' (d) at time $2t_d$. The decrease in magnitude of the magnetisation vector between stages (a) and (d) provides a measure of T_2 (Eq. (18.6)). All 'reversible' contributions to the T_2 process are removed by the application of the $(\pi)_{y'}$ pulse

response in which the envelope of the decay in the time domain and hence the width, $\Delta\nu$, of the frequency domain signal is characterised by:

$$T_2^* = \frac{1}{\pi\Delta\nu} \quad (18.5)$$

The decay of the coherent magnetisation aligned along y' , due to spin-spin interactions but not magnetic field heterogeneities, is characterised by the time constant T_2 and measured using a Hahn (1950) spin echo pulse sequence as shown in Fig. 18.5.

T_2 characterises the loss of phase coherence of the individual spin isochromats in the transverse plane within the spin ensemble comprising the total magnetisation vector M_0 . A spin isochromat represents a group of spins which experiences the same homogeneous magnetic field and which therefore behaves in the same way following the excitation pulse. Immediately following the excitation r.f. pulse the individual isochromats become asynchronous and are thus said to "lose phase coherence" with each other. The loss of phase coherence is a result of irreversible spin-spin interactions and local variations in B_0 .

T_2 relaxation may be defined as:

$$M_y(\tau) = M_0 \exp\left(-\frac{\tau}{T_2}\right) \quad (18.6)$$

where τ is the (variable) time between the excitation pulse and maximum of the echo at $2t_d$. The generic Hahn spin echo sequence shown in Fig. 18.5, has widespread use in MR methods, far beyond simple measurement of T_2 . In short, by using

an echo sequence, instead of exciting the system and then allowing the magnetisation to decay to zero as in Fig. 18.4, the majority of the magnetisation can be recovered for use in subsequent measurements. The simple Hahn echo sequence shown in Fig. 18.5 is ubiquitous in MR imaging pulse sequences. However, one of the problems associated with the measurement of T_2 relaxation times, and hence the back calculation (quantification) of the true spin population at time $t=0$ of the species of interest, using the simple Hahn echo sequence is that molecular motion in the form of diffusion (and perhaps flow) can occur during the time interval τ . The (random) self-diffusion of molecules into spatial regions of different local magnetic field can cause irreversible signal loss in the Hahn echo experiment and thus the measured exponential decay will be faster than expected. This type of behaviour was first realised by Hahn and Eq. (18.6) has to be modified (Callaghan 1993) to account for diffusion in a linear magnetic field gradient giving:

$$M_y(\tau) = M_0 \exp\left(-\frac{\tau}{T_2}\right) \times \exp\left(-\frac{1}{12}\gamma^2 G^2 D (2\tau^3)\right) \quad (18.7)$$

where G is the magnitude of the magnetic field gradient strength and D is molecular self-diffusion coefficient of the species being studied. The influence of molecular diffusion in linear magnetic field gradients on the measurement of T_2 relaxation times may be minimised by adopting the so called Carr, Purcell, Meiboom and Gill (Carr and Purcell 1954; Meiboom and Gill 1958) T_2 measurement which is essentially a repeated Hahn spin echo consisting of a series of π refocusing pulses that are phase shifted by $\pi/2$ from the initial excitation pulse. The delay between the initial r.f. excitation pulse and the π refocusing pulse is kept to a minimum to minimise the diffusive signal losses during the successive refocusing periods. Thus the CPMG T_2 experiment is a better reflection of the true T_2 relaxation time of a sample than the simple Hahn echo experiment.

3 Magnetic Resonance Imaging

So far, the discussion on NMR theory has been limited to spectroscopic measurements from the whole sample. This type of multi-dimensional measurement is still used in abundance by chemists and biochemists whose common goal is essentially to determine the composition, structure, bonding and dynamic properties of molecular systems. Our goal now is to introduce the concepts and theory that will allow us to obtain local/spatially resolved information from a sample of interest as opposed to the whole sample itself. We chose here a simple one-dimensional spin echo imaging sequence to illustrate the principle behind the techniques. More specific imaging sequences are discussed later in Sect. 4.

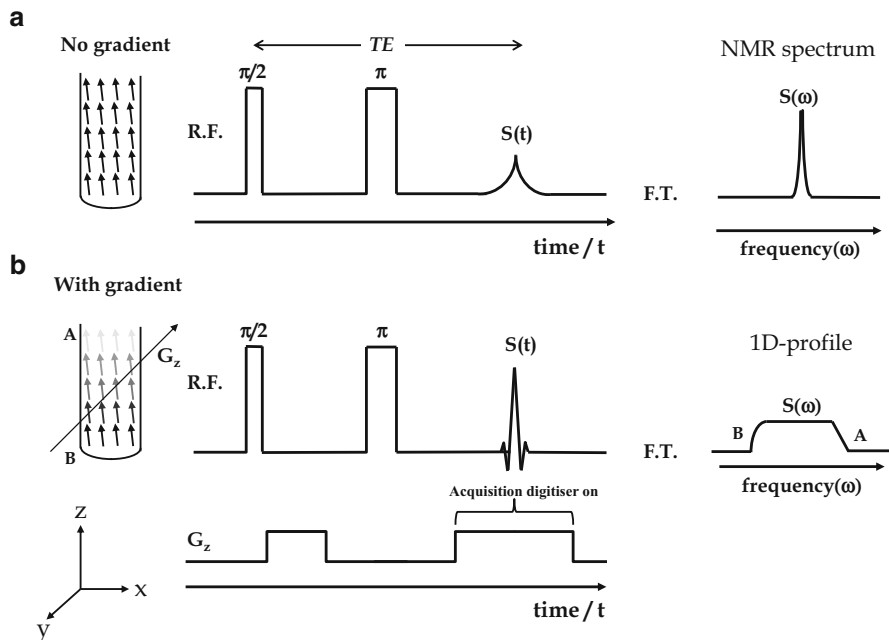


Fig. 18.6 (a) A Hahn spin echo applied to a water sample and its resulting ^1H NMR spectrum. (b) A simple 1D-Hahn spin echo profile sequence applied to the sample in the z -direction. Note the different shades of *grey* indicate the different Larmor frequencies that are set-up when a magnetic field gradient is applied. The Fourier transform of the resulting FID yields a simple 1D-image

3.1 One Dimensional Image Profiling

Consider a 20 mm outer diameter glass tube filled to 2.0 cm depth of water which is placed at the centre of a 7.05 T superconducting magnet and is surrounded by a 25.0 mm birdcage r.f. coil. Normally, for imaging systems the r.f. coil is then surrounded by a shielded 3-axis magnetic field gradient system. As we have seen a simple Hahn spin echo r.f. pulse sequence applied to the ^1H nuclei within the sample will, upon Fourier transformation and appropriate phase correction (Levitt 2002), yield a single narrow line at the basic Larmor frequency (see Fig. 18.6a).

Spatial resolution of the water sample is achieved by the addition of a pair of linear magnetic field gradient pulses (in say the laboratory z -direction) that are inserted (i) between the $\pi/2$ and π pulse and (ii) during the acquisition according to Fig. 18.6b. The acquisition (digitisation) of the analogue ^1H MR signal occurs during the application of the second z -magnetic field gradient following the π pulse. The resulting raw data now contains a range of Larmor precession frequencies, which depend upon the magnitude of the applied gradient and the position of the individual water nuclear magnetic moments in the sample tube. Mathematically,

the resonance frequency of a nuclear spin in this one-dimensional imaging or *profiling* experiment² may be written as:

$$\omega(\mathbf{r}) = \gamma(B_0 + \mathbf{G} \cdot \mathbf{r}) \quad (18.8)$$

where $\omega(\mathbf{r})$ is the resonance at position \mathbf{r} in the sample and \mathbf{G} the gradient of the linear applied magnetic field gradient vector. If now we consider the local volume element dV within our tube of water then the number of spins in this element if the local spin density is $\rho(\mathbf{r})$ is then $\rho(\mathbf{r})dV$. The NMR signal from this element may then be written as:

$$dS(\mathbf{G}, t) = \rho(\mathbf{r})\exp[i\omega(\mathbf{r})t]dV \quad (18.9)$$

Inserting Eq. (18.8) into Eq. (18.9) gives:

$$dS(\mathbf{G}, t) = \rho(\mathbf{r})\exp[i(\gamma B_0 + \gamma \mathbf{G} \cdot \mathbf{r})t]dV \quad (18.10)$$

Obviously at this stage we have neglected to include any relaxation effects and thus the dephasing of the magnetisation is due purely to the term in the exponent of Eq. (18.10). A transformation into the rotating frame of reference followed by explicit integration over all space allows us to write Eq. (18.10) in terms of the observed signal S as a function of time and therefore becomes:

$$S(t) = \iiint \rho(r)\exp[i\gamma \mathbf{G} \cdot \mathbf{r} t]d\mathbf{r} \quad (18.11)$$

Where the symbol $d\mathbf{r}$ represents integration overall all space.

3.1.1 k-Space Formalism

Mansfield and Grannell (1973) simplified the meaning of Eq. (18.11) by introducing the concept of \mathbf{k} -space (whilst \mathbf{k} is a vector quantity the bold face type for \mathbf{k} is dropped in the main text for convenience), which may be defined by:

$$\mathbf{k} = \frac{\gamma \mathbf{G} t}{2\pi} \quad (18.12)$$

²The 1D-profiling experiment is a very useful quick imaging experiment to ensure that the sample under investigation is suitably located with respect to its position inside both the r.f. coil and gradient coil set which is normally fixed inside the main magnet. Often researchers will use the 1D-profiling experiment in real time acquisition mode to physically position their sample in the r.f. coil and orientate the sample with respect to the laboratory frame of reference.

The k-space vector unit is a reciprocal space unit, i.e., m^{-1} . Equation (18.12) shows that values (or different regions) of k-space may be traversed by either varying the time for which the magnetic field gradient is applied or by varying the amplitude of the magnetic field gradient. Inserting the expression for the reciprocal space vector \mathbf{k} given in Eq. (18.12) into Eq. (18.11) gives an expression which relates the time domain (frequency encoded) signal, i.e., that which is actually acquired in an MRI experiment as:

$$S(t) = \iiint \rho(\mathbf{r}) \exp[i2\pi \mathbf{k} \cdot \mathbf{r}] d\mathbf{r} \quad (18.13)$$

The NMR signal that is acquired in the time domain is in reciprocal space and is generally non-intuitive. Hence it is commonplace to interpret NMR data in the frequency domain. Fourier transformation of the above equation gives:

$$\rho(\mathbf{r}) = \iiint S(\mathbf{k}) \exp[-i2\pi \mathbf{k} \cdot \mathbf{r}] d\mathbf{k} \quad (18.14)$$

Taken together, Eq. (18.13) and Eq. (18.14) tell us that $S(\mathbf{k})$ and $\rho(\mathbf{r})$ form a mutually conjugate Fourier transform pair. In order for a fully resolved image to be acquired at the desired field-of-view and spatial resolution it is necessary to traverse and acquire all desired points in k-space. For this reason the concept of k-space is useful in designing and explaining magnetic resonance imaging pulse sequences.

3.2 Two-Dimensional Slice Selective Imaging

In order to see how k-space is traversed in terms of magnetic resonance imaging pulse sequences it is useful to draw upon a simple example. Consider a standard two-dimensional slice selective spin echo pulse sequence (Callaghan 1993) applied to our tube of water as shown in Fig. 18.7a. The first slice selective³ $\pi/2$ excitation pulse, also known as a “soft-pulse” rotates the equilibrium magnetisation vectors from within the selected slice into the transverse plane and takes us to the center of the k-space diagram.

Immediately after the slice selective excitation pulse we now apply a magnetic field gradient of fixed magnitude and duration in the x direction. Figure 18.7b shows that this has the effect of moving to the right hand side of the k-space *raster* ($+k_x^{max}$, 0). At the same time we also apply a gradient in the y direction. The diagram shows

³ Slice selection is achieved by applying a “soft” radio frequency pulse at the same time as an applied magnetic field gradient. The magnetic field gradient spreads out the Larmor precession frequencies and because of the narrow frequency bandwidth of the selective excitation pulse, only a limited region or “slice” of the samples Larmor frequencies is excited.

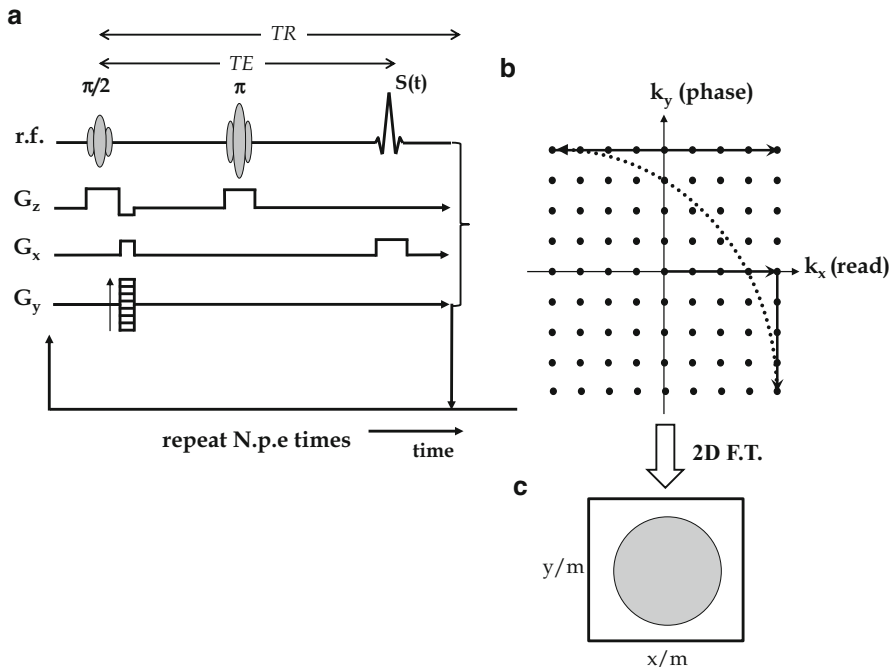


Fig. 18.7 (a) Schematic of a simple slice selective two-dimensional spin echo pulse sequence. (b) The corresponding k-space raster used to show how we may interpret the pulse sequence. Following a sufficient T_1 relaxation period the whole sequence is repeated $N.p.e.$ times to produce the full k-space data set. TE and TR represent the echo time and recycle time of the experiment respectively. (c) A two dimensional Fourier transform of the raw data acquired in (b) results in a two-dimensional slice selective spin-density "image" from the tube of water. See the main body text for a detailed description of this sequence

that this gradient actually has a number of different values but it is usual to assume that the first value is $-k_y^{max}$. This has the effect of moving the magnetisation to the bottom right hand corner of the k-space diagram, i.e., $+k_x^{max}$, $-k_y^{max}$. The application of the k_x and k_y gradients is performed simultaneously in order to minimise T_2 relaxation time contrast between the r.f. excitation and detection of the magnetisation. The result can therefore be attained by simple vector addition of the individual k-space components. At the end of the first two readout/phase gradient events a slice selective π refocusing pulse is applied to the spin system which has the effect of inverting the phases of all spins through the center of k-space. In terms of the k-space raster shown in Fig. 18.7b, the magnetisation now resides at the top left hand corner of k-space ($-k_x^{max}$, $+k_y^{max}$). Application of the second x gradient (the readout gradient) at this point along with the switching on of the digitiser, traverses k_x from left to right, and data is then acquired at a specific digitisation rate. M complex data points, typically 128 or 256, are acquired in the presence of the second x gradient, which has twice the duration but the same amplitude as the first gradient. To re-iterate, the k-space NMR signal that is

acquired in the presence of a magnetic field gradient, where spins at different positions have different frequencies, is said to be *frequency encoded*. Frequency encoding gradients are also termed *read* or *readout* gradients. The acquisition of complex data points in the presence of a constant magnitude ‘read’ gradient yields a straight line k-space data trajectory whose direction is defined by the Cartesian orientation of the gradient. A linear equally spaced k-space trajectory will always result so long as the read amplitude gradient is kept constant and the digitisation (acquisition) rate of the complex data is fixed. The echo time (TE) of this basic spin echo pulse sequence is defined by the time that elapses between half way through the initial excitation pulse and the acquisition of the maximum signal for k-space values k_x and $k_y = 0$. The time symmetry of the pulse sequence either side of the π refocusing pulse must be preserved for successful imaging.

Following the acquisition of the first line of M complex frequency encoded points in k-space, the spin system is then allowed to relax for a total time, TR , via T_1 relaxation, before the whole sequence is repeated. In the subsequent pass (and subsequent passes thereafter) through the pulse sequence, all that changes is the magnitude of the k_y phase encoding gradient. Phase encoding is differentiated from frequency encoding by the fact that the application of phase encoding gradient takes one to a specific point in k-space before the acquisition of the signal. Typically k_y is ramped from $-k_y^{max}$ to $+k_y^{max}$ in $N.p.e.$ steps to eventually yield a complete data matrix of $M \times N.p.e.$ frequency/phase-encoded points on a rectilinear grid. A two-dimensional Fourier transform of this data matrix followed by modulus correction will then give a two-dimensional spin density map⁴ (see Fig. 18.7c). The acquisition time for this type of single imaging sequence is given by $(TR \times N.p.e.)$ and typically takes a few minutes to execute which is considered slow by today’s standards though it is still widely used because it is more robust than many faster techniques. Through both advanced pulse sequence design and improved commercially available hardware, much faster imaging sequences, in the order of several tens of milli-seconds, are routinely available nowadays.

To produce an image of the required resolution and field-of-view (FOV), data must be acquired of a suitable range and increment of k . From Fourier theory it follows that the range of k defines the image resolution and increment of k defines to the field-of-view such that:

$$FOV = \frac{1}{\Delta k}, \Delta l = \frac{1}{k_{range}} \quad (18.15)$$

Where Δk is the increment in k , Δl is the image resolution and k_{range} is the total range of k sampled from $-k$ to k .

⁴Note the two-dimensional FT produces a frequency encoded spin density map in both orthogonal (xy) directions. The axes conversion to real space units is usually performed by the computer software from knowledge of the initial desired field of view (FOV) and digitisation rate.

4 MRI Protocols for Solid Dosage Form Pharmaceutical Research

One unique advantage of the nuclear magnetic resonance experiment is that it can, under the right conditions, reveal exactly what type of substance is present in a system, how much there is of it, and moreover, how it behaves with time. The term “nuclear spin-density” is often used amongst the magnetic resonance community and simply means how much of a particular substance we have within a specific volume element. In order for an image to be quantitative in terms of nuclear spin density one must essentially be able to measure the magnitude of the magnetisation immediately after the initial excitation pulse. This is, in general, not possible when using standard imaging protocols⁵ (Weiger et al. 2011; Robson et al. 2003) with finite echo times. For standard imaging protocols it is necessary to acquire a series of images at different T_2 or T_2^* weighting: for spin echo imaging this can be achieved by (i) CPMG or Hahn-echo T_2 -preconditioning of the magnetisation before image acquisition or (ii) by varying the echo-time (TE) within the imaging sequence itself. For gradient-echo based imaging the time TE , and hence T_2^* is also usually varied within the imaging sequence itself. In either case, following Fourier transformation of the raw k -space data, the signal intensity from each pixel, i , in the image is then fitted to Eq. (18.6) (replacing T_2 with T_2^* as necessary) as a function of TE , and thus a complete map of M_{0i} and T_{2i} is obtained. Similarly, the spatial variation in T_1 can be mapped throughout the image by a similar T_1 -preconditioning procedure either via saturation or inversion recovery (Callaghan 1993). In practice, the easiest way to avoid having to account (and hence correct) for T_1 relaxation contrast in an image is to ensure that the ones allows at least 3–5 times the longest T_1 relaxation time constant expected in the sample (of course this may have to be measured at some stage) between successive r.f. excitation pulses, i.e., $TR = 3\text{--}5 \times T_1$. Clearly this approach can have its disadvantages in that the total acquisition time of the image, which is essentially governed by the time allowed between successive r.f. excitations for any image protocol where more than one average is required, may become unacceptably long.⁶ The following sections now describe a series of image protocols that are commonly used to obtain quantitative information from solid dosage forms.

Before proceeding further it is worth stressing that, in general, we do not “see” the MR signal from solid substances because the T_2^* values are generally far too short; they are usually around a few micro-seconds. Following initial spin system excitation, MRI protocols generally require that 1–2 ms elapse before we can

⁵ There are specialist pulse sequences such as zero echo time (ZTE, see for example Weiger et al. 2011) and ultra short echo time (UTE, see for example Robson et al. 2003) imaging that are considered quantitative in terms of spin density without correction, but they are not commonly used in non-clinical MR research.

⁶ This can be avoided by choosing saturation recovery T_1 pre-conditioning over inversion-recovery T_1 preconditioning.

digitise the signal; thus for solids that signal has been irreversibly lost before we can actually do anything useful with it.⁷ So to clarify, when we talk about “imaging solid dosage forms” we are generally describing systems where:

- the solid is porous and we image the uptake of a liquid into that solid
- the solid is initially a rigid porous organic polymer that, under certain conditions, e.g., exposure to water, undergoes a glass transition, then becomes a gel and thus allows us to image the water behaviour within the gel
- the solid is completely soluble and thus will physically reduce in size during an imaging experiment allowing us to track the physical changes of the non-dissolved solid
- if the porous solid matrix is itself insoluble, it may contain soluble components (excipients) which, when contacted with water, will themselves dissolve and thus a NMR signal will result from the water solution.

There are a multitude of imaging strategies that can be designed according to the type of quantitative information that is required from the image, i.e., chemical composition, species concentration, velocity and diffusion. We have shown that in order to acquire a basic image it is necessary to acquire all points on the k-space raster followed by Fourier transformation. This is generally achieved using two families of imaging protocols: gradient echo sequences and spin echo sequences.

4.1 Gradient Echo MRI

In gradient echo (GE) imaging (Callaghan 1993), the spin system is refocused by the applied magnetic field gradients alone and a generic example of a two-dimensional gradient echo imaging sequence is shown in Fig. 18.8. In this sequence, a slice from the sample is excited by the simultaneous application of a small tip angle⁸ slice selective soft pulse, G_{S1} , and a magnetic field gradient.

As the initial slice selective gradient lobe passed through zero ($t = t_a$), a negative refocusing slice selective, G_{S2} , phase encoding, G_{PE} , and negative dephasing readout gradient, G_{R1} , are then applied all at the same time to minimise the inherent T_2^* weighting in the image. In terms of the k-space raster at time $t = t_b$ (using Fig. 18.8) this process will have taken us to the bottom left hand corner of k-space. At time $t = t_b$ all gradients are now zero and at this point the magnetisation is fully dephased. From $t_b < t < t_d$ the readout gradient is switched on and the digitiser is also switched on and the first line of k-space is acquired and then stored in

⁷ In addition to UTE and ZTE imaging there are a number of MR pulse sequences that can begin to image solid matter, such as single point imaging (SPI) techniques, but again their use is not routine. The reader is referred to (Mantle 2011) for a further discussion regarding SPI.

⁸ In GE imaging a small tip angle is usually employed as one wants to make the acquisition of the image fast (sub-second) and free from T_1 relaxation artefacts. This is why the FLASH protocol is usually adopted for GE imaging.

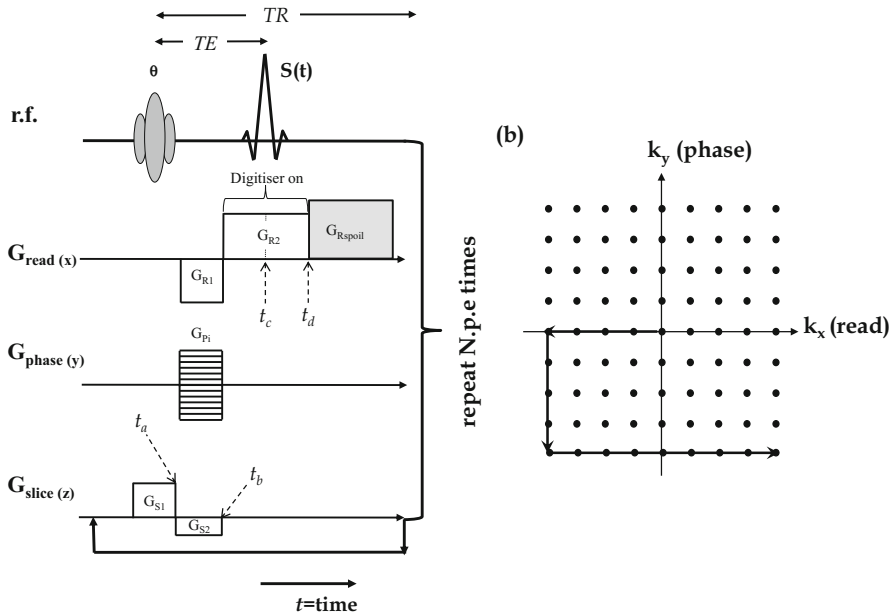


Fig. 18.8 Schematic showing the principles of two-dimensional slice selective gradient echo imaging (see main body text for details)

memory.⁹ Usually the order of the phase encoding gradient is chosen such that k -space is traversed from $-k^{max}$ through $k=0$ to $+k^{max}$ and thus in this case the first line of k -space appears to have no actual signal at $t=t_c$. In order to visibly see the “echo signal” from the sample on a computer display one has to ensure that the total gradient time integral for all gradients is zero, $k_{x,y,z}=0$, and this occurs at $t=t_c$ at which point the spins are said to be refocused and a ‘gradient echo’ is formed.¹⁰ From $t=0$ to $t=t_c$, dephasing of the spin magnetisation will also occur due to T_2^* relaxation processes and thus the digitised signal will be T_2^* weighted, which essentially means that signal is lost during the so called echo time period, TE . The most common form of gradient echo imaging is the Fast Low Angle Shot (FLASH) sequence (Haase et al. 1986). The major downside of gradient echo imaging is that it is not suited to systems that have short T_2^* values on the order of a few milli-seconds. We have seen that T_2^* can be estimated using the full width half maximum of the resonance line from the sample as a whole. Considering two

⁹ Often an additional “readout spoiler” gradient is applied after the digitiser has been switched off in order to destroy any spurious magnetisation. Similarly, r.f. spoiling is often also used in GE imaging.

¹⁰ It is always very useful when working on any pulse sequence development to turn off all phase encoding gradients, i.e., set their values to zero, to see where and what form the echo signal takes using only the readout gradients. This “trick” is also used to ensure that the receiver gain is set correctly at the point where the center of k -space is acquired.

different samples one with a FWHM of 50 Hz and the other with a FWHM of 500 Hz corresponding to T_2^* values of approximately 6 ms and 600 μ s respectively. The T_2^* signal losses at $t = t_c$ from two such samples using a gradient echo sequence with a minimum echo time in the 1 ms range are given by:

$$\% T_2^* \text{ Signal loss} = [1 - \exp\left[-\frac{TE}{T_2^*}\right]] \times 100 \quad (18.16)$$

which for our FWHMs of 50 and 500 Hz correspond to signal losses of 16 and 81 % respectively. Practically, one would always measure the inherent line width of the frequency spectrum of the sample under investigation using a simple “pulse acquire”, followed by Fourier transformation, and then calculate the signal loss expected from a gradient echo based sequence. Quantitative gradient echo imaging is possible by acquiring a series of T_2^* weighted images at different TE times and fitting the individual pixel intensities from each weighted image data set to Eq. (18.6). However, because of the generally short T_2^* s that occur in solid dosage form MRI research it is not usually possible to acquire more than 3–4 images for the fitting procedure as the signal decays so quickly in the first place. Fitting using 3–4 points for each pixel in an image is feasible but the very nature of FLASH GE imaging means that signal averaging to improve the overall signal-to-noise is not practical for systems that change with time. Hence the fitting of FLASH T_2^* weighted data to obtain M_0 and T_2^* values will likely be “noisy” yielding fitting results with large error bars.

In order to illustrate the features from the various imaging protocols discussed in this section images will be shown from a model solid dosage form (Chen 2014) undergoing dissolution in a standard USP-IV dissolution cell. The model tablet is made from hydroxypropylmethyl cellulose (HPMC-K4M, Colocron, Dartford, UK) with 30 % wt. of trifluoperazine dihydrochloride (Sigma-Aldrich, UK) added as the active pharmaceutical ingredient (API). These were then mixed by a powder blender (Turbula[®]Mixer T2F, Manesty, UK) for 1 h. Tablets were prepared by a manual hydraulic press (Specac, USA) equipped with two flat-faced punches (o.d. 13 mm) and evacuable dies (i.d. 13 mm). The 13 mm o.d. tablets were prepared under compression force of 50 kN for 1 min, and the powder was pre-weighted to obtain a tablet of 250 ± 1 mg with thickness of 2 ± 0.1 mm. The dissolution media used in the experiments was 500 mL 0.01 M PBS (pH = 7.4) prepared from a powder sachet (Sigma-Aldrich, UK). Figure 18.9 shows a schematic of the MRI system and USP-4 dissolution cell illustrating the tablet orientation as well as the UV-Vis spectrometer. The temperature of the dissolution media was conditioned at 37 °C in the USP-IV flow-through cell regulated by a water bath (Grant Instrument, UK). A peristaltic pump (205S, Watson Marlow, USA) was used in the experiment and the dissolution media flow rate was set to 8 mL/min. The tablet was placed vertically in the USP-IV dissolution cell and held in place by use of a nylon cage; the location of the horizontal (xy) MRI slice was taken through the middle of the tablet which was determined from initial ‘pilot’ vertical slices (zx)

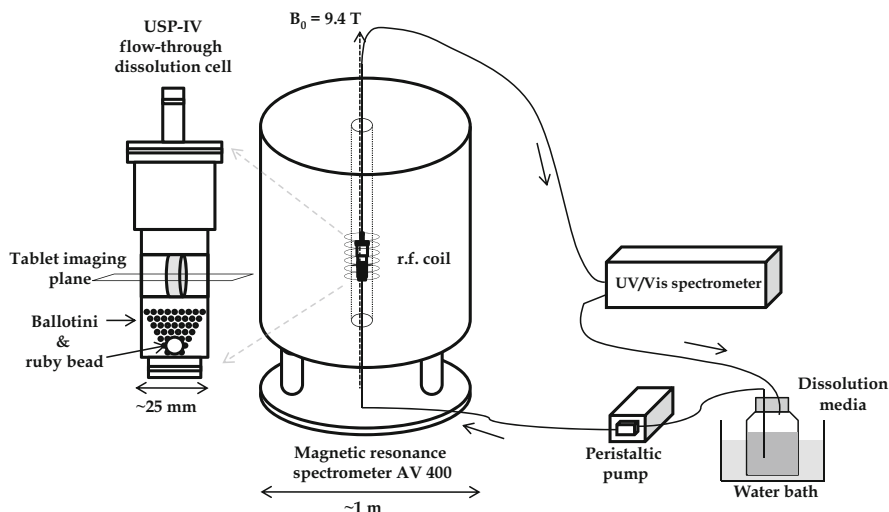


Fig. 18.9 Schematic of the USP-IV/MRI experimental setup with on-line UV-Vis spectrometer

taken at the start of the experiment using the Bruker Biospin Paravision™ 4.1 software interface.

Figure 18.10 shows a time series of two-dimensional 1 mm thick slice selective ^1H FLASH-GE images taken through the plane of the tablet indicated in Fig. 18.9. Details of the imaging parameters are included in the figure caption. The images show that water penetrates into the tablet with the penetration fronts meeting at approximately 5 h. The black area at the center of the image from $t = 0$ to $t = 3.5$ h is solid HPMC/TDFH that has yet to be challenged by the PBS solution. Air bubbles present as black dots in the image can be seen to form both within and on the outside of the tablet during the dissolution event. There is also some evidence of flow based image artefacts from the pure PBS solution that is flowing around the tablet from $t = 0$ to $t = 13$ h. The main point to note here are that the differences in magnetic susceptibility between air, PBS and solid matrix highlight the presence of air bubbles. Note the scale bar is in arbitrary units as these images have not been corrected for T_2^* relaxation. Substantial swelling of the tablet is also evident in both the radial and axial directions.

4.1.1 Radially Sampled Gradient Echo Imaging

Whilst gradient echo imaging sequences suffer from a T_2^* weighting and thus sometimes a poor signal-to-noise ratio, e.g., when the FWHM of the samples spectral line is in the 100's of Hz range, one way to improve the signal-to-noise value is to adopt a radial k-space sampling strategy (Haacke et al. 1999) as shown by Fig. 18.11.

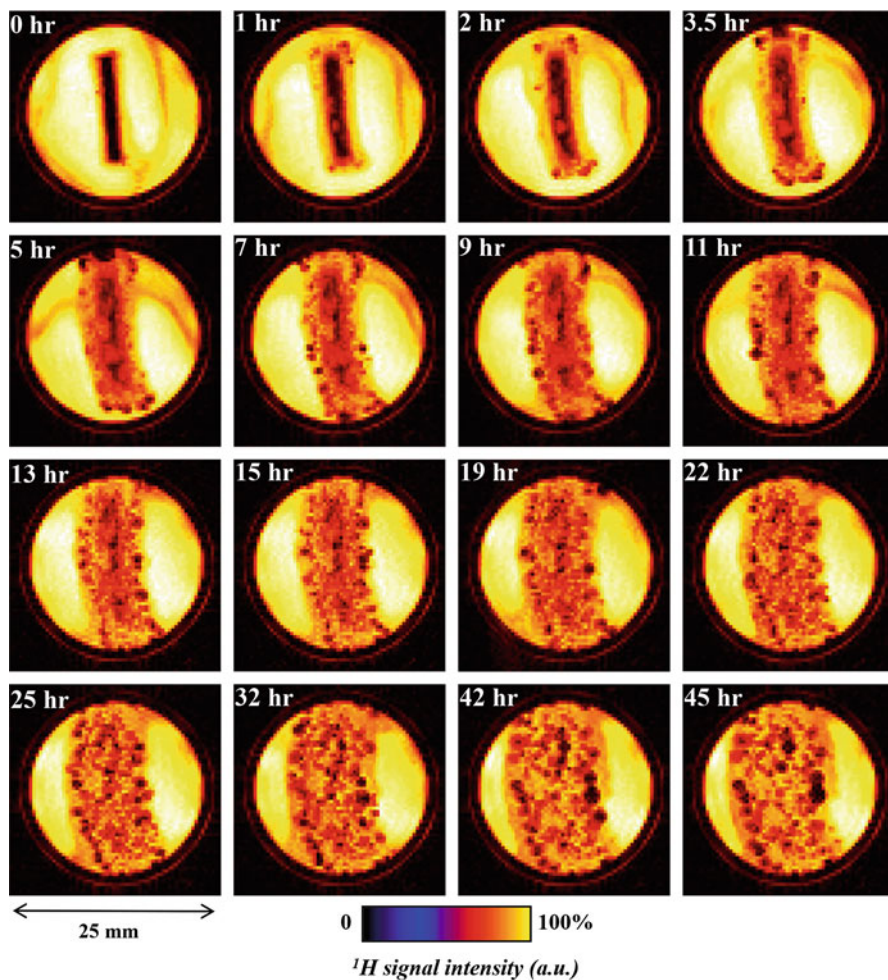


Fig. 18.10 A time series of ^1H two-dimensional 1 mm thick slice selective images taken through the imaging plane illustrated in Fig. 18.9 for a HPMC/TFDH model tablet at different hydration times. Initially the dry core of the tablet can be seen as areas of black signal surrounded by flowing PBS solution (yellow/white colour). The formation of air bubbles around the outer surfaces as well as from within the tablet is evident. Considerable swelling in both axial and radial directions is also visible. ^1H FLASH imaging parameters: ^1H frequency 400.23 MHz; Acquisition bandwidth = 100,000 Hz; $TE = 1.09$ ms; $TR = 100$ ms; FOV 25 mm; data matrix size 64×64 ; image pixel resolution = 391 mm; soft pulse tip angle $\theta = 10^\circ$. Number of averages = 128; total imaging time 13 min

Here, k-space is sampled on a polar grid which gives a better SNR than Cartesian sampling albeit at the cost of a loss in spatial resolution. However one of the drawbacks of the radial sampling technique is that a Fast Fourier Transforms (FFT) cannot be used to reconstruct the raw data to give a meaningful image. Instead the common way to reconstruct data that is acquired on a polar as opposed

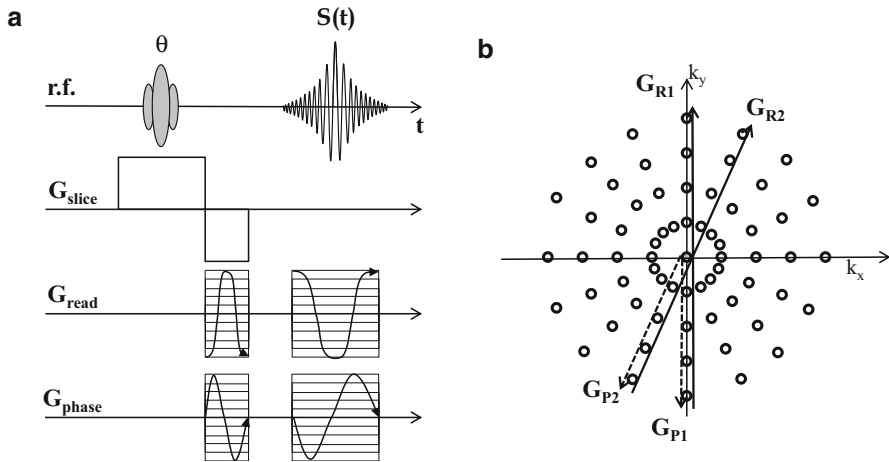


Fig. 18.11 (a) Schematic of the radial FLASH pulse sequence illustrating the cosine/sine modulation of both readout and phase gradient waveforms used to acquire the data on a polar grid. (b) corresponding polar co-ordinate k -space trajectory.

to rectilinear grid is to use filtered back projection FBP which was originally developed for X-ray computed tomography (Block et al. 2007). Other techniques (Fessler and Sutton 2003) such as non-uniform fast Fourier transforms (NUFFT) can be used but are beyond the scope of this chapter and only FBP is considered here. For FBP MR imaging, a fast Fourier transform is performed for each acquired radial spoke in k -space; the projected profiles are then further reconstructed to an image via a filtered inverse radon transform (see Fig. 18.12).

Originally developed for X-ray computed tomography, the inverse radon transform can be applied to obtain the image by casting all projection profiles over a matrix in corresponding directions (Block et al. 2007; Mistretta et al. 2006). Figure 18.12a shows how an image can be converted to a matrix of projections of the image via a radon transform. The inverse radon transform with appropriate filtering, therefore, converts the projection profiles into the original image. Figure 18.12b shows two key steps of filtered back projection: (i) the radially sampled k -space is Fourier transformed to obtain the projection profiles of the image; (ii) the projection profiles then can be transformed into an image by inverse radon transform. Note the image obtained with filter represents a much better reconstruction than the one without filter. This is because prior to the inverse radon transform, it is necessary to compensate for the oversampling of the k -space centre, usually via the application of a frequency filter. The Ram-Lak filter is a ramp filter, which filters out low frequencies and allows high frequencies to pass through, with a linear behaviour between two extremes of k -space. The Ram-Lak filter works well for projection reconstruction, but it magnifies the noise from projection data (Ramachan and Lakshmin 1971). Several other filters are commonly used to overcome the noise sensitivity issue. For example, the Shepp-Logan filter multiplies the Ram-Lak with a ‘sinc’ function (Shepp and Logan 1974); the Hamming filter multiplies the

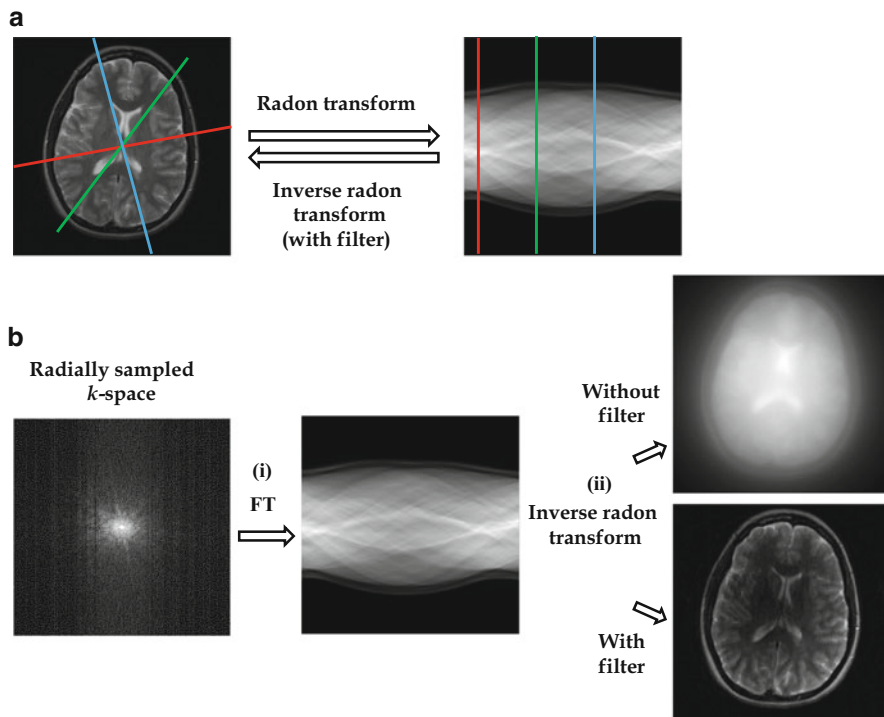


Fig. 18.12 (a) Illustration of radon transform and inverse radon transform. The red/green/blue 'spikes' in the brain image correspond to the coloured lines in the radon transform domain. (b) Key steps in filtered back projection method used to reconstruct the image.

Ram-Lak filter with a Hamming window. Recently Quodbach et al. (2014) used radial real time high resolution UTE-GE imaging to investigate the disintegration process of tablets containing disintegrants. A temporal resolution of 75 ms and a spatial resolution of $80 \times 80 \mu\text{m}$ with a section thickness of only $600 \mu\text{m}$ were achieved. Further examples of radial FLASH imaging and its use to study directly API behaviour in solid dosage forms during dissolution testing are given in Sect. 4.4.

4.2 Quantitative Spin Echo MRI

An alternative to the gradient echo sequence is the spin echo sequence already shown in Fig. 18.7a. In this case a π refocusing pulse is inserted at the midpoint of TE which has the effect of reversing the spin dephasing due to magnetic field inhomogeneities and thus the signal is said to be refocused at TE and a spin echo is formed; the signal at this point is now T_2 weighted as opposed to T_2^* . Another

difference to note is the polarity of the dephasing readout gradient; the π refocusing pulse inverts the phase of the spins and therefore the effective polarity of the gradient. In this case, the dephasing readout gradient must have the same polarity as the rephasing gradient since they are separated by the π refocusing pulse. Although this is termed a spin echo experiment, two echoes are formed—the spin echo at TE and the gradient echo at $k = 0$ —and these are usually chosen to coincide. In this sequence the data will be T_2 weighted compared to T_2^* for the gradient echo sequence. In solid dosage forms samples undergoing dissolution testing we have several material boundaries and T_2 can be much greater than T_2^* . Therefore it is advantageous to adopt spin echo imaging protocols to obtain quantitative images with minimal contrast in them; alternatively of course when quantitation is not required a gradient echo sequence may be used to highlight heterogeneities in the sample. All MRI images will have some ‘relaxation weighting’—signal loss from the effects of relaxation—which will change the image intensity. We have seen that T_1 weighting can be ignored if one chooses that the repetition time of the experiment to be in the $3\text{--}5 \times T_1$ range. It is generally more important to account for T_2 signal losses which are described by Eq. (18.6) where t is the time between excitation and data acquisition, i.e., the echo time TE . Here M_{xy} is the measured signal intensity and M_0 is proportional to the absolute material density. Any signal loss can be minimised by making $\frac{TE}{T_2} \ll 1$ such that $M_{xy} \approx M_0$ but this may not be possible in some situations where T_2 is particularly small. In such systems, a series of images can be acquired with increasing values of t and then the pixel measured intensities, M_{xy} , fitted to Eq. (18.6) with M_0 and T_2 as fitted parameters. The final image of material concentration or spin density is proportional to M_0 (see Fig. 18.13) whilst the image of T_2 contains information on local molecular mobility as shown in Fig. 18.14.

Figure 18.13 shows the equivalent quantitative 1 mm thick RARE spin echo images for the model HPMC/TDFH pharmaceutical dosage form from exactly the same sample as that depicted in Fig. 18.10 taken using a T_2 -CPMG precondition fast spin-echo RARE sequence (T_2 -RARE) (Chen et al. 2010). Note the scale bar is now representative of absolute water concentration and there is now less contrast between the flowing PBS solution surrounding the tablet and the water that has penetrated the tablet. The reason for this is that the GE-FLASH image was not corrected for T_2^* weighting and is more susceptible to material magnetic susceptibility differences.

It is particularly important to realise that the water concentration map C_{wat} (which is equivalent to the absolute spin density (I_0) map) and T_2 map obtained from the fitting procedure for each pixel are examined together. Inspection of Figs. 18.13 and 18.14 shows that the outer boundary of the HPMC/TDFH tablet and the flowing PBS solution is much more clearly defined in the T_2 map than the I_0 map. Recently, Chen et al. (2010) gave the first report of a quantitative RARE based ultra-fast two-dimensional magnetic resonance imaging protocol to follow the water uptake of hydroxypropylmethyl cellulose (HPMC). Quantitative maps of absolute water concentration, T_2 -spin-spin relaxation times were obtained at a spatial resolution of $469 \mu\text{m}$ in less than 3 min each. These maps allowed the dynamic development of the medium release rate HPMC/water system to be

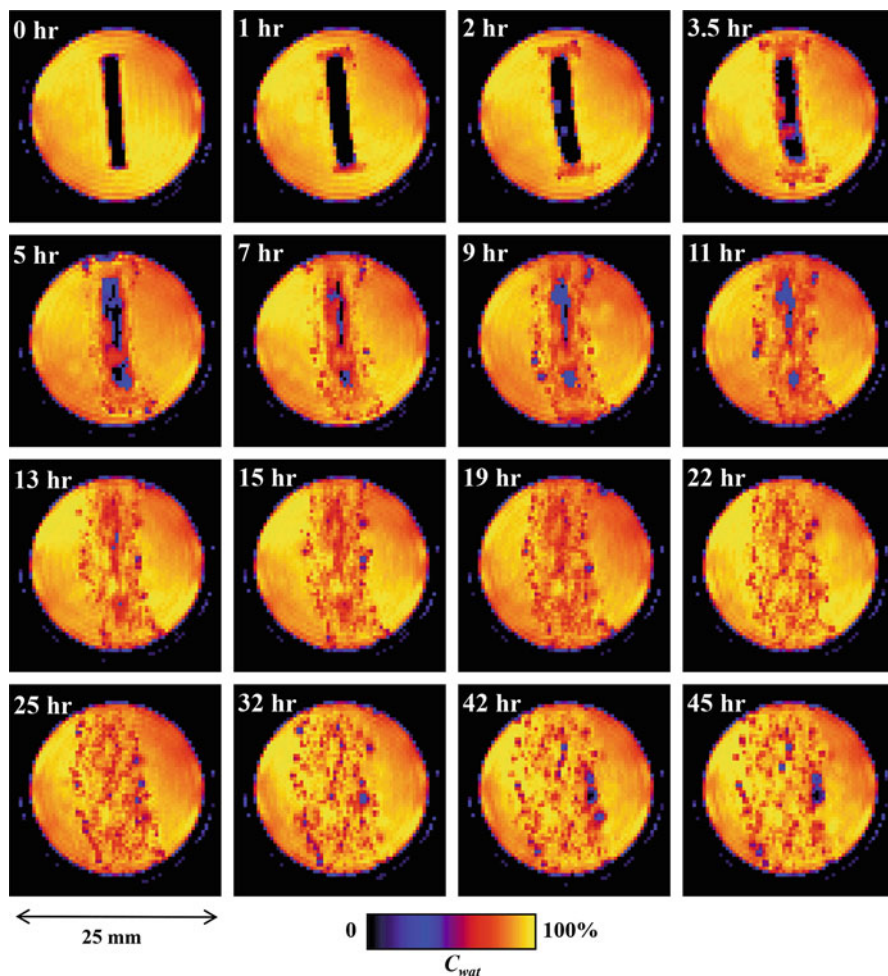


Fig. 18.13 A time series of two-dimensional 1 mm thick slice selective water concentration maps, C_{wat} , obtained from the fitting of ^1H T_2 -RARE spin echo imaging data of the HPMC/TFDH to Eq. (18.6) of the model tablet at different hydration times. Note these images are from exactly the same sample as used to obtain Fig. 18.10. ^1H T_2 -RARE imaging parameters: ^1H frequency 400.23 MHz; Acquisition bandwidth = 200,000 Hz; $TE = 2.54$ ms; $TR = 10$ s; FOV 25 mm; data matrix size 64×64 ; RARE factor = 64; image pixel resolution = 391 μm . Number of averages = 2; total imaging time 3 min. Number of CPMG T_2 weightings used = 8. Split echo acquisition mode. Even echo times $TE_E = 23.34$ ms, 25.34 ms, 29.34 ms, 53.34 ms, 85.34 ms, 277.34 ms, 533.34 ms, 1045.34 ms; Odd echoes times $TE_O = 23.02$, 25.02 ms, 29.02 ms, 53.02 ms, 85.02 ms, 277.02 ms, 533.02 ms, 1045.02 ms) Phase encode start value (PESV) = -0.22

followed. This details behind this imaging protocol has recently been reviewed (Mantle 2011) and exploited by workers from the same group to study the dissolution of Lescol XL tablets under pharmacopeial conditions (Zhang et al. 2011; Chen et al. 2014).

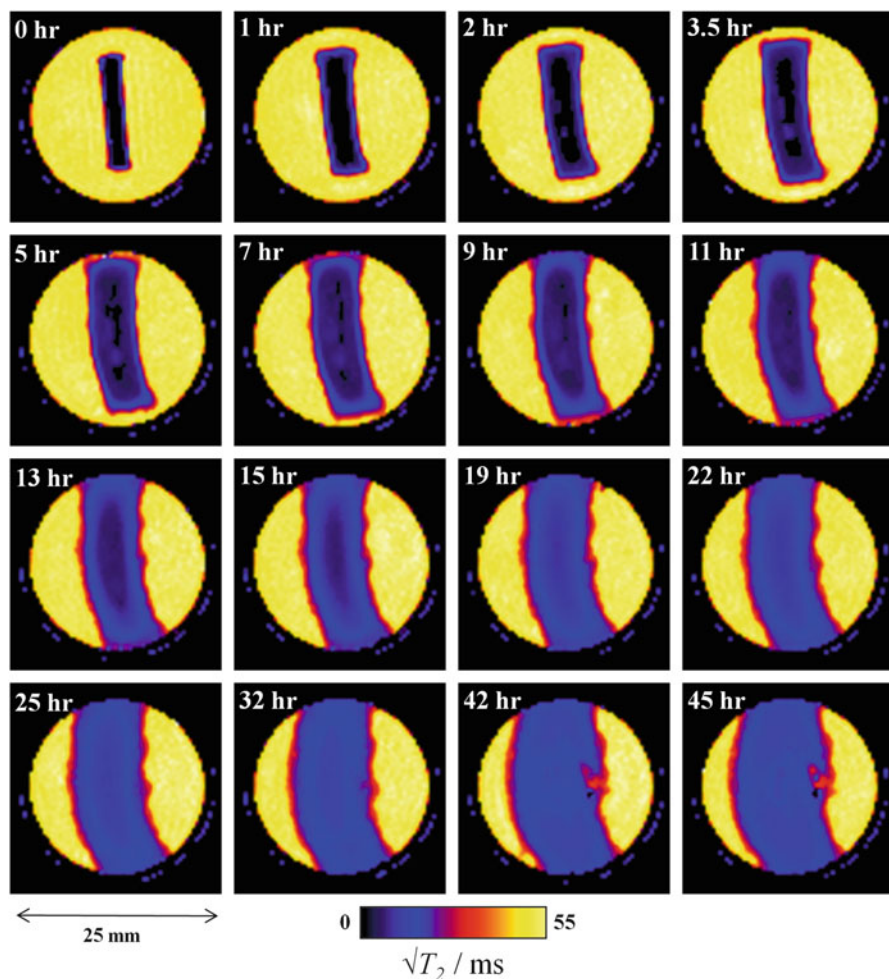


Fig. 18.14 Time series of two-dimensional 1 mm thick slice selective ^1H - T_2 -maps obtained from the fitting of ^1H T_2 -RARE spin echo imaging data of the HPMC/TFDH to Eq. (18.6) of the model tablet from Fig. 18.13 at different hydration times. Note the square root dependence of the scale bar has been chosen to highlight the large range in T_2 values observed (25–3000 ms)

4.3 Quantifying Mass Transport Using MRI

Another defining property of magnetic resonance is its ability to measure mass transport in the form of incoherent self-diffusive motion and coherent motion in the form of flow. For a detailed account behind the theory and application of mass transport as measured by magnetic resonance the reader is referred to several reviews (Fukushima 1999; Mantle and Sederman 2003; Elkins and Alley 2007; Callaghan 2011). This section briefly introduces the theory behind diffusion and flow imaging techniques.

4.3.1 Molecular Self-Diffusion MRI

Self-diffusion may be defined as random molecular motion in the absence of any gradients in chemical potential, i.e., $\nabla\mu = 0$, where μ in this context is the chemical potential of a molecular species. Random molecular motion also causes random fluctuations of the Larmor frequency of the individual magnetic moments within the spin system and thus any signal acquired may be considered as a superposition of pulse sequence imparted frequency/phase encoded signal and that due to the residual phase shifts resulting from random motion. The experimental determination of molecular self-diffusion coefficients by magnetic resonance is achieved by the application of a simple pulsed (magnetic) field gradient spin echo (PFG-SE) as first realised by Stejskal and Tanner (Stejskal and Tanner 1965). This experiment consists of a standard r.f. $\pi/2$ --- π --- spin echo with the additional incorporation of a pair of incremented pulsed magnetic field gradients of duration δ , amplitude G , with a time between the centres of the pulsed magnetic field gradients of Δ , either side of the π r.f. refocusing pulse (see Fig. 18.15).

In practice, the NMR signal is acquired for different values of the pulsed magnetic field gradient strength whilst keeping the durations, δ and Δ constant. The measured NMR signal intensity, I , is then plotted as a function of the gradient strength G and a numerical fit of the data according to:

$$\frac{I}{I_0} = \exp\left(-\gamma^2\delta^2G^2D\left(\Delta - \frac{\delta}{3}\right)\right) \quad (18.17)$$

is then performed. A plot of the logarithm of the signal intensity versus $-\gamma^2\delta^2G^2(\Delta - \delta/3)$ will yield a straight line (for Brownian diffusion) whose gradient is the self-diffusivity D . The interpretation and measurement of NMR data for systems exhibiting random (Brownian) diffusion is simple enough, but a more complex behaviour of the signal intensity is often observed in non-Brownian systems (Callaghan 1993). The method just described was a description of how molecular self-diffusion could be measured using PFG-NMR from the whole sample. A spatially resolved *diffusion image*, i.e., one where a map of self-diffusion coefficients from each individual pixel within an image can be extracted, is easily acquired by pre-conditioning a spin echo (or gradient echo) (Callaghan 1993) imaging sequence with a varying amount of diffusion weighting. One thus obtains a data set that contains several images (usually at least eight) with a different amount of diffusion weighting between each image. The intensity of each pixel in the image is then extracted and fitted to the Stejskal-Tanner equation (Stejskal and Tanner 1965) (Eq. (18.13)) to obtain the diffusion map. Diffusion weighted imaging (DWI) as it is more commonly known, is an important tool in clinical research and has also been exploited in the pharmaceutical research (Chen et al. 2010). Figure 18.16 shows a time series of ^1H water molecular self-diffusion coefficient maps in units of m^2s^{-1} for exactly the same sample as those presented in Figs. 18.10, 18.13 and 18.14 for the HPMC/TDFH compact using a diffusion

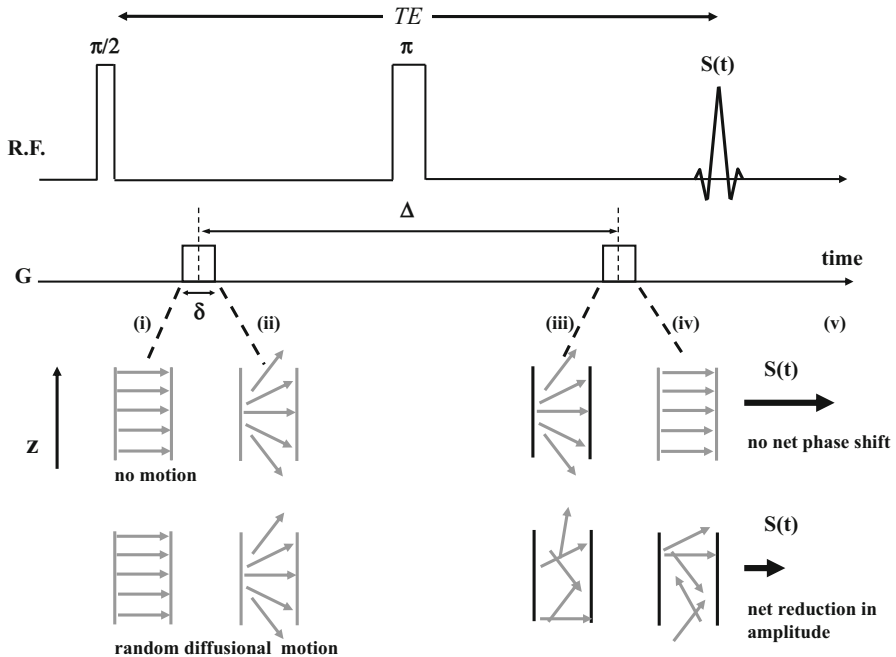


Fig. 18.15 The principle of self-diffusion measurements using the ‘phase shift’ approach. Two pulsed magnetic field gradients (of magnitude G and duration δ) are applied a time Δ apart. The action of the first pulsed magnetic field gradient is to introduce a phase shift to each nuclear spin with respect to its orientation if no field gradient were to have been applied. The phase offset non-invasively ‘labels’ the position of the nuclear spin. A π degree refocusing pulse then inverts the phase of the spins. At a time Δ later, the spin system receives an equal pulsed magnetic field gradient. If the spins have not moved, the spins receive an equal and opposite phase offset and return to their initial alignment in the x' - y' plane. Incoherent motion (i.e. diffusion and dispersion) causes a loss of alignment of the nuclear spins within the sample; the resulting attenuation in the received signal provides a measure of the distance travelled by the ensemble of spins during the observation time, Δ . The figure shows the relative phase offset of five adjacent spin isochromats, initially lying at different locations along the direction of the applied pulsed magnetic field gradients: (i) after r.f. excitation and before application of the first gradient pulse the spin isochromats are aligned along y' ; (ii) immediately after application of the first gradient pulse; (iii) after the system has been phase inverted by the π degree refocusing pulse it then is allowed to evolve for the time Δ ; (iv) after application of the second gradient pulse. (v) represents the resulting net magnetisation vector characterising the system after application of the two gradient pulses. The whole sequence is then repeated for different magnitudes of the pulsed gradient G to yield data that is then fitted using Eq. (18.17) with the self-diffusion coefficient D as the only free parameter

preconditioned fast spin echo RARE imaging sequence, D -RARE (Chen et al. 2010).

The water self-diffusion coefficient (SDC) maps reflect very similar features to the T_2 relaxation time maps. For example, Fig. 18.16 ($t = 13$ h) shows three main regions: (i) free flowing water coloured in white ($SDC > 3.5 \times 10^{-9} \text{ m}^2\text{s}^{-1}$);

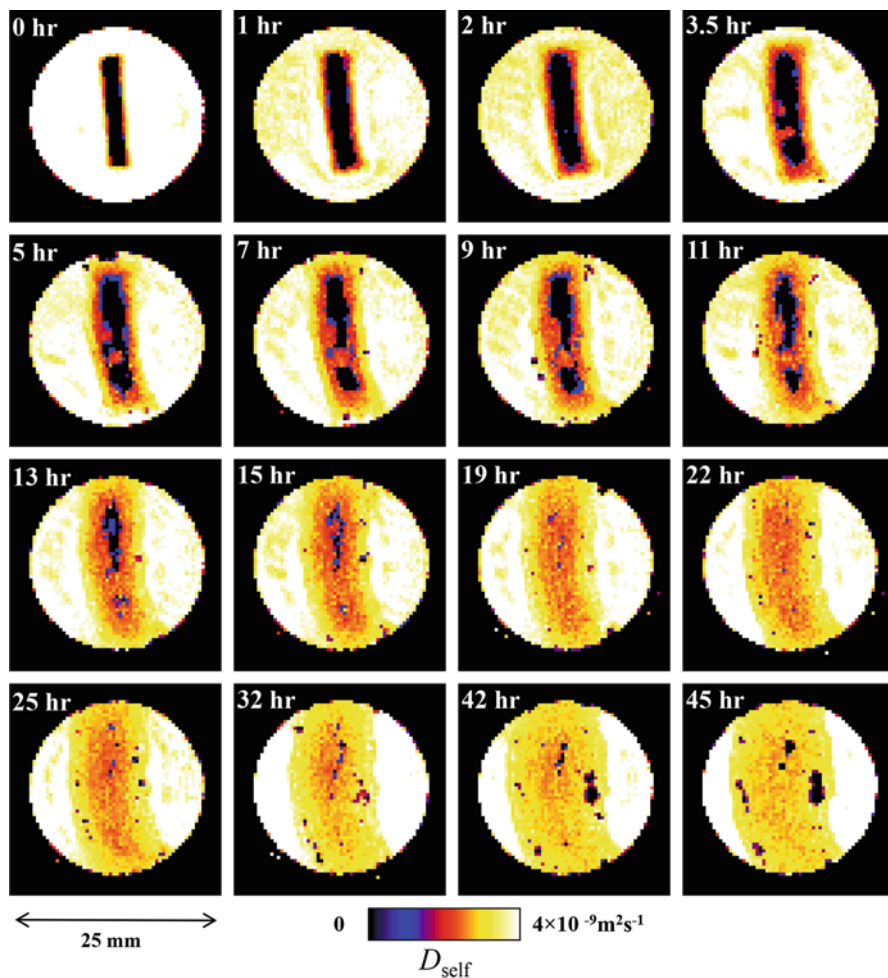


Fig. 18.16 Time series of two-dimensional 1 mm thick slice selective ^1H -self-diffusion coefficient, D , maps obtained from the fitting of ^1H D -RARE spin echo imaging data of the HPMC/TFDH to Eq. (18.13) of the model tablet used in Fig. 18.13 at different hydration times. ^1H - D -RARE imaging parameters: ^1H frequency 400.23 MHz; Acquisition bandwidth = 200,000 Hz; TE = 2.54 ms; TR = 10 s; FOV 25 mm; data matrix size 64×64 ; RARE factor = 64; image pixel resolution = 391 μm ; number of averages = 2; total imaging time 3 min; G diffusion weightings = 5.9, 11.4, 16.9, 22.4, 27.8, 33.3, 38.8 and 44.3 G/cm; $\delta = 1$ ms; $\Delta = 50$ ms

(ii) water on outer region of the swollen tablet ($(2.8 \times 10^{-9} \text{ m}^2\text{s}^{-1}) < SDC < 3.5 \times 10^{-9} \text{ m}^2\text{s}^{-1}$); (iii) water within inner region of the swollen tablet ($(1 \times 10^{-9} \text{ m}^2\text{s}^{-1}) < SDC < 2.8 \times 10^{-9} \text{ m}^2\text{s}^{-1}$). The water SDC within the gel layer is lower than the free water in the dissolution cell, because the polymeric matrix significantly restricts the self-diffusion of the water and agrees with previous reports in literature (Ferrero et al. 2008; Zhang et al. 2011; Kikuchi et al. 2012).

Note that the *SDC* maps show a slightly enlarged dry core region compared to the I_0 map (Fig. 18.13) and T_2 relaxation time map (Fig. 18.14). The reason for this loss of signal at the interface is due to the extra T_2 weighting of around 4 ms that the diffusion pre-conditioning introduces before the acquisition of the image (Chen et al. 2010).

4.3.2 Phase Shift Velocity Imaging

Phase-shift or phase-contrast displacement measurement is perhaps the most robust and quantitative way of measuring flow by magnetic resonance. The dynamic range of phase-shift velocity imaging can be adjusted from as little as a few $\mu\text{m s}^{-1}$ up to 10–100 m s^{-1} . It is limited at lower velocities to displacements due to self-diffusion and at higher velocities to residence time in the measurement volume of the MR spectrometer. The principle of phase-shift velocity imaging can be understood by considering the effects of the applied gradient $\mathbf{G}(t)$ on the phase of moving spins. The basic imaging equation (Eq. (18.8)) showed that the precession frequency was dependent upon its position \mathbf{r} . If we now invoke the condition that this is time dependent, $\mathbf{r}(t)$; then the phase shift $\phi(t)$ is given by:

$$\phi(t) = \gamma \int_0^t \mathbf{G}(t) \mathbf{r}(t) dt \quad (18.18)$$

Elementary kinematics shows that if the time-dependent position of this spin can be expanded as:

$$\mathbf{r}(t) = \mathbf{r}_0 + \mathbf{v}_0 t + \frac{1}{2} \mathbf{a}_0 t^2 + \dots \quad (18.19)$$

Then the time-dependent phase accrued by the spins will be:

$$\phi(t) = \gamma [\mathbf{r}_0 \int_0^t \mathbf{G}(t) dt + \mathbf{v}_0 \int_0^t \mathbf{G}(t) t dt + \mathbf{a}_0 \int_0^t \mathbf{G}(t) t^2 dt + \dots] \quad (18.20)$$

The integrals are the successive moments ($M_0, M_1, M_2 \dots$) of the gradient with time:

$$\text{Zeroth moment, } M_0 = \int_0^t \mathbf{G}(t) dt \quad (18.21)$$

$$\text{First moment, } \mathbf{M}_1 = \int_0^t \mathbf{G}(t) t dt \quad (18.22)$$

$$\text{Second moment, } \mathbf{M}_2 = \int_0^t \mathbf{G}(t) t^2 dt \quad (18.23)$$

The zeroth moment, \mathbf{M}_0 , causes a phase shift proportional to position \mathbf{r}_0 and the first moment, \mathbf{M}_1 , causes a phase shift proportional to velocity \mathbf{v}_0 etc. Therefore gradient waveforms can be designed that have a non-zero \mathbf{M}_1 (but zero \mathbf{M}_0) and thus the measured phase will be proportional to the velocity. Velocity encoding is usually achieved using a bipolar pulsed gradient pair as already shown in Fig. 18.15 and the velocity can be calculated from the measured phase since \mathbf{M}_1 is known. Experimentally¹¹ this is often done by acquiring the image twice with two values of \mathbf{M}_1 and a velocity is calculated from the observed phase difference between the two sets of images. Each image in Fig. 18.17 was calculated from eight diffusion weighted images using D-RARE (Chen et al. 2010), and from these images the velocity of the flowing dissolution media can be obtained by tracking phase changes between successive diffusion weighted images. The phase shift map is calculated from the real and imaginary parts of the D map. The relationship between the NMR signal phase change and velocity is:

$$\phi = \gamma G_{inc} \delta \mathbf{v} \Delta \quad (18.24)$$

where ϕ is the phase change, γ is the gyromagnetic ratio, G_{inc} is the difference in gradient strengths between subsequent diffusion/flow gradients applied, δ is the encoding gradient duration, Δ is the observation time, and \mathbf{v} is the flow velocity.

In principle the velocity of a system can be measured in any spatial direction but it is usual to limit this to the 3 orthogonal directions of the Cartesian co-ordinate system. We do note that velocity induced phase can also cause image artefacts. A detailed discussion of these is beyond the scope of this chapter but it is possible to compensate for velocity artefacts by ensuring that any the gradient waveforms have \mathbf{M}_1 equal to zero (Pope and Yao 1993). Figure 18.17 shows the equivalent water v_z velocity maps for the sample already shown in Fig. 18.10, 18.13, 18.14 and 18.16.

Figure 18.17 shows that in the early stages (within 1 h) of dissolution, the velocity maps are heterogeneous, indicative of a non-steady state flow field. At the centre, the black region represents the dry core of the tablet, where no signal is observed. At $t = 1$ h, a static gel layer (in red) is formed surrounding the dry core. From $t = 2$ h to $t = 25$ h, after the formation of the gel layer, the flow becomes more

¹¹ It is a bonus that diffusion preconditioning will also yield velocity information if the data are processed in the correct way. Based on the SDC images obtained by D -RARE, the velocity of the flowing dissolution media can be obtained by tracking phase changes of the diffusion weighted images.

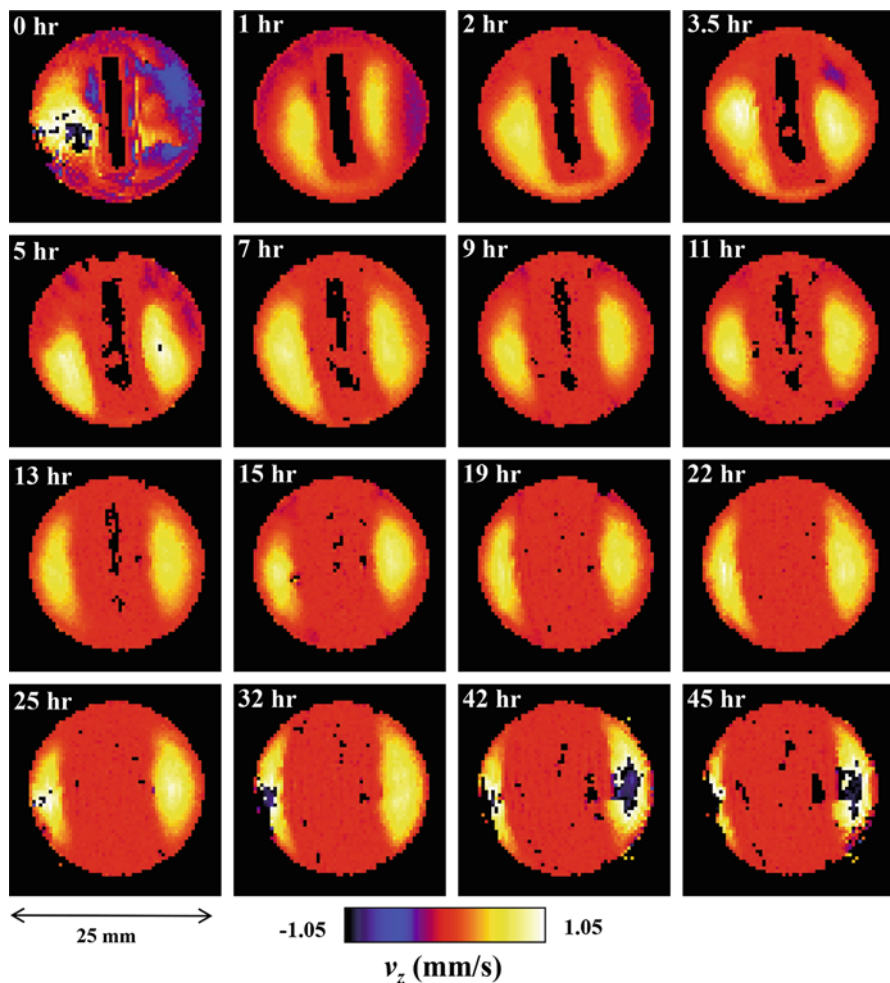


Fig. 18.17 Time series of two-dimensional 1 mm thick slice selective ^1H - v_z velocity maps obtained from the fitting of ^1H D -RARE spin echo imaging data of the HPMC/TFDH to Eq. (18.24) of the model tablet used in Fig. 18.13 at different hydration times. Note the imaging parameters are identical to those given in the caption of Fig. 18.16

evenly distributed outside the gel layer. After 45 h upon hydration, the flowing space around the tablet becomes more heterogeneous as a result of increased swelling and surface roughness, indicating a non-steady state. Such phenomenon has previously been attributed to the increase of surface roughness of the polymer matrix upon dissolution (Zhang et al. 2011).

4.4 Multi-nuclear MRI of Active Pharmaceutical Ingredients (API)

The vast majority of published literature concerning pharmaceutically relevant solid dosage form research has concerned examining the ingress of dissolution media into the dosage form and how the dosage form itself responds to this challenge. Ultimately, it is the API that we are interested in and how it behaves throughout the dissolution testing procedure. However, direct imaging of the APIs during the dissolution process is made difficult by low API concentrations, fast T_2^* relaxation times and the fact that the ^1H s associated with the APIs are completely swamped by the ^1H signal from the water making up the dissolution media. Despite these drawbacks it is possible to image an API unambiguously via the use of ^{19}F NMR/MRI (Zhang et al. 2011; Chen et al. 2014). Figure 18.18 shows the results from a radial FLASH experiment on the same samples as that used in Figs. 18.10, 18.13, 18.14 and 18.16, 18.17. This is made possible by the use of a dual resonance r.f. coil that can be tuned both to ^1H and ^{19}F resonance frequencies and radial sampling of k -space.

Figure 18.18 shows 2D ^{19}F radial FLASH slice selective images which highlight the temporal evolution of the API distribution within the system during the dissolution event. The ^{19}F signal detected in these experiments arises solely from the dissolved TFDH drug that is held within the hydrated HPMC gel layer. No detectable signal can be attributed to the drug dissolved in the flowing media due to inflow/outflow (washout effects) of the dissolution media from the active slice within the MRI radio frequency coil. Also, no signal is detected from the solid state API in the dry core of the tablet due to the short T_2^* it possesses (Zhang et al. 2011). Thus, the ^{19}F images obtained can be uniquely used to monitor the mobilisation, dissolution and distribution of the non-solid state API within the swelling polymeric matrix. In Fig. 18.18 the bright orange/yellow areas correspond to the dissolved TFDH drug residing within the gel. At $t = 0$ h the tablet quickly hydrates upon contact with dissolution media. The 'ring-like' structure surrounding the tablet corresponds to the accumulation of hydrated API. From $t = 1$ h to 9 h, the dry core continues to shrink as more water penetrates into the dry core of the tablet and subsequently hydrates the drug. Meanwhile, the bright orange/yellow areas continue to expand. This behaviour agrees with the expansion of the gel layer as shown by the T_2 -maps in Fig. 18.14. In particular, at $t = 5$ h, the bright yellow/white dots are attributed to the mobilised API in the tablet correspond to a highly hydrated area in C_{wat} (Fig. 18.13, $t = 5$ h, $C_{wat} > 60\%$), the gel region in T_2 relaxation time map (Fig. 18.14 $t = 5$ h, $T_2 > 600$ ms), and the high self-diffusivity region in SDC map (Fig. 18.16, $t = 5$ h, $SDC > 2 \times 10^{-9} \text{ m}^2 \text{ s}^{-1}$). From $t = 13$ h onwards, the size of the bright region starts to decrease as the hydrated drug continues to diffuse out into the bulk solution. This type of imaging has also recently been shown to be viable for real pharmaceutical products (Zhang et al. 2011; Chen 2014). Chen et al. (Chen

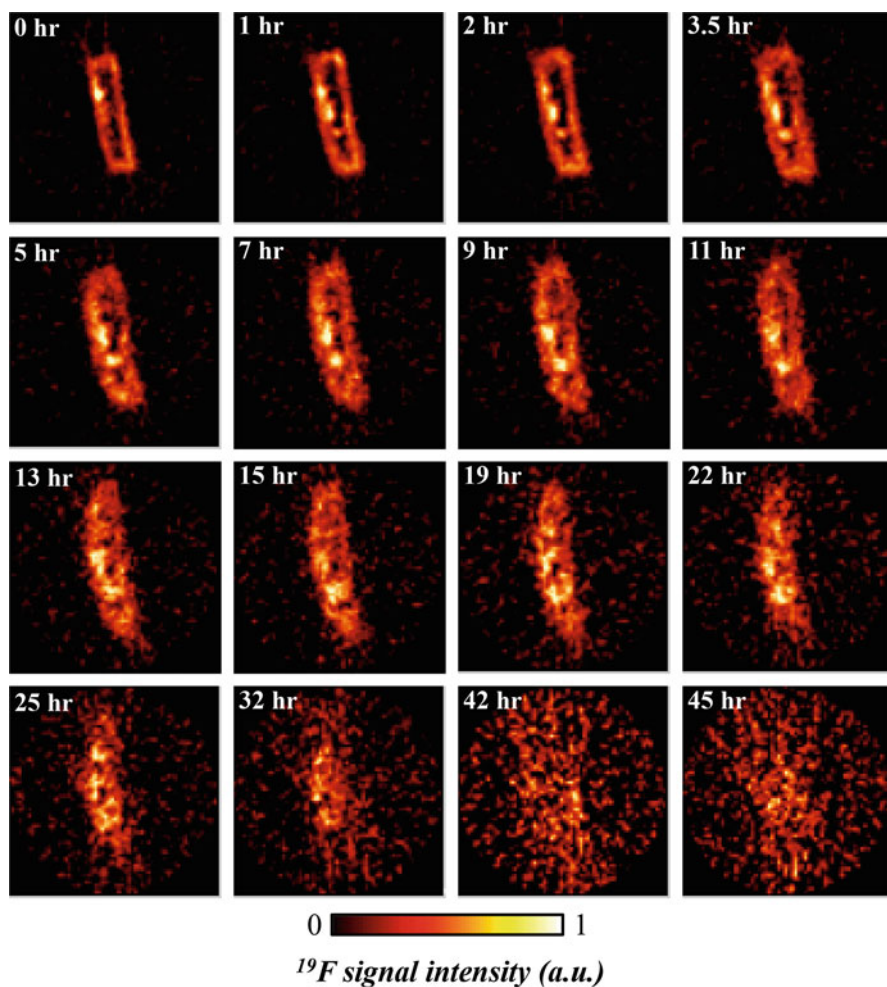


Fig. 18.18 Two-dimensional 2.5 mm thick slice selective ^{19}F radial FLASH maps of the HPMC/TFDH model tablet used in Fig. 18.10 at different hydration times. Radial ^{19}F FLASH imaging parameters: ^{19}F frequency 376.50 MHz; Acquisition bandwidth = 100,000 Hz; $TE = 1.09$ ms; $TR = 100$ ms; FOV 25 mm; data matrix size 64×64 ; image pixel resolution = $391 \mu\text{m}$; soft pulse tip angle $\theta = 10^\circ$. Number of averages = 128; total imaging time 13 min.

2014) showed that both ^1H T_2 relaxation maps and ^{19}F drug mobilisation maps can be co-registered to show the simultaneous behaviour of dissolution media ingress and API mobilisation and exit during the dissolution testing of Lescol XL tablet under pharmacopeial conditions in a USP-IV dissolution cell. Figure 18.19 shows a summary of this type of multi-nuclear co-registered data is currently possible.

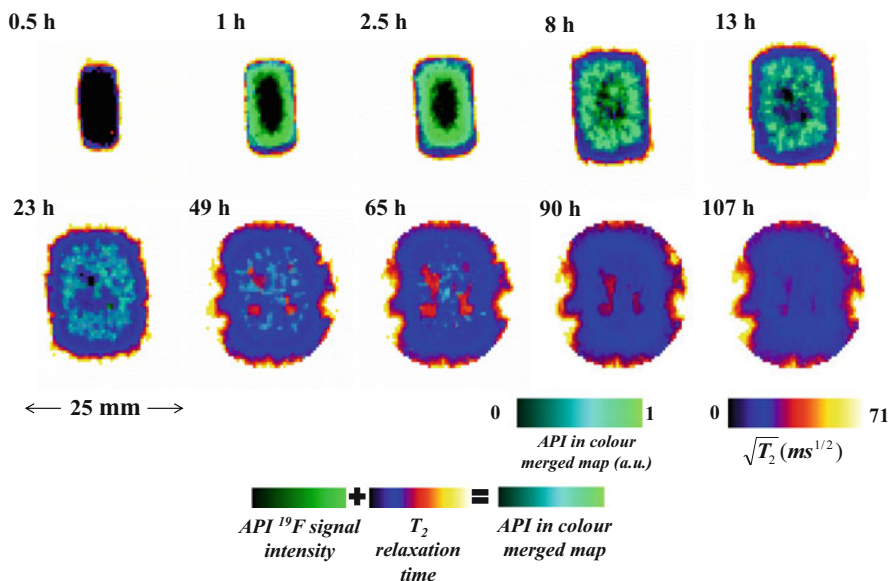


Fig. 18.19 ^{19}F intensity and ^1H - T_2 co-registered maps of Lescol[®] XL tablet at different hydration times. FOV = 25 mm \times 25 mm, pixel resolution = 391 μm \times 391 μm , temporal resolution = 3 min (^1H) and 13 min (^{19}F), slice thickness = 1 mm (^1H) and 2.5 mm (^{19}F). Adapted from Chen et al. (2014).

5 Practical Hints for MRI Imaging of Solid Dosage Forms

Dos

- Calibrate both hard and soft (π and $(\pi/2)$) r.f. pulses by hand each time you use a NMR/MRI spectrometer
- Ensure your r.f. coil and gradient coil are all aligned with the iso-center of the main field, B_0 .
- Measure the FWHM line width¹² of your bulk spectrum. It's useful for calculating the minimum frequency encoding bandwidth and hence maximum digitisation rate to avoid Nyquist aliasing and chemical shift artefact. For example:

- (i) Calculate minimum frequency bandwidth (BW_{\min}) for N frequency encoded pixels using¹³:

¹²For more than one spectral resonance peak, calculate $\Delta\nu_{1/2}$ by subtracting the value of the FWHM of the left most and right most peaks. This will avoid chemical shift artefact (frequency aliasing) if sufficient bandwidth and gradient strength are available (which may not always be the case!).

¹³The factor of 2 in the expression below is due to the fact that the acquired readout data is complex, i.e., it has real and imaginary components.

$$BW_{\min} = 2 \times N \times \Delta v_{1/2}.$$

(ii) Calculate maximum digitisation rate (DR) as:

$$DR_{\max} = 1/BW_{\min}$$

- Perform a simple T_1 and T_2 and self-diffusivity, D , bulk measurement on your sample so you can begin to formulate your imaging protocols and appreciate what relaxation and signal losses you might expect.

Don'ts

- Rely solely on automated set-up of pulse sequences, parameters and imaging protocols included by the manufacturers of spectrometer. Often they will work, but they may not be optimised for the system you are investigating.
- Use/copy historic data sets and parameters when starting a new set of experiments. Always start and calibrate your next experiment from first principles.

6 Final Remarks

The general aim of this chapter was to highlight the theory behind nuclear magnetic resonance phenomena and show how one can obtain a variety of non-invasive, spatially resolved, quantitative information from pharmaceutically relevant solid dosage forms under pharmacopeial conditions. Understanding the principles behind the common imaging techniques found on modern spectrometers is key to being able to adapt, develop and optimise existing MR protocols to push further the limits of quantitative imaging in “difficult” samples such as solid dosage forms. Two families of MR techniques were discussed in some detail: gradient echo based techniques that are sensitive to sample magnetic susceptibilities and spin echo based techniques that are generally insensitive to T_2^* effects which under the right conditions provide us with useful measurements of for example absolute species concentration, molecular self-diffusivity and coherent motion. The chapter also highlighted the ability of multi-nuclear MR methods, specifically ^1H and ^{19}F , to gain unparalleled insights into API behaviour within a model solid dosage form during dissolution. MR imaging in pharmaceutical research, and in particular that applied to understanding the dissolution behaviour of solid dosage forms and their APIs, is now at a stage that is producing meaningful results which should ultimately be incorporated into the Quality by Design approach to pharmaceutical research and development. As ever, the acquisition of higher fidelity, quantitative MR images in shorter acquisition remains a challenge, but MR technologists and research workers alike are beginning to apply state-of-the-art advanced techniques such as sparse sampling (Lustig et al. 2007, Holland et al. 2010) and Bayesian methods (Holland et al. 2011a, b, 2012) to address the future challenges in general MR research.

Acknowledgement The author wishes to thank Dr Chen Chen (Charlie) for his assistance in preparing the manuscript and for expertly performing the data acquisition and processing of the results from the dissolution experiments on the model HPMC/TDFH dosage form.

References

- Block KT, Uecker M, Frahm J (2007) Undersampled radial MRI with multiple coils. Iterative image reconstruction using a total variation constraint. *Magn Reson Med* 57:1086–1098
- Callaghan PT (1993) Principles of nuclear magnetic resonance microscopy. Oxford University Press, New York
- Callaghan PT (2011) Translational dynamics and magnetic resonance. Oxford University Press, Oxford
- Carr HY, Purcell EM (1954) Effects of diffusion on free precession in nuclear magnetic resonance experiments. *Phys Rev* 94:630–638
- Chen C (2014) Quantitative magnetic resonance imaging studies of extended drug release systems. Cambridge
- Chen YY, Hughes LP, Gladden LF, Mantle MD (2010) Quantitative ultra-fast MRI of HPMC swelling and dissolution. *J Pharm Sci* 99:3462–3472
- Chen C, Gladden LF, Mantle MD (2014) Direct visualization of in vitro drug mobilization from Lescol XL tablets using two-dimensional F-19 and H-1 magnetic resonance imaging. *Mol Pharm* 11:630–637
- Elkins CJ, Alley MT (2007) Magnetic resonance velocimetry: applications of magnetic resonance imaging in the measurement of fluid motion. *Exp Fluids* 43:823–858
- Ferrero C, Massuelle D, Jeannerat D, Doelker E (2008) Towards elucidation of the drug release mechanism from compressed hydrophilic matrices made of cellulose ethers. I Pulse-field-gradient spin-echo NMR study of sodium salicylate diffusivity in swollen hydrogels with respect to polymer matrix physical structure. *J Control Release* 128:71–79
- Fessler JA, Sutton BP (2003) Nonuniform fast Fourier transforms using min-max interpolation. *IEEE Trans Signal Process* 51:560–574
- Fukushima E (1999) Nuclear magnetic resonance as a tool to study flow. *Annu Rev Fluid Mech* 31:95–123
- Haacke EM, Brown RW, Thompson MR, Venkatesan R (1999) Magnetic resonance imaging: physical principles and sequence design. Wiley, New York
- Haase A, Frahm J, Matthaei D, Hanicke W, Merboldt KD (1986) FLASH imaging. Rapid NMR imaging using low flip-angle pulses. *J Magn Reson* 67:258–266
- Hahn EL (1950) Spin echoes. *Phys Rev* 80:580–594
- Holland DJ, Malioutov DM, Blake A, Sederman AJ, Gladden LF (2010) Reducing data acquisition times in phase-encoded velocity imaging using compressed sensing. *J Magn Reson* 203:236–246
- Holland DJ, Blake A, Tayler AB, Sederman AJ, Gladden LF (2011a) A Bayesian approach to characterising multi-phase flows using magnetic resonance: application to bubble flows. *J Magn Reson* 209:83–87
- Holland DJ, Bostock MJ, Gladden LF, Nietlispach D (2011b) Fast multidimensional NMR spectroscopy using compressed sensing. *Angewandte Chemie-International Edition* 50:6548–6551
- Holland DJ, Blake A, Tayler AB, Sederman AJ, Gladden LF (2012) Bubble size measurement using Bayesian magnetic resonance. *Chem Eng Sci* 84:735–745
- Kikuchi S, Onuki Y, Kuribayashi H, Takayama K (2012) Relationship between diffusivity of water molecules inside hydrating tablets and their drug release behavior elucidated by magnetic resonance imaging. *Chem Pharm Bull* 60:536–542

- Levitt MH (2001) Spin dynamics: basics of nuclear magnetic resonance. Wiley, New York
- Levitt MH (2002) Spin dynamics. Wiley, England
- Liang ZP, Lauterbur PC (2000) Principles of magnetic resonance imaging: a signal processing perspective, IEEE Press Series in Biomedical Engineering. IEEE, New York
- Lustig M, Donoho D, Pauly JM (2007) Sparse MRI: the application of compressed sensing for rapid MR imaging. *Magn Reson Med* 58:1182–1195
- Mansfield P, Grannell PK (1973) NMR “diffraction” in solids? *J Phys C* 6:L422–L426
- Mantle MD (2011) Quantitative magnetic resonance micro-imaging methods for pharmaceutical research. *Int J Pharm* 417:173–195
- Mantle MD (2013) NMR and MRI studies of drug delivery systems. *Curr Opin Colloid Interface Sci* 18:214–227
- Mantle MD, Sederman AJ (2003) Dynamic MRI in chemical process and reaction engineering. *Prog Nucl Magn Reson Spectrosc* 43:3–60
- Meiboom S, Gill D (1958) Modified spin-echo method for measuring nuclear relaxation times. *Rev Sci Instrum* 29:688–691
- Melia CD, Rajabi-Siahboomi AR, Bowtell RW (1998) Magnetic resonance imaging of controlled release pharmaceutical dosage forms. *Pharm Sci Technol Today* 1:32–39
- Mistretta CA, Wieben O, Velikina J, Block W, Perry J, Wu Y, Johnson K (2006) Highly constrained backprojection for time-resolved MRI. *Magn Reson Med* 55:30–40
- Nott KP (2010) Magnetic resonance imaging of tablet dissolution. *Eur J Pharm Biopharm* 74:78–83
- Pope JM, Yao S (1993) Flow-selective pulse sequences. *Magn Reson Imaging* 11:585–591
- Quodbach J, Moussavi A, Tammer R, Frahm J, Kleinebudde P (2014) Tablet disintegration studied by high-resolution real-time magnetic resonance imaging. *J Pharm Sci* 103:249–255
- Rajabisiahboomi AR, Bowtell RW, Mansfield P, Henderson A, Davies MC, Melia CD (1994) Structure and behavior in hydrophilic matrix sustained-release dosage forms. 2. NMR-imaging studies of dimensional changes in the gel layer and core of HPMC tablets undergoing hydration. *J Control Release* 31:121–128
- Ramachan GN, Lakshmin AV (1971) 3-Dimensional reconstruction from radiographs and electron micrographs—application of convolutions instead of Fourier transforms. *Proc Natl Acad Sci USA* 68:2236
- Richardson JC, Bowtell RW, Mader K, Melia CD (2005) Pharmaceutical applications of magnetic resonance imaging (MRI). *Adv Drug Deliv Rev* 57:1191–1209
- Robson MD, Gatehouse PD, Bydder M, Bydder GM (2003) Magnetic resonance: an introduction to ultrashort TE (UTE) imaging. *J Comput Assist Tomogr* 27:825–846
- Shepp LA, Logan BF (1974) Fourier reconstruction of a head section. *IEEE Trans Nucl Sci* NS21:21–43
- Stejskal EO, Tanner JE (1965) Use of spin echoes in a pulsed magnetic-field gradient to study anisotropic, restricted diffusion and flow. *J Chem Phys* 42:288–292
- Weiger M, Pruessmann KP, Hennel F (2011) MRI with zero echo time: hard versus sweep pulse excitation. *Magn Reson Med* 66:379–389
- Zeitler JA, Gladden LF (2009) In-vitro tomography and non-destructive imaging at depth of pharmaceutical solid dosage forms. *Eur J Pharm Biopharm* 71:2–22
- Zhang Q, Gladden L, Avalle P, Mantle M (2011) In vitro quantitative H-1 and F-19 nuclear magnetic resonance spectroscopy and imaging studies of fluvastatin (TM) in Lescol (R) XL tablets in a USP-IV dissolution cell. *J Control Release* 156:345–354

Chapter 19

Mass Spectrometry Imaging of Pharmaceuticals: From Tablets to Tissues

Ivan M. Kempson and Clive A. Prestidge

Abstract Drug efficacy is dependent upon effective and controlled release for delivery to the target site. The properties of a drug product effecting delivery are carefully manipulated by a variety of ingredients/excipients serving various purposes. As such, there is high dependence on the optimal construction and spatial arrangement of all ingredients. The subsequent fate of the active pharmaceutical ingredient then ultimately determines therapeutic and toxic effects. Mass spectrometry imaging offers high sensitivity, specificity, high mass resolution and high mass ranges for imaging component distributions in solid forms and in biological tissues. This chapter reviews mass spectrometry imaging techniques most commonly utilised in these research areas. Examples are then provided of imaging various components in solid form products and on the exciting area of label-free imaging of pharmaceuticals and metabolites in animal tissues. A small section is also provided on micro-array imaging of biologicals. Due to the relative immaturity of the field, a special focus on future perspectives and emerging potential concludes the chapter.

Keywords Mass spectrometry • Imaging • ToF-SIMS • LA-ICPMS • MALDI • Active pharmaceutical ingredients • Excipients • Analysis • Small molecules • Biologicals • 3D • Metabolism

1 Introduction

High resolution spectral imaging offers many opportunities in the development of pharmaceutical and biomedical products. Mass spectrometry imaging (MSI) offers significant promise for pharmaceutical imaging but is far from being fully utilised at a basic science level or in assisting transfer of pharmaceutical products onto the

I.M. Kempson (✉)

Future Industries Institute, University of South Australia, Mawson Lakes, SA 5095, Australia
e-mail: Ivan.Kempson@unisa.edu.au

C.A. Prestidge (✉)

School of Pharmacy and Medical Sciences, University of South Australia, City East Campus, Adelaide, SA 5001, Australia
e-mail: Clive.Prestidge@unisa.edu.au

market. This is primarily due to only recent technological development and application in the biological and pharmaceutical arenas. However, MSI can be utilised in a range of applications including quality screening and identification of adulterants (Lanzarotta et al. 2012) and counterfeits (Nyadong et al. 2009), foreign matter identification (Pajander et al. 2013), and can play an integral role in product development (Bugay 2001).

Imaging inherently provides information on spatial arrangement of an analytes' partitioning, heterogeneity and distribution that coincide with product performance; either in the tablet, driving dissolution rates, or fate in biology, ultimately impacting on drug efficacy. The purpose of this is to enable product transfer onto the market and offering greater compliance and safer products with greater efficacy in a more efficient and cost-effective manner. Heterogeneity, for example, may lead to poor dissolution, which could be refined by adjusting process parameters in formulation and manufacturing. Failures of coatings on solid dosage forms may lead to crystallization of amorphous active pharmaceutical ingredients (API's) and detract from patient treatment, or a loss of lubrication impacting product quality, patient comfort and perception of a product.

Imaging is also under increasing demand by regulatory bodies such as the FDA in initiatives to ensure product quality. Infrared and Raman imaging techniques are already finding place in this regard. MSI however offers complementary information with distinct advantages that can promote understanding of a product and identification of key parameters in relation to product performance which is being increasingly needed for regulatory approvals. Mass spectrometry has particular advantages for specificity, sensitivity and parallel detection (in general). The nature of spectral information is highly complex, however the high mass-resolution means there is little detrimental feature overlap, hence the unique identification of molecules is generally feasible. Detection limits are often as low as ppm and even ppb. Secondary ion modalities also enable spatial resolution down to 10s of nanometres; well beyond diffraction limits encountered for optical interrogation. Analysis by MSI is furthermore becoming increasingly rapid, especially with microscopy (as opposed to 'mapping' or 'rastering') modalities.

In this review, we assess the most typical MSI approaches that have been utilised for imaging pharmaceutical materials and products as well as imaging the fate of these products *ex-vivo* after administration. We subsequently review, in a logical manner, MSI of active pharmaceutical ingredients (APIs), APIs and excipients in product, screening approaches in biopharmaceutical development, and the exciting area of API and metabolite imaging in tissue sections. Due to the developmental nature of many of these MSI techniques, considerable attention is finally given to perspectives on future developments.

2 Introduction to Mass Spectrometry Imaging Techniques

All mass spectrometry techniques are characterised by a mode of ablation and ionisation of the surface of a material and then the subsequent collection and separation of ions in a mass resolving analyser. Importantly in this review is that either the analyser provides spatial resolution or the sample is rastered for spot-by-spot analysis to create a chemical map. The most dominant forms of MSI techniques that have been applied to pharmaceutical research are summarised in Tables 19.1 and 19.2 and described in the follow sub-sections.

2.1 Time-of-Flight Secondary Ion Mass Spectrometry (ToF-SIMS)

Time-of-Flight Secondary Ion Mass Spectrometry (ToF-SIMS) operates via the focusing and rastering of a primary ion beam (often Ga⁺, Bi cluster, Au cluster or C60 as examples) upon a sample surface. The impact and momentum transfer of the primary ions leads to ejection from the surface of its constituents as elemental species, molecular fragments or partial fragments due to bond breakage in the impact and emission process. Charged species within the sputter plume are extracted, accelerated and transported to a spatially and temporally resolved

Table 19.1 Major MSI techniques and their advantages and disadvantages

	Advantages	Disadvantages
ToF-SIMS	Absolute surface analysis	Ultra-high vacuum
	High spatial and spectral resolution	Smaller area of analysis
	Detects all elements, as well as molecular information	Limited to a mass range of a few thousands mass units
DESI	Ambient atmospheric operation	Mass range of ~100–1000
		Slow imaging
		Low spatial resolution
MALDI	Very high mass range for detecting protein molecular ions	General need for matrix Limited elemental information

Table 19.2 Comparative performance of major MSI techniques

	ToF-SIMS	MALDI	DESI
Sensitivity	xxxxx	xxxx	xx
Spatial resolution	xxxxx	xxxx	xx
Analysis speed	xxxxx	xx	xx
Ambient conditions	No	Possible	Yes
Cost	x	xxx	xxxx
Mass range	xxx	xxxxx	xx
Surface sensitivity	xxxxx	xxx	x

detector via ion optics. Within the analyser and prior to the secondary ions reaching the detector, the ions navigate a time-of-flight region. Over this well-defined distance, an ions' transit time is measured and due to the relation between kinetic energy (known from the ion extraction and acceleration process) and velocity, a mass-to-charge ratio can be determined. Thus for each primary ion pulse, an entire mass spectrum is generated. The spatial arrangement is preserved in the detector plane and images of windowed spectral features are formed. The nature of this probe is highly surface sensitive, detecting effectively only the first monolayer, and for larger molecules such as proteins, may probe sub-monolayer depths. The typical sub-micron spatial resolution achieved with Liquid Metal Ion Guns (LMIG) enables highly detailed imaging.

Importantly for imaging and retrospective analysis of data, full spectral information at every pixel is acquired. This facilitates statistical data processing and exploratory research where the most valuable spectral features may not be immediately apparent during the time of data acquisition. Images are 256×256 pixels with a variable field of view used from roughly 50–200 μm and require on the order of 1–5 min for acquisition.

Perhaps the biggest drawback with ToF-SIMS is the need for measurements to be performed in an ultra-high vacuum environment. This gives immediate limitations on the sample that can be analysed. This usually is not an issue for solid materials but does require biologicals to be dried down onto a surface. However while the native state is not preserved, there is information retained in the nature of how the molecules adsorb on the surface that relate to their form in solution. Due to the surface sensitivity, contamination of samples by particularly prevalent silanes is commonly an issue.

While ToF-SIMS has a smaller mass range than MALDI for instance, it obtains greater fragmentation which can provide significant information on structure. The mass range of up to one to a few thousand mass units is typically adequate for detecting molecular ions of solid form drugs and small biologicals.

2.2 *Matrix Assisted Laser Desorption Ionization (MALDI) MS*

MALDI-MSI naturally relies on the MALDI process for generation of ions from a sample. Directing a laser (typically nitrogen or Nd:YAG lasers emitting in the UV) onto a sample in short high energy pulses leads to ablation of material and ionization. The ionization yield can be dramatically enhanced by the use of a 'matrix' material coating the sample that is selected for optimal absorption of the laser wavelength utilised. This in turn promotes energy transfer to the sample and greatly improves efficiency in the desorption process. The matrix material used is generally an organic acid that can donate protons and absorbs strongly in the UV region, corresponding with the laser used. Infrared lasers and matching matrix are

also used but are less common. The ions are subsequently extracted and passed through a mass analyser which often utilises TOF or an ion trap for discrimination.

Imaging is generally conducted by incrementing the sample stage in the x and y axis to generate a 2D distribution. Spectra acquisition at each point (pixel) can take from one to several seconds. The acquisition of an entire image therefore requires a significant dedication of instrument time. However, recent developments have seen sub-diffraction limit resolution achieved with a ‘microscope’ mode implementing a pixelated array detector (Soltwisch et al. 2014).

A significant advantage of MALDI is the mass spectral range spanning up to ten’s to hundreds of kilo-daltons. This enables detection of molecular ions from large molecules such as proteins. Operation has conventionally been done in vacuum, but atmospheric systems are also available which adds ease to the sample handling and analysis. While quantification can be achieved, reproducibility relies heavily on sample preparation (especially having a strong dependence on the matrix and homogeneity of the coating) and instrument operation which is not always a trivial achievement. Micron resolution can be achieved however several to 10s of microns is commonplace.

2.3 Desorption Electrospray Ionization (DESI) MS

DESI operates by a desorption process created by focusing accelerated charged droplets from an electrospray source onto the sample. This liquid film undergoes rapid solid–liquid extraction. Droplets from the surface are then ejected due to momentum transfer from the incoming jet and are then extracted and analysed (Nyadong et al. 2009). This technique operates in ambient conditions, greatly improving application, and needs little or no sample preparation. The energy transfer to the sample is also efficient such that no matrix is needed, as is required for MALDI. However, the selective extraction from the desorption solvent used appears to be a significant challenge (Earnshaw et al. 2010). Imaging resolution is often limited to hundreds of microns although sub-hundred micron resolution is achievable and relies on rastering a sample beneath the probing beam. The mass range is somewhat limited at around 100–1000 mass units although this is suitable for detecting many solid form APIs. Desorption efficiency can vary due to hardness of samples and this can induce artefacts across a sample that may be of varying density, such a compressed tablet for example.

2.4 Laser Ablation Inductively Coupled Plasma (LA-ICP) MS

Laser Ablation Inductively Couple Plasma Mass Spectrometry (LA-ICP-MS) has so far demonstrated minimal use in analysis of pharmaceuticals. This is largely due

to sensitivity being limited to elemental isotopes. Ablation of material from a sample (up to several microns deep) is performed with a laser. Ionisation is performed within a surrounding plasma and ions are extracted for mass differentiation, generally utilising a quadrupole analyser. This mode of analysis however typically operates for selected specific ions rather than full spectra. It is therefore imperative that exact ions of interest are known beforehand, which is however conducive with the typical experimental design for LAICPMS imaging. Again, incremental 'spots' need to be acquired individually to generate an entire image. Quantification can be achieved by comparison to appropriate standard materials and can reach excellent detection limits. Analysis is conducted under ambient conditions and most often provides spatial resolution of about 50–100 μm although a few microns is achievable. A variety of other ambient ionization techniques exist but as yet have had little application in the pharmaceutical field (Harris et al. 2008).

3 Small Molecule API and Excipient Analysis

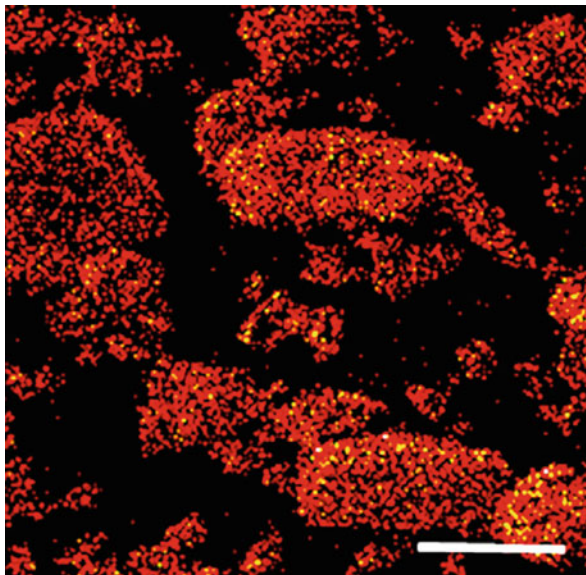
3.1 *Crystal/Powder Mixtures and Coatings*

Solid form drugs occur as powders or pressed into tablets. The particles' structural properties (such as amorphous versus crystal forms and relating to dissolution behaviour) and surface physico-chemical properties (influencing particle agglomeration, adhesion and flow) subsequently have strong influence on scale up and manufacturing processes, and product efficacy.

Surface compositional properties and how they relate to physical behaviour of flow, stickiness and dispersion impacting drug delivery performance are especially critical for inhalation powders (Shur and Price 2012). To promote powder lubrication and dispersion of dry particle inhalation products, magnesium stearate is often used as a coating. Zhou et al. (2011), utilised ToF-SIMS to image individual particles to assess such coatings and demonstrated sufficient resolution and sensitivity to quantify inter-particle heterogeneity for coatings of <1% (w/w) on 20 μm diameter lactose particles (Fig. 19.1). Subsequently, the surface coverage and composition were identified to be of greater significance to particle cohesion and flow than the particle morphological parameters. The surface sensitivity of ToF-SIMS was particularly well demonstrated in this work. At magnesium stearate incorporation levels achieving effective particle coverage, the chemical signature of lactose was effectively invisible to the ToF-SIMS. Most spectroscopic imaging techniques would not have such sensitive discrimination between the surface and the underlying particle.

The ultra-high surface sensitivity of ToF-SIMS is further demonstrated in the work of Chan et al. (2013), who imaged triple API composite particles of sub-micron diameter. The surface sensitivity enabled identification of which API preferentially distributed at the surface of the particles during spray drying

Fig. 19.1 Image of Mg, indicative of magnesium stearate coating on lactose particles at a coverage of 0.5% (w/w). Bar = 50 μm . Reproduced with permission from Elsevier from Zhou et al. (2011)



manufacture. The API forming at the core was barely identifiable in the ToF-SIMS imaging. Furthermore, ToF-SIMS has been especially useful in its use in identification and characterisation of foreign material in solid formulations, however with most relevance for relatively homogenous and low concentration contaminants (Pajander et al. 2013).

3.2 *Imaging API in Product*

Solid form pharmaceuticals are most commonly delivered via a tablet comprising compressed API with excipients such as bulking agents, lubricants and disintegrants. Distribution, particle size and coating all play important roles in the performance of a product. Infrared and Raman imaging have been implemented for screening and failure analysis. While these approaches are effective in many regards, there are distinct advantages offered by MSI for analysing the API and other ingredients directly in compressed tablets.

MALDI MS Imaging was perhaps published for the first time for a whole tablet cross section in 2010 (Earnshaw et al. 2010). The image shown in Fig. 19.2a gives the distribution of API in a tablet cross-section and the authors could examine such distributions as a function of the formulation. Interestingly, this image shows apparent concentration variation in regions of greater density due to the tablet compression process, i.e., the outer edge of the tablet appears to indicate greater compression than the centre.

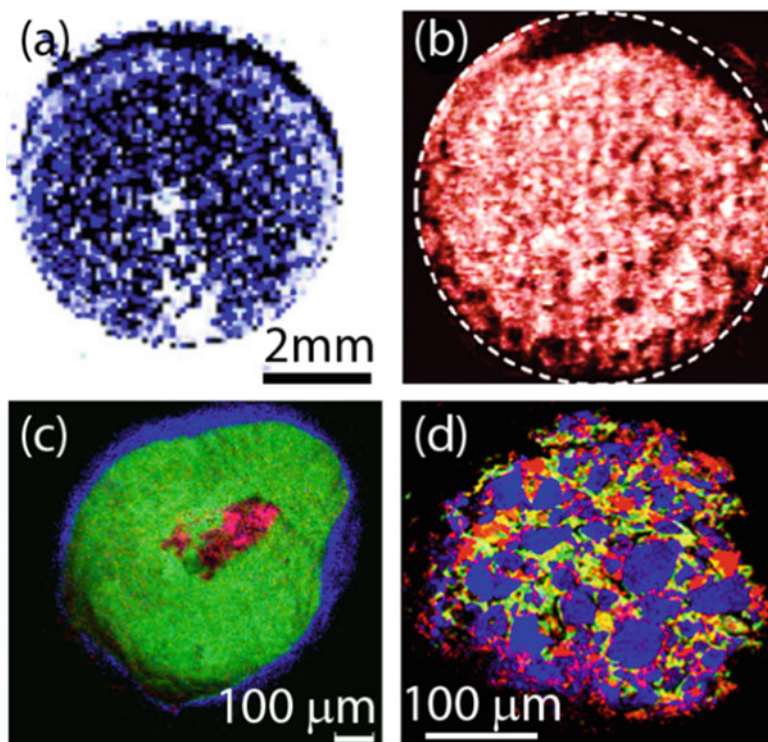


Fig. 19.2 (a) MALDI image of API in a tablet. Reproduced with permission from John Wiley and Sons from Earnshaw et al. (2010). (b) Imaging of API in a tablet with DESI MS. Reprinted with permission from Nyadong et al. (2009). Copyright 2009 American Chemical Society. Some artefacts are apparent at the edges of the tablets in (a) and (b) inherent to the techniques. (c) and (d) show tri-(artificial) colour maps of products acquired with ToF-SIMS. (c) red = silicon, green = API, blue = ethycellulose. Reproduced with permission from Physical Electronics. (d) red = API, Green = HPC binder, blue = sucrose. Reproduced with permission from Physical Electronics, 2010

On a coarser spatial scale, an ambient ionization approach of infrared laser ablation metastable-induced chemical ionization (IR-LAMICI) has more recently been introduced and was demonstrated, as proof-of-principal, on the analysis of a counterfeit antimalarial tablet (Galhena et al. 2010). A 300 μm analysis area was scanned with an X-Y stage over a Tylenol tablet to reconstruct a compositional image over 14×7 mm which took 40 min to acquire. The greatest advantage here is the ease in operating the analysis in ambient conditions, however this is still of quite a coarse resolution. Also useful for its ambient operation is DESI. Figure 19.2b presents an image of artesunic acid in an antimalarial tablet achieved with 75 μm resolution. The data in that research was used in characterization of differences in formulation used in counterfeit drugs (Nyadong et al. 2009). While these approaches yield valuable information on spatial segregation relating to mixing and individual components, there are limitations with respect to the spatial resolving power.

Superiority of ToF-SIMS' spatial resolution over the other MSI techniques reviewed here in application of studying pharmaceuticals is demonstrated in the images in Fig. 19.2c and d. In these striking images, the various components of these solid form products are clearly identified in the spectral features used for their characterization. The spatial scales are also well suited to the granular feature sizes. The clarity in delineation of each component is inherent to ToF-SIMS due to the extremely surface sensitive nature of its analysis. Subsequently there is effectively no sub-surface sampling which can blur or distort features. ToF-SIMS has also been used for imaging drug (alendronate sodium) in ultra-high molecular weight polyethylene matrices used as an articulating material in joint replacement (Liu et al. 2009). Local controlled release relies on proper API distribution within the polymer and needless to say, should not compromise the mechanical properties of the polymer. The drug itself however can potentially impact on the mechanical integrity of the polymer. In this work, the material properties were assessed and determined to be maintained with specific drug loading and homogenous API distribution was confirmed with MSI.

4 Imaging Biologicals and Array Analysis

Distinct from solid form small molecule drugs are biologicals (e.g., peptides, proteins and RNA/DNA), which are most commonly stored and administered in solution forms. Many techniques are used for the characterisation of biological drugs in these forms and spatial distributions are rarely of interest or consequence. However, some specific examples of MSI of biologicals have been reported and are mentioned here. Specifically, potential exists in the study of biomolecules and proteins on surface patterned substrates or structures, micro-array analysis in product development and study of biomolecule structure and binding.

The first example is given in Fig. 19.3 which shows the 3D distribution of sirolimus (also known as rapamycin), an immunosuppressant, in a PLGA polymer stent coating matrix (Fisher et al. 2009). The API here was imaged as a function of elution time using ToF-SIMS. Alternating between the surface sensitive analysis and a direct-current (DC) sputter beam, depth profiling was conducted to produce consecutive images to be reconstructed into a 3D rendering. From the 3D reconstruction it was possible to observe large areas of the surface as well as subsurface channels containing the drug. In this case, ToF-SIMS was used to characterise the depletion of the drug from the PLGA matrix as a function of elution time and provided valuable information on the characterization of the stent product.

For screening and development, array analysis is a very recent area of extension in mass spectrometric analysis. Array analysis of samples has provided visually exciting representation of populations, for example imaging protein distribution in human eye lens tissue with MALDI (Grey and Schey 2009). While that study was not specifically regarding pharmaceutical imaging, it stands as excellent example of MSI in the biotechnology field. ToF-SIMS has also been proven successful in

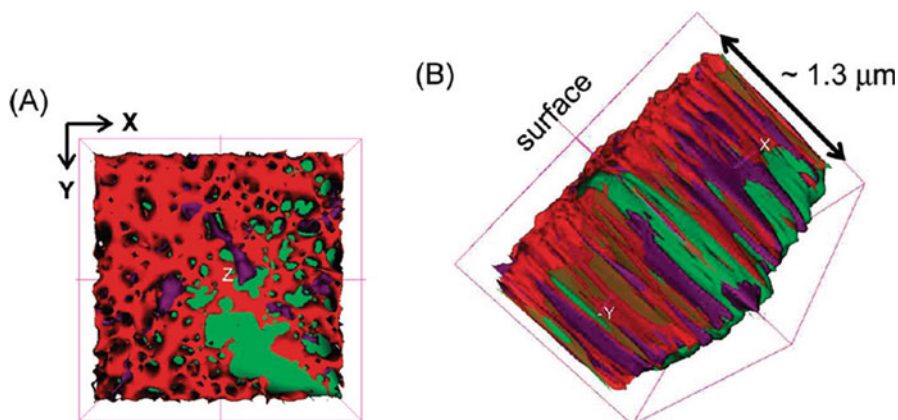


Fig. 19.3 A 3D rendering from ToF-SIMS analysis of API in a stent coating. Red: $C_5H_{10}N^+$ (sirolimus, an immunosuppressant drug used to prevent rejection in organ transplantation). Green: $C_3H_4O^+$ (PLGA, a biocompatible copolymer). Purple: Na^+ (from elution medium). Reprinted with permission from Fisher et al. (2009). Copyright 2009 American Chemical Society

quality control screening and analysis in micro array patterns (Wendeln et al. 2010). Possibly the earliest example of ToF-SIMS to micro-array analysis was by Braun et al. 1999. In that work, atto-mol quantities of organic molecules were analysed and imaged after printing into ‘vials’ produced in an array with volumes down to 30 femtolitres. The arrays contained 10,000 samples per 1.4 cm^2 . And each sample was acquired in a time on the order of 100 ms. There is clear potential in extending this type of analysis into the pharmaceutical and biotechnology development arenas, especially considering the sensitivity of ToF-SIMS to molecular interactions and subtle changes in condition parameters (Kempson et al. 2010; Kempson et al. 2013). In the latter two publications, it was shown how ToF-SIMS coupled with multivariate analysis could identify extremely subtle changes in protein interaction with a surface depending on thermal exposure and misfolding. This approach is further highlighted in Fig. 19.4. Particularly worthy of note in this work is that distinct spectral features have not been imaged, rather chemical classifications as determined by the statistical analysis have been imaged. The images have been produced from a study into the heterogeneity of drug and polymer formulations printed onto a microarray. This example shows 5 discretely separated components. Component 1 indicated the substrate material while component 3 and 5 were polymer and drug respectively. Where this approach is most valuable is in identifying areas of overlapping/mixed material, discriminating chemically very similar material, exploratory analysis and identification of materials generated in the processing that are not represented by the initial ingredients.

Following from this is the prospect of correlating fluorescence images of arrays with mass spectroscopic analysis (Finnskog et al. 2004), or other parameters that can be correlated with the beneficial matrix sensitivity of mass spectrometry. Progress in this general area is demonstrated by Al-Bataineh and Short in Fig. 19.5, where such arrays can then be utilised in the study of molecular interactions including proteins, peptides, drugs and other biological molecules.

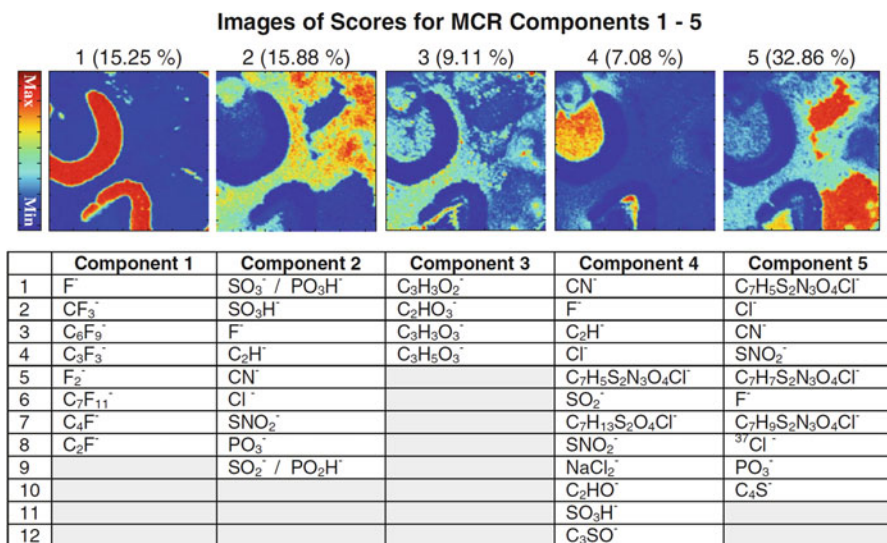


Fig. 19.4 Multivariate curve resolution (MCR) images of scores for components 1–5 of a hydrochlorothiazide (HCT) printed spot and a corresponding table showing significantly loaded negative secondary ions for the respective MCR components. Reproduced with permission from Scoutaris et al. (2012)

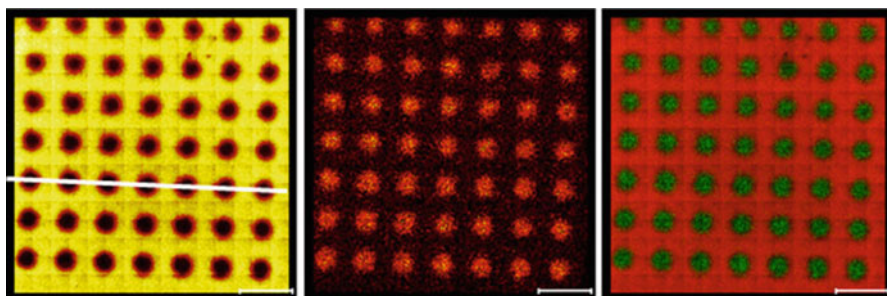


Fig. 19.5 Imaging of ToF-SIMS fragment ions from an array showing the substrate (*left*), the plasma polymer treated array (*centre*) and the overlay of the two (*right*). Bar = 1 mm. Reproduced with permission from John Wiley and Sons, from Al-Bataineh and Short (2014)

5 Label-Free Imaging in Organs and Tissues: Molecule Metabolism and Fate

In developing pharmaceutical products to enter the market, exceptional potential exists with MSI in assisting with more economical screening and assessment of drug distribution in-vivo. MSI is capable of imaging animal cross sections to ascertain molecular metabolism and fate. Such information is critical for translation

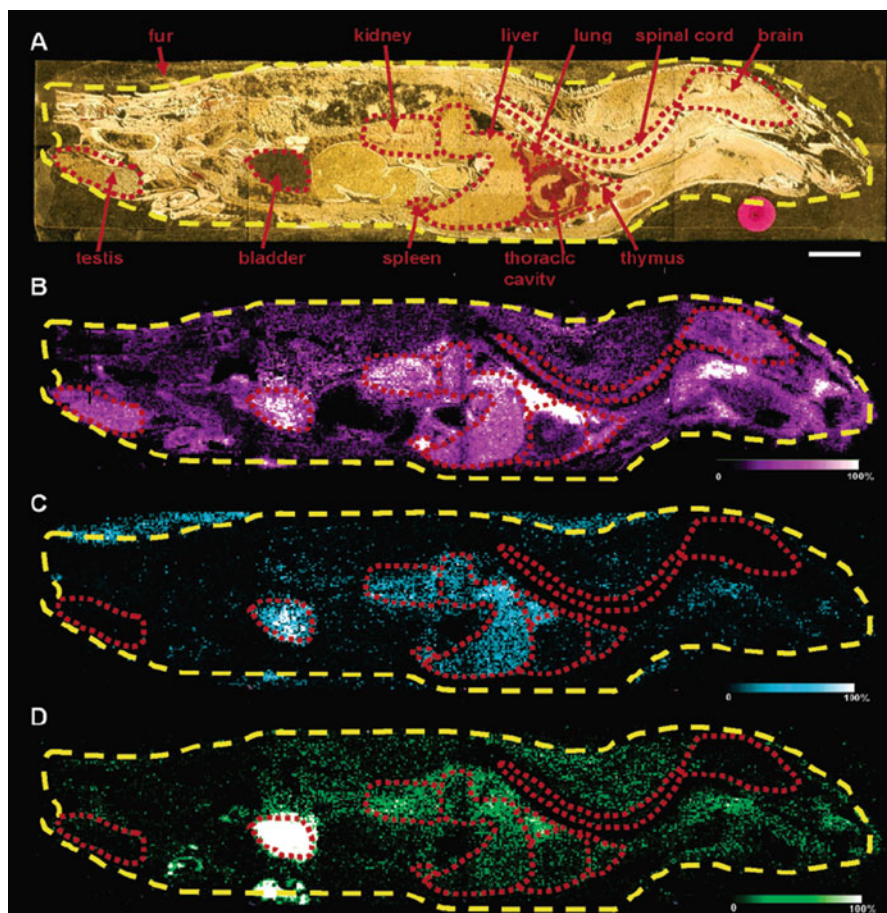


Fig. 19.6 MALDI-MSI of drug and metabolite distribution 2 h after dosage in a whole-rat sagittal section. The optical image in (a) outlines specific organs. MS/MS ion images of parent drug (b) and metabolites N-desmethyl metabolite (c) 2-hydroxymethyl (d) are shown respectively. Bar, 1 cm. Reprinted with permission from Khatib-Shahidi et al. (2006). Copyright 2006 American Chemical Society

of drugs to the market place and is conducted without need for stains, or fluorescent or radio-isotope labelling (Fig. 19.6). This is, in principal, molecular histology and true molecular imaging.

Label-free imaging of biological and drug molecules is enabling tracking of specific molecules of interest, especially in metabolism where labels can interfere or are lost in metabolic transformation and avoids the limitations associated with labeling. While highly attractive and clearly powerful to image without labels, this comes at the price of complexity in many instances in how the specific molecule of interest can be clearly distinguished from the complex biological environment. The potential and challenges are objectively reviewed by Heeren et al. 2009, in their

article “Imaging Mass Spectrometry: Hype or Hope?”. MS for imaging of tissues for biomedical analysis in general has been reviewed thoroughly elsewhere (Chughtai and Heeren 2010), and also for MALDI (Fournier et al. 2008) and ToF-SIMS specifically (Jones et al. 2007). Critical comparison between MSI of tissue and other labelling techniques has also been made elsewhere (Ait-Belkacem et al. 2012). The primary motivation in this field of research is more thorough and rapid appreciation of drug delivery and mechanistic interactions at specific sites such as the target organ for efficacy, and other organs for toxicity and side effects.

This area of research is dominated by the advantages of MALDI-MSI with large mass-spectral range. Imaging MALDI-MS began to appear in a more popular fashion soon after the year 2000, although some pharmaceutical imaging work had been conducted as early as the mid-1990s (Gusev et al. 1995). One of the earliest studies was that by Bunch et al., imaging Nizoral penetration into a porcine skin model (Bunch et al. 2004). Around this time, MALDI-MS imaging had also been used to image changes in protein expression due to drug induced regulation (Reyzer et al. 2004). The technique evolved quickly from this point to imaging drugs and metabolites in organs (Rohner et al. 2005) and then in whole-rat sections, for instance by Khatib-Shahidi et al. 2006 (Fig. 19.6). This work exemplified the potential to come, by imaging olanzapine and its metabolites as well as proteins distributed among the organs of rats at varying time points after drug administration. This was primarily motivated by pre-clinical screening in drug discovery and development. In further development such imaging has become fully quantitative (Takai et al. 2012).

Particular hurdles that challenge the application of MALDI MS have been the selection of a suitable matrix, improved spatial resolution, analyte extraction and sensitivity. Thawing of frozen samples has also been identified to lead to changes in analyte concentration depending on rate and duration (Goodwin et al. 2012). However, successful application has been providing important information for understanding and screening in drug development in many areas, for instance in delivery to the brain (Hsieh et al. 2007; Liu et al. 2013; Hsieh et al. 2010). Developments here are genuinely exciting for pharmacology, understanding disease etiology and progression and therapy as given in the inspiring perspective of Schwamborn and Caprioli, Fig. 19.7 (Schwamborn and Caprioli 2010).

A particularly interesting article in two regards is one by Eijkel et al. 2009. Their report presented images from SIMS and MALDI of a 10 μm thick section of human cerebellum which enabled a direct comparison of the two techniques (Fig. 19.8). The SIMS image contained $16,384 \times 16,384$ pixels, each with a full mass spectrum from 0 to 2000 Da. In this range, SIMS is sensitive to elements, small molecules and lipids. The MALDI image was produced with a mass range from a few hundred to a few thousand Da. This could be extended depending on sample preparation. The image was 48×46 pixels of $200 \times 200 \mu\text{m}$ and presents distribution of peptides. The second key point in their research was that the data from each of these images were processed statistically for further correlative analysis. The application of these algorithms can dramatically increase the amount of data extracted with greatly improved interpretation. For SIMS however, particular attention needs to be paid to

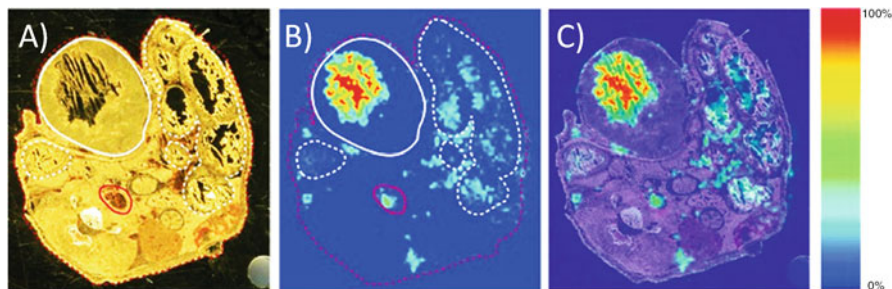


Fig. 19.7 A transverse section of a mouse (a) imaged with MALDI, showing API distribution (b) and overlay (c). T anti-cancer drug is shown with high concentrations in the tumour (*white solid line*), and is also detected in the digestive system (*dotted white line*) and major blood vessels (*solid red line*). Reproduced with permission from Nature Publishing Group from Schwaborn and Caprioli (2010)

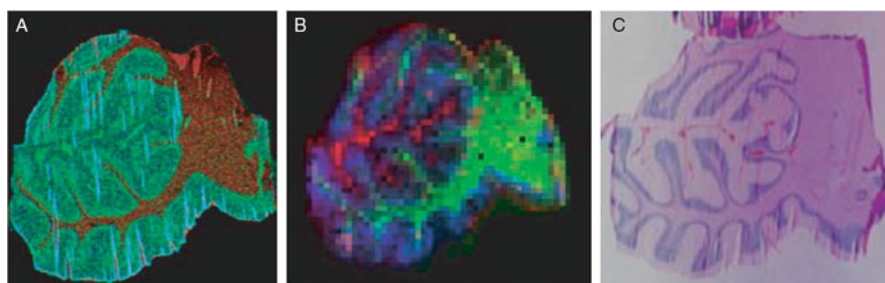


Fig. 19.8 Images of human cerebellum. (a) A SIMS (red: cholesterol, m/z 386; green: phosphocholine, m/z 184). (b) MALDI (green: m/z 3926, blue: m/z 1756, and red: m/z 2817), and (c) optical imaging after the tissue was stained with H&E showing grey matter (light pink), white matter (pink), and granular layer (purple). Reproduced with permission from John Wiley and Sons, from Eijkel et al. (2009)

the sample preparation and handling due to the surface sensitive nature of this technique. Preliminary ablation of surface contamination is likely to be a common requirement (Lee et al. 2008).

In one of the few demonstrations of LA-ICP-MS, Izmer et al. (2012), with interest in comparison to radio-luminography imaging, produced images of drug in rat organs at varying time points after administration. LA-ICP-MS could be used in this case due to the drug of interest being a Br labelled anti-tuberculosis molecule and the inorganic element is detectable by the analysis system. Conventionally an organic molecule would not be detectable by this method. Microtomed sections of rat were prepared and quantified distributions were imaged with detection limits down to $0.1 \mu\text{g g}^{-1}$. This approach was arguably easier due to the ambient analysis and quantifiably more accurate than other MS techniques. Acquisition time is still a hindrance however, in this case needing 8 h for acquisition of an entire rat section.

Other MSI techniques are less commonly applied to imaging of tissue. Liquid extraction surface analysis mass spectrometry also has some limited potential for imaging at low resolution or complementary corroboration of data at specific analysis points (Schadt et al. 2012). The potential here along with associated challenges were well represented by Parson et al. 2012.

6 Emerging Approaches and Future Perspectives

Imaging typically provides a 3-dimensional data set, i.e., spectral information for every pixel in a 2-dimensional array. Not surprisingly, analytics become increasingly challenging with increasing dimensionality of the data. Furthermore, there is clear value to evolve imaging beyond simple mapping of a spectral peak, but to image spectral trends and correlations. For instance, statistics comparing spectra can identify specific spectral trends that correlate rather than indicating a specific peak of interest. Otherwise statistical approaches can extract very subtle differences in samples, even when compositionally identical. An example of this is principal component analysis that can semi-quantify the amount of a denatured protein in a protein mixture (Kempson et al. 2010; Kempson et al. 2013). In this instance, composition is absolutely identical, however the interplay between peak intensities identifies key spectral correlations identify underlying trends in the data.

This opens up two avenues of particular relevance to this chapter. I—significant improvements in the characterisation of active ingredients and products; and II—extracting vital information concerning the imaging of biological systems.

With regard to the first point, researchers are now conducting statistical analysis across all spectral features for all pixels in images. This moves away from the conventional concept of imaging a tangible material component. Rather, it enables much more interesting and valuable information. A particularly effective application of this concept is the work by Brito et al. (2010). In that research, ToF-SIMS was used to image particles in a standard approach by imaging Si and other specific spectral features relating to composition. However, statistical analysis enabled correlating the spectral features with the physico-chemical property of water contact angle, a measure of wettability. Subsequently this physico-chemical property can be imaged and provides an entirely new understanding of heterogeneity. There is clearly immense value in such imaging, but this is limited by the complexity involved to establish and validate each system analysed. Ultimately such approaches can offer immense value in correlating material properties with material behaviours such as flow and dissolution.

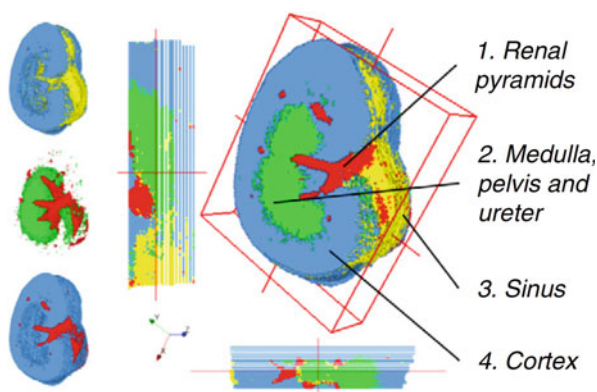
Statistical analysis will also likely increase in providing discriminant analysis or cluster mapping images, for example, such as shown in Fig. 19.4 above. Such statistical approaches are emerging as a powerful analytical tool for ToF-SIMS and are demonstrated in the characterization of biological tissues, comparing homeostasis with morbidity (Bulet et al. 2010).

These statistical analyses will also play important roles with regard to the second point above, i.e., for biological imaging. The work by Eijkel et al. (2009), is one example of this development and highlights the potential in cross-correlative spectroscopies. It is clearly advantageous to incorporate different modalities in pharma characterization for a more complete picture (Lanzarotta et al. 2012; Shur and Price 2012). The actual process can go beyond the direct overlay of information, but incorporation of statistical analysis correlating key and often subtle features between spectroscopies. For ex-vivo work, the biology, metabolism and anatomy also need great appreciation for assessing tissue/protein and drug co-localisation. Imaging in biology for label free study of APIs requires ‘friendly’ compounds clearly distinguished by the imaging modality, or greater sophistication in the analytical ability to distinguish specific organic molecules in the complex bio-environment. Compounding the complexity here is the metabolism and structural change and association of molecules in-vivo. As commonly recognised for enabling research, cross-discipline collaborations will be vital to effective development, requiring statistics, image and data processing as well the understanding of the physical chemistry and pharmaceutical sciences.

Extension into further dimensions will also become increasingly common as instrumental and computing power increases. With increasing speed of analysis, array analytics, time resolved studies and 3-dimensional rendering will become more easily achievable. For example it is conceivable that we will soon see mass spectrometry imaging used for 3 dimensional molecular reconstruction of organs and the entire distribution of drugs and metabolites. A prelude to this is the work by Oetjen et al. demonstrating a full reconstruction of a mouse kidney in Fig. 19.9 (Oetjen et al. 2013). Coupling with this massive increase in data acquired, i.e., full spectral information in multiple dimensions, is a need for data handling, storage and processing capability (Klinkert et al. 2014).

With the ever increasing desire and challenges to bring new medicines to the market, there is no doubt that mass spectral imaging will play an increasingly important role in advancing the research and development of pharmaceutical products.

Fig. 19.9 A 3D reconstruction of a mouse kidney using MALDI-MSI. Reproduced with permission from Elsevier, from Oetjen et al. (2013)



References

- Ait-Belkacem R, Sellami L, Villard C, DePauw E, Calligaris D, Lafitte D (2012) Mass spectrometry imaging is moving toward drug protein co-localization. *Trends Biotechnol* 30(9):466–474
- Al-Bataineh SA, Short RD (2014) Protein patterning on microplasma-activated PEO-like coatings. *Plasma Processes Polym* 11(3):263–268
- Braun RM, Beyder A, Xu J, Wood MC, Ewing AG, Winograd N (1999) Spatially resolved detection of attomole quantities of organic molecules localized in picoliter vials using time-of-flight secondary ion mass spectrometry. *Anal Chem* 71(16):3318–3324
- Brito E, Abreu S, Brien C, Skinner W (2010) ToF-SIMS as a new method to determine the contact angle of mineral surfaces. *Langmuir* 26(11):8122–8130
- Brulet M, Seyer A, Edelman A, Brunelle A, Fritsch J, Ollero M, Lapr evote O (2010) Lipid mapping of colonic mucosa by cluster TOF-SIMS imaging and multivariate analysis in cfr knockout mice. *J Lipid Res* 51(10):3034–3045
- Bugay DE (2001) Characterization of the solid-state: spectroscopic techniques. *Adv Drug Del Rev* 48(1):43–65
- Bunch J, Clench MR, Richards DS (2004) Determination of pharmaceutical compounds in skin by imaging matrix-assisted laser desorption/ionisation mass spectrometry. *Rapid Commun Mass Spectrom* 18(24):3051–3060
- Chan JGY, Chan HK, Prestidge CA, Denman JA, Young PM, Traini D (2013) A novel dry powder inhalable formulation incorporating three first-line anti-tubercular antibiotics. *Eur J Pharm Biopharm* 83(2):285–292
- Chughtai K, Heeren RMA (2010) Mass spectrometric imaging for biomedical tissue analysis. *Chem Rev* 110(5):3237–3277
- Earnshaw CJ, Carolan VA, Richards DS, Clench MR (2010) Direct analysis of pharmaceutical tablet formulations using matrix-assisted laser desorption/ionisation mass spectrometry imaging. *Rapid Commun Mass Spectrom* 24(11):1665–1672
- Eijkel GB, Kaletař BK, Van Der Wiel IM, Kros JM, Luider TM, Heeren RMA (2009) Correlating MALDI and SIMS imaging mass spectrometric datasets of biological tissue surfaces. *Surf Interface Anal* 41(8):675–685
- Finnskog D, Ressine A, Laurell T, Marko-Varga G (2004) Integrated protein microchip assay with dual fluorescent- and MALDI read-out. *J Proteome Res* 3(5):988–994
- Fisher GL, Belu AM, Mahoney CM, Wormuth K, Sanada N (2009) Three-dimensional time-of-flight secondary ion mass spectrometry imaging of a pharmaceutical in a coronary stent coating as a function of elution time. *Anal Chem* 81(24):9930–9940
- Fournier I, Wisztorski M, Salzet M (2008) Tissue imaging using MALDI-MS: a new frontier of histopathology proteomics. *Expert Rev Proteomics* 5(3):413–424
- Galhena AS, Harris GA, Nyadong L, Murray KK, Fern andez FM (2010) Small molecule ambient mass spectrometry imaging by infrared laser ablation metastable-induced chemical ionization. *Anal Chem* 82(6):2178–2181
- Goodwin RJA, Iverson SL, Andren PE (2012) The significance of ambient-temperature on pharmaceutical and endogenous compound abundance and distribution in tissues sections when analyzed by matrix-assisted laser desorption/ionization mass spectrometry imaging. *Rapid Commun Mass Spectrom* 26(5):494–498
- Grey AC, Schey KL (2009) Age-related changes in the spatial distribution of human lens α -crystallin products by MALDI imaging mass spectrometry. *Invest Ophthalmol Vis Sci* 50(9):4319–4329
- Gusev AI, Vasseur OJ, Proctor A, Sharkey AG, Hercules DM (1995) Imaging of thin-layer chromatograms using matrix-assisted laser desorption/ionization mass spectrometry. *Anal Chem* 67(24):4565–4570
- Harris GA, Nyadong L, Fernandez FM (2008) Recent developments in ambient ionization techniques for analytical mass spectrometry. *Analyst* 133(10):1297–1301

- Heeren RMA, Smith DF, Stauber J, Kükrer-Kaletas B, MacAleese L (2009) Imaging mass spectrometry: hype or hope? *J Am Soc Mass Spectrom* 20(6):1006–1014
- Hsieh Y, Chen J, Korfmacher WA (2007) Mapping pharmaceuticals in tissues using MALDI imaging mass spectrometry. *J Pharmacol Toxicol Methods* 55(2):193–200
- Hsieh Y, Li F, Korfmacher WA (2010) Mapping pharmaceuticals in rat brain sections using MALDI imaging mass spectrometry. *Methods Mol Biol* 656:147–158
- Izmer A, Ghlop D, De Houwer K, Cuyckens F, Vanhaecke F (2012) A pilot study on the use of laser ablation-ICP-mass spectrometry for assessing/mapping the distribution of a drug and its metabolites across the body compartments of rats. *J Anal At Spectrom* 27(3):413–418
- Jones EA, Lockyer NP, Vickerman JC (2007) Mass spectral analysis and imaging of tissue by ToF-SIMS—the role of buckminsterfullerene, C₆₀⁺, primary ions. *Int J Mass Spectrom* 260(2–3):146–157
- Kempson IM, Martin AL, Denman JA, French PW, Prestidge CA, Barnes TJ (2010) Detecting the presence of denatured human serum albumin in an adsorbed protein monolayer using TOF-SIMS. *Langmuir* 26(14):12075–12080
- Kempson IM, Chang P, Bremmell K, Prestidge CA (2013) Low temperature thermal dependent Filgrastim adsorption behavior detected with ToF-SIMS. *Langmuir* 29(50):15573–15578
- Khatib-Shahidi S, Andersson M, Herman JL, Gillespie TA, Caprioli RM (2006) Direct molecular analysis of whole-body animal tissue sections by imaging MALDI mass spectrometry. *Anal Chem* 78(18):6448–6456
- Klinkert I, Chughtai K, Ellis SR, Heeren RMA (2014) Methods for full resolution data exploration and visualization for large 2D and 3D mass spectrometry imaging datasets. *Int J Mass Spectrom* 362(1):40–47
- Lanzarotta A, Crowe JB, Witkowski M, Gamble BM (2012) A multidisciplinary approach for the analysis of an adulterated dietary supplement where the active pharmaceutical ingredient was embedded in the capsule shell. *J Pharm Biomed Anal* 67–68:22–27
- Lee TG, Park JW, Shon HK, Moon DW, Choi WW, Li K, Chung JH (2008) Biochemical imaging of tissues by SIMS for biomedical applications. *Appl Surf Sci* 255(4):1241–1248
- Liu X, Qu S, Lu X, Ge X, Leng Y (2009) Time-of-flight secondary ion mass spectrometry study on the distribution of alendronate sodium in drug-loaded ultra-high molecular weight polyethylene. *Biomed Mater* 4(6):065008
- Liu X, Ide JL, Norton I, Marchionni MA, Ebling MC, Wang LY, Davis E, Sauvageot CM, Kesari S, Kellersberger KA, Easterling ML, Santagata S, Stuart DD, Alberta J, Agar JN, Stiles CD, Agar NY (2013) Molecular imaging of drug transit through the blood-brain barrier with MALDI mass spectrometry imaging. *Sci Rep* 3:2859
- Nyadong L, Harris GA, Balyssac S, Galhena AS, Malet-Martino M, Martino R, Parry RM, Wang MD, Fernández FM, Gilard V (2009) Combining two-dimensional diffusion-ordered nuclear magnetic resonance spectroscopy, imaging desorption electrospray ionization mass spectrometry, and direct analysis in real-time mass spectrometry for the integral investigation of counterfeit pharmaceuticals. *Anal Chem* 81(12):4803–4812
- Oetjen J, Aichler M, Trede D, Strehlow J, Berger J, Heldmann S, Becker M, Gottschalk M, Kobarg JH, Wirtz S, Schiffler S, Thiele H, Walch A, Maass P, Alexandrov T (2013) MRI-compatible pipeline for three-dimensional MALDI imaging mass spectrometry using PAXgene fixation. *J Proteom* 90:52–60
- Pajander J, Haugshøj KB, Bjørneboe K, Wahlberg P, Rantanen J (2013) Foreign matter identification from solid dosage forms. *J Pharm Biomed Anal* 80:116–125
- Parson WB, Koeniger SL, Johnson RW, Erickson J, Tian Y, Stedman C, Schwartz A, Tarcsa E, Cole R, Van Berkel GJ (2012) Analysis of chloroquine and metabolites directly from whole-body animal tissue sections by liquid extraction surface analysis (LESA) and tandem mass spectrometry. *J Mass Spectrom* 47(11):1420–1428
- Physical Electronics, Inc., USA (2010) TOF-SIMS imaging of a drug pellet cross-section using a Bi₃²⁺ cluster ion beam

- Reyzer ML, Caldwell RL, Dugger TC, Forbes JT, Ritter CA, Guix M, Arteaga CL, Caprioli RM (2004) Early changes in protein expression detected by mass spectrometry predict tumor response to molecular therapeutics. *Cancer Res* 64(24):9093–9100
- Rohner TC, Staab D, Stoeckli M (2005) MALDI mass spectrometric imaging of biological tissue sections. *Mech Ageing Dev* 126(1):177–185
- Schadt S, Kallbach S, Almeida R, Sandel J (2012) Investigation of figopitant and its metabolites in rat tissue by combining whole-body autoradiography with liquid extraction surface analysis mass spectrometry. *Drug Metab Disposition* 40(3):419–425
- Schwamborn K, Caprioli RM (2010) Molecular imaging by mass spectrometry—looking beyond classical histology. *Nat Rev Cancer* 10(9):639–646
- Scoutaris N, Hook AL, Gellert PR, Roberts CJ, Alexander MR, Scurr DJ (2012) ToF-SIMS analysis of chemical heterogeneities in inkjet micro-array printed drug/polymer formulations. *J Mater Sci Mater Med* 23(2):385–391
- Shur J, Price R (2012) Advanced microscopy techniques to assess solid-state properties of inhalation medicines. *Adv Drug Del Rev* 64(4):369–382
- Soltwisch J, Göritz G, Jungmann JH, Kiss A, Smith DF, Ellis SR, Heeren RMA (2014) MALDI mass spectrometry imaging in microscope mode with infrared lasers: bypassing the diffraction limits. *Anal Chem* 86(1):321–325
- Takai N, Tanaka Y, Inazawa K, Saji H (2012) Quantitative analysis of pharmaceutical drug distribution in multiple organs by imaging mass spectrometry. *Rapid Commun Mass Spectrom* 26(13):1549–1556
- Wendeln C, Heile A, Arlinghaus HF, Ravoo BJ (2010) Carbohydrate microarrays by microcontact printing. *Langmuir* 26(7):4933–4940
- Zhou Q, Qu L, Gengenbach T, Denman JA, Larson I, Stewart PJ, Morton DAV (2011) Investigation of the extent of surface coating via mechanofusion with varying additive levels and the influences on bulk powder flow properties. *Int J Pharm* 413(1–2):36–43

Chapter 20

Applications of AFM in Pharmaceutical Sciences

Dimitrios A. Lamprou and James R. Smith

Abstract Atomic force microscopy (AFM) is a high-resolution imaging technique that uses a small probe (tip and cantilever) to provide topographical information on surfaces in air or in liquid media. By pushing the tip into the surface or by pulling it away, nanomechanical data such as compliance (stiffness, Young's Modulus) or adhesion, respectively, may be obtained and can also be presented visually in the form of maps displayed alongside topography images. This chapter outlines the principles of operation of AFM, describing some of the important imaging modes and then focuses on the use of the technique for pharmaceutical research. Areas include tablet coating and dissolution, crystal growth and polymorphism, particles and fibres, nanomedicine, nanotoxicology, drug-protein and protein-protein interactions, live cells, bacterial biofilms and viruses. Specific examples include mapping of ligand-receptor binding on cell surfaces, studies of protein-protein interactions to provide kinetic information and the potential of AFM to be used as an early diagnostic tool for cancer and other diseases. Many of these reported investigations are from 2011 to 2014, both from the literature and a few selected studies from the authors' laboratories.

Keywords Atomic force microscopy (AFM) • Bacteria and bacterial biofilms • Cantilevers • Drug crystal growth • Drug-protein interactions • Live cells • Nanomedicine • Nanotoxicology • Pharmaceutical science • Protein-protein interactions • Scanning force microscopy (SFM) • Viruses

D.A. Lamprou (✉)

Strathclyde Institute of Pharmacy and Biomedical Sciences (SIPBS), University of Strathclyde, 161 Cathedral Street, Glasgow G4 0RE, UK
e-mail: dimitrios.lamprou@strath.ac.uk

J.R. Smith

School of Pharmacy and Biomedical Sciences, University of Portsmouth, St Michael's Building, White Swan Road, Portsmouth PO1 2DT, UK

1 Introduction

Atomic force microscopy (AFM) continues to find ever wider applications in the fields of materials characterisation and life sciences. By using a small tip to scan across the sample's surface, the requirement to focus light and electrons as with light and electron microscopies is eliminated; this overcomes the Rayleigh criterion resolution limit, enabling nanometre and sometimes atomic resolution imaging, depending on the sample and/or imaging regime, to become routine. AFM can be operated without the need for conducting or stained samples and therefore can be operated in physiological media. Further, the probe can be used to push into or pull away from sample surfaces, yielding quantitative nanomechanical and adhesion data, which can also be displayed graphically. This chapter will discuss the fundamentals of AFM and highlight a few recent applications with relevance to pharmaceutical science.

1.1 Background

The atomic force microscope (AFM; scanning force microscope, SFM) is the principal member of a number of related scanning probe microscopes (SPM). The first of these was the scanning tunnelling microscope (STM), invented by Binnig and Rohrer, whom received the Nobel Prize for Physics, in 1982 after revealing the first atomic resolution images (Binnig and Rohrer 1982). By applying a bias potential across a small gap between a sharp metallic tip and a conducting sample, it was possible for electrons to tunnel across the forbidden energy gap; if the probe was simultaneously scanned across the sample, the tunnelling current yielded an image related to the topography (strictly, the local density of states) of the sample. The technique necessitated the use of conducting specimens, with the exception of DNA, proteins and other small molecules, and so was restrictive for the study of thicker biological samples and other insulating materials, such as polymers. To overcome this issue, the imaging method was developed, by the same inventors, to measure forces on a cantilever, to which the tip was mounted, rather than tunnelling currents: this became the AFM instrument (Binnig et al. 1986). In 1992, SPMs capable of both STM and AFM, became commercially available and very soon afterwards a vast array of derivative techniques and modes, almost solely AFM-based, were developed. AFM has finally come of age, with new imaging modes and related techniques continually coming to market; highlights of these are summarised later in this chapter.

1.2 Principles of Operation

Before discussing the multitude of acquisition modes, some of the fundamentals of AFM will be presented. AFM operates by scanning a small, usually square pyramidal shaped tip, prefabricated onto a cantilever, across a sample, mounted on a

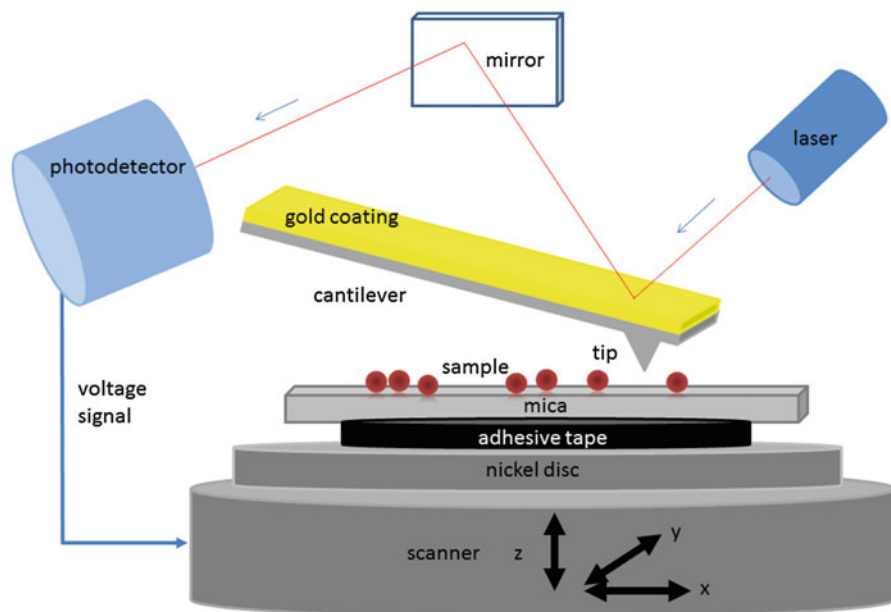


Fig. 20.1 A schematic of the main components of a typical AFM, with particles on a mica surface

stub, which is magnetically held into place on top of a piezoelectric ceramic scanner. Piezoelectric crystals change shape on the application of a voltage, the relationship being roughly proportional and accurate to 0.1 \AA ; it is this feature that provides AFM with its high resolution capability. The piezos are arranged in the scanner (tripod or the more usual tube design) to provide x , y and z (height) movement, the former two of which allow the scanning motion. The arrangement here describes a sample-scanning rather than tip-scanning instrument, i.e., the sample scans a stationary tip. It is often more convenient, however, to imagine the tip scanning the sample, as will be discussed here.

The cantilever is often coated with a gold layer to make it reflective, so that a laser can be reflected from the cantilever onto a photodetector, via a mirror (Fig. 20.1). This laser assembly serves as a tracking system so that the position of the tip in relation to the surface can be continuously monitored. In contact mode, the simplest of operations, the probe (tip + cantilever) is brought into contact with the sample until a small deflection of the cantilever, corresponding to a repulsive force (the set-point), is detected via a displacement on the photodetector. The probe is then scanned across the surface causing the cantilever to move vertically corresponding to variations in topography (height) of the sample. As the probe begins to go over a high feature on the specimen, for example, the cantilever will start to deflect more (bending will increase) causing the laser spot on the photodetector to move. So as not to cause damage to the sample, and/or tip, a voltage signal from the photodetector is sent to the scanner, to which the sample is mounted, causing the scanner to retract. This then lowers the sample, relieving the increased

deflection (above the set-point) on the cantilever. Upward movement of the piezo, and sample, is also allowed when, for example, the probe moves over a low feature, such as a pit. This cycle is repeated as the sample is scanned, so that the deflection of the cantilever is kept constant by means of this feedback loop. The potential required to maintain the set-point via the feedback circuit is used, alongside the x and y coordinates, to create the contact mode AFM image. Some practical steps on how to acquire contact mode images are given in the Appendix.

1.3 Operating Modes

There are three operating modes in AFM: contact mode, Tapping Mode[®] (a trade mark of Bruker, and also known as intermittent contact mode) and non-contact mode. The last two modes are referred to as ‘ac’ techniques while contact mode is referred to as ‘dc’. Each has their own advantages and disadvantages. Contact mode is the simplest, where the cantilever moves along the surface maintaining a set force. If too much force or too little force is detected, the height will be adjusted using the piezoelectric motors through the feedback loop (Sect. 1.2). Tapping Mode[®] is probably as widely encountered as contact mode. Here, to minimise potentially damaging lateral forces being exerted on the sample, the cantilever is oscillated at its resonant frequency during scanning; the measurement is made only at the moment when the tip touches the specimen, and for the most part, while the scanner moves the sample, the tip is safely retracted. Tapping Mode[®] is often used for imaging delicate biological samples, such as DNA, and this can also be carried out in physiological media.

With most commercial AFM instruments, different image channels can be acquired at the same time as the topography (height) image. For example, in contact mode, the error signal (raw signal detected by the photodetector) and the friction response (or lateral force microscope, LFM image, derived from the horizontal component of the photodetector’s signal as the cantilever twists during scanning) may be obtained. Similarly, in Tapping Mode[®], in addition to the error signal, the phase image (not to be confused with other definitions of this term in microscopy) and amplitude image may be obtained (Schmitz et al. 1997). These respectively correspond to the time (phase) lag and amplitude of the driven tapping sine wave signal relative to the response wave after interacting with sample. For example, variations in viscoelastic and/or adhesion properties of the sample across the surface may modify the phase and/or amplitude signals. These modes often give more defined visual contrast than their simultaneously acquired topography images, although the exact mechanism behind their complex origin is poorly understood.

In addition to imaging, force data can be obtained by pushing the tip into or pulling the tip away from a sample’s surface; this is often referred to as force spectroscopy (Butt et al. 2005). This can be explained with reference to a force vs. distance plot (force curve; Fig. 20.2), where a tip approaches a surface, typically experiences a short-range attraction event and then is pushed into the surface (Cappella and Dietler 1999; Butt et al. 2005). The gradient of the force curve in

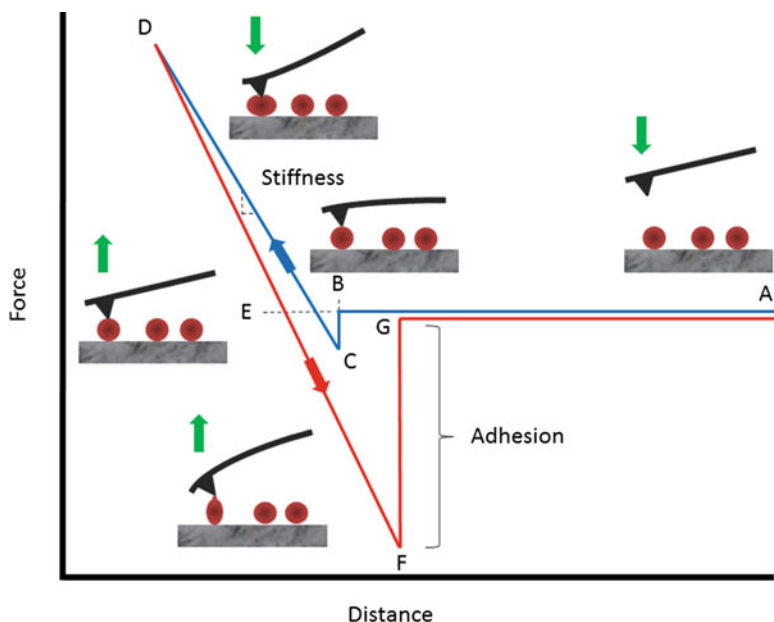


Fig. 20.2 A schematic showing the some key features of an AFM force vs. distance plot: *Blue line*: approach curve, *red line*: retract curve; regions (A–B) tip approaches the surface, (B–C) tip-surface attraction, (C–D) tip driven into the surface combined with cantilever bending (where stiffness/compliance information may be extracted), (D) point at which applied load is withdrawn and tip pulled away from the surface, (E) no net attractive or repulsive forces between tip and sample, (E–F) tip is adhered to sample, (F) applied load overcomes adhesion force and tip released from surface (maximum adhesion force), (F–G) adhesion force, (G) tip away from surface, (G–A) continued withdrawal of the tip

this region is a combination of indentation of the tip into the sample and cantilever bending, and with a suitable hard reference surface and use of mathematical models, quantitative nanoindentation (Young's modulus) data can be extracted. After a user-defined selected total force (or deflection), the applied load on the cantilever can be reduced, and the tip may eventually become adhered to the surface. Overcoming this force leads to an adhesion event, the importance of which becomes significant when the tip is suitably chemically derivatised or biologically functionalised (Sect. 1.4). Typically, only one-half of the force curve (an approach or retract curve) is relevant for any given experiment.

Nowadays, force measurements are combined with the scanning capability to produce local physical property maps, e.g., indentation, Young's modulus, adhesion and friction. These can be quantitative or qualitative depending on the extent of pre-calibration. Instrument manufacturers tend to have their own trade mark names for these modes, such as Torsional Resonance (TR) Mode[®] and PeakForce Tapping[®] (PFT).

In the TR mode, the tip is parallel rather than vertical to the surface, and the forces between the tip and the sample cause a change in resonance behaviour that

can be used to track the surface at a constant distance. The TR mode has the advantage that the tip remains at a constant distance from the surface at all times. Song and Bhushan (2006) investigated the dynamics of the tip-cantilever system when it is operated in TR mode, with or without tip-sample interaction, and they also described the basic methodology to extract in-plane surface properties in TR mode.

PFT is similar to Tapping Mode[®] AFM, however the PFT oscillation is performed at frequencies well below the cantilever resonance and the force on the tip can be kept constant which differs from Tapping Mode[®] AFM where the probe vibration amplitude is controlled by the feedback loop. A continuous series of force-distance curves is produced and by keeping the peak force constant, the modulus, adhesion force, and deformation depth can be calculated. In PFT, the oscillation combines the benefits of contact and Tapping Mode[®] imaging by having direct force control and avoiding damaging lateral forces. PeakForce Quantitative Nanomechanical Mapping (QNM[®]) (Bruker) is a recent and powerful technique that provides quantitative characterisation of surfaces at the nanoscale level (Lamprou et al. 2013). Individual force curves can be acquired and quantitatively analysed as the tip taps across the surface.

By attaching a ligand onto the tip, it is possible to map receptor-binding sites on cell/substrate surfaces, with a lateral resolution of a few nanometres, whilst simultaneously acquiring the topography image; this is known as topography and recognition imaging (TREC) mode or single-molecule force spectroscopy (SMFS), a single-molecule interaction method (Ebner et al. 2010; Muller et al. 2009).

Outside the scope of this short chapter lie a whole host of related probe techniques (not strictly modes). These, as their names suggest, are able to obtain other local physical properties; they include electrochemical AFM (EC-AFM), magnetic force microscopy (MFM), electrostatic force microscopy (EFM), kelvin probe force microscopy (KPFM), photoconductive AFM (pcAFM), scanning spreading resistance microscopy (SSRM), scanning thermal microscopy (SThM), scanning capacitance microscopy (SCM) and surface potential microscopy (SPoM).

Some of the latest developments include fast scanning, where the typical 1 Hz scan rate (ca. 10 min/scan) can be rapidly increased, and in some cases, for flat samples, to real-time acquisition. This is achieved through the use of small cantilevers.

1.4 Cantilevers and Tips

A wide variety of cantilevers and tips (often jointly named probes, although terms are used interchangeably) are available depending on their intended application. Broadly, contact mode probes tend to be made from silicon nitride, a hard material of approximate stoichiometry Si_3N_4 , whereas Tapping Mode[®] probes are normally formed from silicon, owing to its stiffness, although Si_3N_4 is also sometimes used.

The shapes of the cantilevers also vary, for example, V-shaped (often used for contact mode), beam-shaped (rectangular) and arrow shaped. The cantilever's spring constant (k , N m^{-1}), a proportionality constant used to relate cantilever deflection to force, can be determined from the dimensions (typically, 10–450 μm in length and various widths) and material properties of the cantilever. There are numerous methods for measuring k , such as the thermal noise method, described elsewhere (Clifford and Seah 2005; Lamprou et al. 2010). Accurate determination of this property, for which manufacturers provide approximate ranges, is essential for all AFM studies where force measurements are required.

The tip itself can be a square pyramid (approximating at its apex to a small sphere, the radius R of which may need to be determined for some force measurements), an oxide-sharpened tip (small R), a high-aspect ratio tip or a colloid probe. The latter type includes small entities, such as cells or polymer spheres that can be adhered to a tip-less cantilever to bestow biological functionality or defined contact geometries.

Probes can also be coated on either side for increased laser reflection (top side: Au), chemical functionalisation (underside: Au) or to change physical properties (underside: Pt, diamond-like coatings, magnetic Co alloys). Chemically modified probes are typically prepared by grafting thiol self-assembled monolayers (SAMs) on to Au coated probes or by silanising the surface OH groups of Si/Si₃N₄ probes, which are then used to measure specific short-range intermolecular (usually adhesion) forces. This is often termed chemical force microscopy (CFM; Smith et al. 2003a). Florin et al. (1994) first used functionalised AFM tips and surfaces to measure forces between biotin-avidin ligand-receptor pairs; this area has now been extended to investigate many interacting pairs.

Many different approaches have been used to attach (bio)molecules to AFM probes. For example Sikora et al. (2012) used AFM to investigate protein-protein (the core methylase and the HsdR subunit) interactions within the EcoR124I molecular motor. To do this, they functionalised a tip with a glutathione S-transferase-HsdR complex via a NHS-PEG-MAL linker and probed the core methylase (Fig. 20.3). The NHS end of the PEG linker reacts with amines on an amino-terminated, silanised Si₃N₄ tip, forming a stable amide bond, while the MAL group forms a C-S linkage with the protein. Li et al. (2013) used a similar linker to attach the drug rituximab to an AFM tip.

Riener et al. (2003) developed an 'easy-to-use test system' for investigating single ligand-detectors with AFM, demonstrating this using the avidin-biotin interaction where the AFM tip was biotinylated via a 6 nm PEG linker. Hinterdorfer et al. (1996) functionalised a tip with an antibody via an 8 nm PEG linker and an amino-functionalised Si₃N₄. Cail and Hochella (2005) added a polystyrene microbead to a cantilever to investigate sticking efficiency in colloid systems; spheres were simply glued to the cantilevers with UHU 5-min epoxy glue. The procedure was carried out by placing a tip-less Si₃N₄ cantilever in the AFM apparatus, using the piezoelectric actuators to drive the cantilever into the adhesive and then onto a glass slide covered with microspheres and picking up a single microsphere.

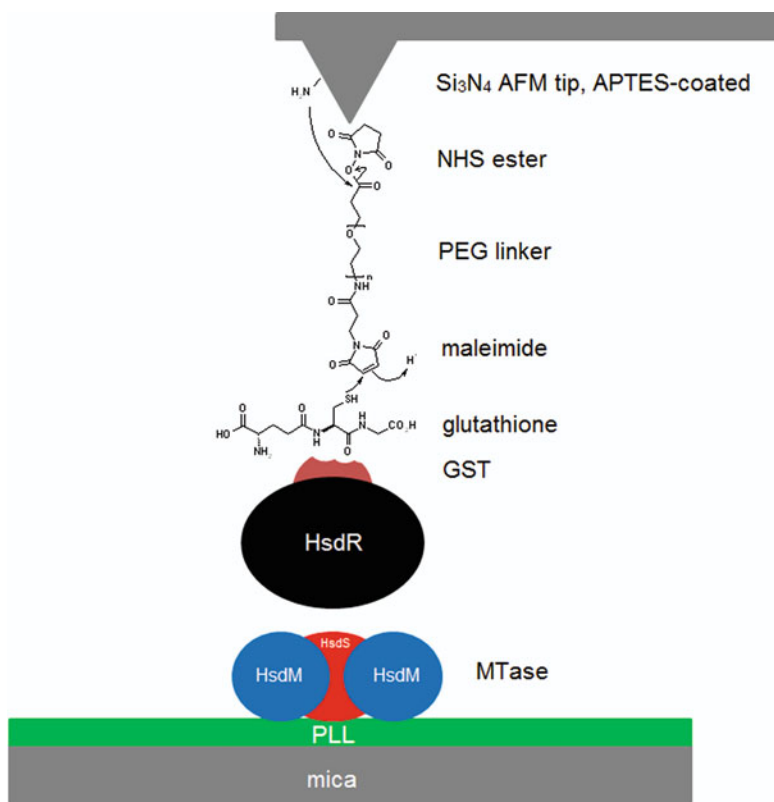


Fig. 20.3 Surface chemistry used to immobilise proteins to a Si_3N_4 AFM tip and a mica surface to study protein-protein interactions, in this case different subcomponents (HsdR/HsdS/HsdM) of a molecular motor (type I restriction-modification enzyme EcoR124I). APTES = (3-aminopropyl) triethoxysilane (to form surface NH_2 groups), PLL = poly(L-lysine) (a polycation to couple proteins to negatively charged mica), GST = glutathione S-transferase. Reproduced with permission (Sikora et al. 2012)

1.5 The Need for AFM in Pharmaceutical Research

The potential of AFM for structural biological studies was recognised since the conception of the technique. Indeed, it was the inability of tunnelling currents in STM to penetrate through the thickness of biological specimens greater than the diameter of proteins that led to the realisation of AFM. Nowadays, with the multitude of operating modes and techniques available, including the ability for real-time imaging in physiological buffer, many questions of interest to those engaged in pharmaceutical research can be answered. For example, ligand-receptor binding on cell surfaces can be measured and mapped, protein-protein interactions can be studied to provide kinetic information and AFM shows potential for use as an early diagnostic tool for cancer and other diseases.

The remainder of this chapter is dedicated to outlining selected examples that highlight the application of AFM in pharmaceutical research, ranging from coatings characterisation through to nanotechnology and biological applications. Many of these investigations have been from the past 4 years, both from the literature and a few from the authors' laboratories.

2 Use of AFM in Pharmaceutical Sciences

2.1 *Tablet Coating and Dissolution*

Pharmaceutical solid dosage forms are usually coated to control drug release, to protect active pharmaceutical ingredients (APIs) from degradation in the stomach or in humid atmospheres, to provide a barrier to taste and smell, and for controlling dissolution (Romer et al. 2008). AFM has been used mainly to acquire topography information, where it has the advantage over SEM in that it can provide quantitative surface roughness and surface area measurements and allow for their study in real-time (Seitavuopio et al. 2005); data on compositional distribution and porosity may also be discerned. Seitavuopio et al. (2003) investigated tablet surfaces using different imaging and roughness techniques, including AFM, and concluded that KCl tablets were smoother than NaCl tablets. A summary of surface roughness parameters that can be readily obtained from AFM topography profiles has been described by Smith et al. (2003b).

The coating materials of tablets are frequently studied as free films so that the effects of the tablet core can be eliminated (Kwok et al. 2004). Seitavuopio et al. (2006) used AFM imaging to examine the surfaces of pharmaceutical tablets that were coated with different aqueous hydroxypropyl methylcellulose films. AFM has been used to assess the quality of montmorillonite/poly(styrene)/poly(butyl acrylate) films prepared using dispersion methods (Csontos et al. 2006); the influence of composition on the form and arrangement of polymer droplets, and also the uniformity of the polymer film surface on the tablets were investigated. AFM can also be used to investigate areas on surfaces that have different properties, such as crystallinity and chemical composition; these are important parameters concerning the dissolution of a tablet.

The mechanisms and dissolution rates of the cholesterol monohydrate (001) surface, of relevance to the removal of gallstones, were investigated by Abendan and Swift (2005). The dissolution rate was found to be closely related to local variations in topography. Danesh et al. (2001) measured the dissolution rates of the (001) and (100) planes of aspirin crystals (0.45 and 2.93 nm s^{-1} , respectively) in 0.05 M HCl . The (001) crystal plane dissolved by receding step edges, whilst the (100) surface showed crystal terrace sinking. Such studies are important as in vitro crystal dissolution is proportional to in vivo drug absorption (Levy 1961).

2.2 *Crystal Growth and Polymorphism*

Drug crystal growth, particle characterisation and tablet coatings are critical elements in the manufacture of solid dosage forms. Thus, microscopic examination is important for the design and evaluation of a pharmaceutical product after the steps in the drug formulation process have been taken.

AFM was first introduced into crystal growth studies by Durbin and Carlson (1992), who detected the growth of steps on the surfaces of lysozyme crystals. Tonglei et al. (2000) used AFM for monitoring the crystal surface and they reported the step velocity of egg-white lysozyme crystal planes on a nanometre-scale using a sealed vessel in the AFM and noted the consequences of controlling the supersaturation. Land and De Yoreo (2000) used an in situ AFM for investigating the growth and activity of dislocation sources as a function of supersaturation during canavalin crystal growth. They reported that growth occurs on monomolecular steps generated either by simple or complex screw dislocation sources, and also visualised 2D nucleating islands that form onto the surface before spreading laterally as step bunches. Onuma et al. (1995) used AFM to investigate the topography of hydroxyapatite single crystals that had been synthesised from hydrothermal solution, and reported that growth proceeded through a layer-by-layer mechanism. Miyazaki et al. (2011) determined crystal growth rates of nifedipine at the surface of amorphous solids with and without polymers using AFM; they found the technique to be useful for studying the crystallisation kinetics of amorphous solids by targeting the crystals at the surface. Thompson et al. (2004), utilised AFM to assess the growth on the (001) face of aspirin crystals at two supersaturations, elucidating both the growth mechanisms and kinetics at each supersaturation. They also assessed the capability of AFM to follow the structural transformations of crystals that can occur in unstable pharmaceutical compounds. Thakuria et al. (2013) used AFM to observe the phase changes at crystal surfaces where the transformation is supplemented by changes in the spacing between layers of molecules. They analysed the thermodynamically stable form of the caffeine-glutaric acid cocrystal continuously in situ using intermittent-contact mode AFM. Further information on the applications of AFM for the visualisation of crystal growth can be found in two review papers by McPherson et al. (2001) and Chow et al. (2012).

Different polymorphs have different physicochemical properties, which could affect the solubility, dissolution and stability, and therefore polymorphic characterisation is an important parameter in pharmaceutical industry. AFM can be applied both in situ and ex situ to study the growth of crystals from solution, and in particular for investigating the crystallisation of proteins, nucleic acids and viruses (McPherson et al. 2001). Yip and Ward (1996) used AFM to identify the polymorphic forms of insulin and Danesh et al. (2000) mapped the distribution of polymorphs on the drug cimetidine. The author's group (DL) have investigated the nanocrystalline growth of dibenz[a,c]anthracene using a FastScan AFM (Fig. 20.4).

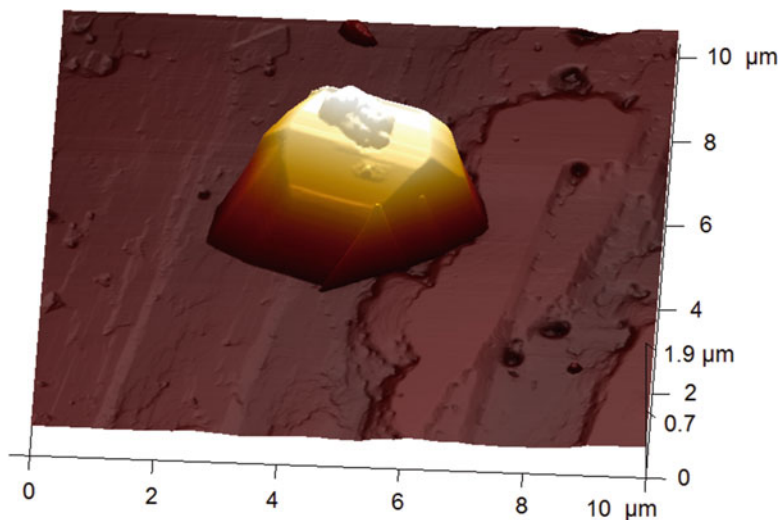


Fig. 20.4 AFM image of a dibenz[a,c]anthracene crystal grown on top of a similar structure crystal

2.3 Particles and Fibres

AFM offers particular advantages over TEM and SEM for the characterisation of particles and fibres, such as height measurement, minimal sample preparation, the ability to operate under atmospheric pressure and in liquids, and the acquisition of nanomechanical/adhesion data. These advantages facilitate the study of loaded and empty delivery systems.

AFM is an excellent technique for visualising particles with sizes ranging from 1 nm to 10 μm , allowing quantitative particle size measurements. These are not prone to problems experienced when using SEM, such as conducting coating thickness, astigmatism, penetration depth and absence of height information. SEM and dynamic light scattering (DLS) may also cause slight deformations of soft particles, such as liposomes (Fig. 20.5; Onyesom et al. 2013). Since x, y and z distances may be recorded using AFM, parameters such as diameter, volume and surface area can be calculated. AFM is one of the most important techniques for the characterisation of lipid drug delivery systems (Potta et al. 2011), which have been successfully used as drug carriers for the treatment of many cancers.

Recently, AFM has been used to study the scale-up and shelf-stability of curcumin-encapsulated poly(lactic acid-co-glycolic acid) (PLGA) nanoparticles (NPs), which were found to be stable for periods up to 6 months; the particles were spherical and had smooth surfaces (Gramma et al. 2013). AFM has been also used to characterise Au NPs with sizes 25, 55 and 90 nm, for investigating the stability of the naked, PEGylated, and Pt-conjugated NPs as a function of time under various conditions (Craig et al. 2012).

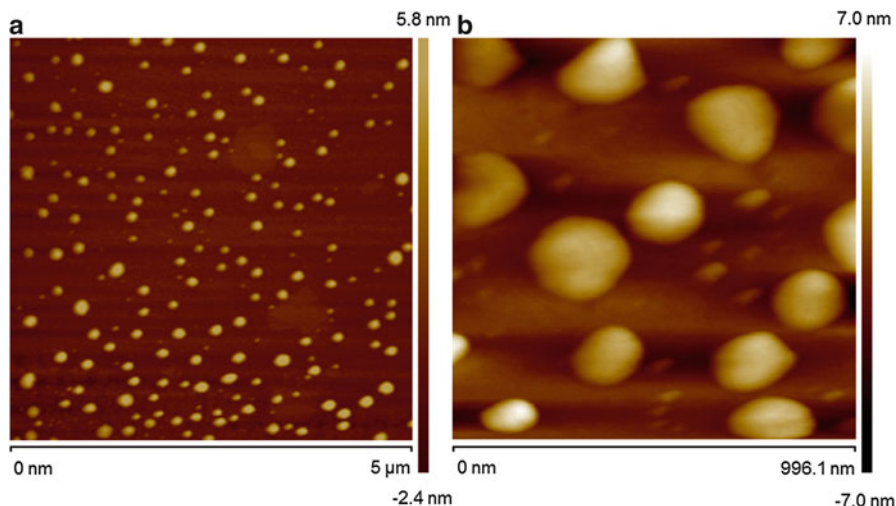


Fig. 20.5 AFM topography images (using PeakForce QNM[®] mode in air) of cholesterol-stabilised, dipalmitoylphosphatidyl choline (DPPC) Stealth liposomes. (a) unloaded, (b) sirolimus-loaded. Reproduced with permission (Onyesom et al. 2013)

Tsukada et al. (2004) developed AFM colloid probe techniques to mount a 1–3 μm spherical polycrystalline drug particle on a cantilever to measure adhesion to an α-lactose monohydrate layer for developing formulations for dry powder inhalers (DPI). Begat et al. (2004) used a similar arrangement to investigate adhesive and cohesive force characteristics of DPI systems containing budesonide or salbutamol sulphate to α-lactose monohydrate.

AFM has recently been used for the analysis of amyloid fibrils, an important research area in diseases such as Parkinson's, Alzheimer's, and type II diabetes (Chiti and Dobson 2006). For example, Mains et al. (2013) used drug-loaded lysozyme amyloid hydrogels, prepared by misfolding lysozyme in the presence and absence of drugs, such as atenolol, propranolol hydrochloride or timolol tartrate (Fig. 20.6). Different amyloid fibre structures were formed depending on the type of drug used. Adamcik and Mezzenga (2012) stated that AFM can contribute to research of amyloid fibrils by providing important information concerning fibril structure and fibrillation processes, and also to analyse some important properties of amyloid fibrils, such as their strength and Young's modulus. The contour length is also a very useful structural parameter of amyloid fibres that can be determined from AFM imaging; the property can be used to interpret the cellular response to the presence of amyloid fibrils of different sizes after fragmentation. Shorter fibrils have been found to have enhanced cytotoxicity compared to longer fibrils (Xue et al. 2009).

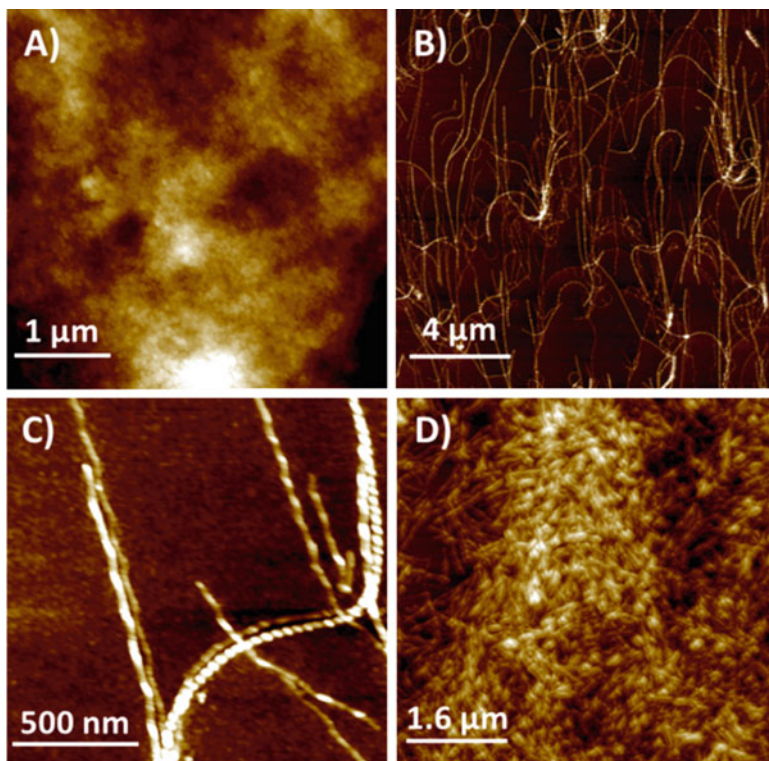


Fig. 20.6 AFM height images of drug loaded amyloid hydrogels. Drugs: (a) atenolol; (b) propranolol; (c) propranolol, with image showing both long and short range periodicity fibres; (d) timolol. Reproduced with permission (Mains et al. 2013)

2.4 Nanomedicine

Nanomedicine is an interdisciplinary field encompassing the detection, prevention and treatment of diseases at the nanometre scale (Karagkiozaki et al. 2012), which includes the longer term goals of producing personalised medicines (Janowski et al. 2012). Materials used in this application area include polymer coatings and nanoscale drug delivery devices, respectively, recently reviewed by Smith and Lamprou (2014) and Sitterberg et al. (2010), the latter of which focuses exclusively on the use of AFM.

AFM phase imaging, in conjunction with TEM and other techniques, has been used to characterise PEGylated lipoplexes for siRNA drug delivery (Belletti et al. 2013). Post-PEGylation was found to yield improved homogeneity with regards to PEG coverage. Karagkiozaki et al. (2013) used Tapping Mode[®] AFM to assess the morphology, surface roughness and cytocompatibility of conducting polymers as nanocoatings for tissue regeneration for cardiovascular implants. The use of these materials for this type of application has been recently reviewed (Smith and Lamprou 2014).

The size and morphology of liposomes for transporting boronated compounds for use in boron neutron capture therapy (BNCT) for targeted cancer treatments have been investigated by Tapping Mode[®] AFM (Theodoropoulos et al. 2013). Carbon nanotubes show promise as drug delivery devices owing to their dimensions, biocompatibility and ease of chemical functionalisation (Bianco et al. 2005). Tapping Mode[®] AFM has been used to show lipids wrapped around single-walled carbon nanotubes to increase their dispersion in aqueous media (Tasis et al. 2008; Roldo et al. 2009; Wise et al. 2008).

Adhesion forces between hematite NPs and *E. coli* immobilised onto a tip-less cantilever have been measured in phosphate buffer solution (Zhang et al. 2011). This fundamental study investigated the interaction forces and contact mechanics of the system, and a new model to describe the interaction was devised.

Lamprou et al. (2013) investigated the use of PeakForce QNM[®] for improving the developments in the field of nanomedicines, by measuring the effect of particles into various tissues (e.g., liver, kidney and small intestines). They also described how this detailed imaging approach may also help scientists address growing concerns in nanotoxicology.

2.5 Nanotoxicology

Nanotoxicology is a relatively new field, developed to study the toxicological effects of NPs (natural or engineered)/nanomaterials in the environment, which can differ markedly from their bulk materials due to their small particle size and large surface area (Donaldson et al. 2004). With the rapidly increasing use of nanomaterials, currently over 1000 commercial products, there is an urgency to determine their toxicity and to control exposure (Arora et al. 2012). There are a number of in vitro techniques that can be used for testing, such as proliferation assays, reactive oxygen species (ROS) generation analysis, flow cytometry, DNA damaging potential assays, gene expression analysis, genotoxicity and microscopic evaluation, including SEM/EDAX, TEM, fluorescence microscopy, MRI and AFM (Arora et al. 2012). Chinnapongse et al. (2011) used AFM to investigate the persistence of citrate-capped Ag NPs (20 nm) in natural freshwaters and synthetic aquatic media. Tetard et al. (2010) observed single-walled carbon nanohorns and SiO₂ NPs buried in cells using various AFM oscillation techniques. The morphology and particle size of TiO₂ NPs, which are being increasingly used in catalysis and as a pigment, were characterised by Thio et al. (2011). The nanotoxicological effects of graphene on human plasma were studied by Mao et al. (2013), who found low molecular weight proteins to have a high affinity for the nanomaterial. Parallel investigations found decreased nuclei numbers and increased ROS after prolonged incubation with Hela and Panc-1 cell lines.

2.6 *Drug-Protein and Protein-Protein Interactions*

The study of drug-protein and protein-protein interactions are key topics in pharmaceutical sciences and are critical for targeting drug delivery (Edwardson and Henderson 2004). Proteins can be used as adapters conjugated to NPs (chitosan, Au, liposomes, silica, self-assembly) for targeting drug delivery. Furthermore, the interaction between protein molecules with drug carriers and cell surfaces is crucial (Bastatas et al. 2012), since cell adhesion to surfaces depends on the availability of specific protein-binding sites. Protein-material interactions also play a significant role in biosensors as a diagnostic tool since ligands can be immobilised on a probe surface and used to analyse the corresponding integrin. In addition, proteins encounter a wide range of surfaces during processing, each of which has the potential to affect their structure if adsorption takes place. If a loss of structure takes place upon surface adsorption, or even a small change in the native fold, subsequent protein-protein interactions may occur, resulting in the formation of aggregates and thus potentially an immunogenic response. Roberts (2005) identified challenges that need to be addressed when AFM adhesion measurements are to be used to study single drug particles interacting with proteins or cells. Couston et al. (2012) studied the interactions between monoclonal antibodies and albumin to surfaces of varying functionality and hydrophobicity by monitoring the adhesion over time and found a two-step interaction process involving an initial, rapid perturbation of the protein surface on contact with the surface, followed by relaxation and unfolding. Fahs and Louarn (2013) investigated the nanomechanical and adhesion properties of 2S albumin and 12S globulin. Differences in tip-protein interaction strength with regard to the nature of the protein and pH of the aqueous environment in terms of protein unfolding were observed. Protein-protein interactions have been studied also by Kao et al. (2012), where B-cell/CD80 was immobilised on an AFM tip and T-cell/CD28 was immobilised to a surface and forces were measured before and after adding cynarine.

2.7 *Live Cells*

The ability to image, probe ligand-receptor interactions and obtain nanomechanical information, all in physiological media, makes AFM particularly suited for studying cells in a therapeutic context.

Kozlova et al. (2013) obtained contact and intermittent contact mode images of the surfaces of red blood cells (RBCs) that had been treated in vitro with various agents (hemin, furosemide, chlorpromazine and zinc ions) to investigate blood intoxication. Images were filtered using a Fourier transform algorithm to detect poorly seen structures on RBC membranes. The study showed that blood intoxication affected the nanostructures present on the RBC membrane surfaces.

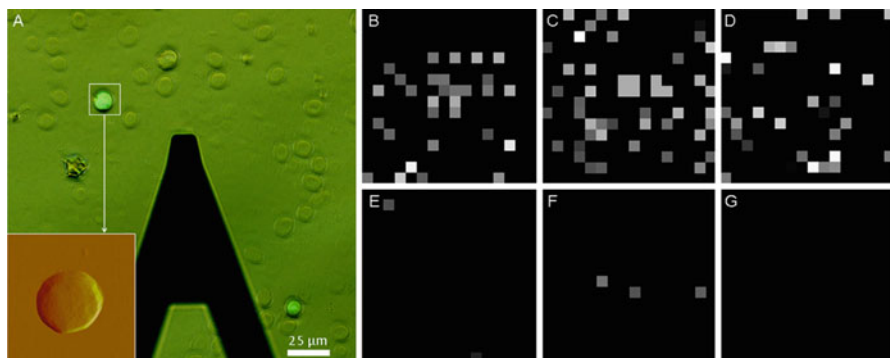


Fig. 20.7 Measuring specific CD20-rituximab interactions on cancer cells using a rituximab functionalised tip. (a) Bone marrow cancer (inset) and cells fluorescently labelled for easy identification; (b–d) CD20 distribution map (xy : $500 \times 500 \text{ nm}^2$, z : 0–100 pN, 16×16 pixels); (e–g) CD20 distribution map after blocking (same scale). Reproduced with permission (Li et al. 2013)

Surface roughness has been suggested to provide a diagnostic measure of the health state of cells (Antonio et al. 2012). Widespread application of this method has been limited by scan-size dependence on surface roughness, although this has been overcome by the work of Antonio et al. (2012).

Li et al. (2013) used SMFS (Sect. 1.3) to map CD20 molecules on surfaces of cancer B cells (fluorescently labelled; mapped area $500 \times 500 \text{ nm}^2$) obtained from patients with B-cell non-Hodgkin's lymphoma (NHL; marginal zone lymphoma; Fig. 20.7). CD20 can be targeted therapeutically with monoclonal antibodies (mAb), such as rituximab. These antibodies were covalently linked to an AFM tip via silanisation and a PEG linker; the density was such that only one CD20-rituximab complex was formed per force curve. RBCs, which do not express CD20, were used as controls. These studies are useful in understanding mechanisms, and developing new anti-CD20 mAbs especially where rituximab resistance becomes a problem.

Numerous nanoindentation studies of cells have appeared in the literature, many describing differences in elastic behaviour between cancer cells and benign equivalents (Cross et al. 2007; Li et al. 2008), where the Young's modulus of the affected cells is often cited as being ca. 70% less stiff than non-cancerous cells (Cross et al. 2007). The differences are usually attributed to rearrangements in the cytoskeleton network and have been suggested to be of early diagnostic value (Cross et al. 2007; Suresh 2007).

Bastatas et al. (2012) used a combination of AFM cell stiffness measurements and cell-substrate adhesion studies, together with calcium imaging and migration studies to investigate prostate cancer metastasis. The Young's modulus was found to be larger for more metastatic cells, in contrast to but also in keeping with other studies, suggesting that mechanical studies cannot be used solely as a biomarker for

metastasis. Indeed, a complicated relationship is found with adhesion and calcium dynamics also playing important key roles.

Quantitative Imaging[®] (JPK Instruments), a rapid tip modulation technique that acquires nanomechanical/adhesion data simultaneously with topography, was used by Chopinet et al. (2013) to investigate a number of different cell types, some of which had very little adhesion to the substrate. Force-volume elasticity and adhesion maps could be obtained rapidly and at high resolution for weakly adhered cells. Heu et al. (2012) used PeakForce Tapping[®] (Bruker), similar to Quantitative Imaging[®] for rapidly obtaining nanomechanical data at high resolution, to study the increase in stiffness of HaCaT keratinocytes (as a model for skin cancer) brought about through exposure to the herbicide glyphosate. A concentration dependence was observed and the addition of quercetin, a common flavonoid considered to provide protection against oxidative injury and inflammation (Wang et al. 2010), reversed this process.

2.8 Bacteria and Bacterial Biofilms

There are numerous reports on the use of AFM for investigating bacteria and bacterial biofilms. A few recent highlights are provided here.

Emerson and Camesano (2004) investigated the adhesion of pathogenic microorganisms, *Candida parapsilosis* and *Pseudomonas aeruginosa* (chosen for their clinical relevance), to biomaterials including the *P. aeruginosa* biofilm to unmodified silicone rubber. The attractive force between *C. parapsilosis*, adhered to a probe tip, and a bare silicon substrate was 4.3 ± 0.25 nN, comparable to the smaller attractive forces between *C. parapsilosis* and the *P. aeruginosa* biofilm (2.0 ± 0.4 nN), although the tip experienced repulsive forces 75 nm away from the biofilm surface (2.0 nN). The magnitude of the attractive forces, both towards silicone rubber and the biofilm, led the authors to suggest that they may allow adhesion and colonisation of these surfaces which, in a clinical setting, would increase the risk of death and disease.

The adhesion of *E. coli* to modified silicones using SEM and AFM was investigated by Cao et al. (2006). Their aim was to find a bacteria-resistant surface by varying hydrophobicity through modification. Octadecyltrichlorosilane (OTS) and fluoroalkylsilane (FAS) were tested against hydrophilic mica, which acted as a bacteria-adhesive control surface. Adhesion was investigated by adhering *E. coli* cells to the AFM probe tip and force measurements were taken from the approach to and retraction from surfaces. With the FAS silicone, as with *C. parapsilosis* and the *P. aeruginosa* biofilm (Emerson and Camesano 2004), a repulsive force was observed at close proximity and the force required to remove the tip was low. In contrast, however, when the tip was coated with heparin, the attractive forces to FAS were high on both approach and retraction. This led the authors to conclude that hydrophobicity of a material alone is not enough to predict bacterial adhesion.

Lau et al. (2009) used ‘microbead force spectroscopy (MBFS)’ to investigate the viscoelasticity of biofilms. A glass bead coated with biofilm was attached to a tip-less cantilever and used as a probe against a flat glass surface. The properties of a *P. aeruginosa* wild-type biofilm were compared with a lipopolysaccharide (LPS)-deficient mutant strain, wapR. Biofilms at different levels of maturity were also compared. When immature, the wapR strain adhered to the glass slide with far more force than the immature wild-type (ranges of 2–13 nN and 0–3 nN, respectively). As they matured, adhesion forces decreased in both strains. AFM has also been used for investigating real-time visualisation of the antibiotic azithromycin with various lipid domains in solution (Berquand et al. 2004).

2.9 Viruses

Viruses consist of an oligomeric protein head, called a capsid, which contains the viral genome; in more complex virus structures, the capsid may also contain other macromolecules, such as proteins and molecular motors (Martinez-Martin et al. 2012; Mateu 2013). A full historical account of the development of AFM studies of viruses has been reviewed in depth by Baclayon et al. (2010); some highlights are provided in this section. AFM was first used to image viruses in 1992, almost immediately after the instruments became commercially available (Thundat et al. 1992), although these studies were mostly confined to exploiting their well-defined geometry to measure AFM tip radii. An interest in the biological structure of viruses, however, soon followed, with contact mode imaging of head and tail components of bacteriophage T4 (Kolbe et al. 1992). Tapping Mode[®] in liquid rapidly became the mode of preference, due to reduced lateral forces (Bushell et al. 1995) and a more relevant imaging environment (Kuznetsov et al. 2001), although contact mode is still widely used (Mateu 2013). Topography imaging has been used to distinguish capsomers, determine the triangulation number (T) of capsids (Kuznetsov and McPherson 2011), revealing exposed nucleic acids subsequent to capsid stripping (Drygin et al. 1998; Kienberger et al. 2004; Plomp et al. 2002) and to observe viral budding from living fibroblast cells (Gladnikoff and Rousso 2008). Treatment of pinostroin, an antiviral, was shown to cause severe disruption to HSV-1 virus morphology, as evidenced from topography and phase imaging (Wu et al. 2011).

In addition to imaging, force vs. distance curves, both tip approach (indentation) and tip retract (adhesion) cycles, have been acquired from immobilised viruses. Head, collar and tail regions of ϕ 29 phage virions were found to exhibit different elasticity values (Melcher et al. 2009). A decrease in Young’s modulus (stiffness) was reported for *E. coli* after infection with filamentous phage M13 (Chen et al. 2009). Concerning adhesion events, spatially-resolved force mapping was used to examine single influenza virus particles (glycoprotein hemagglutinin, HA, surface) using an anti-HA derivatised tip (Liu et al. 2012).

Recent developments in high-speed AFM imaging at high resolution offer even greater opportunities for studying dynamic virus-cell interactions (Ando et al. 2008).

3 AFM Combined With Optical or Spectroscopic Techniques

In the last couple of years, instruments that combine AFM with spectroscopic techniques, such as IR and Raman, and/or improved light microscopy for studying cells conveniently in physiological medium have been made commercially available. These instruments offer considerable potential for *in vitro* studies, where high-resolution imaging can be combined with biochemical measurements. A few examples are provided here.

Dazzi et al. (2012) showed there to be excellent agreement between conventional IR spectroscopy with nanoscale combined AFM-IR data from polymer samples. By combining AFM imaging with mid-IR spectroscopy, Van Eerdenbrugh et al. (2012) examined the micro- and nanostructure and chemical phase composition of felodipine/poly(acrylic acid) blends. Oil inclusions in streptomyces, without the need for staining, were mapped using a combined AFM-IR instrument by Deniset-Besseau et al. (2014). A high-speed AFM for nano/mesoscale analysis of living cell surfaces (HeLa and 3T3 fibroblasts) has been combined with fluorescence microscopy (Suzuki et al. 2013). High-resolution fluorescence imaging (super resolution stimulated emission depletion, STED) has been combined with nanomechanical (stiffness) mapping to investigate COS-7 cells with immunolabelled microtubuli (Harke et al. 2012). Cell biological aspects such as dynamics of mitochondrial movement and drug uptake have also been investigated (Matthaus et al. 2007).

4 Summary

AFM is a high-resolution imaging technique that can be used to study a variety of samples under physiologically relevant conditions. The ability to chemically or biologically functionalise AFM probes combined with various modes that permit the acquisition of spatially-resolved force data allows for the study of systems at the single-molecule level. AFM technology, now frequently using high-speed acquisition, interfaced with spectroscopic modes and light microscopy methods for live cell imaging offer huge potential for the pharmaceutical sciences.

Appendix: Obtaining an AFM Contact Mode Image in Air

As a practical demonstration, this section outlines a typical sequence of the steps necessary for the acquisition of the simplest of AFM operations: a contact mode image to be obtained in air. Most of the details that make the sequence particularly relevant for a specific instrument have been excluded deliberately. Bacteria on a mica surface has been chosen as an example. Mica is an ideal substrate for many AFM studies since it is atomically flat (glass coverslips can appear quite rough for many high-resolution studies); fresh, uncontaminated surfaces can be also prepared, without the need for cleaning, by simply attaching adhesive tape and peeling away the top layer from this layered material (Morris et al. 2001). Mica is negatively charged and so improved adhesion to often negatively charged biological specimens, such as DNA, can be achieved by derivatising the mica surface with a suitable polycation, e.g., poly-L-lysine (Eaton and West 2010).

1. Turn on the AFM instrument and computer, and open the software.
2. Place a piece of mica (1 cm², cut with scissors) on a nickel stub (1.2 cm²) using double-sided adhesive tape. Press it on firmly.
3. Cleave the mica with adhesive tape. Derivatise the mica, if required.
4. Add an aliquot (10 µL) of the solution containing bacteria to the mica surface. Leave the drop of solution in place for 2 min.
5. Carefully rinse the treated mica plate with distilled water to remove buffer salts, which might mask any biological sample features.
6. Allow to air-dry or carefully use a jet of nitrogen gas.
7. Place the sample on top of the AFM scanner; the magnet will hold the nickel disc of the sample in place.
8. Select a contact mode probe (of low spring constant k , ca. 0.06 N m⁻¹) and fix into the AFM head above the sample.
9. Line up the laser (according to manufacturer's instructions).
10. Move the sample and/or probe to select imaging region of interest.
11. Select a required scan range (say, 20 µm) and set the scan rate to 1 Hz. Use an image resolution size of at least 512 × 512 pixels. Select the integral, proportional and derivative (PID, external scanner feedback; Eaton and West 2010) settings outlined by the manufacturer (these will depend mostly on the scanner being used and whether air or liquid is the medium).
12. Lower the probe to just above the sample surface and use the automated approach.
13. Slowly increase the PID settings to maximise image contrast to just below the level that produces noise (piezo ringing). It should also be possible to reduce the applied load (reduce deflection) on the cantilever to improve image quality.

14. Once image settings are optimised, obtain a complete image and save (capture) it.
15. The next typical options will either be to zoom in, move to a different area or change the sample.

References

- Abendan RS, Swift JA (2005) Dissolution on cholesterol monohydrate single-crystal surfaces monitored by in situ atomic force microscopy. *Cryst Growth Des* 5:2146–2153
- Adamcik J, Mezzenga R (2012) Study of amyloid fibrils via atomic force microscopy. *Curr Opin Colloid Interface Sci* 17:369–379
- Ando T, Uchihashi T, Kodera N, Yamamoto D, Miyagi A, Taniguchi M, Yamashita H (2008) High-speed AFM and nano-visualization of biomolecular processes. *Pflugers Arch* 456:211–225
- Antonio PD, Lasalvia M, Perna G, Capozzi V (2012) Scale-independent roughness value of cell membranes studied by means of AFM technique. *Biochim Biophys Acta* 1818:3141–3148
- Arora S, Rajwade JM, Paknikar KM (2012) Nanotoxicology and in vitro studies: the need of the hour. *Toxicol Appl Pharmacol* 258:151–165
- Baclayon M, Wuite GJL, Roos WH (2010) Imaging and manipulation of single viruses by atomic force microscopy. *Soft Matter* 6:5273–5285
- Bastatas L, Martinez-Martin D, Matthews J, Hashem J, Lee YJ, Sennoune S, Filleur S, Martinez-Zaguilan R, Park S (2012) AFM nano-mechanics and calcium dynamics of prostate cancer cells with distinct metastatic potential. *Biochim Biophys Acta* 1820:1111–1120
- Begat P, Morton DAV, Staniforth JN, Price R (2004) The cohesive-adhesive balances in dry powder inhaler formulations I: direct quantification by atomic force microscopy. *Pharm Res* 21:1591–1597
- Belletti D, Tonelli M, Forni F, Tosi G, Vandelli MA, Ruozi B (2013) AFM and TEM characterization of siRNAs lipoplexes: a combinatory tools to predict the efficacy of complexation. *Colloid Surface Physicochem Eng Aspect* 436:459–466
- Berquand A, Mingeot-Leclercq MP, Dufrene YF (2004) Real-time imaging of drug-membrane interactions by atomic force microscopy. *BBA-Biomembranes* 1664:198–205
- Bianco A, Kostarelou K, Prato M (2005) Applications of carbon nanotubes in drug delivery. *Curr Opin Chem Biol* 9:674–679
- Binnig G, Rohrer H (1982) Scanning tunnelling microscopy. *Helv Phys Acta* 55:726–735
- Binnig G, Quate CF, Gerber C (1986) Atomic force microscope. *Phys Rev Lett* 56:930–933
- Bushell GR, Watson GS, Holt SA, Myhra S (1995) Imaging and nano-dissection of tobacco virus by atomic force microscopy. *J Microsc* 180:174–181
- Butt HJ, Cappella M, Kappell M (2005) Force measurements with the atomic force microscope: technique, interpretation and applications. *Surf Sci Rep* 59:1–152
- Cail TL, Hochella MF (2005) Experimentally derived sticking efficiencies of microparticles using atomic force microscopy. *Environ Sci Technol* 39:1011–1017
- Cao T, Tang H, Liang X, Wang A, Auner GW, Salley SO, Ng KYS (2006) Nanoscale investigation on adhesion of *E. coli* to surface modified silicone using atomic force microscopy. *Biotechnol Bioeng* 94:167–176
- Cappella B, Dietler G (1999) Force-distance curves by atomic force microscopy. *Surf Sci Rep* 34:1–104
- Chen YY, Wu CC, Hsu JL, Peng L, Chang HY, Yew TR (2009) Surface rigidity change of *Escherichia coli* after filamentous bacteriophage infection. *Langmuir* 25:4607–4614

- Chinnapongse SL, MacCuspie RI, Hackley VA (2011) Persistence of singly dispersed silver nanoparticles in natural freshwaters, synthetic seawater, and simulated estuarine waters. *Sci Total Environ* 409:2443–2450
- Chiti F, Dobson CM (2006) Protein misfolding, functional amyloid, and human disease. *Annu Rev Biochem* 75:333–366
- Chopinnet L, Formosa C, Rols MP, Duval RE, Dague E (2013) Imaging living cells surface and quantifying its properties at high resolution using AFM in QITM mode. *Micron* 48:26–33
- Chow EHH, Bucar D-K, Jones W (2012) New opportunities in crystal engineering—the role of atomic force microscopy in studies of molecular crystals. *Chem Commun* 74:9210–9226
- Clifford CA, Seah MP (2005) The determination of atomic force microscope cantilever spring constants via dimensional methods for nanomechanical analysis. *Nanotechnology* 16:1666–1680
- Couston RG, Lamprou DA, Uddin S, van der Walle C (2012) Interaction and destabilization of a monoclonal antibody and albumin to surfaces of varying functionality and hydrophobicity. *Int J Pharm* 438:71–80
- Craig GE, Brown SD, Lamprou DA, Graham D, Wheate NJ (2012) Cisplatin-tethered gold nanoparticles that exhibit enhanced reproducibility, drug loading, and stability: a step closer to pharmaceutical approval? *Inorg Chem* 51:3490–3497
- Cross SE, Jin YS, Rao J, Gimzewski JK (2007) Nanomechanical analysis of cells from cancer patients. *Nat Nanotechnol* 2:780–783
- Csontos I, Ronaszegi K, Szabo A, Keszei S, Anna P, Fekete P, Marosi G, Nagy T (2006) Controlled technology for forming a nanostructured polymer coating for solid pharmaceuticals. *Polym Adv Tech* 17:884–888
- Danesh A, Chen X, Davies MC, Roberts CJ, Sanders GHW, Tendler SJ, Williams PM (2000) Polymorphic discrimination using atomic force microscopy: distinguishing between two polymorphs of the drug cimetidine. *Langmuir* 16:866–870
- Danesh A, Connell SD, Davies MC, Roberts CJ, Tendler SJ, Williams PM, Wilkins MJ (2001) An in situ dissolution study of aspirin crystal planes (100) and (001) by atomic force microscopy. *Pharm Res* 18:299–303
- Dazzi A, Prater CB, Hu Q, Chase DB, Rabolt JF, Marcott C (2012) AFM-IR: combining atomic force microscopy and infrared spectroscopy for nanoscale chemical characterization. *Appl Spectrosc* 66:1365–1384
- Deniset-Besseau A, Prater CB, Virolle M-J, Dazzi A (2014) Monitoring triacylglycerols accumulation by atomic force microscopy based infrared spectroscopy in streptomyces species for biodiesel applications. *J Phys Chem Lett* 5:654–658
- Donaldson K, Stone V, Tran CL, Kreyling W, Borm PJA (2004) Nanotoxicology. *Occup Environ Med* 61:727–728
- Drygin YF, Bordunova OA, Gallyamov MO, Yaminsky IV (1998) Atomic force microscopy examination of tobacco mosaic virus and virion RNA. *FEBS Lett* 425:217–221
- Durbin SD, Carlson WE (1992) Lysozyme crystal growth studied by atomic force microscopy. *J Cryst Growth* 122:71–79
- Eaton P, West P (2010) Atomic force microscopy. Oxford University Press, Oxford
- Ebner A, Chhtcheglova LA, Preiner J, Tang J, Wildling L, Gruber HJ, Hinterdorfer P (2010) Simultaneous topography and recognition imaging. In: Bhushan B (ed) Scanning probe microscopy in nanoscience and nanotechnology nanoscience and technology. Springer, Heidelberg, pp 325–362
- Edwardson JM, Henderson RM (2004) Atomic force microscopy and drug discovery. *Drug Discov Today* 9:64–71
- Emerson RJ IV, Camesano TA (2004) Nanoscale investigation of pathogenic microbial adhesion to biomaterials. *Appl Environ Microbiol* 70:6012–6022
- Fahs A, Louarn G (2013) Plant protein interactions studied using AFM force spectroscopy: nanomechanical and adhesion properties. *Phys Chem Chem Phys* 15:11339–11348

- Florin EL, Moy VT, Gaub HE (1994) Adhesion forces between individual ligand-receptor pairs. *Science* 264:415–417
- Gladnikoff M, Rousso I (2008) Directly monitoring individual retrovirus budding events using atomic force microscopy. *Biophys J* 94:320–326
- Gramma CN, Venkatpurwar VP, Lamprou DA, Kumar RMNV (2013) Towards scale-up and regulatory shelf-stability testing of curcumin encapsulated polyester nanoparticles. *Drug Deliv Transl Res* 3:286–293
- Harke B, Chacko JV, Haschke H, Canale C, Diaspro A (2012) A novel nanoscopic tool by combining AFM with STED microscopy. *Opt Nanoscopy* 1:1–6
- Heu C, Berquand A, Elie-Caille C, Nicod L (2012) Glyphosate-induced stiffening of HaCaT keratinocytes, a peak force tapping study on living cells. *J Struct Biol* 178:1–7
- Hinterdorfer P, Baumgartner W, Gruber HJ, Schilcher K, Schindler H (1996) Detection and localization of individual antibody-antigen recognition events by atomic force microscopy. *Proc Natl Acad Sci U S A* 93:3477–3481
- Janowski M, Bulte JWM, Walczak P (2012) Personalized nanomedicine advancements for stem cell tracking. *Adv Drug Deliv Rev* 64:1488–1507
- Kao F-S, Ger W, Pan Y-R, Yu H-C, Hsu R-Q, Chen H-M (2012) Chip-based protein–protein interaction studied by atomic force microscopy. *Biotechnol Bioeng* 109:2460–2467
- Karagkiozaki V, Logothetidis S, Vavoulidis E (2012) Nanomedicine pillars and monitoring nanobio-interactions. In: Logothetidis S (ed) *Nanomedicine and nanobiotechnology*. Springer, Heidelberg, pp 27–52
- Karagkiozaki V, Karagiannidis PG, Gioti M, Kavatzikidou P, Georgiou D, Georganaki E, Logothetidis S (2013) Bioelectronics meets nanomedicine for cardiovascular implants: PEDOT-based nanocoatings for tissue regeneration. *Biochim Biophys Acta* 1830:4294–4304
- Kienberger F, Zhu R, Moser R, Blaas D, Hinterdorfer P (2004) Monitoring RNA release from human rhinovirus by dynamic force microscopy. *J Virol* 78:3203–3209
- Kolbe WF, Ogletree DF, Salmeron MB (1992) Atomic force microscopy imaging of T4 bacteriophages on silicon substrates. *Ultramicroscopy* 42–44:1113–1117
- Kozlova EK, Chernysh AM, Moroz VV, Kuzovlev AN (2013) Analysis of nanostructure of red blood cells membranes by space fourier transform of AFM images. *Micron* 44:218–227
- Kuznetsov YG, McPherson A (2011) Atomic force microscopy in imaging of viruses and virus-infected cells. *Microbiol Mol Biol Rev* 75:268–285
- Kuznetsov YG, Malkin AJ, Lucas RW, Plomp M, McPherson A (2001) Imaging of viruses by atomic force microscopy. *J Gen Virol* 82:2025–2034
- Kwok TSH, Sunderland BW, Heng PWS (2004) An investigation on the influence of a vinyl pyrrolidone/vinyl acetate copolymer on the moisture permeation, mechanical and adhesive properties of aqueous-based hydroxypropyl methylcellulose film coatings. *Chem Pharm Bull* 52:790–796
- Lamprou DA, Smith JR, Nevell TG, Barbu E, Willis CR, Tsiouklis J (2010) Self-assembled structures of alkanethiols on gold-coated cantilever tips and substrates for atomic force microscopy: molecular organisation and conditions for reproducible deposition. *Appl Surf Sci* 256:1961–1968
- Lamprou DA, Venkattpurwar V, Kumar MNVR (2013) Atomic force microscopy images label-free, drug encapsulated nanoparticles in vivo and detects difference in tissue mechanical properties of treated and untreated: a tip for nanotoxicology. *PLoS One* 8, e64490
- Land TA, De Yoreo JJ (2000) The evolution of growth modes and activity of growth sources on canavalin investigated by in situ atomic force microscopy. *J Cryst Growth* 208:623–637
- Lau PCY, Lindhout T, Beveridge TJ, Dutcher JR, Lam JS (2009) Differential lipopolysaccharide core capping leads to quantitative and correlated modifications of mechanical and structural properties in *Pseudomonas aeruginosa* biofilms. *J Bacteriol* 191:6618–6631
- Levy G (1961) Comparison of dissolution and absorption rates of different commercial aspirin tablets. *J Pharm Sci* 50:388–392

- Li QS, Lee GYH, Ong CN, Lim CT (2008) AFM indentation study of breast cancer cells. *Biochem Biophys Res Commun* 374:609–613
- Li M, Xiao X, Liu L, Xi N, Wang Y, Dong Z, Zhang W (2013) Nanoscale mapping and organization analysis of target proteins on cancer cells from B-cell lymphoma patients. *Exp Cell Res* 319:2812–2821
- Liu C-H, Horng J-T, Chang J-S, Hsieh C-F, Tseng Y-C, Lin S (2012) Localization and force analysis at the single virus particle level using atomic force microscopy. *Biochem Biophys Res Commun* 417:109–115
- Mains J, Lamprou DA, McIntosh L, Oswald IDH, Urquhart AJ (2013) Beta-adrenoceptor antagonists affect amyloid nanostructure; amyloid hydrogels as drug delivery vehicles. *Chem Commun* 49:5082–5084
- Mao H, Chen W, Laurent S, Thirifays C, Burtea C, Rezaee F, Mahmoudi M (2013) Hard corona composition and cellular toxicities of the graphene sheets. *Colloids Surf B Biointerfaces* 109:212–218
- Martinez-Martin D, Carrasco C, Hernando-Perez M, de Pablo PJ, Gomez-Herrero J, Perez R, Mateu MG, Carrascosa JL, Kiracofe D, Melcher J, Raman A (2012) Resolving structure and mechanical properties at the nanoscale of viruses with frequency modulated atomic force microscopy. *PLoS One* 7, e30204
- Mateu MG (2013) Assembly, stability and dynamics of virus capsids. *Arch Biochem Biophys* 531:65–79
- Matthaus C, Chernenko T, Newmark JA, Warner CM, Diem M (2007) Label-free detection of mitochondrial distribution in cells by nonresonant Raman microspectroscopy. *Biophys J* 93:668–673
- McPherson A, Malkin AJ, Kuznetsov YG, Plomp M (2001) Atomic force microscopy applications in macromolecular crystallography. *Acta Crystallogr D Biol Crystallogr* 57:1053–1060
- Melcher J, Carrasco C, Xu X, Carrascosa JL, Gomez-Herrero J, de Pablo JD, Raman A (2009) Origins of phase contrast in the atomic force microscope in liquids. *Proc Natl Acad Sci U S A* 106:13655–13660
- Miyazaki T, Aso Y, Kawanishi T (2011) Feasibility of atomic force microscopy for determining crystal growth rates of nifedipine at the surface of amorphous solids with and without polymers. *J Pharm Sci* 100:4413–4420
- Morris VJ, Kirby AR, Gunning AP (2001) Atomic force microscopy for biologists. Imperial College Press, London
- Muller DJ, Helenius J, Alsteens D, Dufrene YF (2009) Force probing surfaces of living cells to molecular resolution. *Nat Chem Biol* 5:383–390
- Onuma K, Ito A, Tateishi T, Kameyama T (1995) Surface observations of synthetic hydroxyapatite single crystal by atomic force microscopy. *J Cryst Growth* 148:201–206
- Onyesom I, Lamprou DA, Sygellou L, Owusu-Ware SK, Antonijevic M, Chowdhry BZ, Douroumis D (2013) Sirolimus encapsulated liposomes for cancer therapy: physicochemical and mechanical characterization of sirolimus distribution within liposome bilayers. *Mol Pharm* 10:4281–4293
- Plomp M, Rice MK, Wagner EK, McPherson A, Malkin AJ (2002) Rapid visualization at high resolution of pathogens by atomic force microscopy: structural studies of herpes simplex virus-1. *Am J Pathol* 160:1959–1966
- Potta SG, Minemi S, Nukala RK, Peinado C, Lamprou DA, Urquhart AJ, Douroumis D (2011) Preparation and characterization of ibuprofen solid lipid nanoparticles with enhanced solubility. *J Microencapsul* 28:74–81
- Riener CK, Stroh CM, Ebner A, Klampfl C, Gall AA, Romania C, Lyubchenko YL, Hinterdorfer P, Gruber HJ (2003) Simple test system for single molecule recognition force microscopy. *Anal Chim Acta* 479:59–75
- Roberts CJ (2005) What can we learn from atomic force microscopy adhesion measurements with single drug particles? *Eur J Pharm Sci* 24:153–157

- Roldo M, Power K, Smith JR, Cox PA, Papagelis K, Bouropoulos N, Fatouros DG (2009) N-Octyl-O-sulfate chitosan stabilises single wall carbon nanotubes in aqueous media and bestows biocompatibility. *Nanoscale* 1:366–373
- Romer M, Heinamaki J, Strachan C, Sandler N, Yliruusi J (2008) Prediction of tablet film-coating thickness using a rotating plate coating system and NIR spectroscopy. *AAPS PharmSciTech* 9:1047–1053
- Schmitz I, Schreiner M, Friedbacher G, Grasserbauer M (1997) Phase imaging as an extension to tapping mode AFM for the identification of material properties on humidity-sensitive surfaces. *Appl Surf Sci* 115:190–198
- Seitavuopio P, Rantanen J, Yliruusi J (2003) Tablet surface characterisation by various imaging techniques. *Int J Pharm* 254:281–286
- Seitavuopio P, Rantanen J, Yliruusia J (2005) Use of roughness maps in visualisation of surfaces. *Eur J Pharm Biopharm* 59:351–358
- Seitavuopio P, Heinamaki J, Rantanen J, Yliruusi J (2006) Monitoring tablet surface roughness during the film coating process. *AAPS PharmSciTech* 7:E1–E6
- Sikora AE, Smith JR, Campbell SA, Firman F (2012) AFM protein-protein interactions within the EcoR124I molecular motor. *Soft Matter* 8:6358–6363
- Sitterberg J, Ozcetin A, Ehrhardt C, Bakowsky U (2010) Utilising atomic force microscopy for the characterisation of nanoscale drug delivery systems. *Eur J Pharm Biopharm* 74:2–13
- Smith JR, Lamprou DA (2014) Polymer coatings for biomedical applications: a review. *Trans IMF* 92:9–19
- Smith DA, Connell SD, Kirkham CR (2003a) Chemical force microscopy: applications in surface characterisation of natural hydroxyapatite. *Anal Chim Acta* 479:39–57
- Smith JR, Breakspear S, Campbell SA (2003b) AFM in surface finishing: part 2 surface roughness. *Trans IMF* 81:B55–B58
- Song Y, Bhushan B (2006) Dynamic analysis of torsional resonance mode of atomic force microscopy and its application to in-plane surface property extraction. *Microsyst Technol* 12:219–230
- Suresh S (2007) Nanomedicine - Elastic clues in cancer detection. *Nat Nanotechnol* 2:748–749
- Suzuki Y, Sakai N, Yoshida A, Uekusa Y, Yagi A, Imaoka Y, Ito S, Karaki K, Takeyasu K (2013) High-speed atomic force microscopy combined with inverted optical microscopy for studying cellular events. *Sci Rep* 3:2131
- Tasis D, Papagelis K, Douroumis D, Smith JR, Bouropoulos N, Fatouros DG (2008) Diameter-selective solubilization of carbon nanotubes by lipid micelles. *J Nanosci Nanotechnol* 8:420–423
- Tetard L, Passian RH, Farahi RH, Thundat T (2010) Atomic force microscopy of silica nanoparticles and carbon nanohorns in macrophages and red blood cells. *Ultramicroscopy* 110:586–591
- Thakuria R, Eddleston MD, Chow EHH, Lloyd GO, Aldous BJ, Krzyzaniak JF, Bond AD, Jones W (2013) Use of in situ atomic force microscopy to follow phase changes at crystal surfaces in real time. *Angew Chem Int Ed* 52:10541–10544
- Theodoropoulos D, Rova A, Smith JR, Barbu E, Calabrese G, Vizirianakis IS, Tsibouklis J, Fatouros DG (2013) Towards boron neutron capture therapy: the formulation and preliminary in vitro evaluation of liposomal vehicles for the therapeutic delivery of the dequalinium salt of bis-nido-carborane. *Bioorg Med Chem Lett* 23:6161–6166
- Thio BJR, Zhou D, Keller AA (2011) Influence of natural organic matter on the aggregation and deposition of titanium dioxide nanoparticles. *J Hazard Mater* 189:556–563
- Thompson C, Davies MC, Roberts CJ, Tendler SJ, Wilkinson MJ (2004) The effects of additives on the growth and morphology of paracetamol (acetaminophen) crystals. *Int J Pharm* 280:137–150
- Thundat T, Zheng XY, Sharp SL, Allison DP, Warmack RJ, Joy DC, Ferrell TL (1992) Calibration of atomic force microscope tips using biomolecules. *Scanning Microsc* 6:903–910

- Tonglei L, Kenneth RM, Kinam P (2000) Influence of solvent and crystalline supramolecular structure on the formation of etching patterns on acetaminophen single crystals: a study with atomic force microscopy and computer simulation. *J Phys Chem B* 104:2019–2032
- Tsukada M, Irie R, Yonemochi Y, Noda R, Kamiya H, Watanabe W, Kauppinen EI (2004) Adhesion force measurement of a DPI size pharmaceutical particle by colloid probe atomic force microscopy. *Powder Tech* 141:262–269
- Van Eerdenbrugh B, Lo M, Kjoller K, Marcott C, Taylor LS (2012) Nanoscale mid-infrared imaging of phase separation in a drug–polymer blend. *J Pharm Sci* 101:2066–2073
- Wang XY, He PY, Du J, Zhang JZ (2010) Quercetin in combating H₂O₂ induced early cell apoptosis and mitochondrial damage to normal human keratinocytes. *Chin Med J* 123:532–536
- Wise JA, Smith JR, Bouropoulos N, Yannopoulos SN, van der Merwe SM, Fatouros DG (2008) Single wall carbon nanotube dispersions stabilised with N-trimethyl-chitosan. *J Biomed Nanotechnol* 4:67–72
- Wu N, Kong Y, Zu Y, Fu Y, Liu Z, Meng R, Liu X, Efferth T (2011) Activity investigation of pinostrobin towards herpes simplex virus-1 as determined by atomic force microscopy. *Phytomedicine* 18:110–118
- Xue W-F, Hellewell AL, Gosal WS, Homans SW, Hewitt EW, Radford SE (2009) Fibril fragmentation enhances amyloid cytotoxicity. *J Biol Chem* 284:34272–34282
- Yip CM, Ward MD (1996) Atomic force microscopy of insulin single crystals: direct visualization of molecules and crystal growth. *Biophys J* 71:1071–1078
- Zhang W, Stack AG, Chen Y (2011) Interaction force measurement between *E. coli* cells and nanoparticles immobilized surfaces by using AFM. *Colloids Surf B Biointerfaces* 82:316–324

Part VI
Techniques to Characterize Particles

Chapter 21

Particle Size Analysis of Micro and Nanoparticles

Elisabeth Kastner and Yvonne Perrie

Abstract Micro- and nanosized particles are extensively used in drug formulation, delivery and targeting with the size of these particles fundamentally influencing their properties. There are a range of methods for measuring the size of these systems. Here, we evaluate and compare the main particle measurement techniques for micro- and nanosized particles, elucidating on the respective measurement principles. Light scattering based particle sizing techniques are described, including the background to dynamic light scattering, laser diffraction and nanoparticle tracking analysis. Pulse sensing particle sizing methods including Coulter Counter and tunable resistive pulse sensing are described. Two case studies provide practical examples of how to interpret particle size analysis data and how to compare between different measurement techniques.

Keywords Dynamic light scattering • Laser diffraction • Particle sizing • Pulse sensing

1 Application of Particle Size Measurement Techniques

With advances in particle engineering, the application of micro- and nanosized particles in drug formulation offers new options for drug delivery and targeting. The application of these constructs is often fundamentally governed by their particulate size, which can dictate dissolution, drug loading and release characteristics, biodistribution, cellular interactions and stability. Therefore it is important that the particle size and heterogeneity of these particulate dosage forms is accurately measured both for understanding the design principles of the system and for their subsequent quality control and quality assurance. Therefore in the development and manufacture of particulate delivery systems, the determination of the

E. Kastner • Y. Perrie (✉)
Strathclyde Institute of Pharmacy and Biomedical Sciences, University of Strathclyde,
Glasgow G4 0RE, Scotland
e-mail: yvonne.perrie@strath.ac.uk

particle population characteristics and its distribution is crucial and ultimately linked to the correct interpretation of the particle size measurement technique.

Particles are defined as a discrete portion of a substance with physical dimensions that can be described or measured in mass or volume. Particles considered in this chapter range from nanometer to millimetre in size and by EU definition, the term nanomaterial comprises a particle population with more than 50 % of present particles providing a diameter of less than 100 nm (Bleeker et al. 2013). When discussing particle size, it is important to remember the size is generally reported as a diameter and therefore makes the assumption the particle is a sphere. However, obviously particles are three-dimensional objects which will have a length, breadth and height which need not be equal. Therefore, non-spherical particles can give different particle sizes depending on the sizing techniques used.

Most particulate based systems used pharmaceutically are not monodisperse, and the polydispersity of those particles is commonly described by a particle distribution. A particle can be described in many ways; often depending on quality requirements or product characteristics, described by assessing the maximum or minimum length of a particle as well as by its average diameter. The sedimentation rate is related to the specific density of a particle and depends on the particle porosities; this can influence the stability of a product and its distribution e.g. when delivered via the pulmonary route. The surface area is also an important factor for surface chemistry and adsorption (Allen 1997). However when considering micro- and nanoparticles for drug delivery, the volume of a particle and the three dimensional shape is often the most important factor and this factor, combined with a measure of heterogeneity, is nominally used as one of parameters in a product specification. A variety of methods for analysing a particle distribution are available, each based on a measurement principle related to a specific particle characteristic (Fig. 21.1). Yet, the determined diameter of a particle can depend on the method chosen and on the suspending media (ionic strength, pH, temperature) and can differ from any particle measurement technique that relies on the adsorption of a particle on a surface, such as in microscopy analysis (Stanley-Wood et al. 1992; Bell et al. 2012; Anderson et al. 2013). Therefore, interpreting particle size measurements effectively requires an understanding of the technique used and the calculations underpinning the reported particle sizes. For example, particle size analysis conducted using microscopic techniques or image analyzers base particle size on number distribution; this approach counts the number of particles in each size range assigned. In contrast, particle sizes determined from laser diffraction can report results based on volume distribution. Therefore, the particle size of a suspension can be reported in two different ways. For example, consider a particulate mixture containing four particles of 100 nm, four particles of 200 nm and four particles of 300 nm. The particle size based on the number and volume distribution is shown in Fig. 21.2. When represented as a number distribution, each particle size accounts for 1/3 of the total, whereas when converted into a volume distribution, 75 % of the total volume results from the 300 nm particles. Given this difference in the way the results can be reported, it is important that the background to the particles sizes reported is understood. Thus within this chapter, the main particle sizing techniques are highlighted, with their respective limitations and benefits. We

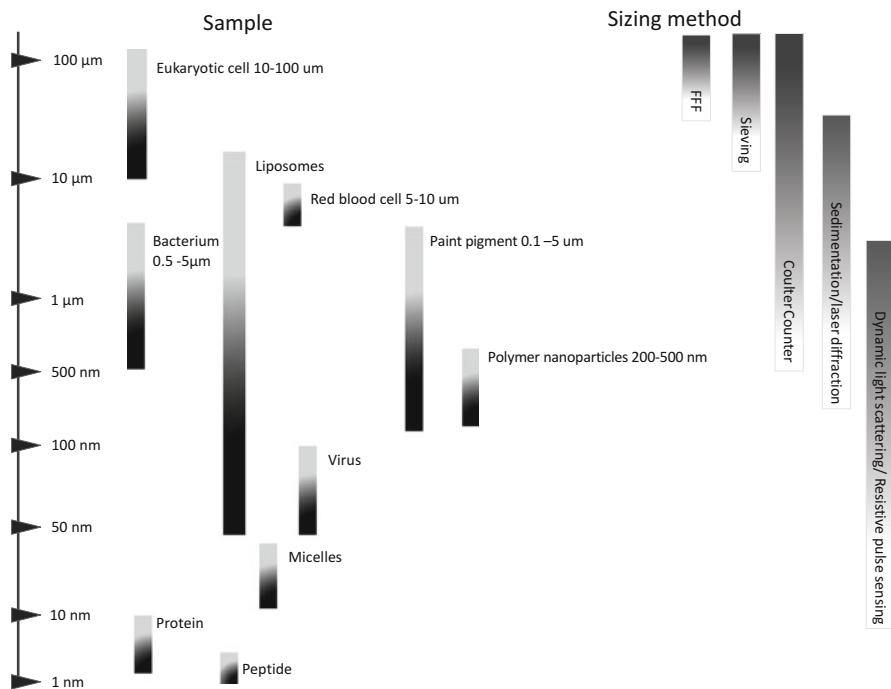


Fig. 21.1 Overview of averaged sized particles and measurement techniques applicable in pharmaceutical and biopharmaceutical industry

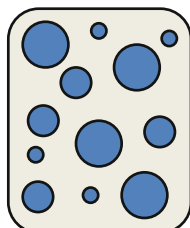
categorize the most commonly used particle analysing methods according to laser diffraction principles (dynamic and static light scattering, tracking analysis), differential centrifugal sedimentation, and the pulse sensing method (tunable resistive pulse sensing, coulter counter).

2 Light Scattering Based Particle Sizing

A wide range of techniques have been developed for determining particle size distribution; however, light-scattering based methods are currently the most widely used option. This is due to the fact that it is a non-destructive method that can be adopted for a wide range of samples and can be performed relatively quickly.

2.1 Dynamic Light Scattering

Dynamic light scattering (DLS) is also known as photon correlation spectroscopy (PCS) and quasielastic light scattering (QELS); it is a frequently applied method for



Particle mixture

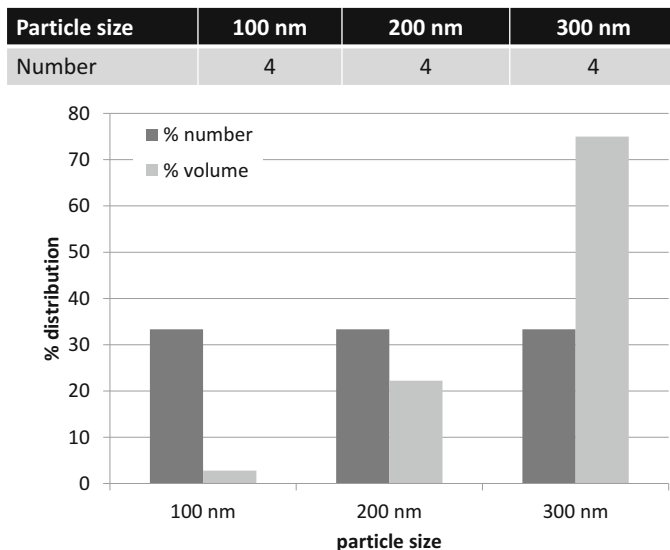


Fig. 21.2 The impact of calculating particle size distribution based on number and volume

Table 21.1 Key features of dynamic light scattering

Size range	1 nm to 8 μ m
Concentration range	Max 40 % w/v Limits generally dependent on refractive index and particle size
Required sample volume	10–500 μ L (dependent on concentration)
Key parameters	Average hydrodynamic diameter Intensity, volume and number based particle size distribution
Application areas	Wide range of colloids, dispersions, suspensions

determining the hydrodynamic diameter of particles (down to the nanometer range) in solution. Typically, this technique is applied for particle suspensions below the micrometer range, it provides rapid analysis, it can measure small sample volumes and is applicable to a range of particulate systems, therefore is a commonly adopted particle sizing method. Typical features of this method are outlined in Table 21.1.

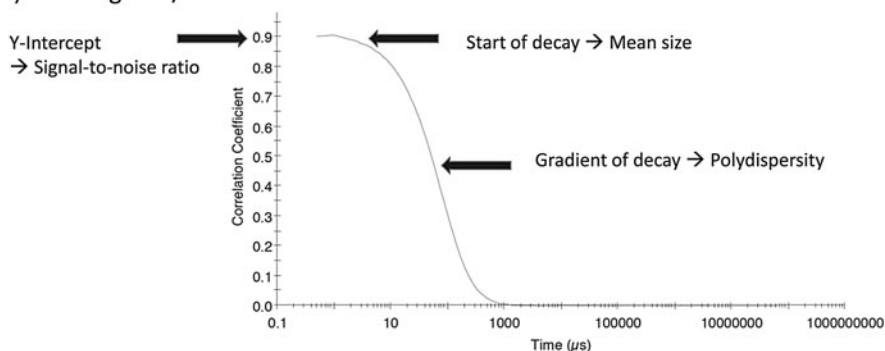
Dynamic light scattering measures the time-dependent intensity scattering fluctuation of a particle in suspension. These scattering fluctuations are used to approach the diffusion constant (D) based on the Stokes-Einstein relationship, which is used to derive the hydrodynamic diameter (d_H) of a particle; dependent on the viscosity of the suspending media (μ), the absolute temperature (T) and the Boltzmann constant (k) (Eq. (21.1)).

$$d_H = \frac{k T}{3\pi\mu D} \quad (21.1)$$

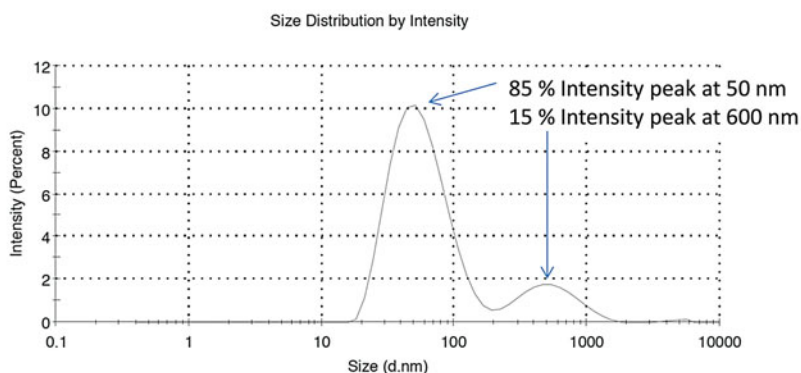
The determined diffusion coefficient depends on a number of assumptions, namely a spherical particle size, as well as known viscosities for the particle and suspending media. However, in practice, particles in a solution are dynamic and rarely perfectly spherical. The diameter measured by DLS is the hydrodynamic diameter (d_H) and represents how the particles diffuse in suspension. Therefore, the hydrodynamic diameter that results from diffusion measurements of the particle is only indicative of the actual size of the particle. The determined hydrodynamic diameter, which is also called Stokes-Diameter, corresponds to a hypothetical sphere that comprises an equal translational diffusion coefficient to the measured particle (Chu and Liu 2000).

Particles move under the Brownian motion, which is induced by collisions between the particles themselves and molecules in the suspending medium. During the particle size measurement, a monochromatic light beam illuminates the particles suspended in a liquid; the light hitting those particles is scattered. In the instrument, a detector, placed at 90° or 173° to the laser beam inlet, is used to collect the scattered light intensity. The intensity of the light scattered depends on the size of the particles; small particles move more rapidly, which results in more rapid intensity fluctuations over time compared to the ones obtained from larger particles. The fluctuations over time can be linked to the diffusion of the particles in suspension using a correlation curve (Fig. 21.3a) (Chu and Liu 2000; Pecora 2000). This correlation curve (or correlation function) should be a single exponential decay function for a monomodal size distribution, and is used to fit the decay to the diffusion of the particles measured. The correlation curve is fitted to an exponential function, which is used to derive the diffusion coefficient (D) that is proportional to the duration of the decay function. Once the diffusion coefficient is determined, the hydrodynamic diameter can be determined by using the Stokes-Einstein relationship. The mean size of a particle population is determined by a cumulants method and can be indicated by the start of the decay (Fig. 21.3a); the polydispersity (a measure of the heterogeneity of the particle suspension) of the samples can be indicated by the steepness and the gradient of the decay. Here, the correlation function is fitted with a least square method in order to assess the decay rate. The Y-intercept on the correlation curve, the intersection of the decay function with the Y-axis in the correlogram, is significant to judge the quality of the data. It can be used to qualitatively determine the signal-to-noise ratio, with an ideal sample giving an intercept at 1 and good intercepts are located within the range of 0.6–0.9. The count rate is also a useful parameter to assess the sample quality, where its stability over time is monitored and represents the number of photons per second detected. This is useful to set the measurement duration and the attenuator in the measurement, as the intensity of the laser beam is adjusted according to number of particles present in the sample (therefore, a highly diluted sample will require a higher attenuator and longer measurement duration).

A) Correlogram / Correlation Function



B)



C)

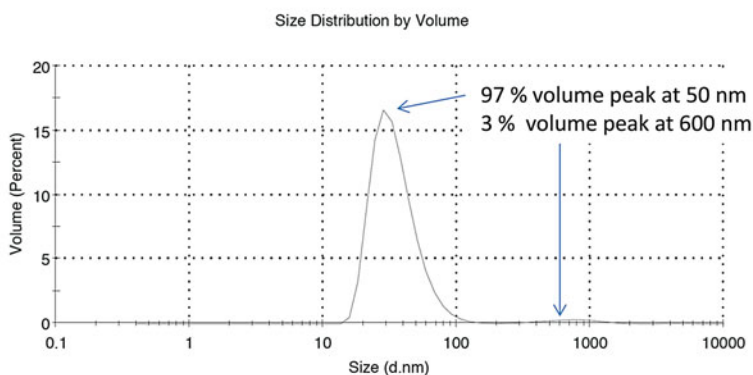


Fig. 21.3 Outcome of DLS measurement; (a) correlation function, (b) intensity-based and (c) volume-based particle size distributions (*bottom*)

The primary and most accurate measurement obtained from DLS measurement is the z-average size (also known as the cumulants mean), which is defined as the intensity averaged particle diameter. Because it is an intensity based calculated value, it cannot be compared directly to a number based size. The z-average is the

best value to report and is defined in the ISO standards, but should only be used for a monomodal (single peak) size distribution, and is not comparable to any other size determination in a multimodal size distribution. This is because, the z-average is very sensitive to changes in the suspending media, including the presence of a small number of aggregates, which more notably affect the intensity-based distribution compared to the volume distribution. This is highlighted in Fig. 21.3b, c, where the same sample is measured using intensity based size distribution and then converted to volume based size distribution; the small proportion of 600 nm particles in the mixtures makes a 15 % contribution to the size distribution when based on intensity (Fig. 21.3b) compared to a 3 % volume peak when the size is based on volume (Fig. 21.3c).

As shown in Fig. 21.3, whilst a DLS measurement typically results in an intensity-based distribution, number and volume distributions can also be derived from the intensity based measurements, and this can be important for generating an estimation of the relative proportions of the particles in a sample (Chu and Liu 2000; Ito et al. 2004). With the intensity-based distribution, the size distribution is weighted according to the intensity of the scattered light from each particle. The scattered light intensity is proportional to the molecular weight of the particle squared and the diameter of the particle to the power 6 (Fig. 21.4). Therefore, the intensity distribution tends to bias towards larger particles within a mixture and may be misleading, as a small amount of larger particles present may overshadow the distribution, identifying any larger contaminants in the sample. Hence, the intensity-based distribution can be converted to a number or volume distribution using the Mie theory (Fu and Sun 2001) where the respective proportion (volume %) in the

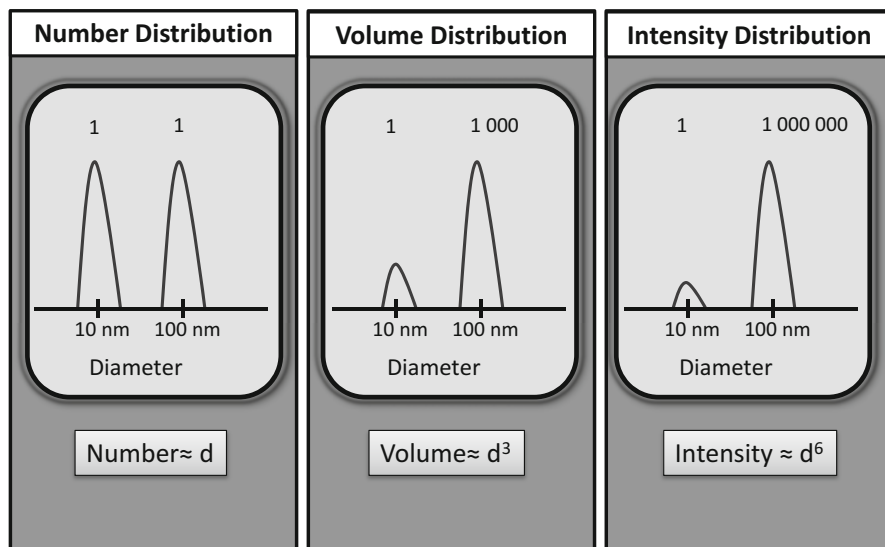


Fig. 21.4 Difference in number-based, volume-based and intensity-based particle size distribution in DLS measurement

sample is identified, based on known optical properties of particle and suspending medium. The volume distribution describes the particles in a suspension based on the volume being proportional to the diameter cubed (Fig. 21.4). However, this conversion relies on a number of assumptions, namely that all particles are spherical, there is a homogenous particle size distribution, that the refractive index of the particles are known, and that there is no error in the intensity-based measurement.

In addition to the reported particle size, a measure of the heterogeneity of the particle suspension is important. With DLS, this is reported as the polydispersity index. The polydispersity index is dimensionless, and the lower the value the more homogeneous the particle size range. Generally a value >0.7 indicates a very broad size distribution and particle size measurements based on DLS will not be reliable.

DLS is a relatively quick method for analysing particle size, without extensive operator training. Its popularity is linked to a rapid analysis together with minimum requirements for calibration and maintenance. Measurements are generally very reproducible for monomodal particle size distributions. Its limitations lie in the sensitivity to the presence of the larger particles or aggregates, which will skew the measurement and the outcome in the intensity measurement (as shown in Fig. 21.3b vs. c) (Chu and Liu 2000; Ito et al. 2004), overall making the method less suitable for characterizing heterogeneous or multimodal particle size distributions (Bell et al. 2012). Also, the correct dilutions need to be determined, in order to reduce the signal-to-noise ratio during the measurements and avoid multiple light scattering. Possible light absorption of the medium may interfere with the measurement. Filtered media and clean cuvettes are indispensable to avoid contamination.

2.2 Laser Diffraction

As opposed to dynamic light scattering, laser diffraction or static light scattering relies on time-averaged intensity measurements. Angles of detection can be fixed or variable, where intensity of the scattered light is recorded at different detection angles. Laser diffraction should be used for particles ranging from the submicron (approximately 500 nm or above depending on the system) to millimetre size range. Generally particles that have sedimentation velocities that exceed Brownian motion should be measured using laser diffraction. Laser diffraction measures particle size distributions by measuring the angle of diffraction of scattered light as a laser beam passes through the particle dispersion and this sizing technique relies on the fact that the diffraction angle is inversely proportional to particle size. Therefore, large particles scatter light at smaller angles compared with smaller particles. The intensity of the light scattering can be used to calculate the particle size using the Mie theory (where the optical properties of the sample are known) or the Fraunhofer theory (which does not require the optical properties but may be less accurate with particles below 50 μm or where particles are relatively transparent). Normally the volume mean diameter (VMD or $D(4,3)$) is reported, and the distribution percentiles can also be reported; $D(10)$, $D(50)$ and $D(90)$ represent the volume of

sample (10 %, 50 % and 90 % respectively) with a diameter up to the value stated. It is fairly typical that the VMD is larger than the D(50), and will indicate a asymmetric distribution profile. The standard deviation or span gives an indication of the uniformity of the overall distribution of sizes, and the span is calculated as $(D90-D10)/D50$. Example particle size plots generated by this method are shown in Fig. 21.5. In all three cases (Fig. 21.5a–c), presentation of the plot is important as the particle size distribution is multimodal in nature; whilst reporting the span for these suspensions will give an indication of the heterogeneous nature of the particle size distribution, inclusion of the plot allows for clearer interpretation of the data.

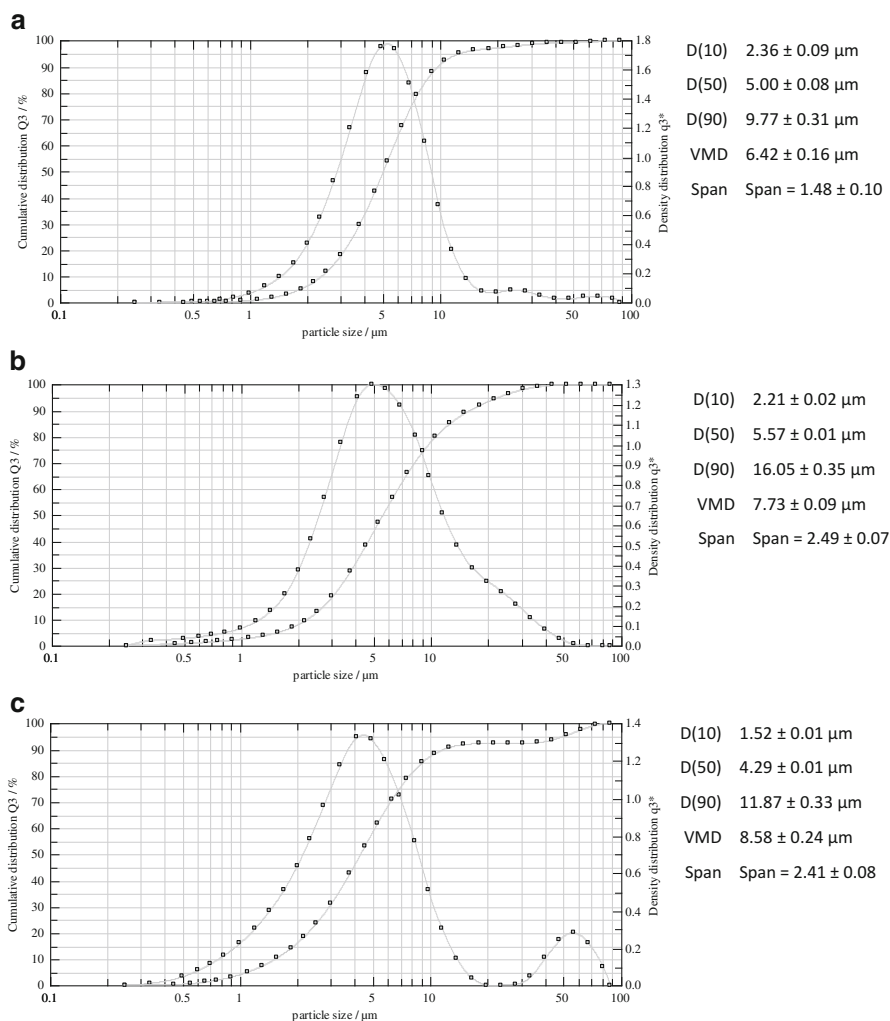


Fig. 21.5 Size plots and particle sizes of microparticles using laser scattering with multi-modal size distributions with the presence of a second larger particle size becoming more apparent from (a) to (c)

Table 21.2 Key features of nanoparticle tracking analysis

Size range	10 nm to 2 μm
Concentration range	10^7 – 10^{10} particle/mL
Required sample volume	10–100 μL (dependent on concentration)
Key parameters	Hydrodynamic diameter
	Particle concentration
Application areas	Wide range of colloids, dispersions, suspensions, synthetic and biological particles

2.3 Nanoparticle Tracking Analysis

Nanoparticle tracking analysis (NTA) is based on the analysis of scattered light and Brownian motion to assess particle size distributions of particles suspended in a liquid, similar to the DLS measurement technique. A laser beam passes through a prism and into the suspension of particles, which scatter the laser light, and this is then captured with a camera on an optical microscope. A video file is recorded by the camera, which allows to track each particle in the frame and its specific movement under the Brownian motion (Carr and Wright 2008; Gardiner et al. 2014; Carr et al. 2009). This method can be employed for particles between 10 nm and 2 μm and has the advantage of allowing single particle sizing and particle concentration measurements (Table 21.2).

Within this method, the first step is to select the field of view comprising $100 \times 80 \times 10 \mu\text{m}$ in space, where each particle is visualized and can be viewed by eye through the camera or projected onto a computer live tracking system (Fig. 21.6, Step 1). Following that, a video file is recorded, with typically 30–60 s duration. The centre of each particle is localized and each particle is tracked on a frame-by-frame basis for the duration of the recording time selected (Fig. 21.6, Step 2). For each particle the average distance in x and y direction is then analysed. Similar to the DLS measurement, this distance travelled can be used to calculate the diffusion coefficient using the Stokes–Einstein equation, based on the viscosity of the media (η), the absolute temperature (T) and the Boltzmann constant (k), used to determine the hydrodynamic diameter (d_H) of the particles (Eq. (21.2)).

$$d_H = \frac{k T}{3\pi\eta D} \quad (21.2)$$

The distances of each particle in the frame travelled are converted into a real-time particle size distribution (Fig. 21.6, Step 3). Finally, data fitting allows displaying the intensity and number based distributions as well as the particle concentration (Fig. 21.6, Step 4). In order to detect the correct concentration of particles suspended, samples should be diluted to the range of 10^7 – 10^{10} particles/mL. A concentration below that threshold will require a prolonged analysis time in order to gather enough data to get a statistically valid particle size and concentration

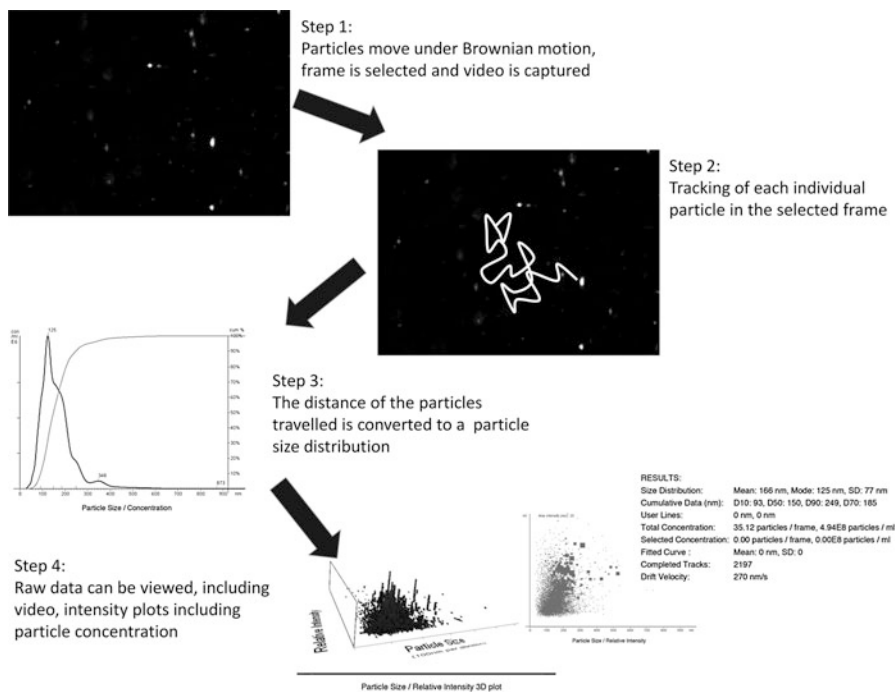


Fig. 21.6 Stepwise procedure in a NTA analysis

measurement. At concentrations higher than 10^{10} particles/mL, the Brownian motion of the particles may be interfering with each other, leading to invalid measurements. The volume of the view field is known (depth of laser beam of $10\ \mu\text{m}$, channel dimensions of $100 \times 80\ \mu\text{m}$), allowing for determination of the scattering volume, dependent on particle size and refractive index, as well as the laser characteristics (wavelength, power, dimensions). With the determined number of particles in the optical field, the concentration of particles can be extrapolated, which is the main difference to the DLS measurement principle. The system settings are normalized against polystyrene latex beads and a calibration is recommended for samples that differ from the properties of the standardized beads, to allow for accurate and precise concentration determination (Carr and Wright 2008; Carr et al. 2009).

The smallest size that can be measured by NTA depends on the scattered light intensity. Factors affecting the scattered light intensity include not only the size of the particle, but also the laser power, wavelength and angle, as well as the refractive index of particle and suspending medium and the shape of the particle. The lower limit of particles being detected depends on the particles refractive index; gold particles with a relatively high refractive index can be detected down to a size of $10\ \text{nm}$, whereas biological samples of lower refractive index usually have a lower detection limit of $20\text{--}30\ \text{nm}$. The lower detection limit for polymers, exosomes and

liposomes is around 40 nm. The upper size detection limit depends on the Brownian motion, which decreases with increasing particle size, leading to inaccuracies at sizes around 1–2 μm .

Unlike DLS, NTA measures the hydrodynamic diameter of each particle tracked; this circumvents intensity-based weighing problems seen with larger particles or aggregates present in a sample, as it is not the sum of the motion that is analysed, but the motion of each particle on its own. In theory, this allows for a higher resolution for mixed populations, as it is a direct number-weighted size determination method. Furthermore, the system can be used to analyse fluorescent particles and their dependent fluorescence behaviours (Braeckmans et al. 2010). Nevertheless, well-trained operators and expertise are required to yield an accurate measurement and selecting the field of view is susceptible to user bias. The time for completing a measurement usually exceeds that of a measurement with DLS. Also, the measurement chamber needs to be cleaned manually after each measurement.

2.4 Differential Centrifugal Sedimentation

Differential centrifugal sedimentation (DCS) uses the particle sedimentation principle for particle separation and size-related settling rates. It can be used over a large size range (10 nm to 50 μm) with high resolution and is applicable to a wide range of systems (Table 21.3). Given that this method involves particle size separation before sizing, it can offer advantages when considering multi-modal size populations.

Upon a gravitational field (g), particles settle according to Stokes' law. The sedimentation velocity (v_{sed}) is proportional to the diameter of a particle squared (d_p^2), the density difference between particle (ρ_p) and liquid (ρ_f) and the viscosity of the surrounding medium (η) (Eq. (21.3)); given that the velocity of sedimentation is proportional to the diameter of the particle squared (Eq. (21.4)), a small difference in particle size has a significant effect to the particle's sedimentation velocity.

$$v_{\text{sed}} = \frac{\rho_p - \rho_f}{18\eta} d_p^2 g \quad (21.3)$$

$$v_{\text{sed}} \approx d_p^2 \quad (21.4)$$

Table 21.3 Key features of differential centrifugal sedimentation

Size range	10 nm to 50 μm (dependent on particle density)
Key parameters	Absolute size distribution
Application areas	Wide range of colloids, dispersions, suspensions, synthetic and biological particles, polymers, abrasives

The disadvantages of using sedimentation as a method for particle separation is that small particles may require a long time to sediment. Therefore, centrifugal forces are applied to enhance the separation process. In the disk centrifuge, a hollow disk spins at constant speeds (up to 15,000 rpm). The disk cavity includes the particles dispersed in a spin fluid (often a sucrose solution), creating a density gradient. Spin fluids can be chosen with desired choice on viscosity and density, which allows for flexibility and suitability for almost any kind of particle with desired size and density characteristics.

The time for the particles to settle is proportional to the square of the particle diameter (Oppenheimer 1983) and particles will separate according to differences in size, density and shape (Anderson et al. 2013). Particles move to the outside of the disc centrifuge under high centrifugal forces until they collide with the wall. Particles of the same size travel with the same velocity and form a band of particles on the channel wall, which are analysed by the detector at the same time, with larger particles being detected before smaller ones. The detector is based on the light diffraction principle, similar to the DLS and SLS techniques. The detector measures the extinction of a light beam that continually passes through the sample (McFadyen and Fairhurst 1993). The resulting particle size distribution is computed based on a known correlation between particle size and sedimentation kinetics. Optical properties are required for a conversion of the light extinction using the Mie theory (Fu and Sun 2001).

Disk centrifugation is an absolute method (McFadyen and Fairhurst 1993), a standard of known size and density is usually applied as a reference check (Anderson et al. 2013). The method is limited for small particles with equal diffusion and sedimentation rate, low-density particles at a minimum 50 nm and denser particles around 10 nm. The disk centrifuge can be run at various centrifugal speeds, which also allows for very small particles to be collected and analysed. The resolution of particle separation and analysis by disk centrifugation is very good. Application areas include chemical industry (polymers, abrasives, particles) as well as biological and pharmaceutical industry (virus particles, cell fragments, proteins, liposomes, particles and drug particles).

3 Pulse Sensing Particle Sizing Methods

As an alternative to light scattering, resistive pulse sensors can also be used for the quantitative sizing of micro and nanoparticles. These systems are based on a relationship between particle volume and change in electrical resistance across a pore.

Table 21.4 Key features of a Coulter counter

Size range	400 nm to 1500 μm
Key parameters	Number and volume of particles
	Particle concentration
Application areas	Wide range of cell types, colloids, dispersions in electrolyte, microorganisms, viruses

3.1 Coulter Counter

The Coulter principle for particle analysis goes back to the 1940s, where Wallace H. Coulter developed the technique for particle size analysis based on impedance measurements, a resistive method of particle size analysis. The principle is common for cell analysis as well as for several particulates (Shibata 1971; Coulter 1953). The measurement principle is based on impedance detection of the analytes suspended in an electrolyte. Two electrolytes that are submerged in the suspension of analytes provide an electric field, where the impedance between both electrodes is measured. Particles that pass through this “sensing zone” displace a volume of electrolyte, proportional to the particles volume. This can be captured by a change in impedance whilst the particle travels through the electric field, which is measured as a voltage pulse proportional to the volume of a particle, converted to a particle size distribution (Hurley 1970; DeBlois and Bean 1970). Particles from 400 nm to 1500 μm can be sized using this method and advantages in this system include the ability to size and count particles, therefore it gives particle volume and concentration (Table 21.4). Like NTA sizing is done on a particle-by-particle basis.

When using a coulter counter, particles must be suspended in an electrolyte solution. Furthermore, conductive particles might act as insulators in the measurement and require adjustments of the applied voltage. A measurement might be problematic for porous particles, as volume displaced by a porous particle might not be represented by its volume and size. Particle sizing by the coulter method is however a very rapid analytical method, with an average recording time of less than 1 min.

3.2 Tunable Resistive Pulse Sensing

Tunable resistive pulse sensing (TRPS) is a direct particle-by-particle characterization method of micro- and nanosized particles, similar to the principles involved in the above mentioned Coulter Counter method, which is adapted to the nanoscale and allows for sizing nanoparticles. In contrast to the previously introduced laser diffraction technologies like DLS or NTA, this method is independent of optical technologies and measures particle size, concentration, charge as well as dynamic properties (Table 21.5) (Kozak et al. 2011, 2012).

Table 21.5 Key features of tunable resistive pulse sensing

Size range	50 nm to 10 μ m
Concentration range	10^5 – 10^{12} particle/mL
Required sample volume	40 μ L (dependent on concentration)
Key parameters	Absolut size distribution (particle-by-particle analysis)
	Particle concentration
Application areas	Wide range of colloids, dispersions, suspensions, synthetic and biological particles, diagnostics, viruses

Nanopores are used as the heart of the analysis, made out of flexible thermo-plastic polyurethane, which provide a dynamically resizable pore that can be stretched along the x and y axis for adjustments by nanometers. This size of the tunable pore is the main difference to many commercially available Coulter Counters (Sowerby et al. 2007) and can easily be adjusted by stretching the membrane in real-time to the size of the particles being analysed. A voltage is applied over a fluid cell, which incorporates an electrolyte, and by optimization of pressure and voltage the particle transport through the nanopore is optimized (Willmott et al. 2010, 2012). Ions are allowed to move between electrodes, which produce a baseline current across the nanopore (Fig. 21.7a). The stretch of the nanopore can now be altered and adjusted, which will affect the baseline current and improves measurement sensitivity and resolution (Roberts et al. 2010). At a lower stretch, the nanopore is smaller which allows for fewer ions to move. Due to more resistance in the circuit, the baseline current is lower. A high stretch allows for a reduced resistance, which will result in a higher baseline current (Fig. 21.7b). Upon addition of the sample, the particles passing through the nanopore displace a certain volume of electrolyte, which interrupts the baseline current. The particle increases the resistance of the circuit and the current measured is temporarily decreased, which results in a blockade event, visible as a drop in the baseline current. The magnitude of the blockade event is proportional to the volume of the particle: smaller particles with a lower resistance result in a smaller drop in the baseline current, larger particles have more resistance, and result in a blockade event of larger magnitude. This change in the current allows for sizing and counting of each particle that travels though the nanopore. The convective forces that allow for particle motion due to pressure differences across the membrane are influenced by a pressure module, which provides pressure and vacuum control during the analysis. The convection is directly influenced by either increasing the stretch on the nanopore, which allows for more fluid flow, or by increasing the pressure difference.

The particle volume is directly proportional to the resistance pulse signal ΔR , which is generated by each particle traveling through the nanopore. As the particle volume is proportional to the particle diameter cubed, a small change in particle diameter will result in a notable change in the resistance pulse signal. The effective particle diameter is calculated by the relationship in Eq. (21.5), where the diameter

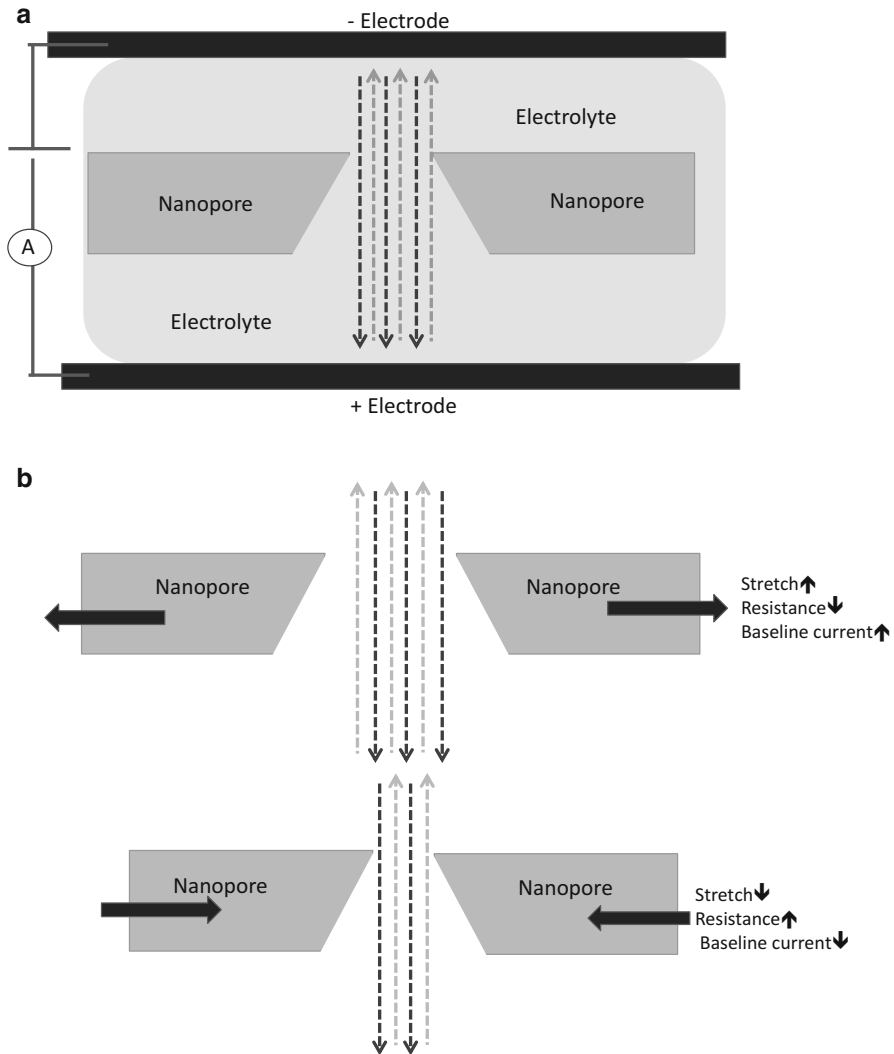


Fig. 21.7 (a) Schematic overview of a TRPS measurement cell. (b) Schematic overview of a TRPS measurement cell with different pore sizes

of a particle (d_p) is extrapolated from the relationship of the resistance signal (ΔR), the pore diameter (d_{pore}) and the resistance of the suspending electrolyte (δ).

$$\Delta R = \frac{4 \delta d_p^3}{\pi d_{pore}^4} \tag{21.5}$$

TRPS determines the actual physical diameter (rather than the hydrodynamic diameter as in the case light-scattering methods) of the particles and the size of

each individual particle is measured (particle-by-particle analysis). One of the main features using this technique is the ability to determine the effective particle concentration. Each particle that passes through the nanopore is counted, and resulting particle concentration measurements are generally independent of particle size or zeta potential. The number of particles counted over a specific time frame (particles/min) is proportional to the actual particle concentration, in a direct linear correlation (Roberts et al. 2012).

TRPS can be used to characterise a wide range of drug delivery systems including liposomes, polymers, microparticles, exosomes and nanobubbles. In microbiology, TRPS is used for analysis and quantification of extracellular vesicles, viruses, bacteria and yeast. Industrial applications also include the analysis of paint pigments, metallic and magnetic particles, as well as for silica, polystyrene and polymers. Compared to particle sizing techniques based on light scattering, this technique is not biased by a small population of larger particles present in the suspension (Merkus 2009) and no assumptions of particle properties prior to the measurement are required (Bell et al. 2012). Nevertheless, analysis depends on a high ionic strength buffer and necessitates the stability of the measured particles in the respective medium. The absolute diameter of the particles may depend on the suspended media and particular swelling behaviour. Blockage of the pore might occur if particles are too big or attracted to the surface of the pore. This pore blockage is limited by the effective size, which makes the analysis of very polydisperse samples difficult using the same nanopore. Nevertheless, the pore geometry can be altered to create a wider application range (Anderson et al. 2013) to measure polydisperse samples over a range of nanopores. In contrast, small particles might be overlooked if they don't displace enough electrolyte larger than the background noise. This can lead to difficulties in the selection of the right nanopore if the average diameter is unknown prior to the measurement. Furthermore, the machine needs to be calibrated prior to every measurement, which also requires a certain level of training and expertise of the operators. A comparison between TRPS and the two other commonly adopted laboratory methods for particle sizing is given in Table 21.6.

4 Case Studies

4.1 *Bimodal Populations Measurements by DLS*

In the formulation of particulate drug delivery systems, bi- or even multimodal populations in the formulations may be present; this can have a major impact on the therapeutic outcome of the system. For example, drug loading and the pharmacokinetic profiles can be influenced by particle size. Therefore, when measuring and reporting particle sizes it is important that the modality of the particle size distribution is known. To consider this, we prepared liposome suspensions containing a

Table 21.6 Comparison of main attributes of DLS, NTA and TRPS

	DLS	NTA	TRPS
Size range	1–8000 nm	10–2000 nm	50–10,000 nm
Concentration range	N/A	10^7 – 10^9 particles/mL	10^5 – 10^{12} particles/mL
Sample volume	100–200 μ L	10–50 μ L	10–50 μ L
Accuracy	Good accuracy for monodisperse samples, inaccurate at higher polydispersities	Good accuracy for low and high polydispersity samples	Good accuracy for low and high polydispersity samples
Resolution	Low at less than threefold difference in diameter	High, higher than 0.5-fold in diameter	Very high
Reproducibility	High	Lower (frame selection by user)	High (particle-by-particle analysis)
Sample preparation	Removal of large contaminants by filtration or centrifugation	Removal of large contaminants by filtration or centrifugation	Removal of large contaminants by filtration or centrifugation
		Appropriate dilutions required	Appropriate dilutions required
Contamination	Large particles influence measurements (intensity measurements)	Contaminants more easily detected, lower influence of larger particles	Selection of different nanopores allows for accurate detection of contaminants
Output	Z-average, intensity, volume and number distribution, polydispersity	Absolute particle diameter	Absolute particle diameter
		Particle concentration	Particle concentrations
Visualization	No	Yes (video recording over measurement period)	No
Device	User-friendly, little sample preparation, disposable cuvettes	Several adjustments required (dilutions, microscope settings), cleaning of chamber after each measurement, operator experience required	Adjustments required (pressure, voltage), nanopore stretch, calibration, baseline current and buffer selection
Average recording time	2–5 min/measurement	5–10 min/measurement	5–10 min/measurement
Application	Sizing, size distribution	Sizing, size distribution, particle concentration	Sizing, size distribution, particle concentration

mixture of two different liposome size populations and measured the particle size using dynamic light scattering with a Malvern Nanosizer ZS (Malvern Instruments Worcestershire, UK). In this study a commonly investigated liposomal adjuvant composed of dimethyldioctadecylammonium (DDA) and D-(+)-trehalose 6,6'-dibehenate (TDB) (Avanti Polar Lipids, Inc. (Alabaster, AL); purity >99%)

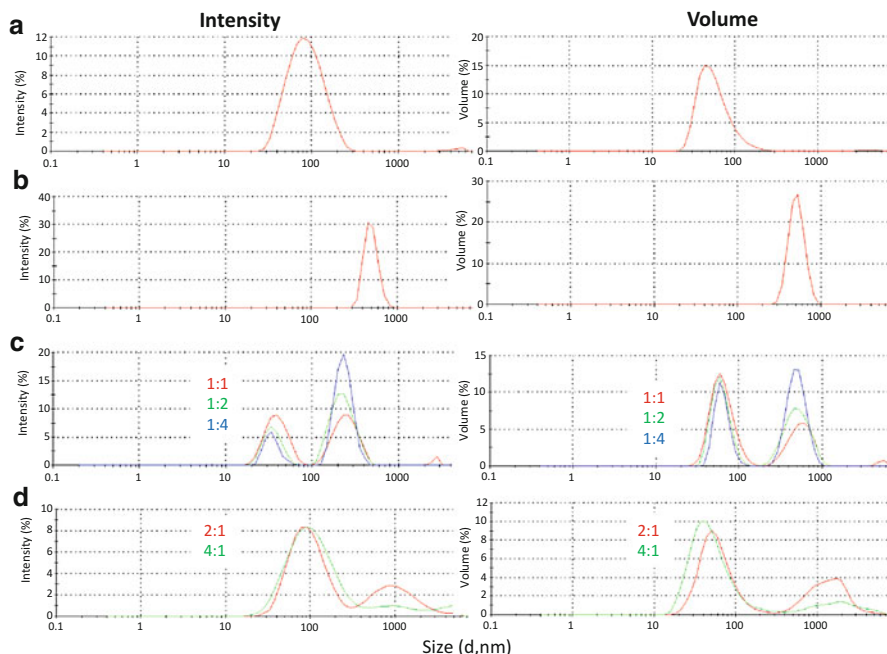


Fig. 21.8 Bimodal liposome distributions analysed by DLS as intensity and volume distribution of (a) liposomes ~80 nm, (b) liposomes ~500 nm, (c) a mixture of the 500 nm and 80 nm liposomes in a 1:1 lipid weight ratio and (d) a mixture of the two liposome populations at a 1:4 ratio

were prepared (Christensen et al. 2007). Two size populations of liposomes were produced; liposomes were manufactured by rotary evaporation to generate a larger population of ~500 nm vesicles and were subsequently sonicated to generate a smaller sized liposome population of ~80 nm. Given that both formulations contained equal lipid concentrations, it can be assumed that the 80 nm population contained a larger number of liposomes. Both populations were initially analysed by DLS to detect the respective size and polydispersity (Fig. 21.8a, b) before bimodal populations were prepared by mixing the two different liposome systems at different ratios (Fig. 21.8c, d).

Mixing the 500 and 80 nm populations in a 1:1 lipid weight ratio (Fig. 21.8c) reveals a near equal-sized intensity plot with 51 % of the distribution at 500 nm and 47 % of the distribution at 80 nm. In contrast, when plotted as Volume %, the 80 nm liposome population has a higher proportion (34 % for the 500 nm sized population and 65 % for the 80 nm sized population; Fig. 21.9). In this case, clearly reporting the z-average diameter would be inappropriate given the two sub-populations present (Table 21.7); however, by comparing the number distribution we are able to consider the ratio of the two populations present. Increasing the concentration of 500 nm liposomes present in the mixture (Fig. 21.9) continued to give good peak separation for the two liposome size population, with the ratio between both the

Table 21.7 Z-average particle size measured from various liposome mixtures

80:500 nm size ratio	Z-average diameter (nm)	PDI
1:0	78.1	0.196
0:1	502.2	0.704
1:1	175.6	0.594
1:2	298.0	0.595
1:4	407.0	0.636
2:1	117.9	0.413
4:1	101.1	0.387

intensity and volume peaks reflecting the increase in 500 nm liposomes (Fig. 21.8c). Here, the z-average diameter shows an increase with a higher amount of larger-sized population added (Table 21.7), exemplifying that the z-average diameter is an inappropriate representation of the two populations. When considering the volume distribution, at a 1:4 ratio of 80:500 nm liposomes resulted in approximately equal distribution plots for both sub-populations, suggesting there is an approximately 4 times higher concentration of the smaller (80 nm) liposomes relative to the larger (500 nm) liposomes (Fig. 21.8c).

In contrast, when the ratio of smaller liposomes was increased (Fig. 21.8d), resolution between the two size populations became less clear. At a ratio of 4:1 for 80:500 nm liposomes, the larger 500 nm liposome population was difficult to accurately detect due to reduced resolution, a shift and broadening of the peaks both with intensity and volume distribution plots (Fig. 21.8d), and the corresponding z-average reading (Table 21.7) approaches the actual diameter of the 80 nm sized population with the increase in ratio of the smaller liposomes, whereas the higher polydispersity values still represent the mixed population.

From this case study, we can see that the evaluation of both the intensity- and volume-based distribution plots is useful in understanding particle size distribution. However the resolution between differently sized populations depends on the concentration of the particles in each sub-population, with small proportions of sub-populations being difficult to detect.

4.2 DLS and NTA Measurement of Liposomes

To consider the impact of particle sizing methodology on reported sizes, liposomes were also sized using dynamic light scattering (performed with a Malvern Nanosizer ZS, Malvern Instruments) and NTA (NanoSight NS300, Malvern Instruments, Worcestershire, UK). Liposomes were formulated from phosphatidylcholine (PC) and cholesterol (Avanti Lipids and Sigma-Aldrich Ltd respectively). PC: cholesterol liposomes in a 16:4 molar ratio were manufactured by a standard rotary evaporation protocol, and liposomes were sonicated in order to reduce their size. Analysis with the DLS method yielded a Z-average of 119 nm, with a polydispersity of 0.121 (Fig. 21.9). Both the intensity and volume-based distribution showed a

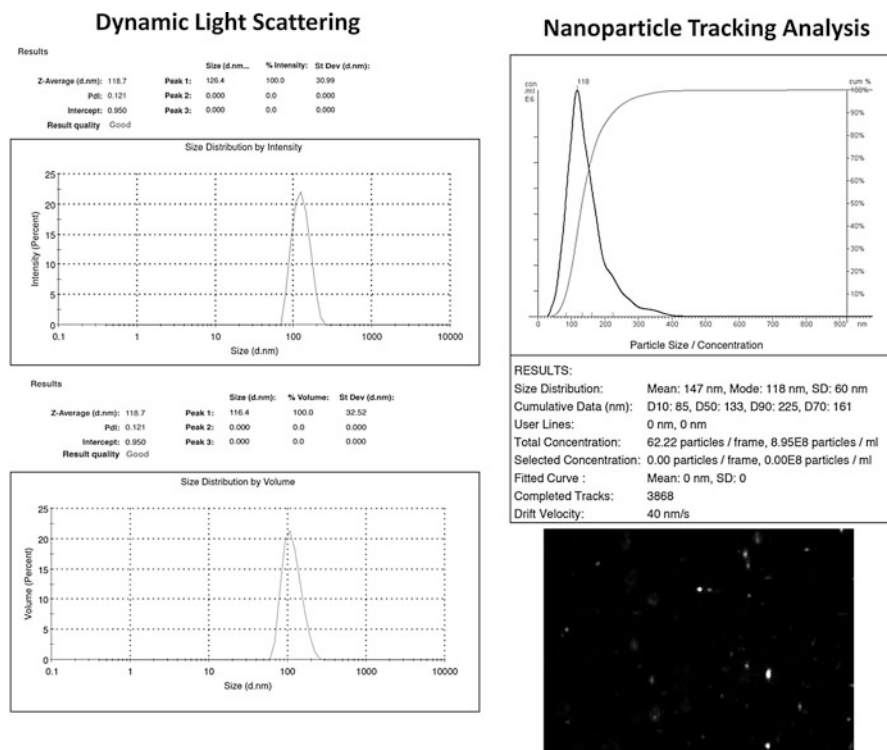


Fig. 21.9 Comparison of DLS and NTA measurement for a liposome sample

monomodal size distribution, with 100 % intensity at 126 nm and 100 % volume at 116 nm (Fig. 21.9), indicating that no larger aggregates were detected in the sample. For the same liposome batch, the NTA method yielded a mean diameter of 147 nm, a mode of 118 nm and a standard deviation of 60 nm (Fig. 21.9). The particle concentration determined was 8.9×10^8 particles/mL. Also, a visual image and video recording of the liposomes during the analysis was recorded, showing the scattered laser light in the selected frame (Fig. 21.9). From these results, we highlight the importance of providing the details of the particle size methodology as depending on the parameter reported that particle size can be correctly described as 116, 126 or 147 nm, with the z-average obtained by DLS measurement matching with the mode diameter obtained from the NTA analysis.

of their physico-chemical attributes is vital to ensure clinical reproducibility and appropriate quality control and assurance. With new methods becoming available, the ability to measure the size and concentration of particulate delivery systems is now standard practise; however, a shared good-practice policy has yet to be adopted. Furthermore, it must be remembered that the particle size provided by the systems discussed are representative of a sphere which may not match the true attributes of the particles being sized. Whilst the above described methods are rapid and easily adopted, it is important to remember that accurate size analysis of multi-modal size populations can present difficulties and for non-spherical particles different sizing techniques will give different answers. Therefore with any particle size method adopted there remains a need to validate measurements, with microscopy remaining the most important reference method.

Acknowledgments The authors gratefully acknowledge Sameer Joshi who generated the plots presented in Fig. 21.5 and Robert Vogel (Izon Science) for reviewing the manuscript. This work was part funded by the EPSRC Centre for Innovative Manufacturing in Emergent Macromolecular Therapies and Aston University.

References

- Allen T (1997) Particle size measurement, vol 2, Surface area and pore size determination. Springer, New York
- Anderson W et al (2013) A comparative study of submicron particle sizing platforms: accuracy, precision and resolution analysis of polydisperse particle size distributions. *J Colloid Interface Sci* 405:322–330
- Bell NC et al (2012) Emerging techniques for submicrometer particle sizing applied to stober silica. *Langmuir* 28(29):10860–10872
- Bleeker EA et al (2013) Considerations on the EU definition of a nanomaterial: science to support policy making. *Regul Toxicol Pharmacol* 65(1):119–125
- Braeckmans K et al (2010) Sizing nanomatter in biological fluids by fluorescence single particle tracking. *Nano Lett* 10(11):4435–4442
- Carr B, Wright M (2008) Nanoparticle tracking analysis. *Innovations Pharm Technol* 26:38–40
- Carr B et al (2009) Applications of nanoparticle tracking analysis in nanoparticle research--A mini-review. *Eur J Parenter Pharm Sci* 14(2):45
- Christensen D et al (2007) Cationic liposomes as vaccine adjuvants. *Expert Rev Vaccines* 6:785–796
- Chu B, Liu T (2000) Characterization of nanoparticles by scattering techniques. *J Nanopart Res* 2(1):29–41
- Coulter WB (1953), Itteajls fofe counting mrtictes, Google Patents.
- DeBlois R, Bean C (1970) Counting and sizing of submicron particles by the resistive pulse technique. *Rev Sci Instrum* 41(7):909–916
- Fu Q, Sun W (2001) Mie theory for light scattering by a spherical particle in an absorbing medium. *Appl Opt* 40(9):1354–1361
- Gardiner C, Dragovic R (2014) Nanoparticle tracking analysis. Extracellular vesicles in health and disease, p 261
- Hurley J (1970) Sizing particles with a Coulter counter. *Biophys J* 10(1):74–79

- Ito T et al (2004) Comparison of nanoparticle size and electrophoretic mobility measurements using a carbon-nanotube-based coulter counter, dynamic light scattering, transmission electron microscopy, and phase analysis light scattering. *Langmuir* 20(16):6940–6945
- Kozak D et al (2011) Advances in resistive pulse sensors: devices bridging the void between molecular and microscopic detection. *Nano Today* 6(5):531–545
- Kozak D et al (2012) Simultaneous size and ζ -potential measurements of individual nanoparticles in dispersion using size-tunable pore sensors. *ACS Nano* 6(8):6990–6997
- McFadyen P, Fairhurst D (1993) High-resolution particle size analysis from nanometres to microns. *Clay Miner* 28(4):531–537
- Merkus, H.G., *Particle size measurements: fundamentals*. Practice, Quality, 2009: p. 1-7.
- Oppenheimer LE (1983) Interpretation of disk centrifuge data. *J Colloid Interface Sci* 92 (2):350–357
- Pecora R (2000) Dynamic light scattering measurement of nanometer particles in liquids. *J Nanopart Res* 2(2):123–131
- Roberts GS et al (2010) Tunable nano/micropores for particle detection and discrimination: scanning ion occlusion spectroscopy. *Small* 6(23):2653–2658
- Roberts GS et al (2012) Tunable pores for measuring concentrations of synthetic and biological nanoparticle dispersions. *Biosens Bioelectron* 31(1):17–25
- Shibata K (1971) Measurement of size distribution with the Coulter counter. *Methods Enzymol* 24:171–181
- Sowerby SJ, Broom MF, Petersen GB (2007) Dynamically resizable nanometre-scale apertures for molecular sensing. *Sens Actuators, B* 123(1):325–330
- Stanley-Wood N, Lines RW (1992) Particle size analysis, vol 102. Royal Society of Chemistry, London
- Willmott G et al (2010) Use of tunable nanopore blockade rates to investigate colloidal dispersions. *J Phys: Condens Matter* 22(45):454116
- Willmott GR, Platt M, Lee GU (2012) Resistive pulse sensing of magnetic beads and supraparticle structures using tunable pores. *Biomicrofluidics* 6(1):014103

Chapter 22

Particle Size Measurements in Aerosols

Regina Scherließ

Abstract Pharmaceutical aerosols comprise a wide range of drug products which all are dispersed as droplets (wet aerosol) or particles (dry aerosol) in a gas for application. Hence, the device being used for dispersion plays a very important role as it impacts the dispersion efficiency and significantly influences the resulting aerosol particle size. For an aerosol's therapeutic effect it is important how the particles behave in the gas they are dispersed in, i.e. how they distribute and deposit. Therefore, aerodynamic particle size is important in addition to a geometrical particle size—unlike many other formulations where only geometrical particle size is looked at. The chapter defines the differences in particle sizes and gives an overview of measurement techniques to determine aerodynamic particle size as well as other sizing techniques in use for aerosol particle sizing. Pharmacopoeial requirements are summarized and physiological implications as well as ideas to closer mimic the in vivo situation are discussed.

Keywords Accessories to mimic in vivo situation • Aerodynamic particle size • Cascade impaction • Geometric particle size • Particle deposition mechanisms • Pharmacopoeial requirements • Sample dispersion

Aerosols are dosage forms consisting of droplets or dry particles being dispersed in a gas. They can be administered as topical spray, nasal spray or via (naso-)oral inhalation to the lung. For all dosage forms, a device generating the aerosol prior to or during administration is needed. Particle size of aerosols is important for aerosol particle deposition and distribution of the active pharmaceutical ingredient (API) and with this has implications for drug action. Once airborne, particles deposit due to impaction, sedimentation, diffusion or interception (Fig. 22.1).

For topical sprays fine and uniform particle size is preferred which allows even distribution of the spray without splashing and dripping. Particle size should also be large enough to allow a directed spray to and impaction in the area to treat without major loss of the dose due to diffusion of very fine particles. Nasal sprays are

R. Scherließ (✉)

Department of Pharmaceutics and Biopharmaceutics, Kiel University,
Grasweg 9a, 24118 Kiel, Germany
e-mail: rscherliess@pharmazie.uni-kiel.de

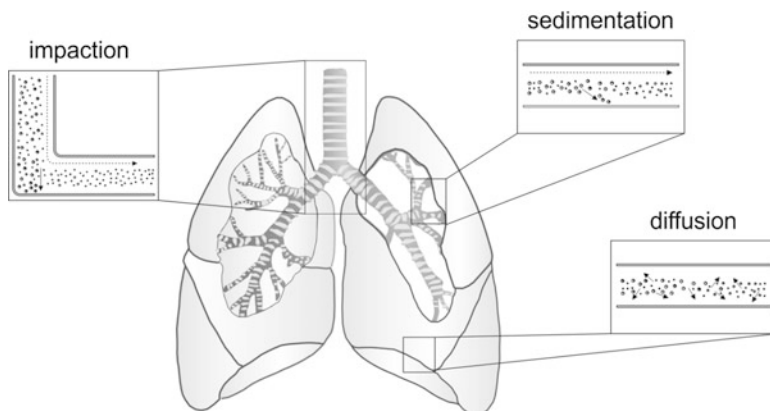


Fig. 22.1 Particle deposition mechanisms in the lung

required to have a particle size distribution where the vast majority is above $10\ \mu\text{m}$ in order to obtain preferential nasal deposition without an inhalable fraction. For pulmonary delivery, an aerodynamic particle size below $5\ \mu\text{m}$ ($2\ \mu\text{m}$ for alveolar targeting) is requested. The proportion of particles probably reaching the lungs is then given as fine particle dose (FPD) according to pharmacopoeial requirements.

Aerosol particle size of liquid formulations is determined by formulation parameters such as viscosity and size of suspended particles and is also affected by device parameters such as nozzle size and dispersion force. For dry powder formulations, particle size is determined by the primary particle size of the formulation and dispersion effectiveness of the device. Furthermore, measurement parameters such as flow rate and distance between device and measurement zone can influence the result.

1 Aerodynamic and Geometric Particle Size

If a particle is a sphere, its size can be described by its diameter. Nonetheless, most particles are non-spherical, irregularly shaped and hence, particle size is defined as the size of a sphere of unit density ($1\ \text{g}/\text{cm}^3$) with the same behaviour in the respective measurement. Particle sizes are then viewed in terms of geometrical (e.g. surface, volume, etc.) or behavioral (e.g. sedimentation, aerodynamic) equivalence. Depending on the measurement technique and data analysis, different particle sizes can be defined which are:

- Volume based particle size, which is the diameter of the sphere that has same volume as the measured particle
- Area based particle size, which is the diameter of the sphere that has the same surface area as the measured particle

- Hydrodynamic or aerodynamic particle size equals the diameter of the sphere that has the same drag coefficient as the measured particle (in liquid or air, respectively)

Aerodynamic particle size describes the particle behavior in airflow. It is the size of the particles or droplets that make up the emitted aerosol cloud. Aerodynamic particle size takes into account that particle flight behavior, impaction and settlement also depends on density and particle shape. Aerodynamic diameter (d_{ae}) is given as the diameter of a sphere with unit density (1 g/cm^3) showing the same behavior in the airflow as the measured particle (Eq. (22.1)), where d is the actual diameter of the sphere, ρ is the spherical particle density and ρ_0 is unit density. For non-spherical particles, which are more prone to deposition via interception, the particle shape also influences the aerodynamic diameter and therefore corrections for shape factors (f) are applied).

$$d_{ae} = d \cdot \sqrt{\frac{\rho}{\rho_0}} \cdot f \quad (22.1)$$

For spray dried particles, which normally are of spherical shape, but may have low density due to being hollow or porous, that results in an aerodynamic particle size smaller than their geometric size as measurable by laser diffraction (LD) or in Scanning Electron Microscopy (SEM). Further, particles being able to align in the airflow, such as needle-like particles, will also behave like smaller particles. On the other hand, aerodynamic particle size can also be larger than estimated from SEM if the particles agglomerate and cannot be separated by the airflow and hence, are measured as agglomerates. This effect might be overcome when using higher air velocities or a dispersion device with higher deagglomeration force; hence, aerodynamic particle size is also a function of flow rate and device.

2 Dispersion Techniques

Dispersion of an aerosol can be performed actively with a puff generated by pressurized gas (air, nitrogen, carbon dioxide or propellant (often hydro fluoroalkanes (HFA) such as HFA 134a or HFA 227)), mechanical compression through a nozzle or by application of negative pressure which is created by the patient's inhalation airflow producing a vacuum. Typical dispersion devices for human use are mechanical spray pumps, pressurized aerosol containers, nebulizers, pMDIs (pressurized metered dose inhalers) and DPIs (dry powder inhalers). All these devices create some kind of force disrupting and with this dispersing the formulation. This can be created by the introduction of turbulence in the airflow due to winded air channels, baffles, impaction plates or cyclones. This can also be done by (ultrasound or piezo-induced) vibration, rotation, propellant evaporation or by the expansion and disruption of a spray after being pressed through a nozzle. As the

dispersion mechanism significantly influences the size distribution of the resulting aerosol, the dispersion technique should carefully be selected for aerosol particle sizing in order to obtain meaningful data.

In some cases of dry powder aerosol sizing, it might be needed to maximize the dispersion of a formulation (e.g. to determine the primary particle size of a powder). In this case, a dispersion technique has to be used which is able to fully disperse the formulation such as by pressurized air. Contrary, it can also be wanted not to introduce any dispersion-enhancing principles when measuring dry powder aerosols. Thus, a “deviceless” application of the powder to the measurement is wanted and can be performed by transferring the powder to the airflow in the analysis instrument with the help of an application method eliminating the influence of a specific device (Steckel and Bolzen 2004).

It has to be kept in mind, that the mode and device for dispersion is crucial for the particle size of the generated aerosol. Hence, when testing drug products it is most appropriate to use the device that is dedicated to the respective drug product.

3 Pharmacopoeial Requirements for Particle Size Measurements in Aerosols

The European Pharmacopoeia defines two particle sizing techniques applicable to aerosols: Aerodynamic assessment of fine particles (2.9.18), which has to be used for the determination of fines according to the monograph on preparations for inhalation; and particle sizing by laser diffraction (LD) (2.9.31) which can be used for aerosols in general as well as other preparations. For LD, the Ph.Eur. states that an aerosol should preferably be measured without further dilution in order not to alter particle size by a change in concentration. For the characterization of preparations for nebulization (2.9.44), the Ph.Eur. acknowledges the advantages of laser diffraction such as speed of measurement and explicitly allows the characterization of aerosol fines by laser diffraction if the method is validated against a cascade impaction method despite the impossibility to differentiate between drug and excipient particles in LD.

The US Pharmacopoeia (General Chapter <601>) states that whenever possible “a method to determine the aerodynamic particle size distribution of the drug aerosol leaving the inhaler” should be used.

4 Geometric Particle Size Measurements

4.1 Laser Diffraction

The measurement of particle size by laser diffraction (LD) also named low angle laser light scattering (LALLS) is based on the principle that particles passing through a laser beam will scatter light at an angle that is directly related to their size: large particles scatter at low angles and small particles scatter at wide angles. Laser diffraction is described by the Fraunhofer approximation and the Mie theory with the assumption of spherical particle morphology. The Fraunhofer approximation can be used for calculation of size of particles much larger than the wavelength of the used laser and the diffraction signal is independent from optical properties. For particles below 1 μm Mie theory should be used in order to obtain correct calculations, which in turn requires knowledge of refractive indices.

It has to be taken into account that there might be a set of different optics (lenses) for different size ranges. It should be assured that the particle size distribution is located in the middle of the size range of the selected optic; otherwise the distribution might get cut at one side and with this, the result is adulterated. Further, the space between the device and the measurement zone can influence the result. This is especially true for devices where the particle cloud is altered due to evaporation (in MDI clouds) or further segregation (in a nasal spray). It has to be assured that the particle cloud is fully developed in the measurement zone, while avoiding to measure too far on the edge of the particle cloud. The particle collective to be measured is best dispersed by the device used for aerosol generation as this allows characterization of the interplay of formulation and dispersion characteristics of the device. The dose will only be dispersed as well as the device can do; hence, particles can still be agglomerated in parts when leaving the device. Device actuation can be performed manually, but often semi-automatic modules are applied which standardise device actuation and coordinate actuation and measurement such as the Malvern Spraytec or the Sympatec Sprayer for nasal sprays and Sympatec Inhaler module for pulmonary dosage forms. Here, pharmacopoeial requirements for inhalation products such as the use of a preseparator or an airflow corresponding to a certain pressure drop over the device can be applied either. For dry powder formulations, the particle size distribution upon total dispersion and the size upon device dispersion can differ significantly. In his case, size upon device dispersion in comparison to a completely dispersed sample can be taken as a measure for dispersion efficacy of the device, whereas the size upon dispersion itself gives a hint on aerodynamic behaviour. For pulmonary delivery, a theoretical fine particle fraction (FPF_{th}) can be calculated, which is the cumulative undersize below 5 μm of a fully dispersed (3 bar pressurised air) sample. This gives a first hint on aerodynamic capabilities although it has to be remembered that laser diffraction does not look at particle density and flight behaviour. Then, the same powder is dispersed by the respective device and again, cumulative undersize below 5 μm is determined from the volume distribution. If these two values are put into relation,

relative deagglomeration is calculated (Eq. (22.2)), which describes the ability of the device to fully disperse the powder.

$$Deagglomeration_{rel} = \frac{\text{cumulative undersize upon device dispersion}}{\text{cumulative undersize upon full dispersion (pressurised air)}} \times 100 \quad (22.2)$$

Time-resolved measurements are able to follow the whole spray duration from spray formation to stable phase and spray dissipation (Kippax and Fracassi 2003). These data allow not only determination of spray duration but also uniformity of particle size distribution over spray time. The concomitant measurement of optical concentration further indicates the spray phase where most of the formulation is dispersed. This is especially interesting for liquid formulations as differences in between the phases are more pronounced.

A drawback of the technique is that it cannot distinguish between particles of the active pharmaceutical ingredient (API) and excipient particles. Further, only the particles leaving the device can be measured, whereas it can happen that the majority of particles remain in the device. This can lead to misinterpretation in terms of relative deagglomeration. Here, it is important to look at the emitted dose (ED) as well, which should be as high as possible. Nonetheless, as laser diffraction is a fast technique compared to cascade impactor analysis, it is attractive to use this technique for characterisation of aerosols, although laser diffraction measures a geometric particle size, not a behavioural particle size. For routine analysis, comparative evaluation and development, comprising most in vitro applications, this can be appropriate. Then laser diffraction is highly reliable, can be automated and allows standardisation of the test conditions (de Boer et al. 2002).

4.2 Optical Particle Counters/Sizers

Optical particle counters (OPCs) are routinely used for real-time aerosol characterization in the particle size range of approximately 0.3–20 μm . They can be applied to everything from low concentration measurements such as clean room monitoring in ambient air to highly concentrated industrial aerosols, e.g. for industrial filter testing under realistic conditions (Heim et al. 2008). Most optical particle counters operate with visible or near infrared wavelengths (typically 500–1100 nm) as a very intense light source is needed to detect scattering from single particles. With this most of the aerosol size range is put in the Mie Scattering regime. Recent developments also use a white light source for sizing such as in the “White Light Aerosol Spectrometer” (WELAS) from PALAS (Karlsruhe, Germany).

Optical particle counters also named optical particle sizers (OPS) are an interesting alternative to laser diffraction, due to their accuracy and resolution in

obtaining number-based particle size distributions by measuring particle-induced light-scattering in a defined measurement zone. Whereas particle size can be derived from the scattered signal utilizing the Mie theory as explained for laser diffraction before, particle number can be determined by counting the pulses of scattered light reaching the detector. As this technique cannot handle multiple particles in the measurement zone which create a coincidence error, the challenge is to dilute the aerosol without a change in aerosol particle size and sample the aerosol into the OPC. Similar to laser diffraction, this technique cannot distinguish between excipient particles and drug particles or droplets.

4.3 Microscopy/Image Analysis

In image analysis, dimensions of individual particles (precisely, of two-dimensional projections of the particles) can be defined such as length, width, roundness and roughness. With this, particles can be defined with more parameters than one size value, which is interesting for irregular dry powder particles. Image analysis is used widely following high speed imaging of dispersed particles and can also be performed on Scanning Electron Microscopy (SEM) images, if the particles can be prepared for SEM. As image analysis relies on high number of measured particles, high speed camera-assisted measurement is mostly used. Here, particles need to be several micrometers in their dimensions in order to be capable for accurate measurement due to restrictions in resolution. Therefore, this technique is limited and works well for particles larger than 20 μm . Image analysis of particles in aerosols utilizing SEM images is often rather used for a verification of geometrical particle size being measured with other techniques. It is also useful for determination of habit and visualization of typical powder characteristics in interactive mixtures or engineered powders for inhalation.

5 Aerodynamic Particle Size Measurements

5.1 Cascade Impactor/Impinger

The European Pharmacopoeia (Ph. Eur.) Method Chapter 2.9.18 currently specifies one twin and three multistage impactors for the aerodynamic assessment of fine particles in both MDIs and DPIs:

- Ph.Eur. Apparatus A: Twin Impinger (Glass)
- Ph.Eur. Apparatus C: Multi-Stage Liquid Impinger (MSLI)
- Ph.Eur. Apparatus D: Andersen Cascade Impactor (ACI), (Fig. 22.2, left)
- Ph.Eur. Apparatus E: Next Generation Impactor (NGI), (Fig. 22.2, right)

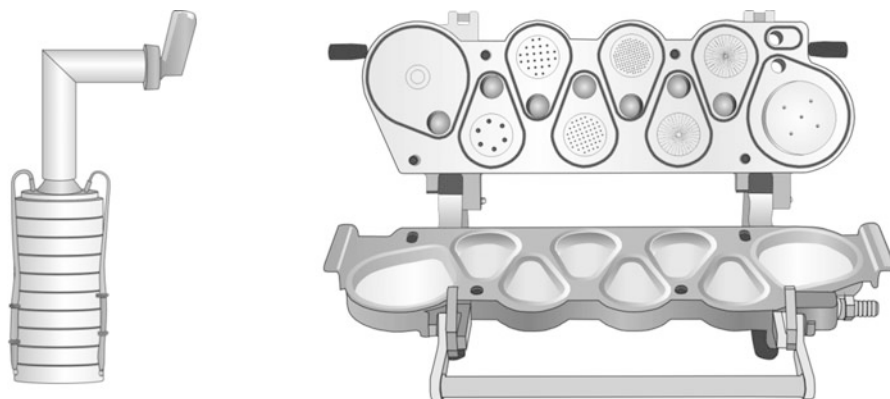


Fig. 22.2 Andersen cascade impactor (*left*) and next generation impactor, open (*right*)

Procedures for Apparatus A—Glass Impinger and Apparatus E—NGI (Chapter 2.9.44) are also specified for nebulizers.

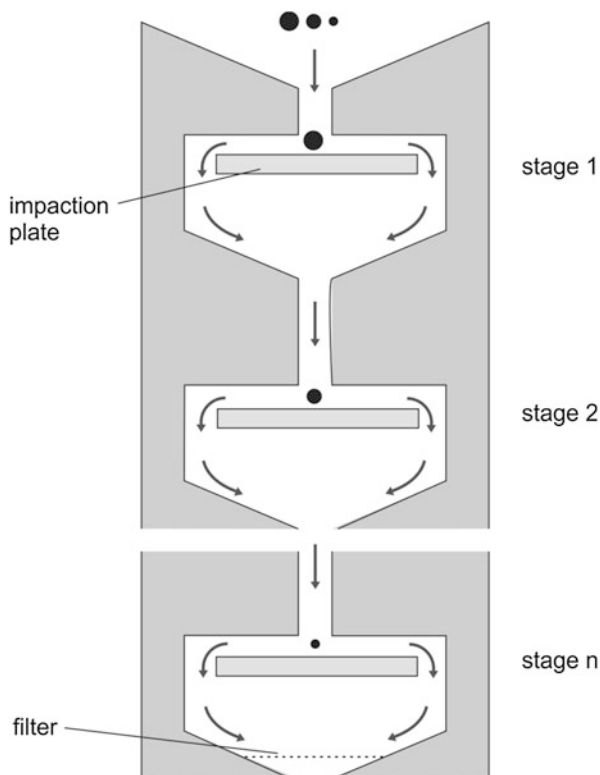
The United States Pharmacopeia (USP) Test Chapter <601> specifies six impactors suitable for aerodynamic size distribution:

- USP Apparatus 1 for MDIs: Andersen Cascade Impactor (ACI)
- USP Apparatus 2 for DPIs: Marple Miller Impactor (MMI)
- USP Apparatus 3 for DPIs: Andersen Cascade Impactor (ACI) + Preseparator
- USP Apparatus 4 for DPIs: Multi-Stage Liquid Impinger (MSLI)
- USP Apparatus 5 for DPIs: Next Generation Impactor (NGI) + Preseparator
- USP Apparatus 6 for MDIs: Next Generation Impactor (NGI)

The fundamental principle of this measurement technique, originally developed for collection of microbiota from air, is the separation of particles according to their flight behaviour in flowing air and collection thereof on different stages where they deposit due to impaction (Fig. 22.3).

In a classical impactor such as the MSLI or the ACI a set of nozzles with decreasing nozzle size is stacked onto each other having collection plates in between. This setup is transferred to horizontal in the Next Generation Impactor (NGI), which is therefore easier to use. With decreasing nozzle size, air velocity is increased and hence, increasingly smaller particles will impact on the respective collection plate. Each stage is designed to have a certain cutoff diameter, which also is a function of flow velocity. Different impactors differ in the cutoff precision and number of stages and continuous calculation of stage cutoffs for a wide range of flow rates (15–100 L/min) is only possible for the NGI (Marple et al. 2003a, b, 2004). The Twin Impinger is only calibrated for 60 L/min and the ACI only for 28.3 L/min. This excludes the use of these apparatus for other flow rates without further validation as it might be necessary for dry powder inhalers.

Fig. 22.3 Principle of particle collection in an impactor



Depending on the impactor used, details of the testing conditions differ. Generally, the impactor is assembled and prepared for collection, which in case of apparatus C requires introduction of collection fluid and in D and E also requires stage coating to minimize particle bounce and to capture particles touching the surface (e.g. by the use of silicon grease or a stage coating). The induction of aerosol is mediated by an induction port ("throat", a stainless steel tube with a 90° angle) on which the dispersion device is fitted by a customized sealing. The requested flow through the instrument is generated by a vacuum pump and must be adjusted prior to aerodynamic assessment. For testing, the device is primed, if necessary, and attached to the impactor inlet by the sealing. In MDI testing, the vacuum pump is started before, whereas for DPI measurements, the flow is started with a trigger box to exactly allow a flow time enough to drain the requested 4 L through the instrument. Actuation is repeated as often as needed to obtain an amount of drug which can be quantified precisely, but normally not more than ten times. Subsequently the apparatus is disassembled, collected particles on each stage are prepared for analysis by an appropriate technique and calculation of results is performed as outlined in the pharmacopoeial methods. A mass balance of 75–125 % recovery compared to the average emitted dose is requested for valid results. Particle size distribution can be displayed as the deposition on the stages and is

normally characterised by the mass median aerodynamic diameter (MMAD) and the geometric standard deviation (GSD). Further, fine particle dose (FPD) is used as a measure for the fraction of particles of the dose probably reaching the lung. Normally, it is defined as the percentage of the dose (total dose or emitted dose) having an MMAD $\leq 5 \mu\text{m}$. If peripheral (alveolar) deposition is targeted, an FPD $\leq 2 \mu\text{m}$ is calculated from the particle size distribution.

According to the European standard, nebulizers shall be tested at 15 L/min which is only possible with the NGI due to availability of a calibration at 15 L/min. To minimize evaporation and with this changes in droplet size, cooling of the impactor to 5 °C is requested which can be performed by cooling it for 90 min in the refrigerator prior to use. As drug output is constant, a mass balance is not meaningful and therefore must be replaced by appropriate recovery experiments. MDI formulations are tested at a flow rate of 28.3–30 L/min with flow continued for 5 s after the last actuation. For DPI assessment, a flow rate is applied which generates a 4 kPa pressure drop over the dispersion device used, but not more than 100 L/min, as specified in the pharmacopoeial method for uniformity of delivered dose. DPIs are often formulated with the use of larger carrier particles, from which the small particles targeting the lung are separated during inhalation; therefore, it is normally recommended to use a preseparator for separating these large carrier particles in order not to overload the first collection stage. A non-pharmacopoeial alternative is the fast screening impactor (Copley Scientific Ltd., Colwick, UK), an impactor which only separates two particle size classes for direct determination of fine particle fraction. Depending on the test airflow, different customized collection plates are available, but this setup does not give further information on particle size distribution.

5.2 *Time-of-Flight Based Measurements*

Time-of-flight analysis is based on differences in particle acceleration in an air stream, which is proportional to particle size and thus gives an aerodynamic size result. Particles dispersed in air are accelerated through a nozzle and pass two focused laser beams. The first scatter signal starts the clock, the second stops the clock. As the particles accelerate due to their aerodynamic size, this can be calculated from the time difference of the two signals and the air flow (Fig. 22.4). Similar to laser diffraction, the measurement cannot distinguish between drug particles and excipient particles (Mitchell and Nagel 1999). The Aerodynamic Particle Sizer from TSI (TSI Inc., Shoreview, MN, USA) concomitantly measures light-scattering intensity and aerodynamic size based on a time-of-flight evaluation of particles between 0.7–20 μm . This size restriction makes it unsuitable for particle sizing of the carrier part in carrier-based dry powder formulations or for other aerosols with larger particles/droplets such as nasal sprays or topical sprays, but it is well suitable for other inhalation drug products. The system originally was used in measurements of filters and diesel exhaust particles, but has been shown suitability

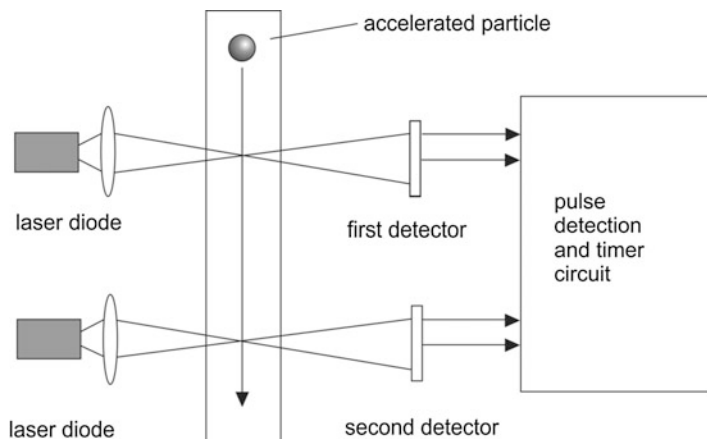


Fig. 22.4 General measurement principle of time-of-flight based particle sizing

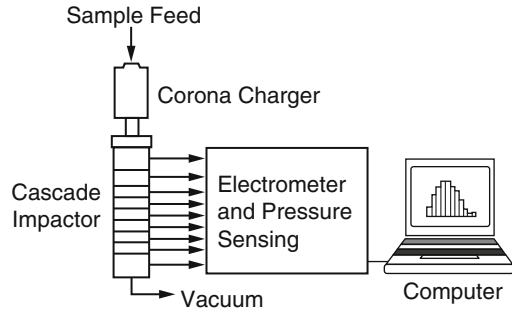
for pharmaceutical aerosols and is able to speed up analysis of MDIs significantly (Stein et al. 2003). It can be equipped with an induction port similar to impactor testing and if desired, it can be connected to a spectrometer to provide a chemically specific estimate of the dose.

5.3 *Electrical Low Pressure Impactor (ELPI)*

The ELPITM operating principle can be divided into three major parts: particle charging in a unipolar corona charger, size classification in a cascade impactor and electrical detection with sensitive electrometers (Fig. 22.5).

The particles are first charged into a known charge level in the charger. After charging the particles enter a cascade low pressure impactor with electrically insulated collection stages. The particles are collected in the different impactor stages according to their aerodynamic diameter, and the electric charge carried by particles into each impactor stage is measured in real time by sensitive multichannel electrometers (Dekati 2010; Marjamäki et al. 2000). This measured current signal is directly proportional to particle number concentration and size; hence, sample collection and quantification from the individual deposition stages is not necessary. A disadvantage of the ELPI is that it is only suitable for particles below 20 μm . As the ELPI is based on the measurement of charges, it can also be modified to be used for charge assessment of pharmaceutical aerosols (Glover and Chan 2004; Kotian et al. 2009) similarly to the electrical NGI (eNGI) (Hoe et al. 2009).

Fig. 22.5 Schematic of an electrical low pressure impactor (© Copyright Dekati Ltd. 2014)



6 Physiological Implication

6.1 Fine Particle Fraction = Lung Fraction?

Fine particle fraction is generally accepted as a measure for the amount of particles probably reaching the lung and hence, being therapeutically effective. The respiratory tract is a branched tree with 23 bifurcations with decreasing diameter and increasing surface. Active inhalation only reaches the major airways, where particles can hence deposit due to impaction. This is dependent on the patient's inhalation speed. The majority of the respiratory tract can only be reached by diffusion of particles, which then settle due to sedimentation. This is a major difference to aerodynamic particle sizing using impactor methods, which is based on the principle of impaction. Further, diffusion and sedimentation requires time and is thus dependent from the inhalation maneuver of the patient in terms of breath holding and speed of exhalation. For these reasons, it is difficult to predict deposition of a certain particle size in a certain region of the respiratory tract *in vivo*. It is widely accepted that smaller particles are able to enter to deeper areas of the lung whereas larger particles tend to deposit in the larger airways. This was confirmed *in vivo* by the use of different monodisperse particle preparations, where deposition *in vivo* could be followed by gamma scintigraphy or similar techniques (Carvalho et al. 2011). It was also reported that there is a certain minimum in particle deposition in the lung when reaching an aerodynamic particle size in the submicron range, whereas lung deposition increases again in the lower nanometre scale (Hinds 1999). Nonetheless, determination of a "respirable fraction" of an aerosol by impactor studies rather allows a qualitative correlation to particle deposition in the peripheral lung (Hickey et al. 1996).

It has to be kept in mind that impactor studies are far from mimicking the *in vivo* situation: The impactor is run at constant airflow, whereas inhalation follows a patient individual profile. The impactor inlet is a 90° angle tube, whereas the human throat is a complicated structure with bends serving as baffles for inhaled particles. Therefore, for coming closer to an *in vitro in vivo* correlation (IVIVC), more realistic anatomical models for parts of the airways (e.g. throat) are investigated

(Byron et al. 2010). Further, computer simulation of particle deposition in realistic anatomical models using computational fluid dynamics (CFD) may be a useful approach (de Backer 2012).

7 Accessories to Mimic the In Vivo Situation

All aerosol particle sizing techniques are significantly different from the in vivo situation; nonetheless there are some possibilities with which in vitro particle sizing and determination of total lung dose gives a more realistic estimate of the total lung dose in vivo.

7.1 *Throat Model*

One accessory is a realistic throat model which can be used instead of the 90° angle induction port for impactor measurements. It is easy to understand that a human throat is far from a stainless steel tube with polished inner walls. Further, the human throat exhibits a highly patient-individual geometry. Therefore, an idealized throat model was developed at the Aerosol Research Laboratory of Alberta, Canada (Stapleton et al. 2000) and has been shown to closely mimic the aerosol and flow motion within a human throat. Currently, different mouth-throat models are available for more realistic in vitro assessment of total lung dose (Byron et al. 2013).

7.2 *Inhalation Profile*

Another important point is the flow rate at which aerodynamic particle size is assessed. It has been shown by numerous studies that even patients with severe inhalation impairment are able to generate a pressure drop of 4 kPa over a dry powder inhalation device resulting in a sufficient airflow to disperse the formulation. But in reality, inhalation flow is not at a constant flow rate, but flow is rapidly increasing, reaching a maximum, before it slowly decreases again. Hence, it would be more realistic to use inhalation flow profiles for testing (Olsson et al. 2013; Byron et al. 2013) which is technically possible by the introduction of a mixing inlet securing constant airflow through the cascade impactor, while varying flow rates are taken through the device mimicking the patient inhalation.

8 Which Technique to Choose?

- Ideally, the measurement technique should not perturb the aerosol being evaluated, since the process of moving the aerosol to the measurement instrument may alter the size distribution by premature deposition, droplet size reduction due to evaporation or size enlargement due to hygroscopicity or aggregation.
- The chosen technique needs to be suitable for the expected size range of the aerosol particles.
- If possible, dispersion for sizing should be performed the same way and utilizing the same device than used with the drug product.
- The chosen instrument should possess a suitable aerosol inlet and possibly a dilution option.
- It has to be thought about the necessity of chemical drug quantification.
- If particle sizing has to be performed within regulatory requirements, choice of technique should take into account the respective regulations.

References

- Byron PR, Hindle M, Lange CF, Longest PW, McRobbie D, Oldham MJ, Olsson B, Thiel CG, Wachtel H, Finlay WH (2010) In vivo–in vitro correlations: predicting pulmonary drug deposition from pharmaceutical aerosols. *J Aerosol Med Pulm Drug Delivery* 23:S59–S69
- Byron PR, Wei X, Delvadia RR, Longest PW (2013) Standardizing in vitro test methods to support aerosol drug evaluation in the clinic. *Respir Drug Deliv* 1:85–92
- Carvalho TC, Peters JI, Williams RO III (2011) Influence of particle size on regional lung deposition—what evidence is there? *Int J Pharm* 406:1–10
- de Backer J (2012) Novel imaging in assessing small airway disease and therapy. In: *Proceedings of DDL 23*. Edinburgh, Scotland
- de Boer AH, Gjaltema D, Hagedoorn P, Frijlink HW (2002) Characterization of inhalation aerosols: a critical evaluation of cascade impactor analysis and laser diffraction technique. *Int J Pharm* 249:219–231
- Dekati (2010) Dekati ELPI: electrical low pressure impactor. Tampere
- Glover W, Chan H-K (2004) Electrostatic charge characterization of pharmaceutical aerosols using electrical low-pressure impactation (ELPI). *Aerosol Sci* 35:755–764
- Heim M, Mullins BJ, Umhauer H, Kasper G (2008) Performance evaluation of three optical particle counters with an efficient "multimodal" calibration method. *J Aerosol Sci* 39:1019–1031
- Hickey AJ, Martonen TB, Yang Y (1996) Theoretical relationship of lung deposition to the fine particle fraction of inhalation aerosols. *Pharm Acta Helv* 71(3):185–190
- Hinds WC (1999) *Aerosol technology—properties, behavior and measurement of airborne particles*. John Wiley & Sons
- Hoe S, Young PM, Chan H-K, Traini D (2009) Introduction of the electrical next generation impactor (eNGI) and investigation of its capabilities for the study of pressurized metered dose inhalers. *Pharm Res* 26(2):431–437
- Kippax P, Fracassi J (2003) Particle size characterisation in nasal sprays and aerosols. LabPlus International

- Kotian R, Peart J, Bryner J, Byron PR (2009) Calibration of the modified electrical low-pressure impactor (ELPI) for use with pressurized pharmaceutical aerosols. *J Aerosol Med Pulm Drug Deliv* 22(1):55–66
- Marjamäki M, Keskinen J, Chen D-R, Pui DYH (2000) Performance evaluation of the electrical low-pressure impactor (ELPI). *J Aerosol Sci* 31(2):249–261
- Marple VA, Olson BA, Santhanakrishnan K, Mitchell JP, Murray SC, Hudson-Curtis BL (2003a) Next generation pharmaceutical impactor (a new impactor for pharmaceutical inhaler testing). Part II: archival calibration. *J Aerosol Med* 16(3):301–324
- Marple VA, Roberts DL, Romay FJ, Miller NC, Truman KG, Van Oort M, Olsson B, Holroyd MJ, Mitchell JP, Hochrainer D (2003b) Next generation pharmaceutical impactor (a new impactor for pharmaceutical inhaler testing). Part I: design. *J Aerosol Med* 16(3):283–299
- Marple VA, Olson BA, Santhanakrishnan K, Roberts DL, Mitchell JP, Hudson-Curtis BL (2004) Next generation pharmaceutical impactor: a New impactor for pharmaceutical inhaler testing. Part III. Extension of archival calibration to 15 L/min. *J Aerosol Med* 17(4):335–343
- Mitchell JP, Nagel MW (1999) Time-of-flight aerodynamic particle size analyzers: their use and limitations for the evaluation of medical aerosols. *J Aerosol Med* 12(4):217–240
- Olsson B, Borgström L, Lundbäck H, Svensson M (2013) Validation of a general in vitro approach for prediction of total lung deposition in healthy adults for pharmaceutical inhalation products. *J Aerosol Med Pulm Drug Delivery* 26(6):355–369
- Stapleton KW, Guentsch E, Hoskinson MK, Finlay WH (2000) On the suitability of k - ϵ turbulence modeling for aerosol deposition in the mouth and throat: a comparison with experiment. *J Aerosol Sci* 31(6):739–749
- Steckel H, Bolzen N (2004) Alternative sugars as potential carriers for dry powder inhalations. *Int J Pharm* 270(1–2):297–306
- Stein SW, Myrdal PB, Gabrio BJ, Obereit D, Beck TJ (2003) Evaluation of a new aerodynamic particle sizer spectrometer for size distribution measurements of solution metered dose inhalers. *J Aerosol Med* 16(2):107–119

Part VII
Rheological Techniques

Chapter 23

Rheology in Pharmaceutical Sciences

Johanna Aho, Søren Hvidt, and Stefania Baldursdottir

Abstract Rheology is the science of flow and deformation of matter. Particularly gels and non-Newtonian fluids, which exhibit complex flow behavior, are frequently encountered in pharmaceutical engineering and manufacturing, or when dealing with various *in vivo* fluids. Therefore understanding rheology is important, and the ability to use rheological characterization tools is of great importance for any pharmaceutical scientist involved in the field. Flow can be generated by shear or extensional deformations, or a combination of both. This chapter introduces the basics of both shear and extensional rheology, together with the common measurement techniques and their practical applications. Examples of the use of rheological techniques in the pharmaceutical field, as well as other closely related fields such as food and polymer science, are also given.

Keywords Elasticity • Extensional rheology • Interfacial rheology • Oscillatory shear deformation • Polymer melts and solutions • Rheology • Steady shear flow • Viscoelasticity • Viscosity

1 Introduction

Traditionally variables such as pH, temperature, surface tension, ionic strength, osmolarity, and composition have been used to characterize liquid or semi-solid formulations. However, complex liquids are dynamic systems with related variables that are hard to distinguish.

Rheology is the science of flow and deformation of matter and is a well-known method in the food industry where it is applied on various food products to analyze e.g. mouth feel, chewability and the ease to swallow. Most pharmaceutical systems contain one or more macromolecular excipients and their physicochemical

J. Aho • S. Baldursdottir (✉)
Department of Pharmacy, University of Copenhagen, Copenhagen, Denmark
e-mail: stefania.baldursdottir@sund.ku.dk

S. Hvidt
The Department of Chemistry – Institute of Science and Environment, Roskilde University,
Roskilde, Denmark

properties are important for the performance of the end product, and thus rheological behavior becomes a critical quality attribute. Additionally, as the human body contains on average 60 % water and thus is mostly composed of various complex fluid systems, physicochemical properties like the rheology of the complex *in vivo* fluids can play a crucial role in the outcome of any pharmacotherapy. Hence, the knowledge on the rheological behavior of many pharmaceutical systems is crucial in order to understand the stability, bioavailability and absorption of the active pharmaceutical ingredient (API) in the human body.

The following chapter will give a short introduction to the theory of rheology and give practical examples of its utility in the field of pharmacy and how both shear and extensional rheology can help in characterizing various pharmaceutically relevant systems.

2 Theoretical Background and Fundamental Concepts

2.1 Shear Rheology

Rheology is the study of flow and deformation of matter. When external forces are applied to a system it can either change form or change volume or a combination of both effects. Simple elongation (simple extension), which will be discussed in Sect. 2.2.1, in general involves both effects (Fig. 23.1c).

Shear deformations are characterized by a change of shape but no volume change. Simple shear and simple elongation give the same information about the material properties as long as the volume does not change during deformations. When forces are applied to a system the deformation response depends on area and height of the system. In order to obtain information about material characteristics relative forces and deformations are therefore needed. Shear stress is defined as the shear force divided by area of system, $\sigma = F/A$, and the relative deformation is given by the strain defined by deformation divided by height, $\gamma = \Delta x/h$ (Fig. 23.1).

A simple shear geometry (cone-and-plate geometry) is illustrated in Fig. 23.2a. This type of deformation is used in most modern rotational rheometers. In this geometry all parts of the sample experience the same strain and the deformation is homogenous. The shear rate, $\dot{\gamma}$, is defined as the time-derivative of the shear strain. In the flow of a liquid between two plates the shear rate is simply given by the rate of the moving plate divided by the distance between the plates shown in Fig. 23.2b. Flow through capillaries and pipes are also used to measure shear deformations, but deformations are inhomogeneous with zero shear rate in the center of the pipe and maximal rates at the pipe surface. Cone-and-plate and concentric cylinder tools (Fig. 23.2c) ensure homogenous deformation in rotational rheometers, whereas the plate-and-plate tools result in inhomogeneous shear deformations.

A rheometer is any instrument that enables determination of rheological properties. Very simple rheometers such as capillaries have been used for centuries to

Fig. 23.1 Deformation (Δx) in (a) simple shear and (b) simple oscillatory shear of a system, with height h , surface area A , and shear stress σ and (c) extensional deformation (extension ratio l/l_0) in simple uniaxial stretching

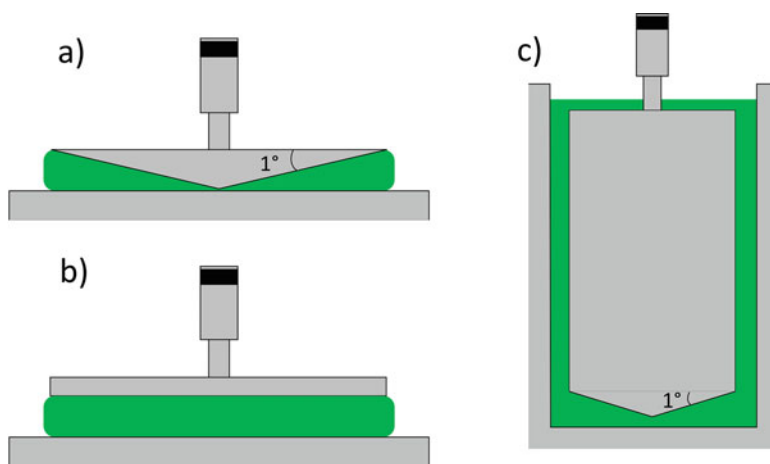
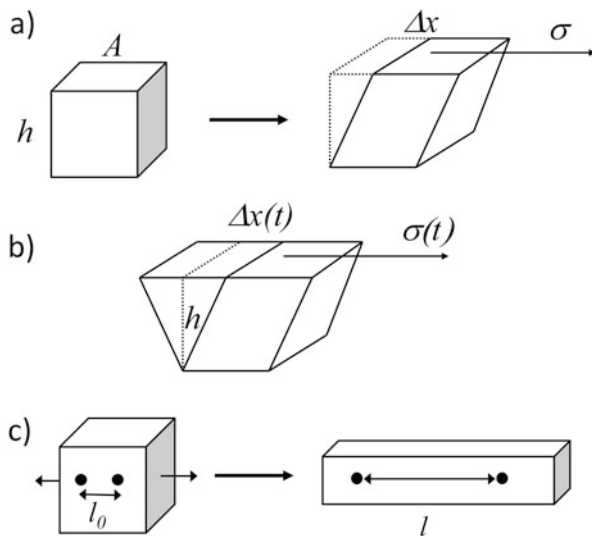


Fig. 23.2 Geometries used in shear rheology measurement on rotational rheometers (a) cone-and-plate, (b) plate-plate, and (c) concentric cylinders (Couette)

determine flow of liquids. Modern rheometers allow a more precise quantification of material properties in well-defined geometries, and they can be divided into two main types. In a controlled rate type (CR) instrument, a motor, often controlled by a computer, deforms the sample in a controlled manner and a force transducer monitors the force or torque resisting the deformation of the sample. The strain or strain rate is controlled and the forces or stresses are measured. In a controlled stress (CS) type instrument, a stress is applied to the sample and the resulting deformation is monitored. The flow of a liquid through a simple capillary viscometer is an

example of a CS type instrument where gravity determines the stress and the flow rate is determined from the flow time of a fixed volume of the flowing liquid.

Most modern rheometers are rotational type instruments. The sample to be measured is confined in a narrow gap between a stationary and a moving part of a measuring cell. Different measuring cells are used depending on the sample properties. The most common measuring cells are cone-and-plate, parallel plate (plate-plate), and concentric cylinders (Couette).

Two signals from a rotational rheometer, the angular position of the moving part and the torque, are used to compute strains and stresses. A position sensor registers the angular position of the moving cell part. The angle of rotation, ϕ , is proportional to the strain and the proportionality constant depends on gap size and geometry. The stress is proportional to the torque (force times lever arm length) and the proportionality constant depends on the cell geometry and especially on the surface area of the measuring tool. Tools with a large area are used for soft materials and low viscosity liquids, whereas smaller tools are used for harder materials. A summary of proportionality constants for various geometries can be found in the book “Viscoelastic properties of polymers” (Ferry 1980).

2.1.1 Ideal Model Systems

Many of the materials encountered in pharmacy are complex systems displaying both viscous and elastic properties. In order to understand such systems knowledge of the characteristic properties of simple model systems is important. These extreme models are the ideal elastic material and the ideal Newtonian liquid. A spring is an example of an ideal Hookean elastic material where the resulting extension of the spring is proportional to the force applied. Ideal isotropic elastic materials in rheology follow Hooke’s law with proportionality between stress and strain

$$\sigma = G\gamma \quad (23.1)$$

The proportionality constant G is the (elastic) shear modulus. Typical values are 10^3 Pa for many gels, 10^6 Pa for rubber networks, and about 10^{10} Pa for wood, glass and metals. For an ideal elastic material G is independent of strain, time, and shear rate, but it will often depend on temperature and to a lesser extent on pressure. A Hookean solid in a deformed state will remain deformed at constant strain as long as the applied stress persists and recover completely when the stress is removed. The energy needed to deform the elastic solid is stored in the sample and can be recovered. Knowledge of the G value enables prediction of the strain or stress in any type of deformation for an ideal elastic system.

In contrast, the other extreme model system is an ideal Newtonian liquid where a constant flow will persist as long as a stress is applied. For an ideal Newtonian liquid the flow rate and hence the shear rate will be proportional to the stress applied

$$\sigma = \eta \dot{\gamma} \quad (23.2)$$

where the proportionality constant, η , is the shear viscosity, which is independent of strain, strain rate, and time for an ideal Newtonian liquid. It does, however, depend on temperature and to a lesser extent on pressure. The SI unit of viscosity is seen from Eq. (23.2) to be Pa · s, and in older literature Poise (P) with $10 \text{ P} = 1 \text{ Pa} \cdot \text{s}$. Typical values at room temperature are $10^{-3} \text{ Pa} \cdot \text{s}$ for water and $1 \text{ Pa} \cdot \text{s}$ for glycerol. When a constant stress is applied to such a liquid it will flow at a constant rate determined by the viscosity of the liquid and the applied stress. When the stress is removed flow will cease and there will be no recovery in strain. The energy needed to maintain the flow will be dissipated as thermal energy in the liquid. Eq. (23.3) shows that the energy needed per volume and time, \dot{E} , to maintain a shear flow is given by

$$\dot{E} = \eta \dot{\gamma}^2 \quad (23.3)$$

Energy dissipation, and hence a resulting temperature increase, should be considered for liquids with high viscosities and at high shear rates. An effective temperature control is therefore especially needed under such conditions. Knowledge of the η value enables prediction of the rate and strain in any type of deformation for an ideal viscous system.

2.1.2 Non-Newtonian Liquids

Real materials are, except for very simple systems, in general neither ideal solids nor ideal liquids. The deformation response depends on how fast the material is deformed. If deformations are fast, molecular rearrangements in materials cannot take place and materials will be deformed elastically. However, if the same material is deformed slowly, the molecules can re-organize and relax and often flow like a liquid. Materials, which exhibit both elastic and liquid-like properties, are called viscoelastic. The practical use of rheological experiments is to quantify the viscoelasticity of materials over as wide a range of time, rate and deformation scales as possible, and often to relate these viscoelastic properties to the molecular structure of the material and different components in formulations.

Non-Newtonian liquids are liquids that cannot be characterized by a constant viscosity. Many pharmaceutical systems, including suspensions, emulsions and polymer solutions, show a constant viscosity only at low shear rates (zero-shear viscosity, first Newtonian plateau) but a decreasing viscosity (shear thinning) above a characteristic shear rate. Flow curves are plots of viscosity against shear rate, most often on log-log scales, and allow determinations of the zero shear rate viscosity, the critical shear rate (onset of shear thinning), and how rapidly the viscosity decreases at high rates. A linear decrease is often observed at high rates on a log-log plot, which shows that the viscosity follows a power-law. An example of

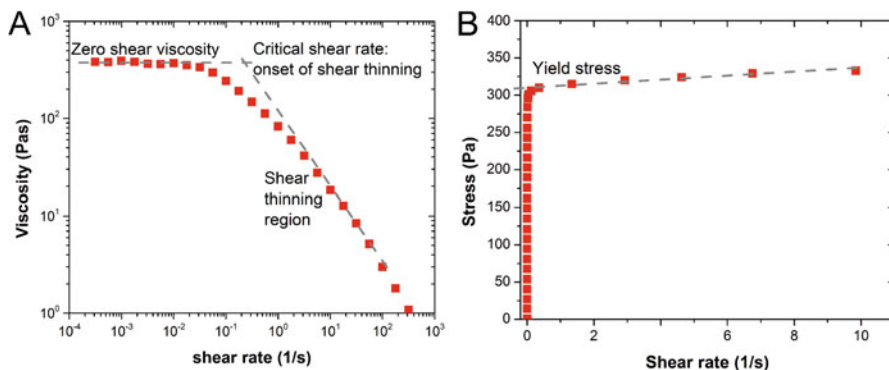


Fig. 23.3 (a) A flow curve of a high molecular mass polymer in semi-dilute solution. (b) A stress ramp is applied to a micellar suspension and shear rates are measured. A vanishing shear rate is observed at low stresses. Above a critical stress the suspension flows and the slope is the Bingham viscosity. The intercept at vanishing shear rates is a measure of the yield stress

a high molecular mass polymer in a semi-dilute solution where the polymers overlap and are entangled is shown in Fig. 23.3a. The exponent should always be between 0 (Newtonian liquid) and -1 (limit of indeterminate flow). The critical shear rate is related to the inverse of the longest relaxation time of the system. At low shear rates the friction in this solution is high because of this entangling of chains. At higher shear rates the polymer chains disentangle and orient in the flow with less friction and hence a lower viscosity.

Flow curves can also be used to determine yield stresses of elastic materials. If the shear rate is measured with increasing steady stresses (stress ramp), the elastic properties will dominate at small stresses, with a vanishing shear (flow) rate (Fig. 23.3b). At stresses above the yield stress, structures will be broken and the system will flow. The example in Fig. 23.3b is typical for many systems and is referred to as a “Bingham liquid”, with a Bingham viscosity, η_B , which is the slope of the curve at higher stresses and a yield stress corresponding to the intercept of this curve at vanishing shear rates. Empirical information about the amount of stress that a sample can withstand before it is damaged and flows, often called a yield stress, is generally useful for studies of samples such as suspensions and gels.

2.1.3 Oscillatory Measurements

When a constant stress is applied to an ideal elastic material, a constant strain is obtained (Eq. (23.1)) and corresponds to zero shear rate (or zero flow). Ideal elastic materials are therefore characterized by an infinite viscosity (Eq. (23.2)). As a result, viscosity measurements of elastic and many viscoelastic systems under steady shear are of limited use. Furthermore, in many cases deformation caused by a steady shear rate will destroy fragile structures in the sample and provide little information about the unperturbed properties of the system.

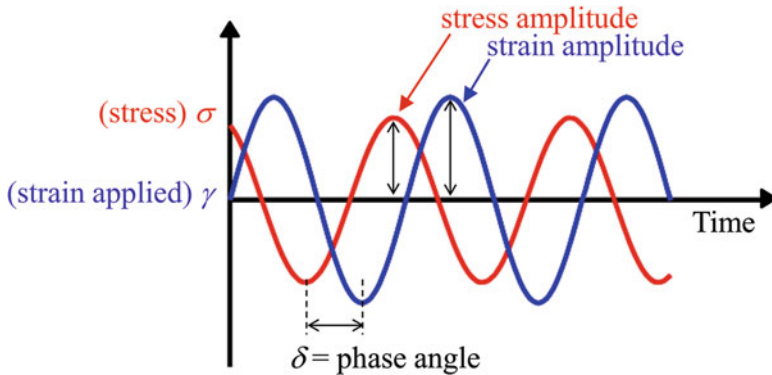


Fig. 23.4 Schematic illustration of the applied force and strain in an oscillatory shear measurement

Viscoelastic materials are therefore frequently studied by applying small amplitude oscillatory stresses or strains to the sample rather than steady flows (Fig. 23.4).

If an oscillatory strain deformation with an amplitude γ_0 and an angular frequency ω is applied, the stress will also oscillate in time t with the same frequency but it will be phase shifted by δ , the phase angle, relative to the strain

$$\gamma(t) = \gamma_0 \sin \omega t \quad (23.4a)$$

$$\sigma(t) = \sigma_0 \sin(\omega t + \delta) \quad (23.4b)$$

where σ_0 is the stress amplitude and the angular frequency ω (in rad/s) equals $2\pi f$, where f is the frequency in Hz. The phase shift δ is always between 0 and 90° . For an ideal elastic system the phase shift is 0° as seen from Eqs. (23.1) and (23.4a), and for an ideal Newtonian liquid it is always 90° as seen from Eqs. (23.2) and (23.4a) (differentiation of the strain with respect to time in Eq. (23.4a) will result in a shear rate which depends on $\cos \omega t$, which is phase shifted by 90° relative to $\sin \omega t$) (Fig. 23.4). Materials with phase shifts between 0 and 90° are viscoelastic and the stress in Eq. (23.4b) can be written as a sum of elastic and loss contributions

$$\sigma(t) = \gamma_0 \left(G' \sin \omega t + G'' \cos \omega t \right) \quad (23.5)$$

In this equation, G' is referred to as the elastic storage shear modulus because it is associated with energy storage. Likewise, G'' is the loss shear modulus because it is related to the viscous properties and associated with energy loss in the sample during an oscillatory deformation. For an ideal Newtonian liquid $G'' = \omega\eta$ and $G' = 0$, which shows that no energy is stored in the sample. For an ideal elastic system $G' = G$ and $G'' = 0$, which shows that no energy is lost during deformation. For viscoelastic materials G' and G'' will in general depend on angular frequency and the elastic properties will often dominate at high frequencies. Small amplitude

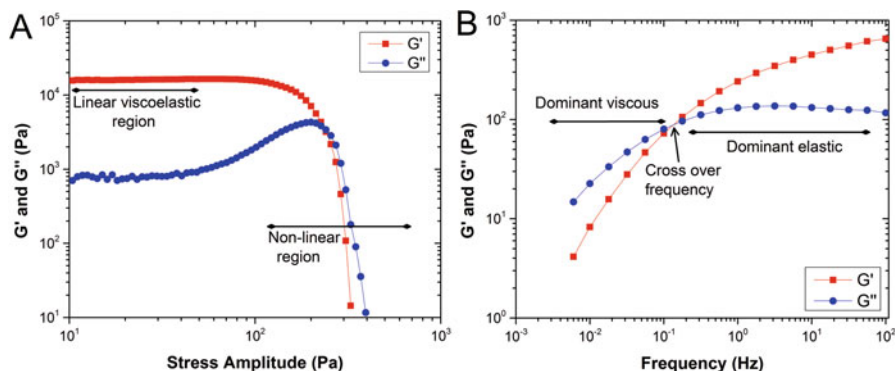


Fig. 23.5 (a) A stress amplitude sweep of a viscoelastic micellar gel and (b) a frequency sweep of a viscoelastic polymer solution

oscillatory measurements are especially useful for monitoring structure development as a function of time or temperature at a fixed frequency.

According to Eqs. (23.1) and (23.4a), stress is proportional to strain or strain amplitude. This is valid for all materials at small strains or amplitudes, and is called the linear elastic or viscoelastic range. At larger strains or strain amplitudes, stress and strain will not be proportional and the material will be in the non-linear range. An example of a stress amplitude sweep is depicted in Fig. 23.5a where the linear elastic or viscoelastic range is seen at stress amplitudes from 10 to 60 Pa, followed by the non-linear range above 60 Pa.

Oscillatory measurements at low strain or stress amplitudes allow a determination of G' and G'' as a function of frequency. Such measurements are important because they can give information about both structure and dynamics. For viscoelastic liquids G'' dominates at low frequencies. At higher frequencies, relaxation of structures cannot take place within the oscillation cycle, resulting in an increase in G' . An example of a frequency sweep is given in Fig. 23.5b, which shows the frequency dependencies of a high molar mass hyaluronic acid solution. The figure illustrates that G'' dominates at low frequencies, where G'' is related to the zero shear rate viscosity and angular frequency through $G'' = \omega\eta$. At higher frequencies G' dominates and a plateau is nearly detected, as expected for an ideal elastic material. The crossover angular frequency is approximately the inverse of the longest relaxation time, which for long polymer chains is strongly dependent on molecular mass and concentration.

2.1.4 Creep and Relaxation Measurements

Steady shear and oscillatory measurements are probably the two most important types of rheological measurements. However, other types of measurements can give more relevant information for some pharmaceutical systems. Suspensions

experience a sustained force due to gravity, and it is therefore also useful to monitor how such systems deform under a constant load or stress. This type of measurement is called a creep experiment, and in such an experiment the strain $\gamma(t)$ is monitored as a function of time for a fixed applied stress σ_0 . The compliance J is then obtained from the time dependence of the strain as

$$J(t) = \gamma(t)/\sigma_0 \quad (23.6)$$

After a certain time period under a constant stress, the stress can be removed and the system's ability to recover towards the original un-deformed state can be investigated in a creep-recovery experiment. Creep experiments are of interest primarily for viscoelastic materials. The elastic properties are seen in the rapid deformation and in the recovery when the stress is applied or removed, respectively. The slow subsequent deformation is characteristic of the viscoelastic time-dependent processes in materials. If this deformation (strain) increases linearly with time, one can obtain the viscosity at a low shear rate based on the inverse relationship between viscosity and the slope. The viscous or plastic deformation can also be calculated from the non-recoverable compliance at long times. Creep tests are of special interest for viscoelastic systems with long relaxation times, because they can be used to measure flow at very low shear rates.

Creep experiments are generally performed on a controlled stress (CS) type instrument, which applies a defined stress and measures the resulting changes in strain with time. A closely related type of experiment, stress relaxation, can be performed on controlled rate (CR) type instruments. In a stress relaxation experiment, the sample is rapidly deformed to a fixed strain, γ_0 , and the stress is monitored as a function of time. The shear stress relaxation modulus, $G(t)$, is then calculated as

$$G(t) = \sigma(t)/\gamma_0 \quad (23.7)$$

The relaxation modulus contains information about how rapidly structures can reorganize and relax to relieve the stress in the system. For an ideal elastic system $G(t) = G$ at all times, and for an ideal Newtonian liquid $G(t) = 0$ since the shear rate and hence the stress is zero at constant strain. For a viscoelastic material $G(t)$ will decrease with time and the decrease will occur on a time scale which is determined by the distribution of relaxation times of the sample. At long (infinite) times the relaxation modulus will either relax to zero (characteristic of all liquids) or reach a constant value which will be the equilibrium elastic modulus of the system characteristic of a viscoelastic solid.

2.1.5 Capillary Flow: Capillary Viscometers

Capillary viscometers have been used for centuries to measure viscosities of especially low viscosity liquids, where even modern rheometers lack their sensitivity and precision. Flow through capillaries, dip-cups, extruders and pumping

through pipes are important in delivery systems and in production. Measurements at low concentrations furthermore enable determination of intrinsic viscosities, which are sensitive to solvent-solute interactions and molar mass of solutes.

In the general case a pressure-drop ΔP is applied over a capillary or pipe with radius R and length l . The flow rate (volume per time) Q of a Newtonian liquid passing through the pipe is given by

$$Q = \frac{\pi R^4 \Delta P}{8 \eta l} \quad (23.8)$$

where η is the shear viscosity. A major problem with capillary and pipe flow is that the flow rate and shear rate are not constant in the liquid. There is maximal flow rate but zero shear rate of the liquid in the center of the pipe, whereas the shear rate is maximal and the flow rate zero at the wall of the pipe. The maximal shear rate at the wall is given by

$$\dot{\gamma}_{max} = \frac{4Q}{\pi R^3} \quad (23.9)$$

The use of capillary viscometers for shear thinning solutions is therefore problematic, since the shear rate is not defined, and plug flow can be expected. Well known examples of plug flow are squeezing pastes and cremes from a tube. In a classical capillary viscometer gravity forces a liquid through the capillary. The time it takes a fixed volume to pass through the capillary is measured. This time is proportional to viscosity divided by density, the so-called kinematic viscosity with units of Stokes. The kinematic viscosity of water at room temperature is 1 cS or 1 (mm)²/s.

2.1.6 Capillary Flow: Capillary Rheometers

For the pressure-driven flow, capillary rheometers with circular or rectangular slit die geometry are commonly used (Fig. 23.6). The sample, usually in granules, pellets or powder form, is fed into the rheometer barrel that is pre-heated to the desired temperature, and the molten material is then extruded through the die at a defined piston speed. When a circular capillary die is used, the melt pressure is recorded in the barrel above the die entrance, and this requires taking into account the extra pressure drop caused by the contraction of the flow from the barrel into the capillary. In a slit die, the flat wall geometry enables measurement of pressure directly in the slit where the flow is fully developed, thus making exact determination of the pressure profile possible. Slit dies are, however, more difficult to assemble and to disassemble and the cleaning of the slit edges requires more effort (Nelson 2003).

The volume flow rate in the barrel can be calculated from the barrel/piston radius R_p and piston speed V_p as $Q = \pi R_p^2 V_p$. The apparent shear rate, that is, the shear rate

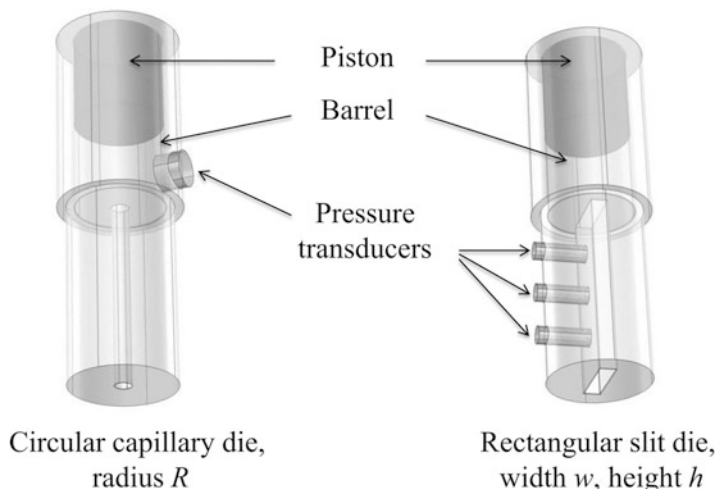


Fig. 23.6 Principle of capillary rheometer with (a) circular capillary die, where the pressure is measured in the barrel before the entrance into the capillary and (b) rectangular slit die, where the slit geometry allows placing the pressure transducer(s) directly on the slit wall

for a Newtonian fluid, at the capillary wall can be determined in a circular capillary die by Eq. (23.9). However, for the rectangular slit die the apparent shear rate at the wall is

$$\dot{\gamma}_{wa} = \frac{6Q}{h^2w} \quad (23.10)$$

where h and w are the slit height and width. The term “apparent” is used because of the plug-like flow profile typical for shear thinning fluids, which means that the shear rate is higher than predicted for Newtonian fluids with a parabolic velocity profile. The true shear rate is calculated by multiplying the apparent values in Eqs. (23.9) and (23.10) by a correction factor achieved using the Rabinowitch correction procedure (for details, see for example (Morrison 2001)). From the pressure measured at the die entrance, Δp , and the additional pressure drop caused by the contraction flow at the capillary entrance, Δp_e , determined using a so called Bagley correction method (Bagley 1957), the true shear stress at the circular capillary die wall is calculated as

$$\tau_w = \frac{\Delta p - \Delta p_e}{2(L/R)} \quad (23.11)$$

where L/R is the length-to-radius ratio of the capillary die. Bagley correction requires measurements with at least two dies that have the same diameter but different length. For a slit die the true wall shear stress is calculated directly from

the pressure profile $\Delta p/l$, the pressure difference between two pressure readings on the die wall at distance l from each other.

$$\tau_w = \frac{h}{2} \frac{\Delta p}{l} \quad (23.12)$$

Conventional, industrial scale capillary rheometer tests usually require a large sample amount (barrel volume $\sim 25 \text{ cm}^3$) particularly for the measurement at high shear rates.

2.2 Extensional Rheology

In extensional flow (also called elongation or elongational flow) the material undergoes stretching *along* the streamlines. Thus it differs from the shear deformation where the distance between two fluid particles on the same streamlines remains constant.

Extensional flow can be classified into three different types. Uniaxial extension is the simplest form of extensional flow: stretching of the material at a velocity, v_I , imposes the strain rate, $\dot{\epsilon}$, in direction x_I and compression ($-\frac{1}{2}\dot{\epsilon}$) in the perpendicular directions x_2 and x_3 . In biaxial extension the velocity profile is the same as for uniaxial flow, but the extension rate is always negative (compression) in the loading direction, whereas for uniaxial flow it is always positive (tension). In planar extension one dimension of the material is extended while the second one is maintained constant and the third one compressed (Fig. 23.7) (Dealy and Wissbrun 1999; Dealy and Larson 2006).

In uniaxial extension the particles accelerate, so that the distance between the particles on the same flow stream lines (depicted in Fig. 23.1c) increases exponentially with time. Thus, typically extension produces a rapid deformation, compared to shear flow:

$$\frac{l}{l_0} = e^{\dot{\epsilon}t} \quad (23.13)$$

where l_0 is the initial sample length and l the length at time t . Stretching at a constant strain rate $\dot{\epsilon}$ results in a final logarithmic strain $\epsilon = \dot{\epsilon}t = \ln(l/l_0)$; note that “strain” in this context is a natural logarithm of the extension ratio, $\ln(l/l_0)$, whereas in the study of solid materials, the simple extension ratio l/l_0 is called “strain”. Usually, in order to distinguish between these, ϵ and $\dot{\epsilon}$ are called Hencky strain and Hencky strain rate, after the German engineer Heinrich Hencky (1885–1951) who committed remarkable pioneering work in the field. The extensional viscosity η_e can be determined analogously to shear viscosity as

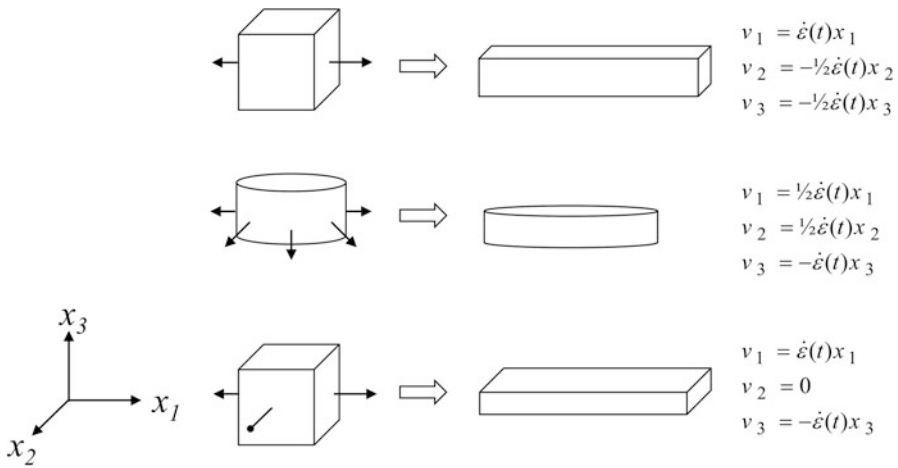


Fig. 23.7 Uniaxial, biaxial, and planar extension and their velocity distributions

$$\eta_e = \frac{\sigma}{\dot{\epsilon}} \tag{23.14}$$

where σ is the extensional stress. The relationship between viscosity of Newtonian fluid shear viscosity and steady state uniaxial extensional viscosity is called Trouton’s ratio, and it is determined as

$$Tr = \eta_{e(steady)} = 3\eta_0 \tag{23.15}$$

This relation is valid also for non-Newtonian fluids, as long as the deformation is sufficiently small, i.e. within the linear viscoelastic region. Thus at small Hencky strain rate ($\dot{\epsilon} \rightarrow 0$), the uniaxial extensional viscosity equals three times the Newtonian shear viscosity. Extensional properties are usually measured in transient start-up flow, and expressed in curves of transient viscosity, η_e^+ , vs. time (Fig. 23.8a). In these plots Trouton viscosity, $3\eta_0$, marks the linear viscoelastic envelope (LVE), obtained from start-up shear experiments at a shear rate within the Newtonian flow region, and is denoted as $3\eta_s^+$.

Uniaxial extension is the simplest extensional flow type to generate and measure under laboratory conditions, and allows most efficiently the detection of non-linear viscoelastic behavior: Strain hardening or strain softening of the material can be seen as deviations from the LVE; in the first case the transient viscosity curve will rise above, and in the latter case below the LVE as described in Fig. 23.8a. After the transient phase the flow should level off to the steady-state, where the viscosity becomes independent of time. However, the steady-state flow may be difficult to observe experimentally, as instability of the sample and limitations of the test device often impair these experiments.

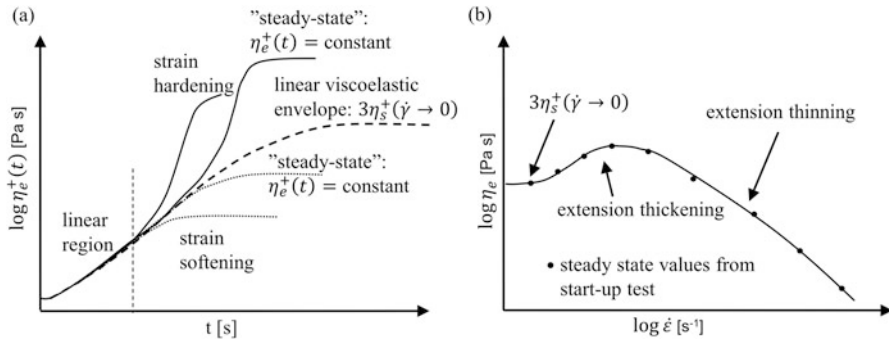


Fig. 23.8 (a) Start-up uniaxial extensional flow of polymer melts. Curves for a typical strain hardening polymer are represented by solid lines and for strain softening polymer by dotted lines, and the dashed line represents the LVE. (b) Typical curve of extensional viscosity vs. Hencky strain rate for an extension-thickening polymer

Strain hardening polymers have a characteristic “hump” or “ridge” in the plot of steady-state extensional viscosity values (from transient start-up flow) against Hencky strain rate; first the flow typically exhibits a constant $\eta_E(\dot{\epsilon})$, then extension thickening at increasing $\dot{\epsilon}$, followed by an extension thinning region in a similar manner to shear flow (Fig. 23.8b). However, achieving the true steady-state in extensional viscosity measurements can be a challenge and is currently under debate (Alvarez et al. 2013; Munstedt and Stary 2013).

Extensional rheology can tell more about intrinsic properties and structure of macromolecular materials than mere shear viscosity measurements; a common example is from the polymer industry: two polymers can have overlaying shear viscosity curves but yet behave differently when they are processed. If extensional viscosity measurements are performed it can be observed that one of them shows strain hardening due to its more branched chain architecture and therefore its elastic properties are more pronounced than for the more linear polymer (Vlachopoulos and Strutt 2003).

Many industrial processes involve both shear and extensional deformation types. Extensional deformation appears in free-surface flow and in closed pipe or channel flow whenever there is a change, either constriction or dilation, of the flow channel cross-section. Shear flow, however, is easier to produce in laboratory conditions and is thus the most commonly used way of characterizing flow behavior.

2.2.1 Extensional Rheometry: Uniaxial Flow

Being a relatively new experimental area, routines for generating and measuring extensional flow are not as well established as for measurements in shear flow. Thus many of the experiments described in the scientific literature have been performed with custom made unique rheometers which are only accessible to a few research groups. Uniaxial extensional flow, also called simple extension or simple

elongation, is a standard rheological flow like simple shear, and it is also the easiest type of extensional flow to generate. Therefore it is the most common flow type measured. Specialized devices for pure planar or biaxial extension are not commonly available (Dealy and Larson 2006).

Rotating Drum Devices

Different devices based on same principle, i.e. stretching the sample strip between counter-rotating drums at a constant rate (Fig. 23.9), have been developed and commercialized. One of such designs is the Sentmanat Extensional Rheometer (SER, Xpansion Instruments) (Sentmanat 2004). A similar design is the extensional viscosity fixture (EVF, TA Instruments) (Franck 2007), with the difference that one drum remains stationary while the other one rotates around it. Probably the first device of this type was the fiber windup fixture (Padmanabhan et al. 1996) where one end of the sample strip is stationary, and the other end fixed on a large-diameter drum which rotates around its axis. Operation principle and calculations related to the SER device are presented here.

Usually the experiments are made in un-steady start-up extension which results in transient viscosity curves presented in the Fig. 23.8a. The Hencky strain rate at constant drum rotating speed Ω is

$$\dot{\epsilon} = \frac{2\Omega R}{l_0} \quad (23.16)$$

The transient extensional viscosity can be calculated as

$$\eta_e^+(t) = \frac{F(t)}{\dot{\epsilon} A(t)} \quad (23.17)$$

The stretching force F is calculated from the measured torque, $M = 2FR$, and the change of the sample cross-sectional area upon stretching is expressed by $A(t) = A_0 \exp[-\dot{\epsilon} t]$, where A_0 is the initial sample cross-sectional area. Reaching the true steady-state flow in transient extension can be challenging. With the SER device the limiting factor in practice is often sample necking and rupture. The maximum drum rotation angle can also be a limiting factor for achieving steady-state flow: If the drums are allowed to rotate over one full revolution, 360° , the sample strip starts to wind up on the clamps, which causes an erroneous peak in the transient viscosity curve (Svrčinova et al. 2009). Due to these limitations, the maximum Hencky strain achieved with the device is $\epsilon_{max} < 4$ (Wagner and Rolón-Garrido 2012).

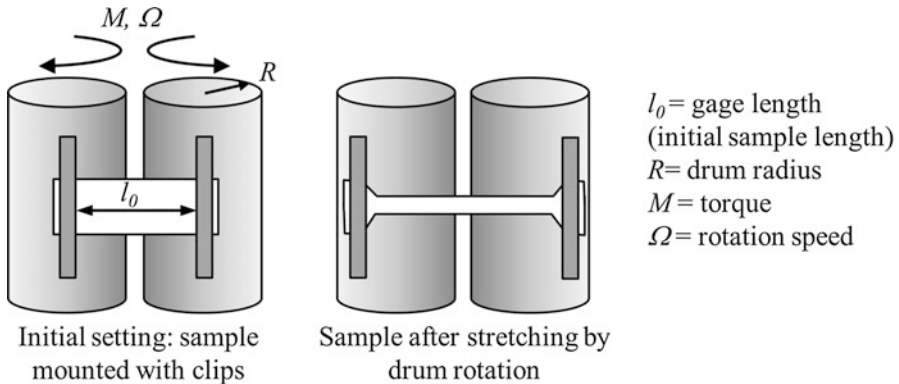


Fig. 23.9 Operation principle of a counter-rotating drum device

Filament Thinning Experiments

In the filament thinning experiments (Fig. 23.10), performed for example with the capillary breakup extensional rheometer (CaBER), the sample is stretched vertically between circular plates by applying a rapid step-deformation with an exponentially increasing separation profile $l(t) = l_0 \exp(\dot{\epsilon} t)$, after which the plates are held at an axial final separation and the thinning of the mid-filament region is observed during the necking and breakup (Anna and McKinley 2001).

The Hencky strain in the filament thinning experiment is $\epsilon = 2 \ln(D_0/D(t))$, and the maximum strain achieved by capillary break-up rheometers $\epsilon_{max} \cong 10$, but can be even above that. The CaBER is designed for capillary break-up experiments of low to mid-range viscosity fluids, where the thinning of the filament is monitored by a laser micrometer. The experiment itself is relatively straightforward, but the analysis may be complicated due to the dynamic nature and time dependence of the fluid flow (Anna and McKinley 2001).

In the filament stretching rheometer (FISER or FSR (Bach et al. 2003; Sridhar et al. 1991) the experimental setting is basically the same as in CaBER, but the plates are separated at a constant deformation rate $\dot{\epsilon} = -(2/R)(dR/dt)$ and the radius R decreases exponentially with time in the mid-point of the sample. The calculation and interpretation of the flow kinematics and fluid response are simpler than in the filament thinning and breakup experiments, but the practical realization of the test can be difficult due to gravitational sagging or instability of the sample (Anna and McKinley 2001). Both these methods produce a pure uniaxial extension in the mid-region of the sample.

Contraction Flow Analysis

The entrance pressure drop in capillary rheometers can be used to evaluate extensional viscosity. The contraction flow analysis method is based on the assumption

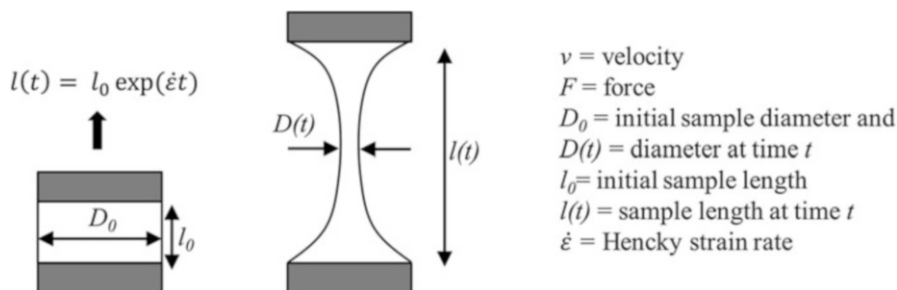


Fig. 23.10 Principle of filament thinning experimental setup

that the pressure drops due to shear and extensional deformation can be calculated separately and that their sum is the total pressure drop. Viscoelasticity of the material causes circulating corner vortices in abrupt contraction (Fig. 23.11) and their size is proportional to the extensional deformation. Additionally the general assumptions of capillary rheometry, discussed in Sect. 2.16, are applied in the contraction flow analysis as well. Cogswell and Binding analyses (Cogswell 1972; Binding 1988) are the most popular techniques for estimating the extensional viscosity from capillary rheometry data.

Testing in Miniature Scale

In pre-screening of pharmaceutical formulations the biggest limitation is often the limited amount of material available, either due to a high price or small trial batches manufactured in laboratory-scale. Viscometer/Rheometer-on-a-Chip (VROC™) is a micro-electro-mechanical systems (MEMS) device that has been developed for measuring viscosity at high shear rates at very narrow passes (Pipe et al. 2008). Basically it is a slit rheometer with micro-scale dimensions, and can be used to measure high-shear viscosity of inks, proteins or pharmaceuticals, in applications where the flow geometry dimensions are very small, such as in microfluidic devices or syringes. This is also an attractive option when only a very small amount of sample is available. Recently, also extensional microfluidic rheometers based on a flow through a hyperbolic die (Ober et al. 2013) and a cross-slot geometry (Haward et al. 2012) have been used for characterization of biological samples in extensional flow.

2.2.2 Extensional Rheometry: Biaxial and Planar Flow

Robust systems for measuring biaxial and planar extension are not commonly available, although some custom made devices for these exist. At least approximate planar extension can be produced in cross-slot devices or lubricated dies by two opposing fluid streams that meet in the middle creating a stagnation flow point,

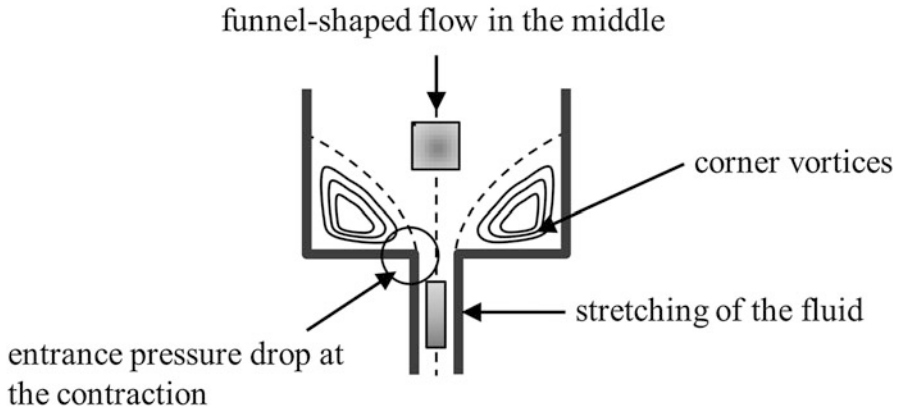


Fig. 23.11 Schematic picture of the contraction flow analysis

where purely planar elongation is expected to occur (Macosko et al. 1982; Auhl et al. 2011). Biaxial flow can be produced for example by sheet inflation (Denson and Gallo 1971) and lubricated squeezing, which is presented in the following section.

Lubricated Squeezing Flow

In lubricated squeezing (Chatraei et al. 1981), biaxial extensional flow is created between plates that are lubricated constantly to prevent the effects of friction between them and the sample. The compression of the sample can be performed using for example a universal material tester or a texture analyzer. Thus the method is widely available and the test setting is relatively simple, but if continuous lubrication cannot be supplied during the measurement, the friction between the sample and the plates will affect the results. Moreover, it is not possible to reach very high extensional strain ($\epsilon_{max} \cong 1$) because of the thinning of the lubrication layer (Kompani and Venerus 2000). Lubricated squeezing flow has been used in food rheology for example to analyze structural changes in cheese due to composition, process parameters and storage time (Brandsma and Rizvi 2001), or fermented milk products, such as kefir (Yovanoudi et al. 2013) or yogurts (Raphaelides and Gioldasi 2005).

3 Practical Issues of Rheological Measurements

3.1 *Shear Rheology in Practice*

3.1.1 Choice of the Right Geometry

The most common measuring cells are cone-and-plate, parallel plate (also called plate-plate), and concentric cylinder (Couette) geometries. The cone-and-plate and Couette geometry are often chosen for liquid samples as all parts of the sample experience the same strain and the deformation is homogenous. The cone-and-plate geometry has the advantage over the Couette geometry in smaller sample size and easier cleaning. However, bigger challenges with evaporation exist, compared to the Couette geometry. Additionally, the gap between the cone tip and the lower plate is very narrow, which must be taken into account when measuring systems that contain particles, as the particle size must be much smaller than the gap size. In the parallel plate geometries the gap can be freely adjusted, thus they do not pose the same strict limitation to the maximum particle size in the sample. However, their disadvantage is that the samples confined between the plates are not deformed to the same degree throughout, because the strain depends on the distance from the center of rotation. The maximum strain is obtained at the perimeter of the measuring plate, whereas the strain is zero at the rotational axis. The surface properties of the measuring cell are also important, since the sample has to adhere to their surfaces during measurements. Slippage between sample and cell surface, e.g. due to syneresis, can be a problem for some pharmaceutical systems. If slippage occurs the sample may not be deformed and the entire deformation or flow may occur in the liquid film layer.

Sample evaporation can be avoided by using solvent traps. Some of these are designed to create saturation of the solvent in a little chamber placed around the sample and will only work after a certain evaporation has taken place. Other solvent traps are designed to hold a low viscosity oil at the sample surface, directly preventing the evaporation. These, however, can increase the adsorption of amphiphilic chemicals to the oil-water interface and lead to a wrong interpretation of the results. Additionally, the solvent trap with oil can only be used with fluids that are totally immiscible with it, so that none of the sample components can diffuse into the oil phase.

3.1.2 Steady Shear Measurements

Flow curves should represent steady state values of the viscosity against shear rate. This means that viscosity should be independent of measurement time. It is important at each shear rate to allow sufficient time for the stress to reach a constant value before the stress is measured. Otherwise the calculated viscosity will not only

depend on shear rate but also on time and past history of the sample. Systems for which the viscosity depends on history are called thixotropic.

At high shear rates the flow may no longer be laminar and turbulent flow may appear, and the viscosity is no longer given by Eq. (23.2). An apparent higher viscosity will be seen due to the extra energy dissipation caused by turbulence.

For the common steady shear power law dependence illustrated in Fig. 23.3a the negative slope must be between 0 (Newtonian liquid) and -1 . This means that the viscosity power law exponent, n , in $\eta \propto \dot{\gamma}^{-n}$ must be between 0 and 1. Values of n greater than 1 correspond to indeterminate flow, in which case an increase in shear rate will demand a smaller stress, as seen from Eq. (23.2), resulting in inhomogeneous flow.

3.1.3 Oscillatory Shear Measurements

Modern rotational rheometers typically cover at least a frequency window from 0.001 to 100 Hz. G' and G'' are only defined in the linear range where both strain and stress are simple sinusoidal curves (Fig. 23.4). In order to ensure this, materials should always be tested as a function of stress or strain amplitude as depicted in Fig. 23.5a. In the linear range G' and G'' are independent of these amplitudes. Oscillatory tests can be performed on both CR and CS instruments. At high frequencies mechanical resonances in the instrument may occur, and it should be ensured that G' never decreases with increasing frequency.

3.1.4 Creep Measurements

Creep tests are also of interest for viscoelastic systems with long relaxation times, because they can be used to measure flow at very low shear rates. Care should be taken to ensure that the experiments are performed in the linear range where the compliance (see Sect. 2.1.4) is independent of the applied stress magnitude. Creep measurements should be performed on CS type instruments.

3.1.5 Capillary Viscometry

Capillary viscometers enable very precise viscosity determinations. Flow times can be measured with an accuracy of typically 0.1 s and for typical flow times in the range of 100–200 s, a viscosity accuracy of 0.1 % is possible. However, a good temperature control is needed and any larger particles in solution should be removed by filtration or centrifugation. The flow times are very dependent on the radius of the capillary, as seen from Eq. (23.8), and a suitable viscometer with flow times greater than about 100 s should be used. Intrinsic viscosities, $[\eta]$, can be determined from a series of measurements at low concentrations. Flow times for the most concentrated solution should be about twice the flow time of the solvent,

where $[\eta]c \approx 1$, and the most dilute solution about 5–10 % of this concentration. The maximal wall shear rate in the capillary is given by Eq. (23.9) with typical values of $\approx 100 \text{ s}^{-1}$. For non-Newtonian liquids, as illustrated in Fig. 23.3a, zero shear rate viscosities cannot be determined unless the critical shear rate exceeds the shear rate in the viscometer.

3.1.6 Capillary Rheometry

Correctly performed capillary rheometer measurements can be quite arduous: In order to achieve the true shear stress, the entrance pressure drop (in case of a circular capillary) needs to be determined, and this requires several measurements with different dies. Moreover, determining the true wall shear rate requires post-experimental data analysis. If these corrections are ignored, the results are merely “apparent” and can only be used for example for internal comparison and quality control purposes. Sometimes the effect of pressure or viscous heating (increase of the temperature due to friction) is relevant and complicates the interpretation of the results. Moreover, the theory of capillary rheometry assumes that the fluid adheres to the die wall (the so called no-slip condition). However, this is not always true: with some materials wall slip can occur when a critical shear stress is exceeded.

3.2 *Extensional Rheology Measurements in Practice*

Despite the variety of available experimental settings for uniaxial extension, a reliable measurement is still not a simple task and each technique has certain limitations (Kaschta and Münstedt 2008). Results between devices based on different principles and even between different laboratories, due to their sample preparation techniques, can differ from each other. Moreover, many of the extensional rheometers are custom built and therefore not available for everyone. Sample uniformity can have a tremendous effect on the results achieved by uniaxial extension tests: The samples for rotating drum devices, for instance, should be cut out from a homogenous film that has a uniform thickness. Depending on the material and the sample preparation technique, a certain degree of molecular and/or particular orientation may be introduced into the sample, and the results will depend on whether the measurement is done in perpendicular or parallel direction to the orientation. Moreover, any inhomogeneity, such as air bubbles or impurities, can cause a premature sample rupture below the maximum achievable strain. Therefore it must be kept in mind that the maximum transient extensional viscosity reached in the measurements, as shown in Fig. 23.8a, can actually be far from a true steady state flow. In fact, it seems that a true steady-state extensional flow cannot be established with many of the extensional devices that are limited by their maximum extensional strain. In the rheological field a lot of debate has been going on about

the steady-state extensional viscosity (Alvarez et al. 2013; Munstedt and Stary 2013).

Gravitational sagging of the sample during the heating phase before the test starts can inflict inconsistency in the uniaxial extension measurements by rotating drum devices. Keeping the sample under a pre-defined small tension in the heating phase can be carried out to avoid the sagging. In this case, the effect of the pre-tension on the initial sample cross-sectional area must be taken into account in the calculation (Aho et al. 2010). Moreover, thermal expansion of the sample when heated to the test temperature causes a change in the sample density, and addressing this correctly will further improve the measurement accuracy. If the device design allows, immersion of the testing system into a buoyant liquid can be used to prevent sagging. In this case proper fixing of the sample is essential to avoid slipping or loosening from the test drums.

In lubricated squeezing flow the greatest problem is the lack of lubrication, and different techniques have been introduced to improve the lubricant supply between the sample and squeezing plate surfaces, such as porous plates through which lubricant can constantly be added during the test (Kompani and Venerus 2000; Venerus et al. 2000).

4 Application of the Technique

4.1 *Shear Rheology of Dosage Forms*

For many years rheology has been used for characterizing polymeric systems, emulsions and suspensions in different industries, e.g. plastic production, food industry, cosmetics, cement industry, etc. Rheology has not been utilized to its fullest extent in the field of pharmaceuticals, however, the examples given below can easily be translated to the use within pharmaceuticals. Rheology has been used in the formulation development and quality assurance for e.g. gels, creams, lotions, ointments, suspensions and pastes (Barnes 2004; Barry and Meyer 1979a, b; Korhonen et al. 2001; Warburton and Davis 1969). Additionally, most dosage forms contain one or more macromolecular excipients and their physicochemical properties are important for the performance of the end product, and thus rheological behavior becomes a critical quality attribute.

Understanding the rheological behavior of emulsions has been of great interest for its strong relationship to many properties of emulsions that are vital for various industrial applications. Saiki et al. (2007) studied the roles of droplet deformability, internal fluid circulation and surface mobility using steady shear rheological measurements (cone-and-plate geometry), and revealed that droplet deformability plays an important role in controlling the shear thinning behavior. A soft emulsion was less shear thinning than a hard emulsion at low volume fractions, due to high level of structural flexibility. At high volume fractions, however, the soft emulsion

exhibited increased shear thinning behavior, presumably due to lateral distortion of droplet structure.

Recent studies have also reported that controlled heteroaggregation of oppositely charged lipid droplets can be used to manipulate the characteristics of emulsion-based products (Mao and McClements 2011, 2012a; Schmitt and Kolodziejczyk 2009). By mixing two emulsions, one containing positively charged droplets and another one with negatively charged droplets, the oppositely charged droplets interact with each other leading to the formation of micro-clusters. A three-dimensional network of aggregated droplets can be formed at sufficiently high particle concentrations leading to elastic-like behavior (Mao and McClements 2012a). These materials may be useful for commercial applications, such as pharmaceuticals, food, and cosmetic products. Mao and McClements (2012b) used a steady shear rheological method (Couette geometry) to measure the influence of particle size, ratio of positively charged to negatively charged particles, and free protein content in such materials and found that the rheological behavior could be tuned by varying these parameters.

The specific semi-solid nature and unsteady behavior of edible gelled systems have resulted in a unique texture experience beyond that of other food textures (Haghighi et al. 2011). This product performance could be transferred to pharmaceuticals, for the use within the design of functional foods, pediatric medicines etc. Fundamental aspects of rheological properties of many polymer-based systems are well described in the literature. However, multifunctional gelled products require precise choice of the ingredients such as gelling agents, sweeteners, colorants, flavors, and some functional and/or technical additives, which can highly influence the properties of the final product. Haghighi et al. (2011) used both steady shear and oscillatory shear rheological measurements (cone-and-plate geometry) to show that pectin-based gel systems have suitable rheological behavior to be considered as a functional, low-calorie gelled dessert. However, sensory and psychorheological evaluations should be carried out to correlate the results to the overall acceptability of this new product.

Furthermore, the conformational parameters of polymer excipients, such as polymer coil radius (R_{coil}), overlap concentration (c^*) and Martin constant (K_m), can be determined from intrinsic viscosity measurements of systems using capillary viscometry, which are dependent on the solvent used to dissolve the polymer. This is crucial in the process of particle design (Antoniou and Alexandridis 2010; Bohr et al. 2012; Son et al. 2004; Vinod et al. 2010).

Recently, the focus has also been on the formulation of *in situ* gelling systems where the rheological behavior is of interest (Baldursdottir and Kjoniksen 2005; Kojarunchitt et al. 2011; Yu et al. 2011). An ideal *in situ* gelling system should be a free flowing, low viscosity liquid at room temperature, that allows the administration either by syringe or as droplets (eye drops) and undergoes gel transition at physiological conditions (Bain et al. 2013). The control over the gelation can thus be achieved by activation of the formulation by an internal stimulus (e.g. pH, salts, temperature etc.) or by an external stimulus (e.g. light, ultrasound, electricity, magnetism etc.) (Sokolovskaya et al. 2014). Thermal gelling properties of different

formulations have been studied both by steady shear (Bhowmik et al. 2013) and oscillatory shear (Kojarunchitt et al. 2011) measurements.

4.2 Shear Rheology of Biological Samples

Physicochemical properties like the rheology of the complex *in vivo* fluids can play a crucial role in the therapeutic outcome of any pharmacotherapy. The physicochemical characteristics of *in vivo* fluids such as saliva, gastric juice, and mucus (intestinal, cervical and pulmonary) have been studied and an increased interest has been on the rheology of the body fluids, since their properties can have an impact on the performance of administered drugs.

Diffusion and dissolution characteristics of small molecules, i.e. drug molecules, have been described by the Stokes-Einstein (Eq. (23.18)) and Noyes-Whitney equation (Eq. (23.19)):

$$D = \frac{k_B \cdot T}{6 \cdot \pi \cdot r \cdot \eta} \quad (23.18)$$

where D is the diffusion coefficient, k_B is Boltzmann constant, T is absolute temperature, η is viscosity, and r is radius of a sphere.

$$\frac{dM}{dt} = -D \cdot A \cdot \frac{C_S - C}{h} \quad (23.19)$$

where dM/dt is the rate of dissolution, D is the diffusion coefficient, A is the surface area, C_S is the saturation solubility, C is the apparent concentration of drug, and h is the thickness of the boundary layer.

The Stokes-Einstein (Eq. (23.18)) and Noyes-Whitney equations (Eq. (23.19)) predict that an increased viscosity decreases the diffusivity and dissolution rate of drugs. Increased media viscosity has been shown to significantly delay tablet disintegration (Anwar et al. 2005; Parojcic et al. 2008; Radwan et al. 2012). The viscosity of the luminal content can have an impact on wettability of the drug and thereby the dissolution of the drug in the luminal fluids, through its effect on diffusivity, mixing, and flow patterns in the gut (Horter and Dressman 2001).

Mucus is a complex aqueous mixture of mucins, lipids, salts and cellular debris, covering many of the epithelial surfaces in the human body. Mucus lines the epithelium of the gastro-intestinal tract (GI-tract) serving as a lubricant facilitating the passage of food and chyme, and forming a protective barrier against contact between the epithelium and e.g. pathogens and pepsin (Atuma et al. 2001; Cone 2009). Consequently, mucus of the GI-tract constitutes an important barrier to oral delivery of therapeutics (Cu and Saltzman 2009), and it is one of the many obstacles for successful oral delivery of biomacromolecules (Boegh et al. 2014).

Mucins are present in human gastro-intestinal fluids, such as saliva, gastric fluid, and intestinal mucus. Mucin oligomers consist of polymerized glycosylated proteins that exist as an entangled network. The mucins are to a large extent responsible for the rheological profile of the GI-fluids. Mucin is a viscoelastic, non-Newtonian gel with shear thinning properties (Allen et al. 1984). The mucins form physical fiber entanglements, and the resistance to flow is exerted by individual fiber segments, and the non-covalent intermolecular interactions are responsible for the rheological behavior of mucins.

When analyzing the rheological properties of biological samples one will observe large heterogeneity within and between individual samples because of the complex nature of the mucus structure and the wide variety of the other substances in the samples.

The steady shear rheology of human whole saliva has been studied and was found to exhibit shear thinning behavior. Although it contains more than 99 % water, saliva is composed of a variety of electrolytes, immunoglobulins, enzymes, mucins and other proteins as well as nitrogenous products such as urea and ammonia (Humphrey and Williamson 2001; Stokes et al. 2007).

Human gastric fluids, sampled from patients in the fasted state, have also been studied; both by oscillatory and steady shear measurements, where they were found to be highly elastic with a strong shear thinning behavior (Pedersen et al. 2013). The mucus rheology can be affected by the composition of mucins and their glycosylation, which varies with age, diet, and the presence of specific antigens. However, the inter-patient variation was not ascribed to any of those parameters (Pedersen et al. 2013).

Boegh et al. (2014) studied porcine intestinal mucus by oscillatory and steady shear measurements and were able to design a biocompatible *in vivo* like mucus, with similar rheological properties to mucus, exhibiting shear thinning and dominant elastic behavior. Thus an *in vivo* representative *in vitro* model was established, where the effect of the mucus layer on drug uptake can be studied by combining biocompatible *in vivo* like mucus with a cell monolayer of mucus deficient epithelial cell lines.

Mucus is also present in pulmonary, cervical and vaginal fluids. The rheological properties of these can be used in the diagnostics of various diseases; e.g. the clearance of mucus is impaired when mucus secretions are too thick, as in patients with cystic fibrosis (Wine and Joo 2004) or chronic obstructive pulmonary disease (Kirkham et al. 2008), while protection against infection is compromised when secretions are too thin, as in women with bacterial vaginosis (Olmsted et al. 2003).

In a study looking at the diagnostics and therapeutic effects of patients treated for cystic fibrosis the oscillatory shear rheology of sputum was found to give good indications on the patients' response to the treatment. The elastic modulus, G' , was found to be dominating for all the patients, with the exception of two cases at high frequencies, and successful treatment seemed to decrease the elastic modulus of sputum (Broughton-Head et al. 2007).

Wang et al. (2013) showed that the shear rheology, both oscillatory and steady shear, and the microstructure of fresh, *ex vivo* human cervicovaginal mucus are

largely stable across a wide range of physiological pH values. Additionally, the studies suggested that this pH stability was likely due to complex biochemical interactions between physically entangled and cross-linked mucins as well as other mucus components, such as lipids, ions, and proteins. The authors speculate that the microstructure and bulk rheology of other human mucus secretions may also be relatively insensitive to pH. Thus reconstituted gels of purified mucins, where these components have been removed, will not give the characteristic rheological and structural properties of native mucus (Bhaskar et al. 1991; Cao et al. 1999; Celli et al. 2007; Kocevar-Nared et al. 1997).

4.3 Extensional Rheology of Dosage Forms and Biological Samples

In the pharmaceutical industry, extensional flow can occur in many processes, such as filling of viscoelastic liquid dosage forms, manufacturing and use of dosage forms that employ spraying, stretching, or free surface flow, such as coating of tablets, fiber spinning, film casting or extrusion. However, extensional viscosity is not commonly reported for the reasons discussed earlier in this chapter. Some examples of the use of extensional rheology are presented here, both in the pharmaceutical field and in other fields, from where they can easily be adapted to characterization of dosage forms or biological samples.

Spraying processes involve very high shear rates. Eccleston and Hudson (2000) investigated the flow properties of different nasal spray formulations by capillary rheometry: the shear viscosity of the investigated formulations was extremely low at the high shear rate, and implies formation of fine atomized droplets upon spraying. However, the extensional viscosity of the same formulations, estimated using contraction flow analysis, was relatively high. The authors suggested that high extensional viscosity, potentially together with surface properties, leads to larger droplet size that prolongs the residence time on the mucosa, which is important for the therapeutic effect of nasal formulations.

Hydrogels consist of water-soluble polymers that after cross-linking can swell and absorb large amounts of water. They are used for example in tissue engineering, wound care, and cosmetic applications. To support tissue regeneration the properties of the hydrogels must match those of the surrounding tissues. Stadler et al. (2013) studied the extensional rheology of different copolymer hydrogels in uniaxial extension using a rotating drum device (EVF) with modified sample fixing. The method was suggested as complementary to the lubricated squeezing flow method, more commonly used to characterize hydrogels.

Hydrocolloids are among the most common materials for wound dressings. Rheology of hydrocolloids has, however, been examined particularly for food-related applications, where different hydrocolloids are used for example as thickeners, or for increasing the elasticity of bread dough to improve its baking

properties. In gluten-free baking, hydrocolloids such as xanthan gum, hydroxypropyl methylcellulose, guar gum, or psyllium husk are used to imitate the gluten networks of the wheat based bread dough, improving the dough elasticity, extensibility, resistance to stretch, mixing tolerance, and gas-holding ability (Lazaridou et al. 2007). These properties are largely related to viscoelasticity and extensional rheology. Bollaín and Collar (2004) have studied the effect of different hydrogel combinations on the wheat bread dough properties in uniaxial extension by texture analyzer and in bi-axial extension using dough sheet inflation. They found that the significance of hydrocolloids together with enzymes and/or emulsifier for the dough quality could realistically be assessed by rheological parameters, including extensibility, resistance to the extension, strain hardening and stress relaxation properties. Bourbon et al. (2010) used a capillary-breakup device to characterize the extensional properties of hydrocolloid food thickeners formed using plant-seed based galactomannans from *Gleditsia triacanthos* and *Sophora japonica*, of which the latter is also known for its hemostatic properties and used in some hemorrhagic conditions.

For digestible fluid or gel like formulations, the mouth feel and the swallowing process are largely affected by both shear and extensional properties of the formulation, and correctly tailored extensional viscosity of the substance is important especially for people suffering from eating and drinking disorders (dysphagia) that can be present in various diseases. Mackley et al. (2013) investigated the extensional properties of dysphagia drink thickeners in a filament break-up device, and the results proved that although the different thickeners showed very similar behavior in shear, their extensional properties differed from each other significantly.

In electrospinning, very thin fibers are spun from a polymer solution. The process subjects the polymer to a large degree of chain orientation and the extensibility of a polymer is dependent on its rheological properties. Dott et al. (2013) used electrospinning to produce drug-loaded nanofiber matrices on a polymeric backing film for oralmucosal drug delivery. Extensibility of the solution was estimated from dynamic oscillatory shear tests and the biaxial extensional properties of the ready fiber-laid films characterized by cylindrical probe penetration using a texture analyzer.

Biological fluids, like most other materials, have primarily been characterized using shear flow. However, the function of many biological fluids is closely related to their extensional rheology, such as circulation of blood, ability of the synovial fluid to lubricate the joints, or saliva flow in the mouth. Haward et al. (2011) proved the suitability of a cross-slot flow device (see Sect. 2.2.1.4) specifically developed for very small sample amounts, for studying the extensional rheology of human saliva.

Changes in the extensional properties of the fluids can indicate an abnormal health status or changes in an already diagnosed disease: For example, the molecular mass/weight of the hyaluronic acid in synovial fluid decreases in patients with degenerative joint diseases. Since the lubrication of joint surfaces involves extensional flow, Haward (2014) investigated the relationship between the extensional

properties and the molecular weight of hyaluronic acid using the aforementioned cross-slot flow device and flow induced birefringence measurements.

In some cases changes of the extensional flow properties of biological fluids can also, directly or indirectly, cause health complications: One reason for a preterm birth can be a bacterial invasion of the uterus during the pregnancy, and this is normally prevented by the cervical mucus that creates a hydrogel plug which helps to maintain the sterile conditions in the intrauterine cavity. Critchfield et al. (2013) studied the extensional rheology of cervical mucus in capillary break-up test and shear rheology in dynamic oscillation in plate-plate rheometer, and found a correlation between the high risk of preterm birth and high extensibility and weak gel-formation of the cervical mucus.

5 Summary

Rheological measurements can add significant knowledge on the behavior of complex fluids that the pharmaceutical field has to deal with. Many rheological techniques can readily be applied from other related fields, such as polymer or food industry. However, choosing the appropriate measurement and sample preparation techniques are crucial for the correct results and their interpretation. Shear rheology has been used for decades for characterizing polymeric systems, emulsions, and suspensions in different industries, and the field of pharmaceutical sciences is catching on. The ability to translate the use of the technique between different fields is of great advantage. The field of extensional rheological techniques is still evolving because of the several limitations of the existing devices. However, recent development of devices for miniature scale testing for both shear and extensional rheology, provide interesting options for the fluid characterization in the pharmaceutical field.

References

- Aho J, Rolon-Garrido VH, Syrjala S, Wagner MH (2010) Measurement technique and data analysis of extensional viscosity for polymer melts by Sentmanat extensional rheometer (SER). *Rheol Acta* 49(4):359–370. doi:[10.1007/s00397-010-0439-8](https://doi.org/10.1007/s00397-010-0439-8)
- Allen A, Cunliffe WJ, Pearson JP, Sellers LA, Ward R (1984) Studies on gastrointestinal mucus. *Scand J Gastroenterol Suppl* 93:101–113
- Alvarez NJ, Marin JMR, Huang Q, Michelsen ML, Hassager O (2013) Creep measurements confirm steady flow after stress maximum in extension of branched polymer melts. *Phys Rev Lett* 110(16):168301. doi:[10.1103/Physrevlett.110.168301](https://doi.org/10.1103/Physrevlett.110.168301)
- Anna SL, McKinley GH (2001) Elasto-capillary thinning and breakup of model elastic liquids. *J Rheol* 45(1):115–138. doi:[10.1122/1.1332389](https://doi.org/10.1122/1.1332389)
- Antoniou E, Alexandridis P (2010) Polymer conformation in mixed aqueous-polar organic solvents. *Eur Polym J* 46(2):324–335. doi:[10.1016/j.eurpolymj.2009.10.005](https://doi.org/10.1016/j.eurpolymj.2009.10.005)

- Anwar S, Fell JT, Dickinson PA (2005) An investigation of the disintegration of tablets in biorelevant media. *Int J Pharm* 290(1–2):121–127. doi:[10.1016/j.ijpharm.2004.11.023](https://doi.org/10.1016/j.ijpharm.2004.11.023)
- Atuma C, Strugala V, Allen A, Holm L (2001) The adherent gastrointestinal mucus gel layer: thickness and physical state in vivo. *Am J Physiol* 280(5):G922–G929
- Auhl D, Hoyle DM, Hassell D, Lord TD, Harlen OG, Mackley MR, McLeish TCB (2011) Cross-slot extensional rheometry and the steady-state extensional response of long chain branched polymer melts. *J Rheol* 55(4):875–900. doi:[10.1122/1.3589972](https://doi.org/10.1122/1.3589972)
- Bach A, Rasmussen HK, Hassager O (2003) Extensional viscosity for polymer melts measured in the filament stretching rheometer. *J Rheol* 47(2):429–441. doi:[10.1122/1.1545072](https://doi.org/10.1122/1.1545072)
- Bagley EB (1957) End corrections in the capillary flow of polyethylene. *J Appl Phys* 28(5):624–627. doi:[10.1063/1.1722814](https://doi.org/10.1063/1.1722814)
- Bain MK, Maity D, Bhowmick B, Mondal D, Mollick MMR, Sarkar G, Bhowmik M, Rana D, Chattopadhyay D (2013) Effect of PEG–salt mixture on the gelation temperature and morphology of MC gel for sustained delivery of drug. *Carbohydr Polym* 91(2):529–536. doi:[10.1016/j.carbpol.2012.08.040](https://doi.org/10.1016/j.carbpol.2012.08.040)
- Baldursdottir S, Kjoniksen A-L (2005) Rheological characterization and turbidity of riboflavin-photosensitized changes in alginate/GDL systems. *Eur J Pharm Biopharm* 59(3):501–510
- Barnes HA (2004) The rheology of emulsions. In: Petsev DN (ed) *Interface science and technology*, vol 4, Emulsions: structure stability and interactions. Elsevier, London
- Barry BW, Meyer MC (1979a) The rheological properties of carbopol gels. I. Continuous shear and creep properties of carbopol gels. *Int J Pharm* 2(1):1–25. doi:[10.1016/0378-5173\(79\)90025-5](https://doi.org/10.1016/0378-5173(79)90025-5)
- Barry BW, Meyer MC (1979b) The rheological properties of carbopol gels II. Oscillatory properties of carbopol gels. *Int J Pharm* 2(1):27–40. doi:[10.1016/0378-5173\(79\)90026-7](https://doi.org/10.1016/0378-5173(79)90026-7)
- Bhaskar KR, Gong D, Bansil R, Pajevic S, Hamilton JA, Turner BS, LaMont JT (1991) Profound increase in viscosity and aggregation of pig gastric mucin at low pH. *Am J Physiol* 261(5):G827–G832
- Bhowmik M, Kumari P, Sarkar G, Bain MK, Bhowmick B, Mollick MMR, Mondal D, Maity D, Rana D, Bhattacharjee D, Chattopadhyay D (2013) Effect of xanthan gum and guar gum on in situ gelling ophthalmic drug delivery system based on poloxamer-407. *Int J Biol Macromol* 62:117–123. doi:[10.1016/j.ijbiomac.2013.08.024](https://doi.org/10.1016/j.ijbiomac.2013.08.024)
- Binding DM (1988) An approximate analysis for contraction and converging flows. *J Nonnewton Fluid Mech* 27(2):173–189. doi:[10.1016/0377-0257\(88\)85012-2](https://doi.org/10.1016/0377-0257(88)85012-2)
- Boegh M, Baldursdóttir SG, Müllertz A, Nielsen HM (2014) Property profiling of biosimilar mucus in a novel mucus-containing in vitro model for assessment of intestinal drug absorption. *Eur J Pharm Biopharm* 87(2):227–35. doi:[10.1016/j.ejpb.2014.01.001](https://doi.org/10.1016/j.ejpb.2014.01.001)
- Bohr A, Yang M, Baldursdottir S, Kristensen J, Dyas M, Stride E, Edirisinghe M (2012) Particle formation and characteristics of Celecoxib-loaded poly(lactic-co-glycolic acid) microparticles prepared in different solvents using electrospraying. *Polymer* 53(15):3220–3229. doi:[10.1016/j.polymer.2012.05.002](https://doi.org/10.1016/j.polymer.2012.05.002)
- Bollain C, Collar C (2004) Dough viscoelastic response of hydrocolloid/enzyme/surfactant blends assessed by uni- and bi-axial extension measurements. *Food Hydrocolloids* 18(3):499–507. doi:[10.1016/j.foodhyd.2003.08.007](https://doi.org/10.1016/j.foodhyd.2003.08.007)
- Bourbon AI, Pinheiro AC, Ribeiro C, Miranda C, Maia JM, Teixeira JA, Vicente AA (2010) Characterization of galactomannans extracted from seeds of *Gleditsia triacanthos* and *Sophora japonica* through shear and extensional rheology: comparison with guar gum and locust bean gum. *Food Hydrocolloids* 24(2–3):184–192. doi:[10.1016/j.foodhyd.2009.09.004](https://doi.org/10.1016/j.foodhyd.2009.09.004)
- Brandsma RL, Rizvi SSH (2001) Effect of manufacturing treatments on the rheological character of Mozzarella cheese made from microfiltration retentate depleted of whey proteins I. *Int J Food Sci Technol* 36(6):601–610. doi:[10.1046/j.1365-2621.2001.00506.x](https://doi.org/10.1046/j.1365-2621.2001.00506.x)
- Broughton-Head VJ, Shur J, Carroll MP, Smith JR, Shute JK (2007) Unfractionated heparin reduces the elasticity of sputum from patients with cystic fibrosis. *Am J Physiol* 293(5):L1240–L1249. doi:[10.1152/ajplung.00206.2007](https://doi.org/10.1152/ajplung.00206.2007)

- Cao X, Bansil R, Bhaskar KR, Turner BS, LaMont JT, Niu N, Afdhal NH (1999) pH-dependent conformational change of gastric mucin leads to sol-gel transition. *Biophys J* 76(3):1250–1258. doi:[10.1016/S0006-3495\(99\)77288-7](https://doi.org/10.1016/S0006-3495(99)77288-7)
- Celli JP, Turner BS, Afdhal NH, Ewoldt RH, McKinley GH, Bansil R, Erramilli S (2007) Rheology of gastric mucin exhibits a pH-dependent sol-gel transition. *Biomacromolecules* 8(5):1580–1586. doi:[10.1021/bm0609691](https://doi.org/10.1021/bm0609691)
- Chatraei S, Macosko CW, Winter HH (1981) Lubricated squeezing flow—a new biaxial extensional rheometer. *J Rheol* 25(4):433–443. doi:[10.1122/1.549648](https://doi.org/10.1122/1.549648)
- Cogswell FN (1972) Converging flow of polymer melts in extrusion dies. *Polym Eng Sci* 12(1):64. doi:[10.1002/pen.760120111](https://doi.org/10.1002/pen.760120111)
- Cone RA (2009) Barrier properties of mucus. *Adv Drug Delivery Rev* 61(2):75–85. doi:[10.1016/j.addr.2008.09.008](https://doi.org/10.1016/j.addr.2008.09.008)
- Critchfield AS, Yao G, Jaishankar A, Friedlander RS, Lieleg O, Doyle PS, McKinley G, House M, Ribbeck K (2013) Cervical mucus properties stratify risk for Preterm birth. *PLoS One* 8(8), e69528. doi:[10.1371/journal.pone.0069528](https://doi.org/10.1371/journal.pone.0069528)
- Cu Y, Saltzman WM (2009) Mathematical modeling of molecular diffusion through mucus. *Adv Drug Delivery Rev* 61(2):101–114. doi:[10.1016/j.addr.2008.09.006](https://doi.org/10.1016/j.addr.2008.09.006)
- Dealy JM, Larson RG (2006) Structure and rheology of molten polymers—from structure to flow behavior and back again. Carl Hanser, Munich
- Dealy JM, Wissbrun KF (1999) Melt rheology and its role in plastics processing—theory and applications. Kluwer Academic, Dordrecht
- Denson CD, Gallo RJ (1971) Measurements on the biaxial extension viscosity of bulk polymers: the inflation of a thin polymer sheet. *Polym Eng Sci* 11(2):174–176. doi:[10.1002/pen.760110213](https://doi.org/10.1002/pen.760110213)
- Dott C, Tyagi C, Tomar LK, Choonara YE, Kumar P, du Toit LC, Pillay V (2013) A mucoadhesive electrospun nanofibrous matrix for rapid oramucosal drug delivery. *J Nanomater* 2013:924947. doi:[10.1155/2013/924947](https://doi.org/10.1155/2013/924947)
- Eccleston GM, Hudson NE (2000) The use of a capillary rheometer to determine the shear and extensional flow behaviour of nasal spray suspensions. *J Pharm Pharmacol* 52(10):1223–1232. doi:[10.1211/0022357001777351](https://doi.org/10.1211/0022357001777351)
- Ferry JD (1980) Viscoelastic properties of polymers, 3rd edn. Wiley, New York
- Franck A. 2007. The ARES-EVF: Option for measuring extensional viscosity of polymer melts. http://www.tainstruments.com/pdf/literature/APN002_V2_ARES_EVF_to_measure_elongation_viscosity.pdf
- Haghighi M, Rezaei K, Labbafi M, Khodaiyan F (2011) On the formulation design and rheological evaluations of pectin-based functional gels. *J Food Sci* 76(1):E15–E22. doi:[10.1111/j.1750-3841.2010.01876.x](https://doi.org/10.1111/j.1750-3841.2010.01876.x)
- Haward SJ (2014) Characterization of hyaluronic acid and synovial fluid in stagnation point elongational flow. *Biopolymers* 101(3):287–305. doi:[10.1002/Bip.22357](https://doi.org/10.1002/Bip.22357)
- Haward S, Odell J, Berry M, Hall T (2011) Extensional rheology of human saliva. *Rheol Acta* 50(11–12):869–879. doi:[10.1007/s00397-010-0494-1](https://doi.org/10.1007/s00397-010-0494-1)
- Haward SJ, Ober TJ, Oliveira MSN, Alves MA, McKinley GH (2012) Extensional rheology and elastic instabilities of a wormlike micellar solution in a microfluidic cross-slot device. *Soft Matter* 8(2):536–555. doi:[10.1039/C1sm06494k](https://doi.org/10.1039/C1sm06494k)
- Horter D, Dressman JB (2001) Influence of physicochemical properties on dissolution of drugs in the gastrointestinal tract. *Adv Drug Delivery Rev* 46(1–3):75–87. doi:[10.1016/S0169-409X\(00\)00130-7](https://doi.org/10.1016/S0169-409X(00)00130-7)
- Humphrey SP, Williamson RT (2001) A review of saliva: normal composition, flow, and function. *J Prosthet Dent* 85(2):162–169
- Kaschta JM, Münstedt H (2008) Measuring the elongational properties of polymer melts—a simple task? Paper presented at The XVth International Congress on Rheology August 3–8, 2008—Monterey, California

- Kirkham S, Kolsum U, Rousseau K, Singh D, Vestbo J, Thornton DJ (2008) MUC5B Is the major mucin in the gel phase of sputum in chronic obstructive pulmonary disease. *Am J Respir Crit Care Med* 178(10):1033–1039. doi:[10.1164/rccm.200803-391OC](https://doi.org/10.1164/rccm.200803-391OC)
- Kocevar-Nared J, Kristl J, Smid-Korbar J (1997) Comparative rheological investigation of crude gastric mucin and natural gastric mucus. *Biomaterials* 18(9):677–681. doi:[10.1016/S0142-9612\(96\)00180-9](https://doi.org/10.1016/S0142-9612(96)00180-9)
- Kojarunchitt T, Hook S, Rizwan S, Rades T, Baldursdottir S (2011) Development and characterization of modified poloxamer 407 thermoresponsive depot systems containing cubosomes. *Int J Pharm* 408(1–2):20–26. doi:[10.1016/j.ijpharm.2011.01.037](https://doi.org/10.1016/j.ijpharm.2011.01.037)
- Kompani M, Venerus DC (2000) Equibiaxial extensional flow of polymer melts via lubricated squeezing flow. I. Experimental analysis. *Rheol Acta* 39(5):444–451. doi:[10.1007/s003970000106](https://doi.org/10.1007/s003970000106)
- Korhonen M, Hellen L, Hirvonen J, Yliruusi J (2001) Rheological properties of creams with four different surfactant combinations - effect of storage time and conditions. *Int J Pharm* 221(1–2):187–196. doi:[10.1016/S0378-5173\(01\)00675-5](https://doi.org/10.1016/S0378-5173(01)00675-5)
- Lazaridou A, Duta D, Papageorgiou M, Belc N, Biliaderis CG (2007) Effects of hydrocolloids on dough rheology and bread quality parameters in gluten-free formulations. *J Food Eng* 79(3):1033–1047. doi:[10.1016/j.jfoodeng.2006.03.032](https://doi.org/10.1016/j.jfoodeng.2006.03.032)
- Mackley MR, Tock C, Anthony R, Butler SA, Chapman G, Vadillo DC (2013) The rheology and processing behavior of starch and gum-based dysphagia thickeners. *J Rheol* 57(6):1533–1553. doi:[10.1122/1.4820494](https://doi.org/10.1122/1.4820494)
- Macosko CW, Ocansey MA, Winter HH (1982) Steady planar extension with lubricated dies. *J Nonnewton Fluid Mech* 11(3–4):301–316. doi:[10.1016/0377-0257\(82\)80037-2](https://doi.org/10.1016/0377-0257(82)80037-2)
- Mao Y, McClements DJ (2011) Modulation of bulk physicochemical properties of emulsions by hetero-aggregation of oppositely charged protein-coated lipid droplets. *Food Hydrocolloids* 25(5):1201–1209. doi:[10.1016/j.foodhyd.2010.11.007](https://doi.org/10.1016/j.foodhyd.2010.11.007)
- Mao Y, McClements DJ (2012a) Fabrication of functional micro-clusters by heteroaggregation of oppositely charged protein-coated lipid droplets. *Food Hydrocolloids* 27(1):80–90. doi:[10.1016/j.foodhyd.2011.08.013](https://doi.org/10.1016/j.foodhyd.2011.08.013)
- Mao Y, McClements DJ (2012b) Modulation of emulsion rheology through electrostatic heteroaggregation of oppositely charged lipid droplets: influence of particle size and emulsifier content. *J Colloid Interface Sci* 380(1):60–66. doi:[10.1016/j.jcis.2012.05.007](https://doi.org/10.1016/j.jcis.2012.05.007)
- Morrison FA (2001) Understanding rheology. Oxford University Press, New York
- Munstedt H, Sary Z (2013) Steady states in extensional flow of strain hardening polymer melts and the uncertainties of their determination. *J Rheol* 57(4):1065–1077. doi:[10.1122/1.4803932](https://doi.org/10.1122/1.4803932)
- Nelson B (2003) Capillary rheometry. In: Lobo HB, Bonilla JV (eds) *Handbook in plastics analysis*. Marcel Dekker, New York
- Ober TJ, Haward SJ, Pipe CJ, Soulages J, McKinley GH (2013) Microfluidic extensional rheometry using a hyperbolic contraction geometry. *Rheol Acta* 52(6):529–546. doi:[10.1007/s00397-013-0701-y](https://doi.org/10.1007/s00397-013-0701-y)
- Olmsted SS, Meyn LA, Rohan LC, Hillier SL (2003) Glycosidase and proteinase activity of anaerobic gram-negative bacteria isolated from women with bacterial vaginosis. *Sex Transm Dis* 30(3):257–261
- Padmanabhan M, Kasehagen LJ, Macosko C (1996) Transient extensional viscosity from a rotational shear rheometer using fiber-windup technique. *J Rheol* 40(4):473–481. doi:[10.1122/1.550792](https://doi.org/10.1122/1.550792)
- Parojcic J, Vasiljevic D, Ibric S, Djuric Z (2008) Tablet disintegration and drug dissolution in viscous media: paracetamol IR tablets. *Int J Pharm* 355(1–2):93–99
- Pedersen PB, Vilmann P, Bar-Shalom D, Müllertz A, Baldursdottir S (2013) Characterization of fasted human gastric fluid for relevant rheological parameters and gastric lipase activities. *Eur J Pharm Biopharm* 85(3):958–965. doi:[10.1016/j.ejpb.2013.05.007](https://doi.org/10.1016/j.ejpb.2013.05.007)
- Pipe CJ, Majmudar TS, McKinley GH (2008) High shear rate viscometry. *Rheol Acta* 47(5–6):621–642. doi:[10.1007/s00397-008-0268-1](https://doi.org/10.1007/s00397-008-0268-1)

- Radwan A, Amidon GL, Langguth P (2012) Mechanistic investigation of food effect on disintegration and dissolution of BCS class III compound solid formulations: the importance of viscosity. *Biopharm Drug Dispos* 33(7):403–416. doi:[10.1002/bdd.1798](https://doi.org/10.1002/bdd.1798)
- Raphaelides SN, Gioldasi A (2005) Elongational flow studies of set yogurt. *J Food Eng* 70(4):538–545. doi:[10.1016/j.jfoodeng.2004.10.008](https://doi.org/10.1016/j.jfoodeng.2004.10.008)
- Rubin BK (2007) Mucus structure and properties in cystic fibrosis. *Paediatr Respir Rev* 8(1):4–7. doi:[10.1016/j.prrv.2007.02.004](https://doi.org/10.1016/j.prrv.2007.02.004)
- Saiki Y, Prestidge CA, Horn RG (2007) Effects of droplet deformability on emulsion rheology. *Colloids Surfaces A* 299(1–3):65–72. doi:<http://dx.doi.org/10.1016/j.colsurfa.2006.11.022>
- Schmitt C, Kolodziejczyk E (2009) Gums and stabilizers for the food industry, vol 15. Royal Society of Chemistry, Cambridge, UK
- Sentmanat ML (2004) Miniature universal testing platform: from extensional melt rheology to solid-state deformation behavior. *Rheol Acta* 43(6):657–669. doi:[10.1007/s00397-004-0405-4](https://doi.org/10.1007/s00397-004-0405-4)
- Sokolovskaya E, Barner L, Braese S (2014) Lahann J (2014) Synthesis and On-Demand Gelation of Multifunctional Poly(ethylene glycol)-Based Polymers. *Macromol Rapid Commun* 35(8):780–786
- Son WK, Youk JH, Lee TS, Park WH (2004) The effects of solution properties and polyelectrolyte on electrospinning of ultrafine poly(ethylene oxide) fibers. *Polymer* 45(9):2959–2966. doi:[10.1016/j.polymer.2004.03.006](https://doi.org/10.1016/j.polymer.2004.03.006)
- Sridhar T, Tirtaatmadja V, Nguyen DA, Gupta RK (1991) Measurement of extensional viscosity of polymer-solutions. *J Nonnewton Fluid Mech* 40(3):271–280. doi:[10.1016/0377-0257\(91\)87012-M](https://doi.org/10.1016/0377-0257(91)87012-M)
- Stadler FJ, Friedrich T, Kraus K, Tieke B, Bailly C (2013) Elongational rheology of NIPAM-based hydrogels. *Rheol Acta* 52(5):413–423. doi:[10.1007/s00397-013-0690-x](https://doi.org/10.1007/s00397-013-0690-x)
- Stokes JR, Davies GA (2007) Viscoelasticity of human whole saliva collected after acid and mechanical stimulation. *Biorheology* 44(3):141–160
- Srvcinova P, Kharlamov A, Filip P (2009) On the measurement of elongational viscosity of polyethylene materials. *Acta Technica* 54:49–57
- Venerus DC, Kompani M, Bernstein B (2000) Equibiaxial extensional flow of polymer melts via lubricated squeezing flow. II. Flow modeling. *Rheol Acta* 39(6):574–582. doi:[10.1007/s003970000107](https://doi.org/10.1007/s003970000107)
- Vinod KR, Vasa S, Sandhya S (2010) Emerging trends in pharmaceutical polymers. *Pharm Lett* 2(1):172–180
- Vlachopoulos J, Strutt D (2003) The role of rheology in polymer extrusion. Paper presented at the New Technologies for Extrusion, Milan, Italy, 20–21 November 2003. <http://www.polydynamics.com/Rheology.pdf>
- Wagner MH, Rolón-Garrido VH (2012) Constant force elongational flow of polymer melts: Experiment and modelling (1978–present). *J Rheol* 56(5):1279. doi:[10.1122/1.4732157](https://doi.org/10.1122/1.4732157)
- Wang Y-Y, Lai SK, Ensign LM, Zhong W, Cone R, Hanes J (2013) The microstructure and bulk rheology of human cervicovaginal mucus are remarkably resistant to changes in pH. *Biomacromolecules* 14(12):4429–4435. doi:[10.1021/bm401356q](https://doi.org/10.1021/bm401356q)
- Warburton B, Davis SS (1969) The oscillatory testing of pharmaceutical semi-solids using a transfer function analyser. *Rheol Acta* 8(2):205–214. doi:[10.1007/BF01984660](https://doi.org/10.1007/BF01984660)
- Wine JJ, Joo NS (2004) Submucosal glands and airway defense. *Proc Am Thorac Soc* 1(1):47–53. doi:[10.1513/pats.2306015](https://doi.org/10.1513/pats.2306015)
- Yovanoudi M, Dimitreli G, Raphaelides SN, Antoniou KD (2013) Flow behavior studies of kefir type systems. *J Food Eng* 118(1):41–48. doi:[10.1016/j.jfoodeng.2013.03.036](https://doi.org/10.1016/j.jfoodeng.2013.03.036)
- Yu T, Malcolm K, Woolfson D, Jones DS, Andrews GP (2011) Vaginal gel drug delivery systems: understanding rheological characteristics and performance. *Expert Opin Drug Delivery* 8(10):1309–1322. doi:[10.1517/17425247.2011.600119](https://doi.org/10.1517/17425247.2011.600119)

Part VIII
Release and Uptake Testing Techniques

Chapter 24

Evaluating Oral Drug Delivery Systems: Dissolution Models

Ragna Berthelsen, Anette Müllertz, and Thomas Rades

Abstract For the past decades a range of dissolution models has been developed and routinely used to evaluate drug release from semisolid and solid oral dosage forms. Their use has been for both research and development, and quality control (QC) purposes. It is thus not surprising that the different dissolution models span a large range in terms of complexity; from simple systems like the pharmacopoeial QC tests to more complex systems like the transfer model and the biphasic dissolution model. In this chapter the basic principle of the dissolution process for orally administered drugs is described alongside a series of different dissolution models including pharmacopoeial models, dissolution models utilising physiologically relevant dissolution media, small volume and biphasic dissolution models, transfer models and combined dissolution-permeation models. All models are evaluated in terms of their common use and limitations.

Keywords Biphasic dissolution • Combined dissolution-absorption models • Dissolution • GI tract • In vitro • Pharmacopoeial models • Physiologically relevant media • Poorly water soluble drugs • Transfer models

1 Dissolution

In order for a drug to be absorbed through the intestinal mucosa and to reach the systemic circulation, it must first dissolve in the intestinal fluids. The dissolution process, which in the context of oral drug delivery commonly takes place in the stomach and/or the small intestine, was first described by Noyes and Whitney in 1897 (Noyes and Whitney 1897). They deduced that the dissolution process could be described as a simple process of diffusion, with the dissolution rate being proportional to the difference between the saturated concentration at the surface

R. Berthelsen (✉) • T. Rades
Department of Pharmacy, University of Copenhagen, Copenhagen, Denmark
e-mail: ragna.berthelsen@sund.ku.dk

A. Müllertz
Bioneer: FARMA, Department of Pharmacy, University of Copenhagen, Copenhagen, Denmark

of the drug and that in the surrounding solution. The relationship between solubility and dissolution rate was further described by Brunner and Nernst in 1904 (Nernst and Brunner 1904), and is now described by the Nernst-Brunner/Noyes Whitney equation (Eq. (24.1)):

$$\frac{dM}{dt} = \frac{D \cdot A}{h} (C_s - C_t) \quad (24.1)$$

where dM/dt is the dissolution rate, D is the diffusion coefficient of the drug in solution, A is the surface area, h is the diffusion layer thickness, C_s is the saturated solubility in the bulk medium and C_t is the amount of drug in solution at time t (Nernst and Brunner 1904; Noyes and Whitney 1897). According to this theory, the dissolution rate of a solid is affected by the particle size, the diffusion layer thickness and the concentration difference between the equilibrium solubility of the drug in the surrounding medium and the dissolved concentration at a given time. When the equilibrium solubility is far higher than the actual concentration, e.g. when a small amount of drug is dissolved in a large volume, the system is said to be under sink conditions ($C_s \gg C_t$). If a solid is dissolving under sink conditions, the dissolution rate will practically not be affected by the amount of drug in solution at time t , and therefore will be directly proportional to the equilibrium solubility. Aside from concentration and saturation solubility, the dissolution rate of a given drug is dependent on the thickness of the diffusion layer, the diffusion coefficient of the drug and the surface area of the dissolving particles. *In vitro*, the diffusion layer thickness is primarily affected by stirring of the system, with a faster stirring rate producing a thinner diffusion layer. The diffusion coefficient of a drug in solution can be mathematically described by the Stokes-Einstein equation (Eq. (24.2)) (Aulton 2013), where D is the diffusion coefficient, a is the radius of the drug molecule (assuming spherical particles or molecules), T is the temperature and η is the viscosity of the medium, R is the gas constant and N_A is the Avogadro constant.

$$D = \frac{R}{N_A} \cdot \frac{T}{6 \cdot \pi \cdot \eta \cdot a} \quad (24.2)$$

This relation shows how the diffusion coefficient is directly proportional to the temperature and inversely proportional to the viscosity of the medium the drug diffuses through, as well as the size of the diffusing particle (Aulton 2013).

2 Dissolution Models

In the following section a selective review of currently used *in vitro* dissolution models developed to predict *in vivo* performance of oral dosage forms is provided. The models are presented in a general order of increasing complexity.

2.1 Pharmacopoeial Dissolution Models

The official pharmacopoeial dissolution models are among the simplest models which have been used to forecast drug performance from oral dosage forms. Over the past decades, dissolution models have been used to evaluate drug release from semisolid and solid dosage forms for both QC and research and development purposes. With respect to QC, dissolution tests are used to detect manufacturing deviations, control batch to batch consistency and ensure continuing product quality and performance upon changes in the composition of the drug delivery system (DDS), the manufacturing process, the site of manufacturing and the scale-up of the manufacturing process (FDA 1997). For product development purposes, dissolution models are mainly used to guide the development of new DDS by providing predictive estimates of *in vivo* drug release (Azarmi et al. 2007).

In order to predict *in vivo* drug release, *in vitro* dissolution models should resemble the *in vivo* conditions that the DDS will encounter when passing through the human gastro-intestinal (GI) tract. Still, the dissolution media listed in different pharmacopoeias (European Pharmacopoeia (Ph.Eur.) and United States Pharmacopoeia (USP)) only show minor resemblances to human GI fluids. They include water, dilute hydrochloric acid, buffers in the physiological pH range of 1.2–7.5 and surfactant solutions (with or without acids or buffers), such as sodium lauryl sulphate (SLS) and polysorbate 80 (The European Directorate for the Quality of Medicines and HealthCare 2014a; The United States Pharmacopoeia and National Formulary 2014a). The typical pharmacopoeial dissolution media volume is 900 mL, but commonly ranges from 500 to 1000 mL (The European Directorate for the Quality of Medicines and HealthCare 2014a; The United States Pharmacopoeia and National Formulary 2014a). These dissolution media (and volumes) are typically chosen to ensure sink conditions, enabling release of the entire dose, even though sink conditions might not be present *in vivo*.

The description of different dissolution apparatus has been harmonised across several pharmacopoeias including the USP and the Ph.Eur. (The European Directorate for the Quality of Medicines and HealthCare 2014a; The United States Pharmacopoeia and National Formulary 2014b). Figure 24.1 depicts the four most popular dissolution apparatus for oral dosage forms; the basket, the paddle, the reciprocating cylinder and the flow-through apparatus. The basket and the paddle apparatus (apparatus 1 and 2) were the first to be introduced into the individual monographs of the pharmacopoeias, and are by far the most widely used dissolution apparatus. The reciprocating cylinder (apparatus 3) is primarily used to test the drug release from modified release (MR) dosage forms and has the advantage that it is possible to change the dissolution medium easily as the cylinder holding the dosage unit can be moved from one dissolution vessel to the next in a series of dissolution vessels. Apparatus 4, the flow-through apparatus, shares the same advantage in terms of media change and use of varying dissolution media volumes. It is therefore also recommended for testing MR formulations.

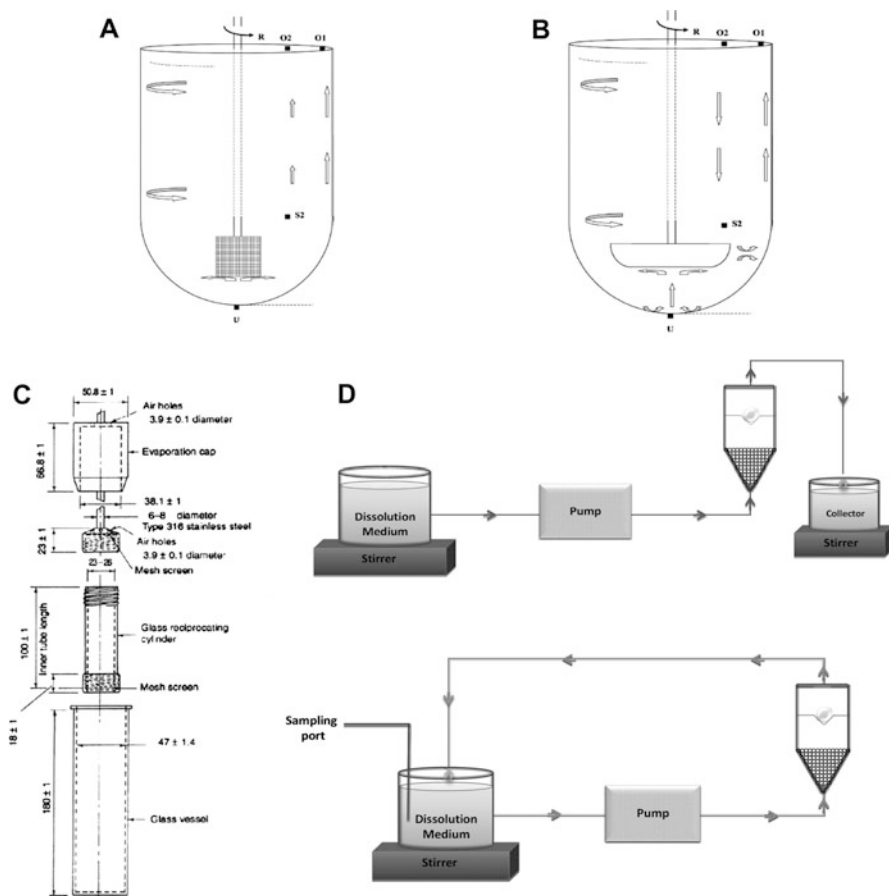


Fig. 24.1 Schematic presentations of dissolution apparatus 1: basket apparatus (a), 2: paddle apparatus (b), 3: reciprocating cylinder apparatus (c), and 4: flow-through apparatus (open loop configuration—upper panel, closed-loop configuration—lower panel). Reprinted from (Kostewicz et al. 2014), with permission from Elsevier (2015)

2.1.1 Apparatus 1 and 2

The basket and the paddle dissolution models are simple, easy to handle, standardised, robust and used worldwide. Furthermore, they are flexible in that they can be used for dissolution testing of a large variety of drugs and drug products. Therefore, these models are generally recommended by the USP (FDA 1997). With respect to dosage form development, compendial apparatus 1 and 2 models have been used to compare various DDS in terms of drug dissolution profiles (reviewed by Kostewicz et al. (2014)).

Particularly for poorly water soluble drugs, the overriding pharmacopoeial desire for sink conditions often results in rather non-physiological models with

large volumes of dissolution media and/or high concentrations of artificial surfactants. Such models typically produce complete release profiles (i.e. with release of min. 80 % of the dose) displaying high dissolution rates, but rarely possess the necessary discriminative power to differentiate between similar formulations. Berthelsen et al. (2014) showed that the suggested dissolution tests described in the USP monograph for fenofibrate capsules (The United States Pharmacopeia and National Formulary 2011), led to similar dissolution profiles for two fenofibrate immediate release (IR) DDS with demonstrated significant *in vivo* differences (C_{\max} and AUC_{0-24h} , clinical data). Also, Shi et al. (2010) found the USP dissolution model to be non-discriminatory when comparing three different formulations of celecoxib. In this study, dissolution was carried out using 900 mL of phosphate buffer (pH 6.8) supplemented with 2 % (w/v) SLS ensuring sink conditions for the tested dose. The tested formulations all displayed very fast dissolution rates with >90 % of the dose released within the first 30 min (Shi et al. 2010).

2.1.2 Apparatus 3

The principle of the reciprocating cylinder apparatus is similar to that of the disintegration tester, with the dosage form retained in an open cylinder with a mesh fitted at the top and bottom (The European Directorate for the Quality of Medicines and HealthCare 2014b; The United States Pharmacopeia and National Formulary 2014b). As the cylinder can be moved between a series of dissolution vessels containing different media (and volumes), the model offers the possibility of obtaining a dissolution profile which covers the entire GI transit. This flexibility in terms of media change is a clear advantage over dissolution apparatus 1 and 2. However, in order to move the dosage form from one vessel to another, it must be a non-disintegrating dosage form. The apparatus has been used successfully to characterise drug release from e.g. enteric coated products (de Campos et al. 2010), lipid filled capsules (Jantratid et al. 2008a) and colon-specific DDS (Li et al. 2002).

2.1.3 Apparatus 4

As an alternative dissolution model, apparatus 4 has also been used to evaluate formulation effects such as particle size and choice of excipients (Perng et al. 2003; Qureshi et al. 1994; Thybo et al. 2008).

The model holds some promise over typical dissolution apparatus 1 and 2 methods; e.g. it is easy to vary the dissolution media to resemble both the gastric and the intestinal fluids, as well as to vary the dissolution media volume from small volumes, resembling a water pocket in the small intestine, to larger volumes providing sink conditions (Fotaki 2011; Perng et al. 2003). However, as the setup for this system is more complex compared to dissolution apparatus 1 and 2;

involving pumps, filters and tubing, several practical aspects may complicate its use.

In terms of physiological relevance and the ability to simulate the events in the GI tract, the compendial dissolution models are far from optimized as the dissolution medium, dissolution medium volume and the hydrodynamics are all far from the conditions described in the human GI tract. Conventional compendial dissolution testing will probably remain critical for QC purposes. However, as these dissolution tests do not accurately reflect the changing conditions of the upper GI tract, compendial dissolution systems are unlikely to produce *in vivo*–*in vitro* correlations (IVIVC) for a broad range of poorly water soluble drugs, and will therefore be of limited use during dosage form development.

2.2 *Physiologically Relevant Dissolution Media*

The properties and composition of the GI fluids has great impact on drug dissolution after oral administration. The pH, buffer capacity, osmolality, surface tension, viscosity, temperature and volume of the varying fluids distributed along the GI lumen will directly affect the degree of ionisation (acids and bases), the apparent solubility and the dissolution rate of a given drug (reviewed by Mudie et al. (2010)). The composition of the human GI fluids has been extensively reviewed and median values for the various physiological factors are readily available in the literature, e.g. Bergström et al. (2014). In the case of poorly water soluble drugs, the apparent solubility in distinct sections of the small intestine will primarily be affected by the content of bile salts (BS) and phospholipids (PL), which form mixed micelles aiding in the solubilisation of the drugs, and the pH, if the drug is ionisable and has a pK_a value in the physiological pH range (Mudie et al. 2010; Sheng et al. 2006). Micelles are aggregates of surfactant monomers, which are formed when the surfactant concentration exceeds a critical value, known as the critical micelle concentration (CMC). Poorly water soluble drugs may be solubilised by incorporation into micelles or mixed micelles formed by one or more types of surfactants, e.g. BS, PL and lipid digestion products (Bakatselou et al. 1991). In doing so, the apparent solubility of the drug will increase thereby increasing the dissolution rate and possibly the drug absorption. Drug partitioning between the micellar phase and the free form is determined by the physicochemical properties of the drug and the composition of the medium (Bates et al. 1966a, b; Vertzoni et al. 2004). In concentrations below the CMC, BS and PL may still increase the dissolution rate by enhancing the wettability of the drug (Bakatselou et al. 1991).

Based on the idea that the dissolution process is the rate limiting step for absorption of poorly water soluble drugs, dissolution tests simulating the *in vivo* dissolution should be predictive for the bioavailability of these drugs. The lack of correlation seen when using compendial dissolution models, described above greatly emphasises the need for more physiologically relevant dissolution models. During the past decades dissolution models have been made increasingly

physiologically relevant, e.g. by the development of physiologically relevant (biorelevant) dissolution media containing BS and PL at physiological relevant concentrations. The first biorelevant media (Fasted State Simulated Intestinal Fluid—FaSSIF) were suggested in 1998 by Dressman and co-workers (Dressman et al. 1998; Galia et al. 1998). Since then a lot of effort has been put into characterising the GI luminal fluids, with the consecutive development of additional media simulating luminal conditions in various parts of the GI tract (Jantratid et al. 2008b; Kleberg et al. 2010; Vertzoni et al. 2005). Today, biorelevant media are used by research groups worldwide as well as most development groups in the pharmaceutical industry (reviewed by Kleberg et al. (2010) and Kostewicz et al. (2014)). Numerous studies have supported the use of biorelevant media, with dissolution studies using these media producing high level IVIVCs for various drugs and DDS (Jantratid et al. 2009; Lobenberg et al. 2000; Lue et al. 2008; Sunesen et al. 2005). A particular use of biorelevant media has been to test food effects by evaluating the drug release in media simulating the pre- and post-prandial states of the stomach and/or small intestine (Galia et al. 1998; Jantratid et al. 2009; Nicolaidis et al. 1999; Sunesen et al. 2005). For example, Nicolaidis et al. (1999) demonstrated a positive food effect, seen *in vivo*, on four poorly soluble drugs (troglitazone, atovaquone, sanfetrinem, cilexetil and GV150013X) *in vitro* using FaSSIF and FeSSIF as dissolution media (Nicolaidis et al. 1999).

Another effort to increase the physiological relevance of *in vitro* dissolution models has been to simulate the *in vivo* volume available for dissolution more closely. Recent MRI studies have demonstrated that the mean fluid volume in the human fasted state small intestine is approximately 100 mL, and that this fluid volume is distributed in several distinct water pockets (Mudie et al. 2014; Schiller et al. 2005). As this volume is considerably smaller than the 900 mL suggested in the pharmacopoeias, there is good reason to evaluate smaller volume dissolution models.

2.3 *Small Volume Dissolution Models*

With the purpose of minimising the required sample size and reducing the dissolution volume, while maintaining the reliability and robustness of the paddle apparatus, a mini paddle apparatus with specially designed small paddles and vessels (250 mL) was developed and is now commercially available (Erweka, Heusenstamm, Germany). Klein and Shah (2008) demonstrated that the Erweka mini paddle apparatus in fact reflected a downscaled version of the standard paddle apparatus; displaying similar hydrodynamics and producing equivalent dissolution profiles (Klein and Shah 2008). Exploiting the small dissolution vessels to mimic the *in vivo* dissolution volume more closely, Berthelsen et al. (2014) used the mini paddle apparatus with a 100 mL of fasted state biorelevant dissolution medium, to evaluate the performance of three fenofibrate IR oral dosage forms (Berthelsen et al. 2014). In this study, drug release profiles from three DDS (145 mg) were

obtained using both the standard paddle apparatus with 1000 mL fasted state biorelevant medium and the mini paddle apparatus with 100 mL of the same dissolution medium. The high dissolution volume model showed no difference between the tested DDS, while the small dissolution volume setup differentiated and ranked the DDS correctly when the amount dissolved after 60 min of dissolution was compared to clinical data (C_{\max} and AUC_{0-8h}). Based on these results, the study showed the importance of mimicking the *in vivo* dissolution volume more closely, in order to obtain an IVIVC. However, the impact of lowering the dissolution volume will depend on both the physicochemical properties of the drug and the chosen DDS. In the present case, the tested DDS were all solid dispersions only varying in the choice and contents of surfactants. The smaller dissolution volume magnified this difference as the surfactant concentrations were increased, thereby enlarging the apparent drug solubility difference caused by the surfactants and allowing DDS discrimination.

For poorly water soluble drugs, the use of a small dissolution volume will often mean that only a small fraction of the dose will be dissolved during the study, e.g. Berthelsen et al. observed dissolution of less than 2% (w/w) of the dose during the small volume dissolution studies (Berthelsen et al. 2014). Such a small amount of dose dissolved makes estimates of *in vivo* dosage form performance rather uncertain. However, if the model is coupled to e.g. an absorption model creating sink conditions, the amount of dose released would increase, potentially providing improvement of the utility of the model. In the particular study by Berthelsen et al. the small dissolution volume data was used as input data for an *in silico* absorption model to predict plasma concentration time profiles (Berthelsen et al. 2014).

The *in vitro* hydrodynamics in the dissolution models discussed in this section do not accurately reflect the hydrodynamics observed in the human GI tract. Furthermore, the hydrodynamics observed within the dissolution vessels used with apparatus 1 and 2 have been reported to vary with location within the vessels (Bai et al. 2007; Baxter et al. 2005). Studies have characterised the hydrodynamic patterns *in vivo* and *in vitro* in the paddle apparatus using different stirring speeds (Scholz et al. 2003). Attempts have been made to correlate the observed patterns, but with inconsistent results (Kostewicz et al. 2014). This means that there is still room for improvement with respect to mimicking the *in vivo* hydrodynamics during *in vitro* dissolution studies, and that the models' ability to predict *in vivo* performance may suffer from this lack of physiological relevance.

Altogether, despite a great progress in increasing the physiological relevance of dissolution models including the introduction of biorelevant media and smaller dissolution volumes, these models still hold some major drawbacks; (1) the hydrodynamics of the models need to better simulate *in vivo* conditions, (2) the models are very static and thereby do not accurately resemble the dynamic changes occurring throughout the GI tract including e.g. shifts in pH as well as shifts in contents of BS, PL and enzymes, and (3) the models lack an absorptive module ensuring removal of dissolved drug and potentially providing biorelevant sink conditions.

2.4 Transfer Models

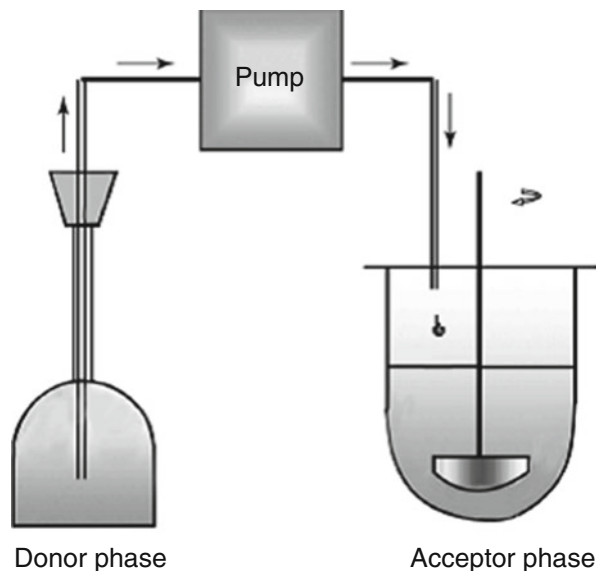
As previously mentioned, the solubility of ionisable drugs is highly dependent on the pH of the GI fluids. As the pH varies widely with location in the GI tract, significant changes in the drug solubility can be expected during GI passage. In the case of poorly water soluble weak bases, dissolution often takes place in the stomach, followed by potential drug precipitation upon entry into the small intestine. However, depending on several factors including the solid state form of the drug, the DDS, and the prandial state under which the drug is administered, the drug may stay in solution for a given time period creating a supersaturated solution (Bevernage et al. 2010, 2013; Carlert et al. 2010). Since supersaturation and drug precipitation will affect the amount of drug available for absorption across the intestinal epithelia, it may be relevant that *in vitro* dissolution models simulate this transfer of fluids from the stomach to the small intestine. Transfer models have been devised to simulate exactly this transfer; out of the stomach into the intestine (Kostewicz et al. 2004). A transfer model is depicted in Fig. 24.2, in which a drug solution in simulated gastric fluid is continuously pumped into simulated intestinal fluid. Varying slightly from this model, some transfer models consist of two consecutive dissolution vessels; one resembling the stomach to which the dosage form is added for dissolution, and one resembling the small intestine to which the gastric solution is continuously transferred and in which the supersaturation-precipitation relationship is analysed (Sugawara et al. 2005). To minimise the amount of drug needed to evaluate potential drug precipitation, the transfer model has also been developed in a miniaturised version utilising the mini paddle apparatus described previously (Klein et al. 2012). The rate at which the simulated gastric fluid is pumped into the intestinal compartment was set to resemble the gastric emptying rate, 0.5–9.0 mL/min (Kostewicz et al. 2004).

A few studies have been conducted using the transfer model, demonstrating IVIVC between the amount of drug solubilised in the intestinal media *in vitro* and the bioavailability, as well as predicting food effects (Kostewicz et al. 2004; Psachoulias et al. 2012).

Similar to other dissolution-type models, the main concerns with respect to predicting the bioavailability of poorly soluble drugs based on results from transfer models, is the non-physiologically relevant hydrodynamics observed in the dissolution apparatus 2, and the lack of an intestinal absorption barrier. The hydrodynamics, including the flow rate at which the gastric drug solution is transferred to the intestinal compartment, may affect the degree and rate of a possible drug precipitation (Carlert et al. 2010; Horn and Rieger 2001). For example Kostewicz et al. observed that a faster transfer rate produced a faster decrease from the maximum concentration of dissolved drug after initiation of precipitation (Kostewicz et al. 2004). The lack of drug removal *in vitro*, may potentially lead to an overestimation of the amount of precipitate as the simulated intestinal drug concentration will be higher than expected *in vivo* due to absorption. In a study by

Fig. 24.2 Schematic setup of a transfer model.

Reprinted from (Kostewicz et al. 2004) with permission from John Wiley and Sons (2015)



Carlert et al. (2010) the precipitation of a poorly soluble weak base (AZD0865) was investigated in three different *in vitro* models including the transfer model and compared to human bioavailability data. All the *in vitro* models predicted rapid drug precipitation, which increased with increasing drug concentration, yet the *in vivo* study indicated a lack of *in vivo* drug precipitation with a dose proportional increase in drug plasma exposure. One of the suggested reasons for this discrepancy was the lack of drug removal *in vitro* (Carlert et al. 2010). The composition and volume of the simulated gastric and intestinal fluids are also of great importance as they will directly impact on the soluble amount of dose and thereby the degree of supersaturation. In a study by Kostewicz et al. (2004) the initial volume of the intestinal acceptor phase was 500 mL, which is probably too high as compared to the available volume in the human small intestine (Kostewicz et al. 2004). Another complicating factor when predicting *in vivo* drug precipitation and oral bioavailability is the presence and conversion of polymorphic and amorphous drugs. As the solubility and dissolution rate of the amorphous form(s) of a drug is higher than any of the crystalline form(s), the bioavailability will depend on which solid state form the drug is administered in and in which form it possibly precipitates, *in vivo*. The last of which may not be accurately captured *in vitro* (Psachoulias et al. 2012).

Particularly for weak bases, the transfer model seems to be a good model to identify drugs and DDS for which drug precipitation may limit the oral bioavailability. However, due to a risk of overestimating the *in vivo* precipitation and a lack of *in vivo* precipitation studies to verify the model mechanistically, the model may not be ideal to accurately predict the bioavailability after oral administration. For non-ionisable drugs, as well as weak acids, the transfer model has very little

relevance, as the most favourable conditions for dissolution and solubilisation are found in the small intestine. For these drugs the model, though fairly simple, is considered too complex, costly and time-consuming.

2.5 *Dissolution Models with an Incorporated Absorption Module*

The models described above all focus on dissolution and precipitation as these processes are expected to be rate limiting for drug absorption. However, ignoring the removal of drug by absorption through the epithelium layer during *in vitro* assessment may compromise the physiological relevance and predictive power of the models. First, the absorption of some poorly water soluble drugs, particularly BCS class IV drugs, is not only limited by solubility, dissolution and precipitation, but also by their permeability. Second, absorption of drugs displaying a moderate to high permeability may create sink conditions that can increase the dissolution and reduce the precipitation (Kostewicz et al. 2014). Third, various enabling formulation strategies aiming at increasing intraluminal drug concentrations, may also affect drug permeability; e.g. addition of the surfactant Kolliphor[®] EL will both aid the solubilisation of poorly water soluble drugs and inhibit the P-gp efflux transporter (Constantinides and Wasan 2007; Ehrhardt et al. 2004). In order to capture these interacting effects a series of advanced *in vitro* models has been developed in which dissolution is coupled with absorption. Examples of such models include the biphasic dissolution model and combined dissolution-permeation (D/P) models.

2.5.1 **Biphasic Dissolution Models**

The biphasic dissolution model represents a fairly easy way of incorporating an absorptive sink into a standard dissolution model. As depicted in Fig. 24.3, the biphasic dissolution model is based on two separate immiscible phases; an aqueous phase for dissolution and an organic phase creating an absorptive sink. After the drug has dissolved in the dissolution medium it will partition between the organic and the aqueous phase based on its lipophilicity (logP). The model concept is relatively old with studies using a similar setup dating back to at least 1967, when Niebergall et al. determined *in vitro* drug dissolution and partitioning rates simultaneously in a biphasic dissolution system (Niebergall et al. 1967). One of the clear benefits proposed by this research group was the possibility of creating sink conditions without using large volumes of dissolution media.

In 2010 Shi et al. used the biphasic dissolution model to evaluate the performance of different DDS of the poorly soluble drug celecoxib. They obtained a rank order correlation of three different DDS (a capsule, a solution and a SNEDDS) by correlating relative *in vivo* AUC and C_{\max} values (clinical data) with *in vitro* AUC

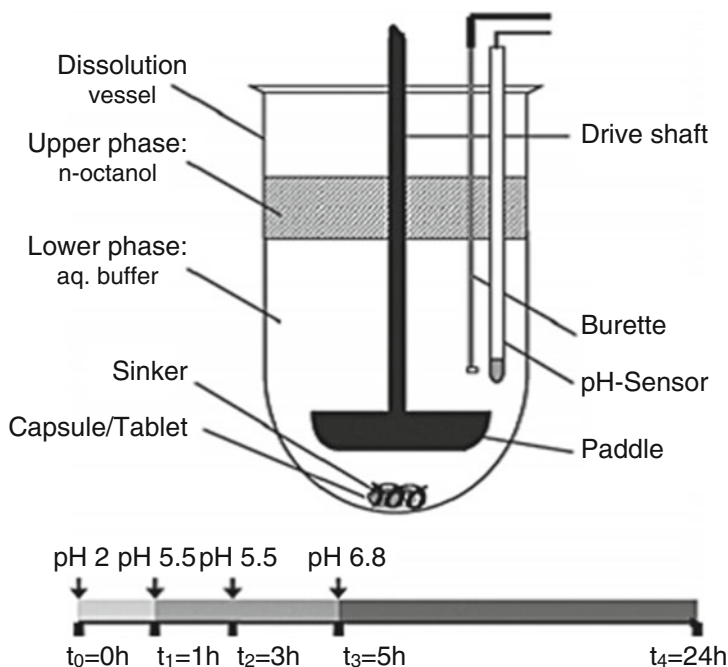


Fig. 24.3 Schematic presentation of a biphasic dissolution apparatus comprising two immiscible phases and a pH controller. Reprinted from (Heigoldt et al. 2010) with permission from Elsevier (2015)

values of the amount of drug in the organic (octanol) phase. Based on this correlation they argued that the amount of drug which partitioned into the octanol phase resembled the amount of drug in the systemic circulation after oral administration, and that the biphasic dissolution model showed great promise to evaluate DDS effects during drug development (Shi et al. 2010). Similarly, an acceptable IVIVC was obtained for MR DDS of two BCS class II drugs (dipyridamole and BIMT 17) using a pH-controlled biphasic model (Fig. 24.3) (Heigoldt et al. 2010). Emphasising the advantages of the biphasic dissolution model, single phase dissolution systems were unable to correctly rank the DDS tested in either of the described examples. The main advantage of the biphasic dissolution model is the sink condition created by the organic layer for drugs with a high logP. Drug removal into an organic phase during dissolution is somewhat comparable to the *in vivo* processes of dissolution followed by absorption. Compared to alternative ways of ensuring sink condition like the use of co-solvents or artificial surfactants, such as sodium lauryl sulphate (SLS), in the dissolution medium, or using very large dissolution volumes, the biphasic approach seems more physiologically relevant. However, an organic layer only shows very little resemblance to the human intestinal membrane lacking e.g. transporters and water channels. Furthermore, the presence of an organic layer may affect the dissolution process in the

aqueous medium as the two phases will never be completely immiscible and the organic phase will tend to work as a co-solvent. If the dissolution medium contains e.g. BS, PL or lipid digestion products (fed state medium), these will also partition into the organic phase altering the dissolution medium and thereby affecting the dissolution process (Phillips et al. 2012). If the dissolution medium or the tested DDS contains surfactants, these will presumably position themselves at interface of the two immiscible phases, again affecting the dissolution/partitioning process. Finally, as for all other models using the paddle dissolution apparatus, the hydrodynamics are not really physiologically relevant.

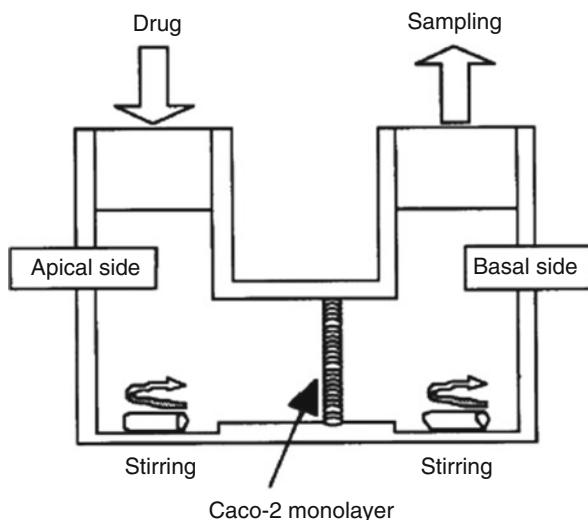
The incorporation of an absorption step into *in vitro* dissolution models has clear advantages related to single phase dissolution systems. Yet, while the biphasic dissolution model may produce good IVIVC for some lipophilic drugs and probably can be used to screen specific DDS effects e.g. surfactant trapping effects, the overall potential of the model used for prediction of the bioavailability of orally administered poorly water soluble drugs is presently considered to be relatively low due to the disturbance of the biorelevant media and the low physiological relevance of the absorption layer.

2.5.2 D/P Models

During the past 15 years different versions of combined D/P models have been developed (Buch et al. 2009; Ginski and Polli 1999; Ginski et al. 1999; Kataoka et al. 2003; Kobayashi et al. 2001; Motz et al. 2007; Sugawara et al. 2005). Figure 24.4 shows an example of a D/P model developed by Kataoka et al. (2003). The systems all consist of at least two chambers separated by a permeability barrier, e.g. a Caco-2 cell monolayer or an artificial membrane, enabling the simultaneous analysis of drug dissolution and permeation. To maintain sink conditions at the basolateral side of the permeability barrier 4.5 % (w/v) BSA is often added, as it has been suggested that BSA works as a reservoir by binding the drug in the basolateral solution (Sawada et al. 1994). In some models, the permeation takes place in a separate absorption module, with the dissolved drug being transported by peristaltic pumps at a predefined flow rate (Ginski et al. 1999). In other models, including that of Kataoka et al. (Fig. 24.4), the absorption is directly integrated in the dissolution module (Kataoka et al. 2003).

Combined D/P models have successfully been used for several purposes including, (1) predicting dissolution-permeation relationships of oral formulations i.e. determining the rate limiting step to absorption (Ginski et al. 1999; Kobayashi et al. 2001), (2) predicting DDS effects and ranking different DDS by the fraction of dose absorbed (Buch et al. 2009; Ginski et al. 1999; Kobayashi et al. 2001; Sugawara et al. 2005), and (3) forecasting food effects (Buch et al. 2009). Data from the *in vitro* studies have been correlated to *in vivo* data to verify the predictive power of the models as well as to locate model weaknesses for improvement and to establish their use and limitations.

Fig. 24.4 Schematic illustration of the D/P model developed by Kataoka et al. (2003). Reprinted from (Kataoka et al. 2003) with permission from Springer (2015)



Overall, D/P models have been shown to produce good correlations to *in vivo* data, providing accurate outcome predictions of pharmacokinetic studies along with a unique insight into the solubility/dissolution and permeability interplay of complex DDS. Yet, like all other models, they have their drawbacks. Working with cell cultures always can create issues in regard to the cell viability. Several studies have shown that BS, surfactants and other formulation excipients are toxic to the cells even at low concentrations (Ingels et al. 2002). Therefore, the dissolution media used in the D/P models is often altered compared to standard biorelevant media (Kleberg et al. 2010) and the added dose of drugs and excipients are usually small. Variations in pressure caused by a pulsatile flow, when applying pumps in consecutive systems, can also damage sensitive cell monolayers such as Caco-2 cells (Buch et al. 2009). Moreover, cell cultures are expensive and very time consuming as they typically take several weeks to differentiate (Hidalgo et al. 1989). The use of artificial membranes instead of cell cultures raises the issue of physiological relevance. Especially, for drugs that are substrates of an active transporter (influx or efflux), the estimated permeability across an artificial membrane will presumably be incorrect. However, for drugs which are only absorbed by passive diffusion, a dialysis membrane with the right cut-off may produce good IVIVC. Another issue with combined D/P models is the ratio between dissolution volume and available absorption surface area. In the human small intestine, the water volume is estimated to be approximately 100 mL, distributed throughout the intestine in small pockets (Mudie et al. 2014; Schiller et al. 2005), and the absorptive surface area of the small intestine is assumed to be approximately 30 m² (Helander and Fandriks 2014). In comparison, the dissolution volume was 8 mL and the cell layer surface area 4.2 cm² in the D/P model by Kataoka et al. (Kataoka et al. 2003). Drugs displaying high permeability may not be affected by this discrepancy, however, for drugs with low or medium GI permeability; the permeability may be wrongly identified as rate limiting for

absorption due to the small surface area. Supporting this notion, Ginski et al.(1999) found that their continuous D/P model qualitatively predicted dissolution-absorption relationships compared to *in vivo* data, but that most predictions overestimated the degree of permeation-rate-limited absorption for both BCS class I, II and III drugs (metoprolol, piroxicam and ranitidine) (Ginski et al. 1999). Conversely, the permeation rate may also be underestimated due to e.g. permeability differences between the human intestinal mucosa and Caco-2 cell monolayer (Lennernäs et al. 1996) or application of a flow rate that is too low for the medium transfer between the different compartments (dissolution/absorption).

If D/P models are to be used as a drug or DDS screening tool, the use of an artificial dialysis membrane as the permeability barrier should be preferred, as cell cultures are sensitive and time consuming to work with. The inclusion of cell layers as the permeability barrier will primarily be interesting for drugs and DDS that are affected or effect cell transporters or are metabolised by the enterocytes.

The combined models show great potential for mechanistic studies, e.g. when testing the effect of supersaturation on absorption, or evaluating the rate limiting step to absorption. However, in all uses, the discrepancy between surface area and dissolution volume and the possible consequences, should be kept in mind.

3 Conclusions

When modelling drug dissolution after oral administration, it is essential to keep in mind that the human GI tract is a very complex system displaying numerous factors influencing drug dissolution. In order to make the best estimate of GI dissolution of a given drug, the *in vitro* tests should simulate this process closely and be as physiologically relevant as possible; mimicking all aspects of the drug's passage through the GI tract. Still, it needs to be acknowledged that the human GI tract is a very complex system with many variable factors influencing the drug dissolution in various ways, therefore, a simple model or even a very complex one, is unlikely to capture every variation or effect.

The presently used *in vitro* dissolution models span a range in terms of complexity; from very simple systems like the pharmacopoeial QC tests to the more complex systems like e.g. the transfer model and the biphasic dissolution model. The simpler models, which are commonly very attractive for the pharmaceutical industry, are generally easy to handle, robust, fast and cheap compared to the more complex models, which in turn are desirable as they often display more physiologically relevant conditions producing better predictions of the bioavailability of a given drug and DDS. As *one* dissolution model is unlikely to be generally predictive of the *in vivo* performance of all drugs, the choice and development of dissolution models must happen on a case by case basis, which is presently the case in both the industry and academia.

References

- Aulton M (2013) Properties of solutions. In: Aulton M, Taylor KMG (eds) *Aulton's pharmaceuticals: the design and manufacture of medicines*. Elsevier, Edinburgh, pp 38–48
- Azami S, Roa W, Lobenberg R (2007) Current perspectives in dissolution testing of conventional and novel dosage forms. *Int J Pharm* 328:12–21
- Bai G, Armenante PM, Plank RV, Gentzler M, Ford K, Harmon P (2007) Hydrodynamic investigation of USP dissolution test apparatus II. *J Pharm Sci* 96:2327–2349
- Bakatselou V, Oppenheim RC, Dressman JB (1991) Solubilization and wetting effects of bile salts on the dissolution of steroids. *Pharm Res* 8:1461–1469
- Bates TR, Gibaldi M, Kanig JL (1966a) Solubilizing properties of bile salt solutions. I. Effect of temperature and bile salt concentration on solubilization of glutethimide, griseofulvin, and hexestrol. *J Pharm Sci* 55:191–199
- Bates TR, Gibaldi M, Kanig JL (1966b) Solubilizing properties of bile salt solutions. II. Effect of inorganic electrolyte, lipids, and a mixed bile salt system on solubilization of glutethimide, griseofulvin, and hexestrol. *J Pharm Sci* 55:901–906
- Baxter JL, Kukura J, Muzzio FJ (2005) Hydrodynamics-induced variability in the USP apparatus II dissolution test. *Int J Pharm* 292:17–28
- Bergstrom CA, Holm R, Jorgensen SA, Andersson SB, Artursson P, Beato S, Borde A, Box K, Brewster M, Dressman J, Feng KI, Halbert G, Kostewicz E, McAllister M, Muenster U, Thinnes J, Taylor R, Mullertz A (2014) Early pharmaceutical profiling to predict oral drug absorption: current status and unmet needs. *Eur J Pharm Sci* 57:173–199
- Berthelsen R, Sjogren E, Jacobsen J, Kristensen J, Holm R, Abrahamsson B, Mullertz A (2014) Combining in vitro and in silico methods for better prediction of surfactant effects on the absorption of poorly water soluble drugs—A fenofibrate case example. *Int J Pharm* 473:356–365
- Bevernage J, Brouwers J, Clarysse S, Vertzoni M, Tack J, Annaert P, Augustijns P (2010) Drug supersaturation in simulated and human intestinal fluids representing different nutritional states. *J Pharm Sci* 99:4525–4534
- Bevernage J, Brouwers J, Brewster ME, Augustijns P (2013) Evaluation of gastrointestinal drug supersaturation and precipitation: strategies and issues. *Int J Pharm* 453:25–35
- Buch P, Langguth P, Kataoka M, Yamashita S (2009) IVIVC in oral absorption for fenofibrate immediate release tablets using a dissolution/permeation system. *J Pharm Sci* 98:2001–2009
- Carlert S, Palsson A, Hanisch G, von Corswant C, Nilsson C, Lindfors L, Lennernas H, Abrahamsson B (2010) Predicting intestinal precipitation—a case example for a basic BCS class II drug. *Pharm Res* 27:2119–2130
- Constantinides PP, Wasan KM (2007) Lipid formulation strategies for enhancing intestinal transport and absorption of P-glycoprotein (P-gp) substrate drugs: In vitro/in vivo case studies. *J Pharm Sci* 96:235–248
- de Campos DR, Klein S, Zoller T, Vieria NR, Barros FA, Meurer EC, Coelho EC, Marchioretto MA, Pedrazzoli J (2010) Evaluation of pantoprazole formulations in different dissolution apparatus using biorelevant medium. *Arzneimittelforschung* 60:42–47
- Dressman JB, Amidon GL, Reppas C, Shah VP (1998) Dissolution testing as a prognostic tool for oral drug absorption: Immediate release dosage forms. *Pharm Res* 15:11–22
- Ehrhardt M, Lindenmaier H, Burhenne J, Haefeli WE, Weiss J (2004) Influence of lipid lowering fibrates on P-glycoprotein activity in vitro. *Biochem Pharmacol* 67:285–292
- FDA (1997) *Guidance for industry: Dissolution testing of immediate release solid oral dosage forms*. Center for Drug Evaluation and Research (CDER), U.S. Department of Health and Human Services, Food and Drug Administration, Silver Spring, August 1997
- Fotaki N (2011) Flow-through cell apparatus (USP apparatus 4): Operation and features. *Dissolution Technol* 18:46–49

- Galia E, Nicolaides E, Horter D, Lobenberg R, Reppas C, Dressman JB (1998) Evaluation of various dissolution media for predicting in vivo performance of class I and II drugs. *Pharm Res* 15:698–705
- Ginski MJ, Polli JE (1999) Prediction of dissolution-absorption relationships from a dissolution/Caco-2 system. *Int J Pharm* 177:117–125
- Ginski MJ, Taneja R, Polli JE (1999) Prediction of dissolution-absorption relationships from a continuous dissolution/Caco-2 system. *AAPS PharmSci* 1, E3
- Heigoldt U, Sommer F, Daniels R, Wagner KG (2010) Predicting in vivo absorption behavior of oral modified release dosage forms containing pH-dependent poorly soluble drugs using a novel pH-adjusted biphasic in vitro dissolution test. *Eur J Pharm Biopharm* 76:105–111
- Helander HF, Fandriks L (2014) Surface area of the digestive tract—Revisited. *Scand J Gastroenterol* 49:681–689
- Hidalgo JJ, Raub TJ, Borchardt RT (1989) Characterization of the human colon carcinoma cell line (Caco-2) as a model system for intestinal epithelial permeability. *Gastroenterology* 96:736–749
- Horn D, Rieger J (2001) Organic nanoparticles in the aqueous phase—Theory, experiment, and use. *Angew Chem Int Ed* 40:4331–4361
- Ingels F, Deferme S, Destexhe E, Oth M, Van den Mooter G, Augustijns P (2002) Simulated intestinal fluid as transport medium in the Caco-2 cell culture model. *Int J Pharm* 232:183–192
- Jantravid E, Janssen N, Chokshi H, Tang K, Dressman JB (2008a) Designing biorelevant dissolution tests for lipid formulations: Case example—lipid suspension of RZ-50. *Eur J Pharm Biopharm* 69:776–785
- Jantravid E, Janssen N, Reppas C, Dressman JB (2008b) Dissolution media simulating conditions in the proximal human gastrointestinal tract: An update. *Pharm Res* 25:1663–1676
- Jantravid E, De Maio V, Ronda E, Mattavelli V, Vertzoni M, Dressman JB (2009) Application of biorelevant dissolution tests to the prediction of in vivo performance of diclofenac sodium from an oral modified-release pellet dosage form. *Eur J Pharm Sci* 37:434–441
- Kataoka M, Masaoka Y, Yamazaki Y, Sakane T, Sezaki H, Yamashita S (2003) In vitro system to evaluate oral absorption of poorly water-soluble drugs: Simultaneous analysis on dissolution and permeation of drugs. *Pharm Res* 20:1674–1680
- Kleberg K, Jacobsen J, Mullertz A (2010) Characterising the behavior of poorly water soluble drugs in the intestine: Application of biorelevant media for solubility, dissolution and transport studies. *J Pharm Pharmacol* 62:1–13
- Klein S, Shah VP (2008) A standardized mini paddle apparatus as an alternative to the standard paddle. *AAPS PharmSciTech* 9:1179–1184
- Klein S, Buchanan NL, Buchanan CM (2012) Miniaturized transfer models to predict the precipitation of poorly soluble weak bases upon entry into the small intestine. *AAPS PharmSciTech* 13:1230–1235
- Kobayashi M, Sada N, Sugawara M, Iseki K, Miyazaki K (2001) Development of a new system for prediction of drug absorption that takes into account drug dissolution and pH change in the gastro-intestinal tract. *Int J Pharm* 221:87–94
- Kostewicz ES, Wunderlich M, Brauns U, Becker R, Bock T, Dressman JB (2004) Predicting the precipitation of poorly soluble weak bases upon entry into the small intestine. *J Pharm Pharmacol* 56:43–51
- Kostewicz ES, Abrahamsson B, Brewster M, Brouwers J, Butler J, Carlert S, Dickinson PA, Dressman J, Holm R, Klein S, Mann J, McAllister M, Minekus M, Muenster U, Mullertz A, Verwei M, Vertzoni M, Weitschies W, Augustijns P (2014) In vitro models for the prediction of in vivo performance of oral dosage forms. *Eur J Pharm Sci* 57C:342–366
- Lennernäs H, Palm K, Fagerholm U, Artursson P (1996) Comparison between active and passive drug transport in human intestinal epithelial (Caco-2) cells in vitro and human jejunum in vivo. *Int J Pharm* 127:103–107
- Li J, Yang L, Ferguson SM, Hudson TJ, Watanabe S, Katsuma M, Fix JA (2002) In vitro evaluation of dissolution behavior for a colon-specific drug delivery system (CODES) in

- multi-pH media using United States Pharmacopeia apparatus II nad III. *AAPS PharmSciTech* 3:1–9
- Lobenberg R, Kramer J, Shah VP, Amidon GL, Dressman JB (2000) Dissolution testing as a prognostic tool for oral drug absorption: Dissolution behavior of glibenclamide. *Pharm Res* 17:439–444
- Lue BM, Nielsen FS, Magnussen T, Schou HM, Kristensen K, Jacobsen LO, Mullertz A (2008) Using biorelevant dissolution to obtain IVIVC of solid dosage forms containing a poorly-soluble model compound. *Eur J Pharm Biopharm* 69:648–657
- Motz SA, Schaefer UF, Balbach S, Eichinger T, Lehr CM (2007) Permeability assessment for solid oral drug formulations based on Caco-2 monolayer in combination with a flow through dissolution cell. *Eur J Pharm Biopharm* 66:286–295
- Mudie DM, Amidon GL, Amidon GE (2010) Physiological parameters for oral delivery and in vitro testing. *Mol Pharm* 7:1388–1405
- Mudie DM, Murray K, Hoad CL, Pritchard SE, Garnett MC, Amidon GL, Gowland PA, Spiller RC, Amidon GE, Marciani L (2014) Quantification of gastrointestinal liquid volumes and distribution following a 240 mL dose of water in the fasted state. *Mol Pharm* 11:3039–3047
- Nernst W, Brunner E (1904) Theorie der Reaktionsgeschwindigkeit in heterogenen Systemen. *Zeitschrift f Physik Chemie* 47:52–110
- Nicolaides E, Galia E, Efthymiopoulos C, Dressman JB, Reppas C (1999) Forecasting the in vivo performance of four low solubility drugs from their in vitro dissolution data. *Pharm Res* 16:1876–1882
- Niebergall P, Patil MY, Sugita ET (1967) Simultaneous determination of dissolution and partitioning rates in vitro. *J Pharm Sci* 56:943–947. doi:10.1002/jps.2600560803
- Noyes AA, Whitney WR (1897) The rate of solution of solid substance in their own solutions. *J Am Chem Soc* 19:930–934
- Perng CY, Kearney AS, Palepu NR, Smith BR, Azzarano LM (2003) Assessment of oral bioavailability enhancing approaches for SB-247083 using flow-through cell dissolution testing as one of the screens. *Int J Pharm* 250:147–156
- Phillips DJ, Pygall SR, Cooper VB, Mann JC (2012) Overcoming sink limitations in dissolution testing: a review of traditional methods and the potential utility of biphasic systems. *J Pharm Pharmacol* 64:1549–1559
- Psachoulas D, Vertzoni M, Butler J, Busby D, Symillides M, Dressman J, Reppas C (2012) An in vitro methodology for forecasting luminal concentrations and precipitation of highly permeable lipophilic weak bases in the fasted upper small intestine. *Pharm Res* 29:3486–3498
- Qureshi SA, Caill'e G, Brien R, Piccirilli G, Yu V, McGilvaray IJ (1994) Application of flow-through dissolution method for the evaluation of oral formulations of nifedipine. *Drug Dev Ind Pharm* 20:1869–1882
- Sawada GA, Ho NF, Williams LR, Barsuhn CL, Raub TJ (1994) Transcellular permeability of chlorpromazine demonstrating the roles of protein binding and membrane partitioning. *Pharm Res* 11:665–673
- Schiller C, Frohlich CP, Giessmann T, Siegmund W, Monnikes H, Hosten N, Weitschies W (2005) Intestinal fluid volumes and transit of dosage forms as assessed by magnetic resonance imaging. *Aliment Pharmacol Ther* 22:971–979
- Scholz A, Kostewicz E, Abrahamsson B, Dressman JB (2003) Can the USP paddle method be used to represent in-vivo hydrodynamics? *J Pharm Pharmacol* 55:443–451
- Sheng JJ, Kasim NA, Chandrasekharan R, Amidon GL (2006) Solubilization and dissolution of insoluble weak acid, ketoprofen: Effects of pH combined with surfactant. *Eur J Pharm Sci* 29:306–314
- Shi Y, Gao P, Gong YC, Ping HL (2010) Application of a biphasic test for characterization of in vitro drug release of immediate release formulations of celecoxib and its relevance to in vivo absorption. *Mol Pharm* 7:1458–1465

- Sugawara M, Kadomura S, He X, Takekuma Y, Kohri N, Miyazaki K (2005) The use of an in vitro dissolution and absorption system to evaluate oral absorption of two weak bases in pH-independent controlled-release formulations. *Eur J Pharm Sci* 26:1–8
- Sunesen VH, Pedersen BL, Kristensen HG, Mullertz A (2005) In vivo in vitro correlations for a poorly soluble drug, danazol, using the flow-through dissolution method with biorelevant dissolution media. *Eur J Pharm Sci* 24:305–313
- The European Directorate for the Quality of Medicines and HealthCare (2014a) European Pharmacopoeia Online 8.2. 5.17.1. Recommendations on dissolution testing, 10 June 2014
- The European Directorate for the Quality of Medicines and HealthCare (2014b) European Pharmacopoeia Online 8.2. 2.9.3. Dissolution test for solid dosage forms, June 10 2014
- The United States Pharmacopoeia and National Formulary (2011) USP 34 - NF 29. Official Monographs/Fenofibrate
- The United States Pharmacopoeia and National Formulary (2014a) USP 37 - NF 32. <1092> The dissolution procedure: Development and validation, June 10 2014
- The United States Pharmacopoeia and National Formulary (2014b) USP 37 - NF 32. <711> Dissolution, June 10 2014
- Thybo P, Pedersen BL, Hovgaard L, Holm R, Mullertz A (2008) Characterization and physical stability of spray dried solid dispersions of probucol and PVP-K30. *Pharm Dev Technol* 13:375–386
- Vertzoni M, Fotaki N, Kostewicz E, Stippler E, Leuner C, Nicolaides E, Dressman J, Reppas C (2004) Dissolution media simulating the intraluminal composition of the small intestine: Physiological issues and practical aspects. *J Pharm Pharmacol* 56:453–462
- Vertzoni M, Dressman J, Butler J, Hemenstall J, Reppas C (2005) Simulation of fasting gastric conditions and its importance for the in vivo dissolution of lipophilic compounds. *Eur J Pharm Biopharm* 60:413–417

Chapter 25

Evaluating Oral Drug Delivery Systems: Digestion Models

Ragna Berthelsen, Philip Sassene, Thomas Rades, and Anette Müllertz

Abstract In order to assess drug release from a digestible drug delivery system (DDS), it is important to simulate the relevant digestion processes as well as the dissolution process. Compared to commonly used dissolution models, digestion models are typically more complex, as they incorporate the digestive enzymes. This also renders these models suitable for the evaluation of food effects on drugs and dosage forms.

In this chapter, the human digestion processes are briefly described, followed by a description of the most commonly used digestion models including the pH-stat controlled lipolysis models, the Dynamic Gastric Model (DGM) and TNO gastrointestinal model (TIM-1). The pH-stat controlled models are examples of relatively simple digestion models commonly used to evaluate the amount of drug solubilised in the aqueous phase during digestion of lipid based DDS (LbDDS), whereas the DGM and the TIM-1 represent two of the more complex dissolution and digestion models available. Emphasis will be on the models suitability to assess LbDDS and will therefore primarily involve lipid digestion.

Keywords Digestion • In vitro • GI tract • Digestible drug delivery systems • Lipid-based drug delivery systems • Food effects • pH-stat controlled lipolysis model • DGM • TIM-1

1 Digestion Processes

The main site of digestion within the human gastrointestinal (GI) tract is the small intestine; however, the digestion processes actually begin in the mouth where amylase is secreted (DeSesso and Jacobson 2001). Previously lingual lipase was

R. Berthelsen • P. Sassene (✉) • T. Rades
Department of Pharmacy, University of Copenhagen, Universitetsparken 2, Building
13, 3rd Floor, 2100 Copenhagen, Denmark
e-mail: dlt527@alumni.ku.dk

A. Müllertz
Bioneer:FARMA, Department of Pharmacy, University of Copenhagen, Copenhagen,
Denmark

thought to be secreted on the tongue by the Von Ebner secretory glands and therefore present in saliva, similar to what is seen in rodents (Hamosh and Burns 1977). This was disproved in 1988 by Moreau et al. who showed, that the only preduodenal lipase present in man, is of gastric origin (Moreau et al. 1988). Thus after ingestion of a meal, lipids are partly digested in the stomach, where gastric lipase is responsible for digesting approximately 5–40% of ingested triacylglycerides (TAG) (Armand 2007; Armand et al. 1994, 1996, 1999; Carriere et al. 1993). The remaining lipid-digestion occurs in the small intestine with complete lipolysis by pancreatic lipases (Carey et al. 1983).

Upon mixing and grinding in the stomach, emulsification of lipids in gastric fluid takes place, ensuring a large interfacial surface area for the lipase to facilitate hydrolysis (Armand 2007; Schulze 2006). The thick semifluid mass of partly digested food (chyme) is subsequently ejected to the duodenum and mixed with pancreatic juice and bile for further digestion before being pushed into the small intestine by peristaltic movements (Schulze 2006). The pancreatic juice contains several enzymes including amylase, proteases and lipases involved in the digestion of carbohydrates, proteins and lipids, respectively, as well as bicarbonate ions serving to neutralize the acid coming from the stomach (Keller and Allan 1967; Dressman et al. 1990). Bile secretions contain bile salts (BS) and phospholipids (PL), which are micelle forming endogenous surfactants, facilitating the lipid digestion process by stabilizing emulsified lipid-droplets and removing lipolysis products from the interfacial contact area between the lipase and substrate (Armand 2007). During intestinal lipid digestion, different colloidal phases are formed, eventually leading to the formation of mixed micelles containing BS, PL, mono-glycerides (MAG) and fatty acids (FAs) (Fatouros et al. 2007a). These micelles presumably diffuse to the intestinal membrane where the different constituents are absorbed (Porter et al. 2007). Figure 25.1 illustrates some of the digestion and drug solubilisation processes taking place in the stomach and the small intestine.

The digestion processes can influence drug absorption, particularly when a drug is administered with a meal or in a LbDDS (Haus 2007; Charman et al. 1997). Ingestion of food can affect drug absorption in several different ways; however, in relation to the digestion processes, the digestion products of e.g. lipids, typically help solubilise poorly water soluble drugs by aiding their incorporation into mixed micelles (Bates et al. 1966). Excipients used in LbDDS commonly need to be digested themselves in order to release incorporated drug (Palin and Wilson 1984).

2 Digestion Models

Digestion models are of primary relevance for dosage forms containing digestible excipients, e.g. tri- and di-acylglycerols and also several surfactants that are hydrolysed by GI esterases (Cuine et al. 2008; Fernandez et al. 2007). In addition, digestion models are needed when a potential food effect on drugs or dosage forms is assessed. Different *in vitro* lipolysis models have been developed to simulate the digestion process in the stomach, duodenum and jejunum. In order to simulate the

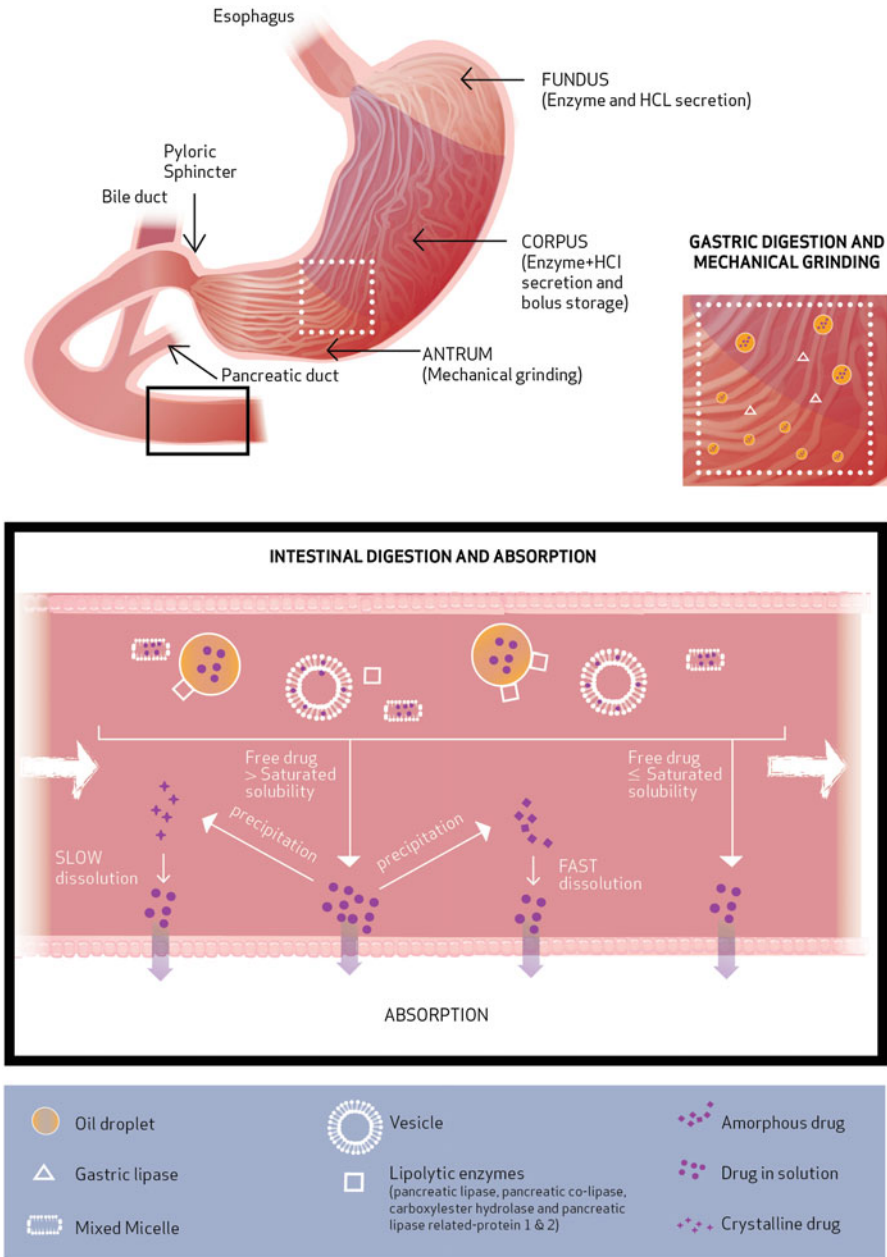


Fig. 25.1 Schematic presentation of lipid digestion, drug solubilisation, precipitation and absorption in the stomach and small intestine.

digestion processes in the GI tract *in vitro*, it has been suggested that the following five aspects should be considered; (1) use of physiologically relevant enzymes and co-enzymes in appropriate amounts, (2) correct physiological pH, as well as addition of relevant co-factors e.g. BS and PL, (3) digestion product removal, (4) appropriate mixing and (5) physiological transit times (Minekus et al. 1995). However, when assessing performance of LbDDS these suggestions are not all needed, as more simple digestion models also have been able to predict drug performance (Larsen et al. 2008; Porter et al. 2004b; Heshmati et al. 2014). This is possible, as *in vitro* evaluation of LbDDS often is performed to pinpoint the most suitable LbDDS by rank ordering a range of formulations, rather than predict the absolute bioavailability. None of the *in vitro* digestion models developed so far meets all five aspects mentioned above. Thus the following sections will clarify the utility of the most commonly used models and how their inadequacy to fulfil the five aspects suggested, results in shortcomings of the respective models.

2.1 pH-Stat Controlled In Vitro Lipolysis Models

The pH-stat controlled lipolysis models primarily consists of three different types; one-compartment pH-stat models, the dynamic *in vitro* lipolysis model and two-compartment pH-stat models (Sek et al. 2001; Williams et al. 2012; Zangenberg et al. 2001a, b; Christophersen et al. 2014; Fernandez et al. 2009; Dahan and Hoffman 2006).

The one-compartment pH-stat models usually simulate intestinal digestion, as it is the primary site of hydrolysis. The *in vitro* lipolysis takes place in a thermostated reaction vessel where the tested DDS is dispersed in biorelevant medium resembling fasted or fed state GI fluid, and digestion is initiated by manual addition of lipase (e.g. porcine pancreatin). The amount of digestion is determined based on the amount of NaOH required to neutralize the pH drop caused by FAs released from enzymatic hydrolysis of triglycerides and other digestible excipients. Mixing of the digesta is usually produced by either overhead or magnetic stirring. This agitation does not mimic the hydrodynamics of the GI tract very well, but is sufficient for evaluation of LbDDS, as the digesta is liquid and easily emulsified. The model lacks an absorption step, so during digestion, lipolysis products build up at the emulsion interface and subsequently inhibit digestion (Pafumi et al. 2002). To avoid this inhibition, calcium is added prior to initiation of the experiment, as calcium is known to form insoluble soaps with FAs and hence remove them from the system. This does on the other hand result in a very fast initial lipolysis, making it difficult to assess how different degrees of digestion impact on the LbDDS. To address this, the dynamic *in vitro* lipolysis model was developed.

Figure 25.2 shows a schematic representation of the dynamic *in vitro* lipolysis model, with continuous pH measurement and addition of NaOH to maintain a predefined pH, continuous addition of CaCl_2 to remove digestion products, stirring and temperature control (Zangenberg et al. 2001a, b). This model is very similar to

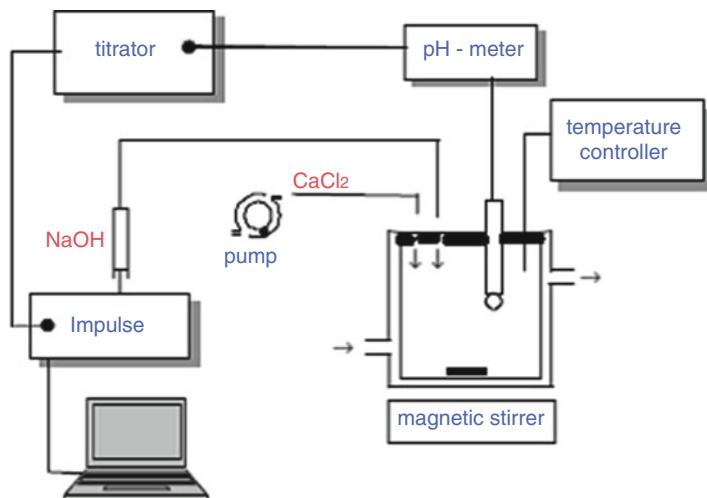


Fig. 25.2 Schematic figure of the dynamic *in vitro* lipolysis setup. Reprinted from (Fatouros et al. 2007b) with permission from Springer (2015).

the one-compartment pH-stat model and only differs, by having no calcium present at the start of the experiment, but adding it continuously during digestion. A result of this is an approximately linear lipolysis, permitting sampling at different stages of digestion, providing a more thorough insight into how lipolysis affects LbDDS (Larsen et al. 2011).

For some purposes, the one-compartment intestinal lipolysis models seem adequate, but for evaluating the impact of low pH and gastric digestion or assessing how sudden pH-changes affect drug and LbDDS, they have proven insufficient. To accommodate this shortcoming, the two-compartment pH-stat model has been developed to mimic both gastric and intestinal digestion (Christophersen et al. 2014; Fernandez et al. 2009). Digestion in the gastric compartment is performed in a medium simulating human gastric fluid and digestion is usually facilitated by microbial or animal-derived gastric lipases, as human gastric lipase (HGL) is not easily obtained. However, as pH-optimum, substrate affinity and stereo selectivity vary between these different lipases, none of the used gastric lipases are ideal as substitutes for HGL. A recombinant HGL (rHGL) may have potential; however, it is not yet commercially available and has consequently not been incorporated into any gastric lipolysis model. Therefore, the impact of gastric lipolysis on the bioavailability of drugs from LbDDS remains to be fully understood (Kostewicz et al. 2014). Subsequent to gastric digestion in the two-compartment pH-stat models, intestinal lipolysis is conducted. For convenience, the transfer of digesta from the gastric compartment to the intestinal compartment is usually performed by adding a concentrated duodenal medium with pancreatic enzymes, instead of gradual gastric emptying to the intestinal compartment (Christophersen et al. 2014).

The general principle of digestion is the same in the aforementioned models and during lipolysis four phases that can be separated by ultracentrifugation, may be formed; an oil phase from undigested lipids, a colloidal phase containing large vesicles, an aqueous phase containing micelles and smaller vesicles, and a pellet phase (Larsen et al. 2011). The oil phase will only be present if the tested DDS contains more lipids, than the surfactants are capable of emulsifying and is mainly present during the initial part of the digestion experiment. To estimate the amount of drug available for absorption, which is thought to be the amount of drug solubilised in the colloidal and aqueous phase, samples are taken throughout the lipolysis experiment to determine the amount of drug solubilised in the different lipolysis phases (Porter et al. 2004a, b; Larsen et al. 2008; Sassene et al. 2010). The pellet phase mainly consists of precipitated FAs in the form of calcium soaps, but will also contain drug in case of drug precipitation. Recently, the pellet has been analysed for the solid state form of the precipitated drug as this has been shown to affect the rate of re-dissolution and thereby possibly the bioavailability of the drug (Sassene et al. 2010; Thomas et al. 2012a, 2013; Stillhart et al. 2014).

As the pH-stat controlled *in vitro* lipolysis models have been used by various research groups, different factors have been reported to vary e.g.: digestion medium contents including type of BS, digestion medium pH, type of lipase (including activity differences), digestion medium volume and digestion duration (Table 25.1).

2.1.1 *In Vivo–In Vitro* Correlations

The potential of *in vitro* lipolysis models has been established by studies showing *in vivo–in vitro* correlations (IVIVC) using one of these models (Dahan and Hoffman 2007; Larsen et al. 2008; Porter et al. 2004b). For example Porter et al. (2004a, b) showed that the use of long chain self-microemulsifying drug delivery systems (LC-SMEDDS) led to a higher oral bioavailability of the BCS class II compound danazol in beagle dogs, when compared to medium chain SMEDDS (MC-SMEDDS). These results were reproduced *in vitro* using the lipolysis model, which showed basically no precipitation from LC-SMEDDS, but high levels of precipitation from MC-SMEDDS (Porter et al. 2004a). Larsen et al. (2008) investigated the predictability of an *in vitro* lipolysis model when applied to different types of lipid based formulations containing the digestible surfactant Labrafil M2125CS (suspensions vs. solutions), and found rank order correlations between the amount of drug (danazol) solubilised in the aqueous phase after 70 min of *in vitro* lipolysis and the bioavailability determined in rats (Larsen et al. 2008).

While some studies have found good correlations, other studies have found the *in vitro* lipolysis models inadequate to predict the *in vivo* performance of oral dosage forms containing digestible excipients. In two separate studies, Griffin et al. (2014) and Thomas et al. (2014) observed that the amount of drug solubilised during *in vitro* digestion studies did not correlate with *in vivo* bioavailability in pigs

Table 25.1 Examples of experimental conditions used for *in vitro* lipolysis

Volume (mL)	Duration (min)	pH	Buffer	Lipase	Bile/phospholipid	Calcium	Substrate	References
9	12	6.5	Tris-maleate 2 mM	Pancreatin 24 TBU/mL	NaTDC 8 mM	10 mM	0.45 mL TG emulsion	Reymond et al. (1988)
5		8.5	Tris-maleate 50 mM	Porcine pancreas 168–280 TBU/mL	NaTDC 0–30 mM/ Lecithin	0–30 mM	0–5 % (w/v) of TG-emulsion (10 %) emulsified with PL	Alvarez and Stella (1989)
10		6–9	Tris-maleate 2 mM	Purified from human pancreatic fluid 1–8 TBU/mL	NaTC NaTDC, or NaCDC, 6 mM	10 mM	0.5 mL olive oil emulsified with gum Arabic	Patton and Carey (1981)
40	30	6.8–7.4	Tris-maleate 50 mM	Porcine pancreatin (8× USP) 1000 IU/mL	NaTC 5 mM L- α -PC	5 mM	0.2–1 g TG	Dahan and Hoffman (2006)
37.5	20–120	7.0	Phosphate 5 mM	Porcine pancreas type II (L3126, Sigma), 100–400 U/mg, 2.4 mg/mL	Porcine bile extract 20 mM	10 mM	0.5 % TG emulsion, different emulsifiers, 1 %	Li and McClements (2010)
300	40–90	6.5	Tris-maleate 2 mM	Porcine pancreatin (3× USP) 300–800 USP units/mL	Porcine bile extract 5–30 mM/ 1–5 mM PC	Continuous addition, 0.045–0.181 mmol/min	15–30 mM TG, 1–3 g SNEEDS	Zangenberg et al. (2001a)
10–40	30–60	7.5	Tris-maleate 50 mM	Porcine pancreatin (8× USP) 1000 TBU/mL	NaTDC 5–20 mM/ 1.25–5 mM lecithin (60 % PC)	5 mM	1 g SEDDS, TG	Kaukonen et al. (2004)

(continued)

Table 25.1 (continued)

Volume (mL)	Duration (min)	pH	Buffer	Lipase	Bile/phospholipid	Calcium	Substrate	References
100	40	6.5	Tris-maleate 50 mM	Pancreatin extract 8 TBU/mg	Bile salts 5 mM/ Lecithin 1.25 mM	5 mM	1 g SEDDS	Ali et al. (2008)
20	35	7.5	Tris-maleate 50 mM	Porcine pancreatic lipase 40,000 IU/g 4000 TBU/mL	NaTDC 5 mM/ 1.25 mM lecithin (92% PC)	5 mM	0.21 g TG, sub-microemulsion	Han et al. (2009)

Reprinted from Thomas et al. (2012b) with permission from Springer

FEA free fatty acids; *NaTC* sodium taurocholate, *NaTDC* sodium deoxytaurocholate, *NaCDC* sodium chenodeoxycholate, *PC* phosphatidylcholine, *PL* phospholipid, *TBU* Tributyrin unit (1 TBU equals the amount of enzyme that can liberate 1 mol of fatty acid from tributyrin per min)

(Griffin et al. 2014; Thomas et al. 2014). In both studies, several LbDDS were evaluated *in vitro* and *in vivo*. And in both studies, the *in vitro* data suggested a significant difference between the tested DDS based on the amount of drug solubilised in the aqueous phase, while the *in vivo* data showed no difference in bio-availability.

In a study by Berthelsen et al. the dynamic *in vitro* lipolysis model was used to understand and explain observed plasma-concentration time profiles (in rats) of a series of fenofibrate-Kolliphor[®] DDS (Berthelsen et al. 2015). As the tested types of Kolliphor[®] (EL, ELP and RH40) are known to be digestible to different degrees (Cuine et al. 2008), the *in vitro* solubilisation of fenofibrate was determined during digestion using the dynamic lipolysis model. The study showed that Kolliphor[®] ELP and EL were digested to a higher degree than Kolliphor[®] RH40. With increasing concentrations of Kolliphor[®] ELP and EL, more fenofibrate was solubilised throughout 60 min of *in vitro* digestion, correlating well with an observed increased bioavailability. In the case of Kolliphor[®] RH40, no difference in the solubilisation of fenofibrate was seen *in vitro*, whereas there seemed to be an optimal Kolliphor RH40 level with an optimal bioavailability. This discrepancy was explained by a micellar entrapment effect, which was not captured by the lipolysis model, as it was unable to capture any permeation effects (Berthelsen et al. 2015). The missing evaluation of the absorption post digestion may generally make the *in vitro* lipolysis models too simple, as other mechanisms, aside from drug solubilisation in the GI lumen and drug permeability, may affect the absorption. Some excipients, including Kolliphor[®] EL, have been shown to inhibit the P-gp efflux pump, which will potentially give rise to an improved absorption of P-gp substrates (Constantinides and Wasan 2007). Very lipophilic drugs may be absorbed by lymphatic uptake, which is stimulated by long-chain lipids (Holm et al. 2003). Furthermore, the gastric emptying rate is typically prolonged by ingestion of lipids allowing longer dissolution and dispersion times (Kossena et al. 2007; Charman et al. 1997). None of these effects are presently captured by the *in vitro* lipolysis model.

The lack of product removal in a physiologically relevant manner is in some examples, resulting in shortcomings of the models. Furthermore, the models are mainly suitable for testing liquid systems, as the hydrodynamics are not physiologically relevant. Thus caution should be taken, if evaluating digestible solid dosage forms in any of the above mentioned models. The relatively simple setup of the pH-stat controlled models, ensures high-throughput and makes them easily adaptable to volumes, pH-levels etc. This is an advantage during the development process, where only small amounts of a new drug candidate are available and small volume testing is needed.

The use of *in vitro* lipolysis models has increased the general understanding of how lipophilic drugs traffic during digestion of lipid vehicles, and for this purpose the models remain interesting. However, in terms of predicting the bioavailability of oral dosage forms, the models need further evaluation and likely further development, e.g. by addition of an absorptive step.

2.2 *Complex Physiologically Relevant Models*

More complex models simulating digestion throughout the GI tract include the dynamic gastric model (DGM) (Mercuri et al. 2008; Wickham et al. 2012) and the TNO gastrointestinal model (TIM-1) (Minekus et al. 1995). These models are especially useful for the evaluation of food effects on dosage forms, but can also be useful for LbDDS. As lipid digestion begins in the stomach and continues in the duodenum and small intestine, a multi-compartment model may well be more physiologically relevant; however, due to the complexity of these models, the throughput is low, often making the simpler lipolysis models more attractive. Nevertheless, the complex models have been used successfully for *in vitro* evaluation of LbDDS and will be introduced in the following sections.

2.2.1 DGM

The DGM is a gastric digestion model developed at The Institute for Food Research (Norwich, UK). It was initially intended for food evaluation, but has also proved useful for pharmaceutical assessment (Vardakou et al. 2011b; Mercuri et al. 2008, 2011). Figure 25.3 shows a schematic overview of the model simulating different regions of the stomach. In the DGM, the stomach is divided into two sections; the main body (a combination of fundus and corpus) and the antrum. The main body primarily serves as a reservoir for the bolus and only limited agitation occurs in this region (Wickham et al. 2012). Secretion of enzymes and gastric acid is computer-controlled and takes place in the upper part of the apparatus, coating the inner surface of the main body. Gentle agitation secures that only the outer layer of the bolus is wetted. The wetted surface layer has a decreased viscosity compared to rest of the bolus, allowing for food migration to the antrum (Wickham et al. 2012). This replicates the events observed *in vivo* with secretion of gastric acid and enzymes in the fundus and corpus regions (upper part of stomach) and local wetting of the bolus. In the antrum shear forces are increased and grinding and mixing of the bolus occurs similar to what is observed *in vivo* (Vardakou et al. 2011a). The DGM also simulates gradual gastric emptying, by sequentially emptying food through an outlet valve. No duodenal or intestinal lipolysis step is incorporated in the DGM, but the secreted chyme can be exposed to further duodenal digestion in e.g. a pH-stat controlled *in vitro* lipolysis model.

The true advantage of the model compared to the simpler pH-stat controlled lipolysis models, is replication of the mechanical stress, which food and pharmaceuticals are exposed to in the stomach. Hence, the DGM is particularly suitable for testing disintegration of tablets or capsule rupture, as well as for food effect studies. Indeed in a study by Vardakou et al. (2011a, b) the authors showed that the DGM was able to predict capsule rupture of three different capsules, whereas a USP dissolution apparatus I was not (Vardakou et al. 2011b). In another study by Mercuri et al. 2011 it was investigated if different shear forces provided by the

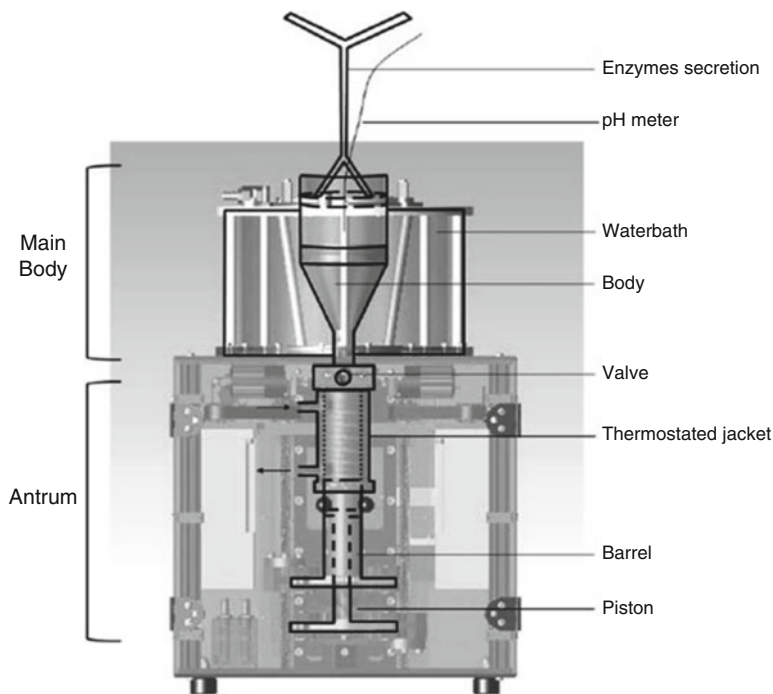


Fig. 25.3 A schematic overview of the DGM. It is divided into two sections; the main body and the antrum. The figure is reprinted from (Mercuri et al. 2011) with permission from Springer.

DGM, USP dissolution apparatus II and shaking the solution in a volumetric flask, affected the droplet size during dispersion of a self-emulsifying drug delivery system (SEEDS). The mechanical stress of the DGM resulted in five- to tenfold smaller droplets compared to the droplet distribution obtained by the other two methods (droplet size range from 3 to 30 μm depending on dispersion method). This was surprising, as SEEDS spontaneously forms an emulsion by gentle agitation. An increase in droplet size was, however, observed during emptying of the last fraction of gastric contents from the DGM, suggesting the presence of oil droplets floating at the top layer. This indicates that the emulsion was not stable and that mechanical forces could influence the droplet size, as seen with dietary lipids. It would therefore be worthwhile to evaluate if shear forces in the stomach influence the droplet size of a stable self micro-emulsifying drug delivery system (SMEDDS) or self nano-emulsifying drug delivery system (SNEDDS). This is of interest, as agitation in the simpler pH-stat models is performed by stirring, assuming mechanical stress is not affecting the formulation. It should be noted however, that in the study by Mercuri et al. 2011, the SEDDS droplet size *in vivo* was not determined; it was assumed that the DGM was predictive as it has been shown to yield droplet sizes in the regions of what has been observed *in vivo* during digestion of a liquid

meal (Mercuri et al. 2011). This might be a plausible assumption, but a more thorough study, would be to evaluate the droplet size *in vivo*, by gastric aspirations.

The DGM does therefore seem to simulate the physical properties of the stomach quite well, but is challenged on a biochemical level. The microbial lipase derived from *Rhizopus oryzae* (ROL), is used as a substitute for HGL, as no appropriate substitute for HGL is currently on the market, as explained in Sect. 2.1. The hydrolysis of lipids in the DGM, might consequently not correspond to what is observed *in vivo*. This can be an issue when evaluating substrates highly susceptible to gastric lipase, as the pharmaceutical excipient Labrasol produced by Gattefossé (Saint-Priest, France) (Fernandez et al. 2007). It could also lead to problems if the DGM is used to evaluate lipid digestion of patients, where HGL is the primary digestive enzyme e.g. people suffering from pancreatitis or cystic fibrosis.

The DGM can be used to simulate the mechanical stress formulations experience in the stomach, but is not ideal for predicting bioavailability of LbDDS, as it does neither include intestinal lipolysis nor absorption.

2.2.2 TIM-1 Model

The TIM-1 model is a multi-compartmental model that dynamically mimics the major events taking place in the upper part of the GI lumen. Figure 25.4 shows a schematic drawing of the system with four serial compartments simulating the stomach, duodenum, jejunum and ileum (Kostewicz et al. 2014). Each compartment has two sections contracting alternately to ensure mixing and simulate peristaltic movements. The temperature is controlled by water jackets, the pH value by automatic addition of acid or base as required according to a pre-defined protocol, appropriate mixing and physiological transit times are simulated with flexible walls and computer controlled pumps and valves (Naylor et al. 2006). Gastric, duodenal, jejunal and ileal secretion fluids containing BS, electrolytes and digestion enzymes are added to the discrete compartments. From the jejunal and ileal compartments of the system, low molecular weight compounds and water are removed continuously via dialysis or filtration. After this simple absorption step, the bio-accessibility (i.e. the solubilised amount available for absorption) of nutritional and pharmaceutical compounds is quantified (Naylor et al. 2006). The model was originally developed as a tool to study the fate of ingested components such as food, microorganisms and drugs, and early studies showed high accuracy in reproducing *in vivo* data on GI transit, pH, BS concentrations and absorption of glucose (Minekus et al. 1995). The model has also been used in the drug product development to predict *in vivo* performance (Naylor et al. 2006), evaluate DDS effects (Barker et al. 2014; Blanquet et al. 2004; Dickinson et al. 2012) and predict food effects (Blanquet et al. 2004; Souliman et al. 2006). Naylor et al. (2006) demonstrated that using bioaccessibility profiles from TIM-1 studies instead of standard USP 2 dissolution data as input data for an *in silico* absorption model, improved the predicted pharmaco-kinetic profile of an immediate release tablet formulation containing paroxetine hydrochlorid hemihydrate (Naylor et al. 2006).

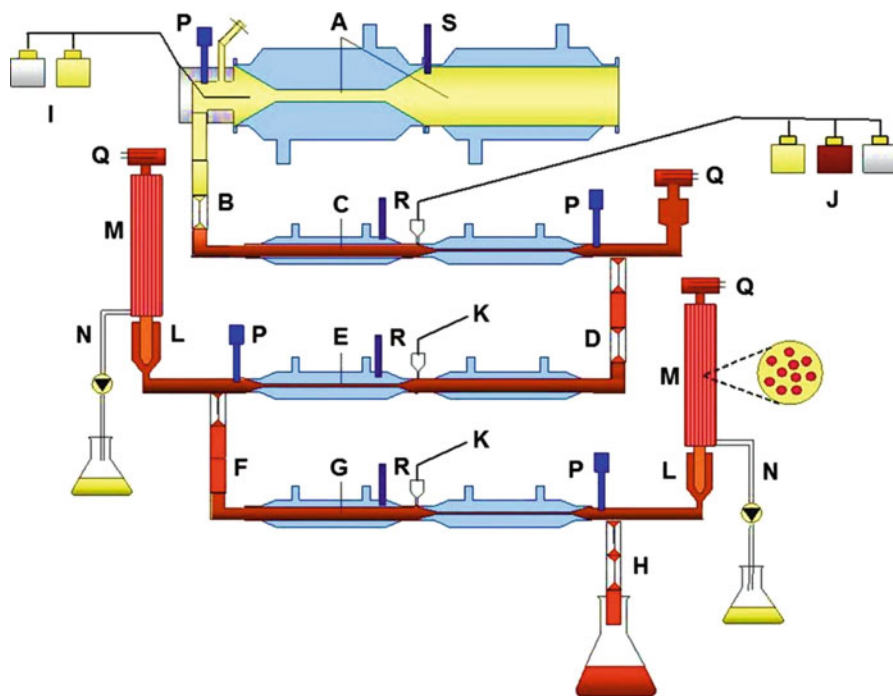


Fig. 25.4 Schematic drawing of the TIM-1 system. *A* stomach compartment, *B* pyloric sphincter, *C* duodenum compartment, *D* peristaltic valve, *E* jejunum compartment, *F* peristaltic valve, *G* ileum compartment, *H* ileo-caecal sphincter, *I* stomach secretion, *J* duodenum secretion, *K* jejunum/ileum secretion, *L* pre-filter, *M* semi-permeable membrane, *N* filtrate pump, *P* pH electrodes, *Q* level sensors, *R* temperature sensor, *S* pressure sensor. Reprinted from (Kostewicz et al. 2014) with permission from Elsevier (2015).

In the early drug product development phase, Dickinson et al. (2012) successfully used the TIM-1 model to evaluate and select an appropriate DDS for a weak base (AZD8055), reducing the need for preclinical *in vivo* studies (Dickinson et al. 2012).

Even though the TIM-1 model has produced some promising results reflecting *in vivo* data on the absorption of both food and drugs, the model also has its disadvantages. First, the model's absorption step is very simplified and lacks physiological relevance, i.e. most *in vivo* processes associated with the intestinal membrane like active transport, efflux and metabolism are not modelled. Therefore, in order to predict oral bioavailability rather than bioaccessibility, TIM-1 samples must be coupled with an intestinal absorption system, like e.g. a Caco-2 cell monolayer (Deat et al. 2009) or an *in silico* absorption model (Sjogren et al. 2013; Naylor et al. 2006). The performance of the TIM-1 will greatly depend on the tested drug and how that interacts with the added fluids and the system itself (Naylor et al. 2006). In a study by Berthelsen et al. (unpublished data), three fenofibrate MeltDos[®] formulations were tested in the TIM-1, but the model was

found unsuitable due to very low recovery; 16.6–29.8 % (w/w) before rinsing and 33.2–59.8 % (w/w) including the rinsing liquid. The low recovery was expected to be due to fenofibrate adsorption to the many plastic surfaces and filters, which is a known problem for lipophilic drugs (Dickinson et al. 2012). Other potential causes of low recovery include drug degradation or precipitation (Naylor et al. 2006).

Due to the relatively long run times and time consuming cleaning processes, the TIM-1 model has a very low throughput making it unfit for most screening purposes. The risk of high levels of adsorption also limits its use to predict oral bioavailability of poorly water soluble drugs. It is furthermore also dependent on ROL for gastric digestion and therefore has the same shortcomings, concerning gastric lipolysis as explained in for the DGM in Sect. 2.2.1. However, for certain drugs and specific evaluations, particularly involving food-related factors like food effects or digestion, of a discrete number of DDSs, the model appears superior to simple models, which only consider dissolution, digestion, or permeability, as well as more advanced models combining e.g. dissolution and absorption, as it allows for a better quantitative prediction of the amount of drug available for absorption. With respect to simulating GI hydrodynamics, peristaltic movements, gastric mixing and grinding, the TIM-1 model seems to be more physiologically relevant than the pH-stat models described in this chapter. It is, however, still inferior to the DGM in simulating shear forces of the stomach. Work has, however, recently been undertaken to improve the stomach section of the TIM-1 model.

3 Conclusions

When modelling drug absorption from orally administered DDS, it is essential to consider all the processes that can influence the drugs ability to reach the systemic circulation e.g. dissolution, precipitation, digestion, solubilisation and absorption, and to keep in mind that the human GI tract is a very complex system displaying numerous factors influencing drug absorption. For digestible DDS it is of key importance to simulate the digestion process, as this will directly impact the drug release profile. The pH-stat controlled lipolysis models and the more sophisticated digestion models such as the DGM and TIM-1 exemplify the range of digestion models used to forecast the drug release from digestible DDS. The models are very different in terms of complexity, advantages and limitations and are therefore often used for different purposes. Improvements of the models are in general needed in order to ensure ability to distinguish *in vitro* between the *in vivo* performances of different DDS. Especially incorporation of physiological relevant absorption, making the models capable of predicting bioavailability, as well as obtaining mechanistic understanding of the limiting factors for drug absorption from LbDDS, is considered to be important.

References

- Ali H, Nazzal M, Zaghoul AA, Nazzal S (2008) Comparison between lipolysis and compendial dissolution as alternative techniques for the in vitro characterization of alpha-tocopherol self-emulsified drug delivery systems (SEDDS). *Int J Pharm* 352(1–2):104–114. doi:[10.1016/j.ijpharm.2007.10.023](https://doi.org/10.1016/j.ijpharm.2007.10.023)
- Alvarez FJ, Stella VJ (1989) The role of calcium ions and bile salts on the pancreatic lipase-catalyzed hydrolysis of triglyceride emulsions stabilized with lecithin. *Pharm Res* 6(6):449–457
- Armand M (2007) Lipases and lipolysis in the human digestive tract: where do we stand? *Curr Opin Clin Nutr Metab Care* 10(2):156–164. doi:[10.1097/MCO.0b013e3280177687](https://doi.org/10.1097/MCO.0b013e3280177687)
- Armand M, Borel P, Dubois C, Senft M, Peyrot J, Salducci J, Lafont H, Lairon D (1994) Characterization of emulsions and lipolysis of dietary lipids in the human stomach. *Am J Physiol* 266(3):G372–G381
- Armand M, Borel P, Pasquier B, Dubois C, Senft M, Andre M, Peyrot J, Salducci J, Lairon D (1996) Physicochemical characteristics of emulsions during fat digestion in human stomach and duodenum. *Am J Physiol* 271(1):G172–G183
- Armand M, Pasquier B, Andre M, Borel P, Senft M, Peyrot J, Salducci J, Portugal H, Jaussan V, Lairon D (1999) Digestion and absorption of 2 fat emulsions with different droplet sizes in the human digestive tract. *Am J Clin Nutr* 70(6):1096–1106
- Barker R, Abrahamsson B, Kruusmagi M (2014) Application and validation of an advanced gastrointestinal in vitro model for the evaluation of drug product performance in pharmaceutical development. *J Pharm Sci* 103(11):3704–3712. doi:[10.1002/jps.24177](https://doi.org/10.1002/jps.24177)
- Bates TR, Gibaldi M, Kanig JL (1966) Solubilizing properties of bile salt solutions. II. Effect of inorganic electrolyte lipids and a mixed bile salt system on solubilization of glutethimide griseofulvin and hexestrol. *J Pharm Sci* 55(9):901–906. doi:[10.1002/jps.2600550906](https://doi.org/10.1002/jps.2600550906)
- Berthelsen R, Holm R, Jacobsen J, Kristensen J, Abrahamsson B, Mullertz A (2015) Kolliphor surfactants affect solubilization and bioavailability of fenofibrate. Studies of in vitro digestion and absorption in rats 12(4):1062–1071. doi:[10.1021/mp500545k](https://doi.org/10.1021/mp500545k)
- Blanquet S, Zeijdner E, Beyssac E, Meunier JP, Denis S, Havenaar R, Alric M (2004) A dynamic artificial gastrointestinal system for studying the behavior of orally administered drug dosage forms under various physiological conditions. *Pharm Res* 21(4):585–591. doi:[10.1023/B:Pham.0000022404.70478.4b](https://doi.org/10.1023/B:Pham.0000022404.70478.4b)
- Carey MC, Small DM, Bliss CM (1983) Lipid digestion and absorption. *Annu Rev Physiol* 45:651–677. doi:[10.1146/annurev.ph.45.030183.003251](https://doi.org/10.1146/annurev.ph.45.030183.003251)
- Carriere F, Barrowman JA, Verger R, Laugier R (1993) Secretion and contribution to lipolysis of gastric and pancreatic lipases during a test meal in humans. *Gastroenterology* 105(3):876–888
- Charman WN, Porter CJH, Mithani S, Dressman JB (1997) Physicochemical and physiological mechanisms for the effects of food on drug absorption: the role of lipids and pH. *J Pharm Sci* 86(3):269–282. doi:[10.1021/Js960085v](https://doi.org/10.1021/Js960085v)
- Christophersen PC, Christiansen ML, Holm R, Kristensen J, Jacobsen J, Abrahamsson B, Mullertz A (2014) Fed and fasted state gastro-intestinal in vitro lipolysis: In vitro in vivo relations of a conventional tablet, a SNEDDS and a solidified SNEDDS. *Eur J Pharm Sci* 57:232–239. doi:[10.1016/j.ejps.2013.09.007](https://doi.org/10.1016/j.ejps.2013.09.007)
- Constantinides PP, Wasan KM (2007) Lipid formulation strategies for enhancing intestinal transport and absorption of P-glycoprotein (P-gp) substrate drugs: in vitro/in vivo case studies. *J Pharm Sci* 96(2):235–248. doi:[10.1002/jps.20780](https://doi.org/10.1002/jps.20780)
- Cuine JF, McEvoy CL, Charman WN, Pouton CW, Edwards GA, Benameur H, Porter CJ (2008) Evaluation of the impact of surfactant digestion on the bioavailability of danazol after oral administration of lipidic self-emulsifying formulations to dogs. *J Pharm Sci* 97(2):995–1012. doi:[10.1002/jps.21246](https://doi.org/10.1002/jps.21246)
- Dahan A, Hoffman A (2006) Use of a dynamic in vitro lipolysis model to rationalize oral formulation development for poor water soluble drugs: correlation with in vivo data and the

- relationship to intra-enterocyte processes in rats. *Pharm Res* 23(9):2165–2174. doi:[10.1007/s11095-006-9054-x](https://doi.org/10.1007/s11095-006-9054-x)
- Dahan A, Hoffman A (2007) The effect of different lipid based formulations on the oral absorption of lipophilic drugs: the ability of in vitro lipolysis and consecutive ex vivo intestinal permeability data to predict in vivo bioavailability in rats. *Eur J Pharm Biopharm* 67(1):96–105. doi:[10.1016/j.ejpb.2007.01.017](https://doi.org/10.1016/j.ejpb.2007.01.017)
- Deat E, Blanquet-Diot S, Jarrige JF, Denis S, Beysac E, Alric M (2009) Combining the dynamic TNO-gastrointestinal tract system with a Caco-2 cell culture model: application to the assessment of lycopene and alpha-tocopherol bioavailability from a whole food. *J Agric Food Chem* 57(23):11314–11320. doi:[10.1021/jf902392a](https://doi.org/10.1021/jf902392a)
- DeSesso JM, Jacobson CF (2001) Anatomical and physiological parameters affecting gastrointestinal absorption in humans and rats. *Food Chem Toxicol* 39(3):209–228. doi:[10.1016/S0278-6915\(00\)00136-8](https://doi.org/10.1016/S0278-6915(00)00136-8)
- Dickinson PA, Abu Rmaileh R, Ashworth L, Barker RA, Burke WM, Patterson CM, Stainforth N, Yasin M (2012) An investigation into the utility of a multi-compartmental, dynamic, system of the upper gastrointestinal tract to support formulation development and establish bioequivalence of poorly soluble drugs. *AAPS J* 14(2):196–205. doi:[10.1208/s12248-012-9333-x](https://doi.org/10.1208/s12248-012-9333-x)
- Dressman JB, Berardi RR, Dermentzoglou LC, Russell TL, Schmaltz SP, Barnett JL, Jarvenpaa KM (1990) Upper gastrointestinal (Gi) pH in young, healthy-men and women. *Pharm Res* 7(7):756–761. doi:[10.1023/A:1015827908309](https://doi.org/10.1023/A:1015827908309)
- Fatouros DG, Bergenstahl B, Mullertz A (2007a) Morphological observations on a lipid-based drug delivery system during in vitro digestion. *Eur J Pharm Sci* 31(2):85–94. doi:[10.1016/j.ejps.2007.02.009](https://doi.org/10.1016/j.ejps.2007.02.009)
- Fatouros DG, Deen GR, Arleth L, Bergenstahl B, Nielsen FS, Pedersen JS, Mullertz A (2007b) Structural development of self nano emulsifying drug delivery systems (SNEDDS) during in vitro lipid digestion monitored by small-angle X-ray scattering. *Pharm Res* 24(10):1844–1853. doi:[10.1007/s11095-007-9304-6](https://doi.org/10.1007/s11095-007-9304-6)
- Fernandez S, Jannin V, Rodier JD, Ritter N, Mahler B, Carriere F (2007) Comparative study on digestive lipase activities on the self emulsifying excipient Labrasol, medium chain glycerides and PEG esters. *Biochim Biophys Acta* 1771(5):633–640. doi:[10.1016/j.bbaliip.2007.02.009](https://doi.org/10.1016/j.bbaliip.2007.02.009)
- Fernandez S, Chevrier S, Ritter N, Mahler B, Demarne F, Carriere F, Jannin V (2009) In vitro gastrointestinal lipolysis of four formulations of piroxicam and cinnarizine with the self emulsifying excipients Labrasol and Gelucire 44/14. *Pharm Res* 26(8):1901–1910. doi:[10.1007/s11095-009-9906-2](https://doi.org/10.1007/s11095-009-9906-2)
- Griffin BT, Kuentz M, Vertzoni M, Kostewicz ES, Fei Y, Faisal W, Stillhart C, O'Driscoll CM, Reppas C, Dressman JB (2014) Comparison of in vitro tests at various levels of complexity for the prediction of in vivo performance of lipid-based formulations: case studies with fenofibrate. *Eur J Pharm Biopharm* 86(3):427–437. doi:[10.1016/j.ejpb.2013.10.016](https://doi.org/10.1016/j.ejpb.2013.10.016)
- Hamosh M, Burns WA (1977) Lipolytic-activity of human lingual glands (Ebner). *Lab Invest* 37(6):603–608
- Han SF, Yao TT, Zhang XX, Gan L, Zhu C, Yu HZ, Gan Y (2009) Lipid-based formulations to enhance oral bioavailability of the poorly water-soluble drug anethol trithione: effects of lipid composition and formulation. *Int J Pharm* 379(1):18–24. doi:[10.1016/j.ijpharm.2009.06.001](https://doi.org/10.1016/j.ijpharm.2009.06.001)
- Hauss DJ (2007) Oral lipid-based formulations. *Adv Drug Deliv Rev* 59(7):667–676. doi:[10.1016/j.addr.2007.05.006](https://doi.org/10.1016/j.addr.2007.05.006)
- Heshmati N, Cheng X, Dapat E, Sassene P, Eisenbrand G, Fricker G, Mullertz A (2014) In vitro and in vivo evaluations of the performance of an indirubin derivative, formulated in four different self-emulsifying drug delivery systems. *J Pharm Pharmacol* 66(11):1567–1575. doi:[10.1111/jphp.12286](https://doi.org/10.1111/jphp.12286)
- Holm R, Porter CJ, Edwards GA, Mullertz A, Kristensen HG, Charman WN (2003) Examination of oral absorption and lymphatic transport of halofantrine in a triple-cannulated canine model after administration in self-microemulsifying drug delivery systems (SMEDDS) containing structured triglycerides. *Eur J Pharm Sci* 20(1):91–97

- Kaukonen AM, Boyd BJ, Charman WN, Porter CJ (2004) Drug solubilization behavior during in vitro digestion of suspension formulations of poorly water-soluble drugs in triglyceride lipids. *Pharm Res* 21(2):254–260
- Keller PJ, Allan BJ (1967) Protein composition of human pancreatic juice. *J Biol Chem* 242(2):281–287
- Kossena GA, Charman WN, Wilson CG, O'Mahony B, Lindsay B, Hempenstall JM, Davison CL, Crowley PJ, Porter CJH (2007) Low dose lipid formulations: effects on gastric emptying and biliary secretion. *Pharm Res* 24(11):2084–2096. doi:10.1007/s11095-007-9363-8
- Kostewicz ES, Abrahamsson B, Brewster M, Brouwers J, Butler J, Carlert S, Dickinson PA, Dressman J, Holm R, Klein S, Mann J, McAllister M, Minekus M, Muenster U, Mullertz A, Verwei M, Vertzoni M, Weitschies W, Augustijns P (2014) In vitro models for the prediction of in vivo performance of oral dosage forms. *Eur J Pharm Sci* 57:342–366. doi:10.1016/j.ejps.2013.08.024
- Larsen A, Holm R, Pedersen ML, Mullertz A (2008) Lipid-based formulations for danazol containing a digestible surfactant, Labrafil M2125CS: in vivo bioavailability and dynamic in vitro lipolysis. *Pharm Res* 25(12):2769–2777. doi:10.1007/s11095-008-9641-0
- Larsen AT, Sassene P, Mullertz A (2011) In vitro lipolysis models as a tool for the characterization of oral lipid and surfactant based drug delivery systems. *Int J Pharm* 417(1–2):245–255. doi:10.1016/j.ijpharm.2011.03.002
- Li Y, McClements DJ (2010) New mathematical model for interpreting pH-stat digestion profiles: impact of lipid droplet characteristics on in vitro digestibility. *J Agric Food Chem* 58(13):8085–8092. doi:10.1021/jf101325m
- Mercuri A, Lo Curto A, Wickham MSJ, Craig DQM, Barker SA (2008) Dynamic gastric model (DGM): a novel in vitro apparatus to assess the impact of gastric digestion on the droplet size of self-emulsifying drug-delivery systems. *J Pharm Pharmacol* 60:4
- Mercuri A, Passalacqua A, Wickham MSJ, Faulks RM, Craig DQM, Barker SA (2011) The effect of composition and gastric conditions on the self-emulsification process of ibuprofen-loaded self-emulsifying drug delivery systems: a microscopic and dynamic gastric model study. *Pharm Res* 28(7):1540–1551. doi:10.1007/s11095-011-0387-8
- Minekus M, Marteau P, Havenaar R, Huisintveld JHJ (1995) A multicompartmental dynamic computer-controlled model simulating the stomach and small-intestine. *Altern Lab Anim* 23(2):197–209
- Moreau H, Laugier R, Gargouri Y, Ferrato F, Verger R (1988) Human preduodenal lipase is entirely of gastric fundic origin. *Gastroenterology* 95(5):1221–1226
- Naylor TA, Connolly PC, Martini LG, Elder DP, Minekus M, Havenaar R, Zeijdner E (2006) Use of a gastrointestinal model and Gastroplus for the prediction of in vivo performance. *Ind Pharm* 12:9–12
- Pafumi Y, Lairon D, de la Porte PL, Juhel C, Storch J, Hamosh M, Armand M (2002) Mechanisms of inhibition of triacylglycerol hydrolysis by human gastric lipase. *J Biol Chem* 277(31):28070–28079. doi:10.1074/jbc.M202839200
- Palin KJ, Wilson CG (1984) The effect of different oils on the absorption of probuco in the rat. *J Pharm Pharmacol* 36(9):641–643
- Patton JS, Carey MC (1981) Inhibition of human pancreatic lipase-colipase activity by mixed bile salt-phospholipid micelles. *Am J Physiol* 241(4):G328–G336
- Porter CJ, Kaukonen AM, Boyd BJ, Edwards GA, Charman WN (2004a) Susceptibility to lipase-mediated digestion reduces the oral bioavailability of danazol after administration as a medium-chain lipid-based microemulsion formulation. *Pharm Res* 21(8):1405–1412
- Porter CJ, Kaukonen AM, Taillardat-Bertschinger A, Boyd BJ, O'Connor JM, Edwards GA, Charman WN (2004b) Use of in vitro lipid digestion data to explain the in vivo performance of triglyceride-based oral lipid formulations of poorly water-soluble drugs: studies with halofantrine. *J Pharm Sci* 93(5):1110–1121. doi:10.1002/jps.20039
- Porter CJH, Trevaskis NL, Charman WN (2007) Lipids and lipid-based formulations: optimizing the oral delivery of lipophilic drugs. *Nat Rev Drug Discov* 6(3):231–248. doi:10.1038/Nrd2197

- Reymond JP, Sucker H, Vonderscher J (1988) In vivo model for ciclosporin intestinal absorption in lipid vehicles. *Pharm Res* 5(10):677–679
- Sassene PJ, Knopp MM, Hesselkilde JZ, Koradia V, Larsen A, Rades T, Mullertz A (2010) Precipitation of a poorly soluble model drug during in vitro lipolysis: characterization and dissolution of the precipitate. *J Pharm Sci* 99(12):4982–4991. doi:[10.1002/jps.22226](https://doi.org/10.1002/jps.22226)
- Schulze K (2006) Imaging and modelling of digestion in the stomach and the duodenum. *Neurogastroenterol Motil* 18(3):172–183. doi:[10.1111/j.1365-2982.2006.00759.x](https://doi.org/10.1111/j.1365-2982.2006.00759.x)
- Sek L, Porter CJ, Charman WN (2001) Characterisation and quantification of medium chain and long chain triglycerides and their in vitro digestion products, by HPTLC coupled with in situ densitometric analysis. *J Pharm Biomed Anal* 25(3–4):651–661
- Sjogren E, Westergren J, Grant I, Hanisch G, Lindfors L, Lennernas H, Abrahamsson B, Tannergren C (2013) In silico predictions of gastrointestinal drug absorption in pharmaceutical product development: application of the mechanistic absorption model GI-Sim. *Eur J Pharm Sci* 49(4):679–698. doi:[10.1016/j.ejps.2013.05.019](https://doi.org/10.1016/j.ejps.2013.05.019)
- Souliman S, Blanquet S, Beyssac E, Cardot JM (2006) A level A in vitro/in vivo correlation in fasted and fed states using different methods: applied to solid immediate release oral dosage form. *Eur J Pharm Sci* 27(1):72–79. doi:[10.1016/j.ejps.2005.08.006](https://doi.org/10.1016/j.ejps.2005.08.006)
- Stillhart C, Durr D, Kuentz M (2014) Toward an improved understanding of the precipitation behavior of weakly basic drugs from oral lipid-based formulations. *J Pharm Sci* 103(4):1194–1203. doi:[10.1002/Jps.23892](https://doi.org/10.1002/Jps.23892)
- Thomas N, Holm R, Mullertz A, Rades T (2012a) In vitro and in vivo performance of novel supersaturated self-nanoemulsifying drug delivery systems (Super-SNEDDS). *J Control Release* 160(1):25–32. doi:[10.1016/j.jconrel.2012.02.027](https://doi.org/10.1016/j.jconrel.2012.02.027)
- Thomas N, Holm R, Rades T, Mullertz A (2012b) Characterising lipid lipolysis and its implication in lipid-based formulation development. *AAPS J* 14(4):860–871. doi:[10.1208/s12248-012-9398-6](https://doi.org/10.1208/s12248-012-9398-6)
- Thomas N, Holm R, Garmer M, Karlsson JJ, Mullertz A, Rades T (2013) Supersaturated self-nanoemulsifying drug delivery systems (Super-SNEDDS) enhance the bioavailability of the poorly water-soluble drug simvastatin in dogs. *AAPS J* 15(1):219–227. doi:[10.1208/s12248-012-9433-7](https://doi.org/10.1208/s12248-012-9433-7)
- Thomas N, Richter K, Pedersen TB, Holm R, Mullertz A, Rades T (2014) In vitro lipolysis data does not adequately predict the in vivo performance of lipid-based drug delivery systems containing fenofibrate. *AAPS J* 16(3):539–549. doi:[10.1208/s12248-014-9589-4](https://doi.org/10.1208/s12248-014-9589-4)
- Vardakou M, Mercuri A, Barker SA, Craig DQM, Faulks RM, Wickham MSJ (2011a) Achieving antral grinding forces in biorelevant in vitro models: comparing the USP dissolution apparatus II and the dynamic gastric model with human in vivo data. *AAPS PharmSciTech* 12(2):620–626. doi:[10.1208/s12249-011-9616-z](https://doi.org/10.1208/s12249-011-9616-z)
- Vardakou M, Mercuri A, Naylor TA, Rizzo D, Butler JM, Connolly PC, Wickham MSJ, Faulks RM (2011b) Predicting the human in vivo performance of different oral capsule shell types using a novel in vitro dynamic gastric model. *Int J Pharm* 419(1–2):192–199. doi:[10.1016/j.ijpharm.2011.07.046](https://doi.org/10.1016/j.ijpharm.2011.07.046)
- Wickham MJS, Faulks RM, Mann J, Mandalari G (2012) The design, operation, and application of a dynamic gastric model. *Dissolution Technol* 19(3):15–22
- Williams HD, Sassene P, Kleberg K, Bakala-N’Goma JC, Calderone M, Jannin V, Igonin A, Partheil A, Marchaud D, Jule E, Vertommen J, Maio M, Blundell R, Benameur H, Carriere F, Mullertz A, Porter CJ, Pouton CW (2012) Toward the establishment of standardized in vitro tests for lipid-based formulations, Part I: Method parameterization and comparison of in vitro digestion profiles across a range of representative formulations. *J Pharm Sci* 101(9):3360–3380. doi:[10.1002/jps.23205](https://doi.org/10.1002/jps.23205)
- Zangenberg NH, Mullertz A, Kristensen HG, Hovgaard L (2001a) A dynamic in vitro lipolysis model. I. Controlling the rate of lipolysis by continuous addition of calcium. *Eur J Pharm Sci* 14(2):115–122
- Zangenberg NH, Mullertz A, Kristensen HG, Hovgaard L (2001b) A dynamic in vitro lipolysis model. II: Evaluation of the model. *Eur J Pharm Sci* 14(3):237–244

Chapter 26

Application of Cell Culture and Tissue Models for Assessing Drug Transport

Carsten Uhd Nielsen and Birger Brodin

Abstract Drug transport in the body is a necessary step, from dosage form administration to the pharmacological target of the drug substance. Absorption (A), distribution (D), metabolism (M) and Excretion (E), i.e. ADME properties of drug substances, all include elements of drug transport. Cell culture and tissue-based models are often used to predict drug ADME properties, and to gain mechanistic insight into these. In the present chapter, the kinetics of drug transport and transport via drug transporters is described. The most common cell culture model for studying intestinal transport, i.e. the Caco-2 cell model is described in detail, and protocols for culturing and studying Caco-2 cells are included as an Appendix. Drug transport via carriers and transporters are important for drug substance ADME properties, and proton-coupled drug transport via the amino acid and peptide transporters PAT1 and PEPT1 in Caco-2 cells are discussed. Renal and hepatic models are also mentioned, as well as *in vitro* models of the blood brain barrier, which are discussed in more details. Even though *in vitro* models are easy to use and provide relatively reproducible results, areas of concerns and potential pitfalls are highlighted.

Keywords Caco-2 cells • Solute carriers (SLC) • ABC-transporters • Blood brain barrier • ADME • In vitro models • P_{app} • Drug transport • PAT1 • PEPT1

1 Introduction to Drug Transport and Drug Transporters

Movement of molecules across cell membranes and diffusion in cellular and extracellular compartments are fundamental for any drug in the process of moving from the site of administration to its site of action. The concentration of the drug at

C.U. Nielsen (✉)

Department of Physics, Chemistry and Pharmacy, University of Southern Denmark,
Campusvej 55, 5230 Odense, Denmark
e-mail: cun@sdu.dk

B. Brodin

Department of Pharmacy, University of Copenhagen, Universitetsparken 2, 2100 Copenhagen,
Denmark

the site of the biologic target mediating its actions is determined by a number of processes involving movement of drug into and out of tissues, and metabolism in these tissues. In the field of pharmaceutical sciences these processes are often described as ADME processes (and for the drug ADME properties), being an abbreviation of absorption, distribution, metabolism and excretion. To gain an understanding of factors determining the action and duration of a drug, it is an advantage to understand the underlying processes, which determine the ADME properties of a drug compound. Cell cultures and tissue preparations are important tools in this respect, and are used routinely to predict drug transport and drug metabolism in both academia and industry.

In the present chapter the application of cell culture and tissue models for assessing various aspects of drug transport is presented. The use of cell cultures or tissue models originates in the quest for detailed simplified information that is difficult to obtain from *in vivo* studies or studies in intact tissues. *In vitro* models may provide insights into transport across a specific biological barrier. This may for example be the intestinal wall in order to obtain an estimate of intestinal permeability and subsequent absorption fraction. It may also be transport across the blood brain barrier in order to estimate the fraction of drug available in the brain. Transport across a cell membrane is sometimes followed by metabolism, and this combined transport and metabolism is particular relevant in hepatic clearance and studied *in vitro* in e.g. hepatocyte cultures. Traditionally, cell culture models have been used for either mechanistic studies or for correlation purposes. The mechanistic studies may be assessing transport pathways such as paracellular versus transcellular, to investigate the effect of a permeation enhancer on transcellular or paracellular transport, or investigating an interaction between a drug candidate and transporters from either the solute carrier family (SLC) or the ATP-binding cassette family (ABC). For correlation purposes, a set of *in vitro* data is obtained and correlated with preferably human *in vivo* data. An example is correlation of permeability across Caco-2 cells with the human intestinal permeability (Artursson and Karlsson 1991) or human fraction of absorption (F_a) (Delie and Rubas 1997) in order to validate that a given *in vitro* model is predictive for a given human parameter.

1.1 Barrier Tissues

In order to get useful and predictive data from *in vitro* transport studies it is important to consider the types of barriers in the body and to have an overview of cell types. Barrier tissues are generally divided into epithelia and endothelia, i.e. barrier tissues facing the outside of the body or barrier tissues of the blood- and lymphatic vessels. The distinction is based upon the germ layer origin of the cell types, epithelia are generally derived from the embryonic endodermal or ectodermal layers, while endothelia are derived from the mesodermal layer. The distinction is therefore not based on physiological functions as such. Endothelia are

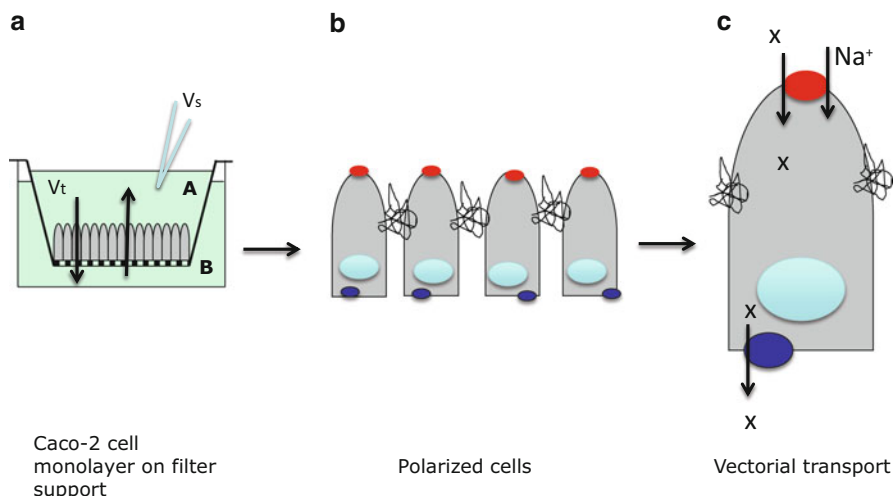


Fig. 26.1 Caco-2 cell monolayers in filter support used for transepithelial transport studies, e.g. from the apical (A) to the basolateral (B) side. V_s is volume of a sample, and V_t is the total volume from which the samples are taken. In tight epithelia cells (in grey) are interconnected at their lateral borders via protein complexes referred to as tight junctions (a). These are vital for the tissue structure and serve the dual role of linking cells together, but also serve as barriers in the cell membrane which restricts lateral movement of proteins in the cell membrane. The presence of the tight junction allows for a polarization (b) of the cells, i.e. allows that the apical and basolateral membrane have different types of transporters in their membranes. This polarization forms the basis for differences in transport rates, i.e. vectorial transport (c), across the individual membranes of the cell as well as across the cell layers

divided into peripheral and central endothelium (see Fig. 26.1), and both are composed of single layers of endothelial cells. The peripheral vascular endothelium is not considered to be a barrier to drug transport due to its leaky nature. The central vascular endothelium on the other hand is, due to its tight nature and presence of enzymes and efflux transporters, a significant barrier to drug transport into the brain. This is discussed in more details later in the chapter. The epithelia are classified according to the number of cell layers, and the shape of the cells (Fig. 26.1). A simple epithelium has a monolayer, a stratified epithelium has more than one cell layer. An epithelium with flat cells is termed squamous, one with cubic cells is termed cuboidal, and an epithelium with cells that are higher than their width, is termed columnar. Cells may furthermore have specialisations such as cilia or microvilli. As an example, cells of the absorptive intestinal epithelium are simple columnar epithelial cells with apical microvilli, whereas crypt epithelium is of the simple cuboidal-type. In tight epithelia and endothelia, the cells are interconnected at their lateral borders via protein complexes referred to as tight junctions. These are vital for the tissue structure and serve the dual role of linking cells together, but also serve as barriers in the cell membrane which restricts lateral movement of proteins in the cell membrane. The presence of the tight junction

allows for a polarization of the cells, i.e. allows that the apical and basolateral membrane have different types of transporters and enzymes, as well as lipids in their membranes. This polarization forms the basis for differences in transport rates, i.e. vectorial transport, across the individual membranes of the cell as well as across the cell layers. The structure of the cells and the degree of cellular differentiation is important to consider when validating and using cell culture models. The presence, polarization and amount of transporters vary with the presence of tight junction, and when using cell culture models, the morphology, polarisation and transporter expression should always be validated.

1.2 Simple Transport Kinetics

Investigations of drug transport across a barrier tissue provide data normally expressed in terms such as flux, permeability or clearance. Considering the simple situation where a non-degraded, non-metabolized drug is transported across a barrier tissue down its concentration gradient without any interaction with transporters, carriers or pumps, samples in a transport study are taken from the donor (starting amount is 100 %) and acceptor side (starting concentration is 0) at various time points in order to measure the concentration of drug on each side of the barrier. At the end of the experiment, the barrier tissue itself is lysed and the amount of drug present herein is quantified. Knowing the amount of drug in all three compartments at the end of the experiment is important, as it allows for an estimation of the mass balance. In case this is notably below 100 % the drug may be either metabolised, be chemical instable, have precipitated, or be adsorbed to surfaces in the *in vitro* setup, and further investigations addressing this are warranted. If mass balance is between 80–120 %, and if the concentration in the acceptor compartment is less than 10 % of that in the donor compartment, the steady-state flux of the compound can be calculated. Initially, mass transfer across the barrier is calculated as the amount of mass accumulated in the acceptor compartment during the experiment:

$$Mass = V_s \left(\sum_{n=1}^n C_{n-1} \right) + C_n V_t$$

Where V_s is volume of the sample, C is the concentration of a number of samples, n , and V_t is the total volume from which the samples are taken (see Fig. 26.1). The mass transferred can then be plotted as a function of time. The steady-state part of the accumulation is the amount transferred per area per time:

$$\frac{Mass}{Area \times Time} = J$$

J is termed the flux, and the unit is e.g. nmol/cm²/s. The flux may be normalized to the starting donor concentration to yield the apparent permeability coefficient (P_{app}), often just termed the permeability:

$$\frac{J}{C_0} = P_{app}$$

The permeability coefficient, which has the unit, e.g. cm/s, is useful for comparisons of values from different laboratories using similar *in vitro* models, e.g. Caco-2 cells. The permeability is dependent on the effective diffusion coefficient, D_{eff} (e.g. m²/s), in the model and the thickness, h (e.g. cm), of the model and the partitioning coefficient between cell/tissue and the solution, $K_{p,eff}$. It should therefore not be used to compare very different models from different cell lines or tissues:

$$P_{app} = \frac{D_{eff} \times K_{p,eff}}{h}$$

In the screening of the permeability of new chemical entities or drug candidates, single point measurements are sometimes used. This is not recommended; as such end-point measurements contain all events in the model system from applying the drug to collecting the final sample. These include potential lag-time, solvent drag induced by either differences in osmotic strength or the application of the solutions, and/or time- and concentration-dependent toxic effects exerted by the compound itself on the *in vitro* model, resulting in altered transport across the model.

1.3 Transport Kinetics in the Presence of Drug Transporters

In the case of transport in cellular systems where transporters influence the total transport, the basic considerations concerning transport studies mentioned in 1.2 still applies, but the interpretation is slightly different. In the case of transport across a membrane where the transporter works to influx compound from a concentration, C , the flux, J , is described by a carrier- and passive component:

$$J = \frac{J_{max} * C}{K_m + C} + P_{app} * C$$

Where J_{max} is the maximal flux, K_m is the Michaelis constant and P_{app} is the passive permeability across the membrane. If the process is only carrier-mediated, the passive part of the equation becomes zero. In the case of multiple influx transporters each expression for the carrier defined by the kinetic parameters J_{max} and K_m is added to describe the total flux across the membrane. One way to estimate the

individual contributions of carriers to the total transport is to use transporter specific inhibitors, as illustrated by Frølund et al. (2010), another is to use knock-down or knock-out cells lines or animals. If the transporter works in the opposite direction of the flux direction investigated, the total transport is described by:

$$J = P_{app} * C - \frac{J_{max} * C}{K_m + C}$$

This phenomenon can occur in barrier tissues where efflux transporters such as p-glycoprotein, multi-drug resistance protein or breast-cancer resistance protein limit the transport of a drug compound. In such cases it may, however, be difficult to get appropriate estimates of the kinetic parameters of the transporter-mediated transport process.

Combinations of these equations may be used to describe the drug transport across biological membranes and tissue barriers, and to estimate the relative contribution of passive versus active transport processes, and thereby to assess the impact of a transporter on drug transport.

2 Cell Culture and Tissue Based *In Vitro* Models

In this section we will discuss cell culture based *in vitro* models for investigations of drug transport, with focus on a small set of selected cell models. There is a large number of cell models described in the literature, and a vast number of immortalized and primary cell lines are available for investigations. Inspiration and information regarding purchase, protocols and security classifications may be found at these vendors: ATCC (<http://www.atcc.org/>), ECACC (<http://www.phc-culturecollections.org.uk/>), DSMZ (<https://www.dsmz.de/>), CellBank Australia (<http://www.cellbankaustralia.com/>).

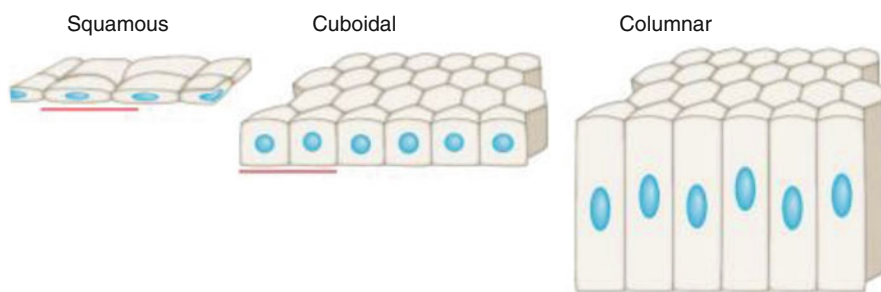
2.1 *Intestinal Cell Models*

A number of models for investigating intestinal drug transport exist. These include intestinal cell cultures, excised tissues mounted in an Ussing chamber, simple everted sacs, *in situ* perfusion studies, and full pharmacokinetic studies. In the present section focus is on *in vitro* cell culture models and their use in investigating intestinal permeability, drug-transporter interactions and application for regulatory purposes.

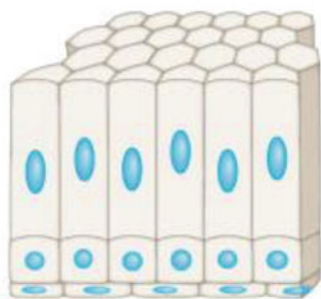
2.1.1 Caco-2 Cell Monolayers

In terms of cell culture based *in vitro* models, Caco-2 cells grown on permeable filters (Fig. 26.2A) is the most commonly used model for *in vitro* investigations of intestinal drug transport, as described in several excellent reviews (Delie and Rubas 1997; Artursson et al. 2001; Sun et al. 2008; Volpe 2008). The Caco-2 cell line was derived from a human colon adenocarcinoma (Fogh et al. 1977), and was first used for transport studies by Hidalgo et al. (1989). In culture the cells have characteristics of both small intestinal enterocytes and colonocytes, and differentiate to various degrees during culture. Caco-2 cells form relatively tight monolayers in culture when cultured on permeable filter support, and this allows for directional studies looking at either transport in the lumen to blood direction (apical to basolateral transport) or blood to lumen transport (basolateral to apical transport). The apical to basolateral flux of a given drug substance/candidate can be used to calculate an *in vitro* permeability of the compound, and this can serve as an estimate of the intestinal permeability in the absorptive direction (see Sect. 1.3, and Table 26.1). Several correlations between the drug permeability in Caco-2 cells

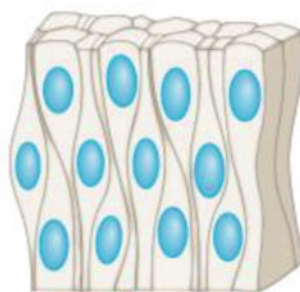
a Simple epithelia



b Stratified epithelia (e.g., columnar stratified)



c Pseudostratified epithelia



TRENDS in Cell Biology

Fig. 26.2 Types of epithelia: Simple epithelia (a) may have flat cells, termed squamous, cubic cells, which are termed cuboidal, or cells that are higher than their width, termed columnar. A simple epithelium has a monolayer (a), whereas a stratified epithelium (b) has more than one cell layer, or (c) just one layer looking like a multi-layer, i.e. pseudo-stratified

Table 26.1 FDA suggested compounds for in vitro permeability validation

Drug	Permeability class	A-B Caco-2 P_{app} ($\times 10^{-6}$ cm/s)	A-B Caco-2 P_{app} ($\times 10^{-6}$ cm/s)	Reference
		pH 7.4/7.4 (Jung et al. 2006)		
Antipyrine	High (IS)	40.9 \pm 5.0	36; 47; 49.5; 28.2	Brayden et al. (2012), Hilgendorf et al. (2000b), Laitinen et al. (2003), and Corti et al. (2006)
Caffeine	High	40.8 \pm 15.8	46.3–53.5; 30.8,	Corti et al. (2006) and Smetanova et al. (2009)
Carbamazepine	High	35.8 \pm 1.8		
Fluvastatin	High	25.4 \pm 1.3	16	Lindahl et al. (2004) and Li et al. (2011)
Ketoprofen	High	16.9 \pm 1.0	45; 10.2; 24.2; 20.1; 44.4	Jung et al. (2006), Laitinen et al. (2003), Corti et al. (2006), and Fischer et al. (2011)
Metoprolol	High (IS)	23.6 \pm 3.5	19; 33; 23.7	Jung et al. (2006), Corti et al. (2006), and Koljonen et al. (2006)
Naproxen	High	24.8 \pm 6.3	47; 39.5	Hilgendorf et al. (2000b) and Corti et al. (2006)
Propranolol	High	14.2 \pm 2.4	32.5; 41.9	Laitinen et al. (2003) and Corti et al. (2006)
Theophylline	High	32.7 \pm 1.3	23.2; 46.5	Corti et al. (2006)
Verapamil	High (ES)	11.7 \pm 0.3	2.3; 23.3; 15.8	Laitinen et al. (2003), Corti et al. (2006), and Koljonen et al. (2006)
Amoxicillin	Low	1.8 \pm 0.6	~1.4	Matysiak-Budnik et al. (2002)
Atenolol	Low	0.2 \pm 0.0	0.13; 0.2	Hilgendorf et al. (2000b) and Corti et al. (2006)
Furosemide	Low	0.2 \pm 0.0	0.12; 0.5	Corti et al. (2006)
Hydrochlorthiazide	Low	5.0 \pm 0.6	0.51	Corti et al. (2006)
Mannitol	Low (IS)	0.5 \pm 0.0	0.14	Hilgendorf et al. (2000b)
α -Methyldopa	Low		0.15	Corti et al. (2006)
Polyethylene glycol (400)	Low	1.8 \pm 0.9		
Polyethylene glycol (1000)	Low			
Polyethylene glycol (4000)	Low (Z)	0.3 \pm 0.1	0.04; 0.06; 0.08	Anderberg et al. (1992)
Ranitidine	Low	0.3 \pm 0.1	0.49	Corti et al. (2006)

Potential internal standards (IS), efflux pump substrates (ES), and zero permeability marker (Z) are also suggested by the FDA. A: apical, B: basolateral

and the human absorption fraction *in vivo* are available (Artursson and Karlsson 1991; Lennernas 1997; Walter et al. 1996). The Caco-2 cell model has also been used for correlation to colonic absorption and peptide transporter-mediated absorption (Bretschneider et al. 1999; Rubas et al. 1996). However, there are a large number of experimental conditions, which may vary between labs, and thus contribute to differences in reported values on transepithelial drug transport. During the actual experiment these include the type of permeable support used, buffer composition and pH, serum albumin concentration, agitation of the cells, temperature, presence of co-solvents, concentration of the drug and its solubility in the buffers used, sampling time and frequency and sample volume. During the culturing of the Caco-2 cells these include the type of permeable support used, culture time, seeding density, source of the Caco-2 cells, passage number, feeding regimen and culture medium. The protocol currently used by our laboratory is included in this chapter as Appendix.

Since Caco-2 cells form monolayers in culture and differentiate into polarized columnar cells, it is possible to study drug or nutrient transport across the apical or the basolateral membrane of the cells. This is particularly important in studies involving transporter investigations. We have routinely used Caco-2 cells as an *in vitro* model expressing hPEPT1 during our research related to developing di/tripeptide based prodrugs targeting the human intestinal di/tripeptide transporter hPEPT1 (SLC15A1). During culturing on permeable filters the apical expression of PEPT1 increased (Bravo et al. 2004a; Nielsen et al. 2001a) and using differentiated cells we could investigate whether compounds had an affinity for hPEPT1, whether they were transported across the apical membrane and whether they were able to be transported through both the apical and basolateral membranes, i.e. showed transepithelial transport (Nielsen et al. 2001b; Thomsen et al. 2003; Vabeno et al. 2004a, b). Some transporters are difficult to express in expression systems, and one of those is the proton-coupled amino acid transporter, PAT1 (SLC36A1). Fortunately, hPAT1 is expressed endogenously in the apical membrane of Caco-2 cells (Chen et al. 2003), and we have used Caco-2 cells to screen for hPAT1 affinity of GABA-mimetics (Larsen et al. 2008, 2009; Frolund et al. 2011), to investigate apical uptake of PAT1-substrates (Frolund et al. 2010; Nohr et al. 2014) and to measure transepithelial transport of PAT1 substrates (Larsen et al. 2008; Frolund et al. 2012). It is fairly straightforward to investigate apically located absorptive transporters such as hPEPT1 and hPAT1. However, it is more difficult to investigate transport across the basolateral membrane, which is part of the barrier function in the transport process from the apical to the basolateral compartment. In the case of oral absorption the transport direction across the basolateral membrane is from the interior of the cell to the extracellular space. This makes it difficult to assess the transport across the basolateral membrane because it is difficult to estimate the intracellular drug concentration in combination with the resulting flux across the basolateral membrane. Moreover, Caco-2 cells are cultured on permeable supports, which limit the direct access to the membrane, as opposed to the direct access to the apical membrane. Transport across the basolateral membrane is therefore often investigated by applying the compound

of interest on the basolateral side of Caco-2 cells for a defined time period, followed by lysis of the cells, quantification of the cellular amount of compound and subsequently an influx rate is calculated (Nielsen et al. 2012).

One of the draw-backs of Caco-2 cell monolayers is that the cells do not produce mucin, which is part of the unstirred water-layer (UWL) found adjacent to the enterocytes in the *in vivo* situation. The UWL may be a diffusion barrier to large hydrophilic molecules such as peptides and proteins, and at the same time protect the cells against direct toxic effects. Since the Caco-2 cell monolayers fail to mimic this feature of the native tissue, they may not be optimal for studies of the transport of larger peptides and proteins. Some compounds may also exhibit toxicity in the *in vitro* model but not *in vivo*, due to the presence of the mucus layer in the *in vivo* situation.

2.1.2 Other Intestinal Cell Culture Models

Other intestinal cell models have therefore been developed and been characterized, e.g. Caco-2 cells and goblet-producing HT-29 co-cultures (Hilgendorf et al. 2000; Walter et al. 1996). Triple cultures have also been developed using Caco-2 cells, HT-29 cell and Raji B lymphocytes, in order to simulate the diversity of the entire intestinal epithelium. The triple cultures are designed so as to include absorptive epithelial cells in the form of Caco-2 cells, goblet producing cells in the form of HT-29 cell and M-cells, which are induced by the presence of Raji B lymphocytes (Antunes et al. 2013; Araujo and Sarmiento 2013).

Another draw-back of the conventional Caco-2 cell model is that the cells require 14–21 days of culture before they are homogeneously differentiated and ready to use for transport studies. Therefore, single cultures of Caco-2 cell cultured with various growth factor and regulators of signal pathways with reduced culture time (3–7 days) in mind have been investigated (Bravo et al. 2004a; Lentz et al. 2000; Liang et al. 2000). However, these may only be useful for certain investigations and cannot serve as a substitute for the conventional 21-day culture Caco-2 cell model.

The Madin-Darby canine kidney (MDCK) cell line is another cell line often used for transport studies. This cell line is derived from a canine kidney, and has two clonal strains, the MDCK I cells which forms non-ciliated, columnar monolayers with high transepithelial electrical resistance, and MDCK II cells which form cuboidal ciliated monolayers of low electrical resistance. MDCK cells, grown on permeable supports have mainly been used for investigations of intestinal permeability, and since it is of renal nature it seems less useful for absorptive processes caused by intestinal carriers, but may be better suited for looking at intestinal efflux processes mediated by e.g. active transport via p-glycoprotein (ABCB1). The MDCK cell lines have also been used for transfection with efflux transporters and serve as surrogate blood-brain barrier models, as mentioned later in the chapter.

2.1.3 Cell Cultures in Permeability Classification

Tissue and cell cultures may also be used to study drug transport in a regulatory perspective. An additional use of Caco-2 cell monolayers is in waivers for *in vivo* bioavailability or bioequivalence studies for immediate release solid oral dosage forms of highly soluble and permeable drug substances (U.S. Department of Health and Human Services Food and Drug Administration Center for Drug Evaluation and Research (CDER) 2000). A key component of the waiver is the assessment of intestinal permeability, which may be estimated from fraction of drug dose absorbed in human, rate of mass transfer across intestinal membranes obtained from *in vivo* or *in situ* studies in human or animals, or from *in vitro* epithelial cell culture methods (U.S. Department of Health and Human Services Food and Drug Administration Center for Drug Evaluation and Research (CDER) 2000). The suitability of the chosen permeability model should be validated using compounds with known high and low intestinal permeabilities. In Table 26.1 the compounds suggested by the US food and drug administration (FDA) is given along with a selection of reported permeabilities. Comparable Caco-2 cell permeabilities obtained from Jung et al. are shown in Table 26.1 (Jung et al. 2006). The experimental setup was based on Caco-2 cells obtained from ATCC, and grown on permeable filters for 21–25 days. The pH of the apical and basolateral HBSS buffer was 7.4, and the donor concentration was 0.1 times the dose divided by 250 mL. It is clear that a certain lab-lab variation in permeability values obtained exist, which argues for the inclusion of well-known compounds for validation purposes.

The cell lines presented in this section are in reality substitutes for using native enterocytes. The practical use of primary cultures is, however, limited since primary enterocytes only can be passaged a limited number of times (3–4 times). They are currently not useful for studies of intestinal drug transport. Alternatives to cell cultures are excised tissues from animals or humans, are mounted in Using chamber setups. The throughput of such studies is however rather low, and also involves ethical aspects.

2.2 Blood-Brain Barrier Models

2.2.1 Introduction to the Blood-Brain Barrier/the Neurovascular Unit and BBB-Models

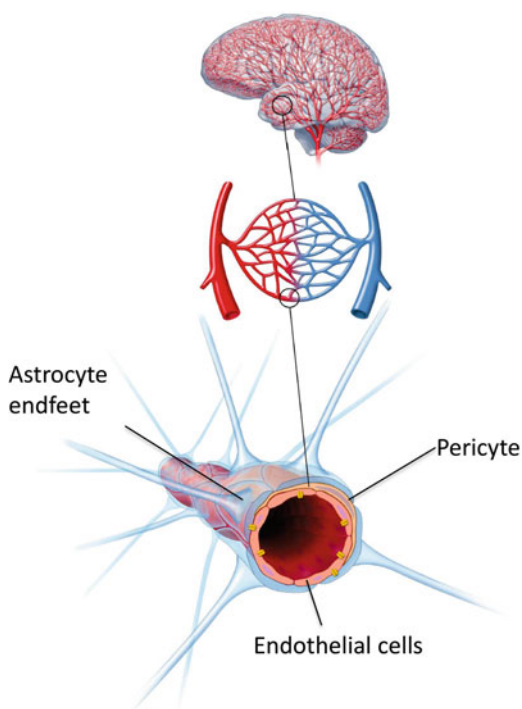
The blood-brain barrier (BBB) limits the uptake of most small molecules and practically all macromolecules. Overcoming low blood-brain barrier permeability is a thus major obstacle in the development of drugs intended to act in the central nervous system (CNS) (Pardridge 2007). An *in vitro* model, reflecting all the properties of the blood-brain barrier in terms of barrier morphology, passive permeability properties, functional transporter expression and enzyme expression, would allow for screening of new drug candidates at an early stage in the drug

development process and a lot of attention has been given to develop predictive *in vitro* BBB models. However, at present there is no standard *in vitro* model of the blood-brain barrier allowing for prediction of all the processes. A number of models are available, each with its own strengths and drawbacks. This section will focus on the most widely used models, with emphasis on the *in vitro* models, which form tight monolayers, making them useful for estimation of transendothelial transport and thus BBB permeability of drug compounds.

The term BBB is a figurative description of the barrier function of the endothelial cells in the brain capillaries. In order to understand the strengths and weaknesses of the various *in vitro* models, it may be helpful to have a general idea of the structure of the brain microvasculature: The brain capillaries are composed of tubes of endothelial cells, partly covered (~30 %) with another cell type, the pericyte. The endothelial cells and pericytes are completely covered with astrocyte protrusions, the astrocyte endfeet (see Fig. 26.3). The endothelium can be innervated, and microglia may also be present in the close vicinity of the endothelium. The endothelial phenotype can be influenced by signalling factors from all these cell types. The most electrically tight *in vitro* models are therefore co-culture models, where endothelial cells are cultured together with astrocytes, pericytes or both (Fig. 26.4).

The endothelial cells in the blood-brain barrier express the efflux transporters P-gp and BCRP as well as MRP's in their luminal (blood-facing) membrane, a range of nutrient transporters such as LAT1, GLUT1 and MCT1 in both their

Fig. 26.3 Schematic overview of the neurovascular unit/the blood-brain barrier. The endothelial cells, lining the capillaries, constitute the blood-brain barrier. Pericytes are embedded in the basement membrane between endothelial cells and astrocytes, and astrocyte endfeet encircle the capillaries and pericytes



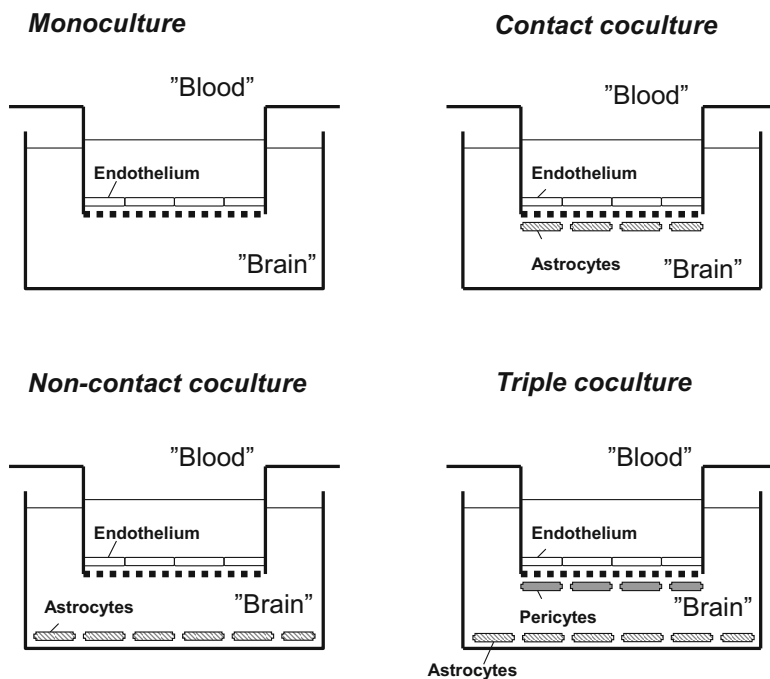


Fig. 26.4 Schematic overview of common cell culture configurations for in vitro blood-brain barrier models. *Upper left Panel:* Monocultures where endothelial cells are seeded on the upper surface of permeable supports. The endothelial cells will form monolayers and orientate themselves with the luminal side facing the upper compartment and the abluminal side facing the lower compartment. *Lower left panel:* Non-contact co-culture. Astrocytes are seeded in the bottom of the culture wells, endothelial cells on the upper surface of permeable supports. *Upper right panel:* Contact co-culture. Astrocytes are seeded on the lower surface of permeable supports; endothelial cells are seeded on the upper surface. *Lower right panel:* Astrocytes are seeded on the bottom of culture wells, pericytes are seeded on the lower surface of permeable supports, endothelial cells on the upper surface

luminal and abluminal (brain-facing) membrane and a range of tight junction proteins including Claudin-5, which give the BBB its tightness towards small molecules. The electrical tightness of the *in vivo* barrier has been estimated to be in the range of $2000 \Omega \cdot \text{cm}^2$ (Crone and Olesen 1982) and the permeability for small molecules like the cell impermeable paracellular flux marker mannitol has been estimated to approximately 10^{-8} cm/s (Amtorp 1980). The BBB is water permeable, but practically impermeable for most hydrophilic solutes, unless they can cross the barrier via transport proteins. Lipophilic solutes may cross the barrier, but the large expression of efflux transporters keep most lipophilic drug compounds out of the brain.

An ideal *in vitro* model of the blood-brain barrier for use in drug development and drug delivery studies should display a permeability *in vitro*–*in vivo* correlation when tested with drug compounds with known *in vivo* permeability. The model

should also fulfil some general criteria listed below (Gumbleton and Audus 2001; Abbott 2014).

- The cell model should have a restrictive paracellular pathway and ideally express the same types of junction proteins as the native barrier.
- The model should possess a cell phenotype morphologically comparable to the native brain endothelium, i.e. large and thin cells (<0.5 μm in thickness at the cell periphery).
- The model should display functional expression of membrane transporters, both ABC-type efflux transporters and SLC-transporters mediating uptake, as well as brain endothelium-specific enzymes such γ -glutamyltranspeptidase and alkaline phosphatase.
- The model should be easy to culture in order to facilitate high throughput screening.

No single *in vitro* model of the blood-brain barrier fulfils these criteria. In general, BBB *in vitro* models fall into two groups, immortalized endothelial cell lines of animal or human origin and primary cell cultures of animal origin. The endothelial cell lines and cultures can be grown alone or in co-cultures with astrocytes and/or pericytes (Fig. 26.4). As a general rule, it can be stated that while immortalized endothelial cell lines often express relevant transporters and are easy to culture, they tend to have poorly developed junctions and do not develop into tight monolayers and can therefore have limited use in drug delivery studies (Veszeka 2011). Primary cultures of endothelial cells do express some of the BBB-specific transporters, although they tend to loose transporter expression rapidly during sub-culturing and therefore only useful in early passages. They possess realistic cell architecture and can form tight monolayers, but they are work-demanding to establish and maintain.

To give an overview of all published blood-brain barrier *in vitro* models is beyond the scope of the present chapter, but a number of excellent reviews cover the subject (Gumbleton and Audus 2001; Abbott 2014; Deli et al. 2005; Wilhelm et al. 2011). In the following we will describe three electrically tight *in vitro* models based on primary endothelial cultures from rat, pig and cow. These models have been tested to varying degrees with respect to tightness, junctional protein composition and transporter expression. They can all, due to their high resistance, be used for transport studies when cultured as monolayers on permeable supports in e.g. Transwell systems.

2.2.2 The Rat Triple Co-culture Blood-Brain Barrier Model

The rat triple co-culture model is a cell model where endothelial cells obtained from rat brains are co-cultured with both astrocytes and pericytes (Nakagawa et al. 2009; Hellinger et al. 2012)). The endothelial cells are seeded on the upper surface of permeable supports, pericytes on the lower surface and astrocytes are seeded at the bottom of the culture wells. In brief, capillary fragments are isolated from rat brains

by mechanical dissociation and enzyme treatment, followed by density gradient centrifugation. The microvessel fragments are seeded on coated culture dishes, cultured with growth factors and a range of supplements, including puromycin which favours the growth of P-gp-expressing endothelial cells (Perriere et al. 2005). The cells are collected by trypsinization and seeded on the permeable supports. Rat astrocytes are obtained by simple mechanical dissociation of cerebral tissue, followed by flask culture. Pericytes are obtained from prolonged culture of microvessels using pericyte-selective conditions, i.e. no puromycin and uncoated culture dishes. The endothelial cells are co-cultured for 4 days, in the presence of hydrocortisone (500 nM). The endothelial cells of the triple co-cultures are thin, have up-regulated expression of ZO-1, occludin and Claudin-5 as compared to monocultures. The endothelial cells express Glut-1, Mrp1 and P-gp at the protein level. They display vectorial transport of the P-gp substrates Rhodamine 123 and digoxin with an efflux ratio of ~ 2.5 , and have a transendothelial electrical resistance in the range of $\sim 350\text{--}550 \Omega \cdot \text{cm}^2$ and a sodium fluorescein (376 g/mol) permeability in the range of $\sim 3\text{--}4 \cdot 10^{-6}$ cm/s (Nakagawa et al. 2009; Hellinger et al. 2012).

This model allows for direct comparison with *in vivo* data from rats, and has the three main cell types of the neurovascular unit included and a decent tightness. Drawbacks of the model are the relatively low yield of cell material from rat brains and the complexity, which arises from the handling of three different cell types during culture.

2.2.3 The Porcine Monoculture Blood-Brain Barrier Model

Blood-brain barrier models are based on endothelial cells from porcine brains, grown on permeable supports in monoculture (Franke et al. 1999). The endothelial cells are generated by isolating microvessels from the cerebral cortex by mechanical dissociation followed by a series of steps including dextran centrifugation, filtration and enzyme treatments (Franke et al. 2000) or, alternatively, by homogenization in a Dounce homogenizer, followed by filtration and enzyme treatment steps (Patabendige et al. 2013). The endothelial cells are cultured on permeable supports coated with rat tail collagen in a serum-free medium, in the presence of hydrocortisone (Hoheisel et al. 1998) for 6–8 days. Cells display endothelial morphology with large, flattened cells. The endothelial cells form tight monolayers expressing ZO-1, Occludin and Claudin-5 at the cell borders (Cohen-Kashi-Malina et al. 2012) and reach resistance values in the range of $400\text{--}800 \Omega \cdot \text{cm}^2$, and display sucrose permeabilities in the range of $1\text{--}6 \cdot 10^{-6}$ cm/s (Franke et al. 1999, 2000; Patabendige et al. 2013; Cohen-Kashi-Malina et al. 2012). The efflux transporters P-gp, BCRP and MRP1 are expressed at the transcript level and BCRP-mediated vectorial transport has been demonstrated functionally (Eisenblatter et al. 2003). Efflux ratios have not been estimated but uptake and transport experiments indicate functional expression of P-gp (Patabendige et al. 2013; Lemmen et al. 2013a, b, c).

It should be noted that the porcine endothelial cells may reach even higher resistances and lower paracellular permeability when grown in co-cultures with astrocytes (Cohen-Kashi-Malina et al. 2012). The porcine *in vitro* model has the great advantage that endothelial monolayers can be generated without accompanying astrocytes. Furthermore, the endothelial cells can be cultured in serum-free media, allowing for more complex investigations of growth factors and signalling components, which normally to some degree are present in serum.

2.2.4 The Bovine Co-culture Blood-Brain Barrier Model

Primary cultures of endothelial cells of bovine origin, cultured on permeable supports, were among the first *in vitro* models of the blood-brain barrier (reviewed in Gumbleton and Audus (2001) and Abbott et al. (2014)). Numerous versions of bovine *in vitro* blood-brain barrier models exist, differing slightly from lab to lab (Audus et al. 1990; Bowman et al. 1983; Dehouck et al. 1990; Gaillard et al. 2001). In our lab we adapted the model developed by Bert de Boers group at the University of Leiden (Gaillard et al. 2001), with modified the culture conditions (Helms et al. 2010) and are using the model for studies of drug delivery (Ballet et al. 2014) and CNS pharmacology (Helms et al. 2012). Our bovine model will thus be used as an example in the present chapter. The endothelial cells are generated by isolating microvessels from the cerebral cortex of calves by scraping of the grey matter, followed by a series of steps homogenization in a Dounce homogenizer, followed by filtration and enzyme treatment steps. The capillaries are stored in cryo-batches for later culture. The endothelial cells are co-cultured with rat astrocytes on coated permeable supports in a serum-containing medium in the presence of dexamethasone for 6 days (for a detailed protocol see Helms and Brodin (2014)). The cells display an endothelial morphology with large, flattened cells. Whereas most endothelial cells in *in vitro* culture has an elongated spindle shape, the bovine endothelial cells in co-culture are broader and with a larger surface area per cell (Helms and Brodin 2014), more closely resembling the native endothelium. The endothelial cells form tight monolayers expressing ZO-1, Occludin and Claudin-5 at the cell borders. The monolayers have resistance values from 800 to 2000 $\Omega \cdot \text{cm}^2$, with individual monolayer resistances reaching well above 2000 $\Omega \cdot \text{cm}^2$. Mannitol permeabilities are approximately $5 \cdot 10^{-7}$ cm/s (Helms et al. 2010). The efflux transporters P-gp, BCRP and MRP1 are expressed at the transcript level, and vectorial transport of P-gp and BCRP substrates have been demonstrated functionally, and flux studies with MRP1 inhibitors also indicate the presence of functionally active MRP1 (Helms et al. 2014). The bovine model has the advantage of being robust and display high tightness. The disadvantages of this model are the high workload involved in the isolation of brain capillaries and the generation of primary endothelial cell cultures, and the sparse availability of bovine brain tissue in some countries. The model is sensitive

to media changes and vectorial transport studies are often performed in growth medium. This procedure may limit drug substance solubility and make it more troublesome to estimate free drug concentrations due to protein binding.

2.2.5 Surrogate Blood-Brain Barrier Models

The *in vitro* models based on primary cell lines are all labour intensive and demands regular characterization of the purity of cell types, i.e. immunocytochemical characterization with antibodies against Von Willebrands Factor (endothelial cell marker), glial fibrillary acidic protein (astrocyte marker), neural growth factor 2 (pericyte marker) and smooth muscle actin- α (pericyte marker). Due to the relative high workload involved in generating blood-brain barrier models originating from brain endothelial cells, immortalized cell lines originating from peripheral tissue are used by some laboratories as surrogate BBB models. As examples, the intestinal cell line Caco-2, sometimes cultured in the presence of vinblastine, in order to increase P-gp expression, and the kidney cell line MDCK, transfected with P-gp and/or BCRP are used by some groups and companies to estimate BBB-permeability. The rationale behind this is that the efflux transporter expression and the passive paracellular and transcellular pathways in these cell lines may be comparable to that of the endothelium in the blood-brain barrier. These cell lines do, however, not have the same SLC-expression profile as the brain endothelium, and compounds permeating the brain endothelium via solute transporters may therefore not show permeability in Caco-2 and MDCK-models or vice-versa (Hellinger et al. 2012). Nor do they have endothelial morphology, junction protein composition and enzyme expression, but they do in general display decent retrospective *in vivo*-*in vitro* correlations for lipophilic drugs permeating passively, or lipophilic efflux transporter substrates (Hellinger et al. 2012; Garberg et al. 2005; Hakkarainen et al. 2012). They do, however, not express the same receptor systems as the brain endothelial cells and are therefore generally not applicable for studies of endothelial receptor-mediated endocytosis.

2.3 Hepatic Models

Hepatic metabolism and excretion of exogenous and endogenous molecules is a major determinant for clearance of drug compounds from the systemic circulation. Hepatocytes play a pivotal role in this process by taking up drugs from the circulation, followed by metabolism and/or extrusion into the bile duct. The transport between the blood and the hepatocyte occurs across the basolateral membrane of the hepatocyte, often referred to as the sinusoidal membrane. Transport occurs across the apical membrane, from the hepatocyte and into the bile canaliculus, and the apical membrane is therefore often called the canalicular membrane. A number of transporters work in concert to influx and efflux drugs

and their metabolites across the membrane of the hepatocytes. A number of influx transporters have been identified in the basolateral membrane, such as the sodium taurocholate cotransporting polypeptide (NTCP, SLC10A1), members of the OATPs, and organic anion and cation transporters (Yang et al. 2013). Efflux transporters present in the basolateral membrane are MRP3 and 4, whereas MDR1, MRP2 and BCRP are present in the apical membrane (Yang et al. 2013). *In vitro* studies of hepatic transport processes and resulting intracellular drug concentrations thus require *in vitro* models capable of expressing correct membrane polarization of the native membrane components.

A number of models are available, such as membrane vesicle preparations and transfected cell lines. However, these models have some draw-backs in terms of being either labour-intensive, technically challenging or limited in terms of transporter expression (Yang et al. 2013). Currently, significant efforts are devoted to develop culture protocols for primary hepatocytes, in order to use them as *in vitro* models for studies of hepatic transport and metabolism. Primary hepatocytes may be either freshly isolated or cryopreserved. Obviously, human hepatocytes are the golden standard for most studies, however getting liver tissues from human donors is a limiting factor. Furthermore, the quality of the primary cells may be a limiting factor for certain culture protocols, and introduce a variability of the results obtained (Yang et al. 2013). Primary hepatocytes are generally cultured either in suspension or in a sandwich culture. Hepatocytes cultured in suspension have proved useful for transport studies investigating movement of drugs similar to the blood-hepatocyte transfer, but not the hepatocyte-bile transfer (Yang et al. 2013). In the sandwich culture, hepatocytes are cultured between two layers of collagen, whereby the hepatocytes develop functional apical membranes. A further use of *in vitro* cell models generated from primary hepatocytes may be to get *in vitro* models from species other than human, e.g. from preclinical species such as mouse, rat, pig or dog. *In vitro* cultures obtained from mice and rats may serve as important mechanistic tools, since data obtained in control cells can be compared with data obtained in cultures from knock-out animals, allowing for the investigations of the role of single transporters and enzymes in the complex hepatic interplay between metabolism and transport.

Another tool for hepatic *in vitro* transport and metabolism studies is the HepaRG cell line. The HepaRG cells were derived from a hepato-cholangiocarcinoma of a female patient and seeded at low density. HepaRG cells proliferate into cultures containing differentiated hepatocytes and primitive biliary cells (Le et al. 2006; Gripon et al. 2002). The hepatocyte-like cells express various phase I and phase II xenobiotic metabolizing enzyme activities, as well as transporters and nuclear receptors at levels close to those measured in primary human hepatocytes (Le et al. 2006). The expression profile of hepatic transporters and enzymes makes the HepaRG the most relevant *in vitro* cell culture model for investigating drug transport in the liver at present (Antherieu et al. 2012).

2.4 Renal Models

Renal clearance is a major component of net systemic drug clearance, and therefore drug transport along with renal secretion and re-absorption is relevant to study as part of the evaluation of drug ADME properties. There are, however, no validated predictive *in vitro* cell culture models for kidney transport available. The epithelium of the kidney may indeed also be hard to model, as the kidney tubules consist of several functionally different segments. Filtration occurs in the glomerulus, reuptake of nutrients and micronutrients occurs in the proximal tubules, while the loop of Henle and the distal parts of the tubules mainly deal with removal of water and salts from the filtrate. The proximal tubule is probably the most important site for drug/transporter interactions, and drugs can be excreted as well as reabsorbed, depending on the drug in question. The optimal renal cell line for investigating renal handling of drug compounds would be a human cell line of proximal tubular origin with high resistance expressing the relevant transporters in quantitative amount. However, even with this model the changes in osmolality found in the nephron would be an *in vitro* challenge.

Due to the lack of cell models, a number of cell-based assays and membrane vesicles as well as transfected cell line and yeast have been used, mainly to study the impact of transport proteins. The major transporters in the kidney are briefly listed here. In terms of reabsorption the apically located the di/tri-peptide transporters PEPT1 and PEPT2 (members of SLC15) are relevant because may transport substrates from the urine back into the renal proximal tubular cells. The apically located organic cation transporters OCTN 1 and OCTN 2 (members of SLC22), the organic anion transporter OAT4 (SLC22A9) and MATE1/2-K as well as the basolaterally located OAT1/2/3 and OCT2 are exchangers and may as such facilitate both reabsorption and secretion. In contrast the apically located MRP2/4, P-gp and BCRP are only involved in the secretion of drugs.

In terms of cell lines, as mentioned in Sect. 2.1, MDCK cells are from the canine kidney, however they have been used for investigating intestinal permeability and do not seem to be suitable for investigating renal drug transport. We have used various renal cell lines to investigate peptide transport, since two isoforms of the di/tri-peptide transporter, PEPT, i.e. PEPT1 and PEPT2 is expressed in the kidney and contributes to reabsorption of certain β -lactam antibiotics (Ocheltree et al. 2004; Shen et al. 2005, 2007; Smith et al. 1998). In the rat kidney proximal tubule cell line SKPT0193 cl.2 we found that PEPT2 is expressed and that luminal transport of dipeptides is PEPT2 mediated, however the cell line apparently does not express a basolateral transporter to facilitate the cellular efflux of a non-metabolized dipeptide substrate, and thus we found no polarized dipeptide transport (Bravo et al. 2004b, 2005). The SKPT cell line may be used to study luminal transport of di/tri-peptides and their mimetics, but not the total transport pathway resembling the re-absorption process. Likewise, the porcine kidney cell line LLC-pk1 express the porcine PEPT2 protein (Sondergaard et al. 2008), and a recent study reveals a reasonable correlation between permeability across LLC-pk1

cell and renal clearance (Kunze et al. 2014). The study suggest that for neutral and cationic drugs the permeability across filter-grown LLC-pk1 cells may be reasonable correlated with the *in vivo* renal clearance, suggesting that secretory and re-absorptive processes are mimicked (Yang et al. 2013). However, a general *in vitro* cell culture model of the proximal kidney tubule epithelium is not yet available.

3 Conclusion

Models for studying drug transport and interactions with transporters are important tools in understanding drug ADME properties, e.g. by estimating intestinal absorption, hepatic metabolism and brain influx. However, care must be taken in performing transport studies, in culturing cells and isolating primary cells. The present chapter has highlighted some of the models available for studying drug transport, and at the same time addressed some of the concerns about model use and transport evaluation.

Acknowledgement The cell culture facility at the Department of Pharmacy (Maria Diana Læssøe Pedersen) is acknowledged for providing information for the appended Caco-2 cell protocol.

Appendix: Culture and Application of Caco-2 Cells

Caco-2 cells from DSMZ (Deutsche Sammlung von Mikroorganismen und Zellkulturen, DSMZ no.: ACC 169. the cells are proliferated and then frozen and kept in storage as stocks in a cryotank.

These Caco-2 cells have been shown to be optimal for use in 17–20 passages after a new thawing. Characterization studies of membrane transporters show that the cells can be used immediately after thawing.

After a new thawing, it takes about a week of culture before the cells are ready for the first trypsinization when two cell vials of cryopreserved cells are cultured in a T75 flask.

Microscopy

All flasks are controlled by light microscopy prior to every trypsinization or change of medium. This is to monitor the growth of the cells and to adjust condition.

Preparation of Growth Medium

Composition

DMEM ⊕:	
Penicillin/streptomycin 10,000 U/mL/10 mg/mL (Pen/Strep)	5.0 mL
L-Glutamine (dissolve precipitate by gentle shaking) (L-Glu)	5.0 mL
Non-Essential Amino Acids (NEAA)	5.0 mL
DMEM ad.	500 mL
DMEM ⊕ + 10 % FBS:	
Foetal bovine serum (FBS)	50 mL
DMEM ⊕ ad.	450 mL

Aseptic Preparation of the Medium

Thaw FBS, pen/strep and L-Glu in a water bath at 37 °C and shake gently before use. Heat NEAA in a water bath to 37 °C.

Add 5 mL Pen/Strep, 5 mL NEAA and 5 mL L-Glu to a bottle of 500 mL DMEM.

This solution is referred to as DMEM ⊕.

Transfer 50 mL FBS to a sterile 500 mL bottle or to the bottle containing excess DMEM ⊕ from the previous medium preparation, then fill up with DMEM ⊕ to a final volume of 500 mL (termed DMEM ⊕ + 10 % FBS)

Trypsinization Procedure (Sub-cultivation)

This is normally carried out at a confluence of approx. 90 %.

Instructions for trypsinization of a 75/175 cm² culture flask (T75/T175 flasks):

The cell culture should be handled aseptically in a LAF-bench.

1. Pre-warm the DMEM ⊕ + 10 % FBS, PBS and Trypsin-EDTA in the 37 °C water bath (approx. 15 min). Trypsin-EDTA × 3 may be used.
2. Control the culture flask visually and subject it to microscopy in order to check the cell layer for normal growth.
3. Remove the culture medium with a Pasteur pipette without touching the cell layer. Rinse the culture with 10/30 mL 37 °C pre-warmed PBS by gently moving the flask back and forth. Then remove the PBS with a Pasteur pipette.
4. Shake the trypsin-EDTA solution gently before use. Measure out 1 mL/T75 and 3 mL/T175 (0.5 mL/T25) and add this to the culture flasks by pouring it down the sides of the bottle. After this is done, move the flask so as to distribute the trypsin over the entire culture.
5. Leave the culture flask in the incubator for approx. 10 min.

6. By holding the flask perpendicular you will be able to see whether the cells have loosened, i.e. whether the trypsinization has lasted long enough. You can also check this by microscopy.
7. Trypsinization is stopped by pouring 10/20–30 mL DMEM \oplus + 10% FBS over the loosened cells on the bottom of the flask (*Serum inactivates the trypsin-EDTA*).
8. Aspirate the medium approx. 4–6 times with the pipette to separate any cell clumps (they can be a little difficult to separate in single-cell suspension. Further aspiration may be necessary for separation of cell clusters).
9. The cell concentration is determined by transferring a small aliquot (9 μ L) of the cell suspension to a MultiCount 10 disposable counting slide using a Pasteur pipette. It may be necessary to dilute the cell suspension further, if the cell concentration is too great (*an optimum count figure is approx. 100 cells/9 fields*). Perform the counting using a conventional light microscope. Count at least 2×9 fields (3×3 fields—magnification $\times 10$, see SOP No. 269-B). The different counts must be approximately equal.
10. The cell density in the suspension is calculated as follows:
Average number of cells/9 fields * 10,000 = number of cells/mL.
11. A new passage is established by diluting the suspension to the desired concentration.

Seeding

Make sure the cells are evenly suspended in the pipette

Seeding in T-75 and T175 Flasks

The number of cells needed for seeding is dependent on passage No. Cell division is slower at the lower passage numbers. Therefore it is a good idea to seed a few more cells in the flasks when carrying out trypsinization during the first weeks after thawing.

Normally, the numbers of cells shown below are seeded, but with older passages it makes good sense to reduce the number of cells/flask a little:

Seed:		
T-75	2.6×10^5 cells/T75	+13 mL DMEM \oplus +10% FBS
T-175	6×10^6 cells/T175	+33 mL DMEM \oplus + 10% FBS

Change medium every second day and trypsinize the flask again 1 week later.

Calculation:

$$\text{Number of mL (cell susp.)} = \frac{2.6 \times 10^5 \left(\frac{\text{cells}}{\text{flask}} \right)}{\text{conc. of cell susp.} \left(\frac{\text{cells}}{\text{mL}} \right)}$$

$$\text{Number of mL (cell susp.)} = \frac{6 \times 10^5 \left(\frac{\text{cells}}{\text{flask}} \right)}{\text{conc. of cell susp.} \left(\frac{\text{cells}}{\text{mL}} \right)}$$

Seeding on Filters

Most often T12-transwells of polycarbonate from Costar are used (T12-cci3401). These filters have a pore size of 0.4 μm , a growth area of 1.12 cm^2 and a diameter of 12 mm.

Various types of filters exist (see www.corning.com/lifesciences).

12-Well Filters (T12)

Prepare a cell suspension of 2.0×10^5 cells/mL. Of this, 0.5 mL is added apically, and 1.0 mL DMEM \oplus 10% FBS is added basolaterally.

(Use $12 \times 0.5 = 6$ mL cell suspension. Prepare a total of 7 mL with 1.4×10^6 cells for 12 wells, corresponding to 1.0×10^5 cells /filter or 8.93×10^4 cells/ cm^2).

Calculation:

$$\text{Number of mL (cell susp.)} = \frac{2 \times 10^5 \left(\frac{\text{cells}}{\text{mL}} \right) \cdot \text{total number of mL}}{\text{conc. of cell susp.} \left(\frac{\text{cells}}{\text{mL}} \right)}$$

Cells seeded on filters are normally used for experiments on days 11–25, the cells must always be used for experiments the day after they have had their medium changed.

Seeding in Trays

12-Well Tray (B12)

Prepare a cell suspension of 2.26×10^5 cells/mL. Add 1.5 mL of this per well.

(Use $12 \times 1.5 = 18$ mL of cell suspension. Prepare a total of 20 mL with 4.52×10^6 cells for 12 wells, corresponding to 3.39×10^5 cells/well or 8.93×10^4 cells/ cm^2).

Calculation:

$$\text{Number of mL (cell susp.)} = \frac{2.26 \times 10^5 \left(\frac{\text{cells}}{\text{mL}}\right) \cdot \text{total number of mL}}{\text{conc. of cell susp.} \left(\frac{\text{cells}}{\text{mL}}\right)}$$

Cells must always be used for experiments the day after they have had their medium changed.

Change of Medium

T75/T175 Flasks

Remove the medium with a Pasteur pipette connected to a tube with vacuum suction.

After this, replace the medium with 13/33 mL DMEM \oplus + 10 % FBS

6 and 12-Well Filters

- Remove the medium with a Pasteur pipette connected to a tube with vacuum suction.
- Empty the wells of medium, first basolaterally and then apically. This must be done without touching the cell layer on the filter (Avoid leaving the cells without medium for too long).
- Then replace the medium with fresh DMEM \oplus + 10 % FBS, first apically and then basolaterally with:

6-well filters:	apically:	2.0 mL
	basolaterally:	2.5 mL
12-well filters:	apically:	0.5 mL
	basolaterally:	1.0 mL

6, 12, 24 and 96-Well Trays

Cells are seeded in the wells once a week. After this, the medium must be changed every other day until the cells are to be used.

- Remove the medium with a Pasteur pipette connected to a tube with vacuum suction. This must be done without touching the cell layer on the bottom.
(Avoid leaving the cells without medium for too long)

- After this, replace the medium with fresh DMEM \oplus + 10 % FBS with:

6-well:	3.0 mL
12-well:	1.5 mL
24-well:	1.0 mL
96-well:	0.2 mL

Freezing Procedure

The freezing of cells is done in an ordinary freshly prepared growth medium DMEM \oplus with 15 % FBS, 5 % DMSO added, where the cell concentration is 2×10^6 cells/mL, corresponding to a cryotube.

In order to protect the cells during freezing, all work done in the period during which the cells are affected by DMSO must be carried out as quickly as possible. The same applies during the thawing procedure.

Preparation of medium for freezing:

1.	90 % DMEM \oplus + 10 % DMSO	(9 mL DMEM \oplus + 1 mL DMSO)
2.	70 % DMEM \oplus + 30 % FBS	(7 mL DMEM \oplus + 3 mL FBS)

NOTE: DMEM \oplus + DMSO must be prepared aseptically and sterile-filtered before use.

Final Concentration in Freezing Medium

DMEM \oplus	80 %
DMSO	5 %
FBS	15 %
Cells	2×10^6 cells/mL

Work Procedure

Normally four (or more) extra T175 flasks are seeded the week before in connection with the trypsinization.

1. The trypsinization procedure is as usual.
The total number of cells is calculated.
2. Then calculate how many cryotubes can be frozen (2×10^6 cells/tube).

3. Put the cells in 15 mL centrifugal tubes with conical bottoms (max. 10 mL cell suspension/tube). Each tube can contain, for instance, 8×10^6 cells, corresponding to four cryotubes.

(There has to be at least 1 mL medium in which the cells can be resuspended after they have been centrifuged. This means that there must be enough cells for at least two cryotubes/centrifugal tubes)

Calculation:

$$\text{Number of mL (cell susp.)} = \frac{8 \times 10^6 \left(\frac{\text{cells}}{\text{mL}}\right)}{\text{conc. of cell susp.} \left(\frac{\text{cells}}{\text{mL}}\right)}$$

The tubes must all contain the same amount of medium. If there are an odd number of tubes, prepare an extra tube containing an equal amount of water. Place the tubes in pairs opposite one another in the centrifuge.

4. Centrifuge the cells at approx. 1000 g for 10 min -4°C .

5.

When preparing cryotubes, mark them with:	Cell type
	Date
	Passage No.
	Cell concentration
	Your initials

(Increase the passage No. by 1 in connection with the trypsinization, so that the new passage no. is noted on the cryotube. On thawing, note the new passage no. on the T75 flask.)

6. Carefully remove the supernatant from the centrifugal tube using suction.
7. Carefully resuspend the cells in 1 mL, corresponding to two cryotubes, DMEM \oplus + 30% FBS per tube (mL DMEM \oplus + 30% FBS depends on how many cells are in the centrifugal tube)
8. Transfer the cell suspension to two cryotubes (with a silicon gasket), each containing 0.5 mL.
9. Carefully add 0.5 mL DMEM \oplus + 10% DMSO drop wise to each cryotube.

The cryotubes are placed in a special freezing box, Nalgene® Cryo 1 $^\circ\text{C}$ Freezing Container (which is usually located in the refrigerator outside the cell room). The freezing box can hold a maximum of 18 cryotubes per freezing. Alternatively, a specially-made polystyrene box can be used for the freezing.

The freezing box/polystyrene box is so adjusted that freezing takes place at a rate of 1 degree/min.

Place the freezing box/polystyrene box in the -80°C freezer for a minimum of 2 h.

10. After freezing at -80°C for at least 2 h, the cryotubes are moved to one of the cryotanks.

This is done either by placing 4–5 cryotubes in a cane (a holder specially made for cryotubes), which is then placed in the appropriate section of the cryotank (small/medium)

The cryotank is divided into several sections, which can each contain a certain number of canes. Number all canes in a section consecutively, and write these numbers with a marker pen on the broad end. Each cane can hold a maximum of six cryotubes.

Each cell line has a special section in the cryotank, which can be seen in the freezing folder.

Or transfer the cryotubes to a special freezing box (which holds 96 tubes) and place in one of the holders in the large cryotank.

11. The freezing tables must be filled in with all the relevant information in the folder for the cell stock.

All work with cells from item 7 to 10 must be carried out as quickly as possible to avoid the cells being damaged during freezing and the transferal to the cryotank.

Thawing Procedure

When thawing new cells received from the DSMZ, follow the thawing procedure found in the “product information sheet” that comes with them.

With other thawing, follow the thawing procedure below.

Work Procedure

1. Add 13 mL of DMEM \oplus + 10 % FBS to a T75 flask and place it in the incubator for approx. 15 min (a T25 with 5 mL DMEM \oplus + 10 % FBS can also be used).
2. Remove the cells from the cryotank and thaw them in a small beaker containing autoclaved water warmed to 37 °C in the water bath (It is important that the thawing is done as quickly as possible, and for this reason the beaker containing 37 °C water must be brought to the cryo tank).

A face shield must be worn, as the cryo tube can burst during thawing.

3. Immediately after thawing, carefully transfer the cells to a culture flask, T75 (T25).

Write the data from the cryo tube on the flask.

4. The cells must have their medium changed the day after thawing.
5. After this, the medium is changed every other day (Mon.-Wed.-Fri.), until the cell layer is confluent, after which they are trypsinized.
6. Write in the folder for the cell stock when the cells were thawed and how the cell growth proceeded up until the date of trypsinization.

Passage Nomenclature

Passage = sub-cultivation.

The passage numbers consist of:

Number1-(number2)-number3

Number1

Passage Number as the cell line is received—if this number is 1—the cell line is received without a passage number.

() + Number2

In () is info on freezing. Number2 is the number of trypsinizations before freezing—if there are more numbers in the brackets means that the cell line is proliferated several times.

Number3

Number of trypsinizations since thawing.

Example:

Received without passage No.—proliferated by two trypsinizations before freezing:	
New passage No. at thawing:	1—(2)—0
After first trypsinization:	1—(2)—1

References

- Abbott J (2014) In vitro models of CNS barriers. In: Hammarlund-Udenaes M (ed) Drug delivery to the brain: Physiological concepts, methodologies and approaches. Springer, New York
- Amtorp O (1980) Estimation of capillary-permeability of inulin, sucrose and mannitol in rat-brain cortex. *Acta Physiol Scand* 110:337–342
- Anderberg EK, Nystrom C, Artursson P (1992) Epithelial transport of drugs in cell culture. VII: Effects of pharmaceutical surfactant excipients and bile acids on transepithelial permeability in monolayers of human intestinal epithelial (Caco-2) cells. *J Pharm Sci* 81:879–887
- Antherieu S, Chesne C, Li R, Guguen-Guillouzo C, Guillouzo A (2012) Optimization of the HepaRG cell model for drug metabolism and toxicity studies. *Toxicol In Vitro* 26:1278–1285
- Antunes F, Andrade F, Araujo F, Ferreira D, Sarmento B (2013) Establishment of a triple co-culture in vitro cell models to study intestinal absorption of peptide drugs. *Eur J Pharm Biopharm* 83:427–435
- Araujo F, Sarmento B (2013) Towards the characterization of an in vitro triple co-culture intestine cell model for permeability studies. *Int J Pharm* 458:128–134
- Artursson P, Karlsson J (1991) Correlation between oral drug absorption in humans and apparent drug permeability coefficients in human intestinal epithelial (Caco-2) cells. *Biochem Biophys Res Commun* 175:880–885
- Artursson P, Palm K, Luthman K (2001) Caco-2 monolayers in experimental and theoretical predictions of drug transport. *Adv Drug Deliv Rev* 46:27–43

- Audus KL, Bartel RL, Hidalgo IJ, Borchardt RT (1990) The use of cultured epithelial and endothelial cells for drug transport and metabolism studies. *Pharm Res* 7:435–451
- Ballet S, Betti C, Novoa A, Tömöböly C, Nielsen CU, Helms HC, Lesniak A, Kleczkowska P, Chung N, Lipkowski A, Bordin B, Tourwé D, Schiller P (2014) In vitro membrane permeation studies and in vivo antinociception of glycosylated Dmt1-DALDA analogues. *ACS Med Chem Lett* 5(4):352–357. doi:10.1021/ml4004765
- Bowman PD, Ennis SR, Rarey KE, Betz AL, Goldstein GW (1983) Brain microvessel endothelial-cells in tissue-culture—A model for study of blood-brain-barrier permeability. *Ann Neurol* 14:396–402
- Bravo SA, Nielsen CU, Amstrup J, Frokjaer S, Brodin B (2004a) In-depth evaluation of Gly-Sar transport parameters as a function of culture time in the Caco-2 cell model. *Eur J Pharm Sci* 21:77–86
- Bravo SA, Nielsen CU, Amstrup J, Frokjaer S, Brodin B (2004b) Epidermal growth factor decreases PEPT2 transport capacity and expression in the rat kidney proximal tubule cell line SKPT0193 cl.2. *Am J Physiol Renal Physiol* 286:F385–F393
- Bravo SA, Nielsen CU, Frokjaer S, Brodin B (2005) Characterization of rPEPT2-mediated Gly-Sar transport parameters in the rat kidney proximal tubule cell line SKPT-0193 cl.2 cultured in basic growth media. *Mol Pharm* 2:98–108
- Brayden DJ, Bzik VA, Lewis AL, Illum L (2012) CriticalSorb promotes permeation of flux markers across isolated rat intestinal mucosae and Caco-2 monolayers. *Pharm Res* 29:2543–2554
- Bretschneider B, Brandsch M, Neubert R (1999) Intestinal transport of beta-lactam antibiotics: analysis of the affinity at the H⁺/peptide symporter (PEPT1), the uptake into Caco-2 cell monolayers and the transepithelial flux. *Pharm Res* 16:55–61
- Chen Z, Fei YJ, Anderson CM, Wake KA, Miyauchi S, Huang W, Thwaites DT, Ganapathy V (2003) Structure, function and immunolocalization of a proton-coupled amino acid transporter (hPAT1) in the human intestinal cell line Caco-2. *J Physiol* 546:349–361
- Cohen-Kashi-Malina K, Cooper I, Teichberg VI (2012) Mechanisms of glutamate efflux at the blood-brain barrier: Involvement of glial cells. *J Cereb Blood Flow Metab* 32:177–189
- Corti G, Maestrelli F, Cirri M, Zerrouk N, Mura P (2006) Development and evaluation of an in vitro method for prediction of human drug absorption II. Demonstration of the method suitability. *Eur J Pharm Sci* 27:354–362
- Crone C, Olesen SP (1982) Electrical-resistance of brain micro-vascular endothelium. *Brain Res* 241:49–55
- Dehouck MP, Meresse S, Delorme P, Fruchart JC, Cecchelli R (1990) An easier, reproducible, and mass-production method to study the blood-brain-barrier invitro. *J Neurochem* 54:1798–1801
- Deli MA, Abraham CS, Kataoka Y, Niwa M (2005) Permeability studies on in vitro blood-brain barrier models: Physiology, pathology, and pharmacology. *Cell Mol Neurobiol* 25:59–127
- Delie F, Rubas W (1997) A human colonic cell line sharing similarities with enterocytes as a model to examine oral absorption: Advantages and limitations of the Caco-2 model. *Crit Rev Ther Drug Carrier Syst* 14:221–286
- Eisenblatter T, Huwel S, Galla HJ (2003) Characterisation of the brain multidrug resistance protein (BMDP/ABCG2/BCRP) expressed at the blood-brain barrier. *Brain Res* 971:221–231
- Fischer SM, Brandl M, Fricker G (2011) Effect of the non-ionic surfactant Poloxamer 188 on passive permeability of poorly soluble drugs across Caco-2 cell monolayers. *Eur J Pharm Biopharm* 79:416–422
- Fogh J, Fogh JM, Orfeo T (1977) One hundred and twenty-seven cultured human tumor cell lines producing tumors in nude mice. *J Natl Cancer Inst* 59:221–226
- Franke H, Galla HJ, Beuckmann CT (1999) An improved low-permeability in vitro-model of the blood-brain barrier: Transport studies on retinoids, sucrose, haloperidol, caffeine and mannitol. *Brain Res* 818:65–71
- Franke H, Galla HJ, Beuckmann CT (2000) Primary cultures of brain microvessel endothelial cells: A valid and flexible model to study drug transport through the blood-brain barrier in vitro. *Brain Res Protoc* 5:248–256

- Frolund S, Marquez OC, Larsen M, Brodin B, Nielsen CU (2010) Delta-aminolevulinic acid is a substrate for the amino acid transporter SLC36A1 (hPAT1). *Br J Pharmacol* 159:1339–1353
- Frolund S, Rapin N, Nielsen CU (2011) Gaboxadol has affinity for the proton-coupled amino acid transporter 1, SLC36A1 (hPAT1)—A modelling approach to determine IC(50) values of the three ionic species of gaboxadol. *Eur J Pharm Sci* 42:192–198
- Frolund S, Langthaler L, Kall MA, Holm R, Nielsen CU (2012) Intestinal drug transport via the proton-coupled amino acid transporter PAT1 (SLC36A1) is inhibited by Gly-X(aa) dipeptides. *Mol Pharm* 9:2761–2769
- Gaillard PJ, Voorwinden LH, Nielsen JL, Ivanov A, Atsumi R, Engman H, Ringbom C, de Boer AG, Breimer DD (2001) Establishment and functional characterization of an in vitro model of the blood-brain barrier, comprising a co-culture of brain capillary endothelial cells and astrocytes. *Eur J Pharm Sci* 12:215–222
- Garberg P, Ball M, Borg N, Cecchetti R, Fenart L, Hurst RD, Lindmark T, Mabondzo A, Nilsson JE, Raub TJ, Stanimirovic D, Terasaki T, Oberg JO, Osterberg T (2005) In vitro models for the blood-brain barrier. *Toxicol in Vitro* 19:299–334
- Gripon R, Rumin S, Urban S, Le SJ, Glaise D, Cannie I, Guyomard C, Lucas J, Trepo C, Guguen-Guillouzo C (2002) Infection of a human hepatoma cell line by hepatitis B virus. *Proc Natl Acad Sci USA* 99:15655–15660
- Gumbleton M, Audus KL (2001) Progress and limitations in the use of in vitro cell cultures to serve as a permeability screen for the blood-brain barrier. *J Pharm Sci* 90:1681–1698
- Hakkarainen JJ, Pajander J, Laitinen R, Suhonen M, Forsberg MM (2012) Similar molecular descriptors determine the in vitro drug permeability in endothelial and epithelial cells. *Int J Pharm* 436:426–443
- Hellinger E, Veszelka S, Toth AE, Walter F, Kittel A, Bakk ML, Tihanyi K, Hada V, Nakagawa S, Thuy DHD, Niwa M, Deli MA, Vastag M (2012) Comparison of brain capillary endothelial cell-based and epithelial (MDCK-MDR1, Caco-2, and VB-Caco-2) cell-based surrogate blood-brain barrier penetration models. *Eur J Pharm Biopharm* 82:340–351
- Helms HC, Brodin B (2014) Generation of primary cultures of bovine endothelial cells and setup of cocultures with rat astrocytes. In: Milner R (ed) *Cerebral angiogenesis: Methods and protocols*. Humana Press, New York
- Helms HC, Waagepetersen HS, Nielsen CU, Brodin B (2010) Paracellular tightness and claudin-5 expression is increased in the BCEC/astrocyte blood-brain barrier model by increasing media buffer capacity during growth. *AAPS J* 12:759–770
- Helms HC, Madelung R, Waagepetersen HS, Nielsen CU, Brodin B (2012) In vitro evidence for the brain glutamate efflux hypothesis: Brain endothelial cells cocultured with astrocytes display a polarized brain-to-blood transport of glutamate. *Glia* 60:882–893
- Helms HC, Hersom M, Kühlmaa L, Badolo L, Nielsen CU, Brodin B (2014) An electrically tight blood-brain barrier model displays net brain-to-blood efflux of the P-gp substrate digoxin and the BCRP substrate estrone-3-sulfate. *AAPS J* 16(5):1046–1055. doi: [10.1208/s12248-014-9628-1](https://doi.org/10.1208/s12248-014-9628-1). Epub 2014 Jun 17
- Hidalgo JJ, Raub TJ, Borchardt RT (1989) Characterization of the human colon carcinoma cell line (Caco-2) as a model system for intestinal epithelial permeability. *Gastroenterology* 96:736–749
- Hilgendorf C, Spahn-Langguth H, Regardh CG, Lipka E, Amidon GL, Langguth P (2000) Caco-2 versus Caco-2/HT29-MTX co-cultured cell lines: permeabilities via diffusion, inside- and outside-directed carrier-mediated transport. *J Pharm Sci* 89:63–75
- Hoheisel D, Nitz T, Franke H, Wegener J, Hakvoort A, Tilling T, Galla HJ (1998) Hydrocortisone reinforces the blood-brain barrier properties in a serum free cell culture system. *Biochem Biophys Res Commun* 244:312–316
- Jung SJ, Choi SO, Um SY, Kim JI, Choo HY, Choi SY, Chung SY (2006) Prediction of the permeability of drugs through study on quantitative structure-permeability relationship. *J Pharm Biomed Anal* 41:469–475
- Koljonen M, Hakala KS, Ahtola-Satila T, Laitinen L, Kostiaainen R, Kotiaho T, Kaukonen AM, Hirvonen J (2006) Evaluation of cocktail approach to standardise Caco-2 permeability experiments. *Eur J Pharm Biopharm* 64:379–387

- Kunze A, Huwyler J, Poller B, Gutmann H, Camenisch G (2014) In vitro-in vivo extrapolation method to predict human renal clearance of drugs. *J Pharm Sci* 103:994–1001
- Laitinen L, Kangas H, Kaukonen AM, Hakala K, Kotiaho T, Kostianen R, Hirvonen J (2003) N₁-in-one permeability studies of heterogeneous sets of compounds across Caco-2 cell monolayers. *Pharm Res* 20:187–197
- Larsen M, Larsen BB, Frolund B, Nielsen CU (2008) Transport of amino acids and GABA analogues via the human proton-coupled amino acid transporter, hPAT1: Characterization of conditions for affinity and transport experiments in Caco-2 cells. *Eur J Pharm Sci* 35:86–95
- Larsen M, Holm R, Jensen KG, Brodin B, Nielsen CU (2009) Intestinal gaboxadol absorption via PAT1(SLC36A1): modified absorption *in vivo* following co-administration of L-tryptophan. *Br J Pharmacol* 157:1380–1389
- Le VM, Jigorel E, Glaise D, Gripon P, Guguen-Guillouzo C, Fardel O (2006) Functional expression of sinusoidal and canalicular hepatic drug transporters in the differentiated human hepatoma HepaRG cell line. *Eur J Pharm Sci* 28:109–117
- Lemmen J, Tozakidis IEP, Bele P, Galla HJ (2013a) Constitutive androstane receptor upregulates Abcb1 and Abcg2 at the blood-brain barrier after CITCO activation. *Brain Res* 1501:68–80
- Lemmen J, Tozakidis IEP, Galla HJ (2013b) Pregnane X receptor upregulates ABC-transporter Abcg2 and Abcb1 at the blood-brain barrier. *Brain Res* 1491:1–13
- Lennernas H (1997) Human jejunal effective permeability and its correlation with preclinical drug absorption models. *J Pharm Pharmacol* 49:627–638
- Lentz KA, Hayashi J, Lucisano LJ, Polli JE (2000) Development of a more rapid, reduced serum culture system for Caco-2 monolayers and application to the biopharmaceutics classification system. *Int J Pharm* 200:41–51
- Li J, Volpe DA, Wang Y, Zhang W, Bode C, Owen A, Hidalgo IJ (2011) Use of transporter knockdown Caco-2 cells to investigate the *in vitro* efflux of statin drugs. *Drug Metab Dispos* 39:1196–1202
- Liang E, Chessic K, Yazdani M (2000) Evaluation of an accelerated Caco-2 cell permeability model. *J Pharm Sci* 89:336–345
- Lindahl A, Sjoberg A, Bredberg U, Toreson H, Ungell AL, Lennernas H (2004) Regional intestinal absorption and biliary excretion of fluvastatin in the rat: Possible involvement of mrp2. *Mol Pharm* 1:347–356
- Matysiak-Budnik T, Heyman M, Candalh C, Lethuaire D, Megraud F (2002) *In vitro* transfer of clarithromycin and amoxicillin across the epithelial barrier: Effect of *Helicobacter pylori*. *J Antimicrob Chemother* 50:865–872
- Nakagawa S, Deli MA, Kawaguchi H, Shimizudani T, Shimono T, Kittel A, Tanaka K, Niwa M (2009) A new blood-brain barrier model using primary rat brain endothelial cells, pericytes and astrocytes. *Neurochem Int* 54:253–263
- Nielsen CU, Amstrup J, Steffansen B, Frokjaer S, Brodin B (2001a) Epidermal growth factor (EGF) inhibits glycylsarcosine (Gly-Sar) transport and hPepT1 expression in a human intestinal cell line. *Am J Physiol Gastrointest Liver Physiol* 281:G191–G199
- Nielsen CU, Andersen R, Brodin B, Frokjaer S, Taub ME, Steffansen B (2001b) Dipeptide model prodrugs for the intestinal oligopeptide transporter. Affinity to and transport via hPepT1 in the human intestinal Caco-2 cell line. *J Controlled Release* 76:129–138
- Nielsen CU, Carstensen M, Brodin B (2012) Carrier-mediated gamma-aminobutyric acid transport across the basolateral membrane of human intestinal Caco-2 cell monolayers. *Eur J Pharm Biopharm* 81:458–462
- Nohr MK, Hansen SH, Brodin B, Holm R, Nielsen CU (2014) The absorptive flux of the anti-epileptic drug substance vigabatrin is carrier-mediated across Caco-2 cell monolayers. *Eur J Pharm Sci* 51:1–10
- Ocheltree SM, Shen H, Hu Y, Xiang J, Keep RF, Smith DE (2004) Role of PEPT2 in the choroid plexus uptake of glycylsarcosine and 5-aminolevulinic acid: Studies in wild-type and null mice. *Pharm Res* 21:1680–1685
- Pardridge WM (2007) Drug targeting to the brain. *Pharm Res* 24:1733–1744

- Patabendige A, Skinner RA, Abbott NJ (2013) Establishment of a simplified in vitro porcine blood-brain barrier model with high transendothelial electrical resistance. *Brain Res* 1521:1–15
- Perriere N, Demeuse PH, Garcia E, Regina A, Debray M, Andreux JP, Couvreur P, Scherrmann JM, Tamsamani J, Couraud PO, Deli MA, Roux F (2005) Puromycin-based purification of rat brain capillary endothelial cell cultures. Effect on the expression of blood-brain barrier-specific properties. *J Neurochem* 93:279–289
- Rubas W, Cromwell ME, Shahrokh Z, Villagran J, Nguyen TN, Wellton M, Nguyen TH, Mrsny RJ (1996) Flux measurements across Caco-2 monolayers may predict transport in human large intestinal tissue. *J Pharm Sci* 85:165–169
- Shen H, Keep RF, Hu Y, Smith DE (2005) PEPT2 (Slc15a2)-mediated unidirectional transport of cefadroxil from cerebrospinal fluid into choroid plexus. *J Pharmacol Exp Ther* 315:1101–1108
- Shen H, Ocheltree SM, Hu Y, Keep RF, Smith DE (2007) Impact of genetic knockout of PEPT2 on cefadroxil pharmacokinetics, renal tubular reabsorption, and brain penetration in mice. *Drug Metab Dispos* 35:1209–1216
- Smetanova L, Stetinova V, Kholova D, Kvetina J, Smetana J, Svoboda Z (2009) Caco-2 cells and Biopharmaceutics Classification System (BCS) for prediction of transepithelial transport of xenobiotics (model drug: caffeine). *Neuro Endocrinol Lett* 30(Suppl 1):101–105
- Smith DE, Pavlova A, Berger UV, Hediger MA, Yang T, Huang YG, Schnerrmann JB (1998) Tubular localization and tissue distribution of peptide transporters in rat kidney. *Pharm Res* 15:1244–1249
- Sondergaard HB, Bravo SA, Nielsen CU, Frokjaer S, Brodin B (2008) Cloning of the pig PEPT2 (pPEPT2) and characterization of the effects of epidermal growth factor (EGF) on pPEPT2-mediated peptide uptake in the renal porcine cell line LLC-PK1. *Eur J Pharm Sci* 33(4–5):332–342. doi: 10.1016/j.ejps.2008.01.001. Epub 2008 Jan 6
- Sun H, Chow EC, Liu S, Du Y, Pang KS (2008) The Caco-2 cell monolayer: Usefulness and limitations. *Expert Opin Drug Metab Toxicol* 4:395–411
- Thomsen AE, Friedrichsen GM, Sorensen AH, Andersen R, Nielsen CU, Brodin B, Begtrup M, Frokjaer S, Steffansen B (2003) Prodrugs of purine and pyrimidine analogues for the intestinal di/tri-peptide transporter PepT1: affinity for hPepT1 in Caco-2 cells, drug release in aqueous media and in vitro metabolism. *J Controlled Release* 86:279–292
- U.S. Department of Health and Human Services Food and Drug Administration Center for Drug Evaluation and Research (CDER) (2000) Waiver of in vivo bioavailability and bioequivalence studies for immediate-release solid oral dosage forms based on a biopharmaceutics classification system. <http://www.fda.gov/cder/guidance/index.htm>
- Vabeno J, Lejon T, Nielsen CU, Steffansen B, Chen WQ, Hui OY, Borchardt RT, Luthman K (2004a) Phe-Gly dipeptidomimetics designed for the di-/tripeptide transporters PEPT1 and PEPT2: Synthesis and biological investigations. *J Med Chem* 47:1060–1069
- Vabeno J, Nielsen CU, Ingebrigtsen T, Lejon T, Steffansen B, Luthman K (2004b) Dipeptidomimetic ketomethylene isosteres as pro-moieties for drug transport via the human intestinal di-/tripeptide transporter hPEPT1: Design, synthesis, stability, and biological investigations. *J Med Chem* 47:4755–4765
- Veszeka ÁKMADS (2011) Tools of modelling blood-brain barrier penetrability. In: Tihanyi K, Vastag M (eds) Solubility, delivery and ADME problems of drugs and drug-candidates. Bentham Science, Washington, pp 166–188
- Volpe DA (2008) Variability in Caco-2 and MDCK cell-based intestinal permeability assays. *J Pharm Sci* 97:712–725
- Walter E, Janich S, Roessler BJ, Hilfinger JM, Amidon GL (1996) HT29-MTX/Caco-2 cocultures as an in vitro model for the intestinal epithelium: In vitro-in vivo correlation with permeability data from rats and humans. *J Pharm Sci* 85:1070–1076
- Wilhelm I, Fazakas C, Krizbai IA (2011) In vitro models of the blood-brain barrier. *Acta Neurobiol Exp* 71:113–128
- Yang K, Köck K, Brouwer KLR (2013) Analysis of hepatic transport proteins. In: Sugiyama Y, Steffansen B (eds) Transporters in drug development. Springer-Verlag, New York, pp 201–223

Index

- A**
- Absorption spectroscopy, 224
 - Acousto-optical tunable filters (AOTF), 68
 - Active pharmaceutical ingredient (API)
 - MIR spectroscopy
 - crystallization, 87–88
 - reaction monitoring, 86–87
 - NIR spectroscopy
 - crystallization, 88
 - drying, 89–90
 - reaction monitoring, 87
 - Active pharmaceutical ingredients (APIs), 157, 558, 623–624, 657
 - Active transport via p-glycoprotein (ABCB1), 800
 - Adiabatic calorimetry, 391, 405
 - Aequorea victoria*, 47
 - Aerosol particle sizing
 - aerodynamic particle size measurements, 703
 - cascade impactor/impinger, 707–710
 - ELPI, 711
 - time-of-flight based measurements, 710–711
 - dispersion techniques, 703–704
 - fine particle fraction, 712–713
 - geometric particle size measurements, 703
 - laser diffraction, 706
 - microscopy/Image analysis, 707
 - OPCs, 706–707
 - in vivo situation, 713
 - pharmacopoeial requirements, 704
 - pulmonary delivery, 702
- AFM. *See* Atomic force microscopy (AFM)
- Alpha amylase (AA), 479
- 5-Aminosalicylic acid (5-ASA), 431
- Amorphous naproxen, 188
- Ampicilline, 80
- Ampoule calorimetry, 393
- Amyloid fibrils, 660
- Amyloid hydrogels, 661
- Analytical ultracentrifugation (AUC), 470
- Andersen Cascade Impactor (ACI), 708
- Anharmonic oscillator, 64
- 1-Anilino-8-naphthalenesulfonate (1,8-ANS), 36, 52
- Anomalous small angle x-ray scattering (A-SAXS), 352–354
- Anti-malarial tablets, 161
- Anti-Stokes, 142
- API. *See* Active pharmaceutical ingredient (API)
- Aripiprazole, 184
- Artificial neural networks (ANN), 71
- Asymmetrical flow field flow fractionation (AF4)
 - accumulation wall, 467
 - aggregation phenomena, 470
 - analytical ultracentrifugation, 475
 - antibody aggregates, immunogenicity testing in vivo, 481–482
 - AUC, 470
 - β -cyclodextrin-dextran polymers, 482
 - cationic polymers, gene delivery, 483
 - cross-flow, 467
 - degradation pathways, antibody-based drug candidates, 482
 - electron microscopy, 474
 - focusing step, 470–471
 - HF5, 469
 - HPLC users, 468

- Asymmetrical flow field flow fractionation (AF4) (*cont.*)
 IgG aggregates, 481
 instrumentation, 471–472
 laminar flow conditions, 467
 nanoparticulate additives, 484
 particulate systems
 DLS, 475
 electron microscopy, 475
 gelatin nanoparticles, 476–477
 HSA nanoparticles, 476
 liposomes, liposomal formulations and lipoplexes, 477–478
 melt extrusion, 477
 non-spherical nanoparticles, 479–480
 polyplexes, 479
 Stokes-Einstein equation, 475
 VLPs
 PLGA nanoparticles, 483
 polymersomes, 484
 preparative use of, 480–481
 protein aggregates, HF5, 482
 SEC, 469
 semi-preparative mode, 470
 separation technologies, 467
 separation/fractionation principle, 468
 steric mode, 473–474
- Atmospheric pressure chemical ionization (APCI), 256
- Atomic force microscopy (AFM)
 cantilevers and tips cantil., 654–655
 operating modes opermod, 652–654
 optical/spectroscopic techniques optical, 667
 pharmaceutical research, 656–657
 pharmaceutical sciences
 bacteria and bacterial biofilms bact., 665–666
 contact mode image image, 668–669
 crystal growth and polymorphism crygrow, 658
 drug-protein and protein-protein interactions, 663
 live cells live, 663–665
 nanomedicine nanaomed, 661–662
 nanotoxicology nanotox, 662
 particles and fibres parfib, 659–660
 tablet coating and dissolution table, 657
 viruses, 666–667
 polymers, 650
 principles of operation prinoper, 650–652
 SPMs, 650
- Atovaquone, 759
- ATP-binding cassette family (ABC), 792
- Attenuated total reflectance/reflection (ATR), 63, 67
- Avrami-Erofeev model, 186
- Azithromycin, 79
- B**
- Backscattered electrons (BSE), 510
- Backscattering geometry, 148
- Bagley correction method, 729
- Band target entropy minimization (BTEM), 544
- Base peak chromatogram (BPC), 266
- Basket apparatus, 756–757
- Batch calorimetry, 393
- Beer-Lambert law, 34, 176
- Bile salts (BS), 758, 774
- Binding analyses, 735
- Bingham liquid, 724
- Biofilms, 666
- Biological fluids, 745
- Bioluminescent phenomena, 29
- Biorelevant media, 759
- Biphasic dissolution apparatus, 764
- Biphasic dissolution models, 763–765
- Blood-brain barrier (BBB), 802
 bovine co-culture, 806–807
 CNS, 801
 endothelial cells and pericytes, 802
 in vitro model, 801, 803
 in vivo permeability, 803
 porcine monoculture, 805–806
 rat triple co-culture model, 804–805
 surrogate BBB models, 807
 transendothelial transport, 802
 transwell systems, 804
- Bohr frequency condition, 31
- Bohr-Grotrian diagram, 32
- Bologna stone, 31
- Boron neutron capture therapy (BNCT), 662
- Bragg's Law, 340
- Bruker Biospin Paravision™ 4.1 software, 610
- C**
- Caco-2 cell model, 793, 797–800
 change of medium, 814–815
 freezing procedure, 815
 growth medium preparation, 811
 microscopy, 810
 passage nomenclature, 818
 seeding, 812–814
 thawing procedure, 817–818
 trypsinization, 810–812
work procedure, 815–817

- Caffeine, 79
- Calorimeters, 389, 390
- DSC (*see* Differential scanning calorimetry (DSC))
 - ice calorimeters, 391
 - IMC (*see* Isothermal microcalorimeters (IMC))
- Candida parapsilosis*, 665
- Capacitively coupled conductivity detection (CCCD), 443
- Capillary-based techniques
- adsorption, 459–460
 - affinity capillary electrophoresis
 - EKC, 446
 - mobility shift affinity CE, 444
 - pre-equilibrium capillary zone and frontal analysis, 447–448 - binding kinetics, 459
 - biomacromolecules, 440
 - charge/size ratio, 460
 - pharmaceutical applications
 - acid dissociation constants (pK_a values), 453–455
 - diffusivity and size, 457
 - interactions, excipients and delivery systems, 457–458
 - partitioning and lipophilicity, 455–456
 - physicochemical properties, 453
 - plasma protein binding, 456 - pharmaceutical sciences
 - analysis, 442
 - bioanalysis, 440 - physicochemical characterization, 454
 - solution media effect, 459
- TDA
- diffusion coefficients, 457
 - FIDA, 450
 - hydrodynamic flow, 449
 - non-covalent interactions, dispersion measurements, 453
- Capillary breakup extensional rheometer (CaBER), 734
- Capillary electrophoresis (CE), 14, 440, 441
- Capillary electrophoresis frontal analysis (CE-FA), 447
- Capillary isoelectric focusing (cIEF), 457
- Capillary rheometers, 729, 739
- Capillary viscometry, 728, 738–739
- Carbamazepine, 80, 186
- CASTEP program, 308
- Celecoxib, 763
- Central nervous system (CNS), 801
- Cetirizine, 432
- Charge-coupled device (CCD), 9, 322, 524, 531
- Chemical force microscopy (CFM), 655
- Chemical ionization (CI), 255
- Chemometric analysis, 399
- Chromophores, 4
- Cilexetil, 759
- Circular dichroism (CD) spectroscopy
- absorbance, 228
 - absorption, BNF–224
 - amino acid alanine, 224
 - background spectrum, no subtraction of, 248
 - calibration and maintenance, 243–245
 - chirality, 224
 - circularly polarized light, 224
 - cuvettes and cell pathlength, 228–229
 - data acquisition, 247
 - instrumentation, 226–228
 - measurement at excessive HT, 247
 - in pharmaceutical sciences
 - advanced drug delivery systems, 239–241
 - biosimilar, development of, 235
 - insulin, 237–239
 - pH values, 235, 236
 - RIME, 241–242
 - synchrotron radiation, 242
 - thermodynamics, 236 - protein structure
 - dialanine, 230
 - far UV and near UV CD spectroscopy, 232–234
 - native state, 230
 - quaternary structure, 231
 - secondary structure elements, 230, 231
 - tertiary structure, 230
 - unfolded state, 232 - reference/baseline spectrum, 229
 - sample preparation, 246–247
 - secondary structure fits, overinterpretation of, 248
- Circularly polarized light (CPL), 224
- Classical least squares (CLS), 543, 561
- Cluster analysis, 561
- Coatl, 30
- Cogswell analyses, 735
- Coherent anti-Stokes Raman scattering (CARS), 21
- Coherent anti-Stokes Raman spectroscopy (CARS), 531
- Collision activated dissociation (CAD), 262
- Collisional quenching, 43
- Collision-induced dissociation (CID), 262, 277
- Column chromatography, 414

- Compendial dissolution models, 758
 Complementary metal oxide semiconductor (CMOS), 12
 Composite sensor array (CSA), 89
 Connes advantage, 148
 Contact mode, 652
 Continuous solvent area model, 326
 Contraction flow analysis, 734–735
 Conventional circular dichroism (cCD) spectrometers, 242
 Correlation coefficient (CV), 71
 Coulter principle, 690
 Counterfeit detection, 161
 Critical micelle concentration (CMC), 458, 758
 Critical quality attributes (CQAs), 89, 91
 Crystalline phonon vibrations, 534
 Crystallisation, 186–187
 Crystallographic Information File (CIF), 311
 Current correction method, 458
 Current good manufacturing practice (cGMP), 475
 Cyclodextrins, 457, 458
 Czemy-Tuner spectrograph, 148
- D**
- Debye models, 175
 Delta Epsilon, 227, 228
 Density functional theory (DFT), 182
 Desorption electrospray ionization (DESI) advantages, 631
 API in tablet, 636
 disadvantages, 631
 imaging resolution, 633
 mass range, 633
 solid–liquid extraction, 633
 Deuterated tri glycine sulphate (DTGS), 525
 Diclofenac sodium, 398
 DICVOL program, 301
 Dielectric spectroscopy, 376
 Differential centrifugal sedimentation (DCS), 688
 Differential scanning calorimetry (DSC), 390
 conventional DSC, 364–366
 hyper DSC, 367–368
 MTDSC, 366–367
 polymorph stability, 396
 power-compensation designs, 391
 purity determination, 396
 Diffractometers, 297
 Diffuse reflectance (DRIFT) spectroscopy, 67
 Diffusion weighted imaging (DWI), 617
- Digestion models
 complex physiologically relevant models
 DGM, 782–784
 TIM-1 model, 784–786
 LbDDS, 776
 pH-stat controlled *in vitro* lipolysis models
 calcium, 776
 experimental conditions, 779
in vivo - *in vitro* correlations, 778–781
 intestinal digestion, 776
 low pH and gastric digestion, 777
 microbial/animal-derived gastric lipases, 777
 pellet phase, 778
 recombinant HGL, 777
 processes
 bile secretions, 774
 drug absorption, 774
 excipients, 774
 gastric lipase, 774
 hydrolysis, 774
 intestinal lipid digestion, 774
 stomach and small intestine, 775
 tri- and di-acylglycerols, 774
 Dimethyldioctadecylammonium (DDA), 694
 Direct orthogonalization (DO), 76
 Direct standardization (DS), 76
 Discrete element modelling (DEM), 202
 Disk centrifugation, 689
 Dissolution models
 absorption module
 biphasic dissolution models, 763–765
 D/P models, 765–767
 equilibrium solubility, 754
 intestinal fluids, 753
 Nernst-Brunner/Noyes Whitney equation, 754
 pharmacopoeial dissolution models
 basket and paddle apparatus, 756–757
 DDS, 755
 flow-through apparatus, 757–758
 modified release dosage forms, 755
 oral dosage forms, 755
 QC and research and development purposes, 755
 reciprocating cylinder apparatus, 757
 physiologically relevant dissolution media, 758–759
 small volume dissolution models, 759–760
 Stokes-Einstein equation, 754
 transfer models, 761–763
 Double-beam UV-vis spectrophotometer, 7
 Dounce homogenizer, 805, 806

- Drug delivery system (DDS), 755
- Drug lipophilicity, 445
- Drug metabolism and pharmacokinetics (DMPK), 282
- Drug molecules, crystal structure of
 crystalline phase transitions, 184–185
 fundamental properties, polymorphism, 183–184
 identification, polymorphism, 177–178
 quantification, 178–181
 terahertz spectra, interpretation of, 181–183
- Drug polymorphism, 157
- Drug transport, 797–801
 ADME properties, 792
 barrier tissues, 792–794
 BBB (*see* Blood-brain-barrier (BBB))
 cell culture and tissue based *in vitro*
 models, 797–800
 hepatic models, 807–808
in vitro models, 792
 paracellular *vs.* transcellular pathways, 792
 renal models, 809–810
 simple transport kinetics, 794–795
 transport kinetics, 795–796
- Dry powder inhalers (DPI), 660, 703
- Dynamic gastric model (DGM), 782
- Dynamic light scattering (DLS), 457, 475, 659, 679, 693–696
- Dynamic mechanical analysis (DMA), 376
- E**
- Eddy diffusion, 423
- Efflux transporters, 796, 808
- Elastic scattering, 530
- Electrical Low Pressure Impactor (ELPI), 711
- Electrochemical AFM (EC-AFM), 654
- Electrochromatograms, 448
- Electromagnetic radiation, 171
- Electron capture dissociation (ECD), 262
- Electron ionization (EI), 255
- Electron microscopy, 571
 electron beam generation and focus, 500
 field emission, 501
 image generating data, 500
 TEM, 502–508
 acceleration voltage, 502
 application, pharmaceutical formulation research, 504–508
 colloidal drug carrier systems
 voltages, 502
 sample preparation and investigation, 502–504
 thermionic emission, 500
- Electron transfer dissociation (ETD), 262
- Electroosmotic flow (EOF), 442
- Electrospinning, 745
- Electrospray ionization (ESI), 257–258
- ElectroSpray Ionization Mass Spectrometry (ESI-MS), 443
- Electrostatic force microscopy (EFM), 654
- Energy dispersive X-ray (EDX) spectrometry, 513, 516
- Enthalpy of solution, 397–398
- Environmental scanning electron microscopy (ESEM), 512–513
- Epidermal growth factor receptor (EGFR), 575
- Erlotinib, 575
- Ethosuximide (ESM), 555
- Ethyl phenyl carbonate, 19, 20
- Etravirine, 377
- European Pharmacopoeia (Ph.Eur.), 755
- Everhart-Thornley detector, 509
- Extensional rheology
 biaxial and planar flow, 735–736
 biaxial extension, 730
 Hencky strain and Hencky strain rate, 730
 measurements (*see also* Shear rheology)
 planar extension, 730
 polymer industry, 732
 strain hardening polymers, 732
 streamlines, 730
 Trouton's ratio, 731
 uniaxial extension, 730
 uniaxial flow
 contraction flow analysis, 734–735
 filament thinning experiments, 734
 miniature scale, testing, 735
 rotating drum devices, 733
- Extracted ion chromatogram (EIC/XIC), 266
- Eysenhardtia polystachya*, 30
- F**
- Fast Fourier transform (FFT), 87, 111, 611
- Fast Low Angle Shot (FLASH)
 sequence, 608
- Fasted State Simulated Intestinal Fluid (FaSSIF), 759
- Fatty acids (FAs), 774
- Felgett advantage, 149, 166
- Felodipine, 381
- Fenofibrate, 757, 781
- Fermi resonance, 65
- Fiber optic probe spectrophotometers, 10–12
- Field-flow fraction (FFF), 468
- Filament stretching rheometer (FISER/FSR), 734

- Film coating
 coating uniformity, 198–200
 functional coatings, 200–204
 in-line sensing, 206–207
 process sensors, calibration of, 204–205
 TPI technique, 196
- Fine particle dose (FPD), 702, 710
- Flory-Huggins lattice based theory, 381
- Flow calorimetry, 393
- Flow field flow fractionation (FFF), 477
- Flow induced dispersion analysis (FIDA), 450
- Flow-through apparatus, 756–758
- Flufenamic acid, 190
- Fluid bed dryer (FBD), 89, 108
- Fluid bed granulation (FBG), 108–109
- Fluorescence, 144–146, 443
 emission, 38, 50
 excitation, 40, 50
 imaging, 493
 lifetime, 36, 51
 microscopy, 45, 572
 phenomenon
 Palo Azul, 30
 polarization, 42
 quantum yield, 37
 quinine sulfate, 31
 Stokes shift, 31
- Fluorescence lifetime image (FLIM), 52
- Fluorescence spectroscopy
 absorption and Beer-Lambert law, 34
 1,8-ANS/serum albumins, interaction of, 53
 emission, 38, 50
 excitation, 40, 50
 lifetime, 36, 51
 markers and reporters, 46–48
 polarization, 42
 quantum yield, 37
 quenching, 43
- Fluorimeter, refractive index (RI) detector, 469
- Fluoroalkylsilane (FAS), 665
- Fluorometers, 35, 48
- Fluorophores, 37
- Focal plane array (FPA), 524, 529
- Focus beam reflectance measurements (FBRM), 87
- Focused beam reflectance measurements (FBRM), 109
- Food and drug administration (FDA), 801
- Förster resonance energy transfer (FRET), 44
- Fourier self deconvolution (FSD), 69, 97
- Fourier transform (FT), 148–149, 531
- Fourier transform infrared (FTIR)
 mAb formulations, 99–102
 polymeric delivery systems, 102–103
 secondary structural analysis, 96
- Fourier transform infrared-photoacoustic spectroscopy (FTIR-PAS), 66
- Fourier transformation (FT), 525
- Franck-Condon principle, 32
- Fraunhofer approximation, 705
- Fraunhofer theory, 684
- Freeze fracture technique, 516
- Frequency domain fluorometry, 53
- Frequency domain method, 51
- Full width of half height (FWHM), 97
- G**
- Gabapentin polymorphs, 184
- Gas chromatography (GC), 89, 368
- Gas chromatography coupled to mass spectrometry (GC-MS), 264
- Gas perfusion calorimetry, 393, 400, 403
- Gastro-intestinal (GI) tract, 742, 755
- G-coupled protein receptors (GPCR), 355
- Geometric standard deviation (GSD), 710
- Gleditsia triacanthos*, 745
- Global molecular mobility, 375
- Global optimisation approach, 307–308
- Goniometer, 322
- Gordon-Taylor (G-T) equation, 374
- Grazing incidence small angle x-ray scattering (GI-SAXS), 354
- Green fluorescent protein (GFP), 47–48
- Griseofulvin, 162, 164
- GV150013X, 759
- H**
- Hahn spin echo sequence, 599
- Hancock-Sharp equation, 396
- Harmonic oscillator approximation, 62
- Heat conduction calorimetry, 391–392, 405
- Hierarchical cluster analysis (HCA), 576
- High performance liquid chromatography (HPLC), 200, 413
 animal experiments, 432
 5-ASA, 431
 components of, 424
 detectors, 429
 drug substances and drugs, analysis of, 430
 mobile phase, 425
 pump, 426
 sample injection, 426
 separation column, 426–428
 troubleshooting, 433

- High shear wet granulation (HSWG), 109–110
 High throughput techniques, 345–346
 Hollow fiber FFF (HF5), 469
 Hooke's law, 722
 Horiba LabRAM ARAMIS system, 555
 Hot-melt extrusion (HME), 112
 Human gastric lipase (HGL), 777
 Human serum albumin (HSA), 53
 Hyaluronic acid, 746
 Hydro fluoroalkanes (HFA), 703
 Hydrocolloids, 744
 Hydrodynamic diameter, 681
 Hydrogels, 744
 Hydrogen/deuterium exchange mass spectrometry (HDX-MS), 278–281
 Hydroxyethyl starch (HES), 479
 Hydroxypropyl methylcellulose (HPMC), 377, 565, 592, 614
- I**
 Ice calorimeters, 391
 Imidafenacin, 79
 Indirect hard modeling (IHM), 88
 Indomethacin, 190, 377
 Inductively Coupled Plasma Mass Spectrometry (ICP-MS), 443
 Inelastic scattering phenomenon, 140
 Infrared laser ablation metastable-induced chemical ionization (IR-LAMICI), 636
 Infrared (IR) spectroscopy, 14, 62
 Inhalation profile, 713
 Inner filter effect, 36
 In-source decay (ISD), 263, 277
 Institute for Food Research (Norwich, UK), 782
 Insulin, 237–239
 Intestinal cell culture models, 800–801
 Intra-tablet coating uniformity, 201
In vivo - in vitro correlations (IVIVC), 758, 778
 Irbesartan, conformational disorder, 184
 Isothermal microcalorimeters (IMC)
 amorphous content quantification, 400
 dosage forms, 402–404
 drug stability, 398–399
 drug-excipient compatibility screening, 395–396
 enthalpy of solution, 397–398
 in vivo applications, 404–405
 kinetics, 391
 pharmaceutical samples, measurement of, 390
 polymorph stability, 397
 preformulation characterisation, 395
 purity determination, 396
 thermodynamics, 391
 time-dependent phase transitions, 390
 ubiquity of heat, 405
 Isothermal titration calorimetry (ITC), 393, 404
- J**
 Jacquinet advantage, 148, 166
 Johari-Goldstein (JG) -relaxation, 187
- K**
 Karl Fischer titration (KFT), 89
 Kelvin probe force microscopy (KPFM), 654
 Kerr-gating, 145
 K nearest neighbours (KNN), 71
 Kolliphor[®], 781
- L**
 Laboratory X-ray powder diffraction instrumentation, 305
 alignment, 300
 crystal structure determination (*see* Structure determination from powder diffraction (SDPD))
 indexing, 301–303
 Pawley refinement, 304
 phase quantification, 311
 phase transitions, 311
 physical form identification, 300–301
 PSD, 297
 radiation source, 296
 refined crystal structure, final check on, 311
 reflection geometry, 297–298, 300
 scintillation-based point detector, 297
 space group identification, 303–304
 transmission geometry, 298, 300
 Laboratory X-ray scattering instruments, 341
 Labrasol, 784
 Lambert-Beer's law, 4–6, 24
 Lanthanum hexaboride (LaB₆), 501
 Larmor precession frequencies, 601
 Laser ablation inductively couple plasma mass spectrometry (LA-ICP-MS), 633, 642
 Laser diffraction (LD), 703, 704
 Latent variables (LV), 70
 Lateral force microscope (LFM), 652

- Light and electron microscopy. *See also*
- Electron microscopy
 - optical microscopy, 493–499
 - general principles of, 493–496
 - pharmaceutical analysis, 498–500
 - special techniques, 496–498
 - pharmaceutical formulation research, 492
 - SEM
 - accelerating voltage, 508
 - electron beam-specimen interactions, 510–512
 - energy dispersive X-ray spectrometry, 513–514
 - ESEM, 512–513
 - Everhart-Thornley detector, 509
 - Faraday cage, 510
 - pharmaceutical application, 514–516
 - sample preparation, 512
 - secondary electrons, 509
 - surface imaging, 508
 - three-dimensional” grayscale images, 508
- Light emitting devices (LEDs), 49
- Light-emitting diode (LED), 67
- Limit of detection (LOD), 283
- Limit of quantitation (LOQ), 283
- Linear discriminant analysis (LDA), 71
- Linear image signature (LIS), 561
- Linearly variable filter (LVF), 68
- Lipolysis model, 778
- Lipopolysaccharide (LPS), 666
- Liposomes, 54
- Liquid chromatography (LC)
 - calibration standards, 435
 - clinical trials and bioanalysis, 433–435
 - detectors, 429
 - drug discovery process, 430
 - drug formulation and stability, 430–432
 - eddy diffusion, 423
 - log P and D values, determination of, 430
 - longitudinal diffusion, 423
 - mass transfer, 423
 - pKa values, 430
 - precolumn, 435
 - retention, 417–418, 422
 - sample preparation, 432, 434
 - separation
 - analytes, partition of, 414
 - efficiency, 419–420, 422
 - mobile phase, 414
 - resolution, 420–421
 - selectivity, 419
 - stationary phase, 414
 - theory of partition, 415–417
 - validation, 435
 - van Deemter equation, 423–424
- Liquid chromatography coupled mass spectrometry (LC-MS), 265–266
- Liquid extraction surface analysis mass spectrometry, 643
- Liquid-liquid extraction (LLE), 266, 286–287
- Liquid metal ion guns (LMIG), 632
- Lissajous analysis, 372
- Localised thermal analysis (LTA), 368
- Locally weighted regression (LWR), 71
- Long chain self-microemulsifying drug delivery systems (LC-SMEDDS), 778
- Low angle laser light scattering (LALLS), 705
- Lubricated squeezing flow, 736
- Luminescence
 - definition, 29
 - fluorescence phenomenon, 30, 31
 - phosphorescence phenomenon, 31
- Lyotropic liquid crystals (LLCs), 345
- M**
- Madin-Darby canine kidney (MDCK), 800
- Magnetic force microscopy (MFM), 654
- Magnetic resonance imaging (MRI)
 - chemical and spatial information, 592
 - chemical shift imaging techniques, 592
 - HPMC, 592
 - NMR
 - origins of, 594
 - spin-lattice relaxation, T_1 , 597–598
 - spin-spin relaxation, T_2 , 599
 - one dimensional image profiling
 - integration, 602
 - k -space formalism, 602–603
 - Larmor frequency, 601
 - relaxation effects, 602
 - solid dosage form pharmaceutical research, 616–622
 - API, 623–624
 - gradient echo (GE) imaging, 609
 - k -space raster, 607
 - nuclear spin-density, 606
 - phase shift velocity imaging, 620
 - quantifying mass transport, 616–622
 - quantitative spin echo, 613–615
 - self-diffusion, 617
 - spin system excitation, 606
 - standard imaging protocols, 606
 - spatial information, 592
 - two-dimensional slice selective imaging, 605

- Main and Interactions of Individual Principal Components Regression (MIPCR), 79
- Malvern Spraytec, 705
- Mannitol, 78
- Mass median aerodynamic diameter (MMAD), 710
- Mass spectrometry (MS), 429, 483
- analyte, 255
 - array collectors, 260
 - capillary electrophoresis, 265
 - data representation, 266–268
 - drug development, 268
 - drug discovery progress, 254
 - electron multipliers, 261
 - Faraday cups, 261
 - gas chromatography, 264
 - hard ionization
 - APCI, 256
 - chemical ionization, 255
 - electron ionization, 255
 - ionization techniques, application range of, 258
 - ion-to-photon detectors, 261
 - liquid chromatography, 265–266
 - mass analyzers
 - characteristics of, 260
 - orbitrap, 259
 - quadrupole, 258
 - resolution, 260
 - 3D/Paul Ion trap, 259
 - TOF, 258
 - microchannel plate detectors, 261
 - point-ion-collectors, 260
 - protein and peptide pharmaceuticals
 - electrospray ionization, 272
 - MALDI, 272
 - mass spectra, interpretation of, 273–276
 - primary structure, 272, 273
 - tandem MS, 276–277
 - quantitative LC-MS, 282–284
 - sample preparation
 - liquid/liquid extraction, 286–287
 - protein precipitation, 284–285
 - solid-phase extraction, 285
 - turbulent flow chromatography, 286
 - sensitivity and low detection limits, 254
 - small molecule drugs
 - chemical synthesis, monitoring of, 269–270
 - drug delivery and stability, 270–271
 - mass spectrum interpretation, 268–269
 - soft ionization
 - ESI, 257–258
 - MALDI, 256–257
 - tandem mass spectrometry (*see* Tandem mass spectrometry (MS/MS))
- Mass spectrometry imaging (MSI)
- advantages, 630
 - applications, 630
 - comparative performance of, 631
 - DESI (*see* Desorption electrospray ionization (DESI))
 - LAICPMS imaging, 634
 - MALDI (*see* Matrix assisted laser desorption ionization (MALDI))
 - ToF-SIMS (*see* Time-of-flight secondary ion mass spectrometry (ToF-SIMS))
- Matrix assisted laser desorption ionization (MALDI), 256–257
- advantages, 631, 633
 - API
 - array analysis, 637
 - in tablet, 635, 636
 - biological and drug molecules, label-free imaging in, 640–641
 - disadvantages, 631
 - mouse kidney, 3D reconstruction of, 644
- Mean dissolution time (MDT), 203
- Meclofenoxate hydrochloride (MF), 398
- Medium chain self-microemulsifying drug delivery systems (MC-SMEDDS), 778
- Melting point depression approach, 381
- Mercury cadmium telluride (MCT), 525
- Mesoscale drug delivery systems
- high throughput techniques, 345–346
 - LLCs, 345
 - spatially resolved, 349–350
 - time resolved studies, 347–349
 - TLC, 345
- Micellar EKC (MEKC), 456
- Michelson interferometer, 148, 525
- Micro-and nanosized particles
- bimodal populations measurements
 - bimodal, 693–696
 - light scattering based particle sizing
 - DCS DCS, 688
 - DLS DLS, 679
 - laser diffraction, 684–685
 - NTA, 686
 - liposomes, DLS and NTA measurement of lipo, 696–697
 - measurement techniques application, 677–679
 - pulse sensing particle sizing methods
 - coulter counter, 690
 - TRPS TRPS, 690
- Microbead force spectroscopy (MBFS), 666
- Microcrystalline cellulose (MCC), 212

- Micro-electro-mechanical systems (MEMS), 68, 735
- Microemulsion EKC (MEEKC), 456
- Micro-thermal analysis (μ TA), 369
- Micro-volume spectrophotometer, 9, 10
- Mid-infrared (MIR) spectroscopy
 absorbance, 62–63
 active pharmaceutical ingredient
 crystallization, 87–88
 reaction monitoring, 86–87
 ATR-IR, 528
 backscattering, transmission and ATR, 527
 freeze-drying process, 116
 FT technique, 65–66
 incandescent silicon carbide/synchrotron, 525
 interferogram signal, 525
 near-field MIR, 528–529
 numerical aperture, 525
 pharmaceutical solid-state characterization
 amorphous/crystalline ratio, 84
 cocrystal characterization, 82–83
 polymorph screening and
 quantification, 80–81
 water content and hydration state
 determination, 79–80
 protein formulation development
 mAb formulations, 99–102
 polymeric delivery systems, 102–103
 secondary structural analysis, 96–98
 sampling techniques
 ATR setup, 67
 DRIFT spectroscopy, 67
 transmission, 66
 signal processing, 69
 skin profiling, 119
 solid dispersions, 91–92
 transitions, 525
 transmission, 528
- Mie theory, 683, 684, 689, 705
- Mirror image rule, 39
- Miscibility, 381
- Modulated temperature differential scanning
 calorimetry (MTDSC), 366–367
- Molar Circular Dichroism, 227
- Monochromatic incident radiation, 296
- Monoclonal antibodies (mAb), 664
- Monoglycerides (MAG), 774
- Moving Block Standard Deviation (MBSD), 105
- Moving window partial least squares
 regression (MWPLSR), 119
- Mucins, 743
- Multi-angle laser light scattering (MALLS)
 detector, 469, 471
- Multiphoton excitation, 33
- Multiple cure resolution (MCR), 156, 544
- Multiple linear regression (MLR), 152
- Multiple reaction monitoring (MRM), 263
- Multiplicative scatter correction (MSC), 70, 540
- Multivariate curve resolution (MCR), 71,
 561, 639
- Multivariate statistical process control
 (MSPC), 81
- N**
- Nanoparticle tracking analysis (NTA), 686
- Nanoparticles (NPs), 659
- Nanostructured lipid carriers (NLCs), 479
- Near infrared (NIR) spectroscopy
 absorption bands
 anharmonicity, 64–65
 combination bands, 64, 65
 Fermi resonance, 65
 overtone band, 64, 65
 active pharmaceutical ingredient
 crystallization, 88
 drying, 89–90
 reaction monitoring, 87
 blend monitoring
 data processing strategy, 105
 qualitative methods, 105–106
 quantitative approaches, 106–108
 sample size, 105
 sampling points, 104
 coating process monitoring, 114–116
 drug dissolution, 91, 94–95
 freeze-drying process, 116–117
 hot-melt extrusion, 112
 instrumentation, 67–68
 laboratory analyzers, 68
 medical monitoring, 118
 multiple CQAs, simultaneous
 determination, 95
 multivariate data analysis
 data pretreatments, 70
 regression methods, 71
 supervised classification, 71
 unsupervised classification, 70
 particle size determination, 92
 pelletization, 112–113
 pharmaceutical solid-state characterization
 amorphous/crystalline ratio, 84, 85
 cocrystal characterization, 83
 polymorph screening and
 quantification, 81–82
 water content and hydration state
 determination, 77–79
 process analyzers, 68

- protein formulation development
 - mAb formulations, 102
 - polymeric delivery systems, 103
 - secondary structural analysis, 98–99
 - qualitative analysis
 - correlation methods, 72
 - distance-based supervised methods, 72
 - supervised classification algorithms, 72
 - threshold value, 73
 - variable selection, 72
 - quantitative analysis
 - β -expectation tolerance intervals, 76
 - calibration maintenance, 76
 - calibration samples, 74
 - calibration transfer, 76
 - multivariate calibration modeling, 74
 - NAS, 75
 - PCP, 75
 - PCR/PLS algorithms, 75
 - reference method, 74
 - representative calibration sample set, 73–74
 - RMSEC, RMSECV, RMSEP, 75
 - sampling strategy, 73
 - spectral resolution, 73
 - TK approach, 76
 - roller compaction, 110–111
 - scatter effects, 65
 - solid dispersions, 91, 92
 - tablet hardness testing, 91, 93–94
 - tableting and capsule filling, 113–114
 - tissue analysis, 119
 - wet granulation
 - fluid bed granulation, 108–109
 - high shear wet granulation, 109–110
 - subphases, 108
 - twin screw granulation, 110
 - Nearly constant losses (NCL), 187
 - Nernst-Brunner equation, 754
 - Net analyte signal (NAS), 75
 - New chemical entity (NCE), 440
 - Next Generation Impactor (NGI), 708
 - Nifedipine, 381
 - Nitrofuantoin, 499
 - Nitrofurantoin, 80
 - Non-contact mode, 652
 - Non-Hodgkin's lymphoma (NHL), 664
 - Non-uniform fast Fourier transforms (NUFFT), 612
 - Normal absorbance spectroscopy, 229
 - Noyes Whitney equation, 742, 754
 - Nuclear magnetic resonance (NMR), 432, 591
 - Numerical aperture (NA), 525
- O**
- Octadecylsilylsilica (ODS), 427
 - Octadecyltrichlorosilane (OTS), 665
 - Oil immersion technique, 493
 - Optical coherence tomography (OCT), 197
 - Optical parametric oscillator (OPO), 556
 - Optical particle counters (OPCs), 706–707
 - Oralmucosal drug delivery, 745
 - Organic cation transporters (OCTN), 809
 - Orthogonal signal correction (OSC), 70
- P**
- Paddle apparatus, 756–757
 - Palo Azul, 30
 - Paracetamol, 190, 377
 - Partial least squares (PLS), 153, 543, 561
 - Partial least squares discriminant analysis (PLS-DA), 71
 - Partial least squares regression (PLSR), 71, 75
 - Particle deposition mechanisms, lung, 702
 - Pawley refinement, 304
 - Peak capacity (PC), 420
 - PeakForce Tapping[®] (PFT), 653
 - Peptide mass finger printing (PMF), 273
 - Perrin-Jablonski diagram, 32
 - Pharmacopoeial dissolution models
 - basket and paddle apparatus, 756–757
 - DDS, 755
 - dosage forms, 755
 - flow-through apparatus, 757–758
 - QC and research and development purposes, 755
 - reciprocating cylinder apparatus, 757
 - Phase contrast technique, 496
 - Phasor analysis, 51
 - Phospholipids (PL), 758, 774
 - Phosphorescence, 29
 - Photocalorimeter, 403
 - Photoconductive AFM (pcAFM), 654
 - Photodiode array (PDA) UV-vis spectrophotometer, 9
 - Photo elastic modulator (PEM), 226
 - Photomultipliers, 49
 - Photo multiplier tube (PMT), 226
 - Photon correlation spectroscopy (PCS), 679
 - Piezoelectric ceramic scanner, 650
 - Planck's constant, 4
 - Polarization microscopy, 496
 - Polarizers, 49
 - Polydispersity index, 684
 - Polyethylene glycol (PEG), 566
 - Polyethylenimine (PEI), 479

- Poly(lactic acid-co-glycolic acid) (PLGA), 659
 Poly(lactic-co-glycolic acid) (PLGA), 553
PolySNAP program, 300
 Polysorbate 80, 755
 Position-sensitive detector (PSD), 297
 Postnova, 471
 Powder X-ray diffraction (PXRD), 296
 crystal structure determination, 294, 295
 cyheptamide form II, pattern of, 294, 295
 laboratory-based PXRD (*see* Laboratory X-ray powder diffraction instrumentation)
 peak intensities, 295
 peak positions, 294
 synchrotron beamlines, 312
 X-ray photon flux, 312
 Power-compensation calorimetry, 391, 405
 Pressurized metered dose inhalers (pMDIs), 703
 Principal component analysis (PCA), 70, 105, 151, 543, 561, 643
 Principal component regression (PCR), 70, 71, 152–153
 Principal components (PC), 70
 Principal Component Scores Distance Analysis (PC-SDA), 105
 Principal components regression (PCR), 75
 Principle of particle collection, 709
 Process analytical technology (PAT), 212
 6-Propionyl-2-dimethylaminonaphtalene (PRODAN), 39
 Protein crystallography, 344
 Proton-coupled amino acid transporter (PAT1), 799
Pseudomonas aeruginosa, 665
 Pseudo-stationary phase, 445
 Pulsed (magnetic) field gradient spin echo (PFG-SE), 617
 Pure-component projection (PCP), 75
 Push-pull osmotic system (PPOS), 200
- Q**
- Quadratic discriminant analysis (QDA), 71
 Quadrupoles, 259
 Quantitative Nanomechanical Mapping (QNM[®]), 654
 Quasielastic light scattering (QELS), 679
 Quinine sulfate, 31
- R**
- Rabinowitch correction procedure, 729
 Raman peak, 50
 Raman scattering, 141
 Raman spectroscopy
 chemometrics
 MCR, 156
 pattern recognition, 151
 PCA, 151
 PCR, 152–153
 PLS, 153
 SIMCA, 155
 unsupervised and supervised techniques, 151
 coherent Raman, 531–533
 counterfeit detection, 161
 experimental methods
 dispersive systems, 147–148
 FT systems, 148–149
 spectral correction, 149–150
 in vivo drug delivery, 159
 near-field effects, 533
 new technologies and experimental protocols
 low frequency Raman spectroscopy, 162–163
 SORS, 163–165
 spatial heterodyne Raman spectroscopy, 166
 transmission Raman, 165
 Raman scattering theory, 140
 ranitidine hydrochloride polymorphism, 157–159
 spontaneous, 530–531
 Ram-Lak filter, 612
 Ranitidine hydrochloride, 157–159
 Raster imaging correlation spectroscopy (RICS), 45
 Rayleigh scattering, 49, 140, 162, 530
 Reactive oxygen species (ROS), 662
 Reciprocating cylinder apparatus, 756, 757
 Refractive index (RI), 241
 Refractive index matched emulsion (RIME) method, 241–242
 Relative humidity (RH), 393
 Relative vapour pressure (RVP), 393
 Reversed phase chromatography, 426
 Rheology, pharmaceutical science
 API, 720
 definition, 719
 dosage forms and biological samples, extensional rheology of, 744–746
 extensional (*see* Extensional rheology)
 shear (*see* Shear rheology)
 Rhizopus Oryzae (ROL), 784

- Rietveld refinement
 chemical restraints, 310
 molecular organic crystal structures, 310
 phase quantification, 311
 programs, 309
 rigid-body, 310
- Rituximab, 664
- Root mean squared error of calculation (RMSEC), 154
- Root mean squared error of calibration (RMSEC), 75
- Root mean squared error of cross validation (RMSECV), 75
- Root mean squared error of prediction (RMSEP), 75, 154
- Red blood cells (RBCs), 663
- S**
- Sanfetrinem, 759
- Scanning capacitance microscopy (SCM), 654
- Scanning electron microscopy (SEM), 474, 492, 500, 558, 703, 707
- Scanning force microscope (SFM), 650
- Scanning probe microscopes (SPM), 650
- Scanning spreading resistance microscopy (SSRM), 654
- Scanning thermal microscopy (S_{Th}M), 654
- Scanning tunnelling microscope (STM), 533, 650
- Science-based calibration (SBC), 116
- Scintillation-based point detector, 297
- Searching combination moving window partial least squares (SCMWPLS), 119
- Second harmonic generation (SHG), 532, 577
- Sedimentation method, 689
- Selected reaction monitoring (SRM), 263, 266
- Self-assembled monolayers (SAMs), 655
- Self-emulsifying drug delivery system (SEEDS), 783
- Self micro-emulsifying drug delivery system (SMEDDS), 783
- Self-modelling curve resolution (SMCR), 561
- Self nano-emulsifying drug delivery system (SNEDDS), 783
- Sentmanat extensional rheometer (SER), 733
- Shear rheology
 biological samples, 742
 capillaries, 720
 rheometers, 729, 739
 viscometry, 728, 738–739
 commercial applications, 741
 cone-and-plate and concentric cylinder tools, 720
 controlled rate type instrument, 721
 controlled stress type instrument, 721
 creep and relaxation measurements, 727
 creep measurements, 738
 deformations, 720
 dosage forms, 740–742
 drum devices rotation, 740
 gelling agents, 741
 geometry, 720, 721
 in situ gelling systems, 741
 lipid droplets, heteroaggregation of, 741
 lubricated squeezing flow, 740
 measuring cells, 722
 non-Newtonian liquids, 723–724
 oscillatory measurements, 725
 right geometry, 737
 rotational type instruments, 722
 steady shear measurements, 737–738
 uniaxial extension tests, 739
- Shepp-Logan filter, 612
- Shifted excitation Raman difference spectroscopy, 146
- Simvastatin, 190
- Single-beam UV spectrophotometer, 7
- Single-crystal X-ray diffraction (SXRD), 293
 absolute structure
 differences and quotients, 329
 Flack parameter, 328
 Friedel pairs, intensities of, 327
 non-centrosymmetric structures, 326–327
 control and data processing software, 323
 crystal lattice, geometry of, 316, 319
 crystal structure, 319–321
 data collection strategy
 centrosymmetric diffraction pattern, 333
 completeness, 333
 data collection time, 334
 diffraction pattern, 332
 redundancy, 333
 resolution, 332
 data processing, 334–335
 detectors, 322
 diffracted intensities, 317, 319
 displacement parameters, 318
 goniometer, 322
 H atoms, 323–324
 metric symmetry, 319
 microfocus source, 322
 Mo/Cu radiation, 331
 non-stoichiometry and disorder, 324–326
 sealed tube, 321
 small drug molecules, 315
 space group, 319
 structure checking procedures, 335–336
 temperature, 331

- Single-molecule force spectroscopy (SMFS), 654
 - Single wall carbon nanotubes (SWNTs), 480
 - Size exclusion chromatography (SEC), 469
 - Small angle x-ray scattering (SAXS), 340, 349
 - A-SAXS, 352–354
 - biological macromolecules, 344
 - grazing incidence, 354
 - liposome drug delivery systems, 343
 - mesoscale structures
 - micellar systems, 343
 - protein crystallography, 344
 - SBDD, 344
 - self nanoemulsifying and microemulsion drug delivery systems, 343
 - Sodium lauryl sulphate (SLS), 755, 764
 - Soft independent modeling of class analogies (SIMCA), 70
 - Solid lipid microparticles (SLMs), 556
 - Solid lipid nanoparticles (SLNs), 479
 - Solid-phase extraction (SPE), 266, 285
 - Solute carrier family (SLC), 792
 - Solution calorimetry, 393
 - amorphous content quantification, 399–400
 - drug formulations, 403
 - enthalpies of solution, 398
 - Sophora japonica*, 745
 - Source for circular dichroism (SRCD), 242
 - Spatially offset Raman scattering (SORS), 163–165
 - Spatially offset Raman spectroscopy (SORS), 161
 - Spectrophotometric detectors, 429
 - Spraying process, 744
 - Sputum, 743
 - Standard normal variate (SNV), 70, 540
 - Staring array, 524
 - Static light scattering (SLS), 484
 - Static quenching, 43
 - Stejskal-Tanner equation, 617
 - Stern-Volmer equation, 43
 - Stimulated Raman scattering (SRS), 560
 - Stimulated Raman spectroscopy (SRS), 531
 - Stokes-Diameter, 681
 - Stokes-Einstein equation, 686, 742, 754
 - Stokes lines, 142
 - Stokes scattering, 530
 - Stokes shift, 31
 - Strickler-Berg equation, 37
 - Structure-based drug design (SBDD), 344
 - Structure determination from powder diffraction (SDPD), 309
 - data collection, 306
 - global optimisation approach, 307–308
 - modified direct methods, 307
 - Rietveld refinement (*see* Rietveld refinement)
 - structure solution, 306, 309
 - Sum frequency generation (SFG), 532
 - Super resolution stimulated emission depletion (STED), 667
 - Support vector regression (SVR), 71
 - Surface-enhanced Raman spectroscopy (SERS), 533
 - Surface potential microscopy (SPoM), 654
 - Sympatec Inhaler module, 705
 - Sympatec Sprayer, 705
 - Synchrotron radiation (SR), 242
 - Synchrotron X-ray scattering, 341
- T**
- Tandem mass spectrometry (MS/MS)
 - application of, 263
 - full scan mode, 263
 - ion activation, 262–263
 - multiple reaction monitoring, 263
 - neutral loss scanning, 263
 - parent ions, 261
 - precursor ion scanning, 261, 263
 - product ion scanning, 261, 263
 - protein and peptide pharmaceuticals, 276–281
 - selected reaction monitoring, 263
 - in space, 261
 - in time, 262
 - triple quadrupole, 261
 - Tapping Mode[®], 652, 654
 - Taylor dispersion analysis (TDA), 440, 451
 - Terahertz electric field peak strength (TEFPS), 194
 - Terahertz interface index (TII), 194
 - Terahertz pulsed imaging (TPI), 191, 562
 - Terahertz radiation, 171–174
 - Terahertz spectroscopy, 534–536
 - Terahertz technology
 - chemical imaging, 207–208
 - tablet microstructure
 - cracks and delamination, 210–211
 - disintegration testing, 212–213
 - porosity, 211–212
 - tablet density/hardness, 209–210
 - terahertz imaging, 195–207
 - film coating (*see* Film coating)
 - instrumentation, 195
 - measurement principle, 191

- terahertz radiation, pharmaceutical analysis, 171–174
 - terahertz spectroscopy, 177–185
 - amorphous drugs below T_g, 187–190
 - amorphous materials, 185–187
 - dielectric relaxation processes, 175
 - drug molecules (*see* Drug molecules, crystal structure of)
 - molecular interactions, 174
 - optical properties, 175
 - VDOS, 174
 - Terahertz time-domain spectroscopy (THz-TDS), 173
 - Thermal analysis
 - differential scanning calorimetry, 363
 - pharmaceutical raw materials
 - amorphous drugs, 376–377
 - polymer blends, 377–378
 - polymers and lipidic excipients, 377
 - physical and chemical phenomena
 - crystallisation, 371
 - dehydration and decomposition, 376
 - glass transition, 372–374
 - molecular mobility, 375
 - polymorphic transformation, 371–372
 - structural relaxation, 375–ENF
 - scanning probe based thermal analysis, 368–370
 - semi-solid and liquid dosage forms, 383–384
 - solid dosage forms
 - amorphous solid dispersions, 379
 - crystallisation tendency, 379
 - drug-excipient miscibility estimation, 381–382
 - micro-scale drug distribution uniformity assessment, 382–383
 - moisture-induced instability, 380
 - physical stability of, 378
 - quantitative analysis of crystallinity, 379–380
 - TGA (*see* Thermogravimetric analysis (TGA))
 - Thermal decoupling process, 188
 - Thermogravimetric analysis (TGA), 368
 - Thermotropic liquid crystal (TLCs), 345
 - Throat model, 713
 - Tikhonov regularization (TK), 76
 - Time-gated detection schemes, 172
 - Time-of-flight (TOF), 258, 710–711
 - Time-of-flight secondary ion mass spectrometry (ToF-SIMS)
 - advantages, 631
 - API, 634
 - crystal/powder mixtures and coatings (*see* Coatings)
 - micro-array analysis, 638, 639
 - stent coating, 3D reconstruction, 637
 - in tablet, 636, 637
 - disadvantages, 631, 632
 - Tip-enhanced Raman spectroscopy (TERS), 533
 - TOPAS program, 301
 - Topography and recognition imaging (TREC), 654
 - Torsional resonance (TR) Mode[®], 653
 - Total ion current chromatogram (TIC), 266–268
 - Transition temperature mapping (TTM) technique, 370
 - Transmission electron microscopes (TEMs), 54, 474, 492, 500, 556
 - Transmission Raman spectroscopy, 165
 - Transretinol, 159
 - Triacetin, 396
 - Triacylglycerides (TAG), 774
 - Tributyrin unit (TBU), 780
 - Troglitazone, 759
 - Trouton's ratio, 731
 - Tunable resistive pulse sensing (TRPS), 690
 - Turbulent flow chromatography (TFC), 286
 - Twin screw granulation (TSG), 110
 - Two-dimensional (2D) FT-IR spectroscopy, 66
 - Two photon excited fluorescence (TPEF), 532, 577
- ## U
- Ultrahigh performance liquid chromatography (UHPLC), 414
 - animal experiments, 432
 - pressure limit, 426
 - separation column, 428
 - troubleshooting, 433
 - Ultra small angle X-ray scattering (USAXS), 342
 - Ultraviolet (UV) imaging
 - CMOS sensor chips, 12
 - components of, 12
 - drug diffusion and release, 24
 - drug dissolution
 - lidocaine, 22–23
 - Sirius SDI UV imaging instrument, 23
 - solid forms, ranking of, 24
 - theophylline, 23
 - wavelength range, 12
 - with in situ Raman spectroscopy, 23, 24

- Ultraviolet-visible (UV-vis)
 spectrophotometry, 24, 469
 CCD spectrophotometers, 9
 components, 6
 dissolution testing, 21
 double-beam spectrophotometer, 7
 equilibrium constants and complexation, 18
 kinetics and reaction monitoring, 18
 Lambert-Beer's law, 4–6
 light, 3
 micro-volume spectrophotometer, 9
 PDA spectrophotometers, 9
 pK_a values, 16–18
 qualitative analysis, 12–14
 quantitative analysis, 15
 single beam spectrophotometer, 7
 UV-vis fiber optic probes, 10–12
 United States Pharmacopoeia (USP), 755
 Unstirred water-layer (UWL), 800
- V**
 Variable count time (VCT), 306
 Vibrational density of states (VDOS), 174, 185
 Vibrational spectroscopic imaging
 bivariate analysis, 542
 comparison of, 537
 definition, 524–525
 drug delivery
 MIR imaging, 572–575
 Raman imaging, 575–579
 selected studies, 573
 drug release and dissolution
 MIR imaging, 565–566
 Raman microscopy, 566–571
 selected studies, 567
 drugs and dosage forms
 MIR imaging, 544–554
 near-infrared imaging, 560–562
 Raman imaging, 554–560
 selected studies, 545
 terahertz imaging, 562–564
 MIR, 525–529
 multivariate analysis
 BTEM, 544
 CLS, 543
 MCR, 544
 PCA, 543
 PLS, 543
 Raman (*see* Raman spectroscopy)
 spectral preprocessing
 baseline correction, 539–540
 noise correction, 536–539
 scaling and scatter correction, 540–541
 spectral artefacts, 536
 terahertz, 534–536
 univariate analysis
 bandwidth, 542
 peak integral, 542
 peak intensity, 541
 Vibrational spectroscopy, 77
 Virus-like particles (VLPs), 478
 Viscometer/rheometer-on-a-Chip
 (VROC™), 735
 Volume Bragg grating (VBG), 162
- W**
 White Light Aerosol Spectrometer
 (WELAS), 706
 Wollaston probe, 369
 Wood's anomaly, 50
 Wyatt Technology, 471
- X**
 XCELL program, 301
 Xenon arc lamps, 49
 X-ray femtosecond lasers, 344
 X-ray microtomography, 193, 196
 X-ray photon flux, 312
 X-ray scattering, 340
 diffraction, 340–341
 SAXS (*see* Small angle X-ray scattering
 (SAXS))
 USAXS, 342
- Y**
 Young's modulus, 653, 660, 664